AD-A111 522 PENNSYLVANIA STATE UNIV UNIVERSITY PARK DEPT OF MECH--ETC F/6 20/4
SYMPOSIUM ON TURBULENT SHEAR FLOWS (3RD), UNIVERSITY OF CALIFOR--ETC(U)
SEP 81 F W SCHMIDT AFOSR-80-0033

UNCLASSIFIED AFOSR-TR-82-0032 NL

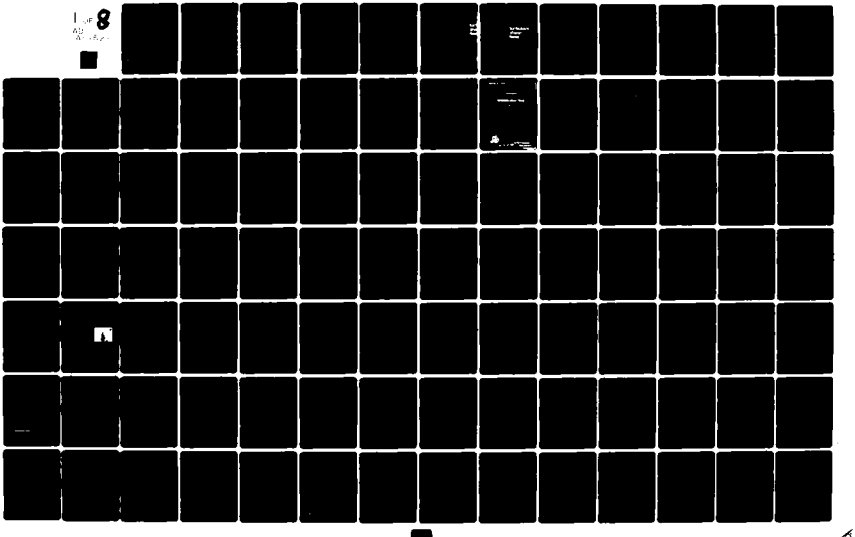

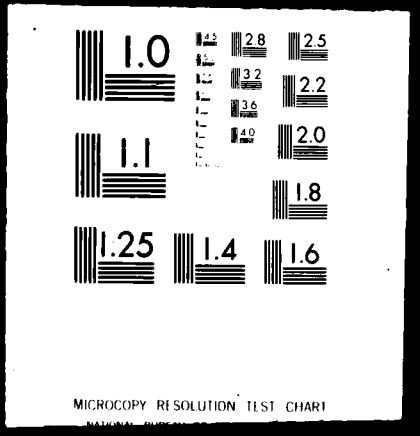

(3)

THIRD SYMPOSIUM ON TURBULENT SHEAR FLOWS

FINAL REPORT

F. W. Schmidt
Mechanical Engineering Department
The Pennsylvania State University
University Park, PA 16802

This material is based upon work supported by the United States Air Force Office of Scientific Research under Grant No. AFOSR-80-0033.

ORGANIZING COMMITTEE

L. J. S. Bradbury
F. Durst
B. E. Launder
F. W. Schmidt
J. H. Whitelaw

PAPERS COMMITTEE

B. E. Launder (chairman)
J.-C. André
I. Gartshore
P. A. Libby
J. H. Whitelaw

ADVISORY COMMITTEE

R. J. Adrian
L. H. Back
H. A. Becker
R. Borghi
S. Corrsin
J. J. D. Domingos
C. du Pont Donaldson
R. Dumas
H. Fiedler
V. W. Goldschmidt
A. D. Gosman
R. Gunther
K. Hanjalic
T. J. Hanratty
J. R. Herring
A. K. M. F. Hussain
W. P. Jones
P. N. Joubert
J. Laufer
J. L. Lumley
O. Martynenko
J. Mathieu
H. McDonald
Y. Mori
K. Owen
W. C. Reynolds
W. Rodi
M. Rubesin
A. K. Runchal
I. Wygnanski
J. Wyngaard

Tuesday, September 8, 1981

Registration: 1500-2200, 565 Oxford Circle, Emerson Lounge
Early Bird Reception: Cash bar 1900 to 2100
Emerson Lounge

Wednesday, September 9, 1981

Registration: 0800-1700, 194 Chemistry Lobby

EQUIPMENT EXHIBITS, 176 Chemistry
Disa Electronics
Spectron Development Laboratories
TSI, Incorporated

PROGRAM

WEDNESDAY, SEPT. 9, 1981
0900-1030
SESSION I — BOUNDARY LAYERS I
194 CHEMISTRY
T. J. Hanratty — Chairman

Evaluation of turbulence models for near-wall and low-Reynolds number flows
V. C. Patel, W. Rodi, G. Scheuerer

Decay of turbulence during a laminar reorganization in pipe flow
P. Vallette, M. Lebouche

A physical interpretation of the spectra of wall turbulence
A. E. Perry, M. S. Chong

*Turbulence and mean flow measurements in an incompressible axisymmetric boundary layer with incipient separation
P. Dengel, H.H. Fernholz, J. D. Vagt

*Measurements in a turbulent boundary layer flow over a two-dimensional hill
A. J. Smits, V. Baskaran, P. N. Joubert

Theoretical prediction of confluent boundary layers
G. W. Brune

1030-1100 COFFEE BREAK

1100-1300
SESSION 2 — BOUNDARY LAYERS II
194 CHEMISTRY
M. Rubesin — Chairman

Three dimensional boundary layer development in an axially rotating pipe
M. Murakami, K. Kikuyama, K. Nishibori

Three-dimensional turbulent boundary layer on a spinning thin cylinder in an axial uniform stream
I. Nakamura, S. Yamashita, T. Watanabe, Y. Sawaki

Turbulent field of a boundary layer very close to an axially roatated cylinder
E. Arzoumanian, M. Leborgne, L. Fulachier

Turbulent flow in unbounded streamwise corners
D. Arnal, J. Cousteix

A near-wall pressure-strain model for turbulent corner flows
F. B. Gessner, H. M. Eppich

Bulk dilatation effects on Reynolds stresses in the rapid expansion of a turbulent boundary layer at supersonic speed
J. P. Dussauge, J. Gaviglio

*PAPER DOES NOT APPEAR IN BOUND SYMPOSIUM VOLUME

1100-1300
SESSION 3 — REACTING FLOWS
179 CHEMISTRY
H. A. Becker — Chairman

Movements of flame-fronts and their properties in a turbulent diffusion flame
M. Ahlheim, H. Hoffmann, W. Leuckel

A chemically reacting plane mixing layer
S. V. Sherikar, R. Chevray

Study of a turbulent diffusion flame in a channel flow
J. M. Most, N. Harivel, P. Joulain, B. Sztal

Computation and its comparison with experiments of time-mean and fluctuating properties in round jets with and without flame
T. Takagi, S. Kotoh

Investigations on a reaction model for turbulent diffusion flames
H. Eickhoff, K. Grethe

Calculations of velocity-scalar joint PDF's
S. B. Pope

Premixed combustion in a turbulent boundary layer with injection
S. Meunier, M. Champion, J. C. Bellet

Lagrangian-Eulerian calculation of turbulent diffusion flame propagation
W. T. Ashurst, P. K. Barr

1300-1400 LUNCH ON THE LAWN

1400-1530
SESSION 4 — CURVED FLOWS
194 CHEMISTRY
W. Rodi — Chairman

*A generalized algebraic relation for prediciting developing curved channel flow with K-ϵ model of turbulence
J. A. C. Humphrey, F. Pourahmadi

Calculation of a turbulent wall jet on a curved wall with a Reynolds stress model of turbulence
M. M. Gibson, B. A. Younis

Measurements in the heated turbulent boundary layer on a mildly curved convex surface
M. M. Gibson, C. A. Verriopoulos, Y. Nagano

Turbulent shear flows behind cylinder and sphere in curved channels
H. S. Koyama

Effects of stable and unstable free streams on a turbulent flow over a concave surface
S. Nakano, A Takahashi, T. Shizawa, S. Honami

1400-1530
SESSION 5 — CONFINED FLOWS
179 CHEMISTRY
J. J. D. Domingos — Chairman

Prediction and measurement of flow and heat transfer in motored diesel engine swirl chambers
M. M. M. Abou-Ellail, M. M. Elkotb

Comparison of calculated and measured velocities for a turbulent swirling flow inside a cylindrical enclosure
T. Morel, N. N. Mansour, V. Saxena, R. B. Rask

Features of turbulent pipe flows in development and decay
E. M. Laws, E-H. Lim, J. L. Livesey

Calculations of confined coaxial-jet flows
M. A. Habib, J. H. Whitelaw

Experimental and numerical studies of the turbulent shear flow in a pipe with a weakly wavy wall
M. P. Chauve, R. Schiestel

1530-1600 COFFEE BREAK

1600-1730
SESSION 6 — JETS AND WAKES
194 CHEMISTRY
V. W. Goldschmidt — Chairman

A complex turbulent wake
G. Fabris

Measurements in a low momentum jet into a crossflow
J. Andreopoulos

The turbulence characteristics in the near-region of the wall jet issued from a small inclined slot
M. Hatano

Response of a plane turbulent wall jet to the perturbation by a cylinder
I. Nakamura, H. Osaka, H. Yamada

1600-1730
SESSION 7 — OPEN FORUM
179 CHEMISTRY
I. S. Gartshore and P. A. Libby — Chairmen

1830-1930 **CASH BAR** — FACULTY CLUB

1930 **DINNER** — FACULTY CLUB

THURSDAY,
0830-1030
SESSION 8
194 CHEM
L. H. Back

A dynamic
layer
T. Haya
The flow of
E. Gutm
On the pul
L. Sherm
Measureme
unsteady t
G. Binde
A hybrid co
J. D. Ma
Dynamics
P. G. Pa
Influence o
boundary
J. Cous

1030-1100

1100-123
SESSION
179 CHE
J. C. Wyn

Diffusion
layer
P. C. C
Passive
J. E. F
Pressure
J.-C. A
Turbulen
F. Ogi

1400-1530
SESSION 5 — CONFINED FLOWS
179 CHEMISTRY
J. J. D. Domingos — Chairman

Prediction and measurement of flow and heat transfer in motored diesel engine swirl chambers
M. M. M. Abou-Ellail, M. M. Elkotb

Comparison of calculated and measured velocities for a turbulent swirling flow inside a cylindrical enclosure
T. Morel, N. N. Mansour, V. Saxena, R. B. Rask

Features of turbulent pipe flows in development and decay
E. M. Laws, E-H. Lim, J. L. Livesey

Calculations of confined coaxial-jet flows
M. A. Habib, J. H. Whitelaw

Experimental and numerical studies of the turbulent shear flow in a pipe with a weakly wavy wall
M. P. Chauve, R. Schiestel

1530-1600 COFFEE BREAK

1600-1730
SESSION 6 — JETS AND WAKES
194 CHEMISTRY
V. W. Goldschmidt — Chairman

A complex turbulent wake
G. Fabris

Measurements in a low momentum jet into a crossflow
J. Andreopoulos

The turbulence characteristics in the near-region of the wall jet issued from a small inclined slot
M. Hatano

Response of a plane turbulent wall jet to the perturbation by a cylinder
I. Nakamura, H. Osaka, H. Yamada

1600-1730
SESSION 7 — OPEN FORUM
179 CHEMISTRY
I. S. Gartshore and P. A. Libby — Chairmen

1830-1930 **CASH BAR** — FACULTY CLUB

1930 **DINNER** — FACULTY CLUB

THURSDAY, SEPT. 10, 1981
0830-1030
SESSION 8 — PERIODIC WALL FLOWS
194 CHEMISTRY
L. H. Back — Chairman

A dynamical and visual study on the oscillatory turbulent boundary layer
T. Hayashi, M. Ohashi

The flow of a row of turbulent vortex-rings impinging onto a plate
E. Gutmark, Y. Haimovitch, M. Wolfshtein

On the pulsating flow in a pipe
L. Shemer, I. Wygnanski

Measurements of the periodic velocity oscillations near the wall in unsteady turbulent channel flow
G. Binder, J. L. Kueny

A hybrid computing scheme for unsteady turbulent boundary layers
J. D. Murphy, P.M. Prenter

Dynamics of an unsteady turbulent boundary layer
P. G. Parikh, R. Jayaraman, W. C. Reynolds

Influence of Strouhal number on the structure of a flat plate turbulent boundary layer
J. Cousteix, J. Javelle, R. Houdeville

1030-1100 COFFEE BREAK

1100-1230
SESSION 9 — GEOPHYSICAL FLOWS I
179 CHEMISTRY
J. C. Wyngaard — Chairman

Diffusion from an elevated source within the atmospheric boundary layer
P. C. Chatwin, P. J. Sullivan

Passive emissions from point sources in turbulent boundary layers
J. E. Fackrell, A. G. Robins

Pressure effects on triple correlations in turbulent convective flows
J.-C. André, P. Lacarrere, K. Traore

Turbulence measurements in an axisymmetric buoyant jet
F. Ogino, H. Takeuchi, M. Ohki, T. Mizushina

1100-1230
SESSION 10 — HEAT AND MASS TRANSFER IN BOUNDARY LAYERS
194 CHEMISTRY
K. Hanjalic — Chairman

On the similarity between velocity and temperature fields within a turbulent spot
R. A. Antonia, A. J. Chambers, M. Sokolov, C. W. Van Atta

A structural study on a turbulent boundary layer with transpiration
M. Senda, S. Horiguchi, K. Suzuki, T. Sato

The mechanism of turbulent mass transfer at a boundary
J. A. Campbell, T. J. Hanratty

Calculation of a turbulent boundary layer downstream of a sudden decrease in surface heat flux or wall temperature
L. W. B. Browne, R. A. Antonia

Turbulent boundary layers on flat plates and in contracted or expanded channels with angled injection and suction
V. M. Yeroshenko, A. V. Yershov, L. I. Zaichik, A. A. Klimov, V. I. Kondratiev, L. S. Yanovsky

Experimental investigation of a turbulent boundary layer structure in the region of a gas screen
Yu. V. Baryshev, A. I. Leontiev, N. K. Peiker

1230-1400 LUNCH ON THE LAWN

1400-1530
SESSION 11 — COHERENT STRUCTURES I
194 CHEMISTRY
I. Wygnanski — Chairman

Education of the "preferred mode" structure in the axisymmetric mixing layer
K. B. M. Q. Zaman, A. K. M. F. Hussain

Entrainment and mixing in pulsatile jets
V. Sarohia, L. P. Bernal

Large scale motions in turbulent wakes
J. H. Gerrard

Development of the organized vortices in the turbulent near wake of a circular cylinder: an experimental and numerical study
H. C. Boisson, P. Chassaing, H. Ha Minh, A. Sevrain

A theoretcial model of the coherent structure of the turbulent boundary layer in zero pressure gradient
Z. Zhang, G. M. Lilley

1400-1530
SESSION 12 — GEOPHYSICAL FLOWS II
179 CHEMISTRY
J.-C. André — Chairman

How time dependence and variable Froude number can explain more rapid entrainment of the two-layer system in annulus experiments
J. W. Deardorff

A theoretical study of radiative cooling in homogeneous and isotropic turbulence
D. Schertzer, O. Simonin

On the influence of buoyancy on the turbulent Ekman layer
U. Svensson

Sediment transport in stratified turbulent flow
B. A. DeVantier, B. E. Larock

1530-1600 COFFEE BREAK

1600-1730
SESSION 13 — DEBATE
194 CHEMISTRY

MOTION: Modelers disregard essential experimental facts
Chairman: L. J. S. Bradbury

PRO	CON
P. N. Joubert	C. du Pont Donaldson
J. Laufer	W. C. Reynolds

FRIDAY, SEPT. 11, 1981
0830-1030
SESSION 14 — COHERENT STRUCTURES II
194 CHEMISTRY
A. K. M. F. Hussain — Chairman

Coherent structures in the similarity region of two-dimensional turbulent jets
J. W. Oler, V. W. Goldschmidt

Experimental study of coherent structures in mixing layers of coaxial jets
O. Leuchter, K. Dang

*Direct numerical simulations of turbulent free shear flows
R. W. Metcalfe, J. J. Riley

A three dimensional time dependent simulation of transition and early turbulence in a time-developing mixing layer
A. B. Cain, W. C. Reynolds, J. H. Ferziger

Spatial growth of wavy disturbunces in a plane shear layer between two streams
B. V. Johnson, J. D. Lin

*Effects of the subharmonic and fundamental phase relationship on an unsteady mixing layer
C.-M. Ho, Y. Zhang

4

830-1030
ESSION 15 — SCALAR TRANSPORT
79 CHEMISTRY
. J. Adrian — Chairman

urther results on the thermal mixing layer downstream of a rbulence grid
J. C. LaRue, P. A. Libby, D. V. R. Seshadri

odelling of homogeneous turbulent scalar field dynamics
B.A. Kolovandin, N. N. Luchko, O. G. Martynenko

odelling the dissipation rate of temperature variance in a thermal ixing layer
S. Elghobashi, B. E. Launder

tructural features of a uniformly distorted heated plane turbulent ake
J. G. Kawall, J. F. Keffer

heoretical and experimental determination of the turbulent diffusivity nsor in homogeneous turbulent shear flow
S. Tavoularis, S. Corrsin

Turbulent transport in passively heated homogeneous and nhomogeneous flows
K. R. Sreenivasan, S. Tavoularis, S. Corrsin

030-1100 COFFEE BREAK

100-1230
ESSION 16 — RECIRCULATING FLOWS I
179 CHEMISTRY
. McDonald — Chairman

omentum, heat, and mass transfer in backward-facing step flows
B. F. Armaly, F. Durst, V. Kottke

elocity characteristics in the vicinity of a two-dimensional rib
D. Crabb, D. F. G. Durao, J. H. Whitelaw

urbulent shear flow behind hemisphere-cylinder placed on ground lane
S. Okamoto

ow frequency unsteadiness of reattaching turbulent shear layer
J. K. Eaton, J. P. Johnston

essure fluctuations under a turbulent shear layer
R. Hillier, N. J. Cherry

perimental investigations in transonic highly separated, turbulent ow
A. Farcy, V. Mercier, R. Leblanc

400-1230
ESSION 17 — FUNDAMENTALS I
94 CHEMISTRY
. Herring — Chairman

model of three-dimensional transfer in non-isotropic homogeneous rbulence
J.-P. Bertoglio

Approach of non isotropic homogeneous turbulence submitted to mean velocity gradients
C. Cambon, D. Jeandel

Entrainment diagrams for viscous flows
B. Cantwell, G. Allen

Predictability of two- and three-dimensional freely decaying flows: Application to mixing layers
M. Lesieur, J.-P. Chollett

1230-1330 LUNCH ON THE LAWN

1330-1530
SESSION 18 — RECIRCULATING FLOWS II
179 CHEMISTRY
A. K. Runchal — Chairman

Turbulent, backward-facing step flows in two-dimensional ducts and channels
F. Durst, C. Tropea

Prediction of the low Reynolds number laminar flow over a normal flat plate, and its application to turbulent flow calculations
I. P. Castro, K. A. Cliffe, M. J. Norgett

*The assessment of numerical diffusion in upwind-difference calcuations of turbulent recirculating flows
J. J. McGuirk, A. M. K. P. Taylor, J. H. Whitelaw

*Turbulent flow induced by a jet in a cavity — measurements and 3-D numerical simulation
F. Baron, J. P. Benqué, Y. Coëffeé

1330-1530
SESSION 19 — FUNDAMENTALS II
194 CHEMISTRY
J. L. Lumley — Chairman

Pseudo-spectral methods for homogeneous or inhomogeneous flows
Y. Morchoisne

The distortion of turbulent shear flow upstream of a body
J. C. Wyngaard

Second order closure for variable density free shear layer
D. Vandromme, W. Kollmann

A new approach to the analysis of turbulent mixing in variable density flows
H. Ha Minh, B. E. Launder, J. M. MacInnes

Pressure strain: exact results and models
J. J. D. Domingos

Direct simulation of homogeneous turbulent shear flows on the Illiac IV computer: applications to compressible and incompressible modeling
W. J. Feiereisen, E. Shirani, J. H. Ferziger, W. C. Reynolds

Appen

THIRD SYMPOS

tur
she
flow

September 9-1
University of C
Davis, Californ
U.S.A.

Sponsored by the U.S
Scientific Research, F
Army and Navy and t
Foundation in coope
Society of Mechanic
and Fluid Engineerin

Approach of non isotropic homogeneous turbulence submitted to mean velocity gradients
C. Cambon, D. Jeandel

Entrainment diagrams for viscous flows
B. Cantwell, G. Allen

Predictability of two- and three-dimensional freely decaying flows: Application to mixing layers
M. Lesieur, J.-P. Chollett

1230-1330 LUNCH ON THE LAWN

1330-1530
SESSION 18 — RECIRCULATING FLOWS II
179 CHEMISTRY
A. K. Runchal — Chairman

Turbulent, backward-facing step flows in two-dimensional ducts and channels
F. Durst, C. Tropea

Prediction of the low Reynolds number laminar flow over a normal flat plate, and its application to turbulent flow calculations
I. P. Castro, K. A. Cliffe, M. J. Norgett

The assessment of numerical diffusion in upwind-difference calcuations of turbulent recirculating flows
J. J. McGuirk, A. M. K. P. Taylor, J. H. Whitelaw

Turbulent flow induced by a jet in a cavity — measurements and 3-D numerical simulation
F. Baron, J. P. Benqué, Y. Coëffeé

1330-1530
SESSION 19 — FUNDAMENTALS II
194 CHEMISTRY
J. L. Lumley — Chairman

Pseudo-spectral methods for homogeneous or inhomogeneous flows
Y. Morchoisne

The distortion of turbulent shear flow upstream of a body
J. C. Wyngaard

Second order closure for variable density free shear layer
D. Vandromme, W. Kollmann

A new approach to the analysis of turbulent mixing in variable density flows
H. Ha Minh, B. E. Launder, J. M. MacInnes

Pressure strain: exact results and models
J. J. D. Domingos

Direct simulation of homogeneous turbulent shear flows on the Illiac IV computer: applications to compressible and incompressible modeling
W. J. Feiereisen, E. Shirani, J. H. Ferziger, W. C. Reynolds

5

Appendix A

THIRD SYMPOSIUM ON

turbulent shear flows

September 9-11, 1981
University of California, Davis
Davis, California
U.S.A.

Sponsored by the U.S. Air Force Office of Scientific Research, Research Offices of the U.S. Army and Navy and the National Science Foundation in cooperation with the American Society of Mechanical Engineer's Heat Transfer and Fluid Engineering Divisions.

The Third Symposium on Turbulent Shear Flow was held at the University of California, Davis, California on September 9-11, 1981. The objectives of the symposium was to further advance the understanding of the physical phenomena associated with turbulent flows and the existing capabilities for calculating items such as the transport of heat and mass in such processes.

In August 1980 a "Call for Papers" was issued. One hundred and fifty eight abstracts were received. The Papers Committee grouped the abstracts by topics and sent them to members of the Advisory Committee for review. On the basis of the reviews the Papers Committee accepted 100 abstracts and requested the authors to submit 6 page manuscripts. The final program (Appendix A) contained 92 papers. The proceeding volume contained 86 papers. Six authors were unable to meet the publication deadline and thus it was necessary to have their papers distributed individually at the time of the meeting.

In addition to the 17 paper sessions, an open forum and a debate were scheduled. Twelve short 10-minute presentations were given in the open forum. The debate on the motion "Modelers Disregard Essential Experimental Facts" was quite lively.

The total number of registrants for the symposium was 242. They are listed in Appendix B. The technical paper sessions were very well attended with a free exchange of ideas. This exchange was often continued between individuals during coffee and lunch breaks. All of the activities allowed the attendees to assess the present state of our knowledge of turbulent shear flows and to identify areas where basic research in turbulent transport processes is needed.

Appendix B

Mr. T. W. Abou-Arab
Mech. Engr. Dept.
Univ. of Calif.
Irvine, CA 92717 USA

Mr. E. Adams
Mech. Engr. Dept.
Stanford University
Stanford, CA 94305 USA

Prof. R. Adrian
Mech. Engr. Dept.
Univ. of Illinois
Urbana, IL 61801 USA

Mr. B. Afshari
Mech. Engr. Dept.
Stanford Unive ity
Stanford, CA 94305

Mr. G. Allen
Durand Bldg.
Stanford University
Stanford, CA 94305 USA

Dr. J.-C. Andre
Meteorologie (EERM/GMD)
73 rue de Sevres
92106 Boulogne, FRANCE

Dr. J. Andreopoulos
SFB 80
Universitat Karlsruhe
7500 Karlsruhe, WEST GERMANY

Dr. Arnal
ONERA - CERT DERAT
2 Av. E. Belin
31055 Toulouse FRANCE

Dr. W. T. Ashurst
Sandia Laboratories
Livermore, CA 94550 USA

Dr. L. H. Back
Fluid Mechanics Program
Jet Propulsion Lab
4800 Oak Grove Drive
Pasadena, CA 91103 USA

Dr. K. W. Bedford
Civil Engr. Dept.
2070 Neil Avenue
Columbus, OH 43210 USA

Prof. A. Bejan
University of Colorado
Boulder, CO 80309 USA

Ms. D. Bell
Div. 8124
Sandia Laboratories
Livermore, CA 94550 USA

Dr. J.-P. Benque
Electricite de France
6 quai Waiter
Chatou 78400, FRANCE

Ms. M. Bergmann
NASA-Ames Research Ctr.
Moffett Field, CA 94035 USA

Dr. L Bernal
Jet Propulsion Laboratory
CALTECH
Pasadena, CA 91103 USA

Dr. G. Binder
IMG - Lab. Assoc. au CNRS
B.P. 53X
Grenoble-Cedex 38041, FRANCE

Dr. S. F. Birch
M.S. 41-52, P.O. Box 3999
Boeing Military Airplane Co.
Seattle, WA 98124 USA

Dr. C. R. Bobba
General Elec. Co.
Mail Drop. G-49
Cincinnati, OH 45215 USA

Dr. J.-P. Bonnet
CEAT
route de l'Aerodromme
8600 Poitiers FRANCE

Dr. R. Borghi
ONERA

Dr. B. Bower
McDonnell Douglas Res. Lab.
P.O. Box 516
St. Louis, MO 63166 USA

Dr. L. J. S. Bradbury
Mech. Engr. Dept.
University of Surrey
Guildford, Surrey, ENGLAND

Dr. J. E. Broadwell
CALTECH 105-50
Pasadena, CA 91125 USA

Dr. Jim Brown
NASA-Ames Research Ctr.
Moffett Field, CA 94035 USA

Dr. L. W. B. Browne
Mech. Engr. Dept.
Univ. of Newcastle
N.S.W., 2308 AUSTRALIA

Dr. G. W. Brune
The Boeing Company
P.O. Box 3707
Seattle, WA 98124 USA

Dr. A Cain
Aero. & Mech. Engr. Dept.
Notre Dame Univ.
South Bend, IN USA

Dr. C. Cambon
Lab. de Mecanique des Fluides
69130 Eucly, FRANCE

Prof. B. Cantwell
Durand Bldg.
Stanford University
Stanford, CA 94305 USA

Dr. L. Carr
Air Mech. Lab. - US Army
NASA-Ames Research Ctr.
M.S. 215-1
Moffett Field, CA 94035 USA

Dr. I.P. Castro
Mech. Engr. Dept.
Univ. of Surrey, Guildford, ENGLAND

Dr. A. J. Chambers
Mech. Engr. Dept.
Univ. of Newcastle
N.S.W., 2308, AUSTRALIA

Dr. M. Champion
L.A. 193 ENSMA
rue Guillaume VII
86240 Poitiers FRANCE

Mr. S.-N. Chang
Mech. Engr. Dept.
Univ. of Calif.
Berkeley, CA 94720 USA

Prof. D. R. Chapman
Mech. Engr. Dept.
Stanford University
Stanford, CA 94305 USA

Dr. R. S. Chapman
212 Sherwood Garden Apts.
Vicksburg, MS 39180 USA

Mr. P. Chassaing
Inst. de Mecanique
des Fluides
31071 Toulouse, FRANCE

Dr. P. Chatwin
Dept. of Appl. Math.
Univ. of Liverpool
Liverpool, ENGLAND

Mr. K. S. Chen
Mech. Engr. Dept.
Univ. of Calif.
Berkeley, CA 94720 USA

Mr. T. Cheung
8G McFarland House
Stanford University, CA 94305 USA

Prof. R. Chevray
SUNY @ Stony Brook
Dept. of Mech. Engr.
Stony Brook, NY 11794 USA

Mr. K. A. Cliffe
AERE Harwell
Oxford, ENGLAND

Dr. T. J. Coakley
NASA-Ames Research Ctr.
Moffett Field, CA 94035 USA

Prof. D. Coles
321 Guggenheim Lab.
CALTECH
Pasadena, CA 91125 USA

Prof. S. Corrsin
Mechs. & Mats. Sci. Dept.
The Johns Hopkins Univ.
Baltimore, MD 21218 USA

Dr. J. Cousteix
ONERA-CERT
2 Avenue E. Belin
31 Toulouse FRANCE

Dr. A. Cutler
Mech. Engr. Dept.
Stanford University
Stanford, CA 94305 USA

Dr. Q. I. Daudpota
NASA-Langley Res. Ctr.
Hampton, VA 23665 USA

Mr. Bruce DeVantier
Civil Engr. Dept.
Univ. of Calif.
Davis, CA 95616 USA

Prof. James W. Deardorff
Atmos. Sci. Dept.
Oregon State Univ.
Corvallis, OR 97331 USA

Dr. R. W. Ibble
Div. 8523
Sandia Laboratories
Livermore, CA 94550 USA

Prof. J. J. D. Domingos
Instituto Superior Tec.
Lisbon 1096 Codex, PORTUGAL

Dr. C. du Pont Donaldson
ARAP
1800 Old Meadow Rd. #114
McLean, VA 22102 USA

Dr. F. T. Dunckhorst
Westinghouse Elec. Corp.
P.O. Box 79
West Mifflin, PA 15122 USA

Prof. F. Durst
SFB 80
Universitat Karlsruhe
75 1 Karlsruhe, WEST GERMANY

Dr. J.-P. Dussauge
IMST
12 Av. General Leclerc
13003 Marseille, FRANCE

Prof. J. Eaton
Mech. Engr. Dept.
Stanford University
Stanford, CA 94305 USA

Dr. S. E. Elghobashi
Mech. Engr. Dept.
Univ. of Calif.
Irvine, CA 92717 USA

Dr. H. M. Eppich
Mech. Engr. Dept. Univ. of Washington
Seattle, WA 98195 USA

Dr. H. Fack

Dr. J. Fackrell
Marchwood Engr. Labs
Marchwood
Southampton SO4 4ZB, ENGLAND

Dr. A. Farcy
CEAT
Route de l'Aerodrome
86000 Poitiers, FRANCE

Dr. W. Feiereisen
Brown-Boveri-ZKE
Baden 5430 SWITZERLAND

Prof. H. H. Fernholz
Hermann-Fottinger Inst.
Technische Universitat
D-1000 Berlin, WEST GERMANY

Prof. J. Ferziger
Mech. Engr. Dept.
Stanford University
Stanford, CA 94305 USA

Prof. H. E. Fiedler
Hermann-Fottinger Inst.
Technische Universitat
D-1000 Berlin, WEST GERMANY

Dr. C. Flokstra
Delft Hydraulics Lab
P.O. Box 177
2600 MG Delft, HOLLAND

Mr. C. J. Freitas
250 Curtner Ave. #25
Palo Alto, CA 94306 USA

Dr. M. Frota
Mech. Engr. Dept.
Stanford University
Stanford, CA 94305 USA

Prof. I. S. Gartshore
Mech. Engr. Dept.
Univ. of British Columbia
Vancouver V6T 1W5 CANADA

Prof. F. B. Gessner
Mech. Engr. Dept.
Univ. of Washington
Seattle, WA 98195 USA

Dr. C. H. Gibson
Mech. Engr. Dept. - B-010
Univ. of Calif.-San Diego
La Jolla, CA 92093 USA

Dr. M. M. Gibson
Mech. Engr. Dept.
Imperial College
London SW7 2BX, ENGLAND

Prof. V. W. Goldschmidt
Mech. Engr. Dept.
Purdue University
Lafayette, IN 47907 USA

Dr. K. Grethe
Universitat Karlsruhe (TH)
7500 Karlsruhe, WEST GERMANY

Dr. R. Gunther
Lehrstuhl und Bereich
Feuerungstechnic
Univ. Karslruhe
7500 Karlsruhe, WEST GERMANY

Dr. E. Gutmark
Dept. of Aerospace Engrg.
Univ. of Southern Calif.
Los Angeles, CA 90007 USA

Dr. E. Guyon
24 rue Rausard
Limoux, FRANCE 91470

Dr. L. Hackman
Mech. Engr. Dept.
Univ. of Waterloo
Waterloo Ontario, CANADA N2L 3G1

Dr. D. Halley
Defense Res. Est.-Atlantic
Dartmouth, Nova Scotia
CANADA

Dr. H. Ha Minh
Inst. de Mecanique
des Fluides - CNRS
31070 Toulouse, Cedex, FRANCE

Prof. K. Hanjalic
Masinski Fakultet
71000 Sarajevo, YUGOSLAVIA

Prof. T. J. Hanratty
205 R.A.L.
Univ. of Illinois
Urbana, IL 61801 USA

Dr. R. G. Hartman
G.E. Corporate R&D
P.O. Box 8
Schenectady, NY 12301 USA

Dr. W. H. Harch
Aero. Research Lab.
P.O. Box 4331
Melbourne, AUSTRALIA 3001

Dr. M. Hatano
Dept. of Aero. Engrg.
National Defense Academy
Yokosuka, 239 JAPAN

Dr. J. R. Herring
N.C.A.R.
P.O. Box 3000
Boudler, CO 80307 USA

Dr. H. Higuchi
229-1 NASA-Ames Res. Ctr.
Moffett Field, CA 94305 USA

Dr. R. Hillier
Aeronautics Dept.
Imperial College
London SW7 2BY, ENGLAND

Dr. C. M. Ho
Dept. of Mech. Engr.
Univ. of Southern Calif.
Los Angeles, CA 90007 USA

Dr. S. Honami
Mech. Engr. Dept.
Sci. Univ. of Tokyo
Kagurazaka, Shinjuku
Tokyo, Japan/62

Dr. C. C. Horstman
NASA-Ames Research Ctr.
Moffett Field, CA 94305 USA

Dr. R. Houdeville
ONERA - CERT DERAT
2 Av. E. Belin
31055 Toulouse, FRANCE

Dr. L. J. Huey
Owens Corning Fiberglas Corp.
172 Mill Race Rd.
Granville, OH 43023 USA

Prof. J. A. C. Humphrey
Mech. Engr. Dept.
Univ. of Calif.
Berkeley, CA 94720 USA

Prof. A.K.M.F. Hussain
Mech. Engr. Dept.
Univ. of Houston
Houston, TX 77004 USA

Mr. R. Jayaraman
Mech. Engr. Dept.
Stanford University
Stanford, CA 94305 USA

Mr. A. Jeans
Mech. Engr. Dept.
Stanford University
Stanford, CA 94305 USA

Dr. J. Jimenez
IBM, SAE/Scientific Ctr.
P°Castellana, 4/Madrid-1
Madrid, SPAIN

Dr. B. V. Johnson
United Tech. Res. Ctr.
400 Main Street - M.S. 17
E. Hartford, CT 06108 USA

Prof. J. Johnston
Mech. Engr. Dept.
Stanford University
Stanford, CA 94305 USA

Prof. P. N. Joubert
Mech. Engr. Dept.
Univ. of Melbourne
Parkville, Melbourne
Victoria 3052 AUSTRALIA

Mr. S. Kale
Mech. Engr. Dept.
Stanford University
Stanford, CA 94305 USA

Dr. N. Kasagi
Mech. Engr. Dept.
Stanford University
Stanford, CA 94305 USA

Prof. J. F. Keffer
Mech. Engr. Dept.
University of Toronto
Toronto, CANADA M5S 1A4

Mr. R. M. Kerr
NASA-Ames Res. Ctr.
Mail Stop 202A-1
Moffett Field, CA 94035 USA

Dr. A. Kerstein
Sandia Laboratories
Livermore, CA 94550 USA

Dr. G. J. Kirouac
GE/Knolls Atomic Power Lab
Box 1072
Schenectady, NY 12301 USA

Mr. J. R. Koseff
Box 9124
Stanford, CA 94305 USA

Dr. H. S. Koyama
Mech. Engr. Dept.
Tokyo Denki Univ.
2-2 Kanda-Nishikicho
Tokyo, 101, JAPAN

Dr. R. Kretschmer
Postfach 1580
D 6638 Dillingen, WEST GERMANY

Dr. P. Krogstad
Iowa Inst. of Hydr. Res.
Iowa City, IA 52242

Dr. I. Kuznetsov
Moscow
USSR

Dr. R. Lai
APL
Johns Hopkins Univ.
Laurel, MD 20707 USA

Prof. B. Larock
Civil Engr. Dept.
Univ. of Calif.
Davis, CA 95616 USA

Prof. J. LaRue
AMES Dept. - B-010
Univ. of Calif.-San Diego
La Jolla, CA 92093 USA

Prof. J. Laufer
Aerospace Engineering Dept.
Univ. of Southern Calif.
Los Angeles, CA 90007 USA

Prof. B. E. Launder
Mech. Engr. Dept.
UMIST - P.O. Box 88
Manchester M60 1QD, ENGLAND

Dr. E. Laws
Aero. & Mech. Engr. Dept.
University of Salford
Salford M5 4WT, ENGLAND

Mr. M. Lee
Mech. Engr. Dept.
Stanford University
Stanford, CA 94305 USA

Mr. M. Lee
Mech. Engr. Dept.
Stanford University
Stanford, CA 94305 USA

Dr. M. Leschziner
Mech. Engr. Dept.
UMIST - P.O. Box 88
Manchester M60 1QD, ENGLAND

Dr. Lesieur
Univ. of Grenoble
Grenoble, FRANCE

Dr. O. Leuchter
ONERA
9232 Chatillon, FRANCE

Dr. P. Li
Ford Motor Company
P.O. Box 2053
Dearborn, MI 48121 USA

Prof. P. A. Libby
AMES Dept. - B-010
Univ. of Calif.-San Diego
La Jolla, CA 92093 USA

Prof. G. M. Lilley
Aero. & Astro. Dept.
Univ. of Southampton
Southampton, ENGLAND

Prof. E. J. List
Keck Lab 138-78 - CALTECH
Pasadena, CA 91125 USA

Dr. P Lowery
Mech. Engr. Dept.
Stanford University
Stanford, CA 94305 USA

Dr. M. Lubert
GE/Knolls Atomic Power Lab
Box 1072
Schenectady, NY 12301 USA

Prof. J. L. Lumley
238 Upson
Cornell University
Ithaca, NY 14853 USA

Prof. R. E. Luxton
Dept. of Mech. Engr.
Univ. of Adelaide
GPO Box 498
Adelaide, SA 5001 AUSTRALIA

Dr. N. N. Mansour
General Motors Res. Lab.
Warren, MI 48090 USA

Dr.-Ing. O. G. Martynenko
Heat & Mass Trans. Inst.
15 Podlesnaya, Minsk
BSSR, USSR

Dr. J. G. Marvin
NASA-Ames Research Ctr.
Moffett Field, CA 94035 USA

Dr. W. T. Mayo, Jr.
3303 Harbor Blvd. #G-3
Costa Mesa, CA 92626 USA

Mr. H. McDonald
Scientific Research Assocs.
P.O. Box 498
Glastonbury, CT 06033

Prof. A. A. McKillop
Mech. Engr. Dept.
Univ. of Calif.
Davis, CA 95616 USA

Mr. J McMichael
FM - 105
National Bureau
of Standards
Gaithersburg, MD 20760 USA

Prof. W. Melnik
David Taylor Naval Ship
Research & Dev. Ctr.
Bethesda, MD 20884 USA

Dr. R. Metcalfe
Flow Research Co.
21414 - 68th Ave. S.
Kent, WA 98031 USA

Dr. E.-S. A. Mogahed
403 H. Eagle Heights
Madison, WI 53705 USA

Dr. P. Moin
Mech. Engr. Dept.
Stanford University
Stanford, CA 94305 USA

Dr. H. C. Mongia
Garrett Turbine Eng. Co.
P.O. Box 5217
Phoenix, AZ 85010 USA

Dr. Y Morchoisne
ONERA - 29 Av. Div. Leclerc
Chatillon-SS-Bagneux
92320 FRANCE

Dr. T. Morel
16W 260 83rd St.
Hinsdale, IL 60421 USA

Dr. J.-M. Most
G.R.C.P.C.
Station d'essais du Deffend
Mignaloux Beauvoir 86800, FRANCE

Dr. J. Murphy
NASA-Ames Research Center
Moffett Field, CA 94035 USA

Dr. T. Nagamatsu
Mitsubishi Heavy Ind. Ltd.
3-48 Bunkyo-Machi
Nagasaki, 852, JAPAN

Dr. Y Nagano
Mech. Engr. Dept.
Stanford University
Stanford, CA 94305 USA

Mr. M. W. Nansteel
2747 Harte St. #27
Berkeley, CA 94704 USA

Dr. K. Nishibori
Mech. Engr. Dept.
Nagoya Univ., Furocho
Chikusaku, Nagoya, 464, JAPAN

Dr.-Ing. G. Oertel
Inst. fur Stromungslehre
und Stromungsmaschinen
Universitat Karlsruhe
7500 Karlsruhe, WEST GERMANY

Dr. F. Ogino
Chem. Engr. Dept.
Kyoto University
Kyoto, JAPAN

Dr. M. Ohashi
Civil Engr. Dept.
Chuo University
Kasuga 1-13-27, Bunkyo-ku
Tokyo, 112, JAPAN

Dr. S. Okamoto
Mech. Engr. Dept.
Shibaura Inst. of Tech.
Shibaura 3-9-14, Minato-ku
Tokyo, 108, JAPAN

Dr. T. Okamoto
Mech. Engr. Dept.
Tokyo Inst. of Tech.
Ookayama 2-12-1, Megura-ku
Tokyo, 152, JAPAN

Dr. J. W. Oler
Mech. Engr. Dept.
Texas Tech. University
Lubbock, TX 79409 USA

Dr. P. Orlandi
Inst. Di Aerodinamica
Via Eudossiana 16
Roma 00184 ITALY

Dr. H. Osaka
Mech. Engr. Dept.
Yamaguchi University
Ube, 2557, JAPAN

Dr. T. Osborn
Dept. of Oceanography
Univ. of British Columbia
Vancouver, B.C., V6T 1W5 CANADA

Dr. K. Owen
NASA-Ames Research Ctr.
Mail Stop 227-8
Moffett Field, CA 94035 USA

Prof. P. J. Pagni
Mech. Engr. Dept.
Univ. of Calif.
Berkeley, CA 94720 USA

Dr. S. Paolucci
P.O. Box 969
Livermore, CA 94550 USA

Dr. P. Paranthoen
Laboratoire Thermodynamique
B.P. 67
76130 Mont Saint Aignam, FRANCE

Prof. P. Parikh
Mech. Engr. Dept.
Stanford University
Stanford, CA 94305 USA

Dr. H. Pearson
Keck Lab 138-78 - CALTECH
Pasadena, CA 91125 USA

Dr. A. E. Perry
Mech. Engr. Dept.
Univ. of Melbourne
Parkville, 3052,
Melbourne, AUSTRALIA

Dr. N. Peters
Aufder Hoin 103
Aachen, WEST GERMANY

Dr. H. Pfeil
Breslauer Pl. 3
61 Darmstadt, WEST GERMANY

Prof. A. Pollard
Mech. Engr. Dept.
Queen's University
Kingston, Ontario, CANADA

Prof. S. B. Pope
MIT - 3-339
Cambridge, MA 02139 USA

Dr. A. Postan
Aerospace & Mech. Engr.
Univ. of Arizona
Tucson, AZ 85721 USA

Mr. F. Pourahmadi
Mech. Engr. Dept.
Univ. of Calif.
Berkeley, CA 94720 USA

Prof. W. C. Reynolds
Mech. Engr. Dept.
Stanford University
Stanford, CA 94305 USA

Mr. H. Rhee
2-F Hulme, Escondido
Stanford, CA 94305 USA

Dr. J. Riley
Flow Research Co.
21414 - 68th Ave. S.
Kent, WA 98031 USA

Dr. S. K. Robinson
NASA-Ames Research Ctr.
Moffett Field, CA 94035 USA

Prof. W. Rodi
SFB 80
University of Karlsruhe
7500 Karlsruhe, WEST GERMANY

Dr. A. Roshko
CALTECH - 105-50
Pasadena, CA 91125 USA

Dr. A. K. Rothapalli
Dept. of Aero. & Astro.
Stanford University
Stanford, CA 94305 USA

Dr. M. W. Rubesin
NASA-Ames Research Ctr.
Moffett Field, CA 94035 USA

Dr. A. K. Runchal
12029 Clover Avenue
Los Angeles, CA 90066 USA

Dr. B. R. Sanders
P.O. Box 969
Sandia Laboratories
Livermore, CA 94550 USA

Dr. A. M. Savill
Physics Dept.
Cavendish Lab
Cambridge CB3 OHE, ENGLAND

Dr. D. R. Schamber
Civil Engr. Dept.
University of Utah
Salt Lake City, UT 84112 USA

Dr. J. Schetz
VPI
Blacksburg, VA 24061 USA

Dr. G. Scheuerer
SFB 80
Postfach 6380
7500 Karlsruhe WEST GERMANY

Prof. F. W. Schmidt
Mech. Engr. Dept.
The Pennsylvania State Univ.
University Park, PA 16802 USA

Dr. M. Senda
Mech. Engr. Dept.
Doshisha University
Kyoto, 602, JAPAN

Dr. L. Shemer
School of Engineering
Tel-Aviv University
Ramat-Aviv, 69978 ISRAEL

Dr. T. W. Simon
Mech. Engr. Dept.
Univ. of Minnesota
Minneapolis, MN 55455

Dr. J Simonich
Mech. Engr. Bldg. 500
Stanford University
Stanford, CA 94305 USA

Prof. R. L. Simpson
Sch. of Engrg. & Appl. Sci.
Southern Methodist Univ.
Dallas, TX 75275 USA

Dr. K. R. Sreenivasan
2159, Yale Station
Yale University
New Haven, CT 06520 USA

Dr. M. Stanislas
Inst. de Mecanique
des Fluides
5 bd Paul Painleve
59000 - Lille, FRANCE

Mr. T. Strawa
Durand Bldg.
Stanford University
Stanford, CA 94305 USA

Prof. R. L. Street
Sch. of Engineering
Stanford University
Stanford, CA 94305 USA

Prof. A. B. Strong
Dept. of Mech. Engr.
University of Waterloo
Waterloo, Ontario, CANADA N2L 3G1

Mr. R. Subbarao
Durand Bldg.
Stanford University
Stanford, CA 94305 USA

Dr. A. Sugavanam
1865 Vintage Ct. 'E'
Marietta, GA 30060 USA

Prof. J. P. Sullivan
Aerospace Sci. Lab Hangar #3
Purdue University
West Lafayette, IN 47906 USA

Prof. P. J. Sullivan
Dept. of Appl. Math.
Univ. of Western Ontario
London, Ontario, CANADA N6A 5B9

Dr. S. G. Sundkvist
Thermo. & Fluid Dyn. Dept.
Chalmers Univ. of Tech.
Gottenburg, SWEDEN S-41296

Dr. K. Suzuki
Mech. Engr. Dept.
Kyoto University
Kyoto, 606, JAPAN

Dr. U. Svensson
Water Res. Engr. Dept.
Univ. of Lulea
S-95187 Lulea, SWEDEN

Dr. T. Takagi
Mech. Engr. Dept.
Osaka University
Suita, Osaka, 565 JAPAN

Dr. K. Takeuchi
Owens Corning Fiberglas Corp.
172 Mill Race Rd.
Granville, OH 43023 USA

Prof. S. Tavoularis
Mech. Engr. Dept.
Univ. of Ottawa
Ottawa, Ontario KN1N 6N5 CANADA

Dr. A. Taylor
Mech. Engr. Dept.
Imperial College
London SW7 2BX, ENGLAND

Mr. W. M. To
Mech. Engr. Dept.
Univ. of Calif.
Berkeley, CA 94720 USA

Dr. A. Tsinober
School of Engineering
Tel Aviv University
Tel-Aviv 69978 ISRAEL

Dr. M. Udo
M.S. 229-1
NASA-Ames Research Ctr.
Moffett Field, CA 94035

Dr. J. P. Vallet
Lab. Dynam. des Fluides
40 Ave secteur Pineau, Bat H
86022 Poitiers, Cedex, FRANCE

Dr. P. Vallette
LEMTA
24 rue Lionnois
5400 Nancy, FRANCE

Dr. C. Van Atta
AMES - B-010
Univ. of Calif.-San Diego
La Jolla, CA 92093 USA

Dr. B. Van den Berg
NLR
Ant. Fokkerweg 2
Amsterdam, NETHERLANDS

Dr. D. F. Van Der Merwe
44 Canyon
Berario, Johannesburg
Transvaal, SOUTH AFRICA

Dr. D. VanDromme
MS 202A
NASA-Ames Research Ctr.
Moffett Field, CA 94035 USA

Dr. C. A. Verriopoulos
Mech. Engr. Dept.
Imperial College
London SW7 2BX, ENGLAND

Dr. J. R. Viegas
NASA-Ames Research Center
Moffett Field, CA 94035 USA

Dr. N. S. Vlachos
Mech. Engr. Dept.
Imperial College
London SW7 2BX, ENGLAND

Dr. R. V. Westphal
Mech. Engr. Dept.
Stanford University
Stanford, CA 94305 USA

Prof. J. H. Whitelaw
Mech. Engr. Dept.
Imperial College
London SW7 2BX, ENGLAND

Dr. M. Wolfshtein
Aero. Engr. Dept.
Technion City, Haifa ISRAEL

Mr. C. T. Wu
Mech. Engr. Dept.
Stanford University
Stanford, CA 94305 USA

Prof. I. Wygnanski
College of Engineering
University of Arizona
Tucson, AZ 85721 USA

Dr. J. Wyngaard
N.C.A.R.
P.O. Box 3000
Boulder, CO 80307 USA

Dr. S. Yamashita
Mech. Engr. Dept.
Nagoya University
Nagoya, JAPAN

Dr. Yeroshenko
Moscow
USSR

Dr. P. Youssefmir
Mech. Engr. Dept.
Stanford University
Stanford, CA 94305 USA

Dr. A. J. Yule
Mech. Engr. Dept.
UMIST - P.O. Box 88
Manchester M60 1QD, ENGLAND

Dr. K. B. M. Q. Zaman
Mech. Engr. Dept.
Univ. of Houton
Houston, TX 77004 USA

Dr. Z. Zhang
Aero. & Astro. Engrg. Dept.
Southampton University
Southampton SO9 5NH, ENGLAND

Dr. C. Zoltani
Ballistics Research lab.
Aberdeen Proving Grounds
Aberdeen, MD 21005 USA

ADDENDUM TO LIST OF PARTICIPANTS

TURBULENT SHEARS FLOWS 3

Ms. P. Barr
Div. 8523
Sandia Laboratories
Livermore, CA 94550 USA

Dr. H. E. Eickhoff
Bismarck Str. 34
Rosrath, FRG

Dr. P. Gresho
L-262
LLNL, P.O. Box 808
Livermore, CA 94550 USA

Dr. W. J. McCroskey
N-202A
NASA-Ames Research Ctr.
Moffett Field, CA 94035 USA

Dr. F.K. Owen
Complete Inc.
Palo Alto, CA 94302 USA

Dr. M. F. Platzer
Naval Postgraduate Sch.
Monterey, CA 94940 USA

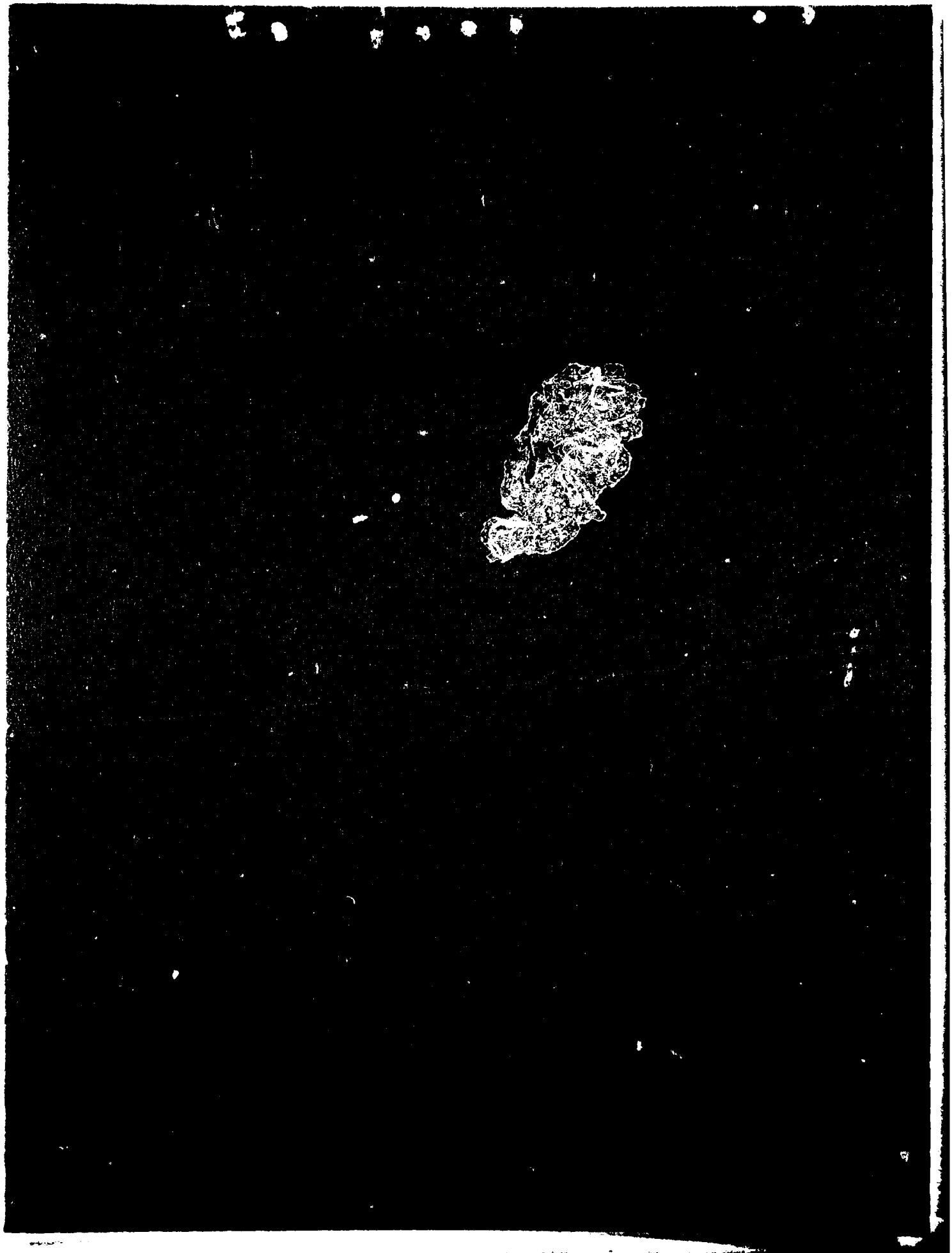

and a debate were also scheduled. Twelve short 10-minute presentations were given in the open forum. A total of 242 registrants attended the meeting.

THIRD SYMPOSIUM ON

turbulent shear flows

Organizing Committee

L. J. S. BRADBURY
Mechanical Engineering Department
University of Surrey
Guildford, Surrey, UK

F. DURST
Sonderforschungsbereich 80
University of Karlsruhe
75 Karlsruhe 1
West Germany

B. E. LAUNDER
Department of Mechancial Engineering
University of Manchester
Institute of Science and Technology
Manchester, M60 1QD, UK

F. W. SCHMIDT, SECRETARY
Department of Mechanical Engineering
The Pennsylvania State University
University Park, PA 16802, USA

J. H. WHITELAW
Department of Mechanical Engineering
Imperial College
London SW7 2BX, UK

PREFACE

This volume contains the papers to be presented at the 3rd Symposium on Turbulent Shear Flows held at the University of California, Davis in the period September 9-11, 1981. The meeting continues the series of biennial international symposia launched at the Pennsylvania State University in 1977 and continued at Imperial College, London in 1979. The aim of the Symposium, like that of its predecessors, has been to provide a forum for airing new developments across the multitude of activities that comprise turbulence research in the 1980's. The papers, which provide the formal record of the meeting, were selected following review of each of the 160 extended abstracts offered for the meeting by two members of the Advisory Committee. The assistance thus provided by the Committee, whose membership appears in the Symposium programme, is most warmly appreciated. The final composition and format of the meeting was set by a Papers' Committee consisting of Jean Claude André, Ian S. Gartshore, Brian E. Launder, Paul A. Libby, and James H. Whitelaw with the assistance of Frank W. Schmidt as secretary.

The Organizing Committee wishes to acknowledge financial support kindly provided by the National Science Foundation, the U.S. Air Force Office of Scientific Research, the U.S. Army Research Office, and the U.S. Office of Naval Research. The cooperation of the Fluids Engineering and Heat Transfer Divisions of the American Society of Mechanical Engineers and the considerable assistance provided by the Conferences and Campus Services of the University of California, Davis are also gratefully acknowledged.

L. J. S. Bradbury F. J. Durst B. E. Launder
F. W. Schmidt J. H. Whitelaw
Organizing Committee

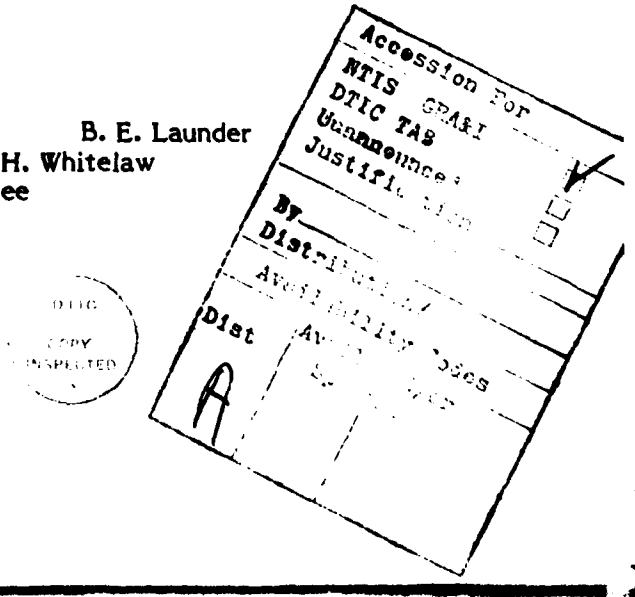

SESSION 12 - GEOPHYSICAL FLOWS II

J.-C. Andre - Chairman

SESSION 14 - COHERENT STRUCTURES II

A. K. M. F. Hussain - Chairman

SESSION 15 - SCALAR TRANSPORT

R. J. Adrian - Chairman

SESSION 18 - RECIRCULATING FLOWS II

A. K. Runchal - Chairman

SESSION 19 - FUNDAMENTALS II

J. L. Lumley - Chairman

SESSION I - BOUNDARY LAYERS I

T. J. Hanratty - Chairman

EVALUATION OF TURBULENCE MODELS FOR NEAR-WALL AND LOW-REYNOLDS NUMBER FLOWS

by

V.C. Patel*, W. Rodi and G. Scheuerer

University of Karlsruhe
Karlsruhe, W. Germany

* on leave from the University of Iowa, Iowa City, USA

ABSTRACT

Several low-Reynolds-number two-equation turbulence models have been utilized, in conjunction with a single numerical scheme, to verify their performance against data sets in a variety of external pressure gradients. It is shown that none of the models yields uniformly accurate results, but three show sufficient promise to justify further refinement. A primary defect of all models is that they do not reproduce the law of the wall which has been observed over a range of pressure gradients. This may be due to the use of near-wall functions which continue to influence the flow well into the logarithmic region. Additional tuning of these functions and the length-scale determining equations is required before such models can be used for the accurate calculation of wall-proximity and low-Reynolds-number effects.

I. INTRODUCTION

It is well known that the success enjoyed by the recent turbulence-closure models in the prediction of wall-bounded flows has depended in large measure upon the application of the so-called wall functions, by which surface boundary conditions are transferred to points in the fluid removed from the boundaries. The finite-difference solutions therefore avoid the regions of very large gradients near the walls and can be carried out with considerable saving in computing times. The validity of this procedure is restricted, however, to situations in which universal wall functions are well established. There are a number of instances in which this approach has to be abandoned, e.g. the turbulent boundary layer at low Reynolds numbers, three-dimensional, unsteady and separated flows, the flow over surfaces with mass- or high heat-transfer, and in the modeling of transition.

Over the past few years, many suggestions have been made for the extension of turbulence closure models to enable their use right up to a solid wall. Quite often the resulting modified models have been referred to as "low-Reynolds-number" turbulence models since it is claimed that they can also be applied to flows in which some characteristic Reynolds number of the turbulence is low. There is therefore an unfortunate confusion of terminology. Some modifications to a basic high Reynolds number model are obviously necessary to account for two physically distinct effects: one is the influence of low Reynolds number, where viscous stresses and transport are comparable with the Reynolds stresses and turbulent transport, and the other is the influence of wall proximity, arising from the preferential damping of the turbulence and local effects on the fluctuating pressure field and pressure-velocity correlations. It is possible for either effect to be present in the absence of the other. However, the fact that both effects are present in the vicinity of a wall has led to the aforementioned confusion of terminology, and these cannot be readily separated within the framework of the models being examined.

The simplest example of a near-wall modification to a turbulence model is the famous van Driest (1) damping function for the mixing length. More advanced models incorporate either a wall damping effect, or a direct effect of molecular viscosity or both, on the empirical constants and functions in the turbulence-transport equations which were devised originally for high Reynolds-number, fully-turbulent flows remote from walls. In the absence of reliable turbulence data in the immediate vicinity of a wall or at low Reynolds numbers, these modifications have been based largely upon numerical experiments and comparisons between calculations and experiment in terms of global parameters. Unfortunately, the results of each model were compared by their proponents with different and rather limited class of flows and, as the issue can be judged at the present time, it is not clear which of the many proposed models can be used with confidence.

The research to be described in this paper was undertaken with the objective of making a systematic evaluation of the merits of the various existing two-equation "low-Reynolds-number" turbulence models. Eight different models have been used, together with a single well-tested calculation procedure to calculate a variety of boundary layers to assess their relative performance. The test cases include not only boundary layers at low Reynolds numbers, but also the standard high Reynolds number, equilibrium and separating boundary layers. The latter have been included specifically to ascertain that the extended models continue to perform at least as well as the parent models which were devised for such flows.

II. OUTLINE OF COMPETING MODELS

Eight models, namely those of Chien (2), Dutoya (3), Hassid and Poreh (4), Hoffman (5), Jones and Launder (6), Lam and Bremhorst (7), Reynolds (8) and Wilcox and Traci (9) were selected for a detailed evaluation. The first seven are variants of the k-ε-model which uses transport equations for the turbulent kinetic energy k and the rate of its dissipation ε. Wilcox and Traci employ an equation for the kinetic energy of the velocity fluctuations normal to the wall, which is similar to the k-equation. Their model is completed by a transport

$$-\rho\overline{UV} = \mu_t \frac{\partial U}{\partial y} \quad (1.1), \qquad \mu_t = C_\mu \cdot f_\mu \cdot \rho \frac{k^2}{\varepsilon} \quad (1.2)$$

$$\rho U \frac{\partial k}{\partial x} + \rho V \frac{\partial k}{\partial y} = \frac{\partial}{\partial y}\left[\left(\mu + \mu_t/\sigma_k\right)\frac{\partial k}{\partial y}\right] + \mu_t\left(\frac{\partial U}{\partial y}\right)^2 - \rho\varepsilon + D \quad (1.3)$$

$$\rho U \frac{\partial \varepsilon}{\partial x} + \rho V \frac{\partial \varepsilon}{\partial y} = \frac{\partial}{\partial y}\left[\left(\mu + \mu_t/\sigma_\varepsilon\right)\frac{\partial \varepsilon}{\partial y}\right] + C_{\varepsilon 1} f_1 \frac{\varepsilon}{k} \mu_t \left(\frac{\partial U}{\partial y}\right)^2 - C_{\varepsilon 2} f_2 \cdot \rho \frac{\varepsilon^2}{k} + E \quad (1.4)$$

$$R_T = \frac{\rho k^2}{\mu\varepsilon} \quad (1.5), \qquad Ry = \frac{\rho k^{1/2} y}{\mu} \quad (1.6), \qquad R_y^* = \frac{\rho y U_\tau}{\mu} \quad (1.7)$$

MODEL	CODE	ε_w-B.C	C_μ	$C_{\varepsilon 1}$	$C_{\varepsilon 2}$	σ_k	σ_ε	f_μ	f_1	f_2	D	E
BASIC HIGH-RE	HR	WF	0.09	1.44	1.92	1.0	1.3	1.0	1.0	1.0	0	0
JONES-LAUNDER	JL	$\varepsilon=0$	0.09	1.44	1.92	1.0	1.3	$\exp\left[\frac{-3.4}{(1+R_T/50)^2}\right]$	1.0	$1-0.3\exp(-R_T^2)$	$-2\mu\left(\frac{\partial\sqrt{k}}{\partial y}\right)^2$	$2\mu\mu_t\left(\frac{\partial^2 U}{\partial y^2}\right)^2$
HASSID-POREH	HP	$\varepsilon=0$	0.09	1.45	2.0	1.0	1.3	$1-\exp[-0.0015R_T]$	1.0	$1-0.3\exp(-R_T^2)$	$-2\mu\frac{k}{y^2}$	$-2\mu\left(\frac{\partial\sqrt{k}}{\partial y}\right)^2$
HOFFMANN	HO	$\varepsilon=0$	0.09	1.81	2.0	2.0	3.0	$\exp\left[\frac{-1.75}{1+R_T/50}\right]$	1.0	$1-0.3\exp(-R_T^2)$	$-\frac{\mu}{y}\frac{\partial k}{\partial y}$	0
DUTOYA	DU	$\varepsilon=0$	0.09	1.35	2.0	0.9	0.95	$1-0.86\exp\left[-\left(\frac{R_T}{500}\right)^2\right]$	$1-0.04\exp[-(\frac{R_T}{50})^2]+\frac{0.25\lambda}{y}]^2$	$1-0.3\exp[-(\frac{R_T}{50})^2]-0.08(\lambda/y)^2$	$-2\mu\left(\frac{\partial\sqrt{k}}{\partial y}\right)^2$	$-C_{\varepsilon 2} f_2 \rho \frac{D}{k}$
CHIEN	CH	$\varepsilon=0$	0.09	1.35	1.8	1.0	1.3	$1-\exp[-0.0115R_y^*]$	1.0	$1-0.22\exp[-(R_T/6)^2]$	$-2\mu\frac{k}{y^2}$	$-2\mu\frac{\varepsilon}{y^2}\exp[-0.5R_y^*]$
REYNOLDS	RE	$\varepsilon=\nu\frac{\partial^2 k}{\partial y}$	0.084	1.0	1.83	1.69	1.3	$1-\exp[-0.0198R_y]$	1.0	$[1-0.3\exp(-(R_T/3.7)^2)]f_\mu$	0	0
LAM-BREMHORST	LB	$\varepsilon=\nu\frac{\partial^2 k}{\partial y}$	0.09	1.44	1.92	1.0	1.3	$[1-\exp(-0.0165R_y)]^2(1+\frac{20.5}{R_T})$	$1+(0.05/f_\mu)^3$	$1-\exp[-R_T^2]$	0	0
LAM-BREMHORST	LB*	$\frac{\partial\varepsilon}{\partial y}=0$	0.09	1.44	1.92	1.0	1.3	----	----	----	0	0

Table 1: Equations, constants and functions for the k-ε group of models

equation for a pseudo-vorticity w. Tables 1 and 2 summarize the basic equations and the low-Reynolds-number functions and constants recommended by the various authors.

$$-\rho\overline{UV} = \mu_t \frac{\partial U}{\partial y} \quad (2.1), \qquad \mu_t = \rho^2 \frac{k}{W} \quad (2.2)$$

$$\rho U \frac{\partial k}{\partial x} + \rho V \frac{\partial k}{\partial y} = \frac{\partial}{\partial y}\left[\left(\mu + \mu_t/\sigma_k\right)\frac{\partial k}{\partial y}\right] + \sqrt{C_\mu}\, f_\mu \rho k \frac{\partial U}{\partial y} - C_\mu k W + D \quad (2.3)$$

$$\rho U \frac{\partial W^2}{\partial x} + \rho V \frac{\partial W^2}{\partial y} = \frac{\partial}{\partial y}\left[\left(\mu + \mu_t/\sigma_w\right)\frac{\partial W^2}{\partial y}\right] + C_{w1} f_1 \rho W^2 \frac{\partial U}{\partial y} - C_{w2} f_2 W^3 E \quad (2.4)$$

$$L = \frac{\rho k^{1/2}}{W} \quad (2.5) \qquad R_T = \frac{\rho^2 k}{\mu W} \quad (2.6)$$

MODEL	CODE	C_μ	C_{w1}	C_{w2}	σ_k	σ_w	f_μ	f_1	D	E
WILCOX-TRACI	WT	0.09	0.33	0.15	2.0	2.0	$1-0.91\exp[-2R_T]$	$1-0.91\exp[-\frac{R_T}{2}]$	0	$-\frac{2}{\sigma_w}\left(\frac{\partial L}{\partial y}\right)^2 W^2$

Table 2: Equations, constants and functions for the model of Wilcox and Traci

It is seen that the models differ from their basic versions by inclusion of viscous diffusion and functions f to modify the constants c which were found to be adequate for high-Reynolds-number flows. Also, some authors introduce additional terms, denoted by D and E, mainly to improve the near wall behaviour. In the subsequent paragraphs the different proposals are examined in the light of physical and experimental evidence.

a) The k-ε Group of Models

Consider first the seven modifications to the k-ε model listed in Table 1. The first entry indicates the constants associated with the basic high-Reynolds-number version of the model; the values listed are due to Rodi (10) and are generally accepted as standard values. Table 1 shows that different authors have adopted somewhat different values for these high-Reynolds-number flow constants in addition to making other modifications. These differences may be quite significant insofar as they may contribute to the overall performance of the low-Reynolds-number version. Extensive calculations of free shear layers by Launder et al. (11) indicate that, at least for those flows, the results are indeed very sensitive to the precise values of $c_{\varepsilon 1}$ and $c_{\varepsilon 2}$.

The various "low-Reynolds-number" functions and correction terms D and E in Table 1 are discussed together with the boundary conditions for k and ε at a wall since they are intricately related. Consider first the function f_μ modifying the Prandtl-Kolmogorov relation. Such a function is necessary to account for the two separate effects mentioned in the

Introduction, namely those of low turbulence Reynolds number and wall proximity. One may therefore expect f_μ to depend upon the turbulence Reynolds number, R_T and the nondimensional distance from the wall R_y or R_{y+}. Most authors however use only a single parameter in f_μ.

Although reliable turbulence data very close to a wall are not available to establish f_μ directly, some information can be obtained from an examination of the boundary conditions at a solid wall. On the basis of such considerations, Hinze (13) has deduced that

$$\overline{u'v'} \sim A'y^2 + B'y^3$$

$$\nu_t \sim Ay^3 + By^4$$

where the coefficients depend upon the gradients of the velocity fluctuations at the wall. There is some evidence that A is negligible in flows which do not vary in the streamwise direction, and that $\nu_t \sim y^4$, in conformity with van Driest's damping function for ν_t. In general, however, Hinze suggests that $\nu_t \sim y^3$. It is interesting to see how the different f_μ-functions compare with these observations.

Since the velocity fluctuations vanish at the wall, simple Taylor series expansion shows that

$$k_w = \left(\frac{\partial k}{\partial y}\right)_w = 0 \quad \text{and} \quad k \sim y^2$$

and the expression for the dissipation at the wall reduces to

$$\varepsilon_w = \nu\left[\overline{\left(\frac{\partial u'}{\partial y}\right)^2} + \overline{\left(\frac{\partial w'}{\partial y}\right)^2}\right] = \nu \frac{\partial^2 k}{\partial y^2}$$

indicating ε to be finite at the wall. Using the data of Kreplin and Eckelmann (14), this wall value may be estimated as

$$\frac{\varepsilon_w \nu}{u_\tau^4} \sim 0.1$$

The exponents x in $\nu_t \sim y^x$ implied by the various models may be obtained by expanding the corresponding f_μ function in a power series. These are listed in Table 3. It is seen that three of the models do not conform with the cubic variation implied by Hinze's analysis.

MODEL	JL	HP	HO	DU	CH	RE	LB	LB$^+$
x	3	3	3	3	3	6	4	4

Table 3: Values of the exponent x in $\nu_t \sim y^x$ for the different models

With regard to the dissipation at the wall, most models employ $\varepsilon_w = 0$, following the suggestion of Jones and Launder, who cited "decisive computational advantages" as the reason for this change. Since this makes the k-equation inconsistent at the wall, Jones and Launder added a term D (see Table 1) and pointed out that ε should not then be identified with the physical dissipation, at least in the wall region. The need for the addition of an arbitrary term in the k-equation can be avoided if the finite value of ε_w is incorporated as a boundary condition in the solution procedure, as is done by Lam and Bremhorst. One possibility which, to the authors' knowlegde, has not been considered so far, is to set the gradient of ε to zero at the wall so that ε_w is determined as a part of the solution. The performance of such a boundary condition has been explored in connection with the model of Lam and Bremhorst (LB$^+$) in the present work.

The function f_2 is introduced to serve two purposes. First, it attempts to incorporate genuine low Reynolds number effects in the destruction term. The physical basis for this is provided by experiments in the final period of the decay of isotropic grid turbulence. The second purpose is to ensure consistency of the ε-equation at the wall with the assumed ε_w boundary condition. A finite non-zero value of ε_w would require $f_2 \sim y2$ in the absence of the additive term E. As noted earlier, however, most models employ $\varepsilon_w = 0$; f_2 may then take any value at the wall and it should not be necessary to add an extra term such as E. If a finite wall value of ε is used without additional term E in the equation, then f_2 must tend to zero at the wall. It is seen that the models of Lam and Bremhorst and Reynolds accomplish this in different ways; the former by simply omitting the factor 0.3 in the function of Jones and Launder, and the latter by choosing $f_2 = g(R_T)\cdot h(Ry)$. It should be noted that the model of Reynolds has not been used thus far making low Reynolds number flow calculations, partly because a constant in the h function is not specified; we have set h equal to f_μ in the calculations since this incorporates the influence of wall proximity. Finally, we note that Dutoya also retains the influence of the wall on the destruction term in the ε-equation by a function involving the Taylor-microscale, approximated by $\lambda = \sqrt{10\nu k/\varepsilon}$, which serves to reduce the destruction of ε.

Three different proposals have been made for the additional term D in the k-equation, all giving the same value at the wall. A word of caution is needed with regard to the use of the formulation of Jones and Launder. This term can be discretized starting from three different expressions:

$$2\mu\left(\frac{\partial k}{\partial y}\right)^2 = \frac{1}{2}\mu\left(\frac{1}{k}\frac{\partial k}{\partial y}\right)^2 = \frac{1}{2}\frac{\mu}{k}\left(\frac{\partial k}{\partial y}\right)^2$$

and calculations show that the manner in which this is done influences the results appreciably. Therefore, simpler formulations, such as those of Hassid and Poreh and Chien, may be preferable from a numerical standpoint.

Table 1 shows that several models employ an additional empirical term E and/or function f_1 in the ε-equation. Although their physical basis is not entirely clear, their near wall behaviour can be examined. Starting with the model of Jones and Launder, it is seen that E is zero in the viscous sublayer of a flat plate boundary layer and decreases as y^4 in the log-region. Consequently, the maximum is located in the buffer layer. The term is then likely to increase the dissipation rate there, resulting in a lower energy peak. In the models of Hassid and Poreh and Chien, the E-terms allow ε to grow quadratically with distance from the wall. An argument cited for this is that the length scale, $L = k^{3/2}/\varepsilon$ then becomes linear in y in the neighborhood of the wall in agreement with some experimental and numerical evidence.

Two of the models under consideration, namely those of Dutoya and Lam and Bremhorst incorporate a function f_1 in the generation term in the ε-equation. Dutoya reduces the generation of ε as a function of the Reynolds number and increases it in the vicinity of the wall. The f_1-function of Lam and Bremhorst can not readily be assessed since, as noted above, the model is used with an ε-boundary condition different from the others. However, the effect of f_1 is to raise generation of ε in order to keep the k-distribution in accordance with measurements.

b) The Model of Wilcox and Traci (9)

The basic equations of this model are cited in Table 2. It is seen that Wilcox and Traci employ an equation somewhat similar to the k-equation for determining the velocity scale in the eddy viscosity. However, they interpret k as a "mixing energy" which is more closely related to the normal component of the Reynolds stress, viz $k \tilde{=} 9/2\ \overline{v'^2}$. Since a direct relationship with the turbulent kinetic energy is now absent it is difficult to make comparisons with conventional turbulence measurements. The same is true for the length-scale determining variable w, which is a product of a "pseudo-vorticity" ω and the local density. Wilcox and Traci extended Saffman's (15) original proposal for a ω^2-transport-equation by adding an extra term E, named gradient dissipation, which stems from a comparison with the ε-equation. The structual difference between the k-ε and k-w models lies in the way the production term in the k-equation is treated. Wilcox and Traci's production, $c_\mu^{1/2}\partial u/\partial y$ implies the use of structural similarity rather than the eddy-viscosity hypothesis. However, as Reynolds (8) has pointed out, this might be advantageous, since it reflects the experimental observation that the near-wall turbulence structure is virtually independent of the mean rate of strain. Examination of the constants in Table 2 shows that these are not grossly different from those used in the k-ε models. Wilcox and Traci's eddy-viscosity formula shows that unlike all k-ε-type models it does not contain a low Reynolds number function. This suggests that viscous and wall-proximity effects are incorporated indirectly in the k and w^2-equations. It is noteworthy that only two functions, f_μ and f_1, are required in this model, both decreasing the production rates in the transport equations as a function of a turbulence Reynolds number. Leaving f_2=1.0 means that the model cannot simulate the decay of grid turbulence in the late, viscosity-dominated stages.

The boundary conditions for this model present some interesting questions. In the k-ε approach they are more or less fixed by the known behaviour of the physical quantities. In the Wilcox and Traci model this is not feasible and hence greater freedom can be exercised in setting these values. In fact the boundary value of w at the wall is made a function of parameters like roughness and blowing/suction rates, whereas physical arguments would require $w \to \infty$ at the wall, independent of the particular flow.

c) Concluding Remarks

The foregoing summary of the various models shows that most modifications to the basic high Reynolds number turbulence models lack sound physical basis, although some rely upon internal consistency of the equations near a solid boundary. In the absence of reliable pertinent data, support for the models is provided largely by comparisons of the results with the gross parameters of shear flows. However, a review of the literature indicates that only two of these, namely the models of Jones and Launder and Wilcox and Traci, have been used extensively. The former has been used over a much larger class of flows, including free shear layers, while the latter has been employed primarily for boundary layers with special emphasis on compressible flows. Additional comparative tests of the other models are thus required to determine if they represent significant improvements.

III. SELECTION OF TEST CASES

Before describing the results of the calculations, it is necessary to discuss two aspects which may influence the conclusions. The first concerns the criteria by which success or failure is to be judged. Among those considered important are the following: (a) the model should reproduce results of the parent high-Reynolds-number model for flows which are not dominated by low-Reynolds-number, and (b) the model predictions in the wall region and for flows in which low-Reynolds-number effects are present should show acceptable agreement with the available experimental evidence. While we shall elaborate upon these criteria later on, they raise the second question, namely that of selecting the test cases against which all calculations are to be compared. In the present study, attention is focussed upon incompressible two-dimensional boundary layers, and calculations have been performed for the following test cases:

1. Flat plate boundary layer, Wieghardt and Tillmann (16)
2. Equilibrium, adverse pressure gradient boundary layer, Anderson et al. (17)
3. Strong adverse pressure gradient boundary layer, Samuel and Joubert (18)
4. Strong favorable pressure gradient (relaminarizing) boundary layers:
   (a) Simpson and Wallace (19)
   (b) Patel and Head (20)

It should be noted that all data sets, with the exception of 2) and 4b) have also been selected as test cases at the 1980-81 Stanford Conference after careful review of the data for completeness and reliability. The choice of the first three for the present work is guided by the first criterion. The relaminarizing flows have been selected since they are obviously dominated by wall proximity and low-Reynolds-number effects.

IV. CALCULATION PROCEDURE

The numerical method used is an adapted version of the implicit marching procedure of Patankar and Spalding (21). 100 cross-stream grid nodes were used to obtain grid-independent solutions and, for an accurate representation of the large gradients in the vicinity of the wall, roughly half of those were located within $y^+ < 50$. At the beginning of the calculations the first grid point was normally located at $y^+ = 0.2$ and it was ensured that this value did not exceed $y^+ = 4$ in the course of the computation.

The streamwise step-size was taken as 0.25 θ, where θ is the momentum thickness. In order to resolve changes in the viscous sublayer, the maximum streamwise step-size was restricted to five sublayer thicknesses, i.e. $\Delta x < 25\nu/u_\tau$.

Initial profiles for the mean velocity were usually obtained by curve-fits to the available data. A representative flat-plate distribution was used for the k-profile. The starting condition for the rate of dissipation ε was generated from a formula given by Hassid and Poreh (see Gibson et al., 22). In general the initial conditions exerted a minor influence on the results.

The calculations were carried out on a BURROUGHS B7700 computer. Computation times per step were of the order of 0.15 s, with little difference between the various models, as could be concluded also from Tables 1 and 2, because all involve about the same

number of arithmetic operations. This observation is at variance with those of Hoffman and Chien who reported large differences in computation times between their model and that of Jones and Launder.

V. RESULTS AND DISCUSSION

Figures 1,2,3 show the results of the calculations for the simplest test case, namely the flat-plate boundary layer. The model of Reynolds is not included since it did not yield consistent results due to the uncertainty mentioned earlier. In the interest of brevity, the comparisons are limited to the skin-friction coefficient, the velocity profiles in wall coordinates and the distribution of turbulent kinetic energy in the near-wall region. The skin-friction data in Figure 1 are deduced from the measurements of Wieghardt. Figure 2 includes the generally accepted semi-logarithmic law, while Figure 3 shows the data of Kreplin and Eckelmann in channel flow. Coles (23), in a review of near-wall turbulence measurements, favors the data of Kreplin and Eckelmann as more reliable among the many, rather scattered, data sets. Moreover, these represent an average of the available measurements. They are included here more as a guide than as a basis for strict comparison.

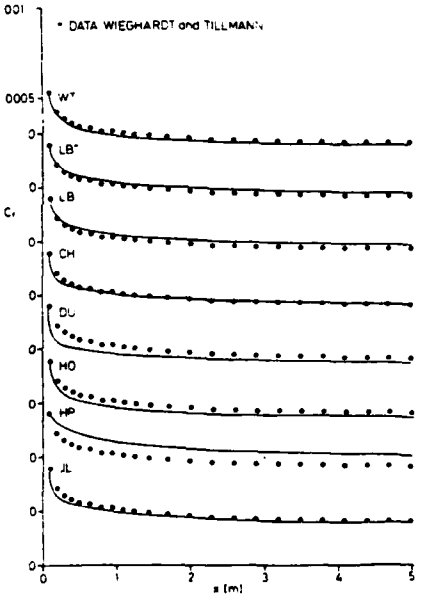

Figure 1: Measured and calculated skin friction coefficient for a flat plate boundary layer

It is obvious from the figures that there is considerable diversity among the results of the various models. Figures 1 and 2 show a strong correlation between the ability of a model to reproduce the standard law of the wall and the corresponding prediction of the wall shear stress. Thus, for example, the overshoot in the law of the wall in DU and, to lesser extents in WT and JL, results in an under-estimation of c_f. The models of HP, LB, LB^+ confirm this correlation with results in the opposite direction. The HO model gives a very small logarithmic region and rather peculiar profile shapes in the outer layer, due presumably to the use of the large diffusion coefficients. The best fit to

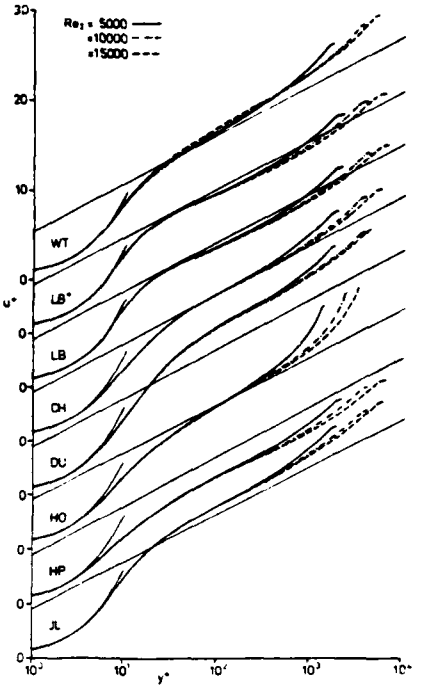

Figure 2: Calculated velocity profiles at different Reynolds-numbers, lines are $u^+ = y^+$ and $u^+ = 1/\kappa \ln y^+ + c, \kappa = 0.418$, $c = 5.5$

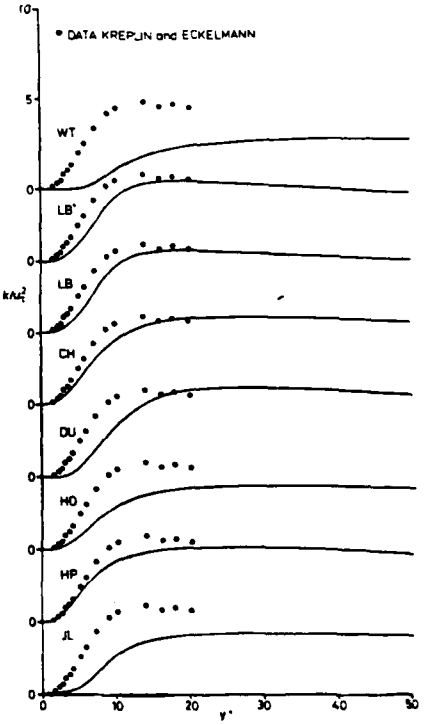

Figure 3: Measured and calculated turbulent kinetic energy profiles in the near wall region

the law of the wall is achieved by CH and then c_f is predicted quite accurately. This consistency is all the more important in establishing the successful features of the models in view of the fact that c_f has been determined for each case from the slope of the velocity profile at the wall and not by recourse to the logarithmic region. Figure 3 shows that the shape of the turbulent kinetic-energy distribution is better predicted by those models which yield good agreement with respect to the wall law and c_f, with the exceptions of WT and JL. The former is not surprising in view of the uncertainty concerning the relationship between k and the "mixing-energy" in the WT model. The poorer performance of the JL model, on the other hand, remains inexplicable although a possible source is the additional terms D and E in the model equations and the manner in which D is discretized. It is also apparent from Figure 3 that none of the models fit the channel data of Kreplin and Eckelmann but the results with LB, LB^+ and CH show fair agreement with the location and magnitude of the energy maximum. Finally, the results of LB and LB^+, obtained with the different ε boundary conditions at the wall discussed earlier, are identical. Since the zero gradient condition at the wall (LB^+) is easier to apply in numerical solutions, and was found to yield $\nu\varepsilon_w/u_\tau^4$ in good agreement with the experimental value, this boundary condition has been used in all subsequent calculations with the LB model.

The foregoing results indicate that not all of the available low-Reynolds-number models reproduce the most basic features of a flat-plate boundary layer. Only the more promising models, namely JL, CH, LB^+ and WT, will therefore be discussed in the context of the remaining test cases.

The results for the second test case, namely an equilibrium boundary layer, are shown in Figure 4. Also included here are the calculations with the high Reynolds-number version of the k-ε model in which wall-functions have been applied at $y+ = 50$. It is seen that the three k-ε based models (CH, JL, LB^+) all lead to an over-estimation of c_f by as much as 50%. The shape parameters G (and H, not shown) are correspondingly lower than the experimental values. The WT model yields the best results although the c_f is still over-predicted by about 15%. It is interesting to note that all models predict nearly constant shape parameters beyond $x = 0.6$ m. Thus, a different equilibrium flow is predicted in each case.

From Figure 5 it is evident that the performance of the four models in an adverse pressure gradient boundary layer is somewhat similar to that observed in equilibrium flow insofar as the skin friction is over-estimated and the velocity profiles in wall coordinates shows systematic departures from the experimental data. From the profiles it appears that the various functions introduced to account for wall proximity and low Reynolds-number effects continue to operate deep into the full turbulent (logarithmic) part of the boundary layer. The rather large differences in the wake component, on the other hand, may be attributed to an inadequacy of the length-scale determining equations in the parent high-Reynolds-number models.

The results of the calculations for the two favorable pressure gradient boundary layers are shown in Figures 6 and 7. Recall that the low-Reynolds-number model were constructed primarily to describe such flows since the accelerations lead to a reduction in the Reynolds number, thickening of the sublayer and eventual relaminarization. Figure 6 indicates again the tendency of all models to over-

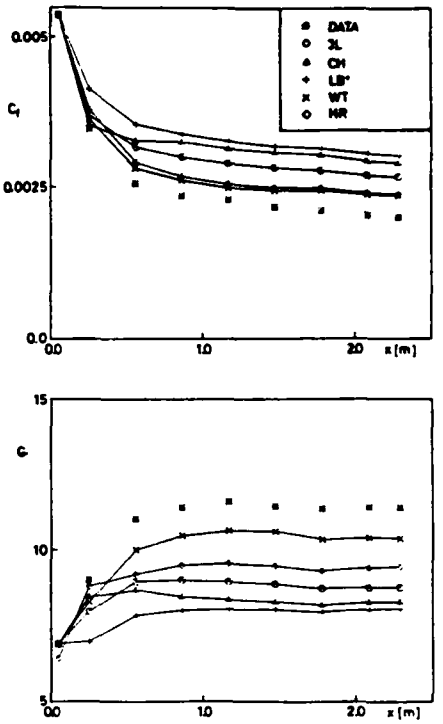

Figure 4: Comparison of model results with the data of Anderson et al.

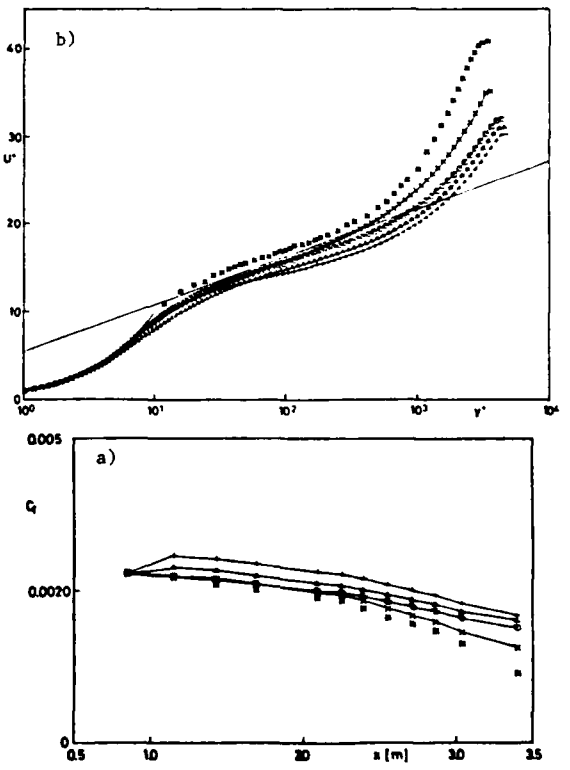

Figure 5: Comparison of model results with the data of Samuel and Joubert, a) skin friction coefficient; b) velocity profiles at x=3.4m (key as for Fig. 4)

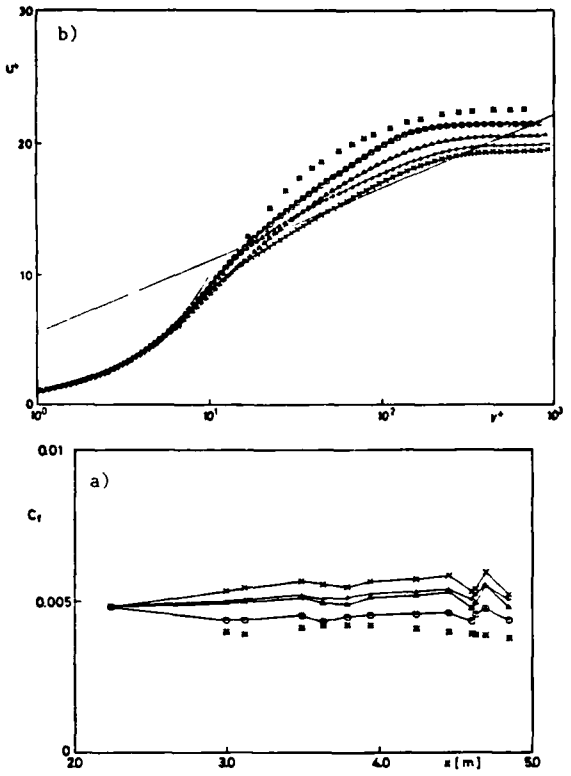

Figure 6: Comparison of model results with the data of Simpson and Wallace, a) skin friction; coefficient; b) velocity profiles at x=4.604m (key as for Fig. 4)

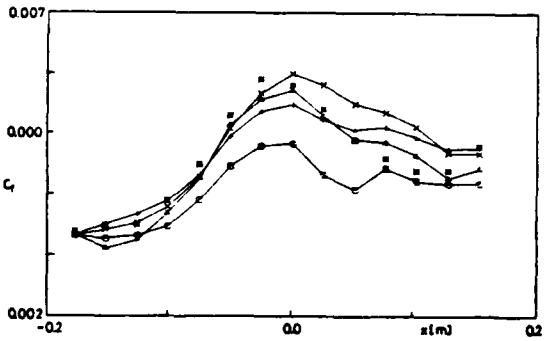

Figure 7: Comparison of model results with the data of Patel and Head (key as for Fig. 4)

predict c_f in the case of Simpson and Wallace. The calculated velocity profiles now show a departure from the usual law of the wall as indicated by experiments but the predicted thickening of the sublayer is not as rapid as that observed in the experiments. In the case of Patel and Head (s. Fig. 7), where the acceleration is more severe, the calculations with three of the models show fair agreement with the data. In particular, the initial increase in c_f, and the subsequent decrease, associated with relaminarization, are reproduced quite well. The accompanying decrease and increase in the shape parameter (not shown here) are also predicted with satisfactory accuracy.

VI. CONCLUSIONS

The results presented here are, for reasons of brevity, somewhat limited with respect to the details such as the velocity-profile shapes and turbulence parameters. Nevertheless, they are sufficient to indicate clearly the relative performance of the various models that have been proposed to describe the near wall flow. It is clear that not all of the models considered here yield satisfactory results. From an examination of the results for all the test cases as a whole, it appears that the models of Chien (2) and, to some extent, Lam and Bremhorst (7) based on the k-ε model, and that of Wilcox and Traci (9), yield comparable results and perform considerably better than the others. However, even these need further refinement if they are to be used with confidence to calculate near-wall and low-Reynolds-number flows. The calculations presented thus far suggest that the performance of these models can be improved by modifications that ensure the reproduction of the law of the wall over a range of pressure gradients for which the boundary layer remains turbulent and selecting damping functions whose influence is restricted only to the sublayer and the buffer zone. The former would undoubtedly imply changes on the existing length-scale determining equation.

ACKNOWLEDGEMENTS

This research was performed while the first author (VCP) was on a Faculty Developmental Leave from the University of Iowa during 1980-81 at the Institut für Hydromechanik of the Universität Karlsruhe under the sponsorship of the Senior U.S. Scientific Award of the Alexander von Humboldt Foundation. The support of all three Institutions is gratefully acknowledged. The authors are also grateful to Dr. M.M. Gibson for setting up an initial version of the computer program and to Gaby Bartman for typing the manuscript so efficiently.

REFERENCES

1 van Driest, E.R., "On Turbulent Flow Near a Wall", J.o. Aeronautical Sci., Vol. 23, 1956, pp. 1007-1011.

2 Chien, K.Y., "Prediction of Channel and Boundary Layer Flow with a Low-Reynolds-Number Two-Fquation Model of Turbulence", AIAA-Paper, 80-0134, 1980.

3 Dutoya, D., "A Program for Calculating Boundary Layers and Heat Transfer along Compressor and Turbine Blades", ONERA-TP 1979-88, 1979.

4 Hassid, S., Poreh, M., "A Turbulert Energy Dissipation Model for Flows with Drag Reduction", J. Fluids Eng., Vol. 100,1978, pp. 107-112.

5 Hoffmann, G., "Improved Form of the Low Reynolds Number k-ε Turbulence Model", Physics of Fluids, Vol. 18, 1975, pp. 309-312.

6 Jones, W.P., Launder, B.E., "The Prediction of Laminarization with a Two-Equation Model of Turbulence", Int. J. Heat Mass Transfer, Vol. 15, 1972, pp. 301-314.

7 Lam, C.K.G., Bremhorst, K.A., "Modified Form of the k-ε Model for Predicting Wall Turbulence", Univ. o. Queensland, Dept.Mech.Eng., Res.-Rept. 3/78, 1978.

8 Reynolds, W.C., "Computation of Turbulent Flows", Ann. Rev. Fluid Mech.,Vol. 8, 1976, pp. 183-208.

9 Wilcox, D.C., Traci, R.M., "A Complete Model of Turbulence", AIAA-Paper 76351,1976.

10 Rodi, W., "Turbulence Models and Their Application in Hydraulics",Int. Association for Hydraulic Research-Publication, Delft, 1980.

11 Launder, B.E., Morse, A.P., Rodi,W. Spalding, D.B., "The Prediction of Free Shear Flows-A Comparison of the Performance of Six Turbulence Models", NASA SP 320, 1973.

12 Launder, B.E., "Progress in the Modelling of Turbulent Transport", VKI,Lecture Series 76, 1975.

13 Hinze, J.O., "Turbulence", 2nd Edition, McGraw Hill, N.Y., 1975.

14 Kreplin, H.P., Eckelmann, H., "Behaviour of Three Fluctuating Velocity Components in the Wall Region of a Turbulent Channel Flow", Physics of Fluids, Vol. 22, 1979, pp. 1233-1239.

15 Saffman, D.G., "A Model for Inhomogeneous Turbulent Flow", Proc. Roy. Soc, A, Vol. 317, 1970, p. 417.

16 Wieghardt, K., Tillmann, W., "On the Turbulent Friction Layer for Rising Pressure", NACA, TM 1374, 1957.

17 Andersen, P.S., Kays, W.M., Moffat, R.J., "The Turbulent Boundary Layer on a Porous Plate: An Experimental Study of the Fluid Mechanics for Adverse Free-Stream Pressure Gradients", Stanf. Univ., Thermo.Div., Rept.-No. HMT-15,1972.

18 Samuel, A.E., Joubert, P.N., "A Boundary Layer in an Increasingly Adverse Pressure Gradient", J. Fluid Mech., Vol. 66, 1974, pp. 481-505.

19 Simpson, R.L., Wallace, D.B., "Laminarescent Turbulent Boundary Layers; Experiments on Sink Flows", Proj. SQUID, Tech.Rept.No. SMU-2-PU, 1975.

20 Patel, V.C., Head, M.R., "Reversion of Turbulent to Laminar Flow", J. Fluid Mech., Vol. 34, 1968, p. 371.

21 Patankar, S.V., Spalding, D.B., "Heat and Mass Transfer in Boundary Layers", Intertext, 2nd Ed., 1970.

22 Gibson, M.M., Spalding, D.B., Zinser, W., "Boundary-Layer Calculations Using the Hassid-Poreh One-Equation Energy Model", Letters in Heat and Mass Transfer,Vol. 5, 1978, pp. 73-80.

23 Coles, D., "A Model for Flow in the Viscous Sublayer", Workshop on Coherent Structure of Turbulent Boundary Layers, Lehigh Univ., 1-3 May, 1978.

DECAY OF TURBULENCE DURING A LAMINAR REORGANIZATION IN PIPE FLOW

P. VALLETTE

M. LEBOUCHE

Laboratoire d'Energétique et de Mécanique Théorique et Appliquée (LEMTA)
CNRS - ERA n° 893
Institut National Polytechnique de Lorraine ; Université de Nancy I
24, rue Lionnois 54000 Nancy, France

ABSTRACT

We study the reorganization of a turbulent flow wich becomes subcritical after a singularity (Re = 1700). We mesure velocity gradient at the wall and velocity in the core ; we use mainly electrochemical method.

Simultaneous measurements at different points, at the wall or in the flow, allows a spatio-temporal description of this flow ; it shows the main mechanisms of degradation of turbulent energy, with their typical scales ; it leads us to expect the insulation of turbulent structures in a more and more coherent flow. A conditional analysis of velocity profiles given by a multiple anemometric probe shows the development, evolution and vanishing of these structures during reorganization, until obtaining of a POISEUILLE flow. Comparison of the results obtained dowstream enlargments with different angles shows that the mechanisms previously described are characteristic of any turbulent degradation in a pipe.

NOMENCLATURE

d	diameter of the pipe
e(f)	spectral density of energy : $\int e(f)df = 1$
E(k)	spectral density of energy $\int E(k)dk = 1$
f	frequency of fluctuations
i	intensity of electric current
$\mathcal{G}$	intercorrelation coefficient

$$\mathcal{G}_{s\varphi}(x,\varphi_1,\varphi_2,\tau) = \frac{\overline{s(x,\varphi_1,t)\, s(x,\varphi_2,t+\tau)}}{\sqrt{\overline{s^2(x,\varphi_1,t)}\;\overline{s^2(x,\varphi_2,t)}}}$$

$$\mathcal{G}_{sx}(x,\overline{x},o,\tau) = \frac{\overline{s(x,t)\cdot s(x+\overline{x},t+\tau)}}{\sqrt{\overline{s^2(x,t)}\cdot\overline{s^2(x+\overline{x},t)}}}$$

$$\mathcal{G}_{us}(x,\overline{x},y^*,\tau) = \frac{\overline{s(x,t)\cdot u(x+\overline{x},y^*,t+\tau)}}{\sqrt{\overline{s^2(x,t)}\cdot\overline{u^2(x+\overline{x},y^*,t)}}}$$

$$\mathcal{G}_{u\eta}(x,\eta_1,\eta_2,\tau) = \frac{\overline{u(x,\eta_1,t)\cdot u(x,\eta_2,t+\tau)}}{\sqrt{\overline{u^2(x,\eta_1,t)}\cdot\overline{u^2(x,\eta_2,t)}}}$$

$k = 2\pi f/\overline{U}$	wave number
L_x	Integral longitudinal scale of turbulence
P_s	Probability of occurence of class S_s and $\overline{S}$
Q	Rate of flow
Re	REYNOLDS number $R_e = V_q d/\nu$
S	Wall velocity gradient
$\mathcal{S}$	Mean duration of life of a class S
$\overline{U}$	Instantaneous longitudinal velocity
$\overline{U}$	Mean value of longitudinal velocity
u	fluctuation of longitudinal velocity
V_q	Mean velocity (spatial)
V_x	longitudinal convection velocity
x	distance from singularity
y	distance from the wall
$y^* = \frac{2y}{d}$	reduced distance from the wall
$\delta_q = \overline{Q}\int_{-1}^{+1}\frac{\overline{U}_i - \overline{U}}{V_q}\eta\, d\eta$	asymmetry of flow rate
$\eta = \frac{2r}{d}$	reduced distance from the axis
ν	kinematic viscosity
$\sigma = \sqrt{\overline{u^2}}/\overline{U}$	relative intensity of turbulence
τ	incremental lag
φ	azimuthal angle
$X = \frac{x}{d}$	reduced distance from singularity

INTRODUCTION

The reorganization from turbulent to laminar flow in a pipe has already been the purpose of some experimental studies, among which we refer to those of LAUFER (1), SIBULKIN (2) and LEFORT (3). In each case, the law of decrease of turbulent intensity into the flow was given

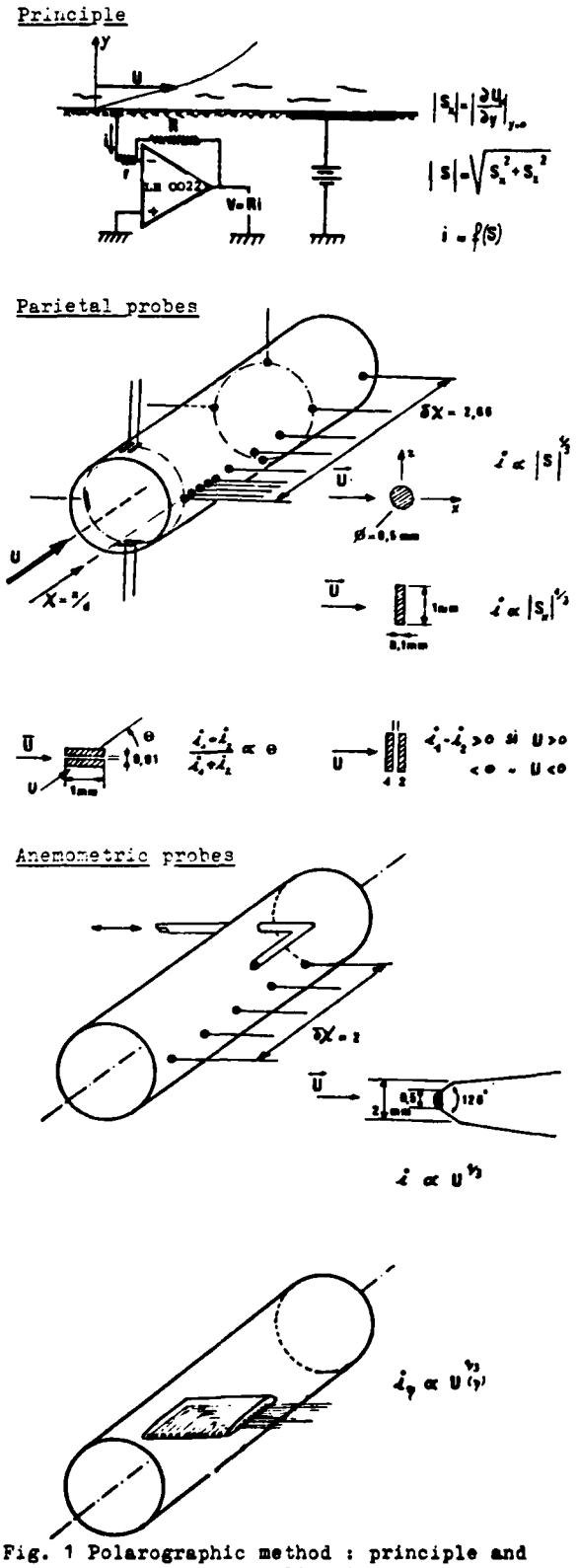

Fig. 1 Polarographic method : principle and applications.

and evolution of the spectral distribution of turbulent energy during reorganization was noted. From these works, it was possible to give the length necessary to obtain the establishment of a laminar flow and to show which parameters give a good description of the evolution toward this state. If, from an Eulerian description, these works show a continuous degradation of the turbulent energy, spectral analysis exhibits an unsteady phase of the velocity fluctuations during regorganization (4). A Lagrangian description made by use of many parietal electrochemical probes and one velocity probe in such a flow (5) shows the coexistence, during reorganization, of two kinds of domains, one corresponding to a frozen flow and the other having features of turbulence. In order to develop this hypothesis, we have followed the development and history of these domains, by reading the informations given simultaneously by eleven velocity probes, distributed over a same diameter of the pipe.

EXPERIMENTAL SET UP

It was already described in a precedent paper (5) ; it gives in the upstream pipe (diameter : 1cm) a turbulent flow, fully developed, at a REYNOLDS number equal to 5100. This flow is incompressible (water or polarographic solution) ; it enters the downstream pipe (diameter : 3 cm) by a sudden or conical enlargment. In this test pipe , we study the reorganization at a REYNOLDS number equal to 1700, over 120 diameters (X=120).

After preliminary results obtained by LDA or hot film anemometry, all measurements near the wall and spatio-temporal analysis of the flow use electrochemical method. This was first employed for wall shear stress measurements by HANRATTY et al.(6) (7) (8) ; it was also developed in our Laboratory by LEBOUCHE (9) COGNET (10) and DELAGE (11). The intensity i of the current obtained at a flush mounted electrode during a diffusion controlled reaction allows the determination of the instantaneous value of the wall velocity gradient S. Extented to the use of double parietal electrodes and of conical probes in the core, this method gives also the direction of flow near the wall and the velocity. Figure 1 remind the main applications. For velocity measurements, it must be noted that the current is proportional to the 1/3 power of the incident velocity (Stoke's flow around the probe induces proportionality between shear stress and velocity). We never took account of corrections due to the frequency response of the electrodes ; this approximation is reasonable because the frequencies of all fluctuations are less than 30 Hz in the studied region.

GENERAL DESCRIPTION OF THE FLOW

For sections near the enlargment, the use of LDA in the core and of electrochemical probes at the wall allowed us to show the development of the recirculating zone (5). This, very unstable and tridimensional,can extend as far as X = 5, while mean position is located at X = 3,6. Downstream,examination of mean velocity ($\bar{U}$) and relative turbulent intensity (σ) profiles gives us an inkling of three main stages in the reor-

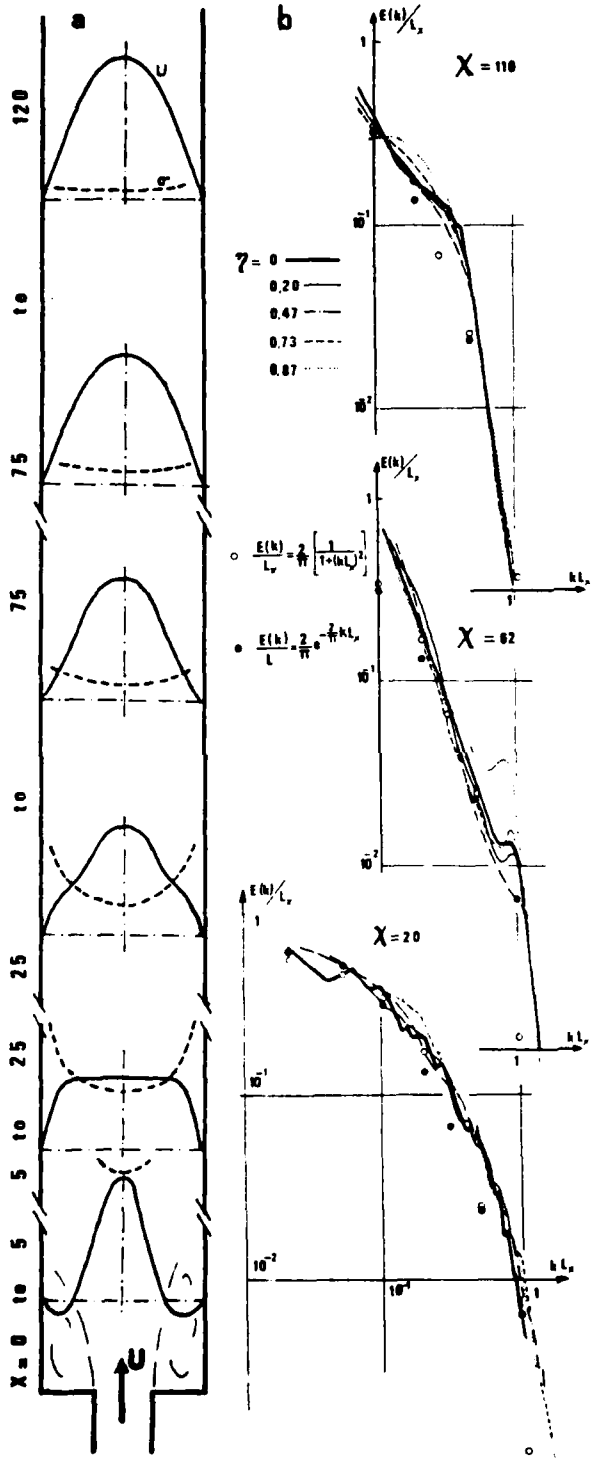

Fig. 2 General characteristics of the flow:
a- Scheme of mean velocity ——— and of relative turbulent intensity-----profiles.
b- Spectral analysis of axial velocity fluctuations.

ganization. A diagram of the profiles, which magnifies their features, is presented on figure 2-a :

- downstream the expansion cone where direct flow cohabits with recirculating one, as far as X =20, the profiles show the main characteristics of a turbulent flow.
- on the other hand, for distances greater than 75 diamteres from the enlargment, we observe a progressive reorganization which leads to the well known parabolic profile. The turbulent level is then lower than 1% in the core.
- in the middle, the evolution of relative turbulent intensity profiles show a considerable energetic reorganization. The aspect of the mean velocity profiles is more complex and exhibits inflexion points. Analysis of velocity histograms leads us to consider that, in this zone, exists an intermittency between two types of flows, not established but well distinct.

Spectral analysis of the velocity fluctuations is summarized on figure 2-b. It is presented in nondimensional space $(E(k)/L_x, kL_x)$ This analysis confirms the distinction of the three stages previously cited :

- in the first stage, all the spectra obtained in a same section show a good agreement with the empirical formulations recommended for description of turbulent flows. They recall production of turbulent energy by breaking and degradation by diffusion in the core and viscous dissipation near the wall.
- in the middle stage, this agreement is much less obvious : the frequency distribution on the axis of the pipe, similar to the previous one, is quite different from the frequency distribution near the wall. If we note that viscous dissipation exists in the whole section, we remark also that the spectra show, over one decade, the slope -2 which characterizes unstable phenomena.
- far downstream, this distribution becomes again unvarying in the section, but takes the appearance of a square function, which we must explain by missing of production of turbulent energy.

Statistical analysis of the fluctuations of wall velocity gradient summarizes quite well the features of this reorganization. The exponential decreasing of σ^2, up to X = 75 is in good agreement with the law of energetic decreasing already known near the wall (5). Nevertheless, the evolution of skewness and flatness factors shows the alteration of the features of the wall velocity fluctuations, between X = 30 and X = 60. The spectra of these fluctuations (see figure 3) remind, up to X = 20, the one of turbulence which is continuous. For X = 50, they send back the unstable character of the flow ; downstream, they show a downstep function marked by a preferential frequency band. This last cannot be imputed to a periodic pulsation of the flow ; it has probably his origine in the aleatory passage of structures with determined length, which will be shown only by a spatio-temporal analysis.

SPATIO-TEMPORAL DESCRIPTION OF THE FLOW

The arrangement of the electrochemical probes allows the determination of intercorrelation functions in time, which connects the events ob-

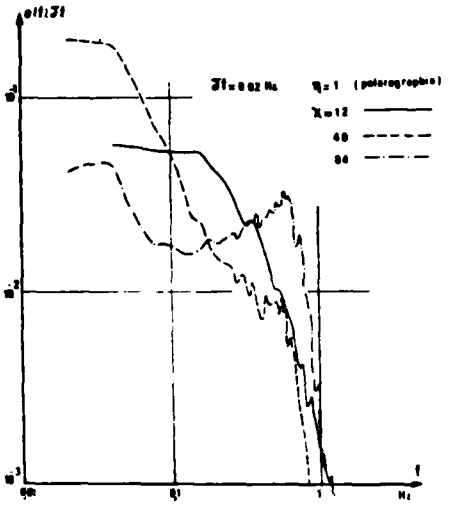

Fig. 3 Fluctuations of wall velocity gradient : Spectral analysis .

served at the wall on two points of a given generating line (ϑ_{sx}) or those observed on two points of the wall in a same section ($\vartheta_{s\gamma}$),or those observed on two points of the same diameter in the core ($\vartheta_{u\gamma}$) or on the wall and in the core (ϑ_{us}). The determination of the best incremental lags and of the corresponding correlation coefficients, as fonctions of the distance between two probes, allows the calculation of the velocities of the perturbations and a valuation of their zone of influence.

-Thus,within the first stage of the reorganization ($X < 25$), we can show that the velocity of axial propagation of the disturbances is almost constant in the whole section and is observed from the wall itself ; it corresponds to an eddy convection of which group velocity is equal to 0.9 time the mean velocity. The evolution,with η , of the best incremental lag of the functions ϑ_{us} and $\vartheta_{u\gamma}$ can be interpreted as a radial convective diffusion. Oriented from the core toward the wall, it is disclosed only in this stage of the reorganization and its velocity is equal to 0.1 time the mean velocity.

-Within the middle stage, ($25 < X < 75$), the measurements of axial velocity of propagation

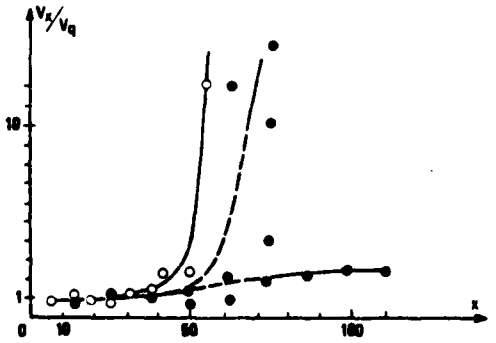

Fig. 4 Axial velocity of propagation :
○ Wall measurements ,
● Wall-Core measurements .

exhibit a change in the character of the parietal flow. Rapidly (near X = 50), a propagation mode of the disturbances with a very high velocity takes the place of the eddy convection (figure 4). This is characteristic of the setting up of a frozen flow. In the core, this second mode appears later and we observe this mode and the eddy convection simultaneously. The respective evolutions of the maxima of the functions ϑ_{us} show that fields containing frozen flow spread out to the detriment of turbulent fields (figure 5). Eddy convection is more and more confined to the axis of the pipe and its velocity approximate velocity on the axis (figure 4). During this transition , we attend the stabilization of the integral length scales and the disappearing of the radial diffusion .

-Within the last stage of the reorganization, the frozen flow get settled in the whole annular zone. Eddy convection is still disclosed near the axis, but its character is much less marked than this of the frozen flow. In this stage, the determination of the length or time scales leads to unsharp results by the fact that these scales loss their meaning in such a flow.

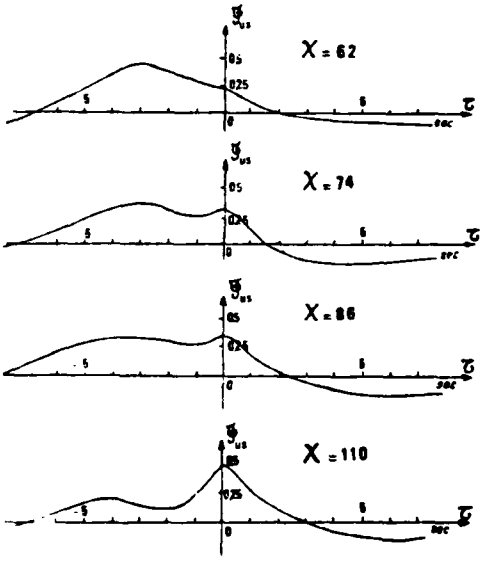

Fig. 5 Transversal intercorrelation us for X =0 and y*=0.5

The compiling of the coefficients $\vartheta_{u\gamma}$ measured without lag for different values of η and X gives space correlation functions along some diameter of the pipe. This study allows the determination of the transversal length scales of the perturbations ; it also reveals the general organizing of the flow. The result of this description seems to be that, in the middle stage, particularly between X =40 and X =70, the registered disturbances inside the flow, at =1/3 , are such than they oblige the surrounding flow to organize itself around them. At these distances, the axial scales are large and the frequencies of the fluctuations quite low. Then , we can think that, in this region, the flow is disturbed by long unsymmetrical structures of which effect must be observable on the velocity profiles .

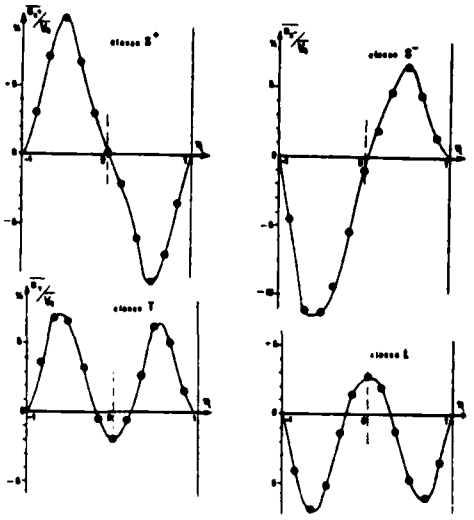

Fig. 6 Classification of velocity profile: for X = 39

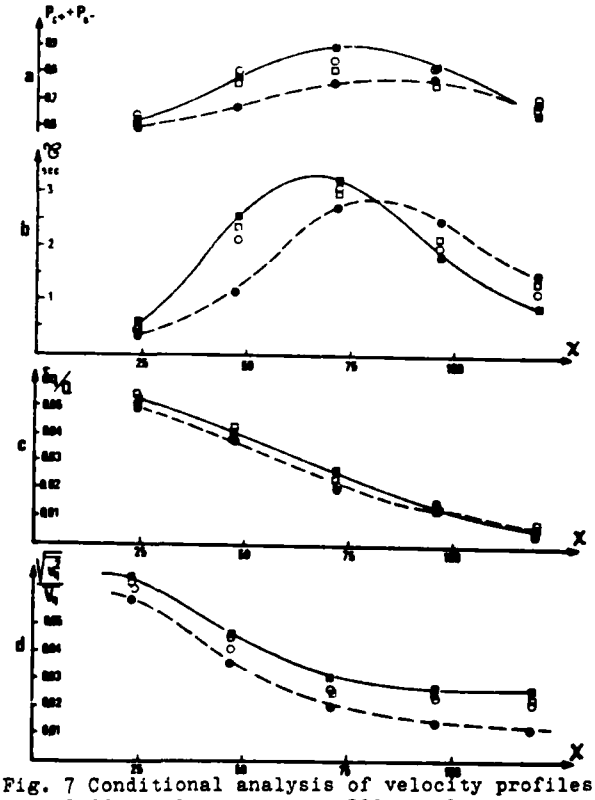

Fig. 7 Conditional analysis of velocity profiles
Sudden enlargment ; 30° enlargment
60° " ; progressive " (4°)
a- probability of occurence of asymmetrical flow
b- mean duration of asymmetrical flow
c- asymmetry of flow
d- fluctuations of the overall velocity.

CONDITIONAL ANALYSIS OF THE VELOCITY PROFILES

The eleven probes velocimeter, with his original conditionning, gives an off line restitution of the evolution with time of the instantaneous velocity profiles, for a given diameter. Downstream the sudden enlargment, the visualization of these profiles confirms that they exhibit unsymmetrical deformations, more or less durable and of variable significance, according to the observation abcissa. Besides, we noticed that they lead to admit, for the mean velocity, slow fluctuations of which amplitude is changing whith the abcissa (fig. 7-d). This result is not consistent with the law of continuity and we are then obliged to consider that the disturbances are generated by the travelling of structures with variable sizes and of which observation from a diameter of the pipe is incomplete. For determine their arrangement, we have normalized each profile by his mean velocity and, after difference with the mean profile, we have divided the results in four classes (fig.6):

- two classes S^+ and S^- which correspond to asymmetrical profiles
- the class L exhibits over-velocity near the axis
- the class T exhibits over-velocities near the wall.

Then, we have essentially studied the probability of occurence and duration of life of the S classes Upstream X = 20, the turbulent level of the flow does not allow any reading of this conditional analysis.

Downstream this abscissa, the increasing probability of occurence of asymmetrical flow (fig. 7-a) corresponds to the transversal spreading of the whirling structures. Simultaneously, we note (figure 7-b) a very important increasing of the mean duration of these periods ; this is the result of a lengthening of the structures, which can be explained only by their coalescence. Beyond 70 diameters, the opposite phenomena must, in return, reflect the breaking of the structures, which is probably due to a too weak energetic level. Indeed, when we study the evolution of the asymmetry of flow observed in the wake of area which shows overvelocity, we notice (fig. 7-c) the decreasing of this quantity during the last stage of the reorganization. Then, we may think that the axial and orthoradial spreading of the structures occurs with some degradation of their properties and that they disappear inside the reorganized frozen flow. In order to know if these structures are typical of such kind of singularity and have for exemple their beginning in the recirculatning zone, or if they are inherent in every turbulent-laminar transition, we have made the same measurements downstream enlargments with various angles. As Sibulkin's experiments foreshadowed it, the results of our mean measurements have shown, downstream X = 20 , a great similarity as much for the evolution of the velocity profiles as for those of relative turbulent intensity. In the same way, the results given by conditional analysis of the instantaneous velocity profiles (presented figure 7) shows the great similarity of behaviour of the flow downstream the different enlargments. Nevertheless, it seems that the structures observed downstream

the progressive (4 degrees) enlargment are slightly less developed and consequently less energetic than in the other cases. The greatest difference noted at the end of this analysis appears when we mesure the fluctuations of instantaneous overall velocity (fig. 7-d). But this difference must not be attributed to the reorganization itself ; indeed, having observed the similarity of the evolution laws of the r.m.s. values of these fluctuations, we have notice that this one is still a function of the enlargment shape for the great value of X. At these sections, it must be attributed to a weak pulsation inside the flow loop, which is a consequence of the interaction between the direct flow and the return flow. For a given flow rate, the amplitude of this pulsation must then depend on the loss of pressure through the whole loop and particularly across the singularity.

CONCLUSION

Downstream the zone where the flow is directly under the influence of the reciruclation or of the enlargment cone, we must consider three stages in the turbulent-laminar reorganization which is presented here.

- Within the first stage, for $X < 25$, if we notice an important degradation of turbulent energy, the mechanisms of production, diffusion and dissipation are present here and the fluctuating fiels seems to satisfy the pattern of turbulence. Nevertheless, the dissipation near the wall is so considerable that at the end of this stage, the mean wall velocity gradient reach a value close to the theoretical one obtained for laminar flow.
- In a second stage, for $25 < X < 75$, we notice the development, from the wall, of laminar areas which repulse and confine near the axis the pre-existing turbulence. Without any production, we observe a coalescence of the structures. Consequently, we observe the forming of stretched cells, of which passage through a given section marks the neighbouring flow.
- In the last stage of the reorganization, these structures have not enough energy to play a dynamic part in the flow. They break and disappear inside the reorganized frozen flow, which we may consider as laminar.

The whole resuls established lead us to think that these phenomena are characteristic of all turbulent-laminar transition downstream an enlargment in a pipe and that the shape of the singularity is determinant only for the value of the loss of pressure over a distance of about 20 diameters.

BIBLIOGRAPHY

1 Laufer J. "Decay of a nonisotropic turbulent fields." Mizzellaneen der Angerwandten Mechanik. Gottingen 1962 pp. 166-174

2 Sibulkin M. "Transition from turbulent to laminar pipe flow". The physics of fluids Vol 5 n° 3 1962 pp. 280-284

3 Lefort M. "Réorganisation d'un écoulement turbulent développé dans une conduite circulaire rectiligne". Thèse doctorat ès sciences 1973 NANCY

4 Vallette P. et Lebouché M. "Mise en évidence d'une phase instable dans la réorganisation en aval d'un élargissement brusque". C.R. Acad. Sc. Paris t. 287 série B 1978 pp 65-68

5 Vallette P., Lebouché M. et Martin M. "Etude spatio - temporelle de la réorganisation d'un écoulement en aval d'un élargissement brusque". Journal de Mécanique Appliquée. Vol. 3 n°4 1979 pp. 389-410

6 Mitchell J.E. and Hanratty T.J. "A study of turbulence at a wall using an electrochemical wall shear-stress meter". Journal of Fluid Mechanics. Vol. 26 part. 1. 1966 pp. 199-221

7 Sirkar K.K. and Hanratty T.J. "The limiting behaviour of the turbulent transverse velocity component close to a wall". Journal of Fluid Mechanics Vol. 44 part. 3. 1979 pp. 605-614

8 Fortuna G. and Hanratty T.J. "Frequency response of the boundary layer on wall transfer probes" International Journal of Heat and Mass Transfert.Vol. 14.1971 pp 1494-1507

9 Lebouché M. "Contribution à l'étude des mouvements turbulents des liquides par la méthode polarographique" Thèse doctorat ès sciences 1968 NANCY

10 Cognet G. "Contribution à l'étude de l'écoulement de Couette par la méthode polarographique". Thèse de doctorat ès sciences. 1968 NANCY

11 Delage Ph. "Contribution au développement de moyens de mesure adaptés à l'étude des écoulements turbulents au voisinage des parois". Thèse de docteur ingénieur 1978 NANCY

A PHYSICAL INTERPRETATION OF THE SPECTRA OF WALL TURBULENCE

by

A.E. PERRY & M.S. CHONG

University of Melbourne

ABSTRACT

Turbulence spectra, which has all the correct properties for wall turbulence, can be generated by the use of eddy signatures derived from potential flow vortices which have characteristic directions. The distribution of energy among the scales follows directly from the scaling laws needed to give the logarithmic mean velocity profile and constant Reynolds shear stress. The use of local isotropy and energy cascades do not appear to be relevant.

INTRODUCTION

Recent work at the University of Melbourne on turbulent spots has shown that a spot consists of a forest of "Λ" shaped vortices which are leaning in the downstream direction (see Perry, Lim and Teh (1)). This picture of wall turbulence is consistent with the smoke tunnel experiments of Bandyopadhyay and Head (2) and Head and Bandyopadhyay (3) who took laser beam cross-sections of eddies in a fully developed turbulent boundary layer. Perry and Chong (4) (see also Perry, Lim, Chong and Teh (5)) have shown that a physical model of wall turbulence can be constructed from this idea. It is assumed that vorticity and heat are carried away from the surface by hairpin or "Λ" shaped vortices which are being strained in a special way by their own mutual induction together with their images in the wall. This hypothesis has received encouraging support by Perry and Chong (4) who applied the Biot-Savart law to isolated "Λ" vortices.

This model is similar to Townsend's (6) attached eddy hypothesis. However, in the Perry and Chong model, eddies are stretched into elongated vortex pairs which cause them to "die" by vortex cancellation and so the resulting debris and fluid surrounding the more active Λ vortices is assumed to be irrotational. According to the smoke observations of Head and Bandyopadhyay (3), groups of vortices have a "granular appearance" with a characteristic direction and lean approximately at 45° in the downstream direction. Thus velocity signatures in wall turbulence can be generated by a forest of potential flow vortices.

Perry and Chong have shown that in order to obtain a logarithmic profile in mean velocity which extends to large $z_+ (= zU_\tau/\nu)$ for $\Delta_E U_\tau/\nu \to \infty$ (where z is the distance normal to the wall, U_τ is the friction velocity, ν is the kinematic velocity and Δ_E is the boundary layer thickness) it is necessary to have hierarchies of geometrically similar eddies with scales which are distributed in a geometrical progression and that a constant characteristic velocity scale for each hierarchy is needed to obtain a constant Reynolds shear stress through the logarithmic region. Figure 1 shows a discrete system of hierarchy scales, and it is conjectured that the smallest eddies in the first hierarchy scale according to the Kline (7) scaling on a smooth surface. Townsend (6) used a

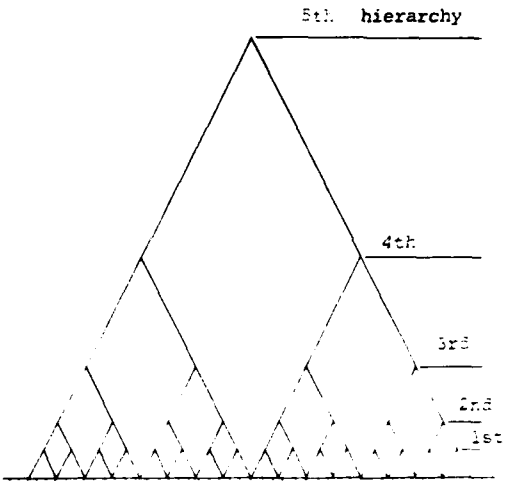

Fig.1 Symbolic representation of a discrete system of hierarchies. View looking downstream.

continuous inverse power law p.d.f. for the distribution of scales which is the continuous analog of the discrete geometrical progression. For simplicity, the authors are using the discrete distribution, where the scales are taken to go in "quantum" jumps with a factor of 2. This is consistent with the spread in hierarchy scales resulting from a vortex pairing process. However, this approach is not essential and other plausible mechanisms result in the continuous distribution of scales used by Townsend which leads to the same general conclusions. In the Perry and Chong model eddies in a given hierarchy are not geometrically similar since they are undergoing stretching. However, it is assumed that the hierarchies are geometrically similar and that the "representative" Λ vortex can be used for each hierarchy for the purposes of deriving spectra.

THE SPECTRUM OF WALL TURBULENCE

Fourier transforms and the power spectral density of signals produced by turbulence are very difficult to interprete or understand. Nevertheless, they are easy to measure and give an indication of how the energy is distributed among the scales. This work was motivated by the idea that modelling of wall turbulence should be consistent with measured spectra and should be linked to the broad-band and mean flow results.

Unlike models of the past, local isotropy is no longer operative and a new explanation or argument must be devised for the existence of the -5/3 law.

At high frequencies or wave numbers, the power spectrum is influenced mainly by the shape of the eddy signatures while at lower wave numbers or frequencies, the spectrum is influenced more by how the energy is distributed among the scales. The detailed shape of the signatures become unimportant at these lower wave numbers. One very useful rule (Bracewell (6)) for the high frequency end of the spectrum is that if n is the number of times one has to differentiate a signal to convert it to a delta function, then the smoothed power spectral density P(k) will asymptote to a law, $P(k) \sim k^{-2n}$. Here k is the wave number or frequency. It has been felt by many workers (eg. see Townsend (6)) that the finest scale motions of turbulence are generated by vortex sheets passing the hot wire probe and these dissipate the energy of turbulence. From the flow visualization work of Head and Bandyopadhyay (3) and Perry, Lim and Teh (1) these vortex sheets are wound up into rods. The rods could be thought to consist of a "scroll" of vortex sheet material. As such rods are cut through by a sensing probe, the high-pass filtered signal will be of a saw-tooth form provided the vortex sheets are very thin and sharp. Using the Bracewell rule, this should give $P(k) \sim 1/k^2$. This scroll could be something like a Kaden spiral (eg. see Pullin Phillips(9)) and one would intuitively feel that since the signature of this is one scale removed from the scale of the sheet itself, then this should be responsible for the -5/3 law. With viscous diffusion the sheet will not be perfectly sharp and at very high wave numbers, the waveform would appear to have the properties of a triangular wave. Using the Bracewell rule, this leads to $P(k) \sim 1/k^4$. It can be seen that the -5/3 law simply does not fit into this scheme. Out of curiosity, the authors devised a wave form with a -5/3 law spectrum to see what it might look like. Using the Bracewell rule, together with the concept of "fractional differentiation", a wave with a 1/6th power-law cusp would give the required result. This needs to be differentiated "5/6th times" to give n = 5/6 and hence the -5/3 law. This was also checked numerically using a fast Fourier transform computer program. It seems unlikely that the -5/3 law comes from such eddy signatures. Rather, if it exists, it seems more likely to be related to the distribution of scales of signatures.

The authors found that a far more fruitful approach to the question was to ignore the details of the rods altogether, or at least assume that the vorticity is smeared out to give a region of solid body rotation within the rod. It is found that all of the salient properties of the spectrum can be generated from the signatures and distribution of the signatures existing in the irrotational fluid surrounding the vortex rods.

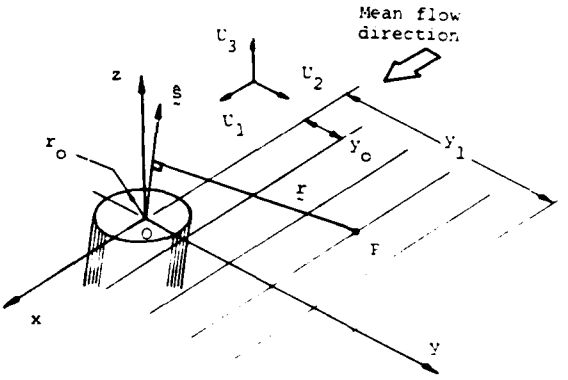

Fig.2 Definition of coordinates and vectors for velocity signature analysis.

In order to keep the description simple and analytical, some simplifications will be made. Let it be assumed that the spectral contributions from each hierarchy can be derived from one representative eddy. Figure 2 shows one "leg" of the eddy being sectioned by a plane of constant z. If we imagine we have a hot-wire probe held stationary and the eddy being convected past in the x direction, then the signature as seen by the probe can be calculated by determining $\underline{U}$ along the lines of constant y in the xy plane. To avoid the complications involved with convection velocities, imagine that the vector field is temporarily "frozen" and the signatures will be decomposed in terms of x component wave number k.

By applying the Biot-Savart law, it can be shown

$$\underline{U} = \frac{K}{2\pi} \frac{(\underline{\hat{s}} \times \underline{r})}{|\underline{r}|^2} \quad \text{for } |\underline{r}| > r_c$$

$$\underline{U} = \frac{K}{2\pi} \frac{(\underline{\hat{s}} \times \underline{r})}{r_c^2} \quad \text{for } |\underline{r}| < r_c \qquad (1)$$

where K is the circulation of the vortex rod and r_c is the rod radius. All other symbols are defined in figure 2.

We will imagine that we are making a series of "cuts" of uniform probability between $y_c (= r_c)$ and y_1. The magnitude of the signatures reaches a maximum at y_o and for $0 < y < y_o$ it drops rapidly to zero for the U_1 component for all x. The distance y_1 represents the maximum distance from the rod we can go before experiencing the influence of the other legs or the legs of other vortices. The analysis is therefore using the signatures of one isolated rod. Of course, in future studies, the full vortex and arrays of such vortices should be used in a computer simulation.

Equation (1) gives the following velocity signature for U_1

$$U_1 = -\frac{\zeta}{y} \left\{ \frac{1}{x_*^2 + h^2} \right\} \qquad (2)$$

where $Q = \frac{KA_1h^2}{2\pi g}$ where A_1, h and g are constants which depend on direction cosines of vector $\tilde{s}$. This is expressed in its simples form by an appropriate choice of the origin for x. Also $X_* = (x-a)/y$, where a is the shift in the origin for x and a/y depends on the direction cosines. It can be shown that the amplitude of the signature $\sim 1/y$.[+] The U_1 signature is an even "bell-shaped" function and the other components are a combination of an even and an odd function.

The Fourier transform of the U_1 velocity signature defined by

$$X_1(k) = \int_{\infty}^{\infty} U_1(x)\, e^{ikx}\, dx \qquad (3)$$

turns out to be

$$X_1(k_1) = - \frac{Q}{h}\, e^{-k_1 y} \qquad (4)$$

where $k_1 = kh$, h being a constant of order unity and depends on direction cosines of the vector $\tilde{s}$. It can be shown that the functional form given by (4) is applicable for all three components of velocity.

Consider only the U_1 signature given by equation (4). This is the Fourier transform of a transient pulse and if a train of such pulses are arranged randomly in the x direction with a mean spacing S, it can be shown that the power spectral density is given by

$$P(k_1,y) = \frac{2\pi |X_1(k_1,y)|^2}{S} \qquad (5)$$

This will be true provided cross products between neighbouring pulses make no contribution to the spacially averaged two-point correlation coefficient for points separated along the x direction. However, if this is not true, then the power spectral density may have to be smoothed.

It will be assumed that the contribution to spectral energy by "cuts" $y < y_o$ are negligible.

Imagine that we have a collection of signature trains all at different y and given the probability of all "cuts" in the interval $0 < y < y_1$ are equally likely, it can be shown that the ensemble averaged or smoothed power spectral density is then given by

$$F(k_1) = \frac{1}{y_1} \int_{y_o}^{y_1} P(k_1,y)\, dy \qquad (6)$$

[+] The symbol "$\sim$" means "to scale with".

From equations (5) and (6)

$$F(k_1) = \frac{1}{y_1}\, \frac{\pi^3 Q^2}{S}\, \frac{1}{k_1 h^3} \left\{ e^{-2k_1 y_o} - e^{-2k_1 y_o (y_1/y_o)} \right\} \qquad (7)$$

Since all hierarchies are geometrically similar, all length scales will scale with y_o and Q will scale such that $Q \sim U_\tau y_o$ where U_τ is the characteristic velocity scale of all the hierarchies.

Let equation (7) represent the smallest observed hierarchy which will be labelled n=1. If the total number of observed hierarchies is N_o, the resulting power spectral density Φ will be given by

$$\frac{\Phi(k_1 y_o)}{U_\tau^2} \sim \sum_{n=1}^{N_o} \frac{1}{k_1 y_o} \left\{ e^{-2k_1 y_o 2^{(n-1)}} - e^{-2k_1 y_o (y_1/y_o) 2^{(n-1)}} \right\} \qquad (8)$$

Here Φ is the energy per unit non-dimensional wave number $k_1 y_o$. The scale y_o for the n^{th} hierarchy is $y_o 2^{(n-1)}$.

From figure 1, it can be seen that as we go away from the wall, the total number of observed hierarchies diminishes, i.e. N_o decreases. Also, y_o is the smallest length scale of the smallest observed hierarchy and this will decrease as we approach the wall and the smallest value will be proportional to the Kline scaling on a smooth surface. The ratio y_1/y_o will be universal and is associated with the geometry of the representative eddy of a given hierarchy. A continuous distribution of scales would give much the same result but an exponential integral is involved.

Figure 3 shows equation (8) for different hierarchies with $y_1/y_o = 11$, i.e. it is assumed that the rod diameter to leg spacing is of this order. It can be seen that as the wave number is decreased, the spectrum goes from an "exponential-like" law to a -1 power law with a short section which could be interpreted as a -5/3 law. However, the authors feel that this is not of significance and that the law where the various hierarchies "peel-off" is the -1 power law. The scale y_1 determines the low wave-number cut-off or "levelling-out" and y_c determines the high wave-number "cut-off". The spectral results of Perry and Abell (10) taken in the wall region of a pipe are shown in figure 4. The existence of a -1 power law is obvious. This law was deduced by Perry and Abell by a "region of overlap" argument based on dimensional analysis. The departure from the -1 power law occurs at approximately $k_1 z = 1$ in the experiments and at $k_1 y_o \approx 10^{-1}$ according to equation (8). This implies that at level z, the smallest "representative eddy" of significance has $y_1 \approx O(z)$. This is of the right order.

It is very instructive to look at spectra far from the wall. Here, the number N_o of observed hierarchies falls off considerably and the spectra should follow the pattern given in figure 4. Figure 5(a) shows some results of Abell and Perry (11) for a smooth pipe. Again, the similarity with the computed results given in figure 3 is very encouraging. As

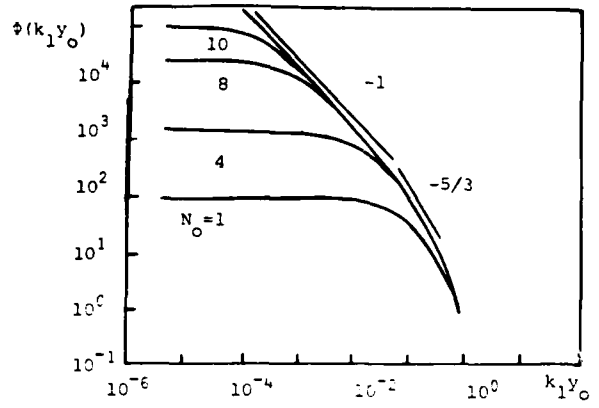

Fig. 3. Equation (8) for various number of observed hierarchies. Log Φ $(k_1 y_o)$ versus log $(k_1 y_o)$. $y_1/y_o = 10$.

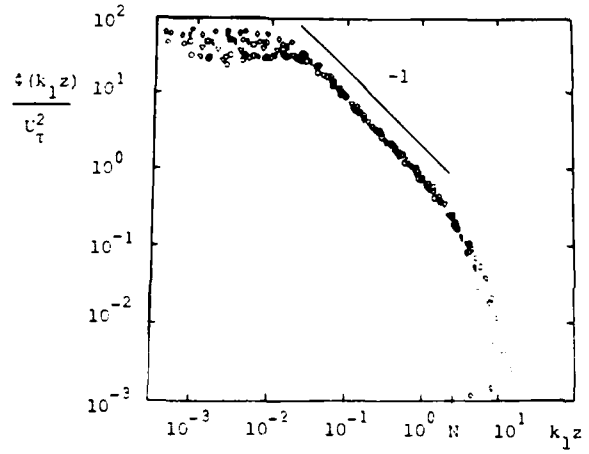

Fig. 4. Smooth-wall longitudinal spectra for the wall similarity range $z_+ > 100$ and $z/R < 0.1$. Reynolds number range = 80×10^3 to 260×10^3, symbols as for figure 11 of Perry and Abell(12). R is the pipe radius.

Here $\int_0^\infty \Phi(k_1 z)\, d(k_1 z) = \overline{u_1'^2}$ †

a matter of interest, figure 5(b) shows some rough wall results taken outside the wall similarity region. The results show a similar behaviour. We would expect the smallest hierarchy scale y_o or y_1 at the wall to scale with k, the roughness scale. Unfortunately, no measurements exist for the wall similarity region for this case.

The model is of course simplified. Spectral information concerned with the vortex shape and the vortex stretching process is missing. However, the authors contend that the inclusion of this information will not alter the general behaviour and will simply be hidden or "buried" in the -1 law region or else will be removed by smoothing.

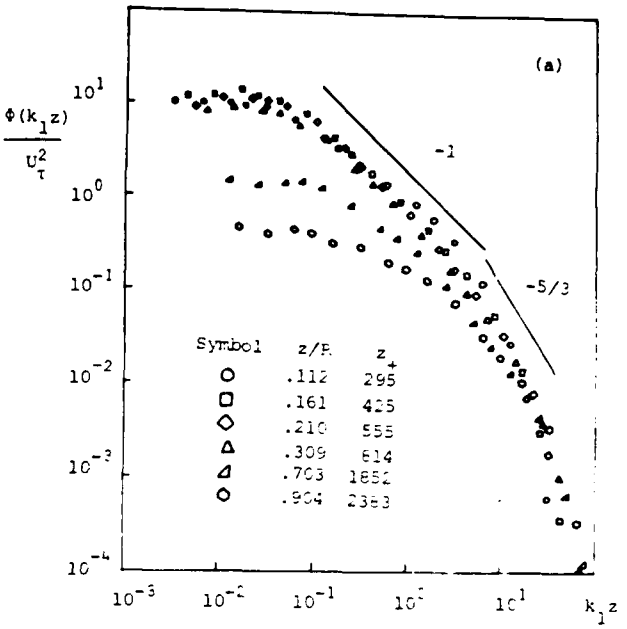

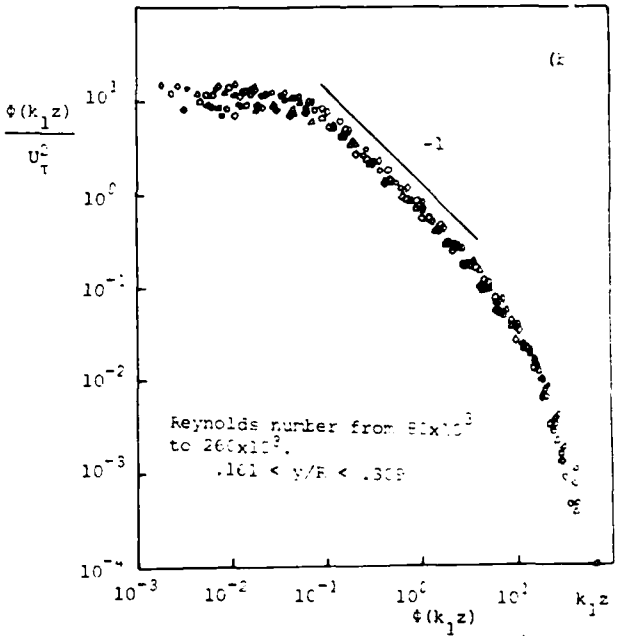

Fig. 5. Measured spectrum function $\frac{\Phi(k_1 z)}{U_\tau^2}$ in a pipe for regions beyond the wall similarity zone. (a) Smooth pipe. (b) Rough pipe.

Here $\int_0^\infty \Phi(k_1 z)\, d(k_1 z) = \overline{u_1'^2}$

† $\overline{u_1'^2}$ is the broad-band turbulent intensity distribution.

The scaling of the Perry and Abell (10) results given in figure 5 suggest that for the wall region but beyond the buffer zone,

$$\frac{\Phi(k_1 z)}{u_\tau^2} = f(k_1 z) \qquad (9)$$

and this appears valid right up to high wave-numbers. This is reasonable since at a given z, the smallest eddy of significance observed will scale approximately with z since, if it is smaller, it will not be seen and if it is larger, it will not be the smallest eddy.

In the energy containing region

$$\frac{\Phi(k_1 z)}{u_\tau^2} = \frac{A}{k_1 z} \qquad (10)$$

where A is a universal constant. Equations (9) and (10) lead to the Townsend result for the broad-band turbulence intensity distribution thus;

$$\frac{\overline{\partial u'^2}}{\partial z} = -\frac{A u_\tau^2}{z} \qquad (11)$$

Although Perry and Abell (10) also incorporated the -5/3 law in their scaling scheme by a further "region of overlap" argument, it would appear that this law is a "red herring", at least in wall turbulence. However, the existence of the law is very obvious in other types of turbulence. If we return to equation (8) and redistribute the energy among the hierarchies such that

$$\frac{\Phi(k_1 y_o)}{u_\tau^2} = \sum_{n=1}^{N_o} \frac{\frac{2}{3}(n-1)}{k_1 y_o} \left\{ e^{-2k_1 y_o 2^{(n-1)}} - e^{-2k_1 y_o (y_1/y_o) 2^{(n-1)}} \right\} \qquad (12)$$

then one obtains a family of spectra for different N_o as shown in figure 6. All low wave number "peel-off's" occur from a -5/3 line. Figure 7(a) shows a turbulent jet. The eddy structure in this jet is quite granular with a characteristic direction but the resulting spectra given in figure 7(b) shows an extensive -5/3 law without any evidence of a -1 law. Thus, it would appear that there are different sorts of turbulence and the -5/3 law results from a different distribution of energy from that found in wall turbulence. This probably is related to the fact that in wall turbulence, new vorticity is continually being generated at the wall, whereas in a jet, no further vorticity is generated beyond the jet outlet. The physical reasons for the -5/3 law distribution need to be pursued.

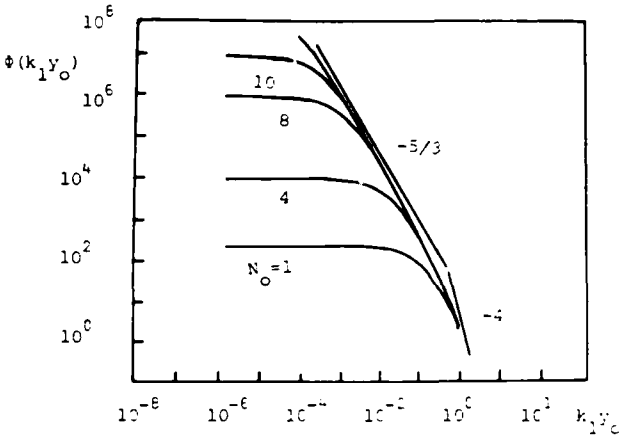

Fig.6. Equation (12) for different number of observed hierarchies.

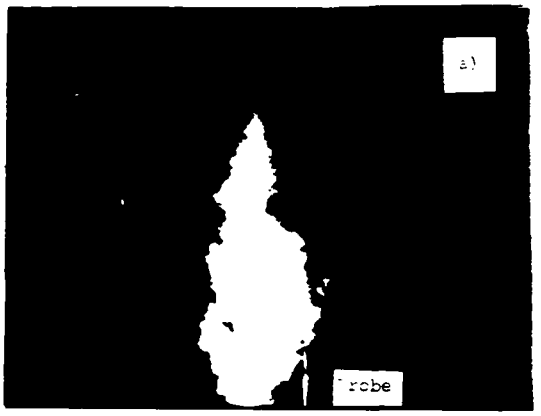

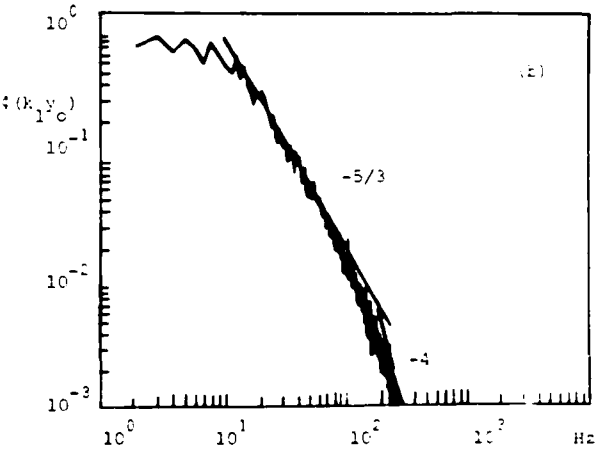

Fig.7. Turbulent jet.
(a) Flow pattern.
(b) Measured spectrum; ensemble average of 40 runs.
Reynolds number based on tube outlet diameter = 3000.

CONCLUSION

By modelling the turbulent boundary layer as a forest of Λ shaped vortices and without the use of local isotropy, the spectrum of wall turbulence can be derived from the signatures and distribution of the signatures in the irrotational fluid surrounding the legs of the vortices. A comparison of the generated spectra with experimental spectra is encouraging. The results show that for wall turbulence, the law where the various hierarchies "peel-off" is the -1 power law and an "exponential like" law is obtained in the so-called dissipation region. By redistributing the energy among the hierarchy scales, the -5/3 power law replaces the -1 law and this has been observed in jets.

ACKNOWLEDGEMENTS

The authors wish to acknowledge the financial assistance of the Australian Research Grants Committee, The National Energy Research, Development and Demonstration Council and the Australian Institute of Nuclear Science and Engineering.

References

1. Perry, A.E., Lim, T.T. and Teh, E.W. "A visual study of turbulent spots". Journal of Fluid Mechanics, Vol.104, 1981, pp.285-403.

2. Bandyopadyay, P. and Head, M.R. "Visual investigation of turbulent boundary layer structure". Engineering Department, Cambridge. (Film) 1979.

3. Head, M.R. and Bandyopadhyay, P. "New aspects of turbulent boundary layer structure". Journal of Fluid Mechanics, 1981 (in the press).

4. Perry, A.E. and Chong, M.S. "On the mechanism of wall turbulence". Submitted to Journal of Fluid Mechanics, 1981.

5. Perry, A.E., Lim, T.T, Chong, M.S. and Teh, E.W. "The fabric of turbulence". AIAA 13th Fluid and Plasma Dynamics Conference, July, 1980, Snowmass, Colorado.

6. Townsend, A.A. The structure of turbulent shear flow. Cambridge University Press, 1976.

7. Kline, S.J. "Observed structural features in turbulent and transitional boundary layers". Fluid Mechanics of Internal Flow. (ed. G. Sovran), Elsevier, Amsterdam, 1967.

8. Bracewell, R.N. The fourier transform and its application. McGraw-Hill Book Company, 1978.

9. Pullin, D.I. and Phillips, W.R.C. "On the generalization of the Kaden's problem". Journal of Fluid Mechanics, Vol.104, 1981, pp.45-53.

10. Perry, A.E. and Abell, C.J. "Asymptotic similarity of turbulence structures in smooth-and rough-wall pipes". Journal of Fluid Mechanics, Vol.79, 1977, pp.785-799.

11. Abell, C.J. and Perry, A.E. "Smooth and rough wall pipe flow longitudinal turbulence spectral data" Internal Report FM-6, Department of Mechanical Engineering, University of Melbourne, 1976.

12. Perry, A.E. and Abell, C.J. "Scaling laws for pipe flow turbulence". Journal of Fluid Mechanics, Vol.67, 1975, pp.257-271.

THEORETICAL PREDICTION OF CONFLUENT BOUNDARY LAYERS

by
G. W. Brune
Boeing Commercial Airplane Company
Seattle, Washington

ABSTRACT

A computational method for the prediction of confluent boundary layer flow is presented, as it may exist on the upper surface of slotted multielement airfoils operating at low speeds. The method is based on the twodimensional incompressible form of the turbulent boundary layer equations, and the two-equation turbulence model of Jones and Launder, modified to account for the effect of curved airfoil surfaces. A Crank-Nicholson-type finite difference solution is employed together with law of the wall boundary conditions. This paper emphasizes those aspects of the computational method and turbulence model which are important in engineering applications: the proper choice of initial values; the validity of the law of the wall boundary conditions; and the limitation of the streamwise step size due to the turbulence model. Test-theory comparisons for streamwise velocities, turbulent shear stress, and turbulent kinetic energy of confluent boundary layers are also included.

NOMENCLATURE

C	law of the wall constant
C_1, C_2, C_μ, C_ϵ	empirical coefficients of turbulence model
k	turbulent kinetic energy
N	number of grid points normal to surface
O, P, Q, R	coefficients of algebraic equations
P	time average of static pressure
R	radius of surface curvature
$Re_{\Delta x}$	step size Reynolds number
S_t	grid stretch factor
U, V	streamwise and normal components of mean velocity
u_τ	friction velocity
$\overline{uv}$	Reynolds shear stress
x,y	streamwise and normal coordinates
Δx	step size in streamwise direction

Greek Symbols

δ	boundary layer thickness
δ^*	displacement thickness
ϵ	dissipation of turbulent kinetic energy
$\eta = y/\delta^*$	
κ	law of the wall constant
ν	kinematic viscosity of air
ν_τ	eddy viscosity
ρ	density
σ_k, σ_ϵ	empirical coefficients of turbulence model
τ_τ	turbulent shear stress
ϕ	general dependent variable

Superscript and Subscripts

$\overline{(\ )}$	variable at midpoint of step Δx
e	outer edge of boundary layer
p	potential flow velocity
s	value at surface

INTRODUCTION

Confluent boundary layers form when turbulent wakes merge with adjacent turbulent boundary layers. Such turbulent wall shear layers may exist on the upper surface of slotted multielement airfoils. Figure 1 shows an example of this type of shear layer on an airfoil consisting of a wing section with a slotted leading edge flap and a double slotted trailing edge flap. Profiles of streamwise velocity and Reynolds stresses of confluent boundary layers are very complex.

The occurrence of confluent boundary layers depends on the number of airfoil elements, their shapes and relative positions, and on flight condition. Angle of attack and the gap between adjacent airfoil elements are the main parameters determining their formation.

Figure 2 illustrates how the lift of a slotted two-element airfoil changes with the size of the gap between the wing section and the flap (ref. 1). In this figure, the airfoil lift is compared with the lift that the same airfoil would generate in a hypothetical potential flow field. The

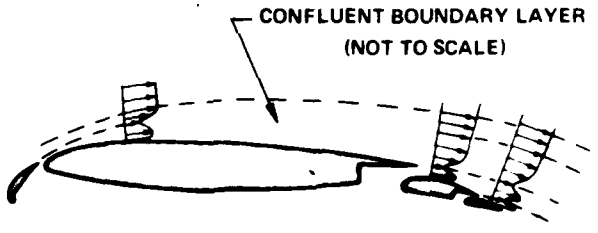

Figure 1.–Confluent Boundary Layer on Upper Surface of Slotted Multielement Airfoil

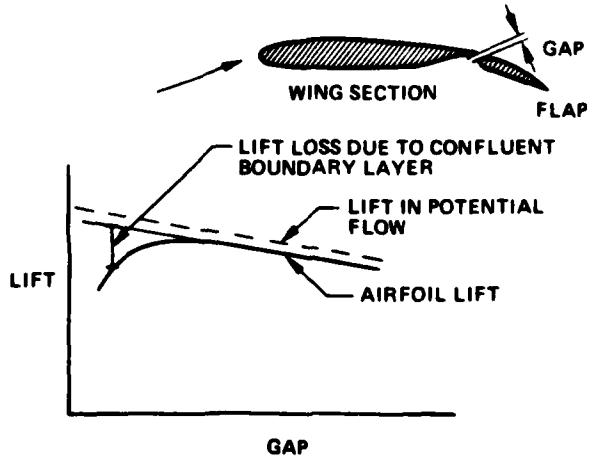

Figure 2. – Viscous Lift Loss of Slotted Airfoil at Constant Angle of Attack Below Stall

viscous lift loss is defined as the difference between the potential flow lift and the true airfoil lift. At a constant angle of attack well below stall, airfoil lift varies nonlinearly with gap size. The optimum gap size corresponds to a flow situation, where the wake of the wing section is divided from the boundary layer on the upper flap surface by a region of inviscid flow, and merging of the two layers begins in the vicinity of the flap trailing edge. At smaller gaps, a confluent boundary layer forms further upstream causing significant viscous lift losses. At larger than optimum gaps, lift again decreases, but at a rate predicted by potential flow theory, the associated viscous lift losses being due to ordinary boundary layers.

The method described in this paper was designed to predict, with the same degree of computational efficiency and accuracy, both the confluent boundary layer of a two-element airfoil and more complex flow situations resulting from a larger number of merging shear layers. This requirement excluded the use of algebraic turbulence modeling and integral solutions. Instead, a high degree of flexibility was achieved by the choice of a two-equation turbulence model in conjunction with a finite difference solution.

Several other confluent boundary layer methods are available for applications to multielement high-lift airfoils (refs. 2 and 3).

COMPUTATIONAL METHOD

Mean Flow Equations

The equations are chosen on the basis of the following assumptions:

a) The mean flow is twodimensional and incompressible.
b) Boundary layer approximations apply.
c) The radius of surface curvature R is of the order of the airfoil chord length.
d) The boundary layer thickness δ is small by comparison with the local value of R.

Hence, the equations governing the mean flow read:

$$\frac{\partial U}{\partial x} + \frac{\partial V}{\partial y} + O\left(\frac{\delta}{R}\right) = 0 \tag{1}$$

$$U\frac{\partial U}{\partial x} + V\frac{\partial U}{\partial y} = -\frac{\partial}{\partial x}\left(\frac{P}{\rho}\right) + \frac{\partial}{\partial y}\left(\nu_T \frac{\partial U}{\partial y}\right) + O\left(\frac{\delta}{R}\right) \tag{2}$$

$$\frac{\partial}{\partial y}\left(\frac{P}{\rho} + \frac{2}{3}k\right) = \frac{U^2}{R} + O\left(\frac{\delta}{R}\right) \tag{3}$$

Here, the x, y-coordinates are measured in the streamwise direction and normal to the surface. The symbols U, V, P, and ρ denote mean values of streamwise and normal velocity components, static pressure, and density of air, respectively. The equations are written in a form anticipating application of the high Reynolds number version of the k, ϵ-model of turbulence to provide the eddy viscosity ν_T and the turbulent kinetic energy k.

The mean flow equations are simplified by noting that the x-momentum equation (2) does not contain explicit surface curvature terms and, consequently, uncouples from the y-momentum equation (3). The latter equation, therefore, can be solved separately (ref. 4) to obtain the pressure gradient in streamwise direction as a function of the potential flow velocity U_e at the outer edge of the boundary layer.

$$-\frac{\partial}{\partial x}\left(\frac{P}{\rho}\right) = U_e\frac{dU_e}{dx} + O\left(\frac{\delta}{R}\right) \tag{4}$$

In deriving this equation from the y-momentum equation, turbulent kinetic energy terms have been neglected, consistent with the order of the neglected terms of the x-momentum equation. Equation (4) is also the correct limiting form of the x-momentum equation at the outer edge of the boundary layer.

Turbulence Model

The k, ϵ-model of turbulence (refs. 5, 6, 7), modified to account for moderately curved convex surfaces, is employed to compute the eddy viscosity ν_T. For curved surfaces, ν_T is defined by the following equation for the turbulent shear stress τ_T:

$$\frac{\tau_T}{\rho} = \nu_T\left(\frac{\partial U}{\partial y} - \frac{U}{R+y}\right) \tag{5}$$

In the k, ϵ-model, ν_T is obtained from:

$$\nu_T = C_\mu\frac{k^2}{\epsilon} \tag{6}$$

where the turbulent kinetic energy k and its dissipation ϵ, in turn, are computed from the following conservation equations, written in boundary layer form.

$$U\frac{\partial k}{\partial x} + V\frac{\partial k}{\partial y} = \frac{\partial}{\partial y}\left(\frac{\nu_T}{\sigma_k}\frac{\partial k}{\partial y}\right) + h\nu_T\left(\frac{\partial U}{\partial y} - \frac{U}{R+y}\right)^2 - h\epsilon + O\left(\frac{\delta^2}{R}\right) \tag{7}$$

$$U\frac{\partial \epsilon}{\partial x} + V\frac{\partial \epsilon}{\partial y} = \frac{\partial}{\partial y}\left(\frac{\nu_T}{\sigma_\epsilon}\frac{\partial \epsilon}{\partial y}\right) + C_1^*\frac{\epsilon}{k}h\nu_T\left(\frac{\partial U}{\partial y} - \frac{U}{R+y}\right)^2 - hC_2\frac{\epsilon^2}{k} + O\left(\frac{\delta}{R}\right) \tag{8}$$

$$\text{with} \quad h = 1 + \frac{y}{R}$$

These equations predict the effect of surface curvature in two ways. First, by formal surface curvature terms in their production and destruction terms which, as is well known (refs. 4, 6), will only account for a small part of the total curvature effect. Second, by an empirical correction of the production term of the dissipation equation (8) The coefficient C_1 of the basic form of the k, ϵ-model is redefined to be a linear function of the term $(k/\epsilon)(U/(R+y))$.

$$C_1^* = C_1\left(1 + C_R\frac{k}{\epsilon}\frac{U}{R+y}\right) \tag{9}$$

C_R is an empirical coefficient whose value is given below for convex curvature. There is no theoretical justification for this particular empirical correction, but the term $(k/\epsilon)(U/(R+y))$ is the simplest possible nondimensional group that can be formed with the main variables. The reader should note that for positive values of C_R, the above empirical correction will increase the dissipation on convex surfaces where R is defined to be positive. This, in turn, will decrease turbulent kinetic energy and shear in agreement with the physics of curved turbulent shear flows (ref. 4).

The six empirical coefficients of the turbulence model are:

$C_\mu = 0.09$ $\sigma_k = 1$ $\sigma_\epsilon = 1.3$ $C_1 = 1.44$ $C_2 = 1.92$ $C_R = 1.25$

The described high Reynolds number form of the k, ϵ-model is not valid in the viscous sublayer and, therefore, can only be used with a wall function method such as the one discussed below.

Wall Function Method

A wall function method, in which the law of the wall boundary conditions are applied outside the viscous sublayer, is utilized to ensure the computational efficiency of the prediction method. A finite difference solution of the flow in the sublayer, where flow variables change rapidly in direction normal to the surface, would require additional computational grid points and would, therefore, increase computer time and storage.

A two-point technique, illustrated in figure 3, is used to patch the logarithmic profile of the streamwise velocity to the outer part of the boundary layer. The velocity profile is assumed to be logarithmic at the two computational grid points closest to the surface. Neglecting the effect of surface curvature on the law of the wall, the boundary conditions at grid point 1 can be stated as:

$$U_1 = u_\tau\left(\frac{1}{\kappa}\ln\frac{y_1 u_\tau}{\nu} + C\right) \tag{10}$$

$$k_1 = \frac{u_\tau^2}{C_\mu^{1/2}} \tag{11}$$

$$\epsilon_1 = \frac{u_\tau^3}{\kappa y_1} \tag{12}$$

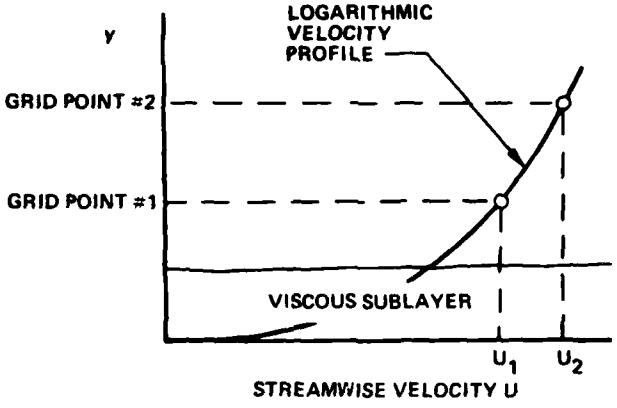

Figure 3. – Two-Point Wall Function Method

These boundary conditions are expressed in terms of the friction velocity ($u_\tau = \sqrt{\tau_s/\rho}$, with τ_s being the shear stress at the surface), which is obtained from the assumption that the velocity profile is logarithmic at grid point 2.

For ordinary boundary layers on smooth surfaces, the law of the wall constants are approximately $\kappa = 0.4$ and $C = 5.5$. The corresponding values for confluent boundary layers are not well known but are most likely affected by the merging of the shear layers. In the absence of any better information, the values cited for ordinary boundary layers have been used for all computed results presented in this paper.

Outer Edge Boundary Conditions

At the outer edge of the boundary layer (subscript e), the boundary conditions $k_e = 0$ and $\epsilon_e = 0$ are chosen for convenience (ref. 8).

The edge velocity U_e for curved surfaces is obtained from the surface value of the potential flow velocity U_{ps} using the relation

$$\frac{U_e}{U_{ps}} = \frac{R}{R+\delta} + O\left(\frac{\delta^2}{R^2}\right) \tag{13}$$

Finite Difference Solution

The equations governing mean flow and turbulence are parabolic, therefore they can be solved by stepping along the surface beginning with known boundary layer profiles at the upstream surface station.

In order to implement the finite difference solution, the equations are discretized in x, η-coordinates, where $\eta = y/\delta^*(x)$. Here, the displacement thickness δ^* is being used as a convenient reference variable to enlarge the grid point spacing in the physical domain, in regions of increasing boundary layer thickness. δ^* is defined by

$$\delta^*(x) = \int_0^\delta \left| 1 - \frac{U}{U_p} \right| dy \tag{14}$$

with U_p representing the local potential flow velocity. Note that taking the absolute value of the integrand avoids zero and negative values of δ^* for confluent boundary layers.

The grid point spacing in the computational domain can be varied in the direction of the surface normal using a suitable stretch factor S_f. Grid point coordinates are obtained from $\eta_{j+1} = \eta_j + S_f(\eta - \eta_j)$, $j = 2, 3, \ldots N-1$.

The equations are solved employing a modification of the Crank-Nicholson finite difference method due to Mellor and Herring (ref. 9). Briefly, the governing equations are written at the midpoint between two consecutive surface stations x_{i-1} and x_i. Denoting by ϕ any dependent variable or term of the equations, the value and x-derivative of ϕ at this midpoint are

$$\bar{\phi} = \frac{1}{2}\left(\phi_i + \phi_{i-1}\right) \qquad \frac{\overline{\partial\phi}}{\partial x} = \frac{\phi_i - \phi_{i-1}}{x_i - x_{i-1}} \tag{15}$$

The η- derivatives of ϕ at any surface station are expressed by central differences as follows:

$$\left.\frac{\partial\phi}{\partial\eta}\right|_j = \frac{\phi_{j+1} - \phi_{j-1}}{\eta_{j+1} - \eta_{j-1}} \tag{16}$$

$$\frac{\partial}{\partial\eta}\left(\nu_T \frac{\partial\phi}{\partial\eta}\right)_j = \frac{(\nu_T)_{j+1/2}\dfrac{\phi_{j+1} - \phi_j}{\eta_{j+1} - \eta_j} - (\nu_T)_{j-1/2}\dfrac{\phi_j - \phi_{j-1}}{\eta_j - \eta_{j-1}}}{\frac{1}{2}(\eta_{j+1} - \eta_{j-1})} \tag{17}$$

with $2(\nu_T)_{j+1/2} = \nu_{T_{j+1}} + \nu_{T_j}$ and $2(\nu_T)_{j-1/2} = \nu_{T_j} + \nu_{T_{j-1}}$

Assuming that all variables are known at the previous station x_{i-1}, their values at the new station, $x_i = x_{i-1} + \Delta x$, are computed by solving the algebraic equations which result from the outlined finite difference approximations. The x- momentum equation and the k, ϵ-equations have the general form

$$O_j \phi_{ij+1} + P_j \phi_{ij} + Q_j \phi_{ij-1} = R_j \tag{18}$$

where ϕ_{ij} stands for any of the unknown variables U_{ij}, k_{ij}, ϵ_{ij}. These equations are nonlinear since the coefficients O, P, Q, R are functions of the unknowns and, hence, are solved iteratively at each surface station.

Initial Values

The solution method requires initial values of all boundary layer variables at the upstream surface station (subscript 1). Two options are provided, one requiring a complete set of boundary layer profiles consisting of streamwise velocity $U_1(y)$, kinematic Reynolds shear stress $\overline{u_1 v_1}(y)$, and turbulent kinetic energy $k_1(y)$. In this case, an initial profile of the dissipation $\epsilon_1(y)$ is computed from the input values combining equations (5) and (6) with $\tau_T = -\rho\overline{uv}$.

Since in many cases, turbulence data are not available to start the computation, a second option is provided in which only the streamwise velocity profile $U_1(y)$ is required. Profiles $k_1(y)$ and $\epsilon_1(y)$ are generated by solving the k, ϵ-equations (7) and (8) assuming that U, k, ϵ are functions of the independent variable η only, i.e., similar profiles are assumed.

NUMERICAL PROPERTIES

Surface Curvature

The described modification of the k, ϵ-turbulence model for the effect of surface curvature differs from other methods such as the one of Launder et al. (ref. 6). For this reason, the results of the test-theory comparison used to calibrate the method are discussed. The empirical curvature coefficient C_R has been determined on the basis of the experimental data of So and Mellor (ref. 10) for a turbulent boundary layer developing on a convex surface. This test case is well suited for such a calibration since the boundary layer thickness is about 10 percent of the local radius of surface curvature, a ratio which is representative of many confluent boundary layers. Furthermore, streamwise pressure gradients are absent so that the calibration could be performed by concentrating solely on curvature effects.

Results of this calibration are shown in figure 4. They were obtained by starting the theoretical predictions about 13 boundary layer thicknesses upstream of the station for which the test-theory comparison is given. Only experimental streamwise velocities were used at this initial station, whereas profiles of turbulence data were generated assuming similar profiles for U, k, ϵ. The value $C_R = 1.25$ gave the best match of theory with experiment, accurately predicting the greatly reduced turbulent activity in the outer half of the boundary layer. For comparison, the theoretical results predicted with formal surface curvature terms, but without any additional empirical correction ($C_R = 0$), are included. The need for such an empirical correction is apparent.

Initial Values

The confluent boundary layer experiment of Pot (refs. 11, 12), illustrated in figure 5, served to study the effect of the two described op-

tions for initial values on the solution accuracy. The experimental data include detailed measurements of streamwise velocity and profiles of Reynolds stresses of a single turbulent wake merging with a single boundary layer in zero pressure gradient. The wake and boundary layer were generated by two parallel flat plates, sufficiently removed from each other to allow a region of potential flow to exist between them initially.

The theoretical predictions were started at the end of this embedded potential core (x = 522mm) with different initial values (figure 6). In one case, all required initial boundary layer profiles were taken from the experiment. In the other case, only the measured streamwise velocity profile was used, and initial values for turbulence data were calculated assuming similar profiles. The two starting techniques produced virtually identical velocity profiles at subsequent surface stations which are in excellent agreement with the experiment. Turbulent shear stress and turbulent kinetic energy profiles, computed by the two starting techniques, are considerably different at upstream surface stations but match very well downstream. Only fair agreement with experimental data of turbulent quantities could be achieved, which is of little concern in aerodynamic applications as long as velocity profiles or equivalently boundary layer integral parameters and skin friction are accurately predicted.

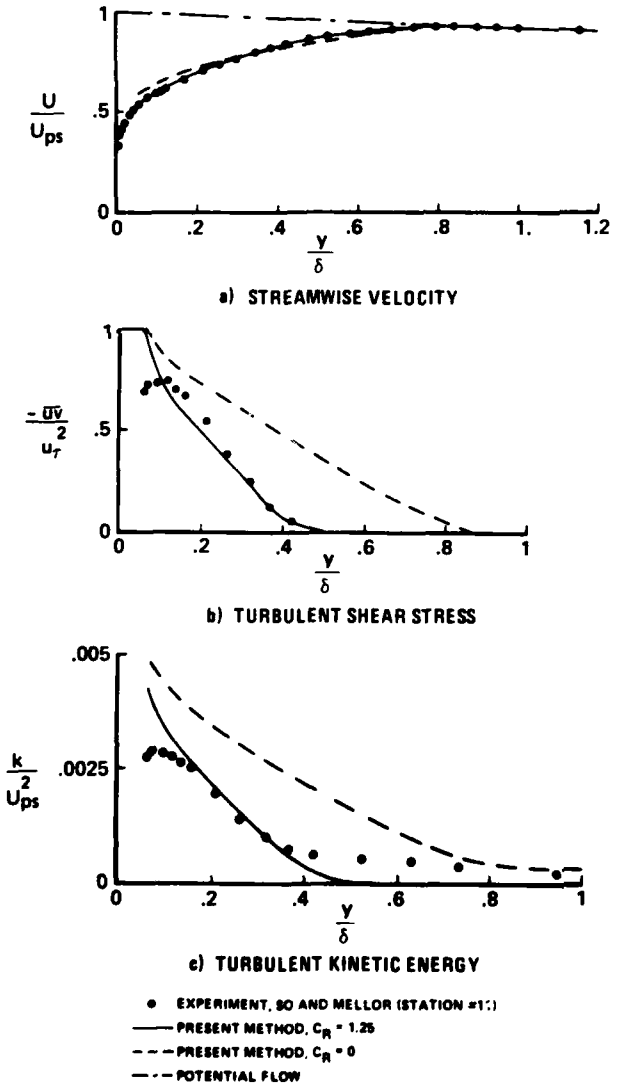

Figure 4. – Effect of Curvature Coefficient C_R on Boundary Layer of Convex Surface

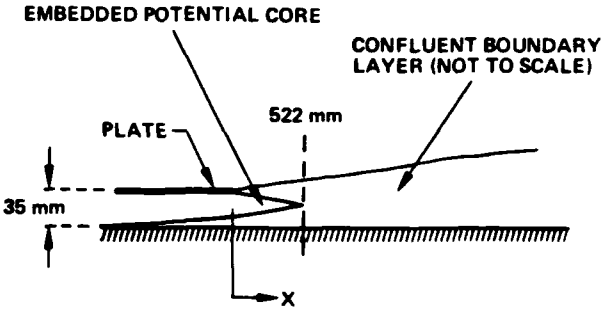

Figure 5. – Confluent Boundary Layer Experiment of Pot

Streamwise Step Size Limitation

The prediction method leads to converged solutions only if the streamwise step size is limited to small values, usually about one half of the local boundary layer thickness. At the initial surface station, the maximum step size is restricted to a small fraction of the boundary layer thickness.

The cause of this step size limitation was investigated by employing a criterion recently applied by Wilcox (ref. 13) to determine the stability limits of a similar computational method. This criterion requires diagonal dominance of the tridiagonal matrix equations (18) for a converged solution of the nonlinear algebraic equations at each new surface station. Application of this criterion, written as

$$|P_j| \geq |O_j + Q_j| \tag{19}$$

gives the following results:

a) The solution of the x-momentum equation is unconditionally stable for all streamwise step sizes Δx.

b) The solution of the k, ϵ-equations is unconditionally stable if the destruction terms are larger than the generation terms.

c) If the destruction terms are smaller than the generation terms, the k, ϵ-equations will only converge if the streamwise step size is limited. In the absence of surface curvature effects, the k-equation imposes the following limit on the step size Δx

$$\Delta x \leq \frac{2\bar{k}\bar{U}}{\bar{\nu}_T\left(\frac{\partial \bar{U}}{\partial y}\right)^2 - \bar{\epsilon}} \tag{20}$$

where all variables are written at the midpoint of the step. The ϵ-equation gives a similar but less restrictive formula.

In order to prove the validity of equation (20), a profile of the step size Reynolds number $Re_{\Delta x} = (U_e \Delta x)/\nu$ was plotted at the initial station of a flat plate boundary layer calculation (figure 7). This profile shows rapid changes caused by an initial velocity profile that was not smoothed. The maximum allowable step size is given by the absolute minimum of $Re_{\Delta x}$ which occurs very close to the surface. This theoretical value of Δx_{max} is $\delta/8$ which very closely agrees with the step size limitation of $\delta/6$ found by numerical experimentation. The result confirms numerically that the streamwise step size of the computational method is limited by the use of the conservation equations for k and ϵ. For two-dimensional boundary layer computations, this step size limitation does not inhibit the economy of the calculation, since converged solutions at each surface station can be obtained in a few iteration cycles.

Embedded Potential Core

For some multielement airfoil configurations and flight conditions, regions of inviscid flow separate neighboring wakes and boundary layers. The length of such a region, termed potential core, must be accurately predicted since merging of the shear layers and associated

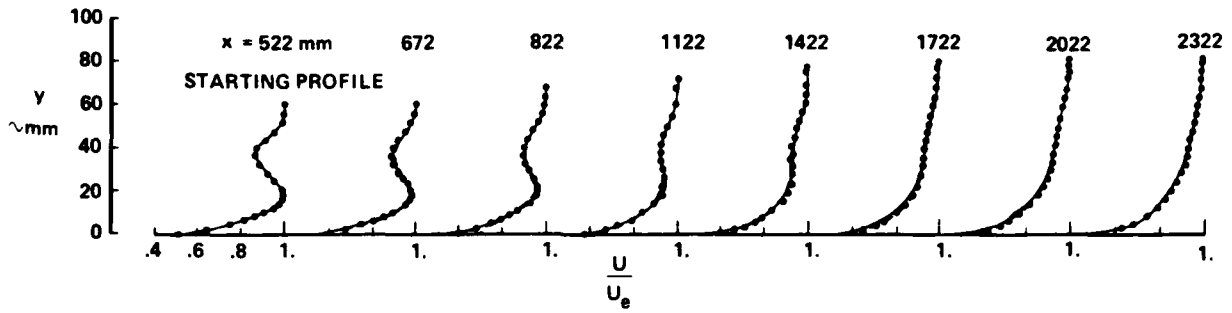

a) STREAMWISE VELOCITY

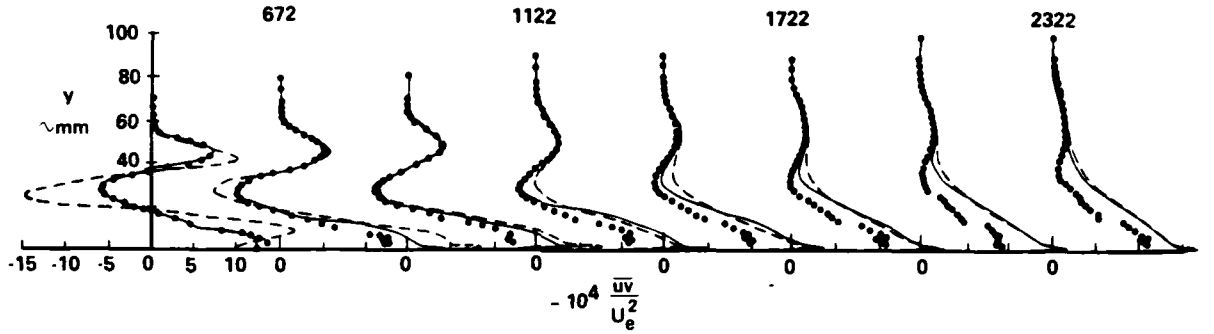

b) TURBULENT SHEAR STRESS

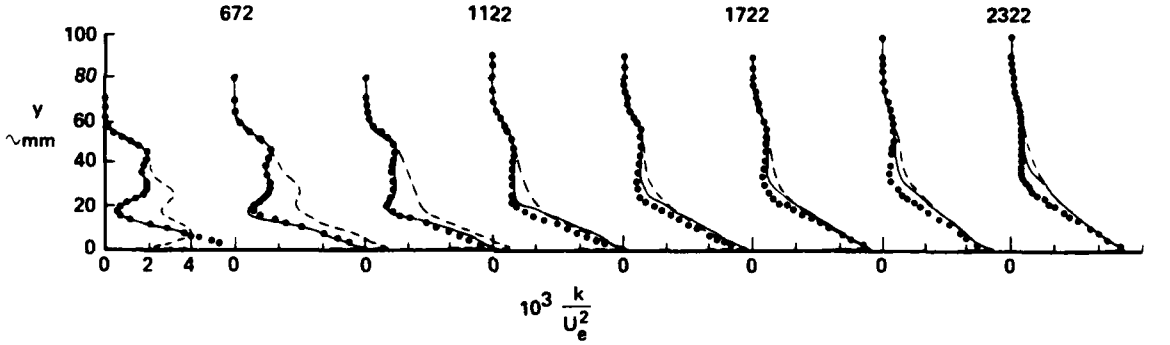

c) TURBULENT KINETIC ENERGY

● EXPERIMENT, POT
—— PRESENT METHOD: ALL INITIAL VALUES FROM EXPERIMENT
– – – PRESENT METHOD: ONLY U(Y) FROM EXPERIMENT

Figure 6. – Effect of Initial Values on Prediction of Confluent Boundary Layer

significant changes in airfoil performance begin with the disappearance of this potential core. The k, ϵ-model of turbulence is well suited for such a prediction since the type of flow region, either boundary layer, wake, or potential flow, need not be specified ***a priori*** and can be predicted with one and the same computational method. Accurate mean flow predictions of shear layers with an embedded potential core are shown in figure 8 , using the data of Pot (ref. 12) upstream of the previously discussed test-theory comparison based on the same experiment. Corresponding turbulence data are also compared in this figure.

In order to perform reliable calculations in flow regions with a very low level of turbulence, care must be taken to eliminate numerical noise from the values of the dissipation ϵ. The latter variable is the denominator in equation (6) for the eddy viscosity ν_T, so that in flow regions with little dissipation very small errors in ϵ can lead to large errors of ν_T. For this reason, the present prediction method utilizes only those values of ϵ which are at least one order of magnitude larger than the corresponding values of turbulent kinetic energy k.

Adverse Pressure Gradient

The main assumption of the described two-point wall function method concerns the existence of a logarithmic velocity profile at the two grid points closest to the surface. This requirement is difficult to satisfy for boundary layers in adverse pressure gradients, since the relative width of the logarithmic layer is greatly reduced when separation is approached. To illustrate this problem, figure 9 gives an example of the size of the logarithmic layer in the computational x, η-domain based on the data of Schubauer and Spangenberg (ref 14)

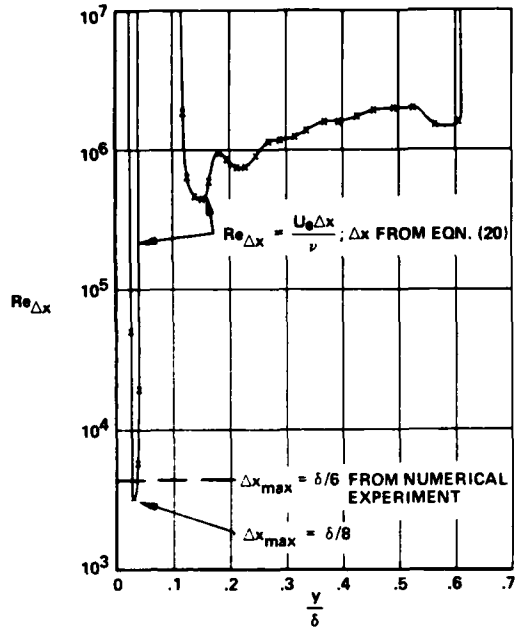

Figure 7.– Limitation of Streamwise Step Size at Initial Station of Flat Plate Boundary Layer ($Re_x = 0.63 \times 10^6$)

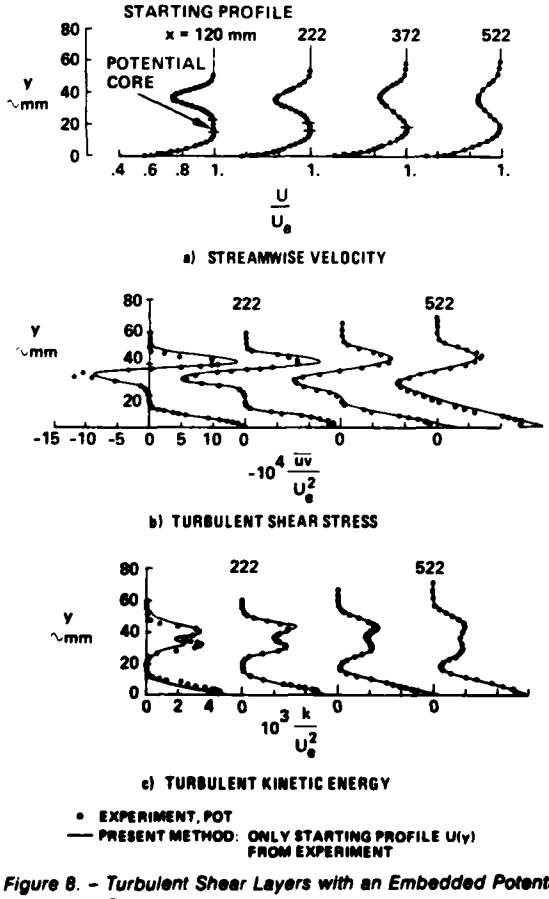

Figure 8. – Turbulent Shear Layers with an Embedded Potential Core

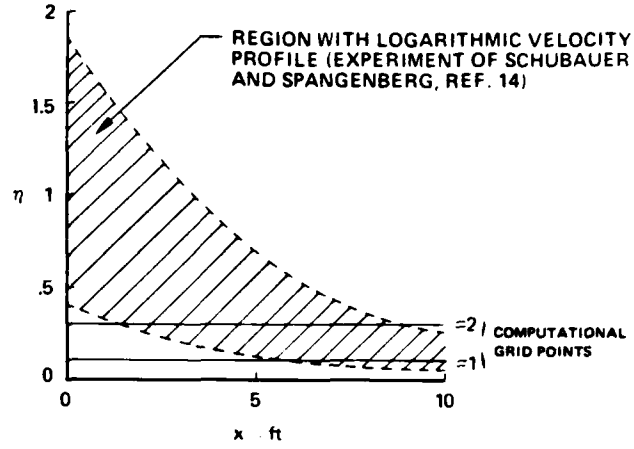

Figure 9. – Check on the Validity of the Two-Point Wall Function Method in the Presence of Adverse Pressure Gradients

Accurate predictions of the boundary layer properties can only be performed if the grid point 2 is chosen such that it will stay inside this region. Numerical experimentation has shown that the location of grid point 1 does not affect the solution accuracy.

Very few experimental data on confluent boundary layers in adverse pressure gradients are available. Goradia and Colwell (ref 15) conducted a wall jet experiment on a flat surface with an imposed pressure gradient simulating the confluent boundary layer of a two-element high-lift airfoil. A comparison of the present theory with measured mean velocity profiles, given in figure 10, shows excellent agreement even though turbulence data were not available to start the computation. Figure 11, showing a test-theory comparison for only one velocity profile on the upper flap surface of a high-lift airfoil (refs 16, 17), is included to emphasize the need for additional experimental data. The author of this paper is not aware of any other published experimental data of attached confluent boundary layers that are available in sufficient detail for a further evaluation of the present prediction method.

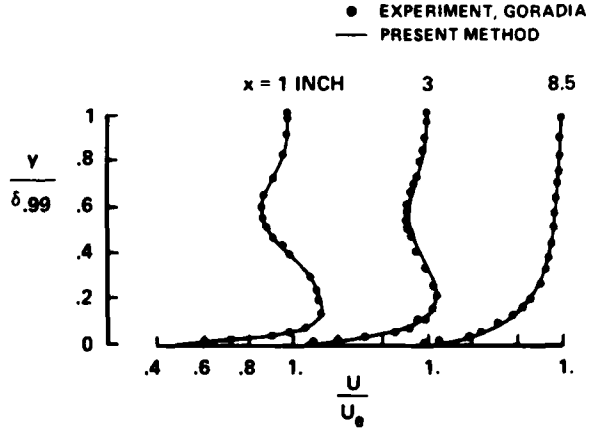

Figure 10. – Velocity Profiles of Confluent Boundary Layer in Adverse Pressure Gradient ($\delta_{.99} = 0.24$ Inches at Initial Station)

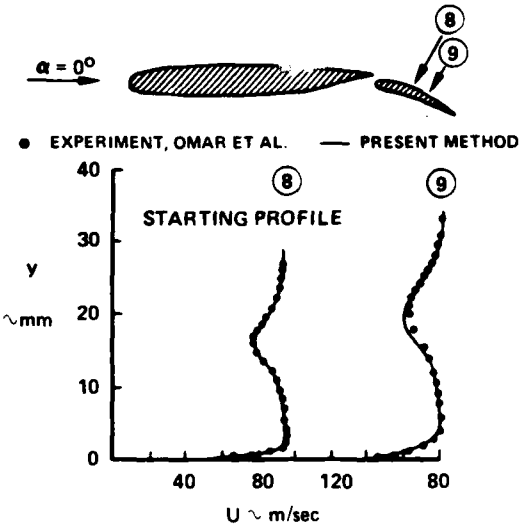

Figure 11. – Velocity Profiles on Upper Flap Surface of High-Lift Airfoil

CONCLUSIONS

The described computational method is applicable without modification to many different types of turbulent wall flows. Test-theory comparisons for ordinary boundary layers, wall jets, and confluent boundary layers support the following conclusions:

a) The method provides an accurate prediction of those turbulent shear flows that exist on slotted multielement airfoils operating at low free stream Mach numbers.
b) Accurate predictions of mean flow can be made in cases where initial values of turbulence data are not available.
c) The use of the k, ε-model of turbulence and a finite difference solution method, provide sufficient versatility to predict the merging of different types of turbulent shear flows.
d) The method is computationally efficient and numerically reliable even though the application of a two-equation turbulence model has severely limited the grid spacing in the streamwise direction. This limitation must be removed before the method is extended to predict economically threedimensional flows.
e) The application of law of the wall boundary conditions is computationally efficient but causes difficulties in boundary layers approaching separation.
f) There is need for additional experimental data of confluent boundary layers comprising streamwise velocity profiles, skin friction, and Reynolds stresses.

ACKNOWLEDGEMENT

The work reported in this paper was sponsored by the Independent Research and Development Program of The Boeing Company.

REFERENCES

1. Küchemann, D., The Aerodynamic Design of Aircraft, Pergamon Press, Oxford, 1978
2. Stevens, W.A., Goradia, S.H., and Braden, J.A., "Mathematical Model for Twodimensional Multicomponent Airfoils in Viscous Flow", NASA CR-1843, July 1971.
3. Dvorak, F. A., "Calculation of Turbulent Boundary Layers and Wall Jets Over Curved Surfaces", AIAA Journal, Vol. 11, No. 4, 1973, pp. 517-524
4. Bradshaw, P., "Effects of Streamline Curvature on Turbulent Flow", AGARDograph No. 169, 1973
5. Jones, W. P. and Launder, B. E., "The Prediction of Laminarization With a Two-Equation Model of Turbulence", International Journal of Heat Mass Transfer, Vol. 15, 1972, pp. 301-314
6. Launder, B. E., Priddin, C. H., and Sharma, B. I., "The Calculation of Turbulent Boundary Layers on Spinning and Curved Surfaces", Journal of Fluids Engineering, 1977, pp. 231-239
7. Launder, B. E. and Spalding, D. B., "The Numerical Computation of Turbulent Flows", Computer Methods in Applied Mechanics and Engineering, Vol. 3, 1974, pp 269-289
8. Cebeci, T. and Meier, H. U., "Modelling Requirements for the Calculation of the Turbulent Flow Around Airfoils, Wings, and Bodies of Revolution", AGARD-CP-271, 1979
9. Herring, H. J. and Mellor, G. L., "Computer Program for Calculating Laminar and Turbulent Boundary Layer Development in Compressible Flow", NASA CR-2068, 1972
10. So, R. M. C. and Mellor, G. L., "Experiment on Convex Curvature Effects in Turbulent Boundary Layers", J. Fluid Mech., Vol 6.0, Part 1, 1973, pp. 43-62
11. Pot, P. J., "A Wake-Boundary Layer Mixing Experiment", Second Symposium on Turbulent Shear Flows, Imperial College, London, 1979
12. Pot, P. J., "Measurements in a 2-D Wake and in a 2-D Wake Merging into a Boundary Layer, Data Report," NLR-TR 79063L, 1979
13. Wilcox, D. C., "Algorithm for Rapid Integration of Turbulence Model Equations in Parabolic Region", AIAA Journal, Vol. 19, No 2, 1981,pp. 248-250
14. Kline, S. J. (ed.) et. al., "Proceedings, Computations of Turbulent Boundary Layers—1968 AFOSR-IFP-Stanford Conference", 1969
15. Goradia, S. H. and Colwell, G. T., "Parametric Study of a Twodimensional Turbulent Wall Jet in a Moving Stream with Arbitrary Pressure Gradient", AIAA Journal, Vol. 9, No. 11, 1971, pp. 2156-2165
16. Omar, E., Zierten, T., and Mahal, A., "Twodimensional Wind Tunnel Tests of a NASA Supercritical Airfoil with Various High-Lift Systems—Volume I, Data Analysis", NASA CR-2214, 1977
17. Omar, E., Zierten, T., Hahn, M., Szpiro, E., and Mahal, A., "Twodimensional Wind Tunnel Tests of a NASA Supercritical Airfoil with Various High-Lift Systems-Volume II, Data Analysis", NASA CR-2214, 1977

SESSION 2 - BOUNDARY LAYERS II

M. Rubesin - Chairman

Three Dimensional Boundary Layer Development in an Axially Rotating Pipe

M. Murakami, K. Kikuyama and K. Nishibori

Department of Mechanical Engineering
Nagoya University
Chikusa-ku, Nagoya, Japan.

ABSTRACT

Experimental results of the boundary layer development in the inlet portion of a rotating pipe are presented. An undeveloped flow with a rectangular velocity distribution was introduced into the pipe rotating about its axis. It has been shown that the flow in the boundary layer is affected by two counter effects. One is a destabilizing effect due to an increase of the relative velocity of fluid at the wall surface caused by the pipe rotation, and the other is a stabilizing effect due to the suppression of turbulence brought about by the centrifugal force of the swirling flow component. Whether the stabilizing effect is dominant or not depends on the through-flow Reynolds number and the rotational speed of the pipe.

It has been verified experimentally that a certain combination of the two parameters causes a reverse transition from turbulent to laminar flow in the boundary layer flow.

NOMENCLATURE

- a : pipe radius
- d : pipe diameter = $2a$
- H : form parameter = $\delta^*/\theta x$
- N : rotation rate = V_o/U_m
- Re : axial Reynolds number = $U_m d/\nu$
- Rex': inlet length Reynolds number = $U_m x'/\nu$
- r : radial distance
- s : running clearance at the pipe entrance
- U, V, W: time mean velocity components in x, y, and z directions, respectively
- $\tilde{U}$: instantaneous velocity component in x direction
- U_e : value of U at outer edge of boundary layer
- U_m : mean axial velocity
- V_o : peripheral speed of rotating pipe
- x : axial distance from the inlet section of rotating pipe
- x' : axial distance from the assumed leading edge of boundary layer
- y : circumferential distance along pipe periphery
- z : radial distance from pipe wall
- γ : intermittency factor
- δ : thickness of boundary layer
- δ^* : displacement thickness of boundary layer in x direction
$$= \int_0^{\delta} (1 - U/U_e)\ (r/a)\, dz$$
- θx : momentum thickness of boundary layer in x direction
$$= \int_0^{\delta} (U/U_e)(1 - U/U_e)(r/a)\, dz$$
- θxy: momentum thickness of boundary layer in y direction
$$= \int_0^{\delta} (U/U_e)\ (V/V_o)\ (r/a)^2 dz$$
- ν : kinematic viscosity

INTRODUCTION

When a flow from a stationary pipe enters an axially rotating pipe, a tangential component of velocity is given to the flow by the moving wall, which causes a large change both in the axial velocity profile and the turbulent structure in the flow. This type of flow prevails in the inlet parts of fluid machinery, heat exchangers, and cooling system of rotors.

The decrease in the hydraulic loss in rotating pipes when a fully developed turbulent flow was introduced into the pipe was examined by Levy(1) and White(2). Murakami and Kikuyama(3) measured both the hydraulic loss and velocity profiles in axially rotating pipes when the flow was turbulent and found that the pipe rotation stabilized the flow and reduced the hydraulic loss in the pipe. In this case the axial velocity profile tended to approach the laminar flow profile in the downstream region of the rotating pipe. Using a visualization technique, Cannon and Kays(4) found two kinds of flow regions: one being the core region without a rotational component, and the other being the wall region with a rotational component. In the latter region the turbulence was observed to be suppressed.

Pedley(5) analyzed theoretically the stability of a laminar flow in a rotating pipe when the flow had a solid rotation type swirling velocity component, and showed that the pipe rotation destabilized the laminar flow state if the axial Reynolds number exceeded 82.9.

From the authors' study cited above, it may be seen that the pipe rotation stabilizes or destabilizes the flow in accordance with the states of flow in the pipe. The occurrence of the same phenomena can be expected in the developing boundary layer in the inlet region of the rotating pipe.

This paper describes the effects of the pipe rotation on the transition and suppression of turbulence in this developing boundary layer.

EQUIPMENT AND METHOD OF EXPERIMENT

A schematic outline of the experimental apparatus is shown in Fig. 1(a). The air discharged from a centrifugal blower flows through a rectifying tank, a nozzle, and a rotating pipe, successively, and is returned to the blower through a stationary pipe and a filter. In order to make the velocity distribution uniform over the inlet section of the rotating pipe and to homogenize the turbulence structure, a honeycomb (20 mm square and 100 mm long) and six screens (mesh size : 1.0 ~ 2.62 mm, screen wire dia. : 0.26 ~ 0.56 mm) were provided in the rectifying tank and the air stream from the tank was throttled by the nozzle in the ratio of 12.3 : 1.

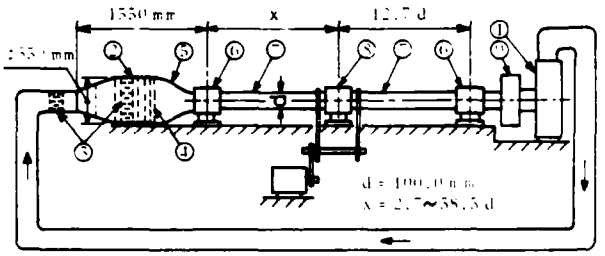

1. Blower
2. Rectifying Tank
3. Honeycomb
4. Gauze Screen
5. Nozzle
6. Bearing Box
7. Rotating Pipe
8. Measuring Section
9. Filter

Fig. 1 (a) Schematic outline of Experimental apparatus

The rotating pipe had a diameter of 100 mm and a hydraulically smooth surface. To check the effect of the running clearance between the nozzle and the rotating pipe on the flow, the tests were made at two clearances of s = 1.6 mm (s/d = 0.016) and 0.2 mm (s/d = 0.002), respectively.

Measurements of velocities were made at the sections of x/d = 0, 2.7, 5.7, 9.7, 12.7, $\cdots\cdots$, and 38.5, where a hot wire probe and a three-hole Pitot tube were inserted. These probes were mounted on a narrow stationary ring of 10 mm length placed between two rotating sections and the probes were inserted into the rotating section through a small hole drilled in the stationary ring. Details of this measuring section are shown in Fig. 1(b). The leakage of the air through the running clearances was prevented by the oil-seals.

The experimental ranges of the axial Reynolds number Re and the rotation rate N were $6 \times 10^4 \leqq Re \leqq 9 \times 10^4$, and $0 \leqq N \leqq 0.83$, respectively.

EXPERIMENTAL RESULTS AND DISCUSSIONS

Velocity Distributions Figure 2 shows the velocity profile at the entrance section of the rotating pipe (x/d = 0) when the pipe is held stationary (N = 0) and Re = 7.5×10^4 Both the uniformity and axi-symmetricity are seen to be established well except for a narrow region near the wall, the thickness being $\delta^*/a = 0.015$. The turbulence intensity u'/U_e was measured to be less than 0.003 in this uniform velocity field.

Figure 3 shows the velocity profiles in the boundary layer at different sections when the pipe is stationary (N = 0) and the clearance is held to be 1.6 mm. The radial distance z is made dimensionless

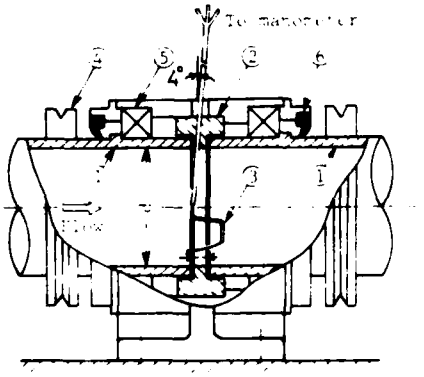

1. Rotating Pipes
2. Stationary Ring
3. Pitot Probe
4. Pulley
5. Bearing
6. Oil-seal

Fig. 1 (b) Details in measuring section

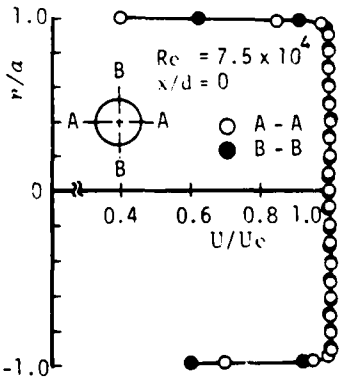

Fig. 2 Axial velocity distribution at the entrance section

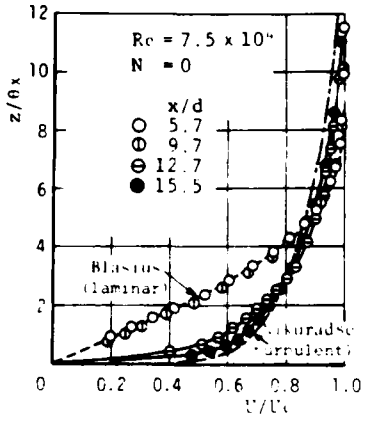

Fig. 3 Velocity profiles for N = 0 (s = 1.6 mm)

by the momentum thickness θx in the figure. At the sections of x/d = 5.7 and 9.7, the velocity profiles coincide well with the Blasius' velocity curve for the flow on a flat plate with no pressure gradient. Thus, the flow in this stationary pipe is considered to be laminar. The velocity profile is changed abruptly at the downstream sections, x/d = 12.7 and 15.5. The velocity curve at x/d = 15.5 shows the same profile as measured by Nikuradse in a fully developed turbulent pipe flow (Re = 1.1×10^5) as shown by a chain line in this figure. When the pipe is rotating, the flow receives a tangential velocity component and this component brings about a change in the axial velocity distribution.

Figures 4(a), (b), (c), and (d) show the axial and tangential velocity curves for different sections when the pipe is rotated at the rates of N = 0.25, 0.35, 0.5 and 0.63, respectively. For reference, the velocity curves obtained by Blasius (laminar flow) and Nikuradse(turbulent flow), respectively, are also plotted in these figures. Judging from the velocity profiles for N = 0.25, the flow is said to be laminar in all sections upstream of x/d = 12.7, but at the downstream section x/d = 15.5, the flow has turned into a turbulent state. Comparing this results with that for N = 0, it may be considered that the pipe rotation in this case stabilizes the flow, since the

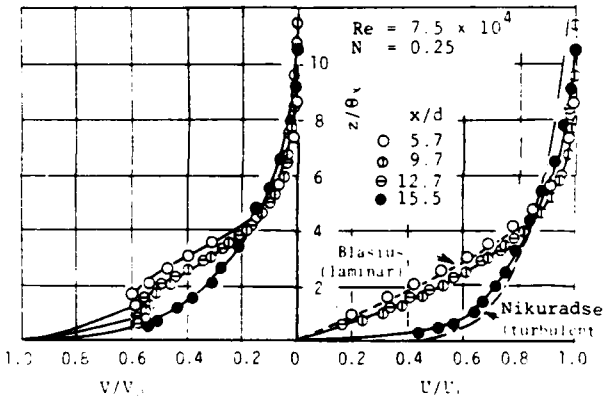

Fig. 4(a) Changes in velocity profiles for N = 0.25 (s = 1.6 mm)

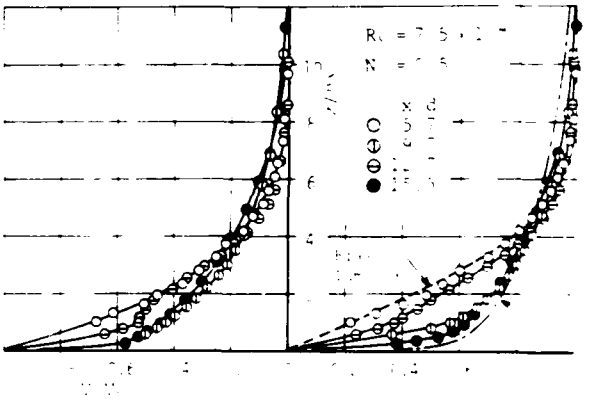

Fig. 4(c) Changes in velocity profiles for N = 0.5 (s = 1.6 mm)

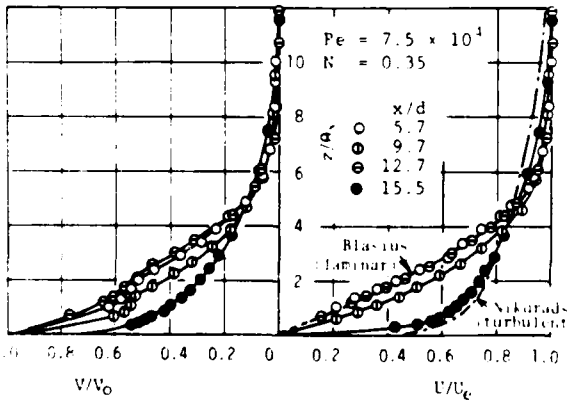

Fig. 4(b) Changes in velocity profiles for N = 0.35 (s = 1.6 mm)

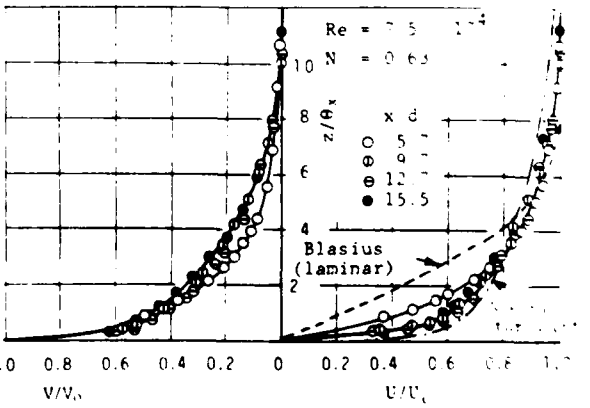

Fig. 4(d) Changes in velocity profiles for N = 0.63 (s = 1.6 mm)

transition of flow from laminar to turbulent is seen in farther downstream sections in the rotating state.

The curves of the tangential velocities V/V_0 in different sections show a similar tendency within the range of $x/d \lesssim 12.7$, and a discontinuity observed at about the point of $V/V_0 = 0.6$ will be due to a local instability caused by a large shear near the moving wall. At the section $x/d = 15.5$, this discontinuity cannot be seen in the velocity curve.

When the rotation rate is increased to $N = 0.35$ (Fig. 4(b)), the axial velocity profile at the section $x/d = 5.7$ exhibits a laminar flow pattern and at the section $x/d = 9.7$ the profile begins to turn into a turbulent state. But they are again returned in a laminar state by the stabilizing effect of the swirling velocity component as shown in the profile of $x/d = 12.7$. In the farther downstream section $x/d = 15.5$, however, they are almost in a turbulent flow pattern. The stabilizing and destabilizing effects of the pipe rotation become more dominant when the rotation rate is increased to $N = 0.5$ as shown in Fig. 4(c). Both of the axial and tangential velocity profiles in the section of $x/d = 5.7$ exhibit a laminar flow pattern, but in the section of $x/d = 9.7$ the flow pattern becomes a turbulent one. Farther downstream, at $x/d = 12.7$, the flow pattern again becomes laminar, namely a "relaminarization phenomenon" is seen to occur. In this section, there is a slight discontinuity in the curve of V/V_0, corresponding to a local instability. This laminar state of flow becomes again turbulent at the section of $x/d = 15.5$. At the rotational speed of $N = 0.63$ (Fig. 4(d)), the axial velocity profile is of a turbulent flow type in every section.

To confirm the above description, a hot wire probe was inserted at the section $x/d = 12.7$, and its instantaneous output was recorded. The results are shown in Fig. 5, in which the distance z of the probe from the pipe wall is made to be 0.9 mm ($z/\theta x = 0.5 \sim 1.0$) and the Reynolds number is adjusted as $Re = 7.5 \times 10^4$. The output corresponding to the turbulent velocity component $\tilde{U}$ in the stationary

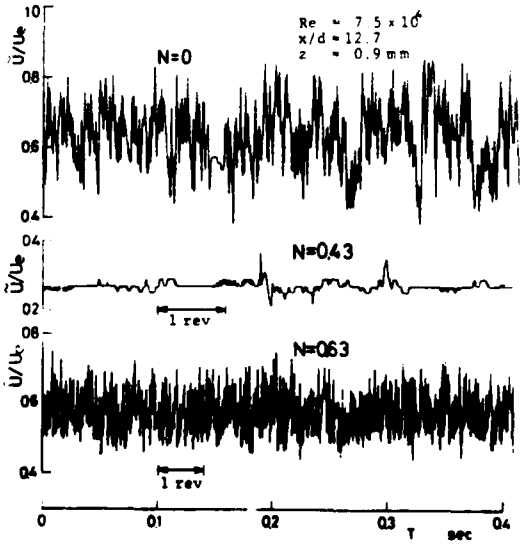

Fig. 5 Output signals of hot wire probe for $x/d = 12.7$, $Re = 7.5 \times 10^4$, and $z/d = 0.009$ ($s = 1.6$ mm)

state $N = 0$ is seen to fluctuate just as in a turbulent flow. If the pipe is made to rotate and its rate is elevated to $N = 0.43$, this intensive turbulent fluctuation dies away and the flow almost becomes laminar. A further increase of N to 0.63, however, again brings about an intensive fluctuation characterizing a turbulent flow. The above results on the fluctuation of velocities will confirm well the reason for the change in the velocity profiles in Figs. 3, and 4(c) and (d).

Momentum thickness and form parameter Changes of the momentum thicknesses both in the axial and tangential components θx and θxy along the pipe axis are shown in Fig. 6, where $Re = 7.5 \times 10^4$ and $s/d = 0.016$. Already at the inlet section of the rotating pipe, the boundary layer is seen to be developed, which shows the effect of the nozzle wall before the inlet. To account for this, an equivalent pipe length is introduced, at the end of which the boundary layer that would have been developed is the same amount as that observed at the exit section of the nozzle. This length can be assumed to be 1.5d, irrespective of the Reynolds number, and the axial distance x' from the assumed leading edge is expressed as

$$x' = x + 1.5d$$

where x denotes the distance measured from the leading edge of the rotating pipe. In the figure, x/d and also $Rex' = U_m x'/\nu$ are taken as the abscissa.

When the pipe is stationary ($N = 0$), θx has a comparative high increase near the section corresponding to $Rex' = 10^6$ or $x/d = 12.7$. Near this section the boundary layer is expected to change from laminar to turbulent. When the pipe is rotated at the rate of $N = 0.15 \sim 0.5$, the point of the transition shifts to the downstream side and comes to the section $Rex' \fallingdotseq 1.2 \times 10^6$. The same change can be seen in θxy when $N \lesssim 0.5$. When the rotation rate N is increased to 0.65, the point of the transition is seen to move upstream. This shift of the transition corresponds well to the results described already.

The form parameters H for different Reynolds numbers are plotted against Rex' in Fig. 7, when $N = 0$. The values of $H = 1.7$ and 2.5 are also shown in this figure by broken lines: $H = 1.7$ corresponds to a

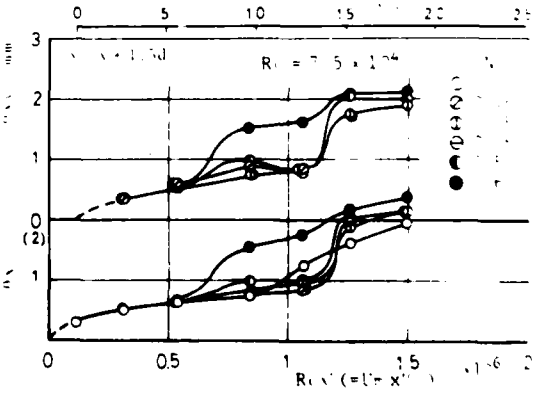

Fig. 6 Changes of θx and θxy along the pipe for $s/d = 0.016$

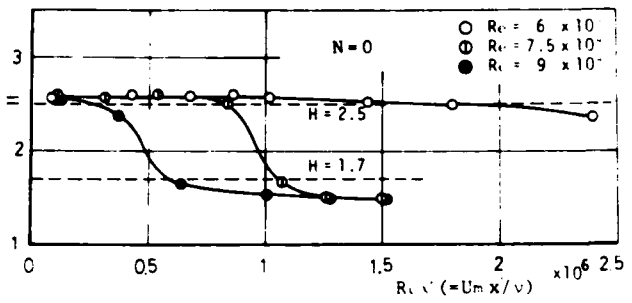

Fig. 7 Changes of H along the pipe for N = 0 and s/d = 0.016

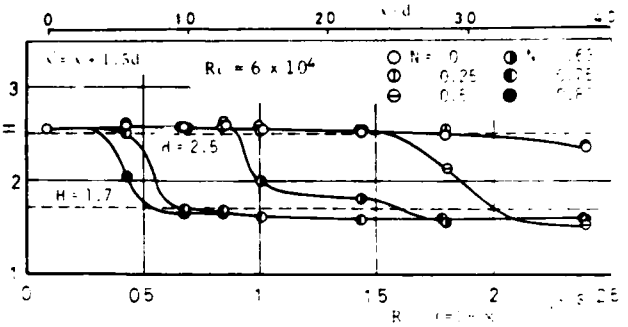

Fig. 8(a) Changes of H along the pipe for Re = 6 × 10^4 and s/d = 0.016

developed turbulent flow and H = 2.5 to a developed laminar flow. Increasing the axial Reynolds number Re, the transition point moves upstream as is expected from the foregoing results.

Figures 8(a), (b) and (c) show the changes of the form parameter H along the pipe when Re = 6.0 × 10^4, 7.5 × 10^4 and 9.0 × 10^4, respectively. When Re = 6 × 10^4 (Fig. 8(a)), the transition point moves upstream gradually as the rotation rate N is increased, and at N = 0.85 this point reaches the section where Rex' ≒ 0.35 × 10^5.

When the Reynolds number Re is increased to Re = 7.5 × 10^4 as in Fig. 8(b), a different situation occurs and the transition point in the rotating state of N = 0.15 comes to a section situating downstream of the transition in the stationary state N = 0. This delay of the transition in the rotating pipe is caused by a stabilizing effect of the swirling flow component. If N is increased further to N = 0.25, however, the pipe rotation disturbs the flow and the transition from laminar to turbulent flow occurs at an early section. In this case the turbulent flow again becomes laminar in the downstream sections and H changes in a wavy form along the pipe. This wavy change in H is seen only in the range of 0.25 ≦ N ≦ 0.5. When N is increased beyond this range, namely, to N = 0.65, the flow transition occurs earlier, and H decreases gradually along the pipe, showing no wavy form. At the Reynolds number Re = 9 × 10^4 (Fig. 8(c)), the point of the transition moves downstream as N is increased when N is in the range of N ≦ 0.35 but it moves upstream when N is increased beyond the limit. The curve of H in N = 0.5 comes near to that in the stationary state of N = 0.

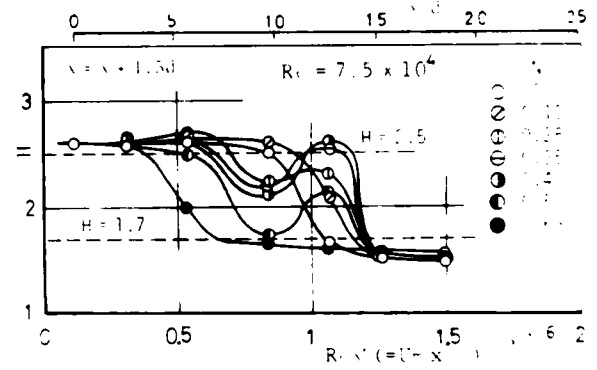

Fig. 8(b) Changes of H along the pipe for Re = 7.5 × 10^4 and s/d = 0.016

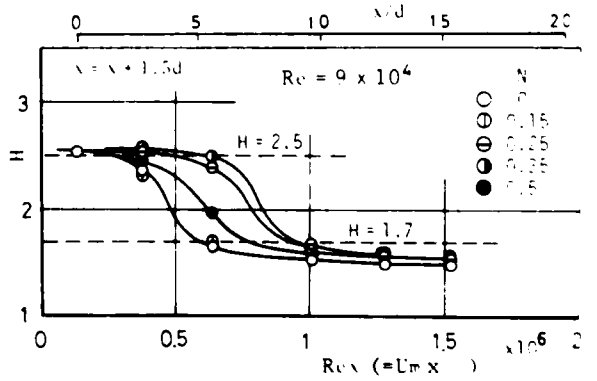

Fig. 8(c) Changes of H along the pipe for Re = 9 × 10^4 and s/d = 0.016

Flow regimes in rotating pipe With knowledge of the form parameters H obtained from the velocity profiles and the intermittency factors γ measured by the hot wire anemometer, the flow regimes in the rotating pipe can be constructed. Figures 9(a) and (b) exhibit the flow regimes obtained for the inlet running clearances of s/d = 0.016 and 0.002, respectively. In these figures the following classifications are adopted, depending on γ and H:

(1) laminar state : when γ ≦ 0.05 or H ≧ 2.5,
(2) transition state : when 0.05 < γ < 0.9 or 2.5 > H > 1.7,
(3) turbulent state : when γ ≧ 0.9 or H ≦ 1.7.

When the running clearance is made to be s/d = 0.016 (Fig. 9(a)), the laminar region becomes narrower as Re increases. In the case of Re = 6 ×

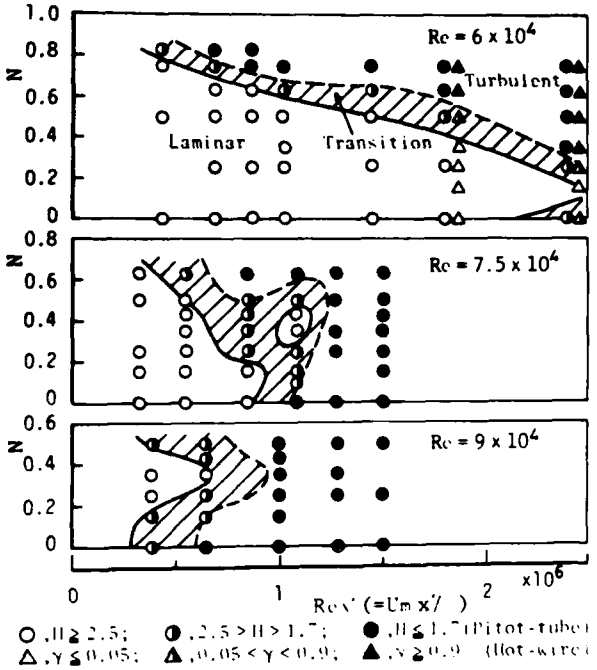

Fig. 9(a) Flow regime for s/d = 0.016

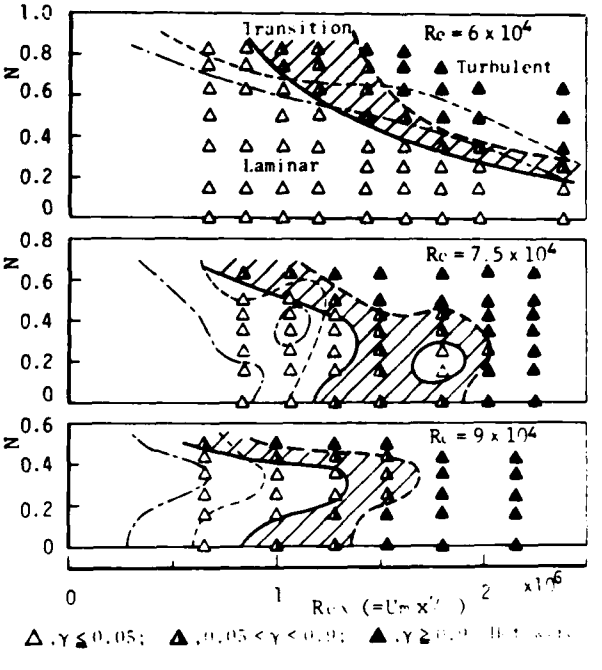

Fig. 9(b) Flow regime for s/d = 0.002

10^4, the pipe rotation can stabilize the flow only when $N < 0.15$, and if N is increased beyond this limit, the flow is disturbed and an early transition is brought about. When the rotation rate exceeds the value $N = 0.8$, the flow becomes turbulent shortly after the inlet section of the rotating pipe.

The flow regime map at $Re = 7.5 \times 10^4$ differs remarkably from that at $Re = 6 \times 10^4$. In the case of $Re = 7.5 \times 10^4$, the dimension of the laminar flow region situated near the inlet section decreases as N increases. Another isolated laminar flow region is seen inside the transition flow territory. This laminar region appears only within the rotation range $0.3 < N < 0.45$.

When Re is increased to 9×10^4, the laminar flow region after the inlet section becomes narrower and the stabilizing effect of the rotating pipe is observed only in a small range of $0.2 < N < 0.5$.

Generally, the transition phenomenon is very sensitive to the upstream condition of flow, and the running clearance at the rotating pipe inlet will exert some influence on the flow regimes explained above. The results for another running clearance of $s/d = 0.002$ are shown in Fig. 9(b), where the results for $s/d = 0.016$ are also plotted. It is seen that the wider clearance causes much disturbance to the flow and an early transition is brought about, but the flow regime maps for both clearances do not exhibit any qualitative differences.

CONCLUSIONS

An undeveloped uniform flow was introduced to an axially rotating pipe, and the velocity distribution and turbulence intensity were measured in the ranges of the Reynolds number $Re = 6 \sim 9 \times 10^4$ and the rotation rate $0 \leq N \leq 0.83$. The results obtained are summarized as follows:

(1) Pipe rotation causes a stabilizing effect or a destabilizing effect on the boundary layer flow according to the values of Re and N. A relaminarization phenomenon is observed in the rotating pipe within certain boundaries of Re and N.

(2) Transition of the flow is sensitively affected by the running clearance between the rotating pipe and the upstream stationary nozzle, but if the clearance ratio s/d is made to lie in the range of $s/d = 0.002 \sim 0.016$, the size of the clearance does not give any qualitative change in the flow.

REFERENCES

(1) Levy, F., "Strömungserscheinungen in Rotierenden Rohren," Vereines Deutscher Ingenieure Forschungsheft, No. 535, 1929, pp. 18-45.

(2) White, A.,"Flow of a Fluid in Axially Rotating pipe," Journal of Mechanical Engineering Science, Vol. 6, No. 1, 1964, pp. 47-54.

(3) Murakami, M., and Kikuyama, K.,"Turbulent Flow in Axially Rotating Pipes," ASME Journal of Fluids Engineering, Vol. 102, No. 1, Mar. 1980, pp. 97-105.

(4) Cannon, J. N., and Kays, W. M.,"Heat Transfer to a Fluid Flowing inside a Pipe Rotating about its Longitudinal Axis," ASME Journal of Heat Transfer, Vol. 91, No. 1, 1969, pp. 135-139.

(5) Pedley, T. J.,"On the Stability of Viscous Flow in a Rapidly Rotating Pipe," Journal of Fluid Mechanics, Vol. 35, No. 1, 1969, pp. 97-115.

THREE-DIMENSIONAL TURBULENT BOUNDARY LAYER ON A SPINNING THIN CYLINDER IN AN AXIAL UNIFORM STREAM

Ikuo NAKAMURA, Shintaro YAMASHITA and Takashi WATANABE
Department of Mechanical Engineering, Nagoya University, Nagoya, Japan

Yutaka SAWAKI
Department of Mechanical Engineering, Mie University, Tsu, Japan

ABSTRACT

An analysis and experiments are presented about a turbulent boundary layer on a cylinder rotating in an axial flow. A non-orthogonal and non-inertial frame is used to clarify the characteristics of the boundary layer in the near-wall region. Exploration of the boundary layer equation leads to a novel type wall variable and then new sublayer and logarithmic layer velocity distributions. The mean velocity profiles obtained in the experiments confirmed the novel velocity distribution law. Power spectra measured near the wall exhibited a mild but clear peak. Discussion was made as to the origin of the peak, and attention was drawn to a possible large eddy structure.

NOMENCLATURE

a	= radius of the cylinder
P	= static pressure
Re	= $U_m a/\nu$, reference Reynolds number
r	= $a + x^3 = a + z$, radial coordinate
T^{ij}	= contravariant component of the stress tensor
T_{ij}	= physical component of the stress tensor
U_e	= free stream velocity outside of the layer
U_m	= reference free stream velocity at x = 0
U_R	= $\sqrt{U_e^2 + (r\omega)^2}$, relative velocity of the inviscid flow with respect to the rotating frame
U_{R0}	= $\sqrt{U_e^2 + (a\omega)^2}$, value of U_R at the cylinder surface
U,V,W	= mean velocity components in the x-, y- and z directions respectively
U^i	= contravariant component of the mean velocity
U_i	= physical component of the mean velocity
U_{relo}	= $\sqrt{U^2 + (a\omega - V)^2}$, relative velocity in the boundary layer to the rotating cylinder
u^i	= contravariant component of the fluctuating velocity
u_i	= physical component of the fluctuating velocity
V_o	= $a\omega$, peripheral velocity of the cylinder
x^i	= coordinates of the rotating streamline frame, Fig. 1
$\bar{x}^i$	= coordinates of the non-inertial Cartesian reference frame, Fig. 1
x,y,z	= stationary cylindrical coordinates; axial, peripheral and radial coordinates respectively, z = r - a
Ω	= V_o/U_e, local speed ratio
Ω_m	= V_o/U_m, reference speed ratio
Ω_i	= component of the angular velocity of the rotating Cartesian frame with respect to the stationary frame
ω	= angular velocity of the cylinder
Φ_{u^*}, Φ_{v^*}	= normalized one-dimensional energy spectra of fluctuating velocities

Oberbars are used to designate the Cartesian non-inertial reference frame.

INTRODUCTION

The turbulent shear flow along a flat plate has a multi-layered structure as the most fundamental feature of the mean velocity field. On the other hand, the details of the multi-layered structure of the general complex turbulent shear flow along a wall are still unknown. In this report the turbulent boundary layer on a rotating cylinder in an axial flow is treated as one of the complex turbulent flows; this is affected by both the transverse curvature and the centrifugal force. This flow is perhaps one of the simplest of general three-dimensional flows. One of the main objectives of the present paper is to analyse the similarity of the near-wall flow in order to establish a universal velocity distribution law which is similar to the classical law of the wall.

Lohmann (1) and Arzoumanian et al. (2) insisted that the relative velocity to the rotating cylinder show the same logarithmic profile as for flat-plate flow. We earlier made a suggestion on the same formulation of the law of the wall (3). This law might be valid in a thin boundary layer having negligible effects of the transverse curvature and the centrifugal force. If the boundary layer is thick, it does not show the above-mentioned logarithmic law, as will be shown in our experimental results. This phenomenon may also be inferred from the large deviation of the mixing length distribution from that of the two-dimensional case as described in a previous paper (4).

In order to clarify this crucial point, we derive the boundary layer equations expressed by a non-orthogonal coordinate system rotating with the cylinder which reflects well the features of the present flow, and obtain a novel logarithmic law. Experiments have also been performed by use of a rotating cylinder in an axial flow. The mean velocity distribution measured definitely confirms the novel logarithmic law. Power spectra of turbulence obtained exhibited a particular characteristic which implied a special large eddy.

DERIVATION OF BASIC EQUATIONS AND LOGARITHMIC LAW

Boundary Layer Equations in a Rotating Streamline Frame

Let us suppose that the non-inertial Cartesian reference frame (coordinates $\bar{x}^i$) is firmly attached to the cylinder spinning at the angular velocity ω. A set of coordinates x^i with respect to the non-inertial curvilinear frame is defined as shown in Fig. 1. Supposing an inviscid flow of velocity U_e in the x^3-direction in the stationary frame, we define the curved x^1-

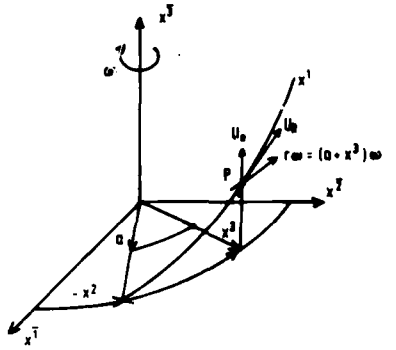

Fig. 1 Rotating streamline coordinates

coordinate line as a line whose tangent is in the direction of the relative velocity vector with respect to the rotating frame. The x^3-coordinate curve is radial straight line. The surface x^1-x^3 is a helicoid. The x^2-coordinate curve is chosen parallel to the leading edge of the cylinder considering the rotational symmetry of the flow. The x^1-coordinate is the length normalized to the projected length on the cylinder surface, the x^2-coordinate is the azimuthal angle, and the x^3-coordinate is the length measured from the cylinder surface. A set of coordinates x^i is thus a non-inertial non-orthogonal curvilinear system. In what follows, we term this system a rotating streamline coordinate system, and x^1-direction a streamline direction.

The coordinate transformation is given by

$$\left.\begin{aligned} x^{\bar{1}} &= (a+x^3)\cos(x^2 - \omega\textstyle\int_0^{x^1}(1/U_{R0})dx^{1'}),\\ x^{\bar{2}} &= -(a+x^3)\sin(x^2 - \omega\textstyle\int_0^{x^1}(1/U_{R0})dx^{1'}),\\ x^{\bar{3}} &= \textstyle\int_0^{x^1}(U_e/U_{R0})dx^{1'}, \end{aligned}\right\} \quad (1)$$

where $U_{R0} = \sqrt{U_e^2 + (a\omega)^2}$. Using the relations (1), we can obtain the basic equations with respect to the rotating streamline frame, following non-Cartesian tensor analysis (5). Various geometric coefficients, i.e., the transformation matrix elements, the metric tensor, the Christoffel symbols and so on, are required for the present purpose. The metric tensor g_{ij} is obtained as

$$g_{ij} = \begin{pmatrix} (1/\lambda)^2 & -\omega(a+x^3)^2/U_{R0} & 0 \\ -\omega(a+x^3)^2/U_{R0} & (a+x^3)^2 & 0 \\ 0 & 0 & 1 \end{pmatrix}, \quad (2)$$

where $\lambda = U_{R0}/U_R$ and $U_R = \sqrt{U_e^2 + (r\omega)^2}$. Other quantities can be obtained after some algebra.

Let $\Omega_{\bar{i}}$ be the angular velocity of the rotating frame relative to the stationary frame. The present study deals with the case of a steady rotation with $\Omega_{\bar{1}} = \Omega_{\bar{2}} = 0$ and $\Omega_{\bar{3}} = -\omega$. From the conservation equation of mass and momentum of fluid with respect to a non-inertial non-Cartesian frame (see, for example, (5)), we obtain the following continuity equation and Reynolds equation for incompressible fluid:

$$U^i{}_{,i} = 0, \quad (3)$$

$$U^jU^i{}_{,j} + 2\varepsilon^{ijk}\beta_j^{\bar{k}}g_{k\ell}\Omega_{\bar{k}}U^\ell + \varepsilon^{ijk}\beta_j^{\bar{k}}\beta_k^{\bar{\ell}}\Omega_{\bar{k}}(\varepsilon_{\bar{\ell}\bar{j}\bar{m}}\Omega^{\bar{j}}x^{\bar{m}}) = (T^{ij} - \rho\overline{u^iu^j})_{,j}/\rho. \quad (4)$$

Here we assume a steady turbulent flow. In these equations, the comma denotes the covariant differentiation, ε^{ijk} and $\varepsilon_{\bar{\ell}\bar{j}\bar{m}}$ are permutation tensors, and $\beta_j^{\bar{k}}$ are the transformation matrix elements. The averaged stress tensor T^{ij} is defined in incompressible fluid by the constitutive equation,

$$T^{ij} = -Pg^{ij} + \mu(g^{in}U^j{}_{,n} + g^{\ell j}U^i{}_{,\ell}). \quad (5)$$

Introducing all the geometric coefficients into Eqs.(3) and (4), we can obtain, after some algebra, the basic equations for a turbulent flow with respect to the rotating streamline coordinate system. In what follows, the contravariant physical components are written with subscripts.

Using the physical components and assuming the axisymmetry of the mean flow, the continuity equation is

$$\partial_{x^1}(\lambda U_1) - \partial_{x^1}(\gamma_0)\lambda U_1/\gamma_0 + \partial_{x^3}U_3 + U_3/(a+x^3) = 0, \quad (6)$$

and the Reynolds equations become,

$$\begin{aligned} &\lambda U_1\partial_{x^1}(\lambda U_1) + U_3\partial_{x^3}(\lambda U_1) - \partial_{x^1}(\gamma_0)(\lambda U_1)^2/\gamma_0 = \\ &= [\gamma_0{}^2\partial_{x^1}(T_{11}/\gamma^2) + \partial_{x^3}\{(a+x^3)\lambda T_{13}\}/(a+x^3)]/\rho - \\ &- [\gamma_0{}^2\partial_{x^1}(\overline{u_1{}^2}/\gamma^2) + \partial_{x^3}\{(a+x^3)\lambda\overline{u_1u_3}\}/(a+x^3)], \end{aligned} \quad (7a)$$

$$\begin{aligned} &\lambda U_1\partial_{x^1}U_2 + U_3\partial_{x^3}U_2 + \omega(a+x^3)\partial_{x^1}(U_{R0})(\lambda U_1/U_e)^2 - \\ &- 2\omega\lambda U_1U_3/U_{R0} + U_2U_3/(a+x^3) + 2\omega U_3 = \\ &= [\omega(a+x^3)\partial_{x^1}(U_{R0})\lambda^2T_{11}/U_e{}^2 + \gamma_0\partial_{x^1}(T_{12}/\gamma) - \\ &- 2\omega\lambda T_{13}/U_{R0} + \partial_{x^3}\{(a+x^3)^2T_{23}\}/(a+x^3)^2]/\rho - \\ &- [\omega(a+x^3)\partial_{x^1}(U_{R0})\lambda^2\overline{u_1{}^2}/U_e{}^2 + \gamma_0\partial_{x^1}(\overline{u_1u_2}/\gamma) - \\ &- 2\omega\lambda\overline{u_1u_3}/U_{R0} + \partial_{x^3}\{(a+x^3)^2\overline{u_1u_3}\}/(a+x^3)^2], \end{aligned} \quad (7b)$$

$$\begin{aligned} &\lambda U_1\partial_{x^1}U_3 + U_3\partial_{x^3}U_3 - (a+x^3)\{\omega(\lambda U_1 - U_{R0})/U_{R0} - \\ &- U_2/(a+x^3)\}^2 = [-\omega^2(a+x^3)\lambda^2T_{11}/U_{R0}{}^2 + \\ &+ 2\omega\lambda T_{12}/U_{R0} + \gamma_0\partial_{x^1}(T_{13}/\gamma) - T_{22}/(a+x^3) + \\ &+ \partial_{x^3}\{(a+x^3)T_{33}\}/(a+x^3)]/\rho - \\ &- [-\omega^2(a+x^3)\lambda^2\overline{u_1{}^2}/U_{R0} + 2\omega\lambda\overline{u_1u_2}/U_{R0} + \\ &+ \gamma_0\partial_{x^1}(\overline{u_1u_3}/\gamma) - \overline{u_2{}^2}/(a+x^3) + \\ &+ \partial_{x^3}\{(a+x^3)\overline{u_3{}^2}\}/(a+x^3)], \end{aligned} \quad (7c)$$

where $\partial_{xi} = \partial/\partial x^i$, $\gamma = U_R/U_e$ and $\gamma_0 = U_{R0}/U_e$. The evolution of the constitutive equations with respect to this coordinate system is straightforwards but considerably tedious, and is not presented here.

Assuming, for the present, that the free stream velocity U_e is constant, the equations for the thick turbulent boundary layer read as follows:

$$\partial_{x^1}(\lambda U_1) + \partial_{x^3}\{(a+x^3)U_3\}/(a+x^3) = 0, \quad (8)$$

$$\begin{aligned} &\lambda U_1\partial_{x^1}(\lambda U_1) + U_3\partial_{x^3}(\lambda U_1) = -\gamma_0{}^2\partial_{x^1}P/\rho + \\ &+ \partial_{x^3}\{(a+x^3)\lambda\tau_1\}/\rho(a+x^3), \end{aligned} \quad (9a)$$

$$\begin{aligned} &\lambda U_1\partial_{x^1}U_2 + U_3\partial_{x^3}U_2 + U_2U_3/(a+x^3) - 2\omega U_3(\lambda U_1 - U_{R0})/ \\ &/U_{R0} = -\gamma_0\omega(a+x^3)\partial_{x^1}P/\rho U_e + [-2\omega\lambda\tau_1/U_{R0} + \\ &+ \partial_{x^3}\{(a+x^3)^2\tau_2\}/(a+x^3)^2]/\rho, \end{aligned} \quad (9b)$$

$$\begin{aligned} &(a+x^3)\{\omega(\lambda U_1 - U_{R0})/U_{R0} - U_2/(a+x^3)\}^2 = \partial_{x^3}P/\rho - \\ &- (a+x^3)\overline{\{\omega\lambda u_1/U_{R0} - u_2/(a+x^3)\}^2} + \\ &+ \partial_{x^3}\{(a+x^3)\overline{u_3{}^2}\}/(a+x^3), \end{aligned} \quad (9c)$$

Where τ_1 and τ_2 are shear stress components in the x^1- and x^2-directions, respectively, defined by

$$\tau_1 = \mu\partial_{x^3}(\lambda U_1)/\lambda - \rho\overline{u_1u_3}, \quad (10a)$$

$$\tau_2 = \mu(a + x^3)\partial_{x^3}\{U_2/(a + x^3)\} - \rho\overline{u_2u_3}. \quad (10b)$$

Boundary conditions are

$$x^3 = 0;\ U_1 = U_2 = U_3 = 0,\ u_1 = u_2 = u_3 = 0, \quad (11a)$$
$$x^3 \to \infty;\ U_1 \to U_R,\ U_2 \to 0,\ u_1, u_2, u_3 \to 0. \quad (11b)$$

Note that U_2 is not assumed to be small in Eqs.(9a)-(9c); these equations and Eq.(8) are general basic equations for the turbulent boundary layer on a thin cylinder spinning in a uniform axial flow.

It is noticed that the pressure gradient in x^1-direction can be eliminated from Eqs.(9a) and (9b). This pressure is produced due to the rotating boundary layer as expressed by Eq.(9c). Therefore it can be interpreted that the effects of rotation through the pressure gradient on U_1 and on U_2 cancel out each other. Elimination of the pressure gradient from Eqs.(9a) and (9b) leads to

$$\lambda U_1\partial_{x^1}(\lambda U_1) + U_3\partial_{x^3}(\lambda U_1) - \gamma_0 U_e\{\lambda U_1\partial_{x^1}U_2 + U_3\partial_{x^3}U_2 + U_2U_3/(a + x^3)\} + 2U_3(\lambda U_1 - U_{R0})/(a + x^3) = [\partial_{x^3}\{(a + x^3)^3\lambda\tau_1\}/(a + x^3)^3 - U_{R0}\partial_{x^3}\{(a + x^3)^2\tau_2\}/\omega(a + x^3)^3]/\rho. \quad (12)$$

Universal Velocity Distribution Law

The components of mean velocity U_i (i = 1, 2, 3) in this coordinate system are related to the axial, peripheral and radial components, U, V and W, respectively, in the stationary cylindrical coordinate system as

$$U_1 = \gamma U,\ U_2 = V - r\omega(1 - U/U_e),\ U_3 = W. \quad (13a, b, c)$$

If $U_2 = 0$, the generalized quasi-collateral relationship (6) follows, that is,

$$1 - U/U_e = (a/r)V/V_0. \quad (14)$$

The previous experiments (6) have shown that this relationship is nearly satisfied in the turbulent boundary layer, and also the present experiment will confirm this relationship. It is reasonable to assume that U_2 is small, an assumption which assures the advantage of using the rotating streamline system.

Neglecting the terms including U_2 in Eq.(12) for the first approximation, we obtain

$$\lambda U_1\partial_{x^1}(\lambda U_1) + U_3\partial_{x^3}(\lambda U_1) + 2U_3(\lambda U_1 - U_{R0})/r = \partial_{x^3}(r^3\lambda\tau_1)/\rho r^3, \quad (15)$$

Here the Reynolds stress $-\rho\overline{u_2u_3}$ is thought to be zero in this case because of the axisymmetric nature of statistical quantities.

Near the wall, the inertia terms on the right-hand side of Eq.(15) may be neglected:

$$\partial_{x^3}(r^3\lambda\tau_1)/\rho r^3 \approx 0, \quad (16)$$

whence follows

$$r^3\lambda\tau_1 = \text{const.} = a^3\tau_{01}, \quad (17)$$

where τ_{01} is the x^1-component of the wall shear stress. Substituting the Eq.(10a) into Eq.(17) and introducing a new dimensionless argument

$$z^+ = (U_{1\tau}a/\nu)(r^2 - a^2)/2r^2, \quad (18)$$

we obtain

$$\partial_{z^+}(\lambda U_1/U_{1\tau}) - \lambda(r^3/a^3)\overline{u_1u_3}/U_{1\tau}^2 = 1, \quad (19)$$

where $U_{1\tau} = \sqrt{\tau_{01}/\rho}$. We may expect the solution of Eq.(19) to be

$$\lambda U_1/U_{1\tau} = F(z^+). \quad (20)$$

This is the law of the wall in this turbulent boundary layer, and z^+ defined by Eq.(18) is the relavant wall variable.

In the viscous sublayer, the Reynolds stress can be neglected in Eq.(19), and the velocity distribution becomes

$$\lambda U_1/U_{1\tau} = z^+ = (U_{1\tau}a/\nu)(r^2 - a^2)/2r^2. \quad (21)$$

Outside the viscous sublayer, the universal velocity distribution may be deduced on the basis of Eq.(20) using various more or less sophisticated methods similar to those in the case of two-dimensional flow. This becoms

$$\lambda U_1/U_{1\tau} = A_1\log[(U_{1\tau}a/\nu)(r^2 - a^2)/2r^2] + B_1, \quad (22)$$

where A_1 and B_1 are empirical constants.

Inserting Eqs.(13a) into Eq.(22), we obtain the logarithmic velocity distribution in the axial direction:

$$U/U_\tau = A_X\log[(U_\tau a/\nu)(r^2 - a^2)/2r^2] + B_X, \quad (23)$$

where U_τ is the friction velocity in the x-direction, and

$$A_X = A_1/(1 + \Omega^2)^{1/4}, \quad B_X = [A_1\log(1 + \Omega^2)^{1/4} + B_1]/(1 + \Omega^2)^{1/4}. \quad (24)$$

In the same way, using Eq.(13b) with $U_2 = 0$, the peripheral velocity distribution becomes,

$$\{V_0 - (a/r)V\}/V_\tau = A_Y\log[(V_\tau a/\nu)(r^2 - a^2)/2r^2] + B_Y, \quad (25)$$

where V_τ is the friction velocity in the y-direction, and

$$A_Y = A_1\Omega^{1/2}/(1 + \Omega^2)^{1/4}, \quad B_Y = [A_1\log\{(1 + \Omega^2)^{1/4}/\Omega^{1/2}\} + B_1]\Omega^{1/2}/(1 + \Omega^2)^{1/4}. \quad (26)$$

Equation (25) agrees completely with the expression in the previous study (6).

EXPERIMENTAL APPARATUS AND PROCEDURES

The wind tunnel used is shown in Fig. 2. In order to obtain a uniform oncoming flow to the rotating cylinder, the boundary layer developing on the front supporting rod is sucked through the slit, and it goes through the hollow rod to the blower. There is no strut which disturbs the inlet flow. Hot-wires for measurement are made of tungsten 5 μm in diameter. A special copper plating method was devised to make parts of the prongs, which were usually made of sewing

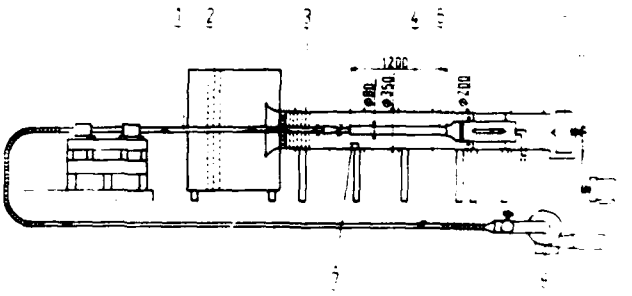

Fig. 2 Schematic diagram of apparatus. 1, supporting hollow rod; 2, filters; 3, gauze screens; 4, duct casing; 5, spinning cylinder; 6, fan; 7, reference probes; 8, suction blower

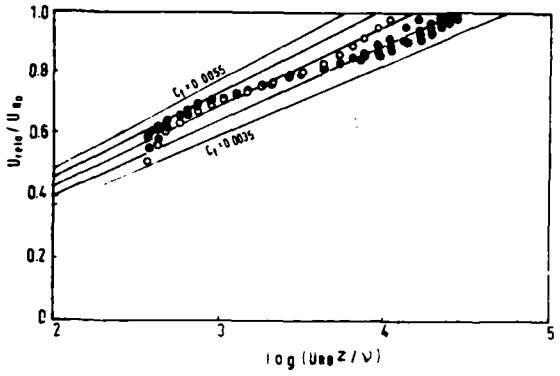

Fig. 3 Two-dimensional Clauder's plots of the relative velocity distribution to the rotating cylinder surface: Ω_m = 1. ○, x = 350 mm; ⊕, 550; ⊖, 750; ⊖, 850; ●, 950

needles or similar.

Measurements were made using a V-type hot-wire probe so designed that the plane including the two wires is parallel to the surface of the cylinder wall, and partly using a rotated hot-wire probe of I-type especially in the near-wall region. n X-probe was also used but not extensively. A three-hole cobra probe was used jointly in the mean flow measurements.

Reynolds number based on the cylinder radius a and the reference free-stream velocity U_m was kept constant: $R_e = 3 \times 10^4$, and the speed ratio $\Omega_m = V_0/U_m$ was varied: 0, 0.5, 1 and 1.5, although the experiments at these speed ratios did not cover all the measuring stations.

RESULTS AND DISCUSSION

The distribution of the velocity components U_1 and U_2, and the polar diagram based on Eq.(14) were plotted at Ω_m = 1 over the range from x = 25 mm to 950 mm. These results showed that U_2 was very small in the turbulent boundary layer beyond the station of x = 350 mm; the assumption of U_2 = 0 for the first approximation made in the preceding section is acceptable.

Logarithmic Velocity Distribution

Lohmann (1) and Arzoumanian et al.(2) presented their experimental data for the relative velocity employing a two-dimensional wall variable. Figure 3 shows the present results for the relative velocity plotted on a two-dimensional Clauser's chart, where U_{relo} is the relative velocity to the cylinder surface. It is impossible to find a line which corresponds to the experimental data, as is clearly seen from Fig. 3. Bissonnette and Mellor (7) considered a modification of the similarity law of the velocity near the wall, but it does not seem successful.

We have derived the logarithmic law for the x^1-direction, Eq.(22), to take the place of the earlier propositions. We must, first of all, determine the values of A_1 and B_1. The specially designed hot-wire probe made it possible to measure the velocity profiles near the wall and then to deduce the wall shear stress. Fortunately, the velocity near the wall with rotation is so large that the influence of the wall on a hot-wire signal is thought to be relatively small and negligible.

Thus, we deduced the wall shear-stresses from the velocity profiles measured near the wall with various

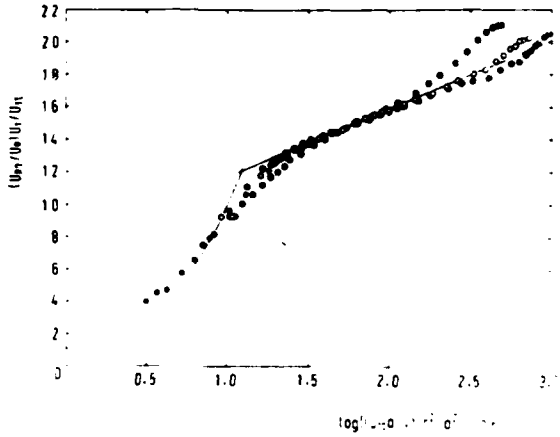

Fig. 4 Law of the wall representation of the velocity distribution in the x^1-direction, based on Eqs.(21) and (22) with Eqs.(27a, b): x = 850 mm. ⊕, Ω_m = 0.5; ○, ●, 1; ⊖, 1.5

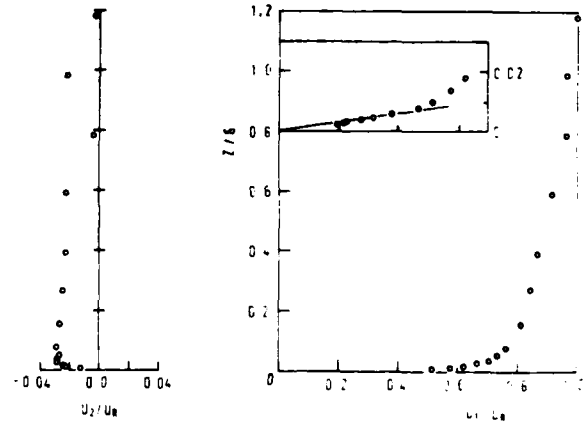

Fig. 5 Velocity profiles in the x^1- and x^2-directions with respect to the rotating streamline frame: Ω_m = 1, x = 850 mm

speed ratio (Ω_m = 0.5, 1 and 1.5), but only at the station of x = 850 mm. Using these wall shear-stresses, the experimental results were plotted, on the basis of the logarithmic law for the x^1-direction. It implied that the logarithmic portions of the velocity distribution collapse into one single line independent of the speed ratio within the present experimental condition. The optimum line gave

$$A_1 = 4.2, \quad B_1 = 7.5. \qquad (27a, b)$$

In Fig. 4, the experimental results are replotted according to the Eq.(22) with Eqs.(27a, b). The wall shear-stresses used in these plots have been determined by Clauser's chart based on these equations. The velocity distribution very close to the wall measured by means of I-probe at Ω_m = 1 are also presented. The figure shows that the logarithmic law (22) with the constants deduced above and the sublayer expression (21) describe very well the experimental results.

Figure 5, the velocity distributions in the x^1- and x^2-directions, is presented in illustration of the

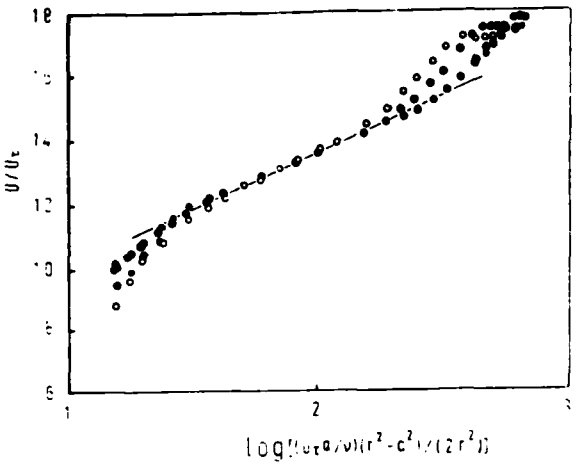

Fig. 6a Logarithmic velocity distribution in the axial direction based on Eq.(23) with A_x = 3.6 and B_x = 6.6: Ω_m = 1. ○, x = 350 mm; ⊙, 550; ⊖,750; ⊖, 850; ●, 950

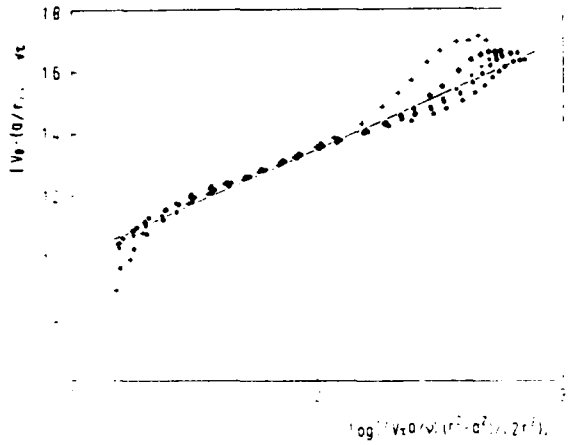

Fig. 6b Logarithmic velocity distribution in the peripheral direction based on Eq.(25) with A_y = 3.5 and B_y = 6.5: Ω_m =1. +, x = 350 mm; ⊕, 550; ×, 750; ⊙, 850; ⊖, 950

correctness of the value of the wall shear-stress determined in the way mentioned above. Attention is focussed on the profile very close to the wall, and the profile near the wall is enlarged in the figure. The gradient of the line in the figure corresponds to the wall shear-stress in the x^1-direction. The experimental points lie on the line showing the validity of the present law of the wall, and the correctness of the value of the $U_{1\tau}$ is confirmed.

We further examine the propriety of this logarithmic law (22) and the universality of the velues of A_1 and B_1, using the experimental results at various stations. Let us use the logarithmic velocity distributions in the x- and y-directions, Eqs.(23) and (25) respectively. The experimental results at various stations with Ω_m = 1 are presented in Figs. 6a and 6b. The wall shear-stresses were determined, in the same way as mentioned above, on the basis of the logarithmic laws (23) and (25). Here the coefficients A_x and B_x, and A_y and B_y are computed from Eqs.(24) and (26). These values vary with the local speed ratio Ω, but were nearly constant in this experiment when Ω_m = 1.

Figures 6a and 6b show that the logarithmic laws, Eqs.(23), (25) and also (22), describe extremely well the experimental results at various stations. Using the wall shear-stress values estimated here, a momentum-integral check was made comparing the two sides of the momentum integral equations (6) in the x- and y-directions. The two sides of each equation agreed excellently with each other, and the correctness of the wall shear-stress values was confirmed.

Turbulence Structure

The authors reported details of the turbulent field in the boundary layer on a rotating conical body with its radius decreasing in the downstream (4). The data were accumulated by use of various single wire rotation. In the present experiment measurements were performed with I-, V- and X-probes in order to increase accuracy. There are many points to be discussed about the turbulent field, energy balance, Reynolds stress balance and so on, but here we will be concerned with the turbulent energy spectra.

In principle we may expect that the fluid dynamically meaningful turbulent structure will be reflected in its power spectrum. Let u* and v* be the fluctuating velocity components in the directions of local mean velocity U* in the stationary frame and perpendicular to it, respectively. The power spectra Φ_{u*} and Φ_{v*} are presented in Figs. 7a and 7b, where they are normalized by $\overline{u^{*2}}$ and $\overline{v^{*2}}$, respectively, and the wave number k is given by the relation $k = 2\pi f/U^*(r)$, where f is the frequency. The spectra of u* near the wall exhibit a mild but explicit hill or peak, and it disappears in the outer layer. Φ_{v*} shows a similar hill near the wall, but it still appears in the outer layer. However, it should be considered as a particular feature of the transverse spectrum (see, for example, (8)). In the inner layer the hill is superposed on this inherent trend of the Φ_{v*} curve. Lohmann reported some curves of Φ_{u*} obtained by conventional I-probe (11), and the result measured at z/δ = 0.04 showed a very slight but perceptible hill. However, he made no comment about this phenomenon. In the present experiment, the probe has come down to $z/\delta \simeq 0.005$ at z = 0.1 mm much nearer the wall than reached by Lohmann's probe, and then the hill became evident. In the cases of other speed ratios, this slight peak was also seen.

There are various possible reasons for such a hill appearing in the spectrum. The first type derives from the characteristics of the apparatus used, and it may be classified as (a) a wake produced by some still obstacles in front of the rotating cylinder, and (b) excentricity of the rotating cylinder or irregularity of the cylinder surface. The second type originates in the instricsic flow pattern of this boundary layer. It may be classified as (c) the reminiscence of the laminar-turbulent transition, which perhaps consists of a T-S wave process mixed with the Taylor-Görtler instability (9), and (d) the strong excitation or production of the velocity fluctuation in a certain spectral region in this turbulent boundary layer.

Although the value of the wave number at the hill varies with the distance from the wall and with the speed ratio, the frequency at the hill in the spectra of the inner layer is about 250 Hz and independent of z and Ω_m. Both the cases (a) and (b) are denied by the consideration of the nature of hot-wire signal produced by possible disturbances originating from (a) and (b). We are compeled to think that the hill in the spectrum originates in (c) or (d).

The wave length λ_x of the large structure in the axial direction can be evaluated as $\lambda_x = \lambda U_e/U^* = U_e/f \simeq$ 40 mm using $U_e \simeq$ 10 m/s and f ≃ 250 Hz, and it is in-

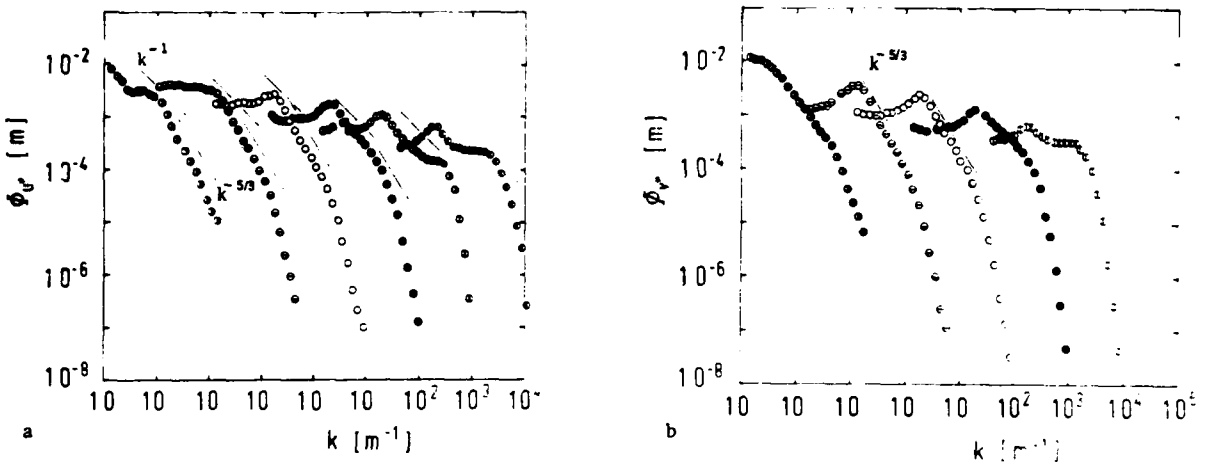

Fig. 7 Power spectra of the fluctuating velocity components in the directions of mean velocity and perpendicular to it: $\Omega_m = 1$. a, Φ_{u^*}; b, Φ_{v^*}. ◐, z = 0.1 mm; ◑, 0.2; ●, 0.7; ○, 2.5; ⊖, 15.0; ◉, 35.0

dependent of Ω_m. If we assume the helical Taylor vortex system as a simple model, it consists of six vortices around the circumference at $\Omega_m = 1$. Since the actual flow is turbulent and has a continuous spectrum, it may not be correct to imagine such a regular pattern, but we should expect a so-called eddy. It may be said that there is a relatively strong eddy around the hill of the present spectrum. Perhaps it relates to some instability of this turbulent boundary layer which resembles the Görtler vertices in the turbulent boundary layer envisaged at first by Tani (10). The eddy is most evident in the buffer layer as seen from Figs. 7a and 7b, and it may regulate the "burst." The eddy structure could be elucidated by space-time correlation measurements.

CONCLUDING REMARKS

Theoretical and experimental investigation were conducted on the thick and skewed turbulent boundary layer on a rotating thin cylinder in the uniform axial flow. The following conclusions were obtained.

First, a non-inertial non-orthogonal curvilinear coordinate system fitting the flow geometry is introduced to depict the flow field. The boundary layer equations deduced in this coordinate system suggest the relevant non-dimensional distance from the wall as $(U_{1\tau}a/\nu)(r^2 - a^2)/2r^2$. The logarithmic law which must hold in the x^1-direction is Eq.(22). The logarithmic law in the axial direction follows as Eq.(23), and the assumption of generalized quasi-collaterality yields Eq.(25) for the peripheral direction.

Secondly, the experimental results show clearly the inadequacy of the two-dimensional logarithmic law in the relative streamline direction. The proposed logarithmic laws, Eqs.(22), (23) and (25) were confirmed by the experiments.

Thirdly, the power spectra of the fluctuating velocity components were measured. In the inner layer, they exhibited an obvious hill in the region of the energy containing eddy. Discussion on the origin of this hill suggested it derives from a particular large eddy inherent in this boundary layer.

REFERENCES

1 Lohmann, R.P., "The Response of a Developed Turbulent Boundary Layer to Local Transverse Surface Motion," Journal of Fluids Engineering, Vol. 98, 1976, pp. 354-363.

2 Arzoumanian, E., Fulachier, L. and Dumas, R., Experimental Investigation of the Three-Dimensional Turbulent Boundary Layer on an Axially Rotated Cylinder," 2nd Symposium on Turbulent Shear Flows, Imperial College, London, 1979, pp. 4.28-4.33.

3 Furuya, Y. and Nakamura, I., "Velocity Profiles in the Skewed Boundary Layers on Some Rotating Bodies in Axial Flow," Journal of Applied Mechanics, Vol. 37, 1970, pp. 17-24.

4 Nakamura, I., Yamashita, S. and Furuya, Y., "Experiments on Turbulence Properties in the Thick Turbulent Boundary Layer on a Rotating Conical Body of Radius Decreasing Toward Downstream," Turbulent Shear Flows 2, ed. by L.J.S. Bradbury et al., Springer, 1980, pp. 99-115.

5 Robert, K. and Grundmann, R., "Basic Equations for Non-Reacting Newtonian Fluids in Curvilinear, Non-Orthogonal and Accelerated Coordinate Systems," Deutsche Luft- und Raumfahrt, Forschungsbericht, 76-47, 1976, pp. 1-42.

6 Furuya, Y., Nakamura, I. and Yamashita, S., "The Laminar and Turbulent Boundary Layers on Some Rotating Bodies in Axial Flows," Memoirs of the Faculty of Engineering, Nagoya University, Vol. 30, No. 1, 1978, pp. 1-58.

7 Bissonnette, L.R. and Mellor, G.L., "Experiments on the Behaviour of an Axisymmetric Turbulent Boundary Layer With a Sudden Circumferential Strain," Journal of Fluid Mechanics, Vol. 63, 1974, pp. 369-413.

8 Tennekes, H. and Lumley, J.L., A First Course in Turbulence, The MIT Press, 1972, pp. 248-287.

9 Kobayashi, R., Kohama, Y. and Takamadate, Ch., "Spiral Vortices in Boundary Layer Transition Regime on a Rotating Disk," Acta Mechanica, Vol. 35, 1980, pp. 71-82.

10 Tani, I., "Production of Longitudinal Vortices in the Boundary Layer Along a Concave Wall," Journal of Geophysical Research," Vol. 67, 1962, pp. 3075-3080.

TURBULENT FIELD OF A BOUNDARY LAYER VERY CLOSE TO AN AXIALLY ROTATED CYLINDER

E. ARZOUMANIAN, M. LEBORGNE, L. FULACHIER

Institut de Mécanique Statistique et de la Turbulence
Laboratoire associé au CNRS N° 130

12, Avenue Général Leclerc
13003 Marseille, FRANCE

ABSTRACT

A fully developed two-dimensional boundary layer on a cylinder is submitted to a sudden transversal distorsion by rotation of the downstream part of the wall. In these experiments the wall speed is of the same order as the outer velocity. This paper deals with the experimental results concerning the turbulent velocity field. In order to analyse the evolution of three-dimensional effects, two measurement stations have been explored. Emphasis has been placed on the very-close-to-the-wall regions up to the sublayer. The influence of the rotation on the standard deviations of longitudinal and transverse velocity fluctuations and their correlations has been examined. In these regions, $\overline{u'v'}$ and $\overline{w'v'}$ Reynolds stresses can be attained only by integrating the statistical momentum equations. Actually, it will be shown that interpretation of most of these results must be done by considering a relative coordinate system spinning with the cylinder. In particular, comparison can be made between the results obtained with rotation, and considered in these axes, and those obtained with no rotation.

NOMENCLATURE

a	Cylinder radius, m
$\bar{q}$	Mean velocity vector, $\bar{q}$ $(\bar{u},\bar{w})$, ms^{-1}
q_e	Free stream velocity, $q_e=(U_e^2+W_o^2)^{1/2}$, ms^{-1}
$\bar{q}_r$	Relative mean velocity vector (see Fig. 5), ms^{-1}
R	Correlation coefficient of u' and w'
U_o^*	Friction velocity defined by $U_o^*=U_o^* q_e/U_e$, ms^{-1}
U_o^*	Friction velocity with no rotation, ms^{-1}
u,v,w	Velocity components in S(x,y,z) system, ms^{-1}
U_e	Local axial free stream velocity, ms^{-1}
U_{e_o}	U_e for X = -30 mm, ms^{-1}
W_o	Velocity of the wall, ms^{-1}
X	Axial distance along rotating wall, m
$x,y,z,$	Coordinates in fixed system S(see Fig. 1), m
y^+	Distance from the wall, $y^+=yU_o^*/\nu$
γ	Angle defined in Fig. 5, degree
δ	Local boundary layer thickness ($\bar{u}$), m
δ_o'	Boundary layer thickness for X=-30 mm ($\bar{u}$=.99U_e), m
ψ_o	Angle defined on Fig. 5·degree
$(\,)',(\bar{\ })$	Fluctuation and mean value of ( )
$(\,)$	Quantities in relative system S(x,y) (see Fig. 5)

INTRODUCTION

Measurements in three-dimensional boundary layer are still rare and fails to establish turbulence models for the computation of boundary layer flows. The main purpose of the present investigation is to provide such experimental tools in the case of an axially rotated cylinder with special emphasis in the region very close to the moving wall. This body has a forward stationary part along which a two-dimensional boundary layer is developing.

In a first set of experiments, presented in the previous Turbulent shear flows symposium (1), the mean velocity field had been explored in a region

sufficiently far away the origin of the spinning part. In that region the reorganization of the three-dimensional boundary layer into a two-dimensional one - in a relative coordinate system - is in an advanced phase. The present paper is entended to give last experimental results which concern the turbulent field. Moreover, in order to determine the evolution of the rotation effect, measurements have been carried out nearer the origin where the three-dimensionality is stronger. In particular, it is pointed out that, when measurements results related to the moving wall are analysed in the same coordinates system as in the stationary case, their interpretations can be very misleading.

EXPERIMENTAL CONDITIONS AND PROCEDURES

A detailed description of the model and the wind tunnel has been already given (1), (2).

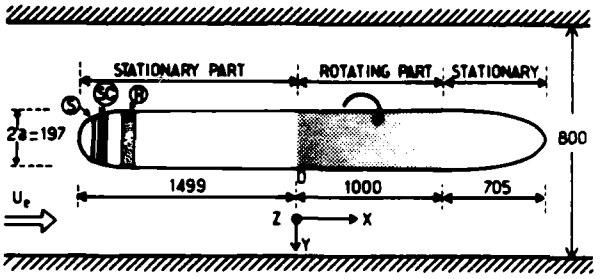

Fig. 1 : Schematic arrangement of apparatus (dimensions in mm). R : roughnesses, S : stripe, SC : scores.

The scheme (Fig. 1) recalls geometrical configurations to mind. The aerodynamical conditions are summarized hereafter :

- for $X/\delta'_o = -1.3$, just upstream the rotating part :

  $U_{e_o} = 12.38\ ms^{-1}$, $\delta'_o = 22.5$ mm ($\delta_o = 28$ mm),

  $R_{\delta_o} = U_e\delta_o/\nu = 23\,000$, $U^*_o = .47\ ms^{-1}$,

- at the measurement station $X/\delta'_o = 5.5$:

  $U_e = 12.40\ ms^{-1}$, $\delta = 29$ mm ($\delta' = 24$ mm)

- at the measurement station $X/\delta'_o = 28$:

  $U_e = 12.42\ ms^{-1}$, $\delta = 34$ mm ($\delta' = 28{,}3$ mm).

The stream static pressure gradient is weak, the Clauser parameter (1) being small : $\pi = -.026$.

The peripheral wall speed is $W_o = 10.8\ ms^{-1}$, i.e. $W_o/U_{e_o} = .88$.

The measurement stations have been selected from the longitudinal evolution (Fig. 2) of the deviation γ of the relative velocity vector q_r defined on Fig. 5. This angle γ characterizes the effect of three-dimensionality. All along the x direction, two laws can be pointed out for the variation of the

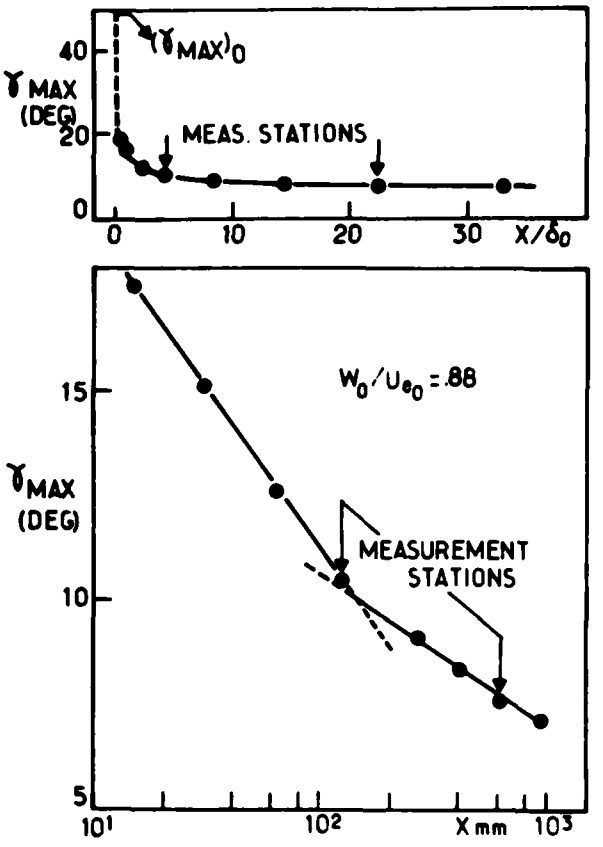

Fig. 2 : Longitudinal variation of the maximum of the γ angle.

maximum γ angle (Fig. 2). These results are deduced from $\bar{u}$ and $\bar{w}$ velocity profiles (1,2).

Concerning the instrumentation, various types of difficulties have been got over, in particular, for the investigation of very-close-to-the-wall region ($y^+ > 2$). Measurement procedure of the modulus and the direction of mean velocity vectors have been previously reported (1), (2). While the wall effects plays an important role in the stationary wall case (for $y < 1$ mm), no correction seems to be necessary in the rotating wall case in the aforecited experimental conditions. This is owing to the relatively high velocities which prevail in these regions.

Turbulent quantities need more elaborate techniques. A data acquisition system and a digital treatment have been used in connection with a single straight rotating hot wire. A three equation system corresponding to the different positions of the wire yields $\overline{u'^2}$, $\overline{w'^2}$, $\overline{u'w'}$. Thermal drifts, calibrations and experimental conditions variations are numerically taken into account. Moreover the hot wire is sensitive to the tangential component of the velocity vector and this influence is not negligible for the incidences of the wire presently adopted ($\phi = \pm 40°$). The contribution of this component has been taken into account for measurements corresponding to $X/\delta'_o = 5.5$.

In the contrast, direct measurements of the tangential turbulent stresses $\overline{u'v'}$ and $\overline{w'v'}$ are no

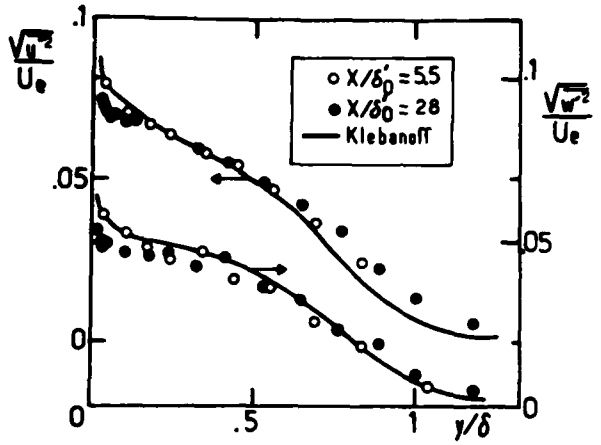

Fig. 3 : Standard deviations of longitudinal and transverse velocity components (no rotation).

more possible in the sublayer and the buffer layer owing to the dimensions of the probe. Therefore these terms have been computed by integrating the corresponding momentum equations from mean velocity measurements (1).

EXPERIMENTAL RESULTS AND INTERPRETATIONS

No Rotation Case

Fig. 3 and 4 give results related to longitudinal and transversal standard deviations at the two measurements stations. Far away the wall ($y/\delta > .03$, fig. 3) results have a similar behavior as these obtained in the boundary layer of a flate plate by Klebanoff (3). Very close to the wall ($y^+ < 30$, Fig. 4), the variation of $(\overline{u'^2})^{1/2}/U_o^*$ are in agreement with Klebanoff (3) and Laufer (4) measurements. At the contrary, it appears that $(\overline{w'^2})^{1/2}/U_o^*$ yields values noticely higher than those of Laufer (4) and Sirkar (5). This could be due to the differences of

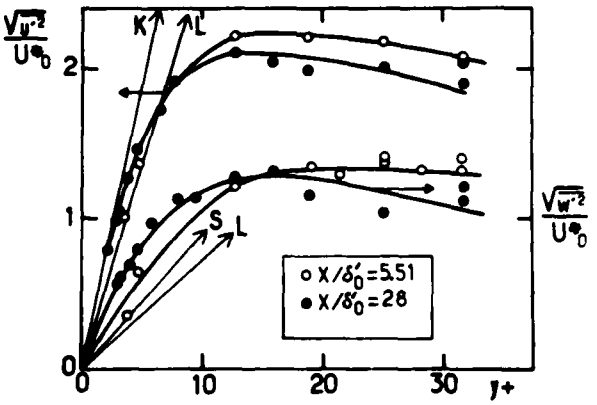

Fig. 4 : Standard deviations of longitudinal and transverse velocity components close to the wall (no rotation). K : (3), L : (4), S : (5).

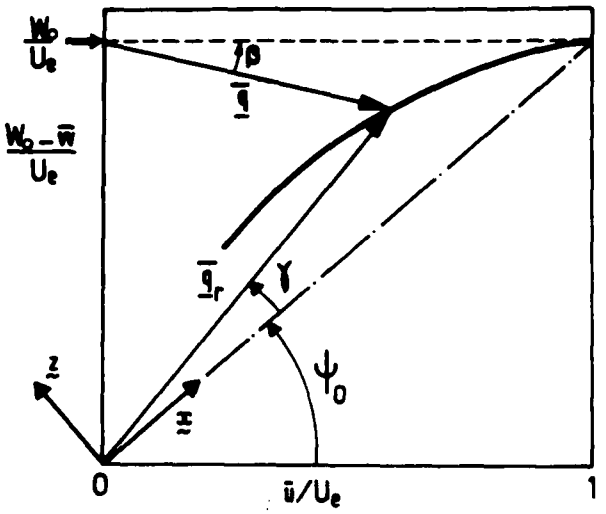

Fig. 5 : Definitions of velocities and angles in the hodograph plane.

the wall geometry.

As concerns the correlation $\overline{u'w'}$ the values obtained (Fig. 7, 9, 10, 11) even near the wall are practically null as one might expect.

Definitions

Fig. 5 shows, in the hodograph plane, the definitions of different quantities which will be used hereafter. In this representation $(u/U_e, (W_o - w)/U_e)$ the transverse velocity is null at the wall and outward the boundary layer, the velocity vector direction is defined by the ψ_o angle. In the case of an

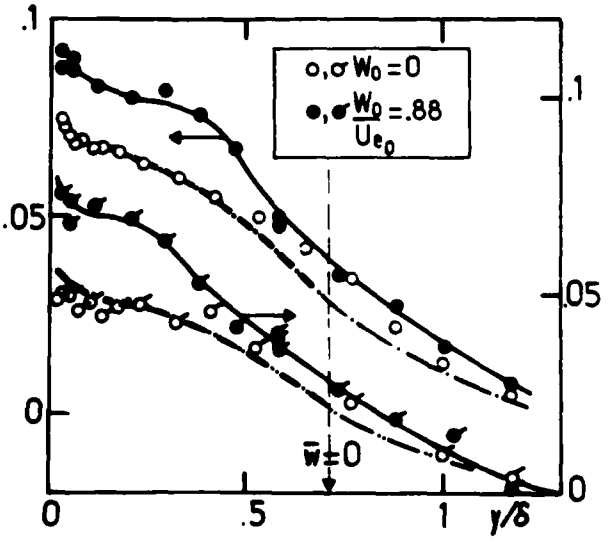

Fig. 6 : Standard deviations of longitudinal and transverse velocity components for $X/\delta'_o = 28$. •, o $(\overline{u'^2})^{1/2}/U_e$; σ, σ $(\overline{w'^2})^{1/2}/U_e$; — · — $(\overline{u'^2})^{1/2}/q_e$; — ·· — $(\overline{w'^2})^{1/2}/q_e$.

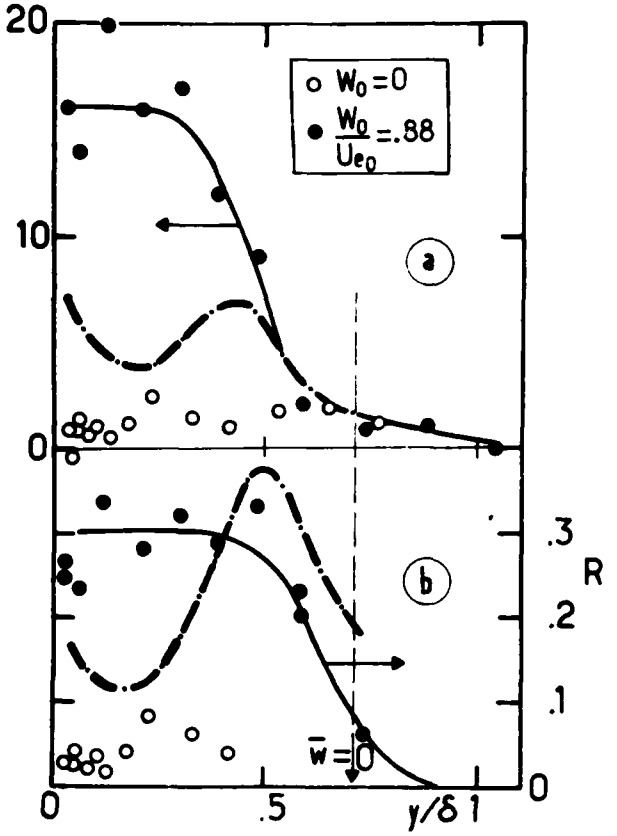

Fig. 7 : Correlations and correlation coefficients of longitudinal and transverse velocity components for $X/\delta_o' = 28$

(a) : ●,○ $[(-\overline{u'w'})/U_e^2]\ 10^4$;

— · — · — $[(-\overline{u'w'})/q_e^2]\ 10^4$

(b) : ● ○ R , — · — R

infinitely long cylinder, q_e would be colinear to that direction, the flow would become colateral and would be considered as two-dimensional in the (x,z) coordinates system S . So, in the same way that γ (with $tg\ \gamma = \bar{w}/\bar{u}$) characterises, for the mean flow, the level of the three-dimensionality, it would be necessary to consider the turbulent quantities in the S system. In the case of an infinite rotating cylinder, we would have $\bar{w} = 0$ and on the other hand $\bar{u}/q_e$ and turbulent quantities similar to the values obtained, at the same distance X, on a stationary cylinder, not with an outer velocity U_e but with an outer velocity q_e. The component (u,w) of the velocity vector q_e in S system are deduced from (u,W_o-w) by a rotation of an angle ψ_o (Fig. 5). For instance :

$$u' = u'(U_e/q_e) - w'\ (W_o/q_e)$$

$$w' = -\,u'(W_o/q_e) - w'\ (U_e/q_e)$$

The influence of the rotation on the turbulent quantities and the three-dimensional effects which are induced are pointed out by comparing respectively

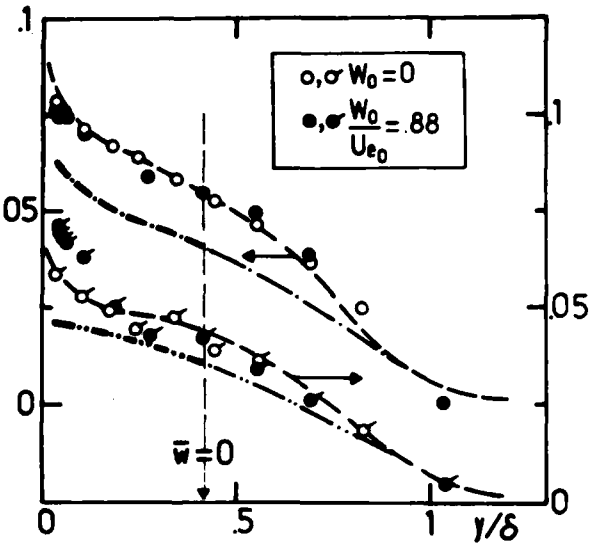

Fig. 8 : Standard deviation of longitudinal and tranverse velocity components for $X/\delta_o' = 5.5$
See caption Fig. 6 (- - - Klebanoff(3))

$(\overline{u'^2})^{1/2}/q_e$, $(\overline{w'^2})^{1/2}/q_e$, $\overline{u'w'}/q_e^2$, $\overline{u'v'}/q_e$, $\overline{w'v'}/q_e$ (at $W_o \neq 0$) to $(\overline{u'^2})^{1/2}/U_e$, $(\overline{w'^2})^{1/2}/U_e$, $\overline{u'w'}/U_e^2$, $\overline{u'v'}/U_e^2$, $\overline{w'v'}/U_e^2$. Close to the wall,

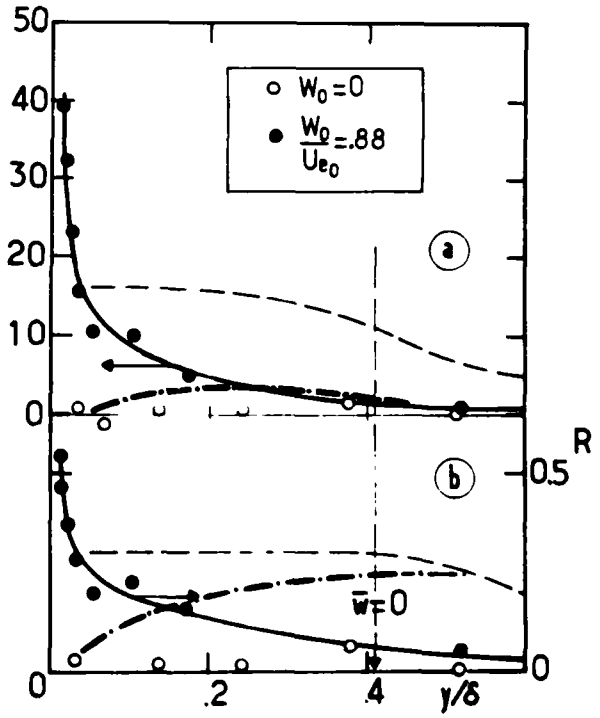

Fig. 9 : Correlations and correlation coefficients of longitudinal and transverse velocity components for $X/\delta_o' = 5.5$
See caption Fig. 7 (- - $X/\delta_o' = 28$)

the normalization is made with $\underset{\sim}{U}^*_o$ and U^*_o respectively

Results far from the wall

At $X/\delta'_o = 28$, sufficiently far from the origin of the spinning part, the influence of the rotation on $(\overline{u'^2})^{1/2}$ and $(\overline{w'^2})^{1/2}$ seems important in the absolute reference system (Fig. 6). Actually, when $\underset{\sim}{S}$ system is considered, $(\overline{u'^2})^{1/2}/q_e$ and $(\overline{w'^2})^{1/2}/q_e$ values are coïncident practically with $(\overline{u'^2})^{1/2}/U_e$ and $(\overline{w'^2})^{1/2}/U_e$ respectively, with no rotation. Of course, this interpretation is to be made only in the region bounded to the influence zone of the rotation (where $w \neq 0$). In the contrast, the correlation $\overline{u'w'}$ and the coefficient correlation R seems more modified (Fig. 7) than standard deviations. It can be also noticed that R presents, in the wall region, a constant value of about -.3. Furthermore this value is approximately of the same order as those obtained from a theoritical law (6) which gives $R \simeq -0.2$. However this law is not valid in the low Reynolds number region very-close-to-the-wall where measurements reveal an increase of R.

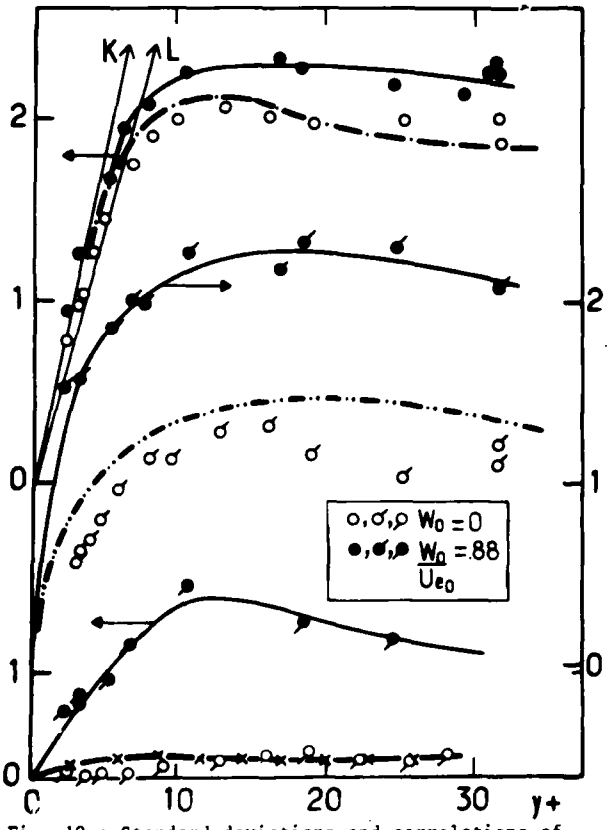

Fig. 10 : Standard deviations and correlations of longitudinal and transverse velocity components close to the wall (X/δ'_o=28)
●, o $(\overline{u'^2})^{1/2}/U^*_o$; ◜, σ $(\overline{w'^2})^{1/2}/U^*_o$;
●, ρ $(-\overline{u'w'})/U^{*2}_o$; — · — $(\overline{u'^2})^{1/2}/U^*_o$;
— ·· — $(\overline{w'^2})^{1/2}/U^*_o$; — x — x — $(-\overline{u'w'})/U^{*2}_o$;
K (3), L (4)

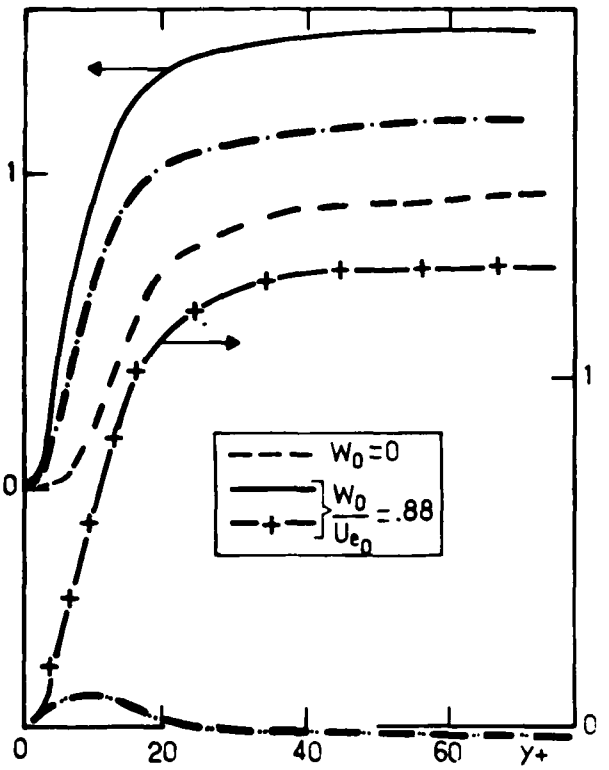

Fig. 11 : Reynolds stresses close to the wall (X/δ'_o = 28)
— , - - - $(-\overline{u'v'})/U^{*2}_o$ — + — + — $(\overline{w'v'})/U^{*2}_o$
— · — $(-\overline{u'v'})/U^{*2}_o$, — ·· — $(\overline{w'v'})/U^{*2}_o$

At X/δ'_o = 5.5, in the absolute coordinates system, the effect of the rotation on $(\overline{u'^2})^{1/2}$ seems practically negligible even in the region where $w \neq 0$. This would suggest that the longitudinal velocity fluctuations have a strong memory. In the $\underset{\sim}{S}$ system the trend to the two-dimensionality is then in defect. Concerning the correlations, their high level obtained in absolute axes, for $.03 < y/\delta < .2$, are misleading as it is shown on Fig. 9, in the $\underset{\sim}{S}$ representation. It can be noticed, at this station, the correlation coefficient has no more a constant value about the theoretical value of -.2 as for X/δ'_o = 28.

Results close-to-the-wall

In these regions, the parameter corresponding to U^*_o (with no rotation) in the $\underset{\sim}{S}$ system must be $\underset{\sim}{U}^*_o = \underset{\sim}{U}^*_o \, q_e/U_e$ which is linked to the skin friction of a boundary layer in which the outer velocity would be q_e and the wall conditions W_o=0. Indeed, the skin friction coefficient is irrelevant inasmuch as it is practically independent of the velocity when this one varies from U_e to q_e.

At X/δ' =28, Fig. 10 shows for the longitudinal velocity fluctuations a similar behaviour as farther from the wall (Fig. 6) : in the $\underset{\sim}{S}$ system, one finds again the values corresponding to W_o=0, what shows that for this component all is so that the boundary

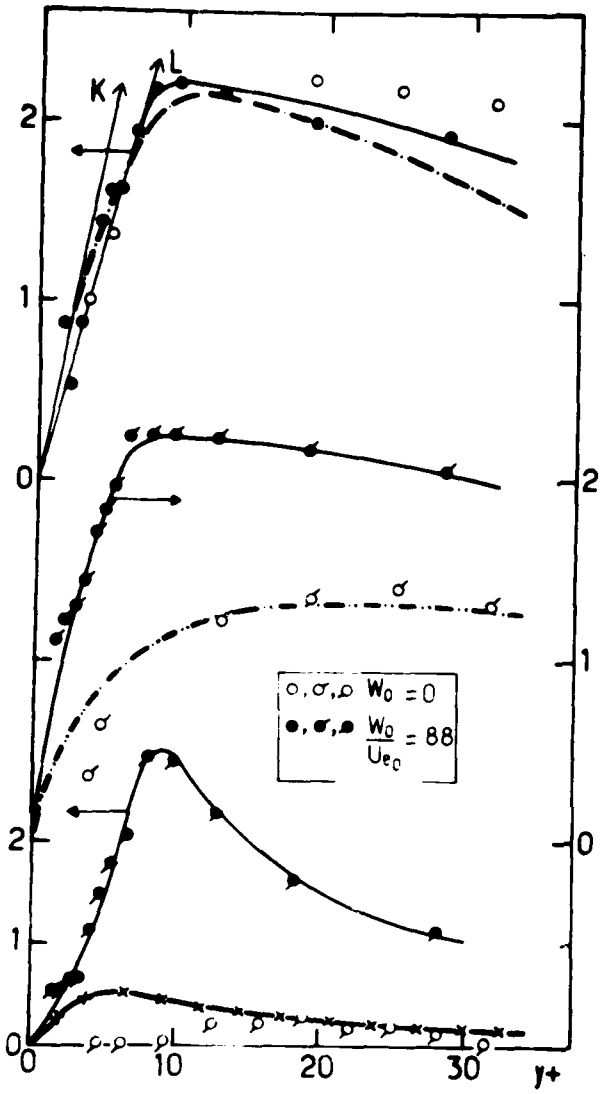

Fig. 12 : Standard deviations and correlations of longitudinal and transverse velocity components close to the wall (X/δ'_o = 5.5) See caption Fig. 10.

layer would be entirely reorganized into a two-dimensional structure. The slight three-dimensional effects observed at this station, and in this region of the boundary layer, appear partly through the transverse velocity component. The correlations $\overline{u'w'}/U^{*2}_o$ and $\overline{u'w'}/U^{*2}_o$ are very similar. Besides, in the same order of idea, it is found (Fig. 11) that $\overline{w'v'}$ is practically null. The three dimensionality seems to be revealed principaly through $\overline{u'v'}$, as it is displayed, as an example, on Fig. 11.

At X/δ'_o = 5.5, Fig. 12 points out that the standard deviations of longitudinal and transverse velocity and the correlation of corresponding fluctuations have a similar behaviour as at the previous stations. This result would show that, even at this small longitudinal distance of the origin of the spinning part, the three-dimensional effect would be weak close to the wall. This would be consistent with the collaterality of the flow, in these wall regions, and with the existence of an inflexion point in the hodograph (1, 2, 7).

CONCLUSION

The turbulent field of a complex wall flow has been investigated. The experiments are carried out in the boundary layer of an axially rotating cylinder up to the inner part of the sublayer. The interpretation of results must be made in a relative coordinates system linked to the moving cylinder with an x-axes corresponding to the outer relative velocity. Far from the origin (X/δ'_o = 28)of the spinning part, the turbulent quantities are very slighty influenced by the three-dimensional effects, except the Reynolds stress $\overline{u'v'}$. A similar result is obtained nearer (X/δ'_o = 28)in the very-close-to-the-wall region. This suggests that,in this region, the flow has a behaviour of a two-dimensional boundary layer, what is consistent with the collaterality of the mean flow the direction of which has been found aligned with the external relative velocity. In the contrast, at this station (X/δ'_o = 5.5), the three-dimensional effects are well marked far from the wall. So, the zone where the flow is collateral, is developed from the wall. This occurs from X-distance relatively small (X/δ'_o = 5). Actually, the strong three-dimensional effects spread from the wall to the whole boundary layer in the very initial zone of the spinning part of the cylinder.

ACKNOWLEDGMENT

The authors are indebted to Dr. DUMAS R. for his advice ant to Mr. ASTIER M. for his technical assistance during the investigation.

REFERENCES

1 Arzoumanian, E., Fulachier, L., and Dumas, R., "Experimental Investigation of the Three-Dimensional Turbulent Boundary Layer on an Axially Rotated Cylinder", Proceedings of 2nd International Symposium on Turbulent Shear Flows, London, 1979, pp. 4.28-4.33.

2 Arzoumanian, E., Fulachier, L., Cousteix, J., and Aupoix, B., "Couche Limite Turbulente Tri-Dimensionnelle : Restructuration d'un Ecoulement Axysymétrique Soumis à une Discontinuité de la Vitesse de Paroi", AGARD Conference Proceedings N° 217, The Hague, 1979, pp. 19.1-19.11.

3 Klebanoff, P.S., "Characteristics of Turbulence in a Boundary Layer with Zero Pressure Gradient" N.B.S., NACA 3178, 1954.

4 Laufer, J., "The Structure of Turbulence in Fully Developed Pipe Flow", NACA TN 2954, 1953.

5 Sirkar, K.K., and Hanratty, T.J., "The Limiting Behaviour of the Turbulent Transverse Velocity Component Close to a Wall", Journal of Fluid Mechanics, Vol. 44, 1970, pp. 605-614.

6 Cousteix, J., Private communication.

7 Fulachier, L., Arzoumanian, E., Dumas, R., Cousteix, J., and Aupoix, B., "Wall Region of a Complex Turbulent Boundary Layer on an Axially Rotated Cylinder", XVth International Congress of Theoritical and Applied Mechanics, Toronto, 1980.

Turbulent Flow in Unbounded Streamwise Corners

D. Arnal

J. Cousteix

Aerothermodynamics Department

ONERA / CERT

2 av. E. Belin 31055 Toulouse Cedex

ABSTRACT

This paper deals with a numerical study of turbulent corner flow. The basic equations are the streamwise momentum equation, the streamwise component of the vorticity equation and two equations of Poisson's type for the secondary velocities. The various kinds of secondary flows are discussed. In the case of a straight corner with a uniform external velocity, the modelling of the Reynolds stresses is crucial to predict correctly the development of second kind secondary flows. The boundary conditions imposed to secondary velocities are also discussed. First results relative to corner flow with positive pressure gradient are presented. In a general manner, the overall agreement with experiments seems to be good, but the extent of the vortices is underestimated.

NOMENCLATURE

Cf	skin friction coefficient
H	shape parameter
k	turbulence kinetic energy
p	static pressure
p'	pressure fluctuation
U, V, W	mean velocity components
$\overline{u'v'}$, $\overline{u'w'}$, $\overline{v'w'}$	Reynolds shear stress components
$\overline{v'^2}$, $\overline{w'^2}$	normal Reynolds stress components
x, y, z	Cartesian coordinates
δ	boundary layer thickness
ϵ	isotropic dissipation rate
μ	viscosity
ν	kinematic viscosity
ν_t	eddy viscosity
ρ	fluid density
ξ, η, ζ	vorticity components

Subscript

∞	two-dimensional quantity (y or z $\rightarrow \infty$)

INTRODUCTION

Developing turbulent flow along an unbounded, streamwise corner represents a usual example of complex three-dimensional flow and has some practical importance. The main feature of such a flow is the presence of mean transversal vortex-like motion (secondary flow), which alters the primary flow in the corner region. This pattern provides a good tool for examining the validity of turbulence models. Indeed, the main objective of this paper is to evaluate the importance of the closure problem for calculating the secondary flow.

Experimental studies of incompressible corner flow had been done by several authors, for zero pressure gradient (Mojola and Young / 1 /, Bragg / 2 /) and non zero pressure gradient (Mojola and Young / 1 /, Toan / 3 /). Another problem close to the corner flow problem is the duct flow problem for which experimental data are available (Gessner et al. / 4 /, Melling and Whitelaw / 5 /).In the latter case, the axial velocity must be calculated step by step by ensuring the total mass conservation ; on the contrary, the external velocity distribution is a datum for the corner flow problem. Moreover, the boundary conditions are less obvious for the corner flow than for the duct one, where the geometry imposes simple symmetry conditions. This problem will be discussed later on in this paper.

GEOMETRY AND EQUATIONS

The considered geometry and the governing equations are given in Figure 1. The corner is formed by two semi-infinite planes intersecting at right angle ; the intersection line is parallel to the external velocity Ue.

This work was sponsored by the Société Technique des Programmes Aeronautiques under Grant STPA n° 80.95.004

The equations to be solved are the following ones :

$$U\frac{\partial U}{\partial x} + V\frac{\partial U}{\partial y} + W\frac{\partial U}{\partial z} = -\frac{1}{\rho}\frac{d\bar{P}}{dx} + \frac{\partial}{\partial y}\left(\nu\frac{\partial U}{\partial y} - \overline{u'v'}\right) + \frac{\partial}{\partial z}\left(\nu\frac{\partial U}{\partial z} - \overline{u'w'}\right) \quad (1)$$

$$U\frac{\partial \omega}{\partial x} + V\frac{\partial \omega}{\partial y} + W\frac{\partial \omega}{\partial z} = \omega\frac{\partial U}{\partial x} + \omega_y\frac{\partial U}{\partial y} + \omega_z\frac{\partial U}{\partial z} + \nu\left(\frac{\partial^2\omega}{\partial y^2} + \frac{\partial^2\omega}{\partial z^2}\right) + \frac{\partial^2}{\partial y\partial z}\left(\overline{v'^2} - \overline{w'^2}\right) + \left(\frac{\partial^2}{\partial z^2} - \frac{\partial^2}{\partial y^2}\right)\overline{v'w'} \quad (2)$$

$$\frac{\partial^2 W}{\partial y^2} + \frac{\partial^2 W}{\partial z^2} = \frac{\partial \omega}{\partial y} - \frac{\partial^2 U}{\partial x\partial z} \quad (3)$$

$$\frac{\partial^2 V}{\partial y^2} + \frac{\partial^2 V}{\partial z^2} = -\frac{\partial \omega}{\partial z} - \frac{\partial^2 U}{\partial x\partial y} \quad (4)$$

with : $\omega = \frac{\partial W}{\partial y} - \frac{\partial V}{\partial z}$,

$$\omega_y = \frac{\partial U}{\partial z} - \frac{\partial W}{\partial x}\ ,\ \omega_z = \frac{\partial V}{\partial x} - \frac{\partial U}{\partial y} \quad (5)$$

These equations are: the streamwise momentum equation, the equation for the streamwise component of the vorticity, and two Poisson's equations for the secondary velocities V and W. Equations (3) and (4) are deduced from the continuity equation and from the definition of ω (equation 5). The x-diffusion terms and the first derivatives of the Reynolds stresses in the streamwise direction are neglected ; $\frac{\partial U}{\partial y}$ and $\frac{\partial U}{\partial z}$ are assumed to be the preponderant derivatives of the mean velocity ; in the x-momentum equation (1), the pressure $\bar{P}$ is supposed to be a given function of x.

This set of assumptions, which constitutes an extension of the usual boundary layer hypothesis, leads to a parabolized system in the x direction. For solving the elliptic equations for V and W in each (y, z) plane, a double-sweep procedure is used / 6 /.

The equation for ω contains terms of particular importance : the first term of the right-hand side describes the "vortex stretching" ; the two following terms describe the production of "Prandtl's first kind secondary flows" by skewing of the mean shear ; these terms are very small in the present study. The last two terms of the right-hand side appear only in turbulent flow, they are responsible for maintaining "Prandtl's second kind secondary flows". The experimental results given in Figure 2 (/ 1 /, / 2 /) show examples of such secondary flows as they appear in an unbounded corner. These secondary flows consist of two "vortices", the presence of which is shown by a distorsion , towards the corner, of streamwise longitudinal velocity contours. So an accurate description of the anisotropy of turbulence is necessary to reproduce the vortex-like pattern observed in experiments.

CLOSURE RELATIONSHIPS

Two turbulence models (TM1 and TM2) have been tested.

TM1 model

This model constitutes an extension of Boussinesq's assumption :

$$\overline{u_i'u_j'} = \frac{2}{3}\delta_{ij}k - \nu_t\left(\frac{\partial U_i}{\partial x_j} + \frac{\partial U_j}{\partial x_i}\right) \quad (6)$$

δij is the Kronecker's symbol, k the turbulence kinetic energy ($k = \frac{1}{2}\overline{u'^2}$) and ν_t the eddy viscosity. ν_t is expressed by a classic mixing length relationship :

$$\nu_t = F^2\ell^2\left[\left(\frac{\partial U}{\partial y}\right)^2 + \left(\frac{\partial U}{\partial z}\right)^2\right]^{\frac{1}{2}}, \text{ with :}$$
$$\frac{\ell}{\delta_\infty} = 0.085\ th\left(\frac{0.41}{0.085}\frac{d}{\delta_\infty}\right),\ d = Min(y, z) \quad (7)$$

δ_∞ represents the "two-dimensional" boundary layer thickness when y (or z) goes to infinity. F is a damping function for the near-wall regions ; its form constitutes an extension of Van Driest's formula:

$$F = 1 - \exp\left(\frac{-\ell}{10.7\mu}\sqrt{\tau\rho}\right),\ \tau = (\mu + \rho\nu_t)\left[\left(\frac{\partial U}{\partial y}\right)^2 + \left(\frac{\partial U}{\partial z}\right)^2\right]$$

TM2 model

It should be possible to solve the transport equations for $\overline{u_i'u_j'}$:

$$\underbrace{U_k\frac{\partial \overline{u_i'u_j'}}{\partial x_k}}_{\text{Convection}} = -\underbrace{\left(\overline{u_j'u_k'}\frac{\partial U_i}{\partial x_k} + \overline{u_i'u_k'}\frac{\partial U_j}{\partial x_k}\right)}_{\text{Production}}$$
$$\underbrace{-2\nu\left(\overline{\frac{\partial u_i'}{\partial x_k}}\right)\left(\overline{\frac{\partial u_j'}{\partial x_k}}\right)}_{\text{Dissipation}} + \underbrace{\overline{\frac{p'}{\rho}\left(\frac{\partial u_j'}{\partial x_i} + \frac{\partial u_i'}{\partial x_j}\right)}}_{\text{Redistribution}} \quad (8)$$
$$\underbrace{-\frac{\partial}{\partial x_k}\left[\overline{u_i'u_j'u_k'} - \nu\frac{\partial \overline{u_i'u_j'}}{\partial x_k} + \overline{\frac{p'}{\rho}\left(\delta_{jk}u_i' + \delta_{ik}u_j'\right)}\right]}_{\text{Diffusion}}$$

To simplify the numerical work, it is interesting to neglect the convection and diffusion terms ; it is also assumed that $2\nu\left(\overline{\frac{\partial u_i'}{\partial x_k}}\right)\left(\overline{\frac{\partial u_j'}{\partial x_k}}\right) = \frac{2}{3}\delta_{ij}\varepsilon$, with $\varepsilon = \nu\left(\overline{\frac{\partial u_i'}{\partial x_k}}\right)^2$; the modelling of the redistribution terms proposed by Launder-Recce-Rodi / 7 / is adopted ; if the derivatives of the mean velocity other than $\frac{\partial U}{\partial y}$ and $\frac{\partial U}{\partial z}$ are neglected, the Reynolds stress components are expressed by analytical formulae. In particular, we have :

$$\overline{v'^2} - \overline{w'^2} = \frac{4}{C_1}\frac{(4C_2-1)}{11}\frac{k}{\varepsilon}\left(\overline{u'v'}\frac{\partial U}{\partial y} - \overline{u'w'}\frac{\partial U}{\partial z}\right)$$
$$\overline{v'w'} = \frac{2}{C_1}\frac{(4C_2-1)}{11}\frac{k}{\varepsilon}\left(\overline{u'v'}\frac{\partial U}{\partial z} + \overline{u'w'}\frac{\partial U}{\partial y}\right) \quad (9)$$
$$-\overline{u'v'} = \nu_t\frac{\partial U}{\partial y}$$
$$-\overline{u'w'} = \nu_t\frac{\partial U}{\partial z}$$
with $\nu_t = \frac{1}{C_1}\left(\frac{4}{15} + \frac{-6C_2^2 - 12C_2 + 2}{33C_1}\right)\frac{k^2}{\varepsilon}$

This procedure, proposed by Launder / 8 / has been used by Gessner et al. / 9 /, / 10 / for calculating turbulent flows in ducts.

Two constants, C_1 and C_2, appear in the model.

Let us set $C_2 = 0.25$.

Then $\overline{v'^2} - \overline{w'^2} = 0$, and the turbulent production terms in equation (2) are equal to zero. This means that no second kind secondary flow can be generated.

The eddy viscosity ν_t has been calculated, by using the same mixing length formula as in TM1, instead of solving the k-ε equations. The

dissipation rate ε is obtained from the simplified k-equation (convection and diffusion neglected) :

$$\varepsilon = -\overline{u'v'}\frac{\partial U}{\partial y} - \overline{u'w'}\frac{\partial U}{\partial z}$$

and the turbulent kinetic energy from $\nu_t = C_\mu \frac{k^2}{\varepsilon}$

INITIAL AND BOUNDARY CONDITIONS

For estimating the U, V, W and ω fields in the initial (y,z) plane, we extend Carrier's formulation / 11 /, initially used for the laminar corner flow problem. With the dimensionless quantities $\bar{y} = y/\delta_\infty$ and $\bar{z} = z/\delta_\infty$, the mean velocities are expressed by :

$$U = U_e \frac{\partial^2 g}{\partial \bar{y} \partial \bar{z}}$$

$$V = U_e \frac{d\delta}{dx}\left(\bar{y}\frac{\partial^2 g}{\partial \bar{y}^2 \partial \bar{z}} - \frac{\partial g}{\partial \bar{z}}\right)$$

$$W = U_e \frac{d\delta}{dx}\left(\bar{z}\frac{\partial^2 g}{\partial \bar{y}^2 \partial \bar{z}} - \frac{\partial g}{\partial \bar{y}}\right)$$

These relations allow the continuity equation to be satisfied. Moreover, the function g is given by :

$$g = f_0(\bar{y}) f_0(\bar{z}) \quad \text{with} \quad f_0(\bar{z}) = \int_0^{\bar{z}} f' \, d\bar{z}$$

where f' represents the classic two-dimensional boundary layer profile, and $d\delta/dx$ is estimated by :

$$\frac{d\delta}{dx} = \frac{0.304}{R_x^{0.2}}$$

ω is calculated from its definition. It can be pointed out that the two vortices responsible for the secondary flow are not included in the initial conditions.

The calculation grid is shown in Figure 3. The equations are solved in the (Y, Z) coordinates defined by :

$$Y = z^2 - y^2 \quad \text{and} \quad Z = 2yz$$

The boundary conditions are :

. along boundary 1 : U = V = W = 0

. along boundary 2 : $\frac{\partial U}{\partial z} = \frac{\partial V}{\partial z} = \frac{\partial W}{\partial z} = 0$

. along boundary 3 : $\frac{\partial U}{\partial y} = \frac{\partial V}{\partial y} = \frac{\partial W}{\partial y} = 0$

. along boundary 4 : U = Ue ; V = V (A) ; W = W (B)

The boundary conditions for W are obtained by using the derivatives $\frac{\partial V}{\partial z}$ and $\frac{\partial W}{\partial y}$, calculated at the upstream station.

NUMERICAL RESULTS OBTAINED WITH TM1

Figure 4 shows the results obtained at Δx = 0.4 m and Δx = 0.9 m, with a constant external velocity (Ue = 22 m/s) ; Δx is the distance measured from the initial station. The turbulent production terms are small, and the iso-velocity lines remain close to the initial distribution. This turbulence model is unable to reproduce the secondary flow, as it is observed in the experiments.

NUMERICAL RESULTS OBTAINED WITH TM2

Influence of C_2

Four values of C_2 have been tested : 0.20, 0.25, 0.30 and 0.40. An example of initial distributions of $\overline{v'^2} - \overline{w'^2}$ is shown in Figure 5, for C_2 = 0.20 and 0.30. These distributions are practically opposite because the quantity 4 C_2 - 1, which appears in equation (9), changes sign, and k does not depend very much on C_2. With C_2 = 0.40, the magnitude of $\overline{v'^2} - \overline{w'^2}$ becomes three times greater than the one obtained with C_2 = 0.30. Let us recall that C_2 = 0.25 gives $\overline{v'^2} = \overline{w'^2}$ Similar observations can be made for the other turbulent production term, $\overline{v'w'}$.

The results obtained at Δx = 0.9 m for C_2=0.20, 0.25 and 0.30 are plotted in Figures 6 to 8. The external velocity is still equal to 22 m/s. These Figures give the streamwise iso-velocity contours, the secondary velocities (indicated by arrows) and the iso-ω lines.

For C_2 = 0.20, below the bisector, a clock-wise rotating secondary flow associated with positive values of ω is observed (Fig. 6). Along the bisector, V and W are positive, inducing an outward bulging of the streamwise velocity contours. These results are completely at variance with the experimental results. Therefore, this value of C_2 is not acceptable.

For C_2 = 0.25 (Figure 7), no second kind secondary flow can be generated. As with the TM1 model, the numerical results do not change very much from the initial conditions.

Better results are obtained for C_2 = 0.30 (Figure 8). The secondary flow rotates as expected, and the iso-velocity lines begin to be distorded near the bisector. The tendency is the same for C_2 = 0.40, but the intensity of the streamwise vortices grows downstream without bound. On the contrary, the calculation remains stable with C_2 = 0.30, and this value will be used in the following calculations.

Comparison with the experiments of Mojola and Young

Figure 9 allows comparison between prediction and experimental data of Mojola and Young / 1 /. The external velocity is constant and equal to 30 m/s. The calculation starts at x = 0.15 m (distance from the leading edge of the plates), and the comparison is made at x = 1.091 m. The overall pattern of the experimental contours is correct, but the calculation underestimates the extent of the distorted region : see in particular the iso-velocity line U/Ue = 0.70. This observation becomes clearer by comparing the experimental and calculated secondary flow patterns (Figure 10). Another observation is that, outside the vortex region, the experimental secondary flow becomes practically parallel to the y-axis, whereas the calculated secondary flow is parallel to the bisector. This problem will be discussed later.

IMPROVEMENTS OF THE MODEL

Modification of the mixing length formula

In order to investigate the effects of the algebraic form given to the mixing length, the expression of d given by equation (7) has been modified. The new expression is deduced from Buleev's formulation:

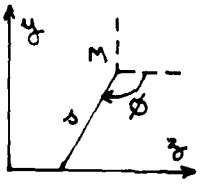

$$\frac{1}{d(M)} = \int_0^{\phi_F} \frac{d\phi}{\delta} \qquad (10)$$

In the case of the corner flow, $\phi_c = 3\pi/4$ and d takes the following form :

$$d = \frac{1}{2} \frac{y z}{(y^2+z^2)^{1/2} + y + z}$$

Note that, when z/y (respectively y/z) goes to infinity, d is equal to y (respectively z), which corresponds to the classic two-dimensional mixing length formulation.

The advantage of this expression is to give a smooth evolution of the mixing length near the corner bisector. In fact, the numerical results are almost similar. The secondary velocities are a bit smaller, but the distorsion of the longitudinal velocity lines remains practically unchanged.

Modification of the boundary conditions

The problem is to reproduce the experimental pattern of the secondary flow outside the vortex region. For this, the condition $\frac{\partial V}{\partial y} = 0$ imposed along boundary 3 is replaced by $V = 0$, and the condition $\frac{\partial W}{\partial z} = 0$ imposed along boundary 4 is replaced vy $W = 0$.

Figure 11 shows the calculated secondary flows obtained at $\Delta x = 0.9$ m with the old and the new boundary conditions. The latter leads to a better qualitative agreement with experiments, without important changes in the iso-velocity contours.

FIRST CALCULATIONS WITH POSITIVE PRESSURE GRADIENT

Mojola and Young have performed measurements in a corner flow with positive pressure gradient / 1 /. Figure 12 shows the external velocity distributions and the evolution of the shape parameter, and of the skin friction coefficient far from the corner. It can be seen that at the last station (x = 1.245 m), the two-dimensional boundary layer is near separation.

Figure 13 compares experimental and calculated evolutions of $\tau_t / \tau_{t\infty}$ with the lateral distance, for different x-stations. At x = 1.19 m, both experiments and calculations indicate a separation near the corner itself, the two-dimensional regions far from the corner being not separated. At x = 1.245 m, the separated region is extended (the accuracy of the calculation is certainly poor, due to the parabolized treatment of the equation). It appears also that the region where vortices are present is characterized by a kink in the $\tau_t / \tau_{t\infty}$ curves ; as in the zero pressure gradient case, the extent of this region is underestimated by the calculations.

CONCLUSIONS

An accurate description of the anisotropy of turbulence is needed to reproduce the vortex-like pattern of the secondary flow observed in experiment. However, when lateral curvature is involved, a refined turbulence modelling could be less important ; in this case, indeed, the first kind secondary flows are likely to be larger than the second kind ones (Johnston, in Bradshaw / 12 /).

When positive pressure gradients are present, separation appears at first near the corner itself ; other calculations are necessary to study the influence of the turbulence modelling on the separation location.

In a general manner, the extent of the secondary flow region remains too small when compared with experiments. Possibly, this problem is related to the very simple mixing length formula used in calculations ; improvements could be obtained by solving transport equations for k and ε, especially in the cases where lontitudinal pressure gradients are important.

REFERENCES

1 Mojola, O.O., and Young, A.D., "An Experimental Investigation of the Turbulent Boundary Layer Along a Streamwise Corner," AGARD CP-93, Agard Symposium on Turbulent Shear Flows, 1972.

2 Bragg, G.M., "The Turbulent Boundary Layer in a Corner," Journal of Fluid Mechanics, Vol. 36, Part 3, 1969, pp. 485-503.

3 Toan, N.K., "Couche limite turbulente à l'intérieur d'un dièdre avec gradient de pression," Thesis, University of Laval (Canada), 1968.

4 Gessner, F.B., Po, J.K., and Emery, A.F., "Measurements of Developing Turbulent Flow in a Square Duct," Proceedings of the Symposium on Turbulent Shear Flows, University Park, Pennsylvania, April 18-20, 1977.

5 Melling, A., and Whitelaw, J.H., "Turbulent Flow in a Rectangular Duct," Journal of Fluid Mechanics, Vol. 78, Part 2, 1976, pp. 289-315.

6 Patankar, S.V., and Spalding, D.B., "A calculation Procedure for Heat, Mass and Momentum Transfer in Three-Dimensional Parabolic Flows," Int. J. Heat Mass Transfer, Vol. 15, 1972, pp. 1787-1806.

7 Launder, B.E., Reece, G.J., and Rodi, W., "Progress in the Development of a Reynolds Stress Turbulence Closure," Journal of Fluid Mechanics, Vol. 68, Part 3, 1975, pp. 537-566.

8 Launder, B.E., "Progress in the Modelling of Turbulent Transport," V.K.I. Lecture Series "Prediction Methods for Turbulent Flows," 1975

9 Gessner, F.B., and Emery, A.F., "A Length Scale Model for Developing Turbulent Flow in a Rectangular Duct," Journal of Fluids Engineering, June 1977, pp. 347-356.

10 Gessner, F.B., and Emery, A.F., "The Numerical Prediction of Developing Turbulent Flow in Rectangular Ducts," Proceedings of the 2nd Symposium on Turbulent Shear Flows. Imperial College London, July 2-4,1979.

11 Carrier, G.F., "The Boundary Layer in a Corner," Quart. Appl. Math. 4, 1947, pp. 367-370.

12 Bradshaw P. (Editor), "Turbulence," Topics in Applied Physics, Vol. 12, 1976.

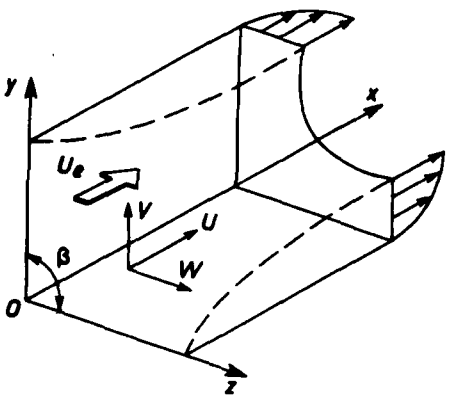

Fig. 1 : Geometry and notations

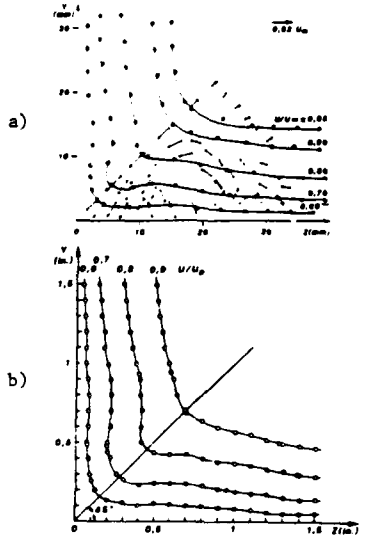

Fig. 2 : Examples of experimental results
a) Mojola and Young /1/
b) Bragg /2/

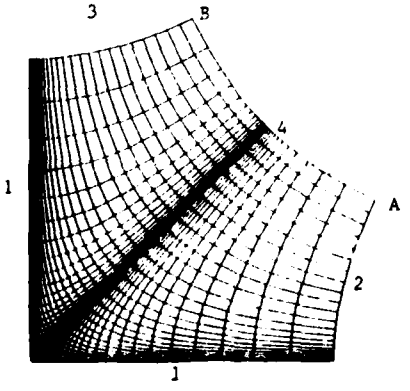

Fig. 3 : Calculation grid

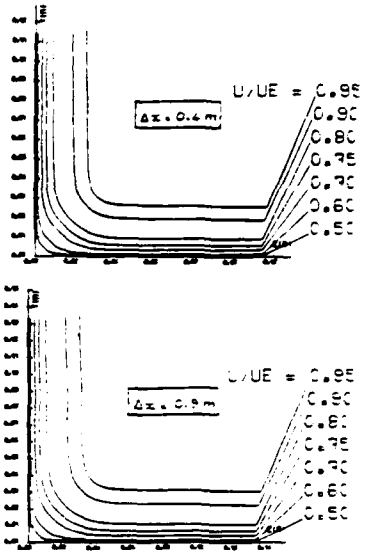

Fig. 4 : Results obtained with TNT

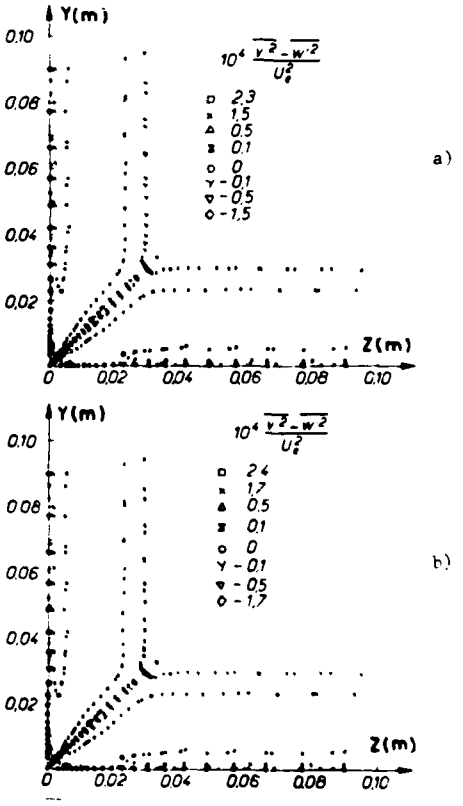

Fig. 5 : Initial distributions of $\overline{v'^2} - \overline{w'^2}$,
a) $C_2 = 0.20$ b) $C_2 = 0.30$

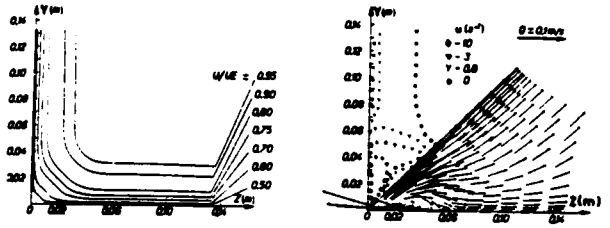

Fig. 6 : Results obtained with $C_2 = 0.20$

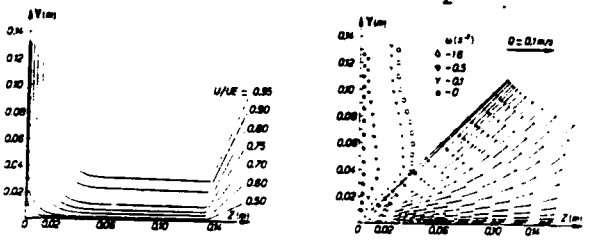

Fig. 7 : Results obtained with $C_2 = 0.25$

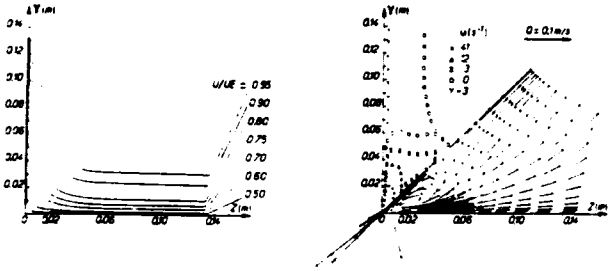

Fig. 8 : Results obtained with $C_2 = 0.30$

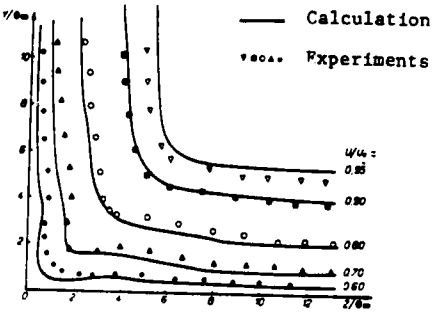

Fig. 9 : Comparison with the experiments of Mojola and Young

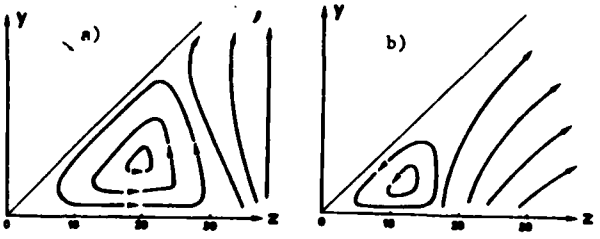

Fig. 10 : Secondary flow pattern :
a) Experiments b) Calculation

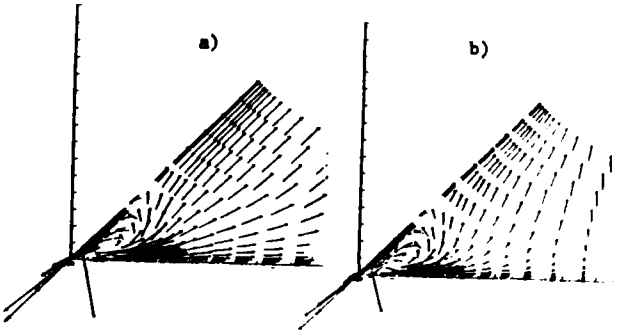

Fig. 11 : Influence of boundary conditions :
a) Old boundary conditions
b) New boundary conditions

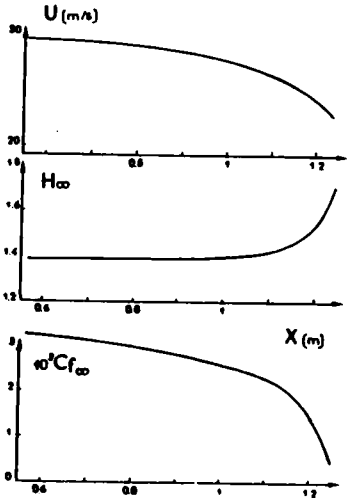

Fig. 12 : Experiments with positive pressure gradient : external velocity distribution, shape factor and skin friction coefficient far from the corner

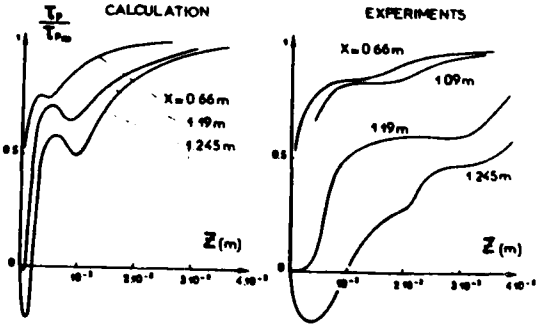

Fig. 13 : Comparison of $\tau_p / \tau_{p\infty}$ (experiments with positive pressure gradient)

A NEAR-WALL PRESSURE-STRAIN MODEL FOR TURBULENT CORNER FLOWS

F. B. Gessner
Professor

H. M. Eppich
Research Assistant

Department of Mechanical Engineering
University of Washington
Seattle, Washington 98195

ABSTRACT

The formulation of a pressure-strain model for 90-degree corner flows based on the method of images is described. Experimental results are analyzed in order to compare the model with the superposition model proposed by Reece. On the basis of these comparisons, some preliminary conclusions are drawn about the relative merits of each model.

NOMENCLATURE

a	duct half height
b	duct half width
$c_1, c_2, \ldots$	primary coefficients
$c_{1,1}, c_{1,2}$	wall correction coefficients
$c_{2,1}, c_{2,2}, \ldots$	corner correction coefficients
$c_1', c_2', \ldots$	correction coefficients (final)
c_f, k_f	empirical coefficients
k	turbulence kinetic energy
ℓ, ℓ_p	length scales
n	normal coordinate
p	fluctuating static pressure
P	turb. kinetic energy prod. rate
r, r_1, r_2, r_3	separation distances (Fig. 1)
R_T	turb. Reynolds no. ($R_T \equiv k^2/(\nu\varepsilon)$)
Re_b	bulk Reynolds no. ($Re_b \equiv 2aU_b/\nu$)
u,v,w	fluctuating velocity components in the x, y, and z directions, respt.
$\overline{u^2}, \overline{v^2}, \overline{w^2}$	Reynolds normal stress components
$-\overline{uv}, -\overline{uw}, -\overline{vw}$	Reynolds shear stress components
U	mean velocity component in x dir.
U_b	bulk velocity
U_τ	friction velocity ($U_\tau \equiv \sqrt{\tau_w/\rho}$)
V, V_ℓ	integration volumes
x,y,z	cartesian coordinates (Fig. 1)
y_1, z_1 or y',z'	reference positions (Fig. 1)
α	corner angle (Fig. 1)
$\ldots$	primary coefficients
$\ldots$	wall correction coefficients
ε	dissipation rate
$\ldots$	empirical coefficients
ν	kinematic viscosity
ξ	prod. rate/dissipation rate ($\xi \equiv P/\varepsilon$)
ρ	density
τ_w	wall shear stress

Subscripts

s	plane homogeneous shear flow
cb	corner bisector
wb	wall bisector

INTRODUCTION

This paper presents a near-wall pressure-strain model for turbulent corner flows which is an extended form of the model proposed by Launder, Reece, and Rodi (1975) for two-dimensional wall flows. Rather than superimposing effects near the bounding walls of a corner to model pressure-strain behavior in the corner layer, as suggested by Reece (1977), a more rigorous development is pursued which is based on the method of images. More specifically, the volume and surface integrals which model the pressure-strain correlation are replaced by a volume integral which includes image point distances in the integrand. The integral form is an extended version of the form originally proposed by Irwin (1974) for two-dimensional boundary layer flows. Implicit in both formulations is the assumption that the normal derivative of the fluctuating static pressure along a bounding wall is negligibly small, which is a reasonable approximation on the basis of arguments presented by Kraichnan (1956) and Irwin (1974).

In terms of modelling this effect, the condition that $\partial p/\partial n$ be identically zero at all points along the bounding walls of a 90-degree corner can be satisfied by the image point pattern shown in Fig. 1a. If a pressure fluctuation is interpreted as originating from a source at (y',z'), than a source of equal strength must be located at the image point (-y',z') to satisfy the condition that $\partial p/\partial n$ be zero on the wall y=0 at points distant from the corner. By similar reasoning, a source must also be located at the image point (y',-z') to ensure that $\partial p/\partial n$ will be zero on the wall z=0 when y is large. In the near vicinity of the corner, however, sources located only at (y',-z) and (y',-z') will cause $\partial p/\partial n$ to be non-zero along each bounding wall. This situation can be corrected by considering a source to be present at a third image point, (-y',-z'), located as shown in Fig. 1a. Under these conditions $\partial p/\partial n$ will be identically zero at all points along each wall, regardless of corner proximity.

The above arguments can be extended to other corner flow situations when the included angle between intersecting walls (α) is different from 90 degrees. When α=60 degrees, for example, five image points are required (Fig. 1b), and the number of image points increases to seven when α=45 degrees (Fig. 1c). In more general terms, if the imaged point in the flow is included (y',z'), the total number of points (N) which influence the pressure-strain correlation at the point of interest (y_1, z_1) must be such that $N\alpha = 2\pi$ (α in radians) where N is an even integer. This relationship implies that pressure-strain effects can be modelled conveniently only in certain corner flows, for unless $2\pi/\alpha$ is an even integer, the normal derivative boundary condition cannot be satisfied exactly, regardless of the number of image points used.

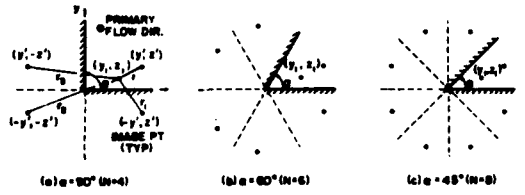

Fig. 1 Typical image point locations for various corner configurations

THEORETICAL CONSIDERATIONS

Model Formulation

In order to develop a working relationship for the pressure-strain correlation which applies for 90-degree corner flows, the influence of fictitious fluctuations at the three image point locations shown in Fig. 1a must be taken into account. If these effects are superimposed (cf. Eppich 1981), then

$$\frac{p}{\rho} = \frac{1}{4\pi}\int_R \left(\frac{1}{r_{eff}}\right)\left[\left(\frac{\partial^2 u_\ell u_m}{\partial x_\ell \partial x_m}\right)' - \left(\frac{\partial^2 \overline{u_\ell u_m}}{\partial x_\ell \partial x_m}\right)' + 2\frac{\partial \bar{U}_\ell}{\partial x_m}\left(\frac{\partial u_m}{\partial x_\ell}\right)'\right] dV \quad (1)$$

where $1/r_{eff} = 1/r + 1/r_1 + 1/r_2 + 1/r_3$. If eq. (1) is multiplied by $(\partial u_i/\partial x_j + \partial u_j/\partial x_i)$ and time averaged, then

$$\overline{\frac{p}{\rho}\left(\frac{\partial u_i}{\partial x_j} + \frac{\partial u_j}{\partial x_i}\right)} = \phi_{ij} + \phi_{ji} + \sum_{n=1}^{3} (\phi_{ij} + \phi_{ji})_{wn} \quad (2)$$

where

$$\phi_{ij} = \frac{1}{4\pi}\int_R \left[-\overline{\left(\frac{\partial^2 u_\ell u_m}{\partial x_\ell \partial x_m}\right)'\left(\frac{\partial u_i}{\partial x_j}\right)} + 2\frac{\partial \bar{U}_\ell}{\partial x_m}\overline{\left(\frac{\partial u_m}{\partial x_\ell}\right)'\left(\frac{\partial u_i}{\partial x_j}\right)}\right]\frac{dV}{r} \quad (3)$$

and

$$\phi_{ij,w_1} = \frac{1}{4\pi}\int_R \left(\frac{r}{r_1}\right)\left[-\overline{\left(\frac{\partial^2 u_\ell u_m}{\partial x_\ell \partial x_m}\right)'\left(\frac{\partial u_i}{\partial x_j}\right)} + 2\frac{\partial \bar{U}_\ell}{\partial x_m}\overline{\left(\frac{\partial u_m}{\partial x_\ell}\right)'\left(\frac{\partial u_i}{\partial x_j}\right)}\right]\frac{dV}{r} \quad (4)$$

with similar expressions applying for ϕ_{ij,w_2} and ϕ_{ij,w_3}. The first contribution to the volume integral for ϕ_{ij} will be modelled by means of Rotta's hypothesis (1951) and, following Launder, Reece, and Rodi (1975), the second contribution will be modelled as the product of the mean-rate-of-strain tensor and a fourth-order tensor subject to certain kinematic constraints imposed by assumed local homogeneity of the turbulent field. Accordingly, we let:

$$\phi_{ij} + \phi_{ji} = -c_1\frac{\varepsilon}{k}\left(\overline{u_i u_j} - \frac{2}{3}\delta_{ij}k\right) + \frac{\partial \bar{U}_\ell}{\partial x_m}\left(a^{mi}_{\ell j} + a^{mj}_{\ell i}\right) \quad (5)$$

where

$$a^{mi}_{\ell j} \equiv \frac{1}{2\pi}\int_R \overline{\left(\frac{\partial u_m}{\partial x_\ell}\right)'\left(\frac{\partial u_i}{\partial x_j}\right)}\frac{dV}{r} \quad (6)$$

with

$$a^{mi}_{\ell j} = \alpha\delta_{\ell j}\overline{u_m u_i} + \beta\left\{\delta_{m\ell}\overline{u_i u_j} + \delta_{mj}\overline{u_i u_\ell} + \delta_{i\ell}\overline{u_m u_j} + \delta_{ij}\overline{u_m u_\ell}\right\} + c_2\delta_{mi}\overline{u_\ell u_j} + \left[\eta\delta_{mi}\delta_{\ell j} + \nu\left(\delta_{m\ell}\delta_{ij} + \delta_{mj}\delta_{i\ell}\right)\right]k \quad (7)$$

In view of the similarity between eqs. (3) and (4), the effect of the first image point (r_1) will be modelled by letting

$$(\phi_{ij}+\phi_{ji})_{w_1} = \left[-c_1\frac{\varepsilon}{k}\left(\overline{u_i u_j} - \frac{2}{3}\delta_{ij}k\right) + \frac{\partial \bar{U}_\ell}{\partial x_m}\left(b^{mi}_{\ell j} + b^{mj}_{\ell i}\right)\right]\overline{\left(\frac{r}{r_1}\right)} \quad (8)$$

where $b^{mi}_{\ell j}$ is a fourth order tensor subject to the same kinematic constraints as $a^{mi}_{\ell j}$, and $\overline{(r/r_1)}$ is the integrated volume average of r/r_1 over a sphere of radius ℓ where ℓ is a length scale indicative of the size of the energy containing eddies. An explicit form for $\overline{(r/r_1)}$ can be developed by restricting the distance ℓ to be less than or equal to the distance between the wall and the point of interest. In accordance with this point of view, we let

$$\overline{\left(\frac{r}{r_1}\right)} \equiv \frac{1}{V_\ell}\int_{V_\ell}\frac{r}{r_1}\,dV \quad (9)$$

where, with reference to Fig. 2,

$$r_1^2 = r^2 + 4yr\cos\phi + 4y^2$$

so that

$$\overline{\left(\frac{r}{r_1}\right)} = \frac{3}{4\pi\ell^3}\int_0^{2\pi}\int_0^{\pi}\int_0^{\ell}\frac{r^2\sin\phi}{(r^2+4yr\cos\phi+4y^2)^{1/2}}\,dr\,d\phi\,d\phi \quad (10)$$

Integration yields

$$\overline{\left(\frac{r}{r_1}\right)} = \frac{3}{4}\frac{\ell}{y}\left\{\frac{(3-10y^*)}{12}(1+2y^*)^2 - \frac{(3+10y^*)}{12}(1-2y^*)^2 + 2y^{*2}\left[(1+2y^*)^2 - (1-2y^*)^2\right](1-2y^*) - \frac{8}{3}y^{*3}\right\} \quad (11)$$

where $y^* \equiv y/\ell$. Since ℓ/y lies between the limits of zero and unity (refer to Fig. 2), the interval of interest for y^* is $1 \geq y^* \geq \infty$, for which the bracketed term in eq. (11) has a unique value (0.5) for all y^* values within this interval. It follows, therefore, that

$$\overline{\left(\frac{r}{r_1}\right)} = \frac{3}{8}\frac{\ell}{y} \quad (12)$$

which is directly analogous to the linear decay function assumed by LRR in their development.

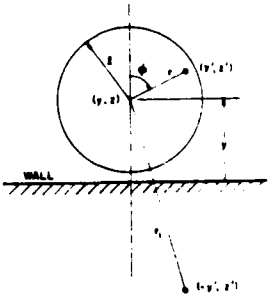

Fig. 2 Geometric configuration for volume averaging procedure

By means of arguments similar to those employed in developing eqs. (8) and (12), analogous expressions for $(\phi_{ij}+\phi_{ji})_{w_2}$ and $(\phi_{ij}+\phi_{ji})_{w_3}$ can be developed, so that the net effect of the image points on the pressure-strain correlation can be represented as:

$$\sum_{n=1}^{3}(\phi_{ij}+\phi_{ji})_{wn} =$$

$$\left[-c_{1,1}\frac{\varepsilon}{k}\left(\overline{u_iu_j}-\frac{2}{3}\delta_{ij}k\right)+\frac{\partial\overline{U}_\ell}{\partial x_m}\left(b^{mi}_{\ell j}+b^{mj}_{\ell i}\right)\right]\overline{\left(\frac{r}{r_1}\right)}+$$

$$\left[-c_{1,2}\frac{\varepsilon}{k}\left(\overline{u_iu_j}-\frac{2}{3}\delta_{ij}k\right)+\frac{\partial\overline{U}_\ell}{\partial x_m}\left(d^{mi}_{\ell j}+d^{mj}_{\ell i}\right)\right]\overline{\left(\frac{r}{r_2}\right)}+$$

$$\left[-c_{1,3}\frac{\varepsilon}{k}\left(\overline{u_iu_j}-\frac{2}{3}\delta_{ij}k\right)+\frac{\partial\overline{U}_\ell}{\partial x_m}\left(g^{mi}_{\ell j}+g^{mj}_{\ell i}\right)\right]\overline{\left(\frac{r}{r_3}\right)} \quad (13)$$

where

$$\overline{\left(\frac{r}{r_2}\right)} = \frac{3}{8}\frac{\ell}{(y^2+z^2)^{1/2}}\,, \qquad \overline{\left(\frac{r}{r_3}\right)} = \frac{3}{8}\frac{\ell}{z}$$

and $d^{mi}_{\ell j}$ and $g^{mi}_{\ell j}$ are fourth-order tensors having the same functional form as $b^{mi}_{\ell j}$. If equal weight arguments are applied for the influence of each bounding wall of the corner, then $g^{mi}_{\ell j}$ and $b^{mi}_{\ell j}$ must be identical in form, which implies that $c_{1,3}$ must equal $c_{1,1}$. By considering the linear nature of $a^{mi}_{\ell j}$, $b^{mi}_{\ell j}$, $d^{mi}_{\ell j}$, and $g^{mi}_{\ell j}$, equations (2), (5), and (13) can be combined to yield a composite model for the pressure-strain correlation of the form:

$$\overline{\frac{p}{\rho}\left(\frac{\partial u_i}{\partial x_j}+\frac{\partial u_j}{\partial x_i}\right)} = -c_1^*\frac{\varepsilon}{k}\left(\overline{u_iu_j}-\frac{2}{3}\delta_{ij}k\right)+\frac{\partial\overline{U}_\ell}{\partial x_m}\left(a^{*mi}_{\ell j}+a^{*mj}_{\ell i}\right) \quad (14)$$

where

$$a^{*mi}_{\ell j} = \alpha^*\delta_{\ell j}\overline{u_mu_i}+\beta^*\left(\delta_{m\ell}\overline{u_iu_j}+\delta_{mj}\overline{u_iu_\ell}+\delta_{i\ell}\overline{u_mu_j}+\delta_{ij}\overline{u_mu_\ell}\right)$$
$$+c_2^*\delta_{mi}\overline{u_\ell u_j}+\left[\gamma^*\delta_{mi}\delta_{\ell j}+\nu^*\left(\delta_{m\ell}\delta_{ij}+\delta_{mj}\delta_{i\ell}\right)\right]k \quad (15)$$

with

$$c_1^* = c_1+c_{1,1}\left[\overline{\left(\frac{r}{r_1}\right)}+\overline{\left(\frac{r}{r_2}\right)}\right]+c_{1,2}\overline{\left(\frac{r}{r_2}\right)} \quad (16)$$

$$c_2^* = c_2+c_{2,1}\left[\overline{\left(\frac{r}{r_1}\right)}+\overline{\left(\frac{r}{r_3}\right)}\right]+c_{2,2}\overline{\left(\frac{r}{r_2}\right)} \quad (17)$$

$$\gamma^* = \gamma+\gamma_1\left[\overline{\left(\frac{r}{r_1}\right)}+\overline{\left(\frac{r}{r_3}\right)}\right]+\gamma_2\overline{\left(\frac{r}{r_2}\right)} \quad (18)$$

where $\alpha^*\beta^*\gamma^*\nu^*$, which always appear as a sum in the expanded form for $a^{*mi}_{\ell j}$ when applied to two-dimensional wall boundary layers or turbulent corner flows. The coefficients α^* and β^* can be expressed in terms of c_2^* by invoking the constraints imposed by Green's third identify and continuity, namely:

$$a^{*mi}_{\ell i} = 2\,\overline{u_mu_i}\ (m\neq i) \quad \Rightarrow \quad 3\alpha^*+4\beta^* = 2 \quad (19)$$

$$a^{*mi}_{\ell i}\frac{\partial\overline{U}_\ell}{\partial x_m} = 0 \quad \Rightarrow \quad \alpha^*+5\beta^*+c_2^* = 0 \quad (20)$$

Solution of eqs. (19) and (20) yields:

$$\alpha^* = \frac{4c_2^*+10}{11} \quad (21)$$

$$\beta^* = -\frac{(3c_2^*+2)}{11} \quad (22)$$

It should be noted here that the above approach differs fundamentally from the approach taken by LRR. In expanded form, the continuity constraint can be written as:

$$a^{*mi}_{\ell i}\frac{\partial\overline{U}_\ell}{\partial x_m} = (2\beta^*+4\nu^*+\eta^*)\delta_{m\ell}\frac{\partial\overline{U}_\ell}{\partial x_m}+$$

$$(\alpha^*+5\beta^*+c_2^*)\,\overline{u_mu_\ell}\frac{\partial\overline{U}_\ell}{\partial x_m} = 0 \quad (23)$$

In LRR's development, the sum $2\beta^*+4\nu^*+\eta^*$ (for both the primary and wall correction coefficients) is set equal to zero. It is not necessary to invoke this condition, however, because $\delta_{m\ell}\,\partial\overline{U}_\ell/\partial x_m = \partial\overline{U}_m/\partial x_m = 0$. If, in fact, the condition $2\beta'+4\nu'+\eta' = 0$ (LRR's notation) is invoked for the wall correction coefficients and β' is set equal to zero (as specified by LRR), then the Green's function condition: $3\alpha'+4\beta' = 0$ and the continuity condition: $\alpha'+5\beta'+c_2' = 0$ cannot be satisfied simultaneously. The above inconsistency is avoided in the present development.

Specification of Model Coefficients

The system of equations given by (14) through (22) implies that nine coefficients must be specified in order to complete the model. These coefficients include three primary coefficients (c_1, c_2, and γ), three wall correction coefficients ($c_{1,1}$, $c_{2,1}$, and γ_1) and three corner correction coefficients ($c_{1,2}$, $c_{2,2}$, and γ_2). The required number of coefficients can be reduced, however, on the basis of the following considerations. Consider the modified form of the RS transport equations suggested by LRR, but with convection and diffusion effects modelled by means of Rodi's approximation (1976), namely:

$$\frac{\overline{u_iu_j}}{k}(P-\varepsilon) = -\left[\overline{u_iu_k}\frac{\partial\overline{U}_j}{\partial x_k}+\overline{u_ju_k}\frac{\partial\overline{U}_i}{\partial x_k}-\frac{2}{3}P_{ij}-\right.$$

$$\left.c_1^*\frac{\varepsilon}{k}\left(\overline{u_iu_j}-\frac{2}{3}\delta_{ij}k\right)+\frac{\partial\overline{U}_\ell}{\partial x_m}\left(a^{*mi}_{\ell j}+a^{*mj}_{\ell i}\right)\right] \quad (24)$$

where $P \equiv -\overline{u_ku_\ell}\,\partial\overline{U}_k/\partial x_\ell$. Following Gessner and Emery (1976), algebraic expressions for the Reynolds stress components in normalized form can be developed from eq. (24). The equations are summarized below:

$$\frac{\overline{u^2}}{k} = (c_1^*+\xi-1)^{-1}\left[\frac{2}{3}(c_1^*-1)-2\xi(\beta^*+2\nu^*-1)-\right. \quad (25)$$

$$\frac{\overline{v^2}}{k} = (c_1^*+\xi-1)^{-1}\left[\frac{2}{3}(c_1^*-1)-2\xi\beta^*+2(c_2^*+\gamma^*)\frac{\overline{uv}}{k}\frac{\partial\overline{U}}{\partial y}-\right. \quad (26)$$

$$\frac{\overline{w^2}}{k} = (c_1^*+\xi-1)^{-1}\left[\frac{2}{3}(c_1^*-1)-2\xi\beta^*+2(c_2^*+\gamma^*)\frac{\overline{uw}}{k}\frac{\partial\overline{U}}{\partial z}-\right. \quad (27)$$

$$\frac{\overline{uv}}{k} = (c_1^*+\xi-1)^{-1}\frac{k}{\varepsilon}\left\{\left[(\alpha^*+\beta^*-1)\frac{\overline{v^2}}{k}+\right.\right.$$
$$\left.\left.(\beta^*+c_2^*)\frac{\overline{u^2}}{k}+\gamma^*\right]\frac{\partial\overline{U}}{\partial y}+(\alpha^*+\beta^*-1)\frac{\overline{vw}}{k}\frac{\partial\overline{U}}{\partial z}\right. \quad (28)$$

$$\frac{\overline{uw}}{k} = (c_1^*+\xi-1)^{-1}\frac{k}{\varepsilon}\left\{\left[(\alpha^*+\beta^*-1)\frac{\overline{w^2}}{k}+\right.\right.$$
$$\left.\left.(\beta^*+c_2^*)\frac{\overline{u^2}}{k}+\gamma^*\right]\frac{\partial\overline{U}}{\partial z}+(\alpha^*+\beta^*-1)\frac{\overline{vw}}{k}\frac{\partial\overline{U}}{\partial y}\right. \quad (29)$$

$$\frac{\overline{vw}}{k} = (c_1^*+\xi-1)^{-1}(\beta^*+c_2^*)\frac{k}{\varepsilon}\left(\frac{\overline{uv}}{k}\frac{\partial\overline{U}}{\partial z}+\frac{\overline{uw}}{k}\frac{\partial\overline{U}}{\partial y}\right) \quad (30)$$

where $\varepsilon \equiv P/\varepsilon$ and $k \equiv (\overline{u^2}+\overline{v^2}+\overline{w^2})/2$. Equations (25) - (30) can be recast into forms which express c_1^*, c_2^*, and γ^* explicitly in terms of the normalized stress

components. Along the corner and wall bisectors of a rectangular duct, the following relationships apply:

Wall Bisector

$$c_1^*,_{wb} = 1-\xi+4\xi\left[12\left(\frac{\overline{u^2}}{k}\right)_{wb} + 3\left(\frac{\overline{v^2}}{k} - \frac{\overline{w^2}}{k}\right)_{wb} - 8\right]^{-1} \quad (31)$$

$$c_2^*,_{wb} = \frac{1}{16}\left[4-11\frac{(c_1^*,_{wb}+\xi-1)}{\xi}\left(\frac{\overline{v^2}}{k} - \frac{\overline{w^2}}{k}\right)_{wb}\right] \quad (32)$$

$$\gamma^*_{wb} = -\frac{(c_1^*,_{wb}+\xi-1)}{\xi}\left(\frac{\overline{uv}}{k}\right)^2_{wb} - \frac{(15c_2^*,_{wb}-1)}{22}\left(\frac{\overline{u^2}}{k}\right)_{wb} - \frac{(c_2^*,_{wb}-3)}{22}\left[2+\left(\frac{\overline{v^2}}{k} - \frac{\overline{w^2}}{k}\right)_{wb}\right] \quad (33)$$

Corner Bisector

$$c_1^*,_{cb} = 1-\xi+4\xi\left[12\left(\frac{\overline{u^2}}{k}\right)_{cb} + 6\left(\frac{\overline{vw}}{k}\right)_{cb} - 8\right]^{-1} \quad (34)$$

$$c_1^*,_{cb} = \frac{1}{16}\left[4-22\frac{(c_1^*,_{cb}+\xi-1)}{\xi}\left(\frac{\overline{vw}}{k}\right)_{cb}\right] \quad (35)$$

$$\gamma^*_{cb} = -2\frac{(c_1^*,_{cb}+\xi-1)}{\xi}\left(\frac{\overline{uv}}{k}\right)^2_{cb} - \frac{(15c_2^*,_{cb}-1)}{22}\left(\frac{\overline{u^2}}{k}\right)_{cb} - \frac{(c_2^*,_{cb}-3)}{22}\left[2+2\left(\frac{\overline{vw}}{k}\right)_{cb}\right] \quad (36)$$

A comparison of eqs. (34) - (36) with eqs. (31) - (33) indicates that

$$\begin{aligned} c_1^*,_{cb} &= c_1^*,_{wb} \\ c_2^*,_{cb} &= c_2^*,_{wb} \\ \gamma^*_{cb} &= \gamma^*_{wb} \end{aligned} \quad (37)$$

provided that

$$\begin{aligned} \left(\frac{\overline{u^2}}{k}\right)_{cb} &= \left(\frac{\overline{u^2}}{k}\right)_{wb} \\ \left(\frac{\overline{uv}}{k}\right)_{cb} &= \frac{1}{\sqrt{2}}\left(\frac{\overline{uv}}{k}\right)_{wb} \\ \left(\frac{\overline{vw}}{k}\right)_{cb} &= \frac{1}{2}\left(\frac{\overline{v^2}}{k} - \frac{\overline{w^2}}{k}\right)_{wb} \end{aligned} \quad (38)$$

In order to investigate whether or not these conditions hold, Reynolds stress measurements were made in the near-wall region of a square duct under fully-developed flow conditions. Distributions measured by Eppich (1981) along both wall and corner bisectors of the duct for three different Reynolds numbers are shown in Fig. 3. Superimposed in Fig. 3a are results based on the measurements of Comte-Bellot (1963) and line distributions representative of the consensus set of values proposed by LRR. Although there is close agreement among the various data sets along each bisector, data measured along the wall bisector are not in complete accord with the consensus values, which indicates that near-wall similarity in incompressible turbulent boundary layers may not be as universal as previously thought. In general, however, Fig. 3b indicates that the conditions imposed by (38) are well satisfied. This result enables eqs. (37) to be written as

$$c_1^* = c_1 + c_1' f \quad (39)$$

$$c_2^* = c_2 + c_2' f \quad (40)$$

$$\gamma^* = \gamma + \gamma' f \quad (41)$$

where the primed quantities now denote the wall correction coefficients with

$$f \equiv k_f\left[\overline{\left(\frac{r}{r_1}\right)} + \overline{\left(\frac{r}{r_3}\right)} + \frac{1}{c_f}\overline{\left(\frac{r}{r_2}\right)}\right] \quad (42)$$

where k_f and c_f are empirical coefficients to be selected so that f is approximately unity throughout the entire near-wall layer. (It should be noted here that the corner correction coefficients ($c_{1,2}$, $c_{2,2}$, and γ_2) have now been effectively eliminated from the model.)

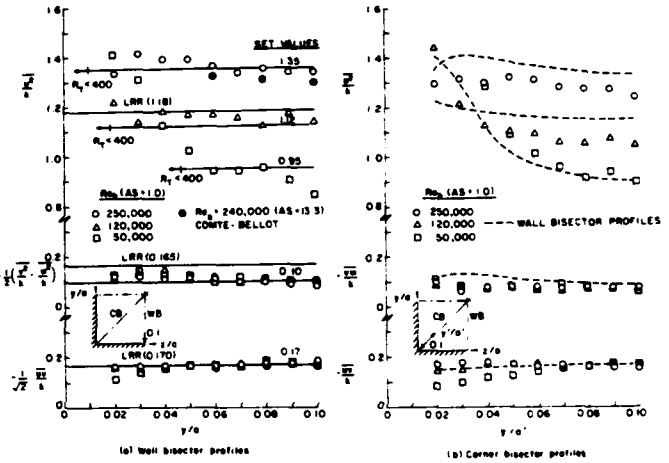

Fig. 3 Normalized stress component distributions in the near-wall region of a rectangular duct

In regions distant from the corner (e.g., in the near-wall region adjacent to the wall y=0 for large z) eq. (42) assumes the following limiting form:

$$\lim_{\substack{y\to 0\\ z\to\infty}} f = \lim_{y\to 0} k_f\overline{\left(\frac{r}{r_1}\right)} = \lim_{y\to 0} k_f\left(\frac{3}{8}\frac{\ell}{y}\right) = 1 \quad (43)$$

or, if $\ell \equiv \ell_p$ and it is noted that $\ell_p = \kappa y$ in this region

$$k_f = \frac{8}{3}\frac{1}{\kappa} \quad (44)$$

On the corner bisector y=z, where $\ell_p = \kappa_1 y$,

$$\lim_{y=z\to 0} f = \lim_{y=z\to 0} k_f\left[2\overline{\left(\frac{r}{r_1}\right)} + \frac{1}{c_f}\overline{\left(\frac{r}{r_2}\right)}\right] = \lim_{y=z\to 0}\frac{\kappa}{\kappa_1}\left(2+\frac{1}{\sqrt{2}c_f}\right) = 1 \quad (45)$$

so that

$$c_f = \frac{1}{\sqrt{2}}\left(\frac{\kappa}{\kappa_1} - 2\right)^{-1} \quad (46)$$

On the basis of measurements by Lund (1977) and Eppich (1981) in the near-wall region of a square duct, κ and κ_1 are approximately equal to 0.40 and 0.23, respectively, for which c_f=-3.0. The final form of the decay function (for an unbounded corner flow) may now be expressed as

$$f = \frac{\ell_p}{\kappa}\left[\frac{1}{y} + \frac{1}{z} + \frac{1}{c_f(y^2+z^2)^{1/2}}\right] \quad (47)$$

or alternatively, for a rectangular duct of arbitrary aspect ratio, as

$$f=\frac{\ell_p}{\kappa}\left\{\frac{1}{a-|a-y|}+\frac{1}{b-|b-z|}+\frac{1}{c_f[(a-|a-y|)^2+(b-|b-z|)^2]^{1/2}}\right\} \tag{48}$$

where a and b are the half-width dimensions of the duct. It should be noted here that for k-ε type predictions, ℓ_p in eqs. (47) and (48) can be replaced by $(ak)^{1/2}/\varepsilon$, but with "a" defined as $(\overline{uv}^2+\overline{uw}^2)^{1/2}/k$, rather than specified as a constant, because $(\overline{uv}^2+\overline{uw}^2)^{1/2}/k$ varies systematically in the near-wall layer (e.g., between 0.23 and 0.29 in the near-wall region of a square duct on the basis of data obtained by Eppich (1981).

With the decay function now defined for both bounded and unbounded 90-degree corner flows, the task which remains is to specify numerical values for both the primary (c_1, c_2, and γ) and wall correction (c_1', c_2', and γ') coefficients which appear in eqs. (39) - (41). In order to determine the primary coefficients, reference will be made to the plane homogeous shear flow data of Champagne, Harris, and Corrsin (1970) and Harris, Graham, and Corrsin (1977), henceforth designated as CHC and HGC, respectively. From the data of both studies, it is possible to determine numerical values for c_1, c_2, and γ from reduced forms of eqs. (31) - (33) applicable to plane homogeneous shear flow. With $\xi\equiv1$ for the CHC data and with $\xi\equiv1.55$ for the HGC data (as suggested by Leslie 1980), the numerical values for c_1 and c_2 are 1.34 and 0.34, respectively, for the CHC data and 1.27 and 0.41 for the HGC data. If one utilizes the average values for c_1 and c_2 generated from these data sets ($\bar{c}_1=1.3$, $\bar{c}_2=0.37$), then the transverse anisotropy calculated from an equation derivable from eqs. (26) and (27), namely

$$\left(\frac{\overline{v^2}}{k}-\frac{\overline{w^2}}{k}\right)_s=\frac{-4\xi(4\bar{c}_2-1)}{11(\bar{c}_1+\xi-1)} \tag{49}$$

is -0.13 when $\xi=1$, and -0.15 when $\xi=1.55$. This spread in values does not simulate the experimentally observed increase in transverse anisotropy which occurs as departures from local equilibrium become significant. (For the HGC data set, for which $\xi=1.55$, $(\overline{v^2}-\overline{w^2})/k=-0.2$, whereas for the CHC data set, $(\overline{v^2}-\overline{w^2})/k=-0.1$ when $\xi=1$. In order to circumvent this shortcoming, a new coefficient, λ^*, will be defined of the form:

$$\lambda^*=\lambda+\lambda'f \tag{50}$$

which effectively replaces c_2^* as an independently specified quantity. If c_2^* is redefined in terms of λ^* as

$$c_2^*=\frac{1}{16}\left[4-11\lambda^*(c_1^*+\xi-1)\right] \tag{51}$$

then eq. (49) can be rewritten as

$$\left(\frac{\overline{v^2}}{k}-\frac{\overline{w^2}}{k}\right)_s=\lambda\xi \tag{52}$$

which yields values for the transverse anisotropy which are in better agreement with the experimental values observed by HGC and CHC than values predicted from eq. (49). (For $\lambda=-0.12$, eq. (52) yields $(\overline{v^2}-\overline{w^2})/k=-0.18$ and -0.12, respectively, when $\xi=1.55$ and 1).

In view of this improvement, λ was specified as -0.12 in the present study to complement the values selected for c_1 and γ (1.4 and -0.12, respectively) which lead to the best overall agreement between calculated and measured stress component values when compared to the data of CHC and HGC. The normalized stress components calculated from reduced forms of eqs. (25) - (28) using the present coefficients and those specified by LRR are compared in Table 1 below.

Reference	$\overline{u^2}/k$	$\overline{v^2}/k$	$\overline{w^2}/k$	$-\overline{uv}/k$
CHC (data)	0.94	0.48	0.58	0.33
Present work (ξ=1)	0.94	0.47	0.59	0.33
LRR (ξ=1)	0.93	0.46	0.61	0.36
HGC (data)	1.00	0.40	0.60	0.30
Present work (ξ=1.55)	0.98	0.42	0.60	0.29
LRR (ξ=1.55)	0.96	0.44	0.60	0.37

Table 1 Normalized stress component values

In general, the present coefficients ($c_1=1.4$, $\lambda=-0.12$), in comparison to those specified by LRR ($c_1=1.5$, $c_2=0.4$), lead to improved agreement between calculated and measured stress component values. On the basis of these results, the primary coefficients chosen in this study were used to determine numerical values for the wall correction coefficients (c_1', γ', and λ').

The coefficient c_1' was evaluated by means of an expression which follows from eqs. (31) and (39) with $f=\xi=1$, namely

$$c_1'=4\left[12\left(\frac{\overline{u^2}}{k}\right)_{wb}+3\left(\frac{\overline{v^2}}{k}-\frac{\overline{w^2}}{k}\right)_{wb}-8\right]^{-1}-c_1 \tag{53}$$

where, for the set values of $(\overline{u^2}/k)_{wb}$ and $(\overline{v^2}/k-\overline{w^2}/k)_{wb}$ indicated in Fig. 3a, c_1' is a Reynolds number dependent coefficient which varies as shown in Table 2 when $c_1\equiv1.4$. The variation is roughly centered about the nominal value for c_1' suggested by LRR (-0.5) for a best fit of the consensus data (near-wall stress values) tabulated in their paper. The coefficient γ' can be determined by differencing eqs. (26) and (27), applying eqs. (22) and (51) with $\xi=1$, and letting f=1 in the defining relationship for λ^* given by eq. (50). This procedure yields

$$\gamma'=\left(\frac{\overline{v^2}}{k}-\frac{\overline{w^2}}{k}\right)_{wb}-\gamma \tag{54}$$

from which $\gamma'=-0.08$ when $\gamma=-0.12$ with $(\overline{v^2}/k-\overline{w^2}/k)_{wb}=-0.020$ on the basis of the set value shown in Fig. 3a.

This completes the number of independent coefficients (5) which must be specified in the present model (c_1, λ, γ, c_1', λ'). The remaining coefficeint, γ', depends on c_1 and c_1', and can be evaluated from an equation which is derivable from eqs. (26), (27), and (28), after λ^* and β^* are written in terms of c_2^* on the basis of eqs. (21) and (22), and then in terms of λ^* and c_1^* from eq. (51), namely

$$\gamma'=\left[\frac{\lambda^*_{wb}}{128}(48-11\lambda^*_{wb})-\left(\frac{\overline{uv}}{k}\right)_{wb}\right](c_1+c_1')+\frac{1}{48}\left[8+15\lambda^*_{wb}-\frac{2}{c_1+c_1'}\right]-\gamma \tag{55}$$

where $\gamma=-0.12$, $(-\overline{uv}/k)_{wb}=0.24$, and $\lambda^*_{wb}=(\overline{v^2}/k-\overline{w^2}/k)_{wb}=-0.20$ on the basis of eq. (54) and the set values shown in Fig. 3a. Table 2 summarizes the numerical values selected for both the primary (c_1, λ, γ) and wall correction (c_1', λ') coefficients utilized in the present development. The corresponding values for c_2 and c_2', as calculated from eq. (51), are also shown in this table. The calculated value for c_2 (0.37) is in close agreement with the value specified by LRR (0.40). The

values for c_2' shown in Table 2 differ in sign from the value specified by LRR (0.06), primarily because the authors let $\beta'=0$ in their development. This condition is equivalent to assuming that essentially no energy is transferred from the $\overline{w^2}$ stress component to the $\overline{u^2}$ component in the near-wall layer. Data obtained in the present study and by Comte-Bellot (1963) show that this is not true, however, for high Reynolds number duct flows, where energy is extracted from both the $\overline{v^2}$ and $\overline{w^2}$ stress components in the near-wall region to elevate $\overline{u^2}/k$ over its plane homogeneous shear flow value. This point will be discussed in more detail shortly.

Re_b	c_1	λ	γ	c_1'	λ'	c_2	c_2'
50,000	1.4	-0.12	-0.12	0	-0.08	0.37	-0.101
120,000	"	"	"	-0.57	"	"	-0.109
250,000	"	"	"	-0.87	"	"	-0.113

Table 2 Primary and Wall Correction Coefficients

In the present development, all model coefficients are constant, except for c_1', which has an apparent Reynolds number dependency. With reference to eq. (31), the different values for c_1' which appear in Table 2 are directly attributable to the different set values for $\overline{u^2}/k$ shown in Fig. 3a. These values were determined by neglecting tail-up behavior of $\overline{u^2}/k$, which occurs in a low Reynolds number region of the flow ($R_T<400$; refer to Fig. 3a) where viscous effects acting on the dissipation rate may be responsible for the observed increase in $\overline{u^2}/k$.

Figure 4a shows distributions of $\overline{u^2}/k$, $\overline{v^2}/k$, and $\overline{w^2}/k$ measured by Eppich (1981) in the near-wall region of a square duct under fully developed flow conditions. In the outer portion of the wall bisector traverse ($0.06\leq y/a\leq 0.10$), there is a relatively strong variation in the level of anisotropy with a change in Reynolds number. In particular, there is an upward shift in $\overline{u^2}/k$ values with an increase in Reynolds number, and a corresponding downward shift in $\overline{v^2}/k$ and $\overline{w^2}/k$ values. Similar shifts are evident in the distributions shown in Fig. 4b, which are based on the measurements of Comte-Bellot (1963) on the plane of symmetry of a high aspect ratio rectangular duct at three different Reynolds numbers. The shift levels shown in Fig. 4a are somewhat higher for a given change in Reynolds number, however, which appears to indicate that the convecting influence of secondary flow along the wall bisector may be responsible, in part, for higher shift levels observed in Fig. 4a. In this figure it can also be seen that normal stress levels measured at the lowest Reynolds number (50,000) are similar to plane homogeneous shear flow (PHSF) levels, which correspond to average values of the CHC and HGC data shown in Table 1, and that deviation of the data from PHSF levels increases with an increase in Reynolds number. Figure 4 also shows that when $Re_b>10^5$, $\overline{v^2}/k$ and $\overline{w^2}/k$ lie below their PSHF counterparts, which implies that energy is transferred from both the $\overline{v^2}$ and $\overline{w^2}$ stress components to the $\overline{u^2}$ stress component in the immediate vicinity of the wall.

A plausible explanation of the shifts shown in Fig. 4 which occur within the interval $0.06\leq y/a\leq 0.10$ is not a simple task. First of all, it may be stated (with reasonable certainty) that the observed shifts are not interpretable as a low Reynolds number effect, because R_T is relatively high within this interval (refer to tabulated values of R_T at $y/a=0.10$ in Fig. 4a). Furthermore, the observed shifts are not associated with some anomalous behavior of the decay function, because $f\simeq 1$ in this region for all three Reynolds numbers. Since k/U_τ^2 is essentially constant and does not vary with Reynolds number, as shown in Fig. 4a, the flow must be in local equilibrium, regardless of the fact that the turbulence kinetic energy is distributed differently among the various stress components. This interpretation is supported by additional data taken by Eppich (1981) which show that $-\overline{uv}/U_\tau^2\simeq 1.0$ within the interval $0.06\leq y/a\leq 0.10$ for all three Reynolds numbers. The near-wall flow in this region is thus a high Reynolds number flow in local equilibrium, which implies that pressure-strain effects (as opposed to dissipation rate phenomena) must be responsible for the shift in anisotropy levels shown in Fig. 4a. As one possibility, one may consider non-linear redistribution effects, but the model proposed by Lumley and Khajeh-Nouri (1974), when applied to the near-wall region, will yield values for $\overline{u^2}/k$, $\overline{v^2}/k$, and $\overline{w^2}/k$ which are identically constant when constant coefficients are specified. The problem can be overcome by assigning a new value to c_1' in the present model whenever there is a change in Reynolds number. Under these conditions, the model will mimic the shift in anisotropy levels shown in Fig. 4a (as indicated by the R1, R2, and R3 levels in the figure), without altering calculated values of $(\overline{v^2}-\overline{w^2})/k$ and $-\overline{uv}/k$ (which should remain constant to be in accord with the data). This is a less-than-satisfying approach, however, and current efforts are being directed toward developing a plausible explanation (and model) for the anisotropy shifts which have been observed in the present study.

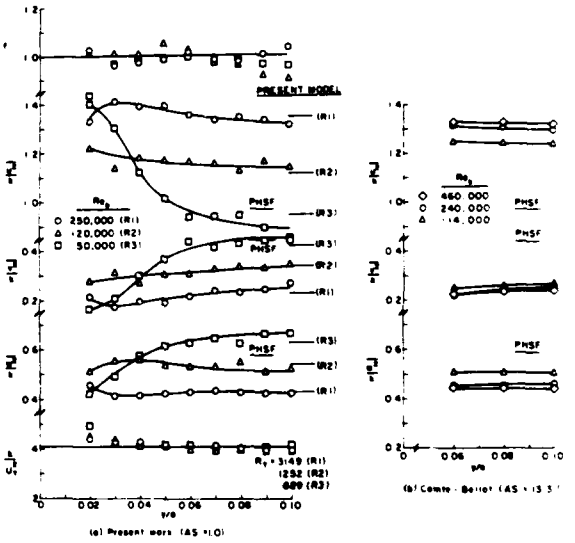

Fig. 4 Normalized stress component distributions along a wall bisector in the near-wall region of a rectangular duct

COMPARISON BETWEEN MODELS

The final form of the pressure-strain model which has been developed in this paper consists of the expression for $(\overline{p/\rho})(\partial u_i/\partial x_j+\partial u_j/\partial x_i)$ given by eq. (1-), with c_2^*, α^*, and β^* defined, respectively, by eqs. (51), (21), and (22), where c_1^*, λ^*, and γ^* ($=\alpha^*+\beta^*$) are defined, respectively, by eqs. (39), (50), and (41) in terms of both primary (c_1, λ, γ) and wall correction (c_1', λ', γ') coefficients whose values are given in Table 2, with γ' to be evaluated from eq. (55), and with f to be evaluated by means of either eq. (47) or (48). The relative merits of this model will be

examined by means of comparisons with the model proposed by Reece (1977).

The decay function developed during the present study is given by eq. (47). An analogous "two-dimensional" expression, which is equivalent to the superposition model suggested by Reece when restricted to the near-wall region, can be written as: $f_{2D}=(\ell_p/\kappa)(1/y+1/z)$. In order to examine the relative behavior of f and f_{2D} in the near-wall region of a square duct, ℓ_p was evaluated from measured primary shear stress components and experimentally determined mean-strain rates by means of the formula: $\ell_p = (\overline{uv}^2 + \overline{uw}^2)^{1/4} \div [(\partial\overline{U}/\partial y)^2 + (\partial\overline{U}/\partial z)^2]^{1/2}$ (Gessner and Emery 1977). The shear stress and mean-strain rate values were determined from data obtained by Lund (1977) and Eppich (1981) at Re_b=250,000 under fully developed flow conditions. Calculated values of f based on κ=0.40 and the data are near unity throughout the entire near-wall layer ($0<y/a\leq 0.1$, $0<z/a\leq 1$). Calculated values of f_{2D} within the same region are approximately unity on the wall bisector (z/a=1), but increase to an average value of 1.14 on the corner bisector.

The consequences of this behavior can be examined by referring to Fig. 5, which shows calculated and measured normalized stress component values in the near-wall region along wall (Fig. 5a) and corner (Fig. 5b) bisectors of the duct. Both models yield results which are in generally good agreement with measured values on the wall bisector, except that Reece's model overpredicts $\overline{w^2}/k$ (refer to Fig. 5a) because the influence of a wall effect on $\overline{w^2}$ is not taken into account in his model. Figure 5b indicates that both models tend to underestimate or overestimate $\overline{u^2}/k$ and $\overline{v^2}/k$ (or $\overline{w^2}/k$) on the corner bisector by approximately the same amount. Reece's model, however, underestimates $-\overline{uv}/k$ by approximately 50% and overestimates $-\overline{vw}/k$ by a factor greater than two on this traverse. In contrast, the present model leads to values for $-\overline{uv}/k$ and $-\overline{vw}/k$ on the corner bisector which are in reasonable agreement with the data. The lack of agreement between Reece's model and measured values of $-\overline{uv}/k$ on the corner bisector is not attributable to the coefficient values specified in Reece's model, but rather to the decay function which exceeds unity on the corner bisector when f_{2D} is used to model decay function behavior. When f is used to calculate $-\overline{uv}/k$ on the corner bisector with Reece's coefficients, the value is 0.166, which is in close accord with the data and with the value calculated by means of the present model (0.170). This does not imply, however, that Reece's model would be entirely suitable if f_{2D} were simply replaced by f, because the $-\overline{vw}/k$ value calculated on the corner bisector using f and Reece's coefficients (0.169) still exceeds experimentally measured values by a factor of two.

In order to compare the present model with Reece's model more fully, additional comparisons involving the balance of production, dissipation, and pressure-strain effects in the flow were made. The Reynolds stress transport equations were first written in reduced form by neglecting transport effects and by assuming local equilibrium, so that the overall dissipation rate could be modelled in terms of the production rate; i.e., $\varepsilon=-(\overline{uv}\,\partial\overline{U}/\partial y + \overline{uw}\,\partial\overline{U}/\partial z)$. The individual terms which appear in the reduced equation for each stress component were then evaluated from data obtained by Lund (1977) and Eppich (1981) in the near-wall region of a square duct. Figure 6 shows normalized pressure-strain distributions for $\overline{u^2}$, $\overline{v^2}$, $\overline{w^2}$, and $\overline{uv}$ along three near-wall traverses (z/a=0.1, 0.6, and 1.0) calculated by means of the present model and Reece's model. Distributions of the rates of production and dissipation are also shown on this figure, as well as the sum of terms (S), which ideally should be zero along each traverse.

Without exception, the sum of terms for each stress component along a given traverse is closer to zero when the pressure-strain term is evaluated by means of the present model, rather than Reece's model. Even along the wall bisector (z/a=1) there is marked improvement in the balance for each stress component. These results are independent of decay function considerations (since $f=f_{2D}=1$ on the wall bisector), which implies that both the unprimed and primed coefficient values specified in the present model are preferable to the values employed by Reece.

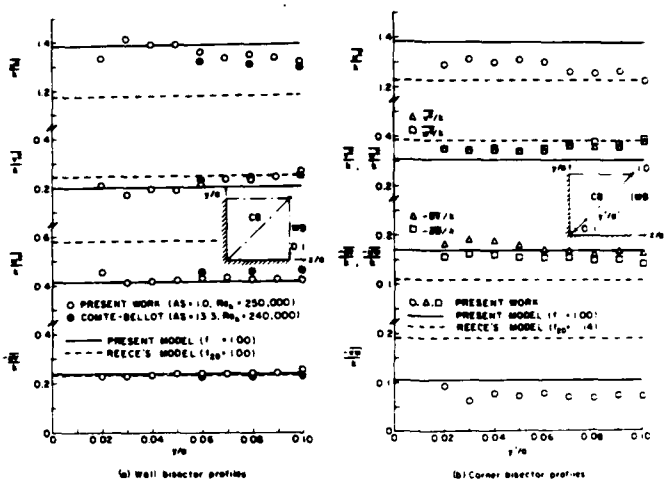

Fig. 5 Comparison of calculated and measured normalized stress component distributions in the near-wall region of a square duct, Re_b=250,000

The sensitivity of the balances to pressure-strain modelling was examined more closely by comparing the sum of effects for the $\overline{v^2}$ and $\overline{uv}$ stress components in the immediate vicinity of the corner. Figure 7 shows the sum of terms associated with redistributive and dissipative effects on the $\overline{v^2}$ stress component (S=PS+D) and the sum of terms associated with production and pressure-strain effects on the $\overline{uv}$ stress component (S=P+PS). From the figure it can be seen that the sum of terms along a given traverse is generally closer to zero when the present model is employed. The differences between the two models are most evident along the traverse closest to the wall (z/a=0.02). Along this traverse, the sum of terms associated with redistributive and dissipative effects on the transverse anisotropy $(\overline{v^2}-\overline{w^2})/k$ is close to zero and varies between $\pm 1.4\times10^{-4}$ within the interval $0.04\leq y/a\leq 0.10$. In contrast, when Reece's model is employed, the sum of terms varies from 8.6×10^{-4} to 11.5×10^{-4} along this same interval, i.e., there is at least a six-fold increase in the imbalance level. Inasmuch as transverse gradients of $\overline{v^2}-\overline{w^2}$ are responsible for the generation of axial vorticity in the flow, it is likely that the present pressure-strain model will lead to improved predictions of the overall flow field (especially in the near-vicinity of a corner) in comparison to Reece's model.

CONCLUDING REMARKS

A near-wall pressure-strain model for 90-degree corner flows has been presented in this paper which is based on a more rigorous approach than that employed in previous studies. The present three-image point model is based on a decay function which is approximately unity in the entire near-wall layer. In contrast, the two-image point (superposition) model leads to a decay function which increases continually as a corner is approached. This behavior leads to calculated normalized stress component values on the corner bisector which are not in complete accord with the data, whereas calculated values based on the present model are in good overall agreement. Modelling

AD-A111 522 PENNSYLVANIA STATE UNIV UNIVERSITY PARK DEPT OF MECH--ETC F/G 20/4
SYMPOSIUM ON TURBULENT SHEAR FLOWS (3RD), UNIVERSITY OF CALIFOR--ETC(U)
SEP 81 F W SCHMIDT AFOSR-80-0033

UNCLASSIFIED AFOSR-TR-82-0032 NL

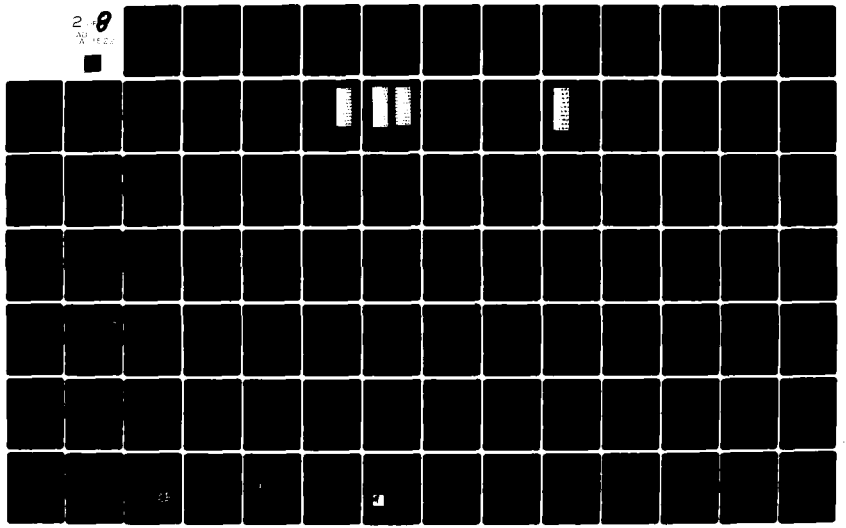

2 OF 8

AD A111522

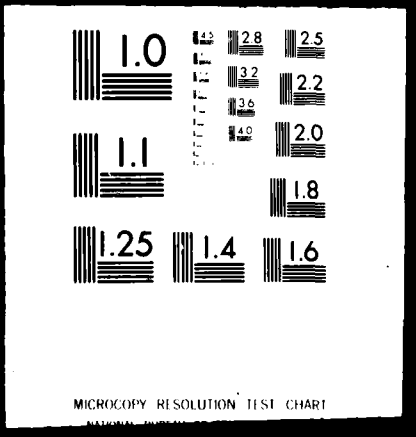

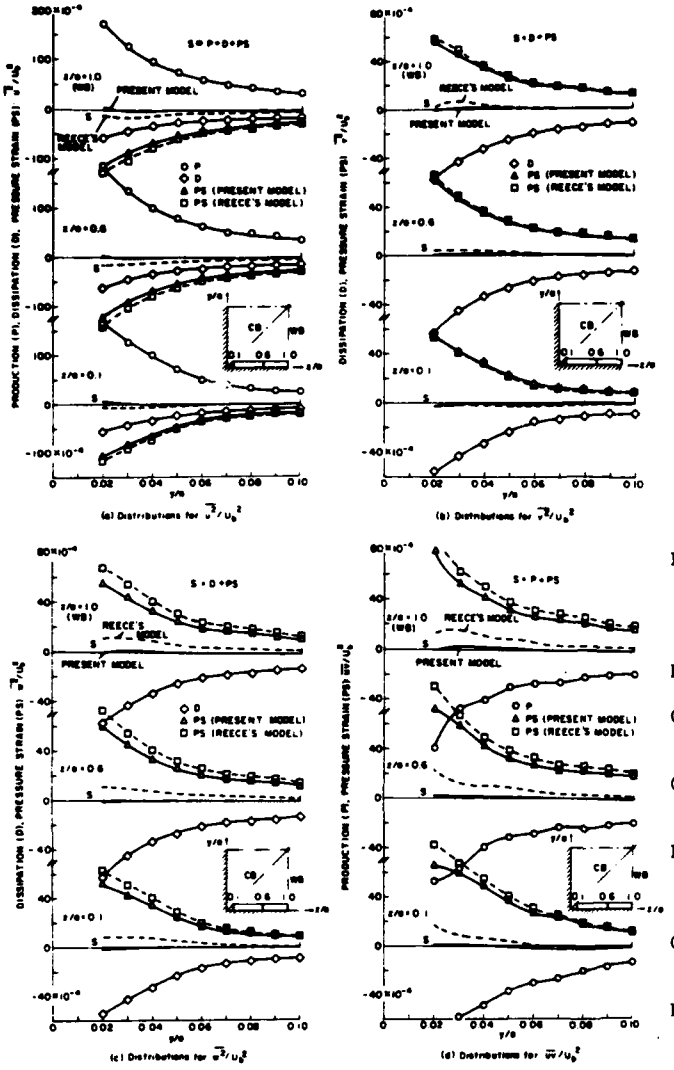

Fig. 6 Production, dissipation, and pressure-strain effects on the Reynolds stress components in the near-wall region of a square duct, Re_b=250,000

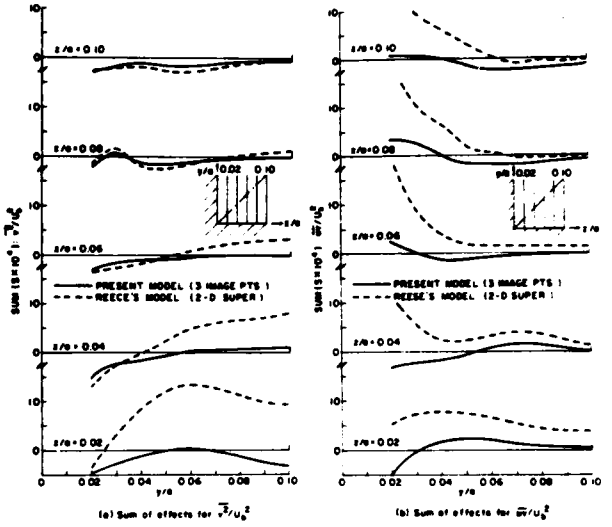

Fig. 7 Sum of production, dissipation, and pressure-strain effects on the $\overline{v^2}/U_b^2$ and $\overline{uv}/U_b^2$ stress components in the near-wall region of a square duct, Re_b=250,000

pressure-strain effects in the Reynolds stress transport equations by means of the present model leads to imbalance levels for each stress component which are significantly less than those associated with Reece's model, even in nominally two-dimensional regions distant from a corner. The comparisons described in this paper indicate that the present model is superior to Reece's model in several respects. Full confirmation of the model must await comparisons with numerical predictions, which is one of our main objectives in future work.

ACKNOWLEDGMENT

This study was sponsored, in part, by the National Science Foundation (ENG 76-11818) and the Office of Naval Research through their Project SQUID program (N00014-79-C-0276). The authors would like to express their appreciation to these agencies for their support of this work.

REFERENCES

Champagne, F. H., Harris, V. G. and Corrsin, S. 1970 Experiments on nearly homogeneous turbulent shear flow. J. Fluid Mech., 41 (1), 81-139.

Comte-Bellot, G. 1963 Turbulent flow between two parallel walls. Ph.D. thesis, University of Grenoble (also available as ARC 31 609).

Eppich, H. M. 1981 Development of a pressure-strain model for turbulent flow along a streamwise corner. M.S. thesis, Dept. of Mech. Engrg., University of Washington.

Gessner, F. B. and Emery, A. F. 1977 A length-scale model for developing turbulent flow in a rectangular duct. J. Fluids Engrg., Trans. ASME, 99, 347-356.

Harris, V. G., Graham, J. A. H. and Corrsin, S. 1977 Further experiments in nearly homogeneous turbulent shear flow. J. Fluid Mech., 81 (4), 657-687.

Irwin, H. P. A. H. 1974 Measurements in blown boundary layers and their prediction by Reynolds stress modelling. Ph.D. thesis, McGill University.

Kraichnan, R. H. 1956 Pressure fluctuations in turbulent flow over a flat plate. J. Acoust. Soc. Amer., 28 (3), 378-390.

Launder, B. E., Reece, G. J. and Rodi, W. 1975 Progress in the development of a Reynolds stress turbulence closure. J. Fluid Mech., 68 (3), 537-566.

Leslie, D. C. 1980 Analysis of a strongly sheared, nearly homogeneous turbulent shear flow. J. Fluid Mech., 98 (2), 435-448.

Lumley, J. L. and Khajeh-Nouri, B. J. 1974 Computational modeling of turbulent transport. Adv. Geophys., 18A, 169-192.

Lund, E. G. 1977 Mean flow and turbulence characteristics in the near corner region of a square duct. M.S. thesis, Dept. of Mech. Engrg., University of Washington.

Reece, G. J. 1977 A generalized Reynolds-stress model of turbulence. Ph.D. thesis, University of London.

Rodi, W. 1976 A new algebraic relation for calculating the Reynolds stresses. ZAMM, 56, T219-T221.

Rotta, J. C. 1951 Statistische theorie nichthomogener turbulenz. Z. Phys., 129, 547-572 (also available as NASA TTF-14, 560).

BULK DILATATION EFFECTS ON REYNOLDS STRESSES IN THE RAPID EXPANSION OF A TURBULENT BOUNDARY LAYER AT SUPERSONIC SPEED

J.P. DUSSAUGE and J. GAVIGLIO

Institut de Mécanique Statistique de la Turbulence
12, Av. Général Leclerc - 13003 Marseille
Laboratoire Associé au C.N.R.S. N° 130
and
O.N.E.R.A. Av. de la Division Leclerc 92320 CHATILLON

ABSTRACT

The rapid distortion of a turbulent motion by a mean bulk dilatation, and the subsequent evolution of Reynolds stresses, are examined. Some properties are given for a solenoïdal velocity fluctuation field. It is shown that mean velocity divergence does not contribute to the rapid part of the pressure-strain correlation terms. Models for these terms are deduced, and a variable which takes in account the mean compressibility effects and behaves like Reynolds stresses in subsonic flows, is defined. These properties are in good agreement with experimental results obtained in a supersonic boundary layer relaminarized by an expansion fan. It is deduced that bulk dilatation and mean pressure gradient contribute largely to relaminarization, and that the solenoidal approximation seems to be valid in distortions like an expansion for moderate supersonic Mach numbers.

NOMENCLATURE

aij = dimensionless Reynolds stress deviatoric
dij = fluctuating strain rate tensor
Dij = mean strain rate tensor
D/Dt = $\partial/\partial t + \tilde{u}j\ \partial/\partial xj$ derivative along the mean motion
L = spatial extent of the distortion
M = Mach number
p = pressure
pt2 = pitot pressure
q' = $(u_1'^2 + u_2'^2 + u_2'^2)^{1/2}$
rij = fluctuating rotation rate tensor
Rij = mean rotation rate tensor
Ruv = correlation coefficient between longitudinal and transversal velocity fluctuations
R:u = correlation coefficient between density and longitudinal velocity fluctuations
R:v = correlation coefficient between density and transversal velocity fluctuations
T = temperature
Tij = $\widetilde{u_i'u_j'}/(\bar{T})^{2/2}$
u = $\tilde{u} + u'$ longitudinal velocity component
ui = $\tilde{u}_i + u_i'$ component of velocity
U = mean velocity modulus
Uo = velocity in the initial external flow
$\widetilde{u_i'u_j'} = \overline{\rho u_i'u_j'}/\bar{\rho}$
v = $\tilde{v} + v'$ transversal velocity component
(s,n,z),(x,y,z) = frames of reference (fig. 1)
δo = initial boundary layer thickness
δ_{ij} = Kronecker symbol
Δ = Laplacean operator
γ = Cp/Cv ratio of specific heats
Λ = integral turbulent scale
$\pi_{ij} = -(\overline{u_i'\partial p'/\partial x_j} + \overline{u_j'\partial p'/\partial x_i})/\bar{\rho}$
ρ = specific mass
τ_w = wall friction

Superscripts :

($\bar{}$) = ensemble average
( ) = Favre average : $\tilde{w} = \overline{\rho w}/\bar{\rho}$
( )' = fluctuation

INTRODUCTION

The classical description of equilibrium supersonic turbulent flows often uses the Morkovin's hypothesis /1/, according to which turbulence structure is supposed to be the same as in subsonic flows. In such conditions, mean compressibility appears only in the variations of the mean specific mass. Moreover, as the flows examined by Morkovin are quasi-parallel and have only very slight longitudinal evolutions, the mean density gradient is nearly perpendicular to the mean velocity, so that the mean velocity divergence is very small, if compared to the mean strain : mean dilatation can then be neglected. When a supersonic flow is subjected to a pressure gradient, the situation is quite different : there are large variations of mean density. Such flows were examined in the last decade /2/,/3/, in order to introduce the dilatation influence in turbulence models. Nevertheless, as noticed by Bradshaw /4/, only few things were known about the effect of longitudinal density variations on turbulent quantities. This paper brings some elements of physical understanding of these phenomena, and compares them to experimental results. The influence of a mean bulk dilatation on Reynolds stresses can be described as the action of mean velocity or associated density gradients on turbulent transfers : the simpler problem of this type is a rapid distortion one. This approximation is here applied to the Reynolds stress equations. Attention is focused on the pressure fluctuation. It is shown that in a rapid distortion, if the fluctuating motion can be considered as essentially incompressible, the pressure fluctuation is given by the same equation as in heated subsonic flows. By assuming that the velocity fluctuation field is solenoidal, the way to adapt to the supersonic case will be deduced, and a new variable will be defined from the Reynolds stress and the mean density, which takes implicitly in account

the effects of mean compressibility. An experiment is presented, in which a turbulent boundary layer subjected to a centered expansion is studied ; turbulence measurements are performed in the expanded zone. The measured evolution of the velocity variance is compared to the evolution deduced from the proposed analysis.

ANALYSIS

Reynolds Stress Equations in a Rapid Distortion

A distortion is "rapid" /5/ if it is applied to a turbulent field during a time which is much lesser than the characteristic time of turbulence. The following inequality must be verified :

$$(q'/U)\ (L/\Lambda) << 1$$

Λ/q' is a characteristic time scale of turbulence
L/U is the time of flight of a fluid particle in the distortion, the spatial extent of which is L.

In such conditions, the rate of dissipation of turbulent kinetic energy per unit mass can be considered roughly as a constant, and equal to its value upstream of the distortion.
We will consider now situations in which the new production terms developped in the distortion are much larger than the dissipation one ; in addition it will be supposed that the flow is not too inhomogeneous, so that the diffusive effects will not change strongly the Reynolds stress evolution, and can be neglected.
With these assumptions, the Reynolds stress equation, expressed for Favre averaged variables /6/, writes :

$$\frac{D}{Dt}\ \widetilde{u_i'u_j'} = -\widetilde{u_i'u_k'}\frac{\partial \tilde{u}_j}{\partial x_k} - \widetilde{u_j'u_k'}\frac{\partial \tilde{u}_i}{\partial x_k} + \frac{\overline{\rho u_i'}}{\bar{\rho}^2}\frac{\partial \bar{p}}{\partial x_j} + \frac{\overline{\rho u_j'}}{\bar{\rho}^2}\frac{\partial \bar{p}}{\partial x_i} - \frac{1}{\rho}\left(u_i'\overline{\frac{\partial p'}{\partial x_j}} + u_j'\overline{\frac{\partial p'}{\partial x_i}}\right) \qquad (1)$$

On the two first lines of the right hand side (r.h.s) member of (1), the production terms in the mean velocity gradient and in the mean pressure gradient are written . The term of the third line is generally of the same order of magnitude as the production, and must be modelled. In the models for turbulent subsonic flows, it is now accepted /7/,/8/,/9/ to represent this term by the sum of two parts. The first called "return-to-isotropy " term, is due to non-linear turbulent mechanisms ; the other, which is only one to be considered in a rapid distortion, is called /9/ the "rapid part of pressure". This rapid part of the pressure is deduced from the pressure equation obtained from the linearized Euler's equations. Only this rapid part is considered here : some limits of validity of such an approximation can be found in ref. /10/.

The Rapid Part of Pressure

By assuming little fluctuations of velocity, density, pressure, deducing a linearized equation for the fluctuation from the Euler's equations, and taking their divergence, an equation for the pressure fluctuation can be obtained. This equation can have very different forms, according as the velocity fluctuation divergence is zero or non-zero. In the Kovasznay's theory /11/, the "acoustic mode" corresponds to the irrotational part of the velocity fluctuation ($\partial u_k'/\partial x_k \neq 0$) while the "vorticity mode" is related to the solenoidal part of the velocity fluctuation ($\partial u_k'/\partial x_k = 0$). For equilibrium flows, a consequence of the Morkovin's hypothesis is that the vorticity mode is presumably predominant. Then, for non hypersonic turbulent flows, it is attractive to assume that the fluctuating motion is essentially incompressible, i.e. $\partial u_k'/\partial x_k = 0$. This basic assumption is made here. This hypothesis is well adapted to equilibrium layers and can also give a good approximation in distortions which do not amplify too much the acoustic mode.
For a solenoidal field of velocity fluctuations, if the mean flow is steady and if the second derivatives of mean velocity can be neglected, the equation for the rapid part of pressure writes :

$$-\Delta p' = 2\bar{\rho}\frac{\partial u_i'}{\partial x_j}\frac{\partial \tilde{u}_j}{\partial x_i} + \frac{\partial \rho'}{\partial x_i}\left(\tilde{u}_j\frac{\partial \tilde{u}_i}{\partial x_j}\right) + \rho'\frac{\partial \tilde{u}_j}{\partial x_i}\frac{\partial \tilde{u}_i}{\partial x_j} + \frac{\partial \bar{\rho}}{\partial x_i}\left(\frac{\partial u_i'}{\partial t} + \tilde{u}_j\cdot\frac{\partial u_i'}{\partial x_j} + u_j'\cdot\frac{\partial \tilde{u}_i}{\partial x_j}\right) \qquad (2)$$

The first two terms of (2) are identical to those found /9/ in subsonic flows with heat sources. In ref. /10/, it is pointed out that for fluctuations associated to small wavenumbers, the last two terms become the more important ones, but for the main part of the spectral range containing energy, it seems reasonable to make the following approximation :

$$-\Delta p' = 2\bar{\rho}\frac{\partial u_i'}{\partial x_j}\cdot\frac{\partial \tilde{u}_j}{\partial x_i} + \frac{\partial \rho'}{\partial x_i}\cdot\left(\tilde{u}_j\frac{\partial \tilde{u}_i}{\partial x_j}\right) \qquad (3)$$

Two additional assumptions are made : we consider flows where mean pressure forces are strong, so that $\partial \bar{p}/\partial x_i = -\bar{\rho}\tilde{u}_j\,\partial \tilde{u}_i/\partial x_j$; at last, it is assumed that, as in equilibrium turbulent flows /12/, the temperature fluctuations are practically isobaric : $\rho'/\bar{\rho} = -T'/\bar{T}$. The final form of (3) is :

$$-\Delta p' = +2\bar{\rho}\frac{\partial u_i'}{\partial x_j}\frac{\partial \tilde{u}_j}{\partial x_i} - \frac{1}{\bar{T}}\frac{\partial T'}{\partial x_i}\frac{\partial \bar{p}}{\partial x_i} \qquad (4)$$

The first term of the r.h.s. member of (4) can be related to the production in the mean velocity gradient, the second one to the production in the mean pressure gradients. According to the contribution of these two terms to the pressure variation can be examined separately ; the first one will be particularly studied hereafter.
A classical separation is used for the velocity gradients. When the divergence of velocity fluctuation is null, $\partial u_i'/\partial x_j$ can be separated into a symmetric part d_{ij} (fluctuating rate of strain), and a antisymmetric part r_{ij} (fluctuating rate of rotation); as the mean flow is compressible, $\partial \tilde{u}_i/\partial x_j$ is separated into an isotropic part $\frac{1}{3}\partial \tilde{u}_k/\partial x_k\ \delta_{ij}$ (mean dilatation rate) and a deviatoric ; the deviatoric is separated in the same way as $\partial u_i'/\partial x_j$:

REPORT DOCUMENTATION PAGE		READ INSTRUCTIONS BEFORE COMPLETING FORM
1. REPORT NUMBER AFOSR-TR- 82 -0032	2. GOVT ACCESSION NO.	3. RECIPIENT'S CATALOG NUMBER
4. TITLE (and Subtitle) THIRD SYMPOSIUM ON TURBULENT SHEAR FLOWS		5. TYPE OF REPORT & PERIOD COVERED FINAL 6. PERFORMING ORG. REPORT NUMBER
7. AUTHOR(s) F W SCHMIDT		8. CONTRACT OR GRANT NUMBER(s) AFOSR-80-0033
9. PERFORMING ORGANIZATION NAME AND ADDRESS THE PENNSYLVANIA STATE UNIVERSITY 308 MECHANICAL ENGINEERING BLDG UNIVERSITY PARK, PA 16802		10. PROGRAM ELEMENT, PROJECT, TASK AREA & WORK UNIT NUMBERS 61102F 2307/A2
11. CONTROLLING OFFICE NAME AND ADDRESS AIR FORCE OFFICE OF SCIENTIFIC RESEARCH/NA BOLLING AIR FORCE BASE, DC 20332		12. REPORT DATE SEPTEMBER 81 13. NUMBER OF PAGES 436
14. MONITORING AGENCY NAME & ADDRESS(if different from Controlling Office)		15. SECURITY CLASS. (of this report) UNCLASSIFIED 15a. DECLASSIFICATION/ DOWNGRADING SCHEDULE

16. DISTRIBUTION STATEMENT (of this Report)

Approved for public release; distribution unlimited.

17. DISTRIBUTION STATEMENT (of the abstract entered in Block 20, if different from Report)

18. SUPPLEMENTARY NOTES

19. KEY WORDS (Continue on reverse side if necessary and identify by block number)

20. ABSTRACT (Continue on reverse side if necessary and identify by block number)

The Third Symposium on Turbulent Shear Flow was held at the University of California, Davis, California on September 9-11, 1981. The objective of the symposium was to further advance the understanding of the physical phenomena associated withturbulent flows and the existing capabilities for calculating items such as the transport of heat and mass in such processes. Of the 158 abstracts received by the papers committee, a total of 92 papers were included in the final program. In addition to the 17 paper sessions, an open forum

DD FORM 1 JAN 73 1473 EDITION OF 1 NOV 65 IS OBSOLETE

UNCLASSIFIED

SECURITY CLASSIFICATION OF THIS PAGE (When Date Entered)

$$\partial u_i'/\partial x_j = d_{ij} + r_{ij} \quad \text{with } r_{ii} = d_{ii} = 0$$
$$r_{ij} = -r_{ji} \; ; \; d_{ij} = d_{ji}$$

$$\partial \tilde{u}_i/\partial x_j = (\partial \tilde{u}_k/\partial x_k)\ \delta_{ij}/3 + D_{ij} + R_{ij} \qquad (5)$$

with $D_{ii} = R_{ii} = 0$ and $D_{ij} = D_{ji}$; $R_{ij} = -R_{ji}$

Applying the rules of tensor algebra, the contribution of the velocity gradients to the pressure fluctuation can be expressed by :

$$\Delta p' = -2\bar{\rho}\,(d_{ij}\,D_{ij} + r_{ij}\,R_{ij})$$

The mean dilatation rate does not contribute to p' , because the fluctuating motion is supposed to be solenoidal. With this assumption, only D_{ij} and R_{ij} have to be considered, as in subsonic flows. The same conclusion can be drawn /10/ for the part of p' related to the mean pressure gradient : if $\partial u_k'/\partial x_k = 0$, the contribution of the mean pressure gradient term to the rapid part of the pressure-strain correlation can be modelled as in subsonic flows.

Models for the Rapid Part of the Pressure-Strain Terms

It follows from the previous considerations, that the way used, for example, by Lumley /9/ or by Launder, Reece and Rodi /8/ to model the pressure-strain correlations can be adapted to the supersonic case. It can be shown /10/ that, with the assumption $\partial u_k'/\partial x_k = 0$, the rapid part of the pressure-strain correlations can be represented by the same function (or functional) of the Reynolds stress and of R_{ij} and D_{ij} as in subsonic flows. The adaptation to the supersonic case is then very simple : the model remains unchanged when expressed in terms of D_{ij} and R_{ij} (but not in terms of $\partial \tilde{u}_i/\partial x_j$). In this paper three models will be used : Launder's model /8/, the quasi isotropic model given by Lumley /9/, and the model used by Naot, Shavit, Wolfsthein /13/. In the latter, which is the simpler one, the modelled terms are proportionnal, for imcompressible flows, to the production of Reynolds stress deviatoric in the mean velocity gradient. They are respectively :

$$-\frac{1}{\bar{\rho}}\left(\overline{u_i'\frac{\partial p'}{\partial x_j}} + \overline{u_j'\frac{\partial p'}{\partial x_i}}\right)_{\tilde{u}} =$$

approximation N° 1 Launder et al. (6)
$$q'^2\left[\frac{2}{5}D_{ij} + 0{,}87\left(a_{qj}D_{iq} + a_{qi}D_{jq} - \frac{2}{3}a_{ql}D_{lq}\delta_{ij}\right) + 0{,}656\left(a_{qi}R_{jq} + a_{qj}R_{iq}\right)\right]$$

approximation N° 2 Naot et al. (7)
$$q'^2\left[\frac{2}{5}D_{ij} + \frac{3}{5}\left(a_{qi}D_{jq} + a_{qj}D_{iq} - \frac{2}{3}a_{ql}D_{lq}\delta_{ij}\right) + \frac{3}{5}\left(a_{qi}R_{jq} + a_{qj}R_{iq}\right)\right]$$

approximation N° 3 Lumley (8)
$$q'^2\left[\frac{2}{5}D_{ij} + \frac{12}{7}\left(a_{qi}D_{jq} + a_{qj}D_{iq} - \frac{2}{3}a_{ql}D_{lq}\delta_{ij}\right)\right]$$

where $a_{iq} = \widetilde{u_i'u_q'}/q'^2 - \delta_{iq}/3$; Index $\tilde{u}$ indicates the contribution of the mean velocity gradient deviatoric : With these three approximations, we used

Lumley's proposal /9/ for the contribution of the mean pressure gradient :

$$-\frac{1}{\bar{\rho}}\left(\overline{u_i'\frac{\partial p'}{\partial x_j}} + \overline{u_j'\frac{\partial p'}{\partial x_i}}\right)_p = -0{,}3\left(\frac{\overline{T'u_i'}}{\bar{\rho}\,\bar{T}}\frac{\partial \bar{p}}{\partial x_j} + \frac{\overline{T'u_j'}}{\bar{\rho}\,\bar{T}}\cdot\frac{\partial \bar{p}}{\partial x_i} - \frac{2}{3}\cdot\frac{\overline{T'u_k'}}{\bar{\rho}\,\bar{T}}\cdot\frac{\partial \bar{p}}{\partial x_k}\delta_{ij}\right) \qquad (9)$$

where $\overline{T'u_i'}/\bar{T} = -\overline{\rho'u_i'}/\bar{\rho}$, if /12/ the low pressure fluctuation level hypothesis is valid.

Definition of an "Incompressible" Variable

Let us consider eq. /1/. Let π_{ij} be the fluctuating pressure term :

$$-\left(\overline{u_i'\partial p'}/\partial x_j + \overline{u_j'\partial p'}/\partial x_i\right)/\bar{\rho} = \pi_{ij}\,(q'^2, a_{ij}, \widetilde{u_i'u_j'}, D_{ij}, R_{ij}, \bar{\rho}, \partial p/\partial x_i)$$

π_{ij} does not depend on $\partial \tilde{u}_k/\partial x_k$. If the separation (5) is used for $\partial \tilde{u}_i/\partial x_j$, and introducing the mean continuity equation, eq. (1) writes :

$$\frac{D}{Dt}\widetilde{u_i'u_j'} = \frac{2}{3}\widetilde{u_i'u_j'}\frac{1}{\bar{\rho}}\frac{D}{Dt}\bar{\rho} + \left[-\widetilde{u_i'u_k'}\,(D_{jk} + R_{jk}) - \widetilde{u_j'u_k'}\,(D_{ik} + R_{ik}) + \frac{\overline{\rho'u_i'}}{\bar{\rho}^2}\frac{\partial \bar{p}}{\partial x_j} + \frac{\overline{\rho'u_j'}}{\bar{\rho}^2}\frac{\partial \bar{p}}{\partial x_i} + \frac{1}{\bar{\rho}}\pi_{ij}\right] \qquad (10)$$

In this equation, the mean dilatation terms appear only in the first term of the r.h.s. member. In addition, as the rôle of π_{ij} is to moderate the production terms due to D_{jk} , R_{jk} and $\partial \bar{p}/\partial x_i$, the production term involving the mean dilatation is the only one which is not reduced by π_{ij}.

In rapid distortions where dilatation effects are predominant, eq. (10) yields :

$$\frac{D}{Dt}\widetilde{u_i'u_j'} = \frac{2}{3}\widetilde{u_i'u_j'}\frac{1}{\bar{\rho}}\frac{D}{Dt}\bar{\rho} \quad ; \text{ if we define}$$

$T_{ij} = (\bar{\rho})^{-\frac{2}{3}}\widetilde{u_i'u_j'}$, it follows that $DT_{ij}/Dt = 0$

After integration, it comes, whatever i and j :

$$T_{ij} = \text{Cst} \quad \text{or} \quad \frac{(\widetilde{u_i'u_j'})^2}{(\widetilde{u_i'u_j'})_1} = \left(\frac{\bar{\rho}^2}{\bar{\rho}_1}\right)^{2/3} \qquad (11)$$

It can be remarked that a mean dilatation, i.e. an homogeneous, isotropic mean distortion does not change the Reynolds stress anisotropy : every component is changed, but at the same relative rate, so that the principal directions of the Reynolds tensor are unchanged. The same type of conclusion was reached in ref. /14/, from a less general analysis involving only the production terms.

Formula (11) was soon given by Batchelor /15/ who used dimensional considerations based on angular momentum conservation. We show here that Batchelor's result is exact for a solenoidal field of velocity fluctuations.

An equation for T_{ij} can be derived from (10). The terms of the r.h.s. member of (10) involving D_{ij} and R_{ij} can be expressed in terms of T_{ij} instead of

$\widetilde{u_i'u_j'}$. Some particular problems appear in the mean pressure gradient terms. For supersonic flows without heat sources /1/, /3/, /10/,/16/, the relations derived from the "Strong Reynolds Analogy" (S.R.A.) may be used to represent $\overline{\rho' u_i'}$ or $\overline{T' u_i'}$:

$$\overline{\rho'u'}/\bar{\rho} = \overline{T'u'}/\tilde{T} = R_{\rho u}\,(\gamma-1)\,M^2\,\widetilde{u'^2}/\tilde{u}$$

$$\overline{\rho'v'}/\bar{\rho} = \overline{T'v'}/\tilde{T} = (R_{\rho v}/R_{uv})\,(\gamma-1)M^2\,\widetilde{u'v'}/\tilde{u}$$

It appears that the production terms and the part of π_{ij} involving $\overline{\rho' u_i'}$ can be related to T_{11} and T_{12}. Then, the equation for T_{ij} has the following form : (no summation on i and j)

$$\frac{D}{Dt}T_{ij} = -T_{ik}\,(D_{jk}+R_{jk}) - T_{jk}\,(D_{ik}+R_{ik})$$

$$+ K_i \cdot \frac{(\gamma-1)M^2}{\bar{\rho}\,u} \cdot T_{1i} \cdot \frac{\partial \bar{P}}{\partial x_j} + K_j \cdot \frac{(\gamma-1)M^2}{\bar{\rho}\,u} \cdot$$

$$T_{1j} \cdot \frac{\partial \tilde{P}}{\partial x_i} + \frac{1}{(\bar{\rho})^{5/3}}\,\pi_{ij}$$

K_i are constants when the correlation coefficients $R_{\rho u}$, $R_{\rho v}$, R_{uv} are fixed : T_{ik} is the only turbulent quantity used in the expression of π_{ij}.

Therefore T_{ij} appears like an "incompressible" *variable because :*

i) its evolution does not depend on the mean dilatation rate;
ii) as far as the action of the mean strain and the mean rotation rates are concerned in a rapid distortion problem, the terms in which these variables appear are identical with the ones found in the equation for $\overline{u_i'u_j'}$ in incompressible flows.

These conclusions are compared to experimental results in the following chapter.

EXPERIMENTS

Description of the flow

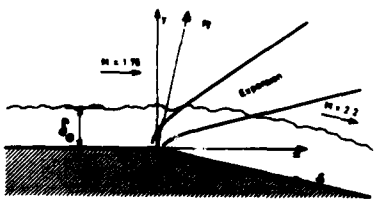

Fig. 1 : Sketch of the flow

The flow in which measurements were performed /10/ is shown on fig. 1. A fully turbulent boundary layer develops on a flat plate ; the external Mach number is 1.76 ; in the outer flow, the stagnation pressure is 40530 N/m^2 and the total temperature is typically 296 K. The wall remperature is, with a good approximation, the adiabatic flat plate recovery temperature upstream of the expansion. In this latter zone, the boundary layer is 1cm thick : the Reynolds number, based on momentum thickness is 5000.
A 12 deg. deflection of the wall around a sharp edge produces an expansion fan ; the boundary layer is deviated without separation. The expansion produces large density and pressure varations. If Δp and τ_w are respectively the pressure drop absolute value and the wall friction in the initial boundary layer, the ratio $\Delta p/\tau_w$ is 100 ; such a value (17),(18) corresponds to a relaminarization of the flow, downstream of the expansion. It seems likely (4) that bulk dilatation contributes to such a relaminarization. At last, in the expansion and out of the viscous sublayer, the mean flow can be computed by neglecting the friction terms in the momentum equation, for the pressure force is very strong. This enables to calculate the mean flow independently from turbulence, and to get an accurate determination of the means gradients contributing to the "source" terms in the equation of T_{ij}.

Measurements methods. Apparatus

The measured mean variables are total pressure and total temperature. Total pressure was measured with Pitot probes and piezo resistant pressure tansducers ; total temperature was measured with hot-wire probes.

Turbulent quantities (variance of temperature fluctuations, of longitudinal velocity fluctuations ; velocity temperature correlation coefficient) were measured by a "constant current" hot-wire anemometer. The bandwidth of the uncompensated amplifier reached *310 kHz. Errors coming from the imperfections of* the time lag compensating circuit were reduced by ad hoc corrections /19/. The Kovasznay's "fluctuation diagram"technique /11/was used. Details of the apparatus and of measurement methods are given in ref. /10/.

Mean flow determination in the expansion

As indicated hereabove, the mean flow out of the viscous sublayer can be computed by resolving the Euler's equations by a method of characteristics. Such a computation is more accurate than measurements for the intrusion of a static pressure probe in the expansion provokes systematic errors. The calculation was made as in ref. /20/ by assuming that mean entropy and mean total enthalpy are constant along streamlines. The results of the computation are in good agreement with Pitot pressure measurements, so that all the information on mean field was deduced from the results of the method of characteristics.

Turbulence Measurements

It was checked from $\widetilde{u'^2}$ measurements that the initial boundary layer is in equilibrium. Fig. 2 gives the results in the representation suggested by Morkovin /1/. τ_w is the wall friction determined from the law of the wall, for compressible turbulent boundary layers. The present results are consistent with the other boundary layer data.

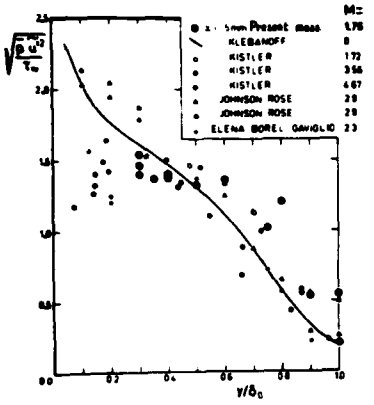

Fig. 2 : Profile of $\widetilde{u'^2}$ in the initial boundary layer

The normal stress $\widetilde{u'^2}$ was measured just downstream of the last expansion characteristic (Fig. 3) and along the streamline whose location in the initial boundary layer is $y/\delta o = 0,3$ (Fig. 4)

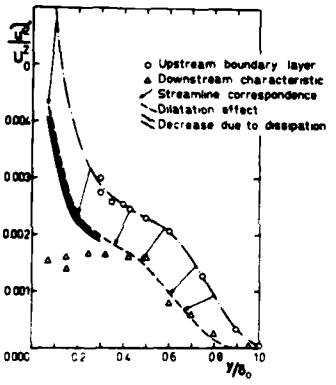

Fig. 3 : $\widetilde{u'^2}$ measurements upstream and downstream of the expansion.

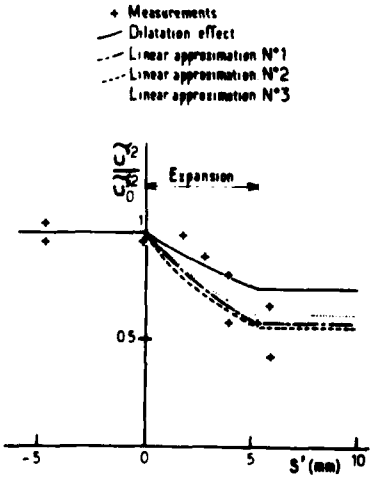

Fig. 4 : $\widetilde{u'^2}$ evolution along the explored streamline.

U_o is the mean velocity in the initial external flow ; $\widetilde{u'^2_o}$ is the initial value of $\widetilde{u'^2}$. On fig. 4, s' is the curvilinear abscissa along the streamline.
The striking fact is the large decrease of $\widetilde{u'^2}$ in the expansion, mainly in the internal half of the boundary layer.
Temperature variance $\widetilde{T'^2}$ and velocity temperature correlation coefficient R_{tu} were also measured. Upstream and downstream of the expansion (Fig. 5)and along the explored streamline, the S.R.A. formula is verified and R_{tu} can be considered as a constant, $R_{tu} \simeq -0,8$. These conclusions are valid only in the non intermittent part of the flow, i.e. $y/\delta o < 0,6$, and will be used in the calculations presented in the next paragraph.

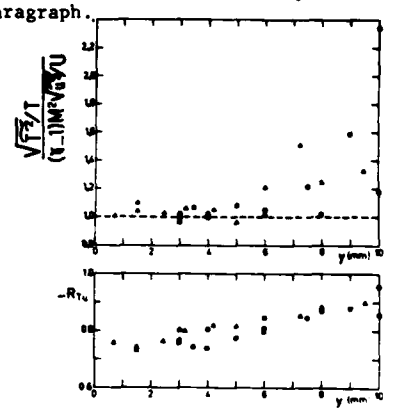

Fig. 5 : Temperature variance ; velocity temperature correlation coefficient, upstream (●) and downstream (▲) of the expansion.

DISCUSSION

Firstly, it was checked that the distortion is rapid. The parameter $q'L/(U\Lambda)$ is roughly 0.1, outside of the viscous sublayer. Secondly, different hypothesis were used to explain the $\widetilde{u'^2}$ evolution. It was at first assumed that bulk dilatation effect is predominant, i.e. T_{ll} is constant. The result, noted "dilatation effect" is shown on fig. 3 and 4 ; it is consistent (Fig. 4) with the measured values of $\widetilde{u'^2}$, in the external half of the boundary layer. In the internal half, the predicted values of $\widetilde{u'^2}$ with the former assumption are much larger than the measured ones. Note that, due to the lack of measurements near the wall, the part of the initial $\widetilde{u'^2}$ profile for $y/\delta o < 0,3$ is extrapoled on the basis of Klebanoff's measurements. Kistler's results (Fig. 2) seem to indicate that near the wall, the supersonic data could be lower than the subsonic ones. Nevertheless, an extrapolation based on Kistler's data, associated with the only dilatation effects, would not reproduce the low u' level observed downstream of the expansion, for $y/\delta o < 0,3$.

The influence of dissipation has been estimated by assuming it is isotropic, constant in the distortion, and equal to production upstream of the expansion. The result is indicated on fig. 3 by a dashed zone. It can be concluded that the contribution of dissipation to the measured evolution is of low importance.

A last approximation is then used, by assuming that for $y/\delta o \leq 0,5$, π_{ij} and all the terms of production can be important, and that diffusive and dissipative effects can be neglected. Formulas (6), (7), (8) to which "linear approximation" N°1,2,3 are

referred on fig. 4, are used to represent the part of π_{ij} involving D_{ij} and R_{ij}. These formulations are used with Lumley's proposal /9/, eq. (10), for the part of π_{ij} depending on $\rho' u_i'$. The Reynolds stress calculation was then made along the mean streamline initiating at $y/\delta o = 0,3$. The equations were written in an "intrinsic" frame of reference, i.e. relative to the mean streamline. The geometry of this streamline (location, radii of curvature) and the mean field are deduced from the results of the method of characteristics. The initial conditions on the Reynolds stresses are given by the $\overline{u'^2}$ measurements and by assuming that the different stresses are in the same proportions as in subsonic equilibrium boundary layers. The results on $\overline{u'^2}$ are given on fig. 4 which shows that the rapid distortion approximations are in good agreement with the measurements. It seems amazing that the three different formulations give practically the same results. An inspection of the source terms in the equation of $\overline{u'^2}$ indicate that the main contribution to $\overline{u'^2}$ is due to the bulk dilatation and to the mean pressure gradient, the terms related to D_{ij} and R_{ij} being very low.

CONCLUSION

The evolution of the normal Reynolds stress related to longitudinal velocity fluctuations in an expansion leading to the relaminarization of a boundary layer at supersonic speed has been analyzed by a rapid distortion approximation. Some properties of the action of a bulk dilatation on a solenoidal field of velocity fluctuations have been given. The results show that, outside of the viscous sublayer, bulk dilatation contributes largely to relaminarization, though the effect of the mean pressure gradient cannot be neglected.

The proposed analysis was based on the assumption that the fluctuating motion is essentially incompressible. Although the used approximations and models can reduce the generality of the conclusions, it seems that this basic hypothesis can be safely used to describe the turbulent fluxes in distortions like a centered expansion, for non hypersonic flows.

ACKNOWLEDGEMENTS

This work was supported by C.N.R.S., and by an O.N.E.R.A. research contract. The authors are indebted to Dr Debieve for valuable comments ant to M. Borel for his efficient technical help.

REFERENCES

1 : MORKOVIN, M.V. Mécanique de la Turbulence, A. Favre ed., C.N.R.S., Paris 1962 pp. 367-380

2 : WILCOX, D.C., ALBER, I.E., Proceedings of the Heat Transfer and Fluid Mechanics Institute, Stanford University, Calif., 1972, pp. 231-252

3 : BRADSHAW, P., Journal of Fluid Mechanics, vol. 63, Part 3, 1974, pp. 449-464

4 : BRADSHAW, P., Theoretical and Applied Mechanics, W.T. Koiter ed., North-Holland, Amsterdam 1976, pp. 103-113

5 : HUNT, J.C.R., XIIIe Biennal Fluid Dynamics Symposium, Warsaw, Poland, Sept. 1977, pp. 121-152

6 : FAVRE A.,KOVASZNAY, L.S.G., DUMAS R., GAVIGLIO J, COANTIC M La Turbulence en Mécanique des Fluides Guathier Villars, Paris 1976, pp. 51-52

7 : ROTTA, J.C., Zeitschrift der Physik, Vol. 129, 1951, pp. 547-572

8 : LAUNDER, B.E., REECE, G.J., RODI, W., Journal of Fluid Mechanics, Vol. 68, N°3, 1975, pp. 537,566

9 : LUMLEY, J.L., V.K.I. Lecture, Von Karman Institute, Rhodes - Saint Génèse, 1975

10 : DUSSAUGE, J.P., Thèse de Doctorat d'Etat, Université d'Aix Marseille II, Marseille, Apr. 1981

11 : KOVASZNAY L.S.G., Journal of Aeronautical Sciences, Vol. 20, 1953, pp. 657-682

12 : LAUFER, J., Proceedings of A.I.A.A. 6th Aerospace Science Meeting, N° 68-41, New-York, 1968

13 : NAOT, D., SHAVIT, A., WOLFSTHEIN, M., Israël J. Tech., Vol. 8 N° 259, 1970

14 : DUSSAUGE, A., GAVIGLIO, J., FAVRE, A., Structure and Mechanics of Turbulence II, H. Fielder ed., Lecture Notes in Physics 76, Springer Verlag, Berlin 1978, pp. 385-395

15 : BATCHELOR, G.K., Vistas in Astronomy, A. Beer ed. Vol. 1, 1955, Pergamon Press, pp. 290-295

16 : DEBIEVE, J.F., GOUIN, H., GAVIGLIO, J., Symposium on the Structure of Turbulence and Heat and Mass Transfer, Dubrovnik Yug., 1980, Hemisphere Publishing Corporation, Washington, D.C., (to be published)

17 : NARASIMHA, R., VISWANATH, P.R., A.I.A.A. Journal, Vol. 13, N° 5, 1975, pp. 693-695

18 : GAVIGLIO, J., DUSSAUGE, J.P., DEBIEVE, J.F., FAVRE, A., The Physics of Fluids, Vol. 20, N° 10, Pt. II, 1977, pp. S 179 - S 192

19 : GAVIGLIO, J., DUSSAUGE, J.P., Proceedings of the Symposium on Flow in Open Channels and Closed Circuits, Gaithersburg, Md, N.B.S. Special Publication N° 484, L.K. Irwin ed., 1977, pp. 649-658

20 : DELERY, J., MASURE, B., La Recherche Aerospatiale, 1969, Vol. 1

SESSION 3 - REACTING FLOWS

H. A. Becker - Chairman

MOVEMENTS OF FLAME-FRONTS AND THEIR PROPERTIES IN A TURBULENT DIFFUSION FLAME

M. Ahlheim, H. Hoffmann and W. Leuckel

Universität Karlsruhe (TH), Karlsruhe, West Germany

ABSTRACT

In an axial jet turbulent diffusion flame issuing from a double concentric burner measurements were made of local ionization, temperature and flow velocity. The ionization signals allow the instantaneous thermal structure and propagation behaviour of the flame front to be explained. Cross correlation measurements with a double ionization probe show that the average value of the absolute flame front velocity is different from the mean flow velocity. Except in the external boundary zone of the flame, flame velocity is slower than flow velocity. Temperature measurements were correlated with ionization and indicate the characteristic differences of combustion progress of the premixed and of the diffusive type.

NOMENCLATURE

d	=	burner diameter
I	=	ionization current
r	=	correlation coefficient
T	=	temperature
t	=	time
x	=	distance from burner exit
y	=	radial distance from flame axis
$\overline{\ }$	=	time mean value
$'$	=	fluctuation value
$\sqrt{\overline{\ }^2}$	=	root mean square value of fluctuation

INTRODUCTION

Investigations on flames using ionization measurements have been known for many years. The first studies in turbulent flames were done by Karlovitz et al./1/ who used the ionization probe to determine the position of turbulent flame fronts. Ahlheim and Günther /2/ found a strong relationship between the ionization measured locally and the local reaction density. The reaction density is defined in this context as the total consumption of methane divided by the total flame surface. This relationship will help in investigating the structure of turbulent diffusion flames by ionization measurements, as carried out before by Ahlheim and Günther /3/ in natural gas flames.

EXPERIMENTAL CONDITIONS

All measurements were made with a 7.9 mm internal diameter tube burner with centric fuel gas flow, surrounded by annular concentric gas flow which was 1.07 times the stoichiometric rate. The flames were stabilized by oxygen issuing from a small annular slit surrounding the fuel tube. The gas velocity was 50 m/s and the air gas velocity rate was 0.29. The Reynolds number was about 26 000. The flame produced by this burner was absolutely non-luminous, i.e. soot free.

IONIZATION MEASUREMENTS

Ionization measurements by Ahlheim and Günther /3/ demonstrate the progress of combustion very clearly. Fig. 1 shows the time mean values of ionization. At $x/d=20$ the reaction has not yet reached the flame axis and is very weak for most of the cross section. At $x/d=40$ the fresh air has penetrated to the flame axis, and a very intensive reaction can be seen across the whole flame cross section. Further on the profile of ionization becomes more and more equalized across the jet due to the advanced mixing of fuel and air. The flame ends at $x/d=100$.

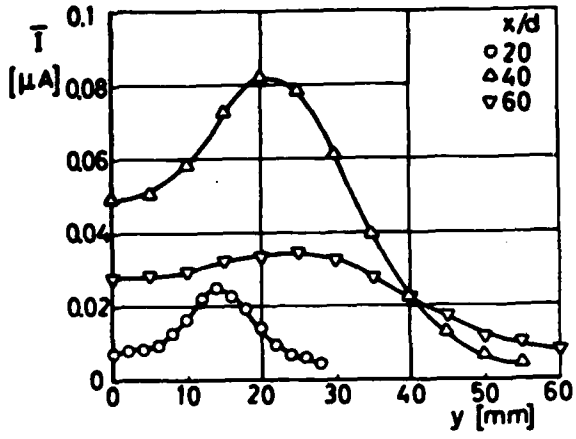

Fig. 1: Time mean values of ionization

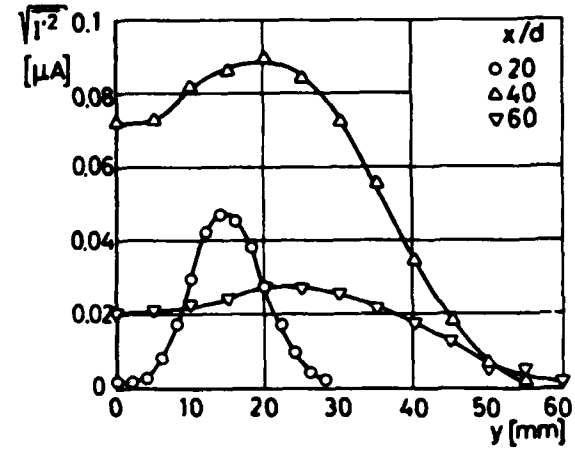

Fig. .. Root mean square values of ionization fluctuations

The fluctuation of ionization (Fig. 2) describes the fluctuation of the reaction density, which is influenced by the mixture of gas and air and by the aerodynamic structure of the reaction zone. In a turbulent diffusion flame there exists any mixture of fuel, air and waste gas. To interpretate the ionization signals measured in a turbulent diffusion flame, some preliminary examinations were made in laminar diffusion flames and in laminar premixed flames. The result of those measurements are shown in Fig. 4.

In a turbulent diffusion flame the simplest model is that of eddies of fuel and air existing side by side, with a flame front possibly existing between fuel and air. Fig. 3 shows a scheme of this model and the corresponding ionization signal. Figs. 4a-4c show the signal measured in a laminar diffusion flame, and Fig. 5a the equivalent signal measured in a turbulent diffusion flame. The measurements of Fig. 4 were made in a flame from a cylindrical burner, so that

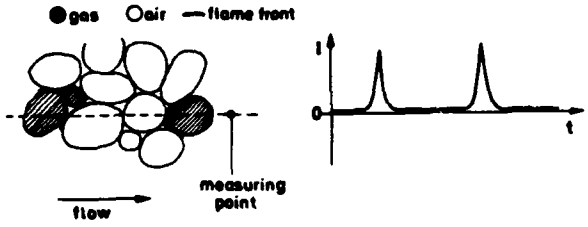

Fig. 3: Scheme of a reacting eddy structure moving over the measuring point

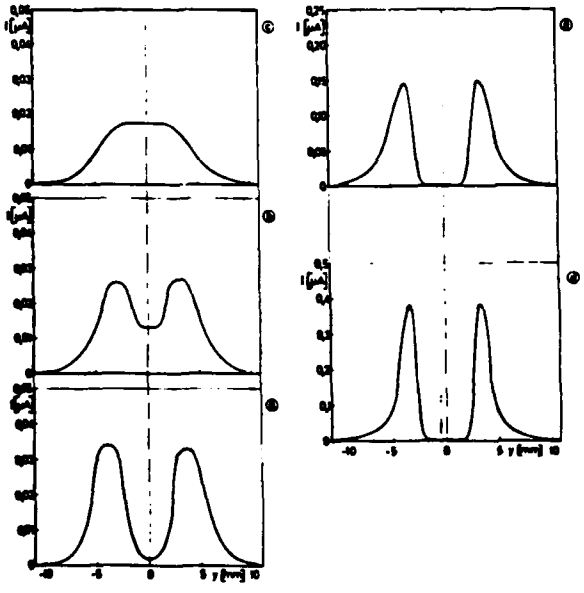

Fig. 4: Ionization profiles of laminar flame fronts
a) diffusion flame, flame root
b) diffusion flame, transition region
c) diffusion flame, flame tail
d) premixed flame, 9.5 Vol % methane
e) premixed flame, 12 Vol % methane

the ionization probe crossing the flame detected two flame fronts. Fig. 4b and 4c show the progress of mixing of fuel and air across the flame axis with increasing downstream distance. It is supposed that in a turbulent diffusion flame two flame fronts with this pattern of ionization do not exist, because in a turbulent eddy fuel is not being continously supplied to the reaction fronts as it is in the laminar flame. The occurence of signals of the type of Fig. 4c, as shown in Fig. 5b, will be explained later in another way. In Fig. 4d and 4e is shown the typical profile of an ionization signal of a premixed flame. The difference to the diffusion flame is obvious. On the fuel side the increase of the ionization signal is steep up to the top of the peak, and on the waste gas side it drops more slowly to the normal zero value, because the ions will gradually decay in the hot waste gas.

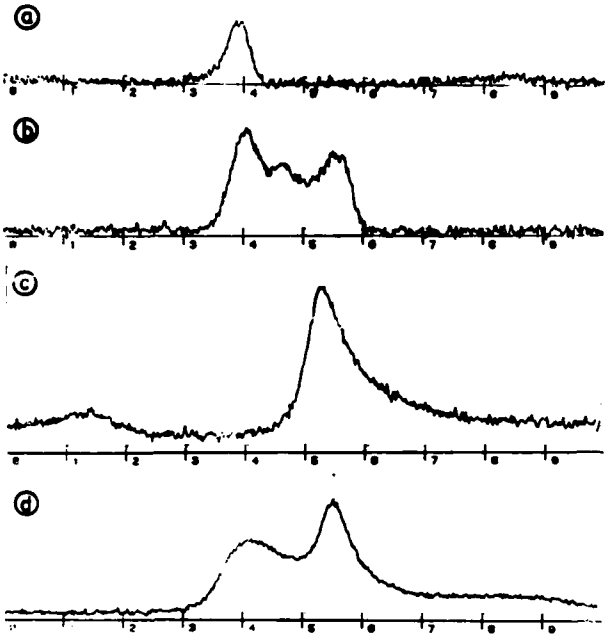

Fig. 5: Various records of ionization signals (see text)

Fig. 6 explains the model of spreading of a premixed flame front in a turbulent diffusion flame. From the ignition point the flame front spreads spherically. Now there are two possibilities of the ionization probe crossing such a flame front (Fig. 6a and 6b), and correspondingly two types of signals can be distinguished.

Fig. 5b shows a typical signal resulting from the probe crossing the flame front once. There is a steep rise in ionization on the fuel side and a much slower decrease on the burned gas side. The rate at which the signal decreases is mainly dependent on the reaction intensity and the local temperature of the burned gas. At higher temperature the ions have longer lifetimes, which leads to a slower decrease of ionization.

Fig. 5c shows the signal corresponding to the model of Fig. 6b. The probe crosses the flame front twice and two sharp ionization peaks are recorded. The level of ionization between them depends on the number of ions remaining in the burned gas, and on the distance between the two crossing points. The gradient is equally large on both sides, since fuel is present on both sides.

Fig. 6c shows a model for the occurrence of the signal of Fig. 5d. In a fuel-rich mixture the excess hot fuel diffuses out of the flame zone. This fuel can react with the air flowing from the surroundings, so that a diffusion flame zone rises in addition to the premixed flame. Unpublished work on laminar flames with incomplete premixing by E. Hoffmann-Berling at the authors' institute confirmed the relationship between flame form and signal shape.

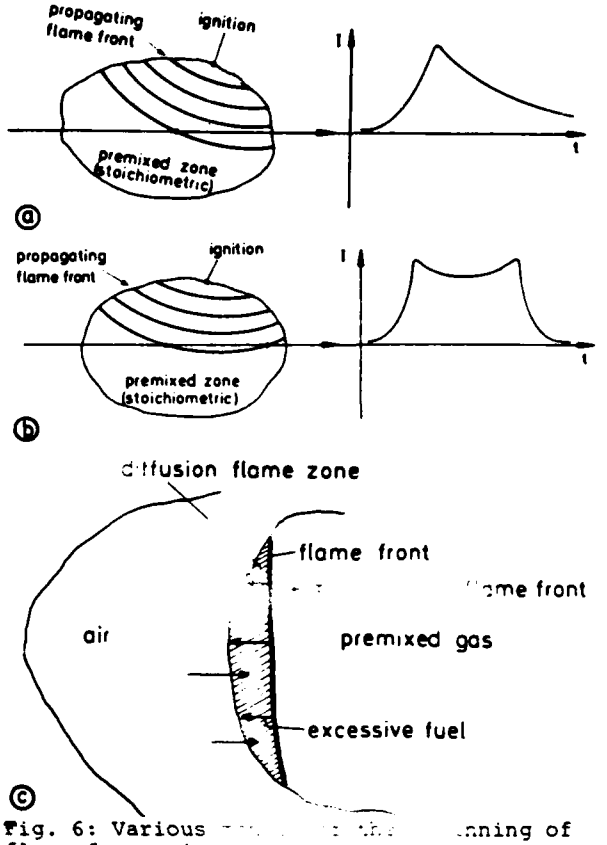

Fig. 6: Various [illegible] of flame-front signals (see text)

In turbulent diffusion flames, the most likely situation will be a simultanous occurrence of both types of combustion, resulting in a practically premixed reaction. The ionization signals from this sort of flame front can not be interpretated without ambiguity.

The ratio of diffusion flames to premixed flames to mixture zone flames was estimated in the present investigation to be about 1:2:7.

EVALUATION OF FLAME PROPAGATION VELOCITY FROM IONIZATION MEASUREMENTS, AND COMPARISON WITH FLOW VELOCITY

In the preceding paragraphs, the relative movement of the flame front in the surrounding gas has not yet been considered. Measurements of the velocity of the flame fronts were made in the diffusion flame by cross correlation with a double ionization probe. From measurements of time intervals in three directions, the magnitude of the velocity of flame fronts and their direction of propagation were calculated. The difference between the velocity of flame fronts and the local flow velocity measured by Seifert /4/ (Fig.8) is important. The relative velocity of flame fronts in the flow is up to 5 m/s. Near the axis, the relative flame speed direction is always upstream. At the beginning of the main

reaction zone (x/d = 40), the movement of flame fronts in the flow change its sign at greater radii, i.e. to downstream direction.

In a premixed flame the movement of flame fronts in the flow was explained by laminar flame speed /5/. In the diffusion flame, the relative velocity reaches up to 5 m/s, but the maximum laminar flame speed of natural gas is only 0.43 m/s. This can be explained by two effects. The preheating of gases before reaction, which occurrs in diffusion flames, increases the laminar flame speed. But even with very high preheat temperatures the burning velocity does not reach more than 1.5 m/s, so this influence can explain only a part of the observed values. The turbulent flame speed cannot be considered here, since it concerns the mean flame surface and not the real instantaneous flame surface which was observed. The second reason for the great difference of flame front velocity and flow velocity must be found in the structure of the turbulent reaction zone.

Whereas the flow velocity is measured continuously, the measurement of flame front velocity is correlated with the occurrence of a flame front. But the occurrence of a flame front itself is correlated with a nearly stoichiometric mixture. The initial fuel velocity is high and that of the air is low, but the stoichiometric mixture consists of about a ten times more mass of air than mass of fuel. Therefore, the observed instantaneous flame front velocities must be strongly correlated with the occurrence of flow velocities.

Direct measurements of this correlation are very difficult. First experiments with Laser-Doppler-Anemometry and simultaneous ionization measurements show a way to get reasonable information on this question, but the results of the preliminary measurements made by now are not yet sufficiently reliable in order to make a clear statement.

CORRELATION OF IONIZATION AND GAS TEMPERATURE

In addition to the measurements of ionization and the correlation of ionization and flow velocity, investigations were made to correlate temperature and ionization. Very useful information can be drawn from those results.

In Fig. 7.1 the mechanism of ignition, propagation and extinction in a fuel-air mixture is shown. When a reaction front passes the probe, there will be an ionization peak as well as a temperature peak (Fig.7.1a). When reaction is finished in such a front, the probe will observe only a temperature peak (Fig. 7.1b). When a reaction spreads over a premixed zone temperature and ionization signals will be found as shown in Fig. 7.1c. The flame moves to one or both sides of this zone, and hence two ionization peaks are found. Between those two reaction zones

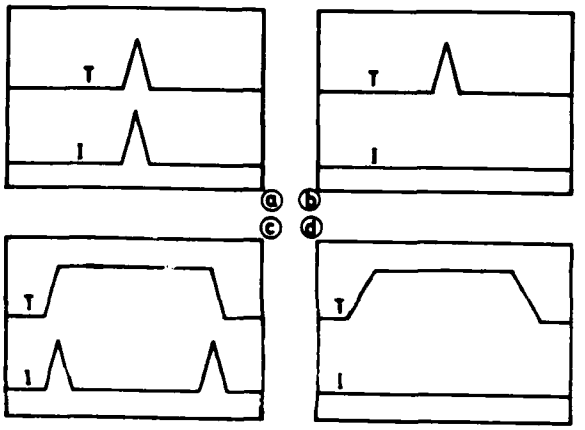

Fig. 7.1: Behaviour of ionization and temperature with reaction in a stationary fuel-air mixture (premixed reaction)
a) Ignition just started
b) Reaction started and extinguished immediately afterwards
c) Reaction propagates to both sides
d) Reaction has propagated across the premixed zone and then extinguished

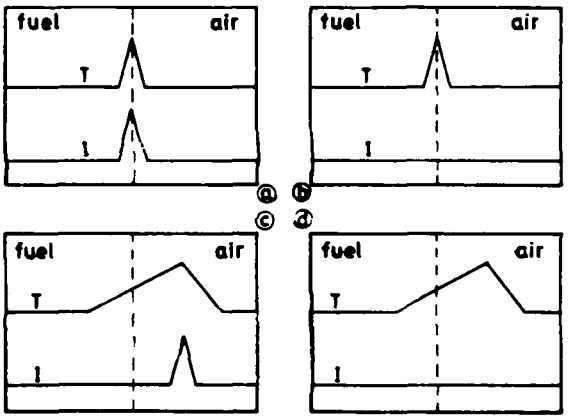

Fig. 7.2: Behaviour of ionization and temperature with reaction in a stationary fuel-air boundary layer (diffusion reaction)
a) Ignition just started
b) Reaction started and extinguished immediately afterwards
c) Diffusive reaction for a longer period of fume
d) Diffusive reaction ceases for a longer period of fume, and then extinguished

there is hot waste gas present. If the reaction zone has extinguished there will be hot waste gas left (Fig. 7.1d).

In contrast to a premixed flame, Fig. 7.2 shows a diffusion flame. First there will be a sharp boundary surface between air and fuel. When both gases start to diffuse into each other and ignite at once, the peaks of ionization and temperature will be very simular to those of a premixed flame (Fig. 7.2a). If the

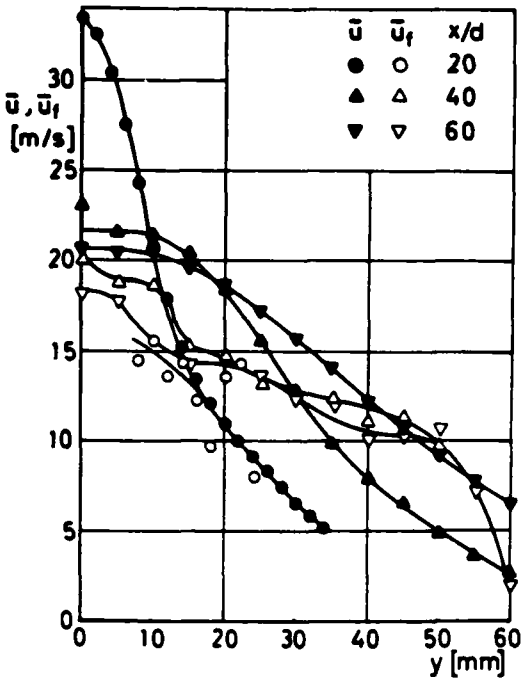

Fig. 8: Flame propagation and flow velocities (from /4/)

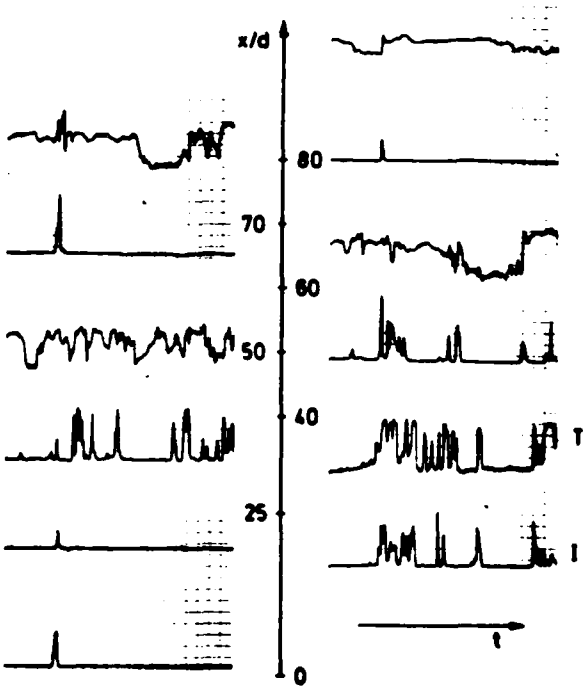

Fig. 9: Instantaneous temperature and ionization signals recorded at different points on the flame axis

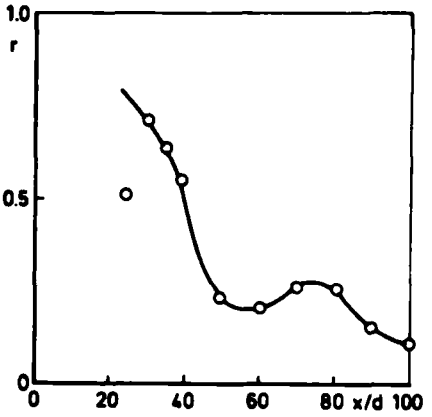

Fig. 10: Correlation coefficient of ionization and temperature along the flame axis

reaction stops at once there will be again no difference to a premixed flame (Fig. 7.2b). But if the reaction goes on for a certain time, the mechanism will become entirely different. Fresh air and fuel have to diffuse to the reaction zone, and hot waste gas moves away. The temperature is proportional to the concentration of waste gas and expands in both directions.The reaction shifts to the side of the air because the reaction needs more air than fuel. For this reason, the temperature profile becomes asymmetric as is shown in Fig. 7.2c. After the reaction has died, the temperature profile will stay the same as in Fig. 7.2d.

There are premixed and non-premixed eddies in a turbulent diffusion flame as can be seen from Fig. 9. There are premixed flames which are accompanied by a temperature step, and non-premixed flames which are surrounded by a field of high temperature.

It is to say that the temperature integrates all reactions along the flow path up to that point (heat transfer neglected), whereas the ionization describes the instantaneous reaction at the measuring point.

Measurements of ionization and temperature fluctuations show the combustion progress along the flame axis (Fig. 10). Near the burner exit (x/d small) only few temperature peaks occur which are always accompanied by ionization peaks. At the beginning of the main reaction zone the frequency of temperature fluctuations increases more than of ionization fluctuations, which is caused by eddies of combustion gases, which do not react but are still hot. This is expressed by the correlation coefficient (Fig. 10) between both. The high correlation coefficient at the beginning is caused by the coincidence of ionization and temperature. This coincidence decreases in the main reaction zone and the correlation coefficient becomes lower, respectively. The weak

maximum at x/d = 80 can be explained by the entrainment of cold air into the hot gases still containing fuel, and resulting in further reactions.

CONCLUSIONS

Measurements of ionization, velocity and temperature were made to get informations of the structure of a turbulent diffusion flame.

It can be concluded:

- the shape of ionization signals give answer over the momentary structure of a flame front in a turbulent diffusion flame
- velocity measurements with a double ionization probe show that absolute flame front velocity is slower than mean flow velocity, exept in the external boundary zone
- correlation measurements of temperature and ionization show the characteristic differences of combustion progress of the premixed and of the diffusive type.

REFERENCES

/1/ Karlovitz, B., Denniston Jr. D.W., Knapschaefer, D.H., and Wells, F.E., "Studies on Turbulent Flames", Fourth Symposium (International) on Combustion, Combustion Institute, Pittsburgh, Pa., pp. 613 - 620

/2/ Ahlheim, M., and Günther, R., "Investigation of Turbulent Reaction Fields by Ionization Measurements", AIAA 18th Aerospace Sciences Meeting, Pasadena, Ca.

/3/ Ahlheim, M., and Günther, R., "Ionization Measurements in Free-Jet Diffusion Flames", Combustion and Flame, Vol. 36, 2, 1979, pp. 117 - 124

/4/ Seifert, H., "Turbulenter Austausch in konzentrischen Luftstrahlen und Erdgas-Diffusionsflammen", Thesis, University of Karlsruhe, West Germany, 1979

/5/ Suzuki, T., Hirano, T., and Tsuji, H., "Flame Front Movements of a Turbulent Premixed Flame", Seventeenth Symposium (International) on Combustion, Combustion Institute, Pittsburgh, Pa.

A CHEMICALLY REACTING PLANE MIXING LAYER

S. V. Sherikar and R. Chevray
Department of Mechanical Engineering
State University of New York at Stony Brook
Stony Brook, N. Y. 11794

ABSTRACT

Flow-visualization has for long been a powerful tool in experimental studies in fluid mechanics. A novel technique utilizing NH_3-HCl reaction is presented and used in order to study the motion of large structures in a plane mixing layer and is shown to be successful. A scheme for studying the interaction of the chemical reaction between NO and O_3 with turbulence in plane mixing layer is discussed and results predicted by Monte Carlo method are presented.

NOMENCLATURE

- c - concentration of species/non-dimensional product concentration
- d - particle diameter
- E - photodetector output/molecular mixing term
- F(d) - total number of particles per unit volume greater than a given diameter d
- f - passive scalar
- I - intensity of light signal with absorption
- I_o - intensity of light signal without absorption by species
- k - reaction rate constant
- k_f - rate constant for NO-O_3 reaction
- k_{nucl} - rate of nucleation of NH_4Cl
- L - path-length of absorption
- m_k - mass fraction of species k in the flow
- N - number of particles per unit volume
- P - pressure
- p - probability density function
- R - correlation coefficient/gas constant
- S - rate of NO-O_3 reaction
- T - temperature
- U - mean flow velocity
- V - velocity of the flow in transverse direction
- W_k - molecular weight of species k
- x - distance along mean flow direction
- y - distance transverse to mean flow direction
- Z_k - $\frac{m_k}{W_k}$
- α - ratio of reactant concentrations, $\frac{(Z_{NO})_1}{(Z_{O3})_2}$
- α_a - absorption constant
- β - defined as $\frac{(Z_{O3})_2}{(Z_{N2})_2}$
- δ - mixing layer width
- Γ - normalised cross-stream distance
- σ - $\frac{d\delta}{dx}$
- τ_t - turbulent diffusivity
- ω - defined as $\frac{Pk_f}{RT}$
- ω_t - turbulent frequency

Subscripts

1 refers to fast stream
2 refers to slow stream

Superscripts

* normalized parameters
' fluctuations in the quantity

INTRODUCTION

One of the simplest free shear flows is the plane mixing layer formed between two parallel streams when they come together. Substantial work has been reported on this in the last decade, whereby some important features of this type of flow have been brought to light (although there is considerable scatter in data from different researchers owing mainly to different experimental conditions). One feature that has been considered of great importance by many is coherent structures and interaction among them put in evidence in low Reynolds number flows by, among others, Browand (1). That this was not a phenomenon of transition and that this mechanism is exhibited also at high Reynolds numbers was shown by Brown and Roshko (2), Dimotakis and Brown (3). With the existing state of art, a clear understanding of the nature of the large structures observed in shear flows seems essential to the understanding of mechanism of entrainment and growth of mixing layer.

Another area which needs attention (and which has been studied much less)is the interaction between turbulence and chemical reaction. Although it was realized long ago that chemical kinetics and turbulent mixing go hand in hand in the study of many systems of interest (combustion, chemical industry, pollution, etc.), the interaction between the two is not well understood. Most of the time complex turbulent flows and complex chemical kinetics are investigated and then getting even a clear qualitative picture of these systems becomes difficult.

Important parameters controlling the turbulent mixing of two chemically reacting species are the velocity ratio, the Reynolds number, the enthalpy ratio, the reaction speed number and the concentration ratio. Velocity ratio has been known to influence the growth of the mixing layer and through this affects the chemical reaction. The Reynolds number comes into the picture because the smallest turbulent length scales can be related to its actual value. Its role in turbulent reaction, however, is not clear yet. Shea (4) concluded that increasing the Reynolds number for a turbulent jet has no systematic effect in product concentration whereas Konrad (5) found a 25% increase in the rate of mixing of a two-dimensional mixing layer above a certain critical value of the Reynolds number. The enthalpy ratio, defined as the ratio of the reaction generated enthalpy and the initial enthalpy of the mixture, defines the importance of exothermicity of the reaction. The reaction speed number (also known as Damkohler number), is the ratio of the time-scale responsible for turbulent mixing to that of the reaction. Whenever this ratio is large, mixing controls the overall process and vice versa for small values of it.

Theoretical approaches in dealing with this problem are many, but none that is completely satisfactory mainly because of closure problems. Formal treatments of turbulent reacting flows with large reaction speed numbers are on firms grounds (Toor (6), O'Brien (7), Bilger (8)) relating them to inert species mixing. Probability methods Dopazo (9) allows for the exact treatment of the turbulent reaction rates and are very advantageous when dealing with a few chemical species. Developments on the conditioned formulation by Libby (10) and Dopazo (11) and their application to fast chemical reactions in turbulent fields permit determination of the local average turbulent reaction rate, once a few conditioned characteristics are experimentally obtained. Monte Carlo technique developed by Pope (12) seems computationally efficient and promising since it can handle a large number of chemically reacting species but its accuracy depends on precise knowledge of initial conditions.

EXPERIMENTAL FACILITIES

A study is being conducted in a wind-tunnel in which two parallel streams of air are kept apart from each other prior to their mixing in the test section. They can thus be seeded with different chemical species to study their reaction occurring in the test section which is 25 cm x 100 cm long (x 15 cm wide). With the velocities used this corresponds to a maximum Reynolds number of 250,000 (based on velocity in the fast stream and maximum distance downstream). Honeycombs and screens are placed in the flow to reduce the turbulence intensity and cut the large scale structures at the inlet of the test section. Initial tests revealed that the boundary layer on the splitter plate was laminar with momentum thicknesses of 0.6 mm and 0.9 mm in fast and slow streams respectively. The splitter plate made out of 1/16" thick stainless steel plate was tapered over 25 cm length to 0.05 mm thickness at the trailing edge. Velocity profile in each section was flat with variations less than 1% when measurements were made with blowers. In addition, an inert gas delivery system was set up to study reactions in which the reactants could react with any of the constituents of air. This system delivers high purity nitrogen from eight bottles simultaneously so that large flow-rates could be obtained. For the study of the NO-O_3 reaction, since the quantities of reactants are large and it is not feasible to put an ozonator on line, we stored ozone in special containers after it had been generated in the laboratory using the T-816 Welshbach ozonator. The species NO, when required, is obtained from bottles commercially available.

Velocity measurements were made using a DISA LDV modular system and the flow was seeded with silicon oil droplets 0.8 mm in mean diameter using a TSI 9306 atomizer. The data acquisition system consists of a PDP - 11/23 minicomputer having 128 KB of RAM with extended memory support. The computer is operated on RT-11 software using extended memory monitor. The system is equipped with a real time programmable clock, 4 channel A/D converter (12 bits), D/A converter and direct memory access. The peripherals include a dual density floppy disk drive, a 20MB Winchester disk drive and a magnetic tape unit with 800/1600 bpi/ 45ips capability. Since runs of 3 minutes with sampling at 50 kHz for 4 channels results in a memory overflow, data transmission to the disk is done simultaneously with data acquisition through buffer tables.

FLOW VISUALIZATION TECHNIQUE

Although NH_4Cl is known to form dense white fumes little effort has been directed in assessing different aspects of NH_3-HCl reaction and its applicability for flow-visualization. While the reaction is very rapid and mixing limited at room temperature, the actual smoke formation can be attributed only to condensation and growth of particles described by colloidal chemistry of NH_4Cl. The generation of solid particles of NH_4Cl can be written in terms of following equations:

$$NH_3 + HCl \xrightarrow{k} NH_4Cl \qquad , k=2\times10^{-17}\ cm^3/_s$$

$$(q+1)\ NH_4Cl\ (gas) \rightarrow (NH_4Cl)_{q+1} \qquad (solid)$$

The first reaction is a chemical phenomenon while the second reaction is a physical process involving homogenous nucleation and definite growth of NH_4Cl, possible when the particles have (q+1) or more monomers. Particles with q monomers are as likely to grow as to disintegrate, and particles with less than q monomers tend to go back to molecular form. The value of q has been cited as 7.5 by Heicklen (13). gravitational settling, wall-deposition and coagulation are unimportant in the condensation of NH_4Cl vapors.

The particle number density can be estimated from the rate law for nucleation given by Heicklen.

$$\frac{dN}{dt} = k_{nucl} [NH_3]^{8.5} [HCl]^{8.5}$$

$$k_{nucl} = 2 \times 10^{-229} \quad cm^{48}/s$$

The smoke generated by formation of NH_4Cl is then poly-dispersed, the particle size distribution being dependent on the extent of mixing and time. It is expected that if F(d) is the total number of particles per unit volume that are larger than a given diameter d and N(t) is the total number of particles at time t, then

$$F(d) = N(t)_e^{-Cd}$$

where C is weakly dependent on time, except for earliest reaction times. Estimates of particle size in the range 0.01 μm to 0.6 μm in the study reported seem reasonable. Furthermore, relaxation time for the largest NH_4Cl particles expected, i.e. 0.6 μm, is of the order of 1.7×10^{-6} s which implies that all the NH_4Cl particles can be expected to follow the flow faithfully.

The use of this reaction to observe coherent structures in shear flow proved valuable as can be seen from plates 1 to 4. They represent three sets of flow-visualization experiments. In the first one (a typical sequence shown in plate 1 & 2), the reacting species were seeded only at the edge of the splitter plate just before mixing so that only thin layers adjacent to either side of the splitter plate were seeded with reactants. The purpose of this was to study the motion of large structures (marked by dense white fumes of NH_4Cl) and transport of a chemically inert quantity, in this case, NH_4Cl, which is possible since reaction is essentially complete very soon after the edge of the splitter plate. In the second set of experiments on flow-visualization (plate 3) the reactants were introduced into the flow facility by passing compressed air over concentrated solutions of reactants in waters and injecting this in the two streams separately. Hence the two streams were uniformly seeded with reactants by the time the gases reached the test section. In the third set of experiments (plate 4), the reactants were introduced just before the two streams entered the test section at positions 1.25 cm above and 1.25 cm below the splitter plate. This permits observing the large structures after the mixing layer becomes larger than a certain width. A 16 mm movie camera was used to record this using typically 4x Kodak film.

NO - O_3 REACTION

It is intended to explore the effect of turbulence on chemical reaction and the mechanisms of mixing in plane shear flow by seeding the two streams with NO and O_3 respectively and monitoring the chemical reaction between the two species in the mixing layer. Air is unsuitable as carrier gas in this case since NO reacts with oxygen at room temperature at moderate rate. Also, presence of any moisture is undesirable since the product NO_2 combines with it immediately creating problems in the measurement of NO_2 concentration. A good choice then is high purity nitrogen commercially available in bottles.

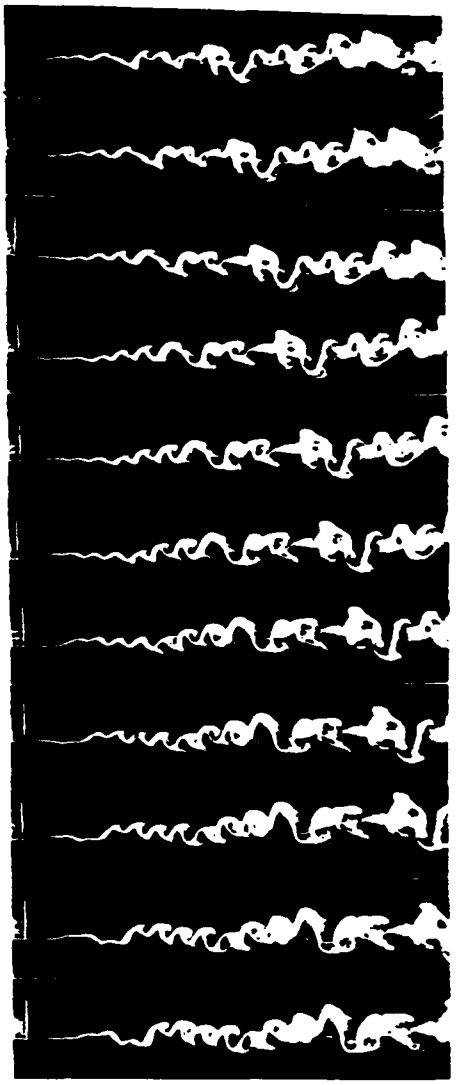

Plate 1: Growth of plane mixing layer. NH_4OH and HCl brushed on either side of splitter plate. $U_2/U_1 = 0.76$

This particular reaction,

$$NO + O_3 \rightarrow NO_2 + O_2 + h\nu$$

is chosen for several reasons. It is well-documented and its homegenous chemical kinetics is well-known; it is simple, second-ordered, fast (mixing limited) and irreversible at room temperature; for low concentrations the heat release effects are negligible; and most important, even at these low concentrations detection and measurements can readily be done using absorptions at 253.7 nm and 435.0 nm respectively. The absorption law

$$\ln \left(\frac{I}{I_o}\right) = \alpha_a [c] L, \text{ where}$$

Plate 2: Growth of plane mixing layer. NH_4OH and HCl brushed on either side of splitter plate. $U_2/U_1 = 0.57$

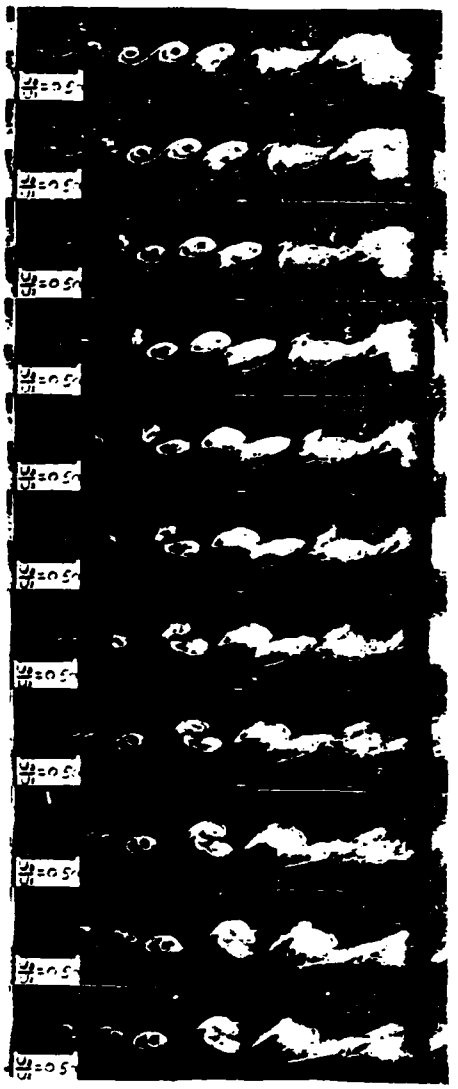

Plate 3: Growth of plane mixing layer. The two streams seeded uniformly with NH_4OH and HCl respectively prior to mixing. $U_2/U_1 = 0.50$

I, I_o - intensities of signal with and without, resp., absorbing species
$[c]$ - mean concentration of species along absorption path
L - path length of absorption
α_a - absorption constant

is exploited in monitoring the concentrations of the two species NO_2 and O_3 in the mixing layer. Table 1 lists the absorption coefficients of the species involved in the reaction. The corresponding signal-to-noise ratio for ozone concentration measurement is 85.

Table 1: Absorption Coefficients for Different Species in NO - O_3 Reaction $(cm^{-1}atm^{-1})$

λ \ Species	NO	O_3	NO_2	O_2	N_2
183.0 nm	40	0.5	0.1	0.1	≈0
253.7 nm	1	139	0.6	≈0	≈0
435.0 nm	≈0	≈0	0.6	≈0	≈0

With E being the output of the photodetector with no absorbing chemical species,

$$\frac{\Delta E}{E} = \alpha_a [c] L \quad ,$$

where ΔE is the attenuation in photodetector output due to absorption by the species. This linear relationship has been verified experimentally with species NO_2 and O_3 independently.

The actual concentration measurements are made with a specially designed fiber optics probe which is a refinement of the technique used by Brodkey (14) and Batt (15). The probe consists of two stainless steel tubes of 1mm outside diameter with 90° bends and separated by 1mm gap. These tubes carry very pure fused silica optical fibres 200um in diameter bundled in 1mm diameter extension cables. The fibre bundle is illuminated by a 100 W short-arc mercury vapor lamp and the signal at the output end is detected with EMI 9781B photomultipliers. A reference channel tracks any drift and fluctuations in the intensity of the lamp, which is important because the level of concentration signals being low, there is more stringent demand on accuracy of measurements. Fig. 1 shows a schematic of this arrangement.

This scheme, although intrusive, allows simultaneous instantaneous concentration measurements of O_3 and NO_2. Computation of microscale of the flow, based on information on plane mixing layer available in existing literature, reveal that probe dimensions are of the same order of magnitude as the Taylor microscale of the flow under investigation. Hence it is reasonable to expect good measurements of concentration fluctuations to be made in this flow. Together with the LDA this system provides a feasible means of making measurements of joint statistics of velocity and concentration in the mixing layer.

PREDICTED RESULTS

Using Monte Carlo method (12), calculations were performed for the turbulent mixing layer with high speed stream carrying NO and slow speed stream carrying O_3. The velocity field is first computed by solving boundary layer equations using finite difference method.

Since there are four species involved in the reaction, four equations for species transport can be written and because they are linearly dependent they can be replaced by just two equations - one for a conserved scalar f and other for a non-dimensional product concentration. A complete statistical description of the scalars in the flow is then provided by the joint pdf of f and c, $p(f, c; x, t)$, defined so that $p(f, c)\, df\, dc$ is the probability that f and c are in the ranges

$$\tilde{f} < f < \tilde{f} + d\tilde{f}$$

and $\tilde{c} < c < \tilde{c} + d\tilde{c}$, where $c = \dfrac{Z_{NO_2}}{(Z_{O_3})_2}$

For two dimensional boundary layer flows, the modelled joint pdf equation (16) is,

$$\langle u \rangle \frac{\partial p}{\partial x} + \langle v \rangle \frac{\partial p}{\partial y} = \frac{\partial}{\partial y} \tau_t \frac{\partial p}{\partial y} + \frac{\partial}{\partial c} \left[p \omega_c S^*(\tilde{f},\tilde{c}) + \omega_t E(\tilde{f},\tilde{c}) \right] \qquad (1)$$

In this equation $S = (Z_{O_3})_2 / (Z_{N_2})_2$,

S^* is given by

$$\frac{S}{(Z_{O_3})_2} = \beta \omega S^*$$

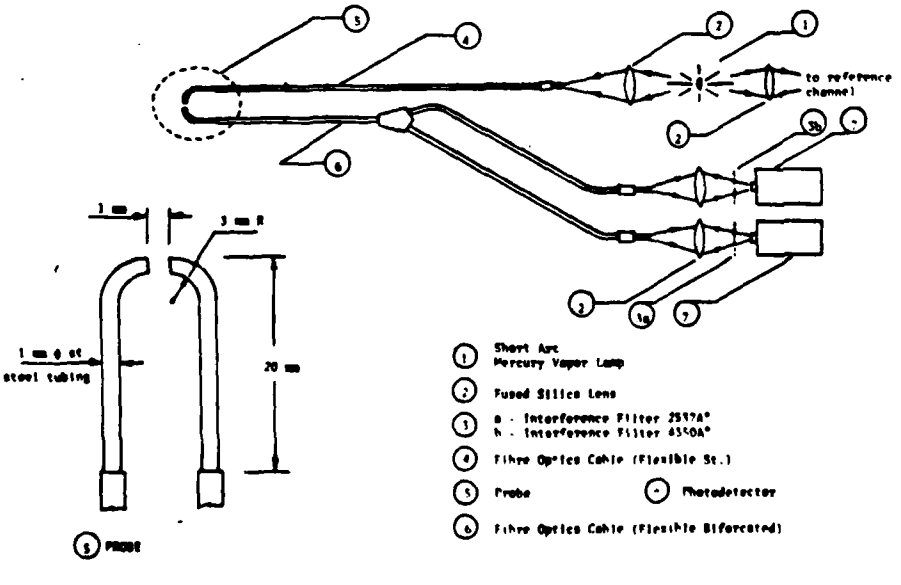

Fig. 1: Optical System (schematic) for monitoring concentrations of NO_2 and O_3

and

$$S^*(f,c) = (\alpha f - c)(1 - f - c),$$

S is the chemical reaction rate and ω is defined as

$$\omega = \frac{P k_f}{(RT)} \qquad k_f \text{ - rate constant}$$

Also,

$$\alpha = \frac{(Z_{NO})_1}{(Z_{O_3})_2} \qquad \text{subscripts 1 and 2 for fast and slow streams respectively}$$

Z_k for species k being defined

$$Z_k = \frac{m_k}{k}$$

where m_k and W_k are mass-fraction and molecular weight respectively for species k. τ_t is the turbulent diffusivity (gradient diffusion model is assumed), turbulent frequency ω_t represents rate of molecular mixing and E represents molecular mixing term which is modelled by Curl's model

$$E(\tilde{f}, \tilde{c}) = 4 \int\int p(\tilde{f}+f^*, \tilde{c}+c^*)p(\tilde{f}-f^*, \tilde{c}-c^*)\, df^*\, dc^* - p(\tilde{f}, \tilde{c})$$

The rest of the terms in eq (1) are exact.

The joint pdf equation can now be cast in dimensionless form by defining the following normalised parameters

$$x^* \equiv x\beta\omega/U_1$$

$$\Gamma \equiv y/\delta$$

$$\sigma \equiv x\left(\frac{d\delta}{dx}\right) = x\sigma$$

$$< U(x, y) > = U^*(\Gamma)\, U_1$$

$$< V(x, y) > = V^*(\Gamma)\, U_1$$

$$\tau_t(x, y) = \tau_t^*(\Gamma)\, U_1\delta$$

$$\omega_t(x, y) = \omega_t^*(\Gamma)\, \frac{\delta}{U_1}$$

and

$$p(\tilde{f}, \tilde{c}, x, y) = p^*(\tilde{f}, \tilde{c}, x^*, \Gamma)$$

The transformed pdf equation is:

$$x^*\sigma U^* \frac{\partial p^*}{\partial x^*} + (V^* - \Gamma\sigma U^*)\frac{\partial p^*}{\partial n} = \frac{\partial}{\partial n}\tau_t^*\frac{\partial p^*}{\partial n} + x^*\sigma\frac{\partial}{\partial \tilde{c}}(p^* S^*(\tilde{f}, \tilde{c})) + \omega_t^* E(\tilde{f}, \tilde{c}) \qquad (2)$$

As can be seen U_1, U_2, β and ω do not appear and U^*, V^*, τ_t^*, ω_t^* and σ are determined by the velocity ratio U_2/U_1 alone. The chemistry enters through the source term $S^*(\tilde{f}, \tilde{c})$ which depends on the conditions only through the concentration ratio α. Thus the solution to eq (2) depends only upon two dimensionless ratios U_2/U_1 and $\alpha\ (Z_{NO})_1 / (Z_{O_3})_2$

The absolute value of U_1 and β determine the scaling factor for downstream distance x,

$$x = \frac{x^* U_1}{(\beta\omega)}$$

The solution for this was obtained using Monte Carlo method for $0 \leq x^* \leq 900$ and for $\alpha = 2$ and $U_2/U_1 = 0.3$. The results are shown in Fig. 4 which will be discussed in details in the next section.

RESULTS AND DISCUSSION

From plates 1-4 it is clear that this novel technique for flow visualization can be very useful in understanding the nature of coherent structures. These pictures clearly underline once again the importance of conditioned sampling in shear layer measurements.

Growth rate and entrainment in the mixing layer are the main features that can be observed in these photographs. From the studies conducted it can be reaffirmed conclusively that pairing of large structures is essential for growth of mixing layer - plate 1 with $U_2/U_1 = 0.76$ showing no signs of pairing between coherent structures and very small rate of growth of mixing layer against plate 2 ($U_2/U_1 = 0.57$) showing a pairing sequence and a larger growth of mixing layer. The average size of coherent structures when plotted against distance downstream for three different velocity ratios (Fig. 2) is representative of dependence mixing layer growth rate on velocity ratio. Another characteristic that can be seen in Fig. 2 is the systematic decrease in growth rate of average size of coherent structures after certain distance downstream, in this case about 65 cm. This is probably because the effect of stretching in the mean flow direction is felt very little when the structures are small and much more at large distances downstream where size of these structures is large.

From plates 2 and 3 it can further be suggested that entrainment in the early part of the mixing layer has contributions from two mechanisms - the major one being the process of engulfing fluid in the surrounding stream and then making the ingested fluid turbulent within the vortex. Small contribution comes from the oscillating interface connecting two large structures where nibbling seems to occur. Also from plate 3, it seems as if the fluid from the fast stream is engulfed first and while it is being made

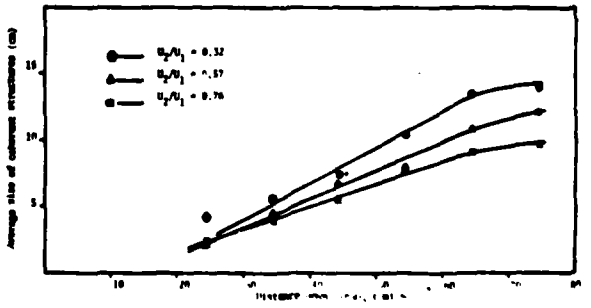

Fig. 2: Growth of size of coherent structures in plane mixing layer

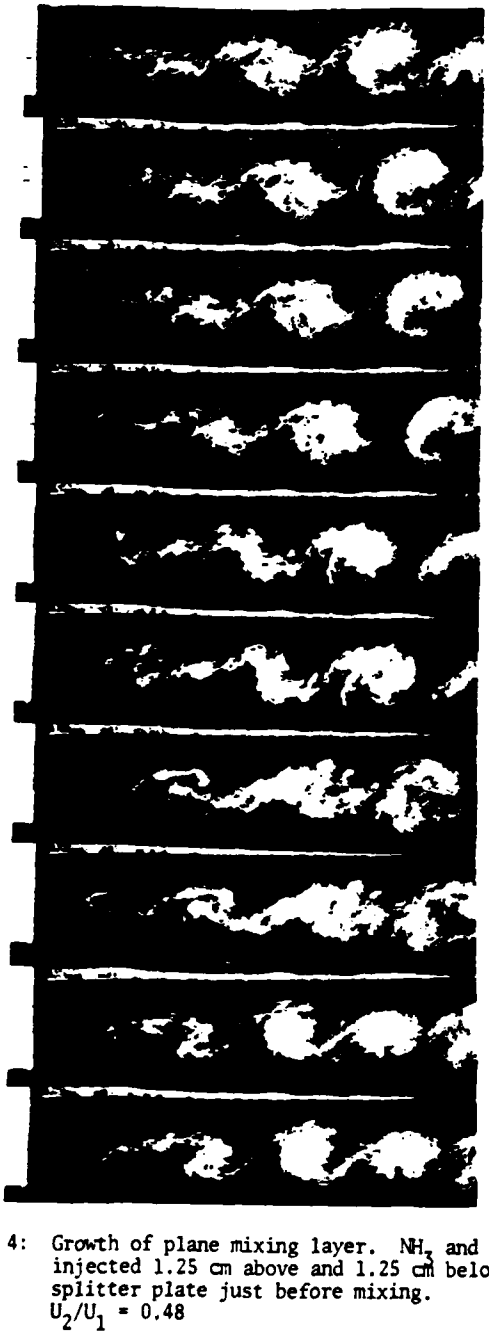

Plate 4: Growth of plane mixing layer. NH_3 and HCl injected 1.25 cm above and 1.25 cm below splitter plate just before mixing. $U_2/U_1 = 0.48$

turbulent the fluid from slow stream is surrounded next. The mixing between the two then is observable if reacting species are present in the two streams (as in plate 3). Nothing much can be said about Plate 4. The large structures appear more turbulent in this case because of the two wakes in the two streams caused by plates from where the flow was seeded.

Results of Monte Carlo calculations are shown in Fig. 4 to 7 with definition sketch shown in Fig. 3. Fig. 4 and 5 show calculated profiles of $\langle c(\eta, x^*)\rangle$ for $.1 \leq x^* \leq 900$. For $x^* > 100$ the profiles are

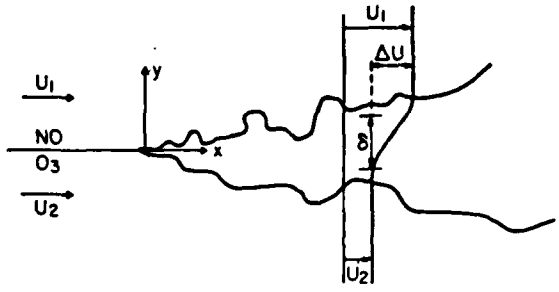

Fig. 3: Definition sketch

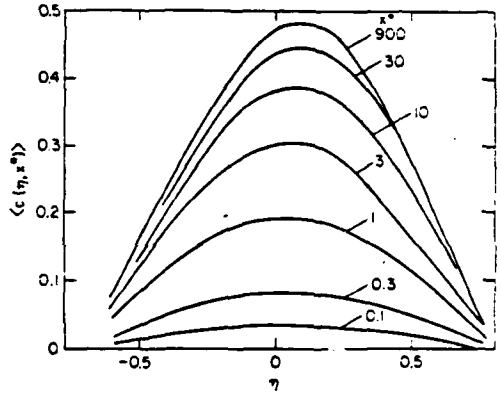

Fig. 4: Mean concentration (normalised) profiles $U_2/U_1 = 0.3$, $[C_{NO}]_1 / [C_{O_3}]_2 = 2$

virtually coincident indicating that chemical equilibrium prevails. Finite reaction rates seem important in the region $0.3 \leq x^* < 10$. It can also be seen that profiles for $\langle \tilde{c}(\eta, x^*)\rangle$ assuming no turbulent fluctuations are typically 20% higher. This is hardly surprising because this reaction being "fast" the probability of coexistence of reactants is very small and since reaction takes place because of contact at molecular level one could think of a reaction surface, the frequency of crossing across which directly determines rate of product formation. In this case of fast chemistry the correlation coefficient $\overline{[C_{O_3}]\,[C_{NO}]} / \overline{[C_{O_3}]}\,\overline{[C_{NO}]}$ is expected to be negative, and in a sense turbulence reduces the mean rate of chemical reaction (17).

Fig. 6 and 7 show profiles of $\langle f'^2\rangle$ and $\langle c'^2\rangle$ and the correlation coefficient

$$R_{cf} \equiv \langle f'c'\rangle \{\langle f'^2\rangle \langle c'^2\rangle\}^{-1/2}$$

at $x^*=3$ and $x^*=300$. The profile of $\langle f'^2\rangle$ which is

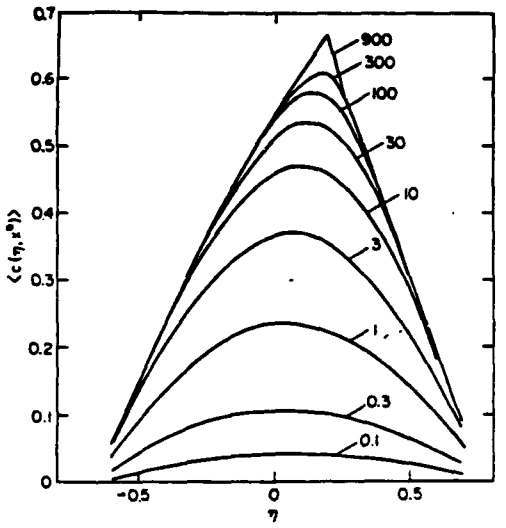

Fig. 5: Mean concentration (normalised) profiles assuming no turbulent fluctuations. $U_2/U_1 = 0.3$, $[C_{NO}]_1 / [C_{O_3}]_2 = 2$

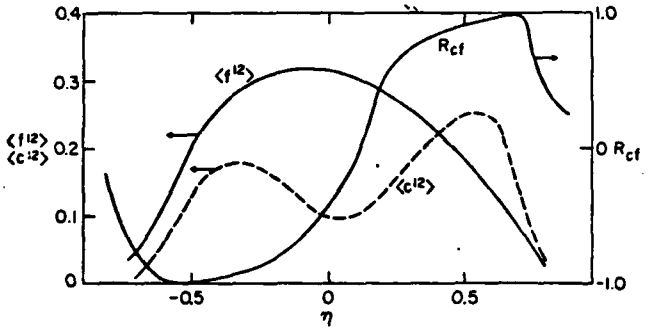

Fig. 6: Second Order moment $x^* = 3$

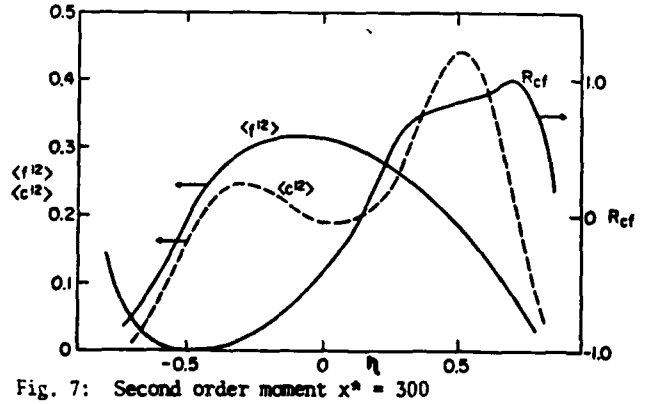

Fig. 7: Second order moment $x^* = 300$

independent of x^*, rises monotonically to its maximum and then decreases monotonically with increasing Γ. The profiles of $\langle c'^2 \rangle$ have two maxima; as expected the values of $\langle c'^2 \rangle$ increase between $x^* = 3$ and $x^* = 300$ and the shape also has changed little.

The correlation coefficient R_{cf} is virtually the same at $x^* = 3.0$ and $x^* = 300$ and the absolute values are surprisingly high on both edges of the mixing layer.

CONCLUSION

From this study the following conclusions can be drawn:

(1) A novel technique is developed for flow visualization in flows in which main stream is air or any colorless gas that does not interfere with NH_3 - HCl reaction.

(2) It is possible with the fibre optics probe and LDA to make simultaneous measurements of concentrations and velocity to obtain joint statistics of the two fields. This can then be compared with the results predicted by Monte Carlo method.

ACKNOWLEDGEMENT

The authors would like to thank the Department of Energy for its generous support under Contract No. DE-AC02-79ER10439.A002. Computations using Monte Carlo method were carried out by Prof. S. B. Pope.

REFERENCES

1. Browand, F. K. and Laufer, J., "The Roles of Large Scale Structure in the Initial Development of Circular Jets", The Proceedings of the 4th Biennial Symposium on Turbulence in Liquids, September 1975, Univ. of Missouri, Rolla, p. 333

2. Brown, G.L. and Roshko, A., "On Density Effects and Large Structures in Turbulent Mixing Layers", J. Fluid Mech., 1974, 64, p. 775.

3. Dimotakis, P.E. and Brown, G.L., "The Mixing Layer at High Reynolds Number: Large-structure Dynamics and Entrainment", J.Fluid Mech., 1976, 78, pp. 535-560.

4. Shea, J., "A Chemical Reaction in a Turbulent Jet", J. Fluid Mech., 1977, 81, p. 317.

5. Konrad, J.H., "An Experimental Investigation of Mixing in Two-dimensional Turbulent Shear Flows with Applications to Diffusion-limited Chemical Reactions", Project SQUID, 1976, Technical Report CIT-8-PV.

6. Toor, H.L., "Mass Transfer in Dilute Turbulent and Non-turbulent systems with Rapid Irreversible Reactions and Equal Diffusivities", A.I.Ch.E. Journal, 1962, 8, 70

7. O'Brien, E.E., "Turbulent Mixing of Two Rapidly Reacting Chemical Species", Physics of Fluids, 1971, 14, 7.

8. Bilger, R.W., "The Structure of Diffusion Flames", Combustion Sci. and Tech., 1976, 13, p. 155.

9. Dopazo, C., Ph.D. Thesis, 1973, State University of New York at Stony Brook.

10. Libby, P.A., "On The Prediction of Intermittent Turbulent Flows", J. Fluid Mech., 1975, 68, pp. 273-296.

11. Dopazo, C., "Relaxation of Initial Probability Density Functions in the Turbulent Convection of Scalar Fields", Workshop on Probability Density Function Method for Turbulent Flows, Aachen, September 1977.

12. Pope, S.B., "A Monte Carlo Method for the PDF Equations of Turbulent Flow", MIT-EL 80-012, 1980

13. Heicklen, J., "Colloid Formation and Growth", Academic Press, 1976, New York.

14. Lee, J. and Brodkey, R.S., "Light Probe for the Measurement of Turbulent Concentration Fluctuations", Rev. Sci. Instruments, 1963, 34, pp. 1086-1090.

15. Batt, R.G., "Turbulent Mixing of Passive and Chemically Reacting Species in a Low-speed Shear Layer", J.Fluid Mech., 1977, 82, p. 60.

16. Pope, S.B., "The Statistical Theory of Turbulent Flames", Trans of the Royal Soc. of London, 1979, 291, pp. 553-557.

17. Libby, P.A. and Williams, F.A., "Turbulent Reacting Flows", 44, Springer-Verlag, 1980.

STUDY OF A TURBULENT DIFFUSION FLAME IN A CHANNEL FLOW

J.M. MOST, Mlle N. HARIVEL, P. JOULAIN, B. SZTAL

Groupe de Recherches de Chimie Physique de la Combustion
E.R.A. n° 160 au C.N.R.S. - Université de Poitiers
Domaine du Deffend - 86800 MIGNALOUX-BEAUVOIR - FRANCE

ABSTRACT

To characterize the behaviour of a turbulent diffusion flame above a solid surface in a channel flow we designed and built an experimental device. The self-sustained diffusion flame was obtained by injecting through a porous wall a gaseous fuel into a mainstream of air. Velocity, temperature and turbulence profiles were obtained by laser doppler velocimetry and compensated thermocouples measurements. We developed a q-ε-g turbulence model and a probabilistic combustion model. Agreement between theory and experiment is particularly good for temperature and velocity mean values. The velocity overshoot is well predicted, though at the present stage the model can't explain all the phenomena experimentally observed (low frequency oscillations, ...).

INTRODUCTION

For several years we have been involved in our laboratory with the study of gas-solid combustion ; our interest being phenomena occuring during fire propagation and inside solid rocket chambers, mainly relationships between burning rates and parameters characterizing heat, mass and momentum transfer.

The model we considered is a reacting gas flowing over a slab of solid material which behaves as a reacting surface. The experimental study showed (1, 2) : the dependence of combustion rates, fluxes at the wall on fluid dynamics and thermodynamic properties ; and the influence of combustion and blowing of gasified solid on the turbulent boundary layer.

In gas-solid combustion the experiment duration is always too short (only a few seconds) to characterize the behaviour of the turbulent diffusion flame above the solid surface. Therefore to study these self-sustained diffusion flames, we designed and built an experimental apparatus to simulate partly these phenomena. The diffusion flames were obtained by injecting through a porous wall a gaseous fuel ($\dot{m}$) into the turbulent main stream of air (G_∞) for different ratio $F = \dot{m}/G$ equal to those observed with gas-solid systems.

EXPERIMENTAL METHOD

The experiments have been carried out using the apparatus described on Fig. 1 which includes :

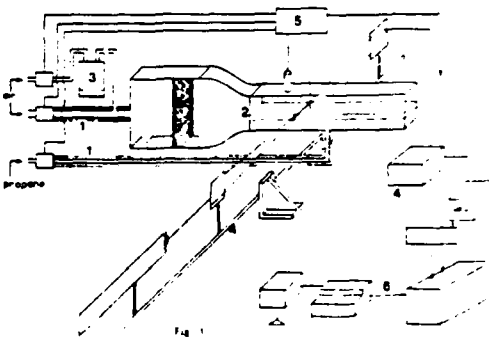

1. A gas feeding installation (insulated and preheated connecting pipes, flow meters, ...).
2. A square duct combustion chamber : 0.03 m x 0.03 m cross section and 0.4 m long. The fuel was injected through a sintered stainless steel porous wall of dimensions 0.03 m x 0.3 m.
3. A fluidized bed aerosol generator to disperse solid powders (1 μ zirconium oxide) for flow seeding.

4. A LDV system (He-Ne 15 mW laser, optics with Bragg cell, photomultiplier, counter, spectrum analyser, oscilloscope, ...).

5. Compensated thermocouples and Pitot tubes.

6. Data acquisition and processing (minicomputer, interfaces and peripherals, ...).

All the experiments were driven by the minicomputer in order to obtain more reliable and accurate measurements.

Data processing was done taking a relatively large sample of values (N). We obtained the mean velocity u, and its turbulent fluctuation $\overline{k}$ considered equal to 1/2 u'^2 :

$$\overline{u} = 1/N \cdot \sum_{1}^{N} u_i, \quad \overline{k} = 1/2\ \overline{u'^2} = 1/2\ N \cdot \sum_{1}^{N} (\overline{u} - u_i)^2$$

To obtain a random probability density function or "pdf", we plotted the number of informations i($\Sigma i = N$) data processing as a function of $(u-\overline{u})/(\overline{u'^2})^{1/2}$ for different coordinates x and y. The same procedure was used for temperature obtained by means of fine (25 and 50 μ diameters Pt - Pt/10 % Rh and chromel-alumel wires) thermocouples, giving as before $\overline{T}$, $\overline{T'^2}$ and the "pdf". Temperature fluctuations were obtained by means of analogue compensated thermocouples. Radiation losses were measured and taken into account.

THEORETICAL STUDY

. Turbulence model. The flows considered include low Reynolds number pipe flow with wall injection. The model of turbulence employed is one where the turbulence energy q and its dissipation rate ε are calculated by way of transport equations which are solved simultaneously with the conservation equations for the mean flow. The closure of Reynolds stress and dissipation rates equations have been made considering the direct influence of viscosity and transport processes (3). The hydrodynamic predictions have been obtained from the resolution of the following system of differential and auxiliary equations.

Streamwise momentum :

$$\rho u \frac{\partial u}{\partial x} + \rho v \frac{\partial u}{\partial y} = \frac{\partial}{\partial y} \left(\mu \frac{\partial u}{\partial y} - \rho \overline{u'v'}\right) - \frac{dP}{dx} \qquad [1]$$

Turbulent viscosity hypothesis :

$$-\rho \overline{u'v'} = \mu_T \frac{\partial u}{\partial y} = C_\mu \frac{\rho q^2}{\tilde{\varepsilon}} \frac{\partial u}{\partial y} \qquad [2]$$

where : $C_\mu = 0.09$ [3]

$$\tilde{\varepsilon} = \varepsilon - (2\mu/\rho)(\partial q^{1/2}/\partial y)^2 \qquad [4]$$

Turbulence energy :

$$\rho u \frac{\partial q}{\partial x} + \rho v \frac{\partial q}{\partial y} = \frac{\partial}{\partial y} \left[(\mu + \mu_T) \frac{\partial q}{\partial y}\right] + \mu_T \left(\frac{\partial u}{\partial y}\right)^2 - \rho \tilde{\varepsilon} - 2\mu \left(\frac{\partial q^{1/2}}{\partial y}\right)^2 \qquad [5]$$

Turbulence dissipation rate :

$$\rho u \frac{\partial \tilde{\varepsilon}}{\partial x} + \rho v \frac{\partial \tilde{\varepsilon}}{\partial y} = \frac{\partial}{\partial y} \left[(\mu + \frac{\mu_T}{1.3}) \frac{\partial \tilde{\varepsilon}}{\partial y}\right] + 1.44 \frac{\tilde{\varepsilon}}{q} \mu_T \left(\frac{\partial u}{\partial y}\right)^2 - 1.92\ \rho \frac{\tilde{\varepsilon}^2}{q} + \frac{2\mu\mu_T}{\rho} \left(\frac{\partial^2 u}{\partial y^2}\right)^2 \qquad [6]$$

q and $\tilde{\varepsilon}$ are equal to zero at the wall.

. Chemical reaction model. It's a fast chemistry model. The Shvab-Zeldovich formulation together with a linear combination of the equations describing the conservation of species yield an equation which has no source term. The dependent variable, the mixture fraction φ, of the resultant equation is defined as :

$$\phi = \frac{(\nu m_{fu} - m_{ox}) + m_{ox,\infty}}{\nu m_{fu,s} + m_{ox,\infty}} \qquad [7]$$

using the Boussinesq assumption :

$$-\rho \overline{u'\phi'} = \mu_T \partial\phi/\partial y \qquad [8]$$

The differential equation for φ can be written as follows :

$$\rho u \frac{\partial \phi}{\partial x} + \rho v \frac{\partial \phi}{\partial y} = \frac{\partial}{\partial y} \left[(\mu + \frac{\mu_T}{0.7}) \frac{\partial \phi}{\partial y}\right] \qquad [9]$$

Then, the assumption of instantaneous chemical equilibrium gives :

$$0 \leq \phi \leq \phi_{st} \quad m_{fu} = 0 \quad m_{ox} = m_{ox,\infty} [1 - \phi/\phi_{st}] \qquad [10]$$

$$\phi_{st} \leq \phi \leq 1 \quad m_{fu} = m_{fu,s} \left[\frac{\phi - \phi_{st}}{1 - \phi_{st}}\right] \quad m_{ox} = 0$$

$$\phi_{st} = m_{ox,\infty}/(\nu m_{fu,s} + m_{ox,\infty}) \qquad [11]$$

$$m_{in} = m_{in,\infty} + \phi(m_{in,s} - m_{in,\infty}) ; \qquad [12]$$

$$m_{pr} = 1 - m_{ox} - m_{fu} - m_{in}$$

. Thermodynamic model. The enthalpy h is defined as :

$$h - h_{ref} = m_{fu} h_c + \int_{T_{ref}}^{T} C_{p_{min}} dT \qquad [13]$$

where $C_{p_{min}} = \Sigma\, m_j C_{p_j}$ and h_c is the heat of combustion per kg of fuel.

Assuming equal turbulent exchange coefficients for diffusion of species and heat, the specific enthalpy is simply obtained from :

$$h = h_s \phi + (1 - \phi) h_\infty \qquad [14]$$

without the need to solve its balance equation. The temperature is obtained from the above enthalpy definition and the density via the perfect gas law.

. Combustion model. SPALDING (4) was the first to assume that the root mean square fluctuating concentration obeys a parabolic differential equation including convection, diffusion, generation and dissipation terms. BRAY and MOSS (5) presented a unified statistical analysis of the premixed turbulent flame supported by a single step global reaction. LOCKWOOD and NAGUIB (6) adapted this method to the prediction of free round turbulent jet diffusion flames. They proposed the following balance equation for $g = (\phi - \bar{\phi})^2$.

$$\rho u \frac{\partial g}{\partial x} + \rho v \frac{\partial g}{\partial y} = \frac{\partial}{\partial y}\left(\frac{\mu_T}{\sigma_{g,eff}} \frac{\partial g}{\partial y}\right)$$

$$+ 2.8\, \mu_T \left(\frac{\partial \bar{\phi}}{\partial y}\right)^2 - 1.82\, \rho\, \varepsilon\, \frac{g}{q} \qquad [15]$$

In the range $0 < \phi < 1$, the probability distribution function is assumed to obey a normal distribution. TAMANINI (7) used a "pdf" generated by the combination of two parabolae. BORGHI and MOREAU (8) for premixed flame, approximated a gaussian-like profile bounded by two Dirac delta functions ; the gaussian profile is approximated by a rectangle ; the delta functions appear for the value $\phi = 0$ and $\phi = 1$. CHAMPION (9) made the same assumption to study a two dimensional probability function. In this work $P(\phi)$ is defined by the rectangular approximation as shown on Fig. 2.

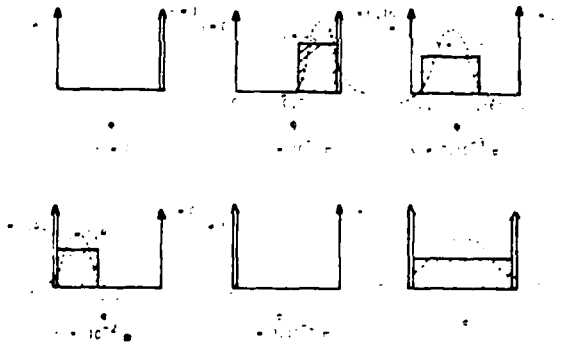

Fig. 2

In the range $\delta < \phi < \eta$ the mixture fraction fluctuation is assumed constant. The unwanted parts of the distribution for $\phi < 0$ and $\phi > 1$ are lumped into Dirac delta function of $\phi = 0$ and $\phi = 1$. The "pdf" may be expressed as :

$$P\langle\phi\rangle = \alpha\, \delta(0) + \beta\, \delta(1) + \gamma[u\langle\phi - \delta\rangle - u\langle\phi - \eta\rangle] \qquad [16]$$

where $u\langle\phi - \delta\rangle$ is the HEAVISIDE function so that the expression $[u\langle\phi - \delta\rangle - u\langle\phi - \eta\rangle]$ has the value 1 in the range $\delta < \phi < \eta$ and zero elsewhere. These characteristic parameters α, β, γ, δ, η are computed from the mean value of ϕ ($\bar{\phi}$ is simply the first moment of the "pdf" about $\phi = 0$) and of g the second moment about $\phi = \bar{\phi}$. The mean mass fraction $\bar{m}_j$, temperature $\bar{T}$, density $\bar{\rho}$ are computed by an analytical integration of the following linear equations.

$$\bar{m}_j = \alpha\, m_{j,\infty} + \beta\, m_{j,s} + \int_{\delta}^{\eta} \gamma\, m_j\, d\phi \qquad [17]$$

$$\bar{T} = \alpha\, T_{\infty} + \beta\, T_s + \int_{\delta}^{\eta} \gamma T\, d\phi \qquad [18]$$

$$\bar{\rho} = \alpha\, \rho_{\infty} + \beta\, \rho_s + \int_{\delta}^{\eta} \gamma \rho\, d\phi \qquad [19]$$

RESULTS

Under appropriate conditions (limited by flame blow-off) of uniform air mass flow rate G_{∞} and of fuel mass flow injection rate $\dot{m}$, a stable turbulent two dimensional diffusion flame was established in the boundary layer over the porous plate.

Without combustion, Fig. 3, the agreement between theoretical and experimental results for $\bar{u}$ and q is quite good and the influence of blowing is consistent with previous work. Then, the turbulence model used seems particularly well adapted.

With combustion, Fig. 4 and 5, a marked feature of the mean velocity profile is the appearance of a velocity overshoot that exceeds the stream mean velocity as for laminar flow. This overshoot can be directly related to the enhancement by combustion of the source term of the momentum equation : $\frac{1}{\rho u}\frac{dP}{dx}$. Starting from the porous wall, q decreases for same distance and then increases drastically up to a certain location which could be assumed to be just above the flame "position". The location of this minimum and maximum of q and the flame stand-off distance increase with $\dot{m}$. The turbulence intensity behaves in a same but less marked way. Far above the flame we have a dissipation of q and of turbulence intensity to their value at the center line. For temperature, the profiles are very similar to those obtained for velocity at the same location. A minimum of $\bar{T}'^2$ corresponds to a maximum of $\bar{T}$ which may correspond to the flame zone. There is a good agreement between theory and experiment for $\bar{u}$ and $\bar{T}$. For q, the agreement is only good below the flame. We can predict the decreasing but not the peak value just above the flame. The discrepancy could be related probably to the experimentally observed low frequency oscillations or to non-stationary boundary conditions.

Fig. 6 shows for a given x location the variation across the boundary layer of the probability density function of fluctuating velocity. Increasing y we observed for both u and T different shapes for the "pdf" : in the flame and below the "pdf" has only one peak, some distance above where $\bar{u}'^2$ and $\bar{T}'^2$ are maximum the "pdf" has two peaks, and further away only one peak appears. The temperature spectrum analysis showed a low frequency sequence (a few Hz) of hot and cold "peaks". The amplitude of these oscillations is minimum in the flame zone and maximum where $\bar{u}'^2$ and $\bar{T}'^2$ are maximum.

On Fig. 7 we plotted the $\bar{u}$ and $\bar{T}$ profiles for three x locations in the flow direction. The maximum

mean velocity increases with x but $\overline{T}_{max}$ seems nearly constant. The presumed flame stand-off distance increases also slightly with x.

The theoretical model can fit relatively well the experimental data obtained for $\overline{u}$ and $\overline{T}$ with and without combustion but can't explain, at the present stage, all the phenomena experimentally observed (low frequency flame oscillations, peak value for q above the flame, discrepancy between theory and experiment for q and turbulence intensity in the core, ...). Meanwhile, as this model can predict the phenomena below the flame it can be used to characterize gas solid turbulent combustion, to obtain the heat flux at the wall and then the mass burning rate.

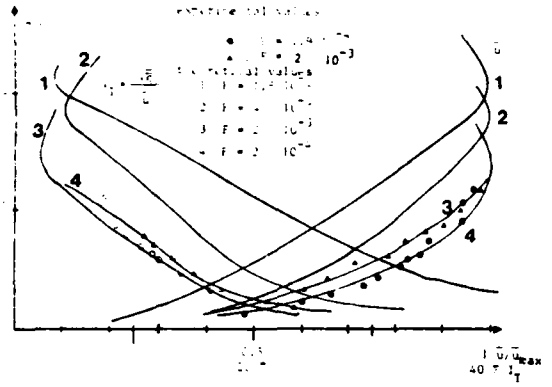

Fig. 3 : Without combustion : the velocity gradient and I_T increase with $\dot{m}$.

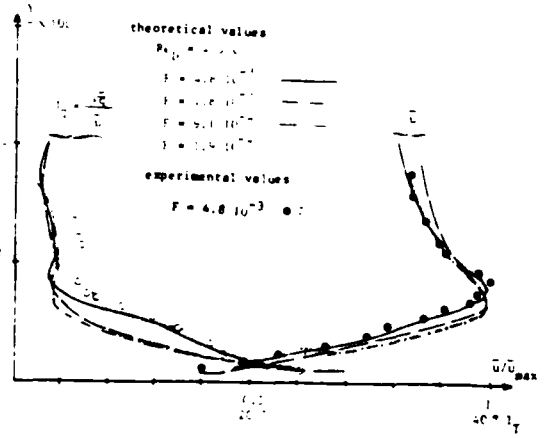

Fig. 4 : For a given F, the shape of the velocity profiles is less dependent on $\dot{m}$ with combustion than without.

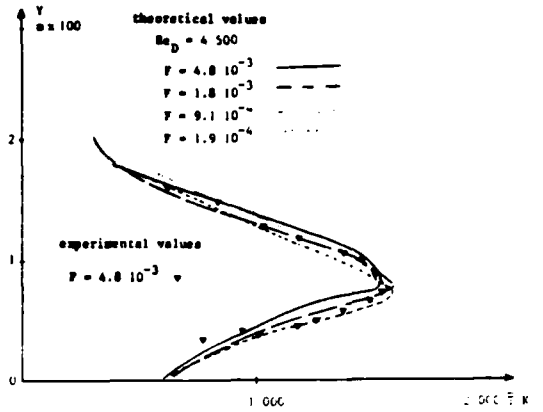

Fig. 5 : The flame "stand-off distance" increases slightly with $\dot{m}$.

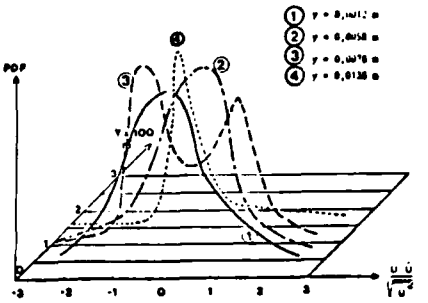

Fig. 6 : Probability density function of fluctuating velocity.

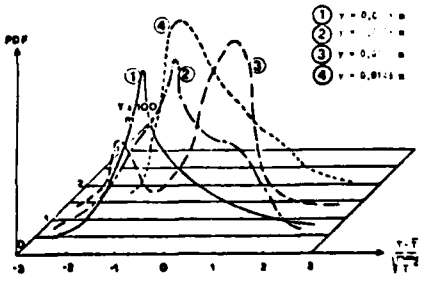

Fig. 6 bis : Probability density function of fluctuating temperature.

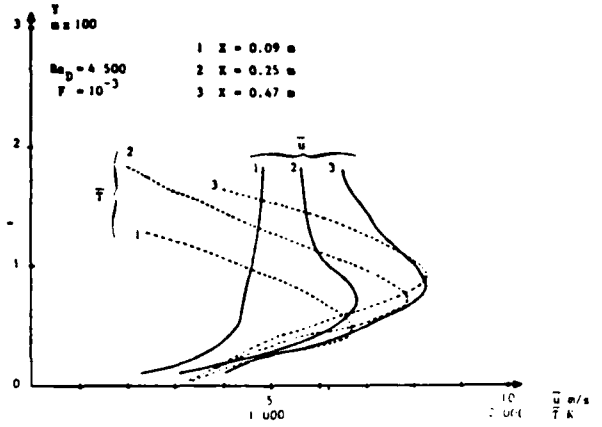

Fig. 7 : Theoretical velocity overshoot, maximum mean temperature and flame "stand-off distance" increase with x.

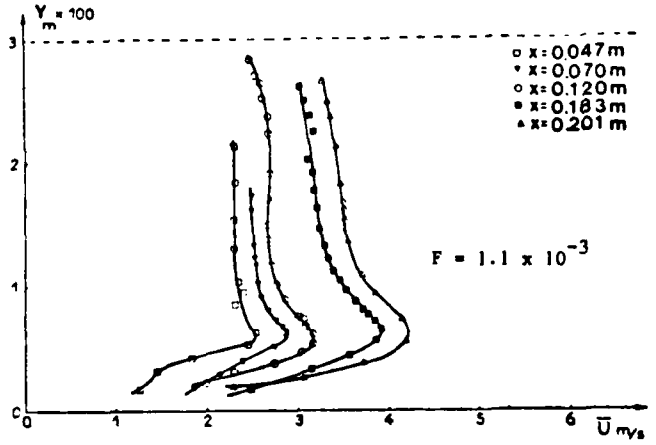

Fig. 7 bis : Experimental mean velocity profiles : influence of x.

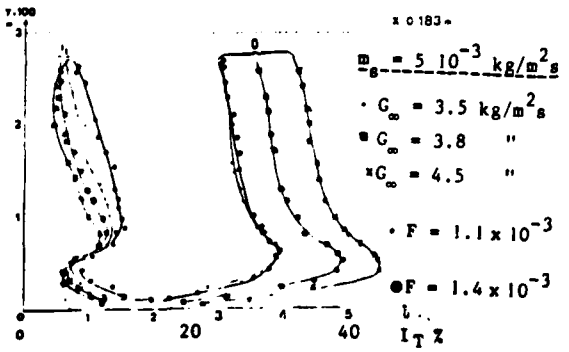

Fig. 8 : Experimental profiles : influence of G and F.

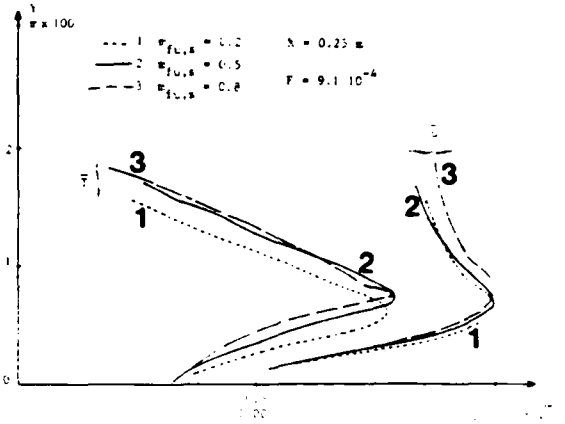

Fig. 9 : Influence of fuel mass fraction on mean velocity and temperature profiles (wall fuel mass fraction fluctuation may explain flame position and velocity overshoot oscillations).

ACKNOWLEDGMENTS

Research was supported by CNRS under ATP n° 2915 and 3984. We also wish to acknowledge MM. BIGEAU and DUPUY who assisted in the design of the experimental apparatus and Professor BERNARD director of the laboratory for providing us all the facilities.

REFERENCES

/1/ JOULAIN P., MOST J.M., FUSEAU Y., SZTAL B., Acta Astronautica, Vol. 5, 1978, pp. 1079-1093.

/2/ JOULAIN P., MOST J.M., FUSEAU Y., SZTAL B., 17th Symposium (International) on Combustion, The Combustion Institute, Pittsburgh, 1979, pp. 1041-1051.

/3/ LAUNDER B.E., "Turbulence transport models for numerical computation of fluid flow" ME-213, winter 1980, University of California, Davis, Cal.

/4/ SPALDING D.B., Chemical Engineering Science, Vol. 26, 1971, pp. 95-107.

/5/ BRAY K.N.C., MOSS J.B., Acta Astronautica, Vol. 4, 1977, pp. 291-319.

/6/ LOCKWOOD F.C., NAGUIB A.S., Combustion and Flame, Vol. 24, 1975, pp. 109-124.

/7/ TAMANINI F., 17th Symposium (International) on Combustion, The Combustion Institute, Pittsburgh, 1979, pp. 1075-1085.

/8/ BORGHI R., MOREAU P., Acta Astronautica, Vol. 4, 1977, pp. 321-341.

/9/ CHAMPION M., Combustion Science and Technology, Vol. 24, 1980, pp. 23-34.

Computation and its Comparison with Experiments of Time-Mean and Fluctuating Properties in Round Jets with and without Flame

Toshimi Takagi and Satoru Kotoh

Faculty of Engineering, Osaka University
Suita, Osaka, 565 Japan

ABSTRACT

Numerical predictions are compared with experimental results of flow velocity, gas temperature, species concentration together with the fluctuation properties such as kinetic energy of turbulence and correlation of velocity and temperature fluctuations in turbulent jets with and without flame. It indicates the validity of the two-equation k-ε turbulence model with a modification for the low Reynolds number effects due to the existence of flame in the lower fuel jet velocity. Effects of the density fluctuation are discussed to imply that neglecting the density fluctuation gives a fairly good approximation for the prediction of the present flow and combustion characteristics.

INTRODUCTION

The numerical prediction of the flow and combustion characteristics in turbulent diffusion flames is one of the subjects of current interest. There have been analytical studies [1],[2] for developing the prediction procedure for turbulent diffusion flames along with the experimental studies [3].

The validity of the prediction procedure must be verified by the comparisons with the experiments because the prediction procedure includes semi-empirical turbulence model and reaction model in turbulent flow fields. The comparisons are desired of the fluctuating properties as well as the time-mean properties because they are directly concerned with the turbulence model.

The experimental data used for the comparison with present calculation are based on the measurements of our own which are planed to include time-mean axial flow velocity, temperature, species concentrations and statistical properties of fluctuations such as kinetic energy of turbulence and correlation of velocity and temperature fluctuation in turbulent jets with and without flame.

Experimental results are compared with the calculated ones which are based on the two-equation k-ε turbulence model paying special attention to the fluctuating properties. Effects of the viscosity increase and the density fluctuation due to the existence of the flame are also discussed.

EXPERIMENTS

The experimental data used for the comparison with calculations are based on the measurements in the turbulent fuel jets with and without flame issuing vertically upward from a round tube nozzle of 4.9 mm inner diameter. The fuel of the nozzle fluid is the mixture of hydrogen and nitrogen whose volume ratio is 0.68 : 1. The average velocity U_j of the fuel jet at the nozzle exit is selected to be 20.4 and 55.7 m/s which is surrounded by coaxial air stream of uniform velocity of 5.1 m/s.

The experimental data include time-mean flow velocity, temperature and species concentrations with statistical properties of fluctuations such as turbulence intensity in axial, radial and circumferential directions, correlation of velocity fluctuation in axial and radial direction $\overline{uv}$, correlation of radial flow velocity and temperature fluctuation $\overline{vT}$ and length scale derived from the velocity or temperature fluctuation.

Time-mean and fluctuating velocity were detected by a laser Doppler velocimeter equipped with a Bragg cell for a frequency shift and a frequency tracker. The fluctuating temperature were measured by a thermocouple (25.4 μm in diameter) compensated electrically for the time lag due to the heat capacity. The gas species concentrations were analyzed by a gas chromatograph after gas sampling by a water-cooled sampling probe.

The details of the experiments are in [4],[5].

ANALYTICAL PROCEDURE

The calculations are based on the time-averaged boundary-layer-type conservation equations of mass, momentum, energy and chemical species in axisymmetric coordinate system.

$$\frac{\partial}{\partial x}(r\rho U) + \frac{\partial}{\partial r}(r\rho V) = 0 \tag{1}$$

$$\rho(U\frac{\partial U}{\partial x} + V\frac{\partial U}{\partial r}) = -\frac{\partial p}{\partial x} + \frac{1}{r}\frac{\partial}{\partial r}(r\mu_{eff}\frac{\partial U}{\partial r}) - \rho g \tag{2}$$

$$\rho(U\frac{\partial h}{\partial x} + V\frac{\partial h}{\partial r}) = \frac{1}{r}\frac{\partial}{\partial r}(r\frac{\mu_{eff}}{\sigma_h}\frac{\partial h}{\partial r}) \tag{3}$$

$$\rho(U\frac{\partial m_j}{\partial x} + V\frac{\partial m_j}{\partial r}) = \frac{1}{r}\frac{\partial}{\partial r}(r\frac{\mu_{eff}}{\sigma_m}\frac{\partial m_j}{\partial r}) + R_j \tag{4}$$

where x or r = axial or radial coordinate, U or V = velocity in axial or radial direction, h = enthalpy, m_j = mass fraction of j species, μ_{eff} = effective viscosity (= laminar viscosity μ_l plus turbulent viscosity μ_t), ρ = density, R_j = reaction rate of j species, σ_h or σ_m = turbulent Prandtl or Schmidt number.

In order to evaluate the turbulent viscosity, k-ε turbulence model is applied. Kinetic energy of turbulence k and its dissipation rate ε are calculated from the following transport equations [6].

$$\rho(U\frac{\partial k}{\partial x} + V\frac{\partial k}{\partial r}) = \frac{1}{r}\frac{\partial}{\partial r}(r\frac{\mu_{eff}}{\sigma_k}\frac{\partial k}{\partial r}) + \mu_t(\frac{\partial U}{\partial r})^2 - \rho\varepsilon \tag{5}$$

$$\rho(U\frac{\partial \varepsilon}{\partial x} + V\frac{\partial \varepsilon}{\partial r}) = \frac{1}{r}\frac{\partial}{\partial r}(r\frac{\mu_{eff}}{\sigma_\varepsilon}\frac{\partial \varepsilon}{\partial r}) + \frac{\varepsilon}{k}\{C_1\mu_t(\frac{\partial U}{\partial r})^2 - C_2\rho\varepsilon\} \tag{6}$$

where C_1, C_2, σ_k and σ_ε are empirical constants. The turbulent viscosity is evaluated by the expression,

$$\mu_t = C_D \cdot f_1 \cdot \rho k^2/\varepsilon \tag{7}$$

$$f_1 = \{1 - \exp(-R_T/A)\}^2 \tag{8}$$

where, $R_T = \rho k^2/\varepsilon\mu_l$ which is a kind of local turbulence Reynolds number, C_D and A = empirical constants. The factor f_1 is introduced in the present calculation to modify the Prandtl-Kolmogorov expression of $\mu_t = \rho C_D \cdot k^2/\varepsilon$ for low Reynolds number (not fully turbulent) flow. The existence of flame results in the significant increase of the kinetic viscosity due to the temperature rise and induces local laminarization [7] especially in low fuel jet velocity. These low Reynolds number effect is taken into consideration by the empirical factor f_1. The expression of f_1 in terms of R_T (= $(\mu_t/\mu_l)/C_D$) and the constant A (=30) is selected so that f_1 tends to unity and eq.(7) is equivalent to the standard Prandtl-Kolmogorov expression for high Reynolds number flow ($\mu_t/\mu_l \gg 1$). The empirical constants in eqs.(3)-(7) are selected to be as follows. C_D = 0.09, C_1 = 1.45, C_2 = 1.95, $\sigma_m = \sigma_h$ = 0.7, σ_k = 1.0, σ_ε =1.3. They are selected referring to [6],[8] and as for C_2, taking into consideration the optimization for the fit of the prediction with the present experiments.

The gas species considered are the main species of reactants and products of N_2, H_2, H_2O and O_2. The one-stage reaction of $H_2 + O_2/2 = H_2O$ is considered. Four species conservation eqs. (4) are converted into the following two differential equations and three algebraic equations based on the stoichiometry of the reaction and the assumption that effective Schmidt number is the same for all species.

$$\rho(U\frac{\partial f}{\partial x} + V\frac{\partial f}{\partial r}) = \frac{1}{r}\frac{\partial}{\partial r}(r\frac{\mu_{eff}}{\sigma_m}\frac{\partial f}{\partial r}) \tag{9}$$

$$\rho(U\frac{\partial m_{H_2}}{\partial x} + V\frac{\partial m_{H_2}}{\partial r}) = \frac{1}{r}\frac{\partial}{\partial r}(r\frac{\mu_{eff}}{\sigma_m}\frac{\partial m_{H_2}}{\partial r}) + R_{H_2} \tag{10}$$

$$m_{O_2} = 8\, m_{H_2} + [m_{O_2}]_O - f(8[m_{H_2}]_F + [m_{O_2}]_O) \tag{11}$$

$$m_{H_2O} = 9f[m_{H_2}]_F - 9m_{H_2} \tag{12}$$

$$m_{N_2} = 1 - m_{H_2} - m_{O_2} - m_{H_2O} \tag{13}$$

f is the so-called mixture fraction which means the mass fraction of the nozzle fluid. Suffix of F or O means the value at the nozzle fluid or surrounding air, respectively. Reaction rate R_{H_2} in eq.(10) is evaluated by the eddy dissipation model [9] which postulates that reaction rate is proportional to the turbulent eddy dissipation rate. Calculations were also tried in the case of the infinite reaction rate which leads to the flame sheet model.

Gas temperature is calculated by the relation,

$$h = \sum_j m_j \int_{T_0}^{T} C_{pj}\, dT + \sum_j m_j H_{0j} \tag{14}$$

where T_0 = reference temperature, C_{pj} = constant pressure specific heat of j species, H_{0j} = standard heat of formation.

Density is evaluated from the ideal gas law.

The above differential equations are solved numerically using a finite difference method based on the procedure developed by Patankar and Spalding [10]. 60 grid points are located in radial direction at nonuniform intervals.

Boundary conditions are selected to correspond to the experimental conditions as much as possible. Initial profiles of k and length scale of turbulence ℓ (ε is obtained by $\varepsilon = C_D k^{1.5}/\ell$) at the exit of the fuel nozzle are given by quadratic profiles similar to that predicted in the fully developed fuel nozzle flow by the same k-ε turbulence model where thin laminar layer is neglected. Length scale in the surrounding air stream is given to be 0.01 times the radius of the throat of the air stream. The selection of the length scale in the surrounding air stream is not sensitive to the calculated results.

RESULTS AND DISCUSSIONS

Comparisons of the experimental results and calculations are made. Plots and solid lines in the Figures are experimental results and calculated ones, respectively unless it is noted.

Non Reacting Flows

In Figs 1 to 5, axial and radial profiles of experimented and predicted flow velocity in axial direction U, gas concentration, kinetic energy of turbulence k and cross correlation of axial and radial velocity fluctuation $\overline{uv}$ are compared for the case of low and high fuel jet velocities (U_j = 20.4 and 55.7 m/s) without flame. The condition of low or high velocity without flame is labelled as RUN CL or RUN CH, respectively as shown in the Figures. L and r in the Figures are axial distance from the fuel nozzle tip and the radial distance from the jet axis, respectively. Predicted $\overline{uv}$ is obtained from the relation,

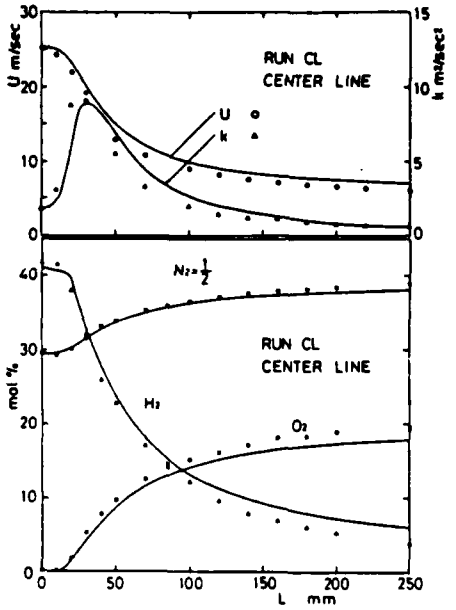

Fig.1 Axial profiles
(U_j=20.4 m/s, Cold)

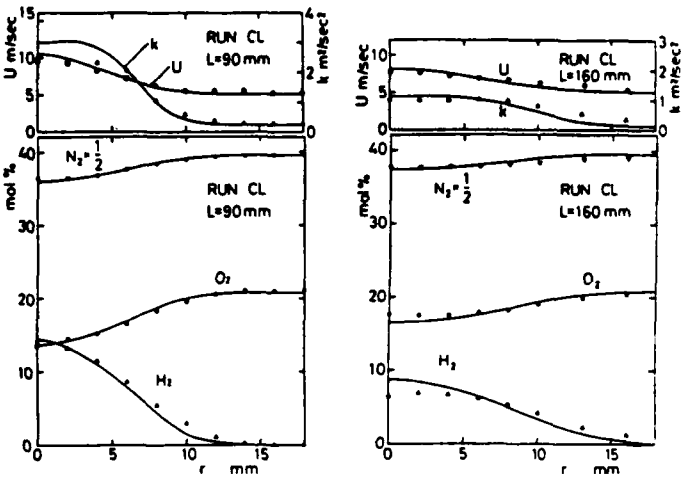

(a) L=90 mm (b) L=160 mm

Fig.2 Radial profiles
(U_j=20.4 m/s, Cold)

$\overline{uv} = -\mu_t(\partial U/\partial r)/\rho$.

It is noted the measured profiles of flow velocity, species concentration for two cases of low and high fuel jet velocities can be well predicted by the present calculations.

The profiles of turbulent kinetic energy along the axis (Figs.1,4) have peak near the nozzle tip and gradually decay along the axis. Such tendency can be well predicted. Radial profiles of k and $\overline{uv}$ are also predicted considerably well. These results indicates that the applied models can describe the fluctuating properties as well as the macroscopic flow and mixing characteristics for the fuel jets without flame.

The factor f_1 in eq.(7) is almost unity in the present fuel jets because the flows are fully turbulent ($\mu_t >> \mu_l$) in the flows without flame.

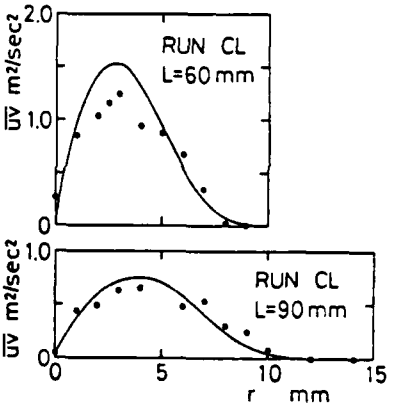

Fig.3 Radial profiles of uv
(U_j=20.4 m/s, Cold)

REACTING FLOWS

In Figs.6 to 11, experimented and predicted axial and radial profiles of flow velocity U, temperature T, gas species concentration, kinetic energy of turbulence k, cross correlation $\overline{uv}$ and $\overline{vT}$ are compared for the case of low and high fuel jet velocitis (U_j=20.4 and 55.7 m/s) with flame. The condition of low or high fuel jet velocity with flame is labelled as RUN FL or RUN FH, respectively as shown in the Figures.

The predicted cross correlation of the fluctuation of velocity and temperature $\overline{vT}$ is obtained from the relation, $\overline{vT} = -\mu_t/\sigma_h(\partial T/\partial r)/\rho$.

Figs.6 to 7 and Figs.10 to 12 indicate that flow velocity, temperature and species concentration can be well predicted in the flames of both low and high fuel jet velocities.

In the flow of the low fuel jet velocity with flame, the ratio μ_t/μ_l decreases at the high temperature region of the outer part near the fuel nozzle tip. This seems to correspond to the local laminarization phenomena observed clearly in the same flame without surrounding air flow [7].

In the low velocity flame, the unmodified turbulence model available in fully turbulent flow overestimates the turbulent viscosity and other transport coefficients. The modification of the turbulence model by the eqs.(7) and (8) gives a better prediction as shown in Figs.6 and 7.

The modification is not necessary for the flame of the higher fuel jet velocity because the μ_t/μ_l is much larger than unity.

The axial profiles of turbulence kinetic energy along the axis (Figs.6 and 10) in the cases with flame increases more gradually along the axis and have peak in the downstream as compared with the cases without flame (Figs.1 and 4). These tendencies are predicted by the calculation as shown in Fig.6 and 10. Predictions of profiles of k, $\overline{uv}$ and $\overline{vT}$ are not very well but the qualitative agreement is fairly well which supports the gradient-transport-model incorporated with the two-equation k-ε turbulence model for

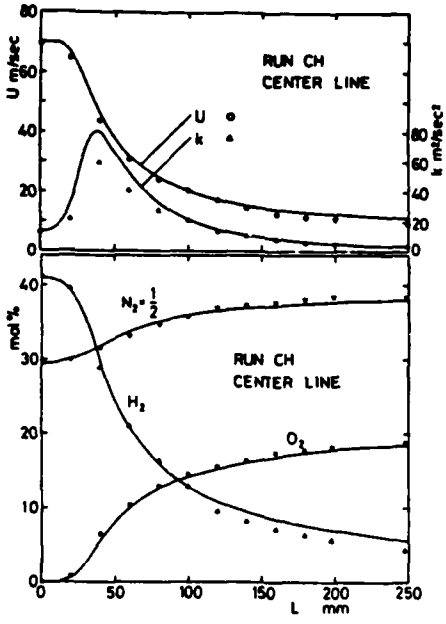

Fig.4 Axial profiles
(U_j=55.7 m/s, Cold)

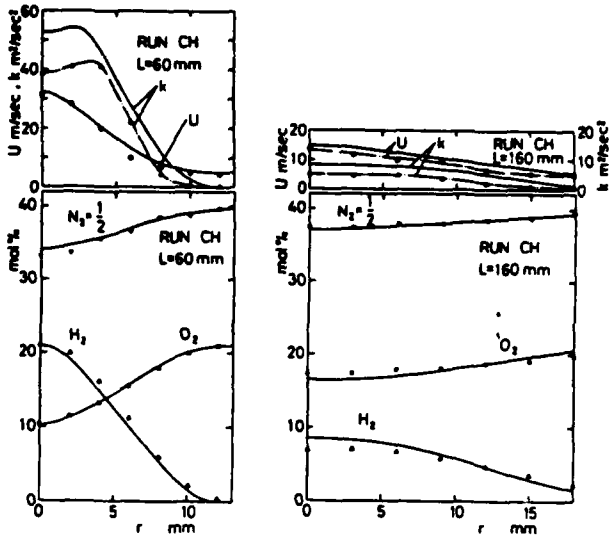

(a) L=60 mm (b) L=160 mm

Fig.5 Radial profiles
(U_j=55.7 m/s, Cold)

the transport of the momentum and heat even in the reacting flows.

DISCUSSIONS

In the turbulent flow fields with flame, significant density fluctuation would prevail and conventional time averaging of the governing equations yields a number of cross correlations including density fluctuation.

The equations used in the preceding section are equivalent to those obtained by neglecting density fluctuation when the variables such as U, T, m_j, etc. in the equations are taken to be conventional time averaging $\bar{U}$, $\bar{T}$, $\bar{m}_j$, etc. Based on the comparisons between the experimental and calculated results described above, it can be said that flow velocity, temperature, species concentration and fluctuating properties can be predicted by the equations neglecting density fluctuation although the spatial variation of density is taken into account.

On the other hand, if the density weighted averaging (Favre averaging) is applied for the variable except for ρ and P, the density fluctuation can be taken into account without any apparent change in the governing equations [1]. In this case, the variables such as U, T, m_j, etc. are supposed to be density weighted averaging $\tilde{U}$ ($=\overline{\rho U}/\bar{\rho}$), $\tilde{T}$ ($=\overline{\rho T}/\bar{\rho}$), $\tilde{m}_j$ ($=\overline{\rho m_j}/\bar{\rho}$), etc. In this case, the prediction yields density weighted avaraging $\tilde{U}$, $\tilde{T}$, $\tilde{m}_j$, etc.

On the other hand, the measured velocity U by a laser Doppler velocimeter and the temperature T by a thermocouple are supposed to be conventional time averating $\bar{U}$ and $\bar{T}$. But, species concentrations measured by gas sampling are supposed to be density weighted averaging $\tilde{m}_j$.

Now, we consider the relations between conventional time averaging and density weighted avaraging as follows.

$$\tilde{U} = \bar{U} \{ 1 - (T'/\bar{T}) (u'/\bar{U}) R_{TU} \}$$

$$\tilde{T} = \bar{T} \{ 1 - (T'/\bar{T})^2 \} \qquad (15)$$

$$\tilde{m}_j = \bar{m}_j \{ 1 - (T'/\bar{T}) (m_j'/\bar{m}_j) R_{Tm_j} \}$$

where T', u' or m_j' is the root mean square of the fluctuation of T, U or m_j and R_{TU} or R_{Tm_j} is the correlation coefficient of the fluctuation of T and U or T and m_j. The equations are derived by the approximation that the density fluctuation is mainly caused by the temperature fluctuation according to the ideal gas law.

The profiles of $\bar{T}$, $\tilde{T}$, $\bar{U}$, $\tilde{U}$, T' and u' are shown in Fig.12 where $\bar{T}$, $\bar{U}$, T', u' are measured ones and $\tilde{T}$ and $\tilde{U}$ are calculated by eq.(15) using the measured R_{TU}, u',T'. It is noted $\tilde{T}$ is always less than $\bar{T}$ and the difference is at most 15 % of $\bar{T}$ at the outer part of the flame where T'/$\bar{T}$ is large. $\tilde{U}$ is larger than $\bar{U}$ at the inner part of the flame where R_{TU} is negative but $\tilde{U}$ is less than $\bar{U}$ at the outer part of the flame where R_{TU} is positive. The difference between $\tilde{U}$ and $\bar{U}$ is less than 10 % of $\bar{U}$.

It can be said that the comparisons between predictions and experiments are available whether the measured or calculated values are conventional time averaged or density weighted averaged and the density fluctuation does not play significant role for the present flame conditions.

SUMMARY

(1) The measured profiles of time mean velocity temperature and species concentration in the fuel jets with and without flame can be well predicted by two-equation k-ϵ turbulence model which is modified for the low Reynolds number effects due to the existence of flame.

(2) The fluctuating properties such as kinetic

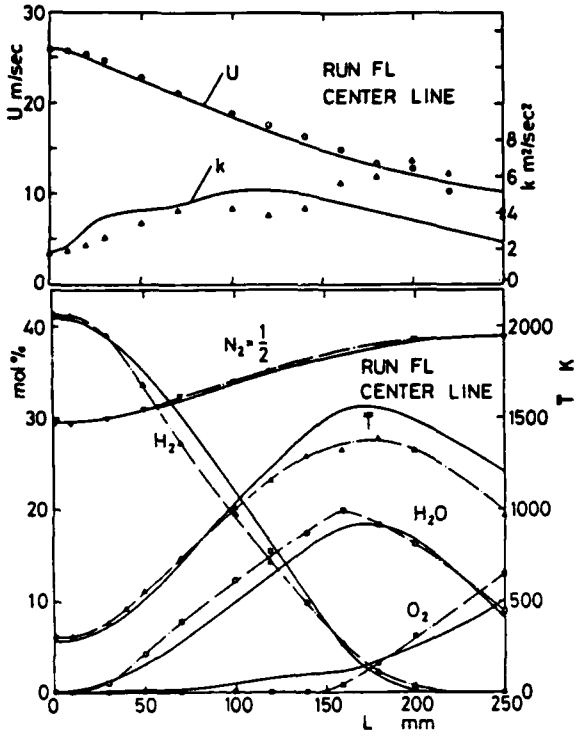

Fig.6 Axial profiles
(U_j=20.4 m/s, Flame)

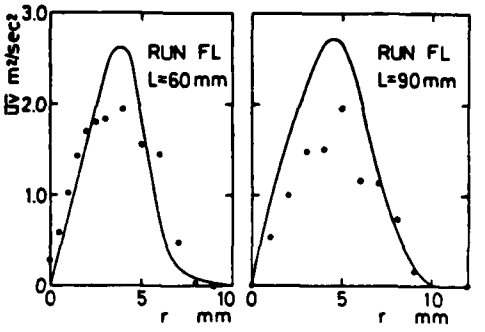

Fig.8 Radial profiles of uv
(U_j= 20.4 m/s, Flame)

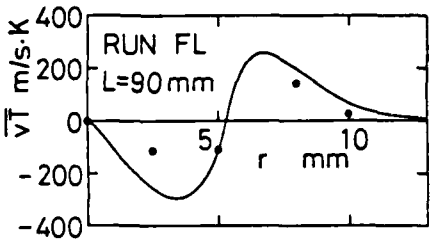

Fig.9 Radial profile of vT
(U_j= 20.4 m/s, Flame)

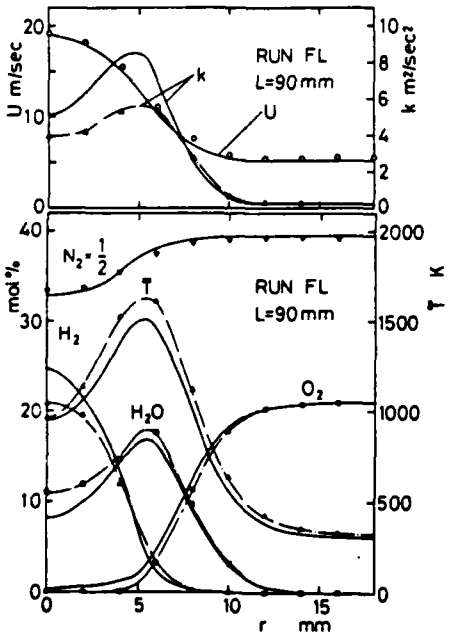

(a) L = 90 mm

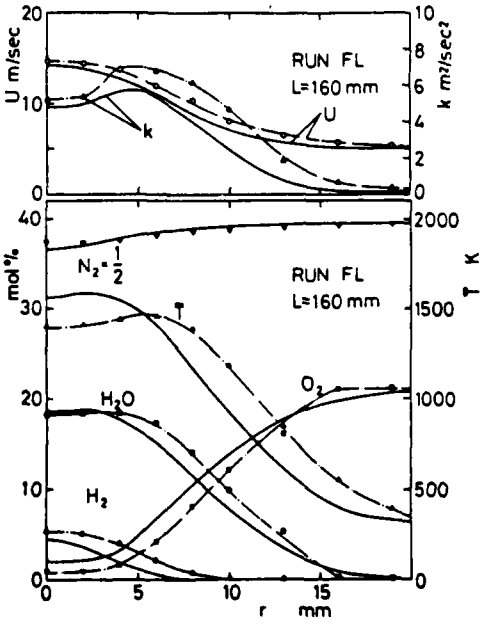

(b) L = 160 mm

Fig.7 Radial profiles
(U_j=20.4 m/s, Flame)

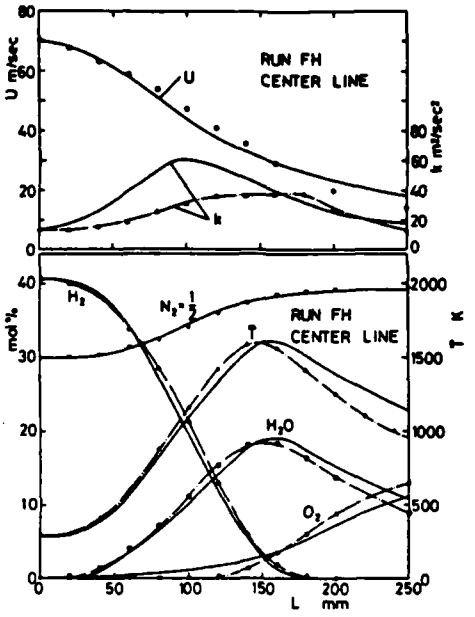

Fig.10 Axial profiles
(U_j=55.5 m/s, Flame)

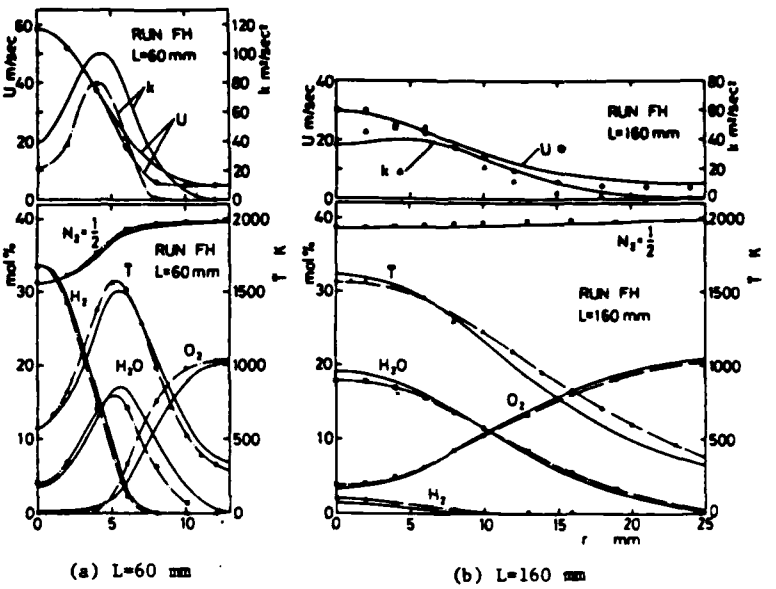

(a) L=60 mm (b) L=160 mm

Fig.11 Radial profiles
(U_j=55.7 m/s, Flame)

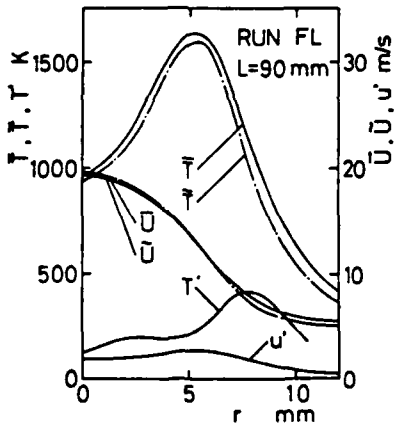

Fig.12 Comparison of $\bar{U}$, $\tilde{U}$ and $\bar{T}$, $\tilde{T}$
(U_j=20.4 m/s, Flame)

energy of turbulence and cross correlations of $\overline{uv}$ and $\overline{vT}$ are also predicted fairly well which support the gradient-transport-model for the turbulent transport of momentum and heat in turbulent diffusion flames.

(3) The difference between conventional time averaging $\bar{U}$ or $\bar{T}$ and density weighted averaging $\tilde{U}$ or $\tilde{T}$ is not so great which indicates that neglecting the density fluctuation gives an fairly good approximation.

ACKNOWLEDGEMENTS

The authors thank Mr. K. Wada, H.D. Shin, A. Ishio and H. Fujita for their assistance. This study is supported by the Fund of the Education Ministry of Japan and the JSME Sub-Committee for the Study on Laser Diagnostics of Combustion.

REFERENCES

1. Kent, J.H. and Bilger, R.W.,"The Prediction of Turbulent Diffusion Flame Fields and Nitric Oxide Formation," Proc. 16th Symposium (International) on Combustion, 1977, pp. 1643-1655.

2. Janicka, H. and Kollman, W., "A Two-Variables Formalism for the Treatment of Chemical Reactions in Turbulent H_2-Air Diffusion Flames," Proc. 17th Symposium (International) on Combustion, 1979, pp. 421-430.

3. Kent, J.H. and Bilger, R.W., "Turbulent Diffusion Flames," Proc. 14th Symposium (International) on Combustion, 1973, pp. 615-625.

4. Takagi, T., Shin, H.D. and Ishio, A., "Properties of Turbulence in Turbulent diffusion Flames," Combustion and Flame, Vol.40, 1981, pp.121-140.

5. Takagi, T., Shin, H.D. and Ishio, A., " A Study on the Structure of Turbulent Diffusion Flame: Properties of Fluctuations of Velocity, Temperature, and Ion Concentration," Combustion and Flame to appear.

6. Jones, W.P. and Launder, B.E., "The Calculation of Low-Reynolds-Number Phenomena with a two-Equation Model of Turbulence," International Journal of Heat and Mass Transfer, Vol.16, 1973, pp.1119-1130.

7. Takagi, T., Shin, H.D. and Ishio, A., "Local Laminarization in Turbulent Diffusion Flames," Combustion and Flame, Vol.37, 1980, pp.163-170.

8. Launder, B.E. and Spalding, D.B., "Mathematical Models of Turbulence," 1972, Academic Press.

9. Magnussen, B.F. and Hjertager, B.H., "On Mathematical Modelling of Turbulent Combustion with Special Emphasis on Soot Formation and Combustion," Proc. 16th Symposium (International) on Combustion, 1979, pp.719-729.

10. Patankar, S.V. and Spalding, D.B., "Heat and Mass Transfer in Boundary Layers," 1970, Intertext Book.

INVESTIGATIONS ON A REACTION MODEL FOR TURBULENT DIFFUSION FLAMES

H. Eickhoff, Deutsche Forschungs- und Versuchsanstalt für Luft- und Raumfahrt E.V., Institut für Antriebstechnik, 5000 köln 90, W.-Germany

K. Grethe, Universität Karlsruhe (TH), Engler-Bunte-Institut, Bereich Feuerungstechnik, 7500 Karlsruhe

ABSTRACT

A study was performed in order to gain new insight into the phenomenology and mathematical modelling of turbulent diffusion flames.
The numerical part of the present investigation treats unsteady one-dimensional laminar diffusion flames using an extended kinetic scheme. The result of these predictions yields the instantaneous substructure of turbulent diffusion flames. In order to check the validity of the model predictions instantaneous peak temperatures as well as time mean concentrations have been measured in turbulent methane diffusion flames.

NOMENCLATURE

$c_{p,i}$	heat capacity of species i at constant pressure
c_p	mixture heat capacity
D_i	binary diffusion coefficient for species i in nitrogen
$F(T^*)$	nondimensional rate of chemical heat release as a function of T
h	mixture enthalpy
h_i	enthalpy of species i
h_i^o	standard heat of formation of species i
NS	number of species
Re	Reynolds-number defined by nozzle diameter and nozzle exit velocity
s	layer thickness
s^o	initial layer thickness
S	stretch rate defined by $-S = \frac{1}{s}\frac{ds}{dt}$
t	time coordinate
T	local temperature
T_o	initial
T_{af}	adiabatic flame temperature
T^o	reference temperature
T^*	nondimensional temperature defined by $T^*=(T-T_o)/(T_{af}-T_o)$
u_o	normal velocity of convective transport through the flame
$\dot{w}_i$	chemical production/consumption rate of species i
x	coordinate normal to the flame zone
γ	Kolmogorov strain rate (reciprocal value of Kolmogorov time scale)
λ	thermal conductivity
ν	viscosity, used in the thermal conduction term of eq. (1) for Prandtl number unity
ω	nondimensional space coordinate normal to the flame zone
ρ	density
σ_i	mole number of species i in 1 kg mixtures
τ	characteristic chemical time scale, defined so that the peak value of $F(T^*)$ becomes unity
$\bar{(\ )}$	time mean values

INTRODUCTION

Combustion of nonpremixed reactants has been investigated in turbulent jet flames with attention focussed on hydrogen combustion. Compared with hydrogen combustion, however, turbulent hydrocarbon diffusion flames introduce additional problems due to the more complex combustion reactions.

An essential feature of some combustion models for turbulent diffusion flames is a unique determination of the instantaneous molecular species concentration by a conserved scalar. The assumption of a one-step irreversible reaction leads to the flame sheet model, with the combustion reactions taking place in an infinitesimally thin flame sheet. If the fast chemistry assumption is not restricted to a one-step irreversible reaction it follows that the products are in chemical equilibrium. Due to the shifting equilibrium reactions a large amount of carbon monoxide is predicted by this model in the fuel-rich region of a diffusion flame, more than is found experimentally in laminar or in turbulent diffusion flames. As it has been shown (1) a turbulent natural gas diffusion flame can be predicted rather well by a chemistry model which is based on the assumption that the instantaneous gas composition in a turbulent flame is that corresponding to local chemical equilibrium over a wide range of mixture strength around stoichiometric, and that the shifting equilibrium reactions freeze at a unique fuel-rich mixture fraction. To check the validity and limitations of this simplified instantaneous reaction model, one-dimensional unsteady laminar diffusion flames have been investigated. These flames are assumed to be representative of the diffusive reactive interfaces between fuel and air eddies in a turbulent flame.

THE UNSTEADY LAMINAR DIFFUSION FLAME

The behaviour of the quasi-laminar substructure of turbulent flames has been discussed qualitatively by Williams (2) in terms of the unsteady, one-dimensional temperature equation

$$\frac{\partial T^*}{\partial t} - \gamma \times \frac{\partial T^*}{\partial x} + u_o \frac{\partial T^*}{\partial x} - \nu \frac{\partial^2 T^*}{\partial x^2} = \frac{1}{\tau} (F(T^*) \qquad (1)$$

This equation is obtained if the coordinate system moves parallel to the reactive layer such that the tangential velocity component becomes zero at the origin of the coordinate system. The second and third term in equation (1) represent convective fluxes due to flame stretch and a velocity component normal to the flame front. In the following these convective fluxes will be neglected, but the stretching process is considered with respect to a decrease of the thickness of the reactive layer as proposed by Spalding (3).The resulting balance equations are

Concentration :

$$\frac{\partial \rho \sigma_i}{\partial t} - \frac{1}{s^2} \frac{\partial}{\partial \omega} \rho D_i \frac{\partial \sigma_i}{\partial \omega} = \dot{w}_i ; \; i=1,\ldots,NS \qquad (2)$$

Energy :

$$\frac{\partial \rho h}{\partial t} = \frac{1}{s^2} \frac{\partial}{\partial \omega} \frac{\lambda}{c_p} \frac{\partial h}{\partial \omega} + \frac{1}{s^2} \sum_{i=1}^{NS} \frac{\partial}{\partial \omega} \left(h_i \left(\frac{\lambda}{c_p} - \rho D_i \right) \frac{\partial \sigma_i}{\partial \omega} \right), \qquad (3)$$

with the non-dimensionalized space coordinate $\omega = x/s$, $0 < \omega < 1$ and

$$h = \sum_{i=1}^{NS} h_i \sigma_i ; \; h_i = h_i^o + \int_{T^o}^{T} c_{p,i} \, dT ; \; c_p = \sum_{i=1}^{NS} c_{p,i} \sigma_i \qquad (4)$$

The following conditions were used for the calculations :

1. As it is difficult to specify the time dependent thickness of the shear layer, a constant stretch S was assumed, which yields (3)
   $s = s_o e^{-S t}$,
   with s_o as the initial shear layer thickness.
2. Initial conditions of the the computations are characterized by a step change in the concentrations of fuel gas and air with a very thin layer of hot gas at the interface.
3. Dimensions of the fuel gas and air volumes are large compared to the thickness of the diffusion layer.
4. 29 elementary reactions were used to describe the oxidation process of methane adopted as a fuel.
5. Binary diffusion coefficients for the gas components in N_2, Lewis number equal to one.

Details of the numerical computations are given in (4).

In order to get information about the properties of flamelets in turbulent diffusion flames, direct thermocouple measurements of instantaneous temperatures were made in free burning turbulent methane flames at various Reynolds numbers (5). The different Reynolds numbers were chosen to get flames with very different flow structures, which were visualized by a schlieren technique. They ranged from orderly coherent structures to fully developed three-dimensional small scale turbulence.

In addition, conventional measurements of mean concentration were performed to get further information about the net influence on the reactions.

RESULTS

In Fig. 1 computed rates of CO and O_2 as functions of the excess air ratio are shown. The effects of diffusion are clearly visible in the changing peak values. The limit for the freezing of the reactions assumed in the flame zone model (1) lies within the area in which the reactions are frozen during the successive time steps. The calculations have been performed for a time period of 25 milliseconds which is beyond the eddy life times of the turbulent flames considered.

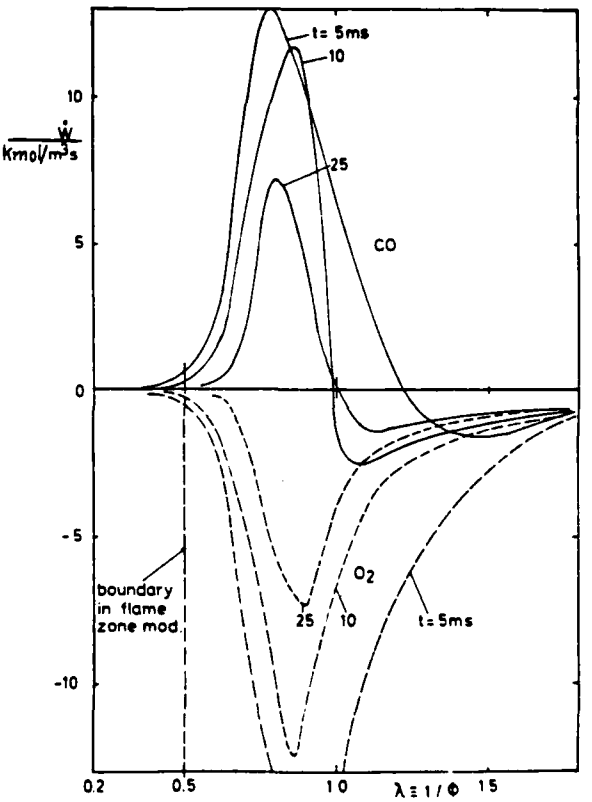

Fig. 1 Production rates of CO and O_2 in a one dimensional unsteady laminar natural gas diffusion flame for different time steps as function of the excess air ratio λ

The concentrations and temperatures shown in Fig.2 do not change significantly during the time period considered. This means that even with very large concentration gradients the conditions at the beginning of the lifetime of an eddy are not very different from those at later time steps. This result, to a certain extent, can justify a posteriori the neglect of the flame stretch which strongly influences the gradients within the reaction zone and can result in quenching under certain conditions.

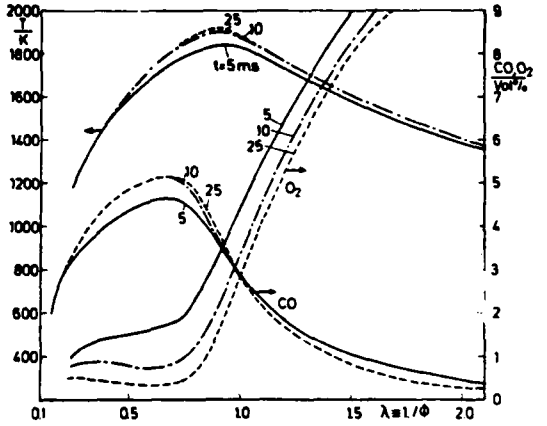

Fig. 2 Concentrations of CO, O_2 and temperature T as functions of the excess air ratio λ

A particularly important result is the fact that the computed peak temperatures of a non-stretched flame zone lie around 1 930 K as did the thermocouple measurements in the turbulent methane diffusion flames. This value is considerably below the adiabatic equilibrium flame temperature of 2 280 K (Fig. 3). The measured peak temperatures of 1 900 - 2 000 K (Figs. 4, 5) in all regions of the turbulent flames at different Reynolds numbers (5) may also be compared to the value of about 2 000 K from Laser Raman measurements (6) in a laminar methane diffusion flame and thermocouple measurements in a different laminar diffusion flame (7).

It follows from Figures 4 and 5 that the maximum peak temperatures in the region of the visible coherent structures ($x/d \leq 20$, Re = 5 500) are approximately equal to this of fully developed three-dimensional turbulence ($x/d = 60$, Re = 37 000). It may therefore be concluded that the instantaneous peak temperatures in turbulent diffusion flames are not significantly affected by turbulence. The measurements of mean concentrations also show that in large parts of the flame the combustion takes place in diffusion flamelets.

The influence of the stretch rate S on the behaviour of the diffusive reactive layer was studied parametrically. In Fig. 6 the predicted time dependent temperatures and concentrations of a stretched layer are shown ($S = 111 s^{-1}$). The decrease of temperature and maximum CO-concentration indicates a decreasing reaction intensity which finally leads to quenching of the reactions.

Concentration measurements in free burning turbulent natural gas diffusion flames of different Reynolds numbers clearly indicate that even in stably burning flames quenched regions occur near the nozzle, through which unreacted oxygen penetrates to the flame axis, Fig. 7. Due to this premixed combustion occurs to a certain extent further downstream. Fig. 8 shows measured axial CO profiles in turbulent flames of different Reynolds numbers. The rapid decrease of downstream CO-concentration in the lower Reynolds number flames is due to mixing enhanced by

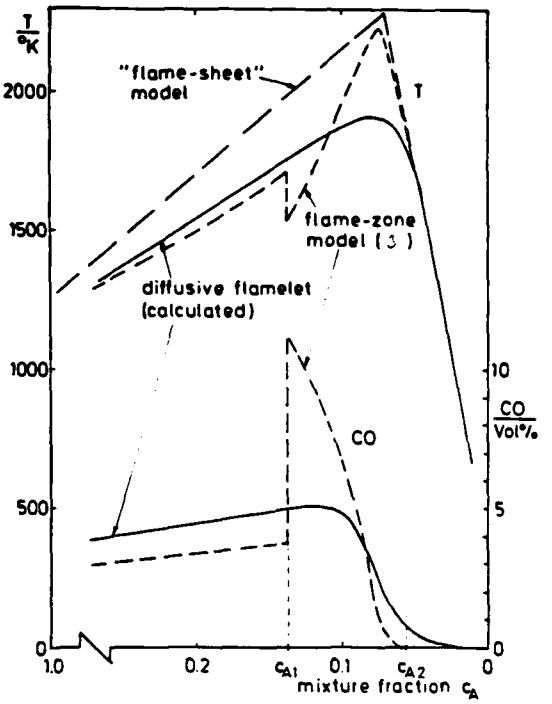

Fig. 3 Comparison of CO-concentration and temperature T calculated by two different flame models and finite kinetics (t = 25 ms)

buoyancy. The dashed curve which refers to flame No.3 represents computed values. The predictions are based on the instantaneous gas composition (Fig. 2), a pdf-representation of the mixture fraction and the k-ε-model for the flow field (8).

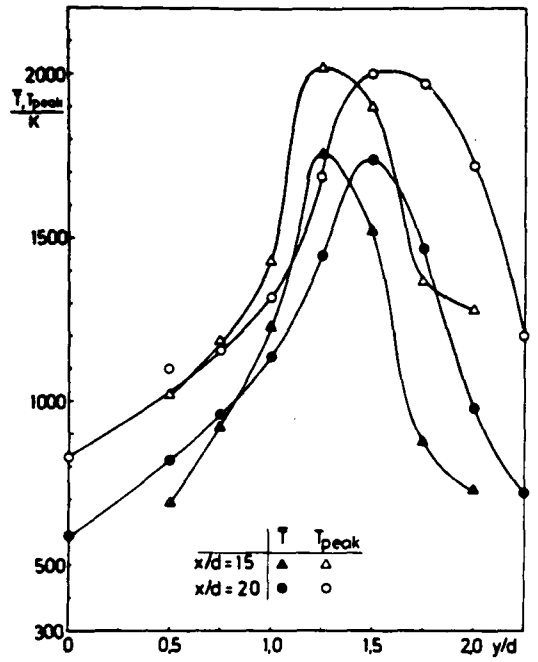

Fig. 4 Radial profiles of measured peak and time mean temperatures in a free burning natural gas flame, Re = 5 500, (5)

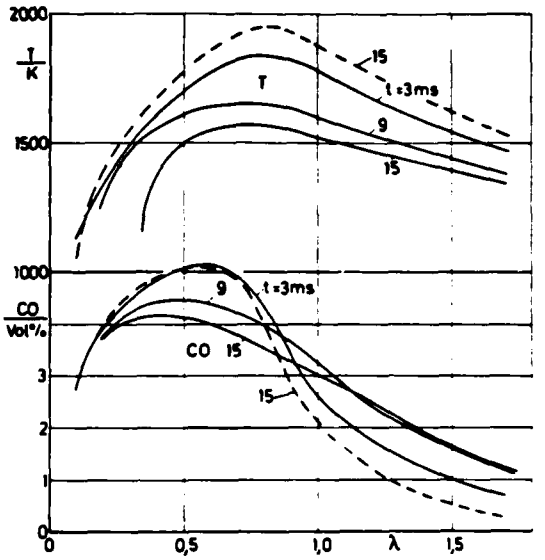

Fig. 6 CO-concentrations and temperatures as function of the excess air ratio λ

—— stretch rate S = 111 s^{-1}
--- without stretch

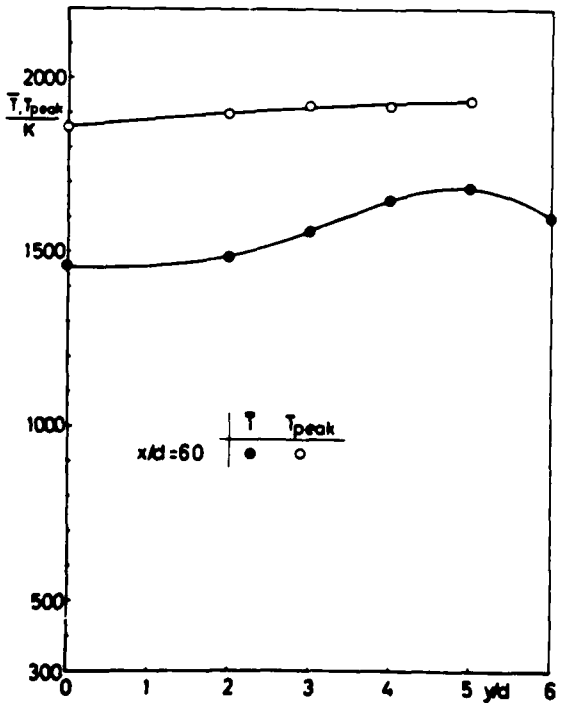

Fig. 5 Radial profiles of measured peak and time mean temperatures in a free burning natural gas flame, Re = 37 000 (5)

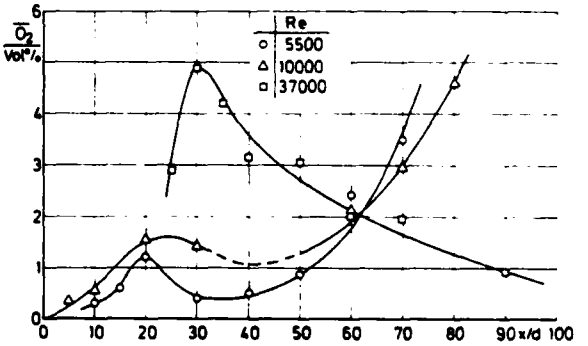

Fig. 7 Measured axial profiles of O_2-concentrations in free burning natural gas diffusion flames at different Reynolds numbers

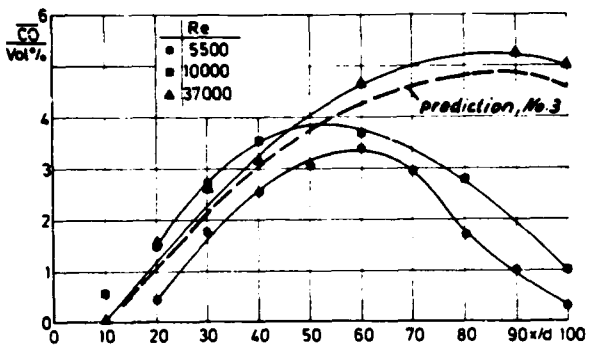

Fig. 8 Measured and predicted axial profiles of CO-concentrations in free burning natural gas diffusion flames at different Reynolds numbers

CONCLUSIONS

1. From comparison of predictions and measurements it can be concluded that turbulent diffusion flames over a large range are composed of laminar diffusion flamelets with instantaneous peak temperatures about 300 K below the adiabatic equilibrium temperature.
   This is an especially useful information with regard to the thermal NO-formation, this being strongly dependent on the peak temperature.
2. Areas of premixed combustion can occur even in flames stably burning at the nozzle exit.
3. The instantaneous temperature and concentration profiles do not change greatly during the most probable life time of an eddy. This result can be compared to some extent to the conclusions of Bilger (9) who found by inspection of measurements in laminar diffusion flames that the gas-composition is independent of the position in the flame and therefore independent of the flow structure.

With a representative profile of the instantaneous gas composition shown in Fig. 3 instead of the one used earlier (1), a turbulent diffusion flame based on the k-ε-model and a pdf of the mixture fraction can be well predicted as long as premixed combustion does not take place.

REFERENCES

1 Eickhoff, H.E. and Grethe, K. , "A Flame Zone Model for Turbulent Hydrocarbon Diffusion Flames", Combustion and Flame 35 (1979), pp. 267-275

2 Williams, F.A., "Recent Advances in Theoretical Descriptions of Turbulent Flames", published in Turbulent Mixing in Nonreactive and Reactive Flows. ed. by S.N.B. Murthy, Plenum Press, New York (1975)

3 Spalding, D.B., "Chemical Reactions in Turbulent Fluids", in Physicochemical Hydrodynamics, Vol.1, ed. by D.B. Spalding, Advance Publications Ltd., London (1977)

4 Grethe, K., "Verification of a Flame-Zone Model for Turbulent Diffusionflames", (submitted Doctor thesis), University of Karlsruhe (TH),(1981)

5 Grethe, K., Kohler, W., Leuckel, W., "Direct Thermocouple Measurements of Instantaneous Temperatures in Turbulent Diffusion Flames", (to be submitted), University of Karlsruhe, Engler-Bunte-Institut (1981)

6 Stricker, W., and Just, Th., "Lokale Temperaturmessung in Flammen mit Laser-Raman-Verfahren", 9. Deutscher Flammentag, Aachen, (1979), VDI-Bericht Nr. 346

7 Yamaoka, I. and Tsuji, H. : "An Experimental Study of Flammability Limits Using Counter Flow Flames", 17. Symp. Inter. on Combustion (1978)

8 Eickhoff, H.E., Grethe, K. and Thiele, F.: "Numerical Investigations on Turbulent Transport and Reaction Phenomena in Jet Flames", 2nd Symposium Turb. Shear Flow (1979)

9 Bilger, R.W., "Reaction Rates in Diffusion Flames", Comb. a. Flame, 30, (1977), pp. 277-284

CALCULATIONS OF VELOCITY-SCALAR JOINT PDF'S

by

S.B. Pope

Massachusetts Institute of Technology
Department of Mechanical Engineering
Cambridge, Massachusetts 02139

ABSTRACT

A joint pdf transport equation has been solved to calculate the properties of the self-similar, plane, turbulent jet. The joint probability density function (pdf) is that of the three velocity components and of the nozzle-fluid concentration, which is a conserved, passive scalar. The advantage of basing a turbulence closure on the joint pdf equation is that convective transport appears in closed form. Consequently, the gradient-diffusion assumption is avoided. For self-similar shear flows, the joint pdf is a function of five variables. Its transport equation is solved by a Lagrangian method with stochastic modelling of the unclosed terms. The calculated Reynolds stresses and triple velocity correlations agree well with the experimental data. Calculated pdf's and joint pdf's are also reported.

NOMENCLATURE

C_R, C_ϕ	model constants
D	velocity dissipation term
E	conditionally-expected value
$f(\underline{V}, \psi)$	velocity-scalar joint pdf
G	scalar dissipation term
$p(\psi)$	scalar pdf
$\langle p \rangle$, p'	mean and fluctuating pressure
R	redistribution term
r,θ, z	polar-cylindrical coordinates
t, δt	time, time interval
$\underline{U}$, $\underline{u}$	velocity, fluctuating velocity
$\underline{V}$	independent velocity variables
x,y,z	axial, lateral and spanwise coordinates
$y_{\frac{1}{2}}$	jet half width

Greek symbols

Γ	molecular diffusion coefficient
ε	dissipation rate of turbulent kinetic energy
η	cross-stream variable $y/y_{\frac{1}{2}}$
μ	molecular viscosity
ϕ, ϕ'	scalar, fluctuating scalar
ψ	independent scalar variable
ω, ω^*	turbulent frequency, normalised frequency

INTRODUCTION

A modelled joint pdf equation [1] has been solved to calculate the one-point statistical properties of the self-similar plane turbulent jet. The equation solved is for the joint probability density function (pdf) of the three velocity components $\underline{U}(\underline{x},t)$ and a conserved passive scalar $\phi(\underline{x},t)$. With θ being the non-dimensional, cross-stream variable, the joint pdf is $f(\underline{V},\psi;\theta)$, where $\underline{V} \equiv V_1, V_2, V_3$ and ψ are the independent variables corresponding to $\underline{U}$ and ϕ. Since $f(\underline{V},\psi;\theta)$ is a function of five variables, the solution of its transport equation by a finite-difference method is impracticable. Instead, the transport equation is solved by a Lagrangian method with stochastic modelling of the unclosed terms. The simplest possible models are used - not the most accurate - the emphasis being on demonstrating the use of the joint pdf equation and the performance of the solution procedure.

Transport equations for pdf's are useful in modelling turbulent flows because non-linear one-point processes (such as convection and reaction) can be treated without approximation [1-3]. The transport equation for the joint pdf of a set of scalars $p(\underline{\psi};\underline{x},t)$ is particularly useful in reactive flows since the term pertaining to reaction appears in closed form, irrespective of the complexity and non-linearity of the reaction scheme. Pope [4] and Janicka, Kolbe and Kollmann [5] have reported accurate calculations of premixed and diffusion flames based on the scalar pdf equation. For more than one or two scalars, finite-difference solutions are impracticable, but a Monte Carlo method [6] has been developed for the general case.

The great advantage of considering the joint pdf of velocity and scalars is that convective transport appears in closed form. Consequently, the assumption of turbulent transport by gradient diffusion is avoided. In fact, for a variable-density reactive flow, the terms pertaining to convection, reaction, buoyancy and the mean pressure gradient all appear in closed form. Only the effects of molecular mixing and the fluctuating pressure gradient need to be modelled. Models for these processes have been given in a recent paper [1] which contains a derivation and discusssion of the joint pdf equation.

Self-similar free shear flows are good test cases for the modelled joint pdf equation. The condition of self-similarity can be used to reduce the number of spatial dimensions to one - namely, the normalized cross-stream coordinate θ. And for self-similar flows there is a wealth of experimental data. The plane jet was chosen for this initial study because of the simple coordinate system and boundary conditions.

In the following three sections, the joint pdf transport equation is presented, the solution procedure is described, and the results of the calculations are reported. The results include profiles of the mean velocity, Reynolds stresses and triple velocity correlations, all of which are compared with the experimental data of Heskestad [7]. Calculated scalar pdf's and joint pdf's are also reported but no data are available for comparison.

JOINT PDF EQUATION

The joint pdf $f(\underline{V},\psi;\underline{x},t)$ contains all the one-point statistical information about the velocity $\underline{U}(\underline{x},t)$ and the conserved, passive scalar $\phi(\underline{x},t)$ in a constant-density turbulent flow. If $Q(\underline{U},\phi)$ is any function of $\underline{U}$ and ϕ, then its mean value (at any $\underline{x},t$) can be determined from the joint pdf by

$$\langle Q(\underline{U},\phi)\rangle = \int\int Q(\underline{V},\psi)\, f(\underline{V},\psi)\, d\underline{V}\, d\psi. \qquad (1)$$

Here and below, $\int d\underline{V}$ represents integration over the whole of the velocity space and, similarly, $\int d\psi$ represents integration over all possible values of ϕ. Substituting $Q(\underline{U},\phi) = U_j$ in equation (1) shows the mean velocity to be

$$\langle U_j\rangle = \int\int V_j\, f(\underline{V},\psi)\, d\underline{V}\, d\psi\,. \qquad (2)$$

Similarly the Reynolds stresses are

$$\langle u_i u_j\rangle = \int\int (V_i - \langle U_i\rangle)\,(V_j - \langle U_j\rangle)\, f(\underline{V},\psi)\, d\underline{V}\, d\psi, \qquad (3)$$

and the scalar fluxes are

$$\langle u_i \phi'\rangle = \int\int (V_i - \langle U_i\rangle)\,(\psi - \langle\phi\rangle)\, f(\underline{V},\psi)\, d\underline{V}\, d\psi. \qquad (4)$$

Thus, any one-point statistic can be obtained from $f(\underline{V},\psi)$.

The pdf of the scalar alone $p(\psi;\underline{x},t)$ is obtained by integrating $f(\underline{V},\psi)$ over velocity space

$$p(\psi) = \int f(\underline{V},\psi)\, d\underline{V}, \qquad (5)$$

and the joint pdf of velocity $g(\underline{V};\underline{x},t)$ is

$$g(\underline{V}) = \int f(\underline{V},\psi)\, d\psi. \qquad (6)$$

Each of the pdf's satisfies the normalization condition

$$\int p(\psi)\, d\psi = \int g(\underline{V})\, d\underline{V} = \int\int f(\underline{V},\psi) d\underline{V}\, d\psi = 1. \qquad (7)$$

A transport equation for $f(\underline{V},\psi;\underline{x},t)$ can be derived from the conservation equations for $\underline{U}$ and ϕ [1]:

$$\frac{\partial f}{\partial t} + V_i \frac{\partial f}{\partial x_i} - \frac{\partial f}{\partial V_i}\frac{\partial \langle p\rangle}{\partial x_i} = \frac{\partial}{\partial V_j}\{f\, E(\partial p'/\partial x_j \,|\, \underline{U} = \underline{V},\ \phi=\psi)\}$$

$$- \frac{\partial}{\partial V_j}\{f\, E(\mu\nabla^2 U_j \,|\, \underline{U} = \underline{V},\ \phi=\psi)\}$$

$$- \frac{\partial}{\partial \psi}\{f\, E(\Gamma\nabla^2\phi \,|\, \underline{U} = \underline{V},\ \phi=\psi)\}. \qquad (8)$$

(The fluid density ρ has been set to unity). The terms on the left-hand side represent convection and the effect of the mean pressure gradient. These terms are in closed form and therefore require no modelling. The terms on the right-hand side of the equation contain (as unknowns to be modelled) conditionally-expected values.

The first term on the right-hand side

$$R(\underline{V},\psi;\underline{x},t) = \frac{\partial}{\partial V_j}\{f\, E(\partial p'/\partial x_j \,|\, \underline{U} = \underline{V},\ \phi=\psi\}, \qquad (9)$$

represents the effects of the fluctuating pressure gradient. The term can be decomposed into three parts [1]: a transport term and two redistribution terms. As in Reynolds-stress models [8], the redistribution terms do not affect the mean velocity or the turbulent kinetic energy, but they redistribute the energy in velocity space. The rapid part of the redistribution is due to pressure fluctuations caused by mean-velocity gradients: the Rotta part [9] is due solely to the turbulence. Models for all three contributions to $R(\underline{V},\psi;\underline{x},t)$ are available [1], but for this initial study only the Rotta term is included.

In Reynolds-stress models, the Rotta term corresponds to a linear return to isotropy, i.e.

$$\frac{\partial}{\partial t}\langle u_i u_j\rangle = \ldots\ldots - C_R\omega(\langle u_i u_j\rangle - 1/3\langle u_i u_i\rangle \delta_{ij}), \qquad (10)$$

where C_R is a constant and $\omega(\underline{x},t)$ is the turbulent frequency (dissipation rate/turbulent kinetic energy). In the joint pdf equation, this term is modelled by a stochastic process that randomly reorientates the energy in velocity space. The effect on the Reynolds stresses is just that given by equation (10).

The second term on the right-hand side of equation (8)

$$D(\underline{V},\psi;\underline{x},t) = -\frac{\partial}{\partial V_j}\{f\, E(\Gamma\nabla^2 U_j \,|\, \underline{U} = \underline{V},\ \phi = \psi)\}, \qquad (11)$$

corresponds to dissipation - it does not affect the mean velocity but decreases the turbulent kinetic energy. Neglecting low-Reynolds-number terms, D is related to the dissipation [1] by

$$\varepsilon = \int\int \tfrac{1}{2} V_i V_i\, D(\underline{V},\psi;\underline{x},t)\, d\underline{V}\, d\psi. \qquad (12)$$

In the joint pdf equation, Curl's coalescence/dispersal model [10] is used to represent this process. (Because the turbulent frequency ω is defined in terms of ε, no additional model constant arises).

The final term in equation (8)

$$G(\underline{V},\psi;\underline{x},t) = -\frac{\partial}{\partial \psi}\{f\, E(\Gamma\nabla^2\phi \,|\, \underline{U} = \underline{V},\ \phi = \psi)\}, \qquad (13)$$

corresponds to scalar dissipation and is analogous to the velocity dissipation term D. The effect of the term is to reduce the scalar variance $<\phi^{*2}>$ without affecting the mean $<\phi>$. Again, Curl's model [10] is used to represent the process. The model involves a constant C_ϕ which is the ratio of the velocity to scalar turbulent time scales. Following conventional modelling [11] we take $C_\phi = 2.0$.

The calculations for the self-similar plane jet are performed in the polar-cylindrical coordinates r, θ, z. The distance from the virtual origin is r, the angle to the plane of symmetry is θ, and z is the spanwise distance. Some of the results are reported in the conventional Cartesian coordinate system (x,y,z) in which x is the axial distance ($x = r \cos\theta$) and y is the lateral distance ($y = r \sin\theta$). The half-width of the jet is $y_{½}$. It is assumed that the turbulent frequency $\omega(r,\theta,z)$ does not vary across the jet - i.e. that ω is independent of θ. Then, the conditions for self-similarity require that the normalised frequency

$$\omega^* \equiv \omega y_{½} / <U>_0 , \qquad (14)$$

be a constant. ($<U>_0$ is the center-line velocity). By transforming equation (8) into polar-cylindrical coordinates and applying the conditions of self-similarity, a transport equation is obtained for the joint pdf $f(V_r,V_\theta,V_z,\psi;\theta,t)$. This equation is obtained without invoking the boundary-layer assumptions and without neglecting any terms. It is solved for $0 \leq \theta \leq \theta_{max} = 0.5$, with symmetry conditions applied at $\theta = 0$ and with the boundary conditions at θ_{max} corresponding to potential flow with $\phi = 0$.

The values of the constants $\omega^* = 0.165$ and $C_R = 4.5$ are chosen to produce approximately the correct spreading rate ($dy_{½}/dx \approx 0.1$) and center-line turbulent kinetic energy ($½<u_i u_i>_0/<U>_0^2 \approx 0.065$). The value of C_R is greater than the usual value $C_R = 1.5$ [8] because the modelled redistribution term has to account for both the Rotta and rapid terms.

To summarize, in the joint pdf equation (Eq. 8), convective transport appears in closed form. Consequently, there are no Reynolds stresses, scalar fluxes or other velocity correlations to be modelled: the gradient-transport assumption is avoided. There are three unclosed terms representing, respectively, redistribution of kinetic energy in velocity space, dissipation of velocity fluctuations, and dissipation of scalar fluctuations. These three terms are modelled by simple stochastic processes, each of which proceeds at a rate proportional to the turbulent frequency ω. For the self-similar plane jet, the turbulent frequency is assumed to be uniform across the jet. A fuller description and analytic expressions for the models can be found in [1].

SOLUTION PROCEDURE

Since the joint pdf $f(V_r,V_\theta,V_z,\psi;\theta,t)$ is a function of five independent variables and time, it is obvious that its transport equation cannot be solved by a standard numerical method. The solution is obtained as the steady state of a transient calculation. The calculation advances from time t to time $t+\Delta t$ in two fractional steps. In the first step, the exact terms are treated by solving the equation

$$\frac{\partial f}{\partial t} + V_i \frac{\partial f}{\partial x_i} - \frac{\partial f}{\partial V_i}\frac{\partial <p>}{\partial x_i} = 0 \qquad (15)$$

by a Lagrangian method. In the second step, stochastic models are used to solve the equation

$$\frac{\partial f}{\partial t} = R + D + G. \qquad (16)$$

After the second step, the result is the pdf at time $t + \Delta t$ (according to eq. 8) plus a truncation error of order Δt^2. The truncation error can be reduced at will by reducing Δt.

In the numerical procedure, the pdf is represented indirectly by a large number (N) of elements in the solution domain $0 \leq \theta \leq \theta_{max} = 0.5$. The n th element is located at $\theta^{(n)}$ and has the properties $U_r^{(n)},U_\theta^{(n)},U_z^{(n)},\phi^{(n)}$. Let $n_1,n_2,\ldots,n_M$ be the M elements in the sub-interval $\theta - ½\Delta\theta \leq \theta \leq \theta + ½\Delta\theta$. (The elements are approximately uniformly distributed and hence $M \approx \Delta\theta N/\theta_{max}$.) At location θ, an approximation to the mean value of any function $Q(\underline{U},\phi)$ is

$$<Q(\underline{U},\phi)> \approx \frac{1}{M}\sum_{m=1}^{M} Q(\underline{U}^{(n_m)},\phi^{(n_m)}) . \qquad (17)$$

Similarly, the pdf at θ can be approximated by the histogram formed from the M elements. In these approximations there is a truncation error (of order $\Delta\theta^2$) and a statistical sampling error of order $M^{-½}$. These errors can, in principle, be reduced at will by decreasing $\Delta\theta$ and increasing $N\Delta\theta$. In practice, for realistic values of N and $\Delta\theta$, the error is large, and a more sophisticated method of determining means based on least-square cubic splines is used. But the principle is the same.

The solution of equation (15) is facilitated by the observation that it is the pdf transport equation for the Lagrangian system:

$$\frac{d\underline{x}}{dt} = \underline{U} , \quad \frac{d\underline{U}}{dt} = -\nabla<p> , \quad \frac{d\phi}{dt} = 0 . \qquad (18)$$

Thus, for the first of the fractional steps, the properties of each of the N elements evolve according to equation (18) for a time Δt.

In the second fractional step, stochastic models are used to solve equation (16). Pairs of elements that are close to each other in physical space interact to cause redistribution and velocity and scalar dissipation - the terms R, D and G. The solution domain is divided into K sub-intervals, of width $\Delta\theta = \theta_{max}/K$, and the ensembles of elements within each sub-interval are treated separately. In Curl's model for the velocity dissipation (D),

each ensemble is treated in turn and, at a rate ωM, pairs of elements are selected at random (M is the number of elements in the ensemble). Denoting the two elements by n and m, their velocities are replaced with the values

$$\underline{U}^{(n)} = \underline{U}^{(m)} = \tfrac{1}{2}\,(\underline{U}_0^{(n)} + \underline{U}_0^{(m)}) \ , \qquad (19)$$

where $\underline{U}_0^{(n)}$ is the value of $\underline{U}^{(n)}$ before the process. This has the effect of decreasing the energy $\langle \underline{U}.\underline{U} \rangle$ without affecting the mean $\langle \underline{U} \rangle$.

The implementation of Curl's model for the scalar dissipation (G) is precisely analogous. Pairs of elements are selected at a rate $C_\phi \omega M$ and the values of ϕ are replaced with

$$\phi^{(n)} = \phi^{(m)} = \tfrac{1}{2}(\phi_0^{(n)} + \phi_0^{(m)}) \ . \qquad (20)$$

In the stochastic model of redistribution (R), at a rate $C_R \omega M$, pairs of elements are selected at random from the ensemble. The velocities of the two elements (n and m) are then replaced with the values

$$\underline{U}^{(n)}_{(m)} = \tfrac{1}{2}(\underline{U}_0^{(n)} + \underline{U}_0^{(m)}) \pm \tfrac{1}{2}\,\underline{\xi}\,|\underline{U}_0^{(n)} - \underline{U}_0^{(m)}| \ , \qquad (21)$$

where $\underline{\xi}$ is a random vector of unit length, uniformly distributed on the unit sphere. This transformation from $\underline{U}_0^{(n)}$, $\underline{U}_0^{(m)}$ to $\underline{U}^{(n)}$,$\underline{U}^{(m)}$ corresponds to a random rotation of the elements in velocity space. Since neither their mean position nor their separation is altered, the transformation conserves both momentum and energy; the effect of the random rotation is to decrease the anisotrophy.

The two fractional steps advance time by Δt. This sequence of operations is repeated until the (statistically) steady state is attained.

For the calculations reported in the next section, there were N = 7,200 elements, and K =48 subintervals in the solution domain $0 \leq \theta \leq \theta_{max} = 0.5$. With a time step of $\Delta t = 0.2\, y^{1/2}/\langle U \rangle_0$, 400 time steps were taken. (The sampling error is decreased by time-averaging: hence the large number of steps). The total CPU time on a VAX computer was 27 minutes, at a cost of $16.

RESULTS

The calculations reported in this section were obtained from the numerical solution of the modelled joint pdf equation. All the results are normalized with the center-line values $\langle U \rangle_0$ and $\langle \phi \rangle_0$. Comparison is made with the hot-wire data of Heskestad [7].

Figure 1 shows the mean axial velocity (in Cartesian coordinates) plotted against the normalised y-coordinate $\eta = y/y_{1/2}$. There is good agreement between the calculated and measured profiles, but it should be remembered that the normalization forces agreement at $\eta = 0$ and $\eta = 1$. Figures 2 and 3 show the normal-stress profiles $\langle u_x^2 \rangle$ and $\langle u_y^2 \rangle$. The profile shapes are calculated quite accurately as are the magnitudes. The profile of $\langle u_z^2 \rangle$ (not shown) is similar to that of $\langle u_y^2 \rangle$ and the level of agreement is the same.

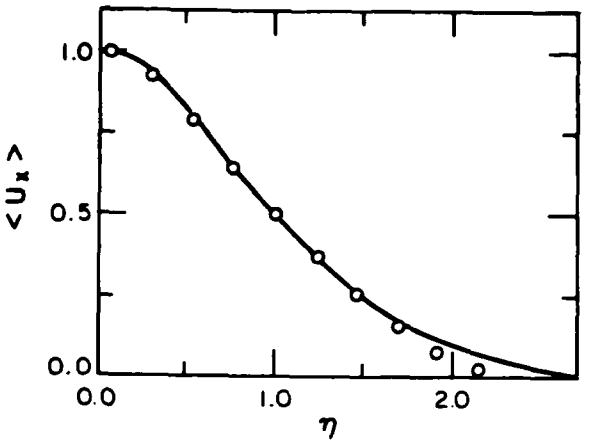

Fig. 1: Mean axial velocity against lateral distance: —— calculation; o experiment [7].

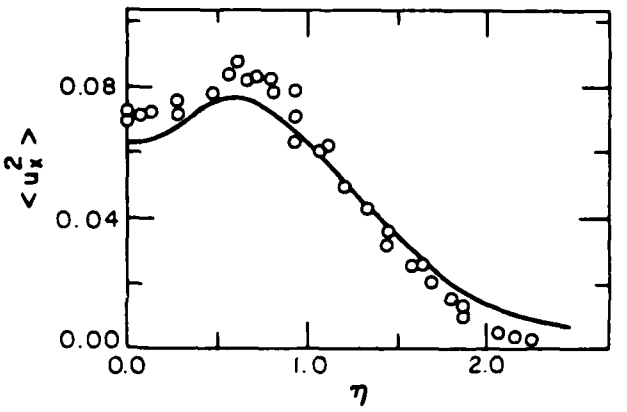

Fig. 2: Mean square axial velocity fluctuations against lateral distance: —— calculation; o experiment [7].

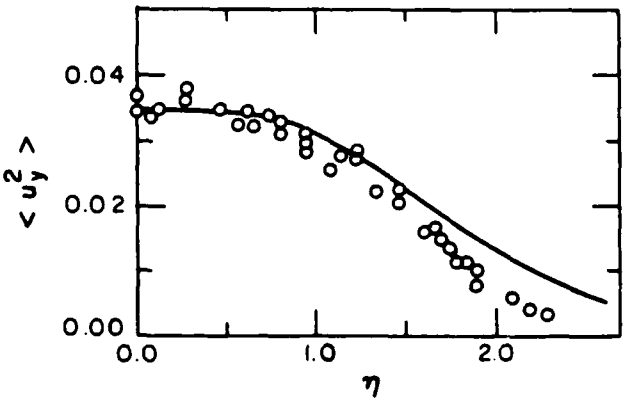

Fig. 3: Mean square lateral velocity fluctuations against lateral distance: —— calculation o experiment [7].

Profiles of the shear stress $\langle u_x u_y \rangle$ are shown in figure 4. It may be seen that the measured values are, typically, 20% lower than the calculations. Using the measured mean velocity and normal stresses, Heskestad used the axial momentum equation to obtain an independent estimate of the shear stress. This estimate (indicated by the broken line) is in good agreement with the calculations. This supports Heskestad's conclusion that the measured values of $\langle u_x u_y \rangle$ are subject to error.

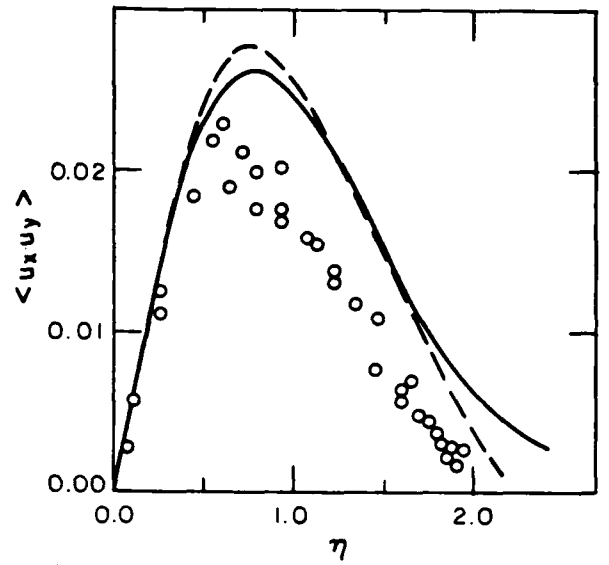

Fig. 4: Shear stress against lateral distance: —— calculation; o experiment [7]; - - - - deduced from measured mean velocity and momentum balance [7].

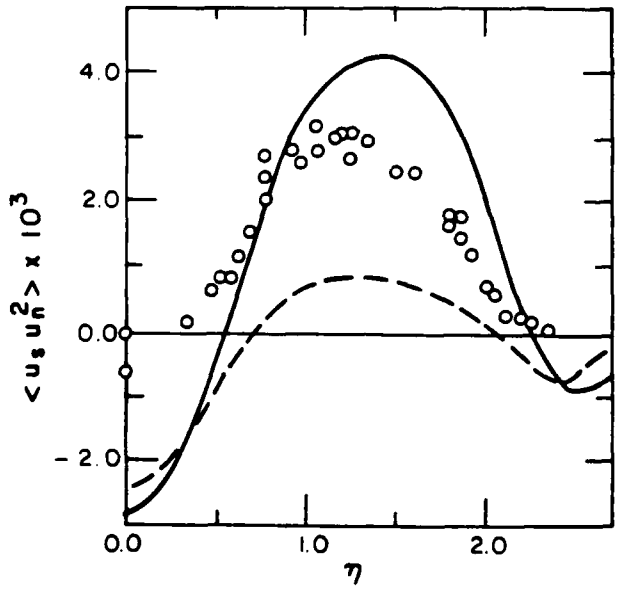

Fig. 5: Triple velocity correlation against lateral distance: —— calculation; o experiment [7]; - - - gradient model [8] evaluated from calculated Reynolds stresses.

Heskestad's results include triple velocity correlations, measured in a local mean-streamline coordinate system. In the x - y plane, the fluctuating velocity components parallel and normal to the mean velocity vector are u_s and u_n. Figure 5 shows measured and calculated values of the triple correlation $\langle u_s u_n^2 \rangle$. Also shown on the figure is the value of the triple correlation obtained from Launder, Reece and Rodi's [8] gradient-diffusion model. Near to the plane of symmetry $0 \leq \eta \leq 0.5$, both the joint-pdf calculations and the gradient model give significant negative values, while the measured values are close to zero. The maximum value of $\langle u_s u_n^2 \rangle$ occurs at $\eta = 1$: the maximum value from the joint-pdf calculation is 30% greater than that measured, while for the gradient model it is 80% less. The level of agreement between the measurements and the joint-pdf calculations is satisfactory considering the likely measurement error and the simplicity of the closure assuptions.

This completes the comparison of calculated velocity statistics with the experimental data of

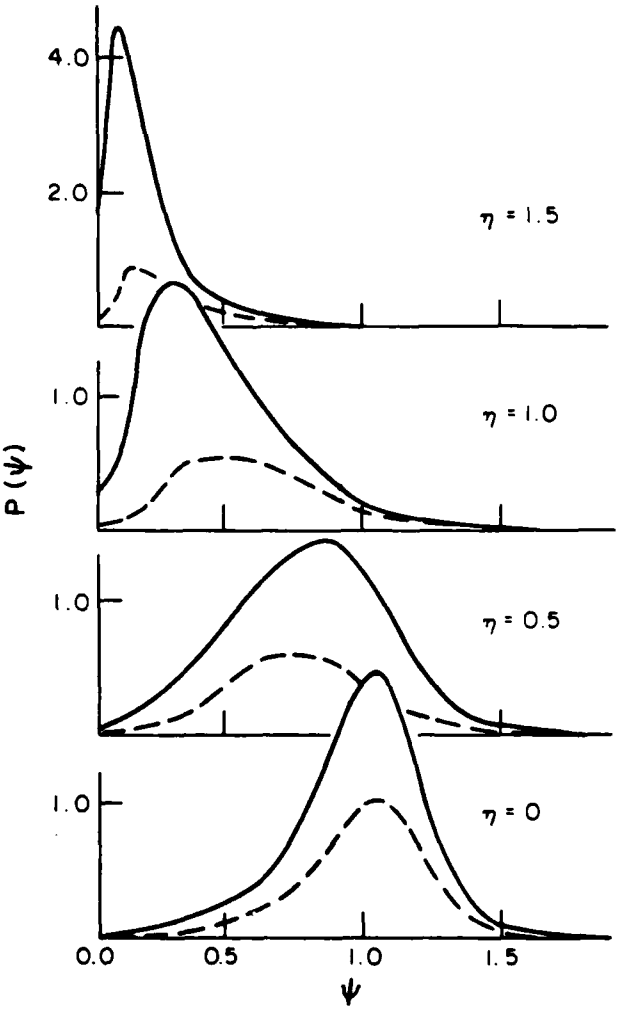

Fig. 6: Scalar pdf's and the contribution from outward-flowing fluid at different lateral positions: —— $p(\psi)$; - - - $p_+(\psi)$.

Heskestad. For the scalar field, the only measurements are for the mean profile, see [12], for example. It is found that for the self-similar plane jet, the spreading rate of the mean scalar is 40% greater than the spreading rate of the mean velocity. In the calculation, however, the scalar spreading rate is 5% less. This disappointing result is undoubtedly due to the simplistic modelling of the fluctuating pressure gradient terms. Future calculations that included the rapid term and the pressure transport term will, hopefully, not suffer from this defect. The normalized scalar profile (not shown) is calculated accurately.

Figure 6 shows the scalar pdf $p(\psi;\eta)$ (for different values of η) and $p_+(\psi;\eta)$, which is the contribution to $p(\psi;\eta)$ from outward-flowing fluid:

$$p_+(\psi;\eta) = \int_{-\infty}^{\infty}\int_{0}^{\infty}\int_{-\infty}^{\infty} f(V_r,V_\theta,V_z,\psi;\eta)\, dV_r dV_\theta dV_z. \quad (22)$$

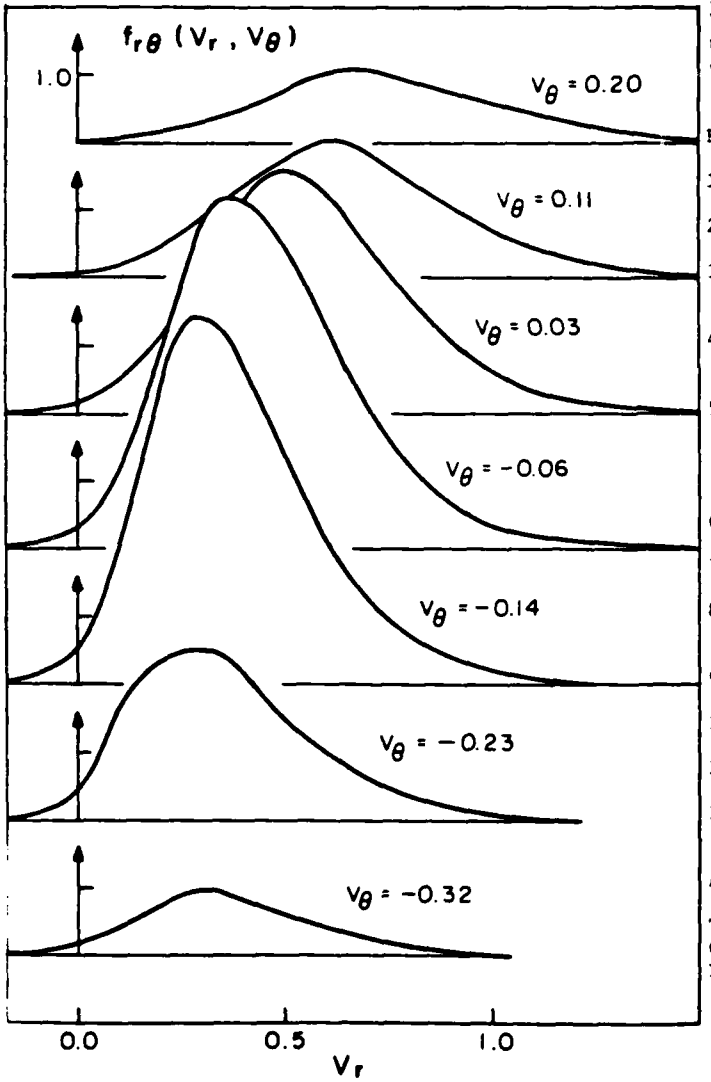

Fig. 7: Joint pdf of radial and circumferential velocity at $\eta = 1.0$.

On the plane of symmetry, $p(\psi)$ is bell-shaped and, because (for $\eta = 0$) inflowing and outflowing fluid are indistinguishable, $p_+(\psi)$ is equal to one half of $p(\psi)$. At the furthest location ($\eta = 1.5$) $p(\psi)$ is centered on low values of ψ corresponding to recently entrained fluid: $p_+(\psi)$ is biased towards larger values of ψsince outward-flowing fluid comes from the interior of the jet where the level of ϕ is higher.

Figure 7 shows the joint pdf of the radial and circumferential velocities at $\eta = 1.0$. This joint pdf is defined by

$$f_{r\theta}(V_r,V_\theta) = \int\int f(V_r,V_\theta,V_z,\psi)\, dV_z d\psi. \quad (23)$$

The figure shows $f_{r\theta}(V_r,V_\theta)$ plotted against V_r for different values of V_θ. At this location ($\eta = 1.0$), the mean circumferential velocity is $\langle U_\theta \rangle = -0.04$, and the mean radial velocity is $\langle U_r \rangle = 0.5$. It may be seen that the joint pdf is a maximum close to $V_r = \langle U_r \rangle$, $V_\theta = \langle U_\theta \rangle$. That the curves of $f_{r\theta}(V_r,V_\theta)$ move to higher values of V_r as V_θ increases indicates that the shear stress $\langle u_r u_\theta \rangle$ is positive (cf. fig. 4).

REFERENCES

1. S.B. Pope: Phys. Fluids 24, 588 (1981)
2. T.S. Lundgren: Phys. Fluids 12, 485 (1969)
3. C. Dopazo, E.E. O'Brien: Acta Astronaut 1, 1239 (1974)
4. S.B. Pope: 18th Symposium (International) on Combustion, The Combustion Institute (1981)
5. J. Janicka, W. Kolbe, W. Kollmann: Proceedings of the Heat Transfer and Fluid Mechanics Institute, Stanford University Press, p. 296 (1978)
6. S.B. Pope: Combust. Sci. Tech. 25, 159, (1981)
7. G. Heskestad: J. Appl. Mech. 32, 721 (1965)
8. B.E. Launder, G.J. Reece, W. Rodi: J. Fluid Mech. 68, 537 (1975)
9. J.C. Rotta: Z. Phys. 129, 547 (1951)
10. R.L. Curl: A.I.Ch.E. J. 9, 175 (1963)
11. D.B. Spalding: Chem. Eng. Sci. 26, 95 (1971)
12. P.E. Jenkins, V.W. Goldschmidt: A.S.M.E. J. Fluids Eng. 95, 581 (1973)

ACKNOWLEDGEMENT

This work was supported in part by grant number CPE8000026 from the National Science Foundation, Engineering energetics program.

PREMIXED COMBUSTION IN A TURBULENT BOUNDARY LAYER WITH INJECTION

S. MEUNIER, M. CHAMPION, J.C. BELLET
Laboratoire d'Energétique et de Détonique
E.N.S.M.A. - rue Guillaume VII
86034 POITIERS Cedex (France)

ABSTRACT

The reactive flow obtained by injecting a fresh mixture of propane and air in a stream of hot gas through a porous plate is studied both theoretically and experimentally. Using Favre averaging and a temperature probability density function the closed set of 7 transport equations is solved. The numerical results are compared with measurements of mean velocity, velocity RMS value and mean temperature.

NOMENCLATURE

- F injection rate
- $\tilde{k}$ mass weighted kinetic energy of turbulence
- $\bar{p}$ mean pressure
- P probability density function
- T temperature
- $\tilde{u}$ mass weighted mean velocity (x component)
- u'' fluctuating part of u (Favre decomposition)
- $\tilde{v}$ mass weighted mean velocity (y component)
- x longitudinal coordinate
- y transversal coordinate
- Y_p product mass fraction
- δ boundary layer thickness
- $\tilde{\epsilon}$ dissipation of $\tilde{k}$
- μ_T eddy viscosity

SUBSCRIPTS

- b burnt gas
- e chemical equilibrium
- f fresh mixture
- w wall

OVERSCRIPTS

- $\bar{}$ conventional average
- $\tilde{}$ mass weighted average

INTRODUCTION

Turbulent boundary layer with injection and combustion is an important problem occuring in many practical devices. In such a configuration, the interaction between turbulence and chemical reactions which occur within the flow can be very strong. Many works have been devoted to the case where the fuel and the oxydiser are not premixed /1-2/ and where it is generally admitted that the flame sheet model is valid i.e. the flow is controlled by turbulent mixing rather than chemical kinetics. In the present work an experimental and theoretical study is made on the structure of a premixed turbulent combustion zone. This zone is obtained by injecting a fresh mixture of propane and air through a porous plate into an incoming flow of hot gas. The purpose of this paper is to describe the structure of this turbulent reactive boundary layer with injection in term of the mean quantities profiles such as velocity $\tilde{u}$, velocity RMS value $\sqrt{\overline{u''^2}}$, mean temperature $\bar{T}$ and to investigate the effect of the combustion on the turbulent flow. A comparison between the experimental results and numerical calculations is made through a model which employs a classical $\tilde{k} - \tilde{\epsilon}$ type of closure and where a probability density function of the temperature is defined in order to express the mean chemical production rate in a closed form.

EXPERIMENTAL APPARATUS

The schematic diagram of the experimental apparatus is shown in Figure 1. It consists of a 10 cm square channel, 21 cm in length, fed with hot burnt gas (1370 K) coming from an upstream burner, and whose lower wall is a porous plate. With a Reynolds number Re which is about 5.10^4 a turbulent boundary layer is formed on this plate. A fresh mixture of propane and air at an equivalence ratio ϕ_f (< 1) and diluted with nitrogen is injected through the plate into this hot boundary layer. Then a combustion zone stabilized by the hot gas is obtained. The injection rate is defined by :

$$F = \rho_f v_f / \rho_b u_b$$

where f and b refer to fresh and burnt gas respectively and its value is varied from 0.01 to 0.02.

The mean stream wise velocity $\bar{u}$ and its RMS value $(\overline{u'^2})^{1/2}$ are measured in the boundary layer by means of a Laser Doppler Anemometry system and bias corrections are made according to Durao et al. /3/. The mean temperature $\bar{T}$ is obtained using a chromel-alumel thermocouple.

THE REACTION AND TURBULENCE MODEL

The combustion is sustained by a global reaction between the fresh mixture M of propane-air and the burnt product :

$$M \rightarrow P$$

whose order is taken to be 1.8 and where N_2 is considered as a diluent.

Moreover the assumption is made that, in the combustion zone itself, i.e. where the chemical production rate ω is not negligible, the change of enthalpy h is due to the heat release only. Then, when the Lewis numbers of the different species are unity, and introducing an instantaneous equation for the conservation of carbon, the temperature T can be

defined as the reaction progress variable /4/. Thus, using mass weighted averaged quantities defined by :

$$g = \tilde{g} + g'' \quad \text{with} \quad \tilde{g} = \overline{\rho g}/\bar{\rho} \quad \forall g \qquad (1)$$

The turbulence compressible reactive flow is described by the following set of transport equations where all turbulent transport and dissipation terms are closed according to a $\tilde{k} - \tilde{\varepsilon}$ model /5-6/. The general following form for those equations is :

$$\frac{\partial}{\partial x}(\bar{\rho}\,\tilde{u}\,\tilde{\phi}) + \frac{\partial}{\partial y}(\bar{\rho}\,\tilde{v}\,\tilde{\phi}) - \frac{\partial}{\partial y}(\bar{\rho}\mu_T^{*}\frac{\partial \tilde{\phi}}{\partial y}) = \bar{S}_\phi \qquad (2)$$

The expression of μ_T^{*} and $\bar{S}_\phi$ for each equation is given in table 1.

to :

$$\widetilde{u''T''} = -C_4 \frac{\tilde{k}}{\tilde{\varepsilon}}\left(\frac{2\mu_T}{\bar{\rho}}\frac{\partial \tilde{u}}{\partial y}\frac{\partial \tilde{T}}{\partial y} + \frac{\widetilde{T''^2}}{\bar{\rho}\,\tilde{T}}\frac{d\bar{p}}{dx} - \frac{\overline{u''\omega_T}}{\bar{\rho}}\right)$$

and following Borghi and Dutoya /8/ the last term of this expression is given by :

$$\overline{u''\omega_T} = \frac{\widetilde{u''T''}}{\widetilde{T''^2}}\overline{\omega_T T''}$$

and finally :

$$\widetilde{u''T''} = -C_4 \frac{\tilde{k}}{\tilde{\varepsilon}}\left(\frac{2\mu_T}{\bar{\rho}}\frac{\partial \tilde{u}}{\partial y}\frac{\partial \tilde{T}}{\partial y} + \frac{\widetilde{T''^2}}{\bar{\rho}\,\tilde{T}}\frac{d\bar{p}}{dx}\right)\Big/\left(1 - C_4 \frac{\tilde{k}}{\tilde{\varepsilon}}\frac{\overline{\omega_T T''}}{\bar{\rho}\,\widetilde{T''^2}}\right)$$

where the constant C_4 has given a value of 0.35 /6/.

equation	$\tilde{\phi}$	μ_T^{*}	$\bar{S}_\phi$
continuity	1	0	0
x momentum	$\tilde{u}$	μ_T	$-\frac{\partial \bar{P}}{\partial x}$
kinetic energy of turbulence	$\tilde{k}$	μ_T	$\mu_T(\frac{\partial \tilde{u}}{\partial y})^2 - \overline{u''}\frac{\partial \bar{P}}{\partial x} - C_3\,\bar{\rho}\,\tilde{k}\,(\frac{\partial \tilde{u}}{\partial x} + \frac{\partial \tilde{v}}{\partial y}) - \bar{\rho}\,\tilde{\varepsilon}$
product mass fraction	$\tilde{Y}_p$	$\frac{\mu_T}{Sc_y}$	$\overline{\omega_y}$
temperature	$\tilde{T}$	$\frac{\mu_T}{Pr_T}$	$\overline{\omega_T}$
dissipation of $\tilde{k}$	$\tilde{\varepsilon}$	$\frac{\mu_T}{\sigma_\varepsilon}$	$\frac{\tilde{\varepsilon}}{\tilde{k}}(C_1\,\mu_T\,(\frac{\partial \tilde{u}}{\partial y})^2 - C_2\,\bar{\rho}\,\tilde{\varepsilon})$
temperature mean square fluctuation	$\widetilde{T''^2}$	$\frac{\mu_T}{Pr_T}$	$\overline{\omega T''} + \mu_T\,(\frac{\partial \tilde{T}}{\partial y})^2 - \bar{\rho}\frac{\tilde{\varepsilon}}{\tilde{k}}\widetilde{T''^2}$

Table 1 - Diffusion coefficients and source terms for governing differential equations.

Values of the various constants appearing in Table 1 are given below :

$\sigma_\varepsilon = 1.3 \quad Sc_y = 1. \quad Pr_T = 0.7$

$C_\mu = 0.09 \quad C_1 = 1.55 \quad C_2 = 2. \quad C_3 = 1.$

and μ_T is the usual eddy viscosity defined by :

$$\mu_T = C_\mu\,\bar{\rho}\,\frac{\tilde{k}^2}{\tilde{\varepsilon}}$$

The dilatation term $C_3\,\bar{\rho}\,\tilde{k}\,(\frac{\partial \tilde{u}}{\partial x} + \frac{\partial \tilde{v}}{\partial y})$ of the $\tilde{k}$ equation has been modeled according to Bray /7/ and represents the change of kinetic energy of turbulence due to the heat release. This term corresponds to a decrease of $\tilde{k}$ and $\widetilde{u''^2}$ and we found it important in the computation. Taking an equation of state into account, the pressure term $-\overline{u''}\,d\bar{p}/dx$ can be written :

$$-\overline{u''}\frac{d\bar{p}}{dx} = -\frac{\widetilde{u''T''}}{\tilde{T}}\frac{d\bar{p}}{dx}$$

The transport term $\widetilde{u''T''}$ is then expressed by assuming that production balances exactly dissipation in the transport equation for this quantity. This leads

It must be noticed that this model implies that μ_T is a positive quantity and then no "counter diffusion", due to an eventual important transversal mean pressure gradient $\partial\bar{p}/\partial y$, occurs /9/. This implicit assumption has to be confirm or infirm by measuring the transport term $\overline{v''T''}$.

The mean chemical rates $\overline{\omega_Y}$ and $\overline{\omega_T}$ are closed by introducing a probability density function $\mathbb{P}(T)$ such that :

$$\overline{\omega_\alpha} = \int_{T_w}^{T_e} \mathbb{P}(T)\,\omega_\alpha(T)\,dT \qquad \alpha = Y,\ T$$

and $$\overline{\omega_\alpha T''} = \int_{T_w}^{T_e} \mathbb{P}(T)\,T\,\omega_\alpha(T)\,dT - \overline{\omega_\alpha}\,\tilde{T} \qquad \alpha = Y,\ T$$

where T_e is the equilibrium temperature corresponding to a product mass fraction Y_p whose value is unity. According to an extended Bray and Moss model /10/ the structure of such a probability density function is taken to be a uniform value between either two Dirac delta peaks in T_w and T_e or two limiting temperatures T_1 and T_2. In any case the

p.d.f. depends on three parameters which are related to $\tilde{T}$ and $\tilde{T}''^2$ by :

$$\tilde{T} = \frac{1}{\bar{\rho}} \int_{T_w}^{T_e} \rho T \, \mathbb{P}(T) \, dT$$

$$\tilde{T}''^2 = \frac{1}{\bar{\rho}} \int_{T_w}^{T_e} \rho \, T^2 \, \mathbb{P}(T) \, dT - \tilde{T}^2$$

$$1 = \int_{T_w}^{T_e} \mathbb{P}(T) \, dT$$

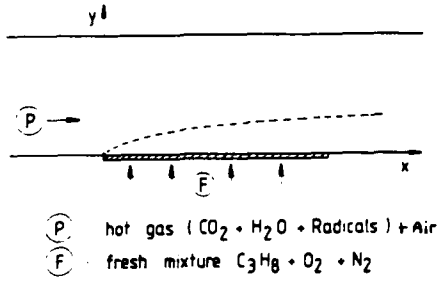

Fig. 1 - Schematic of the 10 cm square channel.

NUMERICAL METHOD

The parabolical partial differential set of equations shown in table 1 are solved by using a procedure which employs a Crank-Nicholson type of discretisation /15/ and where a special treatment of the flow close to the wall has been developed in order to deal with the strong injection rates.

Initial profiles (x = 0) are given from the experiments for mean velocity $\tilde{u}$, the corresponding RMS value $\tilde{u}''^2$, mean temperature $\tilde{T}$ and mean product mass fraction $\tilde{Y}_p$. Different assumptions were made to prescribe the initial values of $\tilde{\varepsilon}$ and $\tilde{T}''^2$ but calculations performed with different initial profiles for those quantities proved that the computed values at the working distance i.e. x = 19 cm are rather insensitive to the initial conditions.

RESULTS AND DISCUSSION

Before discussing the results, it must be emphasized that the measured mean values differ from the mass weighted averages, the difference being given by :

$$\tilde{g} - \bar{g} = \overline{\rho' g'} / \bar{\rho} \quad \forall g$$

In fact, studying a mixing layer with density gradients whose orders of magnitude are about the same as those that we can expected in our present study, Chassaing et al. /14/ showed a good agreement between computed and experimental profiles for mean velocity $\tilde{u}$ and rather small discrepancies for second order correlations such as $\tilde{u}''^2$.

Moreover, it must be pointed out that the only part of $\tilde{k}$ which was measured is $\tilde{u}''^2$. It is the reason why we solved an additive equation for $\tilde{u}''^2$, which, in a closed form, can be written as

$$\bar{\rho} \tilde{u} \frac{\partial \tilde{u}''^2}{\partial x} + \bar{\rho} \tilde{v} \frac{\partial \tilde{u}''^2}{\partial y} + \frac{\partial}{\partial y}\left(\mu_T \frac{\partial \tilde{u}''^2}{\partial y}\right) = + 2 \mu_T \left(\frac{\partial \tilde{u}}{\partial y}\right)^2$$

$$- 2 \overline{u''} \frac{\partial \bar{p}}{\partial x} - 2 \bar{\rho} \frac{\tilde{\varepsilon}}{\tilde{k}} \tilde{u}''^2 - 2 \bar{\rho} \tilde{u}''^2 \frac{\partial \tilde{u}}{\partial x}$$

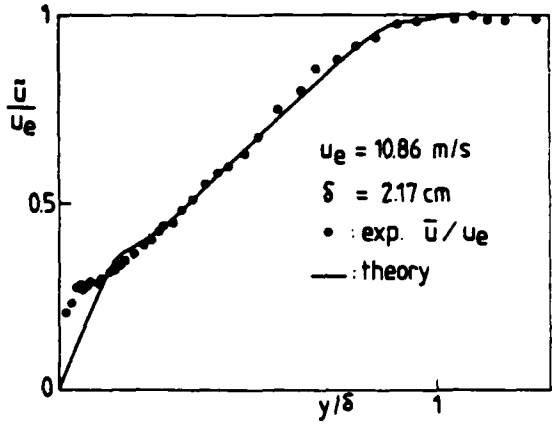

Fig. 2 - Cold flow
mean velocity profile
x = 19 cm, F = 0.02

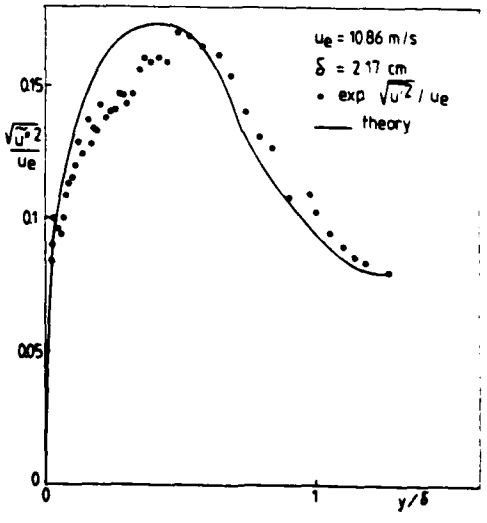

Fig. 3 - Cold flow
Intensity of velocity fluctuations
at x = 19 cm, F = 0.02

As a first step the characteristics of the corresponding cold boundary layer with injection are investigated both experimentally and theoretically ; the flow being obtained by replacing burnt gas and fresh mixture by air at ambiant temperature ($T_b \simeq T_w \simeq 290$ K). This case without chemical reaction and without important density variations was also used to illustrate the computation capability with strong injection rates. Mean streamwise velocity and the corresponding R.M.S. value for F= .02 are shown in figures 2 and 3. It is noticeable that, for such a value of F, the position of maximum $\tilde{u''^2}$ is clearly distinct from the plate.

Experiments with combustion show that a stationnary premixed combustion zone stabilized only by the hot burnt gas is obtained in the turbulent boundary layer if the porous plate is sufficiently cooled by the fresh mixture of propane and air. At an equivalence ratio which is unity, this requirement is full filled by diluting this injected fresh mixture with nitrogen /11/. The mass fraction $y^*_{N_2}$ of added nitrogen is :

$$y^*_{N_2} \simeq 0.2$$

With this value of $y^*_{N_2}$ the temperature T_w of the plate, which is 1000 K at x = 0, is stationnary and slightly decreases with x.

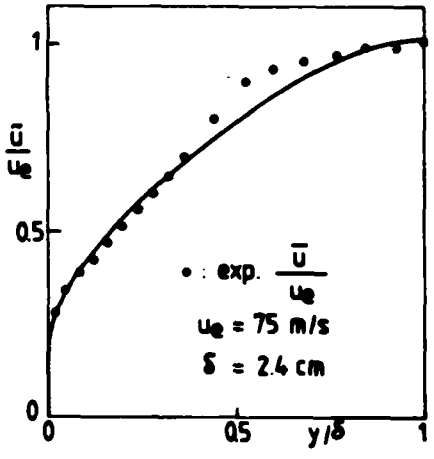

Fig. 4 - Velocity profile, x = 19 cm, F = 0.01

Figures 4 to 6 show the transverse profiles of streamwise mean velocity, streamwise velocity R.M.S. value and mean temperature for F = 0.01. The thickening of the boundary layer which is a result of combustion is found to be not very sensitive to the value of F up to F = 0.02 ($\delta \simeq 2.4$ cm). Figure 5 shows a discripency between the predicted $\tilde{u''^2}$ profiles and measurements at a position which corresponds to the maximum of heat release. This difference is due to the fact that, as it is illustrated by figure 7, the measured streamwise velocity probability density function $\mathbb{P}(u)$ is found to be bi-modal in the zone where the chemical reaction rate is large. This behaviour of the velocity field, which cannot be easily taken into account by our present theoretical model, corresponds to a low frequency oscillation of the combustion zone. This phenomenon has been already observed in others studies of reactive boundary layers, particularly by Cheng et al. /12/ in the case of a

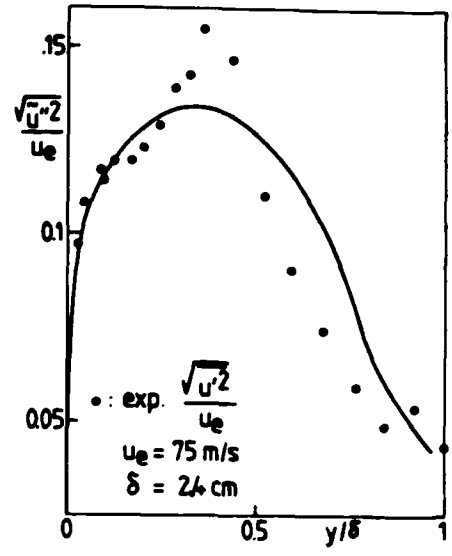

Fig. 5 - Velocity fluctuations profile, x = 19 cm, F = 0.01.

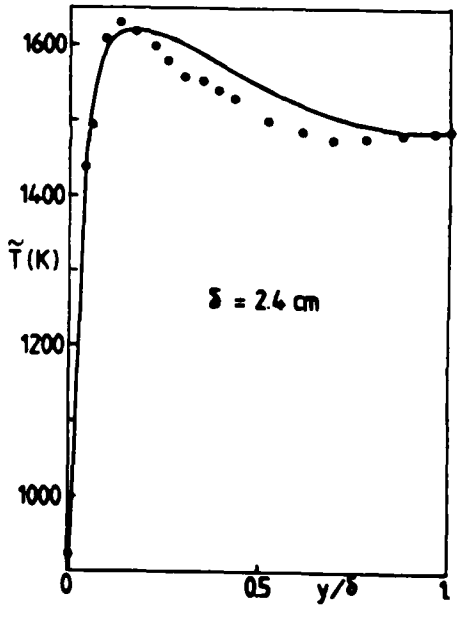

Fig. 6 - Mean temperature profile, x = 19 cm, F = 0.01.

premixed combustion developing over a heated flat plate.

The case with F = 0.014 is illustrated by figures 8, 9 and 10. As far as it concerns the mean velocity and mean temperature profiles through the boundary layer the agreement between computation and experimental results is reasonably good. However it is noticeable that the measured velocity profile exhibits an inflection (already slightly apparent in figure 4 for F = 0.01) and which is not well recovered by the numerical model. This effect which has been also noticed in the case of a diffusion flame over a flat

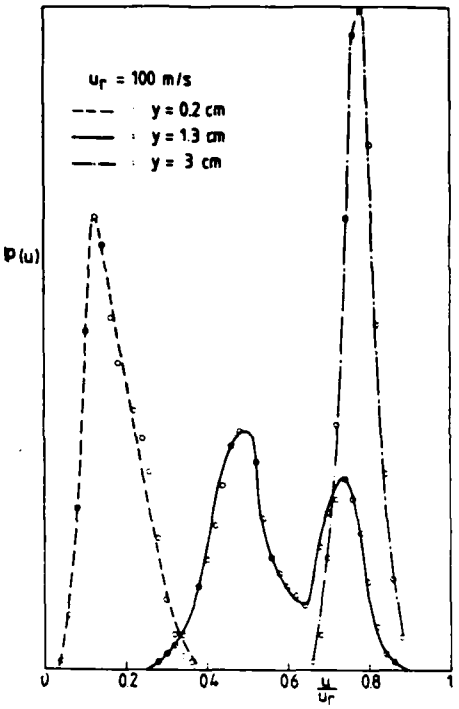

Fig. 7 - Velocity probability density function, x = 19 cm, F = 0.01.

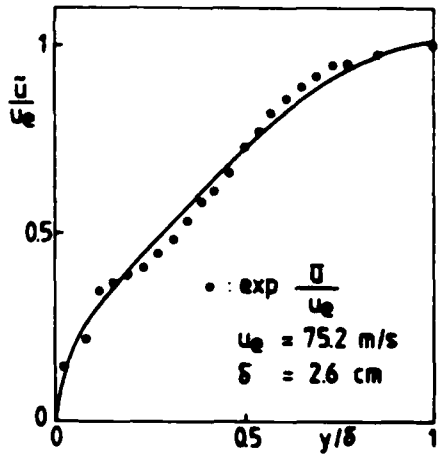

Fig. 8 - Velocity profile, x = 19 cm, F = 0.014.

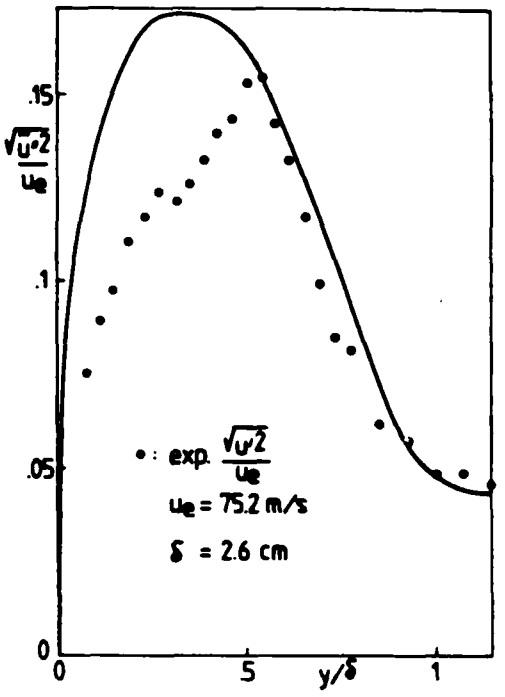

Fig. 9 - Velocity fluctuations profile, x = 19 cm, F = 0.014.

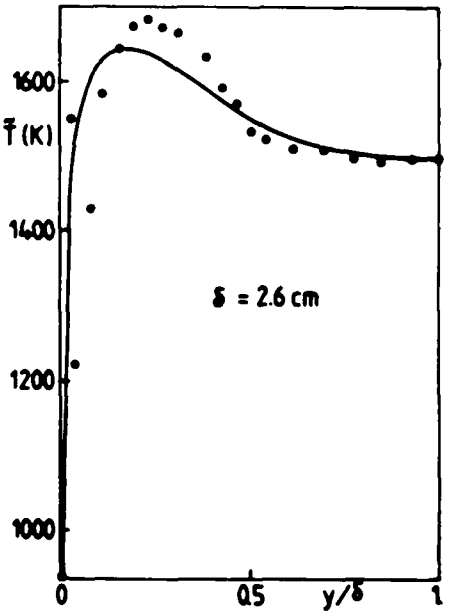

Fig. 10 - Mean temperature profile, x = 19 cm, F = 0.014.

plate by Wooldridge and Muzzy /13/ seems to be due to a transverse pressure gradient $\partial\bar{p}/\partial y$ associated with the accelerating effect of the flame. However pressure measurements through the boundary layer should be performed to confirm this explanation.

The discrepancy which appears between the velocity R.M.S. fluctuation profiles is more difficult to explain since it can be the consequence of different effects. A relative thickening of the combustion zone invalidating the usual closure for dissipation terms /16/ might be the cause of this phenomenon.

CONCLUSION -

The present work reports the first experimental and theoretical results of an investigation of the turbulent boundary layer with wall injection of a propane-air mixture. It demonstrates that there is a good agreement between measurements and computation up to an injection rate of 0.01. For larger injection

rates phenomena due to pressure and probably dissipation effects occur. Pressure measurements should be performed before going further into the model. The finding of a velocity probability density function which is bi-modal at the location of the combustion zone is of interest and this property could be introduced in a more elaborate model.

REFERENCES -

/1/ - ROSNER D.E., "Correlation and prediction of boundary layer energy transfer rates in the presence of chemical reactors and mass injection", Combustion Science and Technology, vol. 10, 1975, pp. 97-108.

/2/ - SENDA M., SUZUKI K., SATO J., "Study on turbulent boundary layer with injection and combustion", Memoirs of the faculty of engineering, Kyoto University 38, 1, p. 21, 1976.

/3/ - DURAO D.F.G., LAKER J., WHITELAW J.H., "Bias effects in laser Doppler anemometry", J. Physics C. Science Inst., vol. 13, 1980.

/4/ - BRAY K.N.C., LIBBY P.A., "Interaction effects in turbulent premixed flames" The Physics of Fluids, vol. 19, n°11, 1976.

/5/ - JONES W.P., LAUNDER B.E., "The prediction of laminarization with a two equations model of turbulence", Int. J. Heat and Mass Transfer, vol. 15, p. 301, 1972.

/6/ - LAUNDER B.E., "Turbulence transport models for numerical computation of fluid flow", Report n° ME-213, Winter 1980, University of California.

/7/ - BRAY K.N.C., "Kinetic energy of turbulence in flames", "Analytical and numerical methods for investigation of flow fields with chemical reactions, especially related to combustion", 1975, AGARD CP-164, p. II.2.1.

/8/ - BORGHI R., DUTOYA D., "On the scales of the fluctuations in turbulent combustion", 17th Symposium (International) on Combustion, 1979, p. 235.

/9/ - LIBBY P.A., BRAY K.N.C., "Counter-gradient diffusion in premixed turbulent flames", AIAA 18th Aerospace Sciences Meeting, Pasadena (Calif.), 1980.

/10/ - CHAMPION M., BRAY K.N.C., MOSS J.B., "The turbulent combustion of a propane-air mixture", Acta Astronautica, vol. 5, 1978, p. 1063.

/11/ - LIBBY P.A., Personnal communication.

/12/ - CHENG R.K., BILL R.G., Jr., ROBBEN F., SCHEFER R., TALBOT L., "Experimental study of combustion in a turbulent boundary layer", Symp. on turbulent shear flow, 1979, Imperial College, London.

/13/ - WOOLDRIDGE C.E., MUZZY R.J., "Measurements in a turbulent boundary layer with porous wall injection and combustion", 10th Symposium (International) on Combustion, 1965, p. 1351.

/14/ - CHASSAING P., HA MINH H., BOISSON H., "Mass transport in turbulent round jet", Symp. on turbulent shear flow, 1979, Imperial College, London.

/15/ - ROACHE P.J., Computational Fluid Mechanics, Hermosa Publishers, Albuquerque, 1972.

/16/ - LIBBY P.A., BRAY K.N.C., "Implications of the laminar flamelet model in premixed turbulent combustion, Combustion and Flame. vol. 39, 1980, p. 33.

ACKNOWLEDGEMENTS -

This work has been supported by the C.N.R.S. under grant A.T.P. n° 3983. The authors wish to thank Dr. P. Cambray for his excellent technical contribution. They are also indebted to Dr. P. Joulain and Dr. J.M. Most for stimulating research discussions and technical assistance.

LAGRANGIAN-EULERIAN CALCULATION OF TURBULENT DIFFUSION FLAME PROPAGATION*

Wm. T. Ashurst and P. K. Barr

Combustion Technology Department

Sandia National Laboratories

Livermore, California 94550

ABSTRACT

This paper explores the effect of time-dependent turbulent flow structure on diffusion of a conserved scalar. The conserved scalar can represent diffusion flame propagation when the flame sheet model is used. The time-dependent flow structure is calculated by the Lagrangian discrete vortex dynamics method. The flow field is two-dimensional and is confined to a square by the use of periodic boundary conditions. The velocity field defined by the known vortex locations determines the convection velocity of the scalar on a fixed Eulerian mesh. The scalar convection and diffusion is calculated with a flux-corrected transport algorithm which allows steep gradients to be computed without exceeding the scalar bounds of zero and one. The effect of turbulence intensity on scalar diffusion has been calculated at three intensity levels at a fixed length scale. The enhanced diffusion effect can be correlated with a linear dependence on turbulence intensity at fixed length scale.

NOMENCLATURE

c_1, c_2 = constants in amplitude time function
c_f = fuel concentration
D = mass diffusivity coefficient
L = reference length unit
N = number of discrete vortices, equals 200
Q = quantity of fuel
r = position vector
r_{core} = vortex core radius
S = conserved scalar concentration
t = time
$\vec{u}$ = Eulerian velocity vector
$\vec{U}$ = Lagrangian velocity vector
x, y = Cartesian coordinate system
$\vec{X}$ = Lagrangian position vector
Γ = vortex circulation strength
δt = discrete time step, equals 0.00625τ
τ = reference time unit
Ψ = vortex produced streamfunction

INTRODUCTION

The ability to calculate chemically reacting flow involving 50 or 100 different reactions is now an accomplished numerical technique for laminar flow. Details of chemical nonequilibrium structure in realistic systems can be studied (Miller and Kee, 1977). In addition to these steady state solutions, non-linear oscillations have been predicted (Margolis, 1980) and experimentally confirmed (Stephenson, 1980) for premixed flames when the flame speed is much smaller than the adiabatic limit. Unfortunately, in most practical applications the flow is turbulent and not laminar. The interplay between turbulent mixing and chemical reaction is not well understood (e.g., see review by Murthy, 1975). Even the observed "turbulent" flame speed may be unique to the overall experiment geometry since both the turbulence intensity and length scale affect the propagation of the reaction zone. Williams and Libby (1980) have reviewed recent progress in the field of turbulent combustion and find the persistent assumption of gradient transport inappropriate for reacting flow. They cite several experiments where the turbulent fluxes are opposed to the mean gradient direction. In order to avoid the gradient transport model, this paper explores the interaction between time-dependent turbulent flow structure and a diffusion flame.

The time-dependent turbulent flow structure has been calculated by the discrete vortex dynamics method. This Lagrangian method has the capability to simulate a turbulent mixing layer (Ashurst, 1979) and two-dimensional separated flow (Ashurst *et al.*, 1980). While the velocity field is described by the Lagrangian solution of the discrete vorticity motion, the conserved scalar transport is calculated with a fixed Eulerian mesh. Following the work of Grötzbach and Schumann (1979), the conservation laws are written for finite grid volumes and a staggered grid is used. The fluxes are defined at the grid volume surfaces and the scalar quantities are defined at the center of the grid volumes. Though in the work of Grötzbach and Schumann, the effect of subgrid-scale motion upon the fluxes required a turbulence model, in this new combined Lagrangian-Eulerian method, a turbulence model is not needed since subgrid-scale fluxes can be directly calculated from the known discrete vortex locations. Thus this hybrid calculational scheme has the advantage that if a model of subgrid motion is needed, it will be needed only at a length scale much smaller than the numerical grid size, i.e., at the vortex core size. Consequently, the results will be less sensitive to turbulence modeling assumptions. In these preliminary results no such model has been used and the subgrid-scale fluxes have been temporarily ignored.

The flame sheet approximation of Burke and Schumann is used to obtain a simple reaction system (see description in Miller and Kee, 1977). Assuming chemical reaction rates that are much faster than turbulent mixing rates produces an infinitely thin reaction zone which is spatially located wherever there is a stoichiometric ratio of fuel to oxidizer. This assumption of infinite reaction rate combined with the conserved scalar technique makes the combustion calculation extremely simple. The conserved scalar equation is created by adding the species equations together in such a way that the chemical reaction rate terms are eliminated. Thus only a single transport equation, which has no chemical source terms, needs to be solved (see Williams and Libby and the work by Bilger cited therein).

For these calculations a constant mass diffusivity coefficient and constant density have been used. Thus the current results focus on the effect of turbulence upon diffusion flame propagation. Relaxation of the constant-density assumption will require incorporation of two effects: 1) perturbation of the vortex produced velocity field by the volume expansion in the reaction zone, and 2) vorticity generation from the density gradient vector crossed with the pressure gradient vector term in the Lagrangian vorticity transport equation. The importance of such a calculation is that it would provide the feedback of chemical heat release upon the turbulence and is the goal of future work.

*This work supported by DOE, Office of Basic Energy Sciences.

FLOWFIELD

The flowfield is two-dimensional and is confined to a square of side length L through the use of periodic boundary conditions. If during the calculation a discrete vortex leaves one edge of the square it will enter the square on the opposite side. Each discrete vortex has a single pairwise interaction with each of the remaining vortices. Because of the periodic boundaries, the largest separation distance of a vortex pair in each coordinate direction is $L/2$. The vortex streamfunction is

$$\Psi = -\frac{\Gamma}{4\pi}\ln(r^2 + r_{core}^2) \tag{1}$$

where r is the distance from the vortex center, r_{core} the vortex core radius, and Γ the circulation strength. In a previous calculation of two-dimensional separated flow in a channel, the Poisson equation for the streamfunction was numerically solved to determine the vortex velocity on the finite-difference mesh. However, as described in that work (Ashurst *et al.*, 1980) the mesh-calculated velocity must be corrected at short range (within 3 cell lengths) to remove non-physical mesh effects. In the current work, direct calculation of velocity and streamfunction has been used and so no mesh corrections are required.

To calculate the transport of the conserved scalar, an Eulerian mesh with a 40-by-40 mesh size is used. The flow is calculated in a periodic two-dimensional square with side length L. The distance L is used to non-dimensionalize all length units. A reference time unit τ is used to reduce all time quantities. Thus, these numerical results may be scaled by L and τ. The transport equation for a conserved scalar S is

$$\frac{\partial S}{\partial t} + \nabla \cdot \vec{u} S = D \nabla^2 S \tag{2}$$

where D is the constant mass diffusivity coefficient ($= 0.0025L^2/\tau$) and the velocity $\vec{u}$ is determined from the streamfunction produced by all the discrete vorticity. The streamfunction produced by the discrete vorticity is calculated at the corner of each mesh cell, and the velocity through the cell face is found by differencing the streamfunction corner values. The cell face scalar value is determined by eighth-order interpolation of the cell values. The transport is calculated with the flux-corrected transport scheme developed by Zalesak (1979). This scheme has recently been evaluated by Barr and Ashurst (1981) for pure convection and for convection with diffusion. One- and two-dimensional Gaussian profiles were convected at constant speed using a Courant number of one-eighth. For the two-dimensional diffusion case during a three unit time period, the Gaussian profile diffused at a rate within a half percent of the desired value and the profile kurtosis changed by only three percent. Thus, numerical diffusion is extremely small in this method.

These good results are in sharp contrast with earlier calculations which defined the cell face scalar value as the average of the two cell values adjacent to that face. Those calculations produced undesirable over- and undershoots of the scalar in regions of steep gradients. While the scalar was conserved, it was not very appealing to have negative values for a scalar bounded between zero and one. The advantage of the flux-corrected scheme is that desired bounds are never exceeded.

While scalar quantities and their transport are described on a mesh, the discrete vortices are not, and to advance the vortex locations in time the velocity at each vortex is calculated from the known vortex locations and their strengths. For the vortex trajectories, Adams-Bashforth two-step integration is used. The new vortex location at time $t + \delta t$ is

$$\vec{X}(t + \delta t) = \vec{X}(t) + (\delta t/2)[3\vec{C}(t) - \vec{C}(t - \delta t)]. \tag{3}$$

This second-order scheme requires a fixed time step ($\delta t = 0.00625\tau$ was used). The scalar transport is advanced from t to $t + \delta t$ by using the streamfunction at t and an interpolated value at $t + \delta t/2$. In the transport subprogram, an Euler prediction is made for values at $t + \delta t/2$ from those values at t, then a leapfrog step from t to $t + \delta t$ is followed by the flux correction [equations 6′ through 14′, 17′ and 18′ in Zalesak (1979)]. In the leap step the convective fluxes are time centered but the diffusion fluxes are time lagged, i.e., the diffusion is based on values at time t.

To start a calculation, N discrete vortices are randomly placed in the square (in these results two hundred such vortices have been used). The vortex circulation strength and core size are also randomly selected within a preset range. After selection, the sum of vorticity is adjusted to be zero. Different initial conditions can be generated by making extra calls to the random number generator. Thus the calculated velocity field has four parameters: 1) number of vortices, 2) range of circulation strength, 3) range of core size, and 4) the particular initial conditions. Notice that none of these parameters would be experimentally measured. Consequently, in order to characterize the velocity field in terms of experimental quantities, several long-time calculations have been made to measure the root-mean-square velocity (RMS) and the velocity spatial and time correlations. The two correlations can be integrated to determine the integral length and time scales (Tennekes and Lumley, p. 252, 1972). The velocity-time correlation, or autocorrelation, was calculated at four equally spaced locations along a diagonal of the square for a time period of 55 τ, where τ is the time unit by which these results may be scaled.

Calculations with a core radius range of zero to 0.32 L were made. With this core range, calculations have been done for three ranges of circulation strength: $\Gamma = \pm 0.1$, ± 0.2, and ± 0.4 in units of L^2/τ, where L is the square edge length. When Γ is $\pm 0.2L^2/\tau$, the RMS velocity is $0.39 \pm 0.04L/\tau$ and the average velocity autocorrelation decays to zero in about 3 τ. Changing only the circulation parameter creates a simple time scaling relation between the results: the velocity scales directly with the circulation strength and the time scales inversely. Therefore, for the weakest case the RMS velocity is 0.20 and the autocorrelation decays to zero at 6 τ, while for the strongest case considered the RMS velocity is 0.78 and the decay time is 1.5 τ.

The effect of the vortex core parameter was determined by reducing the maximum core size by factors of two and thirty and recalculating the long-time correlation. For $\Gamma = \pm 0.1L^2/\tau$ and maximum core size of 0.01 L, the autocorrelation decays to zero at 3 τ (about half of the large core value) and the RMS velocity increases to $0.32 \pm 0.02L/\tau$ (from $0.2L/\tau$). The core value also has a large effect on the spatial structure of the flow. For the two largest core ranges, the correlations indicate that the flow field structure is comparable to the system size whereas the smaller core results in spatial correlations that are one-tenth of the square edge, see Ashurst (1981).

DIFFUSION FLAME RESULTS

Assuming chemical reaction rates to be much faster than turbulent mixing rates produces an infinitely thin reaction zone which is spatially located wherever there is a stoichiometric ratio of fuel to oxidizer. This assumption of infinite reaction rate combined with the conserved scalar technique makes the diffusion flame calculation extremely simple. The conserved scalar equation is created by adding the species equations together in such a way that the chemical reaction rate terms are eliminated. Thus only a single transport equation, which has no chemical source terms, needs to be solved. The conserved scalar will be normalized so that pure fuel corresponds to unity and pure oxidizer to zero. The reaction zone value can be left unspecified for this general study.

The fuel consumption rate is calculated by considering a volume which contains an oxidizer and into which a fixed amount of fuel is introduced at time zero. If the velocity field at time zero is turbulent, then fuel consumption is expected to occur faster than in a pure diffusion experiment, i.e., zero velocity for all time. Thus comparisons will be made with respect to pure diffusion conditions. Because of the flame-sheet-model assumptions, the time-dependent reaction rate is known from the conserved scalar time history. If the reaction value of the conserved scalar is specified, then consumption of all the fuel occurs when the maximum scalar value drops below the reaction value. For this study the reaction value need not be specified and only the maximum scalar value will be recorded as a function of time for comparison with the pure diffusion case.

In an idealized experiment the fuel would be introduced at a point or along a line source of zero radius at time zero. The infinite line source will generate two-dimensional flow in a plane normal to the line and the laminar solution of the diffusion equation for the resulting fuel concentration is:

$$c_f(\vec{r}, t) = \frac{Q}{(4\pi D\, t)}\exp[-r^2/4D\, t] \tag{4}$$

where $r^2 = x^2 + y^2$ and Q is the quantity of fuel. After a finite time duration the solution will be a Gaussian profile with a finite amplitude and it is this type that is used for the numerical calculation. So instead of using a source of zero size, the initial distribution of fuel and oxidizer (i.e., conserved scalar) is confined to a circle in the x, y plane whose radius is 0.2 L, where L is the square edge length. The concentration is unity at the circle center (pure fuel) and decays to zero at its edge (pure oxidizer). A cubic distribution is used with zero concentration gradients at the center and edge of the circle, approximately a Gaussian profile. The calculations are done for a time period of 5 τ, at this time the maximum scalar value is 0.2. By analogy with the source time dependence, the maximum amplitude of the scalar is expected to have a time dependence of $c_1/(c_2 + 4D\, t)$ where c_1 and c_2 are related to the initial conditions. The result of a laminar calculation is shown in Figure 1 along with a curve fit with this functional form. The agreement with the desired coeffient of $0.0025L^2/\tau$ is very good.

Calculations have been done for three ranges of vortex strength: ± 0.1, ± 0.2, and ± 0.4 in units of L^2/τ. Two hundred discrete vortices have been used. In Figure 2, contour plots show the evolution of the conserved scalar interacting with one of the stronger turbulent velocity fields. During this same unit time period, the pure diffusion contours expand by only twenty-five percent and of course remain circular. At time τ, the maximum scalar concentration in Figure 2 is 0.27, whereas in the pure diffusion case the corresponding time to reach 0.27 maximum concentration is 3.5 τ. Thus if a particular fuel-oxidizer system reacted only at this 0.27 scalar concentration, the effect of turbulence in this case would be an apparent fuel consumption rate 3.5 times the laminar value.

For each range of vortex strength, an ensemble average was formed by using five different initial conditions obtained with different random numbers in selecting the initial vortex locations and core sizes. The variation in the scalar contours produced by the weakest vortex field after two time units are shown in Figure 3. Figure 4 shows the average time history of the maximum scalar amplitude and the standard deviation about the mean. In addition, a curve fit with the form of $c_1/(c_2 + 4D\ t)$ is shown by the chain-dashed line. The initial time period was ignored in determining the curve fit. The apparent values of D are 0.0039, 0.0042 and 0.0050 L^2/τ, in order of increasing velocity field turbulence intensity. A plot of these values versus the turbulence intensity yields a straight line, but the line does not pass through the laminar value of 0.0025. This extrapolation would imply enhanced diffusion at laminar conditions and thus must be rejected. This indicates that instead of forcing the turbulent results to the laminar form, a higher order polynomial should be used.

As another way to summarize the results, the laminar amplitude (Fig. 1) divided by the turbulent value is plotted in Figure 5. This ratio starts at unity because of the identical initial conditions, but then shows increasing diffusion at a linear rate. The linear slope of each curve (ignoring the intial region) is plotted versus the velocity field turbulence intensity in Figure 6. Now a linear variation with turbulence intensity has been obtained which reduces to the laminar value at zero turbulence intensity. This result allows estimation of scalar turbulent diffusion by knowing only the RMS velocity and the laminar time dependence. However, the current results have not investigated the effect of turbulent length scale. In premixed calculations of flow structure on flame speed (Ashurst, 1981), the core range had an important effect on the flowfield length scale and flame speed. Thus the current results may also depend upon the core range of the vortices.

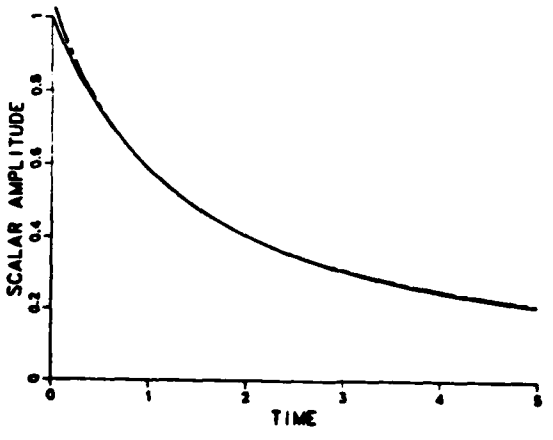

Figure 1. Calculated time dependence of maximum scalar amplitude for pure diffusion (solid line). Note the good agreement with the chain-dash line which represents the analytical source time dependence.

CONCLUSIONS

The combination of a Lagrangian calculated velocity field with an Eulerian scalar transport method allows new insight into turbulent combustion problems. It will now be possible to use the calculated flow structure to generate probability distribution functions of scalar diffusion. These results could be used to improve existing models of turbulent diffusion. The need for turbulence modeling assumptions in this Lagrangian-Eulerian method has been greatly reduced because subgrid-scale fluxes on the Eulerian mesh can be directly calculated from the known discrete vortex locations. In this work, the dramatic effect of turbulent mixing upon diffusion flame propagation has been shown by calculation of time dependent conserved scalar diffusion. Premixed combustion can also be investigated if one calculates transport equations which include chemical reaction rate terms. Extending this work to cover heat release effects upon the turbulence, by adding volume change and the term of density gradient vector crossed with the pressure gradient vector in the vorticity transport equation, will provide a major advance in turbulent reacting flow analysis.

ACKNOWLEDGEMENTS

The authors wish to thank Dr. P. Colella for advice about transport schemes. Discussions with Drs. R. E. Mitchell, S. B. Margolis and J. A. Miller have been very helpful.

REFERENCES

ASHURST, W. T. (1979) "Numerical Simulation of Turbulent Mixing Layers via Vortex Dynamics." *Turbulent Shear Flows I*, edited by F. Durst *et al.* (Springer-Verlag, Berlin) pp. 402-413.

ASHURST, W. T., Durst, F. and Tropea, C. (1980) "Two-Dimensional Separated Flow Experiment and Discrete Vortex Dynamics Simulation." AGARD Conference Proceedings No. 291, *Computations of Viscous-Inviscid Interactions*, paper 24.

ASHURST, W. T. (1981) "Lagrangian-Eulerian Calculation of Turbulence Effects on Premixed Flame Propagation," SAND81-8640, Sandia National Laboratories, Livermore, Calif.

BARR, P. K. and Ashurst, W. T. (1981) "Evaluation of Zalesak's Flux Corrected Transport Algorithm for Convection and Diffusion," SAND81-8233, Sandia National Laboratories, Livermore, Calif.

GRÖTZBACH, G. and Shumann, U. (1979) "Direct Numerical Simulation of Turbulent Velocity, Pressure, and Temperature Fields in Channel Flows," *Turbulent Shear Flows I*, edited by F. Durst *et al.* (Spring-Verlag, Berlin) pp. 370-385.

MARGOLIS, S. B. (1980) "Bifurcation Phenomena in Burner-Stabilized Premixed Flames." *Combustion Science and Technology*, 22, pp. 143-169.

MILLER, J. A. and Kee, R. J. (1977) "Chemical Nonequilibrium Effects in Hydrogen-Air Laminar Jet Diffusion Flames," *Jour. of Physical Chemistry*, 81, pp. 2534-2542.

MURTHY, S. N. B. (1975) "Turbulent Mixing in Chemically Reactive Flows," *Turbulence in Mixing Operations*, edited by R. S. Brodkey (Academic Press, Inc., New York) pp. 167-220.

STEPHENSON, D. A. (1980) "Self-oscillation observed in Flames," Sandia National Laboratories Combustion Research Facility News 2, No. 4, p. 2.

TENNEKES, H. and Lumley, J. L. (1972) *A First Course in Turbulence*, (The MIT Press, Cambridge, Mass.).

WILLIAMS, F. A. and Libby, P. A. (1980) "Some Implications of Recent Theoretical Studies in Turbulent Combustion," AIAA paper 80-0012.

ZALESAK, S. T. (1979) "Fully Multidimensional Flux-Corrected Transport Algorithms for Fluids," *Jour. of Computational Physics*, 31, pp. 335-362.

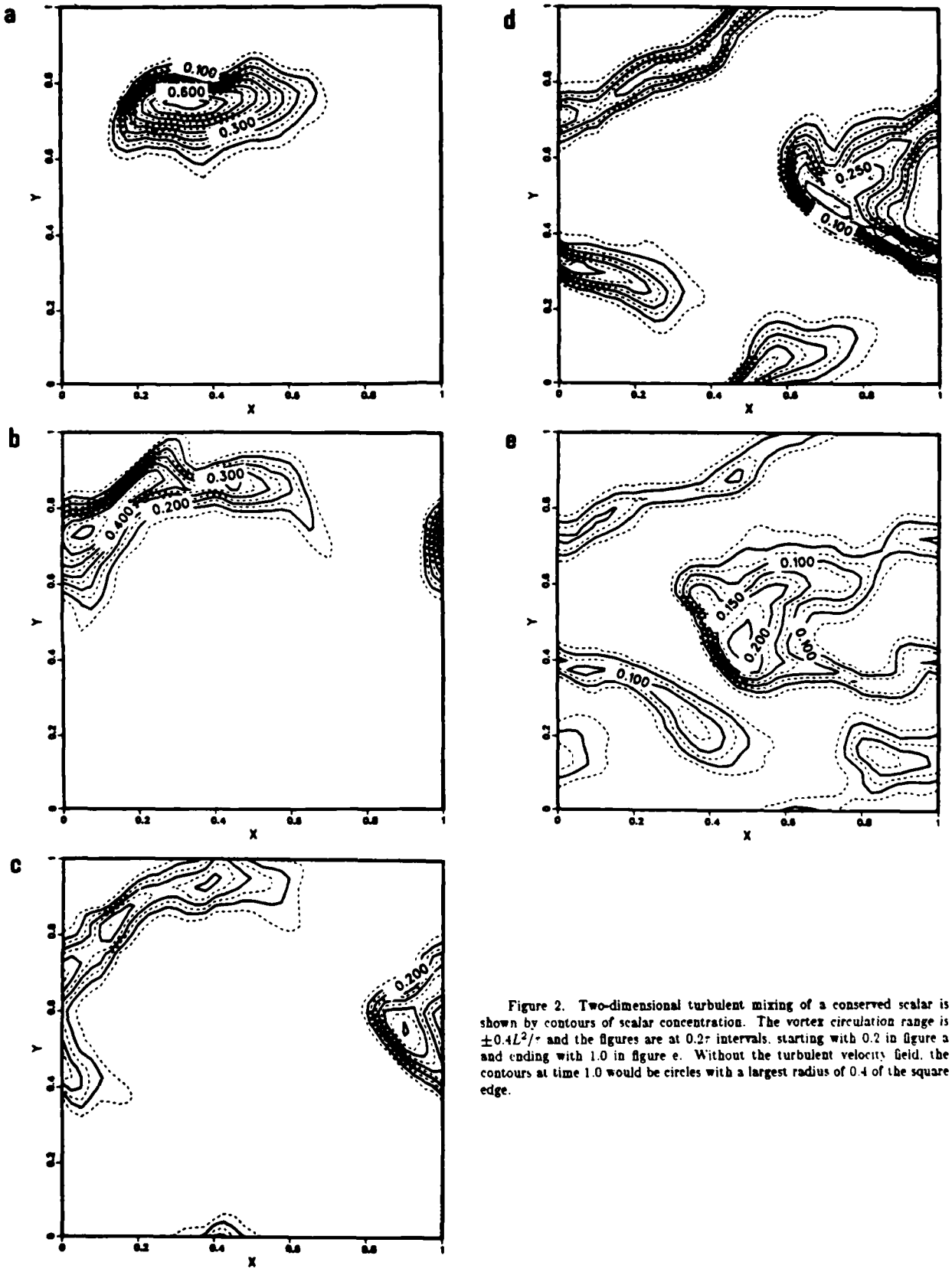

Figure 2. Two-dimensional turbulent mixing of a conserved scalar is shown by contours of scalar concentration. The vortex circulation range is $\pm 0.4L^2/\tau$ and the figures are at 0.2τ intervals, starting with 0.2 in figure a and ending with 1.0 in figure e. Without the turbulent velocity field, the contours at time 1.0 would be circles with a largest radius of 0.4 of the square edge.

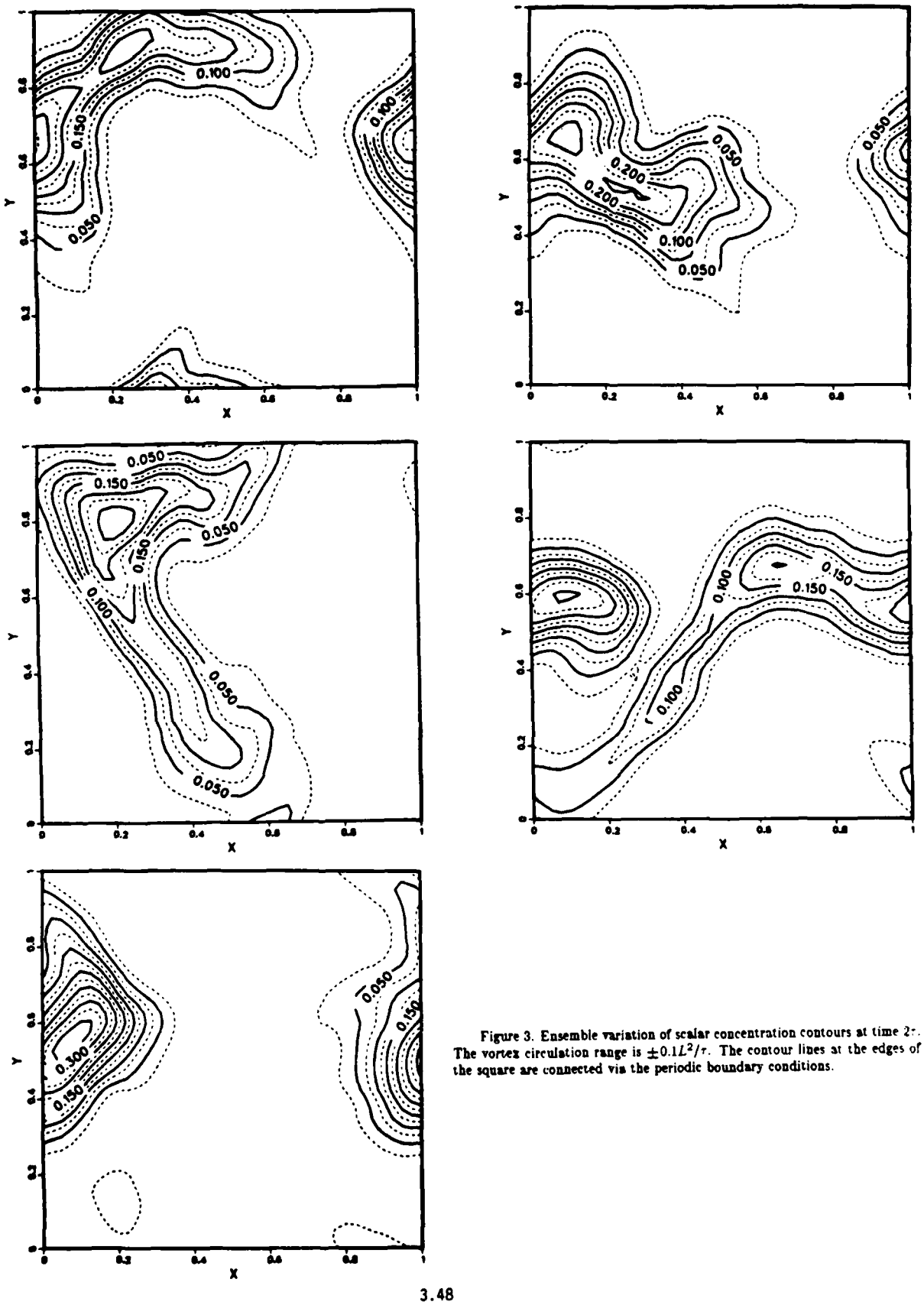

Figure 3. Ensemble variation of scalar concentration contours at time 2τ. The vortex circulation range is $\pm 0.1L^2/\tau$. The contour lines at the edges of the square are connected via the periodic boundary conditions.

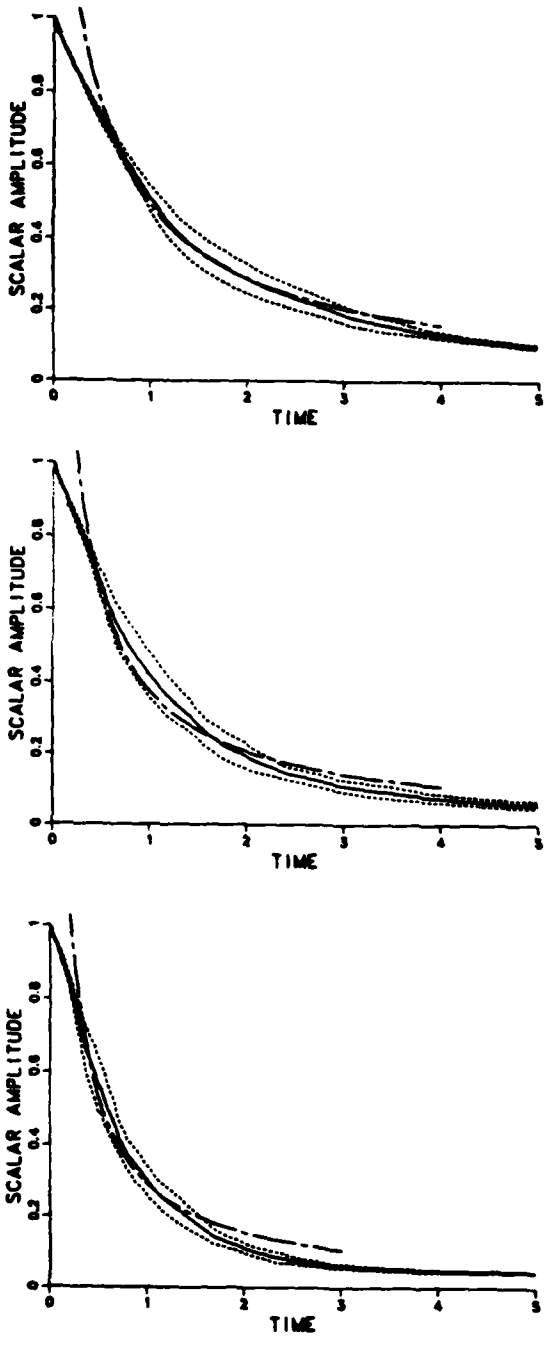

Figure 4. Variation of maximum scalar amplitude with velocity field intensity; from top to bottom the RMS velocity is 0.2, 0.39 and 0.78 L/τ, corresponding to vortex circulation ranges of ± 0.1, ± 0.2 and $\pm 0.4L^2/\tau$. The mean value (solid line), standard deviation about the mean (dash lines) and a curve fit with the laminar functional form (chain dash line) are shown.

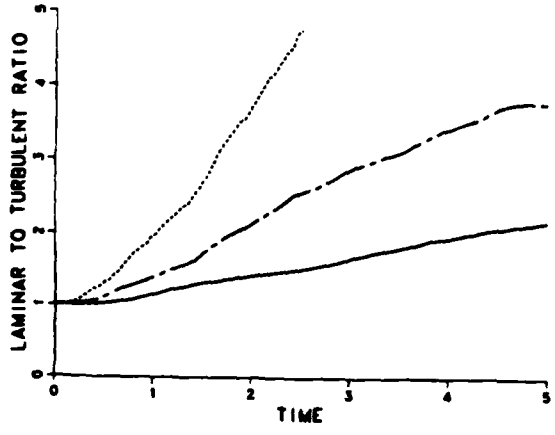

Figure 5. The enhanced turbulent diffusion effect is shown by the ratio of laminar to turbulent scalar amplitude. The RMS velocities are 0.2 (solid line), 0.39 (chain dash line) and $0.78L/\tau$ (dash line).

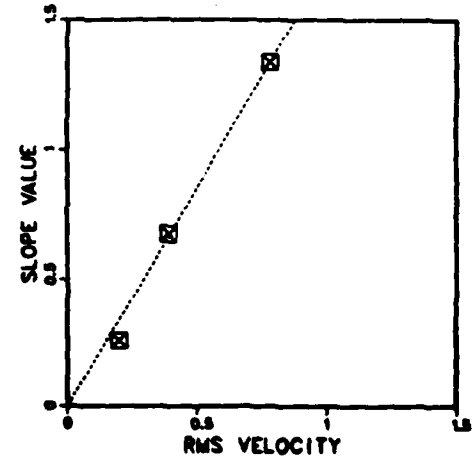

Figure 6. The linear slopes from Fig. 5 are plotted versus the RMS velocity and do reveal a linear dependence on turbulence intensity.

SESSION 4 - CURVED FLOWS

W. Rodi - Chairman

CALCULATION OF A TURBULENT WALL JET ON A CURVED WALL WITH A REYNOLDS STRESS MODEL OF TURBULENCE

M.M. Gibson and B.A. Younis

Mechanical Engineering Department,

Imperial College, London SW7, England.

ABSTRACT

The paper deals with the application of a Reynolds stress closure model of turbulence to the calculation of wall jets developing on plane and convex curved surfaces. Good results are obtained for the mean flow field, the growth rate of the jet and, in particular, the distance between the points of zero shear stress and zero mean velocity gradient which increases as the result of the suppression by convex curvature of the turbulence in the inner layer. The turbulence field is less well predicted although the results are not significantly inferior to those obtained previously for curved wall boundary layers. Deficiencies are identified in the modelling of turbulent diffusion and energy dissipation rate.

NOMENCLATURE

b	jet slot height (Figure 1)
c_f	skin friction coefficient defined with respect to $\frac{1}{2}\rho U_J^2$
F	factor applied to mixing length for curved flow
n	distance measured normal to curved surface
$n_{\frac{1}{2}}$	normal distance to half-velocity point (Figure 1)
P	production rate of turbulent kinetic energy
P_{ij}	production rate of Reynolds stress $\overline{u_i u_j}$
p	fluctuating pressure
$\overline{q^2}$	2 x (turbulent kinetic energy) $= \overline{u^2} + \overline{v^2} + \overline{w^2}$
R	surface radius of curvature
r	local streamline radius of curvature $\simeq R+n$
s	distance measured along curved surface
U	streamwise component of mean velocity
U_∞	velocity at edge of wall jet (plane flow only)
U_m	maximum mean velocity
U_o	$U_m - U_\infty$
U_J	velocity in slot exit plane
u,v,w	components of fluctuating velocity in s,n,z directions
α, β, γ	interdependent constants in pressure strain model, equation (2)
β	empirical constant in mixing length modification, equation (1)
δ	distance from surface of velocity maximum
δ'	distance from surface of point of zero shear stress
ϵ	dissipation rate of turbulent energy

INTRODUCTION

The turbulent wall jet is an interesting flow because it consists of a wall layer and a free shear layer interacting with each other and thus it possesses many of the characteristics of both. It is also an example of a relatively simple shear layer in which the point of turbulent shear stress reversal does not coincide with the point of maximum mean velocity but lies inside it, closer to the wall. This feature of the flow obviously cannot be predicted by simple gradient transport models of turbulence although it turns out that for the wall jet developing on a flat surface, the zeros of shear stress and mean velocity gradient are close enough to one another for the difference to be overlooked so that eddy viscosity models can be used to describe the principal features of the flow (1). In the case of a wall jet developing on a longitudinally curved surface the turbulence structure is affected by the curvature in ways which cannot be satisfactorily accounted for in terms of simple gradient hypotheses. If, for example, the surface curvature is convex the extra strain introduced by it tends to reduce the turbulence intensity and shear stress in the near wall layer where the angular momentum of the flow increases in the direction of the radius of curvature. The reverse occurs in the jet-like layer outside the velocity maximum where turbulent activity is increased by the curvature. Curved wall boundary layers and other curved shear layers without a velocity maximum may be calculated with fair accuracy when the ordinary plane flow mixing length distribution is modified as suggested by the buoyancy analogy (2,3) by a factor

$$F = 1 - \beta\frac{U/r}{\partial U/\partial n} \equiv 1 - \beta S \qquad (1)$$

where U is the streamwise component of the mean velocity, n is the co-ordinate normal to the local flow direction, r is the local streamline radius of curvature and β is an empirical coefficient of order ten. (Figure 1 is a definition sketch for the wall jet). Unfortunately it turns out that β is not universally constant for different types of curved flow and this lack of generality has led to the abandonment of (1) in favour of predictive schemes based on the numerical solution of modelled transport equations for the Reynolds stresses which, in the case of curved flow, contain in exact form extra-strain production terms introduced by the curvature (4,5). The shortcomings of eddy viscosity modelling are yet further emphasised by the curved wall jet. Intuition suggests, and experiment confirms, that the suppression of turbulence in the wall layer and its augmentation in the outer flow result in an inward shift of of the zero shear stress point relative to the velocity maximum. The distance between these two points is too great to be ignored, turbulent stress diffusion assumes an important role, and local conditions depart from the quasi local equilibrium implicitly assumed by the simpler models. It appears

that the minimum requirement for a satisfactory prediction method in this case is that a transport equation for the shear stress be solved and the importance of turbulent transport makes this flow an important and stringent test of transport equation modelling.

The flow in wall jets is well documented and in recent years a number of detailed turbulence measurements have been published. The literature has recently been critically reviewed by Launder and Rodi (6) for the 1980-81 AFOSR-Stanford Conference on the calculation of complex turbulent shear flows. Of four studies of constant-radius convex curved flow the most recent, and by a considerable margin the most detailed, is that of Alcaraz (7, 8) in which a relatively low slot height to radius ratio (b/R = 0.0032) was used to obtain a closely two-dimensional flow. The curvature was, however, large enough to produce measurable effects on the turbulence structure along the lines described above. A self-preserving form is achieved when the wall jet develops on a logarithmic spiral; of three sets of data reviewed in (6) the most closely two-dimensional is that of Guitton and Newman (9) which is also particularly suitable for stress model validation in that (as in 7) hot-wire data are provided for all four non-zero Reynolds stresses.

Proposals for closing the Reynolds stress equations abound in the literature and form the bases for numerous prediction methods which have been applied to complex shear layers with varying degrees of success. Irwin and Arnot Smith (10) first used the method to calculate curved flow with the model of Launder et al (11). The treatment was formally limited to shear layers with mild longitudinal curvature by the use of the plane boundary layer form of the mean momentum equation and the consequent neglect of the cross-stream variation of pressure. Results were obtained for curved wall jets, boundary layers and a curved free jet and demonstrated the capability of Reynolds stress modelling to predict the influence of curvature on flow development, although on account of the limitation noted the agreement with experiment deteriorated for flows of large curvature, the rate of growth of the wall jet (9) being significantly underpredicted. Moreover the limited amount of turbulence (as distinct from mean field) data available at the time of this pioneer study meant that very searching comparisons could not be undertaken.

Irwin and Arnot Smith (10) modelled the difficult pressure strain redistribution terms in the Reynolds stress equations in the way suggested by Launder et al (11):

$$\overline{\frac{p}{\rho}\left(\frac{\partial u_i}{\partial x_j}+\frac{\partial u_j}{\partial x_i}\right)} = \underset{(a)}{-C_1\frac{\varepsilon}{q^2}\left(\overline{u_iu_j}-\frac{1}{3}\delta_{ij}\overline{q^2}\right)} - \underset{(b)}{\alpha\left(P_{ij}-\frac{2}{3}\delta_{ij}P\right)} - \underset{(c)}{\beta\overline{q^2}\left(\frac{\partial U_i}{\partial x_j}+\frac{\partial U_j}{\partial x_i}\right)} - \underset{(d)}{\gamma\left(D_{ij}-\frac{2}{3}\delta_{ij}P\right)} \quad (2)$$

where P_{ij} is the rate of production of $\overline{u_iu_j}$:

$$P_{ij} = -\overline{u_iu_k}\frac{\partial U_j}{\partial x_k} - \overline{u_ju_k}\frac{\partial U_i}{\partial x_k} \quad (3)$$

$$D_{ij} = -\overline{u_iu_k}\frac{\partial U_k}{\partial x_j} - \overline{u_ju_k}\frac{\partial U_k}{\partial x_i} \quad (4)$$

P is the rate of production of turbulent energy $\frac{1}{2}\overline{q^2}$ and C_1, α, β and γ are constants evaluated from simple shear flow data (the last three are simple functions of a single empirical constant). Term (a) in (2), originally due to Rotta (12), represents the wholly turbulent contribution to pressure strain and the remaining three terms are the mean-strain, or rapid, terms which Chou's (13) analysis shows should be present. Equation (2) requires some modification to take account of the influence of the wall on inter-component energy transfer; these effects were modelled differently in (10) and (11) but the details are inessential to the present discussion.

Recently the present authors (5) used an abbreviated form of (2), in which only terms (a) and (b) appeared, to calculate for curved wall boundary layers with fairly satisfactory results. The isolation of the 'anisotropy of production' term (b), which Launder et al (11) in their original paper recognised as the dominant one in the rapid part of pressure strain, permits different interpretations of P_{ij}. When the Reynolds stress equations are transformed from Cartesian to curvilinear co-ordinates there appear extra generation terms due to rotation of axes. Although these have the same form as the other stress generation terms: the product of a Reynolds stress and a mean rate of strain (in this case the 'extra' strain U/r), they do not appear in P_{ij} defined by (3) when this is transformed to curvilinear co-ordinates*. In using the shortened form of (2) the present authors had no inhibitions about interpreting P_{ij} in term (b) as being the total production rate of $\overline{u_iu_j}$ including terms arising from axis rotation. The effects on model predictions for curved flow are significant. In the local-equilibrium limit, when mean flow and turbulent transport become negligible, the Reynolds stress equations reduce to a set of algebraic equations for the stress ratios. Irwin and Arnot Smith showed that for these conditions the pressure-strain model (2) predicts collapse of the shear stress in curved flow when the curvature parameter S (defined in (1)) reaches a critical value of 0.1 in free flow and 0.085 when a near-wall correction factor is applied. In contrast our simpler model, which includes the axis rotation terms, and constants evaluated from plane flow data, predicts (14) collapse at S = 0.17. The measurements of So and Mellor (15) in a boundary layer subjected to severe stabilising curvature suggest a critical value of about 0.15.

The present contribution may be regarded as an extension of our previous curved wall boundary layer calculations (5) to the rather more difficult case of a wall jet on a convex surface. It is unnecessary to repeat here the full description of the turbulence model and calculation method which is given in (5) but it may be helpful to itemise the principal features as follows:

1. the pressure-strain correlation of the Reynolds stress equations is modelled by an abbreviated form of (1)

$$\overline{\frac{p}{\rho}\left(\frac{\partial u_i}{\partial x_j}+\frac{\partial u_j}{\partial x_i}\right)} = -C_1\frac{\varepsilon}{q^2}\left(\overline{u_iu_j}-\frac{1}{3}\delta_{ij}\overline{q^2}\right) - C_2\left(P_{ij}-\frac{2}{3}\delta_{ij}P\right) \quad (5)$$

*In their study of swirling jet flow Launder and Morse (16) used (2) and treated the equivalent extra terms as convection terms.

where P_{ij} is interpreted as discussed above and C_1 and C_2 are constants, equal to 3.6 and 0.6 respectively, evaluated from plane flow data.

2. both terms in (5) are modified by a wall damping factor based on an original proposal by Shir (17) and extended by Gibson and Launder (18) to account for wall effects on density stratified turbulence.
3. turbulent transport of Reynolds stress is modelled by a simple gradient diffusion hypothesis for the triple correlations:

$$\overline{u_i u_j u_k} = - C_t \frac{\overline{q^2}}{\varepsilon} \overline{u_k u_\ell} \frac{\partial \overline{u_i u_j}}{\partial x_\ell} \qquad (6)$$

4. the turbulence energy dissipation rate, ε, is obtained from a modelled transport equation identical in form to that proposed in (11).
5. the cross-stream variation of pressure in curved flow is accounted for in a marching boundary layer procedure by assuming

$$\frac{1}{\rho} \frac{\partial p}{\partial n} = \frac{U^2}{r} \qquad (7)$$

6. near the wall the finite-difference solution is matched to the logarithmic law of the wall consistent with the observed persistence of a logarithmic layer in curved flow albeit much diminished in extent by strong stabilising curvature.

We have also tried the long expression (2) for pressure strain and various alternatives to the triple correlation model (6) whose shortcomings are exposed by the wall jet in which turbulent diffusion is more important than in a boundary layer.

In adapting (2) to wall flow we have used the Shir (17) correction of our other model so that the full wall-flow version differs in detail from those of Irwin and Arnot Smith (10) and Launder et al (11). The additional constants involved (C_1' and C_2' defined in (5)) are set equal to 0.5 and 0.1; these give approximately the correct stress levels for plane wall boundary layer flow. Wall jet predictions are compared with the very detailed measurements of Alcaraz (7, 8) and those of the self-preserving flow studied by Guitton and Newman (9); the data of Irwin (19) are used to check model performance for plane wall jet flow.

RESULTS AND DISCUSSION

We first checked the model and calculation method for plane flow using as a standard the self-preserving wall jet data published by Irwin (19). The jet develops in a moving stream and self-preservation is accomplished in a tailored pressure gradient; the maximum to free-stream velocity ratio is 2.65. Figure 2 shows the measured and predicted development of the mean flow downstream of the injection slot. The symbols are defined in Figure 1 with the exception of δ' which is the distance from the surface of the point of zero shear stress. The ratio δ/δ', in which δ is the distance from the surface of the mean velocity maximum, is about 1.4 and increases very slightly with distance measured downstream, a slight departure from exact self-preservation. This value, and the slight increase, are closely reproduced by the model as are the growth rate, decay of maximum velocity and streamwise variation of skin friction displayed in Figure 2. Profiles of mean velocity and of the four non-zero components of Reynolds stress are shown in Figure 3. Two sets of predictions are represented by continuous and broken lines; the latter were obtained from the Irwin-Smith pressure-strain hypothesis, equation (2), the former from equation (5). The differences here, for plane flow, are within the data scatter; both tend to overpredict the turbulent kinetic energy just outboard of the velocity maximum, mainly because high values of $\overline{u^2}$ are calculated. Otherwise the agreement appears to be very good apart, perhaps, for the slight discrepancies observed at the edge of the jet. We expected good mean field predictions because Ljuboja and Rodi (1) had demonstrated that these were obtainable with the equivalent algebraic stress model (which reduces to an eddy viscosity form). It was pleasing to find that the full stress model reproduced so closely the distance between the points of zero stress and maximum velocity which must have been calculated as coincident in (1).

Turning now to the curved wall jet, Figure 4 shows the predicted development of the mean flow compared with the measurements of Alcaraz (7,8). The agreement, though satisfactory, is not quite as good as for the plane jet and significant differences appear in the results given by the two pressure strain hypotheses, particularly in respect of the ratio δ/δ' which increases sharply, and continues to increase, in the curved flow to double the plane layer value. This increase which, as noted, is due to suppression by curvature of the turbulence in the near wall layer and the reverse in the outer flow, is closely predicted by the model (5), while that of Irwin and Smith (2) tends, relatively, to exaggerate these effects. The predicted cross-stream variation of mean velocity and the Reynolds stresses plotted in Figure 5 show reasonably good agreement with the data. Also plotted is the shear stress profile deduced from the mean flow measurements and momentum equation; this shows some evidence of three dimensionality in the destablised outer layer which possibly accounts for the deteriorating level of agreement there. As expected the Irwin-Smith pressure strain model (broken-line predictions) again predicts higher stress levels in the outer layer; in the inner flow the difference between the two models is less apparent.

Both models give fairly good results for the shear stress and $\overline{v^2}$ in the near wall layer but neither reproduce the redistribution of energy between the other two components and, most noticeably, the significant increase in $\overline{w^2}$ to a value greater than that of $\overline{u^2}$ as the wall is approached. This phenomenon appears to be genuine since it appears also in the measurements of Guitton and Newman (9) presented in Figure 9.

The turbulence energy and shear stress balances presented by Alcaraz provide a welcome opportunity to test the model assumptions in detail. The most noticeable feature of the measured energy balance shown in Figure 6 is the important role apparently played by pressure diffusion in the wall layer. This rises to a sharp peak inboard of the velocity maximum where it is offset to a large extent by velocity (triple correlation) transport of the opposite sign. The net turbulent transport is thus relatively small but by no means insignificant: it and the energy dissipation rate appear to be the dominant terms in this region. The pressure diffusion data reproduced in Figure 6 were not obtained by direct measurement but by difference to complete the energy balance. The net turbulent transport near the wall is quite well represented by the gradient diffusion hypothesis (6) although the level of agree-

ment deteriorates further from the wall. Equation (6) has been criticised because it is not compatible in its symmetry properties since only the left hand side is independent of the order of the indices i, j and k. Lumley (20) has suggested that a possible reason why it usually gives good results for wall flow may be that it absorbs some pressure diffusion which is not symmetrical and which is not modelled explicitly. The present results tend to support this view but we would not press the point too hard. Of the remaining terms in the energy balance the mean flow transport and production rate, which present no problems in measurement or prediction, are reasonably well predicted. The discrepancies noted for turbulent transport are reflected by the significant difference between measured and predicted values of the dissipation rate outside the velocity maximum. This apparent failure to reproduce the dissipation rate is rather surprising in view of good results obtained for $\overline{q^2}$ in this region and may be contrasted with the much better level of agreement obtained in this respect with the same models for a curved (stable) mixing layer (4). The flow in the outer layer is not unlike that in a mixing layer but these results seem to be at variance with those previously reported for such flows (see, for example, the review by Rodi (21)) and with what might be expected intuitively. The dissipation rate was obtained by Alcaraz from the isotropic relation:

$$\varepsilon = 15\nu\overline{\left(\frac{\partial u}{\partial x}\right)^2} \qquad (8)$$

Closure of the modelled equations is effected by solving the simple and widely used equation recommended by Launder et al (11) for the dissipation rate:

$$\frac{D\varepsilon}{Dt} = C_\varepsilon \frac{\partial}{\partial n}\left(\frac{r}{R}\frac{\overline{q^2}}{\varepsilon}\overline{v^2}\frac{\partial \varepsilon}{\partial n}\right) + \frac{\varepsilon^2}{\frac{1}{2}\overline{q^2}}\left(C_{\varepsilon_1}\frac{P}{\varepsilon} - C_{\varepsilon_2}\right) \qquad (9)$$

This equation has given good results for simple shear layers but its usefulness in more complex flows has recently been questioned. For example Launder and Morse (16) identified the modelling of the source terms in (9) as a major weakness in their Reynolds stress model of a swirling jet and Rodi (22) describes empirical modifications which improve performance for the analogous effects of buoyancy and rotation. Hanjalic and Launder (23) now recommend the inclusion in (9) of additional normal stress generation terms. We found that neither of these proposals made significant differences to the predictions (4) of a curved mixing layer and so, for the time being, we are content to retain (9) for curved flow calculations.

The shear stress balance, Figure 7, reveals high measured rates of turbulent transport in the vicinity of the velocity maximum which are not reproduced adequately by the simple gradient transport model (6) where the deficiency is offset in the predictions by an equivalent discrepancy in pressure strain, obtained from the measurements by difference. We have experimented with alternative models for the triple correlation without achieving significantly better results. Figures 6 and 7 show turbulent diffusion calculated from the invariant relationship recommended by Launder et al (11):

$$\overline{u_i u_j u_k} = -C_S\frac{\overline{q^2}}{\varepsilon}\left[\overline{u_i u_\ell}\frac{\partial \overline{u_j u_k}}{\partial x_\ell} + \overline{u_j u_\ell}\frac{\partial \overline{u_k u_i}}{\partial x_\ell} + \overline{u_k u_\ell}\frac{\partial \overline{u_i u_j}}{\partial x_\ell}\right] \qquad (10)$$

The result is to increase the net diffusion near the wall but the change is very small.

The final comparison is made with the data of Guitton and Newman (9) whose nominally self preserving wall jet developed on a logarithmic spiral. The results for s/R = 1 are presented in Figures 8 and 9 and show much the same level of agreement as that noted for the other flows. The ratio δ/δ' cannot be obtained accurately from the published data; the large predicted value of 7.0 appears to be broadly consistent with the measurements.

CONCLUDING REMARKS

The calculations presented in this paper have been carried out as part of an ongoing programme of research motivated by the requirement for a generally applicable predictive procedure for complex shear flows with density stratification, rotation and/or streamline curvature. The work is thus a continuation of our studies of buoyancy (18), curved free flow (4) and curved wall flow (5) with the same turbulence model, and it is a logical extension of the latter. Moreover the wall jet possesses interesting and individual features which are exaggerated when the flow develops on a convex curved surface. One of these, which can only be predicted with a stress equation model, is that the zeros of shear stress and mean velocity gradient occur at different places. The present model accurately predicts the distance between these two points and the extent by which this distance is increased by the stabilising action of convex surface curvature.

ACKNOWLEDGEMENT

We gratefully acknowledge financial support for this work provided by the Central Electricity Generating Board (CERL), Leatherhead, England.

REFERENCES

1. Ljuboja,M. and Rodi,W., Trans. ASME, J. Fluids Eng. 102, 3, 350 (1980).
2. Bradshaw,P., J. Fluid Mech. 36,1, 177 (1969).
3. Bradshaw,P., AGARDograph No. 169 (1973).
4. Gibson,M.M. and Rodi,W., J. Fluid Mech.103,161 (1981).
5. Gibson,M.M.,Jones, W.P. and Younis,B.A., Phys. Fluids 24, 3, 386 (1981).
6. Launder,B.E. and Rodi,W., UMIST rep, Manchester (1980).
7. Alcaraz,E., These d'Etat,Univ. Claude Bernard, Lyon (1977).
8. Alcaraz,E., Charnay, G. and Mathieu,J., Phys. Fluids 20, 2, 203 (1977).
9. Guitton,D.E., and Newman,B.G., J. Fluid Mech. 81,1, 155 (1977).
10. Irwin, H.P.A.H. and Arnot Smith,P., Phys. Fluids 18, 6, 624 (1975).
11. Launder,B.E., Reece,G.J. and Rodi,W. J. Fluid Mech. 68, 3, 537 (1975).
12. Rotta,J.C., Z. Phys. 129, 547 (1951).
13. Chou,P.Y., Quart. Appl. Math. 3, 38 (1945).
14. Gibson,M.M., Int. J. Heat Mass Transfer 21,1609 (1978).
15. So,R.M.C. and Mellor,G.L., J. Fluid Mech. 60,1,48 (1973).
16. Launder,B.E. and Morse,A., Turbulent Shear Flows 1, Springer-Verlag (1979).
17. Shir,C.C., J. Atmos. Sci. 30, 1527 (1973).
18. Gibson,M.M. and Launder,B.E., J. Fluid Mech. 86,3,491 (1978).
19. Irwin,H.P.A.H., J. Fluid Mech. 61,1,33 (1973).
20. Lumley,J.L., in Prediction Methods for Turbulent Flows, Hemisphere (1980).
21. Rodi,W., in Studies in Convection 1,Academic Press (1975).
22. Rodi,W., Proc. 2nd Symposium on Turbulent Shear Flows, London (1979).
23. Hanjalic,K. and Launder,B.E., Trans. ASME, J. Fluids Eng. 102, 3, 34 (1980).

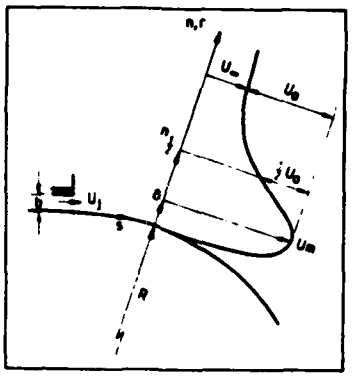

Figure 1. Definition sketch for wall jet

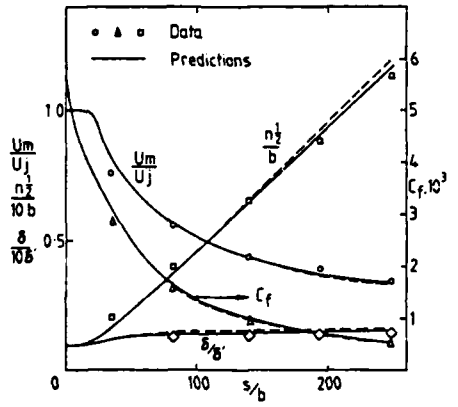

Figure 2. Measured and predicted development of a plane self-preserving wall jet. Data of Irwin (19).
Predictions —— eq (5), ---- eq (2)

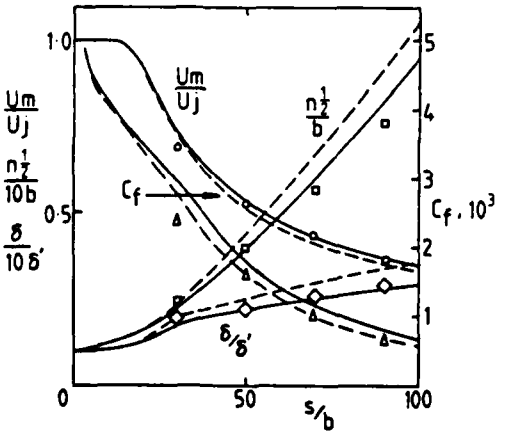

Figure 4. Measured and predicted development of a wall jet on a convex surface.
Data of Alcaraz (7, 8).
Predictions —— eq (5), ----- eq (2).

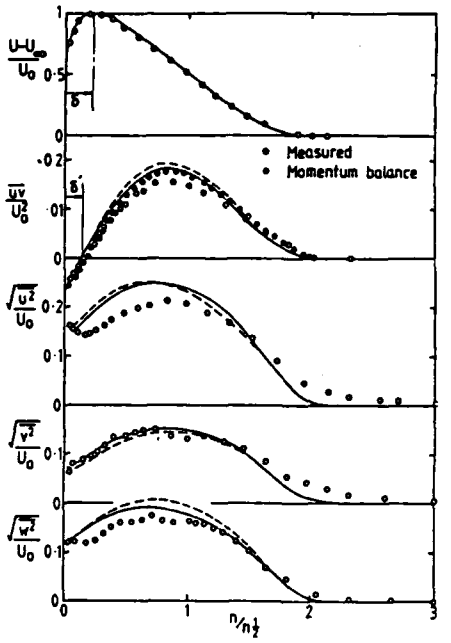

Figure 3. Profiles of mean velocity and Reynolds stresses in a plane self-preserving wall jet. Data of Irwin (19).
Predictions —— eq (5), ---- eq (2).

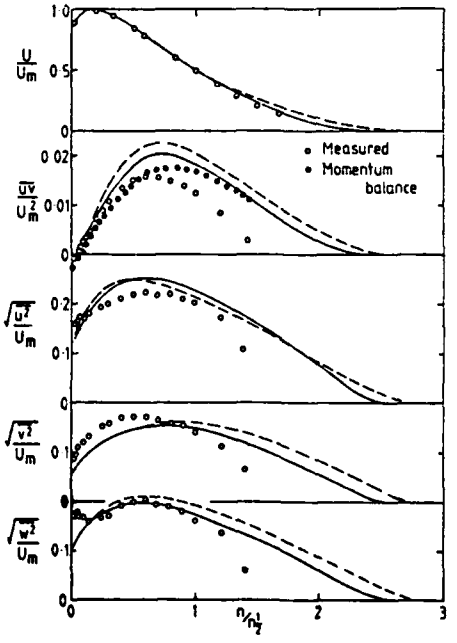

Figure 5. Profiles of mean velocity and Reynolds stresses in a curved wall jet. Data of Alcaraz (7, 8).
Predictions —— eq (5), ----- eq (2).

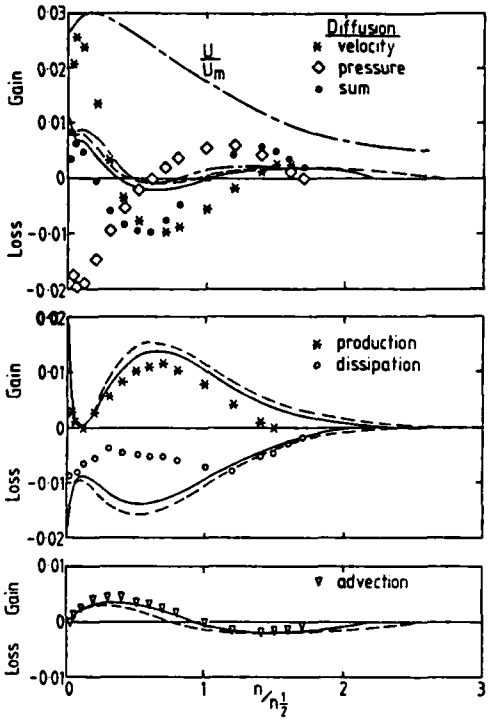

Figure 6. Turbulent energy balance in a curved wall jet. Data (7, 8). Predictions —— eq (5), ---- eq (2), —·— diffusion eq (10).

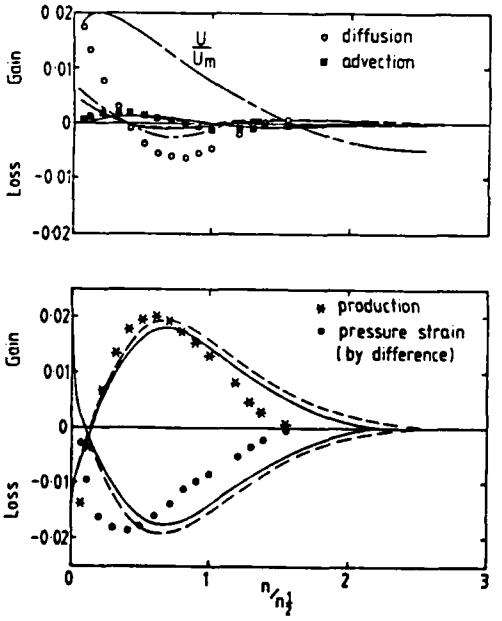

Figure 7. Shear stress balance in a curved wall jet. Data (7, 8), Predictions —— eq (5), ---- eq (2), —·— diffusion eq (10).

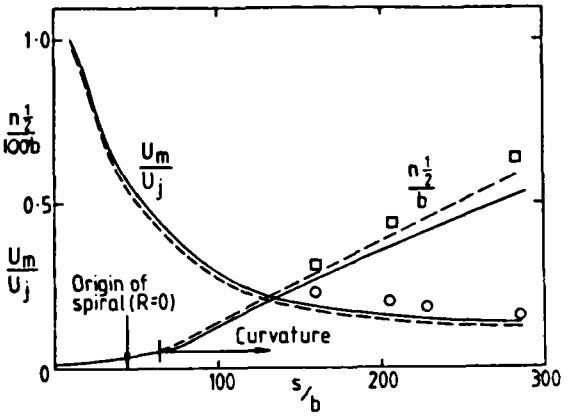

Figure 8. Measured and predicted development of a wall jet on a logarithmic spiral. Data of Guitton and Newman (9).

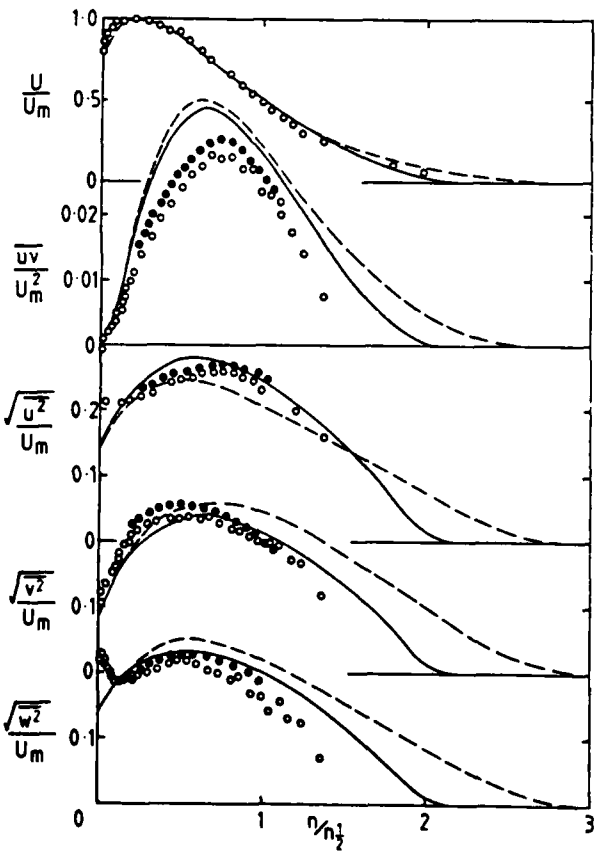

Figure 9. Profiles of mean velocity and Reynolds stresses in a wall jet on a logarithmic spiral. Data (9).
Predictions —— eq (5), ---- eq (2).

MEASUREMENTS IN THE HEATED TURBULENT BOUNDARY LAYER ON A MILDLY CURVED CONVEX SURFACE

M.M. Gibson, C.A. Verriopoulos
(Imperial College, London)

and

Y. Nagano
(Nagoya Institute of Technology, Japan)

ABSTRACT

Measurements of mean velocity and temperature, and of surface heat flux, have been made in a turbulent boundary layer on a heated convex surface of modest curvature ($\delta/R \sim 0.01$). The results show surprisingly large curvature effects on heat transfer: at the end of the curved plate the Stanton number fell by 18 per cent of the predicted flat plate value; the corresponding fall in the skin friction coefficient was 10 per cent.

Profile measurements of temperature and velocity were obtained well into the viscous sublayer.

NOMENCLATURE

c_f	skin friction coefficient, equation (4)
c_p	static pressure coefficient, $2(p-p_{ref})/\rho U^2_{pw}$
	specific heat
$\dot{q}''$	heat flux
R	radius of curvature of plate
s	distance measured along curved wall
T	temperature
T^+	dimensionless temperature, equation (6)
U	velocity
U^+	dimensionless velocity U/u_τ
u_τ	friction velocity, $\sqrt{\tau_w/\rho}$
y	distance measured normal to the wall
y^+	dimensionless distance, yu_τ/ν
Δ_2	enthalpy thickness, equation (2)
δ_2	momentum thickness, equation (1)
δ	boundary layer thickness
ρ	density
τ	shear stress
ν	kinematic viscosity

Subscripts

p	potential flow
w	wall
∞	free stream

INTRODUCTION

The effects of longitudinal curvature on the turbulence in boundary layers are well known. When, for example, a boundary layer develops on a convex curved surface, such as the suction surface of a wing or turbomachine blade, the angular momentum of the flow increases in the direction of the radius of curvature with the result that the shear stress and turbulence intensity are reduced to values often substantially less than those in an equivalent plane wall flow. The reverse occurs in the flow on a concave surface where the turbulence is increased by curvature. In contrast to laminar flow, where the fractional change in shear stress is of the same order as the ratio of the boundary layer thickness to the radius of curvature, turbulent flow measurements show fractional changes an order of magnitude greater. These effects on the turbulent velocity field are now well documented particularly for convex-wall flow. The survey paper by Bradshaw (1) contains details of research up to 1973; since that date a number of detailed hot-wire measurements in isothermal curved flow have been reported (2-6).

In marked contrast to this activity in the study of the hydrodynamics of curved flow the effects of curvature on turbulent heat transfer have received little attention. The supersonic flow measurements of Thomann (7), and the more recent results from an incompressible boundary layer reported by Mayle et al (8), show that the turbulent heat flux is affected in the same way as the shear stress: depressed in flow on a convex surface and augmented in flow on a concave surface. Since, however, the corresponding variation of shear stress is not given in these papers it is impossible to judge whether the heat flux changed by a greater or lesser amount. There is no reason to suppose *a priori* that the changes in these two quantities are equal; on the contrary, in the analogous (9) case of density stratified flow the differences are appreciable. Measurements (10) in the atmospheric surface layer show heat transfer to be significantly more affected by buoyancy than momentum transfer or, stated alternatively, that the turbulent Prandtl number is a strong function of the stratification and increases with increasing stability. The curvature and buoyancy generation terms appear differently in the stress and heat flux equations in each case and suggest that changes of the same order might appear in curved flow (11).

An estimate of the relative changes may be made from the mean temperature and surface heat flux measurements of Simon and Moffat (12) because details of the turbulent velocity field are reported by Gillis et al (13)*. Measurements were made in the boundary layer on a ninety degree bend followed by a flat plate recovery flow. The test wall was constructed of individually heated segments which allowed steady state measurement of the spanwise averaged wall heat flux by energy balance. In two experiments maximum values of δ/R were 0.051 and 0.077. In each case the Stanton number at the end of the curved

*Earlier measurements (3) referred to in (12) were made in a nearly but not quite identical wind tunnel and show slight but significant differences in flow conditions and results.

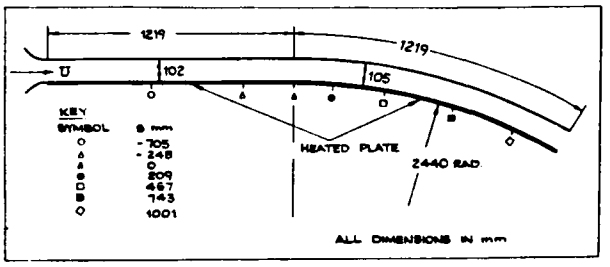

Figure 1. The wind tunnel working section showing traverse stations and symbols.

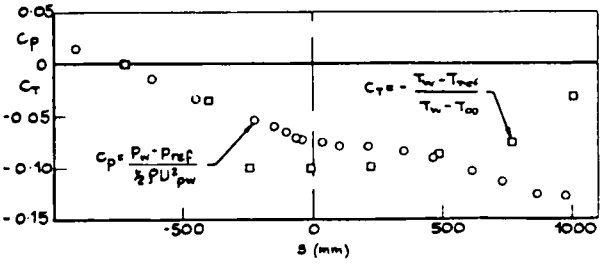

Figure 2. Streamwise variation of wall static pressure and temperature.

section fell by approximately 34 per cent of the calculated plane-flow value while the skin friction coefficient (13) showed only a 30 per cent fall.

The experiment now to be described, which was conceived before we became aware of Simon and Moffat's work, stems from Gibson's (11) speculations based on modelled equations for Reynolds stress and heat flux. The model, which gives good results for heat transfer in density stratified flow (14), suggested that the effects of curvature on heat transfer are less than on shear stress, with the turbulent Prandtl number in local equilibrium flow decreasing with increasing stability. Coincidentally So (15) obtained the contrary result from a different model* and has since (16) used the data of (12, 13) to support his hypothesis. We are not, however, concerned here with the minutae of turbulence modelling. In the present paper we report measurements of mean velocity, mean temperature and surface heat flux made in the boundary layer growing on a moderately curved convex plate for which $\delta/R \approx 0.01$. Previously published data (4,5) show that this degree of curvature is sufficient to produce measurable effects and it was chosen in order to minimise problems with secondary flow which might be exacerbated by heat transfer. Measurements of the mean and turbulent velocity fields have been described elsewhere (6); these exhibit the characteristic features of convex wall flow: a diminished rate of layer growth and a progressive damping of turbulence in the layer.

EXPERIMENTAL ARRANGEMENT AND PROCEDURES

The measurements were made in the boundary layer on the lower, heated, convex wall of an open circuit wind tunnel (Figure 1). The boundary layer developed first on a flat heated plate 1.22 m long to a thickness, δ, of 17 mm at the start of the curved section, also heated, of constant nominal radius of curvature, R, 2.44 m and length 1.22 m. The tunnel cross section in the plane approach flow was constant at 305 x 102 mm^2 but at the start of the curved plate the section height was increased to 105 mm in order to reduce the negative pressure gradient on the test wall. Figure 1 shows the positions of the traverse stations; the reference free stream velocity measured at station 1, 705 mm upstream of the curved plate, was nominally 22.6 ms^{-1} throughout the experiments. The boundary layer was tripped at the start of the flat plate and the momentum thickness Reynolds number at inlet to the curved section was 3300. The maximum value of δ/R, measured at the exit, was 0.011 and the free stream turbulence level was less than 0.4 per cent throughout. Preliminary pressure tube measurements showed that the mean flow was closely two-dimensional up to 150 mm from the curved section exit; in the exit plane the two sides of the mean flow integral momentum equation differed by no more than 10 per cent when the skin friction coefficient was evaluated by the Clauser chart method.

The 12.5 mm thick aluminium test plate was heated to 14 deg C above ambient with an electric blanket. Sets of three copper-constantan thermocouples spaced at 50 mm in the spanwise direction were located at intervals of 120 mm along the flat and curved sections. The variation in plate temperature along the measurement length was found to be within ±0.75 deg C from the mean, the greatest temperatures being recorded around the start of the curved section (Figure 2). Provision was made for inserting miniature heat flux meters at ten locations spaced unevenly (~ 150 mm) on the centre line in downstream half of the flat plate and in the curved section. These meters are of the Schmidt-Boelter multiple thermocouple type, 9.4 mm diameter, and were specially made by the Medtherm Corporation in aluminium so as to be compatible with the plate material. Their sensitivity is 40 mV W^{-1} cm^2 and their accuracy is estimated at ± 2 per cent.

Mean velocity measurements in the boundary layer were made with a flattened Pitot tube except very close to the wall ($y^+ < 25$) where a constant temperature 5 μm tungsten hot wire was employed. Corrections for wall proximity have not been made in view of the evidence (17) that these are significant only for $y^+ < 4$, or roughly the lower limit of the measurements. Mean temperatures at the same traverse stations were measured with a 12 μm chromel-alumel thermocouple of length-to-diameter ratio 580. Errors associated with conduction to the thermocouple supports and radiation from the heated plate were estimated (18,19) to be less than 0.03 deg C. The thermocouple output was amplified (x 1000) in a Precision-Monolithic OP07A low noise amplifier to be digitised and linearised in an Apple II microcomputer. The hot wire and thermocouple were positioned when close to the plate with a micrometer traverse accurate to 10 μm. The wall temperature recorded by the thermocouple probe differed by no more than ±0.1 deg C from the temperatures recorded by the thermocouples set in the plate.

RESULTS AND DISCUSSION

The pressure distribution obtained from static pressure tappings in the test plate before the electric blanket was fitted is shown in Figure 2. The pressure coefficient c_p is defined with respect to reference

*In which the mean strain contributions to the difficult pressure scrambling terms, included by Gibson (11), are omitted.

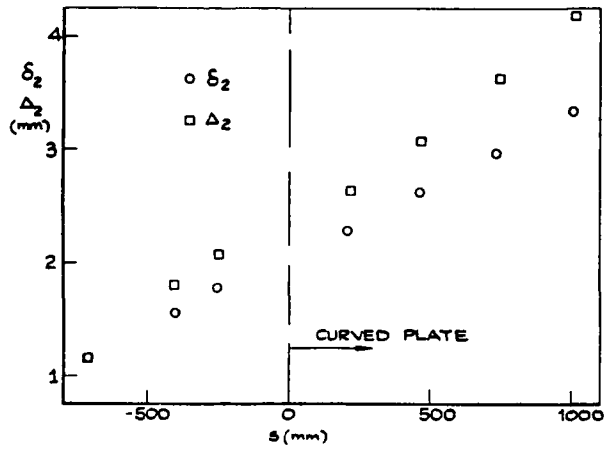

Figure 3. Growth of boundary layer momentum and enthalpy thicknesses.

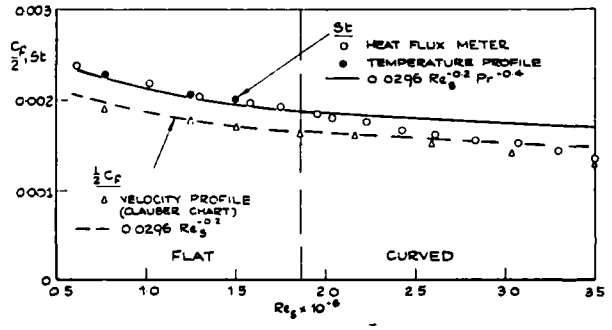

Figure 4. Streamwise variation of skin friction coefficient and Stanton number plotted against length Reynolds number.

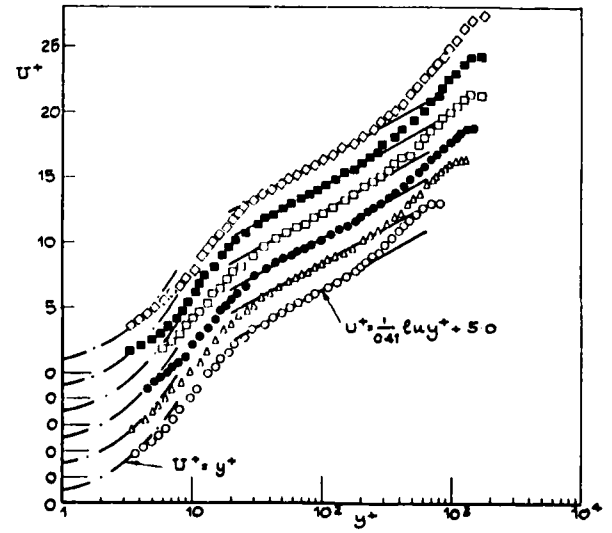

Figure 5. Measured velocity profiles in universal wall co-ordinates.
Symbols defined in Figure 1.

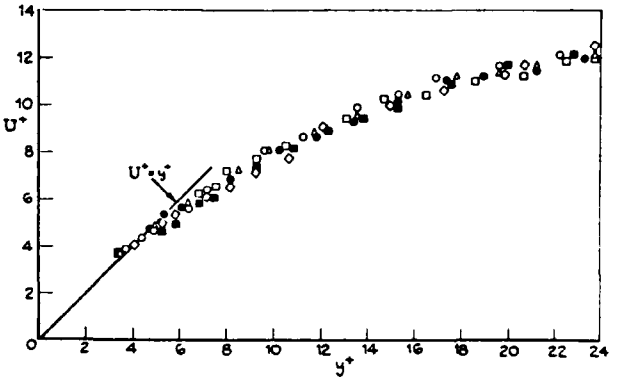

Figure 6. Velocity profiles in the sublayers.

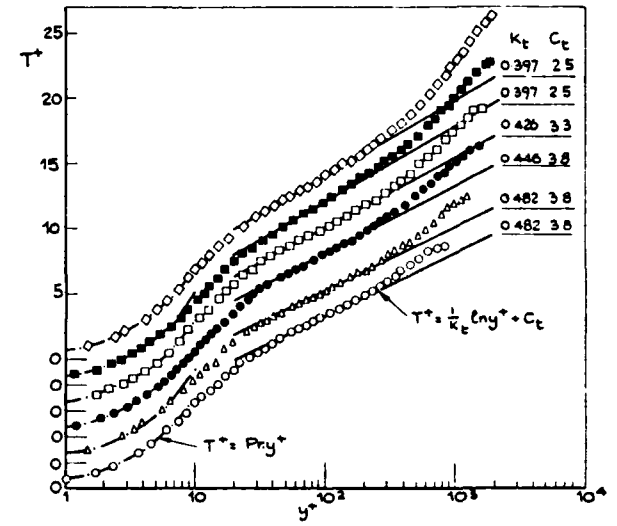

Figure 7. Measured temperature profiles in universal wall co-ordinates.

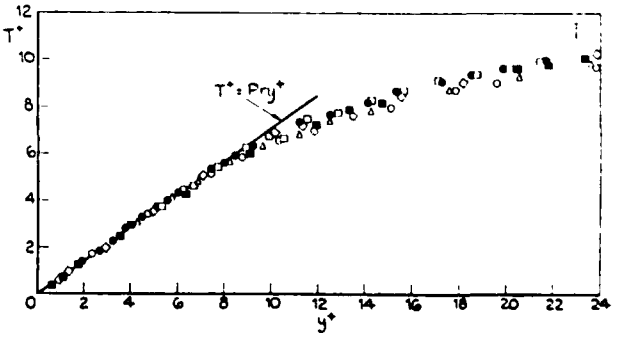

Figure 8. Temperature profiles in the sublayers.

conditions at the first traverse station and the local potential velocity at the wall, U_{pw}. The integral momentum and enthalpy thicknesses evaluated from mean velocity and temperature traverses on the plate centreline are plotted against streamwise distance, s, in Figure 3. These quantities are defined as

$$\delta_2 \equiv \int_0^\infty \frac{U}{U_p}\left(1 - \frac{U}{U_p}\right) dy \qquad (1)$$

$$\Delta_2 \equiv \int_0^\infty \frac{U}{U_{pw}}\left(1 - \frac{T - T_w}{T_\infty - T_w}\right) dy \qquad (2)$$

The observed higher rate of growth of Δ_2 is consistent with values of Stanton number

$$St \equiv \frac{-\dot{q}''_w}{\rho c_p U_{pw}(T_\infty - T_w)} \qquad (3)$$

which are plotted in Figure 4. These are greater than values of one half the skin friction coefficient defined by

$$\frac{c_f}{2} = \frac{\tau_w}{\rho U_{pw}^2} \qquad (4)$$

over the entire measurement length. Fluid property values used in (3) and (4) have been evaluated at the mean, or film, temperature $0.5(T_\infty + T_w)$. In the plane approach flow values of the wall heat flux $\dot{q}''_w$ recorded by the heat flux meters are supplemented by and checked against the local Stanton number obtained by plotting temperature profiles on the thermal equivalent of a Clauser chart. The results are entirely consistent and agree with plane wall values given by the correlation recommended in (20). The Clauser chart method has been used throughout to calculate c_f from the velocity profiles. The most striking feature of the results plotted in Figure 4 is that the Stanton number in the curved flow falls more rapidly from flat plate values than does the skin friction coefficient. Thus at the last traverse station, s = 1 m, St has fallen to 82 per cent and c_f to only 90 per cent of their respective plane flow values. These disproportionate effects are even more marked upstream where in the first half of the curved section a significant drop in St is observed and c_f is but little affected. The results are broadly consistent with those of Simon and Moffat (12); the milder curvature of the present experiment produces smaller falls in St and c_f but not proportionately so. The fall in St relative to c_f is apparently much greater than that reported in (12) and (13) and the effects on c_f in the present case of the mild favourable pressure gradient (Figure 2) must be considered. The pressure gradient term contributes up to 15 per cent of the mean flow momentum balance; this is offset to some extent by the lower growth rate of the accelerated boundary layer (the present measurements of $d\delta_2/dx$ are fully 20 per cent lower than those quoted by Coles (21) for uniform pressure flow) so that the net effect on c_f is relatively small, as is suggested by the excellent agreement with the flat plate correlation in the plane approach flow.

Figure 5 is a semi-logarithmic plot of the mean velocity profiles in universal wall co-ordinates ($U^+ \sim y^+$). These all show clearly defined logarithmic layers which are well fitted in the plane and curved flow by

$$U^+ = \frac{1}{K} \ln y^+ + C \qquad (5)$$

with K = 0.41 and C = 5.0. Profiles in the sublayers ($y^+ < 24$) are also shown in the linear plot of Figure 6. Here the data collapse satisfactorily on a single curve; the scatter appears to be random and within the margins of experimental uncertainty including hot wire positioning error (< 10 μm, unit y^+ corresponds typically to 15 μm). The departure from the $U^+ = y^+$ asymptote at $y^+ = 4$ is attributed to the wall proximity effects documented in (17) for which no correction has been made.

The corresponding plots of T^+ against y^+ are presented in Figures 7 and 8. In contrast to the Simon-Moffat data for stronger curvature these all show well defined logarithmic regions fitted by the expression

$$T^+ \equiv \frac{\rho u_\tau c_p (T - T_w)}{-\dot{q}''_w} = \frac{1}{K_t} \ln y^+ + C_t \qquad (6)$$

A significant difference from the velocity profiles is that the 'constants' K_t and C_t change in the curved flow as indicated on the graph, the slope increasing (K_t decreasing) with distance along the curved plate. The first two profiles of the plane flow are fitted by (6) when $K_t = 0.48$, $C_t = 3.8$ to give an approximate value* of the turbulent Prandtl number near the wall $Pr_t = K/K_t = 0.85$ consistent with values estimated in the Kader and Yaglom (22) survey of flat plate data. Towards the end of the curved plate, however, the profiles are best fitted using $K_t = 0.4$ so that the turbulent Prandtl number rises to approximately 1.03. This result, which is at variance with our model predictions (11), is not as surprising as it might have been had we not seen the Stanford results (12, 13) which, according to So's (16) analysis of the data, exhibit the same trend. Sublayer profiles of T^+ are presented in Figure 8. It was possible to get much closer to the wall with the thermocouple than with the hot wire probe and, within the estimated uncertainty margins indicated by the bars, the profiles collapse satisfactorily on a single curve with asymptote $T^+ = Pr\, y^+$ as $y^+ \to 0$. There is a slight but possibly significant difference from the sublayer velocity profiles of Figure 6 in that scatter is apparently not random but shows a consistent trend for T^+ to increase at a given y^+ as the curved flow develops. It is, however, impossible to be quite certain about this trend in view of the experimental uncertainty.

CONCLUSION

The results of this experiment on a mildly curved heated boundary layer show that convex curvature depresses the surface heat flux by a greater proportionate amount that it does the skin friction. Mean velocity and temperature profiles both exhibit clearly defined logarithmic regions in the curved flow but the gradient of temperature increases as the flow develops. Approximate estimates of the turbulent Prandtl number obtained from the gradients in the logarithmic layer show this quantity to increase from 0.85 at the start of the curved plate to a little over unity at the end. Measurements in the sublayers, in the case of temperature very close to the wall, confirm the internal consistency of the results.

*Assuming uniformity of shear stress and heat flux in the logarithmic layer.

The work presented here is still continuing. Hot-wire measurements of the four non-zero components of Reynolds stress have been made (6) and in the near future we intend to complete our investigation of the velocity field by measuring triple correlations and energy spectra. The mean temperature and surface flux data presented here will be supplemented by profile measurements of the cross-stream and longitudinal components of the heat flux, the temperature variance and the triple correlations.

ACKNOWLEDGEMENT

This study is supported by the Science Research Council under Research Grant No. ER/A76684.

REFERENCES

1 Bradshaw, P., Effect of streamwise curvature on turbulent flows, AGARDograph No. 169 (1973).

2 Smits, A.J., Young, S.T.B and Bradshaw, P., The effect of short regions of high surface curvature on turbulent boundary layers, J. Fluid Mech. 94, 209 (1979).

3 Gillis, J.C. and Johnston, J.P., Experiments on the turbulent boundary layer over convex walls and its recovery to flat-wall conditions, Turbulent Shear Flows 2, 116, Springer-Verlag (1980).

4 Hoffmann, P.H. and Bradshaw, P., Turbulent boundary layers on surfaces of mild longitudinal curvature, Imperial Coll. Aero. Rep. 78-04 (1978).

5 Ramaprian, B.R. and Shivaprasad, B.G., The structure of turbulent boundary layers along mildly curved surfaces, J. Fluid Mech. 85, 2, 273 (1978).

6 Gibson, M.M., Verriopoulos, C.A. and Vlachos, N.S., Measurements in the turbulent boundary layer on a convex wall, Paper presented at Int. Symp. on Applications of Fluid Mechanics and Heat Transfer to Energy and Environmental Problems, Patras, Greece (1981).

7 Thomann, H., Effect of streamwise wall curvature on heat transfer in a turbulent boundary layer, J. Fluid Mech. 33, 2, 283 (1968).

8 Mayle, R.E., Blair, M.F. and Kopper, F.C., Turbulent boundary layer heat transfer on curved surfaces, ASME J. Heat Transfer 101, 3, 521 (1979).

9 Bradshaw, P., The analogy between streamline curvature and buoyancy in turbulent shear flow, J. Fluid Mech. 36, 1, 177 (1969).

10 Businger, J.A., Wyngaard, J.C.,Izumi, Y. and Bradley, E.F., Flux-profile relationships in the atmospheric surface layer, J. Atmos. Sci. 28, 181 (1971).

11 Gibson, M.M., An algebraic stress and heat-flux model for turbulent shear flow with streamline curvature, Int. J. Heat Mass Transfer 21, 1609 (1978).

12 Simon, J.W. and Moffat, R.J., Heat transfer through turbulent boundary layers - the effects of introduction of and recovery from convex curvature, ASME paper 79-WA/GT-10 (1979).

13 Gillis, J.C., Johnston, J.P., Kays, W.M. and Moffat, R.J., Turbulent boundary layer on a convex curved surface, Rep. No. HMT-31, Thermosciences Div., Mech. Eng. Dept., Stanford Univ. (1980).

14 Gibson, M.M. and Launder, B.E., Ground effects on pressure fluctuations in the atmospheric boundary layer, J. Fluid Mech. 86, 3, 491 (1978).

15 So, R.M.C., The effects of streamline curvature on Reynolds analogy, ASME paper 77-WA/FE-17 (1977).

16 So, R.M.C., Wall temperature profiles for turbulent curved shear layers, to be published in ZAMP (1981).

17 Oka, S. and Kostić, Ž., Influence of wall proximity on hot wire velocity measurements, DISA Information 13, 29 (1972).

18 Blackwell, B.F. and Moffat, R.J., Design and construction of a low-velocity boundary layer temperature probe, ASME J. Heat Transfer 97, 2, 313 (1975).

19 Hishida, M., Nagano, Y. and Nakamura, Y., Temperature distribution in the turbulent boundary layer in a circular pipe, Bull. JSME 21, 157, 1175 (1978).

20 Reynolds, W.C., Kays, W.M. and Kline, S.J., Heat transfer in the turbulent incompressible boundary layer, I-constant wall temperature, NASA memo 12-1-58W (1958).

21 Coles, D., The law of the wake in the turbulent boundary layer, J. Fluid Mech. 1, 191 (1956).

22 Kader, B.A. and Yaglom, A.M., Heat and mass transfer laws for fully turbulent wall flows, Int. J. Heat Mass Transfer 15, 2329 (1972).

Turbulent Shear Flows behind Cylinder and Sphere in Curved Channels

Hide S. Koyama
Department of Mechanical Engineering
Tokyo Denki University
Tokyo, Japan

ABSTRACT

Experimental study has been carried out to clarify the effects of centrifugal force on the two- and three-dimensional wakes behind a circular cylinder and a sphere installed in curved channels. From the experimental results, large-scale longitudinal vortices with axis in the streamwise direction were found to exist in the wakes behind the circular cylinder and the sphere on the convex and concave walls. Although the width of the wake behind the circular cylinder was the same size as that of the sphere, one pair and two pairs of vortices were observed in the wakes behind the circular cylinder and the sphere, respectively. The width of the two-dimensional wake behind the circular cylinder, spanning the longest dimension of the cross-section of the channel, was nearly independent of the radius of the curved channel. However, the unstable region was wider than the stable region in the two-dimensional wake.

NOMENCLATURE

- d = Diameter of circular cylinder or sphere, mm
- R = Radius of curved channel, mm
- R_e = Reynolds number, $U_1 d/\nu$
- s = Streamwise coordinate, measured along axis of channel, mm
- U = Freestream velocity at inlet of channel, m/s
- U_1 = Representative velocity, m/s
- $\bar{u}$ = Mean velocity, m/s
- u' = Root-mean square value of fluctuating streamwise velocity, m/s
- y = Transverse coordinate, distance normal to wall, mm
- z = Spanwise coordinate, mm
- ν = Kinematic viscosity, m^2/s

INTRODUCTION

The effects of body force(buoyancy force, centrifugal force due to the curvature of the streamlines, Coriolis force, etc.) on the turbulence shear flows are very interesting problems in physics, engineering and the environmental sciences. The apparent analogy between the stability effects of buoyancy force in density stratified flow, centrifugal force in curved flow and Coriolis force in rotating flow was mentioned by Bradshaw[1][1]. The author investigated the effects of Coriolis force on the turbulence structure of a rotating two-dimensional turbulent boundary layer[2,3]. From the experimental results, Taylor-Goertler type vortices were found to exist inside the turbulent boundary layer on the high pressure side wall. The vortex structure was broken up at the higher rotation number(effects of Coriolis force were stronger). The same phenomena were observed by So and Mellor[4] inside the turbulent boundary layer on a concave wall. The basic equations governing the generation of the secondary vorticity which arises when a non-uniform stream is turned were derived by Squire and Winter[5], Hawthorne[6] and Preston[7]. The author mentioned in [3] that the change in the mean vorticity and the fluctuating vorticity along the streamwise direction is equivalent to the "secondary flow effect" and the "stability effect" of body force in turbulent shear flows. The author also considered that the above-mentioned vortex was broken because the destabilizing effect became much larger than the secondary flow effect. The mechanism of the breaking of the vortex, however, is not yet understood completly.

The object of the present investigation is to make clear the effects, especially the secondary flow effect, of centrifugal force due to the curvature of the streamlines on two- and three-dimensional turbulent shear flows. Thus, quantitative experiments were performed on wakes behind a circular cylinder and a sphere installed at the inlet of straight and curved channels.

EXPERIMENTAL APPARATUS AND MEASUREMENTS

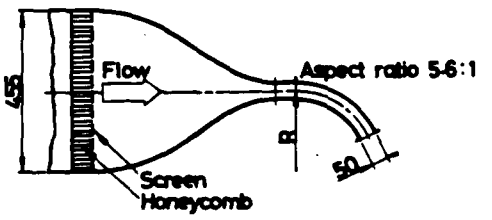

Fig. 1. Experimental apparatus(All dimensions are given in mm)

[1] Numbers in brackets designate References at end of paper

The experimental apparatus employed in the present investigation is shown in Fig. 1. Air is delivered to a wind tunnel by a single-stage Roots blower, having a capacity of 0.5 m^3/s at a delivery pressure of 100 kPa. The air flows through a rectification chamber to the test channel via a 14.8 to 1 contraction chamber. The rectification chamber is made up of several layers of honeycomb flow-straighteners and screens. The contraction chamber is followed by a 210 mm length straight channel (or curved channel), which has a cross section of 280 mm × 50 mm (the aspect ratio 5.6:1). The origin of the coordinates is taken at the inlet of the test channel with the s axis in the streamwise direction, the y axis in the direction perpendicular to the wall, and the z axis in the spanwise direction.

Measurements of the mean velocity and the longitudinal component of turbulence intensity were made using a constant temperature anemometer and an I-type senser with a 5 μm tungsten wire. All measurements were made at the freestream velocity of 10 m/s. The boundary layer at the inlet of the test channel was laminar and its thickness was about 2 mm. The freestream turbulence intensity was about 1.5 %.

A circular cylinder of diameter 2 mm, spanning the longest dimension of the cross-section, was installed as shown in Fig. 2-a to generate a two-dimensional wake at the centre section of the test channel. In this experiment, the Reynolds number was about 1250. To generate two various three-dimensional wakes on the walls, a circular cylinder of diameter 4 mm and a sphere of diameter 4 mm were installed at the inlet of the test channels as shown in Figs. 2-b and 2-c, respectively.

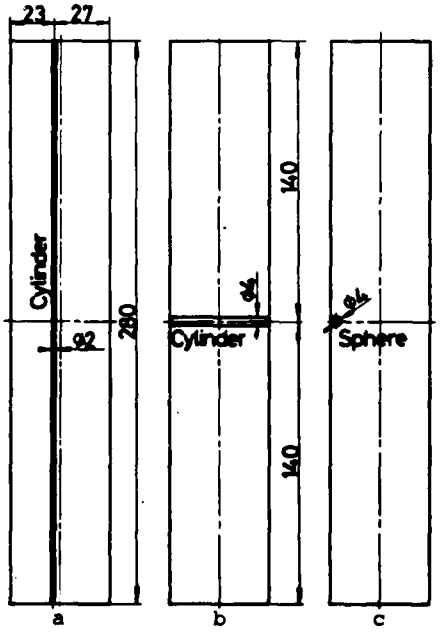

Fig. 2. Three inlet conditions at test channels (All dimensions are given in mm)

EXPERIMENTAL RESULTS AND DISCUSSIONS

Two-dimensional wake behind cylinder

Measurements were performed at the exit of the test channels, 208 mm downstream of the circular cylinder of diameter 2 mm and length 280 mm. Fig. 3 shows the mean velocity and turbulence intensity profiles between the side walls of the straight and curved channels. The wakes behind the circular cylinder at the centre section of the test channel are two-dimensional. The boundary layer on the wall of the straight channel is transitional. The boundary layer on the concave walls of the curved channels (R = 200, 400 mm) are turbulent, whereas on the convex wall (R = 400 mm), the boundary layer is laminar. It is well known that the laminar-turbulent transition is found to be suppressed on the convex wall, while promoted on the concave wall by the effects of centrifugal force due to the curvature of streamlines. In the present results, it is considered that the effect of the boundary layer development on the side walls on the wake is not direct because there are freestream regions between the boundary layers and the wake. The width of the wake is nearly independent of the radius of the curved channel. However, the position of the peak velocity defect is shifted toward the concave wall when decreasing the radius of the curved channel. This means that the unstable region is wider than the stable region of the two-dimensional wake. The turbulence intensity in the unstable region is higher than that of the stable region.

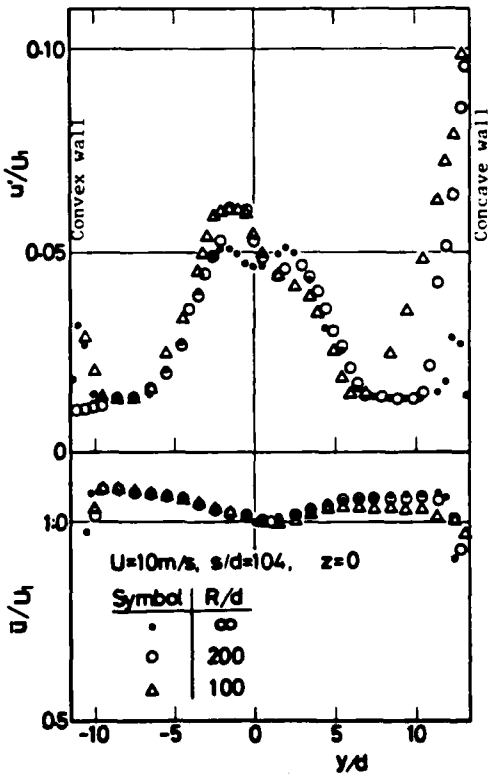

Fig. 3. Mean velocity and turbulence intensity profiles between side walls

Three-dimensional wakes behind cylinder and sphere

Wakes behind circular cylinder. Typical mean velocity profiles in a wake behind a circular cylinder are illustrated in Fig. 4. The basic equations governing the generation of the secondary vorticity which arises when a non-uniform stream is turned were derived by Squire and Winter[5], Hawthorne[6] and

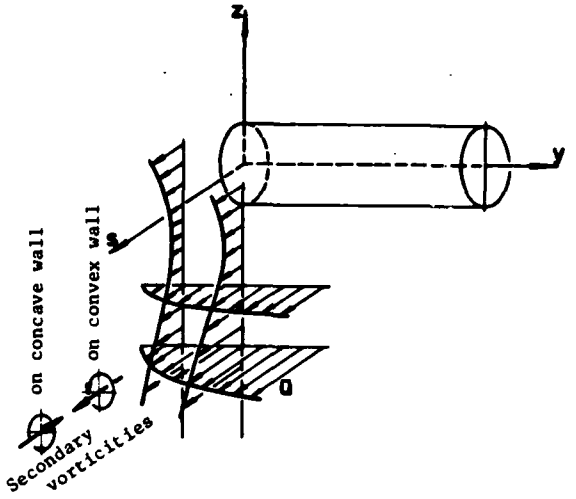

Fig. 4. Secondary vorticities due to spanwise gradient of mean velocity on curved surfaces

Preston[7]. The author mentioned in [3] that the change in the mean vorticity and fluctuating vorticity along the streamwise direction is equivalent to the "secondary flow effect" and the "stability effect" of body force in turbulent shear flows. It is considered that the secondary vorticities as illustrated in Fig. 4 arise due to the spanwise gradient of the mean velocity on the curved surfaces. Therefore, the fluid in the wake behind the circular cylinder installed between the convex and concave walls of the curved channel sweeps from the concave side to the convex side.

Fig. 5 shows the mean velocity and turbulence intensity profiles at the centre section over 120 mm spanwise width. It is observed that the decrease in the mean velocity defect in the curved channel is greater than that in the case of the straight channel. The width of the wake decreases with the decrease in radius of the curved channel. The turbulence intensity profiles with two peaks, where the secondary flows are strong, are also observed. These experimental results demonstrate that the secondary vorticity, which leads to the secondary flow, is a function of the spanwise gradient of the mean velocity and the curvature of the streamlines.

Fig. 6 shows the mean velocity and turbulence intensity profiles at the fixed height (y = 2 mm) from the convex walls over 120 mm spanwise width. The boundary layer outside of the wake is laminar for the case of the radius 400 mm. However, the laminar boundary layer including separation region (dashed lines) was observed outside of the wake for the case of the radius 200 mm. The thickness of the separation region was about 2 mm at the channel exit. The mean velocity in the wake is faster than that outside of the wake. The turbulence intensity at the edge of the wake is higher than that in the central section. From the negative correlation between the mean velocity and turbulence intensity profiles, one pair of large-scale longitudinal vortices with axis in the streamwise direction as illustrated in Fig. 6 is considered to exist in the wake on the convex wall.

Fig. 7 shows the mean velocity and turbulence intensity profiles at the fixed height (y = 2 mm) from the concave walls over 120 mm spanwise width. The boundary layers outside of the wake are turbulent.

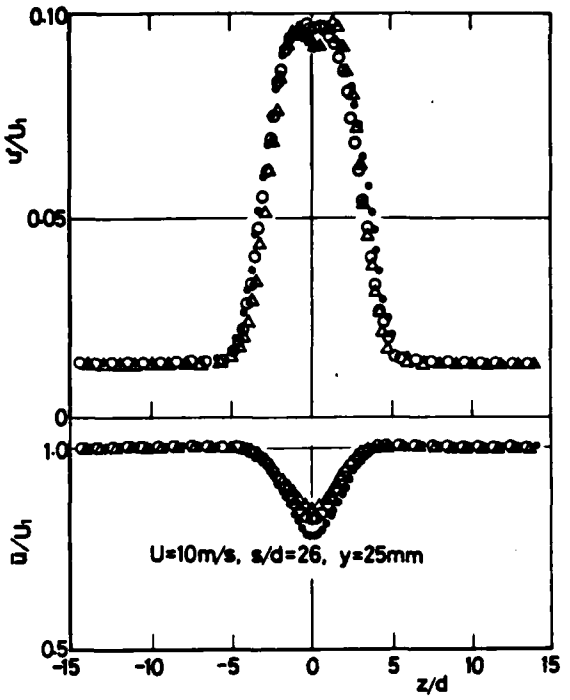

(a) At 26 diameters downstream of cylinder

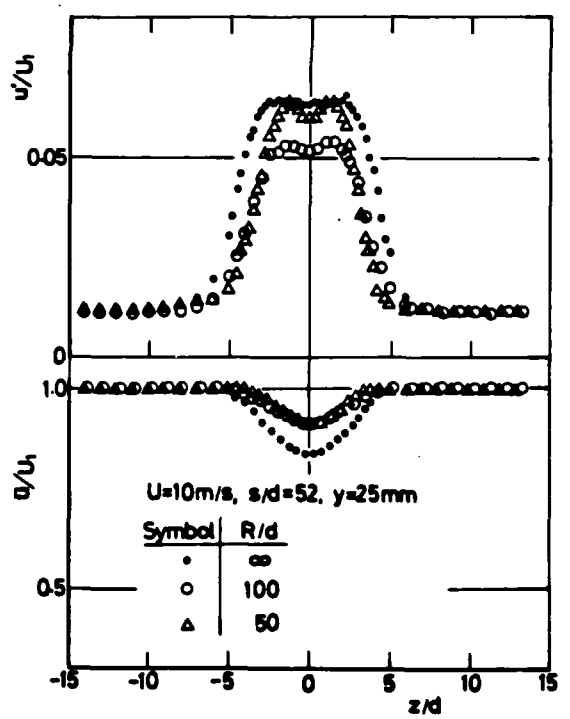

(b) At 52 diameters downstream of cylinder

Fig. 5. Mean velocty and turbulence intensity profiles at centre section over 120 mm spanwise width

in this figure, the dashed lines are the mean velocity and turbulence intensity profiles without circular cylinder at the inlet of the straight channel. There is no difference between the mean velocity profiles in the wakes on the flat, convex and concave walls. Negative correlation between the mean velocity and turbulence intensity profiles is observed for the case of the radius 200 mm. From these results, one pair of large-scale longitudinal vortices with axis in the streamwise direction as illustrated in Fig. 7 is considered to exist in the wake on the concave walls. The vortices convey the fluid of lower mean velocity and higher turbulence near the wall toward the outer layer. The vortices on the concave wall are the same size as that on the convex wall. However, the rotating directions of the vortices on the concave wall are counter-wise as compared with those on the convex wall.

Wakes behind sphere. Fig. 8 illustrate a typical wavy distribution of the mean velocity behind a sphere on a flat surface, and also the secondary vorticities on curved surfaces due to the spanwise wavy variation of the mean velocity.

Fig. 9 shows the mean velocity and turbulence intensity profiles at y = 2 mm, 52 diameters downstream of the sphere over 120 mm spanwise width. The periodic variations of the mean velocity and turbulence intensity are observed in this figure. The negative correlations between the mean velocity and turbulence intensity profiles are also observed. The wavelength of the spanwise variation of the mean velocity and turbulence intensity is nearly independent of the radius of the curvature of the convex wall. From these results, two pairs of longitudinal vortices as illustrated in Fig. 9 are considered to exist in the wake on the convex wall. As mentioned above, the system of the longitudinal vortices is considered to be produced by the secondary flow effect of centrif-

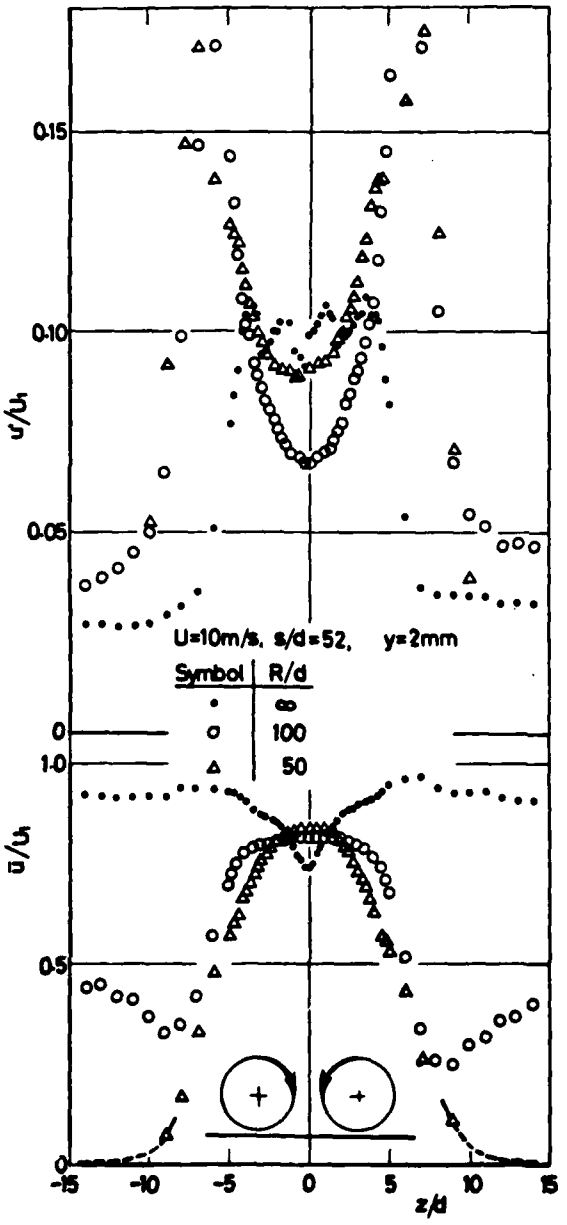

Fig. 6. Mean velocity and turbulence intensity profiles at y = 2 mm over 120 mm spanwise width on convex walls

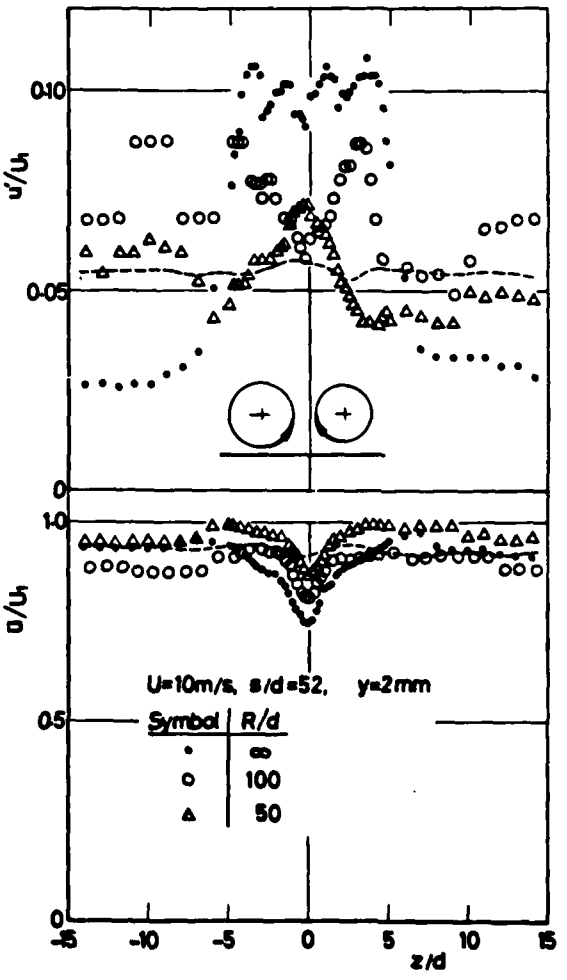

Fig. 7. Mean velocity and turbulence intensity profiles at y = 2 mm over 120 mm spanwise width on concave walls

ugal force due to the spanwise gradient of the mean velocity on the curved surface.

Fig. 10 shows the mean velocity and turbulence intensity profiles in the wakes behind the sphere on the concave walls. The periodic variations of the profiles are observed. The negative correlations between the mean velocity and turbulence intensity profiles are also observed. It is seen from the results that two pairs of the longitudinal vortices with axis in the streamwise direction are found to exist in the wake as illustrated in Fig. 10. The vortices are the same size as that on the convex wall. However, the rotating directions of the vortices on the concave wall are counter-wise as compared with those on the convex wall. Although the width of the wake behind the circular cylinder is the same as that of the sphere, the longitudinal vortex

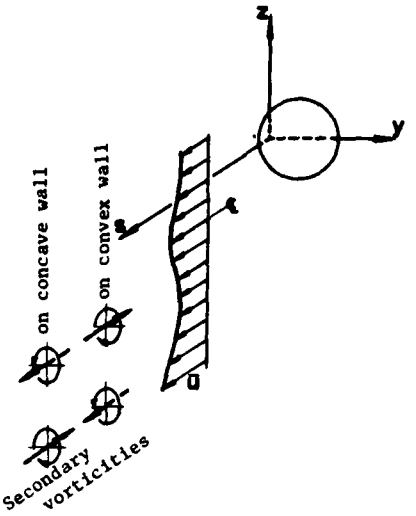

Fig. 8. Secondary vorticities due to spanwise gradient of mean velocity on curved surfaces

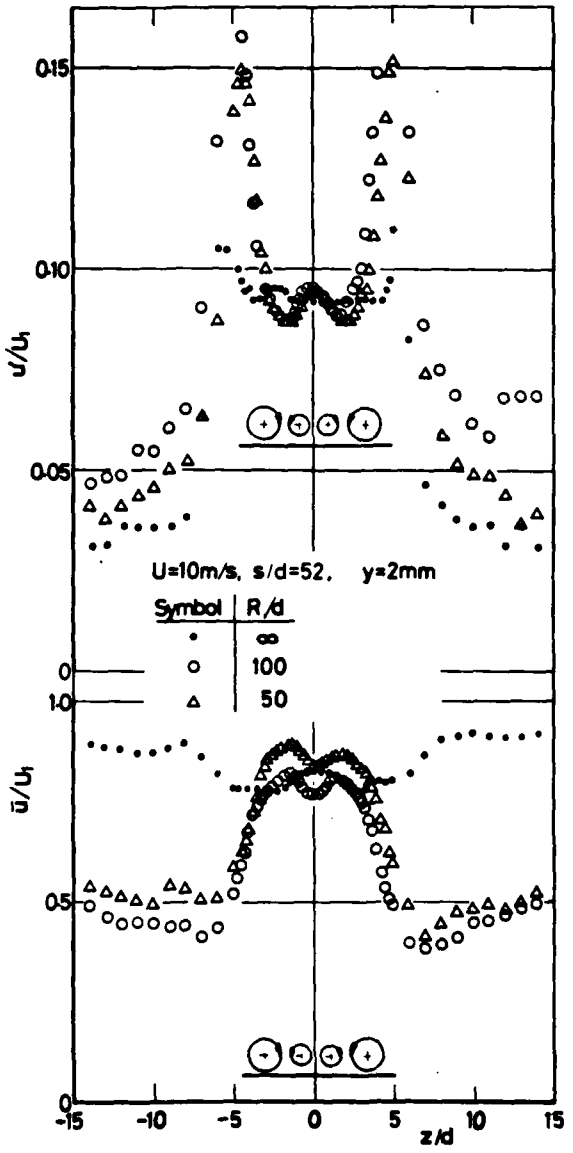

Fig. 9. Mean velocity and turbulence intensity profiles at y = 2 mm over 120 mm spanwise width on convex walls

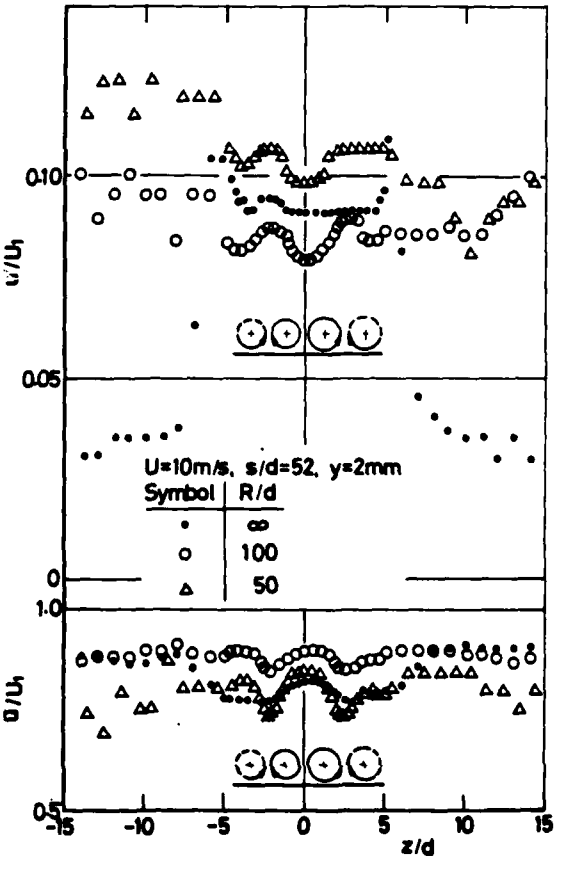

Fig. 10. Mean velocity and turbulence intensity profiles at y = 2 mm over 120 mm spanwise width on concave walls

in the wake behind the circular cylinder is about twice the size of that of the sphere.

CONCLUSIONS

This experimental study has been carried out to clarify the effects of centrifugal force on the wakes behind a circular cylinder and a sphere in curved channels. Conclusions based on the experimental results on the mean velocity and turbulence intensity profiles are summarized as follows:
(1) The width of the two-dimensional wake behind the circular cylinder is nearly independent of the radius of the curved channel. However, the position of the peak of the velocity defect is shifted toward the concave wall when decreasing the radius of the curved channel.
(2) Large-scale longitudinal vortices with axis in the streamwise direction are found to exist in the wakes behind the circular cylinder and the sphere on the convex and concave walls.
(3) Although the width of the wake behind the circular cylinder is the same size as that of the sphere, the longitudinal vortices in the wake behind the circular cylinder are about twice the size of that of the sphere. The rotating directions of the vortices on the convex wall are counter-wise as compared with those on the concave wall.

A 'NOWLEDGMENTS

I wish to express my gratitude to students of Tokyo Denki University who have worked with me and also Mr. T. Endo for his design and manufacture of an electrical equipment. The support of the Research Foundation of Tokyo Denki University is gratefully acknowledged.

REFERENCES

1 Bradshaw, P.,"The Analogy Between Streamline Curvature and Buoyancy in Turbulent Shear Flow," Journal of Fluid Mechanics, Vol. 36,Part 1, 1969, pp. 177-191.

2 Koyama, H., et al.,"Stabilizing and Destabilizing Effects of Coriolis Force on Two-Dimensional Laminar and Turbulent Boundary Layers," Journal of Engineering for Power, Trans. ASME, Vol. 101, No. 1, 1979, pp. 23-31.

3 Koyama, H., et al.,"Turbulence Structure and Three-Dimensionality of a Rotating Two-Dimensional Turbulent Boundary Layer," Proceedings of the 2nd Symposium on Turbulent Shear Flows, 1979, pp. 4.22-4.27.

4 So, R.M.C. and Mellor, G.L.,"Experiment on Turbulent Boundary Layers on a Concave Wall," Aeronautical Quarterly, Vol. 26, 1975, pp. 25-40.

5 Squire, H.B. and Winter, K.G.,"The Secondary Flow in a Cascade of Airfoils in a Non-uniform Stream," Journal of the Aeronautical Sciences, April 1951, pp. 271-277.

6 Hawthorne, W.R.,"Secondary Circulation in Fluid Flow," Proc. Roy. Soc. A, 1951, Vol. 206, pp. 374.

7 Preston, J.H.,"A Simple Approach to the Theory of Secondary Flows," The Aeronautical Quarterly, Vol. V, September 1954, pp. 218-234.

EFFECTS OF STABLE AND UNSTABLE FREE STREAMS ON A TURBULENT FLOW OVER A CONCAVE SURFACE

Susumu Nakano
Graduate Student,
Department of Mechanical Engineering,
Science University of Tokyo

Akiyoshi Takahashi
Copal Electra Co.,
Ashikaga, Tochigi 326, Japan

Takaaki Shizawa
Research Associate,
Department of Mechanical Engineering,
Science University of Tokyo

Shinji Honami
Associate Professor
Department of Mechanical Engineering,
Science University of Tokyo,
Shinjuku, Tokyo 162, Japan

ABSTRACT

Mean velocity and turbulence measurements are described for a turbulent flow over a concave surface with a strong streamwise curvature. Different kinds of uniform shear flow are provided at the inlet to the curved section. Three-dimensional longitudinal vortices are found to occur under all free-stream conditions. In an unstable free stream, turbulent intensities in the boundary layer as well as in the free stream are enhanced. The unstable free-stream condition affects the structure of the boundary layer and of the free stream itself.

NOMENCLATURE

As	Aspect ratio, h / B
B	Channel height
$C_f/2$	Skin friction coefficient
h	Channel width
k	Surface curvature
R	Radius of surface curvature
R_e	Reynolds number, $U_{pw} B / \nu$
R_f	Flux Richardson number, $2k/(\frac{\partial U}{\partial y} + \frac{kU}{1+ky})$
U,V,W	Mean velocities in x, y ,and z coordinates
U_p	Free-stream velocity
U_{pw}	Free-stream velocity extrapolated to the wall
x,y,z	Curvilinear coordinate
u,v,w	Fluctuating velocities in x,y ,and z directions
δ	Boundary layer thickness
δ'	Thickness where vorticity is 95 % of free stream
δ_2	Momentum thickness
ν	Kinematic viscosity
ρ	*Density*
ζ	Vorticity around z-axis, $-\frac{\partial U}{\partial y} - \frac{kU}{1+ky}$

INTRODUCTION

Much attention has been paid to the turbulent boundary layer over a concave surface, since striking changes in turbulence properties can occur, even for a slight surface curvature. Hoffmann & Bradshaw [1] and Hunt & Joubert [2] have provided data on slight surface curvatures. Data reported by So & Mellor [3] shows that over a concave surface, Reynolds shear stress increases and three-dimensional vortices exist.

Furthermore, because concavity increases turbulent mixing [4], the effects of a stable or unstable free-stream velocity gradient on the flow structure and heat transfer over the concave surface have become an important subject of concern. Castro & Bradshaw [5] have explored the effect of streamwise curvature on the free shear layer, but no data on unstable effects has been obtained with the exception of the strongly unstable case described by Margolis [4]. Previous experiments done on the mixing process of free shear layer itself ignored the interaction with the concave boundary layer, indicating that free-stream interaction with a strongly unstable boundary layer is not understood in detail.

The purpose of the present paper is to clarify experimentally the influence of flow conditions upstream from the curved test section on a turbulent structure over a concave surface. These test flow conditions correspond to a stable or unstable free stream.

APPARATUS AND TECHNIQUES

Figure 1 shows the schematic arrangement of the curved wall tunnel used. The tunnel is an open-return suction type. A flow straightener with a honeycomb section, three screens, and a two-dimensional 5-to-1 contraction nozzle are set at the inlet section. The test channel is a 300 mm straight section and a curved test section with a 500 mm radius of concave curvature. A tripping wire 0.6 mm in diameter is attached at the nozzle throat to create a turbulent boundary layer in the test section. While no attempt was made to minimize the secondary flow created by end-wall flow or to separate acceleration or deceleration effects, the use of a large aspect ratio kept secondary flow effects small. The Reynolds number based on channel height is $1.0 - 1.1 \times 10^5$.

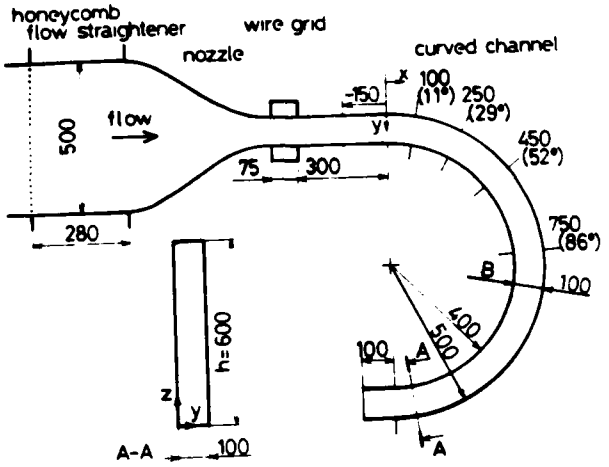

Figure 1 Experimental apparatus : all dimensions in mm s

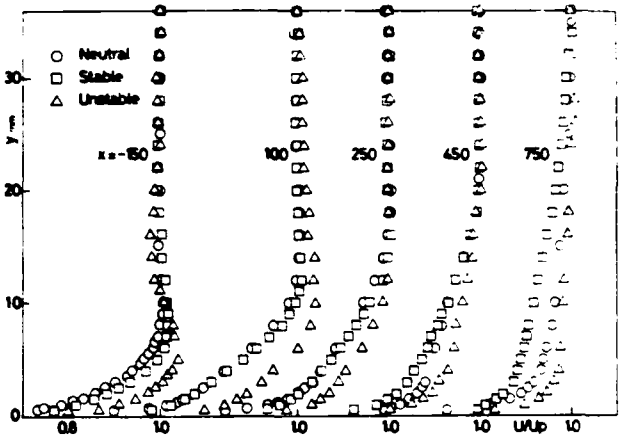

Figure 2 Mean velocity distribution

Different kinds of uniform shear flow were provided at the test channel inlet, with shear changed by means of 1.6 mm diameter wire grids placed normal to the stream at unequal intervals. Wire grid spacing was determined by Owen's method [6]. The same grids could be used for experiments by reversing grid direction in the channel. Inlet conditions obtained in the curved channel's free-stream region are (i) shear free flow, which produced a uniform flow in the upstream straight channel, i.e., the "neutral case," (ii) positive shear flow, and (iii) negative shear flow. Positive shear flows produce a stable free stream in the curved section, while negative shear flows producing an unstable free stream.

Mean and turbulent velocities were measured at five stations in the downstream direction. A hot-wire probe was continuously traversed both spanwise and normal to the wall. The hot-wire anemometer was a linearized constant temperature type. Wire output signals near a wall were not modified to compensate for extra heat loss from the wire to the wall, since no serious error was observed in the wall remote region, i.e., y>1.0 mm.

Reynolds stress measurement was made to involve rotation of the wire around two axes. The normal wire around the z-axis was rotated to provide $\overline{u^2}$, $\overline{v^2}$, and $-\overline{uv}$ in a similar method [7]. The same wire was also rotated around the y-axis to give $\overline{u^2}$, $\overline{w^2}$, and $\overline{uw}$. Accuracy appears to be lessened when rotating normal and slanted wires are used [8], since slanted wire data includes error resulting from the data processing of normal wire.

Hot-wire signals through a low-pass filter and a RMS meter were recorded on an X-Y plotter, then converted manually to digital form. The resulting data was reduced by a computer program including temperature compensation and modification of angle characteristics of the rotating wire. Figures 6 to 9 show the effects of RMS signal scatter on reduced results. The severest uncertainty for $\overline{u^2}$ is 7 % and uncertainty for $\overline{v^2}$ amounts to 6 % near the wall in an unstable free stream

RESULTS AND DISCUSSION

Figure 2 shows profiles of streamwise mean velocity normalized by U_p, with the free stream velocity U_p given as,

$$U_p = \frac{Upw}{1+ky} + \frac{\zeta}{2k}\left\{\frac{1}{1+ky} - (1+ky)\right\} \quad (1),$$

where U_{pw} and ζ were determined by a least square method using velocity data measured in the free-stream region. Their vorticity intensities ζ and free-stream velocities extrapolated to the wall U_{pw} at the first station, x = -150 mm, are shown in Table 1. "Bulging" near the wall region at the straight section, in an unstable case, is produced by the grid arrangement, even though it disappears further downstream. In all cases, comparisons with a flat or convex wall boundary layer flow show a smaller velocity defect near the wall, especially in an unstable free stream, which is quite small in comparison.

In accord with previously obtained results for strong curvature [9,10], the tendency toward a vortex-free flow was obtained even near the concave wall when a fully developed flow was given at a straight section. Hunt [2] classified these flows into two categories depending on curvature, i.e., inertia-dominated and stress-dominated. As Figure 3 indicates,

Table 1 Free Stream Condition at First Station

Flow Condition		Neutral	Stable	Unstable
ζ	sec^{-1}	0	63.8	-37.8
U_{pw}	m/sec	16.3	18.8	12.8
$B\,\zeta/U_{pw}$		0	0.34	0.30
δ	mm	7.5	5.4	6.2 *

* δ' is used

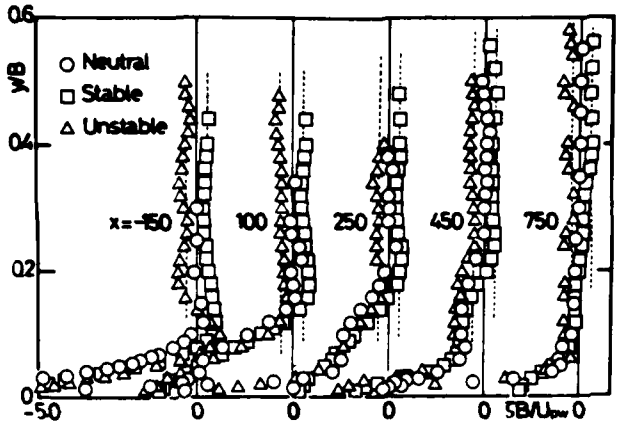

Figure 3 Mean vorticity profile : ---- average free-stream vorticity

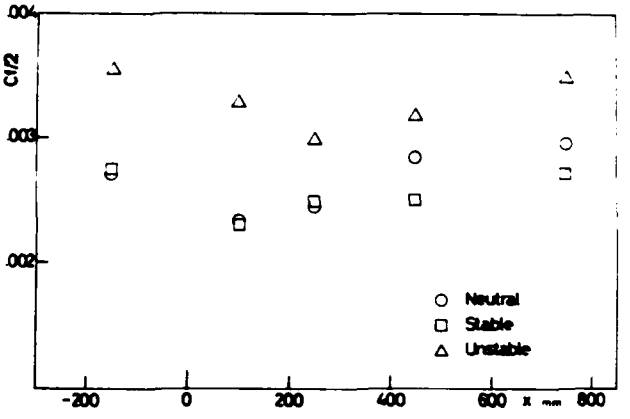

Figure 5 Skin friction coefficient

vorticity in the free-stream region is apparently maintained in the downstream direction. The rate of vorticity change toward zero in the free stream shows a very slow response, while in the boundary layer or for an inertia dominated flow the time constant is shorter.

Figure 4 indicates distributions of momentum thickness, reduced by the usual definition,

$$\delta_2 = \int_0^{\delta} \frac{U}{U_p} \left(1 - \frac{U}{U_p} \right) dy \qquad (2).$$

Although an exact momentum thickness should be defined as

$$\int_0^{\delta_2} U_p^2 \, dy = \int_0^{\delta} U \left(U_p - U \right) dy \qquad (3),$$

the expression for δ_2 in Equation (3) becomes excessively complicated when shear flow is employed. The difference in δ_2 between Equations (2) and (3) was estimated as less than 5 % when $|k\delta| < 0.1$ [11]. Momentum thickness distribution at the first and second stations in an unstable flow is not shown in Figure 4, because the buldging profiles are produced there. Data shows that δ_2 in a stable flow is thicker than in other cases and that it still develops even at the last station, x = 750 mm, though other cases tend to decrease there.

Figure 5 shows distributions of skin friction coefficient, Cf/2, determined from the law of the wall. Some deviation from the law of the wall was certain to occur, thus resulting in a similar tendency [3] containing some doubts about accuracy.

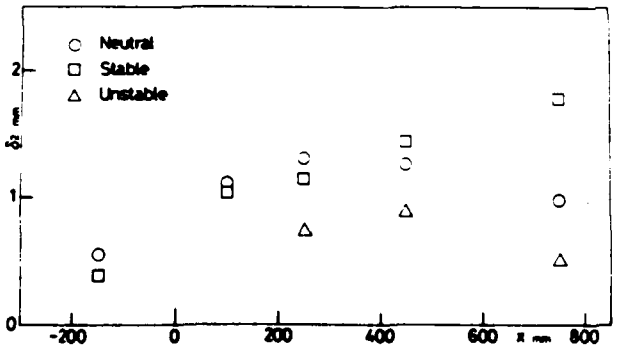

Figure 4 Momentum thickness

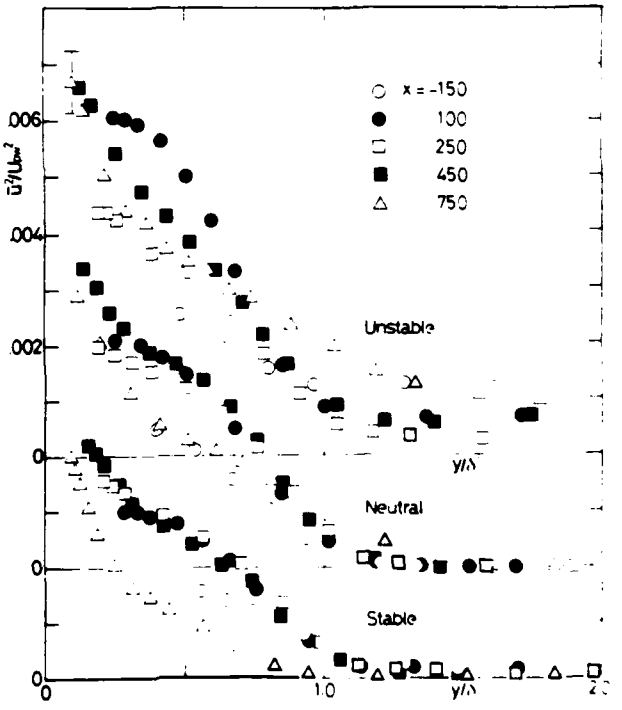

Figure 6 Turbulent normal stress profiles, $\overline{u^2}$

Figures 6, 7, and 8 present the profiles of normal components of Reynolds stress, $\overline{u^2}$, $\overline{v^2}$, and $\overline{w^2}$. Shear stress distribution, $-\overline{uv}$, is also shown in Figure 9. All stresses are normalized by Upw. In figures of unstable case δ', which denotes a thickness where vorticity is 95 % of free stream, is used instead of δ. Reynolds stress, excluding the neutral case, shows some finite values in the free-stream region at the straight section because of the wire grid at the nozzle exit. The boundary layer on the straight wall differs slighty from Klebanoff's data [12], since the upstream straight section is not long enough to provide an equilibrium flow.

Regarding turbulence structure within a boundary layer, the striking feature of $\overline{v^2}$ and $-\overline{uv}$ profiles is that a maximum is observed half way through the boundary layer in all free-stream conditions. Similar maxima located at $y/\delta \simeq 0.4$ were found in mild curvature [1] as well as strong curvature [3], though their free streams were of the neutral case. Of these, a second maximum appears to exist near the boundary layer edge at a position of minima of mean velocity U in the vortex, hereafter refered to as a "trough".

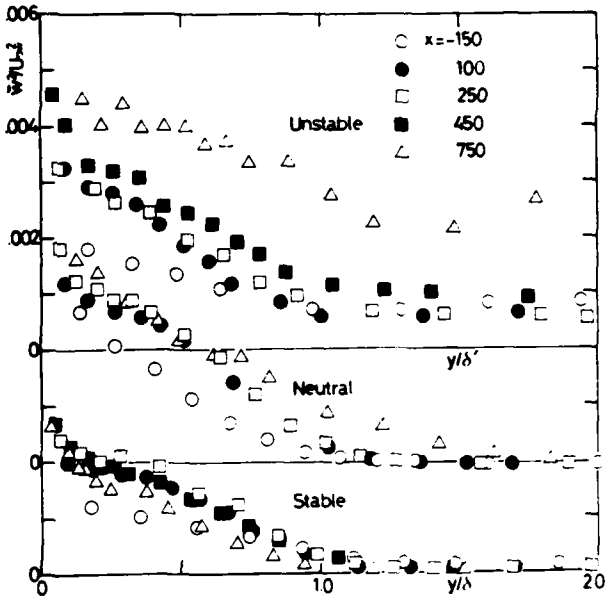

Figure 8 Turbulent normal stress profiles, $\overline{w^2}$

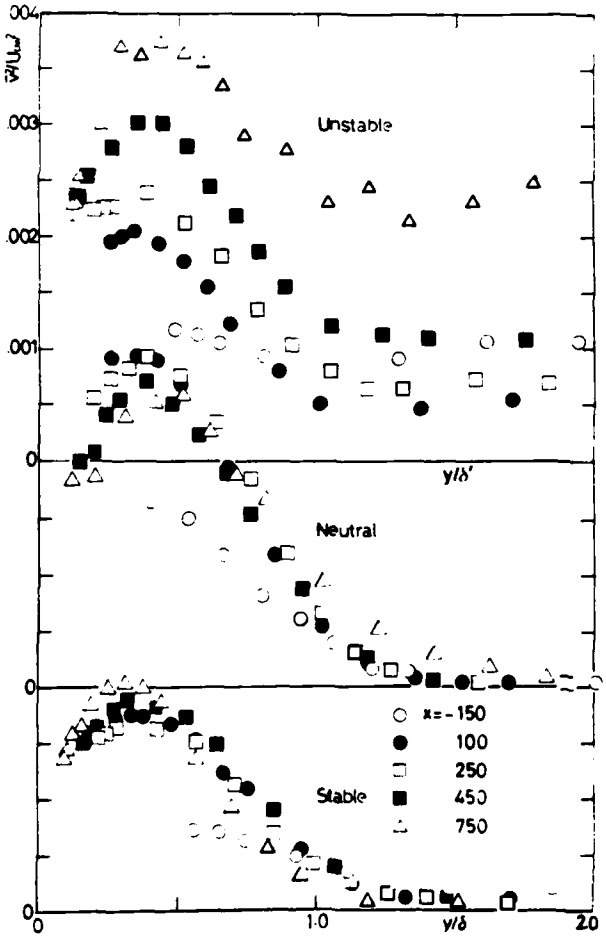

Figure 7 Turbulent normal stress profiles, $\overline{v^2}$

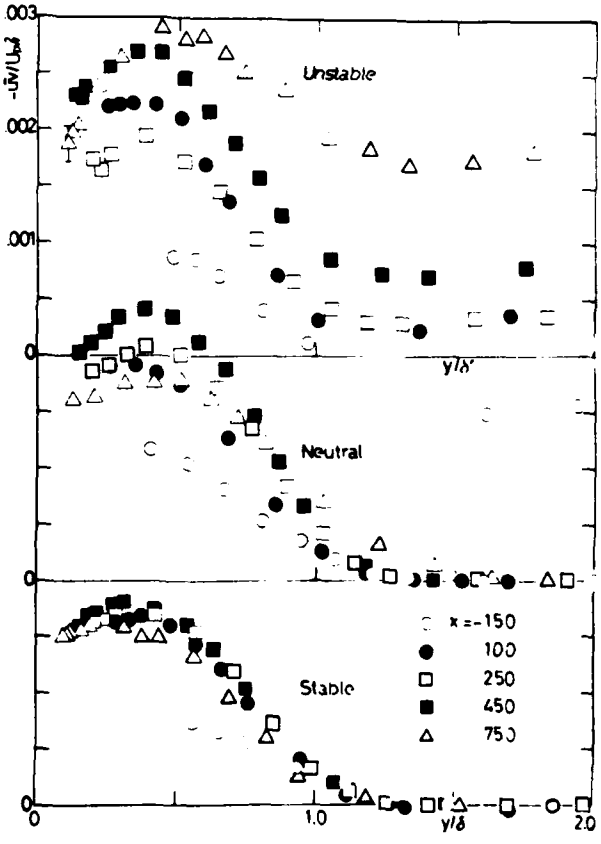

Figure 9 Turbulent shear stress, $-\overline{uv}$

Regarding the turbulence profile in the free-stream region, turbulent intensities in the neutral and stable cases become zero or almost zero. In contrast, an unstable free stream is associated with marked production of turbulence energy. The Reynolds stress trend obtained can be shown to be consistent with the argument that each component is enhanced by an extra term due to curvature together with a mean strain rate based on a thin shear layer assumption. This is easily demonstrated by each production term in transport equations for Reynolds stress given as,

$$-\overline{uv}(1+ky)\left(\frac{\partial U}{\partial y}+\frac{kU}{1+ky}\right) \qquad -\overline{uw}(1+ky)\frac{\partial U}{\partial z}$$

for $\overline{u^2}$ production (4),

$$-\overline{uv}(-2kU) \qquad -\overline{vw}(1+ky)\frac{\partial V}{\partial z}$$

for $\overline{v^2}$ production (5),

$$0 \qquad -\overline{w^2}(1+ky)\frac{\partial W}{\partial z}-\overline{uw}\frac{\partial W}{\partial x}-(1+ky)\overline{vw}\frac{\partial W}{\partial y}$$

for $\overline{w^2}$ production (6),

$$\overline{u^2}(-2kU)+\overline{v^2}(1+ky)\left(\frac{\partial U}{\partial y}+\frac{kU}{1+ky}\right)$$

$$(1+ky)\left\{-\overline{uv}\frac{\partial W}{\partial z}+\overline{uw}\frac{\partial V}{\partial z}+\overline{vw}\frac{\partial U}{\partial z}\right\}$$

for $-\overline{uv}$ production (7).

The first term denotes the production in a two-dimensional curved flow.

Figure 10 shows the production mechanism of $\overline{u^2}$, $\overline{v^2}$, and $-\overline{uv}$ to illustrate the contribution of the above two terms to production of turbulence energy and shear stress. The solid line indicates positive contribution and the dashed line negative. A ratio of the extra strain rate, $-2kU$, to the mean strain rate, $(1+ky)\partial U/\partial y + kU$, is considered a useful measure denoting the effect of curvature on turbulence structure. This ratio corresponds to a flux Richardson number, Rf. A positive $-\overline{uv}$ first introduces the $\overline{u^2}$ production by the mean strain rate, then $\overline{v^2}$ is produced by the extra strain rate through $-\overline{uv}$ generation. Finally, $\overline{v^2}$ goes into $-\overline{uv}$ generation, like a chain reaction. By this cyclic production mechanism, turbulence energy and the shear stress are increased, where an unstable condition is applied, and vice versa.

The effect of the free stream on the production mechanism within a boundary layer is not so straightforward that the mean strain rate in the boundary layer becomes dominant, having a higher order than that

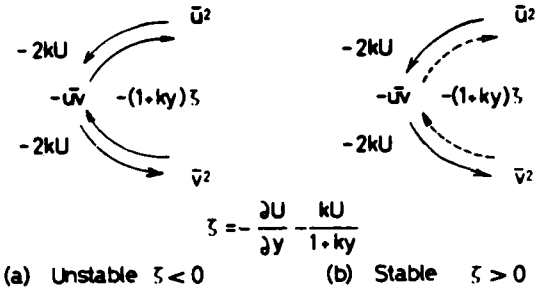

Figure 10 Cyclic production mechanism with concave curvature ; $k<0$

in the free stream and extra strain rate. The free stream may cause only an additional effect, yet remarkable production, even for spanwise component $\overline{w^2}$, is observed within the boundary layer in an unstable case. No extra generation for $\overline{w^2}$ could be expected with the exception of the contribution by pressure fluctuation, if the mean strain rate were confined to a two-dimensional mean flow field.

One reason complicating the turbulence structure is the influence of three-dimensional longitudinal vortices first detected by Tani [13]. Their existence was confirmed by a spanwise flow survey and resulting in wavy profiles of the mean and fluctuation velocity, even in the wall remote region in an unstable case. The spanwise location selected for the experiment corresponds to a central part between the trough and crest of a vortex at channel midspan.

When a mean flow is three-dimensional, each additional term of turbulence energy production and shear stress generation is given as the second term in Equations (4) to (7). One of the additional mean strain rates due to the vortex motion is $\partial W/\partial z$ which denotes a convergent or divergent effect with respect to a plane of symmetry like a crest or trough of the vortex. An additional loss or gain for $\overline{w^2}$ and $-\overline{uv}$ is followed by $-\overline{w^2}(1+ky)\partial W/\partial z$ and $-\overline{uv}\,(1+ky)\partial W/\partial z$. Thus, a mechanism of the extra production for $\overline{w^2}$ and $-\overline{uv}$ in an unstable case might be seen by activity of the longitudinal vortices. However, lack of data at several spanwise positions makes it impossible to demonstrate the three-dimensional production mechanism in detail.

CONCLUSION

Measurements made over a concave surface with different kinds of uniform shear flow at the inlet show marked effects on turbulence structure. In an unstable free-stream condition, Reynolds stresses are increased both in the boundary layer and free stream, even for spanwise component $\overline{w^2}$. The striking feature of $\overline{v^2}$ and $-\overline{uv}$ profiles is that a maxima exists at $y/\delta \approx 0.4$ independent of free-stream conditions. A high level of turbulence intensity is associated with the growth of longitudinal vortices.

ACKNOWLEDGMENTS

This study was supported in part by the Japanese Ministry of Education under the Grant-in-Aid for Scientific Research. The authors wish to thank Messrs M. Katayama and H. Yasukawa who assisted in data acquisition.

REFERENCES

1 Hoffmann, P. H. and Bradshaw, P., "Turbulent Boundary Layers on Surfaces of Mild Longitudinal Curvature," Aero Report 78-04, Dec. 1978, Imperial College, London.

2 Hunt, I. A. and Joubert, P. N., "Effects of Small Streamline Curvature on Turbulent Duct Flow," Journal of Fluid Mechanics, Vol. 91, Part 4, 1979, pp. 633 - 651.

3 So, R. M. C. and Mellor, G. L., "Experiment on Turbulent Boundary Layers on a Concave Wall," Aeronautical Quarterly, Vol. 26, 1975, pp. 25 - 40.

4 Margolis, D. P., "An Investigation of a Curved Mixing Layer," PhD thesis, 1963, Penn. State Univ..

5 Castro, I. P. and Bradshaw, P., "The Turbulence Structure of Highly Curved Mixing Layer," Journal of Fluid Mechanics, Vol. 73, Part 2, 1976, pp. 265 - 304.

6 Owen, P. R. and Zienkiewicz, H. K., "The Production of Uniform Shear Flow in a Wind Tunnel," Journal of Fluid Mechanics, Vol. 2, 1957, pp. 521-531.

7 Fujita, H. and Kovasznay, L. S. G., "Measurement of Reynolds Stress by a Single Rotated Hot Wire Anemometer," The Review of Scientific Instruments, Vol. 39, No. 9, 1968, pp. 1351 - 1355.

8 Bissonnette, L. R. and Mellor, G. L., "Experiments on the Behaviour of an Axisymmetric Turbulent Boundary with a Sudden Circumferential Strain," Journal of Fluid Mechanics, Vol.63, Part 2, 1974, pp. 369 - 413.

9 Wattendorf, F. L., "A Study of the Effect of Curvature on Fully Developed Turbulent Flow," Proc. of the Royal Society, Series A, Vol. 148, 1935, pp. 565 - 598.

10 Eskinazi, S. and Yeh, H., "An Investigation on Fully Developed Turbulent Flows in a Curved Channel," Journal of Aeronautical Science, Vol. 23, 1956, pp. 23 - 34.

11 Honami, S. and Johnston, J. P., "A New Definition of Integral Thickness for Boundary Layer Flow over Longitudinally Curved Surfaces," Report II - 16, Oct. 1980, Thermoscience Division, Stanford Univ..

12 Klebanoff, P. S., "Characteristics of Turbulence in a Boundary Layer with Zero Pressure Gradient," NACA Report 1247, 1955.

13 Tani, I., "Production of Longitudinal Vortices in the Boundary Layer along a Concave Wall," Journal of Geophysical Research, Vol. 67, No. 8, 1962, pp. 3075 - 3080.

SESSION 5 - CONFINED FLOWS

J. J. D. Domingos - Chairman

PREDICTION AND MEASUREMENT OF FLOW AND HEAT TRANSFER IN MOTORED DIESEL ENGINE SWIRL CHAMBERS

M.M.M.ABOU-ELLAIL and M.M.ELKOTB
FACULTY OF ENGINEERING,CAIRO UNIVERSITY,CAIRO,EGYPT.

ABSTRACT

This paper is concerned with the prediction and measurement of flow and heat transfer in motored diesel engine swirl chambers. Measurements are mainly carried out by a temperature-compensated hot-wire anemometer and a high speed camera. Predictions are based on the solution of the finite-difference form of the governing differential equations for the transport of mass, momentum and energy by way of digital computers. In general, the obtained agreement between predictions and measurements is fairly good which confirms the accuracy of the described prediction procedure.

NOMENCLATURE

A_c	influence coefficient
A_p	equal to ΣA_c
C_μ, C_1, C_2	constant of the turbulence model
C_{pm}	mean piston velocity
h	total enthalpy
K	turbulence kinetic energy
$\dot{m}_c$	mass flow rates across cell boundaries
M_p^o	equals to $(\rho V)_p^o/\delta t$ old values at time t
M_p^n	equals to $(\rho V)_p^n/\delta t$ new values at time t+δt
P	pressure
p'	pressure correction
u	tangential velocity
$\vec{u}$	velocity vector at any point
r	radial position
S_p	coefficient of linearized source term
S_u	coefficient of linearized source term
S	source/sink term for variable ϕ
t	time
v	radial velocity
V	cell volume
β	equal to $(\partial\rho/\partial p)T$
Γ_ϕ	effective diffusivity coefficient for variable ϕ
ε	dissipative rate of turbulent kinetic energy
θ	angular position
ϕ	arbitrary dependent variable
μ	laminar viscosity
μ_{eff}	effective viscosity
ρ	density
$\sigma_h, \sigma_k, \sigma_\varepsilon$	constants of turbulence model for h, K & ε.
Σ_c	summation for neighbouring nodes of typical grid node.

Subscripts

E,W,N,S East,West, North and South neighbouring nodes
e,w,n,s midway nodes between each node.

INTRODUCTION

The availability of very large, high speed digital computers has encourage efforts to simulate the compression ignition engines. Complete mathematical model for the calculation of the heat release in a swirl chamber of a diesel engine is still not available. The heat release in multifuel engines depends to a great extent on the hydrodynamic mixing and transport processes, the fuel atomization and evaporation, the chemical reaction mechanism and reaction rates, heat transfer and environmental conditions, all of which vary inside the swirl chamber. The-fuel mixing process perior to autoignition is important in diesel engines, in general, and swirl chambers of diesel engine in particular. Moreover, the mixing process controls combustion which in turn controls the rate of pressure rise, noise emission and pollutant formation in engine cylinders (1,2,3). The study of pure phenomena in subclasses helps in solving more complex combustion phenomena resulting from multifuel combustion.

Therefore, a mathematical prediction model capable of predicting the air velocity inside swirl combustion chambers is required for the development of multifuel engines as well as saving time and cost.

There have been several experimental investigations, as a consequence of the development of swirl chambers; for the determination of the swirl chamber parameters. However, it was found that the study of flow is the more accurate method for determination of swirl chamber parameters. Theoretical investigations have been therefore reported (4,5,6). Most of these investigations are based on the evaluation of the intensity of charge motion which relies on emperical correlations. Moreover, they are based on the application of evaluating parameters recommended from the analysis of present swirl chambers. Such evaluating parameters have a quite wide range that they cannot give sufficient accurate

results. Recently, Elkotb (7) proposed a new theoretical model based on the equality of the moment of momentum resulting from the ejection velocity to the swirl chamber and the moment of momentum of the rotating air inside the swirl chamber provided that the air motion in the central zone is solid vortex and that in periphery is free vortex. This model can define the average velocity to the swirl chamber and the moment of momentum of the rotating air inside the swirl chamber but is not useful in the study of the interaction between fuel and air. Over the past decade a fairly considerable effort has been expended on computational procedures with the aid of mathematical models, for reciprocating engines (8,9,10). These prediction procedures are based mainly on the solution of the finite difference form of the governing differential equations for the transport of mass, momentum and energy.

Although these attempts have been made to predict the properties of turbulent motion by mathematical models, no explicit consideration of the physical properties in swirl chambers is taken.. Moreover, the shape of the combustion chamber with its effect on the air flow was not included.

The objective of this work is to develpp a complete mathematical model for the prediction of the turbulent flow field in swirl chambers. Experimental measurement of the air flow velocity is planned to satisfy careful comparison, over a wide range, with the predicted values to obtain reliable information about the constants of the turbulence model. Actually these constants depend on local turbulence values. This proposed prediction procedure is required to investigate speedily and with reasonable detail and accuracy the combustion of fuel with various chemical properties as well as the effect of various factors on the combustion process needed for the development of multifuel engines.

EXPERIMENTAL INVESTIGATION

A careful comparison over a wide range of data can give, in addition to the mean velocity field, reliable information about the constants of the turbulence model. Therefore an experimental setup has been built up to facilitate measurements of the air velocity components inside the swirl chamber with the highest possible accuracy. The experimental swirl chamber has been built up in one of the engine cylinders of a 2-cylinder, 4-stroke, water cooled medium speed diesel engine. The other cylinder has been used for motoring the engine to the required regime. The engine is directly coupled with hydraulic dynamometer for engine loading and equipped with various instruments required for measuring the main engine parameters.

The scope of this investigation includes the measuring of the instantaneous velocity components and finding out the effect of various constructional and working conditions on the air flow inside swirl chambers. For this reason the cylinder head is modified and a swirl chamber is constructed and attached instead of the original chamber. A schematic drawing of the experimental setup is shown in Fig.(1). A cylinderical combustion

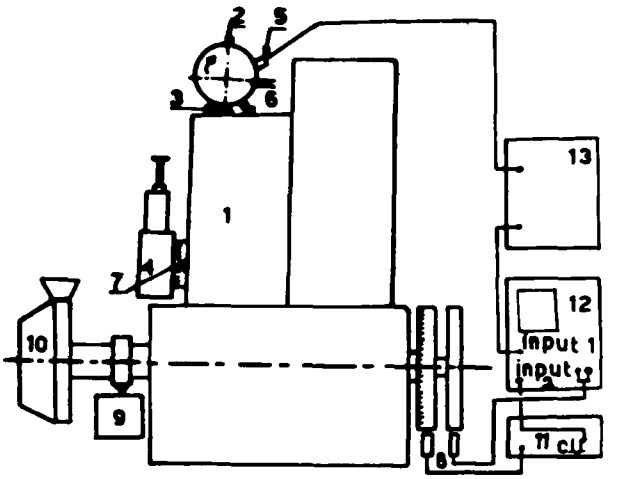

Fig.1 Scheme of experimental setup.(1-engine assembly,2-swirl chamber,3-variable area port 4-injection pump,5-hot wire anemometer,6-thermocouples,7-advance angle adjustment, 8-T.D.C. pickup, 9-tachometer,10-dynamometer,11-degree marker amplifier,12-loop oscillograph, 13-balancing system).

chamber of 48.5 mm diameter,Fig.(2), satisfying a relative swirl chamber volume ratio

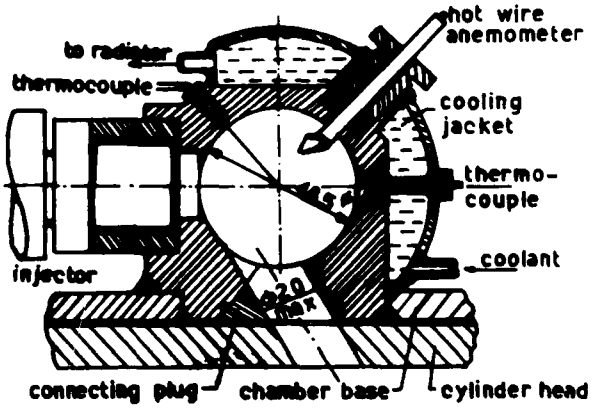

Fig.2 Scheme of the test combustion chamber.

of 0.507 is constructed with an optically flat fused quartz window on one of its sides. The swirl chamber is built up with compression ratio 17. Two oblique washers are fitted on either sides of the quartz plate to avoid stress concentration. The quartz lens is fastened by a self locking screwed collar facilitating easy firm and quick assembly. The test swirl chamber is fitted with a cooling jacket supplied with glysrine from an independent circulating system to control its

surface temperature. Connecting ports with various configurations are constructed to supply air to the swirl chamber from the main chamber. The chamber is designed such that variation of the relative swirl volume ratio, the connecting port area ratio (7) and the connecting port inclination angle are possible. The intake and exhaust manifolds of the test cylinder are separated from those of the second motoring cylinder.

The chamber is equipped with a temperature compensated hot wire anemometer to measure the air velocity components. The probe of the hot wire is connected to an ultra-voilet oscilograph through the compensating bridge. It is equipped also with two ferrous-constantan thermocouples for measuring the surface temperature. The quartz window is used to photograph the air motion inside the swirl chamber with a high speed camera. The gas pressure variations inside the main and swirl combustion chambers together with the crankangle were picked by a highly sensitive Piezo-electric transducers and an external X-generator. The display of the gas pressure is syncronised with the disc displaying the signal of the top dead centre. The data recorded during an engine run include combustion chamber pressure, velocity variation for two inclination angles of the hot wire at each location, crank-angle, top dead centre and two surface thermocouples. Because of the cycle to cycle variations in data recorded and hence in air velocity components, it is required to examine a large quantity of data to obtain a quite sufficient reasonable results. Thus, a high speed multi channel data recording and processing system is applied. The output from the hot wire anemometer is magnified and recorded by a magnetic taperecorder. A calibration signal is recorded at the start of recording. Thereafter, the analog signal representing the air velocity variation at two inclination angles are played back at a lower speed to the analog/digital converter and digitzied at every crank angle for 50 cycles. The output of the 50 cycles is then processed and an average cycle of the velocity variations is determined and recorded on magnetic tape in digital form for subsequent processing on a digital computer to determine the mean velocity and the random velocity.

THE GOVERNING CONSERVETION EQUATIONS

The flow inside diese engine swirl chambers is a transient turbulent flow. For the case of motored engines, thermal radiation may be neglected. The flow is, thus, governed by the differential conservation equations of energy, mass and momentum. In the present investigation, the swirl chamber is cylindrical and the flow may thus be assumed two-dimensional.

The equations govering the flow in a cylindrical swirl chamber of a diesel engine can be obtained by decomposing the velocity, pressure, density and enthalpy into a mean and a fluctuating value respectively(9,11).

The turbulent diffusion fluxes which appear in the governing equations are modeled using Boussinesq approach in terms of the mean flow gradients and eddy diffusivities. These eddy diffusivities are determined by solving additional differential conservation equations for the time-averaged kinetic energy of turbulence k and its dissipation rate ε . This kind of model was originally developed for steady turbulent flows (12) and has been modified , to introduce compressibility effects by analogy with the laminar stress tensor, by Ramos (9).

Within the above framework, the governing set of equations may be compactly represented in terms of a single general equation for an arbitrary dependent variable ϕ ;

$$\frac{\partial}{\partial t}(\rho\phi)+\frac{1}{r}\frac{\partial}{\partial r}(r\rho v\phi)+\frac{1}{r}\frac{\partial}{\partial\theta}(\rho u\phi)-\frac{1}{r}\frac{\partial}{\partial r}\left(r\Gamma_\phi\frac{\partial\phi}{\partial r}\right)$$

$$-\frac{1}{r^2}\frac{\partial}{\partial\theta}\left(\Gamma_\phi\frac{\partial\phi}{\partial\theta}\right)=S_\phi \qquad (1)$$

where ϕ stands for radial velocity v, tangential velocity u, total enthalpy h,k and ε ; t is time; ρ is density; Γ_ϕ and S_ϕ are respectively the effective diffusivity coefficients and source/sink terms for variable ϕ . Equation (1) represents also the continuity equation by replacing ϕ by 1. The definition of Γ_ϕ and S_ϕ are given in table (1). In table (1) μ_{eff} is the effective viscosity which is given by ;

$$\mu_{eff} = \mu + C_\mu \rho K^2/\varepsilon \qquad (2)$$

where μ is the laminar viscosity, C_μ , C_1,C_2, σ_h, σ_k and σ_ε are constants of the turbulence model and are given in ref.(9,11) . $\vec{u}$ is the velocity vector at any point in the swirl chamber.

$$G=\mu_{eff}\left[2\left(\frac{1}{r}\frac{\partial u}{\partial\theta}+\frac{v}{r}\right)^2+2\left(\frac{\partial v}{\partial r}\right)^2+\left(\frac{1}{r}\frac{\partial v}{\partial\theta}+\frac{\partial u}{\partial r}-\frac{u}{r}\right)^2\right]-$$

$$\frac{2}{3}\,\mathrm{div}(\vec{u})\left(\mu_{eff}\,\mathrm{div}(\vec{u})+\rho K\right)$$

BOUNDARY CONDITIONS

The imposition of the boundary conditions for diesel engine swirl chambers is not as straight-forward as it may seem. At chamber walls : the velocity components all obey the no slip conditions; the walls are insulated and hence the wall heat flux is taken equal to zero in this stage; the turbulence fluctuations and their dissipation rate are also zero. Wall functions are used for grid nodes adjacent to the chamber walls to avoid using many grid lines in the boundary sub-layer(13). At the inlet plane, i.e. the tangential port which connects the swirl chamber with the main chamber, the inlet velocity, density and temperature vary with crank angle (or time). They are specified by solving an ordinary differential equation for the flow from the main chamber, or vise versa, through the tangential port, in the manner explained in ref. (14).

THE FINITE-DIFFERENCE EQUATIONS

For the purpose of deriving the finite-difference equations, the swirl chamber is overlaid with a grid of nodes, formed by the

Table (1): Definitions of Γ_ϕ and S_ϕ

ϕ	Γ_ϕ	S_ϕ
v	μ_{eff}	$-\frac{\partial P}{\partial r} + \frac{1}{r}\frac{\partial}{\partial r}(r\mu_{eff}\frac{\partial v}{\partial r}) + \frac{1}{r}\frac{\partial}{\partial \theta}[\mu_{eff}(\frac{\partial u}{\partial r} - \frac{u}{r})] + \rho\frac{u^2}{r} - 2(\mu_{eff}/r^2)(v+\frac{\partial u}{\partial \theta}) - \frac{2}{3r}\frac{\partial}{\partial r}[r(\mu_{eff}.div(\vec{u}) + \rho . K)]$
u	μ_{eff}	$-\frac{1}{r}\frac{\partial P}{\partial \theta} + \frac{1}{r}\frac{\partial}{\partial r}[r\mu_{eff}(\frac{1}{r}\frac{\partial v}{\partial \theta} - \frac{u}{r})] + \frac{1}{r^2}\frac{\partial}{\partial \theta}[\mu_{eff}(\frac{\partial u}{\partial \theta} + 2v)] + \frac{1}{r}\mu_{eff}/r) . (\frac{1}{r}\frac{\partial v}{\partial \theta} + \frac{\partial u}{\partial r}) - \mu_{eff}\frac{u}{r^2} - \rho\frac{uv}{r} - \frac{2}{3r}\frac{\partial}{\partial \theta}(\mu_{eff}.div(\vec{u}) + \rho K)$
1	0	0
h	μ_{eff}/σ_h	$\frac{\partial P}{\partial t} + v\frac{\partial P}{\partial r} + \frac{u}{r}\frac{\partial P}{\partial \theta}$ + small terms
K	μ_{eff}/σ_k	$G - \rho\varepsilon$
ε	$\mu_{eff}/\sigma_\varepsilon$	$\frac{\varepsilon}{K}(C_1 G - C_2 \rho\varepsilon)$

intersections of meridunal lines and circles (Fig.3), at which the scalar variables h,K,ε

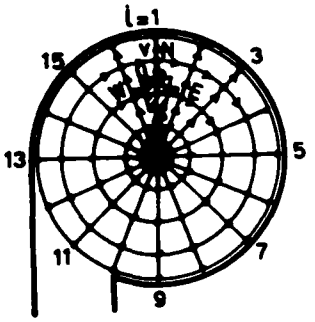

Fig.3 : Computational grid.

and P are stored; while the velocities are located mid-way between the pressures which drive them. Equation (1) is formally integrated over imaginary control volume or 'cell' surrounding each variable and for a time increment δt. The finite-difference approximation to equation (1)is written as :

$$(A_p + M_p^o - S_p)\phi_p^n = \Sigma_c A_c \phi_c^n + M_p^o \phi_p^o + S_u \qquad (3)$$

where; $A_p = \Sigma_c A_c$, Σ_c denotes summation over the four neighbouring nodes of a typical grid node P,c denotes neighbouring node of a grid node P, 'o' and 'n' denote 'old' and 'new' values at times t and t+δt respectively, M_p^o equals $(\rho V)_p^o/\delta t$, V is cell volume, S_p and S_u are coefficients of a linearized source term obtained by integrating S_ϕ. A_c are influence coefficients which give the combined effect of diffusion and convection.

The continuity equation is integrated to give ;

$$M_p^n - M_p^o + \Sigma_c \dot{m}_c = 0 \qquad (4)$$

where $\dot{m}_c$ are mass flow rates across cell boundaries. Equation (3) can be solved for u,v,h, k and ε in space and time domains if the pressure field is known at each time step. The solution of Equation (3) may be obtained economically if coefficients A_c,S_p and S_u are computed at 'Old' time t,leaving ϕ_p^n and ϕ_c^n to be calculated in the 'new' time t+δt. This solution approach parallels that of a parabolic flow which is justifiable because equation (1) is indeed parabolic in time(15). The set of difference equations(3)are linked through pressure differences terms.

OUTLINE OF THE SOLUTION PROCEDURE

At any instant of time t theϕ^o fields of the variables are known, predictions for a time increment δt are then obtained by solving the difference equations for the ϕ^n fields by a marching-integration algorithm. The latter then becomes the ϕ^o for the prediction of the next time step; in this way the solution is marched forward in time until the desired period has been covered. The next section is devoted for the solution of the difference equations.

SOLUTION OF DIFFERENCE EQUATIONS

The energy equation is first solved,using the old fields of h,u,v,p and $(\partial P/\partial t)$, to yield the new enthalpy field (h^n) and hence the new temperature field (T^n).

The next step is to obtain a preliminary set of new velocity components $v^{*n}$and u^{*n} for an estimated new pressure field P^{*n} by solving their difference equations; P^{*n} is actually estimated as equal to the 'old' pressure P^o.

The computed velocities v^{*n} and u^{*n} will not, in general, satisfy the local continuity equation (4) but will produce a net mass source at each grid node. The pressure, density and velocities are then corrected so as to reduce the mass source at each grid node to zero in the following manner ;

$$P^n = P^{*n} + P' \qquad (5)$$

$$\rho^n = \rho^{*n} + \beta P' \qquad (6)$$

$$v_p^n = v_p^{*n} + D_v(P'_p - P'_N) \quad (7)$$

$$u_p^n = u_p^{*n} + D_u(P'_p - P'_E) \quad (8)$$

where the * indicates guessed or preliminary value, p' is pressure correction, β is defined as $(\partial\rho/\partial P)_T$, D_v and D_u are evaluated from the relevant momentum equation, e.g. $D_u = \partial u_p^n/\partial(P_p - P_E)$, subscripts N and E denote neighbouring nodes, as shown in Fig.3.

Equations (6-8) are substituted into the continuity equation (4) to give ;

$$(A_p - S_p)\, P'_p = \sum_c A_c P'_c + S_u \quad (9)$$

where; $A_p = \sum_c A_c$, $S_u = -(M_p^{*n} - M_p^o + \sum_c m_c^*)$ is the local continuity imbalance based on u^{*n}, v^{*n} and ρ^{*n}; S_p and A_c are coefficients which are defined as follows ;

$$S_p = -V_p\beta_p/\delta t - \sum_c (\beta_c \dot{m}_c^*/\rho_c^{*n}) \quad (10)$$

$$A_E = \rho_e^{*n} a_e D_{ue} - 0.5\,\beta_e \dot{m}_e^*/\rho_e^{*n};\ A_W = \rho_w^{*n} a_w D_{uw} + 0.5\,\beta_w \dot{m}_w^*/\rho_w^{*n};$$

$$A_N = \rho_n^{*n} a_n D_{vn} - 0.5\beta_n \dot{m}_n^*/\rho_n^{*n};\ A_S = \rho_s^{*n} a_s D_{vs} + 0.5\beta_s \dot{m}_s^*/\rho_s^{*n} \quad (11)$$

where, subscripts E,W,N,S and e,w,n,s are neighbouring nodes and corresponding nodes mid-way between each node and a typical nodes p respectively (Fig.3). In proving equation (9) terms involve P'^2 were ignored because P' itself should be small. It should be noted that the pressure correction equation does not include P' of 'old' time because there is no question of correcting 'old' velocities and pressure fields.

Equation (9) is solved to yeild the P' field which is required to correct P, ρ, v and u fields. The new K and ε are then computed from their difference equation (3).

OTHER FEATURES

The difference equations (3) & (9) are modified at cells adjoining the swirl chamber boundaries to incorporate the conditions imposed there. In addition to P', a global pressure correction $\bar{P}'$ is computed based on overall continuity balance and is added to the existing pressure field before solving the pressure correction equation (11). The method of solution used to solve equations (3) & (9) is a Gauss-elimination line-by-line double-sweep technique. While equation (3) converges very fast, equation (9) needs more sweeps and some times more than one iteration to reduce the residual mass errors to an acceptable level. The modified form of the pressure correction equation, developed here, gives a fast convergence which reduces the total computational time. The time increment δt used in the present work is 2.22×10^{-4} s which is equivelent to 2° crank angle.

PREDICTION AND MEASUREMENT RESULTS

The computational grid inside the swirl chamber consists of 10 angular and 16 radial locations. Finer grid could be employed at the expense of an increase in computational time. The computations are started at zero time, defined as the time at which the compression stroke has started. The inlet values to the swirl chamber are taken from the previous computational method, reported in (15). Computations are carried out for a diesel engine with a swirl chamber of 48.5 mm diameter, tangential port of diameter 15 mm and inclined an angle 45° to the cylinder axis, engine speed 1500 RPM, and compression ratio 17. The computations are carried out at 2° crank angle intervals. The resulting velocity field computed at various times is shown in Figs.4 and 5 and the corresponding contours of the

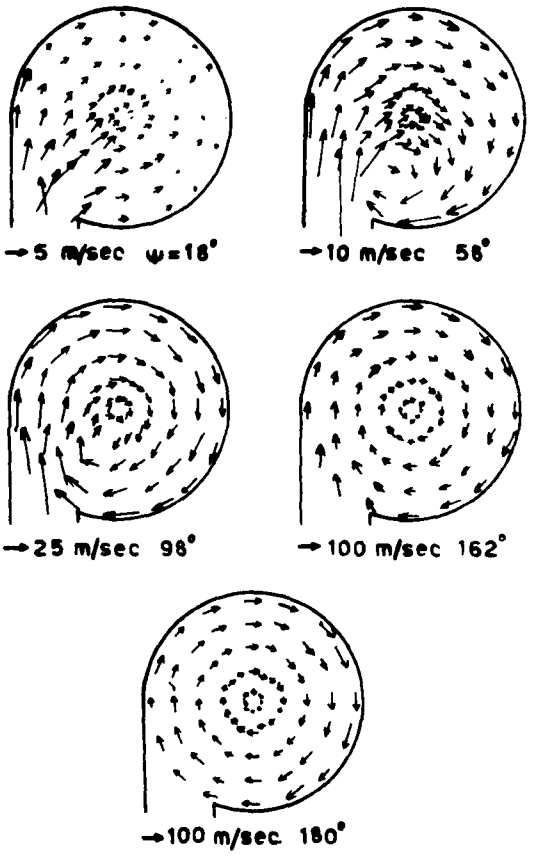

Fig.4 Velocity vector plot during compression stroke.

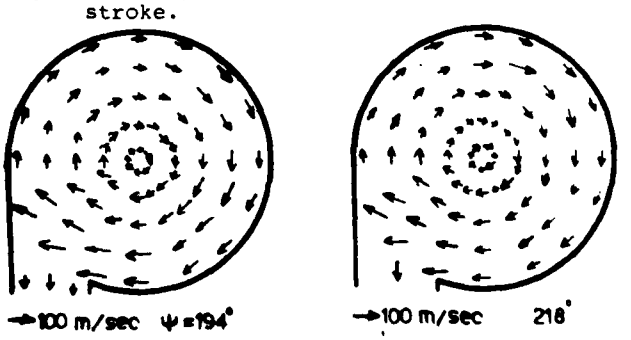

Fig.5 Velocity vector during expansion stroke.

turbulence intensity distributions ($\sqrt{2K/3}/C_{pm}$) where C_{pm} is the mean piston velocity (C_{pm}= 7m/s), are shown in Fig.6.

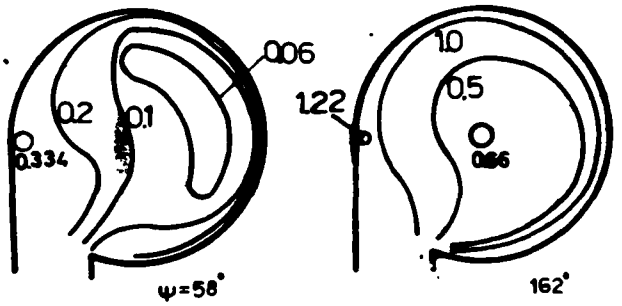

Fig.6 Turbulence intensity contours during compression stroke.

In time sequence, one can observe the features of the flow evolution. At crank angle 18°, it can be seen that the air jet exists at the tangential port with a small velocity which is principally directed from both sides of the port to the opposite wall surface. The flow in the swirl chamber during the initial part of the compression stroke is almost pure radial flow. After some time,for example at 58° crank angle,the pressure gradient built up at the opposite surface have already initiated rotational flow in the bulk of the swirl chamber. Before the initiation of the complete rotational flow a vortex is noticed at the right-hand side of the jet. Before the end of the compression stroke the radial pressure gradient have strengthened to the point of inducing strong flow recirculation which was observed from the high speed photographing of the flow field as shown in Fig.7. The strong recirculating flow inside the swirl chamber produces

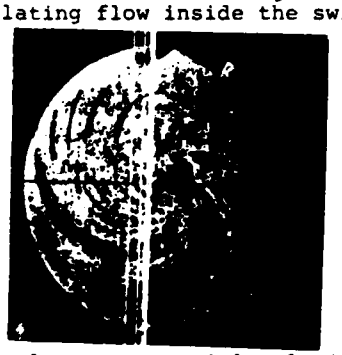

Fig.7 Photography of the flow field at T.D.C.

a large tangential velocity component along the chamber surface and small tangential velocity component at the centre, as shown in Fig.8. It is noticed also that the tangential velocity component increases during compression stroke reaching its maximum value at about 15° crank BTDC, as shown in Fig.9. At the begining of the expansion stroke the recirculating flow is unable to reverse its direction to flow through the tangential port in spite of the absence of a jet flow into the swirl chamber, as shown in Fig.5. Before the complete reverse of the flow a vortex is noticed at the opposite side to the port. It should be mentioned that by this time, the flow velocities are low.

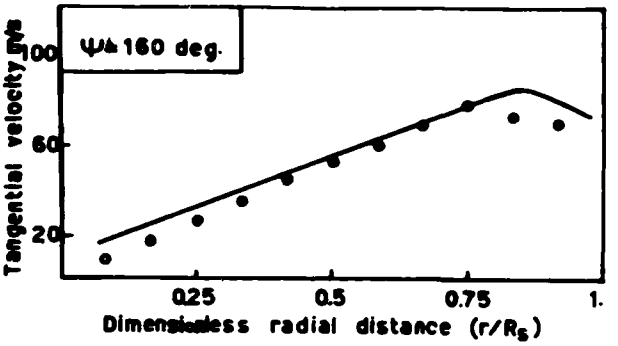

Fig. 8 Predicted and measured tangential velocity in plane 3 at various radii at 20° BTDC.

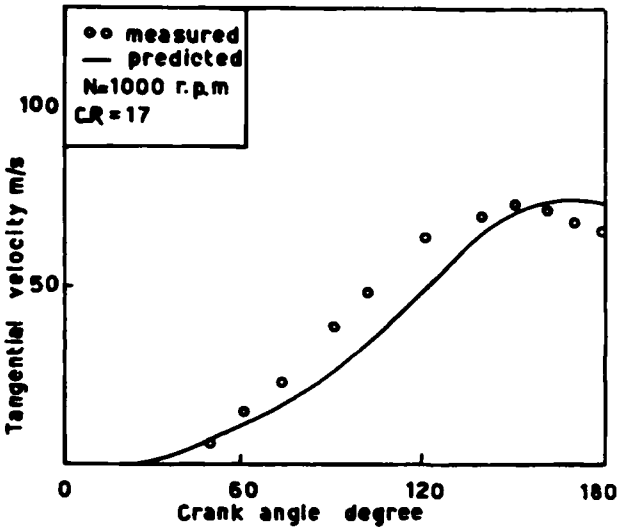

Fig.9 Predicted & measured tangential velocity during compression in plane 3 at 10 mm. from inside surface.

The turbulence contours during compression stroke are also shown in Fig 6 in which it is noticed that the turbulence levels at the begining of the compression stroke are low. By increase of time the inflow to the swirl chamber increases and separates, at the begining, near to the tangential port to form eddies at either sides of the jet. Turbulence intensity generation is particularly strong reaching maximum value of 1.33 near to the entry port. Substantial decrease of the turbulence intensity has been obtained by BTDC where a complete recirculating flow is established. This decrease of turbulence intensity presumably being a consequence of the gradual reduction of the inflow rate by 12° crank angle as the piston approaches the end of the compression stroke.

Figure (10) shows the variation of the turbulence intensity along the radius (plane 3). Maximum turbulence intensity is noticed near chamber walls while the minimum intensity occurs at a radius of about 1.0 mm.

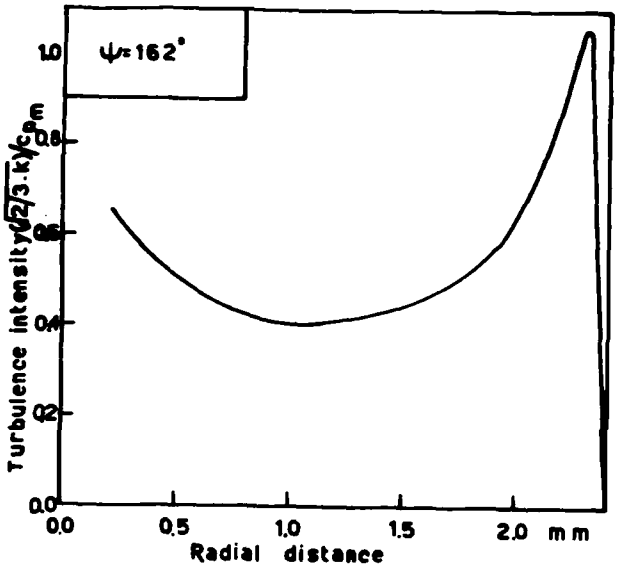

Fig.10 Radial turbulence intensity distribution in plane 3 20° BTDC.

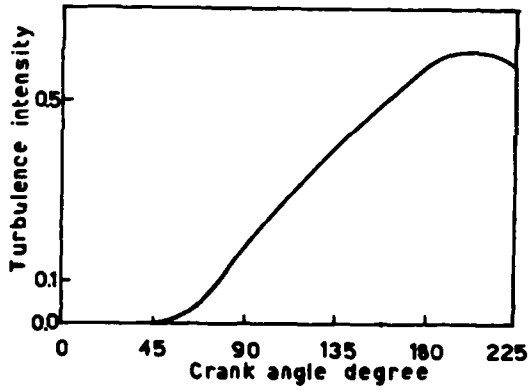

Fig.11 Turbulence intensity during compression at 10 mm from inside surface.

Turbulence intensity variation at 10 mm from chamber walls with crank angle is depected in Fig.11. Turbulence intensity is very low at the begining of compression. It then increases rapidly during the compression stroke reaching a maximum value at the end of compression where the turbulence intensity starts to decrease again during the expansion stroke.

Comparisons of measurements and predictions of tangential velocity in the swirl chamber with the probe located at 10 mm from the wall surface at plane inclined 45° to the port axis. The solid line represents the predicted values. A quite sufficient agreement is noticed as shown in Fig.9, however discrepancy is noticed during the mid of the compression stroke. This discrepancy, may be attributed to the error resulting from the determination of the inclination of the velocity vector by the hot wire anemometer. The measured values are clearly sensitive to this inclination angle which can be defined accurately after the circulating flow has been established.

It is planed to investigate the effect of various geometry parameters of the swirl chamber and working conditions on the flow field to isolate some of the important features of flow and to validate the computational procedure. The present work lays the framework for a more detailed study including spray mixing and combustion which might well prove helpful to the engine designer.

CONCLUDING REMARKS

A measuring technique and a prediction procedure for flow and heat transfer in motored diesel engines swirl chambers are presented. The prediction procedure is based on solving numerically the differential conservation equations for a transient turbulent flow with heat transfer. The obtained agreement between predictions and measurements is fairly good which confirms the accuracy of the prediction procedure. However, the prediction procedure is currently being tested for variables more relevant to turbulence modeling such as the turbulence intensity and the turbulent shear stresses.

ACKNOWLEDGEMENT

The authors are appreciative of the financial support for this work which was provided by the European Research Office, U.S. Army through Grant No.DA-ERO-79-G-0017.

REFERENCES

1. Voiculescu,I.A.and Borman,G.L."An Experimental Study of Diesel Engine Cylinder-Averaged No$_x$ Histories"SAE Paper No. 780228, 1978.
2. Pischinger,F.F. and Klocker,J.J."Single Cylinder Study of Stratified Charge Process with Prechamber Injection" SAE Paper No.741162, 1974.
3. Boni,A.A.et al "Computer Simulation of Combustion Processes in a Stratified Charge Engine"ACTA Astronautica, vol.3. No.3-4, 1976.
4. Fedotenko,F.S."The Effect of Swirl Chamber Volume on the Work of 4-Stroke Self-Ingnition Engines" NAMU, Vol.69, 1953.
5. Bottger "Ursacher der Klapffrein Dieselverbrennung", Kraft , No.8, 1958.
6. Khofax,M.C."Investigation of Mixture Creation in Engines with Devided Swirl Combustion Chamber" Proceeding of the Science Technology Conference,Academy of Science USSR, Moscow 1960.
7. Elkotb, M.M. et al "Theoretical Investigation of Velocity Air Pattern Inside the Swirl Chamber"Bull,of the Faculty of Engng, Cairo University, Paper 17, 1976.
8. Gosman,A.D. et al "Axisymmetric Flow in a Motored Reciprocating Engine" Proc.of Inst. of Mech,Engineers, Vol. 192, No.11,pp.213-223, 1978.
9. Ramos,J.I. et al "Numerical Prediction of

Axisymmetric Laminar and Turbulent Flows in Motored,Reciprocating Internal Combustion Engines" SAE Paper No.790356,1979.
10. Drang, M.S. et al "The Prediction of Heat and Mass Transfer During Compression and Expansion in I.C. Engines, SAE Paper No.760761, 1976.
11. Gosman,A.D. and Watkins,W. "A Computer Prediction Method for Turbulent Flow and Heat Transfer in Piston/Cylinder Assemblies" Paper Presented at Symposium on Turbulent Shear Flows, Pennsylvania, April 1977.
12. Launder,B.E. and Spalding,D.B. "Mathematical Models of Turbulence" Academic Press, 1972.
13. Gosman, A.D. et al "Assessment of a Prediction Method for in-cylinder Processes in Reciprocating Engines" Proc.General Motors Research Symposium on Combustion Modelling in Reciprocating Engines,1978.
14. Elkotb,M.M. et al "Spray Behaviour Inside A Swirl Chamber of A Diesel Engine" Proc. of the 1st Conference of Mech.Power Engng, Feb.1977. Cairo.
15. Patanker,S.V. and Spalding,D.B. "A Calculation Procedure for Heat, Mass and Momentum Transfer in Three-Dimensional Parabolic Flows" Int.J. Heat Mass Transfer, Vol.15 pp. 1787-1806, 1972.

COMPARISON OF CALCULATED AND MEASURED VELOCITIES FOR A TURBULENT SWIRLING FLOW INSIDE A CYLINDRICAL ENCLOSURE

T. Morel, N. N. Mansour, V. Saxena, and R. B. Rask

General Motors Research Laboratories

Warren, MI, 48090

ABSTRACT

This paper presents a comparison of computations with experimental data generated specifically for the purpose of computer code validation. The particular test flow presented here was chosen because of its relevance to flows inside the cylinders of internal combustion engines. The velocity and turbulence measurements were made with a laser Doppler anemometer. The computer code used in the calculations is a time-averaged Navier-Stokes code for time-dependent three-dimensional compressible flows. The turbulence model used is a standard version of the k-ε model; however, new near-wall submodels for velocity and turbulence dissipation rate are employed.

Calculations of the flow inside a cylindrical enclosure containing a steady-state swirling flow reproduced the major overall features of the flow, including the flow pattern, recirculating flow regions, decay of the tangential momentum flux, and turbulent kinetic energy levels. There were some disagreements in the details of the velocity profiles but, overall, the profiles were in good agreement with experiment. It is worth emphasizing that the present flow has a strong swirling component. It has been reported in other investigations that the standard k-ε model does not produce good results for swirling flows, e.g., swirling jets. Nevertheless, for this particular swirling flow, the results obtained were quite satisfactory.

NOMENCLATURE

C_μ	constant in the viscosity model (=0.09)
C_1, C_2	constants in the ε-equation (=1.44, 1.92)
$e_{ij}, \underline{e}$	strain rate tensor
h_{ij}	metric scale factor
h	static enthalpy
k	turbulence kinetic energy
ℓ_ε	dissipation length scale
$\mathcal{M}$	tangential momentum flux (see eqn. 1)
$\mathcal{M}_{ref}$	reference-run tangential momentum flux
n	coordinate in the normal direction
P	*pressure*
r	radial coordinate
R	radius of the cylinder
Re	Reynolds number
T	temperature
T_a	ambient temperature
U,V,W	mean velocity components; radial, tangential, and axial
u',v',w'	rms velocity fluctuations;radial, tangential, and axial
$\bar{U}, \bar{W}$	area-averaged mean velocity
z	axial coordinate
ε	dissipation rate of k
Γ_h	effective enthalpy diffusion coefficient
μ	viscosity
μ_e	effective viscosity (= $\mu + \mu_T$)
μ_T	turbulent viscosity
ρ	density
$\sigma_h, \sigma_k, \sigma_\varepsilon$	Prandtl numbers for h, k and ε (=0.9, 1.0, 1.3)

INTRODUCTION

Swirl is often used in systems of practical interest to provide a certain degree of control over the flow field. In furnace applications, swirl is used to stabilize the flame and enhance the mixing between the reacting gases. In internal combustion engines, swirl is used in different types of engines for different purposes: Diesel engines use swirl to enhance the mixing during injection; direct injection stratified charge engines use swirl to control the flow pattern inside the cylinder as the piston reaches top dead center, and to enhance the mixing in homogeneous-charge engines swirl is used to create a more repeatable flow field to reduce cycle to cycle variability, and to increase the turbulence inside the cylinder. Consequently, the capability of predicting confined turbulent swirling flows is of practical importance.

We are developing a code for predicting the detailed flow field inside cylinders. As part of this work we have compared calculations to detailed measurements of a steady-state (no piston motion) swirling flow in an engine-cylinder-like geometry.

DESCRIPTION OF THE EXPERIMENT

As this paper is primarily concerned with the computation of the first two authors, only a brief description of the experimental results of the third and fourth authors will be provided. the velocity measurements were made with a single-component, counter-based, laser Doppler anemometer operated in the forward scatter mode. A digital tape drive was used to store the data, and an off-line computer system to determine mean velocity and rms velocity fluctuations for all three components. Frequency shift, beam-intersection angle, and counter validation were adjusted on a point-by-point basis to minimize measurement errors.

The geometry of the experiment is described in Figure 1. The flow enters at one end of the cylinder through an inlet ring with 16 equally spaced holes which are inclined at 17° to the local tangential direction. The measured effective inlet

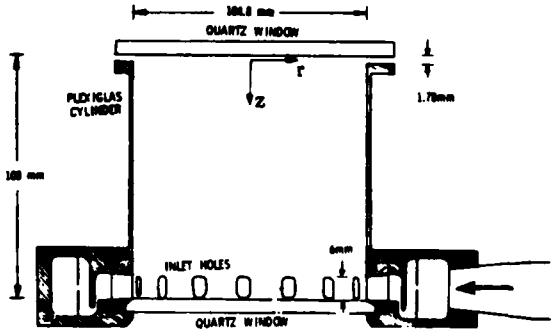

Fig. 1 Schematic of the Experimental Apparatus

hole area is 18.35 mm^2 per hole, or 293.6 mm^2 in total. An effort was made to insure a uniform distribution of the inlet flow over all 16 holes. The flow exits at the opposite end of the cylinder through a narrow circumferential slot. The resulting flow pattern was closely axisymmetric (this was checked by making all measurements on full traverses across the diameter of the cylinder).

The volume flow rate through the experimental set up was fixed at 0.0154 m^3/s, and at that flow rate the average axial velocity through the cylinder was $\bar{W}$ = 1.783 m/s. This velocity was chosen in the present report as the most appropriate normalizing velocity for presentation of data . Reynolds number based on this velocity and the diameter of the cylinder was Re = 12,180.

The average velocity through the inlet holes (through their effective area) was $\bar{U}_{hole}$ = 52.45 m/s, or 29.4 times the reference velocity. The inlet jet Reynolds number based on the effective hole diameter (4.83 mm) was 16,400. The average radial velocity out through the exit slot was $\bar{U}_{exit}$ = 26.28 m/s, or 14.7 times the reference velocity.

Based on geometrical considerations alone, the flow in the vicinity of the inlet holes would be expected to have a radial component of $\bar{U}_{hole} \sin 17° = 0.292\ \bar{U}_{hole}$, a tangential component of $\bar{U}_{hole} \cos 17° = 0.956\ \bar{U}_{hole}$, and approximately zero axial component. However, since the inlet flow was through discrete holes, the actual radial and tangential components downstream of the holes would be expected to drop rapidly to a lower level as the individual inlet jets merge together in the immediate vicinity of the inlet holes.

SET UP OF THE NUMERICAL SIMULATION

The computer code used in these calculations is a derivative of the code MINT described by Gibeling, *et al.* in Reference [1]. It is a time-averaged Navier-Stokes code for time-dependent three-dimensional compressible flows. By making the velocities dimensionless with the average axial velocity $\bar{W}$, the distances with the radius (R) of the apparatus, and the remaining variables with reference values subscripted by D, the modeled equations of motion are given as*:

Continuity

$$\frac{\partial \rho}{\partial t} = -\frac{1}{J}\frac{\partial}{\partial x_i}\left(\frac{J}{h_{i\alpha}}\rho u_\alpha\right)$$

where $h_{ij} = 0$ for $i \neq j$, and for cylindrical polar coordinates $h_{11} = h_{33} = 1$, $h_{22} = r$ and $J = h_{11}h_{22}h_{33}$.

Momentum

$$\frac{\partial}{\partial t}(\rho u_i) = -\frac{1}{J}\frac{\partial}{\partial x_j}\left(\frac{J}{h_{j\alpha}}\rho u_\alpha u_i\right) + G_i - \frac{P_D}{\rho_D \bar{W}}\frac{1}{h_{i\alpha}}\frac{\partial P}{\partial x_\alpha}$$

$$-\frac{1}{h_{i\alpha}}\frac{\partial}{\partial x_\alpha}\left[\frac{2}{3}\frac{\mu_e}{Re}e_{kk} + \frac{2}{3}\rho k\right] + \left[\nabla\cdot\left(2\frac{\mu_e}{Re}\underline{e}\right)\right]_i$$

where $G_1 = \rho u_2^2/r$, $G_2 = -\rho u_1 u_2/r$, $G_3 = 0$, $Re = \rho_D \bar{W} R/\mu_D$, and $\underline{e}$ is the strain rate tensor. In the above equation μ_e is defined as

$$\mu_e = \mu + \mu_T$$

where μ is the laminar viscosity, and $\frac{\mu_T}{Re} = C_\mu \rho\frac{k^2}{\epsilon}$, k is the turbulence kinetic energy and ϵ its dissipation rate.

*All variables are averaged variables but the symbols describing the averaging are dropped. (x_1,x_2,x_3) correspond to the cylindrical-polar coordinate system (r,θ,z) and (u_1,u_2,u_3) correspond to the velocities (U,V,W).

Energy

$$\frac{\partial}{\partial t}(\rho h) = -\frac{1}{J}\frac{\partial}{\partial x_i}\left(\frac{J}{h_{i\alpha}}\rho u_\alpha h\right) + \frac{P_D}{\rho_D h_D}\left(\frac{\partial P}{\partial t} + \frac{u_i}{h_{i\alpha}}\frac{\partial P}{\partial x_\alpha}\right)$$

$$+ \frac{1}{Re}\frac{1}{J}\frac{\partial}{\partial x_i}\left(\frac{J}{h_{i\alpha}h_{\alpha\beta}}\Gamma_h\frac{\partial h}{\partial x_\beta}\right) + \frac{\bar{W}^2}{h_D}\left[\frac{\phi}{Re} + \rho\varepsilon\right]$$

where $\phi = 2\,\underline{e}:\underline{e} - 2/3\,e_{kk}^2$ and $\Gamma_h = \mu_e/\sigma_h$. σ_h is assumed to be constant (=0.9).

For this particular case where the divergence of the flow field is very small, the equation for the turbulence kinetic energy and its dissipate rate are modeled as follows.

Turbulence Kinetic Energy

$$\frac{\partial}{\partial t}(\rho k) = -\frac{1}{J}\frac{\partial}{\partial x_i}\left(\frac{J}{h_{i\alpha}}\rho u_\alpha k\right) + \frac{1}{Re}\frac{1}{J}\frac{\partial}{\partial x_i}\left(\frac{J}{h_{i\alpha}h_{\alpha\beta}}\frac{\mu_T}{\sigma_k}\frac{\partial k}{\partial x_\beta}\right)$$

$$+ \frac{\mu_T}{Re}\,2\,\underline{e}:\underline{e} - \rho\varepsilon$$

Dissipation Rate of Turbulence Kinetic Energy

$$\frac{\partial}{\partial t}(\rho \varepsilon) = -\frac{1}{J}\frac{\partial}{\partial x_i}\left(\frac{J}{h_{i\alpha}}\rho u_\alpha \varepsilon\right) + \frac{1}{Re}\frac{1}{J}\frac{\partial}{\partial x_i}\left(\frac{J}{h_{i\alpha}h_{\alpha\beta}}\frac{\mu_T}{\sigma_\varepsilon}\frac{\partial \varepsilon}{\partial x_\beta}\right)$$

$$+ C_1\frac{\varepsilon}{k}\frac{\mu_T}{Re}\,2\,\underline{e}:\underline{e} - C_2\,\rho\frac{\varepsilon^2}{k}$$

The equations of motion are differenced using a standard (non-staggered) mesh, central differencing in space, and backward (fully implicit) differencing in time. The differenced equations are then linearized in time as described by Briley and McDonald [2], then solved using the Douglas-Gunn [3] technique to generate an Alternate Direction Implicit (ADI) scheme.

The physical flow situation was represented in the calculations as a cylindrical domain, whose length to radius ratio was 2.059. The outflow boundary was represented as a circumferential opening in the cylinder wall flush with the end plane. The size of the opening (slot height) was the same as in the experiment. The calculations were found to be insensitive to outlet slot height, except for the absolute level of the static pressure which depended on the pressure drop across the opening.

The inflow boundary was more difficult to set. To take advantage of the axisymmetry of the flow in the bulk of the domain, the individual inlet holes were not modeled; instead a circumferential slot was used. The individual jets in the experimental apparatus are expected to merge in a short distance downstream from the holes, and the discrepancy between the modeled and the real configuration is expected to be localized and not too serious. The slot height was made the same as the inlet hole height to match the location of the inlet flow separation from the cylinder side wall. Sensitivity runs with different slot heights showed that the results in the bulk of the cylinder were insensitive to inlet slot height. Only near the inlet opening was there an effect, the size of the local separation from the cylinder wall changing with the slot height.

Boundary Conditions on Open Boundaries

Inlet. The inlet radial velocity was prescribed to be uniform over the slot height except for thin boundary layers on top and bottom, with a magnitude such that the total flow rate was the same as in the experiment. The inlet radial velocity was 8.39 m/s, or 55% of the radial component of the average inlet-hole velocity, $\bar{U}_{hole}$.

The tangential velocity was also prescribed to be uniform with thin boundary layers; its magnitude was set at a level deduced from the experimental data taken in a plane passing through the inlet holes (z = 1.99 R) and extrapolated to the cylinder wall. This magnitude was 30 m/s, or only 60% of the tangential component of $\bar{U}_{hole}$. This immediate drop of the inlet tangential velocity by 40%, indicates that the jet merging and intermixing take place very close to the wall, the flow becoming axisymmetric almost immediately. This is a positive sign that the experiment's deviations from axisymmetry, due to discrete jets are restricted to a very small region close to the jet inlets. It is also reassuring that the indicated drop in the tangential velocity is about the same as the drop in the radial velocity.

Other boundary conditions on the inlet opening were: axial velocity set to zero, $\partial^2\rho/\partial n^2 = 0$, $T = T_a$. Turbulence intensity of the inlet flow was fixed at $(2\,k/3)^{1/2}/(U^2 + V^2 + W^2)^{1/2} = 0.14$, *i.e.*, a fairly elevated level consistent with the highly turbulent flow conditions upstream of the inlet holes and with the high turbulence intensity generated by the incoming jets. The dissipation length scale was prescribed to be on the order of 0.1 times the slot height, a typical value for turbulent flows. Experimentation with different inlet velocity profiles, and different levels of both the turbulence intensity and scale, showed only a very small sensitivity of the results to these parameters.

Exit. At the exit opening, where the flow is oriented radially outward, the simple extrapolative boundary condition $\partial/\partial n = 0$ was used on U, V, W, h, k and ε. A prescribed uniform static pressure (=ambient) over the slot-height was used as the boundary condition on the continuity equation.

Near-Wall Submodels at Solid-Walls

At solid-wall boundaries, near-wall submodels were employed to bridge the gap between the wall and the first grid point away from the wall. The same set of submodels was used for all solid walls.

Velocity. The normal velocity component was set to zero at the wall. The velocity components parallel to the wall were handled by a combination of two submodels. One submodel was a wall function based on the law of the wall, and the other one was a "limited slip" submodel developed specifically for regions near flow separation and reattachment. The combination was weighted towards the law-of-the-wall submodel when the flow near the wall was boundary-layer like (in which case the two submodels are similar). When the law-of-the-wall submodel predicted implausible (negative, or too large) wall slip velocities, occurring typically near separation or reattachment, the combination was weighted towards the limited-slip submodel. In this way advantage was taken of the law of the wall wherever its use was appropriate, while avoiding unphysical wall slip velocities elsewhere.

k and ε. $\partial k/\partial n = 0$ was used for the k equation. The dissipation equation at the first point away from the wall (point 2) was replaced by

$$\varepsilon_2 = C_\mu^{3/4} k_2^{3/2}/\ell_2$$

where the dissipation length scale ℓ_2 was obtained by interpolation, assuming that the dissipation length scale varies linearly between its value on the wall ($\ell_1 = 0$) and the value at the second grid point away from the wall ($\ell_3 = C_\mu^{3/4} k_3^{3/2}/\varepsilon_3$).

h and ρ. Fixed wall temperature $T = T_a$ was used for the energy equation. The boundary condition for the continuity equation was $\partial P/\partial n$, calculated from the momentum equation for the normal velocity component evaluated at the wall.

RESULTS

The results of the calculations are compared to the experimental data in Figures 2-4, which show radial profiles of the velocity and rms velocity fluctuation at different z planes, where the z coordinate is measured from the exit end-wall. The axial velocity profile (Figure 2) is seen to be in good agreement with the experiment. The salient features of the axial velocity profile are reproduced: a dominant peak near the wall, reverse flow with a magnitude of about 20% of the maximum velocity near the wall, a small second positive peak, and practically zero axial velocity at the center. The only notable disagreement concerns the location of the reverse flow peak and the second positive peak; both are predicted to be farther away from the wall than the experimental ones. The same findings apply to comparison with data at other z-planes.

The tangential velocity profiles are shown in Figures 3 and 4. The calculations are seen to predict the location of the peak tangential velocity very well, as well as the axial decay of the velocity maximum caused by friction on the cylinder side wall. On the other hand the calculations over predict the swirl at the center of the flow, indicating a solid-body rotation, and with angular velocity approximately constant along the cylinder axis.

The experimental data show a parabolic variation of swirl velocity in the central region, with zero swirl near the axis. It is not obvious what produces the zero swirl near the axis in the experiment. It appears to us that the only mechanism that could be responsible would be friction on the two end walls, opposing the diffusion towards the central region of the tangential momentum of the spinning fluid near the sidewall. However, in that case one would expect that the center-core swirl would be lower in z-planes close to the end walls than in planes away from these walls, but this is not the case: the experimental profiles at z/R = 1.77 and at z/R = 0.31 are practically identical between the centerline and r/R = 0.5.

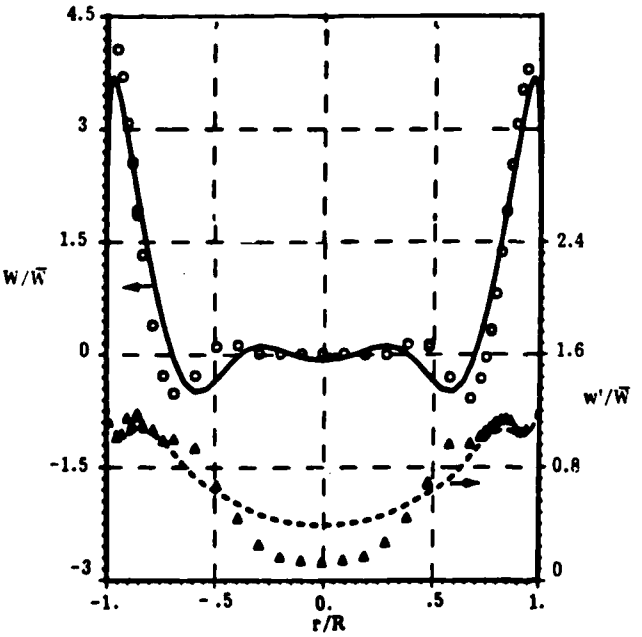

Fig. 2 Axial Velocity at z/R = 0.80
—— Predicted Mean Velocity
- - - Predicted Turbulence Intensity $\sqrt{2k/3}/\bar{W}$.
Symbols are the Experimental Data.

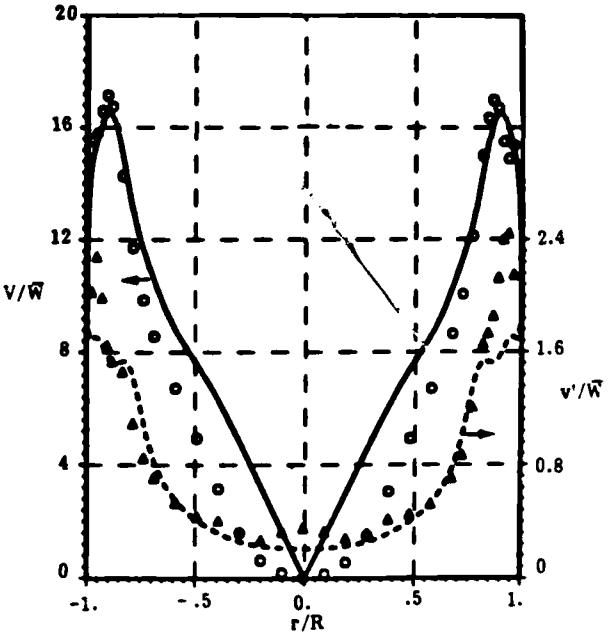

Fig. 3 Tangential Velocity at z/R = 1.77
—— Predicted Mean Velocity
- - - Predicted Turbulence Intensity $\sqrt{2k/3}/\bar{W}$.
Symbols are the Experimental Data.

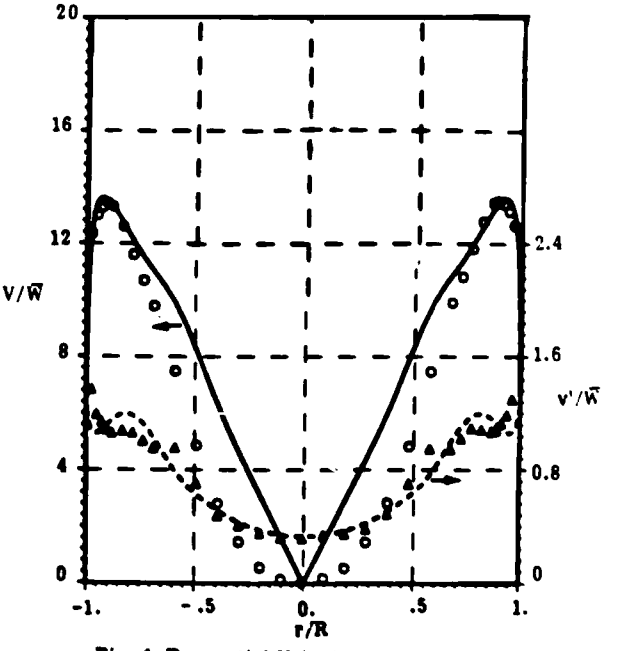

Fig. 4 Tangential Velocity at z/R = 0.31
—— Predicted Mean Velocity,
- - - Predicted Turbulence Intensity $\sqrt{2k/3}/\bar{W}$.
Symbols are the Experimental Data.

Several attempts were made to diagnose the source of the discrepancy between the parabolic variation in tangential velocity observed experimentally and the linear variation obtained with our calculation. One of the attempts was to modify the k-ε model as recommended by Rodi [4], where solid-body rotation is the neutrally stable profile. Also, the recommended modification of Launder, *et.al.*, [5] was tried where the free vortex is the neutrally stable profile. Neither modification changed the center core solid-body swirl results. Since these modifications were so markedly different, and neither offered an improved agreement with experiment, both were abandoned. Finally, several runs were carried out where the skin friction at the top and bottom walls was changed. Again, these results did not change the shape of the tangential velocity profiles. Thus, at the present time we regard the difference as unexplained.

The radial velocities were the smallest of the three velocity components. Because of this they were subject to the largest relative error experimentally (and likely also computationally). Comparisons with experimental data at different axial locations showed a similarity in shape and peaks in approximately the same locations, but the magnitudes were often substantially different. However, the absolute differences between the predictions and the data were not much larger than for the other two components.

The experimental data also include measurements of the three components of rms velocity fluctuation--u', v' and w'. Since the calculations predict only the turbulence kinetic energy k, and not the individual fluctuation components, direct comparison can be made only at planes where all three components were measured and k could be determined. Figure 5 shows the comparison (made at z/R = 1.28) of the

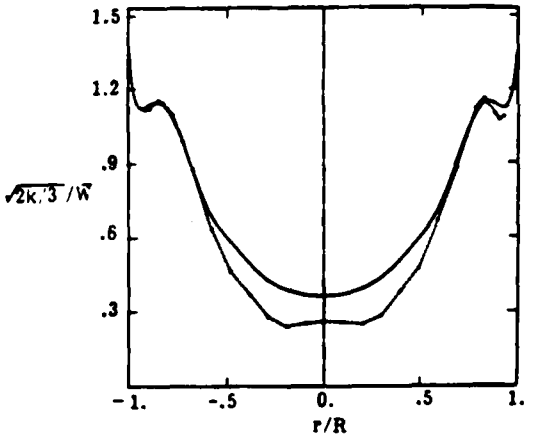

Fig. 5 Profile of Turbulence Intensity at z/R = 1.28
—— Prediction, ---- Experiment

turbulence intensity $\sqrt{2k/3}/\bar{W}$, representing the intensity of velocity fluctuations averaged over the three coordinate directions. The agreement is good in both the shape of the profile and the magnitude of the intensity. The profiles show two peaks, the one right at the wall being due to large shear near the wall, the other to the shear generated on the centerline side of the maxima of the tangential and axial velocity profiles. The only area of disagreement is near the centerline, where the flow is essentially shear-free and so the level of k is set by convection and diffusion from other parts of the flow. This disagreement is fairly typical for slowly moving, or shear-free, portions of any flow field, and is apparently one of the weaknesses of the k-ε model. Those portions of the flow where shear is high, and which usually are the important ones, are handled quite well by the k-ε model. These conclusions appear to hold for other simulations we have made for a variety of different flowfields.

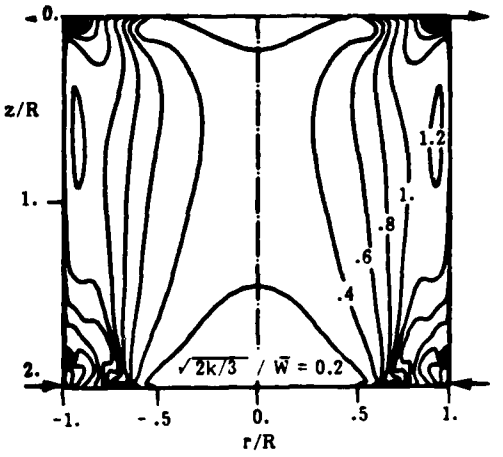

Fig. 6 Contours of Turbulence Intensity, Uniformly Spaced Between $\sqrt{2k/3}/\bar{W}$ = 0 and 5

Inspection of the experimental profiles of u', v', and w' showed that their magnitudes are not too different from each other, and so it made sense to insert into Figures 2-4 the profiles of predicted $\sqrt{2k/3}/\bar{W}$ for comparison with the data. These provide some indication of the capability of the turbulence model to predict the intensity of turbulence.

The contours of turbulence intensity, characterized by $\sqrt{2k/3}/\bar{W}$ in Figure 6, show that the flow inside the chamber has a typical intensity of 0.5-1 times the average axial velocity. The exceptions are the regions around the flow inlet where additional turbulence is generated due to large shear, and at the exit where its level grows rapidly due to higher local velocity levels. The length scale of turbulence (Figure 7) has fairly simple onion-like contours with a maximum of 0.14 R, a value not too different from that found in pipe flows and sudden expansions.

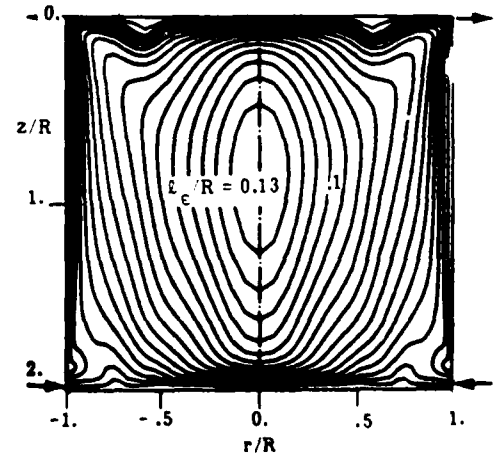

Fig. 7 Contours of Dissipation Length Scale Uniformly Spaced Between ℓ_ε R = 0.0 and 0.13

Effect of Inlet Tangential Momentum Flux

One of the important advantages a calculation scheme has over an experiment is that, once it is set up, parametric studies are much easier to perform than they would be experimentally. Since the predictions that have been reported

AD-A111 522 PENNSYLVANIA STATE UNIV UNIVERSITY PARK DEPT OF MECH--ETC F/G 20/4
SYMPOSIUM ON TURBULENT SHEAR FLOWS (3RD), UNIVERSITY OF CALIFOR--ETC(U)
SEP 81 F W SCHMIDT AFOSR-80-0033

UNCLASSIFIED AFOSR-TR-82-0032 NL

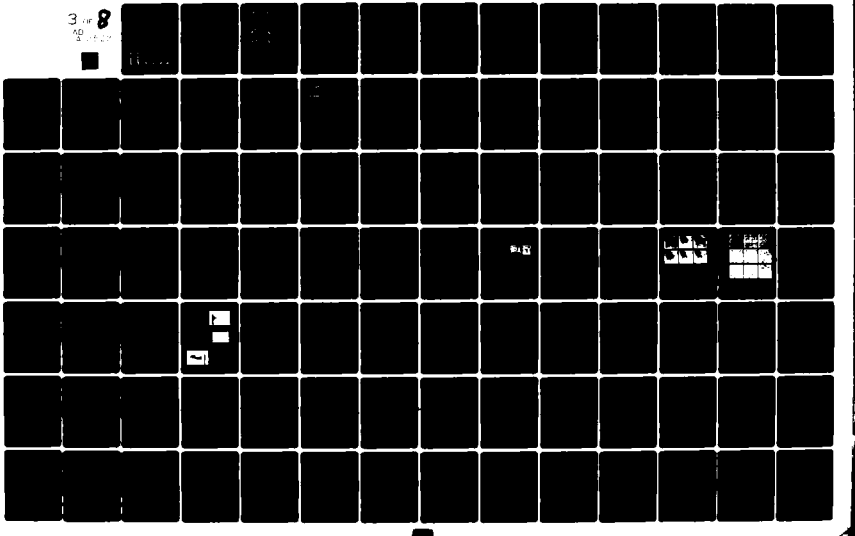

3 OF 8

AD A111522

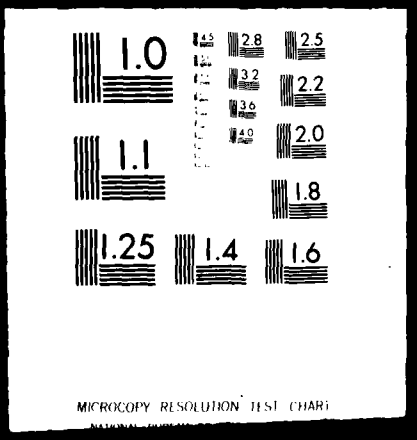

here compared well enough with experiment to give us confidence in the results, it was very tempting to make a parametric calculation. It was of interest to know how the flow would have looked if the experimental apparatus had been constructed somewhat differently. The particular parameter chosen for variation was the inlet flow angle, in effect the inlet flux of tangential momentum.

Calculations were made for five different values of the inlet tangential momentum flux: 2.0, 1.0, 0.5, 0.2, 0.1 and 0.0 times the original value, keeping the flow rate constant. Figure 8 shows the streamline patterns for half the cylinder (the other half can be deduced from axisymmetry) for the different momentum fluxes. These results show that reducing the inlet tangential velocity component leads to progressively milder curvature of the inlet flow as it changes direction from a radial to an axial orientation. This change in curvature must be consistent with the radial pressure gradient set up by the swirling velocity component, which weakens rapidly as the swirl velocity decreases. Concurrently, the size of the separation region grows rapidly, to encompass a large portion of the cylinder volume for zero tangential velocity. The streamlines near the cylinder wall, which were practically parallel over most of the cylinder length in the original case, are progressively less and less parallel. In consequence, the radial velocity profiles grow substantially in magnitude, and both the axial and tangential velocity profile begin to differ to a much greater degree from plane to plane. The tendency for the main flow is to move away from the cylinder wall toward the centerline.

One striking feature of the flow is the presence of recirculating regions in the center of the cylinder. As may be seen in Figure 8, increasing the tangential velocity component increases the number of these regions, taking the shape of alternating fingers protruding from the end walls. There is one recirculating region for M/M_{ref} = 0.1 and 0.2, two for M/M_{ref} = 0.5 and three for M/M_{ref} = 1.0 and 2.0. The changeover from one pattern to another with one more recirculating region is not likely to be abrupt; it is probably a gradual evolution. This may be inferred from the sequence of Figures 8(c), (b) and (a), where the development of the third recirculation region may be observed, starting from a small bulge on the first recirculation region in Figure 8(c). Similarly, a bulge is seen to develop on the second recirculation bubble in Figure 8(a), undoubtedly a precursor of a fourth recirculating region which would emerge at yet higher values of M/M_{ref}.

SUMMARY

1. Calculations using the k-ε turbulence model were found to reproduce the major features of a swirling flow inside a cylindrical engine-like geometry. In particular, the calculations predict well the flow pattern, presence of recirculating flow regions, decay of tangential momentum flux due to wall friction, and turbulence kinetic energy levels.

2. The details of the velocity profiles exhibit some disagreement. The tangential velocity profile is predicted to have solid-body rotation in the vicinity of the centerline, while the experiment shows less rotation in that region. Another difference is in the axial velocity profiles, whose local extrema are predicted to lie closer to the centerline than the experimental ones.

3. A parametric study was run in which the inlet tangential velocity into the cylinder was varied over a wide range, from two times the experimental value down to zero. The results show a strong dependency of the major flow features on this parameter. This demonstrates an attractive feature of numerical simulations: they are very useful for parametric studies around given, experimentally validated, baseline configurations.

REFERENCES

1 Gibeling, H. J., McDonald, H., and Briley, W. R., "Development of a Three-Dimensional Combustor Flow Analysis, Vol. I: Theoretical Studies," AFAPL Technical Report AFAPL-TR-75-59, July 1975.

2 Briley, W. R., and McDonald, H., "Solution of the Multidimensional Compressible Navier-Stokes Equations by a General Implicit Method," J. Comp. Phys., Vol. 24, No. 4, p. 372 (1977).

3 Douglas, J., and Gunn, J. E., "A General Formulation of Alternating Direction Methods," Numerische Math., Vol. 6, 1964, p. 428.

4 Rodi, W., "Influence of Buoyancy and Rotation on Equations for the Turbulent Length Scale," 2nd Symposium on Turbulent Shear Flows, July 1979, Imperial College, London, pp. 10.37-10.42.

5 Launder, B. E., Priddin, C. H., and Sharma, B. I. "The Calculation of Turbulent Boundary Layers on Spinning and Curved Surfaces," Trans. ASME J. Fluid Engineering, March 1977, pp. 231-239.

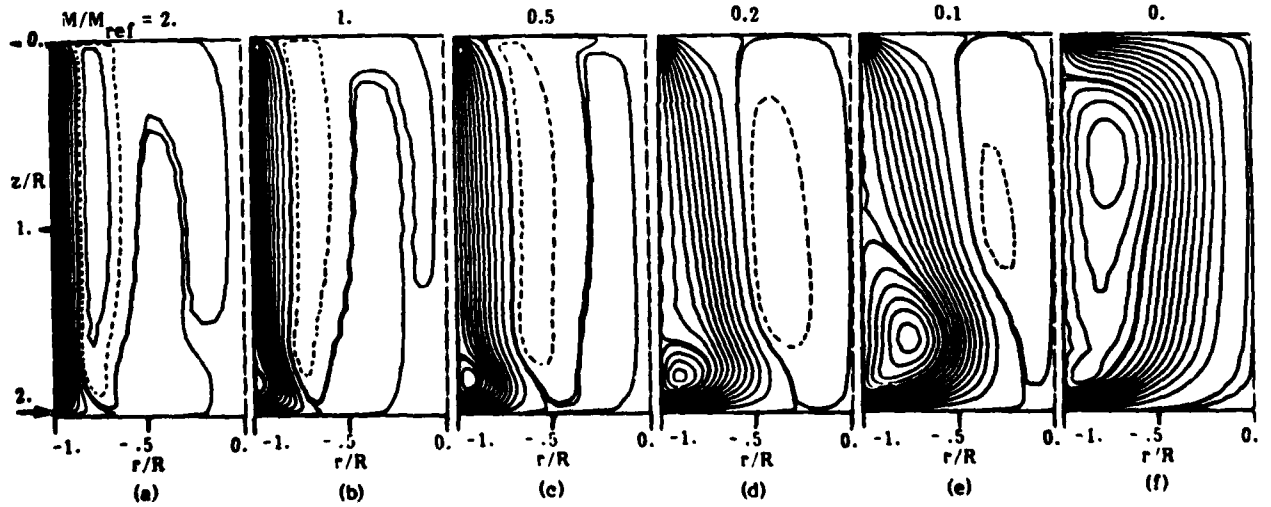

Fig. 8 Streamline Patterns for Six Cases with Different Inlet Tangential Momentum Flux, M

FEATURES OF TURBULENT PIPE FLOWS IN DEVELOPMENT AND DECAY

E.M. Laws, E-H. Lim, J.L. Livesey
Department of Aeronautical and Mechanical Engineering
University of Salford
Salford M5 4WT
England

ABSTRACT

Highly distorted time mean velocity profiles in turbulent pipe flow, given sufficient downstream development length, revert to profiles more typical of established pipe flows.

A detailed study of the decay process for a wide variety of initial conditions has been conducted. The results obtained from this investigation reveal some insight into the mechanism of profile decay and distinguish interesting features associated with the decay process.

In this paper some of this data is presented and a description of the decay of an arbitrary initial velocity profile is suggested.

NOMENCLATURE

D	Pipe diameter
K	Turbulent kinetic energy = $\frac{1}{2}(\overline{u'^2}+\overline{v'^2}+\overline{w'^2})$, $(\overline{v'^2}=\overline{w'^2})$
(r,θ, z)	Polar co-ordinates, $\partial/\partial\theta \equiv 0$
R	Pipe radius
U, V	Axial and radial time mean velocity components
u, v	Non-dimensional time mean velocities U/$\bar{U}$, V/$\bar{U}$
u', v', w'	Fluctuating velocity components
$\overline{u'v'}$	Turbulent shear stress
u_τ	Friction velocity
y	Distance measured from pipe wall
η,ζ	Non-dimensional co-ordinates r/R, z/R
λ(z), μ(z)	Profile decay functions

Subscripts

0	Initial profile
∞	Final, fully developed profile

INTRODUCTION

Few previous investigations have deliberately set out to study the behaviour of highly non-uniform decaying flows. Many examples of such flows can be found in previously reported work. However in most cases the decay process has been secondary to the main objective (for example see Moon and Rudinger[1], Deshpande and Giddens[2], Hussain and Clark[3]).

The decay of a given velocity profile is likely to be most strongly influenced by the initial velocity profile shape and its degree of non-uniformity. Other factors will have some effect in particular the turbulence structure. The turbulence structure will be a result of the combination and interaction of the turbulence present upstream of the profile generator and the turbulence introduced by the method of profile generation (e.g. gauze, baffle plate, grid of rods etc) or the preceding fluid system. Additionally during the decay process a new turbulence structure is established resulting largely from the presence and decay of the high shears in the non-uniform flows and the developing wall boundary layer.

About 10-20 pipe diameters of development is sufficient to achieve an apparent reversion to a pipe-type time mean profile (note however that variations of the other flow quantities are still marked) though this profile will be far removed from the classical fully-developed profile.

In practice the fully-developed profile may never be achieved but will be closely approached after about 100 diameters of development length.

The attainment of fully developed flow starting from the highly distorted inlet condition has been considered by the authors[4] in which interest was focussed on the axial profile changes which occur during the decay.

This paper also considers the decay process but focuses interest on the radial profile changes which occur.

EXPERIMENTAL PROGRAMME

All the experimental work was carried out in an 0.103m diameter smooth pipe preceded by a well designed 16:1 area ratio contraction. The undisturbed pipe inlet profile was practically uniform with a thin inlet boundary layer ($\delta^*/D = 0.02$) with a centre line turbulence level ($\sqrt{\overline{u'^2}}/U$) of about 0.05%. The test Reynolds number based on mean velocity and duct diameter was 2.5×10^5.

All the non-uniform profiles were generated by gauze screens placed close to the contraction outlet. A wide variety of velocity profiles were studied with differing non-uniformity and turbulence structure.

EXPERIMENTAL RESULTS

Some of the results obtained from this investigation are presented here.

Figure 1 shows the axial profiles of non-dimensional velocity u for three different types of profile (marked cases 1, 2 and 3) over a development range extending up to z/D = 76.5. The key to this figure and all subsequent figures follows figure 1.

The three different profiles were selected as being widely different in both profile type (and hence shape) and degree of non-uniformity. Case 1 corresponds to developing pipe flow.

Figures 2, 3 and 4 illustrate the corresponding plots of radial velocity v, turbulent kinetic energy

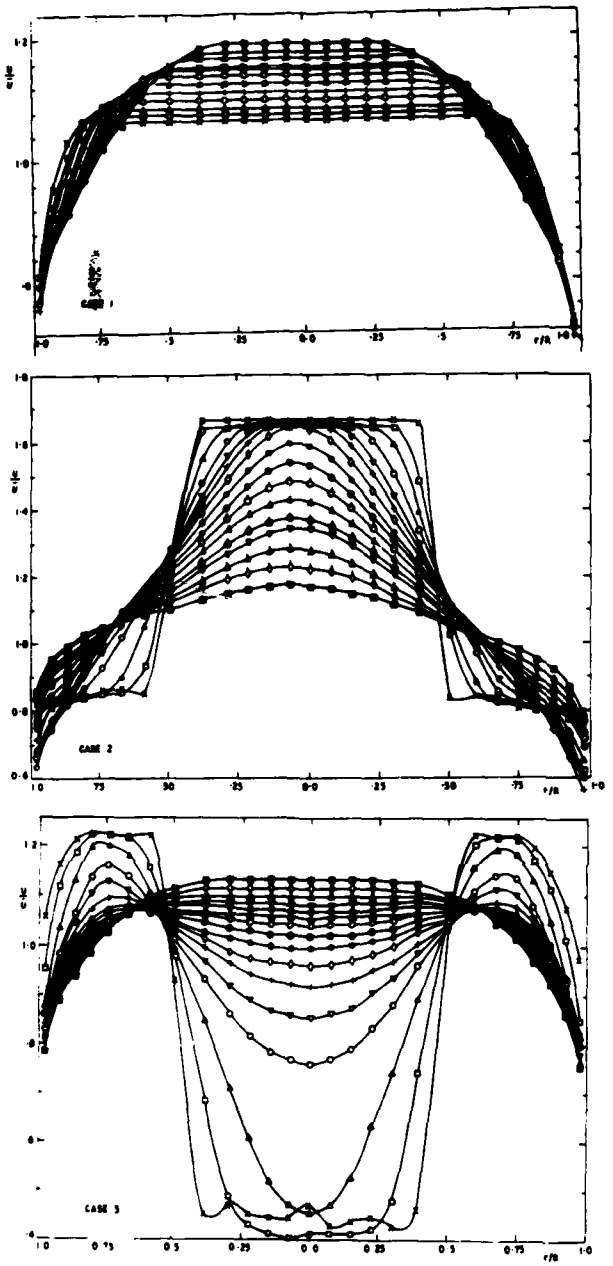

Figure 1 Axial Time Mean Velocity Distributions, $U/\bar{U}$

KEY TO Z/D LOCATIONS
x 0·5, □ 1·5, △ 2·5, ○ 4·0, ▽ 5·0, + 6·0, ◇ 7·0, ✱ 8·0, ● 9·0, ◇ 10·0,
◭ 11·0, ◆ 12·0, ▼ 13·0, ▲ 14·5, ◇ 16·5, ■ 19·5, ◆ 25·5, △ 34·5, ▲ 40·5, ▲ 70·5

K/U^2 and turbulent shear stress $\overline{u'v'}/u_\tau^2$. The axial variation of these quantities has already been illustrated in reference 4. It has been necessary to limit the data included with the paper, more information on the development is available.

The wide difference between the magnitudes and form of the various quantities for case 1 and the corresponding values for the non-uniform flows cases 2 and 3 is very evident particularly for the development range up to z/D = 10. This is clearly illustrated by

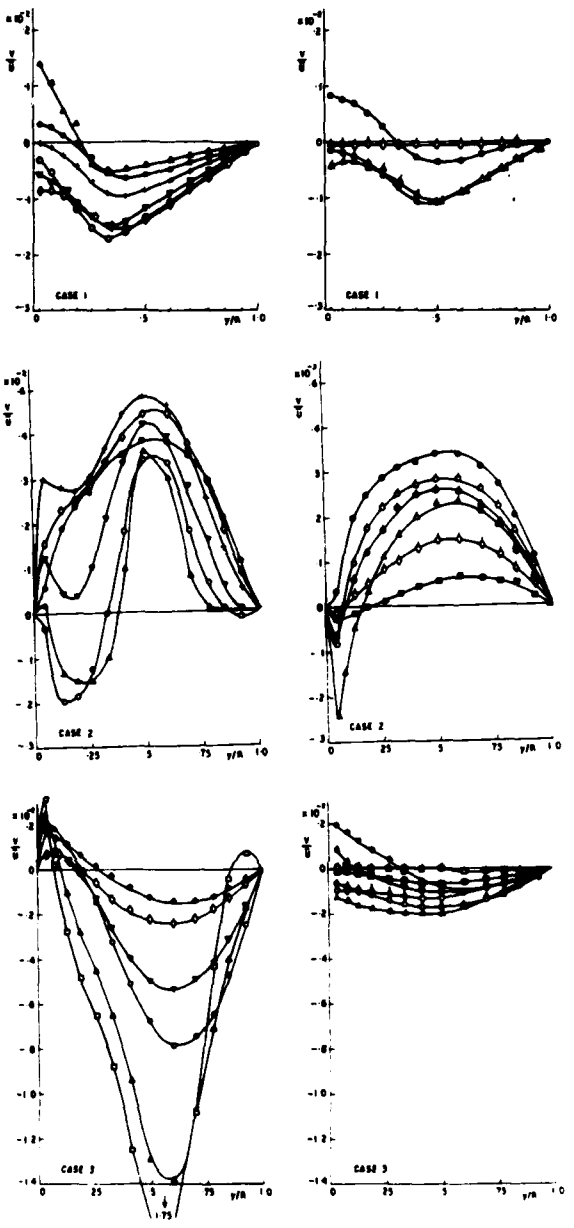

Figure 2 Radial Time Mean Velocity Distribution, $V/\bar{U}$

the turbulent shear stress values for case 2 which increase [illegible] values approaching - 12, in effect an order of magnitude larger than the comparable values for case

In view of the large and striking variations in both axial and radial directions of the various turbulence quantities it is surprising that the time mean flows exhibit such orderly behaviour.

The most striking common feature which was clearly evident from the experimental programme and which figure 1 (cases 2 and 3) illustrate is the occurrence of common intersection points in at least one radial location in each flow.

At this intersection point the axial change in

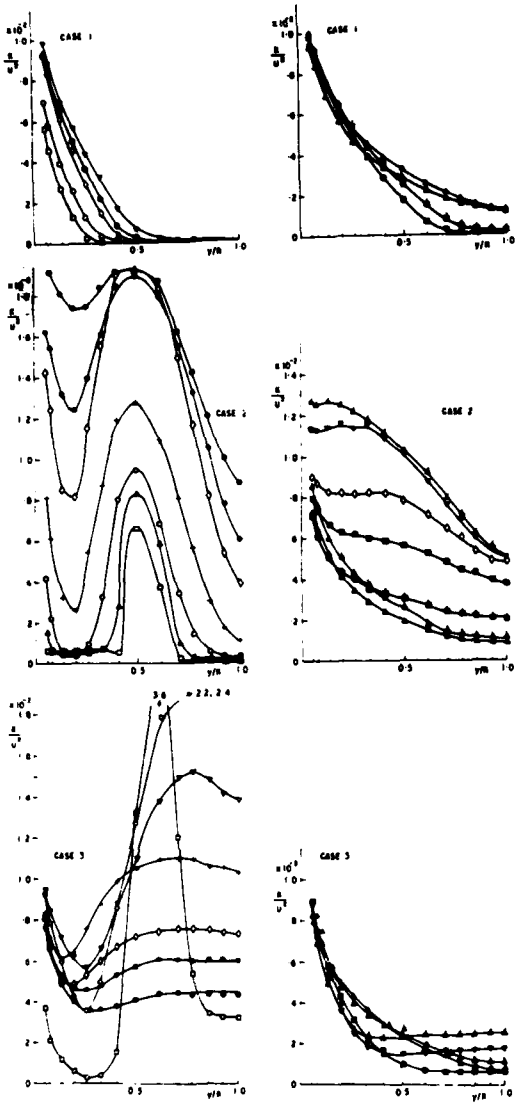

Figure 3 Turbulent Kinetic Energy Distribution, K/U^2

time mean velocity is zero. Thus, on a crude basis, these points act as 'pivots' in the flow with the remainder of the flow either decaying or developing about them.

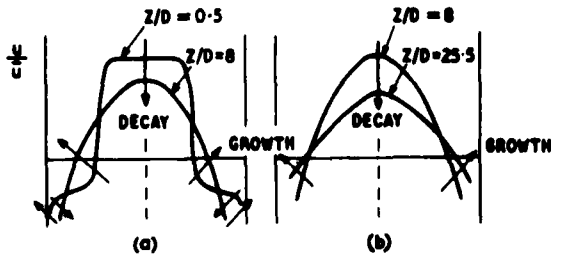

The data of the present investigation and other data quoted in the literature of which references 1-3 provide some examples would suggest that these intersection points are a feature of many flows.

Taking figure 1, case 2 as one example, for $0.5 \leq z/D \leq 8$ at $r/R = 0.87$ and 0.5 the axial velocity remains constant at values of $0.8\bar{U}$ and $1.25\bar{U}$. Thus the development takes the form of sketch (a). Beyond $z/D = 8$ a different type of flow development is found and only one intersection point occurs at $r/R = 0.65$ with a velocity of $1.05\bar{U}$. Again the flow pivots about this point, see sketch (b).

INTERSECTION POINTS

Many examples of common intersection points can be found in published literature, (references 1-3 provide some examples). In the majority of cases however they are not noted as a feature of the studied flows.

Historically Preston[5] and Preston and Norbury[6] established that for a pipe-type profile the non-dimensional velocity u measured at about $y/R = \frac{1}{4}$ gave a fixed value of 1.05. This fact they used to develop the $\frac{1}{4}$ radius flow meter which was designed as a simple method of obtaining the mean velocity in pipe flows.

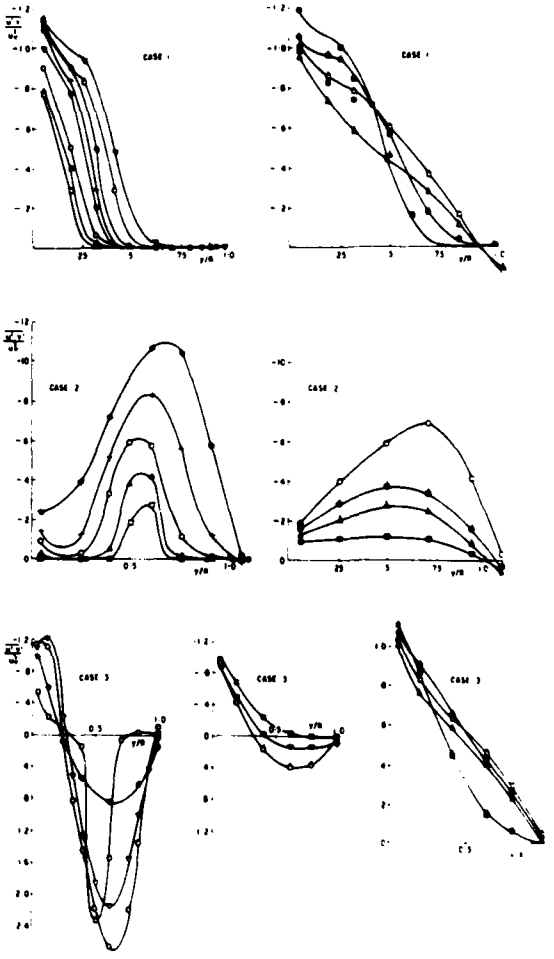

Figure 4 Turbulent Shear Stress Distributions $\overline{u'v'}/u_t^2$

To demonstrate the existence of intersection points in a definitive way is not immediately obvious. Any valid explanation must reflect the fact that the number and position of these points is dependent on the initial profile and allow for the fact that the number and position of the points can change during the profile development.

Studying the profile changes occurring during the decay process the changes in profile can, on a crude phenomenological basis, be seen to contain two main elements:

a) The decay of the initial non-uniform profile accompanied by
b) Growth of a typical pipe flow profile and inevitable interactions.

Therefore, considering an initial profile developing over the range $0 \leq z \leq z_\infty$ (where at z_∞ the profile would have reached the fully developed condition) it should be possible to describe the development in the form:

$$\Delta u_z = \lambda(z)\Delta u_o + \mu(z)\Delta(u_b)_z$$

where

$$\Delta u = u - 1$$

This will be recognised as a defect type formulation and u_o is the initial profile and u_b is the typical pipe profile existing in the absence of the initial flow non-uniformity.

To satisfy the wall boundary condition it is necessary that $\lambda(z) + \mu(z) = 1$ so that:

$$\Delta u_z = \lambda(z)\Delta u_o + (1-\lambda(z))\Delta(u_b)_z \qquad (1)$$

The initial and final conditions will be satisfied by $\lambda(0) = 1$, $\lambda(z_\infty) = 0$ and $\lambda'(z_\infty) = 0$ (implying zero radial velocity).

In the early development stage the decay will be dominated by the first term in the above expression i.e. the damping of the initial profile since $(1-\lambda(z))$ will be small and the contribution from the term u_b significant only near the wall.

Thus for low values of z/D if a point is to exist for which $\frac{\partial u}{\partial z} = 0$ it will occur where $u_o = 1$. Therefore, in the initial development stage the number and position of the intersection points will be governed by the initial profile and the number of times and locations at which it takes its mean value.

Beyond the initial development stage the second term will become significant (at least of the same order as the first) and the location and possibly the number of the points will therefore change.

Referring to figure 1, case 1 which shows the flow development for undisturbed pipe flows it can be seen that beyond z/D = 9 the axial changes which occur between $0.5 \leq \eta \leq 1$ are of small magnitude, though more significant changes are still evident for $0 \leq \eta \leq 0.5$. Beyond z/D = 34.5 (the location of the maximum overshoot position) though profile changes are still obvious these changes are of small magnitude so that the second term will approximate to $(1-\lambda(z))\Delta u_\infty$.

Thus the development would then be approximated by

$$u = \lambda(z)u_o + (1-\lambda(z))u_\infty \qquad (2)$$

When this stage in the flow development is reached (and for many profiles this could be as early as z/D = 9) the intersection points in both number and position will coincide with the points for which $u_o = u_\infty$. At this stage the locus of all intersection points will be the fully developed profile.

This to some extent, provides an explanation for the change in both position and number of the intersection points within the overall profile development. Initially the position of such points is dictated by the condition $u_o = 1$ and subsequently by $u_o = u_\infty$.

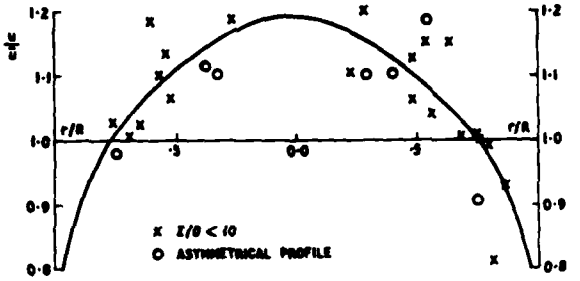

Figure 5 Locus of Intersection Points (z/D < 10) Full line is 'fully developed' profile.

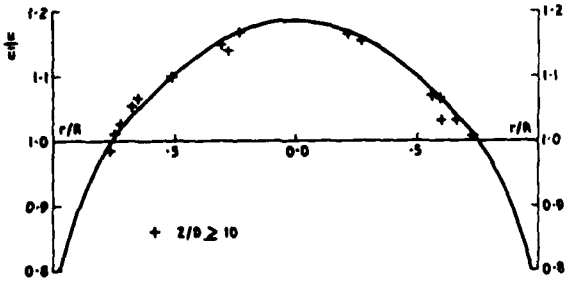

Figure 6 Locus of Intersection Points (z/D ≥ 10)

Figures 5 and 6 show the locus of intersection points obtained from the data for the development range up to z/D = 10 and beyond z/D = 10 respectively. The good agreement obtained between the fully developed profile and the data presented with Figure 6 is obvious.

An identical relationship to equation 2 can be deduced directly from the continuity equation if it is assumed that the radial velocity can be expressed in separable form.

The continuity equation in non-dimensional form gives

$$\frac{\partial}{\partial \eta}(\eta u) + \frac{\partial}{\partial \zeta}(\eta v) = 0$$

so that

$$u(\eta) = u_o(\eta) - \int_0^\zeta \frac{\partial}{\partial \eta}(\eta v)\, d\zeta/\eta \qquad (3)$$

If $\frac{\partial}{\partial \eta}(\eta v)$ can be expressed as a separable function of η and ζ so that

$$\frac{\partial}{\partial \eta}(\eta v) = F(\eta)\, G'(\zeta) \text{ , say, then}$$

equation 3 will imply that

$$u(\eta) = U_o(\eta) - F(\eta)\,\big(G(\zeta)-G(o)\big)/\eta$$

at $\zeta = \zeta_\infty$ where $u(\eta) = u_\infty(\eta)$

$$u_\infty(\eta) = u_o(\eta) - F(\eta)\left(G(\infty) - G(0)\right)/\eta$$

so that

$$\frac{u(\eta)-u_o(\eta)}{u_\infty(\eta)-u_o(\eta)} = \frac{G(\zeta)-G(0)}{G(\infty)-G(0)} = 1 - \lambda(\zeta)$$

thus $$u(\eta) = \lambda(\zeta)u_o(\eta) + (1-\lambda(\zeta))u_\infty(\eta) \qquad (4)$$

This is simply equation 2 written in different non-dimensional form and it would thus imply that common intersection points will occur and that the locus of such points would be the fully developed profile.

Since the basis of the development of the expression is that in effect v can be expressed in separable form it is necessary to consider what restrictions will apply to the applicability of (4).

Since from equation (4)

$$v = -\lambda'(\zeta)\left(\int_o^\eta \eta(u_o(\eta)-u_\infty(\eta))d\eta\right)/\eta \qquad (5)$$

then $v = 0$ at $\eta = 0$ and ∞ and $v = 0$ for all η at $\zeta = \zeta_\infty$. However, if $v = 0$ at some intermediate value of η and ζ, η_x, ζ_x, say, then for 5 to remain valid either v must be zero for all η at ζ_x or v must be zero at η_x for all ζ.

Unless one of these two conditions is satisfied the expression in 4 would no longer be valid over the whole development range.

Referring to figure 2 which shows the plots of radial velocity for the three cases we can see that at many points over the development range the condition $v = 0$ occurs. In some cases one of the above conditions is satisfied but in many cases neither applies. Thus it is likely that the whole profile development range can be split into sections in each of which the decay could be expressed by a modified form of 4.

From figure 2 taking case 3 as an example, the initial development range extends up to $z/D = 4$, a second range up to $z/D = 8$ and the final range from $z/D = 10$. Studying the corresponding time mean profiles in figure 1 the slight shift of intersection point at $z/D = 4$ is clear. Because the profile does not change significantly between $z/D = 8$ and 10 the location of the intersection point beyond $z/D = 4$ lies close to the intersection with the fully developed profile.

DISCUSSION

The assumption of a separable solution has obvious limitations and cannot be used to describe the behaviour of all flows. The best specific empirical profile descriptions (e.g. following Prandtl, Karman, Clauser, Coles) contain both a separable and a non-separable formulation (e.g. law of the wall, law of the wake).

The more general empirical functional description given here, though not universal, enables the occurrence or absence of common intersection points to be better understood.

The existence of common intersection points is demonstrated as being directly relatable to specific conditions on the occurrence of zero local radial time mean velocities.

The formulation is compatible with the oscillatory axial profile development noted by the authors in reference 4.

CONCLUSIONS

An empirical description of the decay of an arbitrary initial profile is suggested. This description can imply the existence of common intersection points in the profile development. At some stage within the profile development the locus of these points must be the fully developed profile.

The analysis, though empirically based, can be of direct application in the areas of profile simulation and characterisation. Though no attempt is made to involve the turbulence structure the data available is of sufficient detail and quality to be of use as test cases for turbulence modelling.

REFERENCES

1. Moon, L F and Rudinger, G "Velocity Distribution in an Abruptly Expanding Circular Duct", Journal Fluids Engineering, Vol 99, 1977, pp 226-230.

2. Deshpande, M D and Giddens, D P "Turbulence Measurements in a Constricted Tube". Journal Fluid Mechanics, Vol 97, 1980, pp 65-89.

3. Hussain, A K M F and Clark, A R "On the Coherent Structure of the Axisymmetric Mixing Layer: a flow visualisation study". Journal Fluid Mechanics, Vol 104, 1981, pp 263-294.

4. Laws, E M, Lim, E H and Livesey, J L "Turbulent Pipe Flows in Development and Decay" 2nd Symposium on Turbulent Shear Flows, Imperial College, London, July 1979, pp 4.6-4.11.

5. Preston, J H "The Three-Quarter Radius Flow Meter", Engineer (London). p 400, 1950

6. Preston, J H and Norbury, J F "The Three-Quarter Radius Flow Meter - A re-assessment" National Engineering Laboratories, Vol 1, pp 46 - 1962.

Calculations of Confined coaxial-jet flows

by

M.A. Habib and J.H. Whitelaw

Imperial College of Science and Technology

London SW7 2BX, England

ABSTRACT

A solution procedure has been developed and applied to the prediction of the flow properties downstream of coaxial jets issuing into a confining duct with an expansion ratio of 2.81. Three turbulence models comprising a mean flow closure (two-equation model) and two Reynolds-stress models were used and the results compared with measured results obtained for two velocity ratios of 1 and 3. The main features of the flow fields are correctly predicted by the three models with the Reynolds-stress models providing better accuracy near and inside the recirculation zone. Discrepancies between measured and calculated flow properties exist, particularly in regions of more than one major component of the velocity-gradient tensor and near the axis of symmetry. The reasons for the discrepancies and the consequent value of the calculation methods are discussed.

INTRODUCTION

Recirculating turbulent flows downstream of coaxial jets, with a sudden expansion, are of relevance to many engineering applications and, in particular, to furnaces and combustion systems. The turbulent mixing which occurs in the vicinity of the shear layers between the two jets and between the outer jet and the reverse flow is the main feature of the present flow. Previous calculations of similar flows are referred to in table (1) and make use of two-equation turbulence models which imply the local isotropy and a generalised Boussinesq effective viscosity concept. In practice, all real flows show some degree of anisotropy and the turbulent stress is usually less directly connected with the mean velocity field than is required by the notion of a turbulent viscosity. As a result, the present investigation includes solutions of transport equations for the Reynolds stresses, and allows comparison with results obtained with the two-equation model. A similar comparison, for bluff body flows, was included in the work of Pope and Whitelaw (1976) and the results appear to have been influenced by numerical effects. As a consequence, the numerical aspects of the present work are considered in some detail.

The calculations are compared with the measurements of Habib (1980) which include values of mean velocity and normal stresses for two different velocity ratios and at high Reynolds number. These results were obtained by laser-Doppler anemometry and the accuracy of the results has been extensively discussed. The flow conditions at exit from the coaxial jet were known to correspond to those of fully developed pipe and annulus flow.

The following section states the differential equations which have been solved in finite-difference form. The solution procedure is described in the third section which deals with boundary conditions and comments on the numerical accuracy and economy. The results of the calculations are then presented and the paper ends with a summary of the more important conclusions.

Differential equations

The time averaged forms of the continuity and momentum equations may be written in the form

$$\frac{\partial U_j}{\partial x_j} = 0$$

$$\frac{\partial}{\partial x_j}(U_i U_j) = -\frac{1}{\rho}\frac{\partial P}{\partial x_i} + \frac{\partial}{\partial x_j}\left(\nu \frac{\partial U_i}{\partial x_j} - \overline{u_i u_j}\right) \quad 2$$

and have been solved in their two-dimensional, axisymmetric form. The Reynolds stresses were represented by the three models represented by the equations indicated below.

Model 1. $$-\rho\,\overline{u_i u_j} = \mu_t\left(\frac{\partial U_i}{\partial x_j} + \frac{\partial U_j}{\partial x_i}\right) - \frac{2}{3}\rho K \delta_{ij} \quad 3$$

$$\mu_t = \rho C_\mu K^2/\varepsilon \quad 4$$

with $$\frac{\partial}{\partial x_j}(U_j K) = \frac{\partial}{\partial x_j}\left(\frac{\nu_{eff}}{\sigma_K}\frac{\partial K}{\partial x_j}\right) - \overline{u_i u_j}\frac{\partial U_i}{\partial x_j} - \varepsilon \quad 5$$

$$\frac{\partial}{\partial x_j}(U_j \varepsilon) = \frac{\partial}{\partial x_j}\left(\frac{\nu_{eff}}{\sigma_\varepsilon}\frac{\partial \varepsilon}{\partial x_j}\right) + C_{\varepsilon_1}\frac{\varepsilon}{K}\overline{u_i u_j}\frac{\partial U_i}{\partial x_j} - C_{\varepsilon_2}\frac{\varepsilon^2}{K}$$

Models 2 and 3 $$\quad 6$$

$$\frac{\partial}{\partial x_\ell}(U_\ell\,\overline{u_i u_j}) = C_s\frac{\partial}{\partial x_k}\left(\overline{u_\ell u_k}\frac{\partial\,\overline{u_i u_j}}{\partial x_k}\right) + G_{ij} + R_{ij} - \frac{2}{3}\varepsilon\,\delta_{ij} \quad 7$$

$$G_{ij} = -\left(\overline{u_i u_k}\frac{\partial U_j}{\partial x_k} + \overline{u_j u_k}\frac{\partial U_i}{\partial x_k}\right)$$

$$R_{ij} = -C_1\frac{\varepsilon}{K}\left(\overline{u_i u_j} - \frac{2}{3}\delta_{ij}K\right) - C_{\phi_1}C_2\left(G_{ij} - \frac{2}{3}G\delta_{ij}\right) - C_{\phi_2}\left[\frac{C_2+8}{11}\left(G_{ij} - \frac{2}{3}G\delta_{ij}\right) + \frac{30C_2-2}{55}K\left(\frac{\partial U_i}{\partial x_j} + \frac{\partial U_j}{\partial x_i}\right) + \frac{8C_2-2}{11}\left(D_{ij} - \frac{2}{3}G\,\delta_{ij}\right)\right]$$

$$D_{ij} = -\left(\overline{u_i u_k}\frac{\partial U_j}{\partial x_k} + \overline{u_j u_k}\frac{\partial U_i}{\partial x_k}\right)$$

In Model 2, $C_{\phi_1} = 1$ and $C_{\phi_2} = 0$ so that there is no account taken of the mean strain which is represented, in Model 3, with $C_{\phi_1} = 0$ and $C_{\phi_2} = 1$. These formulations are in accordance with the work of Launder, Reece and Rodi (1975). The rate of dissipation is again represented by equation 6 with

$$\frac{\partial}{\partial x_j}\left(\frac{\nu_t}{\sigma_\varepsilon}\frac{\partial \varepsilon}{\partial x_j}\right)$$

replaced by $$C_\varepsilon\frac{\partial}{\partial x_j}\left(\frac{K}{\varepsilon}\overline{u_\ell u_j}\frac{\partial \varepsilon}{\partial x_\ell}\right)$$

Calculation Procedures

The equations of the previous section were solved to yield three different solutions of the flow in the confined double coaxial jet. Measured velocities and normal stresses provided the corresponding boundary condition at the inlet to the model furnace and the dissipation rate was determined from

TABLE 1

CALCULATIONS OF RECIRCULATING JET FLOWS BY THE K ∿ ε MODEL

Author	Flow configuration	Flow properties compared with experiments
Gosman et al (1974)	Axisymmetric expansions	U and K
Khalil et al (1975)	Confined flow of an annular jet and sudden expansion	U, K and W
Pope and Whitelaw (1976)	Near-wake flow	U, $\overline{uv}$ and u^2
Pope (1976)	Flow in a diffuser	-
Hutchinson et al (1977)	Axisymmetric expansion	U
Moss et al (1979)	Backward-facing step	U and K
Durst and Rastogi (1979)	Separated flow of a square obstacle in a channel flow	U and K
Gosman et al (1979)	Sudden expansion flows and others	U, W and K
Hyde and Sykes (1979)	Enclosure with divergent quarl angle	U and W
Cebeci et al (1979)	Separated boundary layer flows	U
Habib and Whitelaw (1979)	Confined double coaxial jets	U, K, $\overline{u^2}$

$$\varepsilon = C_\mu\frac{K^{3/2}}{\ell} \quad 8$$

where $\ell = 0.03$ R. In the case of five-equation turbulence models, the shear stress was also available since the flow was known to be fully developed. All axial gradients ($\partial/\partial x$) were presumed zero in the exit plane of the confining tube, i.e. at $x/D_e = 4.8$ (D_e is the enclosure diameter); this corresponds to developed boundary-layer flow at the exit section which is in reasonable accord with the measurement. A symmetry axis was specified with $V = \overline{uv} = 0$ and $\partial/\partial y$ of all other quantities equal to zero at $y = 0$. Zero velocities were specified on all solid surfaces.

Partly to economize computer time requirements, logarithmic wall functions were used to link the near-wall grid lines to wall boundaries, thus:-

$$\tau_w = \frac{U_p}{y_p}\frac{\mu\ \kappa\ y_p^+}{\ln(E_1 y_p^+)} \quad \text{where } y_p^+ = C_\mu^{1/4} K_p^{1/2}\ y_p/\nu$$

where subscript, p, refers to the near-wall node. κ and E_1 are the wall law constants and take the values 0.419 and 9.8 respectively. The value of the kinetic energy of turbulence at point p, K_p, was calculated from the transport equation of K with the flux of energy to the solid wall set to zero. The corresponding value of the dissipation of K, ε,

was prescribed by:-

$$\varepsilon_p = (C_\mu^{1/2} K_p)^{3/2}/\kappa\, y_p$$

and the integral of ε from the wall to y_p, which is required for the kinetic energy or the Reynolds-stress equations given by:-

$$\int_0^{y_p} \varepsilon \, dy = (C_\mu^{1/2} K_p)^{3/2} \frac{1}{\kappa} \ln (E_1 y_p^+)$$

The values of constants used in the models are shown in Table 2. The constants of Model 1 are identical to those of Launder et al (1972) and have been used for the prediction of recirculating flows, see for example Khalil et al (1975). The coefficients of Models 2 and 3 are in accord with Launder et al (1975), and have previously been applied to axisymmetric flow cases by Naot and Launder (1975) and to recirculating flow behind bluff body by Pope and Whitelaw (1976).

TABLE 2

CONSTANTS OF EQUATIONS

Constant	Model 1	2	3
C_μ	0.09	-	-
σ_K	1.00	-	-
σ_ε	1.22	-	-
C_s	-	0.25	0.25
C_ε	-	0.15	0.15
C_1	-	2.50	1.50
C_2	-	0.40	0.40
C_{ε_1}	1.44	1.45	1.45
C_{ε_2}	1.92	1.92	1.92

In the iteration procedure, the initial values were chosen to minimize the instability in the first number of iterations, for example, specification of the mean velocity satisfied continuity throughout the solution domain. In the case of the Reynolds-stress models, the initial values were taken from the results of solutions based on the K-ε model, as indicated on Fig. 1.

Convergence was assessed at the end of each iteration with a convergence factor, taken to be 0.1%, which equals the residual source of each finite difference equation normalised by the fixed flux of the relevant extensive property fed into the solution domain. Under-relaxation was used to improve convergence. It is clear from figure 1 that the number of iterations and, consequently, the computation time required by the Reynolds-stress models is larger than that of the K $\sim$ ε model to achieve the same convergence. The figure indicates also that the rate of decay is much larger in the case of the solution of Model 1 which is due to the lesser number of equations interconnected in the model.

With the small convergence factor noted above, the errors due to the degree of convergence are negligible. The effect of the number and location of grid nodes is more important and, when the Peclet number is large and the flow is inclined to its mesh, donor-cell differencing is used with consequent numerical diffusion. The effects are important where the mean flow component is not aligned with the grid direction and the problem has been examined, for example, by Wolfshtein (1969), Gosman et al (1969) and Raithby (1976). The present number of nodes and their distribution were selected after experiments with fewer nodes and different distributions had indicated that the present arrangement led to results which are reasonably free from numerical errors. Thus, an increase in the number of grid nodes from 396 to 432 led to differences in calculated dependent variables which did not exceed 3% and the trend in values was monotonic for a number of nodes greater than 256. Grid-dependent tests made with (18 x 14) and (30 x 22) nodes and (24 x 18) grid used for subsequent results, are shown in Figs. 2 and 3 and were obtained with the two-equation model. The calculated values are of the mean axial velocity and the kinetic energy of turbulence along the centre-line and at the radial profile of x/D_e = 0.616 and suggest that the numerical accuracy is reasonable even with a 18 x 14 grid. Since the numerical diffusion is likely to be greatest in the same locations where the turbulence control is greatest, it is nearly impossible to provide a more definitive statement.

The finite-difference equations were solved iteratively by a TEACH Fortran program on a CDC 6600 digital computer. The calculation time to convergence is shown on Table 3 for each model; the increase in time in the Reynolds stress models, 2 and 3, is due to the solution of eight dependent variables rather than for five. The storage requirements by the two-equation model was 0.73 of that required by the Reynolds-stress models.

TABLE 3

COMPUTING TIME TO ACHIEVE CONVERGENCE

Model	Number of Iterations	Total Time sec.	Time per Iteration per grid node sec.
1	277	198	0.0017
2	299	373	0.0028
3	333	422	0.0029

Results

The calculations are presented for two velocity ratio (the ratio of the annulus maximum velocity to the maximum pipe velocity, U_a/U_p) of 3 and unity. The axial distributions of the axial mean velocity, normalised by the mean velocity value on the axis at the exit plane of the coaxial jets, are compared with measurements on Fig. 4. The calculated centre-line velocity distribution is in reasonable accord with the measurements except in the region immediately downstream of the exit in the case of the higher velocity ratio where the velocity is underpredicted especially with models 2 and 3. Further downstream and at around x/d_o = 4.0 (d_o is the annulus outer diameter), and again for the higher velocity ratio, the mean velocity maximum is underpredicted by about 15%.

The discrepancy in the calculations by Model 1 has been attributed (see Habib and Whitelaw, 1979) to the incorrect representation of the turbulent diffusion process as a result of the isotropic-viscosity hypothesis and Fig. 4 shows that the same discrepancy occurs with the Reynolds-stress models. This suggests that the predicted mixing is low since the increase in the mean velocity along the centre-line in the case of the higher velocity ratio is attributed to the diffusion of the flow of the outer jet towards the centre-line. The magnitude of the discrepancies attributable to numerical accuracy can be deduced from figures 2 and 3 and is small compared to that associated with the turbulence models.

Fig. 5 represents the normalised variance of the axial velocity fluctuations along the centre-line and is underpredicted by all models; with the Reynolds-stress approach giving better accuracy in most regions. The agreement improves in the downstream region where discrepancies are less than 10% at x/D_e = 4.0. The normal stress distributions predicted by the two Reynolds-stress models are nearly the same and are not affected by the difference in the forms of the redistribution terms. Comparison of measured and calculated values of the kinetic energy of turbulence show similar trends.

The distributions of the normalised rate of dissipation along the centreline are presented on Fig. 6 together with values deduced from the measurements. The rate of dissipation is overpredicted by the three models with the Reynolds-stress models giving smaller discrepancies. These results are consistent with those of Fig. 4 and the overprediction in the values of the rate of dissipation may explain the underestimated values of K along the centre-line. The overprediction of ε and underprediction of K near the centre-line are expected to decrease the transport in the momentum equation by diffusion processes through the decrease in the effective viscosity, μ_{eff} ($\equiv \mu_t + \mu$) as shown from the relation $\mu_t = \rho c_\mu K^2/\varepsilon$, in model 1 and through the decrease in the level of the normal stresses in models 2 and 3. This explains the underpredicted mixing shown by Fig. 4 and discussed above. Fig. 6 also indicates that the inlet distribution of length scale has a large effect on the ε-distribution in the upstream region where the diffusion terms have a large effect in the momentum equations; it has no significant effect in the downstream region where the diffusion effects are small.

Figs. 7 and 8 present the radial profiles of the calculated and measured flow properties at x/D_e of 0.616 and shows that the two Reynolds-stress models give nearly the same distribution for both the two velocity ratios. It can be concluded that the difference in the forms of the redistribution terms has little effect on the mean velocity distribution along the radius. The results of the Reynolds-stress models are more precise for unity velocity ratio and show better agreement than in the case of the higher velocity ratio. The $K \sim \varepsilon$ model predicts the velocity maximum in the 3:1 velocity ratio case more accurately, but shows greater discrepancies in the region of rapid velocity decay, $0.4 < y/R < 0.6$. The width of the recirculation region is underpredicted by the three models with the Reynolds-stress models giving slightly smaller discrepancies and better representation of the mean velocity near the wall.

The calculations of normal stress indicated that the Reynolds-stress models were preferable but still led to significant underprediction in the region of r/R less than 0.3. Pope and Whitelaw (1976) observed similar discrepancies in their calculations for the near-wake flows near the axis of symmetry. The reason may be the gradient assumption embodied in the Boussinesq equation in the two equation model or in the diffusion terms in the Reynolds stress models which break down near the axis of symmetry. The profiles of shear stress showed that the changes in the sign are correctly represented and that no one model can be identified as a clear improvement over any other in the upstream region. At x/D_e = 3.67, the two stress models provide results which are more than 50% larger than those of the K-ε model and are in good agreement with the measurements.

Discussion

The results show that the mean velocity can be represented by the three models with the maxima along the centre-line and radius underpredicted by around 20%. The discrepancies may be attributed to the underprediction of the turbulent diffusion and this is confirmed by the underestimation of normal and shear stresses and their gradients, particularly near the centre-line.

In the case of the $K \sim \varepsilon$ model, the effective viscosity formulation implies that the principal axes of the Reynolds stress tensor are parallel to the principal axes of the strain rate tensor so that any change in the strain rate affects the stresses. This instantaneous change of the Reynolds stresses with the strain rates is not supported by the experimental observations because the Reynolds stresses, due to the vorticity fluctuations, require time to adjust to the new strain rates (Warsi and Amlicke, 1976; Rotta, 1979 and Bradshaw, 1973). The isotropic-viscosity formulation can, therefore, be expected to lead to errors particularly in regions of high velocity gradients, i.e. regions of high rate of strain.

The underestimation of the Reynolds stresses by the models 2 and 3 may be attributed to the incorrect representation of the diffusive mechanism. Ribeiro (1976) suggested that the diffusive mechanism is associated with the larger scales of the motion and can not be represented by second order closures. This is particularly true in regions of high velocity gradients where the local turbulent field is strongly asymmetric and, therefore, the third order correlations play an important role on the transport of the Reynolds stresses. These correlations have been expressed in terms of second order terms and their gradients.

The rate of dissipation of the kinetic energy of turbulence is overpredicted by the three models and is attributed to the strong link between ε and the mean flow field incorporated in the models and represented by the term $G\varepsilon/K$. Dissipation occurs in the finest scales of motion and these do not reflect the local mean strain field. This connection tends to increase the local level of ε, and consequently decreases the level of the kinetic energy of turbulence. The replacement of G by εA (A being the anisotropy of stresses defined as $(\overline{u_i u_j} - \frac{2}{3}\delta_{ij} K)^2/K^2$, Zaman and Lumley (1979), seems physically better but does not work well in practice (Launder and Whitelaw, 1977).

The form of the dissipation equation was also criticised by Bradshaw (1973) and Pope and Whitelaw (1976) particularly in relation to flows with streamline curvature.

In complex flows, where there is more than one major component of the velocity gradient tensor, extra strain rates are added to the generation terms. Bradshaw (1973) suggested that the Reynolds stresses change by amounts which are much larger than the direct effect of these strains and that neither of the effective viscosity model nor the Reynolds stress models represent these changes correctly. In the case of K ∿ ε model, the changes in the shear stresses are directly related to the strain rates through a factor ($\equiv \mu_t (\partial U/\partial y + e)$ where e represents any other strain rather than $\partial U/\partial y$) which is very small with respect to experimental evidence which suggests ($\equiv \mu_t (\partial U/\partial y + ae)$, with a of order 10, see Bradshaw (1975). In the case of the Reynolds stress models, changes of a similar order may also be required in destruction, redistribution and turbulent diffusion terms. This can be achieved in the present models by replacing constants with functions of a parameter which can represent streamline curvature, for example a Richardson number.

It may be noted here that the effect of the extra strain rates is especially important in the regions of $\partial U/\partial y = 0$, near the axis for example. These effects contribute to the underprediction of the Reynolds stresses near the centre-line and it may be anticipated that these effects are of greater importance with the higher velocity ratio. This is consistent with the better agreement between the calculations and experimental results in the case of unity velocity ratio.

Recent attempts to modify the dissipation equation to better represent flows with streamline curvature have been reported. Morse (1979), for example, found it necessary to make the dissipation equation constant c_{ε_1} a function of the Richardson number to increase the rate of spread in his free-swirling flows. A modification of the dissipation equation was also made by Rodi (1979) in which one of the empirical constants in the equation is made a function of the flux Richardson number based on the extra production of the lateral fluctuations of $\overline{v^2}$. Such modifications were shown to be useful in the predictions of swirling jets (Rodi, 1979) and, although so far considered only in the context of boundary-layer flows, are likely to decrease the discrepancies between measurements and predictions for flows with recirculation.

Concluding Remarks

The solution procedure has been applied to the prediction of the flow properties of the confined double coaxial jet for two different velocity ratios and the results compared with corresponding experimental data. The agreement between experimental data and predicted results of the three models are varied according to the flow conditions and, for example, the mean velocity distribution near and inside the recirculation zone was better predicted by the Reynolds-stress models than the eddy-viscosity model. Significant discrepancies exist and the size of the recirculation zone was underprecited by the three models with the Reynolds-stress models giving lower discrepancy. The normal stress was underestimated by the three models particularly near the centre-line and the rate of dissipation overestimated. The discrepancies are associated with streamline curvature and appropriate modifications to the Reynolds stress equations and the equation for the rate of dissipation are required. In the first instance, the application of a Richardson number correlation for C_{ε_1}, as proposed by Rodi (1979), should be evaluated but the need for additional changes can be anticipated for the strong streamline curvatures associated with separated flows.

REFERENCES

Bradshaw, P. (1973) "Effect of streamline curvature on turbulent flow". AGARDograph, 169.

Bradshaw, P. (1975) "Calculation methods for complex flows". VKI Short Course on Prediction Methods for Turbulent Flow, March 3 - 7.

Cebeci, T., Khalil, E.E. and Whitelaw, J.H. (1979) "Calculation of separated boundary-layer flows". AIAAJ, Vol. 17, No. 12, p.1291.

Durst, F. and Rastogi, A.K. (1979) "Theoretical and experimental investigations of turbulent flows with separation". Proc. of the First Symposium on Turbulent Shear Flows, (Eds. F. Durst, B.E. Launder, F.W. Schmidt and J.H. Whitelaw).

Gosman, A.D., Khalil, E.E. and Whitelaw, J.H. (1979) "The calculation of two-dimensional turbulent recirculating flows". Proc. of the First Symposium on Turbulent Shear Flows. (Eds. F. Durst, B.E. Launder, F.W. Schmidt and J.H. Whitelaw).

Gosman, A.D. and Pun, W.M. (1974) "Lecture notes for course entitled - Calculation of recirculating flows". Imperial College, Mech. Eng. Dept.

Gosman, A.D., Pun, W.M., Runchal, A.K., Spalding, D.B. and Wolfshtein, M. (1969) "Heat and mass transfer in recirculating flows". Academic Press, London and New York.

Habib, M.A. (1980) "Confined flows with and without swirl". Ph.D. Thesis, Imperial College, London.

Habib, M.A. and Whitelaw, J.H. (1979) "Velocity characteristics of a confined coaxial jet". ASME J. Fluids Engng., 101, p.521.

Hutchinson, P., Khalil, E.E. and Whitelaw, J.H. (1977) "Measurement and calculation of furnace-flow properties". J. of Energy, 1, p.212.

Hyde, D.J. and Sykes, J. (1979) "A finite difference method for the solution of turbulent, combusting flows in enclosures with a divergent burner quarl". HTFS AERE R5262.

Khalil, E.E., Spalding, D.B. and Whitelaw, J.H. (1975) "The calculation of local flow properties in two-dimensional furnaces". Int. J. Heat Mass Transfer, 18, pp. 775-791.

Launder, B.E., Morse, A., Rodi, W. and Spalding, D.B. (1972) "The prediction of free shear flows - a comparison of the performance of six turbulence models". NASA Conference on Free Shear Flow, Langley Field, Hampton, July.

Launder, B.E., Reece, G.J. and Rodi, W. (1975) "Progress in the development of a Reynolds-stress turbulence closure". J. Fluid Mech., 68, p.537.

Launder, B.E. and Whitelaw, J.H. (1977) "Turbulent flow modelling". Heat Transfer and Fluid Flow Service, AERE Harwell and National Engineering Laboratory, Report AERE-R8635.

Morse, A. (1979) Private communication.

Moss, W.D., Baker, S. and Bradbury, L.J.S. (1979) "Measurements of mean velocity and Reynolds stresses in some regions of recirculating flow". Proc. of the First Symposium on Turbulent Shear Flows. (Eds. F. Durst, B.E. Launder, F.W. Schmidt and J.H. Whitelaw).

Naot, D. and Launder, B.E. (1975). "Numerical calculations of the turbulent swirling and recirculating flows with a Reynolds stress closure". Ben Gurion University of the Negev, Mech. Eng. Dept., Report No. ME-22/75.

Pope, S.B. (1976). "The calculation of turbulent recirculating flows in general orthogonal coordinates" Mech. Eng. Dept., Imperial College Report CHT/76/7.

Pope, S.B. and Whitelaw, J.H. (1976) "The calculation of near-wake flows". J. Fluid Mech., 73, pp.9.

Raithby, G.D. (1976) "A critical evaluation of upstream differencing applied to problems involving fluid flow". Comp. Meth. Appl. Mech. Eng., 9, p.75.

Ribeiro, M.M. (1976) "The turbulence structure of free jet flows with and without swirl". Ph.D. Thesis, University of London.

Rodi, W. (1979) "Influence of buoyancy and rotation on equations for the turbulent length scale". 2nd Symposium on Turbulent Shear Flows, July 2-4, Imperial College, London.

Rotta, J. (1951) "Statistische Theorie nichthomogener Turbulenz". Zeitsch. fur Physik, 129, p.547 and 131, p.51.

Rotta, J.C. (1979) "A family of turbulence models for three-dimensional thin shear layers". Proc. of the First Symposium on Turbulent Shear Flows. (Eds. F. Durst, B.E. Launder, F.W. Schmidt and J.H. Whitelaw).

Warsi, Z.U.A. and Amlicke, B.B. (1976) "Improved algebraic relation for the calculation of Reynolds stresses". AIAAJ, Vol. 14, No.12.

Wolfshtein, M. (1969) "Convection processes in turbulent impinging jets". Ph.D. Thesis, University of London.

Zaman, O. and Lumley, J.L. (1979) "Buoyancy effects in entraining turbulent boundary layers" A second-order closure study" Proc. of the First Symposium on Turbulent Shear Flows (Eds. F. Durst, B.E. Launder, F.W. Schmidt and J.H. Whitelaw).

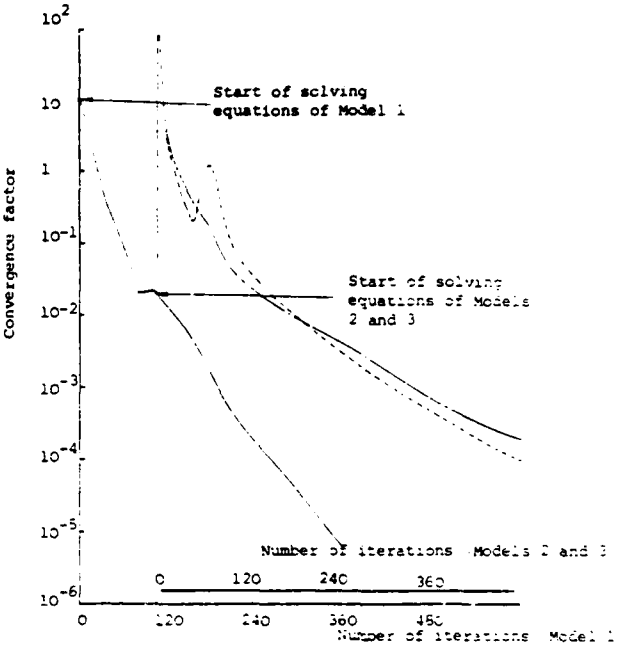

Fig. 1 The Convergence of the Solution Procedure _____, Model 1; ----, Model 2; —.—, Model 3

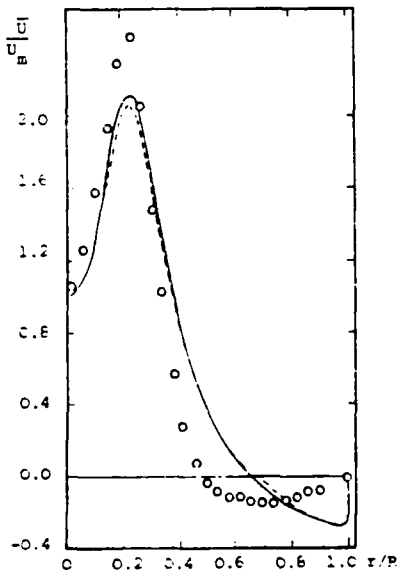

Fig. 2 Effect of Grid Size on the Mean Velocity Values Along the Radius (X/D_e = 0.616 U_a/U_p = 3) ---, 18x14; ——, 24x18; —.—, 30x22

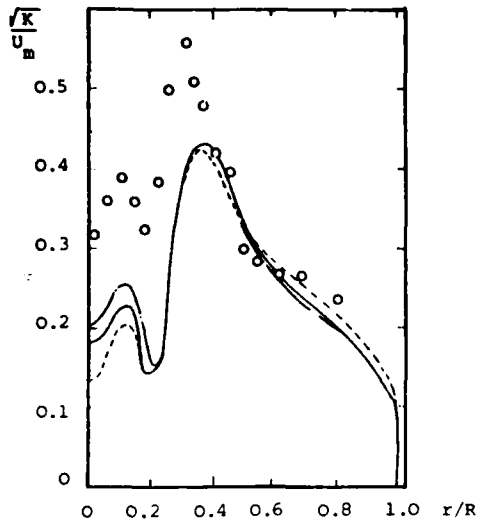

Fig. 3 Effect of Grid Size on the Values of the Kinetic Energy of Turbulence Along the Radius ($X/D_e = 0.616$; $U_a/U_p = 3$) Notation as in Fig. 2

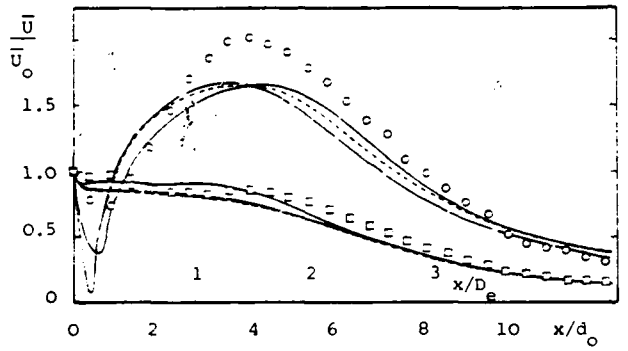

Fig. 4 Axial Distribution of Axial Mean Velocity O, measurements, $U_a/U_p = 3.0$; □ , measurements, $U_a/U_p = 1.0$; _____ calculations, Model 1; - - - -, calculations, Model 2; —·—, calculations, Model 3

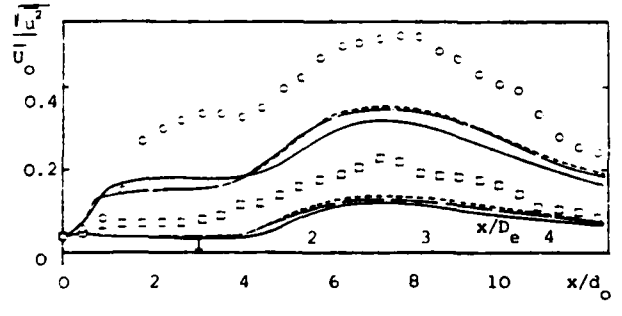

Fig. 5 Axial Distributions of Axial Normal Stress; Notation as in Fig. 4.

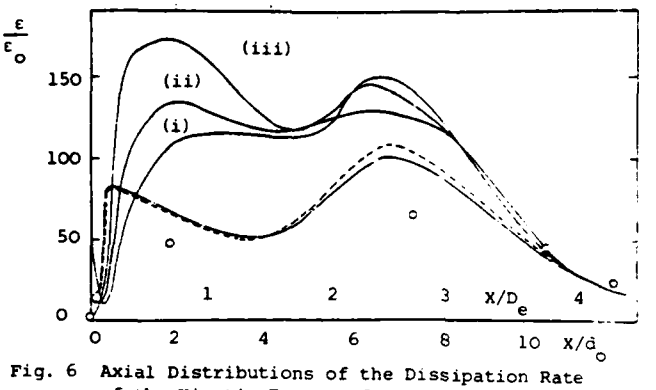

Fig. 6 Axial Distributions of the Dissipation Rate of the Kinetic Energy of Turbulence; (i) $\ell_o = 0.01\, c_\mu R$; (ii) $\ell_o = 0.04\, r_{p,a}$; (iii) $\ell_o = c_\mu^{1/4} \ell_m$. Otherwise as in Fig. 4

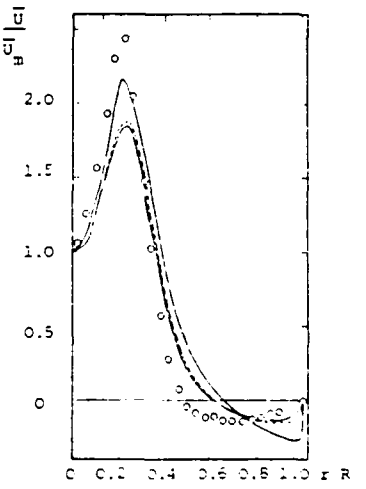

Fig. 7 Radial Profiles of Axial Mean Velocity ($X/D_e = 0.616$, $U_a/U_p = 3.0$); Notation as in Fig. 4.

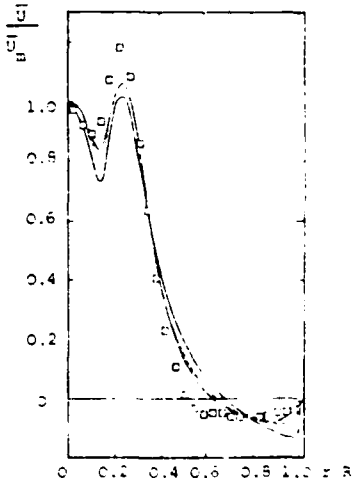

Fig. 8 Radial Profiles of Axial Mean Velocity ($X/D_e = 0.616$, $U_a/U_p = 1.0$); Notation as in Fig. 4

EXPERIMENTAL AND NUMERICAL STUDIES OF THE TURBULENT SHEAR FLOW IN A PIPE WITH A WEAKLY WAVY WALL.

M.P. CHAUVE AND R. SCHIESTEL

Institut de Mécanique Statistique de la Turbulence
CNRS L.A. 130
12, avenue du Général Leclerc
13003 Marseille, FRANCE

ABSTRACT

The complex turbulent flow in a pipe with a weakly wavy wall is studied. Experiments include measurements of mean flow and turbulent quantities in the air and visualizations in water. The flow characteristics proved to be very different from these observed in a usual straight pipe. Moreover an unstationary reverse flow behind every crest has been found. Numerical predictions based on the low-Reynolds k-ε model are performed in order to test usual closure hypothesis in a complex flow. The comparisons with the experimental measurements have shown that such a simple turbulence model give qualitative agreement in several aspects but discrepancies remain on the turbulence quantities that are attributed to the complex character of the flow.

NOMENCLATURE

k	kinetic energy of turbulence
p	pressure
r	radial coordinate
$R(x)$	local radius at abscissa x
R_H	mean radius of the pipe (arithmetic mean between maximum and minimum radius)
$\tilde{R}_H$	Reynolds number $\tilde{R}_H = 2\tilde{u}R_H/\nu$
$\bar{u}$	mean longitudinal velocity
$\tilde{u}$	bulk velocity
$\overline{u'^2}$, $\overline{v'^2}$, $\overline{w'^2}$	turbulent normal stresses
$\overline{u'v'}$	turbulent shear stress
u_{*H}	friction velocity in a straight pipe of radius R_H at the same experimental Reynolds number.
u^+	normalized velocity $\bar{u}/u_{*H}$
$\bar{v}$	radial component of velocity
x	longitudinal coordinate
y	distance from wall
y^+	normalized distance from wall $y\, u_{*H}/\nu$
ε	dissipation rate of turbulent kinetic energy
λ	wavelength
ρ	density
ν	cinematic viscosity
$\tau(x)$	wall shear stress at abscissa x
τ_H	wall shear stress in a straight pipe of radius R_H at the same experimental Reynolds number.

INTRODUCTION

Our aim is to present a study of the turbulent shear flow in a pipe with a weakly wavy wall (fig 1). Several approaches have been used together : an experimental study including measurements in an air flow and some visualizations in water, and a numerical prediction using a classical model of turbulence. Such a flow is a complex one, indeed near wall curvature effects, acceleration and deceleration effects due to section variation are important. In fact the flow characteristics are very different from those obtained in a usual turbulent pipe flow /1/. Besides, the experiments have shown the occurrence of an unstationary reverse flow downstream every crest. We can note that in the literature only few experimental studies are available on this subject ; we mention for instance the work of S.T. Hsu and J.F. Kennedy /2/.

Several numerical predictions of the laminar or turbulent flow above irregular boundaries of various shapes have been made these last years including mainly studies above solid or moving waves /3/, /4/ and constricted pipes /5/,/6/.

Present numerical computation of this flow has been made using the k-ε model of W.P. Jones and B.E. Launder /7/. These calculations of such a complex flow are useful for testing usual turbulence closure hypothesis and for discussing their ability to predict the flow characteristics. Before presentation of the results we first give a brief description of experimental dispositive and conditions for the measurements in the air and for the visualizations in water. We give also the main informations concerning the numerical treatment.

EXPERIMENTAL SET-UP AND PROCEDURES

Pipe characteristics

Mean diameter $2R_H$ = 38.89 mm , total length : 450 mm, wave length of undulation : λ = 55 mm, amplitude : 3 mm, number of undulations : 8. The

shape of the wall undulation are discribed on figure 1.

Instrumentation

The pressure has been measured by a classical static probe connected to a water micromanometer, that allows to distinguish 0.02 mm pressure differences.

Longitudinal mean velocity profiles have been measured with hot wire anemometer, from axis to the viscous sublayer. In all cases the wall distance is determined with 0.01 mm accuracy. The wall shear stress evolution has been obtained from the slope of velocity profiles at the wall. A special correction procedure, based on a probe calibration in a turbulent pipe flow for every distance close to the wall ($y \leq 1$. mm), has been used to take into account near wall effects /8/.

The variances and covariances ($\overline{u'^2}$, $\overline{v'^2}$, $\overline{w'^2}$, $\overline{u'v'}$) have been obtained from single wire and x-wire probe. Moreover to define the unstationary reverse flow region (fig. 2), we use a special probe sketched below :

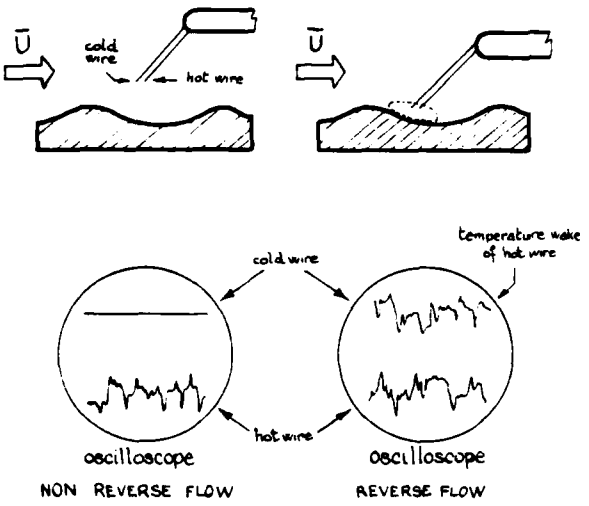

As it can be seen on this sketch if an instantaneous reverse flow happen, we can detect a temperature wake on the upwind cold wire.

Visualization

A similar model to the one for experimental study in the air has been built in plexiglas. A dye of same density than water is injected at different positions of the wall. The flow is driven by gravity. Instantaneous pictures have been taken (fig.4)

Experimental conditions

The Reynolds numbers based on the bulk velocity $\tilde{u}$ and the mean diameter $\tilde{R}_H = 2R_H\tilde{u}/\nu$ are 30 000 and 115 000 for experiments in the air flow and numerical predictions and only 30 000 for visualizations.

NUMERICAL TREATMENT

The numerical treatment /9/ has been developed within the framework of the classical k-ε model of W.P. Jones and B.E. Launder /7/ with low Reynolds number modifications.

Geometric description of the flow

The main difficulty stems from the undulated shape of the wall : a curvilinear grid (fig. 3) is well suited to describe the wavy boundary. The coordinate transformation has been defined by conformal mapping. The shape of the wall boundary has been approximated within a precision of about 0.2 per cent of the pipe radius, that is about 1.5 per cent of the wave amplitude.

Within undulation, the grid presents 22 points in the x direction, 40 points on the radial direction. This latter distribution has been refined in the wall region (half of the points are within the zone $y^+ < 30$), the ratio between two successive steps remaining constant.

Numerical method

The set of partial differential equations governing the flow together with those for turbulence kinetic energy and dissipation rate has been transformed to be formulated in a curvilinear frame of reference. The finite difference counterpart of these equations is derived in the transformed plane using the micro-integral approach. This finite difference scheme embodies upwind-differencing for the approximation of convection terms. Shifted grids are used to calculate $\bar{u}$ and $\bar{v}$ mean velocity components. The solution algorithm is developed on the basis of the calculation procedure of W.M. Pun and D.B. Spalding /10/ for recirculating elliptic flows. The discretized equations, written in a linearized form are solved by iterations using a line-by-line procedure. Solution for all variables on a cross-stream section is performed before advancing the sweep (NEAT method). Cell-continuity is enforced by solving a pressure correction equation but is also preceeded by a strip-wise adjustment of overall continuity with consequent pressure changes over the remainder of the field. This overall correction has been adapted to curvilinear geometry. Due to the nonlinearity and the coupling of the equations, a combination of under-relaxation and linearisation of source terms is necessary to ensure convergence of the overall procedure. Convergence is controlled through residual sources calculation and evolution of variables at preselected modes.

EXPERIMENTAL AND NUMERICAL RESULTS

The pressure and velocity fields have been measured between the 4th and the 5th crests to avoid the entry effect and exit effect.

Numerical calculations have been carried from the entry section down to the 4th crest, undulation after undulation. The entry conditions at the inlet of the first undulation have been obtained from the steady solution in a straight pipe. The inflow conditions in the calculation domain correspond to the values obtained at the exit of the previous undulation. The outflow conditions imposed at a crest

location, where no recirculation happen, assume that the second derivative of each function falls locally to zero. This means the continuity of the variations of the flow quantities.

Pressure field

The evolution of radial distribution of pressure is presented in fig. 5. We find that the maximum of pressure occurs near the wall at the section 3 and the minimum at the crest. This is in accordance with the presence of decelerated and accelerated flow respectively. The pressure gradient vanishes near section 2 (fig.1). The localisation of the inflexion point of the wavy wall is midway between sections 1 and 2 (fig. 1). The evolution of the pressure for Reynolds number 30 000 is delayed compared to the curvature variations of the wall. This point will be discussed later.

Mean velocity field

Fig. 6 and 7 gives the experimental and numerical profiles for the different sections. We note that, due to the presence of undulations, a zone of dynamic equilibrium does not exist as it would be the case for the turbulent flow in a straight pipe. However some discrepancies appears between experimental and numerical values, though the shape of the different profiles at the respective sections is qualitatively the same. Of course, we have verified that the calculated mean velocity profile using the k-ε model in a straight pipe is in good agreement with the universel log. law. Thus, the previous discrepancies come from the complex character of the flow due to curvature effects. We remark also that the use of a calculation grid in expansion from wall to axis diminishes the precision of results near the center of the pipe, but our computer limitations precluded much finer resolution

Reverse flow region and wall shear stress

The existence of an unstationary reverse flow region close to the wall after every crest has been found from measurements with the special probe described previously. It appears that this region diminishes when the Reynolds number increases (fig. 2) Visualizations (fig. 4) in water have confirmed the occurrence of this unsteady reverse flow at Reynolds number of 30 000. We can also observe that the calculated streamlines pattern (fig. 8) at $\tilde{R}_H$ = 30 000 show a bulby deviation of the flow from the wall after every crest, but at $\tilde{R}_H$ = 115 000 the flow direction is closely following the shape of the boundary.

Consequently, the above qualitative observations must be quantitatively described by the evolution of the wall shear stress. Fig. 9 gives the values of the wall shear stress obtained from the slope of the mean velocity profiles in the viscous sublayer. As it can be seen, the Reynolds number influence on these values is taken into account by numerical calculations. The underlying physical mechanisms remain not clearly explained to-day. The increase of turbulent transfers with Reynolds number is a possible explanation of the vanishing of reverse flow at the higher Reynolds number. Consequently the radial pressure gradient at the wall (fig. 5) for $\tilde{R}_H$ = 115 000 is almost only determined by the wall curvature.

Turbulent field

The turbulent kinetic energy (fig. 10) is always higher than in a straight pipe. The experimental determination of normal stresses has shown that the high values of k were mainly due to an increase of $\overline{u'^2}$ component compared to the straight pipe result /1/ and attributed to the effect of undulations.

Numerical results in figure 10 suggest that a peak of energy begins to grow near the wall in the zone of reverse flow and is progessively absorbed by neighbouring regions.

The evolution of the stress is presented in figure 11. The most important difference between experimental and numerical results appears on these terms. In particular the negative values have been calculated near the crest section. It seems that this is a consequence of relatively high values of the term $\frac{\partial \bar{v}}{\partial x}$ which appears in the expression of the Reynolds stress tensor (if $i \neq j$: $\overline{u'_i u'_j} = \left(\frac{\partial \bar{u}i}{\partial x_j} + \frac{\partial \bar{u}j}{\partial x_i}\right)$, in a cartesian system) using turbulent eddy viscosity concept. This point seem to be a limitation to the applicability of the k-ε model to predict a flow with curvature effect.

CONCLUSION

Results presented in the above sections have shown that the flow in a wavy pipe presents many basic differences compared to classical turbulent pipe flow. In addition to the curvature effects, the existence of an unsteady reverse flow region, which is depending on Reynolds number, affect pressure and velocity fields along an undulation, thus adding new complexities. Comparisons between experimental results and numerical predictions have shown that a qualitative agreement is obtained in the description of mean flow. This agreement is rather better at the higher Reynolds number. However, several discrepancies remain attributed to a basic limitation of the simple k-ε closure applied in such a complex flow. In order to take into account curvature effects on turbulence it seems suitable to refine the model by including correction factors in the way proposed by P. Bradshaw /11/. In the long, Reynolds stress closures may probably be useful in such a case, but if they are potentially more general their precise formulation demands a more complete knowledge of turbulent interaction mechanisms in presence of curvature.

REFERENCES

1 : J. LAUFER, the structure of turbulence in fully developed pipe flow, National advisory commitee for aeronautics, report N° 1174, 1954.

2 : S.T. HSU and J.F. KENNEDY, Turbulent flow in wavy pipes. JFM, Vol 47, Pt 3, 1971 pp 481-502.

3 : N.C.G. MARKATOS, Heat, mass and momentum transfer accross a wavy boundary. Computer Meth. in Appl. Mech. and Engng. Vol 14, 1978 pp 323-376.

4 : P.R. GENT and P.A. TAYLOR, A numerical model of the air flow above water waves, JFM Vol 77, pt 1, 1976, pp 105-128.

5 : J.S. LEE and Y.C. FUNG, Flow in locally constricted tubes at low Reynolds numbers. J. of Appl. Mech., Vol 37, Ser E, 1970, pp 9-16.

6 : W.L. OBERKAMPF and S.C. GOH, Numerical solutions of incompressible viscous flow in irregular tubes. Proc. of the Int. Conf. on Computational Methods in non linear mechanics, Austin, Sept 1974, pp 569-579.

7 : W.P. JONES and B.E. LAUNDER, the calculation of low Reynolds number phenomena with a two equation model of turbulence. Int. J. Heat Mass Transfer Vol 16, p 1119, 1973.

8 : M.P. CHAUVE, determination des contraintes de frottement à la paroi par anémométrie fil chaud, colloque Euromech 132, Lyon, 2-4 July 1980.

9 : R. SCHIESTEL, méthode numérique destinée au calcul des écoulements turbulents sur paroi ondulée, Note Interne IMST, March 1980. CEA/IMST Contract SA 8323, 1979.

10 : W.M. PUN and D.B. SPALDING, A general computer program for two dimensional elliptic flows. Imperial college of Science and Technology, HTS Report 76/2, August 1977.

11 : P. BRADSHAW, Effects of streamline curvature on turbulent flow. Agard N° 169, 1973.

ACKNOWLEDGMENTS

For the experimental part of the investigations the authors want to express their thanks to Mr. M. ASTIER for his technical cooperation and to Mr. A. MORAND for instantaneous pictures.

FIGURES

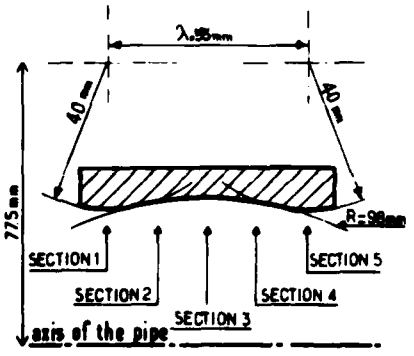

Fig:1 Shape of a Wave.

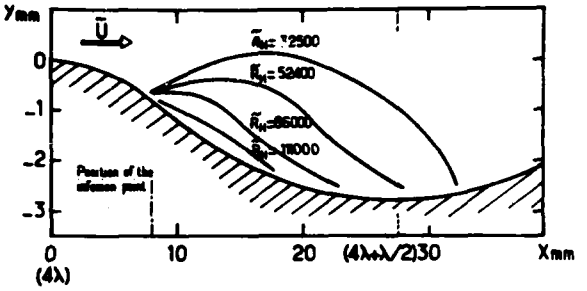

Fig:2 Regions of unsteady reverse flow

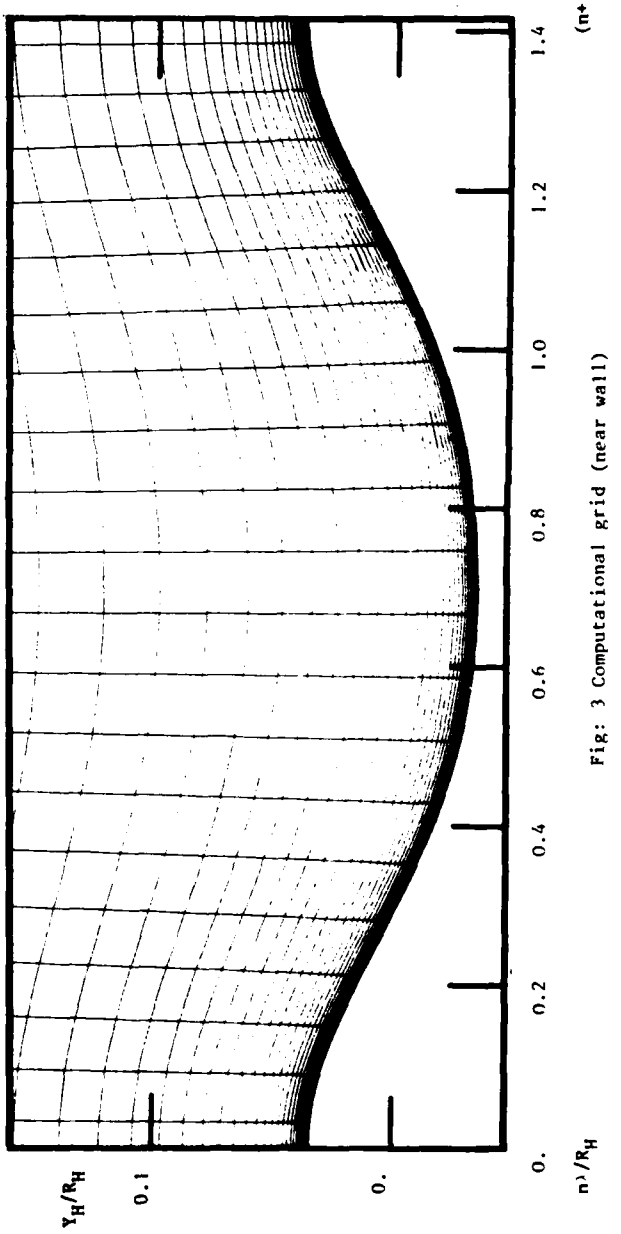

Fig: 3 Computational grid (near wall)

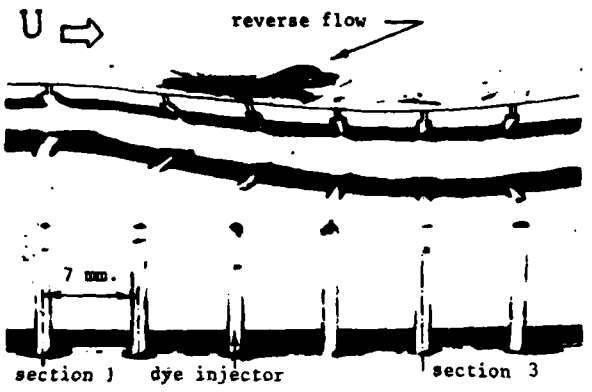

Fig: 4 Instantaneous picture of reverse flow.

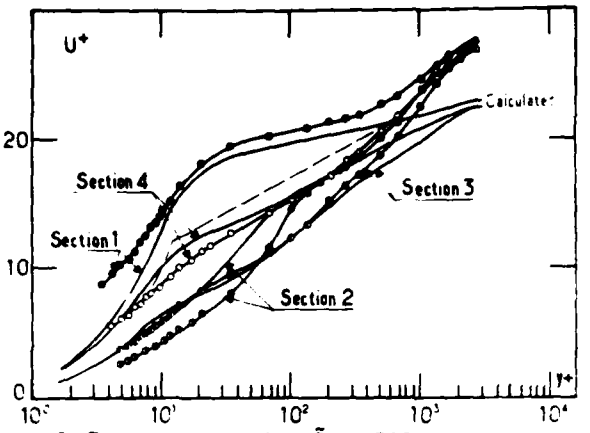

Fig 7 Mean velocity profiles, $\bar{R}_H = 115000$, Universal profile

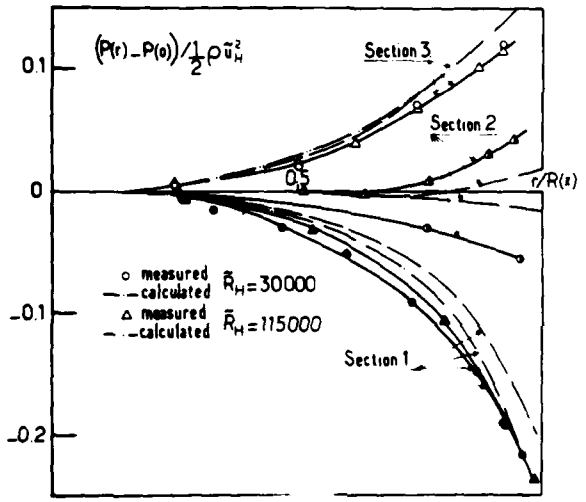

Frg 5 Radial distribution of Pressure

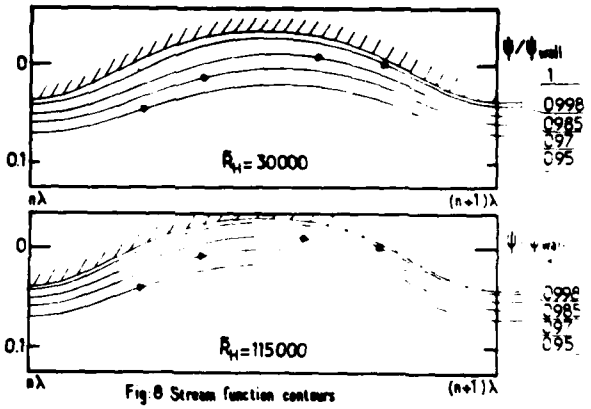

Fig 8 Stream function contours

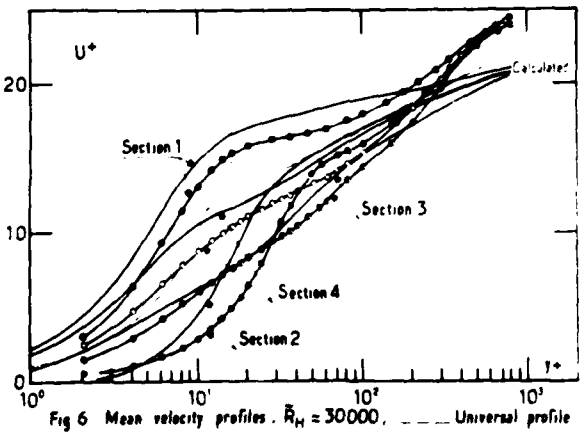

Fig 6 Mean velocity profiles, $\bar{R}_H = 30000$, ____ Universal profile

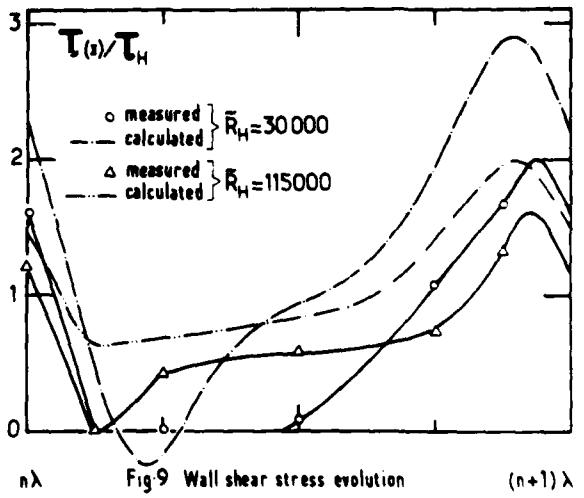

Fig 9 Wall shear stress evolution

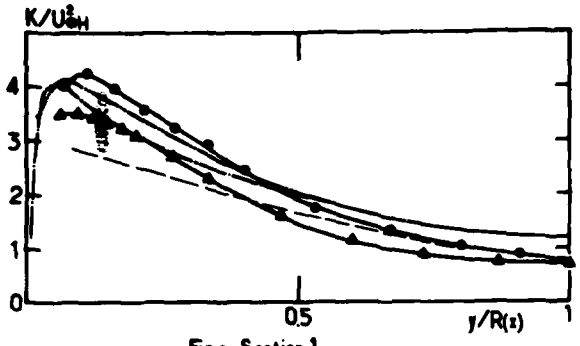

Fig.a: Section 1

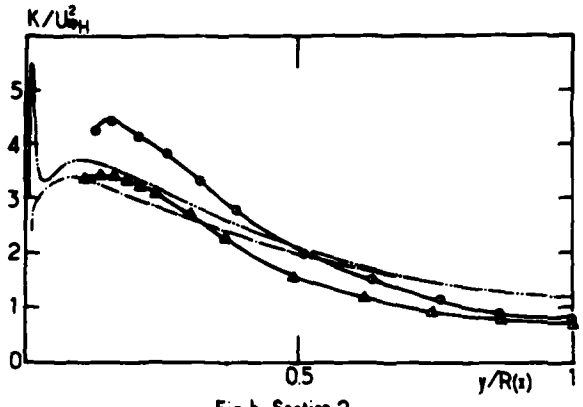

Fig.b: Section 2

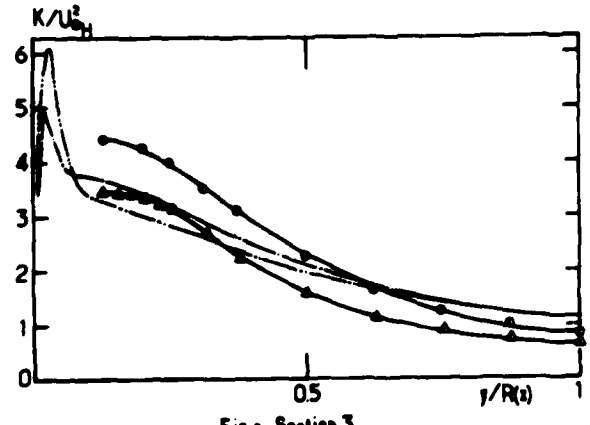

Fig.c: Section 3

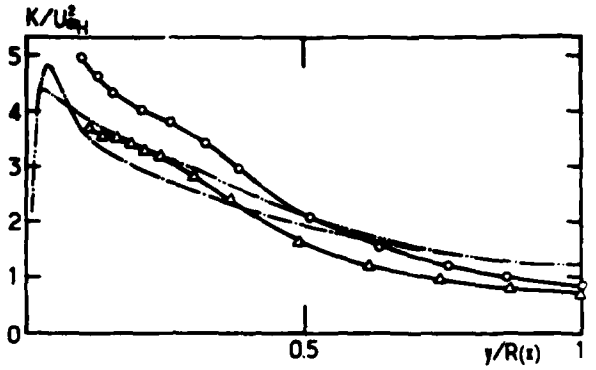

Fig.d: Section 4

Fig: 10 Turbulent kinetic energy profiles
measured $\{^{\circ}\tilde{R}_H=30000$ $_{\Delta}\tilde{R}_H=115000$ calculated $\{\tilde{R}_H=30000$ ——
$\tilde{R}_H=115000$ —·—
Laufer ($\tilde{R}_H=41000$)— — —

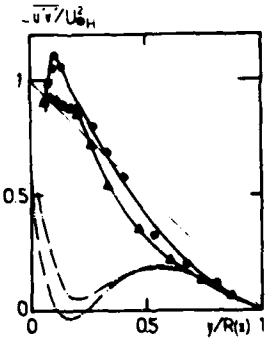

Fig.a Section 1

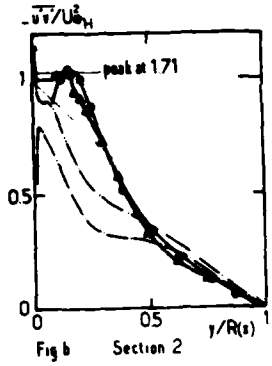

Fig.b Section 2

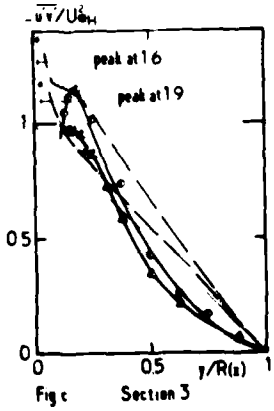

Fig.c Section 3

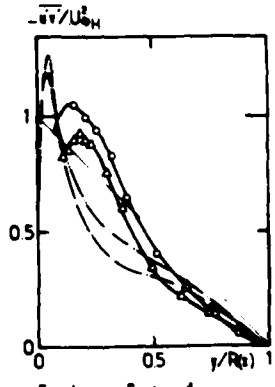

Fig.d Section 4

Fig: 11 Reynolds shear stress profiles
measured $\{^{\circ}\tilde{R}_H=30000$ $_{\Delta}\tilde{R}_H=115000$ calculated $\{\tilde{R}_H=30000$ ——
$\tilde{R}_H=115000$ —·—

SESSION 6 - JETS AND WAKES

V. W. Goldschmidt - Chairman

A COMPLEX TURBULENT WAKE

G. Fabris†
Illinois Institute of Technology
Chicago, Illinois

ABSTRACT

Attention is focused on a complex turbulent flow formed by merging of two two-dimensional far turbulent wakes. Slight heating of only one of the original single wakes provided the temperature trace for a conditional sampling investigation of the interaction process. A special four wire probe and signal processings enabled measurements of extensive number of correlations of predictive and physical interest. Among significant findings are: increased mixing and spread of heat (temperature), enhanced lateral movement of large eddies despite decreasing turbulence intensity in the merging region, increased corrugation of the thermal interface, increased conditional turbulence intensity when eddies originating from the single wake cross the adjacent wake.

INTRODUCTION

Methods of predicting turbulent flows have made remarkable progress during the last decade thanks to the efforts of a number of scientists and advances in available computational power. Additional closure equations have been conceived requiring more detailed information or modeling of third order correlations. The most attention is still focused on about a dozen so called basic turbulent flows. The reason for this interest perhaps being that almost all of the basic flows exhibit features unique enough to frustrate efforts to devise a prediction method of acceptable universality at this time. However most flows of engineering interest are "complex" turbulent flows (1) representing interactions of two or more "basic" turbulent flows. It is safe to assume that complex turbulent flows are likely to possess some "new peculiarities." Accordingly, by redirecting some of the fundamental experimental and predictive research to complex flows gains will be made in the knowledge of turbulence.

The present study represents such an attempt. The complex wake was formed by merging the far fields of two equal cylinder wakes. One cylinder was slightly heated so that the temperature could be used as a tracer and in conjunction with the conditional sampling technique provide detailed insight into the intriguing merging process. Since the single (basic) wake was studied in parallel (2) "reference" was available to judge interacting influence of the second wake. Probe and method developed by Fabris (3), capable of providing accurate instantaneous u, v, w,θ, and at a point, was essential to the quality and completeness of data obtained in this study.

It is encouraging to notice that some predictors have recently made serious attempts (4,5) to use available conditional sampling data in theoretical analysis. These new methods use the intermittency function as one of the variables.

This paper covers conditional mean flow characteristics and second order correlation at downstream station X/D = 400. Interested readers can find data on the third order correlations, statistics of turbulence, including time derivatives at X/D = 200 and 400 in References 6 and 7. Information in the vicinity of the instantaneous thermal interface is also computed.

ESTABLISHMENT OF THE COMPLEX WAKE

Mutual lateral spacing of two cylinders of $\Delta y/D = 8$ was chosen so that the two single "basic" wakes were formed undistorted. This spacing should produce no noticeable coupling of the vortex shedding phenomena (8), (9), (10), (11). The aim was to study merger of their farfields. Downstream development of the velocity defect of the complex wake shown on Figure 1 indicates no interaction at X/D = 25. At that location, von Karman vortex streets have already practically disintegrated (12). At X/D = 50, the defect at the centerline (of the interaction region) is only eight percent of the local maximum defect indicating weak interaction of zones of low turbulent intermittency. At X/D = 100 the centerline defect increases to 35 percent but the region of interaction is still quite narrow. At X/D = 200 the centerline defect grows to 80 percent of the maxima and the interacting region widens considerably. At Z/D = 400 the overall complex wake defect profile begins to resemble the defect of a single wake. There is a rather wide region of weak shear $\partial\bar{U}/\partial Y$ in the merging region of intriguing portent to the turbulence structure and production.

X/D = 200 and 400 locations were chosen for a detailed conditional sampling study of the turbulent structure of the complex wake. However due to limited space only information at X/D = 400 will be presented here.

Figure 1 suggests that at two locations chosen there is a rather rapid transition from two single equilibrium wakes to a complex "transient" wake on a course of further transfiguration to a new wider single self-preserving wake. With this in mind, we shall embark into presenting a few conditional insights into the merging process. (Normalizing factors are: U_R = 6.46 m/s, Θ_R = 0.4227C and D = 6.2484 mm).

† Present Address: Combustion Dynamics and Propulsion Technology Division Science Applications, Inc. Canoga Park, CA 91303

ON CONDITIONAL DISCRIMINATION CRITERIA

A number of criteria has been proposed to distinguish between potential and turbulent fluid on instantaneous basis. Originally different combinations of time derivatives of the streamwise velocity were used (13). There is no guarranty that this kind of discrimination truly detects the correct location of turbulent/potential interface. Comparing traces of generated intermittency function and the velocity provides some subjective judgment. Any passive scalar, such as low level incremental temperature, in air is diffused two orders of magnitude faster in turbulent than in potential flow where diffusion is by conduction only. Accordingly it seems apparent that for flow with at least some positive production of turbulence where potential flow is entrained by turbulent flow the thermal interface will coincide with potential/turbulent interface. There were several publications recently concerning discrimination based on temperature and velocity criteria. Generally it was found that some increased temperature fluid extends into zones called "potential" based on velocity discrimination. The question is: which criteria to trust? Of course, the definition of turbulent fluid is that it possesses vorticity. One would have to compare the three-dimensional instantaneous velocity vector (practically impossible to measure) with the temperature signal. Even if that could be done, the vorticity vector would show short regions of zero vorticity within "the fully turbulent" flow (internal intermittency). Based up on this argument, it seems to the author reasonable to accept that the temperature front coincides to an acceptable degree with the turbulent/potential interface. It appears the most natural to apply a small temperature threshold to detect the thermal front. However, difficulties have been reported (14) such as pronounced variations of computed intermittency factor and bursting rate with the level of the threshold. It was found necessary to introduce a hold time to bridge over quite short "bursts" probably caused by electronic noise and extraneous undulations in the temperature singal. Objections were raised (15) against bridging over short cold spots since a number of them may represent potential fluid rolled up within turbulent eddies. During this study the threshold level and the hold time were changed systematically. However, no appreciable effect on the intermittency factor and the bursting rate was noticed. It is believed that achieved quality of the temperature signal was the reason. Namely the signal to noise ratio was about thirty times higher than had been obtained with standard hot-wire equipment. Examination of the instantaneous temperature trace (2) revealed that within turbulent fluid there were indeed many tongs of colder fluid; however, their temperature was still comfortably above the threshold level. If the temperature went below the threshold then it "stayed" there for a time interval longer than a reasonable hold time.

INTERMITTENCY RESULTS

Since only the lower cylinder was heated, the thermal front bounded the turbulent flow at the lower side of the complex wake. At the upper side the thermal front was within fully turbulent fluid which provided the opportunity to investigate some subtle characteristics of interaction between two turbulent flows. Appropriately the intermittency function was defined as being one in heated, and zero in unheated fluid. This renders results at the lower side of the complex wake, quite similar to those in the single wake (2). In such a way we will be able to infer effects of the second turbulent wake just by comparing results at the upper and lower sides of the thermal part of the complex wake. In a few cases results in the single basic wake will be provided for better contrast.

Intermittency Factor

Figure 2 compares the intermittency factors for the single and the merging wake. Apparently on the lower side results are very similar, as was expected. At the upper side, additional turbulence enhances mixing or the entrainment into the "thermal wake" process, contributing to its more extensive upward spreading. This upward shift is especially pronounced for low intermittency factor suggesting strong lateral penetrations of crests or top portions of the heated turbulent bulges. Plot in the probability coordinates is not provided here, but Figure 2 suggests that approximate Gaussian distribution of γ is retained.

Bursting Rate

Bursting frequency on Figure 3 indicates virtually the same number of heated turbulent bulges in the merging and the single wake. However at $X/D = 400$ the peak number of heated bulges in the merging wake is about 20 percent higher. Only two to four percent of this increase can be attributed to higher convection velocity. It suggests that the turbulent to turbulent fluid entrainment is preferential in this case or occurs in such a way that not only lateral undulations of the thermal interface increase but it also becomes more corrugated.

Distribution of the Intermittent Heated and Cold Fluid

Statistical properties of heated and cold fluid intermittent time intervals were computed. "Complete cycle" intervals were also studied by noting the time elapsed between passage of the backs of two consecutive heated bulges. Figures 4 and 5 display the average durations and its standard deviations of the intermittent time intervals. General trends are as expected with the "full" intervals being the shortest approximately at $\gamma = 0.5$ location. In the interacting region the minimum is 10.5, while at the lower side it is 15.

MEAN FLOW CHARACTERISTICS

Streamwise Velocity

Conditional streamwise velocity defect is given on Figure 6. At the lower side, characteristics are similar to those of the single wake as described elsewhere (2). At the upper side, heated fluid moves significantly more slowly than average flow as compared to results at the lower side even though the lateral mean velocity gradients are the same. The answer should be looked for in faster lateral movements at the upper side (as explained next), or that the upward erupting heated fluid has to cross wider velocity defect region.

Regarding the unheated zones, tendencies are reversed. Namely, potential zones (at the lower side) moves considerably faster than the conventional average. It is easy to find the reason in this case by noticing that at $Y/D = 5$ the cold fluid is fully turbulent. "Fronts" of heated zones move faster than "backs" at both sides of the wake.

An attempt was made to check the superposition method (16,17). However, superimposing the velocity defects of two single wakes resulted in an overestimate of the defect of the merging wake especially at its centerline. It appears that the superposition method could provide acceptable approximation only in the far quasi-similar fully merged wake as proposed by its originators.

Lateral Velocity

Conditional lateral velocity are given on Figure 7. Comparison of the heated and unheated conditional zone velocities at the upper side with those in the single wake (2) leads to the striking realization that the interaction of two wakes caused the lateral movements to be two to three times faster. It appears that counter rotating eddies of two merging wakes enhance each others lateral motion (most of it being in the region of negligible $\partial\overline{U}/\partial y$ and diminished production of turbulent energy). This is contrary to the hypothesis (16) that turbulent bulges from the two separate wakes "collide" and bring the lateral velocity to zero. Figure 8 illustrates the mechanism of enhanced mixing. It had been observed (18) that a heated interface in a uniform turbulent flow spread faster than if the unheated co-flowing region were potential. Here the large-scale motion adds still another factor.

Experimental and predictive analysis of mixing multiple jets in a duct (19) indicated the interesting and puzzling phenomenon of increased decay rate of jets in the overlapping region. It was necessary to increase the eddy viscousity in order to get a good prediction in the overlapping region. It is believed that Figure 7, i.e. enhanced lateral movements, reveals the underlying physics behind it.

FLUCTUATING VELOCITIES - MEAN SQUARES

The Streamwise Fluctuations

The conditional squared streamwise velocity fluctuations are given on Figure 8. The conventional profile has a deep trough in the center, and its maxima are somewhat lower than for the single wake (2) and, again correspond to the region of maximum mean strain rate (see Figure 6). It is most significant that the conventional $\overline{u^2}$ distribution is symmetrical to the accuracy of the measurements. Thus, the differential heating indeed had negligible effect on the dynamics turbulence field. In addition, the measurement technique had fully eliminated cross-contamination of signals. The cold-zone average peaks at almost the same level as the conventional average. However, it exceeds the conventional average just where the cold-zone defect $\overline{U}_d$ had shifted inward with respect to the conventional $\overline{U}_d$ average on Figure 6. Figure 6 discloses how the heat zone defect curve is displaced outwards: the warm lumps have been slowed down (streamwise) in penetrating the cold upper wake. It is curious to see how the fluctuations in the heated lumps follow this outward shift of their mean defect: this conditional average is significantly higher (even when γ-average is used) and is shifted outward. The unheated-zone averages on the lower side of the double wake display no such behavior because the "cold lumps" migrating from the upper cold wake do not remain "fully cold," i.e. below the threshold. Thus despite the presence of these slow "ex-cold lumps," the statistics of the lower part of the double wake follow essentially the behavior of those in the single wake.

The Lateral Fluctuations

Figure 9 displays the variation of conditional $\overline{v^2}$ that is again symmetrical. The most interesting feature in the interacting region are high R-averages in the cold fluid penetrating close to the centerplane and in the warm fluid at the upper edge of the wake. The cold $\overline{v^2}$ averages thus differ from the $\overline{u^2}$ averages near the centerplane. The outward shift of the maxima of the fluctuations in the warm lumps follows the shift of the corresponding averages of $\overline{U}_d$ and $\overline{u^2}$.

The Spanwise Fluctuations

Figure 10 shows that the unheated turbulent fluid interestigly maintains an almost constant intensity of spanwise fluctuations. This would indicate that large countrarotating interacting eddies are primarily two-dimensional, enhancing each other's lateral movement but not the spanwise movement. The heated bulges again exhibit a high level of fluctuation at the wake's periphery. However, the warm peaks are displaced outward less than for the $\overline{u^2}$ and $\overline{v^2}$ cases, a behavior which would be consistent with an increased degree of two-dimensionality of the thermal front interface. Namely, detailed information on basic two-dimensional turbulent flows (instantaneous w trace (2), or smoke visualized mushroom-like formations (20) suggests (21) the existance of eddies possessing strong streamwise vorticity out of phase (direction) with the mean flow vorticity vector. Figure 10 seems to suggest that these eddies of high $\overline{w^2}$ have diminished lateral penetration ability once they encounter another turbulent fluid.

$\overline{uv}$ CORRELATION

This is the most important second-order correlation called they Reynolds shear stress. Multiplied by ρ it represents the turbulent shear stress in the momentum equation. Its product with the mean shear $\partial\overline{U}/\partial y$ is the rate of production of turbulent kinetic energy (that is fed solely to $\overline{u^2}$ fluctuations). Its own production rate is $-\overline{v^2}\,\partial\overline{U}/\partial y$.

The conditional Reynold stresses are given in Figure 11. The conventional average exhibits a wide region of small values near the wake center. The stress changes sign three times times as if it were following the mean velocity graident even in this region of interaction between opposite vorticities and stresses of the component wakes. In the upper part of the wake, the Reynolds stress of the cold zones follows the conventional average but remains more negative as the wake center is approached. This bifurcation apparently reflects the bifurcation of the corresponding defect curve (and their slopes) in Figure 6. The higher peaks in the heated bulges and their outward shift resemble that in the $\overline{u^2}$ case and was previously discussed. Because the "production" depends on the product of $\overline{v^2}$ and $\partial\overline{U}/\partial y$, the outward shift of these two characteristics for the heated zones in Figure 9 and 6 is relevant.

Correlation $\overline{U}_d\overline{V}$ shown on Figure 12 represents rates of lateral transport of the momentum defect. It is clear that in the upper part of flow the heated and unheated bulges transfer much more momentum defect on a conditional basis than on the lower side (which resembles the single wake).

ACKNOWLEDGMENTS

This research was supported by USAFOSR Grant AFOSR-73-2509.

REFERENCES

1. Bradshaw, P. 1976, Turbulence Research Progess and Problems, Proceedings of the 1976 Heat Transfer and Fluid Mechanics Institute, Davis, California.

2. Fabris, G. 1979, Conditional Sampling Study of the Turbulent Wake of a Cylinder. J. Fluid Mech., 94, 673-709.

3. Fabris, G., 1978 A Probe and Method for Simultaneous Measurements of "true" Instantaneous Temperature and Three Velocity Components in Turbulent Flow," Rev. Sci. Instrum. 49/5, 654-664.

4. Dopazo, C. and O'Brian, E. E., 1979, Intermittency in Free Turbulent Shear Flows, in Turbulent Shear Flows I, Springer-Verlag, pp. 6-23.

5. Libby, P. A., 1976, Prediction of the Intermittent Turbulent Wake of a Heated Cylinder, Phys. Fluids, 19/4, pp. 494-501.

6. Fabris, G., 1974, Conditionally Sampled Turbulent Thermal and Velocity Fields in the Wake of a Warm Cylinder and its Interaction with an Equal Cool Wake: Ph.D. dissertation, Illinois Institute of Technology.

7. Fabris, G., 1974, Tables of Conditionally Sampled Data on the Turbulent Wake of a Cylinder and a Merging Wake of Two Cylinders, Illinoise Institute of Technology (714 pages).

8. Spivack, H. M., 1946, Vortex Frequency and Flow Pattern in the Wake of Two Parallel Cylinders at Varied Spacing Normal to an Air Stream, J. Aero. Sci., 13/6, 289-301.

9. Beguier, C., Giralt, F., Fulachier L. and Keffer J. F., 1977, Negative Production in Turbulent Shear Flow, Proceedings of the Symposium on Turbulence, Berlin.

10. Bearman, P. W. and Wadcock, A. J., 1973, The Interaction Between a Pair of Circular Cylinders Normal to a Stream. J. Fluid Mech. 61, 495-511.

11. Zdravkovic, M. M. 1977, Review of Flow Interference Between Two Circular Cylinders in Various Arrangements. Trans. ASME, J. Fluids Engng. 99, 618-633

12. Roshko, A., 1953, On the Development of Turbulent Wakes from Vertex Streets; NACA TN 2913.

13. Kovasznay, L. S. G., Kibens, V. and Blackwelder, R. F., 1970, Large Scale Motion in the Intermittent Region of a Turbulent Boundary Layer; J. Fluid Mech., 41, 2, 283.

14. La Rue, J. C., 1974, The Temperature Characteristics in the Turbulent Wake of a Heated Rod; Ph.D. dissertation, University of California at San Diego.

15. Dean, R. B., Bradshaw, P., 1976, Measurements of Interacting Turbulent Shear Layers in a Duct, J. Fluid Mech., 78/4, 641-676.

16. Bragg, G. M., and Seshagiri, B. V., 1973, Turbulence Measurements in Interacting Wakes, International J. of Heat and Mass Transfer, 16, pp. 1531-1546.

17. Beguier, C., Giralt, F. and Keffer, J. F., 1978 Turbulent Heated Flows with Asymmetric Mean Temperature Profiles, Proceedings of the Sixth International Heat Transfer Conference, Toronto, pp. 353-358.

18. Foss, J. and Corrsin, S., 1974, Molecular Diffusivity Effects in a Half Heated Grid Flow; (private communications).

19. Fabris, G. and Fejer, A. A., 1974, Confined Mixing of Multiple Jets, J. of Fluids Engineering, June, pp. 92-96.

20. Falco, R. E., 1974, Some Comments on Turbulent Boundary Layer Structure Inferred from the Movements of a Passive Contaminant. AIAA paper No. 74-99.

21. Roshko, A., 1976, Structure of Turbulent Shear Flows: A New Look, AIAA J. 14/10, pp. 1349-1357.

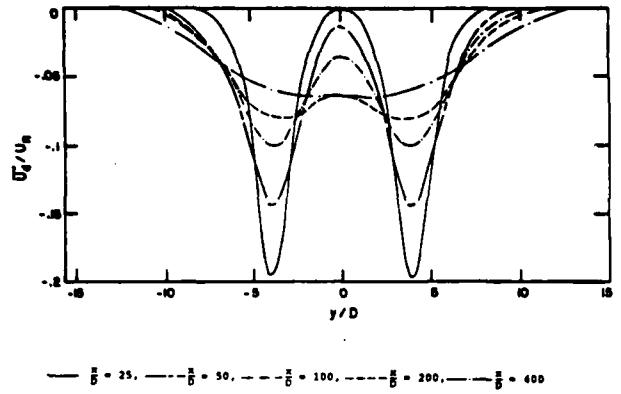

Figure 1. Mean Velocity Defect of the Complex Wake

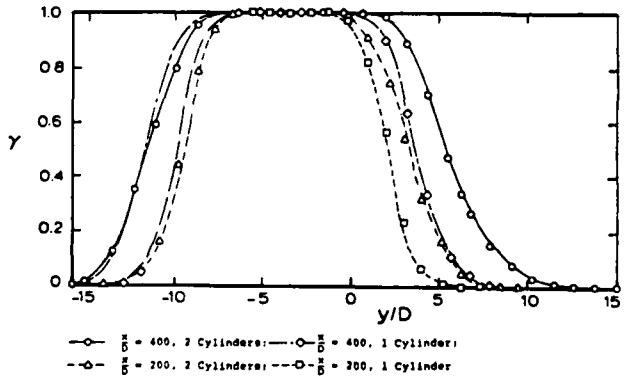

Figure 2. Intermittency Factor

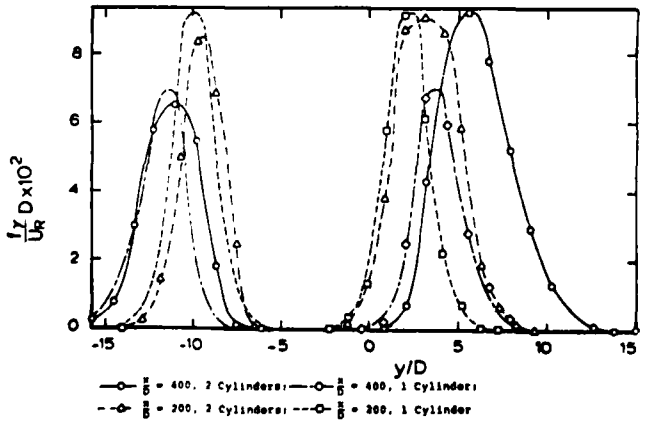

Figure 3. Bursting Rate

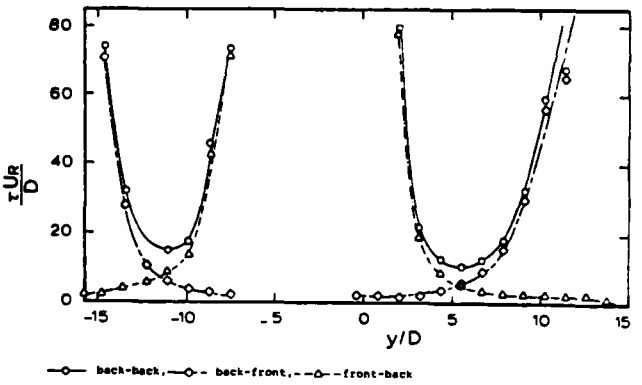

Figure 4. Durations of the Intermittency Intervals; X/D = 400

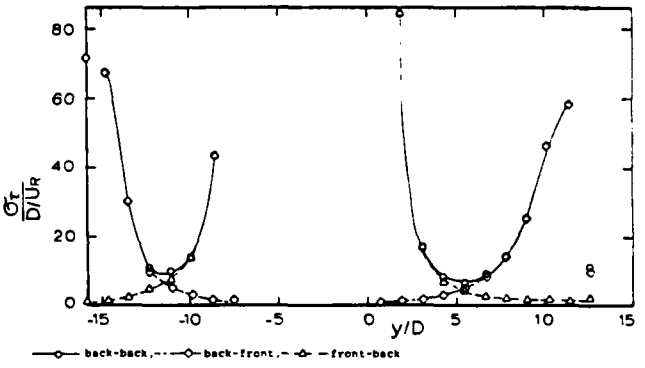

Figure 5. Standard Deviation of Intermittency Intervals; X/D = 400

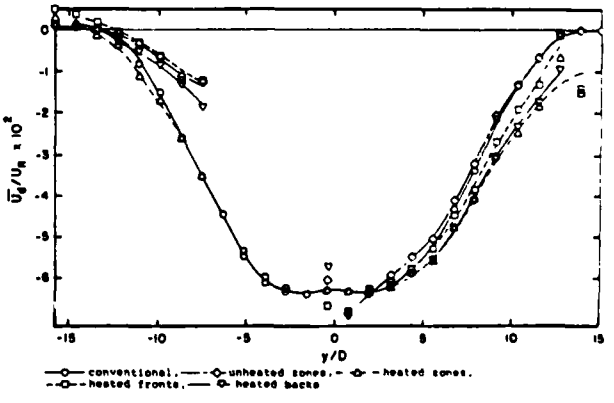

Figure 6. Conditional Streamwise Velocities; X/D = 400

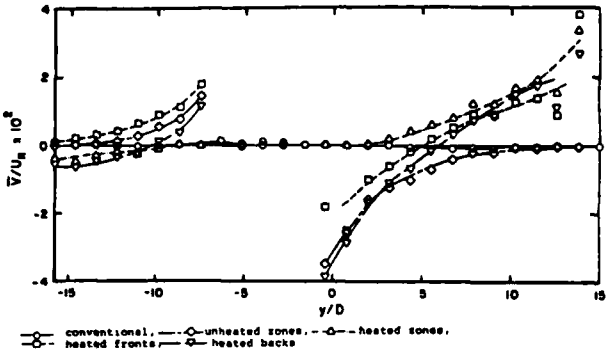

Figure 7. Conditional Lateral Velocity; X/D = 400

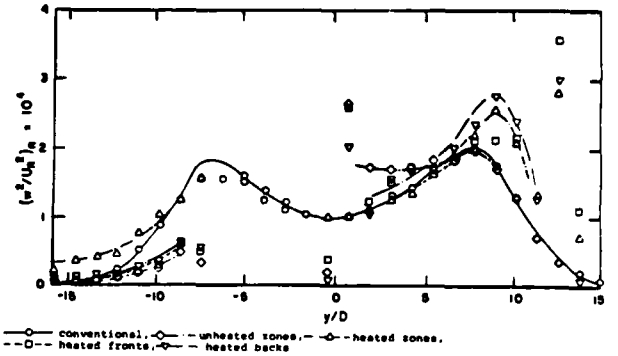

Figure 10. Conditional Spanwise Fluctuations; X/D = 400

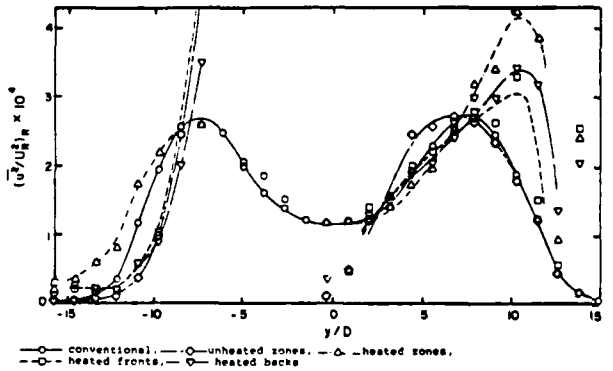

Figure 8. Conditional Streamwise Fluctuations; X/D = 400

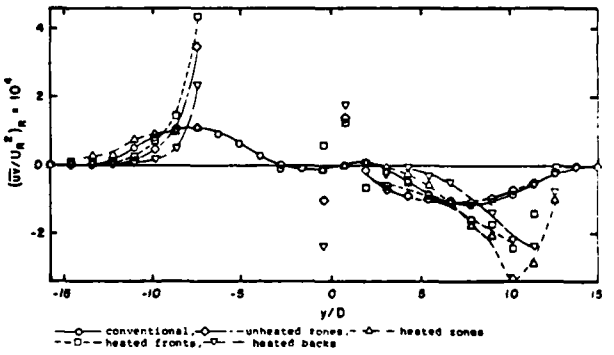

Figure 11. Reynolds Stress; X/D = 400

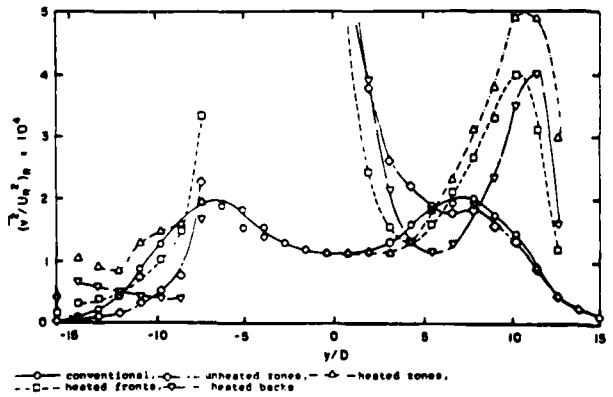

Figure 9. Conditional Lateral Fluctuations; X/D = 400

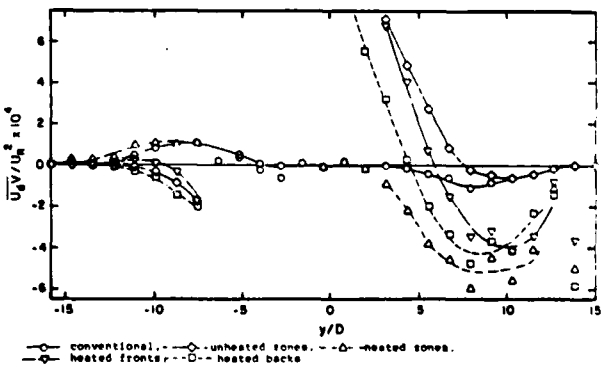

Figure 12. $\overline{U_d V}$ Correlations; X/D = 400

MEASUREMENTS IN A LOW MOMENTUM JET INTO A CROSS FLOW

by

J. Andreopoulos
Sonderforschungsbereich 80

ABSTRACT

Measurements of velocity fluctuations with a triple hot-wire probe are presented for a jet in a cross flow situation at various ratios of the jet to cross flow velocity. Profiles of the three mean-velocity components, the six normal and shear stresses and higher order moments were obtained at different spanwise positions and several down stream stations. It was found that almost all terms involved in the turbulent kinetic energy or shear stress transport equations are of significance. In the lower blowing case most of the Reynolds stresses reach their maximum value after the bending over of the jet fluid streamlines, where the entrainment of cross stream fluid is expected to be high. The presence of two bound vortices which enhance entrainment has also been found in the lower blowing case. The normal spreading rate of the jet in the near field was equal to that of a round jet in a stagnant surrounding while at the far field a gradual reduction occurs to the zero pressure gradient boundary layer. The lateral spreading rate was found to be like that of a plane shear layer and remains constant at all the investigated stations.

b_y, b_z	normal and lateral width of the jet respectively
c_f	skin friction coefficient
D	pipe diameter
E_1, E_2, E_3	hot-wire voltages
R	V_j/U_e, jet to cross-flow velocity ratio
U, V, W	instantaneous velocity components, in x, y, z direction respectively
$\overline{U}$, $\overline{V}$, $\overline{W}$	mean velocity components
u, v, w	fluctuating velocity components
x, y, z	coordinates (see fig. 1), streamwise, normal and lateral respectively
	boundary layer thickness
$\Omega_x, \Omega_y, \Omega_z$	vorticity components in x, y, z directions respectively
φ ϑ	pitch, yaw angles

Subscripts

e	cross-flow at infinity
j	jet-flow at infinity

INTRODUCTION

Numerous experimental and analytical studies of the jet in a cross flow problem are available in the literature due to the relevance which this geometry has in a variety of engineering applications. Depending on the jet-to-cross stream velocity ratio, examples of this flow can be found in turbomachinery, internal flows, aircraft aerodynamics and environmental flows such as plum dispersals and pipe discharges into rivers. Few of these studies, however, include reliable measurements of turbulence quantities throughout the flow. Exceptions to this include investigations by Crabb (4) and Crabb, Durao and Whitelaw (5) who reported data for a relatively high jet to cross flow velocity ratios (R = 2.3 and 1.15). Also some of the basic features associated with larger R values as motivated by the VTOL applications have been presented by Keffer

and Baines (7), Komotani and Greber (8) and Mousa et al (9). Ramsey and Goldstein (10) reported measurements of film cooling effectiveness in a heated jet and Bergeles et al (3) indicated the non-uniformities of the velocity profile at the exit plane of the jet (for low R), although the accuracy of their single sensor hot-wire measurements must be taken into consideration.

The objective of the current research program on the jet in a cross-flow case has to increase the understanding of the flow and to obtain reliable turbulence data throughout the flow field which could be subsequently used for testing and improving numerical calculation methods. The experimental program included a flow visualisation study with dye injection and surface streaking which have been reported on by Foss (6), and measurements inside the discharging pipe to fully document the cross stream effect on the pipe flow upstream of the exit (see Andreopoulos (1)). Here it was found that the non uniformities of the velocity and temperature profiles within the pipe extend as far as 3 pipe-diameters upstream of the exit. The extremely high gradients in x, y, z directions at the exit plane result in high rates of turbulent kinetic energy production, a great part of which is transported outwards by the mean flow of the jet fluid.

EXPERIMENTAL TECHNIQUES AND DATA REDUCTION

The measurements were made in the closed circuit wind tunnel at the Insitut für Hydromechanik, University Karlsruhe, which has a 6 m long by 1.5 m internal diameter octagonally shaped working section. A flat plate was installed at about 0.28 m from the tunnel's floor (see Fig. 1) and the pipe-jet flow was driven by a 2 stage-compressor through a plenum chamber and a heat exchanger to control the air flow temperature. The brass pipe had a 50 mm internal diameter and its exit plane was 12 diameters downstream the plenum chamber. Velocity and turbulence measurements were made with DISA anemometers and DISA miniature slant-wire, cross-wire and triple-wire probes. All signals were digitized at 5 kHz per channel and stored on mag tape for later data reduction, to give statistical averages . The data acquisition system and the statistical analysis program are fully described in (11)

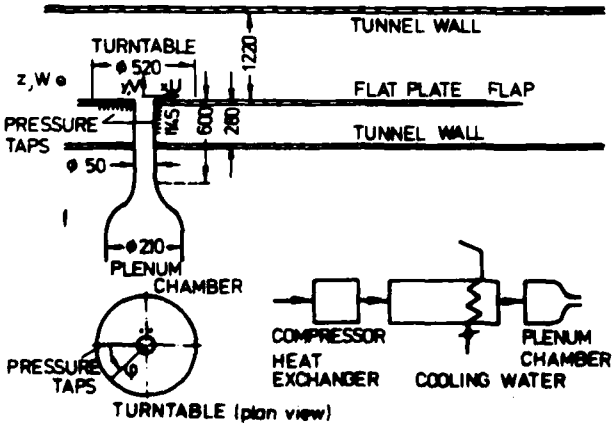

Fig. 1 Experimental arrangements

All mean turbulence quantities which are reported here, have been obtained with a triple hot wire probe DISA type 55P91. The basic feature of such a probe is that its wires are parallel to the axis of an orthogonal coordinates system, so that the tangential component of one wire is the normal for another and binormal for the third. If the instantaneous velocity has components X, Y, Z parallel to the respective axis x, y, z in probe coorinates, then the effective velocity for each wire is given by following:

$$U^2_{eff_1} = k^2(\varphi_1) X^2 + Y^2 + h^2(\vartheta_1) Z^2$$
$$U^2_{eff_2} = h^2(\vartheta_2) X^2 + k^2(\varphi_2) Y^2 + Z^2$$
$$U^2_{eff_3} = X^2 + h^2(\vartheta_3) Y^2 + k^2(\varphi_3) Z^2$$

This system of equations is linear with respect X^2, Y^2, Z^2, has three unknowns, and the instantaneous velocity components in probe coordinates can be obtained easily by the matrix inversion method. A similar technique has been described in (12) where the matrix was inverted using a flow analyser device whose analog output could then be digitized to give velocity components. The present approach is fully digital (no linearisers used) and has the novelty to allow the coefficients k and h to vary with pitch and yaw angles as it has been found in calibrations. Since the yaw and pitch angles of the instantaneous velocity vector are not known "a priori" an iterative numerical scheme has been used to solve the before mentioned system with the matrix corresponding to the true angles. The method which has been documented and tested by Andreopoulos (13) greately improved the performance of the probe.

Both interacting flow fields i.e. the pipe flow and the cross flow, were found to be developing turbulent flows for all the investigated velocity ratios ($0.25 \leq R \leq 3$). At $x/D = -4$ upstream, the jet exit on the plate, where the jet interference on the cross stream was negligible, a friction coefficient $c_f = 0.0034$ and boundary layer thickness $\delta = 0.34$ D at $U_e = 12.8$ m/s were measured. The results which are presented here cover the case with velocity ratio $R = 0.5$ and are nondimensionalized by D and U_e. The corresponding Reynolds number for the pipe flow is $Re = V_j D/\nu = 20500$ i.e. one order of magnitude higher than that in the flow visualisation studies of Foss where both flows were laminar.

RESULTS AND DISCUSSION

Sufficiently strong deflection of mean streamlines in a shear flow can lead to the creation of discrete longitudinal vortices. The "skew-induced" or pressure driven secondary flows (Prandtl's first kind) decay under the action of Reynolds stresses and their generation is basically due to an inviscid mechanism. In the present experiment "skewing" of streamlines takes place in two characteristic directions, namely normal and lateral. Deflection of the streamlines in y-direction leads to the generation of $\Omega_z = \partial\bar{V}/\partial x - \partial\bar{U}/\partial y$ vorticity which, in regions above the dividing streamlines is positive (Ω_{z+}) because $\partial\bar{V}/\partial x$ is drastically increased in the region over the exit and $\partial\bar{U}/\partial y$ is becoming small, (having therefore the same sign as the initial vorticity of the

approaching tube and negative (Ω_{z-}) below the deviding streamline). This negative vorticity can be added to the negative vorticity of the oncoming boundary layer which because of the divergence of streamlines in z-direction is intensified by the lateral positive stretching $\partial\overline{W}/\partial z$. Together these negative vorticity contributions form a "horseshoe vortex" similar to that generated by the atmospheric boundary layer in front of tall buildings. Actually, the oncoming boundary layer separates already upstream of the jet at the saddle point of the skin friction lines; there the separated shear layer rolls up forming a "horseshoe vortex" which wraps around the jet exit as found in the measurements by Andreopoulos (1) and in the flow visualisation and surface steaking patterns in (6).

The lateral deflection of the streamlines is shown in Fig. 2 where the mean $\overline{W}$ velocity is plotted as a function of y/D at z/D = -0.5 for various downstream positions x/D. Mean $\overline{W}$ is zero at z/D = 0 i.e. the plane

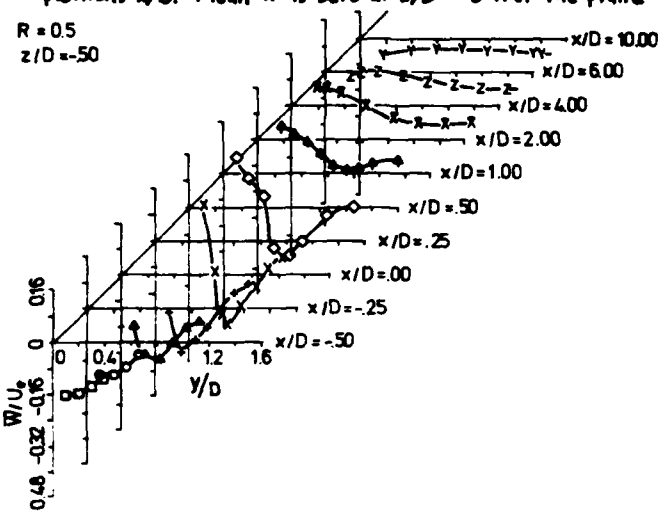

Fig. 2 $\overline{W}$-velocity profiles at z/D = -0.5 as a function of y/D

of symmetry. It is clear that at the two upstream stations x/D = -0.5 and -0.25, $\overline{W}$ can reach values as high as -0.16 U_e at which point $\overline{U}$ takes values of approx. 0.5 U_e (not shown here). The resulting lateral rate of strain is therefore roughly 0.32 U_e/D.

Divergence of streamlines in the z-direction in addition to stretching of Ω_z vorticity can generate also longitudinal or normal vorticity, with opposite sign than the "horseshoe vortex", which with the reoriented and stretched initial vorticity of the approaching flow in the pipe form the "bound vortices". The normal "skew induced" vorticity Ω_y is responsible for the vortex shedding which is present in the high velocity ratio cases (R > 1). However, vortex shedding, strickly speaking shedding of Ω_y vorticity, is quite unlikely to take place in low R cases, at least in the usual sense of regular periodic phenomenon. There was at least no strong evidence in the present investigation to contradict this hypothesis. Strong evidence exists, however, to confirm the existence of the pair of "bound vortices", even in the low velocity ratio case R = 0.5. Two results verify this: first, the change of sign of $\overline{W}$ velocity at

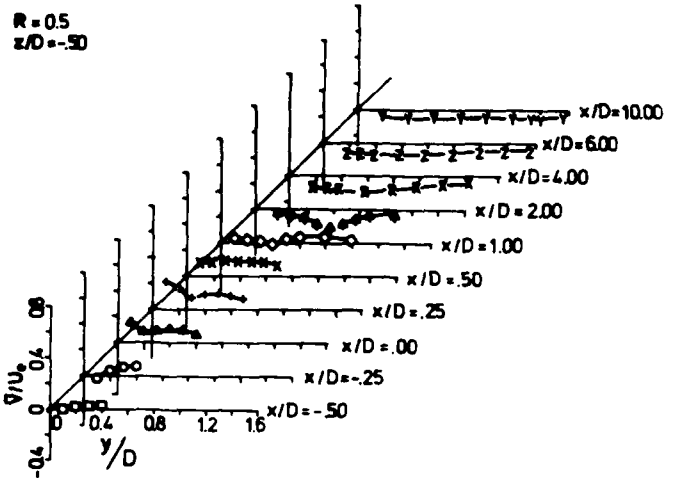

Fig. 3 $\overline{V}$-velocity profiles at z/D = -0.50

x/D = 1, 2 and 4 in Fig. 2 indicating a rather strong contribution of negative $\partial\overline{W}/\partial y$ to Ω_x and second the lateral reduction of mean $\overline{V}$ velocity i.e. $\partial\overline{V}/\partial z > 0$ (see Fig. 3 and 4). Both increase the absolute value of $\Omega_x = \partial\overline{W}/\partial y - \partial\overline{V}/\partial z$. This vortical field of both vorticity components induces a positive $\overline{V}$ velocity in the "common flow" region i.e. in the region between the vortices where the flow is directed outward from the surface, and a negative $\overline{V}$ everywhere else.

But there is another combined effect which has to be taken into account in trying to explain the behaviour of the mean velocity profiles, namely the downwash effect of the streamlines, particularly evident in the outer region. This is due to the low pressure behind the jet. In the "common flow" region these effects are opposing each other and the present results suggest that the low back pressure effect is dominating (see Figs. 3 and 4) except probably

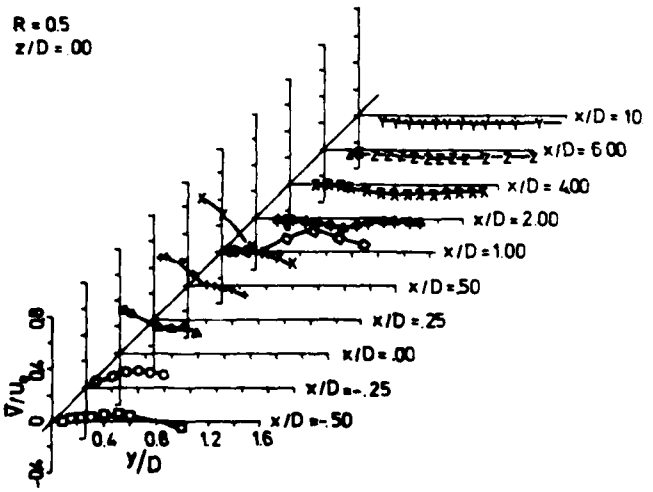

Fig. 4 $\overline{V}$-velocity profiles at z/D = 0.0

very close to the vortex cores, for example at x/D = 1 in Fig. 4. Here the induced $\overline{V}$ velocity is higher - particularly on the plane of symmetry z = 0. In addition Ω_x vorticity is intensified by longitudinal stretching $\partial U/\partial x$ (accelarating flow) in this region.

Fig. 5 shows the $\overline{U}$ velocity profiles at z/D = 0. The approaching boundary layer flow is decelerating i.e. $\partial\overline{U}/\partial x$ is negative while $\overline{V}$ is increased considerably (Fig. 4). In addition it was found in (1) that the mean velocity profiles at the exit plane of the pipe were highly distorted by the presence of the cross flow: at the leading edge of the exit ($x \approx -D/2$) $\overline{V}$ velocity is smaller than V_j i.e. the jet flow in that part of the tube is decelerated under the influence of an adverse pressure gradient which has been imposed by the cross stream, while at the trailing edge the flow is accelerated and $\overline{V}$ is 50 % greater than V_j. The $\overline{U}$, $\overline{V}$ profiles over the exit from x/D = -0.5 to x/D = 0.5 show similar behaviour i.e. $\overline{V}$ increases with x while $\overline{U}$ decreases. Since the jet-streamline curveture commences inside the tube, the jet fluid in the immediate region of the hole acts like a "cover" over the jet exit. The cross stream then is lifted up as the $\overline{V}$ profiles show and flows over and around the "cover" at least in the sense of the mean flow velocities.

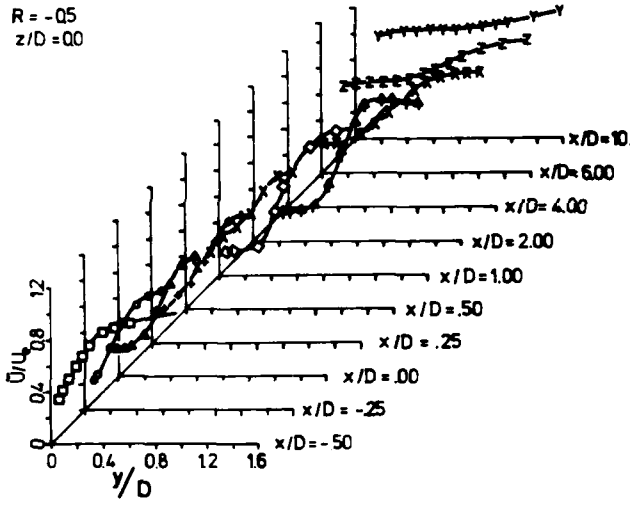

Fig. 5 $\overline{U}$-velocity profiles at z/D = 0.0 as a function of y/D

The profiles downstream of the jet-exit postulate clearly a "wake" like region and/or a "mixing layer" like region with more or less monotonic variation of $\overline{U}$ with y except probably at $x/D \leq 2$ where $\overline{U}$ overshoots its free stream value before it reduces to U_e. In the "wake" like region the longitudinal acceleration is important and the conservation of mass requires fluid from the sides to rush inwards towards the plane of symmetry. The present measurements show clearly that both gradients $\partial\overline{V}/\partial y$ and $\partial\overline{W}/\partial z$ are negative. In fact, checks on the conservation of mass are fairly easy to do because 3-Dimensional velocity profiles exist, and within the limits of graphical differentiation the results are satisfactory.

It is generally agreed upon that a normal yet separates from the exit surface and there always exists a region downstream of the exit where flow reversal takes place. It is not a "close" recirculating flow region because of the high entrainment rates from the cross flow on the sides. This moderates significantly the reverse flow action and the actual reverse flow region is considerably restricted. The surface streaking patterns given by Foss (6) which are time integrated pictures of the flow give a good indication of the extension of that zone. However, occacional flow reversal can happen also at different heights from the wall. A tuft study has been undertaken to investigate the regions in which instantaneous flow reversal may occur. Observations show that within the region 2 diameters downstream 0.4 diameter spanwise from the jet and up to $y \approx 0.1$ D above the floor, instantaneous flow reversal can occur (the probability decreases with y). These results were used to select the measuring points at which to operate the hot wire probe. For lower velocity ratios another separation region was found to exist inside the tube near the leading edge where the adverse pressure gradient is high (see (1)).

Figure 6 shows the turbulent kinetic energy profiles on the plane of symmetry. There are three distinct regions which can be observed in the profiles: the near region over the jet exit where the boundary layer is subjected to high rate of strain $\partial\overline{V}/\partial x$ due to streamlike curveture, resulting in an overshoot of $\overline{q}^2$; the immediate downstream region where high $\overline{q}^2$ is produced; and the far downstream region where $\overline{q}^2$ starts to decay and velocity gradients are smaller. In the first region, where the interaction between the two vortical fields begins to take place, turbulent mixing of the two flows is important even though the mean field picture indicates that the jet fluid acts like a "cover" over the jet. The fluid there is also subjected to lateral divergence leading to an extra component of mean rate of strain $\partial\overline{W}/\partial z$ (> 0) although $\overline{W} = 0$, at z = 0, in addition to $\partial\overline{V}/\partial x$. A positive value of $\partial\overline{W}/\partial z$

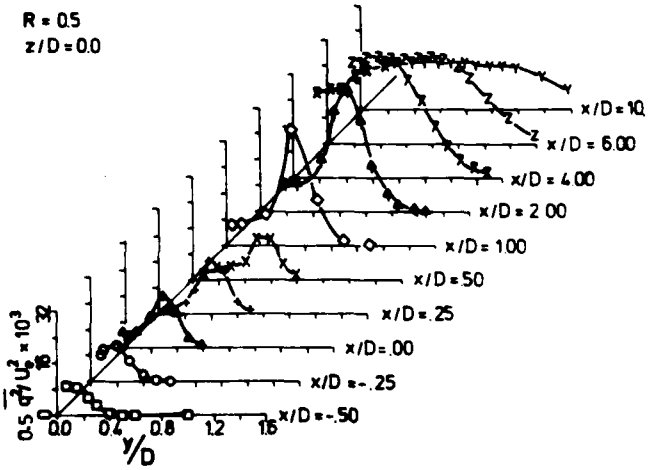

Fig. 6 Turbulent kinetic energy profiles at z/D = 0.0

implies immediately "negative" production of turbulent kinetic energy because of the term $\overline{w^2}\,\partial\overline{W}/\partial z$ in the turbulent kinetic energy transport equation. Furthermore $\partial\overline{W}/\partial z$ must be balanced by negative values of $\partial\overline{U}/\partial x + \partial\overline{V}/\partial y$. In that specific region $\partial\overline{V}/\partial y$ seems to be fairly small but negative and only the longitudinal deceleration

$\partial\bar{U}/\partial x$ balances the lateral divergence which can lead to increased entrainment and mixing. Smits et al (14) found indeed high entrainment velocities in boundary layer with strong lateral divergence, almost three times higher than that of a typical boundary layer with same Re. Most the streamline curveture on the x, y plane takes place from the beginning of the interaction up to $x/D \approx 1$ where $\partial\bar{V}/\partial x$ is becoming negligible. At that point $\overline{q^2}$ starts to increase rapidly and around $x/D \approx 2$ or shortly after reaches its maximum value at the "wake" like region where the flow is accelerating ($\partial\bar{U}/\partial x > 0$). This reduces the energy production, but due to streamlines convergence overall production is strong since both $\partial\bar{W}/\partial z$ and $\partial V/\partial y$ are negative. The last two rates of strain terms together with the positive $\partial\bar{U}/\partial y$ are mainly responsible for the high levels of turbulent kinetic energy which are evident at $x/D \cong 1$.

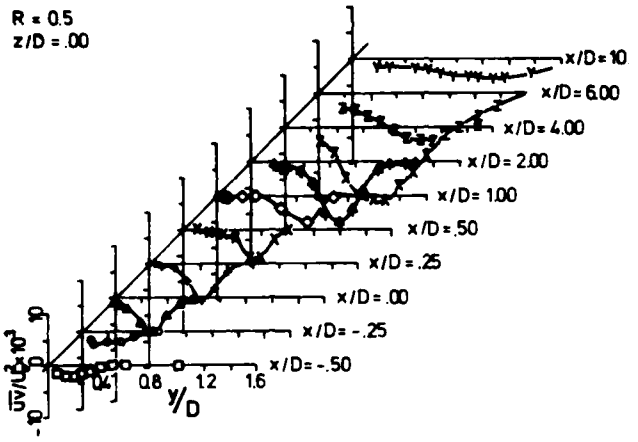

Fig. 7 $\overline{uv}$-profiles at z/D = 0.0

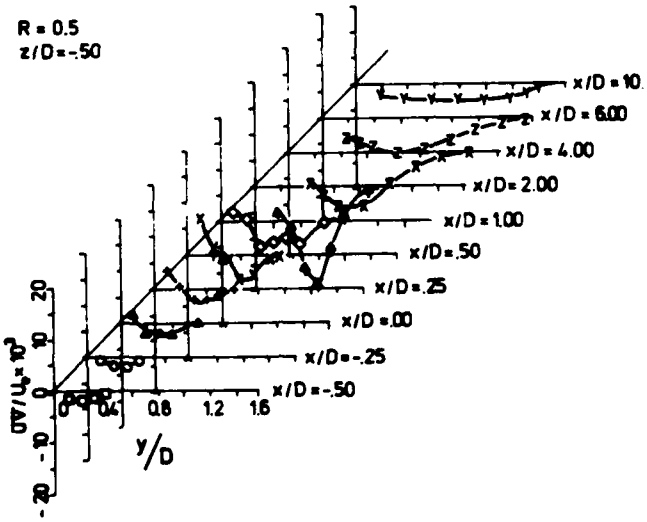

Fig. 8 $\overline{uv}$-profiles at z/D = -0.50

Figure 7 and 8 show profiles of $\overline{uv}$ at two lateral positions z/D = 0 and -0.5 for different downstream positions. Generally the peaks in the $\overline{uv}$ profiles correspond to positions of maximum $\partial\bar{U}/\partial y$ which is one of the main mean strain rates in producing turbulent kinetic energy or shear stress ($\overline{uv}$). At the plane of symmetry this term, like $\partial\bar{U}/\partial y$, does not change sign. However, at z/D = 0.5 it does change sign at various positions over the exit and at the x/D = 1. Here the sign changes do not correspond closely to similar changes of $\partial\bar{U}/\partial y$. Similar behaviour is observed at the $\overline{uw}$ distributions at x/D = -0.5 (Fig. 9) where two zero crossings of $\overline{uw}$ occur at the immediate downstream station x/D = 1 and 2, while $\partial\bar{U}/\partial z$ is everywhere negative. The second crossing near the wall occurs

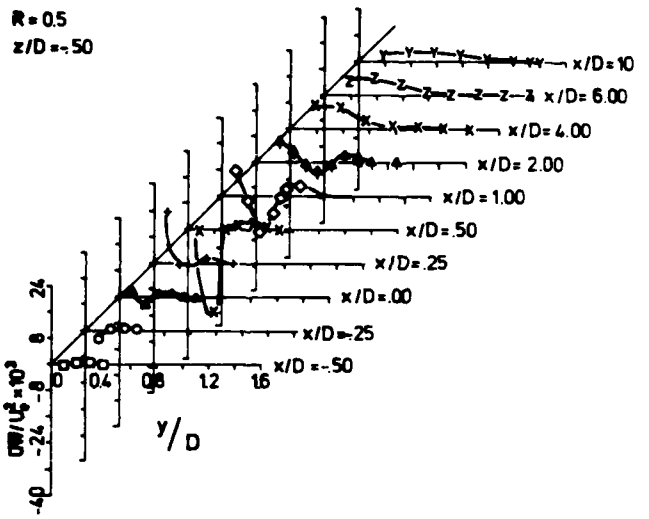

Fig. 9 $\overline{uw}$-profile at z/D = -0.50

in the vicinity of the vortex centre. However, assuming rotation of vortical fluid by 90°, so that the eddies with a contribution to uv after rotation contribute to uw instead, cannot be justified by the present results, since uv and uw profiles do not correspond in any sense. Similar ist the behaviour of vw at z/D = -0.5 shown in Fig. 10. This shear stress has a magnitude almost a third of that of $\overline{uw}$ in the downstream regions but in the upstream stations i.e. in the oncoming boundary layer, it reaches values of the same order of magnitude of $\overline{uw}$.

Although this paper is not directly concerned with calculation methods, it should be pointed out that the eddy viscosity concept $-\overline{uv}/\partial\bar{U}/\partial y$ or even the non-isotropic eddy viscosity $-\overline{uw}/\partial\bar{U}/\partial z$ as it has been introduced in (2) are quite unlikely to give satisfactory results since the longitudinal and normal momentum will be miscalculated and the dissipation rate might be negative if local-equilibrium arguments are involved.

In Figures 11a and b the normal (b_y and lateral (b_z) growth of the jet are plotted as functions of x/D for various values of z/D or y/D respectively. Both have been defined as the points where the shear stress $\overline{uv}$ falls to 0.05 ($\overline{uv}_{max}-\overline{uv}_c$) (where $\overline{uv}_c$ is the assymptotic value of the profile). First it is clear that the width b_y reduces with z as does the growth rate. The growth rate is high

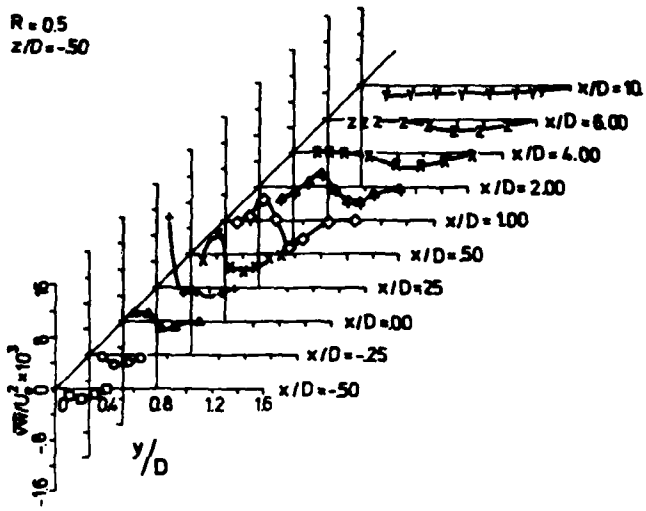

Fig. [illegible] D = -.50

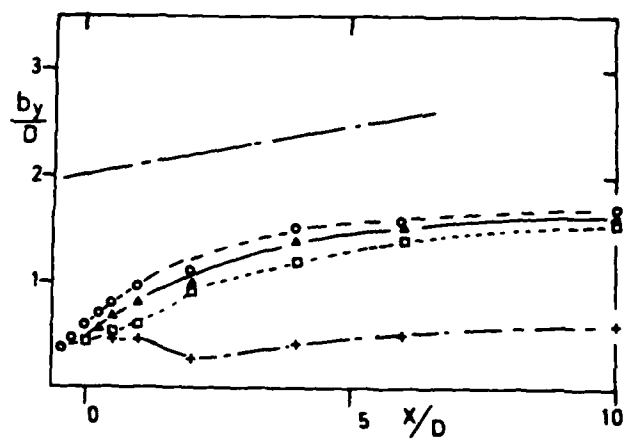

Fig. 11a Normal growth of jet: o z/D = 0.
▲ z/D = 0.5, □ z/D = 0.75, + z/D = 1.0,
Round jet in stagnant surrounding

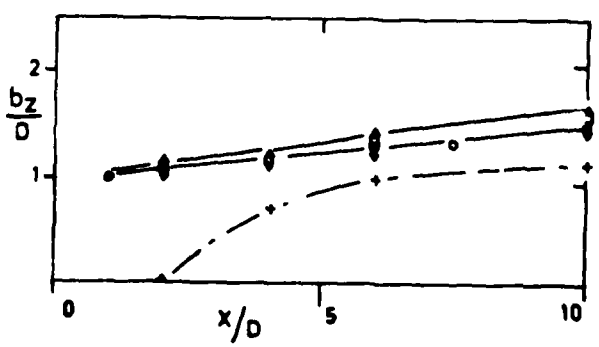

Fig. 11b Lateral growth of jet: ● y/D = 0.18,
o y/D = 0.28, △ y/D = 0.38,
□ y/D = 0.48, ▽ y/D = 0.68
+ y/D = 1.28

close to the exit; roughly equal to 0.32 and is seen to be greater than the lateral spreading rate of 3-Dimensional jets on plane surfaces, which according to the review of Rodi and Launder (15) is equal to 0.26. At the immediate downstream region the spreading rate is gradually reduced up to the station x/D ≈ 5 at which point it takes on a value similar to that of an axisymmetric jet in stagnant surroundings. It then reduces further until the boundary layer growth is asymptotically reached. The lateral spreading rate, however, seems to be fairly constant (0.105) for all the investigated x positions and almost equal to the mixing layer spreading rate. It seems that the bound vortices and the low back pressure greatly effect the spreading of the jet in these two directions. The low back pressure opposes the normal growth of the jet by causing the "downwash" effect in the streamline as it has been shown in the $\overline{V}$-profiles. Here the action of the longitudinal vortices is pressumably suppressed. The lateral spreading of the jet, however, is likely to be controlled by the vortices rather than the back pressure since pressures in this direction are smoothly varying.

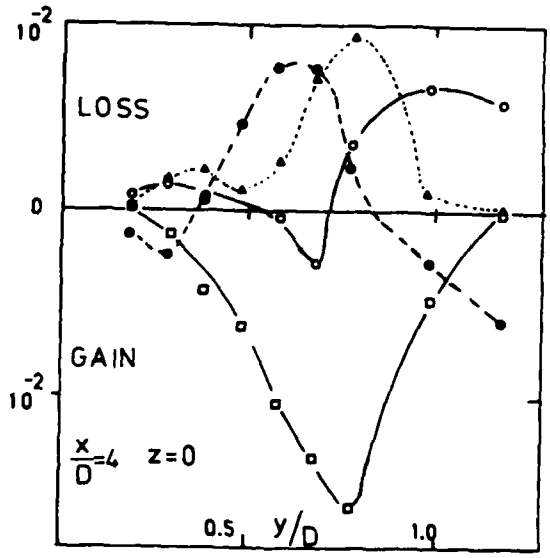

Fig. 12 Turbulent kinetic energy balance
□ Production, o Advection, ● Diffusion
▲ Dissipation

Figure 12 shows the turbulent kinetic energy $\overline{q^2}$ at x/D = 4, on the plane of symmetry z = 0. The terms $\partial\overline{q^2}/\partial z$, $\partial\overline{U}/\partial z$, $\partial\overline{V}/\partial z$ are zero by arguments of symmetry; the remaining terms are as following:

Advection: $\overline{U}\frac{\partial\frac{1}{2}\overline{q^2}}{\partial x} + \overline{V}\frac{\partial\frac{1}{2}\overline{q^2}}{\partial y}$

Production: $\overline{u^2}\frac{\partial\overline{U}}{\partial x} + \overline{v^2}\frac{\partial\overline{V}}{\partial y} + \overline{w^2}\frac{\partial\overline{W}}{\partial z} + \overline{uv}\left[\frac{\partial\overline{U}}{\partial y} + \frac{\partial\overline{V}}{\partial x}\right]$

Diffusion: $\frac{\partial\frac{1}{2}\overline{q^2u}}{\partial x} + \frac{\partial\frac{1}{2}\overline{q^2v}}{\partial y} + \frac{\partial\frac{1}{2}\overline{q^2w}}{\partial z}$

Dissipation is obtained by difference, neglecting the contribution of the pressure-velocity terms $\overline{p'u}$, $\overline{p'v}$ and $\overline{p'w}$ to the diffusion term on grounds described in (16). It is obvious that some changes to the turbulence structure occur: The extremely high gain by production is counterbalanced by loss not only in dissipation but also in diffusion, which also shows a gain at the edges of the jet. This confirms that the transport equations can be reduced to "mean transport" = "turbulent transport" near the outer edge of the jet, where the measured longitudinal and lateral diffusion is small. Then it can be easily argued that the entrainment velocity V_E is high although not equal to $V_q = \overline{q^2v}/\overline{q^2}$ because longitudinal advection $\bar{U}\partial 1/2\ \overline{q^2}/\partial x$ is also high.

CONCLUSIONS

Several interesting features of the jet in a cross flow are brought to light by the present results. The bound vortices which are found to be present at high R were also found at low R ≈ 0.5. These results also support the numerical predictions of Bergeles Grossman and Launder (3) who found weak secondary flows at R≃0.1 but their anisotropic eddy viscosity assumption is not supported. These vortices were found to influence the lateral spreading rate b_z which maintained a constant value of 0.105. Curvature of the jet streamlines begins inside the tube and at the final stages of curvature extremely high Reynolds stresses are developed. These reach a maximum at a downstream distance of about 2 tube diameters where entrainment of free stream fluid is high. The results also show clearly that almost none of the terms involved in the transport equations are negligible and calculation methods based on eddy-viscosity and local equilibrium concepts are not expected to succeed.

The present work has been supported by the Deutsche Forschungsgemeinschaft and has benefited from good colaboration with Prof. J. Foss.

REFERENCES

1 Andreopoulos J. "Measurements in Jet-pipe flow issuing perpendicularly into a cross stream" ASME WA-80/HT-24

2 Bergeles, G., Gosman, A.D. and Launder, B.E. "The turbulent jet in a cross stream at low injection rates: A three dimensional numerical treatment". Num. Heat Transfer, Vol. 1., pp. 217-242 1978

3 Bergeles, G., Gosman, A.D. and Launder, B.E. "The Near-Field Character of a Jet Discharged Normal to a Main Stream". Journal of Heat Transfer, Trans. ASME, Vol. 98, No 3, p 373, 1976

4 Crabb, D. "Jet in a Crossflow" Ph.D. Thesis, London University, 1979

5 Crabb, D., Durao, D.F.G. and Whitelaw, J.H. "A Round Jet Normal to a Cross-Flow". ASME 80-WA/FE-10

6 Foss, J. "Interaction region phenomena for the jet in a cross flow problem". Report SFB 80 E/161, 1980

7 Keffer, J.F. and Baines, W.D. "The Round Turbulent Jet in a Crosswind", J. Fluid Mech., 15, pp. 481-496, 1963

8 Komotani, Y. and Greber, I "Experiments and turbulent jet in a cross flow". AIAA Journal, Vol. 10, No. 11, pp. 1425-1429, 1972

9 Moussa, Z.M., Trischka, J.W. and Eskinazi, S. "The near field in the mixing of a round jet with a cross-stream". J. Fluid Mech. Vol. 80, pp. 49-80, 1977

10 Ramsey, J.W. and Goldstein, R.J. "Interaction of a heated jet with a deflecting stream" Journal of Heat Transfer, Trans. ASME, p. 365, 1971

11 Andreopoulos, J. "Digital Techniques and Computer Programs for Hot Wire Data Processing" Report SFB 80/ME/181 Karlsruhe University, 1980

12 Yavuzkurt, R.J., Moffat, R.J. and Kays, W.M. "Full-coverage film cooling: 3-Dimensional measurements of turbulence structure and prediction of Recovery region hydrodynamics". Report No. HMT-27, Stanford University, 1977

13 Andreopoulos, J. "Some improvements of the performance of triple hot wire probes". Report SFB 80/E/195. Karlsruhe University 1981, submitted to Physics E: Scientif. Instr.

14 Smits, A.J., Eaton, J.A. and Bradshaw, P. "The response of a turbulent boundary layer to lateral divergence". J. Fluid Mech., Vol. 94, pp. 243-208, 1979

15 Rodi, W. and Launder, B.E. "The uniform property turbulent wall jet: a review". To appear in Progress of Aeronautical Science

16 Andreopoulos, J. and Bradshaw P. "Measurements of interacting turbulent shear layers in the near wake of a flat plate". J. Fluid Mech., Vol. 100, pp. 639-668, 1980

THE TURBULENCE CHARACTERISTICS IN THE NEAR-REGION OF THE WALL JET ISSUED FROM A SMALL INCLINED SLOT

Masahide Hatano

Department of Aeronautical Engineering
National Defense Academy
Hashirimizu, Yokosuka 239, Japan

ABSTRACT

An experimental investigation of the turbulence characteristics in the near-region of a steady incompressible turbulent plane wall jet of air injected from a small inclined slot into still surroundings is performed by use of a large apparatus which has a height of injection slot approximately ten times greater than that used by the previous investigators. The present wall jet is injected under the initial conditions of the uniform time-mean velocity distribution and very low turbulence intensity. The turbulence characteristics are obtained in detail by use of the hot-wire anemometers within a nondimensional downstream distance up to about 20 at the injection Reynolds number 6×10^4. It is found that the turbulence characteristics are less affected on the injection conditions and the existence of the corner of small inclined slot than the time-mean characteristics obtained in the previous investigation. The effectiveness of "Coanda Effect" is confirmed also from a view of turbulence characteristics.

NOMENCLATURE

b : width of the wind tunnel
h : height of the injection slot
k : wave number
$Re_j = U_j \times h/\nu$: injection Reynolds number
R_u, R_v, R_w : autocorrelation of u, v, w
t_u, t_v, t_w : time-scales of u, v, w
T : time separation
u, v, w : components of turbulence
u', v', w' : root-mean-square values of turbulence
u_* : friction velocity
U : mean velocity component parallel to the wall
U_j : injection velocity
U_m : maximum value of U at a given section
x : distance measured along the wall downstream from the corner of small inclined slot
x' : distance measured along the nozzle surface
y : perpendicular distance from the wall
y' : perpendicular distance from the nozzle surface
$\delta_{0.5}$: half-jet-width of the wall jet
ν : kinematic viscosity of fluid
θ : inclination angle of the injection slot

INTRODUCTION

Wall jet is formed when a fluid jet is injected from a nozzle along a solid surface. The motivation for investigating such a flow is that the wall jet is very important in connection with many practical applications, such as boundary layer control on aircraft wing, film cooling of rocket engine and prevention of flow separation in diffuser. The another motivation comes from a hydrodynamic interest that the velocity profiles show the combined feature of free jet and boundary layer. Accordingly, a number of investigations have been reported on this flow, since the first paper by Glauert(1). But theoretical and experimental investigations on turbulent wall jet, as well as on turbulent free jet, have been devoted mainly to the mean flow characteristics in the fully developed similar region which is formed sufficiently far downstream from a thin injection slot. In various applications, including the upper surface blowing wing, problems are also concerned with the flow region near the nozzle. For the flow in this near-region of jets, the turbulent mixing and entrainment are quite complicated and largely depend on the injection conditions: for example, geometrical shape of nozzle, injection pressure, velocity profile at nozzle section, and turbulence level and distribution of flow in the nozzle. Then the simple models of turbulence hitherto existed are not adequate, so the analytical treatments are extremely difficult for this near-region.

Moreover, most of the previous measurements are confined to the plane wall jet issued tangentially from the so-called "step slot" type nozzle. But making steps on the surface of the real applications is usually undesirable for the reasons of increasing skin friction and heat transfer. When the "flush slot" type nozzle is used, on the other hand, the jet will separate at the corner of the slot when an external flow is absent.

The present author(2-4) investigated previously the flow in the fully developed region of wall jet issued from a specially designed small inclined "flush slot" using the "Coanda Effect". He also investigated mean flow characteristics in the near-region of wall jet issued from this slot by use of the enlarged apparatus(5).

The purpose of the present investigation is to add the experimental results of the turbulence characteristics to the previous investigation on the time-mean characteristics in the near-region of a steady incompressible turbulent plane wall jet of air issued into still surroundings from the small inclined slot, under the initial conditions of the uniform velocity distribution and very low turbulence intensity at the nozzle section, by use of the cross-wired probe in the same enlarge apparatus as used in the previous investigation, with high degree of accuracy.

EXPERIMENTAL APPARATUS AND PROCEDURE

The small inclined slot shown in Fig. 1 is especially designed by the present author and used in his previous investigations. It has already been confirmed that the jet injected from this nozzle flows around the corner attaching firmly on the wall surface without separation and forms the fully developed similar wall jet in downstream sections, even if there is no external flow. The wall jet with an external flow will be complicated and altered significantly by the velocity ratio and the upper lip thickness, then one had better begin with simpler case. More detailed description of this nozzle can be seen in the previous reports(2-4).

Figure 2 shows the enlarged experimental apparatus used in the present investigation. It was constructed in the testing section of an open-circuit flow-off "blower" type low speed wind tunnel, having a 600mm x 600mm square exit nozzle with large end

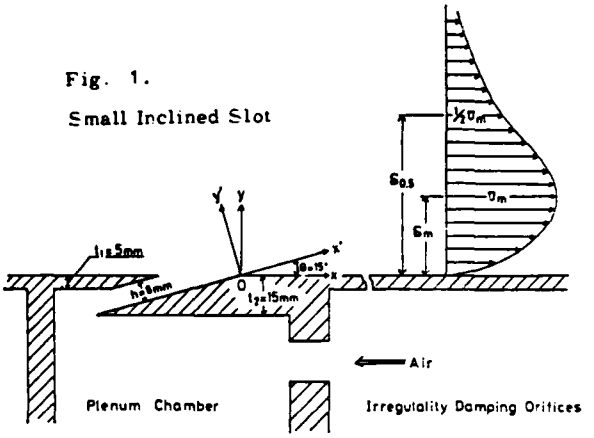

Fig. 1.

Small Inclined Slot

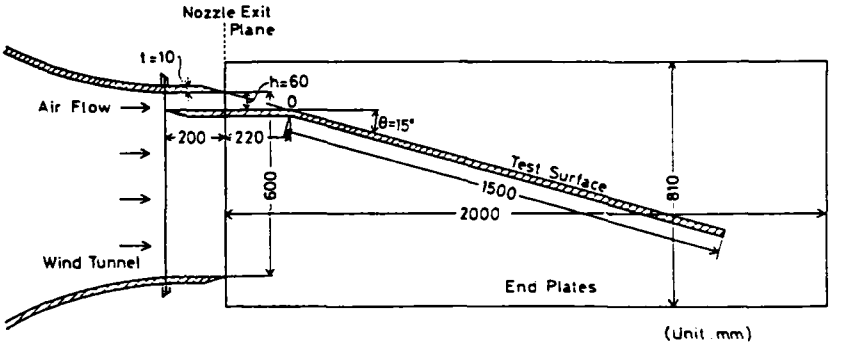

Fig. 2.

Experimental Apparatus

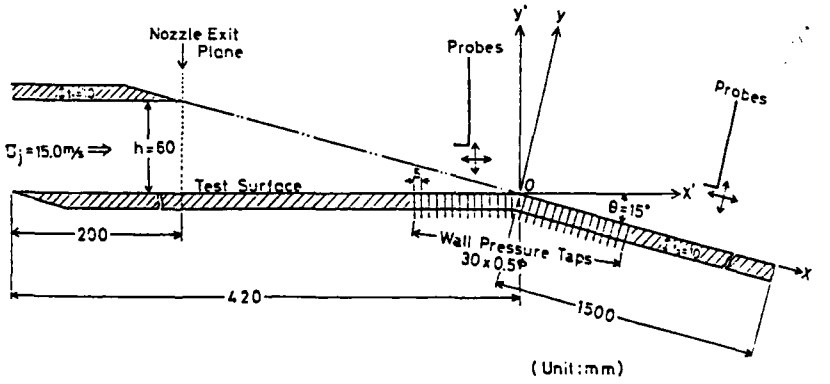

Fig. 3.

Main Part of Apparatus

plates to prevent disturbances from the outside. The geometrical section of this nozzle is exactly similar to the previous one shown in Fig. 1, except that the height of slot (h) is increased to 60mm and axes are rotated clockwise around the corner (0) by an angle of 15 degree.

Figure 3 shows the main part of the apparatus and the coordinate system used in the present investigation. The height of slot is larger than that used in conventional jet studies by about 10 times. The span of nozzle slot is equal to the width of wind tunnel b = 600mm, then the corresponding aspect ratio of nozzle is AR = 10. Using a part of wind tunnel exit as a wall jet nozzle assures the perfect two-dimensionality of wall jet. From Fig. 3, it can be considered that the flow field in the small inclined slot is identical with the one injected tangentially from the new step slot nozzle having same slot height

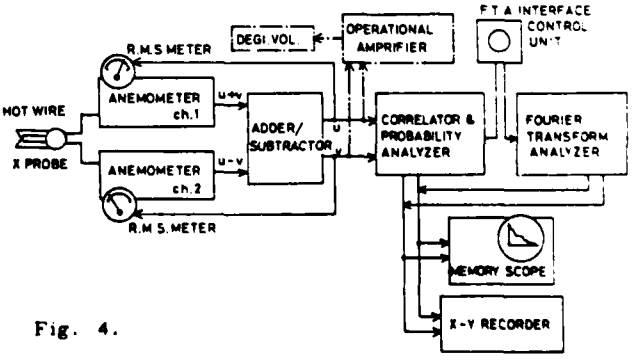

Fig. 4.

Blockdiagram of Instrumentation

and located at the position upstream 220mm from the corner. This flow may be termed "two-dimensional upper surface blowing", as the lower surface of nozzle corresponds to the wing and the test surface corresponds to the flat flap deflected downward by 15 degree.

The experiment was performed at an injection velocity U_j = 15.0m/sec, which corresponded to the injection Reynolds number $Re_j = U_j \times h/\nu = 6 \times 10^4$. The turbulence intensity was measured by the constant-temperature hot-wire anemometers with the standard cross-wired probe. The probe was mounted on the universal traversing mechanism which can shift the probe in the three coordinate directions. Figure 4 shows the block-diagram of the instrumentation for turbulence data processing. This on-line system worked very satisfactorily.

EXPERIMENTAL RESULTS AND DISCUSSION

Injection Conditions

Figure 5 shows the distributions of the mean velocity and the longitudinal relative turbulence intensity at the new nozzle section (x' = -220mm, x'/h = -3.67). It can be seen that the mean velocity U across the nozzle section is uniform over 75% of the height of the injection slot, except in the thin boundary layers on the inside surfaces of nozzle. More precisely, the boundary layer on the inner surface of the upper lip of injection nozzle is much thinner than that on the lower surface. And the relative turbulence intensity u'/U_m in this section is uniform over 60% of the height of the injection slot and has the intensity u'/U_m = 0.0023, which is as low as that in the empty testing section of the low speed wind tunnel used in the present investigation. It is very interesting fact that the respective extent of the constant velocity layer and the constant turbulence layer are different.

Local Turbulence Intensity

The contours of longitudinal local turbulence intensity u'/U in the near-region of wall jet issued from a small inclined slot are shown in Fig. 6. No distinct patterns are seen even in the region around the corner of slot, where the negative peak value of static pressure and the maximum value of mean velocity appeared in the previous investigation.

The one-dimensional turbulence data obtained by means of a cross-wired probe agree very well with the corresponding results obtained by the smaller single-wired probe. This indicates that the influence of cross-wired probe on the turbulence characteristics in the present jet is small.

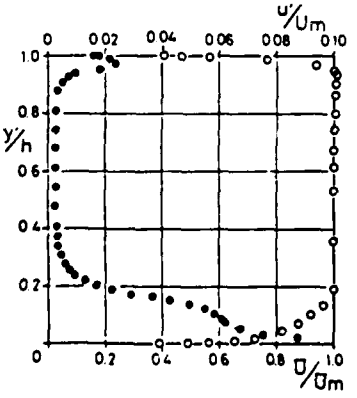

Fig. 5. Measured Profile at Nozzle Section

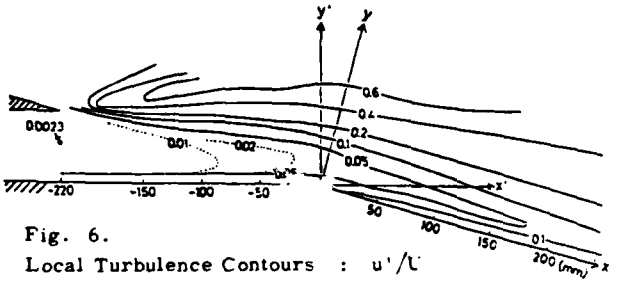

Fig. 6. Local Turbulence Contours : u'/U

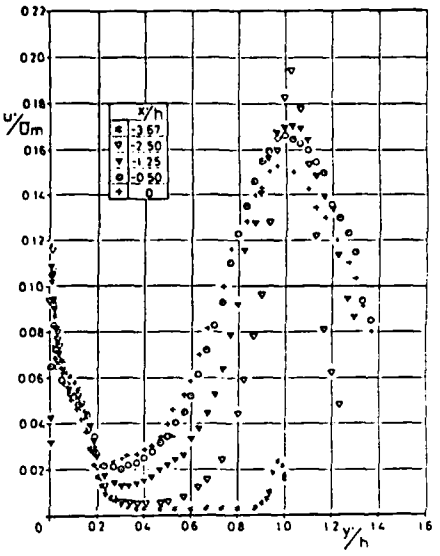

Fig. 7. Relative Turbulence Intensity u'/U_m ($x'/h < 0$)

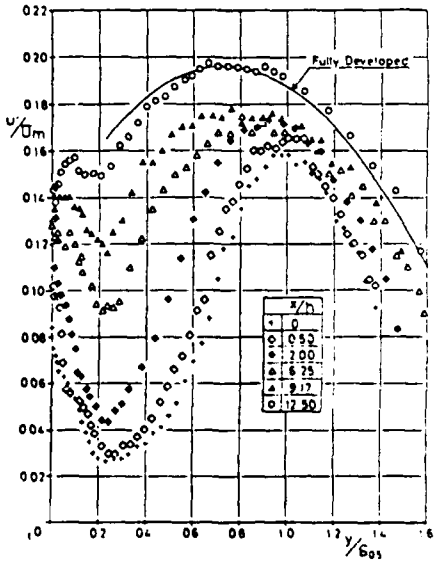

Fig. 8. Relative Turbulence Intensity u'/U_m ($x'/h > 0$)

Relative Turbulence Intensity

The distributions of longitudinal relative turbulence intensity u'/U_m in the sections $x'/h = -3.67 \sim 0$ and $x/h = 0 \sim 18.75$ are shown in Figs. 7 and 8, respectively. Proceeding from the new nozzle section to the downstream sections, the width of the region where u'/U_m = constant becomes narrow and the minimum intensity increases with x. The figures indicate that the longitudinal relative turbulence intensity develops smoothly across the corner sections and reaches the state of similar or self-preserved turbulence at $x/h > 12.5$.

Figures 9 and 10 show the distributions of lateral relative turbulence intensity v'/U_m and w'/U_m, respectively. They show also the smooth development of v'/U_m and w'/U_m.

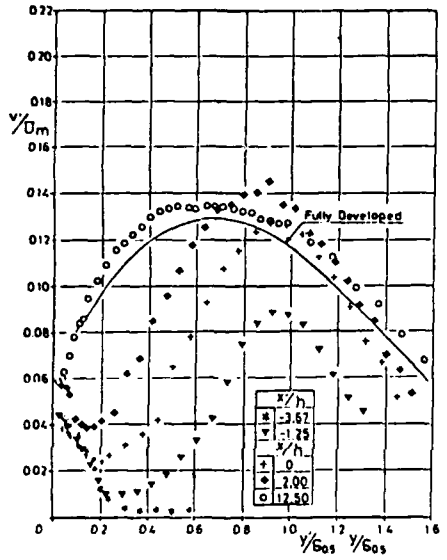

Fig. 9. Relative Turbulence Intensity v'/U_m

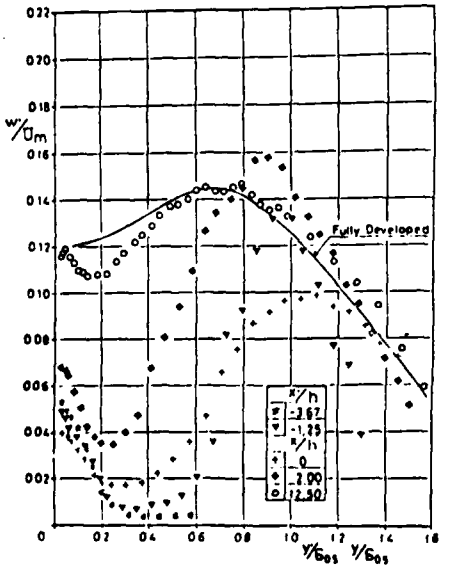

Fig. 10. Relative Turbulence Intensity w'/U_m

Figure 11 indicates that the relative turbulence intensity distributions u'/U_m at the corner sections $x' = 0$ and $x = 0$ agree very well when they are plotted non-dimensionally by use of the same scales. Though the distributions of v'/U_m and w'/U_m in the same sections are shown only by the mean curves in this figure, the scatter of data is as same order as u'/U_m. It is clear that v'/U_m is the highest intensity in the main region $0.2 < y/\delta_{0.5} < 0.8$ at this section. However, it can be seen from Fig. 8 $\sim$ 10 that in the region $x/h \geq 12.5$, the order of three components of relative turbulence intensity is $u' > w' > v'$, as well as in the fully developed region of general turbulent shear flows.

Autocorrelation Curves and Time Scales

The one-point autocorrelation coefficient, e.g. R_u for the turbulent velocity component u, is defined by

$$R_u(x,y,z,T) = \overline{u(x,y,z,t)\cdot u(x,y,z,t+T)} / \overline{u(x,y,z)^2}.$$

The curves for R_u, R_v and R_w were obtained at different positions in the near-region of wall jet issued from a small inclined slot. But only several representative curves of R_u obtained in two sections are shown in Figs. 12 and 13. A curve for the position $x' = -75$mm ($x'/h = -1.25$) and $y' = 20$mm ($y'/h = 0.33$) has the fuller positive portion for small time separation followed by a long negative portion, which indicates the feature observed in the so-called core region of jet. In the downstream sections, for example at $x/h = 15.83$, the autocorrelation coefficients decrease smoothly with time.

The time scales of turbulence can be obtained by the method proposed by Ramaprian(6). The arrows in Figs. 12 and 13 indicate the "last" point for each correlation curve. The time scales t_u, t_v and t_w are nondimensionalized by $\delta_{0.5}/u_*$, where u_* is the friction velocity obtained from the Clauser chart.

Figure 14 shows the time scale t_u, as a representative. It is seen that the distributions of time scale in downstream sections are nearly linear.

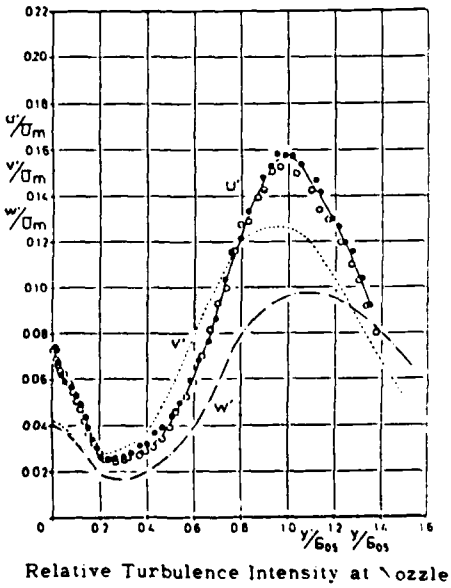

Fig. 11. Relative Turbulence Intensity at Nozzle Section

○: $x' = 0$ ●: $x = 0$

Reynolds Shear Stress

Figure 15 shows the Reynolds shear stress obtained from the one-point cross correlation of turbulence components u and v for the time separation T = 0. The Reynolds shear stress $-\overline{uv}/u_*^2$ has positive value in the boundary layer region and negative value in the free mixing layer region. The curves of the Reynolds shear stress for two regions are connected each other in the so-called core region and become a single smooth curve in the downstream sections x/h ≥ 9.17. The Reynolds stress curves in this region pass through zero at the point nearer to the wall than the position of maximum velocity. This result has been observed in the previous investigations for the fully developed similar flow region of wall jet and lead to the difficulty that there is a definitive difference between the inner layer of wall jet and the conventional boundary layer. This difficulty suggests that the analyses dividing the flow field of wall jet into several layers and regions proposed by Glauert(1) and Myers et al.(7) are not suitable for highly sheared complex turbulent flow. The accumulation of much more detailed and numerous measurements is necessary.

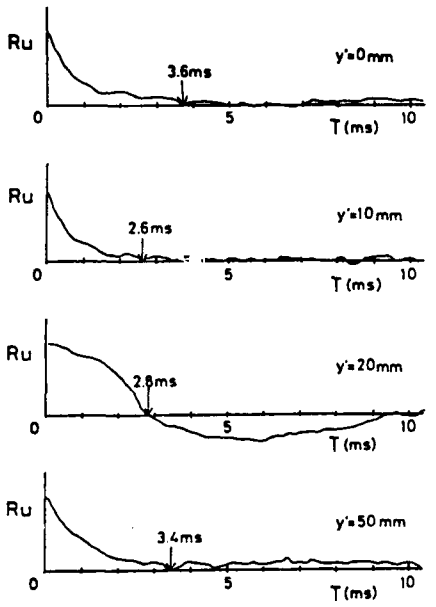

Fig. 12. Autocorrelation Curves R_u
x' = -75 mm , x'/h = -1.25

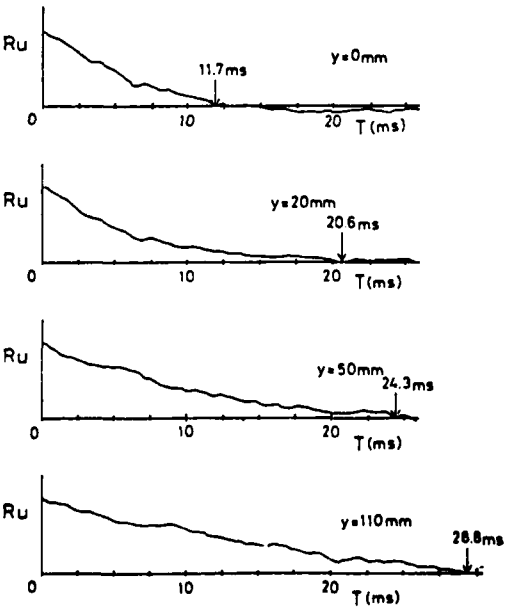

Fig. 13. Autocorrelation Curves R_u
x = 950 mm , x/h = 15.83

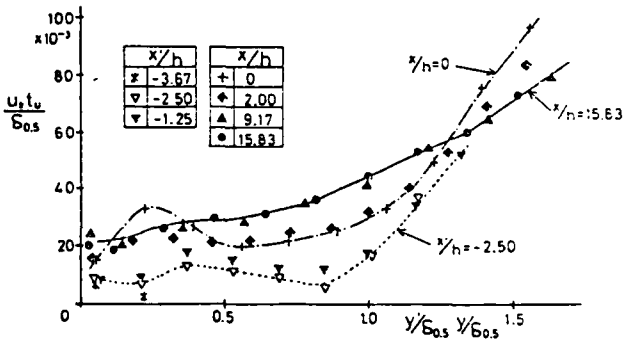

Fig. 14. Distribution of Time Scale t_u

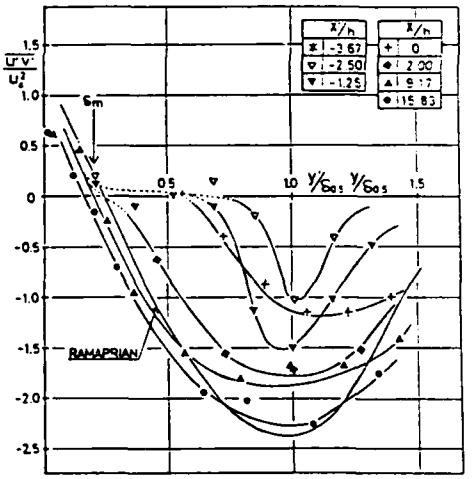

Fig. 15. Distribution of Reynolds Stress

Turbulent Energy Spectra

Figures 16 and 17 show the turbulent energy spectra of u^2 obtained by use of the technique of fast Fourier transformation. The spectra obtained at the position very near to the wall in the section x'/h = -1.25 extend up to nearly 5kHz, but that obtained in the downstream section x/h = 15.83 extend up to 2kHz at most. The local maximum peak in the spectra was not observed even in the t tion just downstream from the corner, which indicates no separation in the flow around the corner of small inclined slot.

CONCLUSIONS

The conclusions of the present investigation on the turbulence characteristics in the near-region of the wall jet issued from a small inclined slot under the initial conditions of the uniform mean velocity distribution and very low turbulence intensity are summerized as follows:-

(1) The effectiveness of the "Coanda Effect" is confirmed not only from a point of view of time-mean velocity characteristics but also from that of turbulence characteristics.
(2) The contours of local turbulence intensity are less complicated than the isobar and the isotach patterns obtained from the time-mean velocity measurement in the previous investigation.
(3) The relative turbulence intensity grows very quickly but smoothly even in the region very near the corner of small inclined slot.

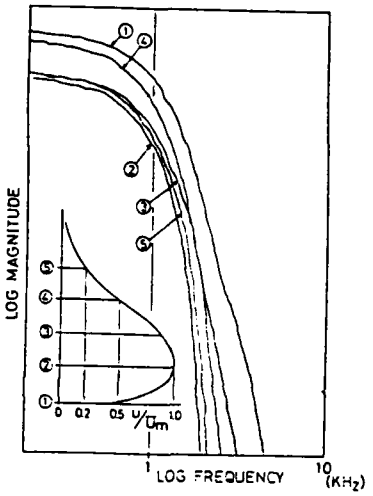

Fig. 16. Energy Spectra of u
x/h = -1.25

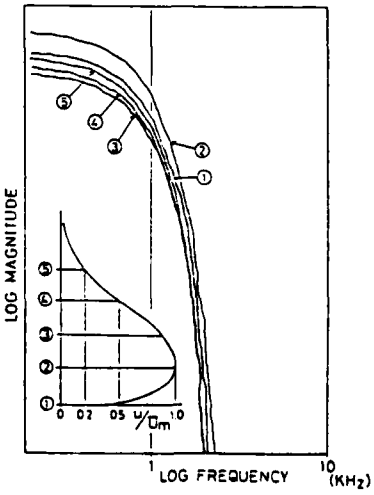

Fig. 17. Energy Spectra of u
x/h = 15.83

(4) The different developing features of correlation coefficient, time scale, Reynolds stress and energy spectra of turbulence cannot lead to the simple characteristic scales which are suitable for complex turbulent flows.
(5) The analysis dividing the flow field of wall jet into several layers and regions is not suitable, and much more careful considerations must be necessary.
(6) It is expected, however, that the accumulation of such a detailed experimental investigation of these highly sheared complex turbulent flows will lead to the comprehensive information on the turbulent flows and more useful models of turbulence than have hitherto existed.
(7) The present investigation is directly concerned with the specially designed small inclined slot using the "Coanda Effect", so that the measurement is performed under the single geometrical condition of injection nozzle. The problem is easily extended to the wall jet on the inclined plate where the inclination angle (θ) and the distance between nozzle and corner may be the important variables. Further investigation on this problem will be made in the future.

ACKNOWLEDGEMENT

The author wish to express his appreciation to Dr. Tetsushi Okamoto, Emeritus Professor of Tokyo Institute of Technology, who guided the research.

REFERENCES

1) Glauert, M.B., "The Wall Jet". Journal of Fluid Mechanics, Vol. 1, Pt. 6 (1956), pp. 625-643.
2) Hatano, M., Okamoto, T. and Suwa, S., "The Experimental Investigation on the Velocity Distribution in the Turbulent Wall Jet Issued from a Small Inclined Slot". Memoirs of Defense Academy, Vol. 9, No.1 (1969), pp. 431-435 and Vol. 11, No.1 (1971), pp. 71-77.
3) Hatano, M., "Experimental Investigation of Incompressible Turbulent Jet along Lateral Convex Wall". Memoirs of Defense Academy, Vol. 9, No.4 (1970), pp. 771-785.
4) Hatano, M., "Experimental Investigation of Incompressible Turbulent Jet along Lateral Concave Wall". Memoirs of Defense Academy, Vol. 9, No.4 (1970), pp. 787-796.
5) Hatano, M. and Okamoto, T., "The Flow in the Near-Region of the Wall Jet Issued from a Small Inclined Slot". Theoretical and Applied Mechanics, Vol. 29 (1980), University of Tokyo Press, Tokyo, pp. 429-439.
6) Ramaprian, B.R., "Turbulence Measurements in an 'Equilibrium' Axisymmetric Wall Jet". Journal of Fluid Mechanics, Vol. 71, Pt. 2 (1975), pp. 317-338.
7) Myers, G.E., Schauer, J.J. and Eustis, R.H., "Plane Turbulent Wall Jet Flow Development and Friction Factor". Transaction of ASME, Series D, Journal of Basic Engineering, Vol. 85, No.1 (1963), pp. 47-54.

Response of a plane turbulent wall jet to the perturbation by a cylinder

Ikuo NAKAMURA
Dept. Mech. Eng., Nagoya Univ., Nagoya, Japan

Hideo OSAKA and Hidemi YAMADA
Dept. Mech. Eng., Yamaguchi Univ., Ube, Japan

Abstract

The change in the turbulence structure and relaxation features of the wall jet disturbed by a circular cylinder which is placed at various distances from the plane wall are investigated experimentally. The results show that the mean and fluctuating properties are considerably affected by the disturbance of the cylinder, and that both the change in the profiles of the turbulent field and the recovery of the turbulent structure from the disturbance exhibit different behaviour according to the locations of the cylinder. Changes in the scale and shape of the perturbing eddy are deduced from the measurements of correlation and spectra. The estimation of various terms of the turbulent energy equation reveals the effect of the disturbance by the cylinder for different cylinder heights.

Nomenclature

a_1 : Bradshaw's parameter ($\equiv -\overline{uv}/\overline{q^2}$)
b_2 : half width
bm : value of y at U/Um = 1
d : diameter of circular cylinder
k : wave number
Lx : integral scale
p : fluctuating pressure
R_{11} : auto-correlation coefficient
S : jet nozzle slot height
U : mean velocity in the x direction
Um : maximum velocity at any x location
u,v,w : fluctuating components of velocity in the x,y and z direction
x : distance measured along wall from the cylinder and in the downstream direction
y : distance normal to wall
y_1 : value of y at 0.5 percent of the maximum turbulent kinetic energy
y_c : height of the cylinder axis
ρ : density of air
ν : kinematic viscosity of air
ν_T : eddy viscosity
$\Phi_{11}, \Phi_{22}, \Phi_{33}$: power spectra of u^2 , v^2 and w^2 respectively

subscript
$(\ast)_r$: value of $(\ast)$ for the undisturbed wall jet

superscript
$\overline{(\ast)'}$: rms value of $(\ast)$

1. Introduction

From the methodological point of view there are two approaches to the shear flow problem. One is to measure the natural development of the flow field and the other is to use Clauser's black box analogy[1]. The latter was proposed about a quarter of a century ago and proved its usefulness in the research of turbulent shear flow as a fundamental method. For example, various responses of the boundary layers to the change of surface condition[2], pressure gradient[3], peripheral speed of the rotating cylinder[4] and the disturbance introduced by a cylinder[5] or a vibrating ribbon[6] were examined. In these studies fundamental concepts, such as inner layer and outer layer, self-preservation, large eddy, coherent structure and so on have been utilized to describe the change of flow field.

A wall jet consists of an inner layer akin to the boundary layer and an outer layer resembling a free shear layer. There is an interaction between the two layers. Although the wall jet has this complex property, it shows a well-defined self-preservation and it is a basic turbulent shear flow. Extensive studies of the wall jet have been carried out, for example, see Townsend[7] and Rajaratnam[8]. The turbulence structure of the wall jet was measured by Irwin(with free stream)[9], Wilson & Goldstein(without free stream)[10] and Kacker & Whitelaw(with free stream)[11].

The present study is different from these experiments since we adopt Clauser's approach, that is, a response of a wall jet issuing in the still ambient air is analized for a disturbance. The current view of turbulent shear flow is that it has an identifiable large-scale structure which controls the development of the shear layer. The disturbance has been introduced simply by a circular cylinder which sheds two-dimensional eddies and makes two shear layers having the opposite sign of mean vorticity. The measurements of various quantities reveal the variation of the mean velocity profile, change of turbulent energy and Reynolds stress balance. The spatial correlation maps with optimal delay time exhibit the deformation of the large eddy.

2. Experimental apparatus and techniques

The wind tunnel used has a rectangular nozzle 10 mm in height and 300 mm in width. A wall jet develops on a smooth flat plate which is made from the aluminium alloy and is 1.67 m in length. Side-boards are attached to the plate to ensure the two-dimensionality of the flow. The configuration of the flow field and nomenclature are shown in Fig. 1. A cylinder of diameter 5±0.01 mm which was made of stainless-steel pipe with very smooth surface was used for the experiment. The streamwise location of the cylinder was fixed at 350 mm downstream from the nozzle exit. The half width and the thickness of the inner layer of the undisturbed wall jet was 33 mm and about 5 mm, respectively, at this station. The space between the cylinder axis and the wall was set at five different values,

the locations yc/d of the cylinder axis being 0.5, 0.8, 3.3, 5.3 and 6.6 above the wall. Measurements have been performed at 6 stations x/d = 6~150 with X-wire probes and a constant-temperature anemometer. The dissipation rate was computed from measurements of the time rate change of the instantaneous velocity. For the measurements of correlation coefficients and spectra a San-ei 7T08 FFT real time data analizer and a Bruel & Kjaer 2112 audio frequency spectrometer was employed. Reynolds number based on a cylinder diameter $U_0 \cdot d/\nu$ was set at 10^4 for all tests. At this time the velocity and turbulence level at nozzle exit was 30 m/s and 0.4% respectively.

The experimental uncertainty of the data is estimated as follows: Primary quantities such as pressure, length, etc., are estimated at ± 1 percent. Mean velocity from hot wire measurements are ± 3 percent and turbulence quantities measurements ± 8 percent.

3. Experimental results and discussion

Change of mean flow field

The undisturbed wall jet showed the self-preserving velocity profile in the region downstream from the station where a cylinder inserted[12]. Figure 2 presents a typical development of the mean velocity disturbed by the cylinder located at yc/d = 0.8, 3.3 and 5.3. At the station of x/d = 6, the positions of maximum velocity deficit almost coincide with the height of the cylinder axis. The relative magnitude of the velocity deficit is larger in the case of the cylinder close to the wall.

Figure 3 shows the decay of the velocity maximum which is usually selected as the velocity scale for all yc/d. In the figure the solid line represents the results of the undisturbed wall jet and coincides well with the measurements of other investigators. When the cylinder locates at yc/d = 3.3, the variation of the velocity maximum is in good agreement with that of the undisturbed wall jet. If the cylinder is set in the region $yc/d \leq 0.8$, the value of U_m/U_0 is lower than that of the undisturbed wall jet. In particular, the velocity deficit has a maximum value for the case of yc/d = 0.8. On the other hand, when the cylinder is set at $yc/d \geq 5.3$ the value of U_m/U_0 is larger than that of the undisturbed wall jet. The decay rate of U_m/U_0 is almost in accord with that of the undisturbed wall jet for each case in the downstream region.

Figure 4 shows the growth of the half width b_2/d along the flow direction. In the figure, the solid line represents the undisturbed wall jet and reflects good agreement with the measurements of other investigators. The value of b_2/d for the cylinder near the wall is larger than that of the undisturbed flow, whereas the results indicate the opposite tendency when the cylinder is away from the wall. The growth rate of b_2/d with x/d almost agrees with that of the undisturbed wall jet for each case in the region greater than approximately x/d = 80.

From the results mentioned above, two possibilities can be inferred in the recovery process of the mean flow field from the disturbance. Possibility 1 is that far downstream from the cylinder position the effect due to the cylinder disturbance effectively disappears, and the flow field becomes exactly the same self-preserving state as for an undisturbed wall jet. Possibility 2 is that although the flow field is also self-preserving, its profile becomes a new equilibrium state differing from the one of the undisturbed case. In this case, we may say that the new equilibrium state bifurcates from the original one asymptotically. The present result seems to suggest possibility 2, according to the considerations of the results mentioned below. This deduction is probable considering that the initial condition for the state of the nozzle exit has a large effect on the development of the free jet[13]. The discussion on the pressure distributions, coefficients of drag and lift of the cylinder and the wall shear stress will be given elsewhere.

Change of turbulent field

Figure 5 shows the distribution of the fluctuating components of velocity for yc/d of 3.3. The figure indicates that u-component of the fluctuating velocity has a maximum value at the region corresponding to both the upper and the lower side shear layers of

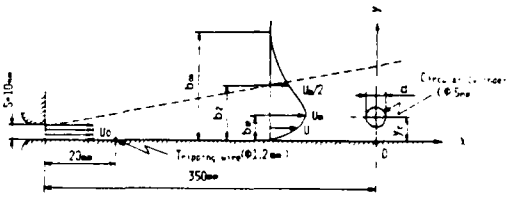

Fig. 1 Configuration of the flow field

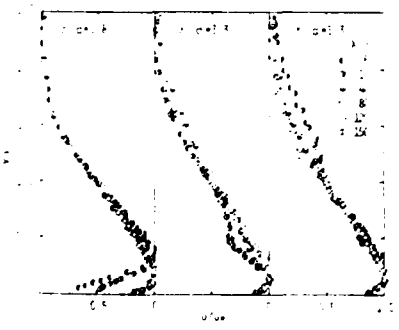

Fig. 2 Profiles of the mean velocity disturbed by the cylinder

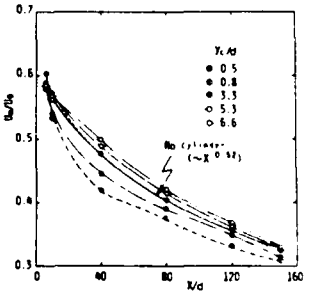

Fig. 3 Streamwise variation of the velocity maximum

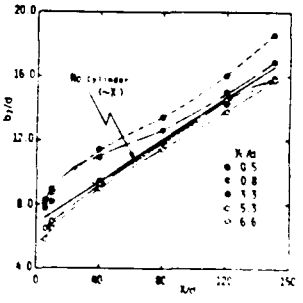

Fig. 4 Streamwise variation of the half width

the cylinder up to x/d=10. This maximum value of the profile is larger in the case of a low cylinder position and perdures for a long distance along the profile of the streamwise fluctuating velocity u'/Um. The contribution to the turbulence intensity by the disturbance shows a more pronounced peak in the profile of v'/Um. For example, at the location of x/d = 6 the result has the order v'/Um > u'/Um > w'/Um[5] in the region corresponding to the lower side shear layer of the cylinder. This is because the mixing length in the y direction become larger than those in the other directions based on the formation of the shear layer. The peak of the profile disappears with increasing x/d, and the distributions of each fluctuating velocity approach those of the undisturbed case.

Figure 6 shows the downstream development of the Reynolds shear stress for values of yc/d of 0.8, 3.3 and 5.3. In the two cases yc/d of 0.5 and 0.8, the distributions of $\overline{uv}/Um^2$ have a counter S-type shape in the region of $x/d \lesssim 10$ and show a maximum value ($\overline{uv}/Um^2 < 0$) in the region corresponding to the upper side shear layer of the cylinder. When $yc/d \gtrsim 3.3$, the profile has a maximum value in the regions corresponding to both side shear layers of the cylinder. At x/d= 40, it is observed that the shear stress profiles are considerably closer to, but still different from, that of the undisturbed wall jet for each case. It may be considered that after x/d=120 Reynolds stress distributions are similar respectively for every case of yc/d, but slightly different from that of the undisturbed case in the same manner as the distribution of the fluctuating velocity components.

Figure 7 shows the turbulent energy difference at x/d= 6, that is $1/2(\overline{q^2} - \overline{q^2}_r)/Um^2$, where $1/2\cdot\overline{q^2}_r$ is the turbulent energy of the undisturbed wall jet. These profiles exhibit a large variation according to the location of the cylinder axis yc/d. When the cylinder is set in the region $yc/d \lesssim 0.8$, the energy difference shows a sharp peak in the region corresponding to the free shear layer generated from the upper side of the cylinder. Then the profile decreases rapidly and again increases in the region of $y/d \gtrsim 5$. The measurement indicated that the second mild peak of the turbulent energy difference for the disturbed case was due to the increase of v component. In the case $yc/d \gtrsim 3.3$, the profile has a maximum in the region corresponding to the lower side shear layer of the cylinder; on the other hand, at the upper side of the cylinder the profile has a minimum. It is notable that the energy in the case of a disturbed wall jet decreases from that in the case of an undisturbed wall jet in the region $y/d \approx 5 \sim 8$ when yc/d = 5.3 and 6.6. This is due to the decrease of u and w components compared with the values of the undisturbed case as shown in Fig. 3.

Turbulent energy balance

The measured values of normal stress and of mean velocity gradient permit the evaluation of the production of Reynolds shear stress $\overline{v^2}\,\partial U/\partial y$. Typical values are shown in Fig. 8 for each case at x/d=6. The solid line in this figure is the result for the case of an undisturbed wall jet. The profiles reveal a more pronounced variation when compared with the one for the undisturbed case. In the case $yc/d \lesssim 0.8$, the negative production of Reynolds shear stress is promoted in the region corresponding to the upper side shear layer of cylinder, while the production of turbulent kinetic energy has a maximum value in that region. The $\overline{v^2}\,\partial U/\partial y$ has a maximum value, which is larger than that of the undisturbed wall jet at $y/b_2 \approx 0.7$. When yc/d=5.3 and 6.6, the production of shear stress does not vary significantly near the wall and has a positive maximum value in the region corresponding to the lower side shear layer of the cylinder, whereas production of turbulent energy has a maximum value in this region. In the case yc/d=3.3, the production of the shear stress has a minimum and a maximum value in the region corresponding to the upper and the lower side shear layer of the cylinder, respectively. The production of turbulent energy has a maximum value in the region corresponding to the lower side shear layer of the cylinder. The pressure distribution around the cylinder is symmetric with respect to the stagnation point for the case yc/d=3.3, and therefore the vortex shedding behind a cylinder whose periodic component contributes strongly to v component of fluctuating velocity exists.

The turbulent energy balance depicts the physical process occurring in the shear layer. Although Kacker and Whitelaw[11] and Irwin[9] estimated the turbulent energy balance of wall jet with a free stream, it seems that only the authors' present experimental[14] are available for the case without the free stream. Figure 9, 10 and 11 show the distribution of various terms of the following turbulent energy equation for the case yc/d=0.8, 3.3 and 5.3 at x/d=40.

$$\left(U\frac{\partial}{\partial x}+V\frac{\partial}{\partial y}\right)\frac{1}{2}\overline{q^2} = -\overline{uv}\frac{\partial U}{\partial y} - (\overline{u^2}-\overline{v^2})\frac{\partial U}{\partial x} - \frac{\partial}{\partial y}\left(\overline{pv} - \frac{1}{2}\overline{q^2 v}\right) - \varepsilon \quad \cdots(1)$$

Advection | Production | Diffusion | Dissipation

The dissipation rate has been evaluated with the aid of the assumption of local isotropy $\varepsilon = 15\nu\overline{(\partial u/\partial x)^2}$,

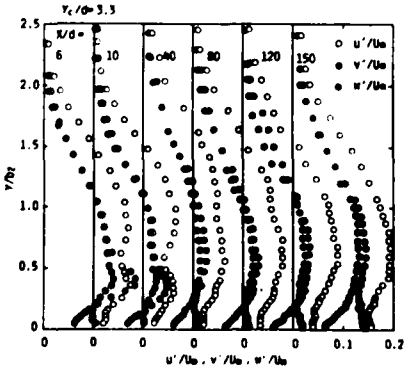

Fig. 5 Profiles of the fluctuating velocity components

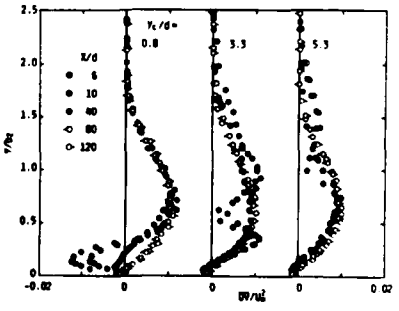

Fig. 6 Profiles of the turbulent shear stress showing large depression

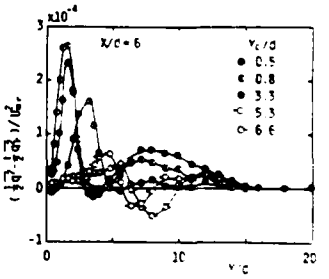

Fig. 7 Profiles of turbulent energy difference between the disturbed and the undisturbed wall jet

and the diffusion has been calculated as the value of $\partial(\overline{vq^2})/\partial y$, so the pressure-velocity correlation has not been measured.

The disturbance generated by the cylinder makes a large contribution to the turbulent energy balance as seen from Figs. 9~11. In all cases, the advection term is very important even in the region far downstream from the cylinder(x/d=40). In the case yc/d $\leq$ 0.8, the advection shows a sharp peak in the region corresponding to the upper side shear layer of the cylinder, and it also exhibits a peak at the lower side shear layer of the cylinder for the case yc/d = 3.3. When yc/d $\geq$5.3, the gain of the advection reveals a deficit in the region of the height of the cylinder axis. The relative increase of the advection may be caused by the large eddies shed from the cylinder. The decomposition of the advection term indicates the large component of $V\cdot\partial(\overline{q^2}/2)/\partial y$. The production term shows a peak in the region corresponding to the height of the cylinder axis. When yc/d=0.8, the gain of this term fairly increases, whereas the gain of the production is not significantly different from that of the undisturbed wall jet for the other cases. The diffusion term has a peak near the region where the production reveals a peak, and the profile shows the same trend as that of the undisturbed wall jet for each case. It may be considered that the pressure-velocity diffusion has an effect on the turbulent energy balance in the region corresponding to the upper side shear layer of the cylinder, comparing the measured value with that obtained by the difference from equation(1). The dissipation does not show a minimum value corresponding to the production term and increases by the cylinder irrespective of its position.

From both results mentioned above and that of the far downstream location, it is noticed that the turbulent energy balance is affected considerably by the disturbance generated by the cylinder, when the latter is near the wall. The recovery from the disturbance is faster when yc/d is smaller after the decision based on possibility 2.

Reynolds shear stress balance is as important as the turbulent energy balance, and Fig. 12 presents a typical profile of the terms of the following $\overline{uv}$ equation at yc/d=0.8

$$\left(U\frac{\partial}{\partial x}+V\frac{\partial}{\partial y}\right)\overline{uv} = -\overline{v^2}\frac{\partial U}{\partial y}+\overline{p\left(\frac{\partial u}{\partial y}+\frac{\partial v}{\partial x}\right)}-\frac{\partial}{\partial y}\left(\overline{pu}+\overline{uv^2}\right) \quad \cdots\cdots (2)$$

Advection Production Transport

In the case of the undisturbed wall jet the advection of the Reynolds shear stress is immaterial, and the Reynolds shear stress is in equilibrium in the sense that production equals transport[15]. It is especially worth noting that the production of the shear stress in the near wall region becomes negative because the production is proportional to the mean vorticity times $\overline{v^2}$, and the mean vorticity changes its sign in the wall jet. The inserted cylinder makes a great change in the shear stress balance as seen in the figure. In the disturbed wall jet the advection term contributes appreciably to the balance and it takes a negative value in the wall region and becomes positive in the middle of the layer. The transverse advection term becomes important in the disturbed wall jet. The importance of the advection suggests that the eddy issued

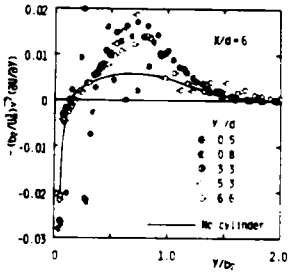

Fig. 8 Production of the turbulent shear stress

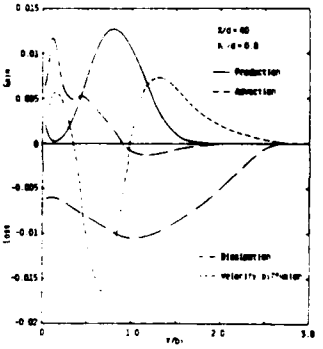

Fig. 9 Turbulent energy balance for yc/d=0.8. Each term is non-dimensionalized by b_2/U_m^3.

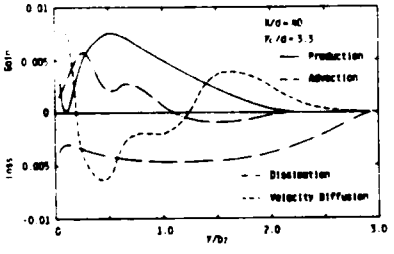

Fig. 10 Turbulent energy balance for yc/d=3.3, see caption to Fig. 9

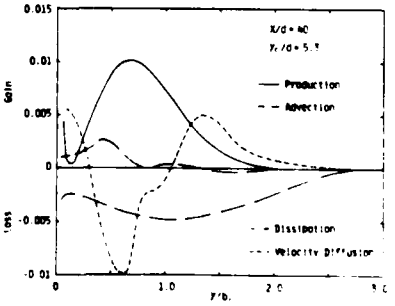

Fig. 11 Turbulent energy balance for yc/d=5.3, see caption to Fig. 9

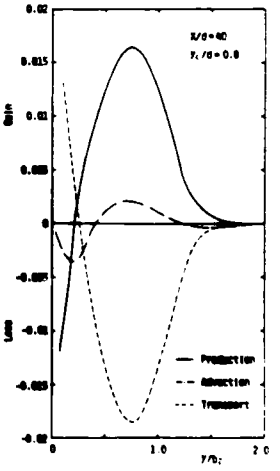

Fig. 12 Balance of terms in the $\overline{uv}$ equation, see caption to Fig. 9

from the cylinder modifies the large-scale structure of the wall jet. The diffusion term is evaluated by the difference from equation(2) and this is balanced by the production term of the shear stress. The disturbance due to the cylinder causes rather large increase of the shear stress production.

Correlation and spectrum

The wake of a cylinder placed in a complete turbulent flow as in the present case may have a complicated structure, but it is reasonable to expect that some dominant freqyency will appear in the power spectrum. Spectra of u^2 , v^2 and w^2 for the case yc/d = 0.5~6.6 at x/d=3 are shown in Fig. 13. The spectrum of v^2 , that is Φ_{22}, reveals more pronounced energy peaks except for the case of yc/d=0.5. This characteristic frequency equals the Strouhal frequency due to the Kármán vortex shedding from the cylinder. From the graph of the spectra it can be inferred that the contribution to the turbulent intensity by the disturbance has the order $\overline{v^2} > \overline{u^2} > \overline{w^2}$. This result corresponds to the variation of the spatial distribution of the turbulent intensity component.

Figure 14 shows the distribution of the integral length scale of the disturbed wall jet calculated from the following definition $Lx = U\int_0^{\tau_0} R_{11}(\tau)\cdot d\tau$, where U is the local velocity and τ_0 is the time delay up to $R_{11}(\tau)=0$. The result in the case of the undisturbed wall jet shown in the figure is nearly constant through the entire cross-section of the wall jet, and it takes Lx/d≒3.2. In the disturbed wall jet, the value of Lx/d increases roughly linear with increasing yc/d, but it is considerably smaller than in the undisturbed case. This result suggests that the large eddy of the wall jet separates into the small eddies due to the disturbance of the cylinder.

Figure 15 and 16 show the so called space-time iso-correlation surface with optimum delay for the cases yc/d=0.8 and 5.3 at x/d=6. The fixed probe is set at the same height of the cylinder axis, respectively. When yc/d=0.8, the space-time iso-correlation surfaces are appreciably narrower than those found in the undisturbed wall jet. The negative value of the iso-correlation line exists in the upper part of the wall jet where the mean velocity causes an excess compared with that of the undisturbed case. In the case yc/d=5.3, the extent of the space-time iso-correlation surface is still smaller than that of the undisturbed case. The iso-correlation line R_{11} = 0.1 has a constriction in the region slightly above the cylinder location. This suggests that the eddies separated by the cylinder disturbance are merged into an eddy in the region downstream from the cylinder position. This trend is markedly evident in the case yc/d = 3.3. In the case yc/d=5.3, the contour line of the

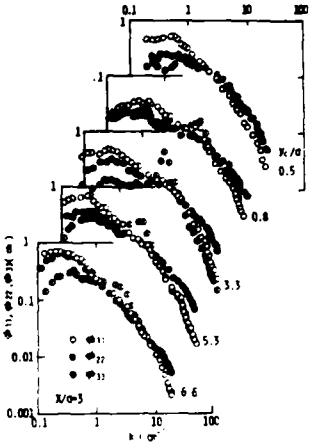

Fig. 13 Spectra of u^2, v^2 and w^2

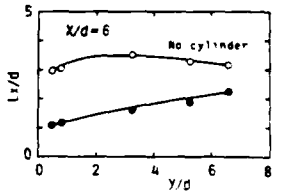

Fig. 14 Integral length scale

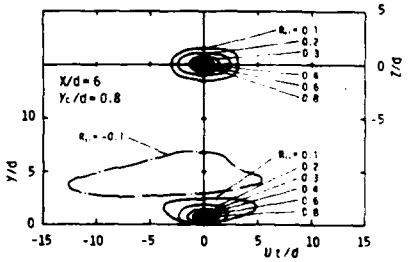

Fig. 15 Space-time iso-correlation surface with optimum delay for yc/d= 0.8, upper side plane view, lower side side view, flow direction is from right to left

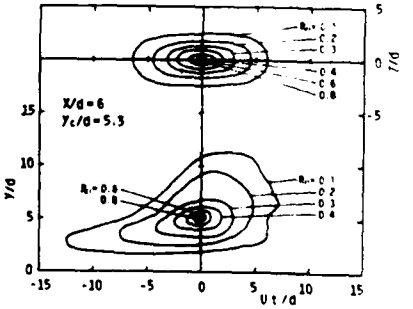

Fig. 16 Space-time iso-correlation surface with optimum delay for yc/d= 5.3

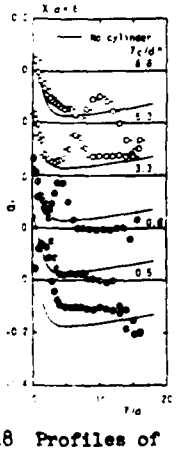

Fig. 18 Profiles of function a_1

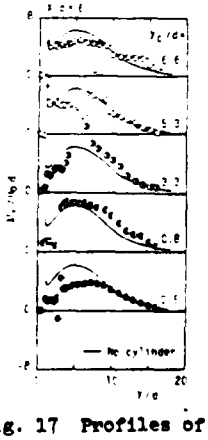

Fig. 17 Profiles of eddy viscosity

iso-correlation extends cosiderably outward to look up at the upstream which indicates the entrainment mechanism. The extent of the iso-correlation for positive Ut/d seems to be smaller compared with that of the undisturbed case.

Prediction model

It is significant to check the typical concepts extensively used in the prediction model. Figure 17 shows the more popular eddy viscosity profile at x/d= 6 which is extensively used. The solid line in the figure indicates the result obtained in the case of an undisturbed wall jet. The profile of ν_T has a maximum value in the region corresponding to the height of the cylinder and also reveals the point of singularity in that region. The value of ν_T is negative near the wall, and thus the physical significance of ν_T is lost. At x/d= 80, the profile is still different from that of the undisturbed case. The profile of the mixing length also indicates the same trends as that of the eddy viscosity.

Figure 18 shows the distributions of the function $a_1 (\equiv -\overline{uv}/\overline{q^2})$. In reference[16], it was shown that a_1 can be regarded as a constant($a_1 = 0.15$) for wall boundary layers. The solid line shown in the figure represents the result of the undisturbed wall jet and agrees with the measurement of Kacker and Whitelaw[11]. The profile of a_1 has a maximum value in the region corresponding to the height of the cylinder axis. Its value is positive for the case $yc/d \lesssim 0.8$ and negative for the case $yc/d \gtrsim 3.3$. It is clear from the figure that the profile of a_1 is complex and so its value is not constant. The distribution of a_1 is still different from that of the undisturbed wall jet at x/d= 80, but it is not seen in the figure.

4. Conclusions

The variation in the turbulent structure of a plane wall jet disturbed by a cylinder and the recovery to the self-preserving state were investigated. Through the experiment the following conclusions have been obtained. First, changing the center height of the cylinder varies the recovery process and it is classified for the case where the cylinder is set in the inner layer of the wall jet and the other case where the one lies in the outer layer. From these results, two possibilities can be inferred for the recovery process of the flow field from the disturbance of the cylinder. Possibility 1 is that the flow field assumes exactly the same self-preserving state as one of the undisturbed wall jets. Possibility 2 is that a new equilibrium state which is bifurcated from the one of the undisturbed flow will be established. According to possibility 2, the wall jet more quickly compensated for its change due to the perturbation when the cylinder was set closer to the wall. This is due to the difference of the disturbing eddy size constrained by the distance from the cylinder to the wall. Secondly, turbulent energy and Reynolds shear stress budget were estimated for the disturbed wall jet. They showed a very large change due to the disturbance. The advection terms which are unimportant for the undisturbed wall jet come to play an important role in the disturbed case. The decomposition of the advection terms indicates that th's increase is due to the transverse term. The turbulent energy balance is more affected by the disturbance generated by the cylinder when yc/d is smaller. Thirdly, energy spectra of u^2, v^2 and w^2 components have been measured. In these spectra, ϕ_{zz} clearly shows a dominant wave number which is most prominent when the cylinder is placed at yc/d = 3.3. The pattern of spectra indicates the v-energy component is affected by the disturbance most intensively in the wave number space. Fourth, auto and space cross correlations have been measured. In the disturbed wall jet, the value of the integral length scale increases roughly linear with increasing yc/d, but it is considerably smaller than that obtained in the undisturbed case. From the space-time iso-correlation surface with optimum delay, it is evident that the large eddy size and its shape are different due to the height of the cylinder, and the scale of the eddy is smaller than that in the undisturbed case. Fifth, the parameters used for the prediction model such as ν_T and a_1 vary significantly in terms of the cylinder height and are not constant. Therefore, predictions based on these models do not suffice.

References

[1] Clauser, F.H., "The Turbulent Boundary Layer," Adv. Appl. Mech., Vol. 4, 1956, pp. 1-51.

[2] Antonia, R.A. and Luxton, R.E., "The Response of a Turbulent Boundary Layer to a Step Change in Surface Roughness. Part 2. Rough-to-Smooth," J. Fluid Mech., Vol. 53, Part 4, 1972, pp. 737-757.

[3] Bradshaw, P. and Ferriss, D.H., "The Response of a Retarded Equilibrium Turbulent Boundary Layer to the Sudden Removal of Pressure Gradient," NPL Aero Rep., No-1145, 1965.

[4] Bissonnette, L.R. and Mellor, G.L., "Experiments on the Behaviour of an Axi-symmetric Turbulent Boundary Layer with a Sudden Circumferential Strain," J. Fluid Mech., Vol. 63, Part 2, 1974, pp. 369-413.

[5] Marumo, E., Suzuki, K. and Sato, T., "A Turbulent Boundary Layer Disturbed by a Cylinder," J. Fluid Mech., Vol. 87, Part 1., 1978, pp. 121-141.

[6] Hussain, A.K.M.F. and Reynolds, W.C., "The Mechanics of an Organized Wave in Turbulent Shear Flow. Part 3," J. Fluid Mech., Vol. 54, Part 2, 1972, pp. 263-288.

[7] Townsend, A.A., "The Structure of Turbulent Shear Flow," 2nd ed., Cambridge Univ., London, 1976.

[8] Rajaratnam, N., "Turbulent Jets," Elsevier, Amsterdam, 1976.

[9] Irwin, H.P.A., "Measurements in a Self-Preserving Plane Wall Jet in a Positive Pressure Gradient," J. Fluid Mech., Vol. 61, Part 1. 1973, pp. 33-63.

[10] Wilson, D.J. and Goldstein, R.J., "Turbulent Wall Jets with Cylindrical Stremwise Surface Curvature," ASME J. Fluids Eng., Vol. 98, No. 3, 1976, pp. 550-557.

[11] Kacker, S.C. and Whitelaw, J.H., "The Turbulence Characteristics of Two-Dimensional Wall-Jet and Wall-Wake Flows," ASME J. Appl. Mech., Vol. 38, No. 1, 1971, pp. 239-252.

[12] Osaka, H. and Yamada, H., "Measurements in a Wall Jet with and without a Trip Wire," Tech. Rep., Yamaguchi Univ., Vol. 2, No. 2, 1978, pp. 115-124.

[13] Goldschmidt, V.W., "Turbulent Transport: Some General Comments," Structure and Mechanisms of Turbulence II, Lecture Notes in Physics, 1977, Berlin.

[14] Kageyama, Y., Osaka, H. and Teruya, I., "Turbulence Structure of the Plane Wall Jet," Prepr. of Jpn. Soc. Mech. Eng. No. 815-1, 1981, pp. 166-168, (in Japanese).

[15] Alcaraz, E., Charnay, G. and Mathieu, J., "Measurements in a Wall Jet over a Convex Surface," Phys. Fluids, Vol. 20, No. 2, 1977, pp. 203-210.

[16] Bradshaw, P., Ferris, D.H. and Atwell, N.P., "Calculation of Boundary-Layer Development Using the Turbulent Energy Method," J. Fluid Mech., Vol. 28, Part 3, 1967, pp. 593-616.

SESSION 7 - OPEN FORUM

I. S. Gartshore and P. A. Libby - Chairmen

SESSION 8 - PERIODIC WALL FLOWS

L. H. Back - Chairman

A DYNAMICAL AND VISUAL STUDY ON THE OSCILLATORY TURBULENT BOUNDARY LAYER

T. Hayashi, and M. Ohashi

Department of Civil Engineering, Chuo University
Kasuga 1-chome, Bunkyo-ku, Tokyo 112, Japan

ABSTRACT

Measurements of velocities in the oscillatory turbulent boundary layer over a horizontal wall have been made using a large oscillating water tunnel. The procedure of periodic ensemble averaging, modified by an application of a finite Fourier series for the estimation of the most probable values of the periodic averages, has permitted the separation of the periodic components and the turbulent fluctuations. From the data separated the vertical profiles and the time variations, of mean velocities, Reynolds stresses and turbulent energy, are obtained.

Turbulent structure of the oscillatory boundary layer has been studied utilizing the flow visualization technique of thin-layered milk method. Visual studies elucidate the results of measurement of turbulent quantities and explain the mechanism of the generation, development and decay of turbulence occurring during each cycle of the oscillatory motion. The large-scale features of turbulence which cause negative Reynolds stresses are examined.

NOMENCLATURE

$\hat{A}_s$	Fourier coefficient of cosine part
$\hat{B}_s$	Fourier coefficient of sine part
a	Free stream amplitude
h	Harmonics number
k	Turbulent energy
T	Period of oscillatory motion
t	Time
U_0	Free stream velocity amplitude
$\overline{u}$	Mean velocity in longitudinal direction
u'	Velocity fluctuation in longitudinal direction
Var	Cumulative variance
w'	Velocity fluctuation in vertical direction
$X_{i,j}$	A measured datum
$\overline{X}_j$	Periodic ensemble mean of data
$\hat{X}_j$	Estimated periodic ensemble mean of data
$\overline{X}$	Overall-time-averaged value of all data
z	Probe height measured from bed
σ^2	Variance
$\hat{\sigma}^2$	Estimated variance
δ	Stokes-layer thickness = $(2\nu/\omega)^{1/2}$
λ	Stokes parameter = $(U_0/2)(2\nu/\omega)^{1/2}/\nu$
ν	Kinematic viscosity of fluid
ω	radian frequency

SUBSCRIPTS

i, j	j-th sample obtained during the i-th cycle
m	Number of sampling during a cycle
n	Number of sampling of cycles

INTRODUCTION

Experimental studies of the oscillatory turbulent boundary layer date back to the work of Jonsson [1], who determined shear stress profiles on the basis of the velocities measured with a micropropeller only. Later, in a similar procedure Jonsson & Carlsen [2] determined turbulent characteristics such as shear stresses, eddy viscosities, energy loss and boundary layer thicknesses. But since the experimental and data processing techniques to study the structure of turbulence in such boundary layers have become available, attention has been forcussed to more refined measurements of oscillatory turbulent boundary layers. The experiments of Hino et al. [3] revealed the fact that turbulence is generated suddenly in the decelerating phase of free stream velocity and that the profile of the velocity distribution changes drastically. Similar observations were reported by Merkli & Thomann [4], who performed experiments on the oscillatory boundary layer in a circular pipe. Detailed measurements of turbulent characteristics such as mean velocity profiles, Reynolds stresses and turbulent energy were made by Cousteix et al. [5]. Measurements of turbulent intensities and Reynolds stresses were also made by Kobashi & Hayakawa [6] for the purpose of studying the effects of unsteadiness of flow on the transition mechanism and development of turbulences in the boundary layer. Experiments by Ramaprian & Mueller [7] showed the profiles across boundary layer, of periodic velocity and ensemble-averaged turbulence intensity in longitudinal direction. Measurements of Reynolds stresses were made by Anwar & Atkins [8], who were in concern primarily with the turbulence characteristics in the tidal flow, the period of oscillation being very large, and the effect of non-steadiness of flow on the structure of turbulence being not remarkable.

Recently, the writers [9] presented the results of detailed measurement of turbulent characteristics and visualization of transition to turbulence, and provided new information on the structure of turbulence. In another recent research, Hino et al. [10] reported the spatial correlations determined for the purpose of elucidating the coherent structure of turbulence in the boundary layer.

In spite of these significant previous studies, a question remains whether the behavior of generation of turbulence to be observed at the end of the decelerating phase of free stream velocity is similar to the behavior of generation of turbulence in the steady uni-directional flow, i.e. the behavior of burst, or not.

Another question to be elucidated is the large-scale features of turbulence which are supposed to exist immediately after the direction of free stream velocity is reversed, i.e. at the beginning of the accelerating phase of the free stream velocity.

The main purpose of this paper is to elucidate these questions performing detailed measurement of turbulence and also visualization of disturbunces.

EXPERIMENTAL APPARATUS AND DATA PROCESSING PROCEDURE

The experiment was conducted in a Lundgren-Sørensen-type water tunnel. This simulates - on a prototype scale - conditions due to the wave motion near the sea bed. The apparatus forms a U-shaped tube consisting of two vertical risers, each with a height of 3.5m, and a horizontal tunnel which is 17.5m long, 0.75m wide and 0.24m deep. By means of a piston the water is made to oscillate in the U-shaped tube with periods and amplitudes as desired. The general view of the apparatus is shown in Fig. 1.

The movement of the water surface in the open riser was recorded by the use of a wave amplitude meter. The phase angle of the oscillatory motion was defined as Fig. 2. Velocities were measured by a X-type hot-film probe. This probe was inserted in the water tunnel, and the height of the probe above the bed was changed with the distances 2mm between z = 0 and 20mm, 3mm between z = 20mm and 35mm, 5mm between z = 35mm and 50mm, and 10mm between 50mm and 120mm.

In order to estimate the most probable values of periodic averages of turbulent quantities of the oscillatory flow out of the data obtained the finite Fourier series described below was adopted to the periodic ensemble means of the data.

Let $X_{i,j}$ be a datum, in which i = cycle ($i = 1,\cdots,n$), and j = number of a datum in each cycle ($j = 1,\cdots, m$). All data obtained are arranged in a matrix form as

$$\begin{bmatrix} X_{1,1} & X_{1,2} & \cdots\cdots\cdots & X_{1,m} \\ X_{2,1} & X_{2,2} & \cdots\cdots\cdots & X_{2,m} \\ \cdot & \cdot & & \cdot \\ \cdot & \cdot & & \cdot \\ \cdot & \cdot & & \cdot \\ X_{n,1} & X_{n,2} & \cdots\cdots\cdots & X_{n,m} \end{bmatrix}$$

Then, the periodic ensemble mean is given as

$$\overline{X}_j = \frac{1}{n} \sum_{i=1}^{n} X_{i,j} \qquad (1)$$

We fit a finite Fourier series with respect to j to the periodic ensemble means obtained by Eq. (1), the finite Fourier series being expressed as

$$\hat{X}_j = \overline{X} + \sum_{s=1}^{h} \left(\hat{A}_s \cos\frac{2\pi sj}{m} + \hat{B} \sin\frac{2\pi sj}{m}\right) \qquad (2)$$

where

$$\overline{X} = \frac{1}{m} \sum_{s=1}^{m} \overline{X}_j$$

$$\hat{A}_s = \frac{2}{m} \sum_{j=1}^{m} (\overline{X}_j - \overline{X}) \cos\frac{2\pi sj}{m}$$

$$\hat{B}_s = \frac{2}{m} \sum_{j=1}^{m} (\overline{X}_j - \overline{X}) \sin\frac{2\pi sj}{m}$$

Now, the problem is to select an optimal number for this h. For this purpose we first calculate the variance of $\overline{X}_j$ from $\overline{X}$ as Eq. (3) and the variance of X_j from the periodic function adopted, as Eq. (4).

$$\sigma^2(\overline{X}_j) = \frac{1}{m} \sum_{j=1}^{m} (\overline{X}_i - \overline{X})^2 \qquad (3)$$

$$\hat{\sigma}^2(\overline{X}_j)_s = (\hat{A}_j^2 + \hat{B}_j^2) / 2 \quad (s = 1,\cdots,h) \qquad (4)$$

With these variances thus obtained we calculate the cumulative variance with respect to s as

$$\text{Var}\ (\overline{X}_j) = [\hat{\sigma}^2(\overline{X}_j)_s / \sigma^2(\overline{X}_j)] \times 100 \quad (s = 1,\cdots,h) \qquad (5)$$

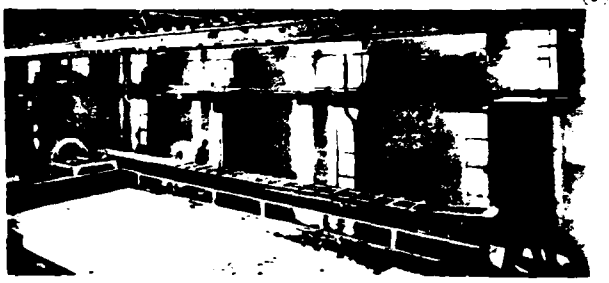

Fig. 1. General view of oscillating water tunnel

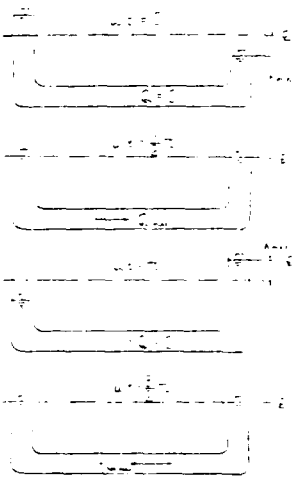

Fig. 2. Definition of the phase angle of oscillating motion

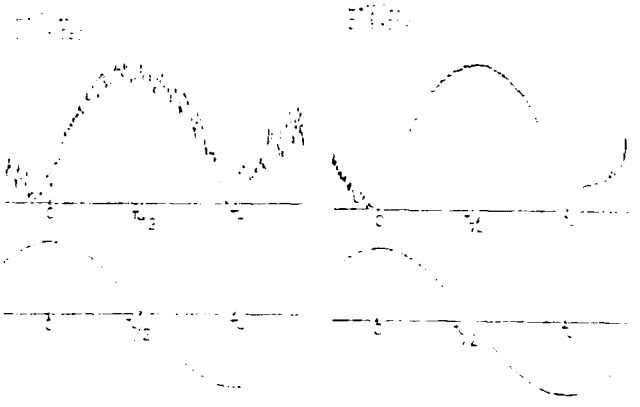

Fig. 3. Records of velocity measurement

The number for h was determined in such a way as to make the value of this cumulative variance 99%. Furthermore, the correlogram was calculated from the autocorrelation of $\overline{X}_j - \hat{X}_j$, and from this correlogram whether the periodic components had properly been eliminated was checked.

EXPERIMENTAL RESULTS

The experimental conditions adopted in this study are listed in Table 1.

Table 1. Experimental conditions

	Run-1	Run-2	Run-3	Run-4
T s	9.8	9.7	11.5	13.5
U_0 cm/s	59.0	67.3	58.8	49.5
ω 1/s	0.63	0.65	0.55	0.47
λ	439	498	473	433
δ cm	0.213	0.208	0.227	0.246
a cm	93.7	103.5	106.9	105.3

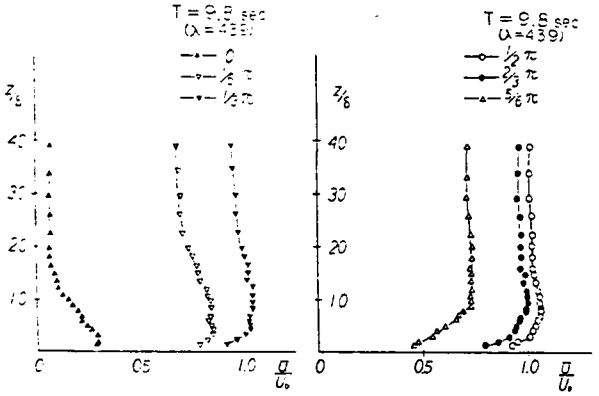

Fig. 4. Mean velocity profiles
(a) During the period of acceleration
(b) During the period of deceleration

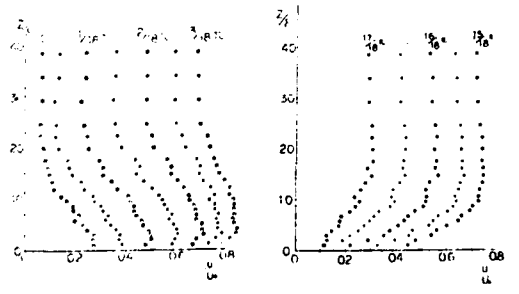

Fig. 5 Mean velocity profiles
(a) At the early stage of acceration period
(b) At the finishing stage of deceleration period

Figs. 4 and 5 show the dimensionless velocity $\overline{u}/U_0$ of Run 1 plotted against dimensionless height from the wall. In these figures, Figs. 4 (a) and (b)

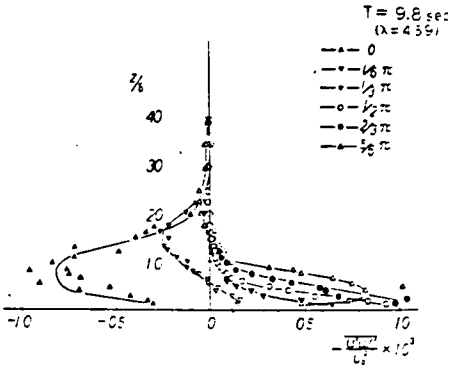

Fig. 6. Reynolds stress distribution (Run-1)

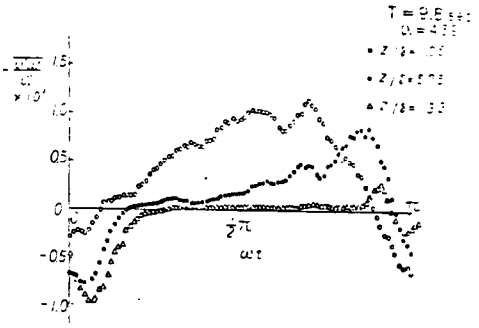

Fig. 7. Time variation of Reynolds stress (Run-1)

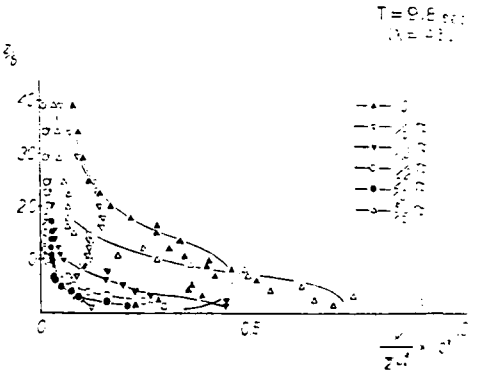

Fig. 8. Turbulent energy distribution (Run-1)

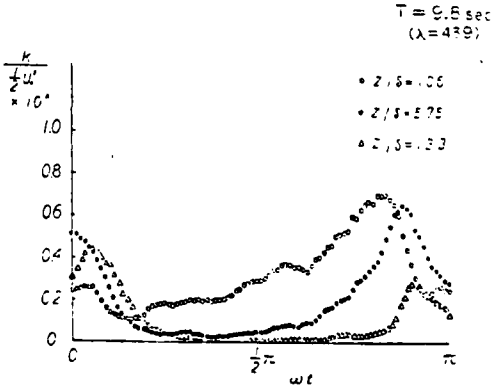

Fig. 9 Time variation of turbulent energy (Run-1)

are for the acceleration period and deceleration period, respectively, of the free stream, and Figs. 5 (a) and (b) are for the early stage of the acceleration period and the finishing stage of the deceleration period, respectively. It is seen from Fig. 4 and Fig. 3 that the phase of velocity advances that of wave amplitude meter by about $\pi/12$.

Figs. 6 and 7 show the the vertical profiles and the time variation, respectively, of turbulent shear stresses in Run-1, and Figs. 8 and 9 show the vertical profiles and the time variation, respectively, of turbulent energy of the same run. Since only two components of turbulent velocity were measured in this study, the turbulent energy k was calculated assumng the formula written below, which formula was used by Eckelmann in his study on low-Reynolds-number turbulence [11].

$$k = (3/4)\ (\overline{u'^2} + \overline{w'^2}) \qquad (6)$$

Figs. 10 and 11 show the time variations of the Reynolds stresses and turbulent energy, respectively of Runs-2, 3 and 4.

It is seen from Figs. 6 ~ 11 that both the Reynolds stress and the turbulent energy are larger in the period of deceleration than in the period of acceleration, of the free stream velocity. It is to be noted also that appearance of the maxima of turbulent shear stress and turbulent energy tend to be delayed as the height of the point of measurement increases.

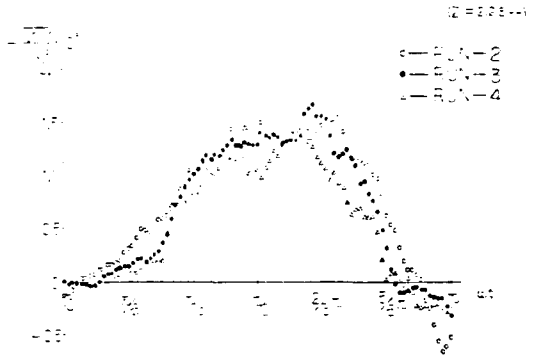

Fig. 10. Time variation of Reynolds stress

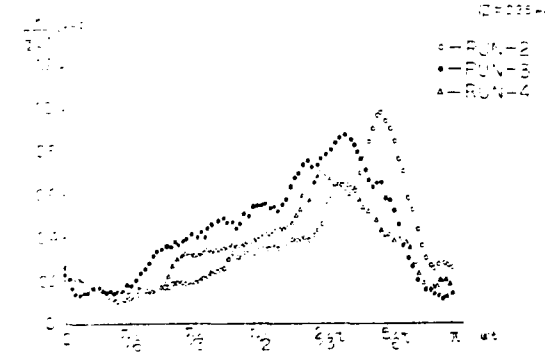

Fig. 11. Time variation of turbulent energy

Runs-2, 3 and 4 have a same free stream amplitude. It is seen from Figs. 10 and 11 that the Reynolds stress does not show distinct difference between these runs, but time of occurrence of the maximum of turbulent energy tends to be delayed as radian frequency increases.

FLOW VISUALIZATION AND OBSERVATION

Flow visualization provides efficient means for the investigation of generation, development and decay of turbulence in oscillatory boundary layer. For the flow visualization the bed of water tunnel was covered by a thin layer of milk whose specific gravity is 1.02. The thickness of the layer was about 1mm. In order to make it possible to observe from vertically upward a lucite part was installed in the upper wall of the water tunnel (Fig. 12). The piston-stroke was started

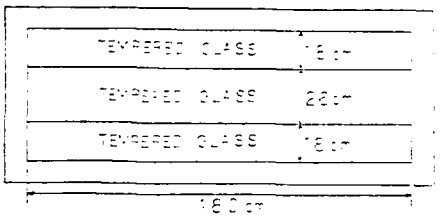

Fig. 12

from rest to a sinusoidal movement (Fig. 13). The movement of milk was recorded photographically with a motor-driven camera set stationary above the tunnel.

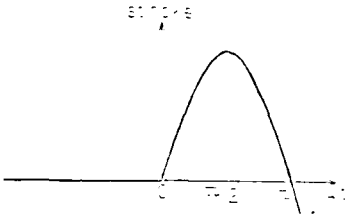

Fig. 13

A series of pictures of Fig.14 show patterns of disturbances occurred on the bed of the tunnel. When the speed of the water flow was maximum, i.e. when $\omega t = \pi/2$ no disturbance was observed on the bed. Disturbances occur after $\omega t = \pi/2$. A series of pictures of Fig. 15 are for nearly a quarter period of oscillation having the instant of no free stream velocity $\omega t = \pi$ in it. This series of pictures was taken employing a micro-lens.

The process of generation and development of turbulence which have been observed from these series of pictures are as follows:

1) The configuration of disturbances formed at first is shown in Fig. 15 (a)
2) The amplitude of these disturbances increases, and the disturbances are deformed to U-shaped loops (Figs. 14 (c) and 15 (b)).
3) The tips of the U-shaped loops move away from the bed owing to the self-induction effect of the loops (Fig. 15 (c)).
4) When ωt approaches π, i.e. when the free stream velocity is decelerated nearly to zero, the U-shaped loops eject turbulent burst (Figs. 14 (e) and 14 (f)).
5) At an early stage of acceleration period a large-scale structure of eddies exists at the outer edge of the boundary layer (Figs. 15 (d), 15 (e) and 15 (f)).
6) These large eddies are decomposed into turbulence having higher frequencies (Fig. 15 (g)).
7) The turbulence tends to be relaminarized during the acceleration period. The clouds of milk already formed make few diffusion and are simply carried back

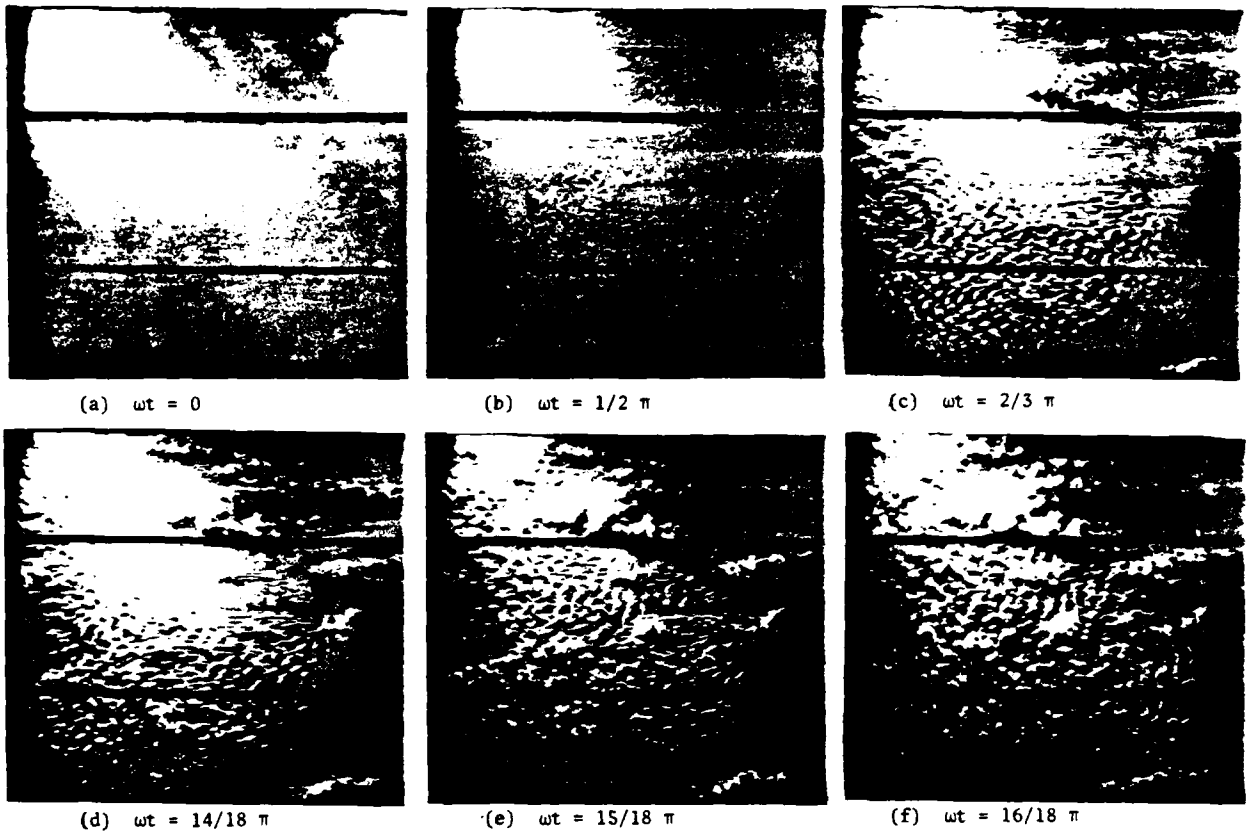

(a) $\omega t = 0$ (b) $\omega t = 1/2\ \pi$ (c) $\omega t = 2/3\ \pi$

(d) $\omega t = 14/18\ \pi$ (e) $\omega t = 15/18\ \pi$ (f) $\omega t = 16/18\ \pi$

Fig. 14. Patterns of disturbances formed (Scope in actual size 64cm x 69cm) (T = 10.0sec)

as a whole by the flow (Figs. 15 (h) and 15 (i)).

It is recognized from these pictures that the flow in the boundary layer does not always remain turbulent during a whole cycle.

Comparison between Fig. 7 and Fig. 15 indicates that the features responsible to the occurrence of negative values of Reynolds stress are such large-scale eddies as shown in Figs. 15 (d), 15 (e) and Fig. 15 (f). It is noticed in Fig. 7 that the absolute value of the negative Reynolds stress increases as the distance from the wall increases up to a certain value, although the value of the positive Reynolds stress decreases as the distance increases. This result of measurement can be interpreted also as the consequence of the formation of the large-scale eddies (Fig. 15 (d), 15 (e) and 15 (f)).

CONCLUSIONS

New details on the nature of turbulence in the oscillatory boundary layer were observed by dynamic measurement of turbulence and also flow visualization technique. Turbulence bursts occur in each cycle of oscillatory flow which bursts are followed by the relaminarization during the same cycle. The process of generation of turbulence in oscillatory boundary layer was elucidated by the flow visualization and compared with the results of dynamic measurements.

BIBLIOGRAPHIC REFERENCES

1. Jonsson, I.G., "Measurements in the turbulent wave boundary layer", Proc. 10th IAHR (London), Vol. 1, pp. 85-92 (1963)
2. Jonsson, I.G., and Carlsen, N.A., "Experimental and theoretical investigations in an oscillatory turbulent boundary layer", J. of Hydraulic Res., IAHR, 14, pp. 45-60 (1976)
3. Hino, M. Sawamoto, M., and Takasu, S., "Experiments on transition to turbulence in an oscillatory flow", J. Fluid Mech., vol. 75, part 2, pp. 193-207 (1976)
4. Merkli, P., and Thomann, H., "Transition to turbulence in oscillating pipe flow", J. Fluid Mech., Vol. 68, part 3, pp. 567-575 (1975)
5. Cousteix, J., Desopper, A., and Houdeville, R., "Structure and development of a turbulent boundary layer in an oscillatory external flow", *Turbulent Shear Flows I*, Springer-Verlag, Berlin, pp. 154-171 (1979)
6. Kobashi, Y., and Hayakawa, M., "The transition mechanism of an oscillating boundary layer", *Laminar-Turbulent Transition*, Springer-Verlag, Berlin, pp. 102-109 (1980)
7. Ramaprian, B. R., and Mueller, A., "Transitional periodic boundary layer study", J. of the Hydraulic Division, ASCE, Vol. 106, No. HY8, Proc. Paper 15908, pp. 1959-1971 (1980)
8. Anwar, H.O., and Atkins, R., " Turbulent mesurements in simulated tidal flow", J. of the Hydraulic Division, ASCE, Vol. 106, No. HY12, Proc. Paper 15609, pp. 1273-1289 (1980)

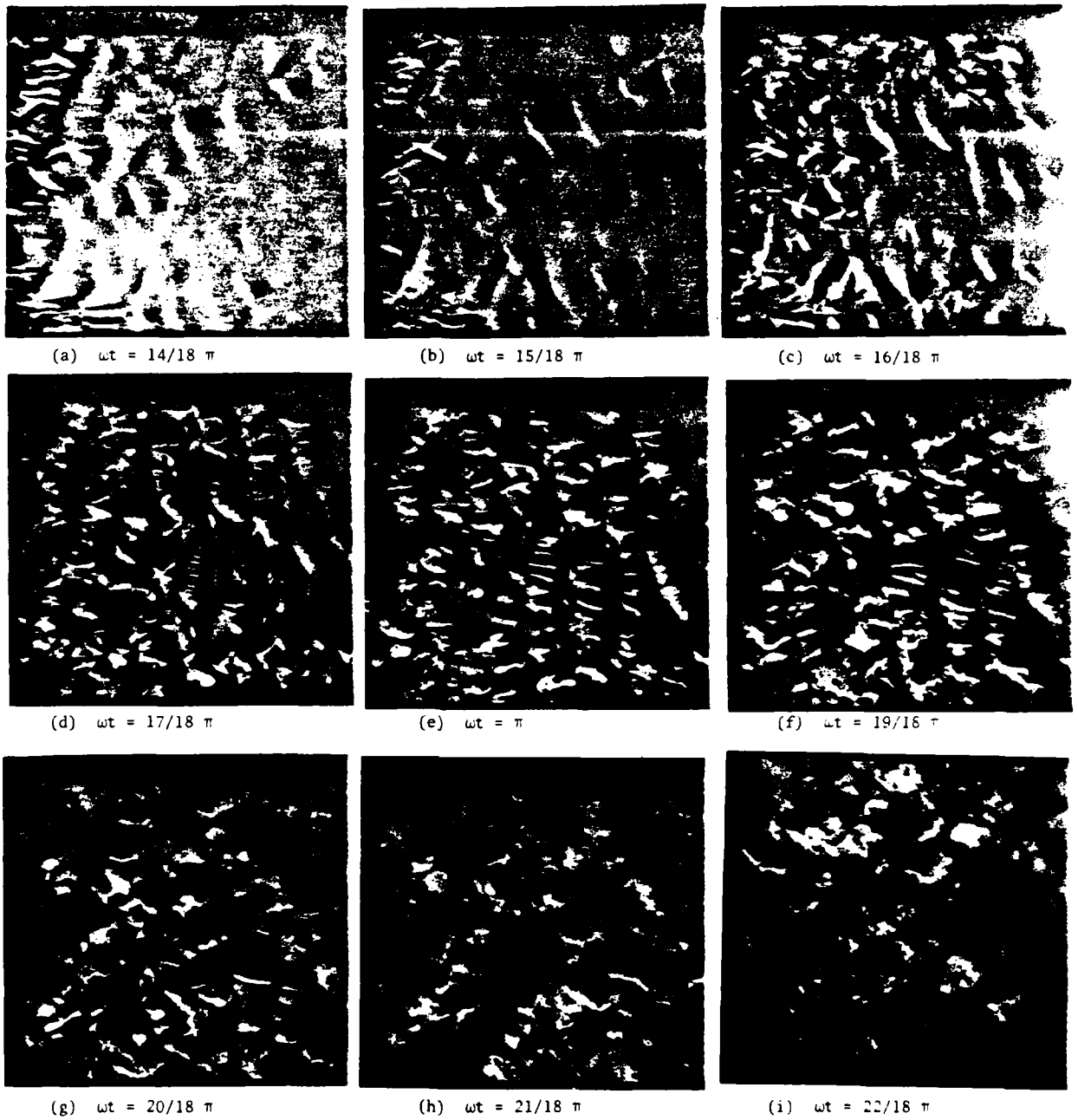

(a) $\omega t = 14/18\ \pi$ (b) $\omega t = 15/18\ \pi$ (c) $\omega t = 16/18\ \pi$

(d) $\omega t = 17/18\ \pi$ (e) $\omega t = \pi$ (f) $\omega t = 19/18\ \pi$

(g) $\omega t = 20/18\ \pi$ (h) $\omega t = 21/18\ \pi$ (i) $\omega t = 22/18\ \pi$

Fig. 15. Large-scale eddies (Scope in actual size 18cm x 21cm)(U_0=49.2cm/s, T=13.0sec, ν=437)

9. Hayashi, T. Ohashi, M., and Takeyasu, S., "Experimental study of the oscillatory boundary layer", Proc. 12th Symposium on Turbulence, Instit. of Space and Aeronautical Science, Univ. of Tokyo, pp. 83-90 (1980) (in Japanese)

10. Hino, M., Kashiyanagi, M., Nakayama, T., and Hara, T., "On the time-space correlation of the turbulence of the oscillatory boundary layer", Proc. 12th Symposium on Turbulence, Instit. of Space and Aeronautical Science, Univ. of Tokyo, pp. 91-97 (1980) (in Japanese)

11. Eckelmann, H., "Experimentelle Untersuchungen in einer turbulenten Kanalströmung mit starken viskosen Wandschichten, Mitt. Max-Planck Inst. f. Strömungsforschung, Göttingen no. 48 (1970)

THE FLOW OF A ROW OF TURBULENT VORTEX-RINGS IMPINGING ONTO A PLATE

By

E. GUTMARK, Y. HAIMOVITCH, M. WOLFSHTEIN
Department of Aeronautical Engineering
Technion - Israel Institute of Technology
Haifa, Israel.

ABSTRACT

The flow field of an axisymmetric turbulent vortex row impinging onto a flat surface was investigated experimentally. The vortices were generated acoustically by a loudspeaker installed in a specially designed ducting system yielding maximum intensity in resonance frequencies. The intensity was further increased using a nozzle of large contraction ratio. Thus, the system could be operated in several resonance frequencies, yielding high velocity fluctuations at the nozzle's exit that resulted in a row of vortices whose geometrical characteristics, velocities, and spacing were governed by those frequencies. Due to the periodic nature of the flow, ensemble averaging was used for data processing.

The results include time histories of the mean and r.m.s. velocities in a basic period, autocorrelations, power spectra and pictures of the flow field using smoke visualization.

The main conclusions are that this flow shows certain similarities to an impinging jet flow in both mean and fluctuating velocities, as well as in the turbulence augmentation by vortex stretching near the stagnation point.

1. INTRODUCTION

1.1 General Description

The initial motivation for this research stems from previous works that were concerned with heat-transfer from a heated flat surface to an impinging flow. It was established in those works that the level of turbulence is increased when the flow approaches stagnation and the heat transfer rates are increased.

In order to study this phenomenon in a controlled flow field Gutmark et al [1] used a round jet that could be excited by a loudspeaker in a predetermined frequency. The flow field of this jet was studied at different excitation frequencies. In special frequencies the amplitude of the velocity fluctuations issued from the nozzle were exceptionally high due to an acoustic resonance of the ducting system. In addition, further augmentation of the turbulence at certain frequencies was generated by the stretching of the flow near the stagnation point. Since the relation between the heat transfer rate and the increased turbulence level in stagnation flow has been established in previous experiments, Gutmark et al [2] checked the heat transfer from a plate to an excited round jet. In these measurements the jet was excited at the resonance frequencies in order to get more energy into the flow in specific frequencies. Some of these measurements were carried out without any net jet-flow, so that the total flow field was created by the loudspeaker generated fluctuations at the nozzle. An interesting observation was that the cooling effect of the acoustic flow was dominant up to a relatively high Reynolds number of the jet flow.

The present research was carried out in order to study the flow characteristics of the acoustic flow, so that its high cooling effect might be explained.

1.2 Literature Survey

The present flow field is similar in some respects to impinging jet flows, and in other respects to the flow of free toroidal vortices. The round impinging jet flow has been investigated experimentally by some authors, e.g. Poreh and Cermak [3], Schauer and Eustis [4], Gutmark et al [1], Donaldson and Snedeker [5] and Yokobori et al [6]. Impingement at a short nozzle to plate distance was reported by Sadeh et al [7]. Similar configuration was studied by Castro and Bradshaw [8].

It is recognized now that vortex stretching near the stagnation point augment the turbulence energy, and that absolute increase of the turbulent fluctuations in the stretched direction occurs at low frequencies. Recently Ho and Nosseir [9] found large scale structures in impinging jet, and these structures are very likely toroidal. Toroidal vortex chains were studied in many papers, for instance Sallet and Widmayer [10], Maxworthy [11], Sullivan et al [12], Yamada and Matsui [13], or Schultz-Grunow [14]. The vortices appear to be very coherent at least near the nozzle. They grow slowly as they move downstream. Usually they reach a fully-developed stage only after 2-3 nozzle diameters.

Theoretical investigation of the toroidal vortices allow prediction of their properties. Saffman [15] formulated a method for such calculations. Although he assumed that the core-diameter is small compared to the diameter of the vortex, his calculations are useful for comparison with the present investigation where this assumption is not satisfied.

In conclusion, vortex stretching near stagnation points plays an important role in such flows, by the augmentation of turbulence which it creates. Apparently, a jet flow shows somewhat similar properties to those of a chain of vortices, and therefore vortex impingement may be of significant practical use. In the present research we study this phenomenon experimentally, using hot wire anemometry, and flow visualization techniques. Our main objective is to understand the basic properties of the mean and turbulent flow.

As the mean flow is periodic, the conventional time-averaging techniques could not be applied here. Therefore we had to develop special sampling and processing techniques, which are described elsewhere [16].

2. EXPERIMENTAL METHODS

2.1 Apparatus and Procedure

A schematic of the experimental rig is shown in Figure 1. The vortex rings are issued form a 2.5 cm diameter nozzle after an area contraction ratio of 1:64.

The nozzle is connected to the settling chamber by a round duct of 203 mm diameter and 984 mm length. At one of the walls of the settling chamber a 50 watt 12 inches diameter loudspeaker is installed. Its vibrations produce the vortex-rings which are issued from the nozzle with increased intensity because of the contraction at the nozzle.

Behind the settling chamber a conical diffuser is installed to enable a proper connection to a blower whenever net flow is superimposed on the acoustic vibrations. The whole system is mounted on a lathe-slide enabling positioning of the nozzle in the two horizontal directions with accuracy of 0.05 mm.

A flat round plate, 1 meter diameter, is installed perpendicular to the nozzle's axis. The plate can be moved in the vertical direction with an accuracy of 0.25 mm. The hot wire probe is protruding through a hole in the center of the plate. The probe may be moved through the hole in a normal direction to the plate. The accuracy of the hot-wire's location was ± 0.25 mm.

The hot-wire probe was operated by a DISA constant-temperature anemometer. It was calibrated against the nozzle velocity while flow was forced by the fan. The hot-wire signal was sampled and processed on a PDP 11/34 computerized data acquisition system as described in Reference [16]. The calibration was performed by the computer as well, using best fit to A, B and n in the anemometer response equation

$$V^2 = A + B\,U^n \ .$$

The calibration errors were about ± 2% at 10 m/s and ± 4% at 1.5 m/s.

The experiments were performed at an acoustic frequency of 15 Hz. The number of sampling points per period was 256. Ensemble averaging was used for processing, and all the members of the ensemble were of equal length. The sampling quality was checked by its autocorrelations. The autocorrelation of the ensemble average was periodic to less than 1% and the autocorrelation of the turbulent fluctuations was stationary.

Very near to the nozzle the axial velocity is negative during a part of the period. We do not report measurements in this region due to the inherent difficulty to identify the direction of flow from hot-wire measurements. The axial velocity became fully positive at about one nozzle diameter from the nozzle.

2.2 Non-Dimensional Presentation

The present flow is governed by the following parameters:

- f - the acoustic frequency
- D - the nozzle diameter
- U - a characteristic velocity of the vortices
- h - the distance between the nozzle and the plate.

These parameters may be arranged in the following dimensionless groups:

Reynolds Number $Re = \frac{UD}{\nu}$

Strouhal Number $St = \frac{f \cdot D}{U}$

Non-dimensional distances h/D ; X/D .

Previous works showed that the viscosity has a secondary effect on the development of the vortices away from the nozzle and from the plate. Thus the Strouhal number is the dominant dimensionless parameter for this flow. This is illustrated in Figure 2, which shows the local Strouhal number (based on local peak velocity) along the axis versus the initial Strouhal number, for various acoustic frequencies and intensities.

The resulting lines correspond to different normalized distances from the nozzle (X/D). A single functional relation is sufficient to describe the behavior at each distance, apart from X/D = 3.10, 3.16, which are very near the wall. The discrepancy at these two locations can be attributed to the high measurement-errors and the increased dependence on

viscosity near the wall.

In most of the measurements the Reynolds number based on the mean absolute nozzle velocity was 7326. This corresponded to Reynolds and Strouhal numbers based on the peak velocity at one nozzle diameter from the nozzle of 16 600 and 0.0375 respectively.

3. EXPERIMENTAL RESULTS

3.1 Flow Visualization

Flow visualization by dry ice was used to clarify the basic characteristics of the flow. In Figure 3 a fully developed vortex can be recognized beginning at $X/D = 1$. In the radial direction it extends to $r/D = 1.5$, which means that its core diameter is about 1D. Figure 4 shows the spreading of the vortex on the plate. The vortex diameter is decreased in this region. The vortex was axially-symmetrical when viewed from the nozzle direction.

3.2 Ensemble Averaged Velocity

Figure 5 depicts a typical hot wire signature, and the loudspeaker input signals. The hot wire signature is positive at all times. High frequency turbulent fluctuations appear following the peak in the velocity. A remarkable difference between the signature of the leading and trailing edges of the vortex is apparent. A typical phase shift between the two signals is evident. This phase shift was found to depend on the distance from the nozzle and from the axis by analysis of many hot wire signatures.

The ensemble-average mean velocity variation of a flow-structure on the axis, at different axial locations is given in Figure 6. The velocity profiles at each location are shifted so that the peak value of each curve coincides with the others. The normalized time is $f \cdot t$; when f is the forcing frequency which equals 15 Hz in the present case, and t is the time, starting from the peak.

The mean velocity $\langle U \rangle$ is normalized by the peak velocity, which is termed $\langle U_m \rangle$. The values of $\langle U_m \rangle$ change from 10 m/sec at $X/D = 1.25$ to about 1m/sec near the plate.

The overlapping of the velocity profiles at different X/D locations along the axis stems from the similarity of the profiles.

The lateral variation of $\langle U_m \rangle$ in different axial locations is given in Figure 7. The velocity is normalized by its value on the center-line. The velocity profiles are also compared with the calculated velocity profile of an inviscid vortex-ring whose total circulation is $\Gamma = 0.32\ m^2/sec$. The shape of the calculated profile fits quite well to the measured one at $X/D = 1.25$ especially in the inner and outer part of the vortex, but not near the core where the viscosity cannot be neglected.

Further downstream the vortex is stretched and entrains more fluid from the ambient air and thus the profile becomes broader and with a more even distribution of the velocity. Near the plate ($X/D = 2.75$) at the outer part of the vortex the velocity measured has a higher contribution of the lateral component.

Figure 8 shows the time-averaged velocity variation in the lateral direction where profiles from different axial locations are similar. The mean velocity is normalized by its center-line value, $\bar{U}_\ell$, and the lateral coordinate Y is normalized by the lateral distance to the point where the mean velocity drops to half its value on the center-line ($Y_{\frac{1}{2}}$). The profiles are compared with the mean velocity profiles of a developed axisymmetric-jet and of a developed plane mixing-layer. The former fits the present results in the outer part of the profile and the later in the inner part.

3.3 Ensemble Averaged Fluctuating Velocities

The root ensemble mean square (R.E.M.S.) axial velocity $(\langle u'^2 \rangle)^{\frac{1}{2}}$, non dimensionalized by the peak velocity $\langle U_m \rangle$ is shown in Figure 9. All profiles were shifted so that the location $f \cdot t = 0$ corresponds to the location of the peak mean velocity of each velocity trace. In this way the relative fluctuations intensity of the leading and trailing edges of the structure can be compared.

The highest relative values of the R.E.M.S. were measured at the leading edge of the structure reaching a level of 20% near the nozzle and 35% near the plate. At the location of the peak mean velocity there's a dip in the normalized R.E.M.S. and another maximum in the R.E.M.S. follows in the trailing edge, but at a lower level. The tail of the structure at each location has a low constant intensity. One exception is the profile closest to the plate at $X/D = 3.16$ where the maximum intensity is located after the peak mean velocity and has a high value of more than 40%, which might lead to large measurement error. Another source of error in this profile is the very low mean velocity in this region which is of the order of 1 m/sec.

The distribution of the axial fluctuating velocity component at $X/D = 2.75$ is given in Figure 10. All the profiles measured in various Y/D feature the same double-peak structure. In most cases the peak in the accelerating side of the vortex is higher than the one corresponding to the decelerating side.

3.4 The Autocorrelation of the Fluctuating Velocities

The autocorrelation of the axial fluctuating component is given in Figure 11 on the axis in different axial locations. All the autocorrelation curves have a typical shape of an isotropic developed turbulence. The autocorrelation decays to zero after less than 10% of the large structures period. Then the curve has a small negative dip, followed by a positive low peak.

The variation along the axis shows a slight narrowing of the autocorrelation in the downstream direction, followed by an increased width near the wall.

3.5 Spectral Distribution of the Fluctuating Axial Velocities

The spectra of the turbulent fluctuations was calculated from the Fourier Integral of the autocorrelation using Wiener-Khinchine relation:

$$p(f) = 4\int_0^\infty R(\tau) \cos 2\pi f\tau \, d\tau \quad .$$

The gradual development of the turbulence towards the plate on the axis is shown in Figure 12. In the beginning most of the energy is concentrated in the low frequency fluctuations of the order of up to 5 times the large structure frequency. The slope in the high frequency range is sharp and thus the energy level of the high frequencies is low. As the plate is approached this slope increases until an inertial subrange can be detected implying that the turbulence becomes more developed and energy is flowing to the higher frequencies.

CONCLUSIONS

The flow field of a row of toroidal vortices impinging onto a plate was investigated experimentally.

It was found that only in a limited zone near the nozzle, of about 1.25 D there is a reversed flow region where the mean velocity could change its direction from forward to backward flow. Following this region the vortices, while entraining flow from the ambient air, gained axial momentum so that there was only forward velocity. The decay of this velocity towards the impingement plate was found to be very similar to that of an impinging jet or a stagnation flow. The profile of the axial mean velocity has also a similar bell shape profile as in the impinging jet but the width of the flow is kept constant till the immediate vicinity of the plate. The width of the mean velocity trace is not changed till a distance of about one wave length from the wall where it starts to decrease as a result of the vortex stretching, caused by the plate. The velocity trace becomes also narrower at the maximum range until a real sharp variation of the velocity can be detected at the crest. Comparing the turbulent R.M.S. values it can be seen that the higher intensities of the turbulent fluctuations are found at the leading edge of the vortex where the flow is in the acceleration phase, indicating a dependence of the intensities on the local Reynolds Number. Similar results were recently found in pulsating flow in a pipe (Shemer & Wygnanski [17]).

The almost perfect periodicity of the large-scale structures is well demonstrated by the autocorrelation measurements.

REFERENCES

1. Gutmark, E., Wygnanski, I. and Wolfshtein, M., "Selective Amplification of Fluctuations In a Turbulent Impinging Jet", Proceedings of the Symposium on Turbulent Shear Flows, Univ. Park, Pennsylvania, April 1977, Vol. 1, pp.3.27-3.33.

2. Gutmark, E., Haimovitch, Y. and Wolfshtein, M., "Heat Transfer Augmentation in Turbulent Impinging Jets", Proceedings of the 2nd Symposium on Turbulent Shear Flows, Imperial College, London, July 1979, pp. 9.1-9.4.

3. Poreh, M. and Cermak, J.E., "Flow Characteristics of a Circular Submerged Jet Impinging Normally on a Smooth Boundary", Proceedings of the Sixth Midwestern Conference on Fluid Mechanics, Univ. Texas, 1959, pp. 198-212.

4. Schauer, J.J. and Eustis, R.H., "The Flow Development and Heat Transfer Characteristics of Plane Turbulent Impinging Jets", Tech. Rep. 3, 1963, Stanford Univ. Stanford, Calif.

5. Donaldson, C. and Snedeker, R.S., "A Study of Free Jet Impingement. Part 1. Mean Properties of Free and Impinging Jets", Journal of Fluid Mechanics, Vol. 45, Part 2, 1971, pp. 281-319.

6. Yokobori, S., Kasagi, N., Hirata, M., Nakamaru, M., and Haramura, Y., "Characteristic Behaviour of Turbulence and Transport Phenomena at the Stagnation Region of an Axisymmetrical Impinging Jet", Proceedings of the 2nd Symposium on Turbulent Shear Flows, Imperial College, London, July 1979, pp. 4.12-4.17.

7. Sadeh, W.Z., Sutera, S.P. and Maeder, P.F., "An Investigation of Vorticity Amplification in Stagnation Flow", Z. Angew. Math. Phys., Vol. 21, Fasc. 5, 1970, pp. 717-742.

8. Castro, I.P. and Bradshaw, P., "The Turbulence Structure of a Highly Curved Mixing Layer", Journal of Fluid Mechanics, Vol. 73, Part 2, 1976, pp. 265-304.

9. Ho, C.M. and Nosseir, N.S., "Large Coherent Structures in an Impinging Turbulent Jet", Proceedings of the 2nd Symposium on Turbulent Shear Flows, Imperial College, London, July 1979, pp. 7.26-7.31.

10. Sallet, D.W. and Widmayer, R.S., "An Experimental Investigation of Laminar and Turbulent Vortex Rings in Air", Z. Flugwiss., Vol. 22, Heft 6, 1974, pp. 207-215.

11. Maxworthy, T., "Some Experimental Studies of Vortex Rings", Journal of Fluid Mechanics, Vol. 81, Part 3, 1977, pp. 465-495.

12. Sullivan, J.P., Widnall, S.E. and Ezekiel, S., "Study of Vortex Rings Using a Laser Doppler Velocimeter", AIAA Journal, Vol. 11, No. 10, Oct. 1973, pp. 1384-1389.

13. Yamada, H. and Matsui, T., "Visualization of Vortex Interaction Using Smoke Wire Technique", Proceedings of the International Symposium on Flow Visualization, Ruhr Universitat, Bochum, Germany, 1980, pp. 518-522.

14. Schultz-Grunow, F., "Sudden Transition to Turbulence Demonstrated by Impinging Laminar Smoke Rings", Proceedings of the International Symposium on Flow Visualization, Ruhr Universitat, Bochum, Germany, 1980, pp. 523-527.

15. Saffman, P.G., "On the Formation of Vortex Rings", Studies in Applied Mathematics, Vol. LIV, No.3, Sept. 1975, pp. 261-268.

16. Gutmark, E., Haimovitch, Y. and Wolfshtein, M., "Computerized Sampling and Processing Technique for Periodic Turbulent Flows", TAE Report No.450, May 1981, Dept. Aero. Engineering, Technion, Israel Institute of Technology, Haifa, Israel.

17. Shemer, L. and Wygnanski, I., Private Communication, 1981.

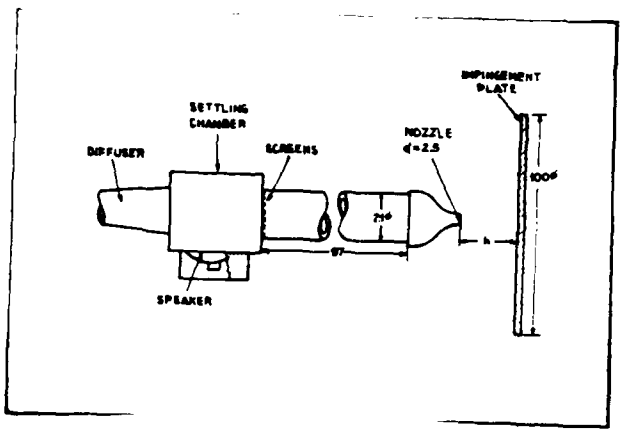

Fig. 1: The experimental rig.

Fig. 4: Visualization of the vortex after impingement. f = 15 Hz, h/d = 3.20.

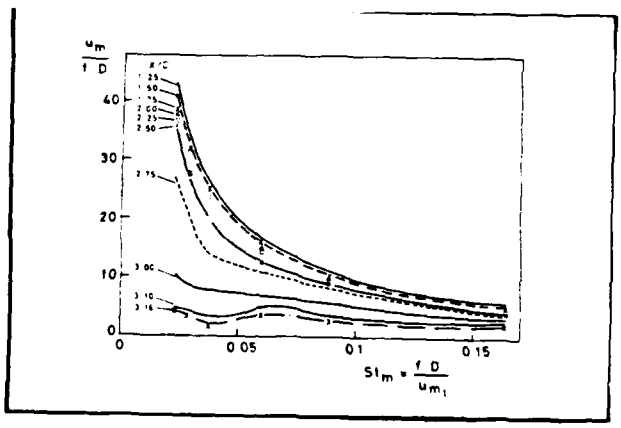

Fig. 2: Variation of the local normalized maximum velocity with Strouhal number.

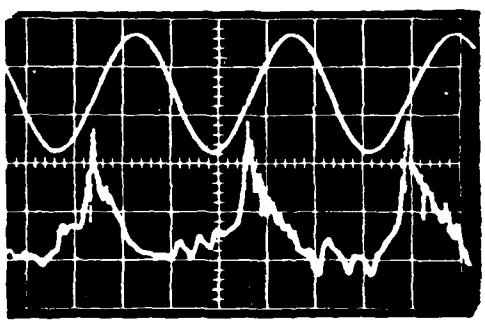

Fig. 5: The exciting signal and anemometer output f = 15 Hz, x/d = 3.0, y/d = 2.08.

Fig. 3: Visualization of the vortex before impingement. f = 15 Hz, h/d = 3.20.

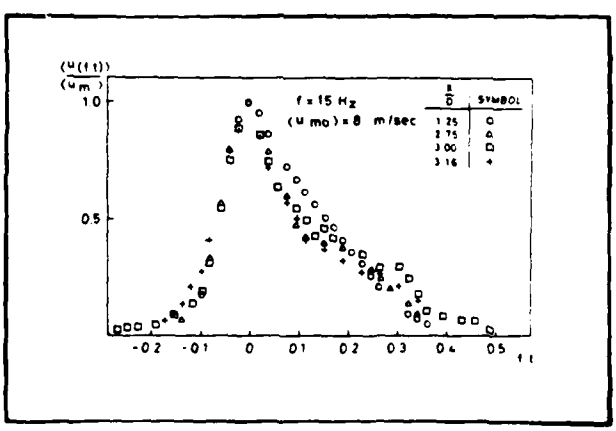

Fig. 6: The ensemble averaged axial velocity distribution for a single period at different axial locations.

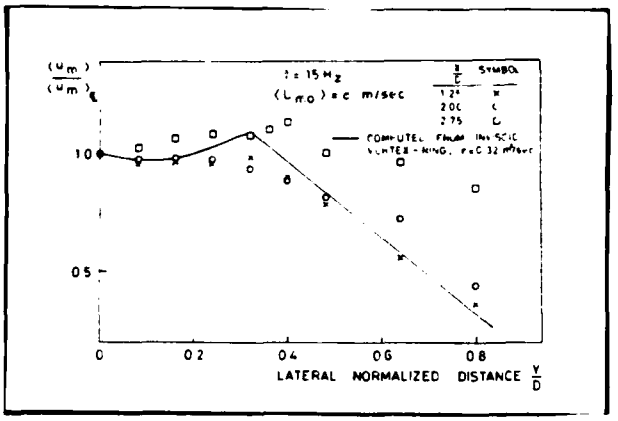

Fig. 7: Lateral variation of ensemble-averaged maximum velocity.

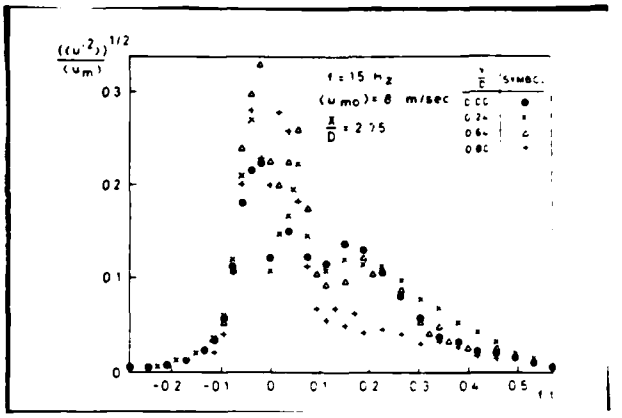

Fig.10: The root-ensemble-mean-square axial velocity fluctuations of different lateral locations.

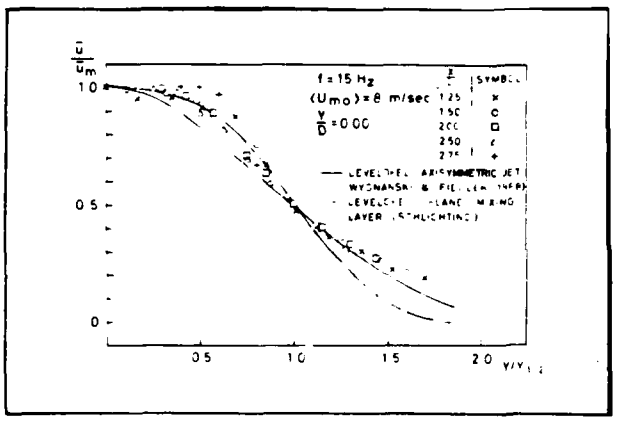

Fig. 8: Lateral distribution of time-averaged longitudinal velocity.

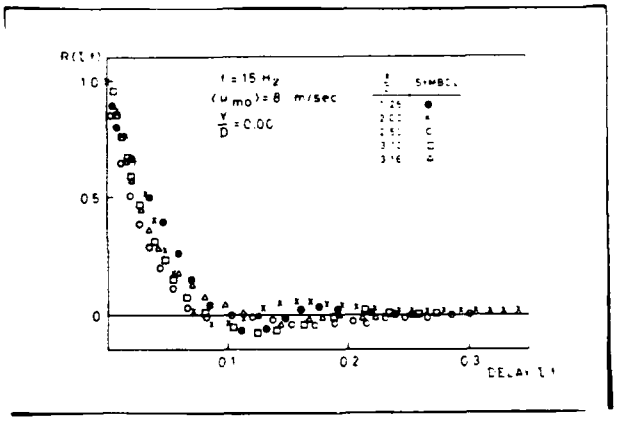

Fig.11: The autocorrelation of the turbulent fluctuations at different axial locations.

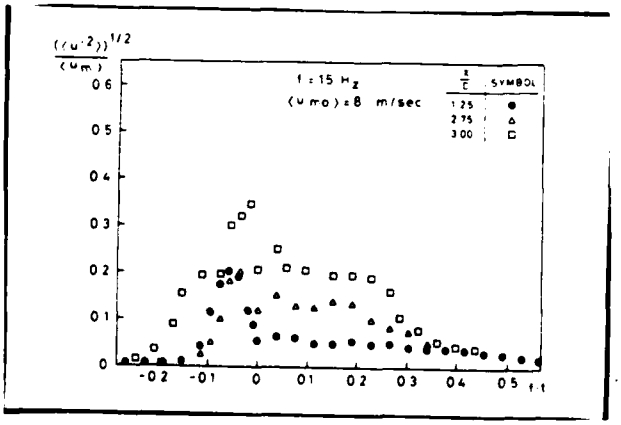

Fig. 9: The root-ensemble-mean-square axial velocity fluctuations at different axial locations.

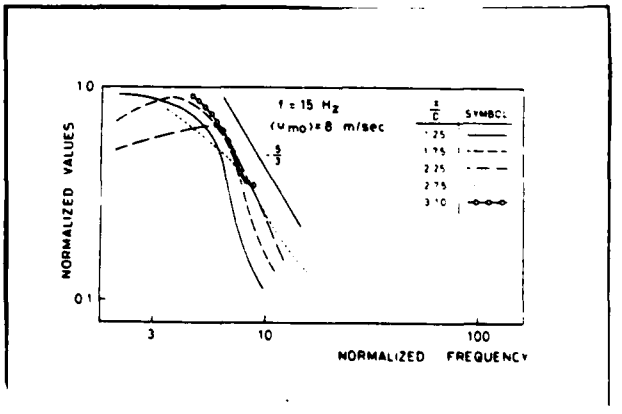

Fig.12: The one-dimensional power spectra of the turbulent fluctuations along the axis.

ON THE PULSATING FLOW IN A PIPE

L. SHEMER AND I. WYGNANSKI
DEPARTMENT OF FLUID MECHANICS AND HEAT TRANSFER
SCHOOL OF ENGINEERING
TEL-AVIV UNIVERSITY, RAMAT-AVIV, TEL-AVIV, ISRAEL.

ABSTRACT

The paper describes velocity and pressure measurments in pulsating pipe flow and a comparison is made between steady and pulsating flows at identical Reynolds numbers in laminar and turbulent regimes. The analysis of the experimental data shows that the response of the turbulent structure lags behind the pulsating flow. An eddy viscosity model allowing for this effect is proposed, and the results of the numerical solution are presented.

NOMENCLATURE

c	=power spectra coefficients
D	=pipe diameter
g,h	=arbitrary functions
f	=frequency
ℓ	=mixing length
L	=length of the pipe
p	=pressure
r	=radial coordinate
R	=radius of the pipe
Re	=UD/ν Reynolds number
t	=time
T	=period of pulsations
u	=axial velocity
u_*	=friction velocity
U	=bulk velocity
v	=radial velocity
x	=axial coordinate
$\vec{x}$	=radius-vector

Greek Letters

α	=$R\sqrt{\omega/\nu}$ frequency parameter
ε	=kinematic eddy viscosity
ε_1	=oscillating eddy viscosity
$\tilde{\varepsilon}$	=complex eddy viscosity
λ	=friction coefficient
ϕ	=phase angle (with the appropriate subscript denotes the angle between the subscript quantity and pressure)
ρ	=density
θ	=relaxation time
τ	=shear stress
ω	=$2\pi f$ cyclic frequency

Subscripts and symbols

1	amplitude of oscillations
cr	critical value
$\langle\ldots\rangle$	denotes phase average
	(overbar) denotes time-mean

A BRIEF DESCRIPTION OF THE APPARATUS AND DATA PROCESSING

The paper describes measurements carried out in a pulsating, fully developed, pipe flow in laminar and turbulent regimes. A detailed description of the original facility was given by Wygnanski and Champagne (1973); a brief account is presented here for the sake of completeness. A straight and smooth aluminum pipe 3.3 cm in diameter and 17 m long was used. The mean flow was supplied by a high pressure (6 atm.) compressor and regulated by a precision regulator. High resistance was introduced between the compressor and a large settling chamber in order that the flow rate would be independent of pressure oscillations and the flow regime in the pipe. As a source of pulsations a valvless piston pump, connected to the settling chamber, was used. The piston diameter was 9 cm., and its displacement could be changed from 0.5 to 7.5 cm in 17 steps. The pump was driven by a 1.5 hp variable speed motor permitting a change in the period of pulsations between 0.5 sec and 5 sec.The repeatability of the time period was better than 0.3%.

Velocity measurements were made with single x-wire or with a rake of 9 hot wires distributed evenly in the radial direction at distances $\Delta r/R=0.12$ between the neighbouring wires; so that when the location of the first wire was on the center line, the 9-th wire was located at $r/R=0.97$. Velocity signals from the hot wire anemometers were digitized by a 12 bit analog to digital converter and processed on a PDP 11/60 minicomputer. All velocity measurments were taken at the exit plane of the pipe.

A pressure transducer (Validyne DP 215-30) placed at the wall of the inlet nozzle monitored the instantaneous static pressure at the entrance of the pipe. An optical senses-witch mounted on the flywheel of the piston provided a trigger signal, which was used as a phase reference. Both pressure and trigger signals were processed digitally.

The period of the oscillations was measured by the computer. Two factors determined the sampling frequency which depended on the period of the oscillations: 1)the number of samples per channel per period had to be a power of 2 for the purpose of using a Fast Fourier Transform; 2) the maximum possible rate of continuous data processing and recording on a magnetic tape provided an upper limit on the total sampling rate which could not exceed 20 KHz. Thus, 1024, 2048 or 4096 points were sampled per period per channel, depending on the frequency of oscillations. The lowest sampling frequency used was 800 Hz. In laminar flow 56 periods were measured for each set of parameters while in turbulent flow the number was 240. In both cases 8 consecutive periods were sampled thus enabling one to ob-

tain spectral information for frequencies lower than those of the forced oscillations.

Most of the measurments were made at mean Reynolds number 4000.The choise of Re was dictated by two main reasons: 1)to ensure that there is no back flow at any radial location, and 2) to assure that the relatively low sampling frequency is adequate for measurments of turbulence. The influence of the mean Reynolds number on the flow was tested and reported by Shemer (1981).

The undisturbed flow was laminar at all Reynolds numbers and frequencies used. Turbulence was triggered artificially by a perturbance (a cylinder 2.5 mm in diameter) which was inserted diametrically into the pipe 20 diameters from the entrance. The disturbance caused the steady flow to become fully turbulent at all Reynolds numbers above 3000. When the cylinder was pulled out of the pipe the flow became laminar, which enabled measurments in laminar or turbulent flow while keeping all other controllable parameters, like mean velocity, displacement amplitude of the piston and frequency of oscillations, constant.

The periodic nature of this flow suggests the decomposition of any flow variable $g(\vec{x},t)$ into 3 components (Hussain and Reynolds (1970))

$$g(\vec{x},t)=\overline{g(\vec{x})}+\langle g(\vec{x},\phi)\rangle+g'(\vec{x},t) \qquad (1)$$

where $\overline{g(\vec{x})}$ is the time mean value of the variable $g(\vec{x},t)$ at point $\vec{x}$

$$\overline{g(\vec{x})} = \lim_{T\to\infty} 1/2T \int_{-T}^{T} g(\vec{x},t)\, dt$$

$\langle g(\vec{x},\phi)\rangle$ is the contribution of the periodic part at a given phase angle at the same point

$$\langle g(\vec{x},\phi)\rangle = \lim_{N\to\infty} \frac{1}{N} \sum_{i=1}^{N} (g_i(\vec{x},\phi) - \overline{g(\vec{x})})$$

and $g'(\vec{x},t)$ is the random part. The difference between pulsating and non-pulsating turbulent flow is determined by the existence of $\langle g\rangle$, which vanishes in the steady case. From the definition of the phase mean component $\langle g\rangle$ it is clear that the following relations must hold for the temporal mean values

$$\overline{g'}=\overline{\langle g\rangle}=\overline{g'\langle h\rangle}=0 \qquad (2)$$

Averaging experimental data at fixed phase angles determines the value of $\langle g\rangle$.

Assuming that the flow is not only periodic, but also harmonic, restricts the oscillating part to a single Fourier component, thus

$$\langle g(\vec{x},\phi)\rangle=\mathrm{Re}(g_1(\vec{x})\exp(i(\omega t+\phi_g)) \qquad (3)$$

where $g_1(\vec{x})$ is the amplitude of pulsations and ϕ_g is the initial phase angle of the quantity g. All phase angles referred to, in this work, are related to the pressure. In general, the time dependent variables can be expanded in Fourier series, so that the right hand side of Eq.(3) becomes the leading term in the expansion.

EXPERIMENTAL RESULTS

Mean Flow: Steady vs. Pulsating Velocities and Pressure

Fig.1[a] represents time mean velocity profile measured by an x-wire in laminar pulsating flow and normalized by the center-line velocity. The profile presented was taken at Re=4000, period T=1.34 sec and a relative amplitude of bulk velocity fluctuations $U_1/\bar{U}$=20%.

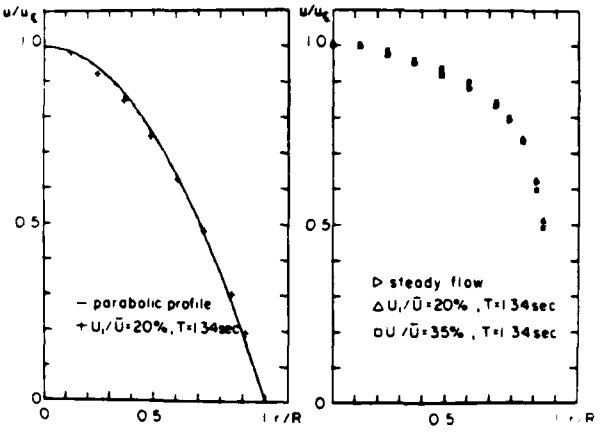

Fig. 1 Time-mean velocity profiles

a) Laminar Flow
b) Turbulent Flow

In Fig.1[b] three measured turbulent velocity are shown; one of the profiles was taken in steady flow at Re=4000, while for the other two the amplitude of pulsations was varied. No significant difference could be observed between steady and pulsating time mean velocity profiles whether in laminar or turbulent flows. This result could be anticipated in fully developed laminar flow, because of the resulting linearity of the Navier-Stokes equations, but in turbulent pulsating flow it indicates, that the time mean Reynolds stresses are not affected by the harmonic oscillations.

The friction coefficient λ, calculated from Darcy's formula

$$p/\rho = \lambda L/D\, \bar{U}^2/2$$

did not show any difference between steady and pulsating flows for both laminar and turbulent regimes. The measured friction coefficient in laminar flow was higher by about 10%, than the theoretically predicted value of 64/Re. In turbulent flow, the measured value of is in fair agreement with the values quoted in the literature for smooth pipes (see H.Schlichting (1975)).

Phase Averaged Values: Laminar vs. Turbulent Flow

Typical time dependencies of the phase averaged velocities in a tubulent pulsating flow are shown in Fig.2 and the concommitant reference pressure oscillations are shown at the top of the Figure. Each velocity trace is normalized by the time mean velocity on the center line of the pipe. The uppermost velocity trace corresponds to r/R=0 (i.e. the velocity was measured on the center line) and the bottom trace represents the velocity at r/R=0.97. During a fraction the period the pressure at the inlet of the pipe is lower than at the exit pointing to the existence of an adverse pressure gradient. The velocity however does not reverse itself at all radial posi-

tions and all phase angles. The validity of the assumption that pressure and velocity oscillations are harmonic may be checked by representing the ensemble averaged signals in Fourier series.

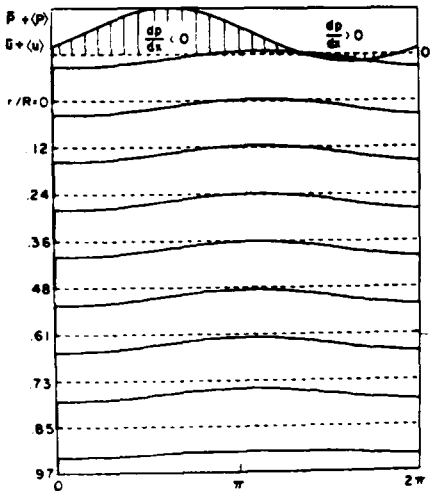

Fig. 2 Phase averaged velocities and pressure

The "power" spectra were calculated, and the ratio of the first two coefficients $c(2\omega)/c(\omega)$, i.e. the coefficient of the fundamental frequency and its first harmonic, was determined. For moderate amplitudes of velocity pulsations, this ratio was less than 3% thus providing the justification for the harmonic assumption. At high amplitudes, in turbulent pulsating flow, partial relaminarization occurs making the contribution of the second harmonic more significant.

The harmonic character of pulsations enables one to represent the instanteneous velocity by an exponential form (Eq.(3)), and aleviates the necessity of describing the temporal and spatial changes in velocity by plotting a large number of phase averaged velocity profiles. Two functions can fully describe the phase averaged component of the velocity at the imposed frequency: (i) the amplitude distribution $u_1(r)$; (ii) the phase angle $\phi_u(r)$ relative to the phase of the pressure oscillations. The fully developed laminar pulsating pipe flow depends on Re and on a dimensionless frequency parameter $\alpha = R\sqrt{\omega/\nu}$ which is referred to at times as Womersley number. In the absence of viscosity, the pressure, being the only driving force, is in phase with the acceleration of the fluid. The velocity lags by 90° behind the acceleration, and thus also lags behind the pressure. The radial distribution of the phase angle is shown in Fig.3 for Re=4000 and for various periods of oscillations. The solid lines show the theoretical prediction of Uchida(1956), while the crosses and the triangles give the measured phase angles in fully developed laminar and turbulent flows, respectively. A good agreement with theory was obtained for the laminar case, with the exception of the very low frequencies which are most sensitive to the influence of the entrance region. The phase lag on the center line of the pipe in laminar flow is usually 90°, and it decreases to approximately 45° near the wall.

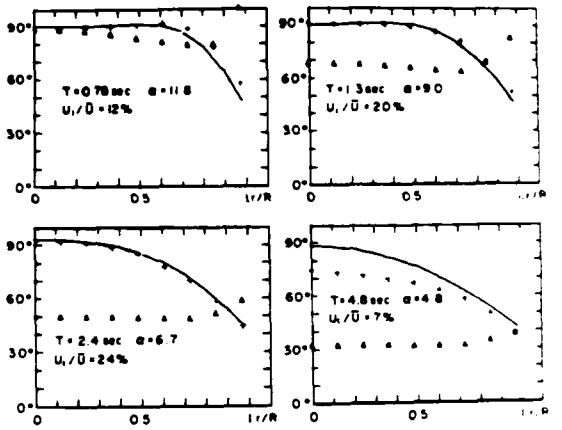

Fig. 3 The radial distribution of ϕ_u in laminar and turbulent flows.

In turbulent flow the results appear to be very different. The frequency parameter $\alpha = R\sqrt{\omega/\nu}$ no longer controls the flow because the relevant viscosity is no longer ν but some turbulent exchange coefficient ε, which is orders of magnitude larger than ν. The effective α is thus much lower, and the angle ϕ_u in the central region of the pipe decreases more quickly with increasing period than in the corresponding laminar flow. In contrast to laminar flow, however, the phase lag increases towards the wall; the qualitative nature of this result was noticed by Ramaprian and Tu (1980). A more detailed explanation of this phenomenon, based on a simple turbulent model will be discussed later.

The qualitative difference between laminar and turbulent pulsating flows also exists in the radial distribution of the amplitudes of the velocity oscillations. In laminar flow, the maximum amplitude of the velocity oscillations occurs in the Stokes layer near the wall, as noticed already by Richardson (1927/28), while in turbulent flow the maximum amplitudes occur in the center of the pipe. The radial distribution of the measured amplitudes of velocity oscillations in laminar and turbulent flows, resulting from identical forcing, is shown in Fig.4. The theoretically calculated amplitudes in laminar flow which were matched on the center line (Uchida (1956)) are shown also in Fig.4 for comparison. In turbulent flow the amplitude is uniform in the central region of the pipe, but decreases rapidly near the wall. The amplitude of pulsations in laminar flow also decreases near the wall. Increasing the mean Re or decreasing the frequency of oscillations leads, in turbulent flow, to a more uniform distribution of the velocity amplitudes.

The Effect of Forcing on Turbulence

There is no doubt, that some information related to the structure of the turbulent flow is lost by the conventional and phase locked averaging proce-

dure. The oscillating part of the velocity during a single period, measured by the hot-wire rake and compared with the signature of the pressure oscillation, is shown in Fig.5.

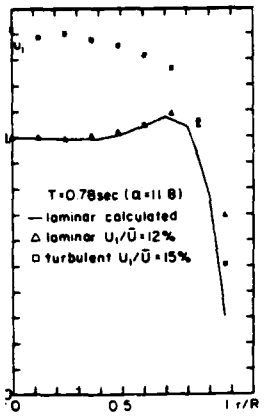

Fig. 4 Radial distribution of velocity amplitude

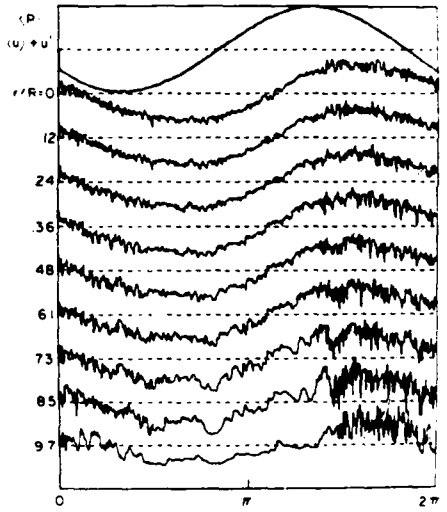

Fig. 5 Perturbation velocity during one period of oscillations

A partial laminarization of the flow is observed during the time at which the velocity is low. The amplitude of the turbulent fluctuations increases quite suddenly while velocity is high, but it decreases gradually during the decelerating portion of the cycle.

Time averaged Reynolds stresses $-\overline{u'v'}$ which were measured by an x-wire, are independent of the flow pulsations (Fig.6a); this was inferred earlier from the similarity of time-mean velocity profiles. The fact that the time mean pressure drop along the pipe is independent of forcing, also indicates, that the pulsations have nearly no effect on the mean Reynolds stresses.

The radial distribution of the oscillating part of the Reynolds stresses for two amplitudes of pulsations is shown in Fig.6[b]. The measured values of $\langle u'v' \rangle$ were rendered dimensionless when divided by the amplitude of the pulsations of u_θ which in turn deduced from the oscillatory component of the pressure drop.

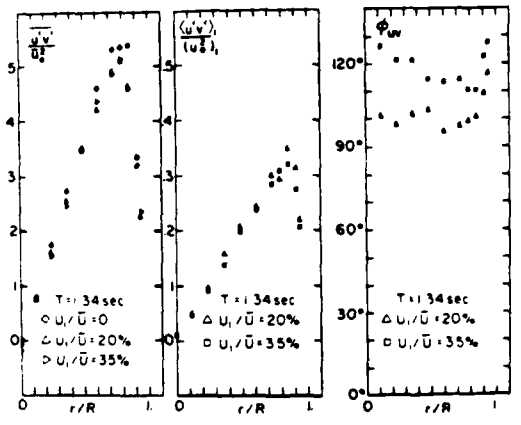

Fig. 6 Radial distribution of u'v' fluctuations
a) time mean $\overline{u'v'}$
b) amplitude
c) phase angle ϕ_{uv}

Normalized in that way, the amplitudes of the Reynolds stress appear to be independent of the amplitude of the pulsating bulk velocity. Qualitatively, the radial distribution of the amplitude of $\langle u'v' \rangle$ resembles the time mean $\overline{u'v'}$, both are proportional to the radial distance r in the central region of the pipe, but the pulsating $\langle u'v' \rangle$, attains a maximum value closer to the wall, than the time mean Reynolds stress.

The phase of $\langle u'v' \rangle$ lags behind the pressure and attains a minimum (Fig.6c) not far from the wall ($0.7<r/R<0.8$). The location of this minimum depends on the amplitude of the forcing.

AN EDDY VISCOSITY MODEL FOR TIME DEPENDENT FLOWS

In pulsating pipe flow, the amplitudes and phase angles of the oscillating pressure, velocity and shear stress are mutually dependent. Therefore the qualitative difference in the radial distribution of ϕ_u between laminar and turbulent flows (Fig.3) results from the different behaviour of the oscillating part of the shear stress in both regimes. The oscillating parts of the laminar and turbulent velocity profiles at high values of α are vaguely similar, suggesting that a proper use of an eddy viscosity model may provide a qualitative answer for the behaviour of the oscillating turbulent flow, in particular for the vastly different radial distribution of the phase.

The eddy viscosity for the time dependent part of the flow is different from the eddy viscosity for the steady flow. Following Maruyama (1974) and using the Prandtl's mixing length approach, the expressions for the shear stress and the eddy viscosity are:

$$\tau = \rho\varepsilon \frac{\partial u}{\partial r} \quad \rho\ell^2\left(\frac{\partial u}{\partial r}\right)^2 \; ; \; \varepsilon = \ell^2 \frac{\partial u}{\partial r} \qquad (4)$$

where ℓ is the mixing length. Introducing the de-

composition for the steady and time dependent parts of the phase averaged velocity $u=\bar{u}+\langle u\rangle$ and substituting into Eq.(4), and neglecting terms of second order yields:

$$\tau = \rho\ell^2 \left(\frac{\partial u}{\partial r}\right)^2 + 2\rho\ell^2 \frac{\partial \tilde{u}}{\partial r}\frac{\partial \langle u\rangle}{\partial r} \qquad (5)$$

thus implying that the eddy viscosity of the oscillating flow is:

$$\varepsilon_1 = 2\ell^2 \frac{\partial \tilde{u}}{\partial r} = 2\varepsilon = \frac{\partial \tau}{\partial(\partial u/\partial r)} \qquad (6)$$

The simple model of Prandtl which uses a constant length-scale, gives for the time dependent part of the shear stress an eddy exchange coefficient ε_1 which is twice the conventional, steady eddy viscosity.

For a more complex model, like the one of Van Driest (Launder and Spalding (1972)), the relation between ε and ε_1 is not as simple. In order to obtain the eddy viscosity which represents the dependence of the shear stress on the velocity profile, the radial distributions of the velocity gradient and of the shear stress were calculated for two slightly different values of the friction velocity u_* from equations of Van Driest. The eddy viscosity for the oscillating flow was then calculated following Eq.(6) from the equation:

$$\varepsilon = -\frac{(r/R)\Delta u_*^2}{\Delta(\partial u/\partial r)} \qquad (7)$$

The use of eddy viscosity suggests that the shear stress is proportional to the instantaneous value of the local velocity gradient, irrespective of to the rate of change of the phase-averaged flow. A careful examination of the experimental data reveals, that this is not always a valid assumption. From the definition of an eddy viscosity one obtaines

$$(\varepsilon_1-\nu)\frac{\partial \langle u\rangle}{\partial r} = -\langle u'v'\rangle \qquad (8)$$

The phase angle of the Reynolds stress is thus related to the velocity gradient $\partial\langle u\rangle/\partial r$. With the radial distribution of both amplitude $u_1(r)$ and phase angle $\phi_u(r)$ of the velocity oscillations known, the time dependent velocity gradient is:

$$\frac{\partial \langle u\rangle}{\partial r} = \left(\frac{\partial u_1}{\partial r} + iu_1\frac{\partial \phi_u}{\partial r}\right) e^{i(\omega t+\phi_u)} \qquad (9)$$

The phase angle of $\partial\langle u\rangle/\partial r$ may thus be calculated from Eq.(9). The experimentally observed radial dependencies of $u_1(r)$ and $\phi_u(r)$ are slowly varying function of r with the exception of the wall area, thus the differentiation of these curves will inevitably result in a large experimental error. Consequently, an accurate evaluation of the eddy viscosity for the oscillating part of the flow from the measured values of $\langle u'v'\rangle$ and $\partial\langle u\rangle/\partial r$ seems impossible in practice.

There exists, however, a point, at which the phase lag $\phi_u(r)$ attains a minimum, resulting in $\partial\phi_u(r)/\partial r=0$ at this particular radial position, and the phase angles of $\partial\langle u\rangle/\partial r$ and $\langle u\rangle$ are identical (Eq.(9)). The experimental data, however, shows a difference in phase of $\langle u\rangle$ and $\langle u'v'\rangle$ at this, as well as at other radial locations. It follows from from Eq.(8), that the turbulent part of the eddy viscosity for the time dependent flow, has to be a complex function which incorporates a phase-shift between $\partial\langle u\rangle/\partial r$ and $\langle u'v'\rangle$. The turbulent structure thus lags behind the instantaneous velocity distribution, and the equation relating the shear stress to velocity gradient has to be modified in order to include a lag in response-time of the Reynolds stress:

$$\langle u'v'\rangle = (\varepsilon_1-\nu)\frac{\partial \langle u\rangle}{\partial r} - \theta\frac{\partial \langle u'v'\rangle}{\partial t} \qquad (10)$$

The second term on the right hand side of Eq.(10) represents the "inertia" of the Reynolds stress, which may be large whenever the change in $\langle u'v'\rangle$ is rapid in comparison with a characteristic time θ, but vanishes for an infinitely slow processes. Substituting into the Eq.(10) the notation of (3) one obtains:

$$\langle u'v'\rangle = \frac{\varepsilon_1-\nu}{1+i\omega\theta}\frac{\partial \langle u\rangle}{\partial r} = \frac{\varepsilon_1-\nu}{\sqrt{1+\omega^2\theta^2}} e^{-i\,\mathrm{arctg}(\omega\theta)}\frac{\partial \langle u\rangle}{\partial r} \qquad (11)$$

which gives an expression for the oscillating eddy viscosity:

$$\tilde{\varepsilon}_1 = \nu + \frac{\varepsilon_1-\nu}{\sqrt{1+\omega^2\theta^2}} e^{-i\,\mathrm{arctg}(\omega\theta)} \qquad (12)$$

Eq.(12) indicates that the argument of the complex eddy viscosity, as well as it's absolute value are frequency dependent. At high frequencies relative to the relaxation time $\theta(\omega\theta >>1)$ the absolute value of the eddy viscosity for the oscillating flow decreases, and the Reynolds stress becomes independent of the phase angle. Thus, the turbulence depends on the mean flow only, while the pulsations are governed by the molecular viscosity and are in this sense laminar; although the mean flow remains fully turbulent.

As mentioned earlier, the phase difference between $\langle u'v'\rangle$ and $\partial\langle u\rangle/\partial r$ is known accurately at *one the radial location only, where the phase* of the velocity gradient equals to the phase of the velocity itself. The experimentally measured ϕ_u at T=1.34 sec and $U_1/U=20\%$ attains a minimum at r/R=0.72, and the phase difference between the velocity and the Reynolds stress is equal at this radial position to 30^0 (see Fig.3 and Fig.6c). The relaxation time θ, obtained from the Eq.(11) is therefore $\theta = (\pi/6)/(2\pi/T)=0.12$ sec. Although the relaxation time, should in general depend on the radial position, it is convenient to assume it to be constant across the pipe. The relaxation time therefore is a universal constant for a given mean Reynolds number. Narasimha and Prahbu (1972) used a similar approach to calculate the influence of the finite relaxation time on the development of the turbulent wake in response to a steep change in pressure gradient. Neglecting the dependence of the relaxation time on the transverse coordinate proved, in their case, to have no significant effect on the results of the calculations nor on the agreement with experimental data.

Following equation (12), one may define a critical frequency of pulsations $f_{cr} = \omega_{cr}/2\pi = 1/2\pi\theta = 1.3$ Hz. At $\omega < \omega_{cr}$ the modulus of $\tilde{\varepsilon}$ is practically independent of frequency and equals to a limiting eddy exchange coefficient for very slow pulsations. At $\omega = \omega_{cr}$ the oscillating eddy viscosity decreases to $1/\sqrt{2}$ of its value at $\omega \to 0$. When $\omega > \omega_{cr}$, and $(\omega\theta)^2 >> 1$ $|\tilde{\varepsilon}| \sim 1/\omega$, the amplitude of oscillations in shear stress decreases rapidly with increasing frequency for a given value of $\partial\langle u\rangle/\partial r$. The corresponding critical period of the pulsations is, in this case, $T_{cr} = 1/f_{cr} = 0.75$ sec. For the turbulent structure to become frozen (i.e. for the oscillating eddy viscosity to vanish) the frequency of pulsations has to be much higher than f_{cr}, as may be

deduced from Eq.(12). On the other hand, even at $f<f_{cr}$ the oscillating eddy viscosity still introduces a significant phase angle between $\langle u'v' \rangle$ and $\partial \langle u \rangle / \partial r$, thus influencing the balance among inertia, pressure and viscous forces (Shemer (1981)).

The eddy viscosity for the infinitely slowly oscillating flow was obtained by modifying the Van Driest model according to Eq.(7). The resulting complex eddy viscosity was substituted into the Navier-Stokes equation which was solved numerically.

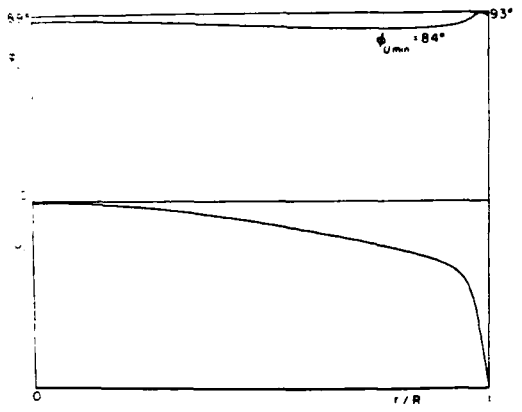

Fig. 7 The calculated radial distribution of $u_1(r)$ and $\phi_u(r)$

The results of the calculations are presented in Fig.7, showing the radial distribution of the amplitudes and phase angles of the oscillating velocity. The calculations were performed for mean Re=4000 and T=1.0 sec. A qualitative agreement with the experimental results was achieved in this way. The calculated radial distribution of ϕ_u is similar to the experimental observation. The calculated angle slightly decreases with increasing distance from the center line, and increases near the wall. It should be noted that efforts to use the real rather than complex value for the oscillating eddy viscosity resulted in the calculated radial distribution of ϕ_u which resembled ϕ_u in laminar flow, and decreased monotonically with increasing r/R.

The calculated values of $\phi_u(r)$ differ from the experimentally measured angles, implying that the theoretical model is not sophisticated enough to provide an exact balance between viscous, inertia and pressure forces, and perhaps it is not adequate for the low Reynolds number used. Nevertheless, even the very simple model which accounts for finite response-time of the turbulent structure to the rapidly changing mean flow appears to be qualitatively correct.

REFERENCES

1. Hussain,A.K.M.F.,and Reynolds,W.C. 1970 J. Fluid Mech. 41, p.241

2. Launder,B.E., and Spalding,D.B. 1972 Lectures in Mathematical Models of Turbulence, Academic Press, London

3. Maruyama,T. 1974 Transport Phenomena in Pulsating Pipe Flow, Kyoto University

4. Narasimha,R., and Prabhu,A. 1972 J. Fluid Mech. 54, p.1

5. Ramaparian,B.R., and Tu,S.W 1980 J. Fluid Mech. 100, p.513

6. Richardson,E.G. 1927/28 Proc. Phys. Soc. 40, p.206

7. Schlichting,H. 1960 Boundary Layer Theory, McGrow-Hill, New-York

8. Shemer,L. 1981 Ph.D. Thesis, Tel-Aviv University

9. Wygnanski,I.J., and Champagne,F.H. 1973 J. Fluid Mech. 59, p.281

MEASUREMENTS OF THE PERIODIC VELOCITY OSCILLATIONS NEAR THE WALL IN UNSTEADY TURBULENT CHANNEL FLOW

G. BINDER and J.L. KUENY

Institut de Mécanique

Université Scientifique et Médicale de Grenoble

Institut National Polytechnique

B.P. 53 X, 38041, GRENOBLE-CEDEX, FRANCE

ABSTRACT

Measurements in turbulent channel flow with forced velocity oscillations of small amplitude have been performed over a wide range of frequencies. The results show that the mean flow and the mean turbulent intensity are not affected by the forced oscillations. The amplitude and the phase shift of the periodic velocity fluctuation follow the laminar Stokes solution at high frequency. A low frequencies near the wall the gradient of the amplitude becomes steeper than in the Stokes flow and the phase shift decreases to slightly negative values. Further from the wall a phase lead is again observed. The results also show that the phase averaged longitudinal turbulent intensity is not simply proportional to the velocity oscillations ; the amplitude ratio is position and frequency dependent. It is shown that the Stokes thickness ℓ_s^+ non-dimensionalized with the mean viscous sublayer thickness is the important parameter.

NOMENCLATURE

A_{nq}	amplitude of n^{th} mode of q
f	frequency of forced oscillations
f_t	characteristic frequency of turbulence
f_v	frequency of validation of the laser Doppler signal
h	channel half hight
$\ell_s = \sqrt{2\nu/\omega}$	Stokes length
$\ell_\nu =$	viscous wall length scale
t	time
T	period of forced oscillations
u	longitudinal velocity
u_τ	shear velocity
x,y	longitudinal and transverse coordinates
ϕ_{nq}	phase lead of n^{th} mode of q
ν	kinematic viscosity
τ	wall shear stress
$\omega = 2\pi f$	
$y_s = y/\ell_s$	
$( )^+ = ( )/\ell_\nu$	
$( )_c$	centerline
$\overline{( )}$	time mean
$\widetilde{( )}$	periodic fluctuation
$( )'$	turbulent fluctuation
$\| \|$	amplitude of periodic fluctuation
$\langle ( ) \rangle = \overline{( )} + \widetilde{( )}$	ensemble average
$q = \bar{q} + \tilde{q} + q'$	for any quantity q
$\langle q \rangle = \bar{q} + \sum_{n=1} A_{nq} \cos(n\omega t + \phi_{nq})$	

INTRODUCTION

Many flows of practical importance in aerodynamics, hydrodynamics, turbomachines, bio-fluid dynamics are unsteady. Yet, in the turbulent regime these flows are not well if at all understood even in the simplest case as the flow over a flat plate.

Experimental investigations of unsteady turbulent boundary layers have so far been rather scarce and have yielded little information on the wall layer. For instance, such vital information as the amplitude and phase shift of the wall shear stress is almost completely lacking. On the other hand, several turbulent closures developped for steady flows have been applied to unsteady flows but their predictions of the wall shear stress differ considerably from one another giving even different trends for its phase shift towards large non-dimensional frequencies (fig. 6 of ref. 6). Since there is little experimental data available with which the various predictions can be confronted, it is difficult to evaluate the merits and defects of the various models.

The need for measurements in unsteady turbulent boundary layers is also patent and has been stressed many times in recent years. The purpose of the present investigation is to provide some data in this field and to contribute to the understanding of unsteady turbulent flows.

APPARATUS. INSTRUMENTATION. DATA ACQUISITION

The measurements are performed in a water channel : length : 2600 mm, height, 2h = 100 mm, span : 1000 mm , u_c = 0-50 cm/s. The test section is 1000 mm long and located at the down stream end. A divergence, adjustable up to about 20°, can be imposed on the section walls in order to subject the flow to a mean unfavourable pressure gradient. The oscillating flow is driven by a reciprocating piston with adjustable speed and stroke mounted on the caisson upstream of the grids and honeycomb. The return flow is via a free surface in order to minimize the effects of unsteady gradients.

The velocities were measured with a laser-Doppler velocimeter operating in the fringe mode. The period of the Doppler signal was determined with a counter. Since one the goals was to perform measurements close to wall it was necessary to minimize the size of the probe volume. The waist of the focused beam was reduced to 0.05 mm by making use of a beam expander (5X). The half angle between the beams was about 6° and the resulting length of the probe volume was 0.8 mm. With this optical arrangement it was possible to make measurements as close as 0.25 mm from the wall corresponding to $y^+ \simeq 2$ for u_c = 17.5 cm/s. No correction for probe volume truncation was necessary. Owing to the small size of the probe volume the shear noise contributed only 3% to the measured turbulent intensity at $y^+ = 3$.

Great flexibility in the characteristics of the emission optics was achieved by use of standart optical components mounted on benches fixed onto a rigid plate.

The Doppler counter is intrinsically a digital period-meter delivering a digital word for every validated Doppler period. This word is fed into a microprocessor were the phase locked ensemble averages are performed. It is also programed to perform simple time integration. The averaged data is transferred to a computer (HONE 10) were it is stored and analysed.

Averaging on the microprocessor is performed directly on the Doppler periods. It may be shown that the mean velocity in turbulent flow obtained from the mean Doppler period is not biased towards the larger velocities as would be the case if the mean frequency were used (TIEDERMAN effect).

AVERAGING PROCEDURE

Ensemble averaging is done at 100 points equally spaced over the period called channels hereafter for the sake of clarity. A problem arises because the phase averaging has to be performed on digital values arriving randomly in time and not from a continuous analog signal as from a hot wire. For this reason, the average in the i^{th} channel is calculated by taking all the values arriving at the microprocessor during the time interval $iT/100$ to $(i+1)T/100$ from the beginning of each cycle. The maximum difference in phase angle between the values averaged in any channel is therefore $\pm 1.8°$. Thus, if f_v is the average frequency at which the validated values occur (roughly equal to the average number of Doppler bursts per second), then the average number of values contributed to the average in one channel during one cycle is $f_v/100f$. In particular, if $f_v < 100\,f$ a sample is not contributed to the average at every cycle.

Let us notice that a systematic error is introduced if the analog output of a counter provided with a circuit holding the previous value between successive validations were periodically sampled by taking one value in each channel at each cycle. It can easily be shown that for a sin-wave the measured amplitude would be reduced by $f_v/\pi f \sin(\pi f/f_v)$ and the phase would lag by $\pi f/f_v$. In addition there would also be an artificial increase in the measured turbulent intensity $\langle u'^2 \rangle$. For $f_v = 10f$ the phase lag would be 18°, also almost half the maximum phase lead of the velocity observed in unsteady boundary layers. This is even more serious because f_v depends upon the rate at which the particles cross the probe volume (proportional to $\langle u \rangle$) and to the quality of the Doppler-signal, two factors which both decay rapidly as the wall is approached. The phase lags of the velocity published previously [6] may be accounted for by this systematic error. Such an error is, of course, avoided by the present phase averaging scheme.

This scheme has in addition the advantage of accelerating the statistical convergence -especially slow near the wall where the turbulence intensity is high- when $f_v > 100f$, as long as roughly $f_v \leq 10 f_t$, where f_t is the characteristic frequency of the turbulent energy containing eddies. This is especially useful at low forcing frequencies which in the present experiments were as small as 0,07 Hz. If in this case only one sample were taken at each point per cycle, than it would take almost four hours to complete one phase average with a sample size of 1000 values per channel. Actually such a sample size proved to be insufficient near the wall even for $\langle u \rangle$ and quite inadequate for $\langle u'^2 \rangle$. The uncertainty on the phase due to insufficient statistical convergence is especially large.

f_v depends upon many factors among which some escape any precise control. The measurements reported here correspond therefore to an average of 5000 samples per channel or an integration over one hour. This proved to be adequate for $\langle u \rangle$ as shown on figures 1 and 2 corresponding to measurements on the centerline and at $y^+ = 4.6$ for $\overline{u}_c$ = 17.5 cm/s. It may be observed that there remains appreciable scatter about the fundamental Fourier mode near the wall. $\langle u'^2 \rangle$ at the same point is shown on fig. 3 ; the periodic variations of

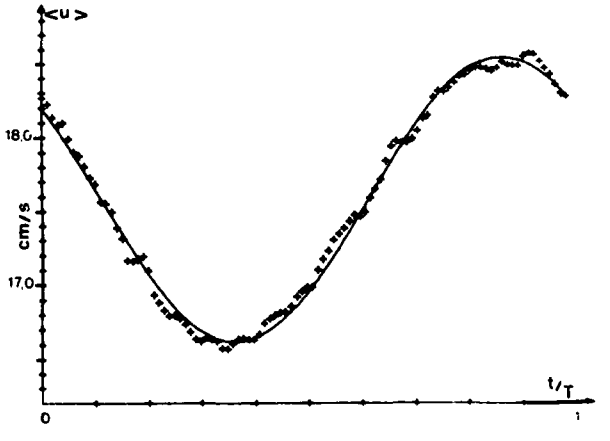

Fig. 1 - Ensemble averaged velocity on channel centerline.
T = 7.32 s - 5000 samples/channel
A_o = 17.6 cm/s A_1 = 3.96 cm/s
A_2/A_1 = 5.5 % - A_3/A_1 = 2.5 %

the turbulent intensity are clearly distinguishable from the random scatter. It should, finally, be remarked that the present measurements correspond to amplitudes of the forced oscillations on the centerline of 5% or less. For larger amplitudes the statistical scatter would be relatively smaller.

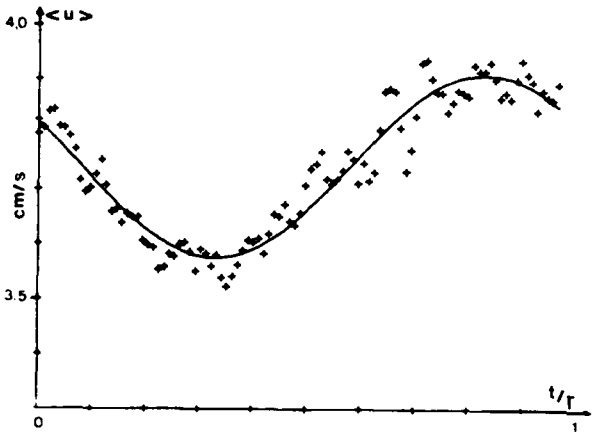

Fig. 2 - Ensemble averaged velocity at $y^+ = 4.6$
$T = 7.32$ s.
5000 samples/channel
$A_o = 3.74$ cm/s $A_1 = 0,166$ cm/s
$A_2/A_1 = 11.3\%$ $A_3/A_1 = 1,7\%$

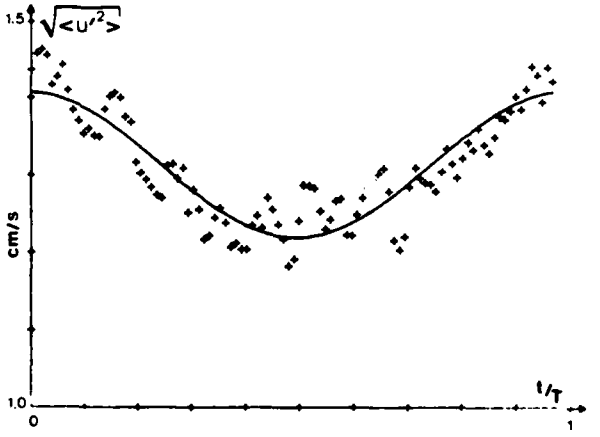

Fig. 3 - Ensemble averaged turbulent intensity at
$y^+ = 4.6$ - $T = 7,32$ s.
5000 samples/channel
$A_o = 1.31$ cm/s $A_1 = 0,094$ cm/s

EXPERIMENTAL CHECKS

The two-dimensionality of the flow was checked at three stations 10 h apart from each other. The mean flow is established at least 10h upstream of the section $X = 2,4$ m where the measurements were taken for the velocity $u_c = 17,5$ cm/s.

The instrumentation and data acquisition were checked in two ways. Firstly in steady turbulent flow in the channel where good agreement was found for both u/u_τ and $\sqrt{\overline{u'^2}}/u_\tau$ vs y^+ with previous measurements (fig. 4,5) and secondly in laminar oscillating flow in an oil channel where good agreement was found for the amplitude A_u and the phase shift φ_{1u} vs y_s with the theoretical values of the Stokes flow.

Vibrations of the wall generated by the oscillating pressure could produce large systematic errors on $\tilde{u}$ especially close to the wall where $\partial\tilde{u}/\partial y$ is large. It should first be remarked that the oscillating pressure in a given section is proportional to $\partial\tilde{u}/\partial t$ and hence to $\omega|\tilde{u}|$. The problem of wall vibrations is therefore most severe with high frequency and large amplitude oscillations. These vibrations were measured with an ultra-sonic depth gage having a sensitivity of 10μm equivalent to $\nu/12$ in the most frequent case. For the highest frequency $f = 0,66$ Hz and an amplitude $|\tilde{u}| = 1.8$ cm/s -almost twice as large as the one used in the experiments reported here-

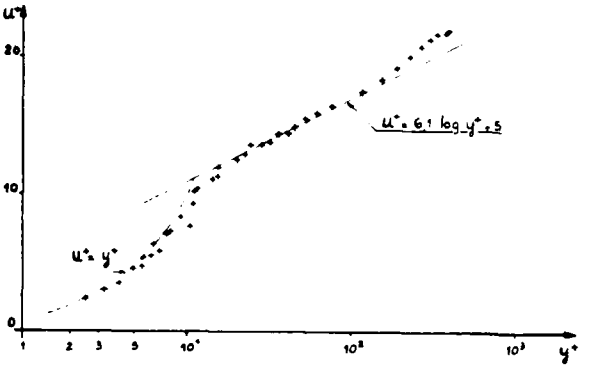

Fig. 4 - Mean velocity in steady and unsteady flow

the wall displacement was to small to be measured. At the same frequency but with an amplitude of 9 cm/s, the maximum displacement was 15 μm. If it is assumed that the displacement is proportional to the amplitude at a given frequency then it is about 1,5 μm also $\nu/80$ in the most severe conditions of these experiments. Since the maximum mean velocity gradient is equal to u_τ/ν at the wall the resulting velocity oscillation is $(\partial\tilde{u}/\partial y)/(\nu/80) = u_\tau/80$. The smallest amplitude measured is about $|\tilde{u}_1|/10$ at $y^+ = 3$. Since $|\tilde{u}_c| \simeq 1$ cm/s and $u_\tau = 0,8$ cm/s in most cases, the largest relative error on the amplitude is about $(u_\tau/80)/(|\tilde{u}_1|/10) = 10\%$. This error decreases with the distance from the wall because $\partial\bar{u}/\partial y$ decreases and $|\tilde{u}|$ increases.

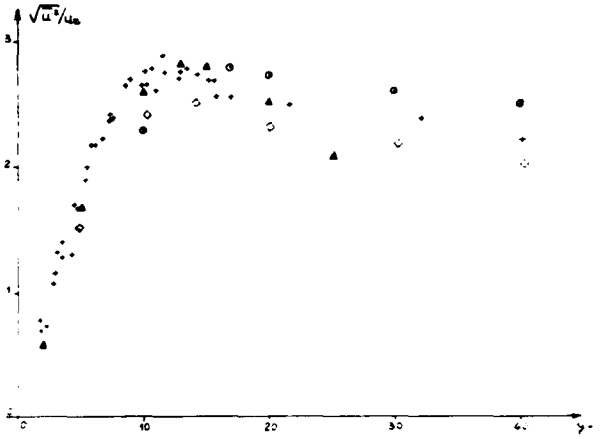

Fig. 5 - Turbulent intensity near the wall in channel flow
Steady flow : ⊙ Comte-Bellot , ▲ Eckelmann
Steady and unsteady flow : ◇ Acharia , + present investigation

An indirect check of the negligible effect of the wall vibrations may be found on fig. 5, where the extrapolations to $y = 0$ of the amplitude data points fall reasonably close to the origine. If the wall vibrations were important the measured amplitudes would not tend to zero with the distance.

EXPERIMENTAL CONDITIONS

All measurements reported here but one set were taken in the following conditions :

$\bar{U}_c$ = 17,5 cm/s u_τ = 1,1 cm/s R_{eh} = 6,5 x 10^3

$A_{u_\tau}/\bar{u}_\tau$ = 5% T = 3,7 - 11,5 s Ω_h = 3,5 - 9,1

The corresponding range of the non-dimensional Stokes length is ℓ_s^+ = 3,5 - 16,6.

In order to obtain smaller reduced frequencies, the centerline velocity had to be increased. The lowest frequency case corresponds to the following conditions :

$\bar{U}_c$ = 50,2 cm/s u_τ = 1,9 cm/s R_{eh} = 25 x 10^4

$A_{u_\tau}/\bar{u}_\tau$ = 2% T = 13,5 s Ω_h = 8,046

ℓ_s^+ = 39,-

Because the piston producing the oscillatory motion has a limited stroke, the amplitude could at most be 2% with this value of $\bar{U}_c$ and f. The amplitude of the second harmonic of the forced velocity oscillations on the centerline was less than 6% of the fundamental and the amplitude of the higher harmonics was less than 1%.

The reproducibility of the oscillating flow on the channel centerline was ± 2,5% r.m.s. for the amplitude and ± 1,1° r.m.s. for the phase of the fundamental mode.

RESULTS AND DISCUSSION

Mean velocity and mean turbulent intensity

Mean velocity profiles measured in oscillating flow are indistinguishable from the steady flow curve at all frequencies tested (fig. 4). This confirms the previously published results (4, 6, 9) but is at variance with the latest data of RAMAPRIAN and SHUEN-WEI (7) whose profile seems to show a point of inflexion near the wall. These authors argue that the mean flow in their experiment has been affected by the periodic oscillations because the forcing frequency f is of the same order as the characteristic frequency f_c of the turbulence ($f \simeq f_c$) and that an interaction between the two types of fluctuations takes place. Since our highest Strouhal number based on the half channel width $\Omega_h \simeq 1,2$ is even larger than the one of RS which was about 0,5 ($R\omega/u_\tau$ in their case ; pipe radius : R), this argument alone cannot explain the differences between these observations. It should be added that the highest frequency in Karlsson's [5] experiment and the two frequencies used by ACHARIA [1] were also such that $f \simeq f_c$ and no effect on the mean flow was observed.

The other parameter which, together with the frequency, would affect the turbulence and therefore the mean flow is the relative amplitude of the oscillation. This parameter is quite different in [7] and the present experiments, being respectively about 35% and 5%. In KARLSSON's measurements at high amplitude (33%) and at a medium or hight frequency, their seems to be a slight effect on the mean velocity but from the plotted data, it is difficult to conclude whether this effect is significant or not. In the present work the amplitude had to be kept small in order to avoid flow reversals near the wall because the laser velocimeter was not equiped with a frequency shifting device.

The mean turbulent intensity (fig. 5) is not affected either by the forced oscillations as observed in other experiments [4, 6, 9]. The data of the turbulent shear stress in [4, 9] point towards the same conclusion but the measurements could of course not be performed as close to the wall as those of $\sqrt{\overline{u^2}}/u_\tau$. The insensitivity of the turbulence to the forced oscillations explains that of the mean velocity which can only be affected by $\overline{u'v'}$ in channel flow the shear stress of the periodic motion $\overline{\tilde{u}\tilde{v}}$ being zero in channel flow because $\partial\bar{u}/\partial x = 0$ and hence from continuity $\bar{v} = 0$. Actually it is shown in [9] that $\overline{\tilde{u}\tilde{v}}$ is small even in an unsteady boundary layer in a mean unfavorable pressure gradient.

Periodic velocity oscillations

The evolutions of the amplitude and of the phase of the fundamental mode of the forced oscillations vs the non-dimensional distance y_s ($y_s = y/\ell_s$) for five cases are shown on figures 6 and 7. The parameter $\ell_s^+ = \ell_s/\ell_\nu$ measures how far the viscous Stokes layer extends into the inner layer of the steady turbulent wall flow. It is clear that small values of ℓ_s^+ correspond to high frequencies.

Despite some differences, it is quite remarkable how close the amplitudes fall to the laminar Stokes layer in all cases for $y_s < 1$. To within about ± 50% the slope $(\partial A_{u_\tau}/\partial y)_w$ at the wall is that of the laminar oscillating flow. This behaviour contrasts sharply with that of the mean flow where the gradient at the wall in the turbulent case u_τ/ℓ_ν is at least an order of magnitude steeper than in the laminar regime $\bar{U}_c/h$, the ratio being $(u_\tau/\bar{u}_c)\cdot(u_\tau h/\nu) = (u_\tau/\bar{u}_c)\,R_{eh}$, where typically $20 < u_c/u_\tau < 40$. The diffusion of the oscillating wall shear stress into the fluid seems also little affected by the presence of the turbulence produced by the mean flow.

In the two high frequency runs $\ell_s^+ = 5,5$ and 7 the amplitude and the phase follow the laminar Stokes curve quite closely. In particular there is a large phase lead near the wall. The scatter of the data points is sufficiently small that the extrapolation to $y = 0$ is significant yielding a 45° phase lead at the wall as in laminar flow. KARLSSON (4) mentions that the largest phase lead obtained was 35° at $y = 0,01"$ for $\ell_s^+ = 11$ inferred from his data. The corresponding Stokes flow at the same distance gives a phase lead of 36° which confirms the present high frequency results despite the difference in ℓ_s^+. PARIKH et al (9) also find a steep raise of the phase with a lead up to 30° near the wall at their highest frequency. An appreciable undershoot of the amplitude for $\ell_s^+ = 5,5$ is observed beyond $y_s = 2$ which does not exist in laminar flow.

ACHARIA's (1) phase results are completely different since he measured a phase difference at the wall of about 180° for $\ell_s^+ = 7,1$. The present $\ell_s^+ = 7$ case was run precisely in order to be as close as possible to ACHARIA's experimental conditions. No plausible explanation for the large discrepancy in the phase angle between the two experiments has been found. But the amplitudes agree qualitatively.

The main features of the high frequency behaviour may be understood if it is recalled that in the steady turbulent wall flow the turbulent shear-stress is smaller than the viscous one for $y^+ < 12$ and if it is observed that the thickness of the viscous Stokes layer is about $2y_s$. Hence, below $y^+ = 12$, $\tilde{u}$ (as $\tilde{u}$) is mainly subjected to viscous diffusion and if $2\ell_s^+ < 12$ than the amplitude and phase of $\tilde{u}$ reach the outer values before the turbulence can actively affect them. It is seen that the present high frequency cases $\ell_s^+ = 5,5$ and 7 approximatly satisfy this requirement.

The evolution of $\tilde{u}$ in the low frequency cases is more complexe. In the proximity of the wall a steeping of the amplitude gradient with respect to the Stokes flow is clearly noticeable for $\ell_s^+ = 16,6$ and 39,4. This is to be expected since most of the variations of $\tilde{u}$ are in the fully turbulent part of the inner layer. Yet, it is surprising that there is so little difference between these two cases though the values differ by a factor of 2,5. For large values of ℓ_s^+ one would expect $\partial\tilde{u}/\partial y$ near the wall to become independent of ℓ_s^+. This does not seem to happen or then the value of 39,4 is still too small. It should be remembered that because of the physical limitations of the pulsating device the amplitude on the centerline was only 2% in the latter case. But it is doutful that at such low levels the amplitude itself influences the flow.

The evolutions of the amplitude for $y_s > 0,5$ at the two lowest frequencies are strikingly different. For $\ell_s^+ = 16,6$ $\partial|\tilde{u}|/\partial y$ keeps roughly the same value until the amplitude reaches the outer level as in the high frequency cases while for $\ell_s^+ = 39,4$ the shope of $|\tilde{u}|$ decreases abruptly, a behaviour reminiscent of the mean velocity's.

The intermediate case $y^+ = 12,2$ is somewhat puzzling since near the boundary $|\tilde{u}|$ varies as in the high frequency cases whereas further away it evolves nearly as in the lowest frequency case.

As ℓ_s^+ increases the phase shifts away from the laminar Stokes curve. In particular, the phase lead at the wall tends to zero and becomes negative. Extrapolation to wall except for $\ell_s^+ = 16,6$ is hazardeous because of the scatter of the data especially for $\ell_s^+ = 39,4$. In this latter case the eduction of $\tilde{u}$ from the turbulence is much slower because of the small value of the centerline amplitude and it has been observed that the phase is quite sensitive to the scatter of the points around the fundamental mode (see fig. 8). There is quite a bit of disagreement on the phase among the various experiments but it is felt that an appreciable part may just come from measurement inaccuracies.

Fig. 6 Relative amplitude of fundamental mode of the periodic velocity oscillations vs non-dimensional distance y_s from the wall. ● $\ell_s^+ = 5,5$, ▲ 7.0, O 12,2, ▲ 16,6, ★ 39,4, — laminar Stokes flow.

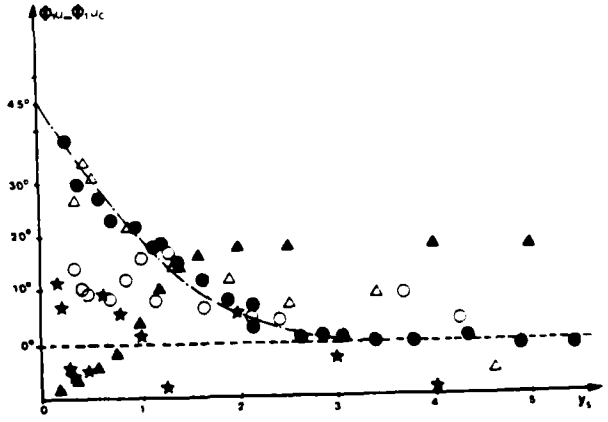

Fig. 7 - Phase of fundamental mode of the periodic velocity oscillations vs non-dimensional distance y_s from the wall for legend see fig. 6

Oscillating wall shear-stress

Since the amplitude of $\tilde{u}$ follows approximately the laminar Stokes solution, the amplitude of the oscillating shear stress is

$$A_{1\tau} \simeq \mu \left(\frac{\partial A_{1u}}{\partial y}\right)_{y\to 0} = \sqrt{2}\,\mu\,\frac{A_{1u_c}}{\ell_s}$$

so that :

$$\frac{A_{1\tau}}{\bar{\tau}} \simeq \sqrt{2}\;\frac{A_{1u_c}}{u_\tau}\cdot\frac{1}{\ell_s^+} \qquad (1)$$

or

$$(A_{1\tau}/\bar{\tau})/(A_{1u_c}/\bar{u}_c) \simeq \sqrt{2}\,(\bar{u}_c/u_\tau)/\ell_s^+ \qquad (2)$$

Let us recall that in a laminar boundary layer this relative amplitude ratio equals $3\sqrt{\Omega_+}$ in the high frequency limit and $h/\sqrt{2}\,\ell_s$ in laminar channel flow. The above relation shows the importance of the non-dimensional Stokes thickness expressed in wall parameters ℓ_s^+. It seems that as long as $\ell_s \ll \delta$ or h that ℓ_s^+ is more relevant than δ/ℓ_s or h/ℓ_s or $\omega\lambda/\bar{u}_c$.

The above relations also show the combined influence of the frequency and of the forcing amplitude on the oscillating shear stress. They further point towards the importance of a mean unfavorable pressure gradient due to the presence of u_τ in the denominator since then $u_\tau \to 0$.

Periodic flow reversal requires $|\tilde{\tau}|/\bar{\tau} > 1$, also :

$$|\tilde{u}|/\bar{u}_c \gtrsim \frac{1}{\sqrt{2}}\,\frac{u_\tau}{\bar{u}_c}\,\ell_s^+ \qquad (3)$$

which shows that the amplitude must be large unless the frequency is very large or u_τ is very small as in a mean unfavorable pressure gradient.

Turbulence is only affected by the strain rate i.e. velocity gradients and not directly by velocity oscillations whatever the frequency so that there can be no effect over the whole layer where $\partial\tilde{u}/\partial y = 0$. The oscillating flow can therefore only modify the turbulence and hence the mean flow if the oscillating gradient $\partial\tilde{u}/\partial y$ contributes substantially to the total gradient $\partial\langle u\rangle/\partial y$ in the wall layer, also if $|\tilde{\tau}|/\bar{\tau} \sim 1$. This requires (3) to hold. In addition, since $\langle uv\rangle \simeq 0$ for $y^+ < 5$ it may be argued that one must also have $\ell_s^+ > 5$ in order to have a substantial contribution to the turbulent production.

Therefore, the mean flow and turbulence can neither be affected if the frequency is low because condition (3) cannot be satisfied unless the amplitude is very large or u_τ very small nor if the frequency is high because ℓ_s^+ is then too small.

Periodic variations of the turbulent intensity

The amplitude of the fundamental mode of the periodic variations of the turbulent intensity $\sqrt{u'^2}$ for four cases are shown on fig. 8 and 9 respectively with respect to u_τ and A_{1u}. As $\sqrt{\overline{u'^2}}/u_\tau$, $A_{1u'}/u_\tau$ tends to zero with y^+, reaches a maximum and slowly decreases to zero as y^+ increases.

Since the amplitude of the run $\ell_s^+ = 39{,}4$ is 2,5 times smaller than in the others, it may be seen that for $\ell_s^+ > 12$ the maximum value of the ratio $\frac{A_{1u'}}{u_\tau}\Big/\frac{|\tilde{u}|}{\bar{u}_c} \sim 4$. The oscillations of the turbulent intensity is also larger than the forcing of the mean flow. It is clear also that these oscillations are much smaller at high frequency as shown by the values for $\ell_s^+ = 7$. This seems to confirm partially the argument above concerning the requirement $\ell_s^+ > 5$ for the turbulence to be affected by the forced oscillations.

These observations are confirmed by fig. 9 where the turbulent intensity variations are referred to the local amplitude of the velocity. It is also seen that the relative intensity near the wall reaches about 50% a value which is twice as large as that of the ratio $\sqrt{\overline{u'^2}}/\bar{u}$ of the means which tends to,24 according to ECKELMANN (3).

There appears also to be an amplification of the turbulent intensity with respect to the imposed velocity oscillations. This should lead to a somewhat weaker requirements than (3) for a modification of the mean turbulence and mean flow.

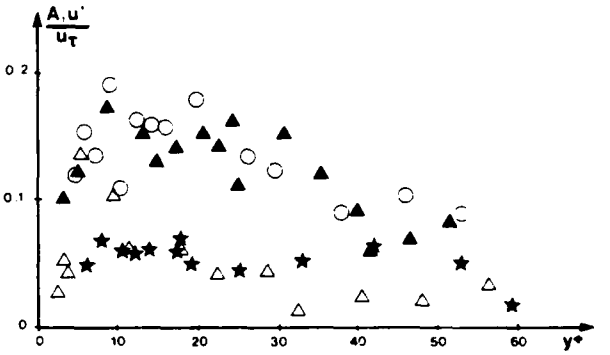

Fig. 8 - Amplitude of fundamental mode of the periodic variations of the turbulent intensity vs y^+. For legend see fig. 6

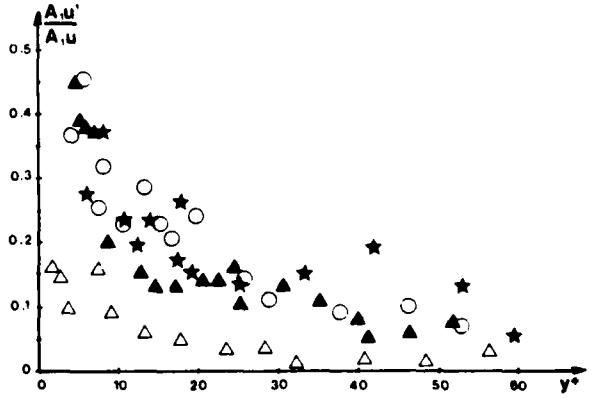

Fig. 9 - Relative amplitude of the periodic variations of the turbulent intensity vs y^+. For legend see fig. 6

ACKNOWLEDGEMENT

Financial support from the Direction des Recherches, Etudes et Techniques from the Ministère des Armées is greatfully acknowledged.

REFERENCES

1. Tellonis, D.P. Unsteady boundary layers separated and attacked, J. Fluids Engineering, 101, 29-43, 1979.

2. Comte-Bellot, G., Ecoulement turbulent entre deux parois parallèles. Publications Scientifiques et Techniques du Ministère de l'Air, 160 p. , 1965.

3. Eckelmann, H., The structure of the viscous sublayerand the adjacent wall region in a turbulent channel flow, J.F.M., 65, 439-459, 1974.

4. Acharya, M., Measurements and predictions of a fully developed turbulent channel flow with imposed controlled oscillations. Stanford Univ., Ph. D., Xeros University Microfilms, Ann Arbor, Mi, réf. 75-25, 492, 1975.

5. Karlsson S.K., An unsteady turbulent boundary layer, J.F.M., 5, 622-636, and Ph. D. Dissertation, The Johns Hopkins University, 1969 (1958).

6. Cousteix, J., Desopper, A., Houdeville, R., Structure and Development of a turbulent boundary layer in oscillatory external flow, Proc. Symp. on Turbulent Shear Flows, Penn. State Univ., Univ. Park, Pa., 1977.

7. Ramaprian, B.R., Shven-Wei Tu, An experimental study of oscillatory pipe flow at transitional Reynolds numbers, J.F.M., 100, 513-544, 1980.

8 Binder, G., Favre-Marinet, M., The inner layer in unsteady turbulent boundary layers, EUROVISC III, Liverpool, 1979.

9 Parikk, P.G., Reynolds W.C., Jayaraman, R., Carr, L.W., Dynamic behaviour of an unsteady turbulent boundary layer, Proceedings IUTAM Symposium on "Unsteady Turbulent Shear Flows" Toulouse, May 5-8, 1981, Springer-Verlag, to appear.

A HYBRID COMPUTING SCHEME FOR UNSTEADY TURBULENT BOUNDARY LAYERS

J. D. Murphy
Ames Research Center, NASA, Moffett Field, California

P. M. Prenter
Colorado State University, Fort Collins, Colorado

ABSTRACT

A new computational procedure for the solution of the unsteady incompressible ensemble-averaged boundary-layer equations is presented. The procedure uses standard second-order accurate finite-difference techniques in the temporal and streamwise marching directions and splined-cubic Hermite polynomials together with orthogonal collocation in the stream normal direction. This latter procedure is fourth-order accurate on a nonuniform mesh. The turbulent shear stress is modeled by means of a scalar eddy viscosity obtained from either the Cebeci-Smith model or the Glushko one-equation model. Any other turbulence model embodying the scalar eddy-viscosity assumption may in principle be incorporated without modification to the solution procedure of the main code. The numerics are verified by comparing the results of the present method with other numerical and analytic solutions for laminar flow with an oscillating free stream. The complete code, including the two turbulence models, is demonstrated by comparing it with other numerical solutions, and with experimental data for oscillating flow over a flat plate and for flow with an oscillating pressure gradient. The results of these comparisons demonstrate that the numerical procedures are satisfactory and that the correct qualitative behavior of unsteady turbulent boundary layers can be predicted with simple turbulence models.

INTRODUCTION

Although unsteady boundary layers have always been important, there appears to be a recent and substantial increase in interest in these flows on the part of both experimentalists and theoreticians. This is a result of the fact that both instrumentation and computation have advanced to the point where many believe they may be usefully brought to bear on the unsteady problem, and to the fact that future high-performance air- and rotorcraft will require the reliable prediction of dynamic flow parameters.

This is not to say that one can expect to predict an arbitrary unsteady turbulent flow reliably but rather that the art of calculation has advanced sufficiently to permit the economical evaluation of various unsteady turbulence models, with some assurance that the purely computational aspects of the study are under reasonable control.

The present method uses splined-cubic Hermite polynomials to represent the stream-normal variation of flow parameters, with the coefficients of these polynomials determined by orthogonal collocation. The streamwise derivatives are represented by classical second-order accurate finite difference approximations and the temporal variation-cum-linearization is accomplished by either a Crank-Nicolson method or by second-order accurate finite differences with Newton-Raphson iteration. The choice of iterative or non-iterative time marching is made by the user. The result is a hybrid finite-element finite-difference scheme which is fourth-order accurate in "Y" and second-order accurate in "X" and "t." The high accuracy in the stream-normal direction is consistent with the boundary-layer assumptions and permits accurate solutions on a relatively coarse mesh.

The present numerical method is a substantial improvement over that of Ref. 1, since it provides the same accuracy with a matrix block size half that of Ref. 1. Applied to the same problem, this would yield a factor of 8 in speed.

In the present paper the new method is applied to turbulent unsteady flows by means of the ensemble-averaged, unsteady boundary-layer equations. In addition, it is assumed that the characteristic frequency of the turbulence is sufficiently remote from that of the mean motion to preclude significant interaction. A scalar eddy viscosity is assumed to provide the relationship between stress and strain tensors. At present, the Cebeci-Smith model (2) and the Glushko turbulence energy equation model (3) have been considered. This latter model has been chosen because it is the simplest model that explicitly includes time dependence.

ANALYSIS

The ensemble-averaged incompressible unsteady boundary-layer equations incorporating a scalar eddy-viscosity relation between stress and strain may be written as:

$$\left.\begin{aligned} &\frac{\partial u}{\partial x} + \frac{\partial v}{\partial y} = 0 \\ &\frac{\partial u}{\partial t} + u\frac{\partial u}{\partial x} + v\frac{\partial u}{\partial y} = -\frac{1}{\rho}\frac{\partial p}{\partial x} + \nu\frac{\partial}{\partial y}\left(1 + \frac{\varepsilon}{\nu}\right)\frac{\partial u}{\partial y} \end{aligned}\right\} \quad (1)$$

Following McCroskey and Phillipe (4), we introduce the coordinate transformation $(x,y,t) \rightarrow (\xi,\eta,\tau)$ where $\xi = x - x_0$, $\eta = (u_e/2\xi\nu)^{1/2}$, and $\tau = \omega t$, yielding

$$\left.\begin{aligned} &\xi\frac{\partial \bar{u}}{\partial \xi} + \frac{\partial V}{\partial \eta} - \frac{\beta_t}{2} + \frac{\bar{u}}{2}(\beta_x + 1) = 0 \\ &\frac{\xi}{u_e}\frac{\partial \bar{u}}{\partial \tau} + \xi\bar{u}\frac{\partial \bar{u}}{\partial \xi} + V\frac{\partial \bar{u}}{\partial \eta} + (\bar{u} - 1)\beta_t + (\bar{u}^2 - 1)\beta_x \\ &\qquad - \frac{1}{2}\frac{\partial}{\partial \eta}(1 + \bar{\varepsilon})\frac{\partial \bar{u}}{\partial \eta} = 0 \end{aligned}\right\} \quad (2)$$

where

$$V = \frac{\eta}{2}\beta_t + \bar{u}\frac{\eta}{2}(\beta_x - 1) + \bar{v}\left(\frac{u_e\xi}{2\nu}\right)^{1/2}, \quad \bar{u} = \frac{u}{u_e},$$

$$\bar{v} = \frac{v}{u_e}, \quad \beta_t = \frac{\omega\xi}{u_e^2}\frac{\partial u_e}{\partial \tau}, \quad \text{and} \quad \beta_x = \frac{\xi}{u_e}\frac{\partial u_e}{\partial \xi}$$

and $\bar{\varepsilon}$ is the dimensionless eddy viscosity. This latter parameter is taken, in the present study, from either the Cebeci-Smith algebraic model or the one-equation model of Glushko. This latter model uses a single differential equation to describe the transport of turbulence kinetic energy in conjunction with an algebraic length scale equation. It is the simplest available model that explicitly admits time dependence in the turbulence field as distinguished from the mean velocity field.

In the stream normal discretization we represent $\bar{u}$, $\partial\bar{u}/\partial\eta$, $\partial^2\bar{u}/\partial\eta^2$, $\bar{V}$, and $\partial\bar{V}/\partial\eta$ in Eqs. (2) by their approximations in terms of cubic Hermite splines. That is,

$$\left.\begin{aligned} \bar{u}(\xi,\eta,\tau) &= \bar{u}_{ijk}N_1(s) + \bar{u}'_{ijk}N_2(s)h_j \\ &\quad + \bar{u}_{ij+1k}N_3(s) + \bar{u}'_{ij+1k}N_4(s)h_j \\ \frac{\partial\bar{u}}{\partial\eta}(\xi,\eta,\tau) &= \bar{u}_{ijk}\frac{N_1'}{h_j}(s) + \bar{u}'_{ijk}N_2'(s) \\ &\quad + \bar{u}_{ij+1k}\frac{N_3'}{h_j}(s) + \bar{u}'_{ij+1k}N_4'(s) \\ \frac{\partial^2\bar{u}}{\partial\eta^2}(\xi,\eta,\tau) &= \bar{u}_{ijk}\frac{N_1''(s)}{h_j^2} + \bar{u}'_{ijk}\frac{N_2''(s)}{h_j} \\ &\quad + \bar{u}_{ij+1k}\frac{N_3''(s)}{h_j^2} + \bar{u}'_{ij+1k}\frac{N_4''(s)}{h_j} \\ \bar{V}(\xi,\eta,\tau) &= \bar{V}_{ijk}N_1(s) + \bar{V}'_{ijk}N_2(s)h_j \\ &\quad + \bar{V}_{ij+1k}N_3(s) + \bar{V}'_{ij+1k}N_4(s)h_j \\ \frac{\partial\bar{V}}{\partial\eta}(\xi,\eta,\tau) &= \bar{V}_{ijk}\frac{N_1'(s)}{h_j} + \bar{V}'_{ijk}N_2'(s) \\ &\quad + \bar{V}_{ij+1k}\frac{N_3'(s)}{h_j} + \bar{V}'_{ij+1k}N_4'(s) \end{aligned}\right\} \quad (3)$$

where $\bar{u}_{ijk}$, $\bar{u}'_{ijk}$, $\bar{u}''_{ijk}$, etc. are the node point values of $\bar{u}$, etc., and their derivatives and N_i's are the cardinal cubic Hermite polynomials on the unit interval, shown in Table 1.

Table 1
Cubic Hermite Polynomials

$N_1(s) = (s-1)^2(2s+1)$	$N_1'(s) = 3s(2s-2)$
$N_2(s) = s(s-1)^2$	$N_2'(s) = (s-1)(3s-1)$
$N_3(s) = s^2(3-2s)$	$N_3'(s) = 6s(1-s)$
$N_4(s) = s^2(s-1)$	$N_4'(s) = s(3s-2)$
$N_1''(s) = 6(2s-1)$	where $s = \frac{y - y_j}{h_j} = S_j(y)$,
$N_2''(s) = 2(3s-2)$	
$N_3''(s) = 6(1-2s)$	$h_j = y_{j+1} - y_j$
$N_4''(s) = 2(3s-1)$	

These relations (3) are substituted into Eqs. (2) which are then collocated at the $2N - 2$ Gauss points to yield $4N - 4$ partial differential equations in X and t. The theoretical background for this procedure is given in Ref. 5.

The X-derivatives are eliminated by the substitution of second-order accurate finite-difference approximations, and the temporal derivatives are treated in either of two ways. For attached laminar flow, the time marching is carried out by a standard Crank-Nicolson method with the usual linearization. If the flow is turbulent or separated (i.e., contains backflow) the time differencing is done by second-order accurate backward differences with Newton-Raphson iteration. The rationale behind this dichotomy is that despite the additional work required by the iteration scheme, the interchangeable module for turbulence modeling is more readily accommodated within the iterative procedure, and the linearization error in the neighborhood of a moving separation point may be significant in comparison with the temporal truncation error.

The resulting linearized algebraic system is advanced one time-step, or one iteration, at each X-station, by the solution of a 4×4 block tridiagonal system having N blocks along the diagonal, where N is the number of mesh points normal to the wall.

The boundary and initial conditions are prescribed as follows:

1. At $x = x_0$ for all y and t, we prescribe $\bar{u}_{ijk}$, $\bar{v}_{ijk}$, $\bar{u}'_{ijk}$, and $\bar{v}'_{ijk}$. This can be accomplished in the present code by calling for steady similarity solutions.

2. At $t = t_0$ for all X and Y, we prescribe $\bar{u}_{ijk}$, $\bar{v}_{ijk}$, $\bar{u}'_{ijk}$, and $\bar{v}_{ijk}$. This can be accomplished in the present code by calling for steady nonsimilar boundary layer solutions.

3. At $Y = 0$, for all X and t, $\bar{u}_{ijk} = 0$ and $\bar{v}_{ijk} = 0$.

4. At $y = y_{max}$ for all X and t, $\bar{u}_{iNk} = 1.0$ and $\bar{v}'_{iNk} + 0.5\,x(\beta_x - \beta_t + 1) = 0$.

Note that the algebraic system solved in $\bar{u}$, $\bar{u}'$, $\bar{V}$, and $\bar{V}'$ requires four boundary conditions as opposed to the three boundary conditions required by the differential system. The additional condition, on $\bar{V}'$ at Y_{max}, above is obtained by collocating the continuity equation at the outer boundary.

The 4 × 4 block tridiagonal matrix has a particular sparcity structure which characterizes these collocation methods. This structure, shown schematically in sketch (a), has been exploited by the construction of a new block solver that is slightly more than twice as fast as the usual dense block solver.

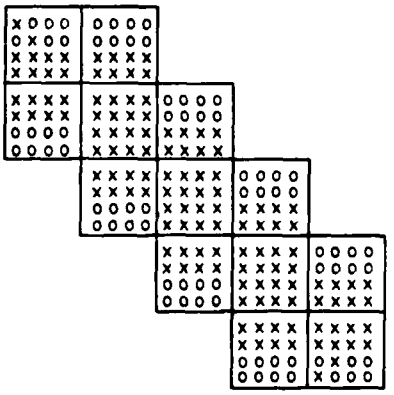

Sketch (a). Schematic of matrix structure; x's denote nonzero entries.

The turbulence model is introduced to the mean flow portion of the code only through the values of $\bar{\varepsilon}$ and $\partial\bar{\varepsilon}/\partial\eta$ which are provided by the EDDY subroutine. As a result, the model may be exchanged for any other eddy viscosity model without major structural changes to the code.

In the present version of the computer code, we have two subroutines defiring the eddy viscosity and its derivatives. The first, denoted Eddy 1, embodies the Cebeci-Smith model (2), which can be written as

$$\bar{\varepsilon} = \min \begin{cases} \bar{\varepsilon}_i \\ \bar{\varepsilon}_o \end{cases}$$

where

$$\bar{\varepsilon}_i = \frac{\varepsilon_i}{\nu} = \frac{[0.4\, y(1 - e^{-y^+/A^+})]^2}{\nu}\left|\frac{\partial u}{\partial y}\right|$$

$$\bar{\varepsilon}_o = \frac{\varepsilon_o}{\nu} = 0.0168\ Re_{\delta^*}$$

where

$$y^+ = \frac{y u_\tau}{\nu}$$

and

$$A^+ = 26$$

$$u_\tau = \sqrt{\tau_w/\rho}$$

Note that if $\tau \equiv 0$ the eddy viscosity damps to zero for all y. This model is very close to those of Refs. 4, 6, and 7. In Refs. 4 and 7 the inner eddy viscosity is modified by incorporating a pressure gradient correction into the parameter

$$A^+ = 26\Big/\sqrt{u_\tau\left[1 - 11.8\left(p_t^+ + p_x^+\right)\right]}$$

where

$$p_t^+ = \frac{\nu}{u_\tau^3}\frac{\partial u_e}{\partial t}, \qquad p_x^+ = \frac{\nu u_e}{u_\tau^3}\frac{\partial u_e}{\partial x}.$$

In Ref. 6, the outer eddy viscosity is modified by an intermittency parameter as

$$\bar{\varepsilon}_o = \gamma\bar{\varepsilon}_o$$

where

$$\gamma = \frac{1}{2}\left\{1 - \operatorname{erf}\left[5\left(\frac{y}{\delta} - 0.78\right)\right]\right\}$$

And in Ref. 7, the outer eddy viscosity is written as

$$\bar{\varepsilon}_o = \alpha\bar{\varepsilon}_o$$

where

$$\alpha = \frac{1.55}{1 + \pi}$$

and

$$\pi = 0.55[1 - \exp(0.243\, Z_1^{1/2} - 0.293\, Z_1)]$$

where

$$Z_1 = \frac{Re_\theta}{425} - 1$$

Based on steady-state experience, for the range of flow parameters considered here, none of the above modifications would be expected to have a first-order effect on the predicted quantities.

The second EDDY subroutine, Eddy 2, embodies the unsteady Glushko model (3). This model relates the eddy viscosity to the turbulence energy described by the equations

$$\frac{\partial e}{\partial t} + u\frac{\partial e}{\partial x} + v\frac{\partial e}{\partial y} = \nu\frac{\partial}{\partial y}\left[1 + \bar{\varepsilon}(\lambda r)\right]\frac{\partial e}{\partial y} + \nu\bar{\varepsilon}(r)\frac{\partial u}{\partial y} - C\nu[1 + \bar{\varepsilon}(\lambda r)]\frac{e}{\ell^2}$$

$$r = \frac{\sqrt{e}\,\ell}{\nu}$$

$$\bar{\varepsilon} = H(r)\alpha r$$

$$H(r) = \begin{cases} \dfrac{r}{r_o} & 0 \le \dfrac{r}{r_o} < 0.75 \\ \dfrac{r}{r_o} - \left(\dfrac{r}{r_o} - 0.75\right)^2 & 0.75 \le \dfrac{r}{r_o} < 1.25 \\ 1 & 1.25 \le \dfrac{r}{r_o} \end{cases}$$

$$\frac{\ell}{\delta} = \begin{cases} \dfrac{y}{\delta} & 0 \le \dfrac{y}{\delta} < 0.23 \\ \left(\dfrac{y}{\delta} + 0.37\right)\Big/2.61 & 0.23 \le \dfrac{y}{\delta} < 0.57 \\ \left(1.48 - \dfrac{y}{\delta}\right)\Big/2.42 & 0.57 \le \dfrac{y}{\delta} < 1.48 \end{cases}$$

The constants used were $\alpha = 0.2$, $r_o = 110$, $C = 3.93$, and $\lambda = 0.4$ as suggested by the author (3). He also proposed the boundary conditions

$$y = 0 \qquad e = 0$$

$$y = y_{max} \qquad e = 0$$

This latter condition is required by the form of the equations for large y.

RESULTS

To verify the numerical accuracy of the present method, the oscillating laminar flow over a semi-infinite flat-plate was solved. Figure 1 compares the phase lead of wall shear as predicted by the present method with the prediction of Cebeci and Carr (8) and with the low- and high-frequency asymptotic solutions of Lighthill (9). The reason for the leading phase angle is that, for unsteady flow,

$$-\frac{\partial p}{\partial x} = \frac{\partial u_e}{\partial t} + \rho_e u_e \frac{\partial u_e}{\partial x}$$

and the low momentum flow near the wall tends to follow $\partial u_e/\partial t$ which, for harmonic variations of u_e, leads u_e by $\pi/2$. The small differences between the results of the present method and those of Ref. 8 are probably due to differences in the temporal integration scheme used to generate the phase angle from the computed unsteady wall shear stress.

Having established that the method is numerically accurate, we can now consider the more interesting problem of the prediction of unsteady turbulent flows.

As in the steady-state case, the only way to assess the utility of an unsteady turbulent boundary-layer code is by comparison with experimental data. Unfortunately, only a relatively small amount of data is available for unsteady turbulent boundary layers and, as always, a substantially smaller amount of reliable data.

There are, however, several programs under way to remedy this situation, notably at Stanford (10), Office National D'Etudes et de Recherches Aerospatiales/Center Etude Recherches de Toulouse (ONERA/CERT) (11), and Southern Methodist University (12). In the past, only Karlsson's data were available and they were used as a test for computational methods. In the present paper, comparisons are made with the data of Karlsson (13) which provides a common base for comparisons with other computational methods, that is, Refs. 4, 6-8, and 14, and with the data of Parikh et al. (10). Although solutions have been obtained for both the Cebeci-Smith and Glushko turbulence models, time and space limitations preclude a detailed discussion of all the results. In the comparison with experiment and the discussions that follow, the emphasis will be placed on the Cebeci-Smith model.

Data of Karlsson

Karlsson (13) measured the turbulent boundary layer on the wall of a wind tunnel with a rectangular cross-section that varied from 12 × 18 in. at the inlet to 13 × 19 in. at the outlet. The mean velocity was 15 to 17.5 ft/sec and the unsteadiness was introduced by four parallel rotating shutters in the tunnel exit plane. This gave rise to a free-stream velocity of

$$u_e(t) = u_o\left(1 + \frac{\Delta u_e}{u_o}\cos \omega t\right)$$

where u_e is the instantaneous edge velocity and u_o the average edge velocity. Amplitudes $(\Delta u_e/u_o)$ varied from 0.08 to 0.34 and frequencies from 0 to 48 Hz. The hot-wire signals were processed to yield

$$\bar{u}(y) = \frac{1}{T}\int_t^{t+T} u(y,t)dt$$

$$A(y) = \frac{\Delta u(y)}{\bar{u}(y)}\cos\phi = \frac{1}{\pi}\int_t^{t+T} u(y,t)\cos \omega t\, dt$$

$$B(y) = \frac{\Delta u(y)}{\bar{u}(y)}\sin\phi = \frac{1}{\pi}\int_t^{t+T} u(y,t)\sin \omega t\, dt$$

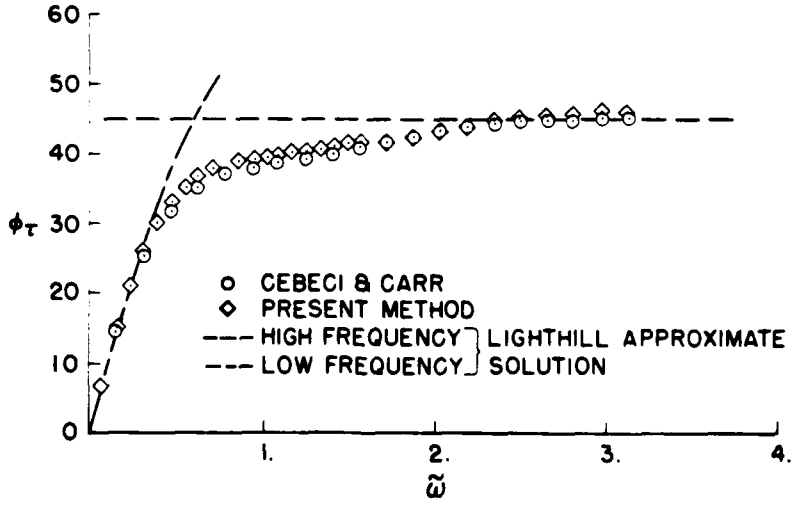

Fig. 1 Phase angle between edge velocity and wall shear stress for an oscillating flow over a flat plate.

where T is the period of the, assumed, purely harmonic oscillation. Note that these three parameters $\bar{u}$, A, and B with the turbulence intensity r(y) constitute the sum of the Karlsson data. Any other parameter must be deduced from those cited above with due appreciation of the experimental accuracy circa 1959.

The predicted results that are compared with the above data were obtained using the following procedure: at time = 0 the code was run in the steady-state mode (i.e., $\partial\bar{u}/\partial t = 0$) with $\Delta x = 0.58$, $\nu = 0.00016$, $u_o = 17.5$, and instantaneous transition at $x = 1.16$. That x, for which $C_f \approx 0.0034$ was chosen as the appropriate value for data comparison. The code was then run in the unsteady mode with a $\Delta(\omega t)$ of 10 deg through two full cycles with the appropriate data-reduction integrations being taken over the second cycle. Parametric studies were carried out with regard to time- and space-step size and will be described subsequently. The starting turbulent energy profile for the Glushko model was taken from Ref. 15.

Figure 2 shows the phase lead between wall shear and edge velocity for an oscillating flow over a semi-infinite flat plate. This figure was first presented by McCroskey (16) and subsequently, with additions, by Cebeci (7). All of the predictions and the experimental data are for the Karlsson experiment. The most disturbing thing about this figure is that the methods of Telionis and Tsahalis (6), Cebeci (7), and McCroskey and Phillipe (4) are all finite-difference methods in which essentially the same turbulence model was used; hence, they should produce nearly indistinguishable results. The fact that these very similar methods produce substantial scatter indicates that the parameter ϕ_τ is very sensitive to the integration time-step. This conclusion is verified by comparing the present results obtained with a time-step of 10 deg of arc and the Cebeci-Smith model, with additional results, at a reduced frequency $\tilde{\omega} = \omega x/u_o$ of 8 with $\Delta(\omega t)$ of 20 deg and 30 deg of arc, shown as the error bar of Fig. 2. We should note that this time-step is the time-step used in the data reduction procedure and not that used in the boundary-layer calculation itself. The in-phase component of velocity is similarly sensitive, and the presentation of data in this form tends to give an erroneous impression of the accuracy of predictions. Since this uncertainty is a function of the time-step used in the data reduction procedure, it may well exist in the analogous procedure applied to the experimental data. In addition, if the angle ϕ_τ is computed from the relation

$$\phi_\tau = \lim_{y \to o} \phi = \tan^{-1} \frac{B(y)}{A(y)}$$

it can be extremely sensitive to the stream normal nodal spacing in the near-wall region because of the rapid variation of ϕ as $y \to o$. This can be clearly seen from Fig. 3. The data appear to reach a maximum near the wall, but these values are questionable since they are ratios of parameters each of which is tending to zero.

In contrast to the above, the mean velocity does not seem to be particularly sensitive to either amplitude or frequency, as can be seen in Fig. 4.

Figure 5 compares the predictions of the present method with Karlsson's data for a frequency of 2 Hz and an amplitude ($\Delta u_o/u_c$) of 0.176. The distance normal to the wall is normalized on the experimental boundary-layer thickness. The difference between mean velocity profiles predicted by the Cebeci-Smith and Glushko models are typical of the differences obtained in steady-state calculations at matching values of C_f. The predicted in-phase components A(y) are in substantial agreement with each other and in qualitative agreement with the rather badly scattered data. The predicted out-of-phase components do not agree nearly so well and, surprisingly, the Cebeci-Smith model appears to be in better agreement with the data, although both models provide the same qualitative behavior.

Figure 6 presents essentially the same information for a frequency of 7.65 Hz and an amplitude of 0.073. Again, both models agree qualitatively with the data, with the Cebeci-Smith model in somewhat better agreement. Comparing Figs. 5 and 6, we note that as the frequency increases, both the predictions and the experiment show a distinct thinning of the region characterized by significant phase shift. This behavior is analogous to the reduction in the depth of penetration with increasing frequency in the laminar flow over an infinite oscillating plate.

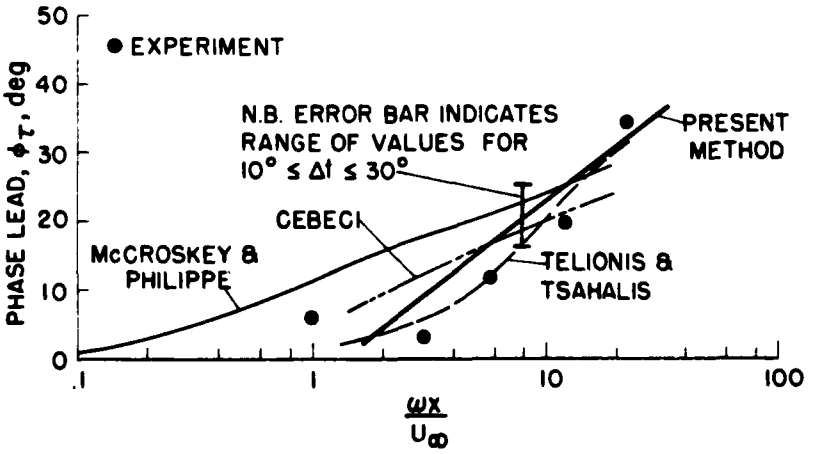

Fig. 2 Phase angle between wall shear stress and edge velocity on an oscillating flat plate.

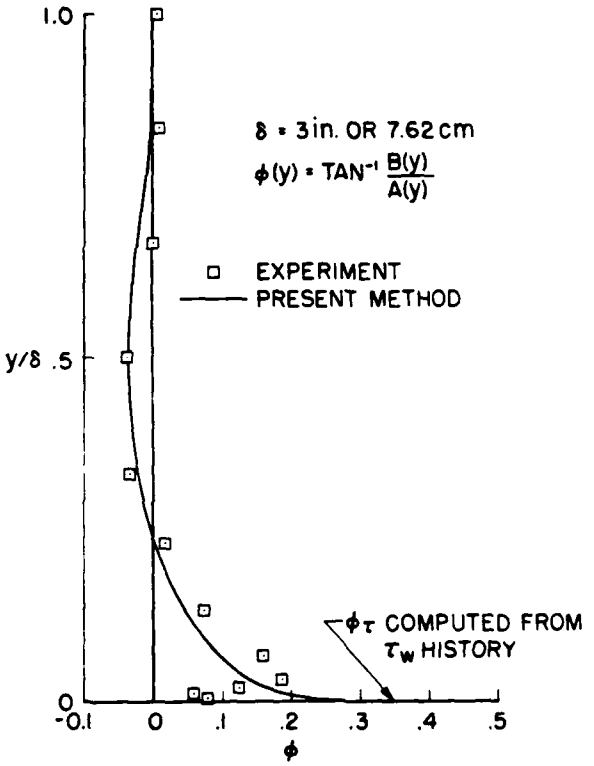

Fig. 3 Phase angle for velocity and wall-shear; data of Karlsson; 2 Hz, amplitude of 0.286.

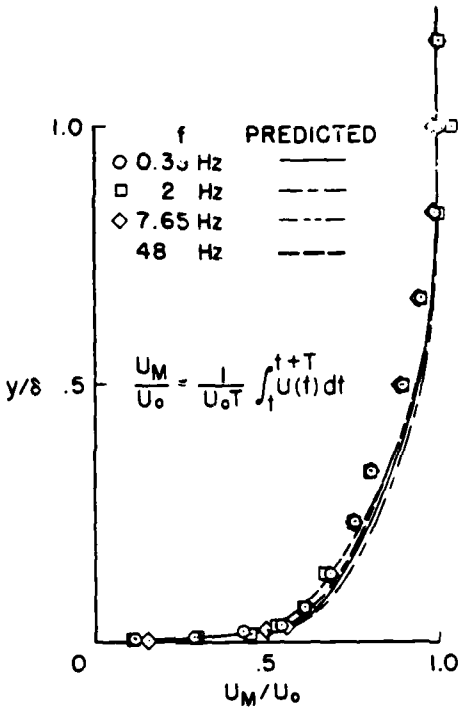

Fig. 4 Distribution of mean velocity for various frequencies; data of Karlsson.

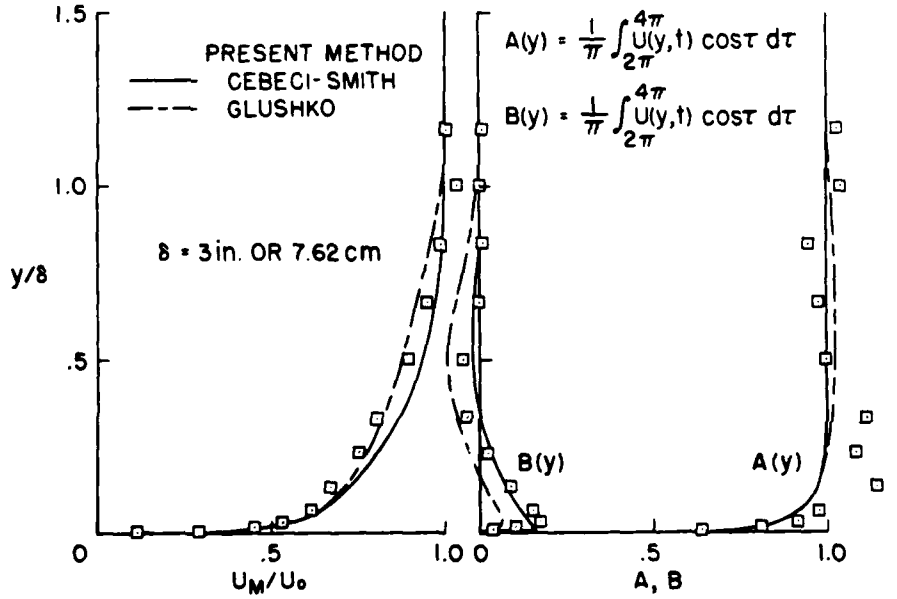

Fig. 5 Comparison of predicted and measured velocity components at 2 Hz with an amplitude of 0.176; data of Ref. 13.

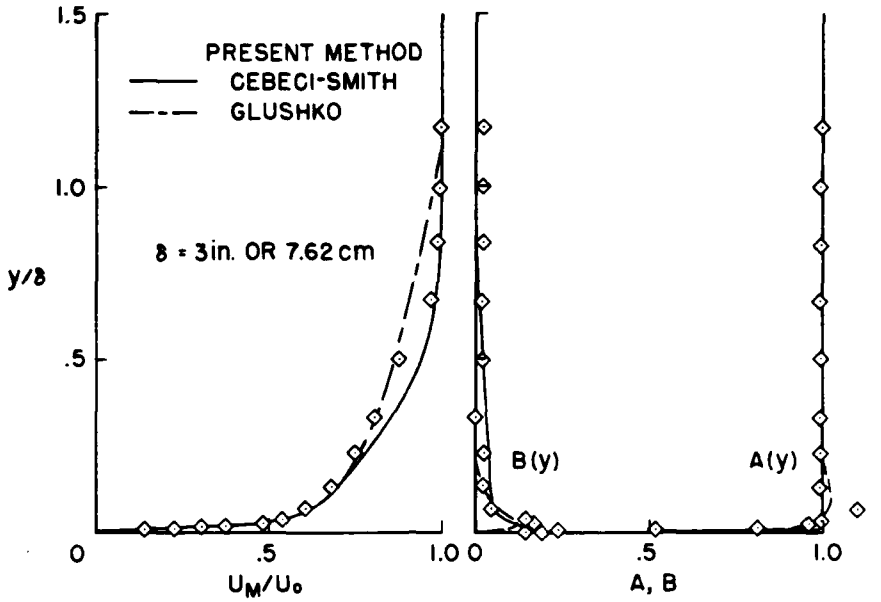

Fig. 6 Comparison of predicted and measured velocity components at 7.65 Hz with an amplitude of 0.073.

To provide the reader with some feeling of the magnitude of the dynamic effects, we present in Fig. 7 the extremes of the computed velocity profiles for the conditions of Karlsson's experiment ($\Delta u/u_o = 0.176$ and $\omega/2\pi = 2$ Hz). These results show that nontrivial excursions in velocity occur and that wall shear-stress

$$C_{f_o} = \frac{\tau_w}{(1/2)\rho_o u_o^2}$$

varies by more than a factor of 2. It is clear that the mean velocity, which can be predicted easily with a quasi-steady method, is meaningless and that if one seeks to predict, for example, the unsteady pressure distribution or drag coefficient, an accurate unsteady calculation scheme is necessary.

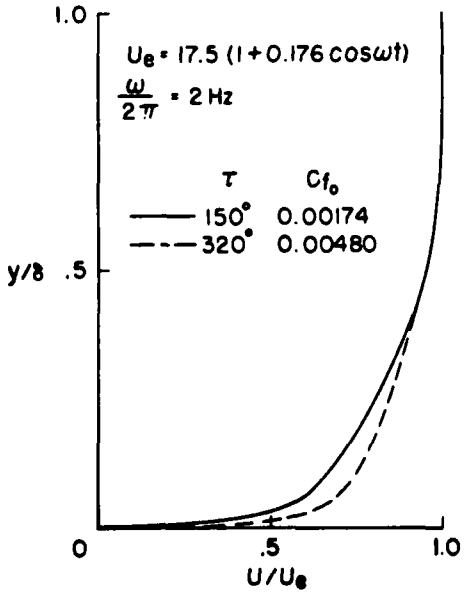

Fig. 7 Comparison of predicted extreme velocity profiles for Karlsson experiment; 2 Hz, $\Delta u_e/u_o = 0.176$.

Data of Parikh, Reynolds, and Jayaraman

The experiment of Parikh, Reynolds, and Jayaraman (10) is again the unsteady flow over a tunnel wall. The edge velocity is given by the relation

$$u_e = 0.73 \text{ m/sec} \qquad x < x_o$$

$$u_e = u_{e_o} - \frac{a_o(x - x_o)}{L}(1 - \cos \omega t) \qquad x \geq x_o$$

where $u_{e_o} = 0.73$ m/sec; $x_o = 2$ m, $a_o = 0.05\, u_{e_o}$ $L = 0.6$; and $\omega/2\pi = 0$, 0.25, 0.5, 2 Hz. At $x = 2.0$ m, the end of the steady flat-plate flow, the experimental and predicted velocity distributions are compared in Fig. 8. The agreement is quite good, as would be expected for a steady flat-plate flow. In fact, since no matching procedure was used, the results are substantially better than might be expected.

Figure 9 shows a comparison of the measured and predicted mean velocity profiles at $x = 2.583$. Note that for $0 \leq \omega/2\pi \leq 2$ Hz these profiles are independent of frequency and equal to the steady profile under the mean pressure gradient. The agreement is everywhere within about 5%, which is quite reasonable.

The present method fails rather badly to predict the skin-friction coefficient, as presented in Ref. 10. This may be due in part to the method of determining the skin-friction in Ref. 10, that is, a Clauser plot which ignores phase differences between velocity and shear stress. Our predictions indicate a 25 to 30 deg phase lead, whereas the data seem to show a significant phase lag; in addition, the predicted variation of $((C_f) - \bar{C}_f)/\bar{C}_f$ is strongly asymmetric (see Fig. 10 in Ref. 10). We do, however, predict an attenuation of amplitude $\Delta C_f/C_f$ at 0.25 and 0.5 Hz. At 2 Hz and higher frequencies, however, the amplitude increases with increasing frequency.

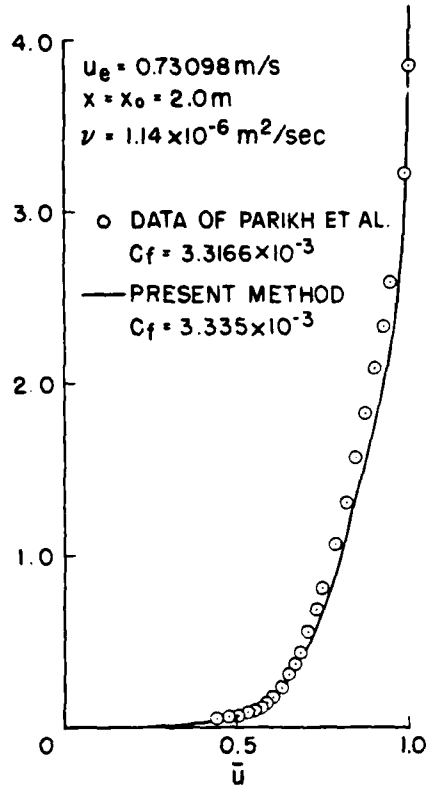

Fig. 8 Initial velocity distribution for the experiment of Ref. 10.

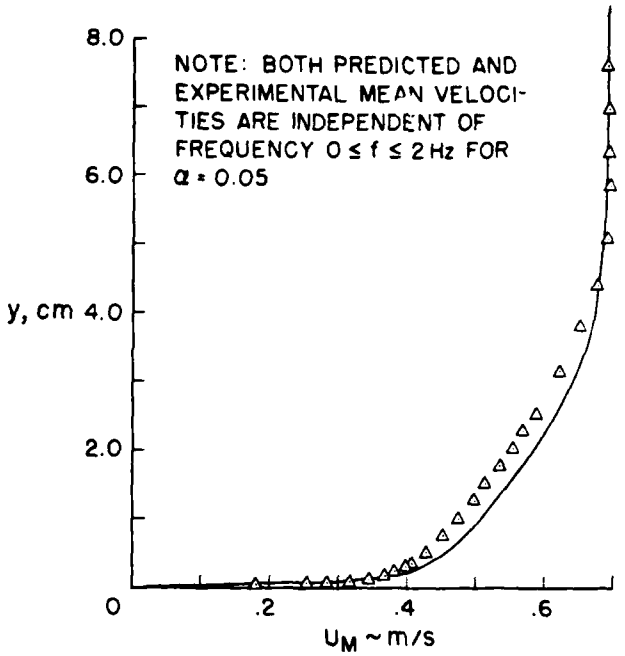

Fig. 9 Comparison of predicted mean velocity distribution with the data of Ref. 10.

Finally, Fig. 10 presents the predicted variation of skin-friction coefficient at a frequency of 2 Hz and an amplitude $\alpha = \Delta u_o/u_e = 0.15$. In Ref. 10 it is noted that this amplitude is sufficient to cause separation during a part of the oscillation cycle. To avoid semantic entanglement as to what constitutes separation, we note merely that the predicted skin friction is negative for $130° \leq \omega t \leq 180°$ where C_f is based on the undisturbed velocity U_o = 0.73 m/sec. No indication of the Goldstein singularity, at $\tau_{\_}$ = 0, was encountered in these calculations.

CONCLUDING REMARKS

One of the major conclusions of the present study is that there is not only a pressing need for additional experimental data, as always, but also an

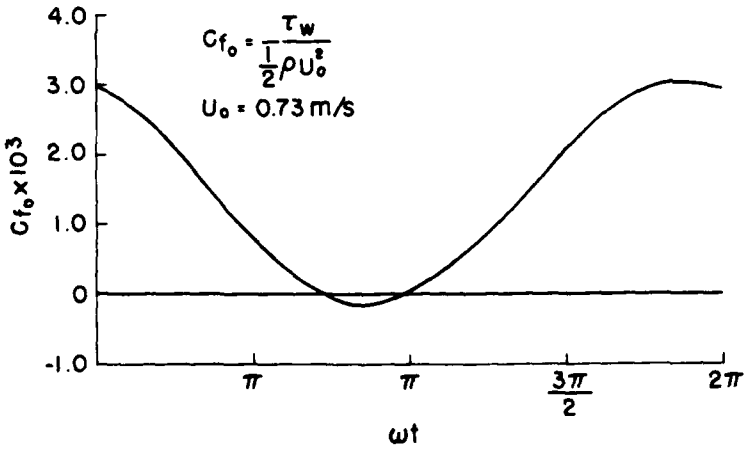

Fig. 10 Predicted variation of skin friction for α = 0.15; 2 Hz.

equally pressing need for a consensus as to what kind of data are required and how they should be presented. The present authors would strongly advocate the use of ensemble-averaged velocity profiles at discrete cycle points as being the nearest thing to common ground between prediction and experiment.

The present numerical method is both accurate and efficient and appears to provide a good qualitative description of the behavior of unsteady turbulent boundary layers with the simplest of turbulence models. One must bear in mind, however, that the streamwise pressure gradients considered here are quite mild. Since the largest variations of parameters occur in the near-wall region, which is also the most difficult region for measurement, we can make no clear quantitative assessment of the turbulence models considered here.

Finally, consistent with earlier studies by authors cited above, we find that the present method can predict the unsteady flow in regions with negative skin friction without difficulty.

ACKNOWLEDGMENT

The authors gratefully acknowledge the assistance of Dr. L. W. Carr of the Ames Directorate USAAMRDL, AVRADCOM for providing them with the digitized experimental data of both the Karlsson and Parikh, Reynolds, and Jayaraman experiments.

REFERENCES

1 Murphy, J. D., "An Efficient Solution Procedure for the Incompressible Navier-Stokes Equations," AIAA Journal, Vol. 15, No. 9, Sept. 1977, pp. 1307-1314.

2 Cebeci, T. and Smith, A. M. O., "A Finite-Difference Solution of the Incompressible Turbulent Boundary-Layer Equations by an Eddy-Viscosity Concept," Proceedings of Computation of Turbulent Boundary Layers, AFOSR-IFP-Stanford Conference, 1968.

3 Glushko, G. S., "Turbulent Boundary Layer on Flat Plate in an Incompressible Fluid," NASA TFF 10.080, 1965, Translation from Izvestiya Akademii Nauk SSSR, Seriya Mekhanika, No. 4, pp. 13-23.

4 McCroskey, W. J. and Phillipe, J. J., "Unsteady Viscous Flow on Oscillating Airfoils," AIAA Journal, Vol. 13, No. 1, Jan. 1975, pp. 71-79.

5 Prenter, P. M., Splines and Variational Methods, John Wiley and Sons, New York, 1975.

6 Telionis, D. P. and Tsahalis, D. Th., "Unsteady Turbulent Boundary Layers and Separation," AIAA Journal, Vol. 14, No. 4, Apr. 1976, pp. 468-474.

7 Cebeci, T., "Calculation of Unsteady Two-Dimensional Laminar and Turbulent Boundary Layers with Fluctuations in External Velocity, Proceedings of the Royal Society, London, Series A, Vol. 355, 1977, pp. 225-238.

8 Cebeci, T. and Carr, L. W., "A Computer Program for Calculating Laminar and Turbulent Boundary Layers for Two-Dimension Time Dependent Flows," NASA TM-78470, Mar. 1978.

9 Lighthill, M. J., "The Response of Laminar Skin Friction and Heat Transfer to Fluctuations in the Stream Velocity," Proceedings of the Royal Society, London, Series A, Vol. 224, June 1954, pp. 1-23.

10 Parikh, P. G., Reynolds, W. C., and Jayaraman, R., "On the Behavior of an Unsteady Turbulent Boundary Layer," paper presented at the Symposium on Numerical and Physical Aspects of Aerodynamic Flows, Jan. 19-21, 1981, California State University, Long Beach, Calif.

11 Cousteix, Jean, "Couches Limite en Écoulement Pulsé," ONERA TN 1979-1.

12 Simpson, R. L., "Features of Unsteady Turbulent Boundary Layers as Revealed from Experiments," Paper No. 220, AGARD CP-227, Unsteady Aerodynamics, Feb. 1978.

13 Karlsson, S. K. F., "An Unsteady Turbulent Boundary Layer," Journal of Fluid Mechanics, Vol. 5, 1959, pp. 622-636.

14 Shamroth, S. J. and Kreskovsky, J. P., "A Weak Interaction Study of the Viscous Flow About Oscillating Airfoils," NASA CR-132425, 1974.

15 Beckwith, I. E. and Bushnell, D. M., "Calculation of Mean and Fluctuating Properties of the Incompressible Turbulent Boundary Layer," Proceedings of Computation of Turbulent Boundary Layers, AFOSR-IFP-Stanford Conference, 1968.

16 McCroskey, W. J., "Some Current Research in Unsteady Dynamics," The 1976 Freeman Scholar Lecture.

DYNAMICS OF AN UNSTEADY TURBULENT BOUNDARY LAYER

P. G. Parikh, R. Jayaraman, W. C. Reynolds
Department of Mechanical Engineering, Stanford University
Stanford, California 94305

Abstract

The response of a well-defined, steady, flat-plate turbulent boundary layer subjected subsequently to two types of oscillations of the free-stream velocity in the test section is studied in this investigation. In the first case, the free-stream velocity decreased linearly in the test section in a time-dependent manner such that the magnitude of the streamwise gradient of the free-stream velocity varied sinusoidally from zero to a maximum value at frequencies ranging from zero to approximately the bursting frequency. In the second case, the mean free-stream velocity decreased in the test section in a nonlinear fashion independent of the oscillation frequency, while the amplitude and phase of the free-stream oscillations varied along the streamwise direction in an arbitrary manner, depending upon the oscillation frequency. Detailed measurements are reported for the first case. It was found that the mean velocity and mean turbulence intensity profiles in the boundary layer were unaffected by the imposed oscillations. The ratio of the amplitude of the periodic velocity component in the boundary layer to that in the free-stream, although as much as 1.7 for quasi-steady oscillations, becomes unity over the outer region of the boundary layer at high frequencies. Also, at high frequencies of imposed oscillations, both the boundary layer thickness and the Reynolds stress distribution across the boundary layer becomes frozen over the oscillation cycle at their mean values. Only the mean velocity profile measurements were carried out in the second case. It was found that, despite the large streamwise variations of the amplitude and phase of the free-stream oscillations, the mean velocity profile in the boundary layer once again remained independent of the imposed oscillation frequency so long as the mean free-stream velocity distribution remained unchanged.

Introduction

The objectives of the Stanford Unsteady Turbulent Boundary Layer Program are: to develop a fundamental understanding of such flows, to provide a definitive data base which can be used to guide turbulence model development, and to provide test cases which can be used by computors for comparison with predictions.

Due to space limitations, work of other investigators will not be summarized here, except to note that all the previous experiments are characterized by unsteady flow at the inlet to the unsteady region. For a comparison of the present experimental parameter range with those of other investigations, see Reference 1. The distinctive feature of the present experiments is that the boundary layer at the inlet to the unsteady region is a standard, steady, flat-plate turbulent boundary layer. It is then subjected to controlled oscillations of the free stream. This feature is especially important from the point of view of a computor, who needs precise specification of boundary conditions for computation of the flow.

Free-Stream Boundary Condition of the Present Experiment

The free-stream velocity distribution $u_\infty(x,t)$ for the first case in the water tunnel built for this work is shown in Fig. 1. u_∞ remains steady and uniform for the first two meters of boundary layer development. It then decreases linearly in the test section; the magnitude of the velocity gradient varies sinusoidally from zero to a maximum value during the oscillation cycle. The mean free-stream velocity distribution in the test section is thus linearly decreasing and corresponds to the distribution at the cycle phase angle of 90°, while the amplitude of imposed free-stream oscillations grows linearly in the streamwise direction, starting at zero at the entrance to a maximum value of a_o at the exit. Hence,

$$u_\infty(x,t) = u_{\infty,o} \quad , \qquad x < x_o$$

$$= u_{\infty,o} - \frac{a_o(x-x_o)}{L}\left[1 - \cos \omega t\right], \quad x_o < x < x_o + L$$

The important parameters of this problem are the amplitude parameter $\alpha = a_o/u_{\infty,o}$ and the frequency parameter: $\beta_\delta = f\delta_o/u_{\infty,o}$. Here $f = \omega/(2\pi)$ and δ_o is the thickness δ of the boundary layer at the inlet to the unsteady region. In the present experiments:

$$u_{\infty,o} = 0.73 \text{ m/s}, \quad \delta_o = 0.05 \text{ m}, \quad 0 < f < 2 \text{ hz},$$

$$0 < \alpha < 0.25, \quad 0 < \beta_\delta < 0.14$$

It should be mentioned that the value of the frequency parameter β_δ at the so-called "bursting frequency" in turbulent boundary layers is about 0.2 [2]. Thus the imposed oscillation frequencies used in the present experiments cover the range from quasi-steady ($f = 0$) to values approaching the bursting frequency. The results reported here are for one non-dimensional amplitude, $\alpha = 0.05$.

In the second case, the mean free-stream velocity distribution was nonlinear along x but was independent of the oscillation frequency, as shown in Fig. 2. The amplitude of the imposed free-

stream oscillations near the test-section exit was comparable to that in the first case (5%). However, the growth of the amplitude from nearly zero at the test section entrance to the maximum value at the exit was nonlinear and frequency dependent, as shown in Fig. 3. Furthermore, the phase of the free-stream oscillations varied dramatically along x and was also dependent on the oscillation frequency, as shown in Fig. 3. The net result at high oscillation frequency was a strong departure of the phase-averaged free-stream velocity distribution from a linear one accomplished in the first case (see Fig. 4).

Experimental Facility

Figure 5 is a schematic of the facility. The 16:1 nozzle contraction is followed by a 2 m long development section, where the test boundary layer is grown on the top wall. A constant head and a constant flow resistance provide a constant flow. The free-stream velocity in the development section is maintained uniform along x by bleed from the bottom wall.

The linear decrease in free-stream velocity in the test section, as desired in the first case, is accomplished by uniformly bleeding off some flow through a perforated plate which forms the bottom wall in the test section. The holes in the perforated plate are sized such that the pressure drop across them is large compared to the dynamic pressure in the test section. To make the amplitude and phase of free-stream oscillations dependent on oscillation frequency, the holes were made larger so that the pressure drop across the perforated bottom plate became small compared to the dynamic pressure. The remainder of the flow exits downstream. Each of these two flows exits the tunnel through slots in an oscillating plate. The design ensures that, regardless of the position of the oscillating plate, the total flow area of the slots remains the same. The slots are the controlling resistance of the entire fluid circuit, hence the constant flow. By sinusoidally oscillating the plate, a periodic free-stream distribution is established in the test section, while the upstream flow in the development section remains steady.

Measurement and Data-Processing Techniques

Pitot tubes are used for mean velocity measurements in steady flow regions. Unsteady velocity measurements use a single-channel, forward-scatter, Bragg-shifted DISA laser anemometer in the tracking mode.

Following Hussain and Reynolds [3], the instantaneous velocity signal from an unsteady turbulent flow may be decomposed into three parts:

$$u = \bar{u} + \tilde{u} + u' \qquad (1)$$

where $\bar{u}$ is the mean, $\tilde{u}$ is the time-dependent, organized (deterministic) component, and u' is the random fluctuation. $\bar{u}$ is determined by long-time averaging of u. Here $\tilde{u}$ is of a periodic nature and may be determined by first phase-averaging the instantaneous velocity signal and then subtracting out the mean. Thus,

$$\tilde{u} = \langle u \rangle - \bar{u} \qquad (2)$$

Here $\langle u \rangle$, the phase average velocity, is determined by averaging over an ensemble of samples taken at a fixed phase in the imposed oscillation. In the present experiments, with harmonic oscillation of the free stream, the response at points within the boundary layer is almost sinusoidal, with higher harmonics contributing less than 5%. Hence, $\tilde{u}$ may also be extracted from the instantaneous signal u by cross-correlation with a sine wave in phase with the oscillation. A digital correlator (HP 3721A) was used to determine cross-correlations leading to the $\tilde{u}$ data reported here. Currently a DEC MINC-11 laboratory minicomputer system is used for automatic data acquisition and processing, allowing the determination of phase averages of u and u'^2.

The measurements reported here were taken at a fixed streamwise location near the end of the test section at $x - x_o = 0.568$ m.

Results and Discussion

Case (i): Linear Phase-Averaged Free-Stream Distribution

The mean velocity profiles measured with the oscillating plate in fixed positions $\theta = 0$, $90°$, $180°$ are fit by dashed curves in Fig. 6. These represent phase-averaged profiles at zero frequency, i.e., quasi-steady profiles. At this amplitude ($\alpha = 0.05$), the response of the boundary layer is almost linear, so that the profile corresponding to $\theta = 90°$ lies nearly midway between the $\theta = 0$ and $180°$ profiles. The $90°$ profile represents the mean profile for quasi-steady oscillations. The difference between the 0 and $90°$ profiles at a fixed y-location represents the amplitude of quasi-steady oscillations at that location in the boundary layer. Note that the quasi-steady amplitudes in the boundary layer are larger than the free-stream amplitude.

The mean velocity profiles measured under oscillatory conditions at 0.5 hz and 2.0 hz are shown as data points in Fig. 6. Note that the mean velocity profiles at various frequencies are identical with the profile measured under stationary condition with pulser angle set at $\theta = 90°$. It may be concluded that the mean velocity profile (at a fixed amplitude $\alpha = 0.05$) is independent of the imposed oscillation frequency in the entire range $0 \leq f \leq 2$ hz. The same behavior persists all the way up to the wall.

This behavior of the mean velocity profile may be explained by an examination of the governing equations. Use of (1) in the momentum equation and time-averaging yields

$$\bar{u}\frac{\partial \bar{u}}{\partial x} + \bar{v}\frac{\partial \bar{u}}{\partial y} = -\frac{1}{\rho}\frac{\partial \bar{p}}{\partial x} + \nu\frac{\partial^2 \bar{u}}{\partial y^2} - \frac{1}{\rho}\frac{\partial}{\partial y}\left[\overline{u'v'} + \overline{\tilde{u}\tilde{v}}\right] \qquad (3)$$

Equation (3) may be recognized as the equation governing an ordinary turbulent boundary layer, except for the addition of the term $\overline{\tilde{u}\tilde{v}}$, which represents Reynolds stresses arising from the organized oscillations.

The time-mean pressure gradient $\partial \bar{p}/\partial x$ may be shown to be independent of the imposed oscillation

frequency and, except for a higher-order term, it is the same as that obtained for $f = 0$ at $\theta = 90°$. Therefore, the mean velocity field will be frequency-dependent if and only if one or both of the following happen:

- The distribution of Reynolds stress $\overline{u'v'}$ is altered under oscillatory conditions and is dependent on the frequency of imposed oscillations.
- The Reynolds stress $\overline{\tilde{u}\tilde{v}}$ arising from organized fluctuations becomes significant compared with $u'v'$.

We shall now argue that neither of the above requirements is met. Figure 7 shows the measured distribution of u'_{rms} under stationary condition with the pulser at $\theta = 90°$ (the mean position) as well as those measured under os illatory conditions at frequencies up to 2 hz. Note that u'_{rms} is independent of the imposed oscillation frequency and, further, that it is the same as that measured at $f = 0$ and $\theta = 90°$. We believe that the same would be true for $\overline{u'v'}$, which at present we cannot measure. Figure 8 gives a comparison between measured values of $\overline{\tilde{u}\tilde{v}}$ at 2 hz with data on $\overline{u'v'}$ obtained by Anderson [4] in a steady adverse pressure gradient boundary layer at comparable conditions. The present data on $\overline{\tilde{u}\tilde{v}}$ were obtained by separate LDA measurements of $\tilde{u}$ and $\tilde{v}$ and their respective phases. It may be seen that the contribution of $\overline{\tilde{u}\tilde{v}}$ to total Reynolds stress is insignificant over almost the entire boundary layer. Hence, $\overline{u'v'}$ is independent of frequency and $\overline{\tilde{u}\tilde{v}}$ is negligible, and so the mean velocity profile is also independent of frequency and is the same as that found at $f = 0$ with $\theta = 90°$.

The behavior of the periodic component $\tilde{u}$ will next be examined. We denote

$$\tilde{u} = a_1(y) \cos[\omega t + \phi(y)] \qquad (4)$$

The profiles of amplitudes a_1 measured in the boundary layer and normalized by the free-stream amplitude $a_{1,\infty}$ are shown in Fig. 6. The profile for quasi-steady ($f \approx 0$) oscillations was determined, as explained earlier, from the mean velocity profiles measured at $f = 0$ with $\theta = 0$, 90°, and 180° (see Figs. 6(a), (b)). Note that, during quasi-steady oscillations, the amplitude in the boundary layer exceeds the free-stream amplitude by as much as 70%. It may be mentioned that data for $f = 0.1$ hz, not shown on Fig. 9, do indeed come very close to the quasi-steady behavior.

As the frequency is increased, the amplitude ewithin the boundary layer is attenuated. The amplitude appears to drop as f is increased and then rise again. At high frequencies, the amplitude in most of the boundary layer is the same as in the free-stream; near the wall the amplitude of the periodic component rapidly drops to zero.

The phase differences between the boundary layer oscillations and free-stream oscillations are shown in Fig. 10. For $f = 0$ there is no phase difference. The largest phase lags in the outer region of the boundary layer were observed at $f =$ 0.25 hz. The effect of increasing the frequency is to reduce the phase lag in the outer region, but to introduce large phase leads in the region very close to the wall. Clearly, the asymptotic behavior of the outer region for high frequencies is once again a zero phase lag with respect to free-stream oscillations, as in the quasi-steady case.

At high frequencies, the combination of the asymptotic behaviors of $a_1/a_{1,\infty}$ and ϕ in the outer region together with the fact that the mean velocity profile is unaffected by imposed oscillations, has the effect of freezing the boundary layer thickness. This is shown in Fig. 11, where the phase-averaged boundary layer thickness $\langle \delta_{.99} \rangle$ is plotted as a function of the cycle phase angle for several frequencies. The quasi-steady behavior of $\langle \delta_{.99} \rangle$ is quite obvious: at $\theta = 0$, the boundary layer in the test section continues to develop under a zero pressure gradient and is the thinnest at this point in the entire cycle. As the phase angle is increased, pressure gradients of increasing adversity are imposed on the boundary layer, causing it to thicken. The maximum thickness is attained at $\theta = 180°$ under the maximum adverse pressure gradient. Hence, at $f = 0$, δ oscillates 180° out of phase with u_∞.

Under oscillatory conditions at $f = 0.25$, 0.5, and 2.0 hz, two things happen: a significant phase lag develops from quasi-steady behavior and the amplitude attenuates with increasing frequency. For the $f = 2.0$ hz case, the variation over the complete cycle is less than 1% and the boundary layer thickness is practically frozen during the oscillation cycle.

It may be shown by a simple argument based on a mixing length model of boundary layer turbulence that the freezing of the boundary layer thickness at high frequencies is also accompanied by freezing of the Reynolds stress over the oscillation cycle. To prove this, we hypothesize that the phase-averaged Reynolds stress distribution may be related to the phase-averaged velocity profile in the same manner as for a steady boundary layer, i.e.,

$$-\langle u'v' \rangle = \varepsilon_m \frac{\partial \langle u \rangle}{\partial y}, \quad \varepsilon_m = \ell^2 \frac{\partial \langle u \rangle}{\partial y} \qquad (5)$$

Now, in the outer region of the boundary layer, the mixing length ℓ may be modeled as

$$\ell = \lambda \langle \delta_{.99} \rangle \qquad (6)$$

where λ is nearly a constant. Now,

$$\langle u \rangle = \bar{u} + \tilde{u} = \bar{u} + a_1(y) \cos[\omega t + \phi(y)] \qquad (7)$$

However, in the high-frequency limit,

$$a_1(y) = a_{1,\infty} = \text{const}, \quad \phi(y) = 0, \quad \text{and} \qquad (8)$$

$$\langle \delta_{.99} \rangle = \bar{\delta}_{.99} = \text{const}.$$

Therefore

$$\frac{\partial \langle u \rangle}{\partial y} = \frac{\partial \bar{u}}{\partial y} \qquad (9)$$

Combining the above, one finds

$$-\langle u'v' \rangle = \lambda^2 \bar{\delta}_{.99}^2 \left[\frac{\partial \bar{u}}{\partial y}\right]^2 = -\overline{u'v'} \qquad (10)$$

i.e., the phase-averaged Reynolds stress in the outer region also becomes frozen at $-\overline{u'v'}$.

Experimental evidence of this stress-freezing behavior was obtained by measurements of phase-averaged normal turbulent stress $\langle u'^2 \rangle$. The quasi-steady ($f = 0$) profiles of $\langle u'^2 \rangle$ are shown in Fig. 12 for three phase angles $\theta = 0°$, 90°, and 180°. Note that the distribution for 90° lies nearly midway between those for 0° and 180°. The distribution of $\langle u'^2 \rangle$ for 90° is the same as the distribution of $\overline{u'^2}$, as seen earlier. Therefore, the difference between the 0° and 90° curves in Fig. 12 represents the amplitude of quasi-steady oscillations of $\langle u'^2 \rangle$ at any point in the boundary layer. This amplitude was determined graphically from Fig. 12 and is plotted in Fig. 13 for the case of $f = 0$. Under oscillatory conditions, the amplitude of the normal stress oscillations in the boundary layer attenuates as the frequency of imposed oscillations is increased from $f = 0$. At $f = 2.0$ hz, the amplitude of stress oscillations across the boundary layer is almost zero over the outer region, as seen in Fig. 13, i.e., the stress is almost frozen over the oscillation cycle.

Case (ii): Arbitrary Phase-Averaged Free-Stream Distribution

In this case, the phase-averaged free-stream distributions become frequency-dependent, as shown in Fig. 4. However, the mean free-stream distribution remained almost the same as that shown in Fig. 2 at all frequencies employed. The mean velocity profiles in the boundary layer were measured at the same axial location as in Case (i). Fig. 14 shows that the mean velocity profile was still unaffected by the imposed oscillations at frequencies ranging from zero to 2.0 Hz. This shows that the mean velocity profile is dependent only on the mean free-stream velocity distribution ahead of the measurement station and is independent of the amplitude and phase distributions of the imposed oscillatory component in the free stream.

Conclusions

The conclusions from our experiments to date may be summarized as follows:

1. The mean velocity profile in the boundary layer is unaffected by imposed free-stream oscillations in the range of frequencies employed, and it is the same as the one measured with a free-stream velocity distribution held steady at its mean value. This is true even if the amplitude and phase of the imposed oscillatory component in the free stream vary arbitrarily along x as functions of imposed oscillation frequency.

2. This behavior of the mean velocity field is a consequence of two observations: (a) the time-averaged Reynolds stress distribution across the boundary layer is unaffected by the imposed oscillations and is indeed the same as the one measured with the free-stream velocity distribution held steady at the mean value; and (b) the Reynolds stresses arising from the organized velocity fluctuations under imposed oscillatory conditions are negligible compared to the Reynolds stresses due to the random fluctuations.

3. The amplitude of the periodic component in the boundary layer under quasi-steady oscillations ($f \to 0$) is as much as 70% larger than the imposed free-stream amplitude. However, at higher frequencies the peak amplitude in the boundary layer is rapidly attenuated toward an asymptotic behavior where amplitudes in the outer region of the boundary layer become the same as the free-stream amplitude, dropping off to zero in the near-wall region.

4. Quasi-steady boundary layer velocity response is in phase with the imposed free-stream oscillations. As the frequency is increased, phase lags begin to develop in the outer region of the boundary layer. The magnitude of this phase lag reaches a maximum and then decreases with increasing frequency until an asymptotic limit is reached where the outer region once again responds in phase with the free stream. Near the wall, however, large lead angles are present at higher oscillation frequencies.

5. A consequence of (3) and (4) above is that the boundary layer thickness becomes nearly frozen over the oscillation cycle at higher frequencies.

6. A consequence of (3), (4), and (5) above is that the Reynolds stress distribution in the outer region of the boundary layer also becomes frozen over the oscillation cycle at higher frequencies.

Acknowledgments

This research is carried out at Stanford in cooperation with and under the sponsorship of the Army Aeromechanics Laboratory, the NASA-Ames Research Center, and the Army Research Office. The authors wish to express their gratitude to Drs. Larry Carr and James McCroskey (AML), Mr. Leroy Presley (NASA-Ames), and Dr. Robert Singleton (ARO) for their continued assistance.

References

1. Parikh, P. G., et al.: "On the Behavior of an Unsteady Turbulent Boundary Layer." Accepted for publication in the AIAA Journal (1981).

2. Rao, K. N., et al.: "The 'Bursting Phenomenon' in a Turbulent Boundary Layer." J. Fluid Mech., 48, 339-352 (1971).

3. Hussain, A.K.M.F., and Reynolds, W. C.: "The Mechanics of an Organized Wave in Turbulent Shear Flow." J. Fluid Mech., 41, 241-258 (1970), and 54, 241-288 (1972).

4. Andersen, P. S., Kays, W. M., and Moffat, R. J.: "The Turbulent Boundary Layer on a Porous Plate: An Experimental Study of the Fluid Mechanics for Adverse Free-Stream Pressure Gradients." Report No. HMT-15, Dept. of Mech. Engrg., Stanford University (1972).

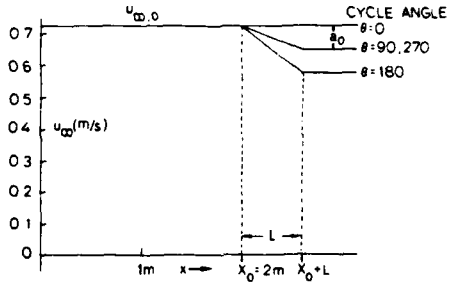

Fig. 1. Free-stream velocity variation, first case.

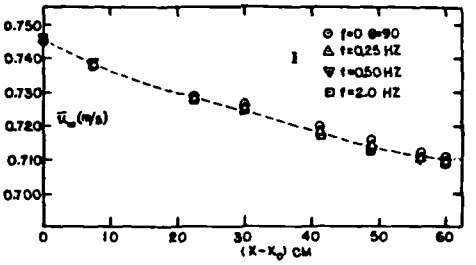

Fig. 2. Free stream velocity variation, second case.

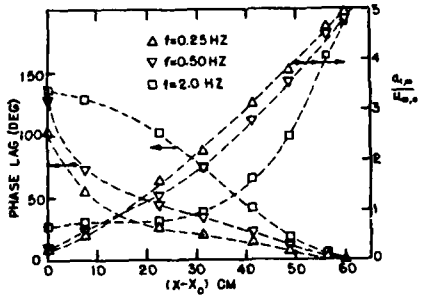

Fig. 3. Streamwise variation of amplitude and phase, second case.

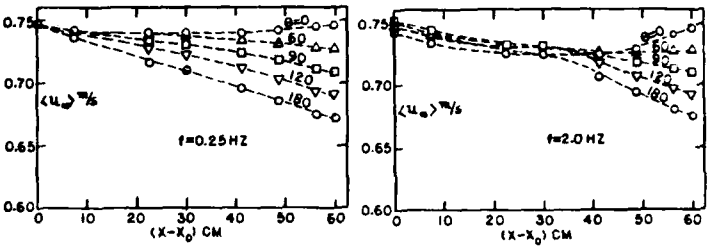

Fig. 4. Phase-averaged free-stream velocity distributions, second case.

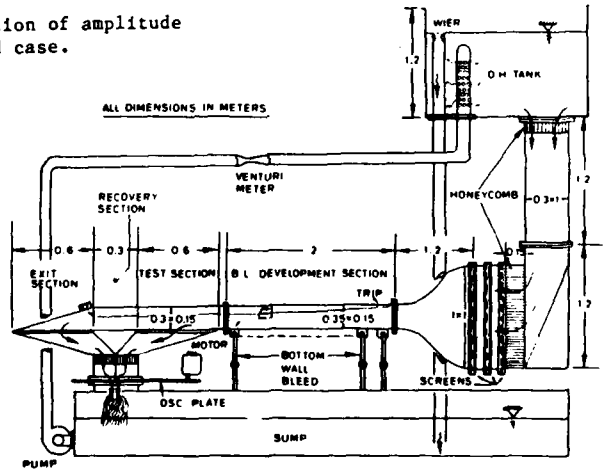

Fig. 5. The apparatus.

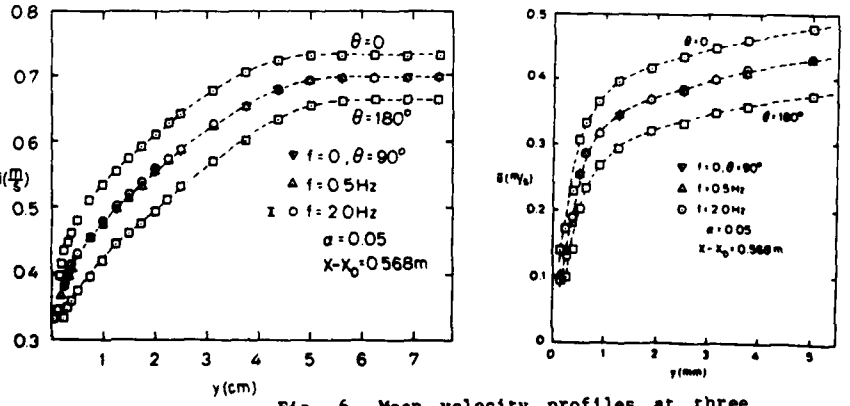

Fig. 6. Mean velocity profiles at three frequencies and profiles at the extremes of the oscillation at zero frequency for $\alpha = 0.05$.

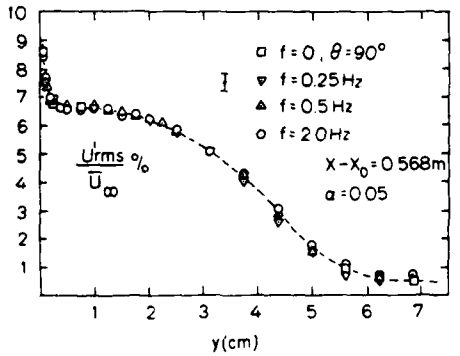

Fig. 7. Mean turbulence profiles at three frequencies for $\alpha = 0.05$.

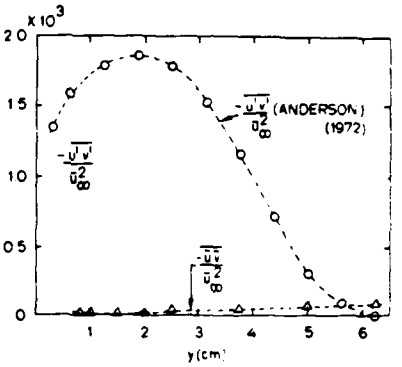

Fig. 8. Turbulent and organized Reynolds stresses for $\alpha = 0.05$.

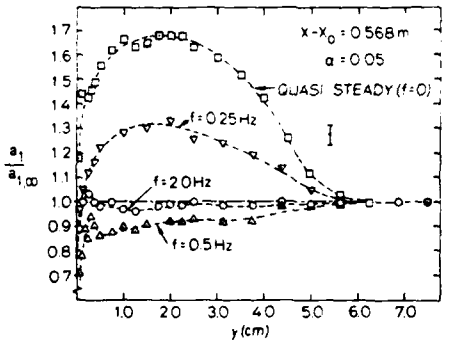

Fig. 9. Amplitude of organized disturbance for $\alpha = 0.05$.

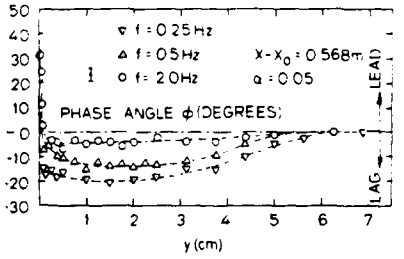

Fig. 10. Phase of organized disturbance for $\alpha = 0.05$.

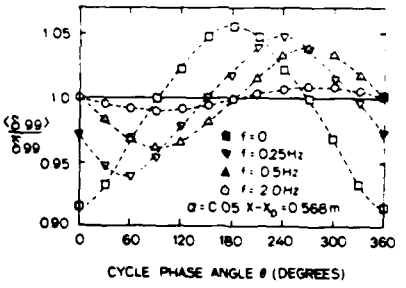

Fig. 11. Phase of boundary layer thickness for $\alpha = 0.05$.

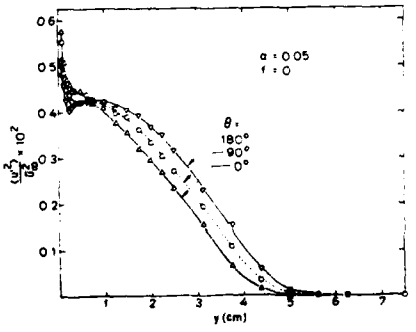

Fig. 12. Phase-average longitudinal fluctuation for $\alpha = 0.05$, $f = 0$.

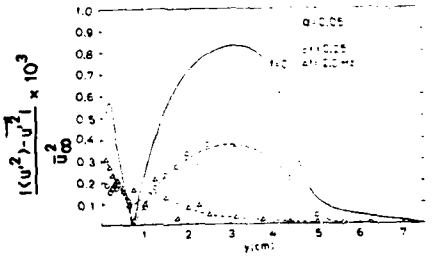

Fig. 13. Reynolds stress oscillations at $\alpha = 0.05$.

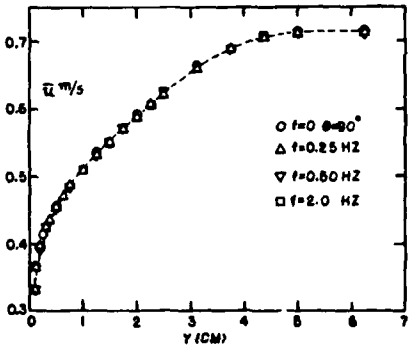

Fig. 14. Mean velocity profiles at different frequencies, second case.

Influence of Strouhal Number on the Structure of a Flat Plate Turbulent Boundary Layer

J. Cousteix

J. Javelle

R. Houdeville

Aerothermodynamics Department

ONERA / CERT

2 av. E. Belin 31055 Toulouse Cedex

ABSTRACT

The development of an oscillating turbulent boundary layer is studied along a flat plate. The Strouhal number, based on a fictitious origine of the boundary layer, varies from 1.5 to 18. Systematic measurements of the velocity profiles are carried out and are presented in the form of the harmonic analysis of the velocity, as well as of the displacement thickness. It is shown that any quantity, for example the phase and the amplitude of the displacement thickness, oscillates as the Strouhal number increases. The period of this oscillation can be correctly estimated from a small perturbation development of the Von Karman momentum integral equation.

The evolution of the phase of velocity profiles near the wall is carefully examined. An estimation of the harmonic analysis of the wall shear stress is given, assuming the validity of the law of the wall and the law of the skin friction coefficient.

The evolution in time of the u-component of the kinetic energy of turbulence and of the correlation coefficient, are presented in a typical case.

INTRODUCTION

The study of unsteady turbulent flows has developed greatly during the last few years, due to the improvement in prediction methods and closure models. Although the number of experimental investigations is also increasing, there exists a lack of experimental data to validate the theoretical work and also, to obtain a better understanding of the physics of the phenomenon. For these reasons, it was felt interesting to undertake the study of the response of a turbulent boundary layer over a flat plate, to an oscillating external velocity field. The simplicity of the boundary conditions, fixed walls and periodic external velocity, allows an extensive and systematic investigation of the boundary layer. This simplicity is also helpful for comparison with other experiments and with predictions.

In the present experiment, the range of the Strouhal number is quite large, between 1.5 and 18, and the velocity profiles are measured at close intervals of Strouhal number, to obtain a detailed description of the response of the boundary layer to the perturbation induced by the oscillation of the external velocity.

NOMENCLATURE

f, T	frequency and period
U	longitudinal velocity
X, Y	longitudinal and normal coordinates
X_o	distance from the ficticious origin of the turbulent boundary layer
S	Strouhal number $S=\omega X_o/\overline{U_e}=2\pi f X_o/\overline{U_e}$
H	shape parameter
R_x	Reynolds number $R_x = U_e X/\upsilon$
C_f	skin friction coefficient $C_f=\tau_w/\frac{1}{2}\rho_e U_e$
$U_\tau=\sqrt{C_f/2}$	
$u^+=U/U_\tau$	$Y^+=YU_\tau/\upsilon$
δ_1	displacement thickness
θ	momentum thickness
τ	shear stress
μ, υ	dynamic and kinematic viscosity
ρ	density
ΔF	amplitude of F
φ_F	phase of F
$\overline{(\ )}$	time mean value
$\langle\ \rangle$	ensemble average
$(\ ')$	random fluctuation

This work was sponsored by the Direction de la Recherche et Etudes Techniques under Grant DRET n° 80.432 (lot n° 6).

Subscripts

o	time mean value
1	complex amplitude
e	external value
w	value at the wall

EXPERIMENTAL SET-UP AND FLOW PARAMETERS

The boundary layer under consideration develops on a 8 m long, .22 m wide and .15 mm thick flat plate. The aspect ratio of the elliptic leading edge is 6. A transverse wire, 0.8 mm in diameter and located 70 mm from the leading edge of the plate, trips the transition of the boundary layer.

The pulsation of the flow is induced by a simple rotating butterfly valve, located 1.3 meter downstream the trailing edge of the flat plate. This valve generates a periodic pressure loss in the suction facility. By choosing the r.p.m. of the butterfly corresponding to the resonance frequencies of the wind tunnel, sinusoïdal variation of the external velocity is easily obtained, with a small harmonic distortion within a few per cent of the fundamental.

The variation of the Strouhal number $\frac{\omega X}{U_e}$ cannot be obtained, only by changing X, which corresponds to a displacement along the plate. Practically, a variation of S from 1.5 to 18 is achieved by choosing two combinations of ω and Ue. Table 1 gives the parameters of the two experiments, as well as a description of the external flow fields in terms of their harmonic analysis. In both experiments, the mean velocity remains constant in the X direction, but the relative amplitude of the fluctuation decreases linearly by a factor 1.5 at $f = 38$ Hz and 3 at $f = 62$ Hz, over a distance of 700 mm. At 38 Hz, the phase difference between the two extreme measurement stations is very small, but it reaches 45° at 62 Hz, which corresponds to a travelling wave with a celerity equal to 450 m/s.

For the calculation of the Strouhal number, a difficulty arises due to the definition of the origin of the turbulent boundary layer. This origin is calculated from the mean momentum thickness, obtained at the first measurement station by using the steady flow flat plate approximation :

$$\frac{\theta}{X_o} = \frac{0.0221}{R_{X_o}^{1/6}} \qquad (1)$$

The quantity X_o in the figures refers to this origin.

MEASUREMENTS AND DATA REDUCTION

Measurements of the longitudinal component of the velocity are done by constant temperature hot wire anemometry. The average velocity is defined using a conditional sampling technique. U being the instantaneous velocity, φ the phase angle in the cycle and n the number of the cycle, we have :

$$\langle U \rangle = \sum_{n=1}^{N} U(nT+\varphi) \text{ with } U = \langle U \rangle + u' \text{ and } \langle u' \rangle = 0$$

The u-component of the turbulence energy is $\langle u'^2 \rangle$ by definition.

In practice, the rotation of the butterfly valve which induces the pulsation of the flow gives the phase information. $\langle U \rangle$ and $\langle u'^2 \rangle$ are obtained at 24 instants per cycle by averaging over 600 cycles /1/.

AVERAGE FLOW FIELD

Mean Flow Field

For both experiments, corresponding to f = 38 and 62 Hz, the average flow field has been compared with the steady configuration at the same Reynolds number. Fig. 1 presents only the results obtained at f = 38 Hz. No influence of the unsteadiness of the flow can be detected at the considered Strouhal numbers, namely between 1.5 and 8. Results corresponding to the case f = 62 Hz extend this conclusion up to S = 18. The skin friction presented in the figure has been obtained using the technique of "Clauser plot", which consists in fitting the experimental velocity profiles by the law of the wall. The results are in good agreement with predictions using an integral method. Moreover, the slope of $\theta(X)$ agrees well with the estimated values of the skin friction coefficient, which indicates a good two-dimensionality of the flow.

Harmonic Analysis Of The Velocity

Profiles of the relative amplitude of fluctuation and of phase shift with respect to the external velocity, are presented in figures 2 and 3 for several stations along the plate. A slight overshoot of $\Delta U/\Delta U_e$ exists at the first station. It increases to reach 20% at $X_o = 0.34$ m. Farther downstream, it decreases and disappears completely at $X_o = .54$ m. Then, this evolution repeats. If the boundary layer is considered as a resonant mechanical system, the observed periodicity along X can be interpreted as the response of the boundary layer to the perturbation induced by the pulsation of the external flow.

$U_e = \overline{U_e} + \Delta U_e \sin(\omega t + \varphi_{ue})$		
F (Hz)	38	62
$\overline{U_e}$ (m/s)	21.9	16.8
$\Delta U_e / \overline{U_e}$	0.152 - 0.0743 $(X_o - 0.047)$	0.118 - 0.114 $(X_o - 0.047)$
$\varphi^\circ_{U_e}$	7.6 $(X_o - 0.047)$	88.9 $(X_o - 0.047)^2$ + 6.66 $(X_o - 0.047)$
X_o (m)	0.14 to 0.77	0.137 to 0.762
$\omega X_o / \overline{U_e}$	1.52 to 8.35	3.2 to 17.8
R_{X_o}	0.2 10^6 to 1.1 10^6	0.15 10^6 to 0.87 10^6
U_{max}/δ (s^{-1})	350 to 120	270 to 90

Table 1 : External velocity and main parameters of the flows

By assuming the existence of a travelling wave which affects the successive profiles, the convective celerity of this wave is of the order of .75 $\overline{U_e}$ .The results obtained at 62 Hz lead to the same interpretation.

The evolution with Strouhal number of the profiles of the phase shift of the velocity, also displays a periodicity, similar to that of the profiles of $\Delta U/\Delta U_e$. An interesting feature of the profiles $\varphi_U - \varphi_{U_e}$ is the maximum phase lead observed around $Y^+ = 50$, corresponding to the logarithmic region of the velocity profile. Simpson /2/ has also observed an extremum in the logarithmic region. This property will be interpreted later.

Integral Boundary Layer Thickness

The relative amplitude of fluctuation of the displacement thickness δ_1 , divided by the relative amplitude of the external velocity,and the phase difference with respect to Ue are presented in figure 4. All the experimental results obtained at ONERA are plotted with those of Karlsson /3/. For the sake of uniformity, the Strouhal number is calculated using a fictitious origin of the turbulent boundary layer. Despite large differences in the initial conditions and the transition process, and although the Strouhal number is not the unique parameter to take into account, an overall good agreement is observed between the various experiments, especially the phase difference with respect to the external velocity. In experiments, this last quantity is measurable with a better accuracy than the relative amplitude of oscillation.

The striking result is the periodic oscillation of the quantities with a small damping as the Strouhal number increases. This oscillation has been previously observed for the shape of the profiles of relative amplitude and phase shift of the velocity. Its period is close to 5. This means that it can be detected only if the boundary layer is measured at close intervals of Strouhal number, which was not the case in the pioneering experiments of Karlsson.

The general feature of the response of the boundary layer to the oscillation of the external velocity, can be easily illustrated from a small perturbation expansion of the Karman's equation :

$$\frac{C_f}{2} = \frac{\partial \theta}{\partial X} + \theta \frac{H+2}{U_e}\frac{\partial U_e}{\partial X} + \frac{1}{U_e^2}\frac{\partial}{\partial t}(U_e \delta_1) \qquad (2)$$

By assuming that all the quantities appearing in equation (2) can be written in the form :

$f = f_o + f_1 e^{i\omega t}$, and the modulus of f_1 , the complex amplitude,being supposed small compared to f_o , the Karman's equation reads :

$$\frac{d\theta_1}{dX} = \frac{C_{f1}}{2} - \frac{i\omega}{U_{eo}}\left(\delta_{11} + \delta_{1o}\frac{U_{e1}}{U_{eo}}\right) \qquad (3)$$

To close equation (3), it is assumed that the shape parameter remains constant and that the skin friction is a function only of R_θ and H,or equivalently in the present case of θ and Ue, but is not explicitely a function of time. Then, equation (3) becomes :

$$\frac{d\theta_1}{dX} + \theta_1\left[i\omega\frac{H_o}{U_{e1}} - \frac{1}{2}\left(\frac{\partial C_f}{\partial \theta}\right)_o\right] =$$

$$\frac{U_{e1}}{2}\left(\frac{\partial C_f}{\partial U_e}\right)_o - i\omega H_o \theta_o \frac{U_{e1}}{U_{eo}} \qquad (4)$$

Using the Strouhal number $S = \omega X/U_{eo}$ instead of X, equation (4) has a solution of the form :

$$\theta_1 = \theta \exp\left[\left(-iH_o + \frac{U_{eo}}{2\omega}\left(\frac{\partial C_f}{\partial \theta}\right)_o\right)S\right] \qquad (5)$$

The period of θ_1 is equal to $2\pi/H_o \simeq 4.5$, which is close to the experimentally observed value of 5.Moreover, the above calculation shows that the damping factor is strongly dependent on the chosen skin friction law.

Skin Friction Coefficient - Phase Shift Near The Wall

Law of the wall

Direct measurement of the wall shear stress being particularly difficult in unsteady flow, it can be interesting to deduce it by using the technique of "Clauser plot" as in steady flow. To do this, the experimental velocity profile is approximated by the law of the wall, which is supposed to remain valid at every instant of the cycle. Following law has been used :

$$U^+ = \frac{1}{\kappa} Ln\, Y^+ + C \qquad (6)$$

with $\kappa = 0.41$ and $C = 5.25$.

In figure 5, profiles measured at a given location but at different instants during a cycle, are plotted in semi-logarithmic coordinates. At each instant, the value of U_τ which gives the best fit with equation (6) is used to calculate Y^+ and U^+ . A good agreement is observed between the experimental velocity profiles and formula (6) over a rather wide range of Y^+ , as in steady flow.

The above method of determining U_τ has been used to obtain the harmonic analysis of τ_W presented in figure 6. The phase shift of τ_W with respect to U_e remains small, less than 20 degrees and decreases when the Strouhal number increases. As regards the relative amplitude of fluctuation of τ_W , the general trend is an increase, to which an oscillation with a period equal to 5.5 is superimposed. One can again notice the weakly damped response of the boundary layer to the perturbation of the external flow.

It has been shown by Simpson /2/ that the existence of a logarithmic region of overlap, between the law of the wall and the law of the wake,implies that the velocity phase shift remains constant in such a region. In fact, this conclusion is a direct consequence of the assumption of the existence of a general universal law of the form :

$$U^+ = f(Y^+) \qquad (7)$$

in which time does not appear explicitely, but only in U^+ and Y^+ through U_τ .

A small perturbation expansion of (7) leads to the following equations, for the time-mean velocity and the complex amplitude :

$$\frac{U_o}{U_{\tau o}} = f\left(\frac{Y U_{\tau o}}{\upsilon}\right) \qquad (8)$$

$$U_1 = U_{\tau_1}\left[f\left(\frac{Y U_{\tau o}}{\upsilon}\right) + \frac{Y U_{\tau o}}{\upsilon}\frac{df}{dY^+}\right] \qquad (9)$$

Equation (8) only indicates that the time-mean velocity profile obeys the steady universal law, which is not surprising. Equation (9) shows that the velocity phase shift is constant and equal to the phase of the shear velocity, or equivalently to the phase of the wall shear stress / 2/ .

Experimentally, the velocity phase shift is nearly constant in the region where a logarithmic behaviour exists. Acutally, a local maximum of the velocity phase lead occurs around $Y^+ = 50$. Despite the fact that the experimental velocity phase lead decreases rapidly near the wall, the phases of the wall shear stress determined by assuming the vali-

dity of the law of the wall, compare well with the maximum velocity phase shift. This can be seen in figure 3, where the triangles correspond to the phase of τ_w .

A possible interpretation of the above results is that a universal law, such as eq. (7), does not cover the whole wall region, from y = 0 to the logarithmic region, but covers only this last region in the immediate vicinity of the wall where $U^+ = Y^+$. In other words, it is possible that the buffer layer does not obey the universal law (7).

Sublayer region

The existence of the universal law of the wall, which is indicated from figure 5, implies that the maximum phase lead of the velocity, observed in figure 3, is equal to the wall shear stress phase shift. For the coherence of the results, the phase of the velocity must increase in the sublayer region. This can be supported by considering the boundary layer equation written in the sublayer region :

$$-\frac{1}{\rho}\frac{\partial P}{\partial X} + \frac{\partial}{\partial Y}\left(\mu \frac{\partial U}{\partial Y}\right) = 0 \qquad (10)$$

By setting $-\frac{1}{\rho}\frac{\partial P}{\partial x} = \frac{\partial U_e}{\partial t}$ and using a small perturbation expansion, the phase of the velocity is given by :

$$\tan(\varphi_U - \varphi_{Ue}) = \frac{\tan(\varphi_{\tau w} - \varphi_{Ue}) - \frac{\omega \upsilon}{2U_{eo}^2}\left(\frac{C_f}{2}\right)^{-\frac{3}{2}} \frac{|U_{e1}|}{|\tau_{w1}|/\tau_{wo}}}{1 + \frac{\omega \upsilon}{2U_{eo}^2}\left(\frac{C_f}{2}\right)^{-\frac{3}{2}} \frac{|U_{e1}|}{|\tau_{w1}|/\tau_{wo}} \tan(\varphi_{\tau w} - \varphi_{Ue})} \qquad (11)$$

This equation shows that the velocity phase shift is not constant near the wall, but decreases as Y increases. Substitution of typical experimental values indicates that for f = 38 Hz, the velocity phase shift decreases by about 6° between $Y^+ = 0$ and $Y^+ = 5$. This decrease is about 13° for f = 62 Hz. The values so obtained agree well with the experimental phase differences plotted in figure 3, the measurement point closest to the wall corresponding to Y^+ between 10 and 6, depending on X_o . The actual behaviour of the velocity phase shift near the wall can be thought of, as given in the figure 7.

In the above discussion, it is assumed that the scaling parameter U_τ which appears in the law of the wall, is equal to $\sqrt{\tau_w/\rho}$. If it was not the case, the velocity phase shift would be constant in the logarithmic region, but not equal to the shift of the wall shear stress phase.

An Expression For The Velocity Phase Shift in The Logarithmic Region

To obtain this expression, it can be assumed that, at each instant, the skin friction coefficient obeys the same law as in a steady flow (4) :

$$\left(\frac{2}{C_f}\right)^{1/2} = \frac{1}{\chi} \operatorname{Ln} \frac{U_e \delta_1}{\upsilon} + D^* \qquad (12)$$

with $D^* = 2\,G - 4.25\,G^{1/2} + 2.12$

and $G = \frac{H-1}{H(C_f/2)^{1/2}}$

By carrying out a small perturbation expansion of equation (12), the phase and the amplitude of τ_w can be expressed as functions of the harmonic analysis of the displacement and momentum thicknesses, and of the external velocity (5). The results obtained from this calculation compare well with those deduced from the law of the wall (figure 6).

TURBULENCE QUANTITIES

Figure 8 shows two cycles of the evolution in time of the u-component of the kinetic energy of turbulence, divided by its mean value. The distance to the wall corresponds to a constant value of Y/δ equal to .8, and the distance between two successive stations is equal to 5 cm. The stars indicate the instants when $\langle u'^2 \rangle$ is maximum. The fact that they are along the dotted straight lines, the slope of which corresponds to .85 Ue, leads to a result similar to that obtained in steady flow from space-time correlation measurements.

An other interpretation of the results of figure 8 is that the free edge of the boundary layer oscillates at the frequency of the external flow, and can be represented by a travelling wave, the celerity of which being equal to .85 Ue.

An important turbulence parameter is the correlation coefficient. In the closure models for calculation methods, it is more or less explicitely assumed constant. The evolution in time of this coefficient is plotted in fig. 9 for two cycles at increasing distances from the wall. Except in the external region where $\langle u'v' \rangle$ vanishes, the correlation coefficient remains constant and equal to the value commonly found in steady turbulent boundary layers, which is 0.45. This result tends to prove that, up to Strouhal number of 5, the development of the turbulence is not strongly affected by the unsteadiness of the flow.

CONCLUSIONS

The experimental study of the response of a turbulent boundary layer over a flat plate to an oscillating external velocity field has confirmed that the mean flow field is not affected by the unsteady effects up to Strouhal number equal to 18. A possible interpretation of the measurements is that the boundary layer responds to the perturbation induced by the pulsation of the external flow as a mechanical system with a small damping.

Although no direct measurement of the wall shear stress has been done so far, an estimation of this parameter can be obtained by assuming that the law of the wall remains valid. A consequence of this assumption is that the phase of the velocity near the wall is constant, and equal to the wall shear stress phase shift. Actually, a maximum of phase lead is measured at Y^+ around 50, but the velocity phase lead decreases near the wall, which tends to prove that the buffer layer does not remain a universal function independent of time.

REFERENCES

1 Houdeville, R., and Cousteix, J., "Couches Limites Turbulentes en Ecoulement Pulsé avec Gradient de Pression Moyen Défavorable," La Recherche Aérospatiale, 1979-1, pp. 33-48 , Nasa Tr. TM 75799-N 8017400.

2 Simpson, R.L., "Features of Unsteady Turbulent Boundary Layers as Revealed From Experiments," Proceedings of the Conference on Unsteady Aerodynamics Ottawa, Sept. 1977, AGARD-CP-227.

3 Karlsson, S.K.F., "An Unsteady Turbulent Boundary Layer," Journal of Fluid Mechanics, Vol. 5, 1959, pp. 622-636.

4 Cousteix, J., and Houdeville, R., "Turbulent Boundary Layer Calculations in Unsteady Flow," Numerical Methods in Applied Fluid Dynamics, Academic Press, 1980, pp. 615-644.

5 Cousteix, J., Houdeville, R., and Javelle J., "Response of a Turbulent Boundary Layer to a Pulsation of the External Flow With and Without Adverse Pressure Gradient," Proceedings of the IUTAM Symposium on Unsteady Turbulent Shear Flows, Toulouse, May 1981 Springer-Verlag.

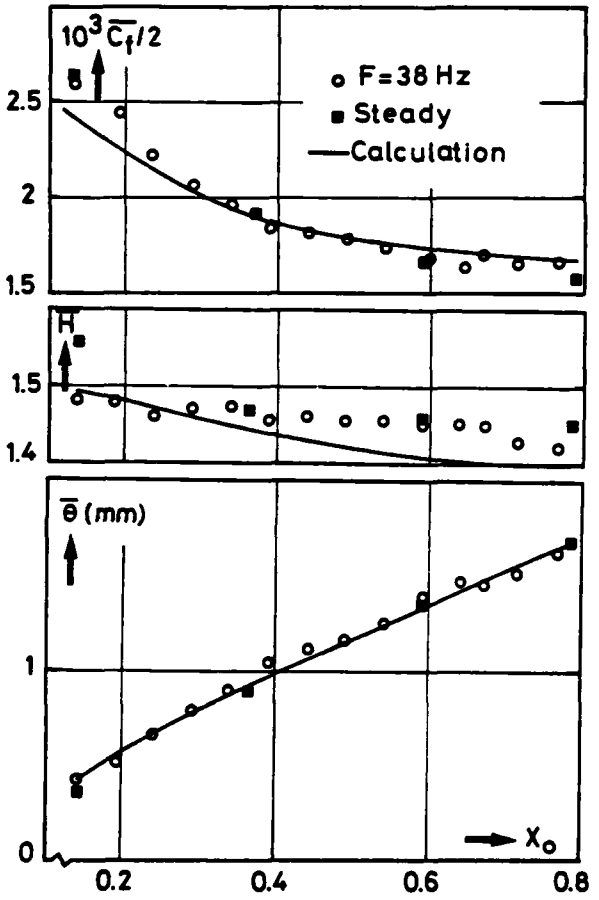

Fig.1:Mean flow field.Evolution of momentum thickness, shape parameter and skin friction along the plate - f = 38 Hz.

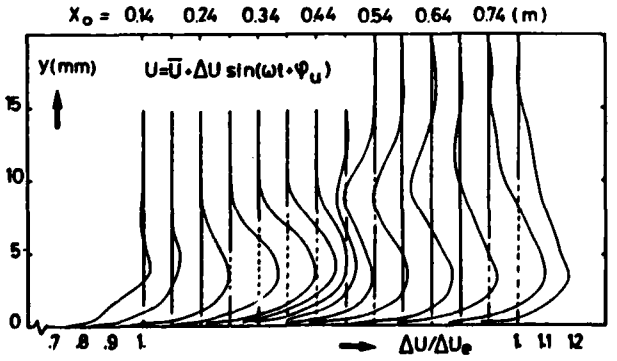

Fig.2:Harmonic analysis of the velocity - Relative amplitude of fluctuation - f = 38 Hz

6 Cousteix, J., Desopper, A., and Houdeville, R.,"Structure And Development of a Turbulent Boundary Layer in an Oscillatory External Flow", Turbulent Shear Flows I, Springer-Verlag, pp. 154-171.

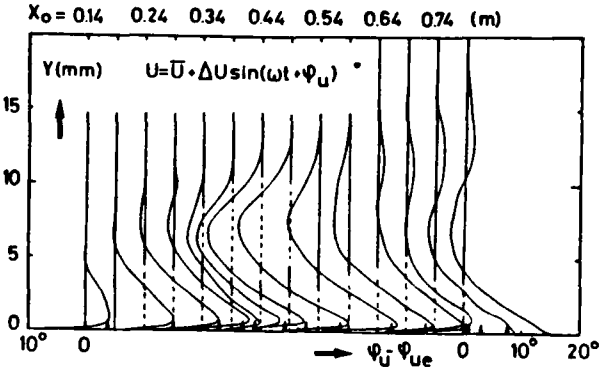

Fig. 3:Harmonic analysis of the velocity - Phase shift - ▲:φ_{TW} calculated from the law of the wall - f = 38 Hz

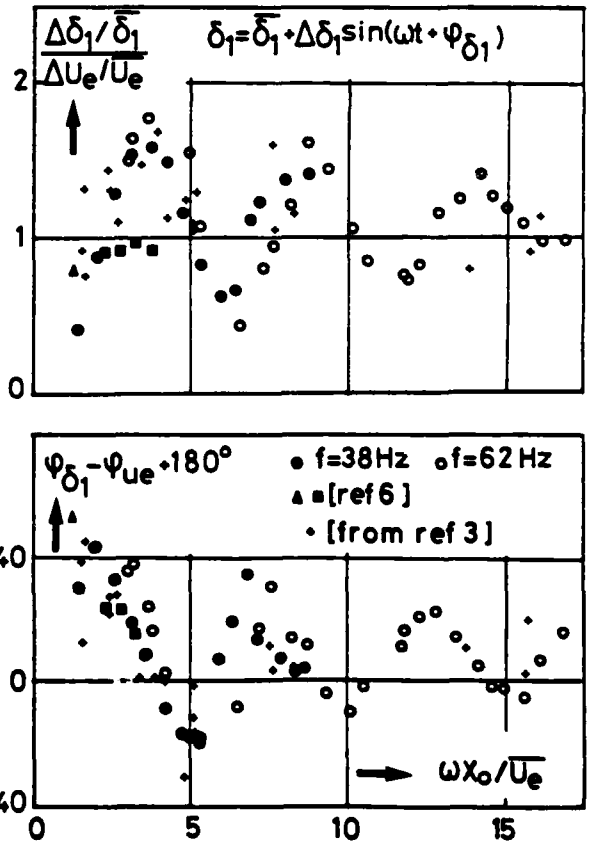

Fig.4:Harmonic analysis of the displacement thickness versus Strouhal number

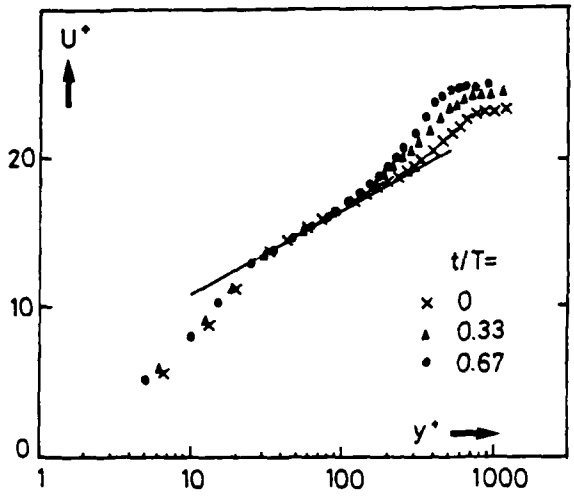

Fig.5:Velocity profiles at different instants - S=5.9-f=38 Hz. ——— Law of the wall (6)

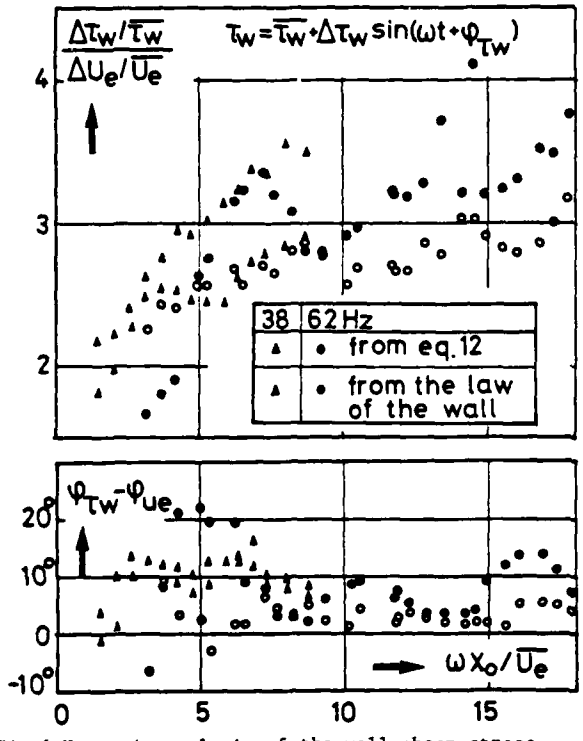

Fig.6:Harmonic analysis of the wall shear stress versus Strouhal number

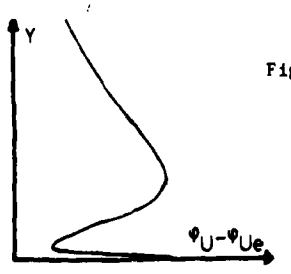

Fig.7:Possible evolution of the velocity phase-shift near the wall

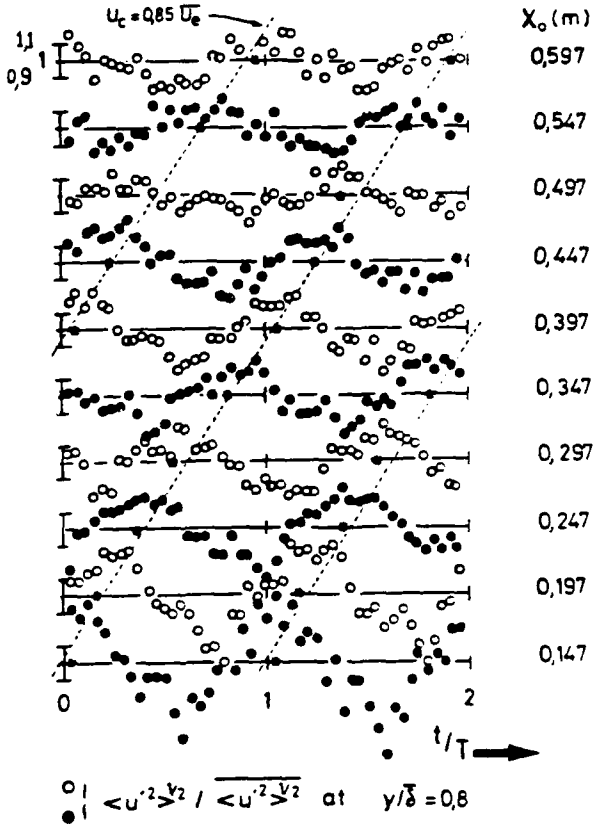

Fig.8:Evolution in time of the turbulence intensity at Y/δ =.8 for different stations along X - f = 62 Hz

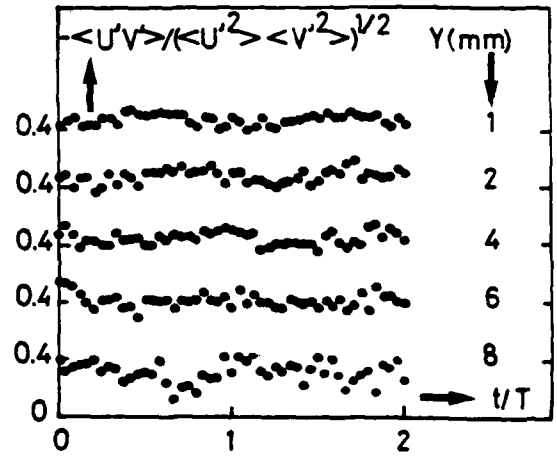

Fig.9:Evolution in time of the correlation coefficient at different distances from the wall, S = 5.

SESSION 9 - GEOPHYSICAL FLOWS I

J. C. Wyngaard - Chairman

DIFFUSION FROM AN ELEVATED SOURCE WITHIN THE ATMOSPHERIC BOUNDARY LAYER

by

P.C. CHATWIN
Department of Applied Mathematics
and Theoretical Physics
The University of Liverpool

and

P.J. SULLIVAN
Department of Applied Mathematics
The University of Western Ontario

ABSTRACT

Concentration distributions that result from contaminant release from an elevated source are found from the solution of the convective-diffusion equation prior to the encounter of an appreciable amount of contaminant with the ground. The important role of the variability of diffusivity in diffusion problems in the atmosphere is clearly exposed.

NOMENCLATURE

a_i, b_i, c_i, d_i = coefficients in a Taylor series expansion of κ_i and u.
α, β, γ = non-dimensional diffusive parameters.
$C(\underset{\sim}{x},t)$ = contaminant concentration.
$D_{ijk}(t)$ = coefficients in Gram Charlier expansion.
ζ = non-dimensional dispersive-parameter.
F, P, Q = conveniently defined functions.
h = release height.
$H_{ijk}(\underset{\sim}{X})$ = Hermite polynomials.
$\kappa_i(x_1)$ = diffusivities.
$M_{m,n,p}(t)$ = moments of $C(\underset{\sim}{x},t)$.
R, r_{ij} = correlation coefficient matrix and elements.
$\sigma_i(t)$ = standard deviation of $C(\underset{\sim}{x},t)$.
σ_ϕ = standard deviation of wind angle.
τ = non-dimensional time scale.
$u(x_1)$, $U(x_1)$ = mean velocity profiles, the former relative to the velocity at the release position.
u_* = friction velocity.
v' = standard deviation for vertical fluctuating velocities.
$\underset{\sim}{x}$, x_i = position vector and components from the release point.
$\underset{\sim}{X}$, X_i = position vector and components relative to the centre-of-mass and normalized with σ_i.
$\bar{x}_i$ = co-ordinates of the cloud centre-of-mass.
x_m = down wind location of the maximum value of ground-level concentration.
z = non-dimensional vertical distance from the ground.

INTRODUCTION

The problem of contaminant release from an elevated source within the earth's boundary-layer is of particular practical importance. The customary procedure (10, 15, 16) for modelling atmospheric diffusion is to assume 'eddy diffusivities' where the principal axes of the diffusion tensor are aligned with the vertical, lateral and streamwise directions. For an instantaneous point source the resulting equations governing contaminant concentration $C(\underset{\sim}{x},t)$ are:

$$\frac{\partial C}{\partial t} + \frac{\partial (uC)}{\partial x_3} = \frac{\partial}{\partial x_1}\left(\kappa_1 \frac{\partial C}{\partial x_1}\right) + \kappa_2 \frac{\partial^2 C}{\partial x_2^2} + \kappa_3 \frac{\partial^2 C}{\partial x_3^2} \qquad (1)$$

when $$\int_{\text{all space}} C(\underset{\sim}{x},t)\, dV(\underset{\sim}{x}) = 1, \qquad (2)$$

and $$C(\underset{\sim}{x},0) = \delta(x_1)\,\delta(x_2)\,\delta(x_3). \qquad (3)$$

The downwind direction x_3 is measured relative to U(0)t so that the velocity profile is

$$U(x_1) = u(x_1) + U(0) \qquad (4)$$

and the lateral direction x_2 and vertical direction x_1 are measured from the release position. $x_2 = 0$ is a plane of symmetry. The large amount of work based on (1) can be found summarized in (16) for example however the bulk of this work is applied to the steady plume model for specific forms of $u(x_1)$ and $\kappa_i(x_1)$. The intrinsically nonstationary character of the diffusion of a cloud in a turbulent shear flow suggests that (1) will be approximate and that the solutions to (1) be closely checked with experiment. Some discussion on this type of approximation is found in (11). It is desirable to assess the validity of (1) by comparison with experimental measurements that are taken before the contaminant has encountered the viscous-dominated or rough boundary region immediately adjacent to the ground. Not only is the detailed flow structure very uncertain in this region but its presence will have a dominant effect on the subsequent cloud evolution. Thus 'near-source' or 'small-time' solutions to (1) are required for a sensitive assessment of the basic modelling.

There are also compelling practical reasons, related to the deposition problem, for the investigation of the near-source diffusion from an elevated source within the earths' boundary-layer. Although some insight is available (mainly for ground-level release) from a Lagrangian similarity analysis (4,5) the extension of this theory to encompass release from an elevated source would appear to require a distance downstream that is large with respect to the distance at which the maximum ground-level concentration occurs(10).

The 'method of moments' (1,17) is used in a new way to investigate the 'small-time' dispersion problem with variable diffusivity as set out in (1), (2) and (3). First all of the moments of the concentration distribution $C(\underline{x},t)$ are found from (1) and the moments are then used to construct $C(\underline{x},t)$ using a generalized Hermite polynomial expansion. Although a great deal of information is contained in the first few moments of the distribution, important considerations such as the value and spatial location of the maximum concentration are not. Advocacy of the use of the Hermite polynomials in the asymptotically large time dispersion problem is found in (7) and for the fluctuation problem in relative turbulent diffusion in (8,9).

Defining moments as:

$$M_{m,n,p}(t) = \int_{\substack{\text{all}\\ \text{space}}} x_1^m x_2^n x_3^p C(\underline{x},t)\,dV(\underline{x}) \quad (5)$$

one derives from (1) the recurrence relationship

$$\begin{aligned} \dot{M}_{m,n,p}(t) &= m[(m-1)a_0 M_{m-2,n,p} + ma_1 M_{m-1,n,p} + (m+1)a_2 M_{m,n,p}] \\ &+ n(n-1)[b_0 M_{m,n-2,p} + b_1 M_{m+1,n-2,p} + b_2 M_{m+2,n-2,p}] \\ &+ p(p-1)[c_0 M_{m,n,p-2} + c_1 M_{m+1,n,p-2} + c_2 M_{m+2,n,p-2}] \\ &+ p\sum_{i=1}^{q} d_i M_{m+i,n,p-1} \end{aligned} \quad (6)$$

when a Taylor series expansion about the point of release and truncated after quadratic terms for $\kappa_i(x_1)$ is used and an arbitrary but finite number q of terms for $u(x_1)$ is used. That is

$$\kappa_1(x_1) = a_0 + a_1 x_1 + a_2 x_1^2 \quad (7a)$$

$$\kappa_2(x_1) = b_0 + b_1 x_1 + b_2 x_1^2 \quad (7b)$$

$$\kappa_3(x_1) = c_0 + c_1 x_1 + c_2 x_1^2 \quad (7c)$$

$$u(x_1) = \sum_{i=1}^{q} d_i x_1^i. \quad (7d)$$

It is apparent that, because of the plane of symmetry $x_2 = 0$

$$M_{m,2n+1,p} = 0. \quad (8)$$

The Taylor series expansion for $\kappa_i(x_1)$ and $u(x_1)$ will describe, locally, all reasonable functions and only as the cloud size grows in time will higher ordered coefficients a_i, b_i, c_i and d_i in (7a - d) be required for an adequate representation. For example, as $t \to 0$ only a_0, b_0 and c_0 are important. In the atmosphere the quadratic terms in (7a-c) represent first approximations to the deviations from the linear values occurring in neutral stratification. The inclusion of x^3 terms in (7a - c) does not permit the simple recursion relationships of (6) so that it is preferable to write the solution to (1) as

$$C(\underline{x},t) = \int_{\substack{\text{all}\\ \text{space}}} C(\underline{y},t-T)C(\underline{x}-\underline{y},t)\,dV(\underline{y}) \quad (9)$$

with the initial conditions (3) and the understanding that T is kept sufficiently small so that (7a - d) will apply at each point throughout the cloud of contaminant. The simple recurrence relationship (6) is ideally suited to recent developments in computer software that provide analytic solutions to such equations (2).

With the moments $M_{m,n,p}(t)$ determined from the solution of (6) a Gram-Charlier series for $C(\underline{x},t)$ is constructed (12,14) such that

$$\begin{aligned} &\sigma_1\sigma_2\sigma_3 C(\underline{x},t) \\ &= (8\pi^3|R|)^{-\frac{1}{2}} e^{-\frac{1}{2}g(\underline{X})} \sum_{\substack{i+j+k\\ =0}}^{\infty} D_{ijk}(t) H_{ijk}(\underline{X}) \end{aligned} \quad (10)$$

where $g(X) = X^T R X$ is a quadratic form in the standardized variable X and R is the correlation coefficient matrix. $H_{ijk}(\underline{X})$ are Hermite polynomials and their coefficients $D_{ijk}(t)$ are conveniently expressible as functions of the moments of $C(\underline{x},t)$

Because of the plane of symmetry in this problem ($x_2 = 0$)

$$D_{i,2j+1,k} = 0 \quad (11)$$

AD-A111 582 PENNSYLVANIA STATE UNIV UNIVERSITY PARK DEPT OF MECH--ETC F/G 20/4
SYMPOSIUM ON TURBULENT SHEAR FLOWS (3RD), UNIVERSITY OF CALIFOR--ETC(U)
SEP 81 F W SCHMIDT AFOSR-80-0033

UNCLASSIFIED AFOSR-TR-82-0032 NL

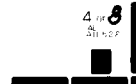

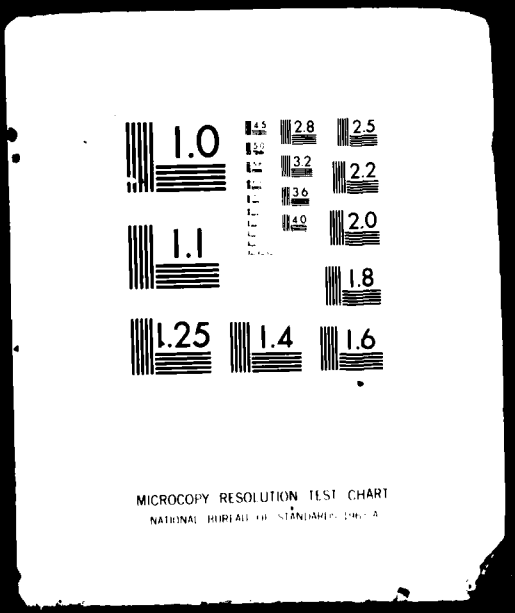

III. PRESSURE PARAMETERIZATION FOR SINGLE-POINT HIGH-ORDER MODELING

in which the parameterization of molecular terms

and the lateral direction x_2 and vertical direction x_1 are measured from the release position. $x_2 = 0$ is a plane of symmetry. The large amount of work based on (1) can be found summarized in (16) for example however the bulk of this work is applied to the steady plume model for specific forms of $u(x_1)$ and $\kappa_1(x_1)$. The intrinsically nonstationary character of the diffusion of a cloud in a turbulent shear flow suggests that (1) will be approximate and that the solutions to (1) be closely checked with experiment. Some discussion on this type of approximation is found in (11). It is desirable to assess the validity of (1) by comparison with experimental measurements that are taken before the contaminant has encountered the viscous-dominated or rough boundary region immediately adjacent to the ground. Not only is the detailed flow structure very uncertain in this region but its presence will have a dominant effect on the subsequent cloud evolution. Thus 'near-source' or 'small-time' solutions to (1) are required for a sensitive assessment of the basic modelling.

There are also compelling practical reasons, related to the deposition problem, for the investigation of the near-source diffusion from an elevated source within the earths' boundary-layer. Although some insight is available (mainly for ground-level release) from a Lagrangian similarity analysis (4,5) the extension of this theory to encompass release from an elevated source would appear to require a distance downstream that is large with respect to the distance at which the maximum ground-level concentration occurs(10).

The 'method of moments' (1,17) is used in a new way to investigate the 'small-time' dispersion problem with variable diffusivity as set out in (1), (2) and (3) . First all of the moments of the concentration distribution $C(\underline{x},t)$ are found from (1) and the moments are then used to construct $C(\underline{x},t)$ using a generalized Hermite polynomial expansion. Although a great deal of information is contained in the first few moments of the distribution, important considerations such as the value and spatial location of the maximum concentration are not. Advocacy of the use of the Hermite polynomials in the asymptotically large time dispersion problem is found in (7) and for the fluctuation problem in relative turbulent diffusion in (8,9).

Defining moments as:

$$M_{m,n,p}(t) = \int_{\substack{\text{all}\\ \text{space}}} x_1^m x_2^n x_3^p C(\underline{x},t)\,dV(\underline{x}) \qquad (5)$$

one derives from (1) the recurrence relationship

$$\begin{aligned} M'_{m,n,p}(t) &= m[(m-1)a_0 M_{m-2,n,p} + ma_1 M_{m-1,n,p} + (m+1)a_2 M_{m,n,p}] \\ &+ n(n-1)[b_0 M_{m,n-2,p} + b_1 M_{m+1,n-2,p} + b_2 M_{m+2,n-2,p}] \\ &+ p(p-1)[c_0 M_{m,n,p-2} + c_1 M_{m+1,n,p-2} + c_2 M_{m+2,n,p-2}] \\ &+ p\sum_{i=1}^{q} d_i M_{m+1,n,p-1} \end{aligned} \qquad (6)$$

when a Taylor series expansion about the point of release and truncated after quadratic terms for $\kappa_i(x_1)$ is used and an arbitrary but finite number q of terms for $u(x_1)$ is used. That is

$$\kappa_1(x_1) = a_0 + a_1 x_1 + a_2 x_1^2 \qquad (7a)$$

$$\kappa_2(x_1) = b_0 + b_1 x_1 + b_2 x_1^2 \qquad (7b)$$

$$\kappa_3(x_1) = c_0 + c_1 x_1 + c_2 x_1^2 \qquad (7c)$$

$$u(x_1) = \sum_{i=1}^{q} d_i x_1^i. \qquad (7d)$$

It is apparent that, because of the plane of symmetry $x_2 = 0$

$$M_{m,2n+1,p} = 0. \qquad (8)$$

The Taylor series expansion for $\kappa_i(x_1)$ and $u(x_1)$ will describe, locally, all reasonable functions and only as the cloud size grows in time will higher ordered coefficients a_i, b_i, c_i and d_i in (7a - d) be required for an adequate representation. For example, as $t \to 0$ only a_0, b_0 and c_0 are important. In the atmosphere the quadratic terms in (7a-c) represent first approximations to the deviations from the linear values occurring in neutral stratification. The inclusion of x^3 terms in 7a - c) does not permit the simple recursion relationships of (6) so that it is preferable to write the solution to (1) as

$$C(\underline{x},t) = \int_{\substack{\text{all}\\ \text{space}}} C(\underline{y},t-T)C(\underline{x}-\underline{y},t)\,dV(\underline{y}) \qquad (9)$$

with the initial conditions (3) and the understanding that T is kept sufficiently small so that (7a - d) will apply at each point throughout the cloud of contaminant. The simple recurrence relationship (6) is ideally suited to recent developments in computer software that provide analytic solutions to such equations (2).

With the moments $M_{m,n,p}(t)$ determined from the solution of (6) a Gram-Charlier series for $C(\underline{x},t)$ is constructed (12,14) such that

$$\begin{aligned} &\sigma_1\sigma_2\sigma_3 C(\underline{x},t) \\ &= (8\pi^3|R|)^{-\frac{1}{2}} e^{-\frac{1}{2}g(\underline{X})} \sum_{\substack{i+j+k\\ =0}}^{\infty} (-1)^{i+j+k} D_{ijk}(t) H_{ijk}(\underline{X}) \end{aligned} \qquad (10)$$

where $g(X) = X^T R X$ is a quadratic form in the standardized variable X and R is the correlation coefficient matrix. $H_{ijk}(\underline{X})$ are Hermite polynomials and their coefficients $D_{ijk}(t)$ are conveniently expressible as functions of the moments of $C(\underline{x},t)$

Because of the plane of symmetry in this problem ($x_2 = 0$)

$$D_{i,2j+1,k} = 0 \qquad (11)$$

and

$$r_{11} = r_{22} = r_{33} = 1,\ r_{23} = r_{12} = 0. \qquad (12)$$

Thus the inertia tensor for the contaminant cloud $C(\underline{X},t)$ will always have principal axes $[0,1,0]^T$, $[1,0,1]^T$, $[1,0,-1]^T$ and with relative magnitudes along these principal axes of 1, $1 + r_{13}(t)$, $1 - r_{13}(t)$ respectively. The Gram-Charlier series expansion for $i+j+k < 3$ in (10) is simply the (generalized) Gaussian distribution

$$C(\underline{X},t) = \frac{e^{-\frac{1}{2}g(\underline{X})}}{(8\pi^3|R|)^{\frac{1}{2}}} \qquad (13)$$

Finally, before proceeding to the problem specifics, it is to be noticed that the solution of (1) for an instantaneous point source is generic in that solutions to continuous plume models and line sources and distributed or non-uniform and time dependent source emissions are retrieved by superposition from (9) by

$$\bar{C}(\underline{X},t) = \int_{-\infty}^{\infty} S(t - T)C(\underline{X},t)dT \qquad (14)$$

where $S(t)$ is the appropriate source emission rate (3).

ANALYSIS FOR $m+n+p \leq 2$

The moments for which $m+n+p \leq 2$ in (5) determine the trajectory of the centre-of-mass of the contaminant cloud and the terms of the inertia tensor and give rise to the Gaussian distribution (13) when used in (10). The first moment, calculated with (6), (7a - d) and setting $q = 2$ in (7d), is for example

$$M_{100} = \frac{a_1}{2a_2}(e^{2a_2 t} - 1). \qquad (15)$$

It is impractical due to the length of the expressions to reproduce more of these moments here.

The trajectory of the centre-of-mass of the diffusing cloud remains on the $x_2 = 0$ plane and has the parabolic form

$$\bar{x}_3 = \left(\frac{a_1 d_1 + 2a_0 d_2}{2a_1^2}\right)\bar{x}_1^2 \qquad (16)$$

provided that

$$t < a_2^{-1} \qquad (17a)$$

and

$$t < \frac{(3/2)(a_1 d_1 + 2a_0 d_2)}{2a_1^2 d_2 + a_2(a_1 d_1 + 6a_0 d_2)} . \qquad (17b)$$

Thus the parabolic form of (16) provides one salient feature of all solutions to (1) which should be readily observed by experiment.

ORDERS OF MAGNITUDE OF $D_{ijk}(t)$

It is useful to define

$$\tau^2 = \left(\frac{a_1^2 t}{2a_0}\right),\ \alpha^2 = \left(\frac{a_0 b_1}{a_1 b_0}\right),\ \gamma^2 = \left(\frac{a_0 c_1}{a_1 c_0}\right)$$

$$\xi^2 = \left(\frac{a_0^3 d_1^2}{a_1^4 c_0}\right),\ \beta^2 = \left(\frac{2a_0 a_2}{a_1^2}\right). \qquad (18)$$

For a typical release in an atmospheric boundary layer at height h

$$a_0 \sim b_0 \sim c_0 \sim u_* h$$

$$a_1 \sim b_1 \sim c_1 \sim u_*$$

$$d_1 \sim \frac{u_*}{hk},\ d_2 \sim \frac{u_*}{2kh^2}, \qquad (19)$$

where u_* is the friction velocity and k is Von Karman's constant, so that α^2, γ^2, and ξ^2 are of order unity. The non-dimensional time scale τ has the interpretation that for the gradient

$$\frac{\partial}{\partial x_1}\kappa_i = a_1 \sim \frac{a_0}{h} \qquad (20)$$

then

$$\tau^2 \sim \frac{a_0^2 t}{2h^2 a_0} = \frac{a_0 t}{2h^2}, \qquad (21)$$

or, $\tau^2 = 0(1)$ is the non-dimensional time required for an appreciable amount of cloud material to reach the ground. It is clear from (18) that α, γ, β all refer to diffusive effects while ξ, which contains d_1, is a measure of relative dispersive effects.

The Gram-Charlier expansion (which follows in 5) shows that the convective effects, as indicated by the presence of ξ in the coefficient appear at lowest order of τ in the term

$$r_{13} = \frac{\xi\tau^2}{QF} \qquad (22)$$

while the effects of a linear gradient in κ_i appear to lowest order in τ as

$$D_{300} = \frac{-\tau}{2Q^3},\ D_{120} = -\tfrac{1}{2}\frac{\alpha\tau^2}{QP^2},\ D_{102} = -\tfrac{1}{2}\frac{\gamma^2\tau}{QF^2}. \qquad (23)$$

Here, for convenience, the following definitions are made.

$$Q^2 = 1 + \tau^2,\ P^2 = 1 + \alpha^2\tau^2,\ F^2 = 1 + \gamma^2\tau^2. \qquad (24)$$

This clearly shows the sequence of events in that a non-constant diffusivity will always be of consequence before the effects of dispersion are experienced by an evolving cloud of contaminant. (See (6) for a comparison with κ = constant case).

MARGINAL DISTRIBUTION ALONG THE VERTICAL DIRECTION

In order to more closely examine the diffusive effects, the marginal distribution--that is when (10) is integrated over x_2 and x_3, along the vertical direction x_1 (which is the most interesting since it is along this direction that the diffusivities vary) is investigated. Here, instead of using central-moments in standard form as the marginal distribution for (10) would literally imply, a slight departure is made in that a conventional one-dimensional Hermite polynomial expansion is used (13) but with a space variable non-dimensionalized as

$$z = \frac{x_1}{\sqrt{2a_0\tau}} . \tag{25}$$

There results

$$C(z,\tau) = \frac{e^{-z^2/2}}{\sqrt{2\pi}} [1 + \tau(H_1(z) + \frac{H_3(z)}{2}) + \tau^2(H_2(z) + H_4(z) + \frac{H_6(z)}{8}) + \beta^2\tau^2(\frac{3}{2} H_2(x) + \frac{H_4(z)}{3}) + 0(\tau^3)]. \tag{26}$$

The advantage in using the representation given in (26) is that the co-ordinate frame remains fixed in space (i.e. $z = 0$ is the release position at all time) as opposed to the use of central moments where $x_1(t)$ does not. It is interesting to notice on Figure 1 that although the skewness is increasing with τ the location of the maximum value of concentration is rather permanent (i.e. $z \doteq 0$).

In figure 1 (26) is compared with a numerical solution, using a Crank Nicholson method, for various values of β and τ. The numerical solutions were checked by decreasing step sizes in space and time such that satisfactorily reproducible and accurate results were achieved. When $\beta = 0$, (26) provides a good representation for all practical times (that is prior to the encounter of an appreciable amount of contaminant with a boundary which occurs at approximately $\tau < .1$ in the numerical solution). It is only when β is approximately 10 that higher order terms than those used in (26) are required for τ greater than about .05. From a review of measurements in (16), where a source height of 50m provided observed values in the location of the maximum value of ground-level concentration x_m of between 300 and 1000m, it was shown that

$$.76 < \frac{h}{\sigma_\phi x_m} < 1.38. \tag{27}$$

By taking the root-mean-square value of wind angle σ_ϕ to be approximately $\sigma_\phi \doteq v'/U(h)$, where v' is the root-mean-square value of vertical velocity fluctuations at the source location, a non-dimensional time for released contaminant to reach the location x_m is approximately given by

$$.7 < \frac{tv'}{h} < 1.4 . \tag{28}$$

Equation (28) corresponds reasonably to both (21) and the numerical estimates above (i.e. $\tau^2 \doteq .3$ which of course must be smaller than the range in (28) since this represents the time at which the wall becomes important).

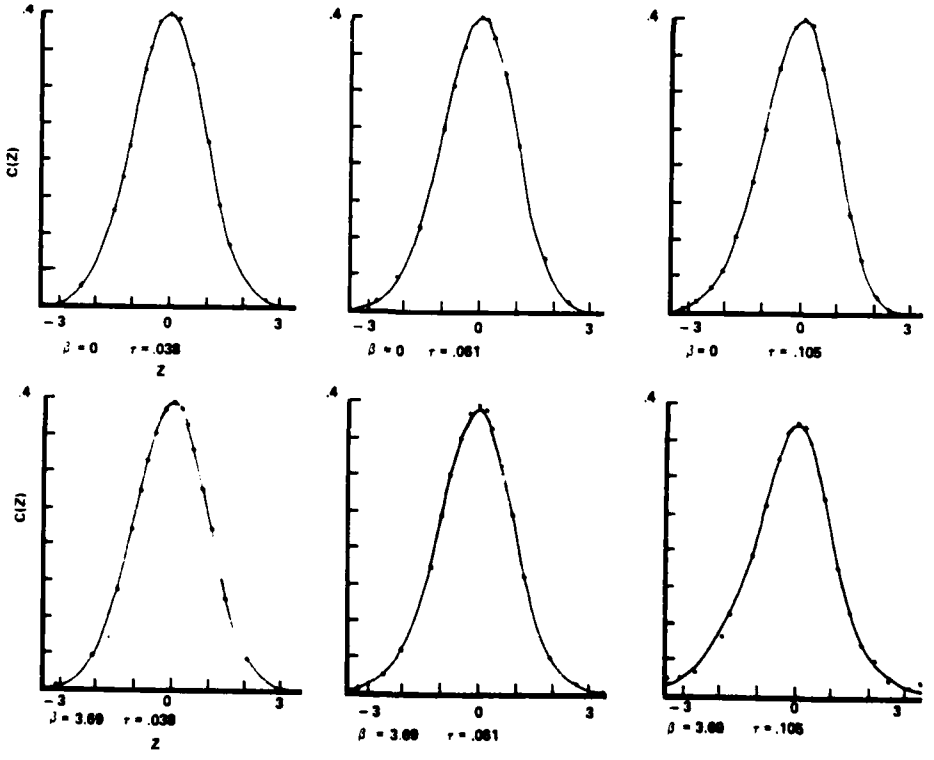

FIGURE 1. A COMPARISON BETWEEN A NUMERICAL SOLUTION (•) AND A GRAM CHARLIER SERIES EXPANSION (SOLID LINE)

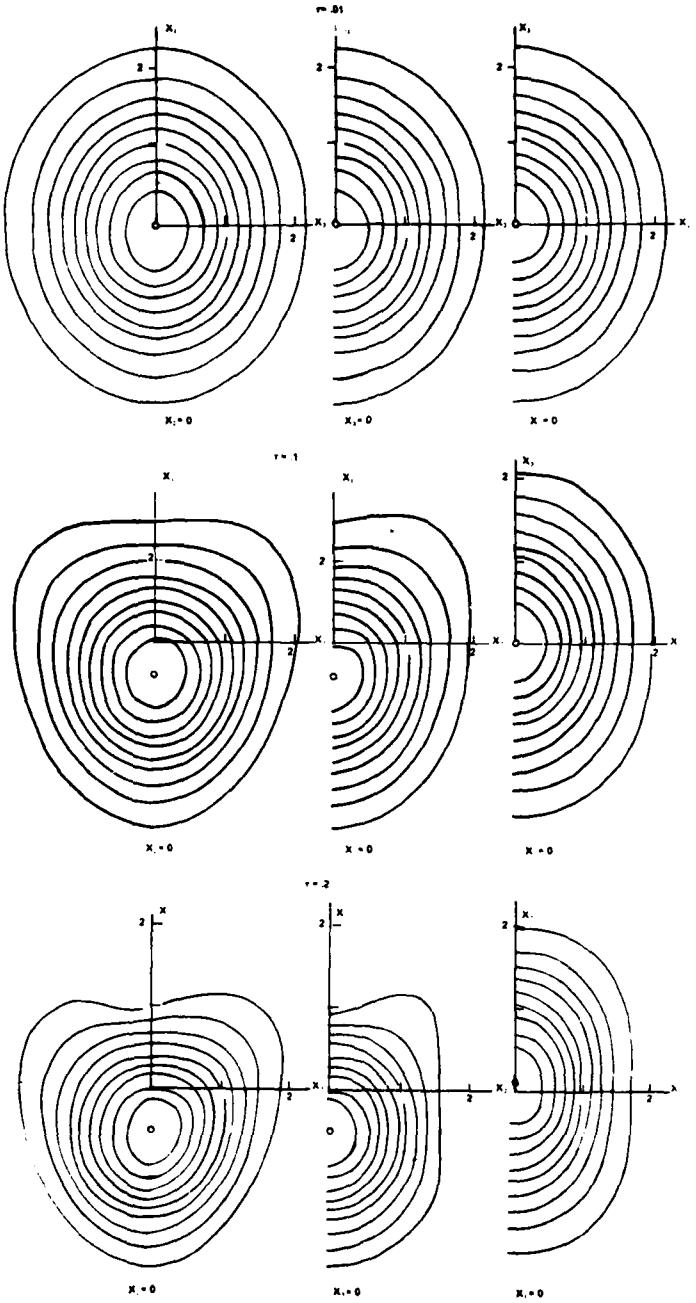

FIGURE 2. GRAM CHARLIER EXPANSION FOR CONCENTRATION $C(\underline{X},\tau)$ AS GIVEN IN EQUATION (10) WITH EQUATION (29) AND $\alpha = \gamma = \xi = 1$. SOLID LINES ENCLOSE CONCENTRATION VALUES FROM 90% (INNERMOST) TO 10% (OUTMOST) OF THE MAXIMUM VALUE OF CONCENTRATION LOCATED BY 0.

It is important to notice here that the quadratic terms in κ_1 in (7a) as indicated by β in (28) only occur at $O(\tau^2)$-- that is along with the convective effects shown in (22), whereas the linear terms in κ_1 take effect at $O(\tau)$.

$C(\underset{\sim}{X},\tau)$ FOR $\beta^2\tau^2 < 1$, $\tau^2 < 1$

The non-zero coefficients D_{ijk} to order τ^2 follow.

$$D_{300} = \frac{-\tau}{2Q^3}\ ,\ D_{120} = -\tfrac{1}{2}\frac{\alpha^2\tau}{QP^2}\ ,\ D_{120} = -\tfrac{1}{2}\frac{\gamma^2\tau}{QF^2}$$

$$D_{400} = \tfrac{1}{2}\frac{\tau^2}{Q^4}\ ,\ D_{040} = \frac{\gamma^4\tau^2}{6P^4}\ ,\ D_{004} = \frac{\gamma^4\tau^2}{6F^4}$$

$$D_{220} = \frac{2}{3}\frac{\alpha^2\tau^2}{Q^2P^2}\ ,\ D_{202} = \frac{2}{3}\frac{\gamma^2\tau^2}{Q^2F^2}\ ,\ D_{022} = \frac{1}{3}\frac{\alpha^2\gamma^2\tau^2}{P^2F^2}$$

$$D_{600} = \frac{\tau^2}{8Q^6}\ ,\ D_{060} = \frac{\alpha^4\tau^2}{24P^6}\ ,\ D_{006} = \frac{\gamma^4\tau^2}{24F^6}$$

$$D_{420} = \frac{\alpha^2\tau^2}{4Q^4P^2}\ ,\ D_{240} = \frac{\alpha^4\tau^2}{8Q^2P^4}\ ,\ D_{402} = \frac{\gamma^2\tau^2}{4Q^4F^2}$$

$$D_{204} = \frac{\gamma^4\tau^2}{8Q^2F^4}\ ,\ D_{222} = \frac{\alpha^2\gamma^2\tau^2}{4Q^2P^2F^2} \qquad (29)$$

Departures of $C(\underset{\sim}{X},\tau)$ from the Gaussian form of (13) result from the terms in (10) with the coefficients given in (29). These departures first occur at $O(\tau)$ from the D_{300}, D_{120} and D_{102} coefficients. In fact, since the r_{13} term that governs the growth along the principal axes of the cloud inertia tensor is $O(\tau^2)$ its contribution will only be made following the distortion caused by D_{300}, D_{120} and D_{102}. On Figure 2 the evolution of $C(\underset{\sim}{X},\tau)$ with $\xi = \gamma = \alpha = 1$ and $\beta = 0$ is shown. Quite significant departures from the Gaussian form of (13) (which would appear as concentric ellipses aligned with axes at forty-five degrees from the axes given in Figure 2) are apparent at small values of τ.

ACKNOWLEDGEMENTS

The authors wish to acknowledge the work of D. Martin who was employed to produce the numerical solution used, and that Sullivan received financial support from the Natural Sciences and Engineering Research Council of Canada.

REFERENCES

1. Aris, R. (1956) "On the Dispersion of a Solute in a Fluid Flowing Through a Tube" Proc. Roy. Soc. A V235, p. 67 - 77.
2. Barton, D. (1970) "Experiments with the Cambridge Algebra System" Bull. IMA V6 No. 1, p. 23.
3. Batchelor, G.K. (1949) "Diffusion in a Field of Homogeneous Turbulence-Eulerian Analysis" Aust. Jour. of Sci. Res., p. 437.
4. Batchelor, G.K. (1964) "Diffusion From Sources in a Turbulent Boundary Layer" Arch. Mech. Stosowancj 3, 16, p. 661.
5. Chatwin, P.C. (1968) "The Dispersion of a Puff of Passive Contaminant in the Constant Stress Region" Quart. Journ. Roy. Met. Soc. 94, p. 350.
6. Chatwin, P.C. (1976) "The Initial Dispersion of Contaminant in Poiseuille Flow and the Smoothing of the Snout" J. Fluid Mech. 77, 3, p. 593.
7. Chatwin, P.C. (1980) "Presentation of Longitudinal Dispersion Data" ASCE V106, No. HY1, p. 71 - 83.
8. Chatwin, P.C. and Sullivan, P.J. (1979) "The Relative Diffusion of a Cloud of Passive Contaminant in Incompressible Turbulent Flow" J. Fluid Mech. 91, 2, p. 337.
9. Chatwin, P.C. and Sullivan, P.J. (1980) "Some Turbulent Diffusion Invariants" J. Fluid Mech. 97, p. 405.
10. Csanady, G.T. (1973) "Turbulent Diffusion in the Environment" D. Reidel, Dordrecht.
11. Dewey, R.J. and Sullivan, P.J. (1979) "Longitudinal Dispersion in Flows That Are Homogeneous in the Streamwise Direction" ZAMP 30, p. 601.
12. Kampe de Feriet, J. (1966) David Taylor Model Basin Report 2013 Naval Ship Research and Development Center, Washington, D.C.
13. Kendall, M.G. and Stuart, A. (1958) "The Advanced Theory of Statistics" VI, Griffin, London, England.
14. Mihaila, I.M. (1968) "Development of the Trivariate Frequency Function in a Gram-Charlier Series" Rev. Roumaine de Math. Pure and App. 13, p. 803 - 813.
15. Monin, A.S. and Yaglom, A.M. (1971) "Statistical Fluid Mechanics: Mechanics of Turbulence" VI. J.L. Lumly ed. The MIT Press, Cambridge, Mass.
16. Pasquill, F. (1974) "Atmospheric Diffusion" (2nd ed.) Ellis Horwood, London.
17. Saffman, P.G. (1962) "The Effect of Wind Shear on Horizontal Spread From an Instantaneous Ground Source" Quart. Jour. Roy. Met. Soc. V88, p. 382 - 393.

PASSIVE EMISSIONS FROM POINT SOURCES IN TURBULENT BOUNDARY LAYERS

J. E. FACKRELL AND A. G. ROBINS

MARCHWOOD ENGINEERING LABORATORIES
CENTRAL ELECTRICITY GENERATING BOARD
MARCHWOOD, SOUTHAMPTON. SO4 4ZB UK

ABSTRACT

Measurements have been made of mean concentration, concentration fluctuations and turbulent fluxes for two passive plumes from an elevated and a ground level source in a turbulent boundary layer. For the concentration fluctuations, results are presented for the variance, the integral time scale and probability density functions and the effect of the ground on these is highlighted. The balance of terms in the variance transport equation is examined and it is shown that most of the production of fluctuations occurs very near the source, then the level of fluctuation decays, roughly in accordance with a balance between advection and dissipation. For the turbulent fluxes of concentration, results are presented for the vertical and lateral fluxes, and the associated behaviour of the vertical and lateral eddy diffusivities deduced. The balance of terms in the transport equations for the fluxes are examined. The essential differences between vertical diffusion from ground level and elevated sources and between near field and far field behaviour are shown to be due to the relative importance of the advection and diffusion terms in these equations.

NOMENCLATURE

C	mean concentration
C_m	maximum mean concentration at any downstream station
C_0	ground level mean concentration
c	fluctuating concentration
c'	rms fluctuating concentration
$\hat{c}$	maximum rms
c_1	peak concentration exceeded less than 1% of the time
D	molecular diffusion coefficient
H	boundary layer height
$p(c)$	probability density function of concentration
p'	fluctuating pressure
U	mean velocity
U_e	mean velocity at edge of boundary layer
u, v, w	velocity fluctuations in x, y, z, directions
u_*	friction velocity
x, y, z	spatial co-ordinates in longitudinal, horizontally transverse and vertical directions
z_0	roughness length
z_s	source height
α, β	constants in pdf
γ	intermittency factor (proportion of time with $C > 0$)
δ_y, δ_z	plume half widths in lateral and vertical directions
$\varepsilon_c, \varepsilon_{wc}, \varepsilon_{vc}$	dissipation of $\overline{c^2}$, $\overline{wc}$ and $\overline{vc}$, respectively
κ_y, κ_z	eddy diffusivities in lateral and vertical directions
ν_t	eddy viscosity
ρ	density
σ_y	plume lateral spread
T^y	integral time scale of concentration fluctuations

An overbar denotes a time averaged quantity

INTRODUCTION

In recent years, due to an increasing interest in environmental problems, considerable attention has been focussed on means of predicting concentration levels downwind of point sources in turbulent boundary layers. In practice, predictions are often required for dispersion in complicated flow fields influenced by buoyancy effects, buildings, topography, etc. By restricting consideration to a passive release into a known boundary layer flow, problems associated with the behaviour of the flow and with source momentum and buoyancy are avoided. Yet, even in this simple case, many aspects of the dispersion, especially the behaviour of the concentration fluctuations and fluxes, are poorly understood. Despite this, the recent tendency has been to attempt to overcome the inherent flaws in the simple gradient transfer approach to dispersion modelling by moving to higher order models, i.e. modelling the transport equations for the fluxes themselves (e.g. Lewellen and Teske, (1); El Tahry et al, (2)). There has been little experimental evidence to guide this work and it has been clear for some time that thorough experimental studies of plume structure and development were required. It is hoped that the present paper will go some way towards fulfilling this need.

A natural development of higher order models lies in the prediction of concentration fluctuations. This is a problem of considerable importance in assessing the likely effects of air pollutants on plants and animals or the hazard from releases of toxic or inflammable gases and in studying some of the chemical processes within plumes.

There is an important distinction to be made between elevated and ground level sources. For a ground level source the vertical scale of the plume always exceeds that of the turbulence, so that vertical dispersion progresses in a 'far field' manner and, consequently, can be adequately described by simple gradient transfer or similarity arguments. This is not the case for an elevated source, or indeed,

for lateral spreading from sources at any height. It has also been found experimentally (Robins and Fackrell, (3)) that many of the statistical quantities associated with a ground level plume exhibit an approximately self preserving form, at least until the plume begins to fill the boundary layer. An elevated plume can also be self preserving whilst it remains fully elevated, but at some stage in its growth the influence of the ground will begin to change its structure until, eventually, it comes to resemble a ground level plume. In the present work, a ground level source and a source at 0.19H (where H is the boundary layer height) were studied. The elevated source height was chosen as being roughly representative of many full scale emissions and because it enabled examination of the change in plume structure from a fully elevated one towards a ground level form within the downstream distance available in the wind tunnel.

Because the main concern is in providing experimental information to aid prediction techniques, results will be presented solely in terms of dispersion in the laboratory boundary layer. However, much of the paper should be of direct relevance to short range dispersion in the neutral atmospheric boundary layer, at least for full scale quantities averaged over fairly short times, of a few minutes to about one hour. In addition, both the flux and fluctuation results should be of wider interest, with, for example, some application to combusting or reacting flows.

EXPERIMENTAL TECHNIQUES

The experiments were undertaken in the Marchwood Engineering Laboratories' 24 x 9.1 x 2.7 m, open circuit, wind tunnel. A 1.2 m high boundary layer was generated in the tunnel by the method of Counihan (4). Plumes from sources at two different heights were studied; $z_s/H = 0.19$ and 0. For the majority of the study the ground level source (GLS) consisted of a horizontal tube, 15 mm diameter, aligned with the flow and placed just above the roughness elements of the floor. It emitted at the average velocity of the flow over its height. The elevated source (ES) was an 8.5 mm diameter tube, similarily arranged, emitting at the velocity at its height. Specifically for the investigation of the importance of source size,a variety of sources were used, their diameters ranging from 3 to 35 mm; all being small compared to the boundary layer height. The source gas consisted of a neutrally buoyant mixture of propane and helium, the former being used as a trace gas for concentration measurement.

Fluctuating concentration measurements were made with a modified flame ionisation detector system. A detailed description of this system, including its use in conjunction with DISA crossed hot wires to obtain the fluxes, is given by Fackrell (5). The -3dB point of the frequency response of the concentration sensing probe was about 300 Hz. This allowed the most energetic fluctuations and some of the inertial subrange to be measured, although excluding the very fine scale structure. Signals from the concentration probe and the hot wires were all processed digitally to obtain the required statistical quantities, with enough samples being taken to achieve good repeatability. No corrections for high turbulence levels have been applied to the hot wire results, since turbulence levels were fairly low, resulting in errors of less than 10% in the shear stress. The accuracy of concentration and flux measurements is probably similar to this, except where the values are small, when the errors will be greater.

RESULTS

Flow Field

The boundary layer used in these experiments was artificially thickened using the method evolved by Counihan (4). A detailed discussion of the structure of such boundary layers is given by Robins (6), from which it follows that the flows are indistinguishable from naturally grown boundary layers beyond a certain distance from the devices used for thickening. The sources in the present case were located to satisfy this requirement and, consequently, the flow field may be assumed to be an ordinary, equilibrium, zero pressure gradient boundary layer, with height H = 1.2 m, roughness length, $z_0 = 2.4 \times 10^{-4}H$ and friction velocity, $u_* = .047\ U_e$.

Mean Concentration Field

Figure 3 shows the variation of maximum mean concentration, C_m, with downstream distance for ground level and elevated sources. For the GLS, the maximum at any downstream station is always at ground level. For the ES it approaches the ground, being at ground level for the furthest downstream position; ground level concentrations, C_0, are plotted separately. Also shown, are the vertical and lateral plume half widths, δ_z and δ_y; where the half width is the distance in which the maximum concentration falls to half its value. The lateral half widths are roughly the same for both sources and increase proportional to x near the source and $x^{\frac{1}{2}}$ far downstream in agreement with statistical theory. The ES vertical half width shows simliar behaviour, but the GLS vertical halfwidth appears to have a power law dependence, consistent with similarity theory, approximately $x^{0.75}$, over all the distance covered by the results. The ES vertical halfwidth is significantly larger than the GLS one.

Vertical profiles of concentration for the ES can be reasonably well represented by a reflected gaussian form, although far downstream and for the GLS the form

$$C = C_0 \exp\ (-.693\ (z/\delta_z)^{1.5}) \qquad (1)$$

gives a better fit. For both GLS and ES the lateral profiles at all stations were closely gaussian and the lateral plume half width was found to be constant with height at any station.

Fluctuating Concentration

There are theoretical grounds for thinking that the observed statistics of a fluctuating concentration field are dependent on both sensor and source dimensions (Durbin (7), Chatwin and Sullivan (8)). For the present work, the former was fixed as described by Fackrell (5), but the latter was varied over a range of source sizes which would normally pass for 'point' sources in experimental work. Figure 2 shows the behaviour of the relative intensity of fluctuations, $\hat{c}/C_m$, with source size and downstream distance. For the ES the effects of source size are large, with the intensity growing to a maximum quite near the source and then decaying, but for the GLS they are not distinguishable from the experimental scatter and the relative intensity stays at a fairly constant level over the downstream distance measured.

Examination of the intermittent signals for the ES suggested that an adaption of the flapping plume model of Gifford (9) might provide a reasonable

description of the fluctuation behaviour, at least near to source. The model developed, described in more detail in Fackrell and Robins (10), uses the theory of Hay and Pasquill (11) to predict mean plume spread and that of Smith and Hay (12) to predict instantaneous plume spread. At the source they both are the same but then increase at different rates. The lines in Figure 2 are predictions due to this model for source sizes corresponding to the experimental ones. There is only one disposable constant in the theory, relating real source size to an initial gaussian spread and it requires as input a specification of the turbulence intensity and transverse integral scales at the source height. The agreement with the ES results is really quite good for such a simple model even in the decaying region. However, the model cannot be applied to a ground level source since it makes no allowance for velocity shear or the surface boundary condition.

The presence of the surface was found to have a pronounced effect on the concentration statistics. The condition of zero (or very small) transfer to the ground ($\partial C/\partial z \to 0$, $z \to 0$) appropriate to most atmospheric plume situations, makes the behaviour near the ground quite different from the situation more usually considered of high (heat or mass) transfer to or from the boundary. It follows that modelling approximations that have been made in the latter case, assuming local equilibrium near the wall, cannot necessarily be applied to plume modelling. The behaviour near the surface of the variance and integral time scale of the concentration fluctuations is illustrated in Figure 3, by results for the GLS (which are also representative of the behaviour of elevated plumes once they are influenced by the ground). The variance has a similar profile at different downstream positions with a maximum at about 0.7 δ_z. There is a decrease in variance values near to the surface, although we cannot say whether $\overline{c^2}$ actually reaches zero since measurements were not made amongst the roughness elements themselves. The integral time scale of the fluctuations, obtained from spectra, increases slightly with downstream distance and is substantially greater near the ground than higher in the plume. The increase in value near the ground is much greater than the decrease in mean velocity, so that a length scale obtained by multiplying T by the local mean velocity would still increase towards the ground, in contrast to the turbulent velocity length scales. The impression given by the concentration signals and from spectra is that the intense small scale eddies near the ground are more effective in mixing and reducing smaller scale concentration fluctuations, leaving the fluctuations due to large scale plume meandering relatively untouched.

The presence of the ground also has a significant effect on the probability density function, p(c), obtained, as illustrated in Figure 4 where the non-dimensional form c'p(c) is plotted against $(c - C)/c'$. For an elevated plume the pdf's obtained are roughly of the form shown for x/H = 0.96, although the exact shape and intermittency factor obtained will vary with downstream distance and source size. This form is well represented by a power law distribution, $p(c) = \alpha c^{-\beta}$, given by the flapping plume theory referred to earlier, as indicated in the figure. After an elevated plume contacts the ground, the distributions near the ground have a tendency towards a more gaussian form, as illustrated by the results for x/H = 4.79. Further downstream, or with a GL source, the near surface pdf's are very close to gaussian, although higher in the plume, where the intermittency factor is lower, the power law shape is still retained. Despite this wide range of pdf shapes, it was found that the peak concentration, defined as the value exceeded for less than 1% of the time, c_1, had a fairly constant relation to the rms c', such that $c_1/c' = 4.5$ to 5.0. Thus, if the rms can be predicted, fairly reliable estimates of the peak concentration can be made.

For the boundary layer flow examined, the variance of the concentration fluctuations obeys a transport equation of the form

$$U\frac{\partial \overline{c^2}}{\partial x} + \{2\,\overline{uc}\frac{\partial C}{\partial x} + 2\overline{wc}\frac{\partial C}{\partial z} + 2\overline{vc}\frac{\partial C}{\partial y}$$

$$+ \{\frac{\partial \overline{uc^2}}{\partial x} + \frac{\partial \overline{wc^2}}{\partial y} + \frac{\partial \overline{vc^2}}{\partial z}\} + 2\varepsilon_c = 0 \qquad (2)$$

where $\varepsilon_c = D\,\overline{\frac{\partial c}{\partial x_j} \cdot \frac{\partial c}{\partial x_j}}$ and D is the molecular diffusion coefficient. The terms represent respectively; advection of $\overline{c^2}$ by the mean velocity; generation by gradients in mean concentration; diffusion by turbulent velocity fluctuations (>> molecular diffusion); and dissipation due to molecular diffusion of the fine scale concentration fluctuations. All the quantities in this equation have been measured directly except the dissipation, which can therefore be obtained by difference, as well as being deduced from the inertial subrange behaviour of spectra as described by for example Bradshaw (13). Results showing the relative importance of the terms for two stations on the centreline of the ground level plume and at 3 stations on the centreline of the elevated plume are given in Figure 5. Except for the elevated case at x/H = 1.92, where diffusion is important, the resultant balances are dominated by advection and dissipation. The production was found to be small relative to the advection in all the measurements (unlike cases with high heat transfer at the surface). Checks at positions off the centreline, where the production is increased by a $\partial C/\partial y$ term, still showed the advection term significantly larger. The near source measurements for ε/C_m given in Figure 2 suggest that most of the production of $\overline{c^2}$ occurs very close to the source and the overall level of the fluctuations is decaying thereafter. Indeed, the value of $\int c^2 \delta_y \delta_z$, roughly proportional to the integral of c^2 over the plume, or the total flux of variance, monotonically decreases with increasing downstream distance from the nearest point of measurement x/H = 0.21. The overall level of the fluctuations is set in the production region near the source and this may pose problems for the numerical modelling of equation 2, since it implies that the near source region will have to be modelled in fairly fine detail.

Concentration Fluxes

It is the magnitude of the turbulent fluxes, $\overline{wc}$ and $\overline{vc}$, which determines the rate of spread of the plume in the vertical and horizontal. Yet despite their importance, there have been very few reports of turbulent scalar flux measurements directly related to the present study. Most measurements that have been made are of heat fluxes in cases with high heat transfer to or from the wall and, as already indicated, a passive scalar with no transfer is a significantly different situation. Note that, since the mean concentration field, away from the immediate vicinity of the source, is observed to be source size independent, the time averaged turbulent fluxes $\overline{wc}$ and $\overline{vc}$ must also be.

Figure 6(i) shows the variation with downstream distance of the vertical flux on the centreline of the

plume from the ES. The flux profiles develop from being anti-symmetric about the source height (.19H) near the source, towards a GLS profile, indicated by the dotted line. The GLS results (not shown explicitly for clarity) were all fairly close to this line, which therefore represents the self preserving form. The lateral variation of $\overline{wc}$ at any downstream position was found to be close to gaussian and similar to that of the mean concentration. The usual first order closure models $\overline{wc}$ as $-\kappa_z \partial C/\partial z$, where κ_z is the eddy diffusivity. The GLS profile for $\overline{wc}$ together with the mean concentration vertical profile described by equation 1, yield an eddy diffusivity which is independent of downstream distance and proportional to the eddy viscosity, such that $\nu_t/\kappa_z = 0.8$. However, for the ES, the vertical eddies are not limited to the plume size, so the eddy diffusivity will be a function of downstream distance. This is illustrated in Figure 6(ii), where, although there is some scatter because of the difficulty of estimating $\partial C/\partial z$ near the ground, the growth in eddy diffusivity with downstream distance can be seen.

Within experimental error it has been found that the lateral profiles of mean concentration at any downstream station are similar and independent of z. This suggests that $C = C(x,z)f(\eta)$, where $\eta = y/\sigma_y$ and $\sigma_y = \sigma_y(x)$. In addition, the results for $\overline{wc}$ indicate that its lateral variation is closely similar to that of the mean concentration, so that writing $\overline{wc} = \overline{wc}(x,z)f(\eta)$ should be a reasonable approximation. It is shown in Robins and Fackrell (3) that these assumptions lead to an expression for the lateral flux at any position of the form

$$\overline{vc} = UC \frac{y}{\sigma_y} \frac{d\sigma_y}{dx} \qquad (3)$$

If the function $f(\eta)$ is gaussian, as the results suggest, and an eddy diffusivity form for $\overline{vc}$ is used, then equation (3) further implies that the eddy diffusivity, $\kappa_y = U/2 \cdot d\sigma_y^2/dx$, i.e. a function of x only. This is the same relation as that obtained from statistical theory for dispersion in a uniform wind, except that in the present case U varies with height. Equation 3 has been tested for the GLS and ES in Figure 7. Although there is some scatter, allowing for likely errors, the results provide fairly good confirmation of equation 3; in particular, the results at each station are fairly uniform with height.

There is an increasing trend towards the use of 'second order modelling' in the calculation of turbulent dispersion, i.e. the modelling of transport equations for the fluxes themselves. It is hoped in this way to account for the advection and diffusion of the fluxes and so make a given calculation set more generally valid. The transport equation for the vertical flux, $\overline{wc}$, as applied to the present two dimensional boundary layer flow, is

$$U\frac{\partial \overline{wc}}{\partial x} + \left(\overline{uw}\frac{\partial C}{\partial x} + \overline{w^2}\frac{\partial C}{\partial z}\right) + \left(\frac{\partial}{\partial x}\overline{uwc} + \frac{\partial}{\partial z}\overline{w^2 c} + \frac{\partial}{\partial z}\frac{\overline{p'c}}{*\rho}\right) + \varepsilon_{*wc} - \frac{\overline{p'}}{\rho_*}\frac{\partial c}{\partial z} = 0 \qquad (4)$$

The terms represent respectively; advection; production; diffusion due to turbulent velocity and pressure fluctuations; dissipation; and a pressure-concentration gradient correlation which acts to limit the growth of the fluxes. With the present measurement system it is not possible to measure those terms marked by an asterisk and they have been lumped together as a difference term to balance the equation. It is expected that final term will make by far the dominant contribution to this difference term and henceforth the two will be treated as being identical (e.g. see Launder, 14). Results for two stations on the centreline of the GL plume are given in Figure 8. At both stations, a balance between production and the difference term dominates, advection and diffusion being much smaller. Also shown are $\overline{wc}$ balances for the ES at 3 downstream stations on the plume centreline and in this case near to the source, advection and diffusion are the same order as the other terms, only becoming much smaller at the furthest downstream position.

A transport equation similar to equation 4 can also be derived for the lateral flux $\overline{vc}$ and $\overline{vc}$ balances obtained for the GLS and ES plume are given in Figure 9. In both cases, there is an approximate balance between production and the difference terms only at the position furthest from the source. Closer to the source, the diffusion and, in particular, the advection become equally important. Note however, that for both the vertical and horizontal fluxes, where the advection and diffusion terms are significant, they do oppose each other, so that their nett contribution is smaller than either term separately. This implies that the diffusion term must be accurately modelled to keep the error in the nett contribution small. In general, whenever plume dimensions are less than the local turbulence scales, any eddy diffusivity term will be fetch dependent, so that using a fixed eddy diffusivity in the diffusion term will lead to errors in that term. By comparing predictions of first, second and third order models for plume dispersion in isotropic turbulence, Deardorff (15) has shown that the resultant error in mean concentration prediction using a fixed eddy diffusivity in the higher order models can be as great as that from doing so in the first order closure. We suspect that the same will be true in the simple boundary layer flow we have examined. Therefore, there may not be a great deal to gain from higher order modelling in such flows, although it may be of advantage in more complex flow situations. Finally, note that, whenever there is a balance between the production and pressure-concentration gradient terms, a fixed eddy diffusivity behaviour should result. For example, modelling the latter term as $\overline{wc}/T$ where T is a time scale, leads to $\overline{wc} = -\overline{w^2}T\,\partial C/\partial z$, the standard eddy diffusivity closure.

ACKNOWLEDGEMENT

The work reported here was carried out at Marchwood Engineering Laboratories and is published by permission of the Central Electricity Generating Board.

REFERENCES

1 Lewellen, W. S. and Teske, M. E. 'Second order closure modelling of diffusion in the atmospheric boundary layer'. Bdry Layer Met., Vol. 10, 1976, pp. 69-90.

2 El Tahry, S., Gosman, A. D. and Launder, B. E. 'The two and three dimensional dispersal of a passive scalar in a turbulent boundary layer'. Int J. Heat Mass Transfer, Vol. 24, 1981, pp. 35-46.

3 Robins, A. G. and Fackrell, J. E. 'Continuous plumes - their structure and prediction'. Proceedings of the Conference on Mathematical Modelling of Turbulent Diffusion in the Environment, Liverpool, Sept. 1978, Ed C. J. Harris, Academic Press, pp. 55-114.

4 Counihan, J. 'An improved method of simulating an atmospheric boundary layer in a wind tunnel'

Atmos. Env., Vol. 3, 1969, pp. 197-214.

5 Fackrell, J. E. 'A flame ionisation detector for measuring fluctuating concentration' J. Phys. E:Sci. Inst., Vol. 13, 1980, pp. 888-893.

6 Robins, A. G. 'The development and structure of simulated neutrally stable atmospheric boundary layers' Jnl. Ind Aero, Vol. 4, 1979, pp. 71-100.

7 Durbin, P. A. 'A stochastic model of two particle dispersion and concentration fluctuations *in homogeneous turbulence*' JFM, Vol. 100, pt. 2, 1980, pp. 279-302.

8 Chatwin, P. C. and Sullivan, P. J. 'The relative diffusion of a cloud of passive containment in incompressible turbulent flow' JFM, Vol. 91, pt. 2, 1979, pp. 337-355.

9 Gifford, F. 'Statistical properties of a fluctuating plume dispersion model' Advances in Geophysics, Vol. 6, 1959 pp. 117-137.

10 Fackrell, J. E. and Robins, A. G. 'Concentration fields associated with emissions from point sources in turbulent boundary layers - part 11 - the effects of source size'. MM/MECH/TF 264, 1980, CEGB Marchwood Engineering Laboratories.

11 Hay, J. S. and Pasquill, F. 'Diffusion from a continuous source in relation to the spectrum and scale of turbulence' *Advances in Geophysics* Vol. 6, 1959, pp. 345-365.

12 Smith, F. B. and Hay, J. S. 'The expansion of clusters of particles in the atmosphere'. Qtr. Jnl. Roy. Met. Soc. Vol. 87, 1961, pp. 82-91.

13 Bradshaw, P. Introductory chapter in Turbulence Ed. P. Bradshaw, Springer-Verlag, Berlin, 1976, pp. 1-44.

14 Launder, B. E. 'Heat and Mass transport' in Turbulence Ed. P. Bradshaw, Springer-Verlag, Berlin, 1976, pp. 231-287.

15 Deardorff, J. W. 'Closure of second and third moment rate equations for diffusion in homogeneous turbulence'. Phys. Fl. Vol. 21, pt. 4, 1978, pp. 525-530.

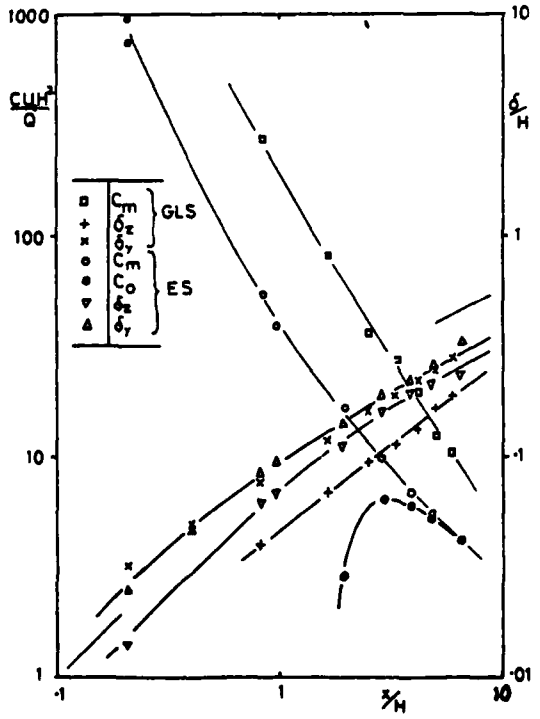

Fig. 1 Mean concentration parameters

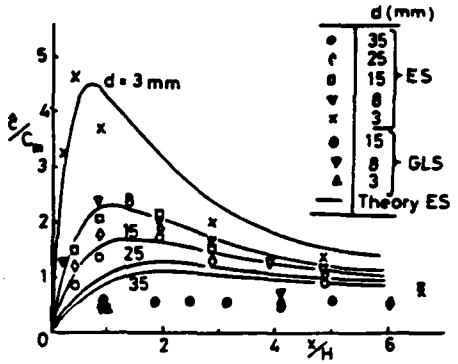

Fig. 2 Variation of fluctuation intensity with source size and downstream distance

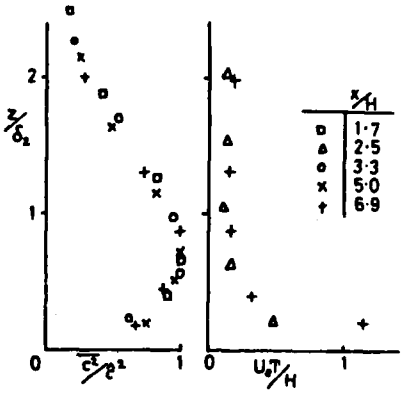

Fig. 3 Vertical centreline profiles of fluctuation variance and time scale, GLS

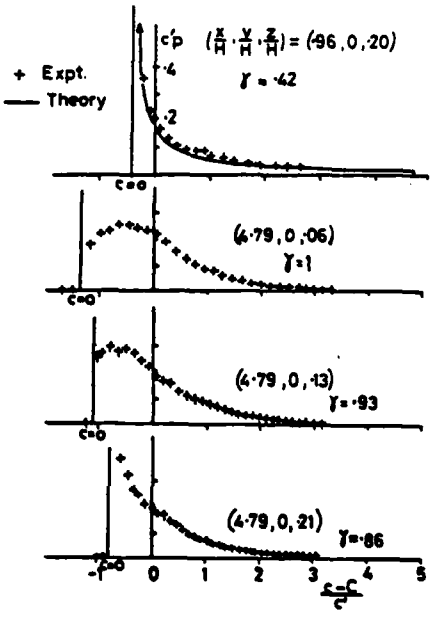

Fig. 4 Probability density functions for ES

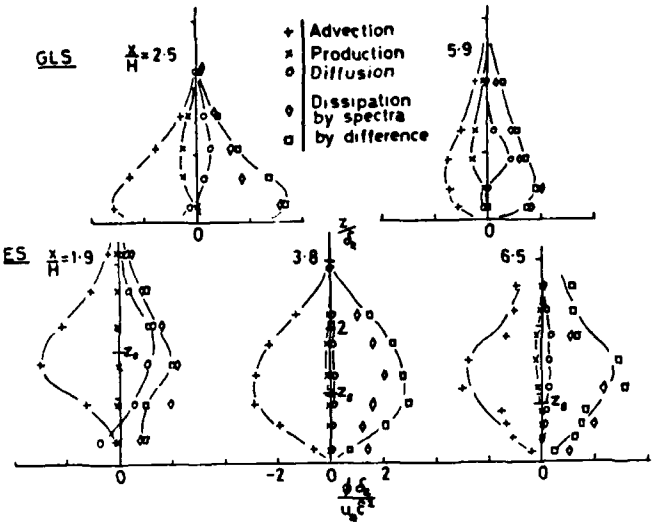

Fig. 5 $\overline{c^2}$ balances on lateral plume centreline, y=0

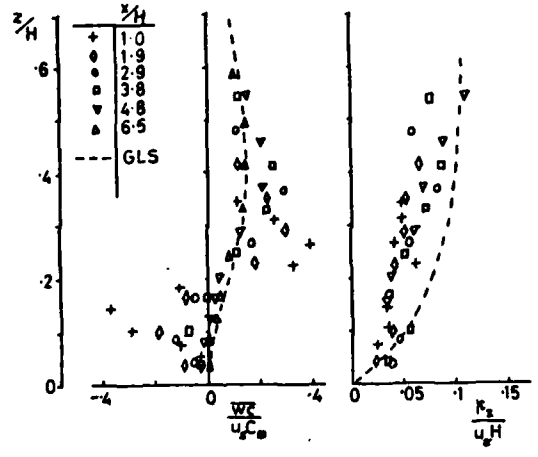

Fig. 6 Vertical flux and eddy diffusivity on lateral plume centreline

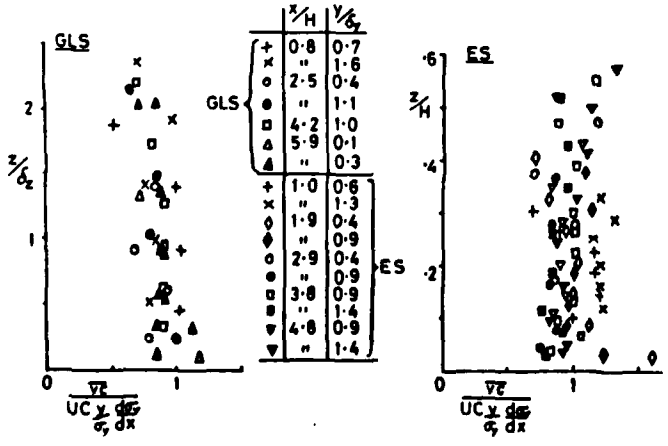

Fig. 7 Lateral flux

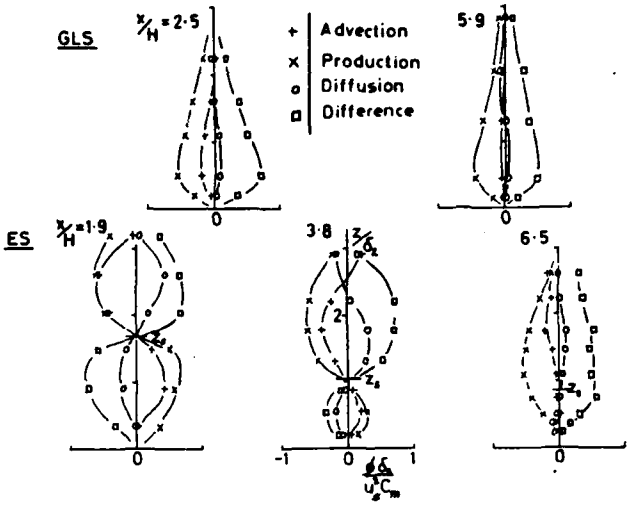

Fig. 8 $\overline{wc}$ balances on lateral plume centreline

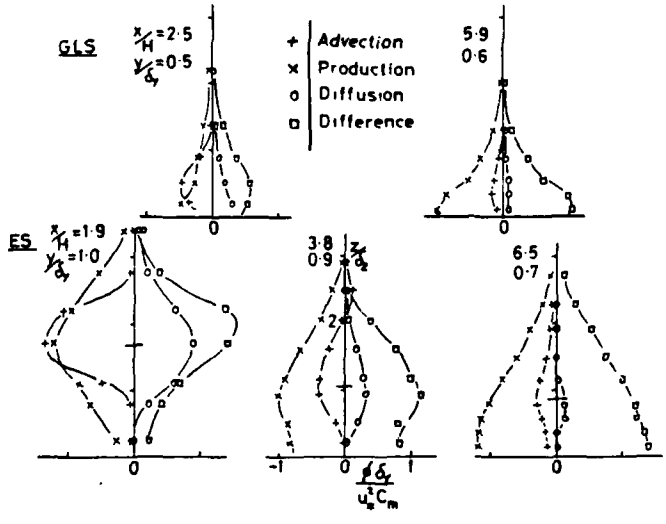

Fig. 9 $\overline{vc}$ balances

PRESSURE EFFECTS ON TRIPLE CORRELATIONS IN TURBULENT CONVECTIVE FLOWS

J.-C. André [1][2], P. Lacarrère [1], K. Traoré [1]

(1) Direction de la Météorologie, EERM/GMD, Boulogne, France

(2) Department of Atmospheric Sciences, Oregon State University, Corvallis, U.S.A.

ABSTRACT

The parameterization of pressure effects on triple correlations is shown to be an important part of the closure problem.

Based on arguments relevant to homogeneous and isotropic turbulence, it is argued that pressure effects are not only of relaxative nature. In the case of turbulent thermal convection, a parameterization scheme including non-linear and rapid effects is proposed and used within the framework of a third-order model. Comparison with experimental results by Ferreira (10) indicates that the rapid part of pressure effects represents an important contribution to the budget of triple correlations and that it prevents the development of spurious stable stratification in the interior of the convective layer.

NOMENCLATURE

C_i	Dimensionless constants
$\overline{e}$	Eddy kinetic energy (per unit mass)
h	Depth of the turbulent layer
i	Square - root of (-1)
$\underline{k},\underline{p},\underline{q},\underline{r},\underline{s}$	Wave-vectors in Fourier space
k,p,q,r,s	Wave-numbers in Fourier space
t	Time
T	Temperature
T_*	Convective temperature scale
$\underline{u}' = (u'_1,u'_2,u'_3) = (u',v',w')$	Fluctuating velocity
$\hat{\underline{u}} = (\hat{u}_\alpha, \alpha = 1 \text{ to } 3)$	Fourier transform of the fluctuating velocity field
w_*	Convective velocity scale
$\underline{x} = (x_1,x_2,x_3) = (x,y,z)$	Position
z	Height
α	Coefficient of thermal expansion
β	Buoyancy parameter
δ_{ij}	Kronecker symbol
ε	Eddy Kinetic energy dissipation rate
ν	Kinematic viscosity
ρ_o	Constant density

I. INTRODUCTION AND MOTIVATIONS

It is now widely known that the turbulent transfers which take place in convectively driven flows do not follow the simple Boussinesq eddy viscosity assumption, i.e. in many cases the turbulent flux of a property 'a' is oriented from regions with low 'a' toward regions with high 'a'. This "counter-gradient" turbulent transport has been documented experimentally for the case of a mean property like the mean temperature $\overline{T}$ (1) and also for the case of a second-order quantity like the eddy kinetic energy $\overline{e} = \frac{1}{2}\rho_o \overline{u'_k u'_k}$ (2). Parameterization methods and numerical simulation techniques for convective flows have consequently undergone a significantly different development as compared to the one which occured in the case of pure shear flows. It is indeed known that even simplified second-order models, like the so-called "k-ε" model, can be used quite successfully for the simulation of a variety of shear flows in different geometrical configurations (e.g. 3), while it has been shown that the numerical simulation of the most simple convective flows requires the use of sophisticated turbulence models (e.g. 4, 5).

These models are presently based :

(i) either on Lumley's idea that Boussinesq eddy diffusivity assumption can be properly generalized in order to account for buoyancy effects and can then be used to relate, in matrix form, third-order correlations to the gradients of second-order ones, in the framework of a more or less complex model (6, 7)

(ii) or on the explicit use of rate equations for the triple correlations (8, 9).

Both of these methods require the knowledge and parameterization of quadruple correlations, molecular and pressure effects on third-order terms. The two former problems are usually solved by retaining respectively the quasi-normal approximation and the assumption of isotropic dissipative scales, while the solution of the latter is based on the idea that pressure effects are indeed relaxative processes. One is then lead to the introduction of a relaxation time which directly determines the value of triple terms in Lumley's method, while the use of rate equations involves not only the above linear relaxation but also allows for more sophisticated, basically non-linear, pressure relaxation effects.

The purpose of this paper is to study these pressure effects on third-order correlations.

Up to now similar studies have been based either on theoretical considerations or on indirect experimental evidence since the only available laboratory measurements were quite scarce and restricted to the so-called case of penetrative convection, where another different physical phenomenon (i.e. entrainment of overlying stably stratified fluid into underlying turbulent convective layer) leads to additional complexity and does not allow for unambiguous determination of pressure effects. In this respect the recent experiment by Ferreira (10), which we will use in the present study, does not suffer from the same difficulties since it deals with non-penetrative convection between rigid boundaries. This experimental study has the further advantage of including more precise thermometric and velocimetric measurements of numerous triple correlations. Unfortunately, the price to pay for the reduction of complexity due to penetrative convection is the introduction of another viscous layer at the upper boundary. Our study will consequently be restricted to the interior of the convective layer, where it can be safely assumed that turbulence is fully developed, and will not deal with the adjacent viscous sublayers.

II. PRESSURE RELAXATION IN HOMOGENEOUS TURBULENCE

Before turning to the subject of convective flows, it is of interest to recall and summarize some general properties of the effects of pressure fluctuations on triple correlations.

The closure problem associated with pressure effects is mainly due to the fact that these effects are non-local in $\underline{x}$-space and involve convolution integrals over the whole domain of the flow. It is consequently of much help to introduce two-point correlations in order to solve, at least formally, the above closure problem. Due to its inherent complexity, it is unfortunately almost impossible to use this formalism in any case different from the simplest, but of much theoretical interest, case of homogeneous turbulence. In this case, and using Fourier transform $\hat{\underline{u}}(\underline{k})$ of the velocity field $\underline{u}(\underline{x})$, the exact rate equations for double and triple correlations read (e.g. 11, 12)

$$\left(\frac{\partial}{\partial t}+2\nu k^2\right)\langle \hat{u}_\alpha(\underline{k})\hat{u}_\beta(-\underline{k})\rangle = -\frac{i}{2}D_{\alpha\rho\sigma}(\underline{k})\int_{\underline{p}+\underline{q}=\underline{k}}\langle \hat{u}_\rho(\underline{p})\hat{u}_\sigma(\underline{q})\hat{u}_\beta(-\underline{k})\rangle d\underline{p} + \left[\begin{smallmatrix}\alpha\rightleftharpoons\beta\\ \underline{k}\rightleftharpoons-\underline{k}\end{smallmatrix}\right] \quad (1)$$

$$\left(\frac{\partial}{\partial t}+\nu(k^2+p^2+q^2)\right)\langle \hat{u}_\alpha(\underline{k})\hat{u}_\beta(\underline{p})\hat{u}_\gamma(\underline{q})\rangle = -\frac{i}{2}D_{\alpha\rho\sigma}(\underline{k})\int_{\underline{r}+\underline{s}=\underline{k}}\langle \hat{u}_\rho(\underline{r})\hat{u}_\sigma(\underline{s})\hat{u}_\beta(\underline{p})\hat{u}_\gamma(\underline{q})\rangle_c\, d\underline{r} - i\,D_{\alpha\rho\sigma}(\underline{k})\langle \hat{u}_\beta(\underline{p})\hat{u}_\rho(-\underline{p})\rangle\langle \hat{u}_\gamma(\underline{q})\hat{u}_\sigma(-\underline{q})\rangle + \left[\begin{smallmatrix}\alpha\rightleftharpoons\beta\\ \underline{k}\rightleftharpoons\underline{p}\end{smallmatrix}\right] + \left[\begin{smallmatrix}\alpha\rightleftharpoons\gamma\\ \underline{k}\rightleftharpoons\underline{q}\end{smallmatrix}\right] \quad (2)$$

where $\langle uuuu\rangle_c = \langle uuuu\rangle - \sum\langle uu\rangle\langle uu\rangle$ is the fourth-order cumulant, $\left[\begin{smallmatrix}\alpha\rightleftharpoons\beta\\ \underline{k}\rightleftharpoons\underline{p}\end{smallmatrix}\right]$ a symbol representing additional terms obtained by the indicated permutations of indices and wave-vectors, and

$$D_{\alpha\beta\gamma}(\underline{k}) = k_\beta\delta_{\alpha\gamma} + k_\gamma\delta_{\alpha\beta} - 2\,k_\alpha k_\beta k_\gamma/k^2 \quad (3)$$

a geometrical tensor taking into account advective and pressure effects, the former being traced to the Kronecker symbol $\delta_{..}$ and the latter described by the term involving k^{-2} (inverse Laplacian operator in $\underline{k}$-space). The fact that pressure effects are always associated with k^{-2} makes it easy to trace their effects. By considering Eq. (2) one is then lead to the following conclusions concerning the effect of pressure fluctuations (i) they are responsible, together with advective effects, for a linear relaxation of triple correlations. It has indeed been shown (11) that the term involving fourth-order cumulants were damping terms which could be approximated by $-\{t(k)+t(p)+t(q)\}\langle \hat{u}_\alpha(\underline{k})\hat{u}_\beta(\underline{p})\hat{u}_\gamma(\underline{q})\rangle$, where the eddy-damping rate $t(k)$ is proportional to a typically positive geometrical coefficient $B(k,r,s)$ constructed from the geometrical tensor D of Eq. (3) :

$$B(k,r,s) = -D_{\alpha\rho\gamma}(\underline{k})D_{\beta\varepsilon\sigma}(\underline{r})\{\delta_{\rho\varepsilon} - s_\rho s_\varepsilon/s^2\} \quad (4)$$

This coefficient is typically positive since

$$B(k,r,s)+B(k,s,r) = \Delta\{k^2(r^2+s^2)+(r^2-s^2)^2\}/4\,k^2r^2s^2 \geq 0$$

where Δ is a totally symmetric quartic positive for k,r and s being the legs of a triangle

$$\Delta = -k^4 - r^4 - s^4 + 2\,k^2r^2 + 2\,k^2s^2 + 2\,r^2s^2.$$

Distinction between advective (A) and pressure (P) effects in Eq. (4) leads to the partition of the geometrical coefficient into

$$B(k,r,s) = B^{(A)}(k,r,s)+B^{(AP)}(k,r,s)+B^{(P)}(k,r,s) \quad (5)$$

where the advective part is positive

$$B^{(A)}(k,r,s) = 5k^2r^2\Delta/4k^2r^2s^2 \quad (6)$$

as well as the pressure-pressure interaction part

$$B^{(P)}(k,r,s) = (k^2+r^2-s^2)^2\Delta/4k^2r^2s^2 \quad (7)$$

and where the pressure-advection interaction part is typically negative

$$B^{(AP)}(k,r,s)+B^{(AP)}(k,s,r) = -\Delta\{2k^4+4k^2(r^2+s^2)+(r^2-s^2)^2\}/4k^2r^2s^2 \quad (8)$$

(ii) they tend to reduce the magnitude of triple correlations, since their contribution leads typically to a decrease of the terms involving products of double correlations in Eq. (2).

In other terms, the above arguments do confirm that pressure fluctuations mainly destroy triple correlations. They also show that (unfortunately!) pressure effects are more complicated than the usually assumed relaxation to isotropy, and that they are not the only mechanism responsible for damping triple correlation, and consequently for preserving the realizability conditions see the discussion by André and Lumley in (13). In the more general case of convective flows, necessary simplicity will nevertheless lead us to adopt a parameterization of pressure fluctuations based on a relaxation assumption, but we shall keep in mind that it would not be reasonable to ascribe every possible unphysical growth of triple correlations to an underestimated pressure-induced relaxation.

III. PRESSURE PARAMETERIZATION FOR SINGLE-POINT HIGH-ORDER MODELING

The simulation of turbulent convective flows which are inhomogeneous along the vertical cannot, at least at the present time, be undertaken in the above presented two-point closure framework.

One has then to turn to the much more efficient single point closures.

Unfortunately, but this is the price to pay, these are less satisfactory from the theoretical point of view. A possible alternative would be to rely on the so-called "modal method" (e.g. 14), in which the simplification due to the use of a relatively crude and prescribed horizontal structure allows for high resolution along the vertical. There is then no need for sophisticated turbulence closure, turbulent transfer being then explicitely described.

The model we shall be dealing with is a third-order model already used for the simulation of various turbulent flows (15, 16). It shoud be noted here that the realizability conditions (8)which were used in the earlier simulations are not necessary anymore for the present study. Indeed, the refinements we shall introduce below for the closure assumptions prevent triple correlations from becoming too large and overshooting their maximum permissible values derived from generalized Schwarz's inequalities.

We shall not go here into all details of the model, its description for the simulation of convective flows being given in André et al. (16), to which the interested reader is referred.

We shall simply recall that the rate equation for triple correlation read, with usual assumptions and standard notations

$$\frac{\partial \overline{u_i'u_j'w'}}{\partial t} = -\overline{w'^2}\frac{\partial \overline{u_i'u_j'}}{\partial z} - \overline{u_j'w'}\frac{\partial \overline{u_i'w'}}{\partial z} - \overline{u_i'w'}\frac{\partial \overline{u_j'w'}}{\partial z} - \varepsilon_{uuw} + \beta\left(\overline{u_i'u_j'T'} + \overline{u_i'w'T'}\delta_{zj} + \overline{u_j'w'T'}\delta_{zi}\right) - \frac{1}{\rho_0}\left(\overline{u_i'u_j'\frac{\partial p'}{\partial z}} + \overline{u_i'w'\frac{\partial p'}{\partial x_j}} + \overline{u_j'w'\frac{\partial p'}{\partial x_i}}\right) \quad (9)$$

$$\frac{\partial \overline{u_i'u_j'T'}}{\partial t} = -\overline{u_i'u_j'w'}\frac{\partial \overline{T}}{\partial z} - \overline{u_i'w'}\frac{\partial \overline{u_j'T'}}{\partial z} - \overline{u_j'w'}\frac{\partial \overline{u_i'T'}}{\partial z} - \overline{w'T'}\frac{\partial \overline{u_i'u_j'}}{\partial z} + \beta\left(\overline{u_i'T'^2}\delta_{zj} + \overline{u_j'T'^2}\delta_{zi}\right) - \varepsilon_{uuT} - \frac{1}{\rho_0}\overline{T'\left(u_i'\frac{\partial p'}{\partial x_j} + u_j'\frac{\partial p'}{\partial x_i}\right)} \quad (10)$$

$$\frac{\partial \overline{w'T'^2}}{\partial t} = -2\overline{w'^2T'}\frac{\partial \overline{T}}{\partial z} - \overline{w'^2}\frac{\partial \overline{T'^2}}{\partial z} - 2\overline{w'T'}\frac{\partial \overline{w'T'}}{\partial z} - \varepsilon_{wTT} + \beta\overline{T'^3} - \frac{1}{\rho_0}\overline{T'^2\frac{\partial p'}{\partial z}} \quad (11)$$

$$\frac{\partial \overline{T'^3}}{\partial t} = -3\overline{w'T'^2}\frac{\partial \overline{T}}{\partial z} - 3\overline{w'T'}\frac{\partial \overline{T'^2}}{\partial z} - \varepsilon_{TTT} \quad (12)$$

in which the parameterization of molecular terms $\varepsilon\ldots$ is based on the assumption of isotropic dissipative scales

$$\varepsilon_{uuw} = \varepsilon_{wTT} = 0$$
$$\varepsilon_{uuT} = c_{10}\frac{\varepsilon}{\bar{e}}\frac{\overline{u_k'u_k'T'}}{3}\delta_{ij} \quad (13)$$
$$\varepsilon_{TTT} = c_{10}\frac{\varepsilon}{\bar{e}}\overline{T'^2}$$

Turning now to the pressure terms, we shall split them as in (15), into three parts : diffusive, diagonal, and trace-free parts. We shall neglect the diffusive part since it is very likely to be of small importance in the interior of convective layers, pressure transport being significant only close to walls or in stably stratified layers. The diagonal part will be modeled as a source term following Launder's (17) recommandation. Finally the trace-free part will be modeled as a redistribution term including a 'slow' return-to-isotropy contribution and a 'rapid' contribution, proportional to the anisotropic part of the production tensor. These two contributions come respectively from the non-linear turbulent and buoyant parts of the Poisson's equation for fluctuating pressure (see 18).

With all these assumptions, and in the particular case of convection in the absence of mean shear, the pressure terms will be given by, in general agreement with the developments of preceding section :

$$-\frac{1}{\rho_0}\left(\overline{u_i'u_j'\frac{\partial p'}{\partial z}} + \overline{u_i'w'\frac{\partial p'}{\partial x_j}} + \overline{u_i'w'\frac{\partial p'}{\partial x_i}}\right) = -c_8\frac{\varepsilon}{\bar{e}}\overline{u_i'u_j'w'} - c_{11}\beta\left(\overline{u_i'u_j'T'} + \overline{u_i'w'T'}\delta_{zj} + \overline{u_j'wT}\delta_{zi}\right) \quad (14)$$

$$-\frac{1}{\rho_0}\overline{T'\left(u_i'\frac{\partial p'}{\partial x_j} + u_j'\frac{\partial p'}{\partial x_i}\right)} = c_9\frac{\varepsilon}{\bar{e}}\overline{u_k'u_k'T'}\delta_{ij} - c_8\frac{\varepsilon}{\bar{e}}\left(\overline{u_i'u_j'T'} - \frac{\overline{u_k'u_k'T'}}{3}\delta_{ij}\right) - c_{11}\beta\left(\overline{u_i'T'^2}\delta_{zj} + \overline{u_j'T'^2}\delta_{zi} - \frac{2}{3}\overline{w'T'^2}\delta_{ij}\right) \quad (15)$$

$$-\frac{1}{\rho_0}\overline{T'^2\frac{\partial p'}{\partial x_i}} = -c_8\frac{\varepsilon}{\bar{e}}\overline{u_i'T'^2} - c_{11}\beta\overline{T'^2}\delta_{zi} \quad (16)$$

where the 'c_9-term' corresponds to diagonal part and the 'c_8-' and 'c_{11}-terms' correspond respectively to the non-linear and rapid parts.

IV. NUMERICAL RESULTS AND SENSIVITY STUDIES

Some "computer optimization" and sensivity studies, which will be reported later, have been used to determine the 'best' values of the constants c_8, c_9, c_{10}, and c_{11} :

$$c_8 = 8.0\ ;\ c_9 = -0.67;\ c_{10} = 6.0\ ;\ c_{11} = 0.2 \quad (17)$$

where the value of c_9 is determined from the realizability constraint (15), $3\,c_9 = c_{10} - c_8$. (18)

The corresponding results, normalized with the aid of Deardorff's (19) convective scaling, are shown in Figures 1 to 4 for respectively $\overline{w'^3}$, $\overline{u'^2w'}$, $\overline{w'^2T'}$ and $\overline{w'T'^2}$. It must be noted here that the experimental results by Ferreira (10) which appear on these figures have been rescaled. The velocity scale

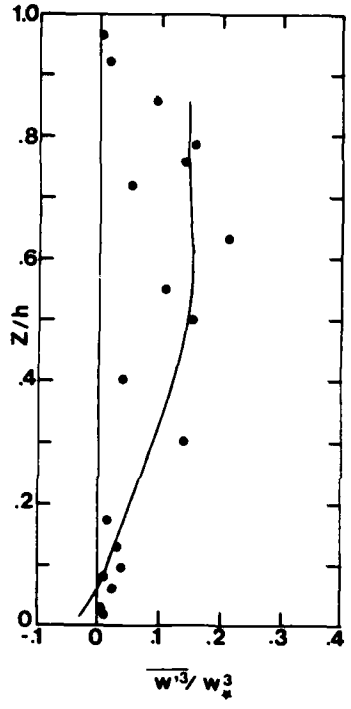

Figure 1 Dimensionless profile of the eddy flux of vertical component of kinetic energy. Points: laboratory measurements; curve: numerical results

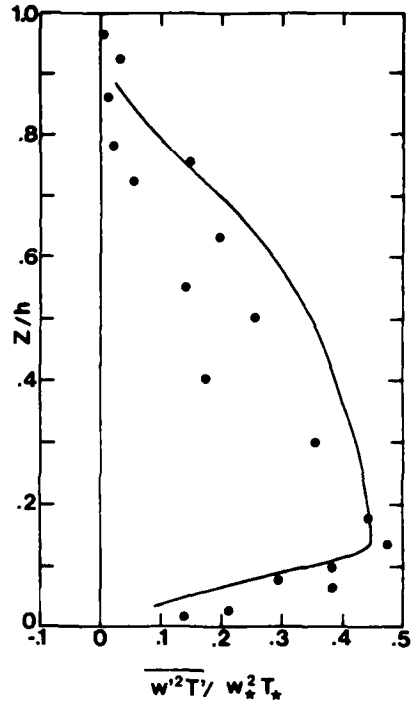

Figure 3 Dimensionless profile of the eddy flux of kinematic turbulent heat flux. Symbols as in Fig. 1

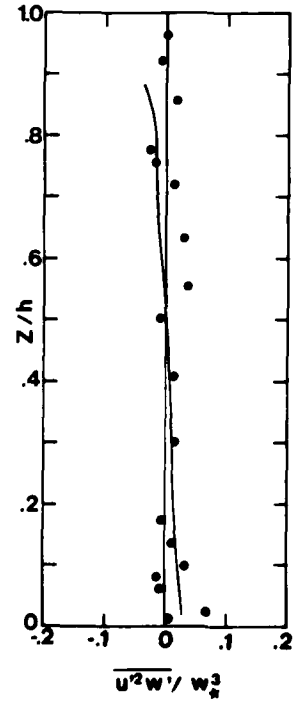

Figure 2 Dimensionless profile of the eddy flux of horizontal component of kinetic energy. Symbols as in Fig. 1

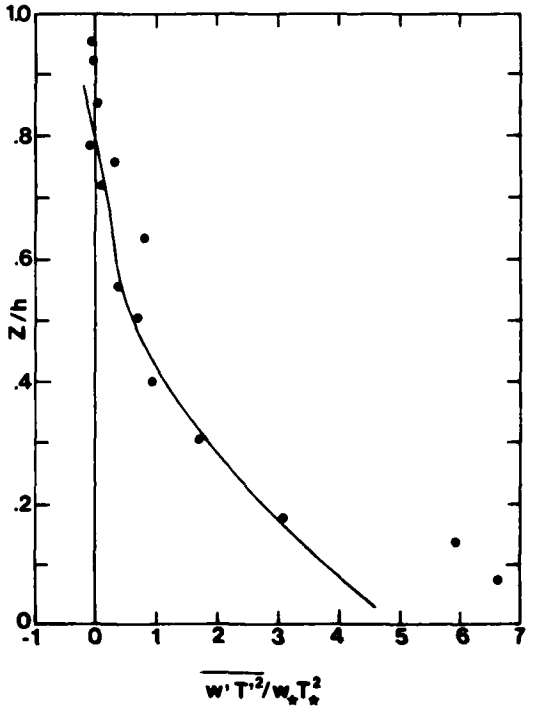

Figure 4 Dimensionless profile of the eddy flux of temperature variance. Symbols as in Fig. 1

w_* used in convective scaling depends in fact on the coefficient of thermal expansion α. Since this coefficient varies significantly (almost linearly) with temperature in the range we are concerned with , we used the exact value of α corresponding to each particular experiment instead of a mean value as in the results shown by Ferreira. This did lead to a change in the dimensionless results by as much as 20% in the case of $\overline{w'^3}$ and $\overline{u'^2 w'}$.

It can be seen that the agreement between our numerical results and the "corrected" measurements by Ferreira (10) is quite satisfactory in the convective layer interior, with the only possible exception that $\overline{w'^2T'}$ is slightly overestimated. This effect could maybe be ascribed to the fact that parameterizations (13) and (15) of molecular and pressure effects in Eq. (10) are not completely consistent with realizability conservation. Indeed, realizability constraint (18) is sufficient to insure that $\partial \overline{w'^2T'}/\partial t = 0$ whenever $w' = 0$ but is not to lead to $\partial \overline{u'^2T'}/\partial t = 0$ when $u' = 0$.

These parameterizations consequently induce an overestimation of $\overline{u'^2T'}$ and $\overline{v'^2T'}$ which in turn, through the c_8-term describing return-to-isotropy, (see Eq. (15)), lead to an overestimation of $\overline{w'^2T'}$. Although a plausible explanation has been found, it has not been possible to derive, at least up to now, a completely satisfactory modification of parameterization (15).

It should also be noticed from Figs. 1 to 4 that, despite the fact that viscous wall layers are not taken into account in the simulation, the numerical results are still in agreement with experimental data close to the lower boundary.

The sensitivity of model results to a ± 20% modification of constants c_8, c_{10} and c_{11} is shown in Table I (c_9 being always determined from (18)).

	c_8		c_{11}		c_{10}	
	-20%	+20%	-20%	+20%	-20%	+20%
$\overline{w'^3}(z/h=0.5)$	+47%	-28%	+ 6%	- 5%	+ 3%	- 2%
$\overline{w'^2T'}(z/h=0.5)$	+36%	- 3%	+ 3%	- 2%	+ 2%	- 1%
$\overline{w'T'^2}(z/h=0.5)$	+21%	-20%	+ 1%	- 1%	+ 7%	- 5%
$\overline{T'^3}(z/h=0.5)$	Less than 1 %				+ 8%	- 7%

TABLE I : Sensitivity of model results to changes in the constants

It can first be checked that an increase in the constants leads to a decrease of triple correlations (and vice-versa), in agreement with the general idea of damping by pressure effects. It must further be noticed that c_8 is the easiest constant to determine since it strongly influences the results, with the only exception that any significant increase of c_8 would lead to an important deterioration of $\overline{w'^3}$ and $\overline{w'T'^2}$ profiles without improving singificantly the $\overline{w'^2T'}$ profile. Such an increase of c_8, i.e. of the linear relaxative effect, would furthermore be in contradiction with the developments of Section 2 and would also lead to much underestimated calculated triple correlations in the case of other turbulent flows like the asymetric channel flow of Hanjalic and Launder (20), see (16). Any significant increase of c_8 being ruled out, one has then to look for another pressure mechanism to efficiently destroy triple correlations. This is the main reason for the introduction of the rapid linear part described by the 'c_{11}-term'.

Another justification for the introduction of rapid linear pressure effects is as follows. For stationary conditions, and near the middle of the convective layer where $\overline{w'^2}$ reaches a maximum, the budget for $\overline{w'^2T'}$ reduces to [see Eqs. (10) with i=j=3 and (13), (15) and (18)] :

$$c_8 \frac{\varepsilon}{\bar{e}} \overline{w'^2T'} = -\overline{w'^3}\frac{\partial \bar{T}}{\partial z} - 2\overline{w'^2}\frac{\partial \overline{w'T'}}{\partial z} + \frac{2}{3}\left(1 - \frac{2}{3}c_{11}\right)\overline{w'T'^2} \quad (19)$$

Adapting to the triple correlation $\overline{w'^2T'}$ an argument developed by Wyngaard and Coté (21) for the double correlation, or kinematic heat flux, $\overline{w'T'}$, it can be said that the introduction of rapid effect (c_{11}-term) decreases the magnitude of the buoyant contribution in Eq. (19), allowing in turn that the budget balances with larger values of $-\overline{w'^3}\partial\bar{T}/\partial z$, i.e. with smaller values of $\partial\bar{T}/\partial z$ or, in other terms, with enhanced unstable stratification. This argument has indeed been verified by running numerical experiments with $c_{11}=0$, and by noting that, in such cases, spurious stable stratification (positive $\partial\bar{T}/\partial z$) did appear in the lower half of the convective layer.

V. CONCLUDING REMARKS

Convective turbulent flows exhibit a lot of peculiar features : existence of countergradient transfer, presence of organized large-scale structures, importance of pressure effects. It is believed that these features are closely related to each other, the key mechanism being probably the appearance of quite regular mean motion at larger scales, even at very high Rayleigh number. These large structures develop in already turbulent flows and are probably the result of secondary instability mechanism (see e.g. 22 for review). They bear some resemblances, from the morphological and also maybe mathematical points of view, to the more familiar convective patterns observed for much smaller Rayleigh number. Their physics and dynamics are however basically different since in this case the dissipative phenomena are due to the 'background' smaller scale turbulent motions, instead of being due directly to viscosity. One can then question about the relevance of 'direct' numerical simulations for the study of these convective turbulent flows. Can they shed some light on flow dynamics ? Can they be of interest for the development of closure schemes and parameterization techniques ? Whatever their precise type is, either "modal" (14) or "three-dimensional" with either subgrid-scale parameterization (e.g. 23) or large eddy simulation techniques (24), they are restricted to relatively small equivalent Rayleigh number.

They indeed can only deal with narrow turbulent spectra due to the limited memory size of presently available computers. Despite this limitation concerning their true physical signification, it is believed (but at least hoped !) that they will help for the understanding of many of the effects

associated with large-scale convective structures.

REFERENCES

1 Deardorff, J.W., "The counter-gradient heat flux in the lower atmosphere and in the laboratory", Journal of Atmospheric Sciences, Vol. 23, No. 5, 1966, pp. 503-506.

2 Willis, G.E., and Deardorff, J.W., "A laboratory model of the unstable planetary boundary layer", Journal of Atmospheric Sciences, Vol. 31, No. 5, 1974, pp. 1297-1307.

3 Launder, B.E., and Spalding, D.B., "The numerical computation of turbulent flows", Computer Methods in Applied Mechanics and Engineering, Vol. 3, North-Holland Publishing Company, 1974, pp. 269-289.

4 André, J.C., De Moor, G., Lacarrère, P., and du Vachat, R., "Turbulence approximation for inhomogeneous flows -Part II. The numerical simulation of a penetrative convection experiment," Journal of Atmospheric Sciences, Vol. 33, No. 3, pp. 482-491.

5 Lumley, J.L., Zeman, O., and Siess, J., "The influence of buoyancy on turbulent transport", Journal of Fluid Mechanics, Vol. 84, Part 3, 1978, pp. 581-597.

6 Zeman, O., and Lumley, J.L., "Modeling buoyancy driven mixed layers", Journal of Atmospheric Sciences, Vol. 33, No. 10, 1976, pp. 1974-1988.

7 Sun, W.Y., and Ogura, Y., "Modelling the evolution of the convective planetary boundary layer", Journal of Atmospheric Sciences, Vol. 37, No. 7, 1980, pp. 1558-1572.

8 André, J.C., De Moor, G., Lacarrère, P., and du Vachat, R., "Turbulence approximation for inhomogeneous flows - Part I. The clipping approximation", Journal of Atmospheric Sciences, Vol. 33, No. 3, 1976, pp. 476-481.

9 Warn-Varnas, A.C., and Piacsek, S.A., "An investigation of the importance of third-order correlations and choice of length scale in mixed layer modelling", Geophysical and Astrophysical Fluid Dynamics, Vol. 13, 1979, pp. 225-243.

10 Ferreira, R.T.S., "Unsteady turbulent thermal convection", Ph. D. Thesis, Sept. 1978, University of Illinois, Urbana Champaign.

11 André, J.C., "Irreversible interaction between cumulants in homogeneous, isotropic, two-dimensional turbulence theory", Physics of Fluids, Vol. 17, No.1, 1974, pp. 15-21.

12 Orszag, S.A., and Kruskal, M.D., "Formulation of the theory of turbulence", Physics of Fluids, Vol.11, No. 1, 1968, pp. 43-60.

13 Lumley, J.L., "A new kind of realizability in turbulence modelling of the planetary boundary layer", Workshop on the Planetary Boundary Layer, American Meteorological Society, 1978.

14 Latour, J., Spiegel, E.A., Toomre, J., and Zahn, J.P., "Stellar convection theory.I. The anelastic modal equations", Astrophysical Journal, Vol. 207, 1976, pp. 233-243.

15 André, J.C., De Moor, G., Lacarrère, P., Therry, G., and du Vachat, R., "Modeling the 24-hour evolution of the mean and turbulent structures of the planetary boundary layer", Journal of Atmospheric Sciences, Vol. 35, No. 10, 1978, pp. 1861-1883.

16 André, J.C., De Moor, G., Lacarrère, P., Therry, G., and du Vachat, R., "The clipping approximation and inhomogeneous turbulence simulations", Turbulent Shear Flows 1, Springer-Verlag, Berlin, 1979, pp. 307-318.

17 Launder, B.E., private communication, 1976.

18 Launder, B.E., "On the effects of a gravitational field on the turbulent transport of heat and momentum", Journal of Fluid Mechanics, Vol. 67, Part 3, 1975, pp. 569-581.

19 Deardorff, J.W., "Convective velocity and temperature scales for the unstable planetary boundary layer and for Rayleigh convection", Journal of Atmospheric Sciences, Vol. 27, 1970, pp. 1211-1213.

20 Hanjalic, K., and Launder, B.E., "Fully developed asymmetric flow in a plane channel", Journal of Fluid Mechanics, Vol. 51, Part 2, 1972, pp. 301-335.

21 Wyngaard, J.C., and Coté, O.R., "The evolution of a convective planetary boundary layer - A higher-order-closure model study", Boundary-Layer Meteorology, Vol. 7, 1974, pp. 289-304.

22 Brown, R.A., "Longitudinal instabilities and secondary flows in the planetary boundary layer : a review", Reviews of Geophysics and Space Physics, Vol. 18, No. 3, 1980, pp. 683-697.

23 Deardorff, J.W., "A numerical study of three-dimensional turbulent channel flow at large Reynolds numbers", Journal of luid Mechanics, Vol. 41, Part 2, 1970, pp. 453-480.

24 Kwak, D., Reynolds, W.C., and Ferziger, J.H., "Three-dimensional time-dependent computation of turbulent flow", TF-5, 1975, Department of Mechanical Engineering, Stanford Univ., Calif.

A THEORETICAL STUDY OF RADIATIVE COOLING IN HOMOGENEOUS AND ISOTROPIC TURBULENCE

D. Schertzer [1], O. Simonin [2] [3]

(1) Direction de la Météorologie, EERM/GMD, Boulogne, France.

(2) Institut de la Mécanique Statistique et de la Turbulence, Marseille, France.

(3) Ecole Nationale Supérieure des Techniques Avancées, Paris, France.

ABSTRACT

We apply two-points closures to study radiative cooling in homogeneous and isotropic turbulence. They should provide a systematic tool in this study.

The radiative dissipation of temperature inhomogeneities intervenes as a linear dissipative term in the equation of advection of temperature fluctuations.

A critical regime is studied which could not be analyzed by phenomenological models. In that regime, a balance occurs between the radiative dissipative term and a non local part of the transfer term. It creates an "intertial-radiative" subrange, where the slope of the temperature spectrum is steeper than -3.

NOMENCLATURE

$B_\nu(T)$	Planck's function
$C_{c.o.}$	Corrsin-Obukhov constant
C_K	Kolmogorov constant
C_p	Specific heat at constant pressure
$\underline{d}$	Unit vector specifying the travelling direction of a ray
$D_R(k) = N(k)/k^2$	Radiative diffusivity
D_θ	Molecular thermal diffusivity
D_R^r	Renormalized radiative diffusivity
D_θ^e	Eddy-diffusivity
E	Turbulent energy spectrum
E_θ	Temperature variance spectrum
$\underline{F}$	Net flux vector of radiative energy
G_ν	Green's function of the radiative transfer equation
i	Square-root of (-1)
$I_\nu(\underline{x},\underline{d},t)$	Specific intensity
$\underline{k}$, $\underline{p}$, $\underline{q}$,	Wave-vectors in Fourier space
k_D	Corrsin-Obukhov wave-number
k_I	Wave-number of injection
k_ν	Komogorov wave-number
K_P	Planck mean absorption coefficient
K_R	Rosseland mean absorption coefficient
K_ν	Absorption coefficient for radiation of frequency ν
$N(k)$	Radiative dissipative term
$P_R = \nu/D_R(o)$	Radiative Prandtl number
P_R^c	Critical radiative Prandtl number
$P_T = \nu/D$	Thermal Prandtl number
$R = \chi v^2/\varepsilon\langle\theta^2\rangle$	Ratio of dissipation time scales
$R_e = v/k_I \nu$	Reynolds number
t	Time
T	Temperature
$T_\theta(k,t)$	Temperature - variance transfer term
$T_\theta^{NL}(k,t)$	Non local temperature variance transfer term
$\underline{U}$	Fluctuating velocity vector
$v^2 = \langle\underline{U}.\underline{U}\rangle$	Eddy kinetic energy
ε	Eddy kinetic energy dissipation rate
ε_c	Critical eddy kinetic energy dissipation rate
θ	Temperature fluctuation
ν	Frequency
ν	Kinematic viscosity
$\Pi(k,t)$	Non linear flux of kinetic energy
ρ	Density
ρ_a	Density of the absorber
σ	Stefan constant
$\tau_e^{(k)}, \tau_D^{(k)}, \tau_R^{(k)}$	Characteristic times of advection, molecular diffusion, radiative diffusion
$\tau_{k,p,q}$	Characteristic time of triple correlation relaxation
$\chi(k,t)$	Non linear flux of temperature variance
χ_D	Molecular temperature variance decay rate
χ_I	Injected flux of temperature variance
χ_R	Radiative temperature variance decay rate
$\phi_\theta(k,t) = k^2 E_\theta(k,t)$	Spectrum of the temperature gradient variance
$\Omega_\theta(k,t) = \int_o^k dk' k'^2 E_\theta(k',t)$	Flux of temperature gradient variance
$\langle . \rangle$	Average value of .

1. INTRODUCTION

Two-point analytical closures have been successfully developped for the study of a passively advected scalar as the temperature field see Leslie (1) for review, and (2) - (5) for new developments .

These closures should provide a systematic tool for the study of interaction between turbulence and long-wave radiation. Coantic (6) analyzes extensively the importance of this interaction in the context of geophysical flows. This interaction seems especially important in nocturnal planetary boundary layers André et al. (7), since the radiative destruction rate of temperature variance, X_R, is then of the same order as the molecular one X_D.

We first discuss a direct derivation in the Fourier space for the divergence of the radiative flux. Due to the fact that the radiative transfer equation is linear, Fourier space is rather convenient to obtain such a result, which has been first obtained by Spiegel (8).

A phenomenological approach, slightly different from the one used by Schved (9), points out the existence of a critical regime.

We characterize it by a critical "radiative Prandtl number" P_R^c. For radiative Prandtl number P_R smaller than this critical value, radiative dissipation becomes of prime importance.

Local and non-local interactions, as analyzed by Lesieur and Schertzer (10), are discussed relatively to their influence.

For radiative Prandtl number P_R larger than P_R^c, local interaction are dominant as in the usual "inertial-inertial" range (i.e. inertial for the temperature and velocity fields). Simple phenomenological models of non linear transfer of temperature variance may be used (11) to model the pertubed temperature spectrum.

On the contrary for lower P_R, non-local interactions become predominant and lead to the existence of an "inertial-radiative" subrange.

In this subrange, which is included within the velocity inertial range, a balance occurs between radiative dissipation (which is not of a pertubative nature anymore) and a non-local part of the non-linear transfer of temperature variance.

The temperature variance spectrum has then a slope notably steeper (< -3) than in the usual "inertial-inertial" range ($-5/3$).

Some consequences of the appearance of such a subrange are discussed.

2. RADIATIVE DISSIPATIVE TERM.

Long-wave radiative cooling is described (6, e.g.) by the divergence of the radiative flux $\underline{F}$:

$$\left[\partial/\partial t \quad T(\underline{x},t)\right]_R = -\underline{\nabla}.\underline{F}/\rho C_p \qquad (1)$$

and introduces a linear dissipative term in the equations for the rate of change of temperature fluctuations $\theta(\underline{x},t)$.

In the Fourier space, this equation and the one for the spectrum of temperature variance $E_\theta(\underline{k},t)$ in homogeneous and isotropic turbulence read :

$$(\partial/\partial t + D_\theta k^2)\ \theta(\underline{k},t) = -N(k)\ \theta(\underline{k},t) - i\,\underline{k}\cdot\int \underline{v}(\underline{p},t)\ \theta(\underline{q},t)\ d\underline{p} \qquad (2)$$
$$\underline{k} = \underline{p} + \underline{q}$$

$$(\partial/\partial t + 2D_\theta k^2)\ E_\theta(k,t) = -2\,N(k)\ E_\theta(\underline{k},t) + T_\theta(k,t) \qquad (3)$$

where $T_\theta(k,t)$ is the non-linear transfer term of scalar variance, D_θ the molecular diffusivity, and $N(k)$ is the radiative dissipative term. It is worthwile to notice that $N(k)$ modifies the Green function of (2), so that it intervens implicitely in the expression of $T_\theta(k,t)$. We will precise this point later.

The reason for this relatively simple radiative term is that the radiative transfer equation (e.g. 12) is linear with respect to $I_\nu(\underline{x},\underline{d},t)$, the specific intensity at point $\underline{x}$ of rays traveling in the direction $\underline{d}$ ($|\underline{d}| = 1$) :

$$\underline{d}.\underline{\nabla}\ I_\nu = -K_\nu\, I_\nu(\underline{x},\underline{d},t) - B_\nu(T(\underline{x},t)) \qquad (4)$$

where K_ν, the coefficient of absorption at frequency ν, is proportional to the mean concentration $\langle \rho_a \rangle$ of the absorber, and has the dimension of a wave-number. B_ν is the Planck function wich is the appropriate source term in case of local thermodynamical local equilibrium (L.T.E.).

Fourier transform of equation (4), respectively to $\underline{x}$, leads then to :

$$I_\nu(\underline{k},\underline{d},t) = G_\nu(\underline{k},\underline{d})\ B_\nu(T(\underline{k},t)) \qquad (5)$$

G_ν being the Green function :

$$G_\nu(\underline{k},\underline{d}) = K_\nu / (i\,\underline{d}.\underline{k} + K_\nu) \qquad (6)$$

From the spectral intensity I_ν, it is then possible to compute the radiative flux and its divergence according to :

$$i\,\underline{k}.\underline{F}(\underline{k},t) = i\int_0^\infty d\nu \int_{|\underline{d}|=1} \underline{k}\,\underline{d}\ I_\nu(\underline{k},\underline{d},t)\ d\,\underline{d} \qquad (7)$$

Equation (2) is then obtained by using a linear approximation for the Planck function B :

$$T(\underline{x},t) = \langle T \rangle + \theta(\underline{x},t)$$

$$B_\nu[T(\underline{x},t)] = B_\nu(\langle T \rangle) + \frac{dB}{dT}(\langle T \rangle)\,\theta(\underline{x},t) \qquad (8)$$

no contribution to the evolution of fluctuations. From (5)-(8), it follows that (11) :

$$N(k) = \int_0^\infty d\nu\, A_\nu K_\nu \left[1 - (K_\nu/k)\arctan(k/K_\nu)\right]$$
$$A_\nu = (4\pi/\rho C_p)\left(\partial B_\nu(\langle T \rangle)/\partial T\right) \qquad (9)$$

In the "grey atmosphere" approximation ($K_\nu = K$), this expression reduces to (8) :

$$N(k) = A\,K\left[1 - (k/K)\arctan(K/k)\right] \qquad (10)$$
$$A = 4\sigma \langle T \rangle^3 / 3\rho C_p$$

Though the approximation of grey atmosphere is not too badly suited for the case of stellar atmospheres (12), it is not accurate enough for the earth atmosphere. In this last case, the dependency on frequency of the absorption coefficient K_ν may classically be taken into account by statistical models of absorption bands (13). The frequency spectrum is then divided into independent bands of frequencies $\Delta\nu$. In each band, K_ν is considered as the cumulative absorption due to randomly distributed lines of absorption, each line having a ran-

domly distributed intensity. Accurate modeling of N (k) can thus be performed (13) for water vapour in the case of the earth atmosphere for infra red radiation. As a first approximation, and following Simonin (14), K_ν will be taken as its average value K_j in the j-th band of characteristic frequency ν_j :

$$N(k) = \sum_j A_j K_j \Delta\nu_j \left[1 - (K_j/k)\arctan(k/K_j)\right] \qquad (11)$$

$$A_j = (4\pi/\rho c_p)\,(\partial B_{\nu_j}/\partial T)$$

We will refer to this last approximation, in the rest of the text, by the expression of "non grey atmosphere".

In each case, it is possible to define the two classical limits (6) :

(i) the opaque limit : $k \to 0$

$$N(k) \simeq D_R(0)\,k^2 \quad ; \quad D_R(0) = (4/3)\int_0^\infty d\nu\, A_\nu/K_\nu = (4/3)\,A/K_R \qquad (12)$$

(ii) the transparent limit : $k \to \infty$

$$N(k) \simeq N(\infty) \; ; \; N(\infty) = \int_0^\infty d\nu\, A_\nu K_\nu = A\,K_P \qquad (13)$$

We may define a radiative diffusivity at each wave number by :

$$D_R(k) = N(k)/k^2 \qquad (14)$$

In the case of a grey atmosphere, the Planck mean absorption coefficient K_P and the Rosseland one, K_R, are both equal to K.

On the contrary, Goody (13) indicates that for the case of water vapour absorption in the lower atmosphere, one has : $K_P/K_R \sim 10^4$.

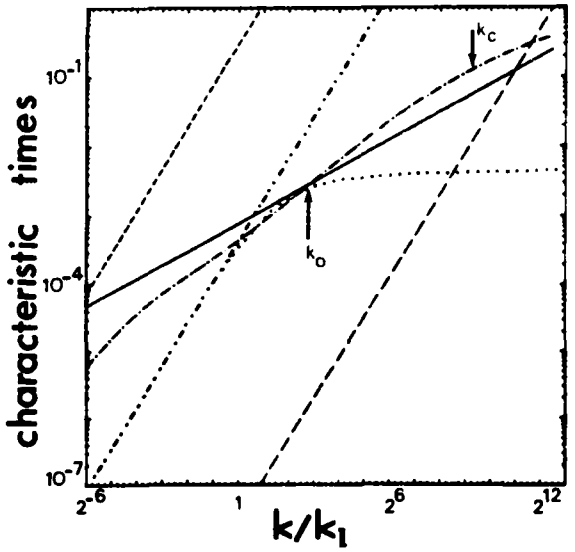

Fig.1 : characteristic times (normalized by $\tau_m = 1/k^2_{max}$) —— : τ_e^{-1} ; - . - : τ_R^{-1} (non grey) ; ... τ_R^{-1} (grey) ; - - - - : $D_R(0)\,k^2$ (non grey) ; - . - . - $D_R(0)\,k^2$ (grey) . ; - - : τ_D^{-1} ;

The main effect of this difference between K_P and K_R is that there exists a large subrange of wave-numbers such that :

$$N(k) \sim k^r \; ; \; r \gtrsim (2/3) \qquad (15)$$

As we will see later, the indicated value (2/3) will be of prime importance.

Figure 1 indicates, in log-log plots, the behaviour of N (k) in the precited cases and will be further commented in the next section.

At this point, we have to emphasize that we have neglected the fluctuations of the concentration of the absorber, as usualy done (13).

3. PHENOMENOLOGY

Classicaly (e.g. : 3), the local characteristic time of turbulent advection is :

$$\tau_e(k) \sim (\varepsilon^{1/3}\,k^{2/3})^{-1} \qquad (16)$$

while the molecular-conductive and radiative ones are respectively :

$$\tau_D(k) \sim (D_\theta\,k^2)^{-1} \; ; \; \tau_R(k) \sim [N(k)]^{-1} \qquad (17)$$

where D_θ is the molecular diffusivity. Recalling that the thermal Prandtl number is defined by :

$$P_T = \bar{\nu}/D_\theta \qquad (18)$$

($\bar{\nu}$ being the kinematic viscosity) we may define a "radiative Prandtl number" P_R by (see equation 12) :

$$P_R = \bar{\nu}/D_R(0) \qquad (19)$$

The inverses of theses times are plotted in figure 1 . A critical regime is obtained when the two curves $\tau_e(k)$ and $\tau_R(k)$ are approximately tangent or intersect.

The possible point of tangency gives a certain critical wave number k_c :

$$k_c \; d\,\mathrm{Log}\,N(k_c)/dk = 2/3 \qquad (20)$$

(in case of a grey atmosphere : $k_c = 2.4768...K$).

When an intersection occurs, we obtain a subrange $[k_o, k_t]$ inside which radiative effects are presumably of prime importance, because $\tau_R(k)$ is the smaller characteristic time. The first point of intersection k_o is on the side of opaque limit (small k), the second one, k_t, on the side of the transparent limit (large k). Of course, if the intersection of $\tau_e(k)$ and $\tau_R(k)$ occurs at a wave-number k'_t smaller than k_t, k'_t, instead of k_t, characterizes the end of the precited subrange. It must be noticed, that we may estimate $P_R \sim 10^{-7}$ from Goody's computations (13), when $P_T \sim 1$.

In the case of a grey atmosphere, using crude (but rather accurate) approximations of N (k) corresponding to its two limits (equations 12 and 13) we may approximate k_o and k_t by :

$$k_o \simeq \varepsilon^{1/4}/D_R(0)^{3/4} \; ; \; k_t \simeq [3\,D_R(0)\,K^2]^{3/2}/\varepsilon$$

In any case (grey or non-grey atmospheres), the case of tangency between τ_e and τ_R is obtained for the critical value ε_c of the rate of destruction of turbulent energy satisfying [k_c being defined by (20)] :

$$\varepsilon_c^{1/3}\,k_c^{2/3} = N(k_c) \qquad (21)$$

and for ε lower than ε_c, we have a critical regime. The relationship (21) can be adimensionalized, by noting that in any case we may write :

$$N(k) = D_R(0)\, K_c^2\, f(k/K_c) \qquad (22)$$

K_c being some characteristic absorption coefficient, and, in the same time, some wave number (because of its dimension, as soon noted). In our study, we choose : $K_c^2 = K_P . K_R$. Using the classical relations (e.g. 1) :

$$R_e \simeq (k_\nu / k_I)^{4/3} \quad ; \quad k_\nu \simeq (\varepsilon / \nu^3)^{1/4}$$

(where R_e is the Reynolds number, k_ν^{-1} is the Kolmogorov length-scale, k_I is the wave number of injection turbulent kinetic energy), one obtains for the critical relationship :

$$(23)$$

P_R^c being what we call the "critical radiative Prandtl". The existence of the subrange $[k_I, k_c]$ is obtained when $\simeq$ is replaced by $\ll$ in (23). A convenient way to say it, is that the radiative Prandtl is lower than its critical value defined by (23) for the given Reynolds number and ratio of scales (K_c/k_I). Otherwise, we could speak of a critical Reynolds number, or a critical ratio of scales.

4. LOCAL INTERACTIONS

For wave-numbers smaller than the radiative Prandtl P_R larger than its [illegible] P_R^c (i.e. for "small" radiative effects) [illegible] be expected that the transfer of temperature variance in Fourier space is dominated by local interactions, as in the case of a simply active scalar (e.g. 3 or 5). That is to say, triad interactions such as $k \sim p \sim q$ give the predominant contribution for the non-linear transfer term $T_\theta(k,t)$ and the non-linear flux of temperature variance in scales smaller than k^{-1} :

$$\chi(k,t) = \int_k^\infty dk'\, T_\theta(k',t) \qquad (24)$$

Dimensionnal analysis, or examination of the local divergence of this flux in the framework of two-point closures (5), leads to :

$$\chi(k,t) = C_{c.o}^{-1}\, k\, E_\theta(k,t)\, \tau_e^{-1}(k) \qquad (25)$$

or :

$$E_\theta(k,t) = C_{c.o}\, k^{-5/3}\, \chi(k,t)\, \varepsilon^{-1/3} \qquad (26)$$

$C_{c.o.}$ being the Corrsin-Obukhov constant. The variation of the flux $\chi(k)$, with respect to k, is due to the radiative dissipation as a quasi-equilibrium is obtained by an injection of a flux χ_I of temperature variance at wave-number k_I :

$$d\chi(k) = -2\, N(k)\, E_\theta(k)\, dk \qquad (27)$$

It follows that :

$$\chi(k) = \chi_I \exp\left[-2\, C_{c.o}\, \varepsilon^{-1/3} \int_{k_I}^{k} dk'\, N(k')\, k'^{5/3}\right] \qquad (28)$$

i.e. a slight modification, with respect to the usual inertial-inertial range.

It may further be approximated, for non critical regime, in noting that in a certain subrange $[k_1, k_2]$ around k_c we have (due to the definition of this wave number, see (21) :

$$N(k) = \varepsilon_c^{4/3}\, k^{2/3} \qquad (29)$$

Thus :

$$\chi(k) \simeq \chi(k_1) (k_1/k)^{2\, C_{c.o.}\, (\varepsilon_c/\varepsilon)^{4/3}} \qquad (30)$$

As noted earlier (15), in case of a non grey atmosphere k_1 may be near of k_I.

This explains the linear dependency of $\chi(k)$ on Log (k/k_I) observed on figure 2. Equations (30) and (27) explain that the radiative dissipation spectrum is rather flat in an area preserving plot (11).

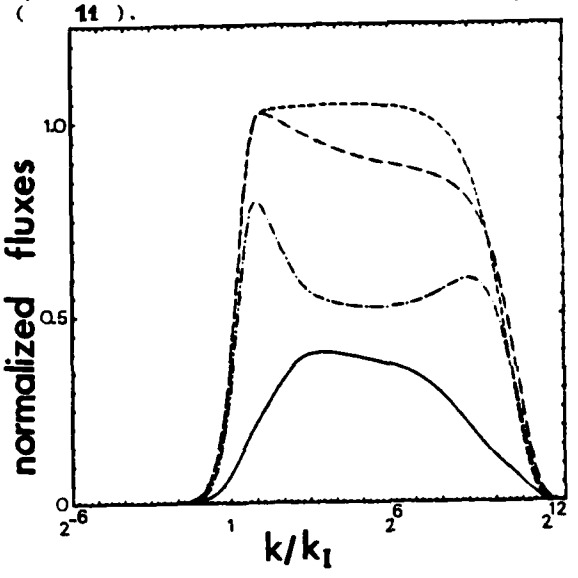

Fig.3 : weak radiative effet (grey atmosphere) $K = 2.k_I$; $P_R = P_R^c/10 = 10^{-3}$: ..... : global energy flux ; — — : global temperature variance flux ; — . — : local temperature variance flux ; —— : non local one.

As soon as ε is near of ε_c (or P_R near of P_R^c) equations (28) or (30) shows that the exponent of the spectrum may largely change. There is consequently no more guarantee that the local interactions are predominant. For instance, if the slope of the spectrum becomes steeper than -3, the spectrum of the temperature gradient $\phi_\theta(k)$ is then concentrated in scales larger than k_o^{-1}. Thus, some integrals intervening in $\chi(k)$ are no more locally divergent. Lousely speaking, what is on the left of the spectrum may wheight more than the rest on the right.

This point is totally missed by phenomenological models leading to (25), even if τ_e is replaced by a time scale taking into account the dissipative one (15).

5. NON LOCAL INTERACTIONS : AN "INERTIAL-RADIATIVE" SUBRANGE

In the physical space, non local interactions mean interactions between very different scales. In the Fourier space a precise definition can be given (e.g. : 10), i.e. a triad ($\underline{k}$, $\underline{p}$, $\underline{q}$) is non local if :

$$\min(k,p,q) / \max(k,p,q) < a \ll 1 \qquad (31)$$

where a is some fixed parameter, defining the amplitude of non-localness.

Suppose now, as the local analysis of the preceding section shows it, that around k_o the slope of the temperature spectrum becomes steeper. The main contribution for the non-linear flux $\chi(k,t)$, $k \simeq k_o$, are given by non local triads of interactions ($\underline{k}$, $\underline{p}$, $\underline{q}$) corresponding to triple correlations $\langle \theta(\underline{k}) \theta(\underline{p}) \psi(\underline{q}) \rangle$ with : $p \ll k_o \ll q \sim k$ (32)

Using the technique developped in Lesieur and Schertzer (10) and applying it to (3), as partialy done in Larchevêque et al. (3), the corresponding part $\mathcal{F}_D^{NL}$ of the non local flux $\mathcal{F}^{NL}$, created by the non local interactions, is of an "eddy diffusivity" type, i.e. :

$$\mathcal{F}_D^{NL}(k,t) = (2/3)\int_k^\infty dk' E(k',t)\int_0^{\alpha(ak',k)} \tau_{k,p,q}\, p^2 E_\theta(p,t) \qquad (33)$$

where E (k,t) is the energy spectrum and $\tau_{k,p,q}$ is the characteristic time of relaxation of triple correlation $\langle\theta(\underline{k})\,\theta(\underline{p})\,\underline{U}(\underline{q})\rangle$.

In the velocity-inertial range, we have, following Larchevêque et al. (3) :

$$\tau_{k,p,q} \simeq [\tau_e^{-1}(k)+\tau_e^{-1}(p)+\tau_e^{-1}(q)+N(k)+N(p)]^{-1} \qquad (34)$$

By derivation, with respect to k, (33) leads to the non local part of the transfer term :

$$T_{\theta,D}^{NL} = (2/3)\,E(k,t)\int_0^{ak} dp\, \tau_{k,p,k}\, p^2 E_\theta(p) - 2D_\theta^e(k,a)k^2 E_\theta(k,t) \qquad (35)$$

$D_\theta^e(k,l,a)$ being the eddy-diffusivity, taking into account the influences of scales smaller than $(k/a)^{-1}$ on the scale k^{-1} :

$$D_\theta^e(k,t;a) = (1/3)\int_{k/a}^\infty dp\, \tau_{p,k,p}\, E(p,t) \qquad (36)$$

As soon as k is larger than k_o, i.e. $N(k) > \tau_e^{-1}(k)$ $\tau_{k,p,k}$ may be approximated by :

$$p < k_o < k : \quad \tau_{k,p,q} \simeq N(k)^{-1} \qquad (36)$$

On the other hand, we may introduce the "renormalized radiative diffusivity" D_R^r (using the renormalization language (16) - (18)) :

$$D_R^r(k,t,a) = D_R(k) + D_\theta^e(k,t,a) \qquad (37)$$

It must be stressed that, equation (37) gives a false appearance of a simple addivity between the radiative diffusivity and an eddy-diffusivity, independant of the radiative diffusivity. This is clearly not the case: an increase in D_R implies (34,36) a decrease in D_R^e. We will comment later this important point.

If we suppose that $T_{\theta,D}^{NL}$ is the leading part of the transfer term T_θ, its balance with the radiative dissipation can be written, with the help of (35, 36 and 37), as :

$$2\,D_R^r(k,t,a)k^2 E_\theta(k,t) = (2/3)\,E(k,t)\,\Omega_\theta(k,t) \qquad (38)$$

Equation (38) ensures the existence of an "inertial-range" between k_o and k_c :

$$E_\theta(k,t) \sim k^{-A} \qquad A > -3 \qquad (39)$$

Because of (36, 37), (38) could be roughly approximated by :

$$E_\theta(k,t) \sim (1/3)C_K \varepsilon^{2/3} k^{-5/3-2r}\Omega_\theta(k_t) \qquad (40)$$

where we use the convergence of Ω_θ, i.e. $\Omega_\theta(k) \sim \Omega_\theta(k_o)$.

After k_c, (40) indicates a return to $k^{-5/3}$ law which is reached around k_t, if this wave-number is far enough in the transparent limit ($r \simeq o$).

Figure 3 shows that in the subrange $[k_o, k_t]$ the exponent of the temperature spectrum remains nearly equal to -3, because r remains itself nearly equal to 2/3.

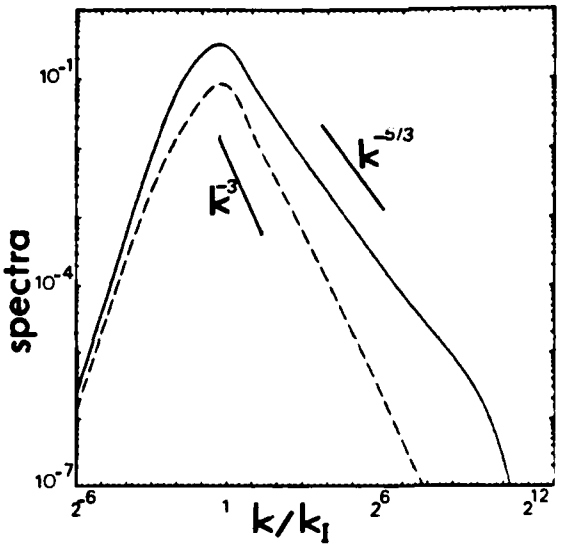

Fig.5 : spectra for non grey atmosphere ($K_c = 2\,k_I$, $P_R = 10^{-7}$) : — : $E(k,t)$; - - - : $E_\theta(k,t)$

Due to (37), we have :

$$N(k) < D_R^r(k,t;a)k^2 < N^r(k,t) = k^2 D_R^r(k,t,q) \qquad (41)$$

(N^r being the "renormalized" radiative dissipative term), we may approximate (38) by :

$$E_\theta(k,t) \gtrsim (1/3)\,E(k,t)\Omega_\theta(k,t)/N(k)\,N(k,t) \qquad (42)$$

$$E_\theta(k,t) \lesssim (1/3)\,E(k,t)\Omega_\theta(k,t)/N^2(k,t) \qquad (43)$$

As noted earlier, equation (40), the non-local equilibrium described tends to create an apparent "inertial-inertial" range near k_t, if this wave-number is far enough in the transparent limit, i.e. $N(k_t) \sim N(\infty)$. For $k > k_t$, a real inertial-inertial subrange takes place up to k_D, the Corrsin-Obukhov wave-number. In this range the flux $\mathcal{F}_D$ of temperature variance which is cascading towards k_D is of course the part of the flux which is left after destruction by radiative dissipation effects, and which will be destroyed by molecular diffusivity.

6. CONCLUDING REMARKS

Above the critical radiative Prandtl number P_R^c, for which advective and radiative time scales are equal, see (23), radiative cooling has only a slight pertubative effect on temperature variance spectrum. It introduces a small exponential correction (a small power correction near k_c, $N(k_c) \sim k_c^{2/3}$) to the $k^{-5/3}$ temperature inertial range spectrum. This range survives, though the flux of temperature variance is no more constant as the radiative dissipation occurs through all the range. The analysis made in section 4, see (28), leads to the following estimation of the molecular dissipation of temperature variance X_D, compared to its injected flux X_I :

$$\mathrm{Log}(\mathcal{F}_D/\mathcal{F}_I) \simeq 2\,\varepsilon^{-4/3}C_{cc}\int_{k_2}^{k_D} dk'\, k'^{-5/3}N(k') \qquad (44)$$

For P_R lower than P_R^c, i.e. larger radiative diffusivity, the spectrum is largely affected by the appearance of an "inertial-radiative" subrange. Non local interactions predominate and determine the

behaviour of the temperature spectrum. The slope of the spectrum being nearly a constant steeper than -3. In the case we have studied, water-vapour in lower atmosphere, this exponent remains very near to -3.

For different absorbers, or different conditions, the value of this exponent could be very different because it depends largely, see (38) - (40), on the behaviour of N(k), the radiative dissipative term.

And, for instance, if N(k) is steeper than the one we used, non-local interactions will be more effective than in our study.

In any case, the variance of the temperature gradient is mainly concentrated on scales larger than k_o^{-1} or smaller than k_t^{-1} (if, of course, an inertial-inertial subrange still developps for $k > k_t$, i.e. if $k_t < k_D$).

On the other hand, the behaviour of the larger scales does not seem too much affected by radiative transfer in the case of grey atmosphere. Thus the ratio of dissipation times :

$$R = \chi \, \nu^2 / \varepsilon \quad < \theta^2 > \qquad (45)$$

remains nearly a constant ($R \simeq 2.2$) in stationnary case. This is not the same for non grey atmosphere, where R may reach 3.5. This difference seems to rely on the fact that in non grey atmoshere the opaque limit (small k) is very slowly reached. Thus the balance, which occurs between the "beating-term" and the eddy-diffusivity in the large scales (see (5)) seems largely affected.

It must be stressed that a cumulative effect of radiative dissipation and molecular one, as modeled by André et al. (7) remains doubtfull due to our remarks on the way the radiative diffusivity is renormalized (37). That is to say, for large radiative effects, the characteristic times of eddy-diffusivity and of radiative diffusivity do not interven in an additive way. This point of view is supported by the corresponding study made by Kraichnan (16) in the case of low thermal Prandtl number.

ACKNOWLEDGEMENTS

The authors would like to thank Pr. M. Coantic for stimulating discussions and Drs J.C. André and U. Frisch for helpfull advices.

REFERENCES

1. Leslie, D.C., Developments in the Theory of Turbulence, 1 st ed., Clarendon Press, Oxford, 1973.

2. Newman, G.R. and Herring, J.R., "A Test Field Model Study of a Passive Scalar in Isotropic Turbulence", Journal of Fluid Mechanics, vol. 94, 1979, pp 163-194.

3. Larcheveque, M., Chollet, J.P., Herring, J.R., Lesieur, M., Newman G.R. and Schertzer, D., "Two-point Closure Applied to a Passive Scalar in Decaying Isotropic Turbulence", Turbulent Shear Flows 2, Springer-verlag, 1980, pp 50-66.

4. Larcheveque, M. and Lesieur, M., "The application of E.D.Q.N.M. to the problem of dispersion of particles in three and two dimensionnal turbulence", Journal de Mécanique, 1980.

5. Herring, J.R., Schertzer, D., Chollet, J.P., Larcheveque, M., Lesieur, M. and Newman, G.R., "A Comparative assessment of Spectral Closures as applied to passive scalar diffusion", NCAR (0901/79-12, Boulder, 1981.

6. Coantic, M.F., "Interaction between Turbulence and Radiation", An Introduction to Turbulence in Geophysics, and Air-Sea Interactions, AGARD ograph No.232, 1978, pp. 175-236.

7. André, J.C., De Moor, G., Lacarrere, P., Therry, G. and Du Vachat R., "Modeling the 24-hour Evolution of the Mean and Turbulent Structures of the Planetary Boundary Layer", Journal of Atmospheric Sciences, vol. 35, No. 10, 1978, pp. 1861-1883.

8. Spiegel, E.A., "The smoothing of temperature fluctuations by radiative transfer", Astrophysical Journal, Vol. 165, 1957, pp. 202-207.

9. Schved, G.M., "Influence of Radiative Transfer on certain Types of Motion in Planetary Atmospheres", Advances in Heat Transfer, Vol.14, 1978, pp. 249-280.

10. Lesieur, M., Schertzer, D., "Amortissement autosimilaire d'une turbulence à grand nombre de Reynolds", Journal de Mécanique, Vol. 17, No.4,1978, pp. 609-646.

11. Coantic, M.F., Simonin, D., and Schertzer, D., "Effet du rayonnement infra-rouge sur la turbulence de température : structure spectrale et taux de dissipation", I.M.S.T., Marseille.

12. Chandrasekhar S., "The equation of Transfer", Radiative Transfer, Dover, New-York, 1953, pp. 1-38.

13. Goody, R.M., "Theoritical basis", Atmospheric Radiation, Part I, Clarendon Press, Oxford, 1964.

14. Simonin, O., "Les interactions turbulence-rayonnement dans les basses couches de l'atmosphère claire", rapport D.E.A., Ecole Nationale Supérieure de Techniques Avancées, Paris, 1978.

15. Hill, R.J., "Models of the scalar spectrum for turbulent advection", Journal of fluid Mechanics, Vol. 88, 1978, pp. 541-562.

16. Kraichnan, R.H., "Shear and Thermally-driven Turbulence", The Physics of Fluids, Vol. 7, No. 7, 1964, pp. 1 048-1 062.

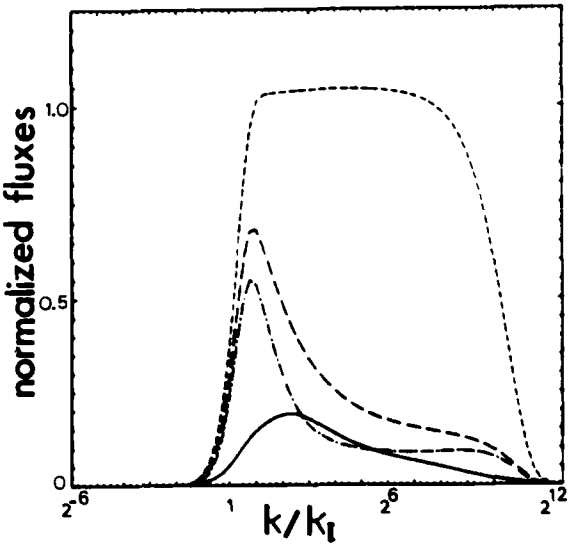

Fig.4 : normalized fluxes (case Fig. 6,8)
.... : global energy flux ; – – : global temperature variance flux ; –.– : local temperature variance flux ; —— : non local one.

TURBULENCE MEASUREMENTS IN AN AXISYMMETRIC BUOYANT JET

Fumimaru Ogino, Hiromi Takeuchi, Masaru Ohki and Tokuro Mizushina

Dept. of Chem. Eng., Kyoto University, Kyoto, Japan

ABSTRACT

Measurements were made of the turbulent fluctuations of vertical velocity and temperature in vertical round buoyant jets. The jets were heated water jets with exit densimetric Froude numbers ranging from 1.3 to 3240. Measurements were carried out with two film probes. One probe was maintained at a constant temperature and the other was operated as a resistance thermometer.

The axial variations of the intensities of velocity and temperature fluctuations and of the streamwise turbulent heat flux in the established flow region of the buoyant jet are presented. It was found that they were well correlated with a scaling law proposed by Chen and Rodi. The radial distributions of the three turbulent properties are also presented. The results show satisfactory similarity profiles in both non-buoyant and plume regions but there is a certain difference in the shapes between the two regions.

NOMENCLATURE

d_0 = discharge nozzle diameter, m

Fr = $U_0^2/[g(T_0-T_\infty)d_0 g]$ = discharge Froude number
g = gravitational acceleration, m/s^2
r = radial coordinate, m
Re = $d_0 U_0 \rho_0/\mu_0$ = Reynolds number

T = time-averaged temperature, K
$T_m^\#$ = $\sqrt{Fr}(T_m-T_\infty)/(T_0-T_\infty)$

U = time-averaged velocity in x-direction, m/s
$U_m^\#$ = $\sqrt{Fr}U_m/U_0$
u = fluctuating velocity in x-direction, m/s

$u_m^\#$ = $\sqrt{Fr}\sqrt{\overline{u_m^2}}/U_0$

$\overline{u\theta}$ = streamwise turbulent heat flux, mK/s
$\overline{u_m\theta_m}^\#$ = $Fr\overline{u_m\theta_m}/[U_0(T_0-T_\infty)]$
X = vertical distance from virtual source, m
$X^\#$ = $X/d_0\sqrt{Fr}$
x = vertical coordinate, m
β = coefficient of volume expansion, 1/K
θ = temperature fluctuation, K

$\theta_m^\#$ = $\sqrt{Fr}\sqrt{\overline{\theta_m^2}}/(T_0-T_\infty)$
μ = viscosity, Pa·s
ρ = density, kg/m^3

Subscripts
m = value at jet centerline
0 = value at jet discharge
∞ = ambient value

Superscripts
$-$ = time-averaged value

INTRODUCTION

The vertical buoyant jet discharged into a uniform stagnant environment is one of the most important flow patterns related with the environmental heat transfer.

A number of methods have been proposed for calculating the practically important cases of turbulent buoyant jets, ranging from simple empirical formulae to complex models involving partial differential equations. The more advanced methods attempt to model details of the turbulent motion (1-3). However, they have not yet been tested widely for buoyant jets because of lack of sufficiently reliable and accurate experimental data.

Measurements have been made of the time-averaged velocity at the axis of the vertical round buoyant jet by Ogino et al. (4) and time-averaged temperature by a number of experimenters, the results showing that the measured values follow a scaling law proposed by Chen and Rodi (5).

Only few data on turbulence quantities are available and they are restricted mostly to the non-buoyant jets. For the plume, both velocity and temperature fluctuations have been measured by George et al. (6) and Nakagome and Hirata (7). Those experimental results have been reviewed in detail by Chen and Rodi (8).

The purpose of this paper is to present more comprehensive result of the measurements of vertical velocity fluctuations, temperature fluctuations and streamwise turbulent heat flux for the vertical round buoyant jet in a uniform temperature ambient.

EXPERIMENTAL APPARATUS AND PROCEDURE

The experimental apparatus is shown schematically in Fig. 1. The test tank was constructed of transparent acrylic plates with internal dimensions of 2 m long, 1 m wide and 1 m deep. Wall thickness was 2.0 cm.

Filtered city water was used as ambient fluid and its temperature was kept uniform during the measurements. For jet flows, three contraction nozzles of different diameters, 0.5, 1.0 and 2.0 cm, were used, so that a wide range of Froude number was covered. The jet fluid was also city water which was heated in a heater and of which temperature was regulated at 310 - 330 K in a head tank. Flow rate was measured by a calibrated orifice meter.

The velocity and temperature were measured with two I-type film probes (TSI 1210-20W) at neighboring

locations in the flow. The spacing of these two probes was 1 mm. The velocity signal was obtained by

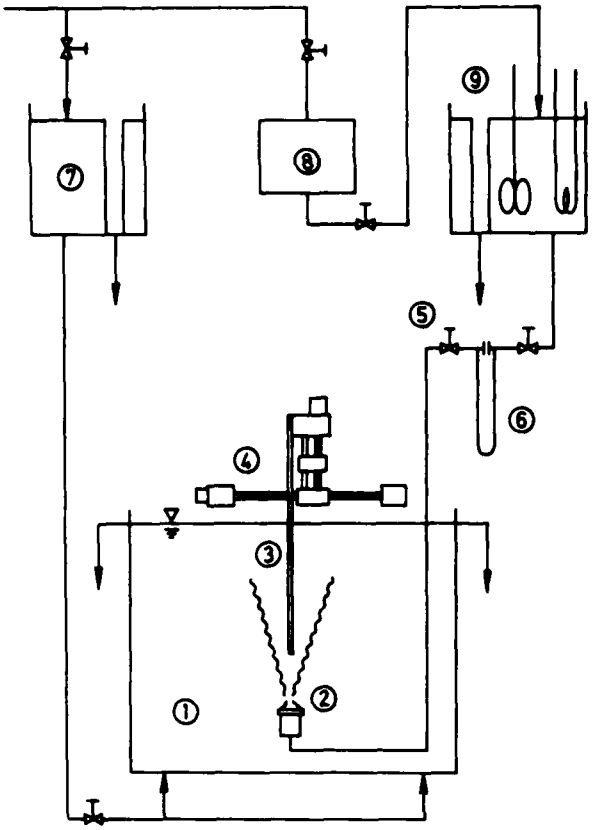

Fig. 1 Schematic drawing of the experimental apparatus
1 Test tank, 2 Contraction nozzle, 3 Probe support, 4 Traverser, 5 Needle valve, 6 Orifice meter, 7,9 Head tank, 8 Heater

a constant temperature anemometer (DISA 55M10), while the temperature signal was obtained by a constant current anemometer (DISA 55M20) operated as a resistance bridge. The outputs from both anemometers were stored in a data recorder (TEAC R-400) and converted to digital signals (FACOM U-200) with a frequency of 200 Hz.

The velocity-temperature calibration curve was then used for calculation of the actual velocity signal from the instantaneous constant temperature anemometer output. A block diagram of the measurement procedure is shown in Fig. 2.

The frequency response of the temperature probe was estimated to be roughly 400 Hz (9). For comparison, the estimated frequency of the energy containing eddies was roughly 40 Hz and that of Kolmogorov microscale was about 300 Hz. Since the velocity probe was operated at constant temperature, its frequency response was orders of magnitude better than the temperature probe.

An error estimate by measured values of skewness and turbulence intensity indicates that the measured values of RMS of vertical velocity fluctuations may be underestimated by about 3% at the jet axis and by about 10% at r/X=0.1 (9).

Reynolds numbers at the nozzle exit ranged from

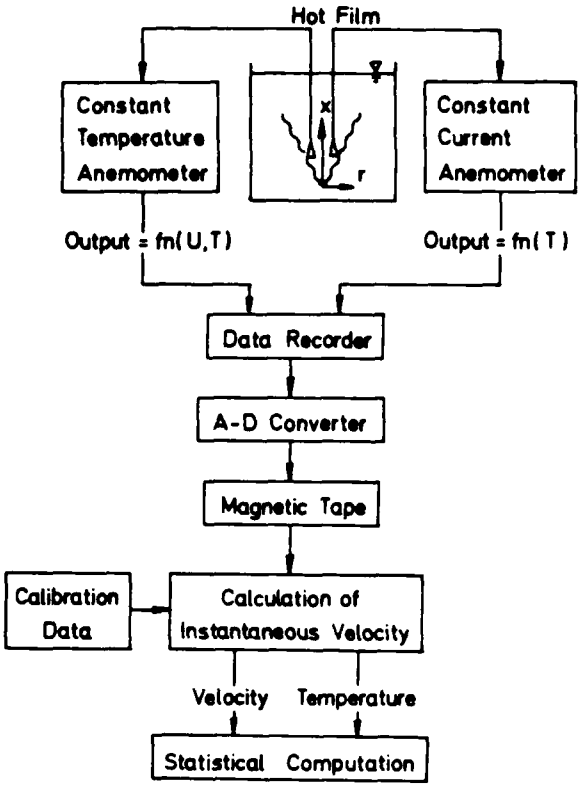

Fig. 2 Block diagram of data acquisition system and data reduction procedure

2280 to 4390 and the discharge Froude numbers were 1.3 to 3240.

EXPERIMENTAL RESULTS AND DISCUSSION

Axial Variation of the Intensity of the Vertical Velocity Fluctuations

The measured values of the relative intensity of vertical velocity fluctuations at the centerline of the buoyant jet are plotted in Fig. 3 along with the experimental results of other investigators (7, 10-13).

As discussed by Chen et al. (3) the turbulent intensity first decays and then increases in the zone of flow establishment. The initial decay is due to the fact that the flow at the nozzle exit is uniformly flat and is being accelerated by a buoyant force. In this condition there will be no generation of turbulence. When the turbulent kinetic energy generated in the mixing layer reaches the centerline by diffusion, the turbulent intensity increases and after the flow is established it then decays again.

The experimental results of the authors, Oosthuizen (13), Nakagome et al. and the result of Corrsin et al. (10) obtained in the jet of large temperature difference at the nozzle exit confirm this expectation, whereas the experimental results obtained in the jet of small temperature/concentration difference by Corrsin et al. and McQuaid et al. (11) show

the continued increase of the relative intensity of

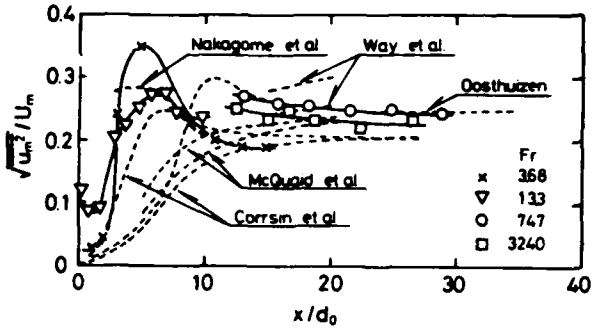

Fig. 3 Axial variation of relative intensity of velocity fluctuations

vertical velocity fluctuations because they have been obtained in the jet with negligible bucyancy.

However, all of the results show that the relative intensity approaches to a constnat value beyond x/d_0 of 20 to 30. The asymptotic value of 0.23 is presented by Oosthuizen and 0.28 by Chen and Rodi (8).

The axial variation of the RMS values of the velocity fluctuations at the centerline of the established jet flow region, normalized with the scaling law proposed by Chen and Rodi (5), is shown in Fig. 4. The abscissa is the normalized distance from the virtual source which have been determined from a plot of $(T_0-T_\infty)/(T_m-T_\infty)$ vs. x/d_0 at the region of $4<x/d_0<20$ as the intercept of the resulting straight line and the x/d_0 coordinate.

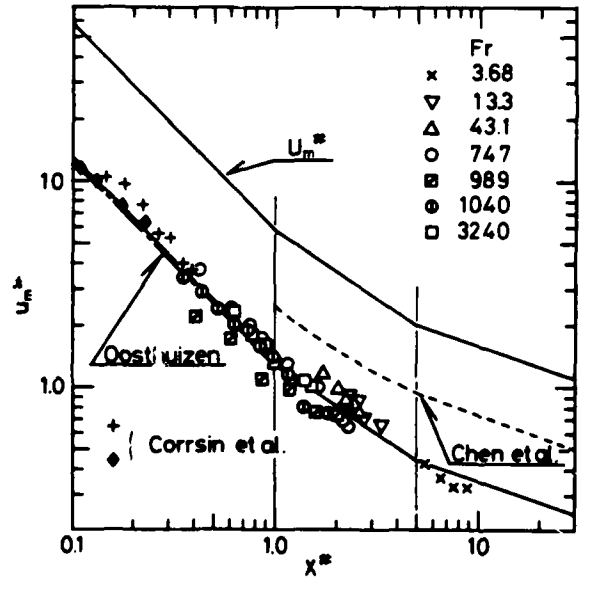

Fig. 4 Axial variation of normalized intensity of velocity fluctuations

The experimental results of Oosthuizen and Corrsin et al. show a fair agreement with the present data. For comparison between the decay of the intensity of the axial velocity fluctuations and that of the time-averaged centerline velocity, the measured result of U_m is also depicted in Fig. 4. Three regions shown in Fig. 4 are respectively non-buoyant, intermediate and plume regions and the demarcations of three regions have been determined by the time-averaged velocity and temperature measurements by Ogino et al. (4).

It is seen from Fig. 4 that the experimental data fall on a single curve and the ratio $\sqrt{u_m^2}/U_m$ is constant, the value being 0.22, over the whole range from non-buoyant to plume regions. The empirical equations of the intensity of the axial velocity fluctuations are given by

$$X^\# \leq 1 \qquad u_m^\# = 1.3\,(X^\#)^{-1} \qquad (1)$$

$$1 \leq X^\# \leq 5 \qquad u_m^\# = 1.3\,(X^\#)^{-2/3} \qquad (2)$$

$$5 \leq X^\# \qquad u_m^\# = 0.76\,(X^\#)^{-1/3} \qquad (3)$$

It should be noted that eq. (3) is not conclusive because of insufficient data in the plume region. However, an analysis by Chen et al. (3) predicts that the turbulent kinetic energy is proportional to $(X^\#)^{-2/3}$, suggesting the intensity of the axial velocity fluctuations to be proportional to $(X^\#)^{-1/3}$. The dashed line depicted in Fig. 4 show the variation of $u_m^\#$ calculated from the result of Chen et al., which predicts higher values than the present experimental data in the intermediate and plume regions.

Axial Variation of the Intensity of Temperature Fluctuations

The experimental result on the axial variation of the relative intensity of temperature fluctuations is presented in Fig. 5. For comparison, the results of some other investigators (6, 7, 10-12, 14-16) are shown in Fig. 5 including the measurements of concentration fluctuations.

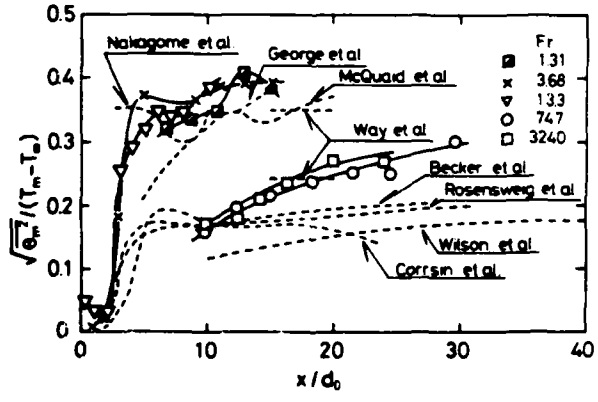

Fig. 5 Axial variation of relative intensity of temperature fluctuations

Although the results show much larger scatter than the results on that of velocity fluctuations, the relative intensities of temperature fluctuations for smaller Froude numbers seem to attain higher asymptotic values while those for larger Froude numbers, the jet with negligible bucyancy, the lower values. Chen and Rodi (8) have recommended as asymptotic value of $\sqrt{\theta_m^2}/(T_m-T_\infty)$ 0.21 to 0.24 for the non-buoyant jet, but the relatively high values of 0.35 to 0.4 have

been reported by George et al. and Nakagome et al. for the plume. This fact suggests that the relative intensity of the temperature fluctuations at the centerline of the buoyant jet may vary from about 0.2 in the non-buoyant region to about 0.3 - 0.4 in the plume region.

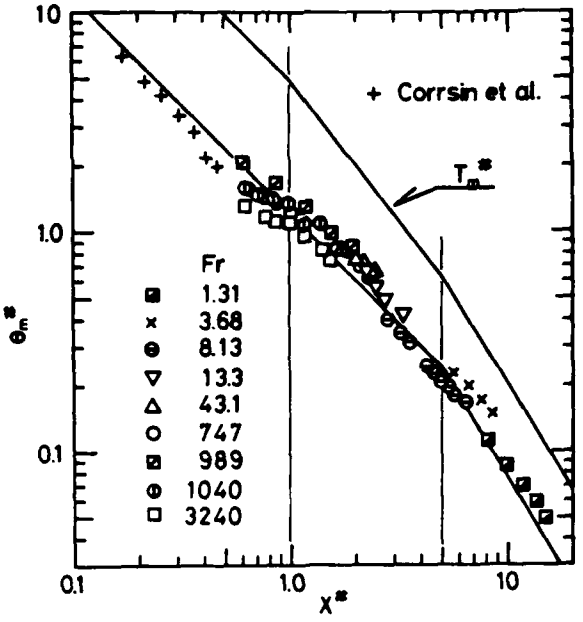

Fig. 6 Axial variation of normalized intensity of temperature fluctuations

In Fig. 6 the normalized intensities of temperature fluctuations in the established region of the buoyant jet are plotted against the normalized distance from the virtual source. The present experimental data and those of Corrsin et al. fall again closely on a single curve and empirical equations are given by

$$X^{\#} \leq 5 \qquad \theta_m^{\#} = 1.2\,(X^{\#})^{-1} \qquad (4)$$

$$5 \leq X^{\#} \qquad \theta_m^{\#} = 3.5\,(X^{\#})^{-5/3} \qquad (5)$$

The distinction of the non-buoyant and intermediate regions cannot be noted in the decay of the intensity of temperature fluctuations within the accuracy of measurements.

The time-averaged temperature at the centerline is also depicted in Fig. 6, from which it is seen that the relative intensity of the temperature fluctuations varies from 0.25 in the non-buoyant region to 0.37 in the plume region.

Axial Variation of the Streamwise Turbulent Heat Flux

Figure 7 shows the axial variation of the streamwise turbulent heat flux at the jet axis. The experimental data are correlated into a single line in the plot of Fig. 7 and no distinction is observed between three regions. The empirical equation is expressed as

$$\overline{u_m\theta_m}^{\#} = (X^{\#})^{-5/3} \qquad (6)$$

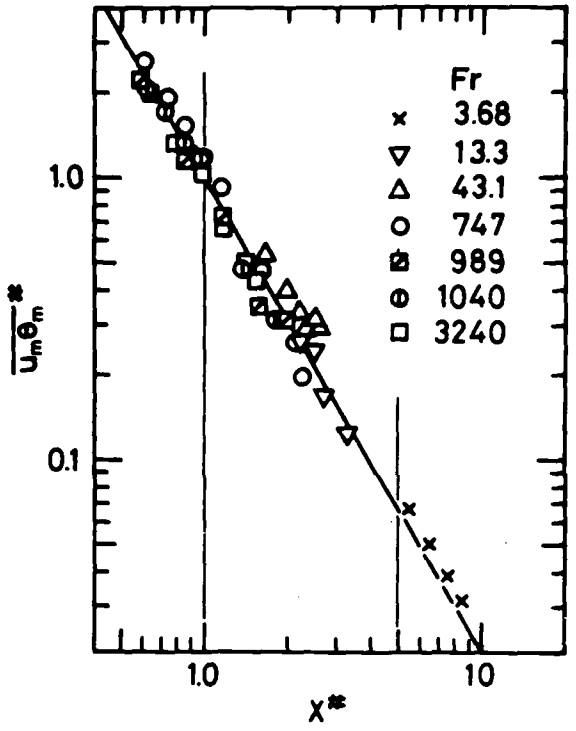

Fig. 7 Axial variation of normalized streamwise turbulent heat flux

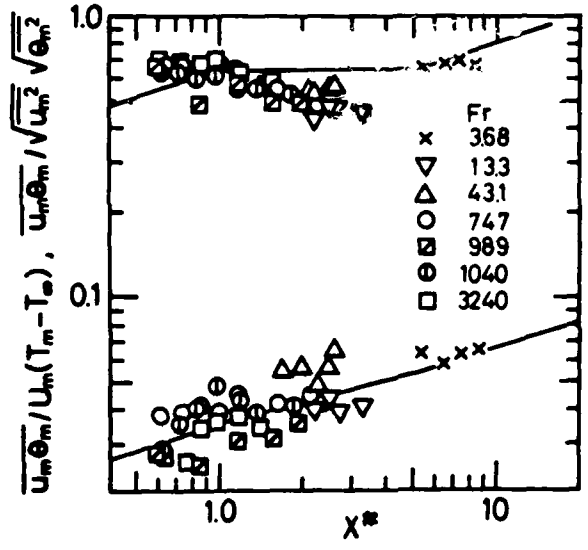

Fig. 8 Axial variations of $\overline{u_m\theta_m}/\sqrt{u_m^2}\sqrt{\theta_m^2}$ and $\overline{u_m\theta_m}/U_m(T_m-T_\infty)$

George et al. reported the value of the correla-

tion coefficient of the streamwise heat flux being 0.65 at the jet axis and this value is in good agreement with the present experimental data in the non-buoyant and plume regions as shown in Fig. 8.

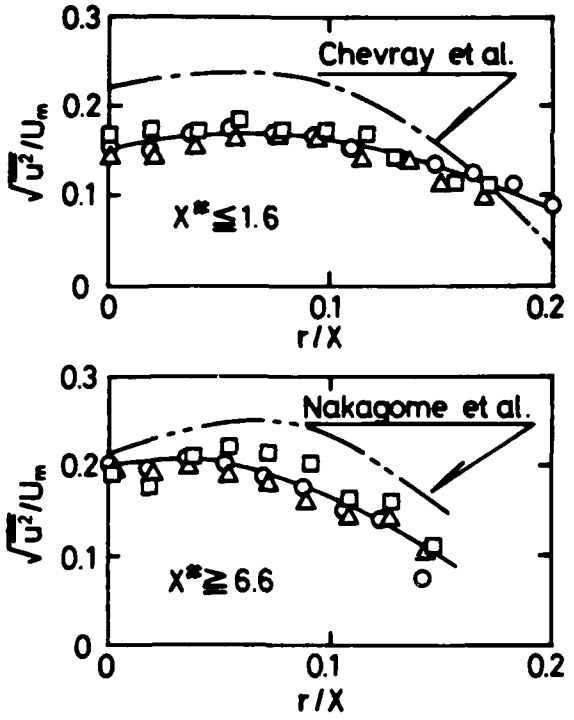

Fig. 9 Radial distributions of relative intensity of vertical velocity fluctuations

The lower values in the intermediate region is mainly due to the higher measured values of $\sqrt{\theta_m^2}$ as shown in Fig. 6. The solid lines are obtained from eqs. (1) - (6). The calculated line in the plume region is not conclusive because the empirical equations for the plume region are based on the insufficient data.

The experimental data of the ratio $\overline{u_m\theta_m}/U_m(T_m-T_\infty)$ are also plotted in Fig. 8 along with the calculated lines. The ratio varies approximately in proportion to $X^{1/3}$ over the whole range of the buoyant jet.

Radial Distributions of the Intensities of the Vertical Velocity and Temperature Fluctuations and the Streamwise Heat Flux

The radial distributions of the intensities of vertical velocity and temperature fluctuations and of the streamwise turbulent heat flux are shown in Figs. 9, 10 and 11, respectively. These turbulence properties are non-dimensionalized with U_m and T_m-T_∞ and plotted against the non-dimensional lateral distance r/X.

The results show satisfactory similarity profiles of $\sqrt{u^2}$, $\sqrt{\theta^2}$ and $\overline{u\theta}$ in both non-buoyant and plume regions, but the shapes of the profiles are different between the two regions. The profiles in the plume region are narrower than those in the non-buoyant region for all three turbulent properties. There exists off-axis peak in the profiles of the intensity of the temperature fluctuations and the streamwise turbulent heat flux in the non-buoyant region as usually observed in the jet with negligible

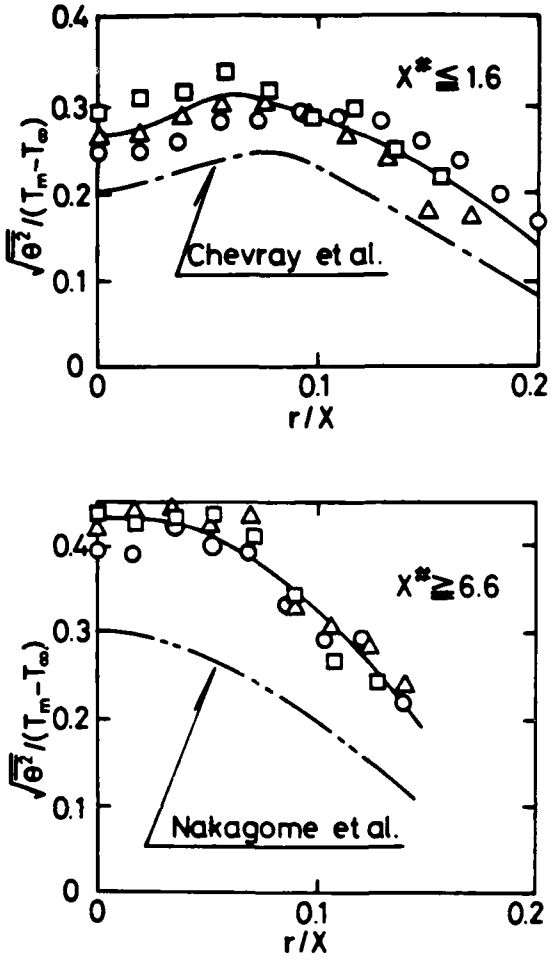

Fig. 10 Radial distributions of relative intensity of temperature fluctuations

buoyancy (10, 14, 15, 17, 18), whereas nearly constant values are observed over the center portion of the jet in the plume region.

For comparison the experimental results obtained by other investigators are also shown in Figs. 9, 10 and 11 from which it is seen that the shapes of the profiles for three turbulent properties vary little between different experimenters, except for the level of the dimensionless properties as was discussed already by considering the values at the axis.

CONCLUSIONS

(1) The intensities of the vertical velocity and temperature fluctuations and the streamwise turbulent heat flux at the axis of the vertical round buoyant jet are correlated well with the same scaling law as that used for correlating the time-averaged centerline velocity and temperature.

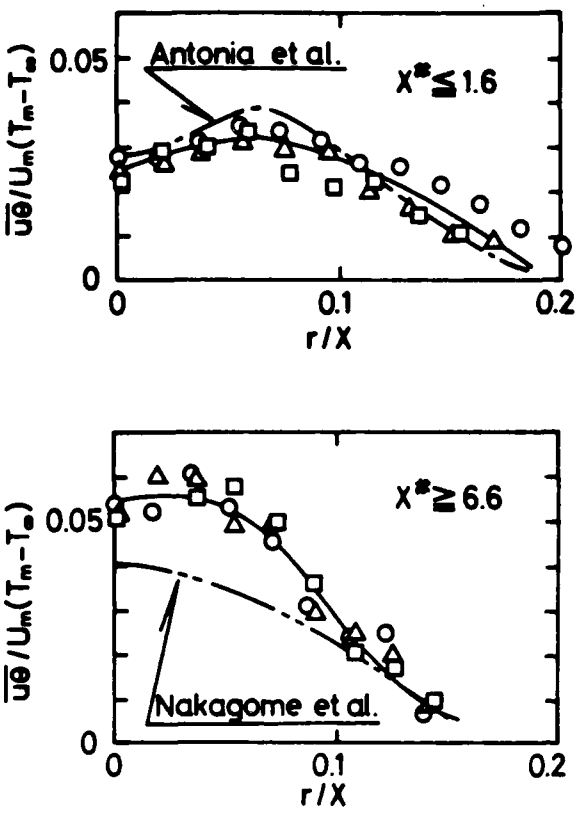

Fig. 11 Radial distributions of streamwise turbulent heat flux

(2) The relative intensity of the axial velocity fluctuations at the centerline is constant at 0.22 in the whole range from non-buoyant to plume regions, whereas that of the temperature fluctuations increases from 0.25 in the non-buoyant region to 0.37 in the plume region. The ratio $\overline{u_m\theta_m}/U_m(T_m-T_\infty)$ veries approximately in proportion to $X^{1/3}$ over the whole range of the buoyant jet.

(3) The radial distributions of the intensities of the vertical velocity and temperature fluctuations and the streamwise heat flux show similarity profiles in both non-buoyant and plume regions, but there is a certain difference in shapes of the profiles between the two regions.

ACKNOWLEDGMENT

This work was supported by the Ministry of Education, Science and Culture through a Grant in Aid for Scientific Research (No. 505557).

REFERENCES

1 Tamanini, F., "The Effect of Buoyancy on the Turbulence Structure of Vertical Round Jets," Transactions of the ASME, Journal of Heat Transfer, Vol. 100, Nov. 1978, pp. 659-664.

2 Chen, C. J. and Nikitopoulos, C. P., "On the Near Field Characteristics of Axisymmetric Turbulent Buoyant Jets in a Uniform Environment," International Journal of Heat and Mass Transfer, Vol. 22, 1979, pp. 245-255.

3 Chen, C. J. and Chen, C. H., "On Prediction and Unified Correlation for Decay of Vertical Buoyant Jets," Transactions of ASME, Journal of Heat Transfer, Vol. 101, Aug. 1979, pp. 532-537.

4 Ogino, F., Takeuchi, H., Kudo, I. and Mizushina, T., "Heated Jet Discharged Vertically into Ambient of Uniform and Linear Temperature Profile," International Journal of Heat and Mass Transfer, Vol. 23, 1980, pp. 1581-1588.

5 Chen, C. J. and Rodi, W., "On Decay of Vertical Buoyant Jet in Uniform Environment," Proceedings of 6th International Heat Transfer Conference, Vol. 1, 1978, pp. 97-102.

6 George, W. K., Alpert, R. L. and Tamanini, F., "Turbulence Measurements in an Axisymmetric Buoyant Plume," International Journal of Heat and Mass Transfer, Vol. 20, 1977, pp. 1145-1154.

7 Nakagome, H. and Hirata, M., "The Structure of Turbulent Diffusion in an Axi-symmetrical Thermal Plume," Proceeding of 1976 ICHMT Seminar on Turbulent Buoyant Convection, Hemisphere Publishing Corporation, 1977, pp. 361-372.

8 Chen, C. J. and Rodi, W., "Vertical Turbulent Buoyant Jets-A Review of Experimental Data," HMT The Science and Applications of Heat and Mass Transfer, Vol. 4, Pergamon Press, Oxford, 1980.

9 Hinze, J. O., "Turbulence," 2nd ed., McGraw-Hill Book Company, New York, 1975.

10 Corrsin, S. and Uberoi, M. S., "Further Experiments on the Flow and Heat Transfer in a Heated Turbulent Air Jet," NACA Technical Notes, No. 1865, 1949.

11 McQuaid, J. and Wright, W., "Turbulence Measurements with Hot-wire Anemometry in Non-homogeneous Jets," International Journal of Heat and Mass Transfer, Vol. 17, 1974, pp. 341-349.

12 Way, J. and Libby, P. A., "Application of Hot-wire Anemometry and Digital Techniques to Measurements in a Turbulent Helium Jet," AIAA Journal, Vol. 9, 1971, pp. 1567-1573.

13 Oosthuizen, P. H., "Vertical Buoyant Air Jets," Proceeding of 1976 ICHMT Seminar on Turbulent Buoyant Convection, Hemisphere Publishing Corporation, 1977, pp. 303-313.

14 Becker, H. A., Hottel, C. and Williams, G. C., "The Nozzle-fluid Concentration Field of the Round, Turbulent, Free Jet," Journal of Fluid Mechanics, Vol. 30, part 2, 1967, pp. 285-303.

15 Rosensweig, R. E., Hottel, H. C. and Williams, G. C., "Smoke-scattered Light Measurement of Turbulent Concentration Fluctuations," Chemical Engineering Science, Vol. 15, 1961, pp. 111-129.

16 Wilson, R. A. M. and Dankwerts, P. V., "Studies in Turbulent Mixing - II. A Hot Air Jet," Chemical Engineering Science, Vol. 19, 1964, pp. 885-895.

17 Chevray, R. and Tutu, N. K., "Intermittency and Preferential Transport of Heat in a Round Jet," Journal of Fluid Mechanics, Vol. 88, part 1, 1978, pp. 133-160.

18 Antonia, R. A., Prabhu, A. and Stephenson, S. E., "Conditionally Sampled Measurements in a Heated Turbulent Jet," Journal of Fluid Mechanics, Vol. 72, part 3, 1975, pp. 455-480.

SESSISON 10 - HEAT AND MASS TRANSFER IN BOUNDARY LAYERS

K. Hanjalić - Chairman

ON THE SIMILARITY BETWEEN VELOCITY AND TEMPERATURE FIELDS WITHIN A TURBULENT SPOT

R. A. ANTONIA, A. J. CHAMBERS

Department of Mechanical Engineering
University of Newcastle, N.S.W., 2308, Australia

M. SOKOLOV

Department of Fluid Mechanics & Heat Transfer
University of Tel Aviv, Tel Aviv, 69978, Israel

C. W. VAN ATTA

Department of Applied Mechanics & Engineering Sciences
University of California at San Diego, La Jolla, 92093, U.S.A.

ABSTRACT

Velocity and temperature fields associated with a turbulent spot developing in a laminar boundary layer reveal a number of similar features. With ensemble averaging performed with respect to a particular feature of the spot, the similarity between ensemble averaged longitudinal velocity and temperature is examined by considering the respective equations for these ensemble averaged quantities. The pressure gradient associated with the spot disturbance may be significant while the measured diffusivities of momentum and heat for the disturbance indicate values for their ratio which are significantly larger than unity.

NOMENCLATURE

c_p Pressure coefficient
f A non-dimensional function, $f' = \langle U\rangle/U_\infty - 1$
g $= U_\ell/U_\infty$
h Spot height, maximum height of 1% contour $\tilde{T}/\Delta T$ m
P Kinematic pressure m^2/s^2
Pr Molecular Prandtl number
R^* Reynolds number based on U_∞ and momentum thickness derived from $\langle U\rangle$ profiles
T Temperature °K
ΔT $\equiv T_w - T_\infty$ °K
t Time s
U Instantaneous longitudinal velocity m/s
u $= U - \langle U\rangle$ m/s
V Instantaneous normal velocity m/s
v $= V - \langle V\rangle$ m/s
W Instantaneous spanwise velocity m/s
x Longitudinal direction m
x_S Distance from spark m
y Normal direction m
z Spanwise direction m
α Molecular thermal diffusivity m^2/s
α_d Disturbance thermal diffusivity m^2/s
ζ $= (z-z_0)/U_\infty(t-t_0)$ $(t_0 = -0.02$ s, $z_0 = 0$ m) non-dimensional spanwise co-ordinate
η $= (y-y_0)/U_\infty(t-t_0)$ $(y_0 = 0$ m) non-dimensional vertical co-ordinate
θ $\equiv T - \langle T\rangle$
ν Kinematic viscosity m^2/s
ν_d Disturbance kinematic viscosity m^2/s
ξ $= (x_S-x_0)/U_\infty(t-t_0)$ $(x_0 = -0.1$ m) non-dimensional longitudinal co-ordinate
ϕ Velocity potential m^2/s

Subscripts

ℓ Laminar
o Evaluated at virtual origin
t Turbulent
w Evaluated at wall
∞ Evaluated in free stream

Averaging Symbols

$\langle\cdot\rangle$ Ensemble average
$\bar{\cdot}$ Conventional average
$\tilde{\cdot}$ Ensemble average relative to laminar value (e.g. $\tilde{U} = \langle U\rangle - U_\ell$ and $\tilde{T} = \langle T\rangle - T_\ell$).

INTRODUCTION

In recent investigations [Van Atta & Helland (1); Antonia *et al (2)*] use was made of a passive temperature-tagging technique to provide some insight into the structure and mixing processes within a turbulent spot. The spot was artificially generated in a laminar boundary layer which developed over a heated flat plate. Temperature measurements obtained in these investigations complemented previous velocity measurements of Wygnanski *et al (3)* and Cantwell *et al (4)*. Contours of the ensemble-averaged temperature disturbance measured relative to the laminar undisturbed (Pohlhausen) profile $T_\ell(y)$ were found to be strongly anti-correlated with corresponding contours of the longitudinal velocity disturbance, measured relative to the Blasius profile $U_\ell(y)$. Using the conical similarity co-ordinates introduced by Cantwell *et al (4)*, Van Atta & Helland *(1)* observed a striking coincidence of the maxima and minima in the temperature disturbance contours meas-

ured on the centreline of the spot with the two stable foci or points of accumulation in the particle paths calculated by Cantwell *et al (4)*. The positions of the temperature maxima could not however be satisfactorily explained in terms of the centreline particle paths. In the present paper, ensemble averaged velocity and temperature fields are compared in a manner similar to that used in considering the analogy between momentum and heat transfer in a fully turbulent boundary layer over a heated flat plate. Equations for ensemble averaged temperatures and longitudinal velocities are first examined and measured values of disturbance diffusivities for momentum and heat are subsequently presented and discussed.

EXPERIMENTAL ARRANGEMENT AND CONDITIONS

A detailed description of the experimental arrangement is given in Van Atta & Helland *(1)* and Antonia *et al (2)*. It is sufficient to indicate here that the spot was generated by discharging a spark between the tips of two sewing needles, separated by about 2 mm in the z direction and protruding about 1 mm in the y direction, mounted in an insulated plug 0.29 m from the leading edge of an aluminium plate. This 1.27 cm thick plate, heated by 0.1 mm thick heating pads bonded to its bottom surface was mounted horizontally in the working section of the low turbulence wind tunnel in the Department of Applied Mechanics & Engineering Sciences at U.C.S.D. The turbulent spot developed along the plate under a small favourable pressure gradient. All measurements were made at a nominal free-stream velocity U_∞ of 11 ms^{-1} and a nominal value of 10 C for the difference ΔT. U and V were measured at distances x_s from the spark of 0.54, 0.84 and 1.12 m with a miniature DISA X-wire while T was measured with a 0.6 μm dia Wollaston wire. A series of U-T measurements was also made at x_s = 1.06 m using a single horizontal hot wire with a cold wire mounted parallel to and 1 mm below the hot wire. Mean velocity and mean temperature profiles were in good agreement with the Blasius and Pohlhausen profiles. Hot and cold wire signals and the square-wave spark generator signal were recorded on a four-track FM tape recorder. These signals were later played back and digitized using a 12 bit analogue to digital converter, at a sampling frequency of 3200 Hz into a digital computer. The frequency of the square-wave used to trigger the spark discharge was 1.5 Hz. Approximately 500 spots were recorded for each value of y but, in the final analysis of the data, only 200 spots were used.

Conical similarity co-ordinates ξ, η, ζ were introduced [Cantwell *et al (4)*] in an attempt to describe the unsteady velocity field associated with the spot in terms of ξ, η, and ζ only. Although conical co-ordinates are used to present data in a later section, it should be noted that the modified similarity co-ordinates proposed by Sokolov *et al (5)* leads to a better representation of the velocity and temperature fields than the conical similarity transformation. For the present experiments, the virtual origins (x_0, y_0, z_0, t_0) were found [Antonia *et al (2)*] to be approximately given by (-0.10 m, 0, 0, -0.02 s).

EQUATIONS FOR ENSEMBLE AVERAGED VELOCITY & TEMPERATURE

In the presence of the quasi-periodic disturbance due to the spot, U, V and temperature T are written

$$U = \langle U \rangle + u$$

$$V = \langle V \rangle + v$$

$$T = \langle T \rangle + \theta$$

where u, v, θ can be identified with the background (random) turbulent fluctuations. Experimental estimates of <U>, <V> and <T> were obtained by first determining the leading edge of the spot and then applying the ensemble averaging operation after aligning individual realizations of U, V and T with respect to the leading edge. Using the above decomposition, the momentum and temperature equations for the disturbance (organized) field can be written, at least on the plane of symmetry (where <W> is assumed to be zero) of the spot

$$\frac{\partial \langle U \rangle}{\partial t} + \langle U \rangle \frac{\partial \langle U \rangle}{\partial x} + \langle V \rangle \frac{\partial \langle U \rangle}{\partial y} = -\frac{\partial \langle P \rangle}{\partial x} + \frac{\partial}{\partial y}\left(\nu \frac{\partial \langle U \rangle}{\partial y} - \langle uv \rangle \right) \quad ..(1)$$

$$\frac{\partial \langle T \rangle}{\partial t} + \langle U \rangle \frac{\partial \langle T \rangle}{\partial x} + \langle V \rangle \frac{\partial \langle T \rangle}{\partial y} = \frac{\partial}{\partial y}\left(\alpha \frac{\partial \langle T \rangle}{\partial y} - \langle v\theta \rangle \right) \quad ..(2)$$

Note that, although the laminar boundary layer develops with zero streamwise pressure gradient, the (kinematic) pressure gradient appears in (1) as a result of the organized pressure field produced by the spot. The quantities <uv> and <vθ> may be interpreted as the shear stress and heat flux that arise from the background fluctuations which rise on the disturbance. If disturbance diffusivities for momentum and heat, denoted by ν_d and α_d respectively, are introduced such that

$$-\langle uv \rangle = \nu_d \frac{\partial \langle U \rangle}{\partial y} \quad ..(3)$$

$$\langle v\theta \rangle = -\alpha_d \frac{\partial \langle T \rangle}{\partial y} \quad ..(4)$$

the ratio ν_d/α_d may be identified with a Prandtl number for the disturbance in analogy to the commonly used turbulent Prandtl number $Pr_t = (\overline{uv}/\overline{v\theta})(\partial\overline{T}/\partial y)/(\partial\overline{U}/\partial y)$. An exact analogy between $\overline{U}$ and $\overline{T}$ in a zero pressure gradient turbulent boundary layer, with identical origins for the momentum and thermal fields, would require that both Pr and Pr_t are equal to unity. Similarly (1) and (2), with assumptions (3) and (4), suggest that an exact analogy between <U> and <T> requires that $\partial\langle P \rangle/\partial x$ is zero, $\nu = \alpha$ or Pr = 1, $\nu_d = \alpha_d$ and that the momentum and thermal fields associated with the disturbance have identical origins. This last requirement is approximately satisfied in the present case since the laminar momentum and thermal layers have the same physical origin.

EXPERIMENTAL RESULTS AND DISCUSSION

The general similarity between velocity and temperature disturbances, relative to the laminar profiles, is in evidence in Fig. 1 which shows contours of $\tilde{U}/U_\infty$ and $\tilde{T}/\Delta T$ obtained at x_s = 1.06 m. The height of the spot is taken, somewhat arbitrarily, as the maximum height (= 2.25 cm) of the 1% contour of $\tilde{T}/\Delta T$. Time t^* = 0 corresponds to the arrival of the spot's leading edge at the wall while Δt^* is the time taken for the spot to travel past the measurement station at the wall.

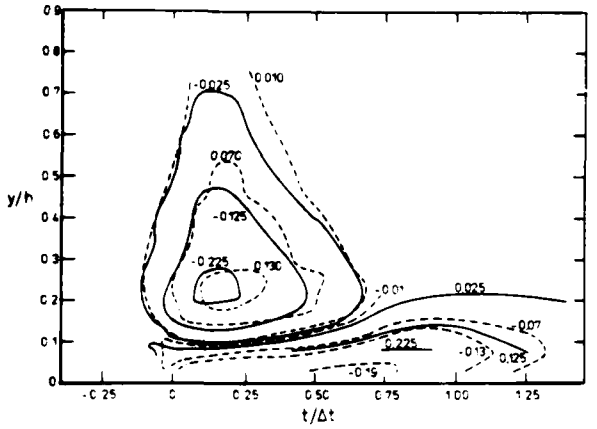

Fig. 1 Contours of $\tilde{U}$ and $\tilde{T}$ at x_s = 1.06 m. Solid and broken curves refer to $\tilde{U}$ and $\tilde{T}$ respectively. (t^* = 0 corresponds to an elapsed period of 130 ms after the spark is fired, Δt^* = 76 ms).

The approximate correspondence between the locations of the minimum value of $\tilde{U}/U_\infty$ and maximum value of $\tilde{T}/\Delta T$ is in agreement with the conclusion of Van Atta & Helland *(1)* who compared their $\tilde{T}$ contours with the $\tilde{U}$ contours of Gilberman *et al (6)*. A quantitative measure of the (negative) correlation between $\tilde{U}$ and $\tilde{T}$ can be obtained by making the rather crude supposition that a fluid particle is displaced, due to the spot disturbance, from one height to another with no change in its temperature or streamwise momentum. If the particle is displaced from height y_1 to height y_2, disturbances relative to the laminar values at y_2 may be written as

$$\frac{\tilde{T}}{\Delta T} = \frac{T_\ell(y_2) - T_\ell(y_1)}{\Delta T} = g(y_1) - g(y_2)$$

and

$$\frac{\tilde{U}}{U_\infty} = \frac{U_\ell(y_2) - U_\ell(y_1)}{U_\infty} = g(y_2) - g(y_1) = \frac{-\tilde{T}}{\Delta T}$$

when Pohlhausen's solution $(T_\ell - T_\infty)/\Delta T = 1 - U_\ell/U_\infty$ is assumed (for Pr = 1) and $U_\ell/U_\infty = f(y)$. Present measurements (Fig. 2) indicate that $\tilde{T}/\Delta T \approx -0.6\ \tilde{U}/U_\infty$.

The ratio $(T_w - \langle T\rangle)/\Delta T$ is plotted against $\langle U\rangle/U_\infty$ in Fig. 3 for different values of ξ at x_s = 1.06 m. Although these data were obtained at a particular value of x_s but different values of time from the spark, it should be noted that conical similarity was found [Antonia *et al (2)*] to provide an approximate description, in terms of ξ and η only, of $\tilde{U}$ and $\tilde{T}$ contours on the plane of symmetry of the spot. The Reynolds number R^* is relatively small (Fig. 3) at the leading and trailing edges of the spot and is largest at a value of t which corresponds roughly to the maximum height of the spot. The distribution at R^* = 1910 appears to show the largest positive deviation from the line of unity slope. The distribution at R^* = 1910 is compared in Fig. 4 with distributions obtained in a laminar boundary layer and a turbulent boundary layer. The laminar results were obtained using the present experimental arrangement while the measurements in the

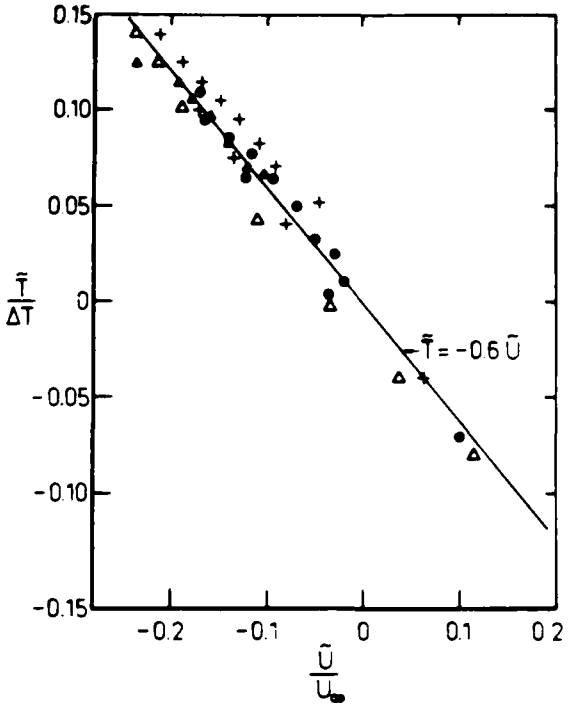

Fig. 2 Relation between $\tilde{T}$ and $\tilde{U}$ at x_s = 1.06 m.

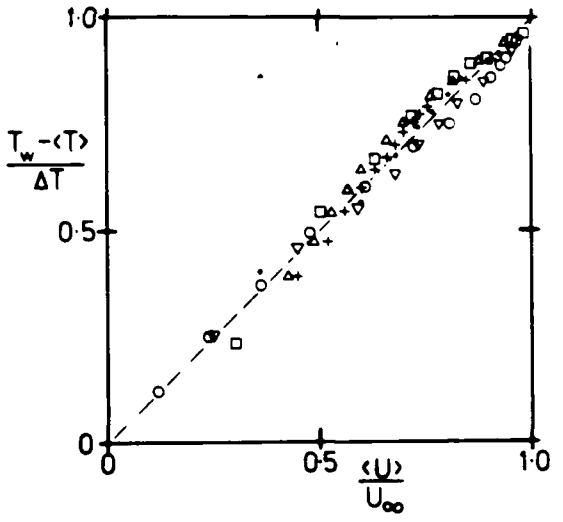

Fig. 3 Ensemble averaged temperature vs velocity at x_s = 1.06 m, ζ = 0. ▽, ξ = 0.53, R^* = 720; ·, 0.59, 1240; +, 0.65, 1660; △, 0.67, 1910; □, 0.71, 1230; ○, 0.76, 670. Broken line has a slope of unity.

slightly heated turbulent boundary layer[1] with zero

[1] The momentum and thermal layers has approximately the same origin.

pressure gradient were obtained at the University of Newcastle [Subramanian & Antonia *(7)*]. Distributions (Fig. 4) for both the laminar and turbulent boundary layers are in reasonable agreement with the line of unity slope. (Note that the unity slope in Figs. 2 or 3 is not related to the slope of -1 given by the equation $\tilde{U}/U_\infty = -\tilde{T}/\Delta T$). As the distributions in the turbulent boundary layer were found to be insensitive to the particular value of momentum thickness Reynolds number R_θ (values in the range 990-7100 were examined), the departure of the spot distribution in Fig. 4 from the other distributions is more likely to be due to an insufficient relaxation time required for the establishment of nearly self-preserving conditions rather than an insufficiently large Reynolds number.

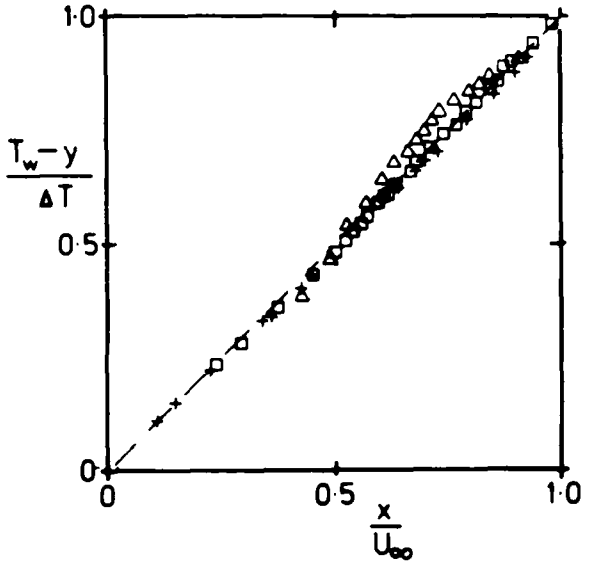

Fig. 4 Comparison of ensemble averaged temperature vs velocity in different flows.
+, laminar boundary layer ($y \equiv T_\ell$, $x \equiv U_\ell$), $R^* = 630$; □, turbulent boundary layer ($y \equiv \tilde{T}$, $x \equiv \tilde{U}$), $R^* = 3100$; Δ, turbulent spot ($y \equiv \langle T \rangle$, $x \equiv \langle U \rangle$), $\xi = 0.6^-$, $R^* = 1910$. Broken line has a slope of unity.

An estimate of the magnitude of $\partial\langle P\rangle/\partial x$, the pressure gradient associated with the spot, can be obtained in a manner analogous to that used by Cantwell *et al (4)*. The free stream flow is assumed to be described by the linearized unsteady Bernoulli equation

$$P_\infty - \langle P\rangle = \frac{\partial\phi}{\partial t} + U_\infty(\langle U\rangle - U_\infty) \qquad ..(5)$$

where P_∞ and U_∞ are the undisturbed free stream pressure and velocity while ϕ is the velocity potential ($\langle U\rangle = \partial\phi/\partial x$). With the assumption of conical similarity, Cantwell *et al (4)* show that

$$\frac{\phi}{U_\infty^2(t-t_0)} = \xi + f(\xi) \qquad ..(6)$$

and

$$c_p \equiv \frac{\langle P\rangle - P_\infty}{\frac{1}{2}U_\infty^2} = -2[f + (1-\xi)f'] \qquad ..(7)$$

where the prime represents differentiation with respect to ξ and $\langle U\rangle/U_\infty = 1 + f'(\xi)$. By integrating experimental values of $\langle U\rangle$ measured outside the spot, Cantwell *et al (4)* obtained an experimental variation of c_p with ξ, shown in Fig. 5. The potential flow disturbance produced by the spot was measured by Van Atta *et al (8)* at different distances above the spot. The measurements indicated that $\langle U\rangle$ was a function[2] of y

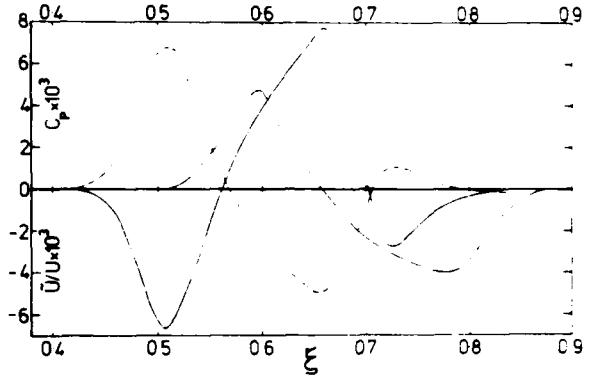

Fig. 5 Distributions of the pressure coefficient c_p and the ensemble averaged disturbance $\tilde{U}$ above the spot.
c_p: — —, present; — · —, Cantwell *et al (4)*; ——, $\tilde{U}/U_\infty$ at $x_s = 1.06$ m, $y = 3.18$ cm.

as well as ξ. It follows that the calculated distribution of c_p by Cantwell *et al (4)* is not universal, at least in the sense that it cannot be regarded as independent of y or η. The potential disturbance measured at $y = 3.18$ cm ($x_s = 1.06$ m) was used for the present calculation. At this value of y the positive and negative potential flow disturbances for the longitudinal velocity are largest. This disturbance corresponds to the distribution of $f'(\xi)$ in Fig. 5, to obtain an appropriate estimate of $\partial\langle P\rangle/\partial x$ for the purpose of comparing terms in (1). After numerically integrating f', c_p was calculated using (7). The resulting c_p distribution (Fig. 5) exhibits a small maximum ($\xi \approx 0.73$) near the leading edge of the spot followed by a larger minimum and a second maximum, these latter two extrema being roughly equal in magnitude. This c_p distribution is in qualitative agreement with the measured wall pressure distributions (the validity of the comparison requires that $\partial\langle P\rangle/\partial y$ is negligible) by Coles & Savas *(9)* and Mautner & Van Atta *(10)*. Cantwell *et al (4)* had concluded, on the basis of their calculated distribution of c_p (Fig. 5), that "streamwise pressure gradients within the spot are probably not important for the dynamics". It was later suggested by Coles & Savas *(9)* that $\partial\langle P\rangle/\partial x$ is appreciably smaller than $\partial\langle P\rangle/\partial y$. The maximum value of $\partial c_p/\partial\xi$, inferred from Fig. 5 is about 0.14 while the magnitude of $|\partial(\langle uv\rangle/U_\infty^2)/\partial\eta|$ in the outer part ($\eta > 2.5 \times 10^{-3}$) of the spot, as inferred from the results at $\zeta = 0$ at Fig. 6, is approximately constant and equal to 0.30. This observation seems to suggest that the pressure

[2] The amplitude of $(\langle U\rangle - U_\infty)$ decreased with increasing y.

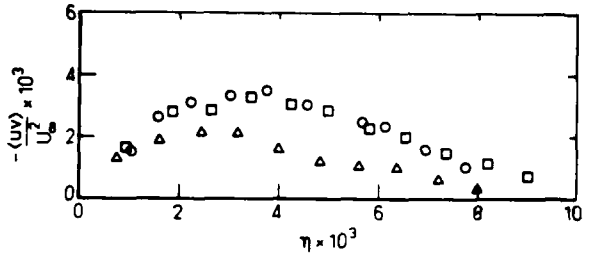

Fig. 6 Ensemble averages of product uv for $\zeta = 0.58$ ($x_s = 0.84$ m).
□, $\zeta = +3.2 \times 10^{-2}$; ○, -3.2×10^{-2}; △, 0.

gradient's influence on the flow need not be negligible since the first and third terms on the right of (1) can be of similar magnitude.

Ensemble averaged distributions (Fig. 6) of $-\langle uv\rangle/U_\infty^2$ at $\zeta = \pm 3.2 \times 10^{-2}$ are almost identical[3] but different from the distribution at $\zeta = 0$. The experimental uncertainty in $\langle v\theta\rangle$ is larger than for $\langle uv\rangle$ and the distributions of $\langle v\theta\rangle$ (Fig. 7) at $\zeta = \pm 3.2 \times 10^{-2}$, while in reasonable qualitative agreement with each other do not exhibit the quantitative agreement of the $\langle\overline{uv}\rangle$ distributions. Values of ν_d/α_d, estimated from the ratio $(\langle uv\rangle/\langle v\theta\rangle)/(\partial\langle T\rangle/\partial\langle U\rangle)$ using the distributions of Figs. 6, 7 and the measured values of $\partial\langle T\rangle/\partial\langle U\rangle$ are shown in Fig. 8 as a function of η. The magnitude of ν_d/α_d for ζ in the range $\pm 3.2 \times 10^{-2}$ decreases from about 8 in the "hot" region of the spot

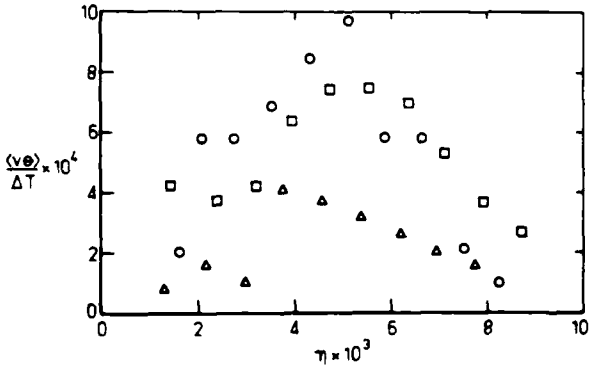

Fig. 7 Ensemble averages of product $v\theta$ for $\zeta = 0.58$ ($x_s = 0.84$ m).
Symbols as for Fig. 6.

(the position of maximum $\tilde{T}$ occurs at $\eta = 3.2 \times 10^{-3}$) to approximately 3 in the outer part of the spot. It is unlikely that the relatively large values of ν_d/α_d reflect a genuine lack of similarity between $\langle U\rangle$ and $\langle T\rangle$. It is more likely that they reflect the inadequacy of assumptions (3) and (4).

Recent flow visualization results by Matsui *(11)*,

[3]Distributions of $\langle U\rangle$ and $\langle T\rangle$ at $\zeta = +3.2 \times 10^{-2}$ are in excellent agreement with corresponding distributions at $\zeta = -3.2 \times 10^{-2}$.

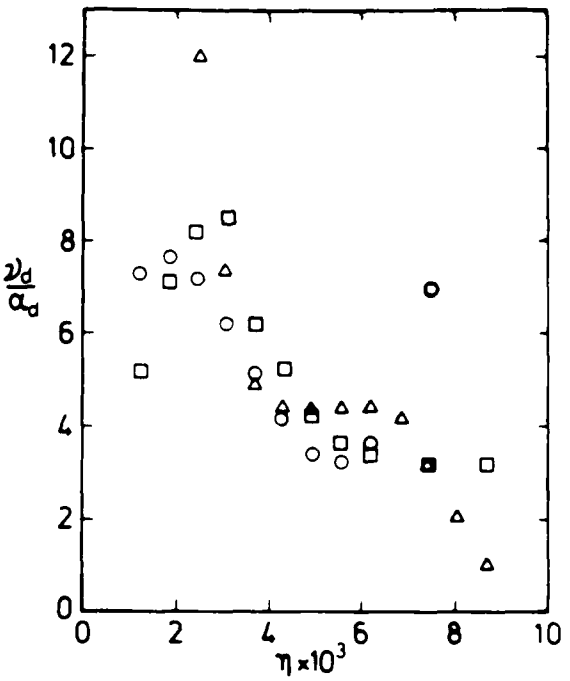

Fig. 8 Ratio of momentum and thermal diffusivities for the disturbance for $\zeta = 0.58$ ($x_s = 0.84$ m). Symbols as for Fig. 6.

Gad-El-Hak *et al (12)* and Perry *et al (13)* suggest that a spot consists of several vortices rather than one large vortex structure as suggested by Coles & Barker *(14)*. Temperature and velocity traces obtained simultaneously [Antonia *et al (2)*; Wygnanski *et al (3)*] at several values of y also support the existence of several coherent structures within each spot. These structures bear considerable similarity to those observed in a fully turbulent boundary layer and it therefore seems likely that a study of these structures in the spot may provide a more meaningful basis for comparison of transfer mechanisms for momentum and heat between the spot and the turbulent boundary layer.

ACKNOWLEDGEMENTS

R.A.A. and A.J.C. acknowledge the support of the Australian Research Grants Committee. C.W.V.A. acknowledges the support of N.S.F. Grant ENG 78-25188.

REFERENCES

1 Van Atta, C. W. and Helland, K. N., "Exploratory Temperature-Tagging Measurements of Turbulent Spots in a Heated Laminar Boundary Layer", *Journal of Fluid Mechanics*, Vol. 100, Part 2, 1980, pp.243-255.

2 Antonia, R. A., Chambers, A. J., Sokolov, M. and Van Atta, C. W., "Simultaneous Temperature and Velocity Measurements in the Plane of Symmetry of a Transitional Turbulent Spot", *Journal of Fluid Mechanics*, Vol. 108, 1981, pp.317-343.

3 Wygnanski, I., Sokolov, M. and Friedman, D., "On the Turbulent 'Spot' in a Boundary Layer Under-

going Transition", *Journal of Fluid Mechanics*, Vol. 78, Part 4, 1976, pp.785-819.

4 Cantwell, B., Coles, D. and Dimotakis, P., "Structure and Entrainment in the Plane of Symmetry of a Turbulent Spot", *Journal of Fluid Mechanics*, Vol. 87, Part 4, 1978, pp.641-672.

5 Sokolov, M., Antonia, R. A. and Chambers, A. J., "A Similarity Transformation for a Turbulent Spot in a Laminar Boundary Layer", *Physics of Fluids*, Vol. 23, No. 12, 1980, pp.2561-2563.

6 Zilberman, M., Wygnanski, I. and Kaplan, R. E., "Transitional Boundary Layer Spot in a Fully Turbulent Environment", *Physics of Fluids*, Vol. 20, No. 10, 1977, pp.S258-S271.

7 Subramanian, C. S. and Antonia, R. A., "Effect of Reynolds Number on a Slightly Heated Turbulent Boundary Layer", to appear in *International Journal of Heat & Mass Transfer*.

8 Van Atta, C. W., Sokolov, M., Antonia, R. A. and Chambers, A. J., "The Potential Flow Signature of a Turbulent Spot", *Proceedings of 7th Australasian Hydraulics & Fluid Mechanics Conference*, Institution of Engineers, Australia, Brisbane, 1980, pp.168-171.

9 Coles, D. and Savas, O., "Interactions for Regular Patterns of Turbulent Spots in a Laminar Boundary Layer" in R. Eppler and H. Fasel (eds.) *Laminar-Turbulent Transition*, Springer-Verlag, 1980, pp.277-287.

10 Mautner, T. S. and Van Atta, C. W., "An Experimental Study of the Wall Pressure Field Associated With a Turbulent Spot in a Laminar Boundary Layer", submitted to *Journal of Fluid Mechanics*.

11 Matsui, T., "Visualization of Turbulent Spots in the Boundary Layer Along a Flat Plate in a Water Flow", in R. Eppler and H. Fasel (eds.) *Laminar-Turbulent Transition*, Springer-Verlag, 1980, pp.288-296.

12 Gad-El-Hak, M., Blackwelder, R. F. and Riley, J. J., "A Visual Study of the Growth and Entrainment of Turbulent Spots", in R. Eppler and H. Fasel (eds.) *Laminar-Turbulent Transition*, Springer-Verlag, 1980, pp.297-310.

13 Perry, A. E., Lim, T. T. and Teh, E. W., "A Visual Study of Turbulent Spots", *Journal of Fluid Mechanics*, Vol. 104, Part 1, 1981, pp.387-405.

14 Coles, D. and Barker, S. J., "Some Remarks on A Synthetic Turbulent Boundary Layer", in S. W. b. Murthy (ed.) *Turbulent Mixing in Nonreactive and Reactive Flows*, Plenum Press, 1975, pp.285-292.

15 Wygnanski, I., Haritonidis, J. H. and Kaplan, R. E., "On a Tollmien-Schlichting Wave Packet Produced by a Turbulent Spot", *Journal of Fluid Mechanics*, Vol. 92, Part 3, 1979, pp.505-528.

A Structural Study on a Turbulent Boundary Layer with Transpiration

M. Senda[+], S. Horiguchi[++], K. Suzuki and T. Sato

Department of Mechanical Engineering
Kyoto University, Kyoto, Japan

ABSTRACT

The method of quadrant analysis of velocity signal obtained near the wall ($y^+ > 30$) has been applied to a transpired turbulent boundary layer, and the effect of transpiration on the statistical features of turbulence has been reexamined from the structural view point.

Near the wall, the contribution from ejection to the mean Reynolds shear stress $-\overline{uv}$ becomes smaller than that from sweep when the injection rate is increased. Another result as to the contribution from ejection to $\overline{uv}$ suggests that the region responsible for the burst moves outward from the wall as the injection rate is increased. These results explain why the magnitude of second-order correlations of velocity fluctuation reduces in this region with increasing the injection rate.

At positions not so near the wall, on the other hand, the contributions both from ejection and sweep become larger with transpiration. Thus, the increase of the second-order correlations of velocity fluctuation found in this region can also be explained. Additionally, the mean bursting period and the mean duration of ejection and sweep events are also discussed, in connection with the average strength of one ejection or sweep event.

NOMENCLATURE

F	= Injection rate
d	= Hole size
$\tilde{d}$	= Hole size defined by Eq.1
M_i	= Number of samples of the instantaneous product uv_i
N_i	= Number of occurrences of the event specified to i-th quadrant
N	= Total number of samples of the instantaneous product uv
T_e	= Mean period of ejection
T_s	= Mean period of sweep
ΔT_e	= Mean duration of ejection
ΔT_s	= Mean duration of sweep
Δt_i	= Duration of one event specified to i-th quadrant
U_e	= Freestream velocity
u_*	= Friction velocity
u, v	= Fluctuating velocity components in the streamwise and normal directions
u', v'	= Root mean square values of u and v
$\overline{uv}$	= Mean Reynolds shear stress
uv_i	= Instantaneous Reynolds shear stress specified to i-th quadrant
$\widetilde{uv}_i, \overline{uv}_i$	= Fractional contribution to $\overline{uv}$ from i-th quadrant
$\langle uv \rangle_i$	= Average strength of the events specified to i-th quadrant, defined by Eq.2
y	= Normal distance from the wall
y^+	= Nondimensional distance from the wall, yu_*/ν
δ	= Boundary layer thickness
ν	= kinematic viscosity

Subscripts

i	= Quadrant number ($i = 1 \sim 4$)
0	= Value with $F = 0$ or $\tilde{d} = 0$

INTRODUCTION

Statistical studies have been made on a transpired turbulent boundary layer by Fulachier (1), Andersen et al.(2), Pimenta et al.(3) and the present authors (4,5). One of the well-known facts of this boundary layer is that the wall shear stress and the wall heat flux can be reduced by transpiration, and the transpiration cooling is an effective method to protect the surface from the hot stream (6). Related with this fact, the Reynolds shear stress $-\overline{uv}$ and the intensities of streamwise and normal fluctuating velocity components, u' and v', decrease near the wall as the injection rate is increased. On the other hand, however, the opposite occurs in the outer layer; $-\overline{uv}$, u' and v' increase in the outer layer with increasing the injection rate (4).

The above mentioned change in the statistical features of turbulence quantities with transpiration should have a relation with the mechanism of turbulence production. In the non-transpired turbulent boundary layer, the bursting phenomenon related to the production of turbulence has been intensively investigated by many researchers, for example, Wallace et al.(7,8), Lu and Willmarth (9), Sabot and Comte-Bellot (10), Blackwelder and Kaplan (11), Nakagawa and Nezu (12), Brown and Thomas (13) and Chen and Blackwelder (14). However, there have been rarely found the structural studies in the transpired turbulent boundary layer.

Present address:
[+] Department of Mechanical Engineering
Doshisha University, Kyoto, Japan
[++] Sakai Works, Nippon Steel Corp., Osaka, Japan

In an usual turbulent boundary layer without transpiration, for example, the bursting event responsible for the production of turbulence kinetic energy occurs most severely in the region very close to the wall, i.e. $y^+ \approx 15$ (15,16). A question may, thus, arise if the same occurs in the transpired turbulent boundary layer. If the characteristics of the bursting phenomenon in the transpired turbulent boundary layer are the same as that in the non-transpired case, the above mentioned change in magnitude of the statistical quantities of turbulence with transpiration is difficult to understand.

To get better understanding of a transpired turbulent boundary layer, some structural studies have been initiated. The present study shows the results of the quadrant analysis of fluctuating velocity signals near the wall, and presents some probable explanation for the above mentioned features of the statistical turbulent quantities.

EXPERIMENTAL PROCEDURE

The experimental apparatus used in this study is the same as that previously used (4), except that the temperature field is homogeneous in the present case. Therefore, only a brief description is given on it below.

A turbulent boundary layer is formed on a bottom flat plate in a low speed wind tunnel, whose cross section is 300 mm × 300 mm. Porous part of the plate starts 1200 mm downstream from its leading edge and covers the length of 900 mm further downstream. Through this porous plate, air is blown uniformly into the developed turbulent boundary layer. The upper wall of the wind tunnel is movable and, prior to the experiments, the upper wall is carefully adjusted so as to remove the pressure gradient in the streamwise direction.

The injection rate F is defined as the mass flow rate ratio of the injection gas to the main flow: $F = (\rho V)_w/(\rho U)_e$, where U and V are the mean velocity components in the streamwise and normal directions, respectively, and ρ the density of the fluid. The subscripts w and e denote the values at the wall and at the freestream. The injection rate distributing uniformly over the porous plate is varied in three steps; 0.0, 0.0021 and 0.0047. The freestream velocity is always kept constant equal to 5.0 m/s. The measurements are carried out at the station 650 mm downstream from the starting position of injection where the transpired turbulent boundary layer is in a state of fully developed condition. At this station, the Reynolds number based on the momentum thickness is in the range between 2500 and 4000, depending on the injection rate.

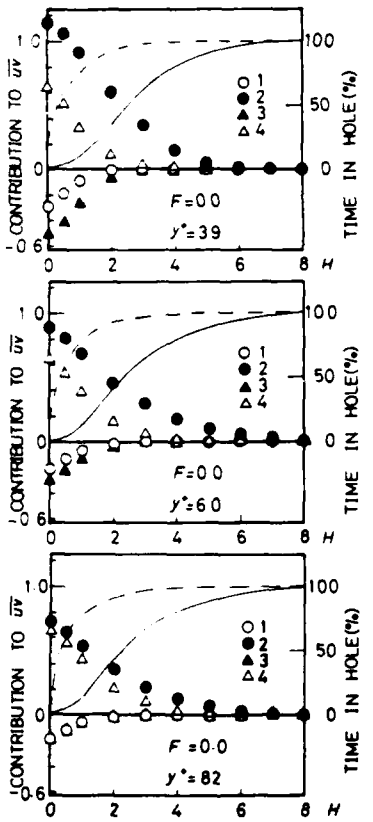

Fig.1 Fractional contribution to $\overline{uv}$ from different events (F = 0.0)

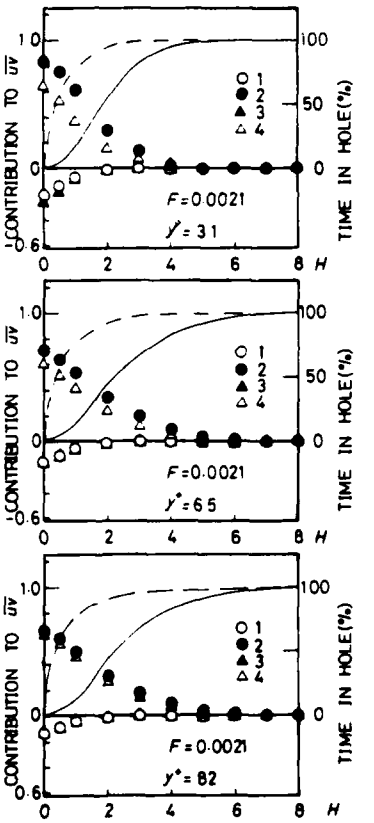

Fig.2 Fractional contribution to $\overline{uv}$ from different events (F = 0.0021)

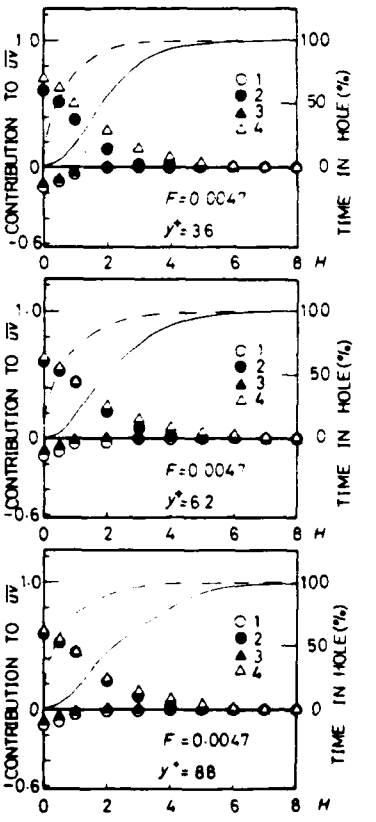

Fig.3 Fractional contribution to $\overline{uv}$ from different events (F = 0.0047)

The measurements of fluctuating velocity signal are made with the hot wires (X-type probe) operated at an constant temperature of overheat ratio of 0.40. Each hot wire consisted of 5μm diameter tungsten wire with copper plated ends has an effective length of 1.0 mm. The spanwise separation of two wires is 1.0 mm. Velocity fluctuating signals both in the streamwise and normal directions, u and v, respectively, are recorded on a digital-magnetic tape recorder by using an A-D converter. Each signal is sampled at a rate of 10 kHz over 60 seconds, and the digitized data are processed with a computer FACOM M-200 at Data Processing Center of Kyoto University.

Following Wallace et al.(7) and Lu and Willmarth (9), u-v plane quadrant analysis is applied in the present study to the transpired turbulent boundary layer. Every instantaneous product uv is classified into one of the four quadrants in the u-v plane according to the four combinations of the signs of u and v. Fluid motion specified by each quadrant may be called as follows.

Quadrant 1	($u>0$ and $v>0$)	Outward interaction
Quadrant 2	($u<0$ and $v>0$)	Ejection-like motion
Quadrant 3	($u<0$ and $v<0$)	Wallward interaction
Quadrant 4	($u>0$ and $v<0$)	Sweep-like motion

At the same time, a threshold parameter H is introduced to classify the magnitude of the instantaneous Reynolds shear stress into two parts; inside a hole $|uv| < Hu'v'$ and outside the hole $|uv| > Hu'v'$. Here, u' and v' are the root mean square values of local velocity fluctuation signals u and v. Signals of small amplitude ($|uv| < Hu'v'$) are stored in the hole, while the remaining signals of large amplitude ($|uv| > Hu'v'$) are classified and stored in one of the four quadrants in a way mentioned above. Analysis is carried out at various values of H.

In the present study, attention is paid mainly on Quadrant 2 and Quadrant 4. The former corresponds to such a fluid motion that the low momentum fluid ejects outward from the region near the wall, and the latter such a fluid motion that the high momentum fluid sweeps out the wall region, respectively. These events will be found to produce almost all of the Reynolds shear stress during bursting in the present case as in the non-transpired turbulent boundary layer.

RESULTS AND DISCUSSION

Figures 1 through 3 show some results of the present quadrant analysis. These figures for different injection rate include the results obtained at three positions from the wall. The coordinate of the figures, $\widetilde{uv}_{i,H}/\overline{uv}$, is the fractional contribution to the local statistical value of the Reynolds shear stress $\overline{uv}$ from the signal specified to the quadrant i and exceeding a hole size of the threshold parameter H which corresponds to the abscissa. One of the curves (dotted line) shows the time fraction occupied by the signal inside the hole, and the other (solid line) shows the contribution from such signal to $\overline{uv}$.

Each figure shows that about a half portion of the time is spent with such weak signal as contributing almost nothing to $\overline{uv}$. On the other hand, such fluid motions as specified to the quadrants 2 and 4 are found to produce larger instantaneous Reynolds shear stress than those specified to other quadrants 1 and 3. For example, about 50 percent of $\overline{uv}$ results from such ejection-like motion (Quadrant 2) and sweep-like motion (Quadrant 4) as exceeding a threshold, above which there is no contribution from the quadrants 1 and 3 to $\overline{uv}$. Similar features have been pointed out by Lu and Willmarth for a turbulent boundary layer without transpiration (9), which corresponds to the case of $F=0.0$ (Fig.1) of the present study. Figures 1 through 3, therefore, demonstrate that these features are not altered by transpiration of a fluid through the permeable wall.

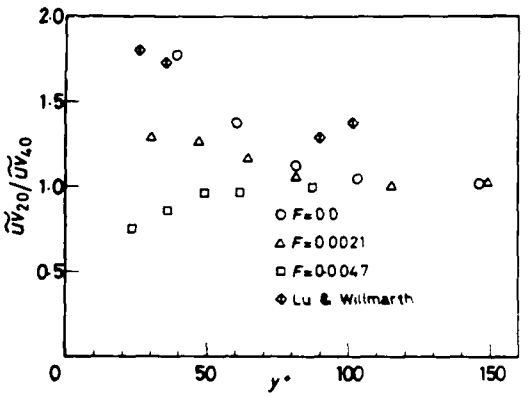

Fig.4 Ratio $\widetilde{uv}_{2H}/\widetilde{uv}_{4H}$ with $H=0$

Studying each figure more carefully, however, a few interesting points can be pointed out concerning with the effect of transpiration on structural features of turbulence. In Figure 4 is plotted the ratio $\widetilde{uv}_{2,0}/\widetilde{uv}_{4,0}$ between the contribution to $\overline{uv}$ from the ejection-like motion and that from the sweep-like motion obtained with $H=0$. In the figure, $y^+ = yu_\tau/\nu$, where y is the normal distance from the wall, u_τ the friction velocity and ν the kinematic viscosity. For comparison, the values of this ratio for a non-transpired case obtained by Lu and Willmarth are also plotted. The present results for a case of $F=0.0$ are in fairly good agreement with their results. With increasing the injection rate, the ratio $\widetilde{uv}_{2,0}/\widetilde{uv}_{4,0}$ is found to decrease, especially near the wall, and in the case of $F=0.0047$ the contribution from the sweep-like motion is larger than that from the ejection-like motion. In the region of large y^+, on the other hand, the ratio is nearly equal to 1.0 independent of the injection rate, which indicates that the contributions from ejection-like and sweep-like motions are almost the same at any injection rate.

As seen easily from the fractional contribution from the different events to $\overline{uv}$ shown in Figures 1, 2 and 3, the small amplitude events contributing almost nothing to $\overline{uv}$ occupy a large fraction of time. In order to eliminate such signals and discriminate the ejection and the sweep more clearly, here is tentatively introduced a threshold level $\widetilde{H}$ defined as follows;

$$\widetilde{H}_i = \frac{\frac{1}{M_i}\sum_{i=1}^{M_i} uv_{i0}}{\overline{u'v'}} \qquad (1)$$

where M_i is the number of the samples of instantaneous product uv_{i0} specified to the quadrant i with zero threshold.

In Figure 5 are shown the ratios $\widetilde{uv}_{2\tilde{H}}/\overline{uv}$ and $\widetilde{uv}_{4\tilde{H}}/\overline{uv}$. Corresponding to the values of $\widetilde{uv}_{2\tilde{H}}/\widetilde{uv}_{4\tilde{H}}$ found to be almost unity at large y^+ position at any injection rate in Figure 4, first of all, $\widetilde{uv}_{2\tilde{H}}/\overline{uv}$ and $\widetilde{uv}_{4\tilde{H}}/\overline{uv}$ are found in this figure to take almost constant value of 0.4 at such positions at any injection rate. In the non-transpired case, the ejection specified to the quadrant 2 is found to contribute much more to $\overline{uv}$ than the sweep does in the region of small y^+. At the injection rate of $F = 0.0021$, the contribution from the ejection is still larger than that from the sweep in the region of small y^+, but the difference between them is smaller compared to the difference found in the case of $F = 0.0$. The contribution to $\overline{uv}$ from the ejection still decreases when the injection rate is increased further. At $F = 0.0047$, the ratio $\widetilde{uv}_{2\tilde{H}}/\overline{uv}$ distributes almost uniformly over the entire y^+ region presently studied and takes a value around 0.4. On the other hand, at $F = 0.0047$, the contribution from the sweep looks to be larger than 0.4 at smaller y^+ position. The combined effect of the reduced contribution from the ejection and the augmented contribution from the sweep is a cause of such a fact found in Figure 4 that the ratio $\widetilde{uv}_{2\tilde{H}}/\widetilde{uv}_{4\tilde{H}}$ is smaller than unity in the region $y^+ < 50$ at the highest injection rate of the present study. Turning back to Figures 1 through 3, another features is found on the magnitude of $\widetilde{uv}_{3\tilde{H}}$ and $\widetilde{uv}_{1\tilde{H}}$. These contribute a little to $\overline{uv}$ in the non-transpired case and much less in the transpired case. These features discussed above suggest that the coherent fluid motion near the wall can no longer remain the same in nature as that of the non-transpired boundary layer when F is raised above zero.

The most interesting result can be drawn from Figure 6, where the value of $\widetilde{uv}_{i\tilde{H}}$ ($i = 2$ and 4) is plotted for three cases of $F = 0.0$, 0.0021 and 0.0047, in the form normalized with $\overline{uv}_0$. $\overline{uv}_0$ is the statistical value of $\overline{uv}$ obtained in the impermeable case, and it distributes almost uniformly over the entire y^+ position studied in the present experiment. In the region of y^+ larger than 50, the values of $\widetilde{uv}_{2\tilde{H}}$ and $\widetilde{uv}_{4\tilde{H}}$ become larger as the injection rate F is increased. This corresponds well to the increase of $-\overline{uv}$, u' and v' with increasing F in this and further outer regions. Additionally, at $F = 0.0047$, both $\widetilde{uv}_{2\tilde{H}}$ and $\widetilde{uv}_{4\tilde{H}}$ decrease toward the wall in the region $y^+ < 50$. This matches the fact that $-\overline{uv}$, u' and v' decrease in such a region close to the wall when F is increased.

The tendency of $\widetilde{uv}_{2\tilde{H}}$ and $\widetilde{uv}_{4\tilde{H}}$ decreasing toward the wall found at $F = 0.0047$ suggests a possibility that the region responsible for the bursting event moves outward from the wall as F is increased. In low Reynolds number oil channel flow without transpiration, Wallace et al.(8) found that the ejection is not so significant as the sweep at a position much closer to the wall than the position where the intensive burst principally originates and that the sweep is the only event occurring in such a region. At two positions of y^+ smaller than 40, $\widetilde{uv}_{2\tilde{H}}$ is found to be smaller than $\widetilde{uv}_{4\tilde{H}}$ in the present case of $F = 0.0047$. This agrees with the finding by Wallace et al., if

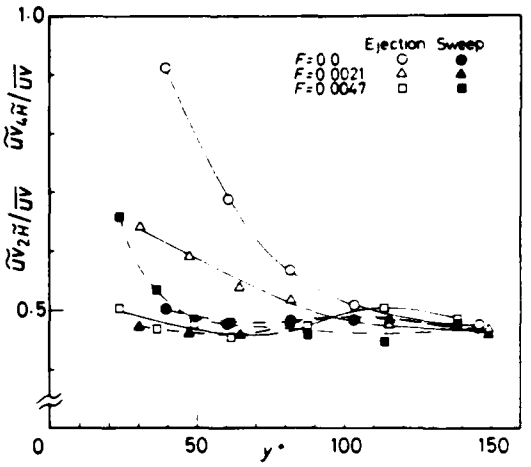

Fig.5 Distributions of $\widetilde{uv}_{i\tilde{H}}/\overline{uv}$ and $\widetilde{uv}_{4\tilde{H}}/\overline{uv}$ as a function of y^+

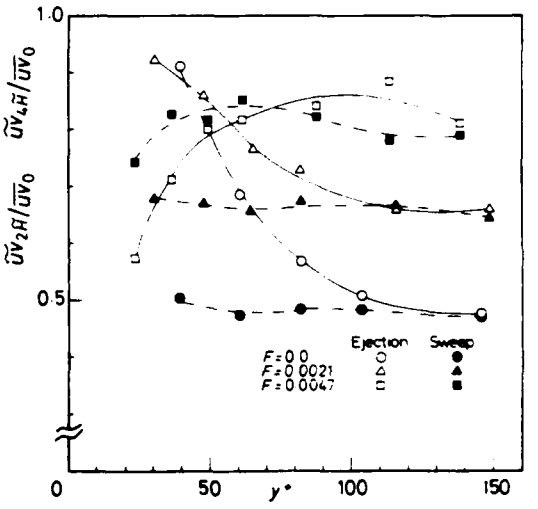

Fig.6 Distributions of $\widetilde{uv}_{i\tilde{H}}/\overline{uv}_0$ and $\widetilde{uv}_{4\tilde{H}}/\overline{uv}_0$ as a function of y^+

actually the position responsible for the bursting event has moved outward to the region of y^+ larger than 50 in the case of $F = 0.0047$.

The mean periods of the ejection T_e and the sweep T_s, and the mean duration of these events, ΔT_e and ΔT_s, are shown in Figures 7 and 8. The mean period and the mean duration are obtained as follows. A portion of such data as continuously specified to the quadrant 2 or 4 with a threshold $\widetilde{H}_i$ is taken as one ejection or sweep event. The mean duration of such sequence is examined and is denoted as the mean duration of the ejection ΔT_e or the sweep ΔT_s. The mean period of the ejection T_e or the sweep T_s is defined as the ratio between the total time observed and the number of occurrences of each event detected.

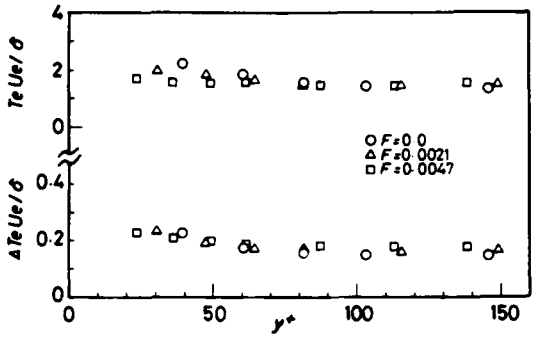

Fig.7 Mean period T_e and mean duration ΔT_e of the ejection

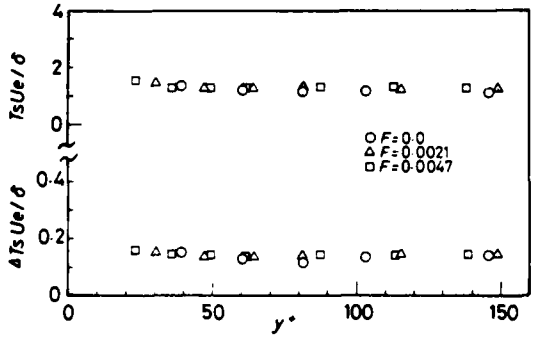

Fig.8 Mean period T_s and mean duration ΔT_s of the sweep

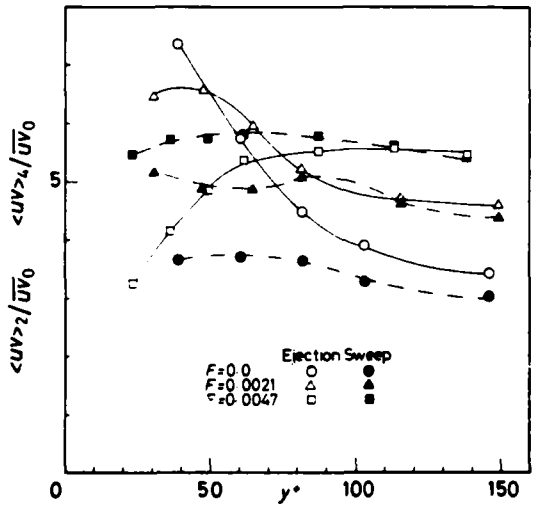

Fig.9 Distributions of the strength for the ejection $\langle uv\rangle_2/\overline{uv}_0$ and for the sweep $\langle uv\rangle_4/\overline{uv}_0$ as a function of y^+

The results are normalized with the parameters of the outer layer; the freestream velocity U_e and the boundary layer thickness δ. This kind of normalization is effective, because the normalized results are found to be independent of the injection rate. The same was found also for the bursting period measured with the correlation function method (17). It was pointed out there that the bursting period normalized with the time scale of the outer layer δ/U_e is independent of both the Reynolds number and the injection rate. These results indicate again that the large scale motion in the outer layer relates to the triggering of bursting phenomenon near the wall (18). The results distribute almost uniformly in the boundary layer both for the ejection and the sweep, but T_eU_e/δ (or $\Delta T_eU_e/\delta$) for the ejection is a little larger than T_sU_e/δ (or $\Delta T_sU_e/\delta$) for the sweep. This result would probably depend on the threshold used in the present study, which differs between for the ejection and for the sweep.

Since δ does not vary so much within the range of F presently studied, these figures show that the bursting period and its duration are not affected so remarkably by transpiration. The present authors have studied the turbulent length scales in the same boundary layer, among others the longitudinal and transverse integral scales and the differential scale of streamwise velocity fluctuation (5). In the reference, it is found that the large scale motion of turbulence in the outer layer is not affected by transpiration. The results between the bursting period and the structure of large scale motion may, therefore, be consistent with each other.

Keeping in mind that the bursting period and its duration vary little with transpiration and reminding that $\widetilde{uv}_2\widetilde{T}$ and $\widetilde{uv}_4\widetilde{T}$ become larger at large y^+ position with increasing F, it is easily inferred that the strength of one ejection event or one sweep event increases at $y^+ > 50$ as the injection rate is increased. Figure 9 confirms the above conjecture, where the average strength of one event is plotted for the ejection and the sweep. The strength is defined as follow;

$$\langle uv\rangle_i = \frac{1}{N_i}\sum_{i=1}^{N_i}\frac{1}{\Delta t_{ik}}\int_0^{\Delta t_{ik}} uv_i\widetilde{T}\,dt \qquad (2)$$

where Δt_{ik} is the duration of one event corresponding to the quadrant i and N_i the number of occurrences of the event.

CONCLUDING REMARKS

The results obtained from the quadrant analysis of velocity signal applied to a transpired turbulent boundary layer have been discussed.

Some qualitative features about the fractional contribution from each quadrant are found not to be altered by transpiration, and the mean frequency and duration of the ejection and the sweep normalized with the time scale of the outer layer are found being almost the same independent of the injection rate. However, the remarkable features suggesting the change in nature of the coherent motion of the fluid near the wall with transpiration have been pointed out. A well-known characteristic of turbulence in the transpired boundary layer that $-\overline{uv}$, u' and v' increase with transpiration at large y^+ position, but decrease

near the wall has been related to the change in nature of the coherent fluid motion.

In the region close to the wall, the contribution from the ejection becomes smaller than that from the sweep with increasing the injection rate. In the non-transpired case, the fractional contribution from the ejection to $\overline{uv}$ decreases monotonously with increasing distance from the wall. Against this, in the highest case of the injection rate studied, it decreases as the wall is approached. This result suggests that the region responsible for the burst moves outward from the wall as the injection rate is increased. These are guessed to be the causes of the fact that the Reynolds shear stress and the intensities of velocity fluctuation decrease with transpiration in this region.

Except near the wall, on the other hand, the contributions both from the ejection and the sweep increase with increasing the injection rate. The average strengthes of these events also increase in this region. Therefore, the increase of the Reynolds shear stress and the intensities of velocity fluctuation in this region is due to the intensification of the bursting with transpiration.

REFERENCES

1 Fulachier, L., "Contribution à l'étude des analogies des champs dynamique et thermique dans une couche limite turbulente: Effet de l'aspiration" Thèse Docteur ès Sciences, Université de Provence, Marseille, 1972.

2 Andersen, P. S., Kays, W. M. and Moffat, R. J., "Experimental Results for the Transpired Turbulent Boundary Layer in an Adverse Pressure Gradient" J. Fluid Mech., Vol. 69, Part 2, 1975, pp. 353-375.

3 Pimenta, M. M., Moffat, R. J. and Kays, W. M., "The Turbulent Boundary Layer: An Experimental Study of the Transport of Momentum and Heat with the Effect of Roughness" Rept. HMT-21, Mech. Engng. Dept., Stanford University, 1975.

4 Senda, M., Suzuki, K. and Sato, T., "Turbulence Structure Related to the Heat Transfer in a Turbulent Boundary Layer with Injection" Turbulent Shear Flows 2 (eds. Bradbury, L. T. S. et al.) Springer-Verlag, 1980, pp. 143-157.

5 Senda, M., Kawaguchi, Y., Suzuki, K. and Sato, T., "Study on a Turbulent Boundary Layer with Injection – Turbulent Scales –" Trans. JSME, Vol. 47, No. 414, 1981, pp.251-258. (in Japanese)

6 Kays, W. M. and Moffat, R. J., "The Behaviour of Transpired Turbulent Boundary Layers" Studies in Convection, Vol. 1 (ed. Launder, B. E.), Academic Press, 1975, pp. 223-319.

7 Wallace, J. M., Eckelmann, H. and Brodkey, R. S., "The Wall Region in Turbulent Shear Flow" J. Fluid Mech., Vol. 54, Part 1, 1972, pp. 39-48.

8 Wallace, J. M., Brodkey, R. S. and Eckelmann, H., "Pattern-Recognized Structures in Bounded Turbulent Shear Flows" J. Fluid Mech., Vol. 83, Part 4, 1977, pp. 673-693.

9 Lu, S. S. and Willmarth, W. W., "Measurements of the Structure of the Reynolds Stress in a Turbulent Boundary Layer" J. Fluid Mech., Vol. 60, Part 3, 1973, pp. 481-511.

10 Sabot, J. and Comte-Bellot, G., "Intermittency of Coherent Structures in the Core Region of Fully Developed Turbulent Pipe Flow" J. Fluid Mech., Vol. 74, Part 4, 1976, pp. 767-796.

11 Blackwelder, R. F. and Kaplan, R. E., "On the Wall Structure of the Turbulent Boundary Layer" J. Fluid Mech., Vol. 76, Part 1, 1976, pp. 89-112.

12 Nakagawa, H. and Nezu, I., "Prediction of the Contributions to the Reynolds Stress from Bursting Events in Open-Channel Flows" J. Fluid Mech., Vol. 80, Part 1, 1977, pp. 99-128.

13 Brown, G. L. and Thomas, A. S. W., "Large Structures in a Turbulent Boundary Layer" Physics Fluids, Vol. 20, 1977, s243-s252.

14 Chen, C. H. C. and Blackwelder, R. F., "Large-Scale Motion in a Turbulent Boundary Layer: A Study using Temperature Contamination" J. Fluid Mech., Vol. 89, Part 1, 1978, pp. 1-31.

15 Corino, E. R. and Brodkey, R. S., "A Visual Investigation of the Wall Region in Turbulent Flow" J. Fluid Mech., Vol. 37, Part 1, 1969, pp. 1-30.

16 Kim, H. T., Kline, S. J. and Reynolds, W. C., "The Production of Turbulence near a Smooth Wall in a Turbulent Boundary Layer" J. Fluid Mech., Vol. 50, Part 1, 1971, pp. 133-160.

17 Senda, M., Kawaguchi, Y., Horiguchi, S., Suzuki, K. and Sato, T., "Study on a Turbulent Boundary Layer with Injection – Measurement of Bursting Period and Calculation with Surface Renewal Model –" Trans. JSME. (to be appeared)

18 Suzuki, K. and Kawaguchi, Y., "Measurement of Bursting Period and Test of Surface Renewal Model in a Turbulent Boundary Layer Disturbed by a Cylinder" Proc. ICHMT/IUTAM Symp. on Heat and Mass Transfer and the Structure of Turbulence, 1980.

THE MECHANISM OF TURBULENT MASS TRANSFER AT A BOUNDARY

JAY A. CAMPBELL AND THOMAS J. HANRATTY

UNIVERSITY OF ILLINOIS
URBANA, ILLINOIS

ABSTRACT

The fluctuating concentration field is calculated from the mass balance equation using measured values of the fluctuating velocity field. It is found that the concentration boundary-layer acts as a filter in that only velocity fluctuations of much lower frequency than the most energetic velocity fluctuations are effective in transporting mass at large Schmidt numbers. Two parameters characterizing the velocity field emerge as being quite important. These are the limiting behavior of the spectral density function of the normal velocity fluctuations for frequency approaching zero and a scale characterizing the spanwise mixing.

NOMENCLATURE

C Concentration of transported species, mole/m^3

C_B Bulk concentration of transported species, mole/m^3

D Molecular Diffusion Coefficient, m^2/s

k Fluctuating part of mass transfer coefficient, m/s

K Mass transfer coefficient, m/s

N Mass transfer rate, mole/m^2s

n Frequency, 1/s

Re Reynolds number = $\frac{d\bar{U}}{\nu}$

S Schmidt number = $\frac{\nu}{D}$

T_B Period of coherent structure, s

u Fluctuating part of velocity in x-direction, m/s

u* Friction velocity, m/s

v Normal velocity, m/s

w Transverse velocity, m/s

W_k Frequency spectrum of k, m^2/s

$W_{\dot{s}}$ Frequency spectrum of $\dot{s}$, $1/m^2s$

x Longitudinal coordinate, m

y Normal coordinate, m

z Transverse coordinate, m

Greek Symbols

a Velocity gradient at the wall in x-direction, 1/s

$\dot{s}$ Velocity gradient at the wall in y-direction, 1/ms

c Velocity gradient at the wall in z-direction, 1/s

δ Thickness of Nernst diffusion layer, m

λ Laterial dimension of coherent structure, m

ν Kinematic viscosity, m^2/s

Superscripts

+ Denotes variable made dimensionless with u^* and ν

BACKGROUND

In 1904, Nernst suggested a model for relating turbulent mass transfer at a boundary to the convective flow. He pictured a stagnant layer of thickness δ existing near a boundary and a well mixed region outside this layer. If the concentration of diffusing species is C_B in this well mixed region, and is zero at the wall then the the rate of mass transfer per unit area, N, is given as

$$N = D \frac{C_B}{\delta} \qquad (1)$$

where D is the molecular diffusion coefficient. Hydrodynamics controls the mass transfer rate by controlling the thickness δ.

A number of attempts have been made to offer alternates to the Nernst diffusion layer concept which recognize that the flow close to the wall is not stagnant. These include surface renewal models, the assumption that the eddy diffusion coefficient is proportional to the eddy viscosity and various pseudo-steady state eddy models. All of these theories are inconsistent with recently obtained measurements of flow close to a wall and of the fluctuations in the local mass transfer rate to a wall.

Studies of the velocity field have revealed the existence of coherent structures close to the wall

which are approximately homogeneous in the flow direction, and which have a lateral dimension of $\lambda^+ = 100$ and a period of $T_B^+ = 100$ [4]. Studies of the fluctuations in mass transfer rate reveal fluctuations of very large amplitude which have a period of at least an order of magnitude larger than T_B^+ at a Schmidt number of 1000 [6,7,9]. This period increases with increasing Schmidt number. As with the fluctuating velocity field close to a wall, the fluctuations in the rate of mass transfer reveal an elongated structure.

At the Second Symposium on Turbulent Shear Flows [3] a model for the mass transfer process was explored which used structural information on the velocity field obtained in recent experiments to relate mass transfer rates to the flow. The time dependent mass balance equation was solved for a regular periodic flow field with period $T_B^+ = 100$ and with a lateral wavelength of $\lambda^+ = 100$. The implication of this analysis is that the observed low frequency concentration fluctuations close to the wall are not contributing to the transport of mass. The Reynolds transport coefficient is assumed to be associated with concentration fluctuations of period T_B^+ which would exist a distance away from the wall.

This calculation was not successful in explaining available measurements. Consequently we have explored a different approach. The results of this new work are reported in this paper. The chief difference is that the assumption of a velocity field periodic in time is abandoned. Rather, the mass balance equations are solved using actual measurements of the fluctuating velocity field close to the wall. Of particular interest is the solution using filtered velocity signals since this reveals whether high frequency velocity fluctuations are playing any role in controlling the mass transfer rate. New measurements of the structure of the fluctuating mass transfer field and of the structure of the low frequency velocity fluctuations close to the wall are also presented.

EXPERIMENTS

The experiments were conducted in a vertical five level flow system which provides a straight entrance length of 15 m for a 20 cm circular test section [7]. The test fluid consists of an aqueous solution of potassium iodide and iodine.

The velocity gradients at the wall were measured in a Plexiglas test section which had an array of 20 pairs of rectangular electrodes mounted flush with the wall around the circumference of the pipe. Each pair was in a chevron arrangement with the two electrode making an angle of 15° to each other. The electrodes formed the cathodes of an electrolysis cell at which the following reaction occurred:

$$I_3^- + 2e^- \rightarrow 3I^- \quad . \qquad (2)$$

At large enough cathode voltages the measured current can be related to the velocity gradient at the wall. The sum of the signals from two of these electrodes gave the component of the velocity gradient in the direction of mean flow, α, and the difference gave the component in the spanwise direction, γ [4,5,7]. At Re = 20,000 the group of electrode pairs covered a distance of $\Delta z^+ = 100$ and the distance between two pairs was $\Delta z^+ = 5$.

In the mass transfer studies, the test section was a nickel pipe plated with platinum. This constituted the cathode of an electrolysis cell. At large enough voltages the current flowing in the electrolysis circuit is proportional to the mass transfer to the test section. A series of circular wires 0.4 mm in diameter were mounted flush with the wall of the test section in an array in the circumferential direction. These were insulated from the test section by a thin layer of epoxy. By measuring the current flowing to one of these electrodes the local fluctuations in the mass transfer rate could be determined.

ANALYSIS

From an order of magnitude analysis, Sirkar and Hanratty [8] have argued that molecular diffusion is important only in the y-direction and that the concentration field is approximately homogeneous in the flow direction. The time dependent mass balance equation can therefore be written as

$$\frac{\partial C}{\partial t} + w \frac{\partial C}{\partial z} + v \frac{\partial C}{\partial y} = D \frac{\partial^2 C}{\partial y^2} \quad . \qquad (3)$$

For large Schmidt numbers the concentration boundary-layer is so thin that w and v may be approximated by a Taylor series expansion so that

$$w = \gamma(z,t)y \qquad (4)$$

and

$$v = \beta(z,t)y^2 \quad . \qquad (5)$$

From the continuity equation the following relation between $\gamma(z,t)$ and $\beta(z,t)$ is obtained if the flow is assumed approximately homogeneous in the flow direction:

$$\frac{\partial \gamma}{\partial z} + 2\beta = 0 \qquad (6)$$

Consequently the mass transfer rate is related to the velocity field either through the specification of $\gamma(z,t)$ or of $\beta(z,t)$.

As a first approximation the influence of spanwise mixing and of the variation of the flow field in the z-direction were ignored. The equation

$$\frac{\partial C}{\partial t} + v(t) \frac{\partial C}{\partial y} = D \frac{\partial^2 C}{\partial y^2} \qquad (7)$$

$$C = 0 \quad y = 0$$

$$C = C_B \quad \text{large } y$$

was solved using actual measurements of $\beta(t)$. These were obtained from the determination of $\partial\gamma/\partial z$ using two pairs of flush mounted mass transfer probes in chevron configurations. The calculated variation of the mass transfer rate, N, with time was found to be similar at Schmidt number = 1000 for an unfiltered $\beta(t)$ and for a $\beta(t)$ for which ~90% of the energy was removed by using a low pass filter (see Figures 1 and 2). This suggests (1) that the fluctuations in the mass transfer rate are being caused by low frequency velocity fluctuations and (2) that the rate of mass transfer is being controlled by velocity fluctuations of much lower frequency than the elongated flow structures that dominate the wall region. Similar conclusions have recently been reached by Campbell [2] who presented solutions to a simplified version of (3) which is linear in the fluctuating quantities.

Solutions of (7) give approximately the same dependency with Schmidt number as found in measurements of the average mass transfer coefficient, $\overline{K}$, and the mean-squared value of the fluctuations in K, $\overline{k^2}$. However, the calculated values of $\overline{k^2}$ and $\overline{K}$ are of incorrect magnitude. This suggests that

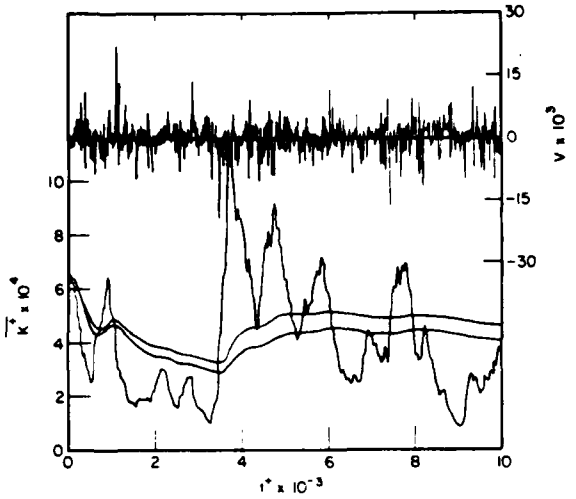

Fig. 1 Dimensionless mass transfer coefficient, K/u*, and dimensionless velocity, v/u*, versus dimensionless time, tu^{*2}/ν, for $t_t^* = 10{,}150$, as Sc = 1000

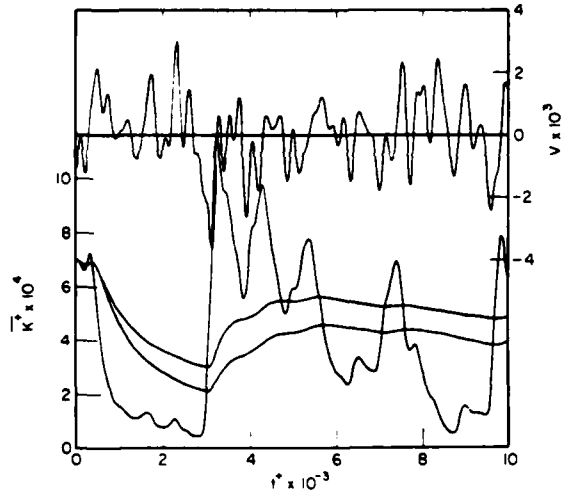

Fig. 2 K/u* versus tu^{*2}/ν for velocity lowpass filtered with $n_{co}^+ = .0041$, $t_t^+ = 10{,}150$, at Sc = 1000

spanwise mixing must be taken into account. The influence of spanwise mixing was assessed by measuring the fluctuations in K simultaneously at multiple wall locations. These revealed a slowly varying pattern with a wavelength approximately equal to $z^+ = 100$. (See Figure 3.) In order to see whether this result is consistent with the finding that the mass transfer is being controlled by low frequency velocity fluctuations, measurements were made of s_z at multiple wall locations. These were treated with a low pass filter so that ~ 90 percent of the energy was removed. Variations of the filtered signals in the spanwise direction had a characteristic wavelength on the same order as that observed for the mass transfer fluctuations. (See Figure 4.)

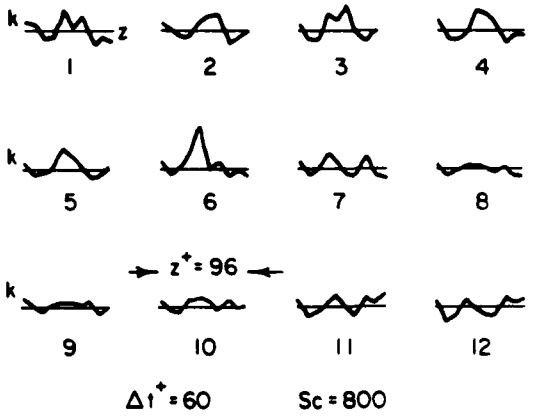

Fig. 3 Instantaneous values of the local fluctuating component of the mass transfer coefficient versus spanwise distance at several consecutive times

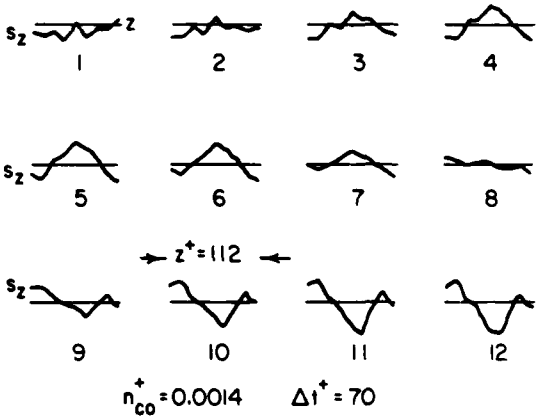

Fig. 4 Instantaneous values of the lowpass filtered spanwise component of the wall velocity gradient versus spanwise direction for several consecutive times

In order to include the effect of spanwise variation of the flow, equation (2) was solved with $v = \bar{s}(t) \cos \frac{2\pi z}{z^+}$. The calculation is not very sensitive to the selection of z^+ if $\bar{s}(t)$ is normalized so as to give a value of $\overline{v^2}$ that agrees with measurements. A comparison of calculated values of $\overline{K}$ and of $\overline{k^2}$ with experiment showed showed good agreement. (See Figures 5 and 6.)

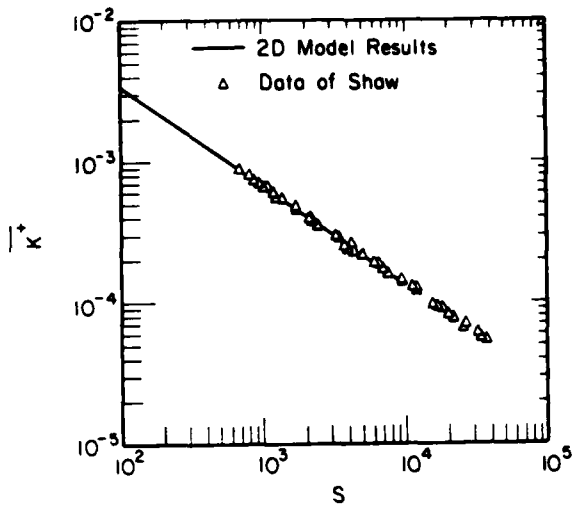

Fig. 5 Comparison of experimental data and results of 2D model for the Schmidt number variation of the average mass transfer coefficient

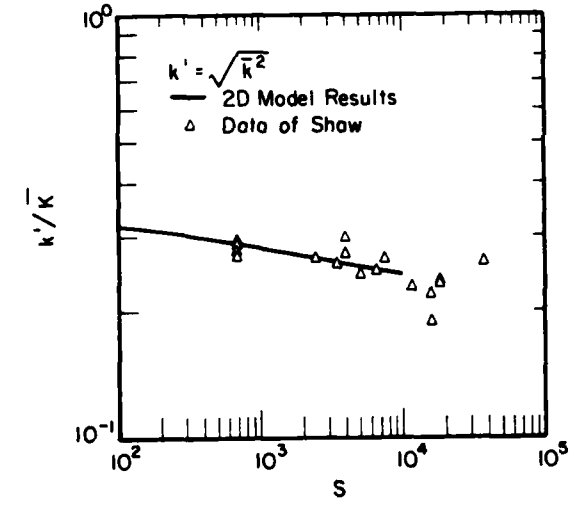

Fig. 6 Comparison of experimental data and results of 2D model for the Schmidt number variation of the relative intensity of the mass transfer coefficient

METHOD OF CALCULATION

The spectral density function for β is represented by W_β and is defined as

$$\overline{\beta^{+2}} = \int_{-\infty}^{\infty} W_\beta^+ (n^+)\, d\, n^+ \qquad (8)$$

where all quantities have been made dimensionless using wall parameters. It is found that for large Schmidt numbers only the low frequency portion of $W_\beta^+ (n^+)$ for which it is constant, $W_\beta^+(0)$, is important.

Solutions of (7) have revealed good agreement between the calculated spectral function for k at large frequencies and predictions based on the solution to the linear equation presented by Sirkar and Hanratty [8].

$$W_k^+ (n) = \frac{\overline{4K^{+2}}\, W_\beta^+ (0)}{(2\pi n^+)^3} \qquad (9)$$

$$n \to \infty$$

Therefore, a comparison of the measurements of $W_k(n)$ by Shaw and Hanratty [8] with (9) allowed the evaluation of $W_\beta(0)$ as

$$W_\beta^+(0) = .010 \quad . \qquad (10)$$

The measured $\gamma(t)$ used to solve (3) and (7) had a $W_\beta(0)$ smaller than given by (10). This suggests that the measurements are in error because of the averaging of small scale motions and because of the neglect of $\partial u/\partial x$ in (6). This was corrected by multiplying the measured $\gamma(t)$ with a constant factor selected to give a value of $W_\beta(0)$ in agreement with (10). Equations (3) and (7) were solved using finite difference techniques which employed upwinding of the advection terms. The one dimensional equation used an implicit method. The two dimensional study used an alternating-direction-implicit method. The calculation was carried out on the University of Illinois Cyber CDC 170/175 Computer. The average computation time for (4) with 10,000 times steps and 20 grid points in the normal direction was 12 seconds. The consistency of the finite difference schemes was tested by varying the number of grid points in time and space and by varying the initial conditions. Both numerical schemes have been shown to be unconditionally stable [1].

CONCLUSIONS

The goal of a theory for mass transfer between a turbulent fluid and a solid is to identify properties of the fluctuating velocity field which are important and to develop a relation between $\overline{K}$ and these properties. The results of the calculations and experiments summarized in this paper present a picture of the process quite different from classical theory.

It is found that at large Schmidt numbers, the concentration boundary-layer close to the surface acts as a filter so that velocity fluctutations of much lower frequency than the most energetic velocity fluctuations are causing turbulent transport. As the Schmidt number increases, smaller and smaller fractions of the turbulence energy are effective in determining the magnitude of $\overline{K}$.

The filtering of measurements of $\gamma(z,t)$ made at multiple locations on the wall reveal no difference in the lateral scale of the low frequency components of $\gamma(z,t)$ and the unfiltered signal.

We therefore find that the mass transfer process is related to the velocity field through $W_\beta(0)$ and a length characterizing the lateral mixing.

ACKNOWLEDGEMENTS

This work is being supported by the National Science Foundation under Grant NSF CPE 79-20990.

REFERENCES

1 Campbell, J. A., "The Use of a Regular Eddy Model to Describe Turbulent Mass Transfer to a Wall," M.S. Thesis, University of Illinois, Urbana, 1979.

2 Campbell, J. A., "The Relation of the Turbulent Velocity Field to Mass Transfer at High Schmidt Numbers," Ph.D. Thesis, University of Illinois, Urbana, 1981.

3 Campbell, J. A. and Hanratty, T. J., "Influence of Turbulent Structure on Mass Transfer at a Solid Surface," Second Symposium on Turbulent Shear Flows, London, 1971.

4 Hogenes, J.H.A., "Identification of the Dominant Flow Structure in the Viscous Wall Region of a Turbulent Flow," Ph.D. Thesis, University of Illinois, Urbana, 1979.

5 Lau, K. L., "Study of Turbulent Structure Close to a Wall Using Conditional Sampling Techniques," Ph.D. Thesis, University of Illinois, Urbana, 1980.

6 Shaw, D. A., "Mechanism of Turbulent Mass Transfer to a Pipe Wall at High Schmidt Number," Ph.D. Thesis, University of Illinois, Urbana, 1976.

7 Sirkar, K. K., "Turbulence in the Immediate Vicinity of a Wall and Fully Developed Mass Transfer at High Schmidt Numbers," Ph.D. Thesis, University of Illinois, Urbana, 1969.

8 Sirkar, K. K. and Hanratty, T. J., "Relation of Turbulent Mass Transfer Rates to a Wall at High Schmidt Numbers to the Velocity Field," J. Fluid Mech., 44, 1970, pp. 589-603.

9 Van Shaw, P. and Hanratty, T. J., "Fluctuations in the Local Rate of Turbulent Mass Transfer to a Pipe Wall," AIChE J., 10, 1964, pp. 475-482.

CALCULATION OF A TURBULENT BOUNDARY LAYER DOWNSTREAM OF A SUDDEN DECREASE IN SURFACE HEAT FLUX OR WALL TEMPERATURE

L. W. B. BROWNE and R. A. ANTONIA

Department of Mechanical Engineering
University of Newcastle, N.S.W., 2308, Australia

ABSTRACT

Results obtained with a calculation method that includes a two-equation model for the turbulence and a turbulent heat flux equation model are compared with the experimental results of a sudden change in surface heat flux or wall temperature. Temperature profiles, heat flux distributions and temperature fluctuation distributions are in reasonable agreement in the case of a sudden decrease in wall heat flux, but the agreement is only qualitative in the case of a sudden decrease in wall temperature. The calculation method yields practically the same results when a constant turbulent Prandtl number is used instead of the turbulent heat flux equation model.

INTRODUCTION

When the temperature difference across a turbulent boundary layer is sufficiently small the temperature may be treated as a passive marker of the layer and hence a useful aid to the study of transport mechanisms in the layer. Several experimental results have been reported on the response of a turbulent boundary layer to sudden changes in the surface temperature or heat flux and where the temperature is such a marker. Antonia *et al* (1) considered a sudden increase in wall heat flux while Fulachier (2), Blom (3) and Perry and Hoffmann (4) carried out experiments with a sudden increase in wall temperature. Subramanian and Antonia (5) examined a sudden decrease in wall heat flux while Charnay *et al* (6) considered a sudden decrease in wall temperature. In all these investigations, the momentum boundary layer developed with nominally zero pressure gradient and was approximately self-preserving immediately upstream of the change in surface condition. For the experiments of Subramanian and Antonia (5) and Charnay *et al* (6) the flow upstream of the change was slightly heated, as illustrated in Fig. 1. Origins for the momentum and thermal layers were approximately coincident and the layers were approximately self-preserving immediately upstream of the change in surface condition.

Browne and Antonia (7) found that their calculated mean temperature $\overline{T}(y)$ and heat flux $\overline{v\theta}(y)$ profiles downstream of a sudden increase in wall temperature were in reasonable agreement with the available measurements when the distance x_s, measured downstream of the change, exceeded about 20 δ_0 (δ_0 is the boundary layer thickness at the position of the change). Antonia and Danh (8) found that a distance of about 10 δ_0 was required before reasonable agreement was obtained between the calculation of Bradshaw and Unsworth (9), based on assuming a constant turbulent Prandtl number Pr_t (= 0.91), and the measurements of $\overline{T}(y)$ and $\overline{v\theta}(y)$ downstream of a sudden increase in wall heat flux. For this experimental situation, the calculation of Launder and Samaraweera (10), which used a transport equation for $\overline{v\theta}$, was in good agreement with the measured $\overline{v\theta}$ profiles for $x_s > 10\,\delta_0$ but indicated poor agreement with the measured mean temperature profiles at all values of x_s/δ_0 (the last measurement station was at 42.9).

In this paper, attention is focused on the calculation of the flow downstream of a sudden decrease in surface heat flux and a sudden decrease in wall temperature. The results from the calculations are compared with the experimental values reported by Subramanian and Antonia (5) and Charnay *et al* (6). The particular calculation method used here is the two-equation model of Wilcox and others (11, 12, 13) which also includes a transport equation for $\overline{v\theta}$.

EXPERIMENTAL CONDITIONS

These are shown in schematic form, in Fig. 1. In all cases the streamwise pressure gradient was negligible.

COMPARISON BETWEEN CALCULATIONS AND THE RESULTS OF SUBRAMANIAN AND ANTONIA (5)

Figures 2 to 5 compare calculations with the experimental results of Subramanian and Antonia (5). For the mean temperature profiles, Fig. 2, two points

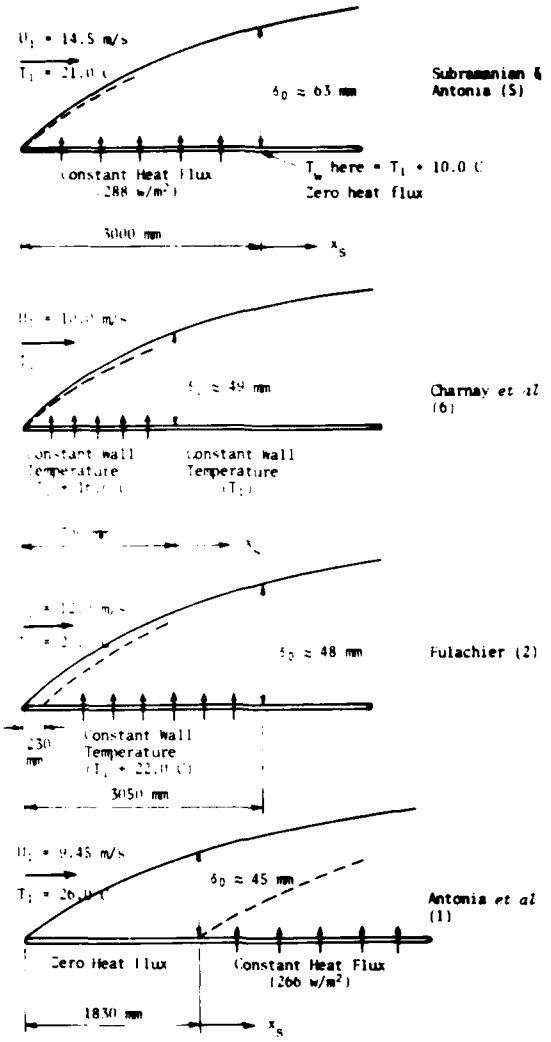

Fig. 1 Schematic layout of experimental arrangements. ——, representation of velocity boundary layer ---, representation of temperature boundary layer.

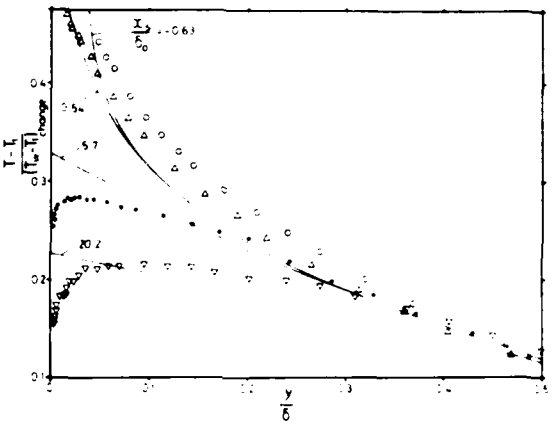

Fig. 2 Comparison between calculated mean temperature profiles and measurements of Subramanian and Antonia (5).
o, experiment $x_s/\delta_0 = -0.63$; Δ, experiment $x_s/\delta_0 = 0.54$; •, experiment $x_s/\delta_0 = 5.7$; ▽, experiment $x_s/\delta_0 = 20.2$; ——, calculation.

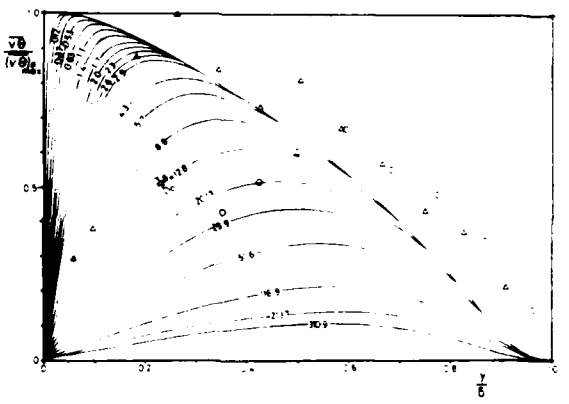

Fig. 3 Comparison between calculated heat flux distributions and measurements of Subramanian and Antonia (5).
Δ, experiment $x_s/\delta_0 = 1.0$; o, experiment $x_s/\delta_0 = 18.6$; ——, calculation.

need to be made. Firstly, it is difficult for the calculation method to simultaneously match the boundary layer thickness, wall heat flux and wall temperature upstream of the surface change, bearing in mind the fact that the effect of the trip used in the experiments could not be satisfactorily included in the calculations. Secondly, it is possible that the experimental wall heat flux at the surface downstream of the change was not quite zero. Mean temperature profiles very near the wall were not made but the mean enthalpy flux, obtained from the measured $U(y)$ and $T(y)$ profiles seemed consistent with $Q_w \simeq 0$. In the calculation, it is of course straightforward to equate Q_w to zero downstream of the change.

The $\overline{v\theta}$ calculations, Fig. 3, highlight the growth of the internal layer downstream of the change. At large distances downstream ($x_s/\delta_0 = 310$) the distributions are still discernable and qualitatively similar to those closer to the step. The few measurements indicate that the profile merge points coincide with those obtained by the calculation.

The agreement between calculated and experimental growth rates of the internal layer is shown in Fig. 4. Here δ_i is the thickness of the internal layer and is inferred in the calculation as the point where the local $\overline{v\theta}$ profile merges with the $\overline{v\theta}$ profile as $x_s/\delta_0 = 0$, while the experimental δ_i was inferred from the merge points of the $\overline{\theta^2}$ profiles. In both cases, the streamline displacement is taken into account in an approximate way by normalising y with the local boundary layer thickness δ.

Calculated and experimental values of $\overline{\theta^2}$, Fig. 5, are in reasonable agreement. The calculated $\overline{\theta^2}$ values were estimated using the equation suggested by

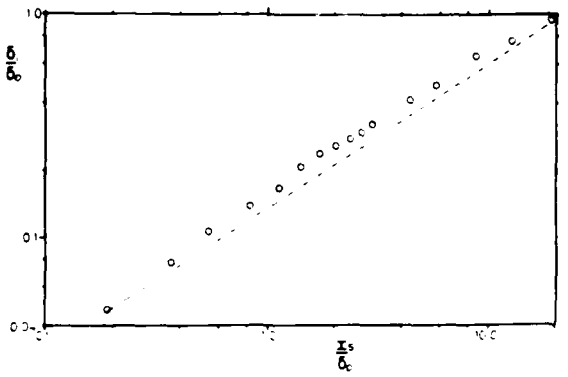

Fig. 4 Growth rate of internal layer downstream from a sudden decrease in heat flux.
---, best fit line to experimental data of Subramanian and Antonia (5); o, calculated values.

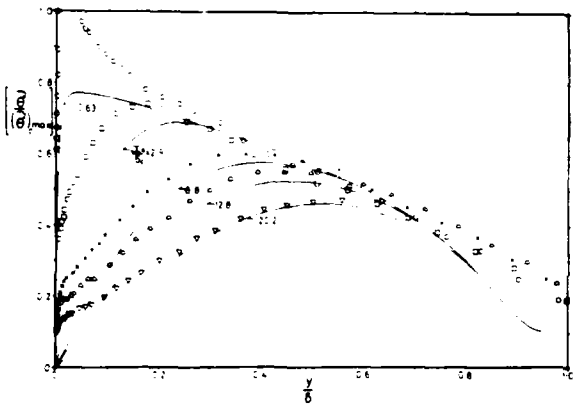

Fig. 5 Comparison between calculated $\overline{\theta^2}$ distributions and measurements of Subramanian and Antonia (5).
o, experiment x_s/δ_0 = -0.63; □, experiment x_s/δ_0 = 2.9; x, experiment x_s/δ_0 = 8.8; Δ, experiment x_s/δ_0 = 12.8; ▽, experiment x_s/δ_0 = 20.2; ——, calculation.

Fulachier (2)

$$\overline{\theta^2} = -\frac{(\overline{q^2})^{\frac{1}{2}}}{B}\,\frac{\left(\frac{\partial \overline{T}}{\partial y}\right)}{\left(\frac{\partial \overline{U}}{\partial y}\right)}$$

where $\frac{1}{2}\overline{q^2} = \frac{1}{2}(\overline{u^2} + \overline{v^2} + \overline{w^2})$ and B is a coefficient. For a fully developed temperature profile, Fulachier found experimentally that B remained remarkably constant, equal to 1.5, for a major part ($0.04 < y/\delta < 0.9$) of the layer. Calculations corresponding to Fulachier's case (cf. Fig. 1) using a B of 1.5 gave $\overline{\theta^2}$ profiles in close agreement with his experimental results. For the calculation curves of Fig. 5, a B value of 1.3 was used. By increasing B from 1.0 at small values of y/δ to 1.5 at large values of y/δ it was possible to obtain much better agreement than using the constant 1.3 value.

The streamwise decay (not shown here) of the maximum value of $(\overline{\theta^2})^{\frac{1}{2}}$ tends to be exponential while the maximum value of $\overline{v\theta}$ decreases a little more rapidly. A comparison of these decay rates with the growth rates corresponding to a sudden increase in heat flux, see Browne and Antonia (7), suggests that the relaxation distance of the flow may be larger in the case of the sudden decrease in heat flux.

COMPARISON BETWEEN CALCULATIONS AND THE RESULTS OF CHARNAY *et al* (6)

Charnay *et al* present mean temperature, $\overline{v\theta}$ and $\overline{\theta^2}$ distributions downstream of a sudden decrease in wall temperature and a comparison with calculations in a manner similar to that for the sudden decrease in heat flux was carried out. Unfortunately the quantitative agreement was poor, although qualitatively similar trends were obtained for distributions of $\overline{T}$, $\overline{v\theta}$ and $\overline{\theta^2}$ across the internal layer. The mean temperature results are shown in Fig. 6. The main problem

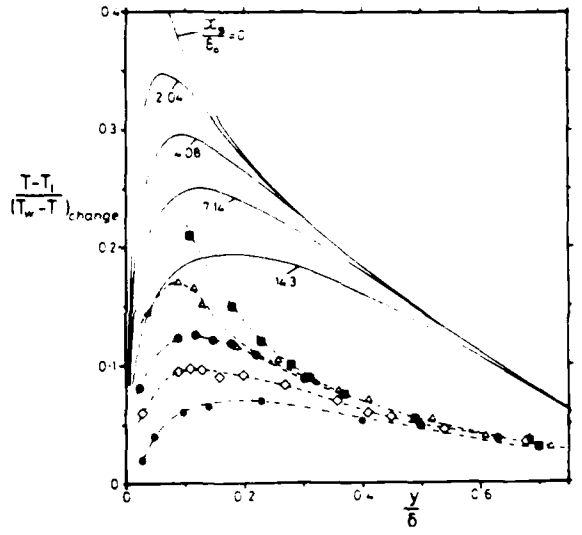

Fig. 6 Comparison between calculated mean temperature profiles and measurements of Charnay *et al* (6). --□--, experiment x_s/δ_0 = 0; --△--, experiment x_s/δ_0 = 2.04; --○--, experiment x_s/δ_0 = 4.08; -- --, experiment x_s/δ_0 = 7.14; --*--, experiment x_s/δ_0 = 14.3; ——, calculation.

seems to be the difficulty of reproducing the initial conditions, i.e. the temperature profile upstream of the change. The Charnay *et al* profile at this point is not in agreement with the general shape obtained in apparently similar experiments by others, for example the experiment (Fig. 1) of Fulachier (2). The calculation method reproduces the Fulachier profile reasonably well.

EFFECT OF USING CONSTANT TURBULENT PRANDTL NUMBER IN THE CALCULATIONS

The calculation method normally uses a diffusion type of equation for $\overline{v\theta}$ to obtain estimates of $\overline{v\theta}$ for input into the energy equation. An option is to use

a constant turbulent Prandtl number, Pr_t, and obtain $\overline{v\theta}$ from $-\alpha_t \partial\Theta/\partial y$, α_t being the eddy diffusivity of heat $= \nu_t/Pr_t$. The eddy diffusivity of momentum ν_t is obtained from the two-equation model of the calculation method.

An interesting result was that the mean temperature profiles, the $\overline{v\theta}$ distributions and the $\overline{\theta^2}$ distributions were practically identical whether the equation for $\overline{v\theta}$ was used or whether a constant turbulent Prandtl number, 0.89 in this case, was used. This is best illustrated by considering the results obtained from calculating the boundary layer downstream of a sudden increase in heat flux case, since Antonia *et al* (1) measured $\overline{v\theta}$ profiles at several stations downstream from the change. The experimental set-up of Antonia *et al* is shown in Fig. 1. The results are shown in Fig. 7 and good agreement is observed between

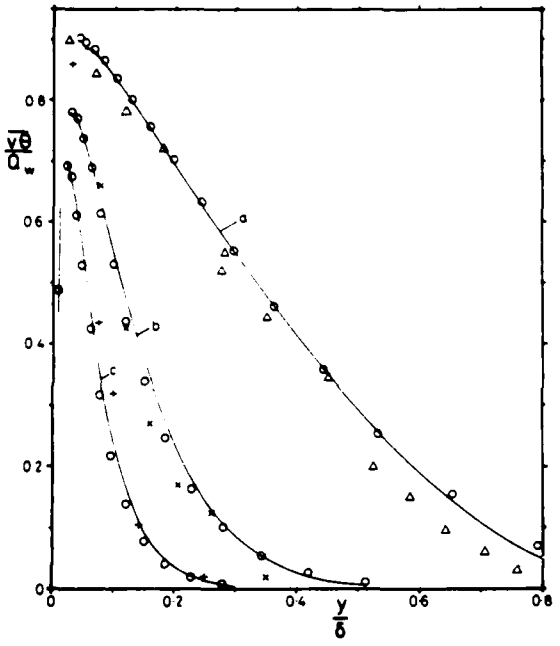

Fig. 7 Comparison between calculated heat flux distributions and measurements of Antonia *et al* (1).
a: $x_s/\delta_0 = 42.9$, Δ, experimental; o, calculation using heat flux model; ——, calculation using constant Pr_t;
b: $x_s/\delta_0 = 5.7$, x, experimental; o, calculation using heat flux model; ——, calculation using constant Pr_t;
c: $x_s/\delta_0 = 2.3$, +, experimental; o, calculation using heat flux model; ——, calculation using constant Pr_t.

calculations, using either the $\overline{v\theta}$ equation or a constant Pr_t (= 0.89), and experiments. When the $\overline{v\theta}$ equation is used, Pr_t can be calculated. Resulting distributions of Pr_t, obtained downstream of the sudden increase in heat flux, are shown in Fig. 8.

Experimental distributions of Pr_t, available in (1), at $x_s/\delta_0 = 2.3$ and 42.9 are slightly larger than unity in the inner region and increase with increasing

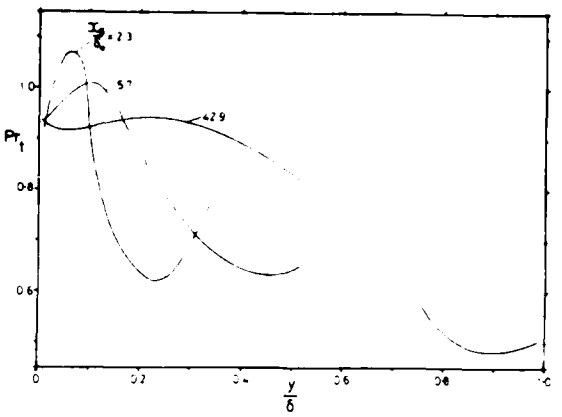

Fig. 8 Turbulent Prandtl number distributions obtained when using a heat flux model to calculate the Antonia *et al* (1) flow.

y/δ in the outer region. However, measured distributions of Pr_t obtained in the range $2.3 < x_s/\delta_0 < 42.9$ could be considered to be in better qualitative agreement with the distributions of Fig. 8. It would appear that the relatively large uncertainty in experimental values of Pr_t would make it difficult to prescribe the variation of Pr_t across the thermal layer (a constant Pr_t does not seem unreasonable!). The good agreement between the calculations and experiment (Fig. 7) for small values of x_s/δ_0 is surprising in view of the non-equilibrium nature of the flow in this region. The budget of $\overline{v\theta}$, measured by Danh (14) indicates that the diffusion term may become significant in comparison with the production and destruction terms. More work is required with regard to both experiments and models to determine the magnitude of each term in the $\overline{v\theta}$ equation, especially for small values of x_s/δ_0.

ACKNOWLEDGEMENT

The authors are grateful to Mr. C. S. Subramanian for making his experimental data available to them. The support of the A.R.G.C. is gratefully acknowledged.

REFERENCES

1 Antonia, R. A., Danh, H. Q. and Prabhu, A., "Response of a Turbulent Boundary Layer to a Step Change in Surface Heat Flux", *J. Fluid Mech.*, Vol. 80, 1977, pp.153-177.

2 Fulachier, L., "Contribution à l'Étude des Analogies des Champs Dynamique et Thermique dans une Couche Limite Turbulente. Effet de l'Aspiration", Thèse Docteur ès Sciences, Université de Provence, Marseille, 1972.

3 Blom, J., "An Experimental Determination of the Turbulent Prandtl Number in a Developing Temperature Boundary Layer", Ph.D. Thesis, Technological University, Eindhoven, 1970.

4 Perry, A. E. and Hoffmann, P. H., "An Experimental study of Turbulent Convective Heat Transfer from a Flat Plate", *Report FM7*, Fluid Mechanics Group, Department of Mechanical Engineering, University of Melbourne, Australia, 1976.

5 Subramanian, C. S. and Antonia, R. A., "A Study of a Turbulent Boundary Layer Downstream of a Sudden Decrease in Wall Heat Flux", to appear in *Int. J. Heat Mass Transfer*.

6 Charnay, G., Schon, J. P., Alcaraz, E. and Mathieu, J., "Thermal Characteristics of a Turbulent Boundary Layer with Inversion of Wall Heat Flux", *Proc. Symposium on Turbulent Shear Flows I*, Penn. State Conference, Pennsylvania State University, U.S.A., 1977, pp.104-118.

7 Browne, L. W. B. and Antonia, R. A., "Calculation of a Turbulent Boundary Layer Downstream of a Step Change in Surface Temperature", *J. Heat Transfer*, Vol. 101, 1979, pp.144-150.

8 Antonia, R. A. and Danh, H. Q., "Calculation of a Turbulent Boundary Layer Downstream of a Step Change in Surface Heat Flux", *Thermofluids Conference*, The Institution of Engineers - Australia, Hobart, 1976, pp.94-97.

9 Bradshaw, P. and Unsworth, K., "An Improved Fortran Program for the Bradshaw-Ferriss-Atwell Method of Calculating Turbulent Shear Layers", *I.C. Aero Report 74-02*, Imperial College, London, 1974.

10 Launder, B. E. and Samaraweera, D. S. A., "Application of a Second-Moment Turbulence Closure To Heat and Mass Transport in Thin Shear Flows - 1. Two-Dimensional Transport", *Int. J. Heat Mass Transfer*, Vol. 22, 1979, pp.1631-1643.

11 Wilcox, D. C. and Traci, R. M., "A Complete Model of Turbulence", *AIAA Paper No. 76-351*, 1976.

12 Wilcox, D. C. and Chambers, T. L., "Streamline Curvature Effects on Turbulent Boundary Layers", *Report No. DCW-R-04-01*, DCW Industries, 4360 Troost Avenue, Studio City, CA 91604, U.S.A., 1975.

13 Wilcox, D. C., "User's Guide for the EDDYBL Computer Program", DCW Industries, 4360 Troost Avenue, Stuido City, CA 91604, U.S.A., 1976.

14 Danh, H. Q., "Turbulent Transfer Processes in Non-Isothermal Shear Flows", Ph.D. Thesis, University of Sydney, 1976.

TURBULENT BOUNDARY LAYERS ON FLAT PLATES AND IN CONTRACTED OR EXPANDED CHANNELS WITH ANGLED INJECTION AND SUCTION

Yeroshenko V.M., Yershov A.V., Zaichik L.I.,
Klimov A.A., Kondratiev V.I., Yanovsky L.S.

Krzhizhanovsky Power Institute, Moscow, USSR

ABSTRACT

Results from both the experimental and theoretical study of turbulent boundary layers on porous and perforated surfaces with angled injection and suction are presented. Effects of the velocity ratio and injection (suction) direction on mean and turbulent flow behaviour are shown

NOMENCLATURE

- δ = injection(suction) parameter $2F/C_{f_0}$
- δ_c = critical injection parameter
- C_f = flow friction factor $2\tau_w/\rho_e u_e^2$
- E = turbulence energy
- f = dissipation rate $E^{3/2}/L$
- F = velocity ratio V_w/u_e
- H_1, H_2 = boundary layer formfactors $\delta_1/\delta_2, \delta_3/\delta_2$
- K = pressure gradient factor $\nu/u_e^2 (du_e/dx)$
- L = length scale
- u, v = streamwise and crosswise mean velocity components
- p = pressure
- Re_e = turbulent Reynolds number EL/ν
- x, y = streamwise and crosswise coordinates
- α = hole axis inclination angle relative to the surface
- δ = boundary layer thickness
- $\delta_1, \delta_2, \delta_3$ = displacement, momentum and energy thicknesses correspondingly
- ε = turbulence intensity
- ε_D = turbulent diffusion coefficient $0.2E^{1/2}L$
- ν = kinematic viscosity
- σ = turbulent shear stress
- τ_w = wall friction
- Ψ = relative flow friction factor C_f/C_{f_0}

SUBSCRIPTS

- 0 = zero injection
- e = outer edge of the boundary layer
- w = wall

1. Introduction

Injection or suction through permeable construction elements is considered to be one of the most effective means of controling flow structure and heat- and mass transfer in turbulent boundary layers. The most of studies on this topic deals with flow and heat- and mass transfer behaviour for the case of the normal injection (suction). The questions of the injection(suction) with angles other than 90^0 have been studied much less and relate generally to laminar boundary layers. Results for turbulent flows with $\alpha \neq 90^0$ have been obtained for the down stream injection through perforated surfaces only [1,2].

The experiments were conducted in the wind tunnel. The test section was a square channel of 40 x 40 mm with the movable upper wall which allowed to control the streamwise pressure gradients [3]. The porous and perforated plates with the uniform permeability of 135x40 were used with hole axis inclination angles relative to the surface α = $15^0, 20^0, 25^0, 45^0, 75^0$ and 90^0. The perforated plates had holes of 0.40 mm staggered with the streamwise and lateral spacings equal nearly to the hole diameter. The porous plates were fabricated by the rolling procedure using packages of stainless steel wire nets.

The isothermal fully developed turbulent boundary layer (the Reynolds number based on

the permeable plate length was $2 \cdot 10^5$) was measured in the range of velocity ratio $F = (-4.7 \div 6.5) \cdot 10^{-2}$ under the adverse and accelerating pressure gradients with $K = (-2.2 \div 4.8) \cdot 10^{-6}$.

The velocity field and turbulent fluctuations were measured using the thermoanemometer "DISA 55 D" in 5-7 sections of permeable plates.

2 Experimental results for the injection

The experiments with $dP/dx = 0$ showed that for a weak injection ($\beta/\beta_c < 0.2$), as the velocity ratio increases the mean velocity profiles tend to be less filled (Fig. 1,a), the turbulent fluctuation velocities near the wall decrease and their maximum shifts into the outer region (Fig.1,b) for all angles α and for both cases of the porous and perforated plates.The comparison of the mean velocity profiles showed that the effects of the weak injection with the angle $\alpha \neq 90^0$ on the mean flow differ a little from those for the normal injection with the same F .This finding can be explained by the fact that the injectant momentum is small as compared to that of the free flow. Hence,only the injection flow rate has a crucial effect on the boundary layer irrespective of the angle and supply way (pores, perforations).

For a moderate injection ($0.2 < \beta/\beta_c < 1$), the change of the velocity profile filling up with F tends to depend on the injection angle α : the profiles are more filled at $\alpha < 90^0$ and less filled at $\alpha > 90^0$ as compared to the normal injection, this trend does not depend on the injectinn way.

For a strong injection ($\beta > \beta_c$), with $\alpha < 90^0$ the character of the velocity profile deformation with F in the inner region over the porous and perforated plates reverses as compared to the normal case,i.e. the filling up of the profiles increases, the effect is higher for smaller injection angles. This result can be explained by the fact that the injectant has here a considerable tangential momentum and, in addition to the flow deceleration due to the normal component of the injection momentum, the acceleration of the flow near the wall is induced. (Fig. 2,c).

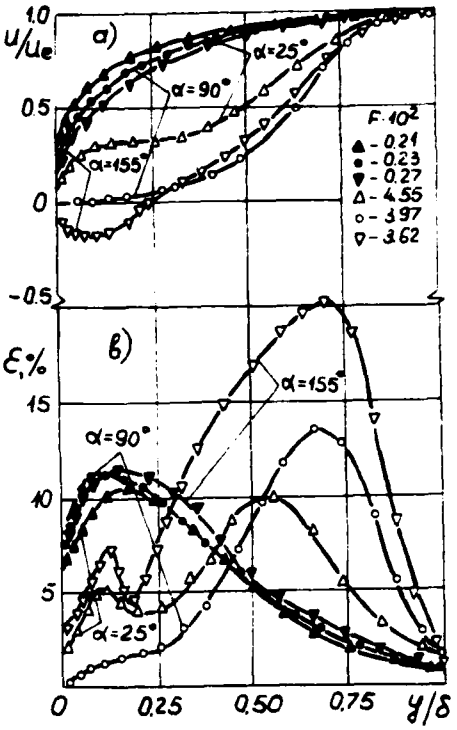

Fig.1 The profiles of the mean and turbulent fluctuation velocities for the porous angled injection with $dP/dx = 0$

Under the conditions of the strong injection with $\alpha > 90^0$ the mean velocity profiles take the S-shape as for the normal injection, i.e. they have a flex point in the outer region. However, in contrast to the normal case, a reverse flow in the upstream direction is induced near the wall (Fig. 2,a). The presense of the reverse flow on the permeable wall for the strong injection $\beta > \beta_c$ evidences the change of the wall friction sign, i.e. the realization of the critical injection condition ($\tau_w = 0$). Thus,an intensive circulation near the wall appears,inside of which the streamline $u = 0$ is located.

The measurements showed that the boundary layer both on the porous and perforated surfaces grows along the plate with the

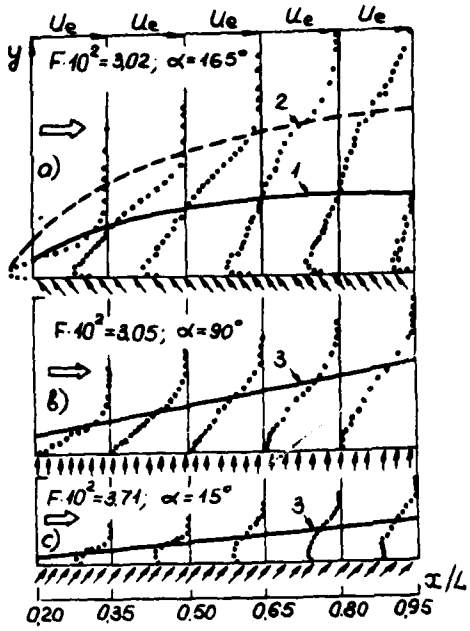

Fig.2 The flow development along the porous plate for the injection with $dP/dx=0$
1 - streamline $U=0$,
2 - circulation zone edge Z: $\int_0^{Z}\rho u\,dy=0$,
3 - dividing streamline Z_1: $\int_0^{Z_1}\rho u/(\rho u)_e=F\cdot x$

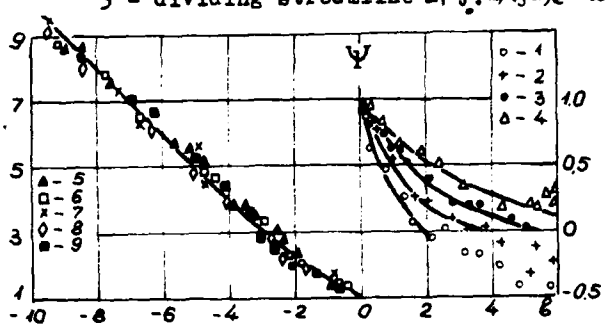

Fig.3 The effects of the angled injection and suction on the relative flow friction factor
K = 0; 1,9 - $\alpha=165°$; 2 - 155°; 3,5 - 90°; 4,8 - 15°; 6 - $K=4\cdot10^{-6}$, $\alpha=90°$; 7 - $K=-1.9\cdot10^{-6}$, $\alpha=90°$

rate depending on the injection angle: the layer thickness slower at $\alpha<90°$ and faster at $\alpha>90°$ as compared to the normal injection with the same F. The displacement thickness δ_1 and the momentum thickness δ_2 show the similar behaviour.

The wall friction τ_w on the porous and perforated surfaces was estimated from the momentum equation. It was found that the dependence of the flow friction factor Ψ on the injection parameter b is different for various angles: the value of C_f decreases slower at $\alpha<90°$ and faster at $\alpha>90°$ as compared to the normal injection (Fig.3).

A general for all α correlation of the wall friction with the injection parameter is found in the paper. The correlation can be fitted by the well-known Kutateladze-Leontiev equation [4] for the normal injection with a correction of the critical parameters on the injection angle:

$$\Psi=\left(1-\frac{b}{b_c}\right)^2 \qquad (1)$$

where

$$\frac{b_c(\alpha)}{b_c(90°)}=1.5-0.5\frac{\alpha}{90°}\quad \text{for } \alpha\le 90°$$

and (2)

$$\frac{b_c(\alpha)}{b_c(90°)}=\frac{\alpha}{90°}\left(2-\frac{\alpha}{90°}\right)\quad \text{for } \alpha\ge 90°$$

Fig.4 shows distributions of the mean and turbulent fluctuation velocities in the flow with the reverse and accelerating pressure gradients. The effect of the adverse pressure gradient results in more intensive

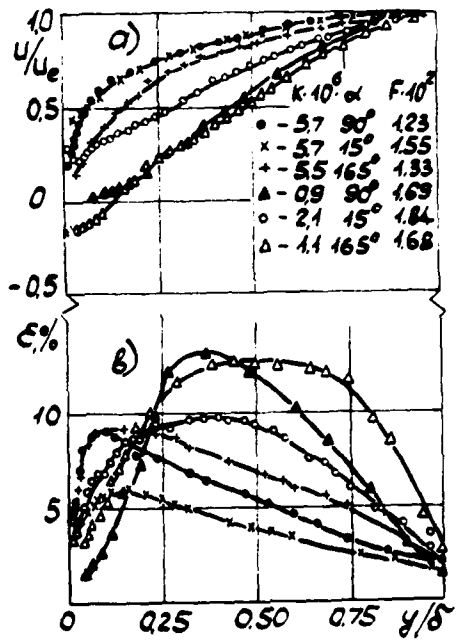

Fig.4. The profiles of the mean and turbulent fluctuation velocities for the porous angeled injection with pressure gradients

velocity profile deformation.The separation of the boundary layer and the appearance of the reverse flow region are observed for the lower velocity ratios than in the nongradient flow,especially in conditions of the upstream injection.

In the case of the downstream injection, S-shaped velocity profiles do not form. As the velocity ratio increases the mean velocity profiles tend to be less filled, the fluctuation maximum rises and shifts from the wall.For velocity ratios $F > 1.7 \times 10^{-2}$ the profile filling up increases across the whole boundary layer in the presence of the adverse pressure gradient and in the inner region only if the pressure gradient is absent.The injection into the flow with the adverse pressure gradient causes the appearing of the second mean velocity maximum at $y/\delta = 0.015$. (Fig.5).

The flow under the accelerating pressure gradient with moderate velocity ratios is characterized by decreasing velocity profile filling up for all injection angles. For a strong injection, the profiles tend to be more filled in the outer region of the boundary layer. The mean velocity profiles for the downstream injection differ from those for the normal case in the vicinity of the wall only (Fig.4): their filling up is higher and the rate of fluctuation decay is much more intensive.For the upstream injection,the velocity profile filling up decreases more rapidly than for $\alpha = 90^0$ and $\alpha = 15^0$ and the fluctuation velocity distribution becomes more filled. The boundary layer separation,however,was not observed for all velocity ratios studied.

3 Experimental results for the suction

Fig.6 shows mean and turbulent fluctuation velocities profiles on the perforated plates for the suction with $\alpha \neq 90^0$ for the nongradient flow. The measurements showed effects of the suction angle on the boundary layer growth.As $\alpha = 20^0$ (the upstream suction) the velocity profiles are less

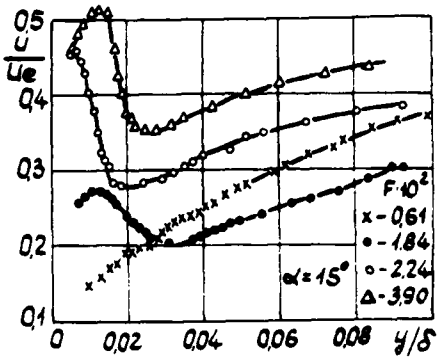

Fig.5 The profiles of the mean velocities near the wall for dP/dx>0

filled than for $\alpha = 90^0$. It can be explained by the contribution of the streamwise suction velocity component which is directed up the main flow.As $\alpha = 160^0$(the downstream suction) the velocity profiles become more filled than for $\alpha = 20^0$ which is due to the streamwise suction component down the flow. For the normal suction ($\alpha = 90^0$) the velocity ratio increase results in the most considerable decay of the turbulent fluctuation.The fluctuation maximum shifts towards the wall at $\alpha \geq 90^0$ and from the wall at $\alpha < 90^0$. The level of turbulent fluctuations for the upstream suction increases in the outer region of the boundary layer.Both for the downstream and upstream suction, the mean velocity profiles are less filled than for $\alpha = 90^0$.

The measurements on the porous plates with $\alpha = 15^0, 75^0, 90^0, 105^0$ and 165^0 did not show considerable differences for all cases mentioned.It is explained by the fact that the pores are so small that the sucked fluid jets can not turn at the corresponding angle.

The comparison of data for the porous and perforated plates shows that for equal velocity ratios,the mean velocity profiles on the perforated plates proved to be more filled,i.e.the suction through a perforated plate is more effective as compared to the porous suction.

Fig.7 shows mean and turbulent fluctuation velocity profiles for the suction through the porous plate in flows with adverse and accelerating pressure gradients. The strongest effects of the suction on the boundary layer is in evidence in the very vicinity of the wall. The magnitudes of the fluctuation maximum both under the adverse and accelerating pressure gradients for the same velocity ratios differ a little from

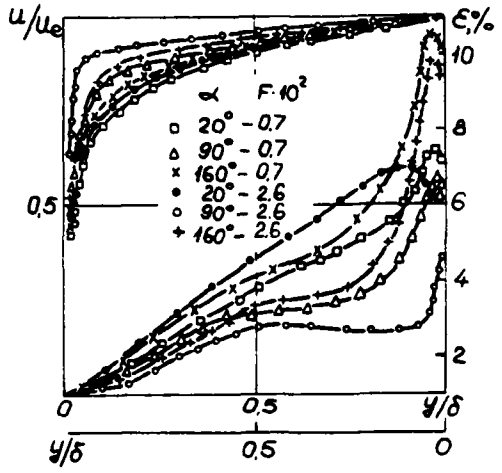

Fig.6. The profiles of the mean and turbulent fluctuation velocities for the perforated angled suction

each other. However, in the outer region of the boundary layer, the level of velocity fluctuations in the presence of the accelerating pressure gradient decreases with velocity ratio stronger than in the case of the adverse pressure gradient.

Fig.3 shows the measured flow friction factors for the porous plates in the flows with $dP/dx > 0$, $dP/dx < 0$ and $dP/dx = 0$. Although C_f depends on the pressure gradient the relative flow friction factor Ψ depends only on β :for $|\beta| > 4$ $\Psi = -\beta$ and for $|\beta| < 4$ $\Psi = (1 + \beta/4)^2$.

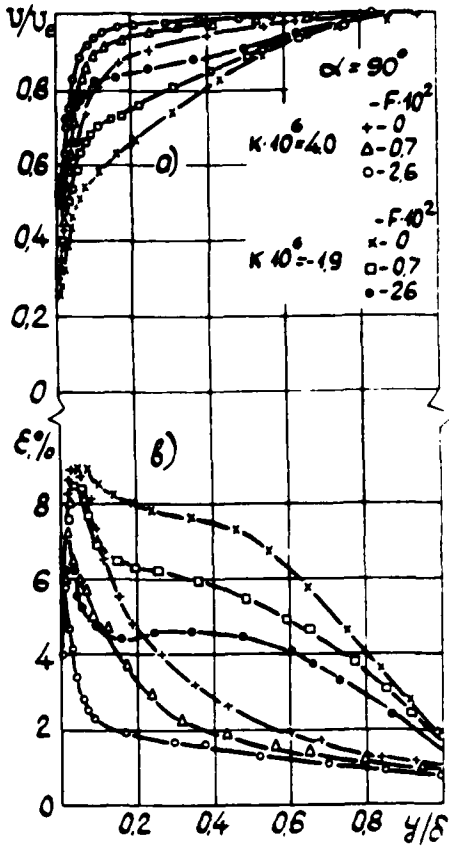

Fig.7 The profiles of the mean (a) and turbulent fluctuation velocities (b) for porous normal suction under pressure gradients

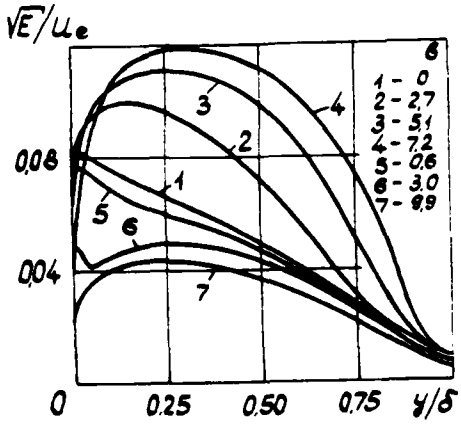

Fig.8 The profiles of turbulence energy in the parallel plate channel

4 Prediction of the developing flow in a parallel plate channel

The report presents also the prediction of the flow behaviour in the entrance region of the parallel plate channel with the normal ($\alpha = 90^0$) injection and suction for the conditions corresponding to the experiments described. An accelerating pressure gradient is induced in the channel by the injection and adverse one - by the suction. A three-parametric turbulence model is used for the turbulent transfer description. The model is based on the transport equations for turbulent energy, Reynolds shear stresses and dissipation rate. Using the boundary layer approximation one governing equation set can be written as follows:

$$u\frac{\partial u}{\partial x}+v\frac{\partial u}{\partial y}=-\frac{1}{\rho}\frac{dP}{dx}+\frac{\partial}{\partial y}\left(\nu\frac{\partial u}{\partial y}+\sigma\right) \qquad (3)$$

$$\frac{\partial u}{\partial x}+\frac{\partial v}{\partial y}=0 \qquad (4)$$

$$u\frac{\partial E}{\partial x}+v\frac{\partial E}{\partial y}=\sigma\frac{\partial u}{\partial y}-\frac{CE^{3/2}}{L}-\frac{C_{1E}\nu E}{L^2}+$$
$$+\frac{\partial}{\partial y}\left[(\nu+\varepsilon_D)\frac{\partial E}{\partial y}\right] \qquad (5)$$

$$u\frac{\partial \sigma}{\partial x}+v\frac{\partial \sigma}{\partial y}=K_1\left[1-\exp(-\gamma Re_E)\right]E\frac{\partial u}{\partial y}-$$
$$-\frac{KE^{1/2}\sigma}{L}-\frac{C_{1\sigma}\nu\sigma}{L^2}+\frac{\partial}{\partial y}\left[(\nu+\varepsilon_D)\frac{\partial \sigma}{\partial y}\right] \qquad (\ )$$

$$u\frac{\partial f}{\partial x}+v\frac{\partial f}{\partial y}=\frac{a\sigma f}{E}\frac{\partial u}{\partial y}-\frac{2CE^{1/2}}{L}-\frac{C_{1f}\nu f}{L^2}+$$
$$+\frac{\partial}{\partial y}\left[(\nu+\varepsilon_D)\frac{\partial f}{\partial y}\right] \qquad (7)$$

The constants in the equations above are: $a = 0.2$; $C = 0.13$; $C_{1E} = C_{1f} = 0.32$; $C_{1\sigma} = 1.92$; $K_1 = 0.2$; $\gamma = 0.06$; $K = 0.35$;

The calculated mean velocity and turbulent energy profiles agree satisfactorily with the experimental data. Fig.8 shows that the turbulent fluctuation maximum increases with the injection velocity, tends to flatten and shifts from the wall. In the suction case the turbulence intensity decreases and two maxima in the turbulence energy profiles appear for some suction velocities which is typical for the flow with the suction under the adverse pressure gradient (fig.7).

The subsequent increase of the suction velocity results in the disappearance of the turbulent energy maximum near the wall.

Fig.9 shows the experimental values of the formfactor H for the nongradient boundary layer in the contracted and expanded channels for $\alpha = 90^0$ as well as a predicted correlation (the curve 1) for the parallel plate channel. It is seen that the formfactor H depends strongly on the pressure gradient in the injection case and weakly in the suction case.

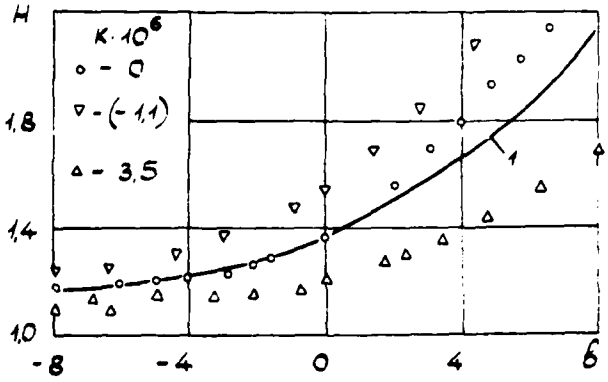

Fig.9 The correlation between the formfactor and velocity ratio

REFERENCES

1 Launder, B.E., and York, I., "Discrete-Hole Cooling in the Presence of Free Stream Turbulence and Strong Favourable Pressure Gradient", International Journal Heat and Mass Transfer, Vol.17, No.11, 1974, pp.1403-1409.

2 Yavuzkurt, S., Moffat, R.P., and Kays, W.M., "Full-Coverage Film Cooling, Part 1. Three-Dimensional Measurements of Turbulence Structure", Journal of Fluids Mechanics, Vol.101, Part 1, 1980, pp.129-158.

3 Yeroshenko, V.M., Klimov, A.A., Motulevich, V.P., and Terentiev, U.N. "An Experimental Study of Velocity and Concentration Profiles in Binary Mixing Zones", "Thermoaerodynamika", Minsk, 1970, pp.58-75.

4 Kutateladze S.S., and Leontiev A.I., "Turbulent Boundary Layers in Compressible Gases", Academic Press, 1964.

EXPERIMENTAL INVESTIGATION OF A TURBULENT BOUNDARY LAYER STRUCTURE IN THE REGION OF A GAS SCREEN

Yu.V.Baryshev, A.I.Leontiev and N.K.Peiker

Institute for High Temperatures, Moscow, U.S.S.R.

ABSTRACT

The paper presents the data on experimental investigation of the structure and integral characteristics of a subsonic turbulent boundary layer in the region of a gas screen downstream of a permeable section over a wide range of injection intensities, j, from 0.003 to 0.04. The data have been obtained ondistribution of local friction coefficients, averaged velocities, their pulsation components and turbulent shear stresses over the entire range of the injection intensities investigated.

NOMENCLATURE

- x, y - longitudinal and transverse coordinates;
- x_1 - permeable plate length;
- δ - dynamic boundary layer thickness;
- y^+ - dimensionless coordinate;
- u, v - averaged velocity projection on the axes x and y, respectively;
- u^+ - dimensionless velocity;
- $\langle u' \rangle, \langle v' \rangle$ - longitudinal and transverse pulsations of the averaged velocity, ;
- δ^{**} - momentum loss thickness;
- ν - cinematic viscosity;
- $j = (\rho v)_w / (\rho u)_0$ - injection intensity;
- τ - tangential stress;
- c_f - friction coefficient;
- $Re_{\Delta x}$, Re^{**} - Reynolds numbers calculated using longitudinal coordinate and momentum loss thickness;
- θ_f - friction efficiency parameter in the region of a gas screen

Indices:

- 0 - undisturbed flow parameters;
- w - wall;
- 1 - end of the permeable section;
- ^{o} - standard conditions;
- t - turbulent

Porous cooling is currently one of the most promising methods of thermal protection. Some attempts have been made to use this method for decreasing the temperature of gas turbune vane surfaces, MHD generator channel walls etc., where it is difficult to create continuous permeable surfaces. Hence the interest in realization of protecting proper -

ties of a "cold" boundary layer downstream of the permeable section, i.e. in the region of a gas screen.

As a rule, a turbulent boundary layer is developed downstream of the permeable surface in the region of a gas screen.

It is known that the turbulent boundary layer equations in the general case are not closed, while for solution of specific problems one of the techniques of approximate closing of equations is used. Closing is usually based on information on integral characteristics and structure of the turbulent boundary layer. The lower-order moments are of greater interest, since their values define the turbulent boun - dary layer properties having an explicit physical sense.

Moments of the first order are represented by the values of velocity, pressure and other quantities, one-point central moments of the second order determine the turbulence energy and the transfer of amount of motion, heat and impurities, while two-point moments of the second order make it possible to judge about the correlation of different-value pulsations at the unevenly-spaced points, thus determining the turbulence spectrum.

This paper presents the results of experimental investigation of the structure and integral characteristics of a dynamic boundary layer downstream of the permeable section over the wide injection intensity range, j= 0.003-0.04.

The experiments were conducted on a small continuous-operation subsonic wind tunnel (Institute of Mechanics of the Moscow State University), the working section of which consisted of a rectangular channel with the cross-section dimensions 0.07 x $0.075m^2$ and the length 0.6 m. The upper wall was a model, and the lower one was flexible and allowed variation, depending on the injection intensity, of the working part height and profile, while maintaining a constant static pressure along the entire length of the working part. The flow parameters were constant and equalled: velocity, 50 m/sec; Reynolds number per 1 m, $3.6 \cdot 10^6$; temperature, 290÷ 300 K; turbulance degree, 0.2÷ 0.3%. The measurement model consisted of a permeable section 0.16 m long, and an impermeable plate with the length 0.22m, erected immediately downstream of the injection section. Description of the experimental set-up of a similar model, supply and injected air control system is given in more detail in /1-2/.

For measurements, the DISA thermoanemometer 55 M0I with the high-speed bridge 55 M0I and auxiliary devices were used. The distance from the wall to the probe thread was determined using the cathetometer KM-8.

Before and after conducting the experiments, the thermoanemometer indicator was calibrated in the working position in the wind tunnel. Careful clearing of the flow /2/ made it possible to maintain stable calibrating dependencies during several hours of the set-up operation. When taking measurements, special attention was given to the equality of temperature of the injected air and that of the main flow, in order to avoid a possible effect of temperature nonuniformity over the boundary layer cros- section on the measurement results /3/.

Calibration experiments without injection have shown that a developed turbulent boundary layer with a universal profile of the averaged velocity in a viscous sublayer and the wall law, flows onto the measurement section.

Figure 1 displays the measured profiles of aversged velocities in the region of a gas screen. It is clear that in the absence of injection the velocityprofile is satisfactorily defined by the universal profile in a viscous sublayer /4/:

$$y^+ = u^+, \quad u^+ = u/u_\tau, \quad u_\tau = \sqrt{\tau_w/\rho} \qquad (1)$$

and the wall law /4/:

$$u^+ = 5.75 \lg y^+ + 5.5 \qquad (2)$$

Accordingly, the local friction coefficients calculated from the measured gradients of averaged velocity in a viscous sublayer (Fig.2) are well described by the friction law /5/. With an increase of injection in-

tensity, velocity profiles deviate from the wall law, while maintaining universal distribution in a viscous sublayer. The larger the injection intensity, the larger the difference between the experimental and universal profiles and the greater the effect of jet turbulence.

Measurements of intensity distributions of turbulent pulsations of averaged velocity demonstrate (Fig. 3) that with an increase of injection intensity an increase of pulsation components is observed, with their intensity maxima forced back from the wall. In the absence of injection, longitudinal pulsations have a pronounced maximum near the wall, while the transverse pulsations maximum is diffuse and displaced further from the wall with respect to longitudinal pulsations. Under the injection conditions, a similarity is observed in the character of longitudinal and transverse pulsations and coincidence of their maxima, which proves that the turbulence near the wall is isotropic during injection and that there are no elongated vortex structures as is the case in the absence of injection. Generation zone of turbulent pulsations is considerably expanded in the external part of the turbulent boundary layer which is a transient region between the pulsation generation zone and free flow, the turbulence structure is universal, which is proved by measurements of averaged velocities.

In Ref / 6 / it is shown that introducing of the parameter of friction efficiency in the region of a gas screen, characterizing momentum transfer in the boundary layer

$$\theta_f = \frac{c_f^o - c_f}{c_f^o - c_{f1}} \qquad (3)$$

makes it possible to generalize the experimental data on friction by a common dependence similar to the calculation of the gas screen efficiency / 6 /:

$$\theta_f = (1 + 0{,}1A)^{-0.8}$$

$$A = Re_{\Delta x} / Re_1^{**1.25}, \quad Re_{\Delta x} = u_0 \Delta x / \nu_0, \qquad (4)$$

$$Re_1^{**} = u_0 \delta_1^{**} / \nu_0, \quad \Delta x = x - x_1$$

Measurements of turbulent shear stresses have shown (Fig. 4) that in the absence of injection the stress maximum is located on the wall and coincides with the local coefficient. With an increase of injection intensity, the friction stress on the wall noticeably decreases, while in the boundary layer it is considerably increased, reaching the maximum displaced from the wall. In this case, the effect of injections essentially decreases in direct proportion to the distance from the permeable section (Fig. 5).

On the whole, the experimental data obtained demonsrate a strong effect of injection on the averaged and pulsation characteristics of a turbulent boundary layer in the region of a gas screen. Analysis of these data makes it possible to define more accurately the local and integral properties of the flow downstream of a permeable surface.

REFERENCES

1. Rozhdestvensky, V.I., Baryshev, Yu.V., and Peiker, N.K. "A Study of Gas Screen Efficiency in the Presence of Longitudinal Pressure Gradient", Report No.1526 of the Institute of Mechanics, Moscow State University, 1974.
2. Baryshev, Yu.V., Leontiev, A.I., and Peiker, N.K. "Turbulent Boundary Layer on Permeable Surface at Intensive Blowing-In", Inzh. Fiz. Zh, Vol. 30, No. 5, 1976, pp. 773-779.
3. Bradshaw, P. "Introduction to Turbulence and Its Measurements", Izd. "Mir", Moscow, 1974.
4. Shlikhting, G. "Boundary Layer Theory", Izd. "Nauka", Moscow, 1974.
5. Kutateladze, S.S., and Leontiev, A.I. "Heat Transfer and Friction in a Turbulent Boundary Layer", Izd. "Energiya", Moscow, 1972.
6. Baryshev, Yu.V., Leontiev, A.I., Peiker, N.K. "The Laws of Heat Transfer and Friction into the Gas Screen Region", Sixth International Heat Transfer Conference,

Toronto, Canada, Vol. 5, 1978, pp. 245-248.

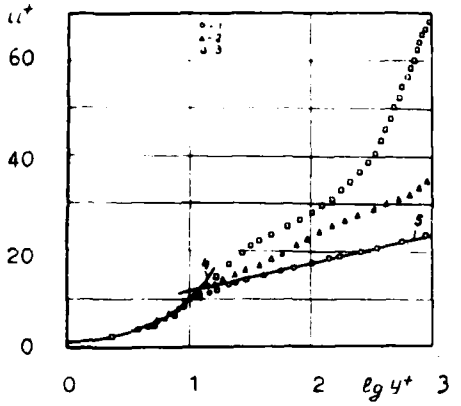

Fig. 1. Averaged velocity profiles in the region of a gas screen ($Re_x = 1.04 \cdot 10^6$).
1- j = 0; 2- 0.003; 3- 0.02;
4- calculation using Eq.1;
5- calculation using Eq.2.

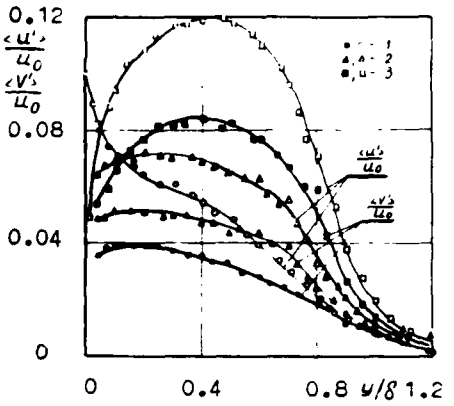

Fig.3. Distribution of averaged velocity pulsations in the region of a gas screen ($Re_x = 1.04 \cdot 10^6$).
1- j = 0; 2- 0.003; 3- 0.02.

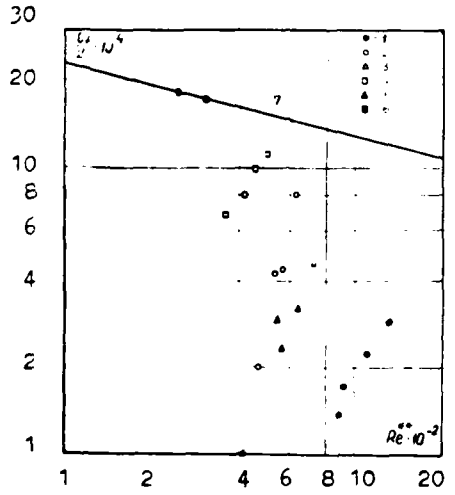

Fig. 2. Experimental data on friction in the region of a gas screen.
1-x_1 = 0.16m, j = 0.02;
2-x_1 = 0.02m, j = 0.02;
3-x_1 = 0.16m, j = 0.011;
4-x_1 = 0.16m, j = 0.003;
5-x_1 = 0.4m, j = 0.04;
6-x_1 = 0;
7- calculation using /5/.

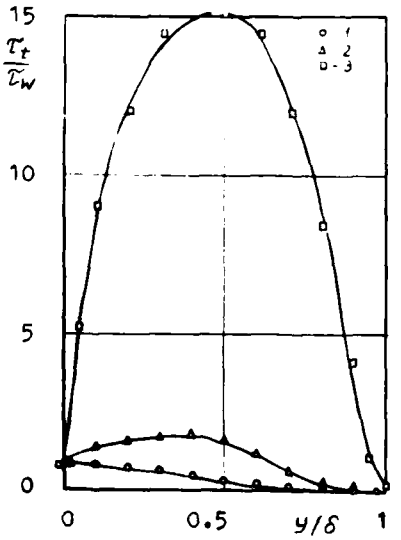

Fig.4. Distribution of turbulent shear stresses in the region of a gas screen ($Re_x = 1.04 \cdot 10^6$).
1- j = o; 2- 0.003; 3- 0.02.

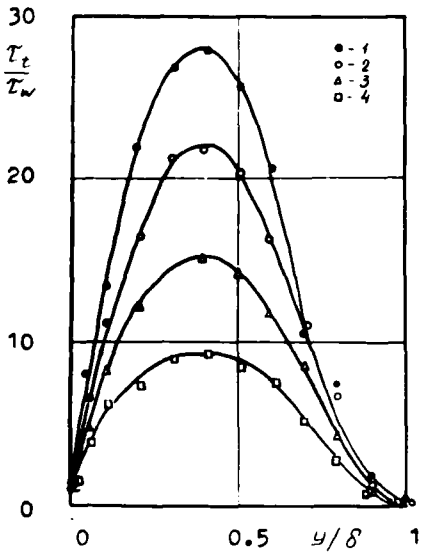

Fig.5. Distribution of turbulent shear stresses downstream of a permeable section (j = 0.02).
1- $Re_x = 0.828 \cdot 10^6$;
2- $Re_x = 0.9 \cdot 10^6$;
3- $Re_x = 1.04 \cdot 10^6$;
4- $Re_x = 1.33 \cdot 10^6$.

SESSION 11 - COHERENT STRUCTURES I

I. Wygnanski - Chairman

COHERENT STRUCTURES IN THE SIMILARITY REGION OF TWO-DIMENSIONAL TURBULENT JETS

by

J.W. Oler
Texas Tech University
Lubbock, Texas

and

V.W. Goldschmidt
Purdue University
West Lafayette, Indiana

ABSTRACT

The strongest indication of an ordered structure in the similarity of plane jet flows is the well-documented (but controversial) apparent "flapping" behavior. Previously, the negative correlation between probes placed on opposite sides of the jet centerline has been attributed to the periodic displacement of the mean velocity profile centerline about its average position, i.e., a flapping motion. The present investigation is directed at evaluating the premise of an essentially two-dimensional von Karman vortex street as being responsible for the apparent "flapping" behavior.

NOMENCLATURE

- b = velocity halfwidth, m
- C_f = dimensionless structural frequency coefficient
- C_ℓ = dimensionless structural wavelength coefficient
- C_u = dimensionless structural convection velocity coefficient
- D = jet exit slot width, m
- f_γ = interface crossing frequency, sec^{-1}
- $f_{\gamma m}$ = maximum interface crossing frequency, sec^{-1}
- f_s = structural passage frequency, sec^{-1}
- I = intermittency
- ℓ_s = structural pattern wavelength, m
- n_s = vortex density, m^{-1}
- R_e = $U_o D/\nu$ = jet Reynolds number
- R_I = correlation coefficient based on intermittency function
- R_u = correlation coefficient based on velocity fluctuations
- u_s = structural convection velocity, m/sec
- u_A, u_B = velocity fluctuation, m/sec
- U_A, U_B = velocity fluctuation intensity, m/sec
- U_o = jet exit velocity, m/sec
- U_m = mean longitudinal centerline velocity, m/sec
- x = streamwise coordinate, m
- x_k = streamwise vortex coordinate, m
- y = lateral coordinate, m
- y_m = lateral position of maximum interface crossing frequency, m
- z = spanwise or homogeneous coordinate, m
- γ = intermittency fraction
- δ = separation distance, m
- Λ = integral lengh scale, m
- ν = kinematic viscosity, m^2/sec

INTRODUCTION

In recent years, there has been a gradual shift in the approach to turbulent fluid mechanics research. It is becoming increasingly clear that much of what has been traditionally considered as random phenomena actually is much more deterministic. In particular, a growing body of experimental evidence is accumulating which demonstrates that much of the physics of turbulent shear flow may be controlled by a finite set of coherent large-scale eddying motions. The relative importance of these large scales has been emphasized in several recent review articles (e.g., References 1, 2, 3, 4, and 5). While the acceptance of the non-random aspects of turbulence is common, it is by no means universal (see References 6, 7, and 8). However, the presence of the large-scale structures and to some extent their importance have become experimentally established facts.

The goal of the research described herein has been to examine the fully-developed plane turbulent jet for evidence of the effects of the large-scale structures characteristic of that flow. During the course of those measurements, the apparent presence of an antisymmetric and periodic vortical structure was noted. Its features suggest an ordered, two-dimensional vortex street pattern similar to that found in two-dimensional mixing layers and wakes (see References 9 and 10) as illustrated in Figure 1.

If, in fact, the vortex street structure does exist in plane jet flows, there are several of its features which should be evident from experimental

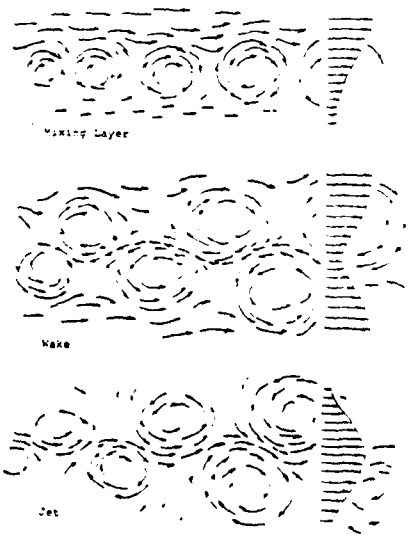

Figure 1. Organized Structures in Two-Dimensional Free Shear Flows

measurements. In particular, measurements related to the large-scale structure should contain indications of (a) structural similarity, (b) spatial coherence and periodicity, and (c) two-dimensionality. The discussion of the experimental results that follows is centered upon the extent to which these structural features are indicated.

EXPERIMENTAL APPARATUS

All measurements for the presently reported investigation were made in the two-dimensional jet apparatus depicted in Figure 2. The test section consists of a 1.27 x 30.4 cm vertical slot in a 91.4 x 30.4 cm wall. The flow is bounded above and below by parallel horizontal surfaces extending 120 cm in the downstream direction. For all measurements, the jet was operated at a constant Re = 1.74×10^5 based upon the exit slot width. The apparatus has the capability for heating the jet flow to a temperature in excess of the ambient. This feature was utilized for making intermittency measurements where heat served as a passive contaminant in the turbulent flow (see Reference 11). A constant overheat of 12 C was used for measurements involving the intermittency function. Otherwise, the overheat was zero.

Fluctuating velocity and temperature signals were derived from the outputs of TSI 1050 series anemometers operated in the constant temperature and constant current modes. The temperature signals were used with an original microcomputer based circuit to formulate continuous, real-time intermittency functions. Cross correlations of velocity fluctuation signals were made using a TSI analog correlator and true rms voltmeter. Correlations of the intermittency function were determined with the aid of an original digital circuit. Detailed descriptions of the intermittency formulation and correlation techniques are given in References 12 and 13.

EXPERIMENTAL RESULTS

Structural Similarity

Structural similarity is a requirement if the large structures are to play a consistent role in the energy transport dynamics throughout the fully-developed or self-preserving region of a plane jet. Experimentally, this characteristic is indicated when the streamwise variations of length, velocity, and frequency scales of the largest structures are compatible with global mean flow scales. In particular, for plane jet flows, length scales should vary as x, velocity scales as $x^{-1/2}$, and frequency scales as $x^{-3/2}$.

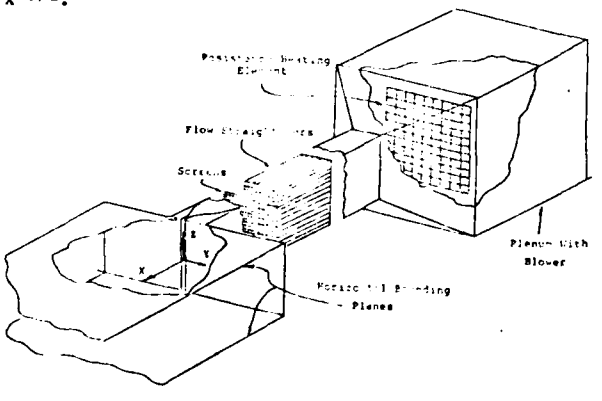

Figure 2 Schematic of Plane Jet Apparatus

It is assumed that the geometry of the interface is controlled by the underlying turbulent structure. Hence, similarity in that structure should also be evident in the interface characteristics such as intermittency and crossing frequency. Transverse distributions of the intermittency fraction and normalized interface crossing frequency at x/D = 15, 20, 30, 40, 50, and 60 were shown in Reference 11. They closely follow the relationships:

$$\gamma = \frac{1}{2} - \mathrm{erf}\left[\frac{1}{.41}\left(\frac{y-y_m}{b} - .11\right)\right] \qquad (1)$$

$$\frac{f_\gamma}{f_{\gamma m}} = \exp\left[-\frac{1}{2}\left(\frac{y-y_m}{.41b}\right)^2\right], \qquad (2)$$

where for x/D > 10 in this jet:

$$\frac{y_m}{b} = 1.6 \pm .05 \qquad (3)$$

$$\frac{b}{D} = 0.098\left(\frac{x}{D} + .619\right) \qquad (4)$$

These distributions exhibit similarity in that the curves from various longitudinal positions collapse on the y/b coordinate.

The mean interface position is given by the point of maximum crossing frequency. At that location, the intermittency fraction is noted to be 0.6 rather than 0.5 as would be required by a symmetric distribution function. Similar observations have been made by other investigators (e.g., References 14, 15, and 16) with the explanation being that the interface is more sharply folded in its troughs than on its crests. In the present investigation, this feature is additionally taken as an indication that the interface and underlying large eddy structure maintain qualitatively similar shapes at all streamwise positions in the fully-developed region since the $\gamma = 0.6$ value at $f_{\gamma m}$ is maintained.

The streamwise variation of the maximum interface crossing frequency was given in Reference 11 as

$$\frac{f_{\gamma m} D}{U_o} = 2.09(x/D + 2.3)^{-3/2}. \qquad (5)$$

Furthermore, it was demonstrated in Reference 13 that the dimensionless maximum crossing frequency coincides with the apparent flapping frequencies of Cervantes [17]. Strong support for the assumption of relatedness between the interface geometry and the underlying structure is given by that comparison. Rather than "flapping" frequency or interface crossing frequency, the term structural passage frequency or simply, structural frequency will be used throughout the remainder of this report.

From similarity arguments for the plane jet, global frequency scales should vary as $x^{-3/2}$. This behavior is verified by the structural frequency data and (5). If a dimensionless frequency is formed from the structural frequency, velocity halfwidth and mean center velocity, a flow constant, $S_s = f_s b/U_m$, results. Values of this constant for the present investigation and those deduced from other reported measurements of "flapping" frequency are given in Table 1. The relatively close agreement suggests a universal instability mechanism which drives the large-scale structure.

From similarity arguments, the convection velocity should decrease in proportion to $x^{-1/2}$, i.e.,

$$\frac{U_s}{U_o} = C_u\left(\frac{x}{D}\right)^{-1/2} \qquad (6)$$

or the ratio of the structural velocity to the mean centerline velocity should be a clearly defined constant. The classical technique for the determination of convective velocities is to determine the space-time correlation function for velocity probes separated in the mean flow direction. By noting the separation distance and the corresponding time delay which yields the peak correlation coefficient, the convection velocity may be determined from their ratio. A variation of the basic technique is to low pass filter the velocity signals prior to forming the correlation function. In this way, only the largest scales contribute to the correlation. It is expected, therefore, that the indicated convective velocity is more closely tied to the velocity of the large-scale structure. Measurements utilizing both techniques have been made by Ott and Young with the results summarized in Reference 21 and Table 2. The difficulty with the results of both techniques is that the indicated convective velocities decrease monotonically away from the jet centerline. There is no clear choice for a single velocity that may be associated with the underlying structural pattern.

Cervantes [17] measured a convective velocity of the "flapping" motion. In addition to the equal spacing of the probes on the opposite sides of the jet centerline, he also introduced a streamwise separation. By observing the shift of the negative peak correlation, the convective velocity was estimated in a manner analogous to that of Young and Ott. The experiment was repeated for two values of the lateral spacing with the results given in Table 2. Again, the convective velocities are noted to be nonconstant.

For the present investigation (in collaboration with Moallemi [22]), the convective velocity of the large eddy structure was determined through a combination of flow visualization and calculations based upon similarity scaling relationships.

Considering the vortex street model of the large eddy structure, the structural convective velocity, wavelength, and frequency are related by $u_s = \ell_s f_s$ or

$$\frac{u_s}{U_o} = C_\ell\left(\frac{x}{D}\right) C_f\left(\frac{x}{D}\right)^{-3/2} . \qquad (7)$$

Comparison of (6) and (7) reveals that $C_u = C_\ell C_f$. If the constants, C_ℓ and C_f, are determined experimentally, then C_u may be deduced and should have a constant value in the similarity region of a plane jet. From table 1, it was noted that $f_s b/U_m \cong 0.1$. For the plane jet flow utilized in the present investigation

$$\frac{f_s D}{U_o} = \frac{f_s b}{U_m}\frac{D}{b}\frac{U_m}{U_o} \qquad (8)$$

$$= 2.36(x/D)^{-3/2}$$

or $C_f = 2.36$.

The pattern wavelength coefficient, C_ℓ, is derived from knowledge of the instantaneous locations of selected vortices in the fully-developed region of a plane jet. This coordinate data was provided by Moallemi [22] who used a smoke-wire flow visualization technique to silhouette the vortices and allow their instantaneous locations to be determined from photographs. In calculating the corresponding wavelengths, provision must be made for the fact that the pattern is growing and decelerating across the photographic frames.

If a dimensionless vortex pattern wavelength is written as $\ell_s/D = C_\ell(x/D)$, then a corresponding vortex density may be defined as

$$n_s D = \frac{2}{C_\ell(x/D)} . \qquad (9)$$

The factor of 2 is a consequence of there being two vortices in each wavelength of the pattern. Consider a vortex instantaneously located at the streamwise station x_0. The next downstream vortex location should be at x_1, such that

$$1 = \int_{x_0}^{x_1} n_s dx$$

Table 1. Summary of Reported Structural Frequencies

$\frac{f_s b}{U_m}$	x/D	R_D	Investigator
0.1 - 0.2↔	44-71	-	Bradbury [18]
0.06*	45	2.6×10^4	Goldschmidt & Bradshaw [19]
0.12‡	12	10^5	Weir & Bradshaw [20]
0.08 - 0.14+	20-100	7.9×10^3 - 1.5×10^4	Cervantes [17]
0.1 - 0.15↔	100	3×10^4	Everitt & Robins [16]
.09↔	10-60	1.7×10^4	Oler & Goldschmidt [13]

* Determined from average peak to peak intervals of the correlation function between velocity fluctuations

\+ Determined by interval to the first peak of the correlation function between velocity fluctuations

‡ Determined by peak in cross-spectral density distribution of velocity fluctuations

↔ Determined from interface crossing frequencies

Table 2. Summary of Structural Related Convective Velocities

u_c/U_m***	y/b	Investigator
1.0	.0	+Ott [21]
.95	.5	
.82	.75	
.68	1.0	
.57	1.5	
.425	0	*Young [21]
.39	.5	
.39	.75	
.38	1.0	
.30	1.5	
.75	.65	‡Cervantes [17]
.61	1.0	
.27	1.6	↔Present
.50	-	**Present

\+ Measured from broad band space-time correlations

* Measured from lowest frequency narrow band correlations

‡ Measured by extension of flapping frequency correlations

↔ Measured from space-time correlations of the intermittency function

** Measured utilizing flow visualization technique

*** The symbol 'u_c' is used to represent all of 'convective' velocities

or

$$1 = \frac{2}{C_\ell} \ell n(\frac{x_1}{x_0}). \qquad (10)$$

If the locations, x_0 and x_1, of the two adjacent vortices have been determined from flow visualization, then (10) may be used to determine the wavelength coefficient, i.e.,

$$C_\ell = 2 \ell n(\frac{x_1}{x_0}). \qquad (11)$$

If the locations of N vortices can be determined from a single photographic frame, then N-1 estimates of C_ℓ may be made using

$$k = \int_{x_0}^{x_k} n_s dx \qquad (12)$$

and

$$C_\ell = \frac{2}{k} \ell n(\frac{x_k}{x_0}), \qquad k=1,2,\ldots,N-1. \qquad (13)$$

The above procedure was followed with the results given in Figure 3. It was found that due to the finite downstream length required for self-preservation to be established, the wavelength coefficient is a function of x that approaches its similarity value asymptotically. The asymptotic value found is $C_\ell \cong 0.5$.

With C_ℓ and C_f thus determined, the convection velocity of the large vortices is

$$\frac{u_s}{U_0} \cong 1.18(\frac{x}{D})^{-1/2} \qquad (14)$$

and

$$\frac{u_s}{U_m} \cong 0.5. \qquad (15)$$

Spatial Coherence and Periodicity

A vortex street structure in a fully-developed jet flow should exhibit specific spatial relationships for the instantaneous velocity field. In particular, counter rotating vortices positioned on opposite sides of the centerline would produce antisymmetric transverse distributions of longitudinal velocity. Additionally, there would be a periodically repeated pattern in the velocity field.

The existence of the spatial relationships described above may be tested experimentally through measurements of cross-correlations between longitudinal velocity fluctuations at separated points in the flow. These correlation coefficients are defined as

$$R_u(\delta_x,\delta_y,\delta_z) = \frac{u_A u_B}{u_A' u_B'} \qquad (16)$$

for points A and B separated by δ_x, δ_y, and δ_z.

The instantaneous asymmetry of the longitudinal velocity distribution is evidence by the distributions of $R_u(0,\delta_y,0)$ given in Figure 4. The most obvious feature of the distributions are the strong negative correlations between the velocity fluctuations on opposite sides of the centerline and extending well into the intermittent regions. Similar results have been reported in References 14, 16, 17, and 19.

The correlation measurements which result from both longitudinal and lateral separation of the velocity probes are presented in Figure 5 in the form of an isocorrelation contour map. The map provides a graphic illustration of the instantaneously antisymmetric velocity and periodically repeatable structural pattern. The actual distance over which the measureable flow organization exists (x/D ≅ 20 to 45) is quite remarkable and strongly supports the possibility of a vortex street eddy pattern.

Two-Dimensionality

The vortex street structure of a fully-developed plane jet flow should exhibit a certain degree of two-dimensionality in the turbulent velocity field, as well as in the interface geometry. Quantification of the degree of two-dimensionality is accomplished experimentally by comparing characteristic streamwise and spanwise integral length scales. These length scales are derived from correlations of velocity and

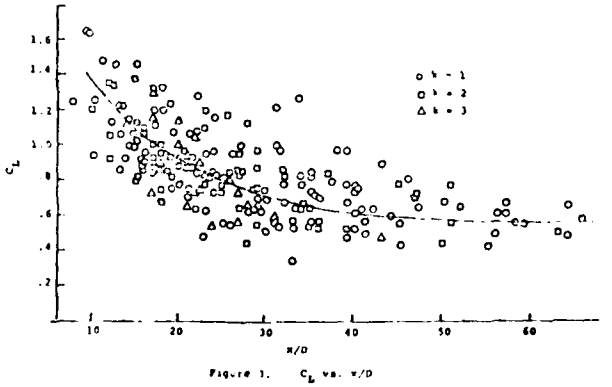

Figure 3. C_ℓ vs. x/D

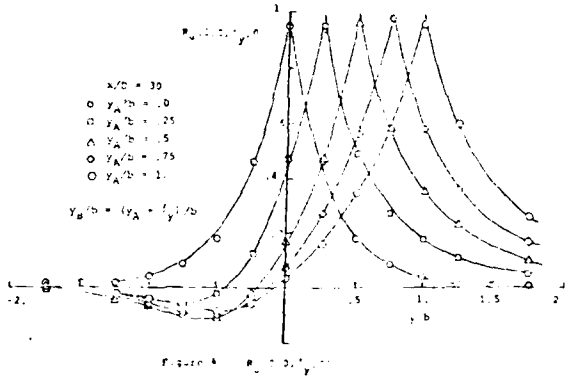

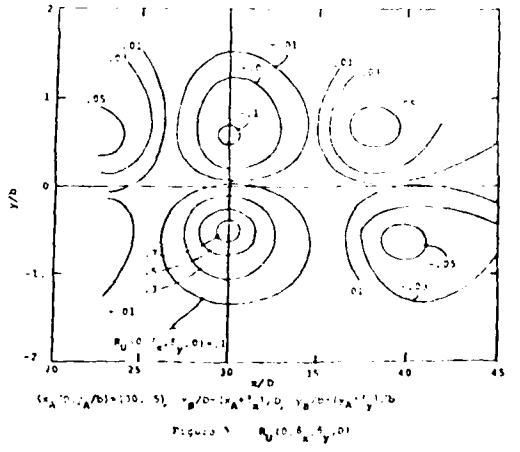

intermittency and are defined as

$$\Lambda_x = \int_0^\infty R(\delta_x,0_y,0_z)\, d\delta_x \qquad (17)$$

$$\Lambda_z = \int_0^\infty R(0_x,0_y,\delta_z)\, d\delta_z \qquad (18)$$

The velocity correlation coefficient is as given in (16) and the intermittency correlation is similarly defined as

$$R_I(\delta_x,\delta_y,\delta_z) = \frac{(I_A-\gamma_A)(I_B-\gamma_B)}{(I_A-\gamma_A)'(I_B-\gamma_B)'} \qquad (19)$$

Figure 6 illustrates typical correlations of the intermittency function at x/D = 30 and γ = 0.5. Similar measurements were taken for $10 \leq x/D \leq 60$. The corresponding integral length scales and their variation with streamwise position are given in Figure 7. Once again, the self-preserving variation of all intermittency length scales is evident. From Figure 7, it is apparent that the longitudinal and vertical length scales are approximately equal, i.e., $\Lambda^I = \Lambda_x^I = \Lambda_z^I$ and $\Lambda^I/b \cong .5$. The near equivalency of integral length scales in the intermittent region has also been noted by Moum, et al., [15].

The integral length scales within the turbulent jet core were determined at x/D = 30, y/b = 0.0, 0.25, and 0.5. In this case, the integrations with respect to δ_x and δ_z were limited to the intervals over which the correlations were positive. A typical result is plotted in Figure 8. The average length scales determined from the correlation curves $\Lambda_x^u/b \cong .65$ and $\Lambda_z^u/b \cong .28$, thereby indicating $\Lambda_x^u/\Lambda_z^u \cong 2$, which is surprising considering the measurements in the intermittent region. However, the results are consistent with those reported by Everitt and Robins [16], i.e., $\Lambda_x^u/b = .47$ and $\Lambda_z^u = b = .23$, which also gives $\Lambda_x^u/\Lambda_z^u \cong 2$.

Another unexpected feature of Figure 11 is the negative lobe in the $R(0,0,\delta_z)$ correlation. Three possible explanations are offered:

1) A combination of streamwise tilting of the large vortices and the streamwise periodicity of the velocity field results in a negative $R(0,0,\delta_z)$ correlation.

2) The vortices undulate periodically along their length and the negative lobe in the correlation is an indication of the first half wavelength.

3) There is a lack of coherence of the vortices in the vertical direction so that the correlation is dominated by the near isotropic smaller scales. The negative lobe is then the result of continuity requirements.

Based on the comparison of integral scales alone, the degree of two-dimensionality characteristic of the large structures is quite limited. However, three points must be noted. First, the flow visualization experiments by Moallemi [22], as well as the correlation contours of Figure 5, strongly suggest a flow structure with significant coherence in the z-direction. Secondly, there is a real possibility that the parallel bounding surfaces intended to maintain the two-dimensionality of the mean flow may actually inhibit the two-dimensionality of the flow structure. Even at an x/D as small as 45, the streamwise wavelength of a vortex street pattern would approach the separation between the surfaces used. And finally, a similar contradiction exists between visualization results and inferences from integral scales concerning the degree of structural two-dimensionality characteristic of the plane mixing layer, (e.g., References 6, 7, and 23).

CONCLUSIONS

From the experimental tests of the validity of a vortex street model for the large scale structure of turbulent plane jets, the following conclusions are found:

1) The global variation of length, velocity, and frequency scales are compatible with similarity requirements.

2) The large, vortex-like motion is periodic.

3) The coherent, vortex-like motion extends

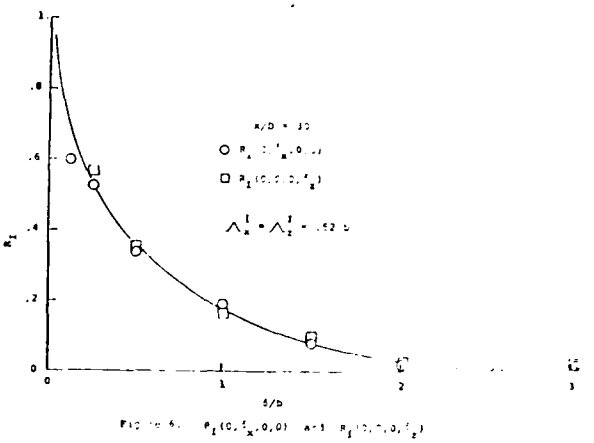

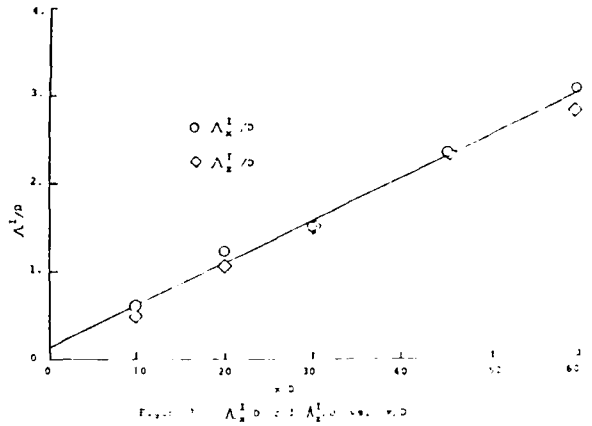

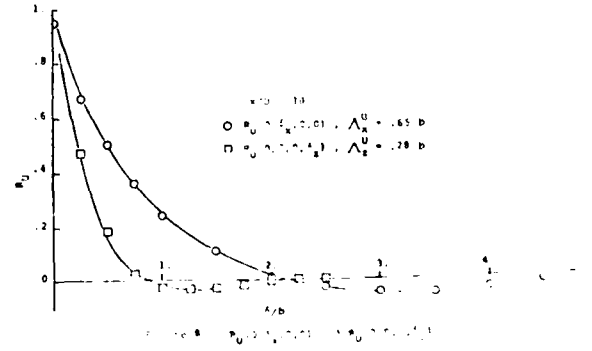

across the entire width of the flow and for considerable up- and downstream distances.

4) The structural organization inferred from the measurements has the instantaneously antisymmetric characteristic expected of a vortex street structure.

5) Only a limited degree of two-dimensionality may be inferred from the measurements.

The presence of these large coherent structures, aligned as in a vortex street arrangement, suggest the need for a re-evaluation of the classical descriptive models which exclude any deterministic aspects of the instantaneous flow.

ACKNOWLEDGMENTS

The major portion of the work reported was conducted under the sponsorship of the ONR and the NSF. Their support is gratefully acknowledged.

REFERENCES

1 Kovasznay, L.S.G., "The Role of Large-Scale Coherent Structures in Turbulent Shear Flows," Proceedings of the Fifth Biennial Symposium on Turbulence, University of Missouri-Rolla, 1977, pp. 379-389.

2 Roshko, A., "Structure of Turbulent Shear Flows--A New Look," AIAA Journal, Vol. 14, No. 10, 1976, pp. 1349-1357.

3 Davies, P.O.A.L. and Lule, A.J., "Coherent Structures in Turbulence," Journal of Fluid Mechanics, Vol. 69 , No. 3, 1975, pp. 513-537.

4 Laufer, J., "New Trends in Experimental Turbulence Research," Annual Review of Fluid Mechanics, Vol. 7, 1975, pp. 307-326.

5 Mollo-Christensen, E., "Physics of Turbulent Flow," AIAA Journal, Vol. 9, No. 7, 1971, pp. 1217-1228.

6 Pui, N.K. and Gartshore, I.S., "Measurements of the Growth Rate and Structure in Plane Turbulent Mixing Layers," Journal of Fluid Mechanics, Vol. 91, No. 1, 1979, pp. 111-130.

7 Chandrsuda, C., Mehta, R.D., Weir, A.D. and Bradshaw, P., "Effect of Free-Stream Turbulence on Large Structure in Turbulent Mixing Layers," Journal of Fluid Mechanics, Vol. 85, No. 4, 1978, pp. 693-704.

8 Bradshaw, P., "Interacting Shear Layers in Turbomachines and Diffusers," A Project Squid Workshop--Turbulence in Internal Flows," (Murthy, S.N.B., Ed.), Hemisphere, 1976, pp. 35-64.

9 Brown, G.L. and Roshko, A., "On Density Effects and Large Structure in Turbulent Mixing Layers," Journal of Fluid Mechanics, Vol. 64, No. 4, 1974, pp. 775-816.

10 Papailiou, D.D. and Lykoudis, P.S., "Turbulent Vortex Streets and the Entrainment Mechanism of the Turbulent Wake," Journal of Fluid Mechanics, Vol. 62, No. 1, 1974, pp. 11-31.

11 Oler, J.W. and Goldschmidt, V.W., "Interface Crossing Frequency as a Self-Preserving Flow Variable," Physics of Fluids, Vol. 23, No. 1, 1980, pp. 19-21.

12 Oler, J.W. and Goldschmidt, V.W., "The Use of Microprocessors for Continous, Real Time Digital Formulation of the Intermittency Function," Proceedings of the Sixth Biennial Symposium on Turbulence, University of Missouri-Rolla, 1979, pp. 379-389.

13 Oler, J.W., "Coherent Structures in the Similarity Region of a Two-Dimensional Turbulent Jet: A Vortex Street," Ph.D. Dissertation, Purdue University, 1980.

14 Gutmark, E. and Wygnanski, I., "The Planar Turbulent Jet," Journal of Fluid Mechanics, Vol. 73, No. 3, 1976, pp. 465-495.

15 Moum, J.W., Kawall, J.G. and Keffer, J.F., "Structural Features of the Plane Turbulent Jet," Physics of Fluids, Vol. 22, No. 7, 1979, pp. 1240-1244.

16 Everitt, K.W. and Robins, A.G., "The Development and Structure of Turbulent Plane Jets," Journal of Fluid Mechanics, Vol. 88, No. 3, 1978, pp. 563-568.

17 Cervantes de Gortari, J.G. and Goldschmidt, V.W., "The Apparent Flapping Motion of a Turbulent Plane Jet - Further Experimental Results," ASME, 80-WA/FE-13, 1980. Also see Cervantes de Gortari, J.G., "An Experimental Study of the Flapping Motion of a Turbulent Plane Jet," Ph.D. Dissertation, Purdue University, 1978.

18 Bradbury, L.J.S., "The Structure of a Self-Preserving Turbulent Plane Jet," Journal of Fluid Mechanics, Vol. 23, No. 1, 1965, pp. 31-64.

19 Goldschmidt, V.W. and Bradshaw, P., "Flapping of a Plane Jet," Physics of Fluids, Vol. 16, No. 3, 1973, pp. 354-355.

20 Weir, A.D. and Bradshaw, P., "Resonance and Other Oscillations in the Initial Region of a Plane Turbulent Jet," Imperial College Report 75-07.

21 Goldschmidt, V.W., Young, M.F. and Ott, E.S., "Turbulent Convective Velocities (Broadband and Wave Number Dependent) in a Plane Jet," Journal of Fluid Mechanics, Vol. 105, 1981, pp. 327-345.

22 Moallemi, K., "Visualization and Characterization of a Two-Dimensional Turbulent Jet," M.S. Thesis, Purdue University, 1980.

23 Wygnanski, I., Oster, D., Fiedler, H. and Dziomba, B., "On the Perserverance of a Quasi-Two-Dimensional Eddy Structure in a Turbulent Mixing Layer," Journal of Fluid Mechanics, Vol. 93, No. 2, 1979, pp. 325-335.

EDUCTION OF THE "PREFERRED MODE" STRUCTURE IN THE AXISYMMETRIC MIXING LAYER

K. B. M. Q. Zaman and A. K. M. F. Hussain

Department of Mechanical Engineering
University of Houston
Houston, Texas 77004

ABSTRACT

In an attempt to educe the preferred mode coherent structure of the unexcited axisymmetric jet, criteria for conditional measurements are examined. It is found that the structures are best educed by triggering on the positive peaks of a reference signal obtained from the high-speed edge of the mixing layer. Positive ũ-peaks are superior to negative ũ-peaks for trigger, because the separation between the trigger probe and the structure is larger in the latter case. The improvement in the eduction achieved by threshold levels higher than twice the standard deviation of ũ is offset by increased experiment time. Above this level, use of a window in the threshold is also of marginal utility. The signals from the high- and the low-speed sides are poorly correlated. Consequently, a criterion based on the simultaneous occurrence of peaks and troughs of two reference signals obtained from the two sides failed to educe the structures in the axisymmetric mixing layer. Tearing and fractional pairing, augmented by the axisymmetric configuration, appear to be responsible for a significantly poorer eduction of the structures from the low-speed side.

INTRODUCTION

Large-scale coherent structures are the focus of many contemporary studies in turbulence. This emphasis stems from the expectation that these structures can serve as the building blocks in newer theories of shear flow turbulence.

Many of the large-scale structure studies have been carried out in the circular jet near field where the structures are found to be quasi-periodic [1-5]. One of the techniques frequency employed in these studies has been controlled excitaton, which helps the formation of the sturctures at controlled phases and thus permits their investigation through phase-locked measurements [1,2,6]. This technique was also employed by us to study the 'preferred-mode' structure evolution as well as its dependence on the Reynolds number and initial condition. The 'preferred-mode' structure was induced by controlled excitation at $St_D = 0.3$ and educed via phase-locked hot-wire measurements [7]. The detailed measures of this structure showed essentially no dependence on the initial condition but a mild dependence on the Reynolds number. However, the question remained as to whether or not these structures, 'enhanced' by the excitation, truly represented the ones in the unexcited mixing layer. This motivated the present work where eduction of the large-scale structures in the natural axisymmetric layer is attempted via conditional sampling.

In this paper, we will primarily focus on the considerations given to the criteria for eduction. The objective was to arrive at a simple eduction scheme for educing the preferred-mode structures in the axisymmetric mixing layer.

EXPERIMENTAL PROCEDURES

The experiments were carried out in a 7.6 cm circular jet; the nozzle boundary layer was tripped with a sand-paper ring located at 4 cm upstream from the exit plane. The efflux boundary layer was fully turbulent as confirmed by the profiles of the longitudinal mean velocity and turbulence intensity and the ũ-spectrum. The jet exited with an axisymmetric top-hat mean velocity profile. Most of the data presented in this paper pertain to a jet Reynolds number of $Re_D = 110{,}000$ and to the downstream station of $x/D = 3$. Data were obtained from standard linearized constant-temperature hot-wire (DISA) anemometers. Data acquisition and analysis were performed by the laboratory mini-computer (HP2100S) together with a magnetic tape and automated probe traversing mechanisms. For further details of the procedures, see ref. [8].

RESULTS

Figure 1 shows the variation of the centerline longitudinal turbulence intensity u_c'/U_e for different Strouhal numbers (St_D) of excitation; the excitation amplitude (u_e'/U_e) measured at the center of the jet exit plane was 2%. The data show that the maximum growth of the imparted disturbance occurs at St_D=0.30, and the trends with different St_D are in qualitative

agreement with the data of Crow and Champagne [1]. The insert in Figure 1 shows variations of the rms amplitude of the fundamental (u_f'/U_e) along the jet centerline for three St_D and confirms that the maximum growth of the fundamental occurs at $St_D = 0.30$. This value of the St_D at which the fundamental receives the maximum amplification is accordingly called the 'preferred mode' of the axisymmetric jet [1,6]. The St_D value that produces the maximum disturbance amplification depends on whether the total or the fundamental of the fluctuation is considered. For example, excitation inducing stable pairing (at $St_D \approx 0.85$) can produce total fluctuation levels considerably higher than that at $St_D \approx 0.3$. Thus, even though Crow & Champagne defined the 'preferred mode' on the basis of the total fluctuation intensity measured on the jet centerline, $St_D \approx 0.3$ is still the preferred mode when it is redefined on the basis of the fundamental amplitude [6].

The spectral evolution on the centerline of the unexcited jet is shown in Fig. 2 for $0 < x/D < 8$. The quasi-periodic passage of the large-scale structures is 'felt' on the jet axis downstream of $x/D \approx 1.5$. The quasi-periodicity in the structure passage, as evident from a clear but broadband peak in the $\tilde{u}$-spectra, is lost beyond $x/D \approx 8$. The frequency of the spectral peak shows a gradual decrease from about $St_D = 0.55$ at $x/D = 1.5$ to about 0.30 at $x/D = 5$. Similar data at a few other Re_D over the range 5×10^4 to 10^6, all having initially turbulent efflux boundary layers and top-hat mean velocity profiles, showed essentially similar variations as in Fig. 2. The mechanism for the 'roll-up' of an initially fully turbulent shear layer remains to be explained. Since the peak in the spectrum on the centerline occurs at the same St_D (≈ 0.55) at all Re_D, this roll-up should not be viewed as an instability of the initially turbulent shear layer, but rather the formation of the 'jet column mode' structures inherent to the axisymmetric configuration.

The frequency of the spectral peak gradually decreases with increasing downstream distances. Such frequency decreases were also observed by others in circular jets [2,9], as well as in a plane mixing layer [10]. In turbulent plane mixing layers and in the initial region of axisymmetric jets with laminar boundary layers, the role of vortex pairing in producing a gradual decrease in the frequency has been clearly demonstrated. However, in the present case of an initially turbulent axisymmetric mixing layer, since the shift in the spectral peak frequency from $x/D = 2$ to 5 is not even by a factor of two and the shift is gradual and not in any discernible step (Fig. 2), whether vortex pairing is the mechanism for the apparent frequency decrease remains to be established. An alternative mechanism is more likely. Noting that the quasi-periodicity under consideration scales on the jet diameter and the initial roll-up occurs at $St_D \approx 0.55$, let us assume that frequencies in the range $0.1 < St_D < 1.0$ are all amplified by the jet column. Different frequency components (and corresponding large-scale structures) occur in the flow at different instants. A lower frequency component receives maximum amplification at a larger axial location [1,6]. Thus, in a time-average measure like the $\tilde{u}$-spectrum, the dominant frequency must decrease with increasing x and the peak in the spectrum at a given x is determined by the disturbance that receives maximum amplification at that x.

The observed initial 'roll-up' at $St_D \approx 0.55$ may appear to be in conflict with previous results which showed that $St_D \approx 0.3$ was the 'preferred mode' of the axisymmetric jet [1,6]. The following points should clarify this apparent anomaly. First, the 'preferred mode' has been defined from excitation studies, which mostly used relatively large (nonlinear) amplitudes of excitation. Second, the dominant frequency component in the natural jet clearly depends on the axial station of measurement (e.g., $St_D \approx 0.45$ observed at $x/D = 3$ in [8] and [11]). Thus, the 'preferred mode' determined from the artificial excitation corresponds to the 'terminal Strouhal number' in the natural jet; this is the structure with the St_D receiving maximum amplification at the end of the potential core. In other words, the 'preferred mode' corresponds to the dominant structure in the natural jet before its breakdown near the end of the potential core, beyond which the velocity signal ceases to indicate any quasi-periodicity. Third, a slight Re_D dependence of the preferred mode St_D has been observed even in excitation studies. Especially at lower Re_D and in jets with initially laminar boundary layers, the preferred mode St_D increases with decreasing Re_D. This should account for at least some of the higher values of the preferred mode found in the literature [2,7,12].

There is, of course, a difference between the natural jet and the jet under artificial excitation. While artificial excitation induces one single large-scale structure (corresponding to the frequency of excitation), an assortment of structures randomly occur in the natural jet. The attractiveness of the excitation in large-scale structures studies is the precipitation of a single structure at controlled phases and elimination of the other structures, which permits application of relatively simpler techniques like phase-averaging to derive the details of the structure. If the 'enhanced' structure under excitation represented the corresponding structure in the natural jet, then structure properties corresponding to different frequencies could be obtained via controlled excitation, and then a suitable distribution of these structures could be used as a model for the flow.

However, it is possible that there may remain some differences between the artificially induced structure and the corresponding structure in the natural jet. Especially, if a high level of excitation is used to induce the structure of interest, it may produce noticeable differences. These motivated the present study where we attempt to educe the naturally-occurring structures via conditionally sampled measurements. These measurements are carried out in the jet with fully turbulent initial boundary layer at $Re_D = 110{,}000$. The axial station chosen for the measurements is $x/D = 3$ where the spectral footprint is relatively the most clear (see Fig. 2).

The measurement technique is schematically shown in Fig. 3. Four 'simultaneous' velocity signals from a reference probe on the high-speed side ($y/D = 0.25$; $U/U_e \approx 0.99$), a reference probe on the low-speed side ($y/D = 0.85$; $U/U_e \approx 0.10$), and $\tilde{u}$ and $\tilde{v}$ signals from a measurement X-wire probe, are recorded by the computer onto the digital magnetic tape. The reference signals from the high- and low-speed sides will be denoted by $\tilde{u}_{r1}$ and $\tilde{u}_{r2}$, respectively. Keeping the two reference probes fixed, the measurement probe was traversed at 15 y-stations under remote computer control, and similar velocity traces were recorded at all stations. These data were later analyzed for eduction of the structures.

The peaks of $\tilde{u}_{r1}$ were first used as triggers for accepting sample functions of $\tilde{u}(t)$ and $\tilde{v}(t)$. Each accepted record of $\tilde{u}(t)$ and $\tilde{v}(t)$ consisted of 64

data points with 31 points preceding and 32 points following the trigger. Ensemble averages <u> and <v> obtained from the accepted realizations were further processed to obtain the coherent azimuthal vorticity Ω_z [$=(1/(0.5U_e))\partial\langle v\rangle/\partial t - \partial\langle v\rangle/\partial x$] distribution in a (τ,y) plane; τ denotes time with respect to the trigger. The Ω_z data are nondimensionalized by the frequency f_m such that $f_m D/U_e = 0.45$. The time axis is nondimensionalized by the corresponding period T_m ($=1/f_m$). Note that in the computation of Ω_z, Taylor hypothesis has been invoked using a convection velocity of $0.5U_e$ [13]. Because of the close resemblance of Ω_z contours with the streaklines and the sensitivity of these contours to the detection criteria, we have used Ω_z contours as the primary measure of the educed structure as well as the bases for evaluation of the conditional sampling technique.

Ω_z distribution obtained by using the $\tilde{u}_{r1}$-peaks discriminated by the threshold level of 2σ (i.e., $\tilde{u}_{r1} > 2\sigma$ criterion) is shown in Fig. 4; (σ denotes the standard deviation). The corresponding distribution obtained by triggering on the negative peaks in $\tilde{u}_{r1}$ below a threshold level of -2σ is shown in Fig. 5. The relative locations of the triggering points are shown by the + signs. The longitudinal spacing of the structures and their transverse extents in Fig. 5 agree quite well with the streamline pattern obtained by Yule [4] who used a similar negative peak criterion in a 5.08 cm diameter jet at $Re_D = 43000$. However, the positive peak criterion clearly results in eduction of the structure having a higher peak vorticity and consequently, larger number of closed contours (Fig. 4). Since a larger core cross-section and a higher peak vorticity represent better approximation of the most energetic structure, the $\tilde{u}_{r1} > 2\sigma$ criterion is clearly superior to the $\tilde{u}_{r1} < -2\sigma$ criterion.

Lesser smearing occurs with the positive peak criterion because the educed structure center at the instant of trigger is physically located at the same x as the reference probe. On the other hand, when triggering on the negative peak of $\tilde{u}_{r1}$, the reference probe is located half-way between two structures. Thus, in the latter case, the structure is educed when centered away from the trigger. The farther away are the measurements from the trigger, the more is the phase jitter, resulting in smeared out educed structures. In spatial measurements, this effect would be equivalent to increasing loss of phase reference with increasing separation between the reference probe and the measurement probe. This is why the positive peak criterion produces less smearing.

In using an amplitude-dependent trigger criterion, one must consider the selection of the optimum threshold level. If the threshold is too high, most of the peaks (or troughs) and thus most of the structures will be rejected. Thus, for a given data volume, threshold levels above a certain value will result in the acceptance of too few realizations and thus produce a lot of scatter in the ensemble averages. In order to obtain convergent ensemble averages, a prohibitively large experiment time may be required at higher threshold levels. On the other hand, if the threshold is too low, the acceptance of dissimilar structures of different scales and strengths will result in unacceptable amounts of smearing. Furthermore, different levels of the peaks in $\tilde{u}_{r1}$ suggest that either structures of different strengths move past the probe, or the structures might be of the same strength but are at different transverse locations as they move past the probe. For either reason, only structures corresponding to reference signal peaks falling in a narrow window level should be ensemble averaged.

Figure 6 shows Ω_z contours obtained by using different threshold levels (A) discriminating the $\tilde{u}_{r1}$-peaks. Values of A in Figures 6(a)-(f) are 0.5, 1, 1.5, 2, 2.5, and 3, respectively. The window criterion has been used for Figs. 6(a)-(d) such that the $\tilde{u}_{r1}$-peaks were above $A\sigma$ but below $1.2A\sigma$. For the levels 2.5σ and 3σ in Figs. 6(e) and (f), use of the window criterion does not produce any noticeable difference from the contours shown which are obtained by the simple $\tilde{u}_{r1} > A\sigma$ criterion.

There is a significant smearing at the lower threshold levels. Thus, the structures which cause the larger peaks in $\tilde{u}_{r1}$ are clearly educed only when peaks above a certain level (say $\tilde{u}_{r1} > 1.5\sigma$) are used for trigger. Comparison of the peak vorticity shows that the smearing effect is less at higher threshold levels, as to be expected. Thus, the area enclosed by the $\Omega_z/f_m = 7$ contour increases as the threshold level is increased. A higher threshold level, therefore, yields better eduction. However, improvements at threshold levels above $\tilde{u}_{r1} = 2\sigma$ do not appear significant. Furthermore, to obtain smooth contours with large threshold levels one requires excessively large experiment times. For a threshold level of 2σ or higher, the window criterion also produces marginal improvements (for example, compare Figs. 6(a) and 4), and thus is not warranted, considering the additional computation time. As a compromise, we conclude that the $\tilde{u}_{r1} > 2\sigma$ threshold criterion yields the optimum result.

While the structure educed with the reference probe at $y/D = 0.25$ was shown in Fig. 4, those educed with the reference probe at $y/D = 0.1$ and 0.33 are shown in Fig. 7(a) and (b), respectively; the threshold criterion of $\tilde{u}_{r1} > 2\sigma$ is used in all three cases. Note that, although the structure center occurs closest to the trigger location in Fig. 7(b), the peak vorticity level is less than that in Fig. 4. This is because the reference probe is inside the shear layer ($U/U_e = 0.95$) in the former case, and turbulent fluctuation in the refernece signal introduces some randomness in trigger and thus smear the educed structures. On the other hand, for $y/D = 0.1$, the structure center is farther away from the trigger location in y and as a result the educed contours are also smeared out. Thus, while the reference probe needs to be as close to the structure as possible so that a sharp footprint is sensed, it cannot be within the structure itself since small-scale fluctuations will introduce smearing in the eduction.

Efforts to educe the large-scale structure using the low-speed side signal $\tilde{u}_{r2}$ as trigger failed. On the low-speed side, the potential footprint being extremely weak due to the axisymmetric configuration, the $\tilde{u}_{r2}$ signal is dominated by random turbulence; this would suggest unavoidable smearing associated with triggering from the low-speed side of the axisymmetric mixing layer. The large peaks and troughs in $\tilde{u}_{r1}$ and $\tilde{u}_{r2}$ were found not to bear any discernible phase relationship. This was observed visually from a large number of simultaneous traces of $\tilde{u}_{r1}$ and $\tilde{u}_{r2}$ as well as by a joint probability computation of the occurrence of a $\tilde{u}_{r2}$ peak relative to a $\tilde{u}_{r1}$-peak. The lack of correlation between $\tilde{u}_{r1}$ and $\tilde{u}_{r2}$ is clearly demonstrated in Fig. 8. The (time-average) correlation co-efficient of the two signals is shown for $-24 < \tau < 24$ ms. The magnitude of the co-efficient is everywhere below 0.05. The small oscillation in the middle are within measurement uncertainty and are not repeatable.

These data thus indicate that, unlike in the plane shear layer at a low Reynolds number studied by Browand and Wiedman [14], any conditional sampling measurement based on a joint criterion on $\tilde{u}_{r1}$ and $\tilde{u}_{r2}$ in the axisymmetric mixing layer will not succeed. Note that Browand and Wiedman not only found definite phase relationship between the peaks in the high- and low-speed side signals but even used the phase relationship to educe different stages of the structure evolution. The present data clearly indicate that the dominant structures in the axisymmetric jets, which scale on the jet diameter and are independent of the initial shear layer state, are very much characteristic of the high-speed or the potential core side only. Presumably, because of the axisymmetric configuration, the structure signatures are dilated on the low-speed side and thus are not detectable.

CONCLUSIONS

It is shown that the quasi-periodic large-scale structures in the near-field of a high Reynolds number axisymmetric jet with fully turbulent initial condition can be educed successfully using a simple criterion of triggering on the extrema of a single wire reference signal. Best eduction is achieved when the reference probe is placed on the high-speed edge of the mixing layer (where $U/U_e \approx 0.99$). Eduction on the positive peaks of $\tilde{u}_{r1}$ is clearly more successful than when triggered on the negative peaks. Between the two, the structure center occurs closest to the positive peaks but is time-shifted relative to the negative peaks, and thus are smeared when the latter is used for trigger. Smearing is larger with increasing separation between the trigger location and the structure center owing to the increasing loss of phase reference (or jitter). Progressively higher thresholds produce sharper contours of the structure properties, and hence less smearing, but threshold levels higher than twice the standard deviation of the signal are not worthwhile because the improvement is marginal at the cost of prohibitively increased experiment time. There is no significant correlation between the high- and low-speed side reference signals $\tilde{u}_{r1}$ and $\tilde{u}_{r2}$. Thus, use of a joint criterion based on $\tilde{u}_{r1}$ and $\tilde{u}_{r2}$, or use of $\tilde{u}_{r2}$ alone, are not effective in educing the large-scale structures. This is due to a significantly weaker organization of the structures on the low-speed side believed to be due to processes like tearing and fractional pairing [15] augmented by the axisymmetric configuration.

REFERENCES

1. Crow, S. C. & Champagne, F. H. 1971 J. Fluid Mech. 48, 547.
2. Browand, F. K. & Laufer, J. 1975 Turb. Liquids, Univ. of Missouri-Rolla, 5, 333.
3. Bechert, D. & Pfizenmaier, E. 1975 J. Fluid Mech., 72, 341.
4. Yule, A. J. 1978 J. Fluid Mech. 89, 413.
5. Bruun, H. H. 1977 J. Fluid Mech. 64, 775.
6. Zaman, K. B. M. Q. & Hussain, A. K. M. F. 1980 J. Fluid Mech. 101, 449.
7. Hussain, A. K. M. F. & Zaman, K. B. M. Q. 1981 J. Fluid Mech. (to appear).
8. Zaman, K. B. M. Q. & Hussain, A. K. M. F. 1981 J. Fluid Mech. (submitted).
9. Davies, P. O. A. L. & Baxter, D. R. J. 1978 Structure and Mechanisms of Turbulence I (ed. H. Fiedler), Springer-Verlag, 125.
10. Winant, C. D. & Browand, F. K. 1974 J. Fluid Mech. 63, 237.
11. Kibens, V. 1978 A. I. A. A. J. 18, 434.
12. Vlasov, Y. V. & Ginevskiy, A. S. 1974 NASA TTF-15, 721.
13. Zaman, K. B. M. Q. & Hussain, A. K. M. F. 1981 J. Fluid Mech. (to appear).
14. Browand, F. K. & Wiedman, P. D. 1976 J. Fluid Mech. 76, 127.
15. Hussain, A. K. M. F. & Clark, A. R. 1981 J. Fluid Mech. 104, 263.

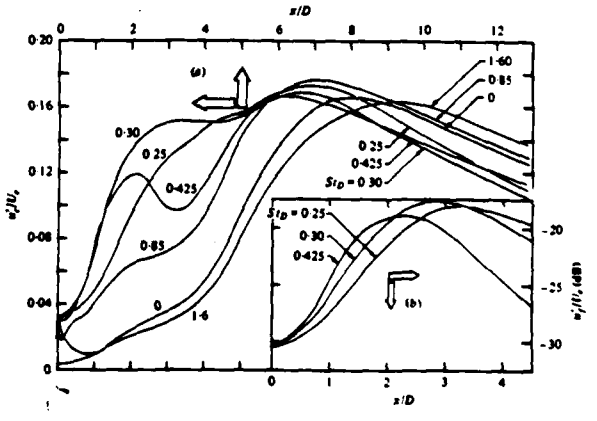

Fig. 1 Variation of u_c^2 with x for different St_D in the 7.62 cm (tripped) jet. For $St_D = 0.25$, $Re_D = 5.0 \times 10^4$; for $St_D = 0.85$, $Re_D = 3.2 \times 10^4$; for all other St_D's, $Re_D = 4.2 \times 10^4$. Insert shows variation of $u_c^2(x)$ for three St_D cases.

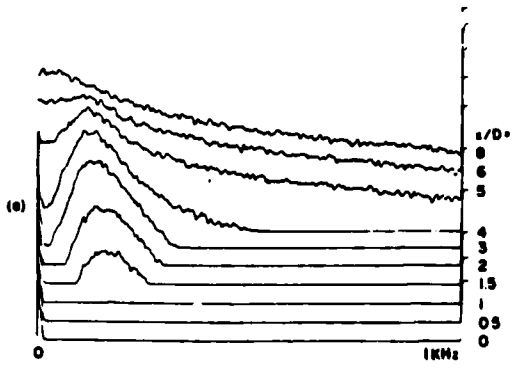

Fig. 2 ũ-spectra in the 7.62 cm (tripped) jet at Re_D = 110,000, for different axial stations on the centerline.

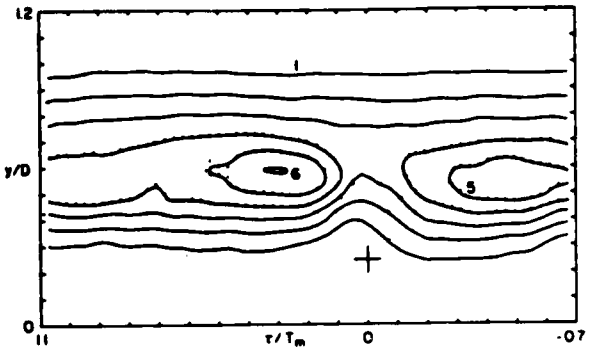

Fig. 5 Ω_z/f_m contours educed by the $\tilde{u}_{rl} < -2\sigma$ criterion.

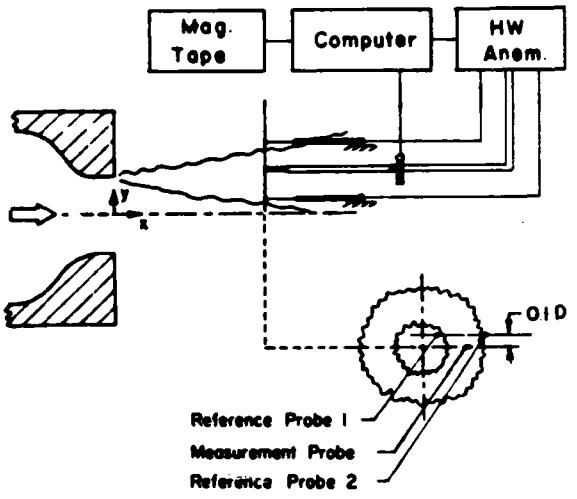

Fig. 3 Schematic of the measurement technique.

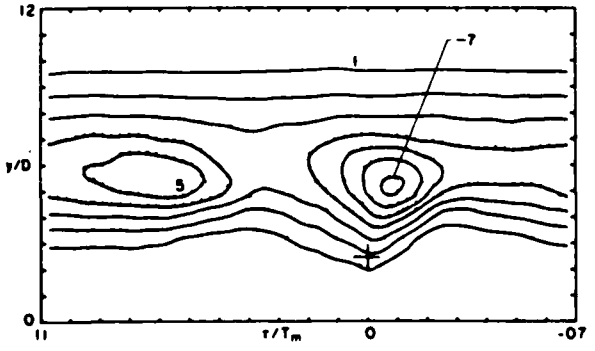

Fig 4. Ω_z/f_m contours educed by the $\tilde{u}_{rl} > 2\sigma$ criterion.

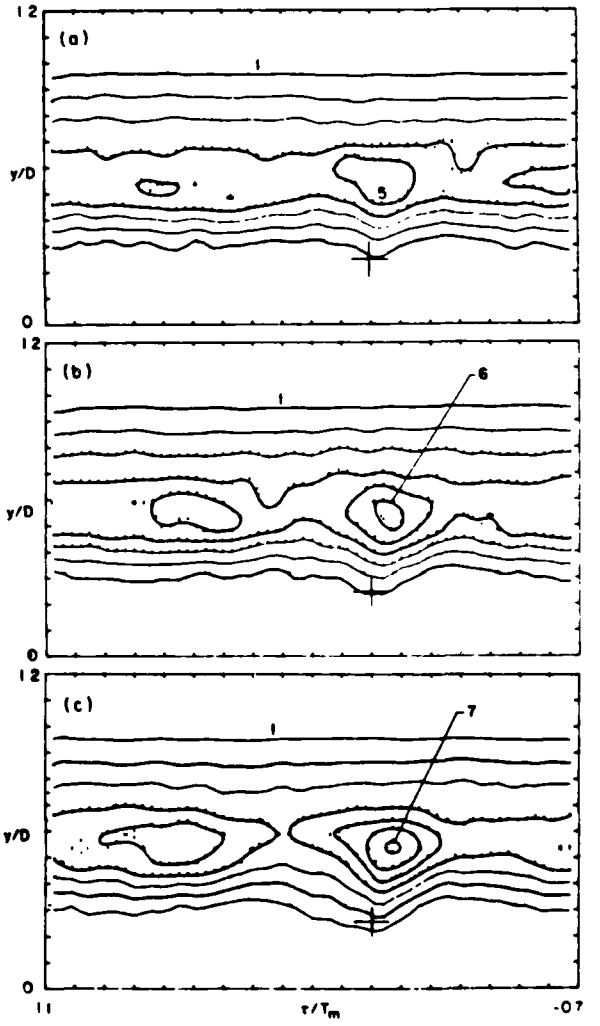

Fig. 6(a),(b),(c) For legend see Fig. 6(d).

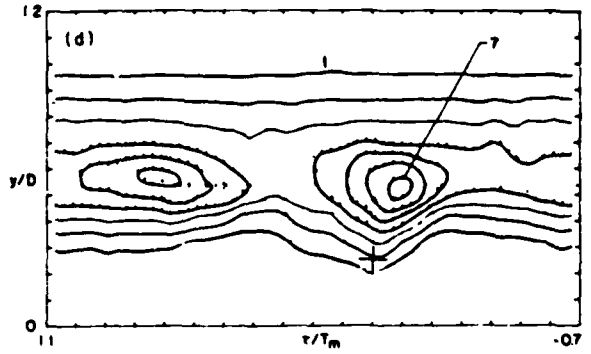

Fig. 6(d) Ω_z/f_m contours educed by the 'window' criterion $A\sigma<\tilde{u}_{r1}<1.2A\sigma$. Values of A are: (a) 0.5, (b) 1, (c) 1.5, and (d) 2.0. A constant ensemble size of 400 is used in all cases.

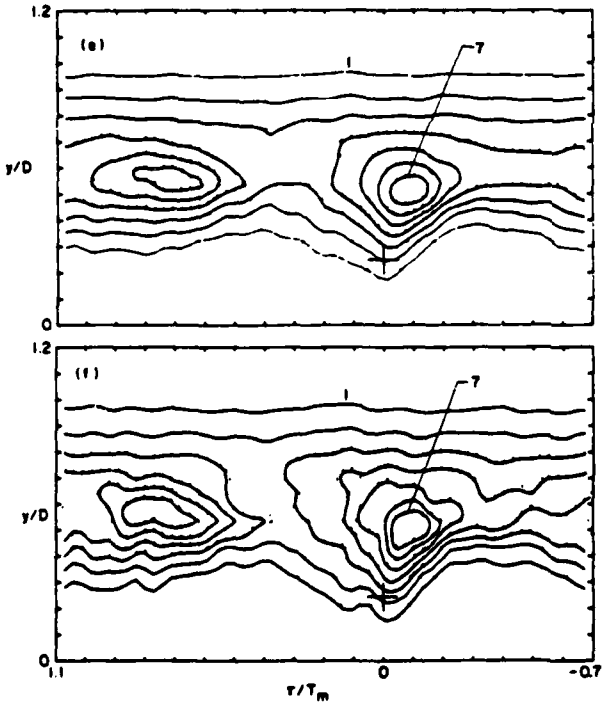

Fig. 6(e), (f) Ω_z/f_m contours educed by the $\tilde{u}_{r1}>A\sigma$ criterion. Values of A are: (e) 2.5 and (f) 3.0. Ensemble sizes are 400 and 75 in (e) and (f), respectively.

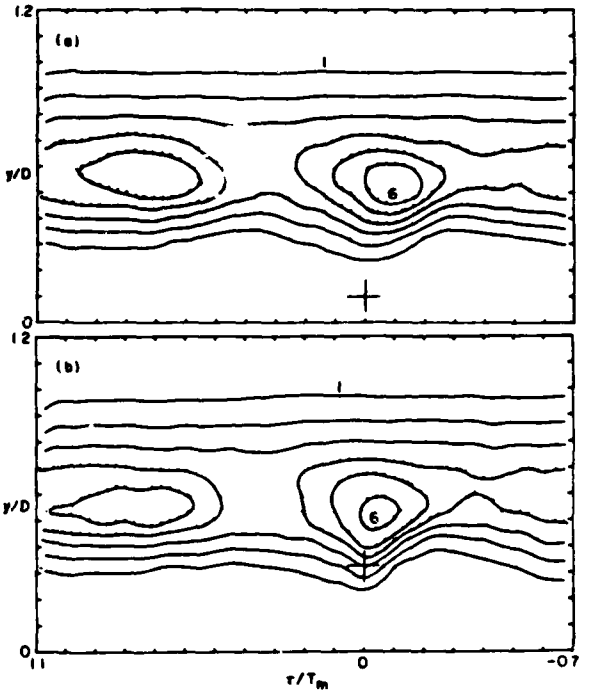

Fig. 7 Ω_z/f_m contours educed by the $\tilde{u}_{r1}>2\sigma$ criterion with different transverse positions of the reference probe: (1) y/D = 0.1 (U/U_e = 1.0); (b) y/D = 0.33 (U/U_e = 0.95).

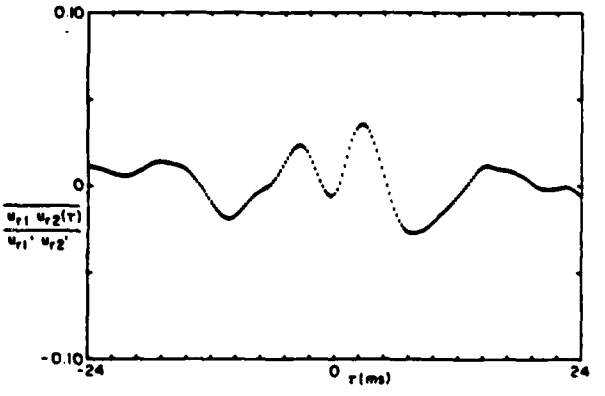

Fig. 8 Correlation of $\tilde{u}_{r1}$ and $\tilde{u}_{r2}$.

LARGE SCALE MOTIONS IN TURBULENT WAKES

J.H. Gerrard

Department of the Mechanics of Fluids

University of Manchester

Manchester M13 9PL, U.K.

ABSTRACT

Wake flows are divided into two categories; those of class 1 are produced by bluff bodies and in these the large scale motions in the wide near wake are the result of interaction of the separated boundary layers; class 2 wakes are without large scale motions in the near wake as in the wake of a slender streamlined body with turbulent boundary layers.

Principally by flow visualisation results the transition to turbulence in a two-dimensional class 1 flow is discussed as also is the development of the wake far downstream. A parallel is drawn between the developments of oscillating laminar and turbulent wakes.

Wakes of class 2 are discussed and the conclusion reached that the necessary experiments, as far as large scale motions are concerned, have yet to be performed.

In two-dimensional class 1 wakes the persistence of large scale motions is demonstrated. It is concluded that it is not yet proved whether large scale motions are spontaneously produced far downstream in wakes of class 2.

INTRODUCTION

Townsend (1) recognised that the large eddies in turbulent shear flow were responsible for the lateral spreading of the turbulence. At that time it was not suspected that the large eddies may possess an ordered motion. The methods of investigation were by hot wire probes and statistical methods. In that measurement environment low frequency motions which are developing at a slow rate and which contain only one fifth of the energy of the fluctuations are easily smoothed out or lost altogether. This Townsend (2) recognises in his 1979 paper. Turbulent self-preservation was found by Reynolds (3) and Keffer (4) to be destroyed by straining the wakes of circular cylinders, because, they said, though the turbulent energy containing eddies responded to the applied strains and reached equilibrium relatively quickly, the large scale motions acted independently of the small scale motions and did not so respond.

It has long been recognised that to understand turbulent shear flows visualisation of the flow is required in order to discover what has to be measured. As with other types of investigation time was needed to see how to use the technique most advantageously and there have been retrogressions as well as advances. The succession may be traced from 1958 to 1981 through the works of Grant (5), Kline and Rundstadler (6), Keffer (4), Brown and Roshko (7), Wynant and Browand (8), Dimotakis and Brown (9), Yule (10), Hussain and Zaman (11) and Hussain and Clark (12). Through this work order was gradually discovered amongst the chaos of the turbulent shear flow. The resultant situation is that there are doubts about the possibility of self preservation in turbulent shear flow. The intrinsic nature of turbulent large scale motions is in doubt, that is, do they appear as a natural consequence of the interactions of turbulence of smaller scale with each other and with the mean shear or are they the remnants of the transition process? This leads to the question of when large eddies are expected to be present and when not. In the last ten years there have been many investigations addressed to this problem. Measurements have ranged over various flow "types", two-and three-dimensional jets, wakes and mixing layers. In terms of self preservation the flow type determines the range of turbulence Reynolds number, R_T, but it became apparent that self preserving shear flows are not so simple that a broad classification in terms of only R_T is possible. Bevilaqua and Lykoudis (13) suggest a hierarchy of self preservation starting from self preserving mean flow profiles and eventually including higher and higher order moments until asymptotically one attains equilibrium fully developed flow with all moments self preserving. Knowing, a priori, which order of self preservation a particular flow will possess cannot yet be determined. It is clear that there are fundamental differences between the various flow types and turbulent shear flows is a class which has subdivisions. Axisymmetric flows are more complex than two-dimensional ones. This is so even at low Reynolds numbers. There has been controversy regarding helical and loop vortices in sphere wakes. There are two classes of turbulent wake flows, (i) those in which turbulence is principally produced by mixing downstream of the body and (ii) those in which the turbulence results principally from boundary shear and the quasi-regular vortex shedding is absent.

We will concentrate on flows of class (i). In particular we will consider turbulent wakes far downstream and their large scale motions. Bevilaqua and Lykoudis have investigated the wakes of a sphere and a porous disc of the same drag. They find that it is some distance (20 diameters) behind the disc before large scale motions appeared and these had smaller transverse spacing than the ones behind the sphere. They attributed the large scales in the disc wake to an active instability of the shear layer. One wonders whether this could be the same as Townsend's suggested mechanism. This work is the closest

approach to a definitive experiment to determine whether large scale motions are spontaneously produced by straining fully turbulent flows. That there are doubts about the interpretation of their results we will see later.

Hussain and Clark (12) describe the types of interaction of large scale structures in turbulent wakes. These include pairing, partial and fractional pairing, slippage, tearing and breakdown or decay. We will find these descriptions useful later.

What I intend to do now is to draw comparisons and recognise similarities between low Reynolds number laminar oscillating wake flows and their higher Reynolds number turbulent counterparts. The development will be more clear if I admit that my feeling is that we can make more than a little progress by viewing the smaller scale turbulent part of wakes with large scale motions as purely random and having the effect of an eddy viscosity.

We will concentrate on the two-dimensional wake of a bluff body and describe the several transitions to the various scales of turbulence which occupy the whole Reynolds number range from about 40 to greater than 10^5. The circular cylinder wake is the most fully investigated flow with large scale oscillatory motions. We will also describe what happens far downstream in laminar and turbulent wakes. Eventually there will be suggestions for further work.

THE PRODUCTION OF TURBULENCE IN WAKES OF THE FIRST CLASS

The mechanics of the transition to turbulence and the resulting length scales produced depend upon the diameter based Reynolds number, Re, of the flow past the body. Transition will be described and discussed for the ranges of Reynolds number which are listed below. This will be illustrated with flow visualisation photographs mostly taken from Gerrard (14) and with some hot-wire oscillograms.

Re < 180

In this range there is only one mechanism for the production of turbulence. The mechanism persists at higher Re but it is more clearly in evidence at low Re. Rarely are the vortices shed from a cylindrical bluff body straight and parallel to the body axis. End effects, which can be minimised only in certain circumstances, produce streamwise vorticity at the ends and along the span of the wake. Spatial nonuniformity of the flow or of the body intermittently produces what we have called "knots" which are localised regions of streamwise vorticity.

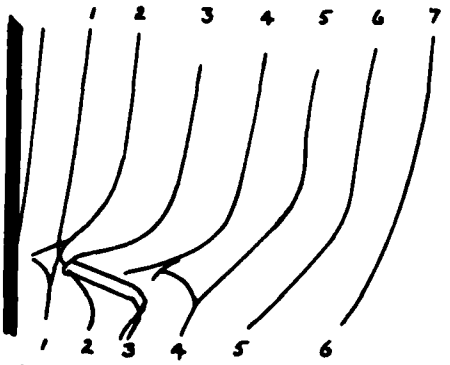

Figure 1 Knots produced by spatial nonuniformity.

Departure from linear vortex lines produces a velocity field which is self-contorting. The vortex lines become mixed up and turbulence of a scale which is large compared with the initial vortex spacing is produced. A sketch illustrating the knot is shown in figure 1. Flow visualisation is produced by dye washed off the rear of the body. This dye mostly accumulates near the vortex centres.

140 < Re < 500

In this range turbulent flow is produced by two additional mechanisms. An instability in the process of vortex formation is triggered by disturbances in the free stream or by feedback from the wake irregularities. This results in periods of irregularity in the rolling up process which lead to the intermittent occurrence of streamwise vorticity at all points along the span. Flow visualisation leads us to describe "fingers" of visualised vorticity pointing back towards the cylinder from the near wake vortex formation region. These lead to turbulence of a scale commensurate with the vortex spacing. This production of irregularity in the wake is special to this Re range.

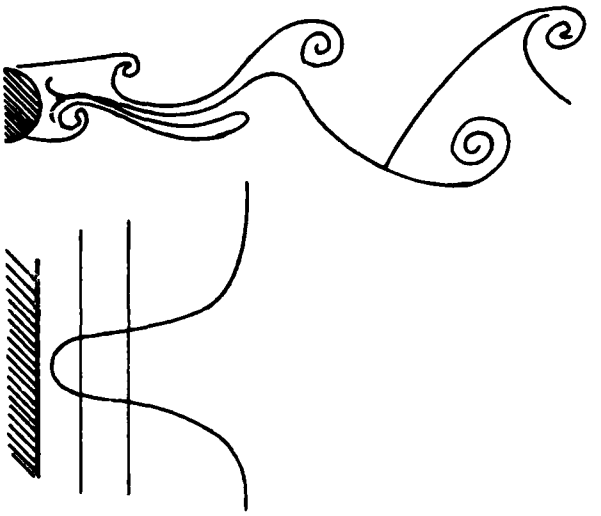

Figure 2. Fingers.

At the upper end of this Re range turbulence of smaller scale is produced by mixing of the fluid from outside the wake into the vortex street. This mixing of outside fluid into the wake takes place at all Reynolds numbers but results in transition only at Re within this range and above. The induction of outside fluid in a transverse flow is attended by a reduction of the vortex spacing ratio and the transition to turbulence within the vortices. Flow visualisation shows that this approaches the cylinder as Re increases and occurs close behind the body at Re > 350. The turbulent scale is less than the vortex sizes. The mechanism of the production of turbulence from mixing of fluid from the two sides of the wake has not been fully explained. Figures 2 and 3 show the filament lines which indicate the mixing. At these low Re the vorticity will have diffused over larger areas than occupied by the filament lines so that fluid of oppositely signed vorticity comes into close proximity in the mixing process as

indicated in figure 3. This represents a seed of instability which at high enough Re results in turbulence production.

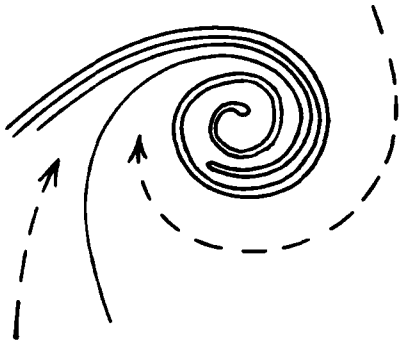

Figure 3. Filament lines and entrainment paths for a vortex in the wake.

Re > 350

The smallest turbulent scales are produced in the transition to turbulence which takes place in the free shear layers before they roll up into vortices. The precursors of this transition are the transition waves observed by Bloor (15). Flow visualisation shows that the mechanism of turbulence production in the transition wave vortices is similar to that at lower Re in the main vortices in the wake.

The transition waves at Re of 1000 to 2000 are seen to interfere with the vortex shedding. In this range the region of vortex formation is long. It is sometimes followed by a turbulent oscillating wake and sometimes by a turbulent wake which does not execute large oscillations until further downstream. The transition in this near wake region is from a diffuse in-line arrangement of vortices to the staggered arrangement of discrete vortices. The results of Bevilaqua and Lykoudis (13) on the wakes of a sphere and a porous disc show a similar transition in the appearance of the envelope of the wake. It would be interesting to repeat their experiment in two dimensions. In this case flow visualisation is easier to interpret. The work of Brown and Roshko (7) shows that the two-dimensional turbulent mixing layer is unstable in the same sort of way as a laminar mixing layer. If the axisymmetric turbulent wake is similarly unstable this could account for the appearance of the wake boundary with its delayed waviness in the work of Bevilaqua and Lykoudis (13).

The wake of a circular cylinder is steady at Re less than about 40. Complete transition to turbulence does not occur until the transcritical range of Re at about $3\ 10^6$ where the boundary layers are turbulent before separation (a class (ii) wake flow). This whole range of Re may be regarded as a range of transition to turbulence. Even the turbulent wake, at higher Re still, begins to be organised again and vortex shedding reappears.

There remains a further cause of irregularity which can produce large scales at all Re and this serves as an introduction to the next section. The irregularities are associated with the imprecise nature of the frequency determining mechanism of the vortex shedding. Vortex shedding is due to the interaction between the separated shear layers and depends on their precise position and strength: it is thus sensitive to small disturbances. The strength and position of the shed vortices varies from cycle to cycle and with position along the span.

DOWNSTREAM DEVELOPMENT INTO THE FAR WAKE

Most experiments on turbulent wakes far downstream of the body have been performed on wakes of the first class which have become turbulent by the processes described above. We will consider the downstream development of large eddies at both low and intermediate Reynolds numbers and show that the development is essentially the same at different Re. The work involves flow visualisation in a towing tank and follows the observations first made by Taneda (16). The towing tank is an appropriate facility in which to study wakes far downstream because the wake moves slowly (at ca. 15% of the body speed) and so remains observable in the tank long after the body has made its traverse. In fact one may observe the wake until it comes to rest provided the background motions are minimised. The wake is constrained by the walls of the tank and lateral growth continues until inhibited by the side walls. Observations of the wake made visible by dye washed off the towed body will be presented at Re at which the wake is essentially laminar, but oscillating, and at which the near wake appears turbulent. Our first observations were reported in an M.Sc. thesis by E. Anagnostopoulos in 1975.

The vortex street can be seen to grow in scale by processes in which the mechanisms described by Hussain and Clark (12) can be recognised. In this way the vortices are rejuvenated. As the vortex increases in age its vorticity becomes more spread by viscous or turbulent diffusion. When the vorticity fields of adjacent vortices overlap interaction ensues. When pairing takes place the combined vortex seems to occupy no greater area than the individuals which combined. The resultant vortex is thus effectively younger. It will be shown that these large scale motions outlive the smaller scale turbulence so that the final state of the wake appears similar.

If the laminar large scale motion is represented by an Oseen vortex of strength K with velocity distribution $(1 - \exp(-r^2/4\nu t))K/2\pi r$ one finds that 72% of the vorticity is contained within the radius of the maximum velocity which is equal to $2.2418\ (\nu t)^{\frac{1}{2}}$ where t is the vortex age. Significant interaction will take place at 25 wavelengths of the vortex street spacing (ca. 125 diameters) down the wake at Re = 100. At higher Re eddy diffusivity takes over from molecular diffusion and its magnitude increases with Re. Approximately, therefore, we expect a similar interaction distance at all Re. As the vortex street scale grows it appears to remain to a first approximation in a vortex street configuration. We infer therefore that there are only small variations in the strength and position of the vortices in the near wake. It is clear that the large scale structures resulting from the downstream development of a vortex street are not coupled to the energy cascade of the other turbulent eddies.

Previous measurements reported as an incidental part of a paper on the three-dimensional structure of the wake (Gerrard, 17) show the same effect in a wind tunnel of the decay of high frequency and persistence of low frequency when the two scales are uncoupled.

The wind tunnel flow had an oscillation at the very low speeds of these experiments. The resulting oscillogram from a hot-wire in the near wake showed a shedding frequency of 6 k Hz with a 200 Hz sinusoidal modulation. At 450 diameters downstream a vortex street at 200 Hz was observed: The 6 k Hz primary vortex street oscillation had decayed to immeasurable size.

To conclude our discussion of wake flows of the first class in which we see a certain amount of parallelism between oscillating laminar wakes and turbulent wakes at higher Re we mention the same similarity in another flow. Photographs of the spread of a jet from a slit in the two conditions above show that the low Re motions still present in the high Re flow could account for the similarity in the rate of spreading.

WAKE FLOWS OF THE SECOND CLASS

There have been many experiments on the wake of a thin flat plate which is one wake of the second class. The turbulent wake produced by the separating turbulent boundary layers is reported to tend towards a self-preserving turbulent state. No measurements seem to have been continued far downstream in this flow. Self-preservation is expected when the scales of the wake motions are all coupled and there is a continuous transfer of energy down the cascade of energy scales from large to small. If the large scale motions are decoupled from the smaller an equilibrium fully developed turbulent flow is not expected.

In the wake of a circular cylinder at transcritical Re (3 to 6 10^6) the wake is relatively narrow at its start and is the result of the coalescence of separating turbulent boundary layers. The turbulent structure of this wake has not been investigated. There is a parallel with the wake of the same body at Reynolds numbers of less than 40. In both cases the near wake is dominated by diffusion, viscous diffusion at low Re, small eddy diffusion in the turbulent wake. (There are also larger scale three dimensional motions in the high Re case). Though the laminar wake can be made to oscillate by disturbances, if it does not oscillate at the body it doesn't start to oscillate further downstream. Is this the case with the turbulent wake or may it develop the oscillations associated with large turbulent eddies?

In hypersonic wakes large scale motions have been found to be absent when turbulent boundary layers produce a turbulent wake but they do appear to possess large scale motions far downstream (Finson, 18). On the other hand Behrens (19) found the appearance of a vortex-street-like array of large eddies far downstream in a hypersonic wake at high Re which he could attribute to an instability of the wake of the bow shock wave.

At low Re Taneda (1978) has produced a circular cylinder wake which is free from oscillations. This was achieved by a rotational oscillation of the cylinder about its axis at a frequency much higher than the normal shedding frequency. If the same (unexplained) effect is present at higher Re a turbulent wake free from large scale motions could perhaps be produced.

It appears that there remain some two-dimensional wake flows which are free from uncoupled large scale motions upon which experiments could yet be made.

CONCLUSIONS

The study of turbulent shear flows has in some respects suffered from having been first approached with the ideas and techniques developed in homogeneous isotropic turbulence. The whole subject of turbulence research has given the impression of struggling for a breakthrough which hasn't been forthcoming. It wasn't surprising that the Boundary Layers and Turbulence meeting in Kyoto in 1966 sent a message to G.I. Taylor noting that the subject of turbulence was essentially still where he had left it in 1938.

In the particular field of large scale motions in turbulent shear flow there has over the years seemed to emerge from the chaos of turbulence the view that there are more regular deterministic structures. The question of whether the large scale motions can appear spontaneously from an equilibrium fully developed turbulent shear flow has still to be answered. They have not been unequivocally observed to do so. It has seemed that the practical and theoretical tools appropriate for the investigation of grid turbulence have not been well suited, at least by themselves, to the study of large scale coherent structures.

We have concentrated here on two-dimensional wakes which, over the whole Reynolds number range, are the most fully investigated flows. Bluff body wakes are peculiar in that they possess a series of transitions to turbulence of different scales over a vast Reynolds number range. There are some similarities between large scale motions in a turbulent wake and the oscillatory motions observed at much lower Reynolds numbers. An understanding of the turbulent wake is to be expected from a study of the unsteady laminar wake because in many wakes the large scale motions appear to be decoupled from the smaller scale motions. There are cases where the relationship between the fluid motion and molecular diffusivity is similar to that between the large scale motions and eddy diffusivity.

Equilibrium fully-developed self-preserving turbulent flow is only possible if the full range of eddy sizes are present and interacting. If large scale motions are decoupled from the cascade of eddy sizes at smaller scales self-preservation is not possible unless one admits the possibility of separate self-preservation of two uncoupled ranges of scales. This is only possible if the large scale motions are part of a fully turbulent range of scales and can pass on mean flow energy to the smallest scales which is an apparent non sequitur.

In an oscillating wake in which "turbulence" of a scale larger than the vortex street spacing certainly exists in the near wake it appears that the interaction between these scales and the vortex street results in a more or less ordered large scale structure. The low frequency disturbances contain a small percentage of the energy at the shedding frequency and determine the scale but not the nature of the downstream development. As far as the large scale motions, into which the vortex shedding develops, are concerned the turbulent smaller scales have a similar effect to that of viscous diffusion at lower Reynolds number.

It is concluded that an experimental investigation of the far wake flows of the second class formed by the coalescence of two turbulent boundary layers yet remains to be performed. In such flows large scale motions appear to be absent in the near

wake. It is possible that the large scale motions produced in the manner suggested by Townsend take a long time to develop in a turbulent wake initially free from large scales. There is only a finite time before the small scale motions in a wake decay and so a spontaneous development of larger scales that is conceptually possible may never occur in practice. A crucial point in the possible production of large scale motions would appear to be whether a turbulent flow is unstable in the same manner as the corresponding laminar shear flow.

In a two-dimensional wake there are various turbulence production mechanisms the effects of which it would be difficult to separate experimentally. Whilst it would be possible to model the downstream development of the vortex street on a computer and thus demonstrate the effects of disturbances of different sorts, a numerical model of a fully turbulent flow which would form a clean model in which to look for large scale motions does not at present seem feasible.

REFERENCES

1 Townsend, A.A., Structure of Turbulent Shear Flow, 1st ed., C.U.P. 1956.

2 Townsend, A.A., Journal of Fluid Mechanics, Vol. 95, 1979, p 515.

3 Reynolds, A.J., Journal of Fluid Mechanics, Vol. 13, 1962, p 333.

4 Keffer, J.F., Journal of Fluid Mechanics, Vol. 22, 1965, p 135.

5 Grant, H.L., Journal of Fluid Mechanics, Vol. 4, 1958, p 149.

6 Kline, S.J., and Rundstadler, P.W., Journal of Applied Mechanics, Vol. 26, 1959, p 166.

7 Brown, G.L., and Roshko, A., Turbulent shear flows AGARD-CP-93, 1971, p 23:1.

8 Wynant, C.D., and Browand, F.K., Journal of Fluid Mechanics, Vol. 63, 1974, p 237.

9 Dimotakis, P.E., and Brown, G.L., Journal of Fluid Mechanics, Vol. 78, 1976, p 535.

10 Yule, A.J., Journal of Fluid Mechanics, Vol. 89, 1978, p 413.

11 Hussain, A.K.M.F., and Zaman, K.B.M.Q., Journal of Fluid Mechanics, Vol. 101, 1980, p 449.

12 Hussain, A.K.M.F., and Clark, A.R., Journal of Fluid Mechanics, Vol. 104, 1981, p 263.

13 Bevilaqua, P.M., and Lykoudis, P.S., Journal of Fluid Mechanics, Vol. 89, 1978, p 589.

14 Gerrard, J.H., Philosophical Transactions of the Royal Society, Vol. 288, 1980, p 351.

15 Bloor, M.S., Journal of Fluid Mechanics, Vol. 19, 1964, p 290.

16 Taneda, S., Journal of the Physical Society of Japan, Vol. 14, 1959, p 843.

17 Gerrard, J.H., Journal of Fluid Mechanics, Vol. 25, 1966, p 143.

18 Finson, M.L., American Institute of Aeronautics and Astronautics Journal, Vol. 11, 1973, p 1137.

19 Behrens, W., American Institute of Aeronautics and Astronautics Journal, Vol. 6, 1968, p 225.

20 Taneda, S., Journal of the Physical Society of Japan, Vol. 45, Pt. 3, 1978.

DEVELOPMENT OF THE ORGANIZED VORTICES IN THE TURBULENT NEAR WAKE OF A CIRCULAR CYLINDER : AN EXPERIMENTAL AND NUMERICAL STUDY

H.C. BOISSON, P. CHASSAING, H. HA MINH and A. SEVRAIN

Institut de Mécanique des Fluides de l'Institut National Polytechnique
Laboratoire associé au CNRS
2, rue Charles Camichel - 31071 TOULOUSE CEDEX FRANCE

ABSTRACT

A method for the prediction of the coherent structures in the turbulent near wake of a circular cylinder is discussed. A comparison is made between the results of an experimental study at a Reynolds number of 52300 and those obtained by the numerical solving of the phase averaged two-dimensional Navier Stokes equations. The properties of the velocity and intermittency fields measured in the turbulent flow are found to be controlled by a vortex pattern similar to the computed one.

NOMENCLATURE

D	Diameter of the cylinder
f	Frequency
f_o	Vortex shedding frequency
I(t)	Intermittency function (1 turbulent ; 0 non turbulent)
I'(t)	Time derivative of I(t)
L	Discrimination threshold
N	Number of periods
$\hat{I}^+(t)$	Positive front indicator = 1.5[I'(t)+|I'(t)|]
$\hat{I}^-(t)$	Negative front indicator = 1.5[I'(t)-|I'(t)|]
R_e	Reynolds number = $U_o D/\nu$
S_t	Strouhal number = $f_o D/U_o$
t	Time
t_n	Reference time station
T_o	Vortex shedding period
U,V	Cartesian instantaneous velocity components
U_o	Upstream mean velocity
X	Downstream location (X = 0 back of the cylinder)
Y	Transverse location (Y = 0 on the axis)
γ	Intermittency factor
f_γ	Crossing frequency of turbulent events
$\hat{f}(t)$	Instantaneous signal
$\bar{f}(t) = \langle f(t)\rangle$; $F(\tau) = \langle \hat{F}(t)\rangle$; $B(\tau) = \langle \hat{B}(t)\rangle$	
τ	Time delay (for phase angle $2\pi f_o \tau$)
ν	Kinematic viscosity (air : $1{,}5\ 10^{-5} m^2/s$)
Ω	Vorticity
<>	Phase average
$(\bar{\ })$	Reynolds average

INTRODUCTION

Numerous research works have been devoted to the study of coherent structures in free turbulent shear flows. A first step is the description of these structures that are often hidden in the turbulent background, but more complex is the theoretical prediction of their dynamical behaviour. As a matter of fact, this second approach can provide a better quantitative determination of their contribution to the overall motion and to some other practical effects such as flow induced vibrations, acoustical generation or turbulent mixing.

Compared with those of jet flows or plane mixing layers, the coherent structures of the near wake have been investigated only in few experimental studies. This is probably the consequence of : i) the complexity of the interactions near the solid body and ii) the difficulty of measuring correctly the velocity components and the corresponding Reynolds stresses in this zone. DAVIES (1) has studied the near wake of a D shape cylinder but he has deduced the spatial structure from only one cross section using the Taylor hypothesis which is probably not verified in such a flow as pointed out by HUSSAIN and DAMAN (2). A more complete study on the coherent structures of the wake of the circular has been performed by CANTWELL (3) using an original hot wire technique for measuring the velocity and a phase locked loop to detect the periodic structure.

Numerical simulation conversely may be a suitable way to obtain a precise information on the dynamics of the flow. Unfortunately it is well known that solving the three dimensional equation for such a random flow with a suitable mesh size would have led to unrealistic computational times. The method of simulation of large eddies based on the filtering technique of LEONARD (4) or a subgrid scale model as proposed by SCHUMANN (5) have not yet been applied to this problem owing to difficulties in their practical setting up. Of a more current use are the methods based upon point vortices in two dimensional potential flows (6), (7), but though some interesting features have been derived in this case, an arbitrary treatment is still necessary near the separation point or at the wall and the results are not always consistent for all the parameters. An alternative method consists of the unsteady simulation of the coherent structures in which the equations are obtained by phase averaging the instantaneous Navier Stokes equations as suggested by HUSSAIN and REYNOLDS (8). Then geometrical considerations are used to obtain two-dimensional equations for the coherent structures. KNIGHT and MURRAY (9) for instance have used this method successfully for the numerical simulation of a plane mixing layer.

In the first part of this paper the fluctuating parameters of the flow behind a circular cylinder at a Reynolds number of 52300 are analyzed experimentally by using of a phase average technique, special attention being paid to the time analysis of turbulent events. In the second one the comparison is made with the numerical solution of the unsteady Navier Stokes equations for the viscous flow which can be considerated as the basis for the equation of the coherent structures and some practical inferences of the turbu-

lent effect are pointed out.

PART ONE : EXPERIMENTAL STUDY

Experimental set up and data processing

A smooth circular cylinder of diameter (D=42mm) spans vertically the test section (60 cm x 70 cm) of a subsonic closed wind tunnel. For all the measurements, the upstream velocity profile was uniform (U_0=10,7 m/s) and the free stream turbulence intensity less than 1,0%. The blockage ratio and aspect ratio are respectively equal to 0,07 and 16,7 which conditions do no cause excessive distorsion of the flow according to WEST and APELT (10)

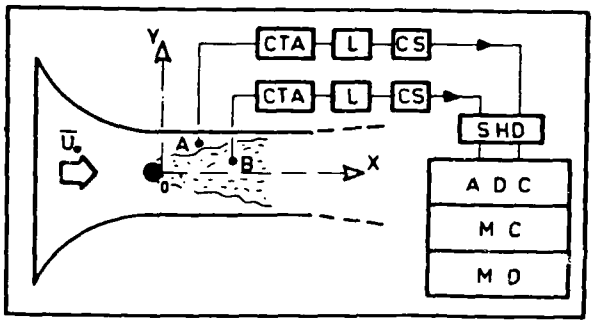

CTA : Constant temperature anemometer ; L : Linearizer ; CS : Conditioning system ; SHD : Sample and hold device ; ADC : Analog to digital converter ; MC : Mini computer Plurimat 400 ; MD : Magnetic disk.

Fig.1. Schematic diagram of the experimental set up

The instrumentation is sketched on fig.1. DISA 55 M 01 constant temperature anemometers and DISA 55 P 11 single wire probes operate with sensor parallel to the cylinder. The signal from a movable probe (B) is analyzed according to a phase reference given by a fixed sensor (A) located at X/D = 2 and Y/D = 2.8. Both signals are identically processed and sampled synchronously by use of a sample and hold device at a frequency of 10 KHz, aliasing being prevented by use of a HEMC low pass filter at 5 KHz (48 dB/Octave). The two synchronous samples of 128 x 2048 points (or 26 seconds) are stored on the magnetic disk of a minicomputer PLURIMAT-S and all further treatments are processed numerically. Spectral analysis operations are performed by use of a microprogrammed Fast Fourier transform routine operating on 2048 points.

The measurements

Velocity signal and vortex crossing detection. The region which is investigated (X/D = 2 and 4) corresponds to the very near wake of the cylinder. The flow in both sections is highly turbulent and accurate velocity measurements require either Lazer Doppler Anemometer or flying hot wire as used by CANTWELL (3). Such an apparatus was not available here. However, the effective cooling velocity of the wire normal to the plane of the wake is, if the effect of spanwise velocity fluctuations is neglected, approximately representative of the modulus of the velocity vector and is poorly sensitive to its angular variations. The signal of such a probe is referred to hereafter as the velocity signal.

Since 1954, using a similar probe, ROSHKO (11) has described some properties of the wake that are confirmed by our measurements. The spectra of the velocity fluctuations displayed on figure 2 are dominated by a principal peak at a Strouhal number S_t=0,197 while on the axis of the wake the first harmonic is observed. The spectral characteristics are interpreted as the footprint of the regular vortex streets issued from the cylinder. But the spectra also contain a continuous power distribution due to the presence of turbulence superimposed to the regular vortices. Under the effect of the turbulent viscosity the peaks are found to disappear in our measurements at a downstream distance of about 15 diameters on the axis and 25 diameters everywhere in the wake.

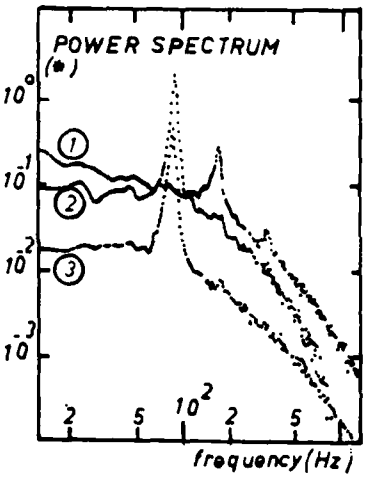

(*) arbitrary scale

1 Y/D = 0
2 Y/D = 0.87
3 Y/D = 1.62

Fig.2. Power spectra of the velocity in the section X/D = 4.

Outside the turbulent wake, the crossing of vortices induces an oscillation of the potential flow so that the peak still exists but the high frequency content of the spectrum is negligible. Thus this signal is choosen as a reference for detecting the organized vortices. Random low frequency modulations of the signal are observed. Discarding a filtering operation that would probably introduce an artificial distorsion of the signal, the occurrence of a maximum of the velocity is choosen as a criterion to detect the crossing of a vortex. Although this criterion does not seem to be the best one, its physical meaning is obvious as changes of sign in the acceleration are clearly linked to the direct influence of the vortex. The histogram of the intervals between two reference time stations, displayed on figure 3, is then different from that of a purely periodic pattern but the most probable value corresponds to the vortex shedding period.

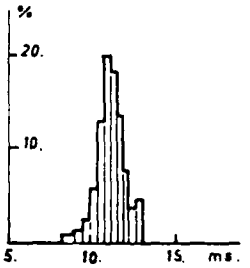

Fig.3. Histogram of the periods of the crossing of a vortex.

Phase average technique. A practice which becomes more and more usual (8), (1), (12) is to obtain the averaged parameters of the coherent structures by ensemble averaging each individual signal conditionned to the crossing of the vortex and referenced to a phase origin (τ= 0). This phase average operation, analogous

to that of the periodic case, is denoted :

$$\langle \phi(t) \rangle = \frac{1}{N} \sum_{n=1}^{N} \phi(t_n + \tau) \quad \text{function of } \tau \qquad (1)$$

For satisfying the double condition of statistical stability and time resolution the values of the phase averages are calculated over a number N of approximately 2300 periods and are displayed on 512 discrete points around the phase reference ($\tau = 0 \rightarrow$ point 256) at a sampling frequency of 10 KHz. Each period of vortex shedding represents 113 points. As the averaging interval is larger than a period, the same point of the signal is averaged several times but at different phase angles.

Turbulent time intervals analysis. Boundary intermittency is very marked in the whole near wake and it is necessary to take account of this aspect in the dynamics of the coherent structures.

The intermittency function is calculated from the second derivative of the velocity signal using a centered difference scheme. On the trace of the signal, figure 4, a large contrast is apparent between turbulent sequences, that is enhanced in the second time derivative. A given threshold "L" can be defined to separate smooth parts from turbulent ones.

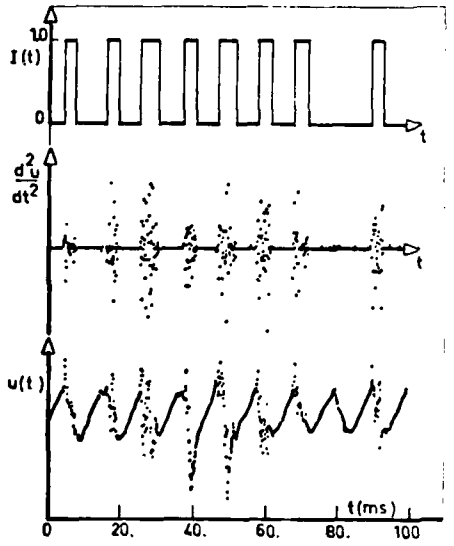

Fig.4. An example of the derivation of the intermittency signal

"L" have been selected from the values in the potential flow and the results are found to be consistent all over a cross section, keeping "L" constant. However the rough intermittency function obtained from this direct treatment needs to be smoothed in order to obtain continuous portions of signal corresponding to the actual state of the flow. Discarding all direct filtering, a validation technique is set up based upon a careful inspection of time intervals - for details see (13) -. In this technique minimum time intervals are prescribed for turbulent intervals (0.2 ms) and for non turbulent intervals (1.5 ms).

Conventional mean values of the intermittency factor γ and the crossing frequency f_γ are presented. Phase averages of the intermittency signal or its front indicators [$\tilde{P}(t)$ and $\tilde{F}(t)$] describe the distribution of turbulence at a given stage of the development of the average structure.

The following functions of the phase angle are defined :

$$\Gamma(\tau) = \langle I(t) \rangle \quad ; \quad F(\tau) = \langle \tilde{F}(t) \rangle \quad ; \quad B(\tau) = \langle \tilde{B}(t) \rangle$$

$\Gamma(\tau)$ is the probability for the flow to be turbulent. $F(\tau)$ and $B(\tau)$ are respectively the probabilities for a front or a back edge of a turbulent zone to be observed.

The results

Velocity field. The phase average of the velocity fluctuation is given in figure 5. Within the accuracy range of the experimental procedure, it can be considered as nearly periodic with respect to the phase angle as far as the first periods surrounding the phase reference are concerned. This periodicity of the averaged signals seems to show that occasional jitters have weak effects as one would have expected then to reduce drastically the correlation for phase angles greater than a period.

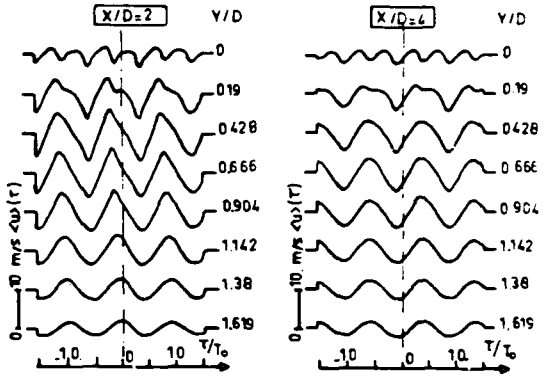

Fig.5. Phase average of the velocity.

At the external part of the wake a nearly pure sinusoïdal signal is observed that is distorted when moving through the axis. On figure 6 the spectral power deduced by Fourier analysis of the phase averaged signal is compared to the Reynolds averaged values.

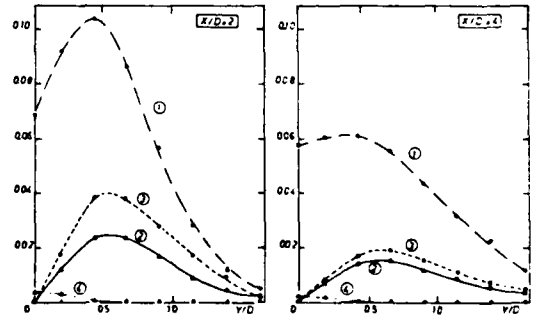

Fig.6. Total and periodic velocity fluctuations (1) total power $\overline{u^2}/U_0^2$; (2) spectral power at f_0 ; Fourier analysis of the phase average : (3) fundamental ; (4) 1st harmonic.

The Fourier components are found the very in the same way in both approaches. It is worthwhile noticing that on the axis the fundamental mode has no contribution and the first harmonic is observed as a conse-

quence of the symmetry of the vortex street with respect to the axis.

Turbulent time intervals analysis. Reynolds averaged parameters deduced from the intermittency function are found to behave differently from those in the far wake. It is obvious from figure 7 that the error function law found by LA RUE and LIBBY (14) or FABRIS (15) is no longer valid in the near wake. The values of intermittency on the axis are substancially different from unity and seems to fall down abruptly at the external edge of the wake. Similarly the crossing frequency f_γ -fig.8- is not gaussian, it takes a non zero value at the axis and reaches its maximum value in the wake, a value which is of the order of the vortex shedding frequency. ($\simeq 1.2\ f_o$)

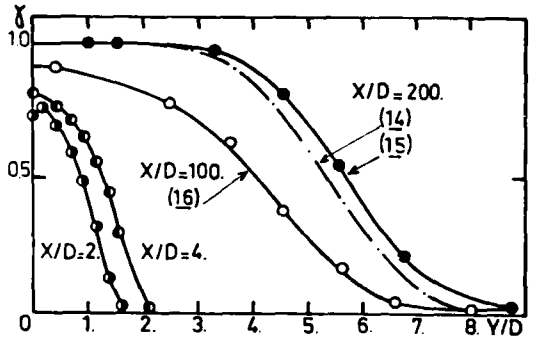

Fig.7. Intermittency profile

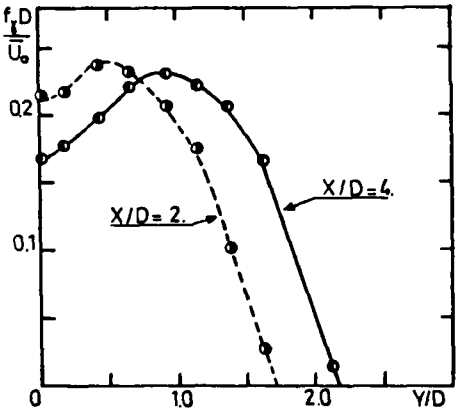

Fig.8. Crossing frequency profile

The phase averaged values of the intermittency function are displayed on figure 9 and the first conclusion to emerge is that the distributions are also periodic showing a severe control of the vortex shedding mechanism on the presence of turbulence. In the external parts of the wake the value of intermittency is found to be very low over a large part of the period and in this region only localized turbulent edges of the vortex cross the otherwise unperturbed potential flow. Near the axis a double distribution is observed that is due to the deep engulfment of potential flow between the turbulent vortices beyond the axis. The zone where the opposite vortex row effect is observed can attain transverse stations of Y/D = 0.67 or 1.14 for sections X/D = 2 and 4 respectively. Conversely in this central zone the intermittency distribution does not fall under a minimum value due to losses in phase lock and to larger turbulent time intervals.

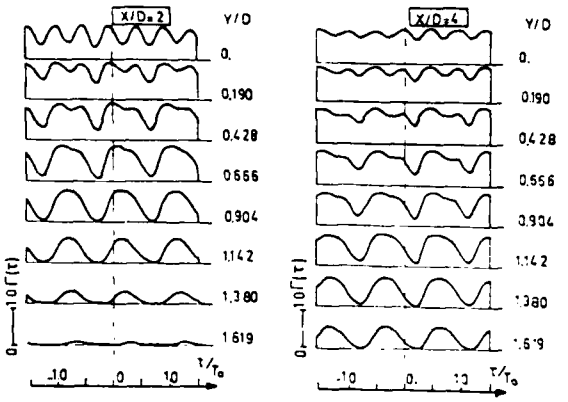

Fig.9. Phase average of the intermittency.

More insight in the organized pattern of the turbulent flow can be obtained by inspection of figures 10 and 11. The probability of occurence of the front of a turbulent event is well localized with respect to the phase angle and it is deduced that the front edge of a turbulent vortex must be a regular sharp edged surface. But for the back of the vortices the situation is not the same as a more spreaded distribution is observed. For both functions, similar features to the phase average of intermittency are found concerning the double distributions due to the alternate influence of the vortex rows.

Concerning the spatial evolution of these parameters, phase lags due to convection of the structures are used to deduce the convection velocity of $0.82\ U_o$ and wavelength of 4.2 D which agrees well with other similar results (1), (3).

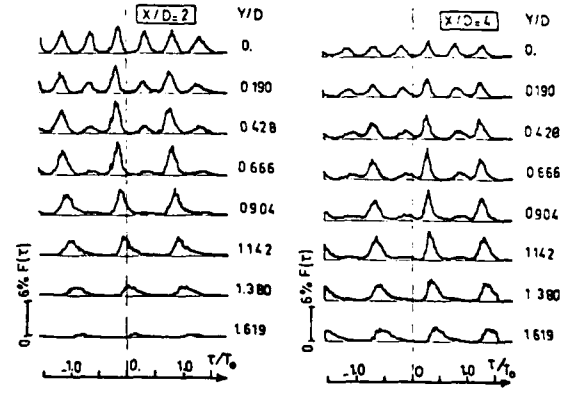

Fig.10. Phase average of the positive fronts.

Comparing the results for the velocity field to those of the time of presence of turbulence, it follows that the phases of the development of the structure where the intermittency level is low corresponds to the accelerations of the phase averaged velocity and that the fronts of turbulent events are mainly localized near the maximum of the velocity. This is

due to the fact that the accelerations derive from the crossing of the high speed potential flow and the turbulent breakdown occurs when the influence of the low speed internal part of the wake is sensible.

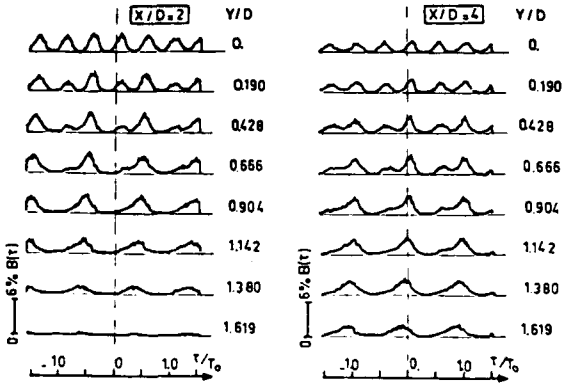

Fig.11. Phase average of the negative fronts.

Conclusion to the experimental part

The averaged structure of the turbulent vortices emerges from the experimental analysis performed here. It is found that the phase average is nearly periodic with respect to the phase angle for both the velocity field and the presence of turbulence. It exists evidences for the entrainment mechanism of large size pockets of potential flow to which the turbulence seems to be transferred from the internal organized vortices. The transfer must be more important near the axis where the interaction is stronger and in this process the back edges of the vortices seem to be more amenable to diffuse their turbulent character.

PART TWO : THEORETICAL APPROACH

Based on the aforementioned experimental analysis the instantaneous motion could be viewed as a combination of "phase coherent" pattern and "phase incoherent" random fluctuations. Generally, the first structures are associated to large-scale determistic characters and the last ones to the fine-scale turbulent motion. Then, an instantaneous flow parameter $\Phi(x_i,t)$ can be decomposed according to (2),(6) :

$$\Phi(x_i,t) = \langle\Phi(x_i,t)\rangle + \phi(x_i,t) \qquad (2)$$

where $\langle\Phi(x_i,t)\rangle$ is the phase averaged value of $\Phi(x_i,t)$ and $\phi(x_i,t)$ is the random contribution. While it is possible to assume in some circumstances that the phase coherent motion is unsteady and spatially two-dimensional, it is clear by contrast that the random contribution $\phi(x_i,t)$ is essentially three dimensional.

Using this decomposition (2) the equations for unsteady flows are :

$$\frac{\partial\langle U_i\rangle}{\partial x_i} = 0 \qquad (3)$$

$$\frac{\partial\langle U_i\rangle}{\partial t} + \frac{\partial}{\partial x_k}\langle U_k\rangle\langle U_i\rangle = -\frac{1}{\rho}\frac{\partial\langle P\rangle}{\partial x_i} + \nu\frac{\partial^2\langle U_i\rangle}{\partial x_k\partial x_k} - \frac{\partial\langle u_i u_k\rangle}{\partial x_k} \qquad (4)$$

It is nevertheless more convenient to introduce, like HUSSAIN and ZAMAN (2), the vorticity vector Ω_i : by taking the curl of (4) it is possible to obtain the transport equation for this quantity.

$$\frac{\partial}{\partial t}\langle\Omega_i\rangle + \langle U_k\rangle\frac{\partial}{\partial x_k}\langle\Omega_i\rangle = \langle\Omega_k\rangle\frac{\partial}{\partial x_k}\langle U_i\rangle + \nu\frac{\partial^2}{\partial x_k\partial x_k}\langle\Omega_i\rangle + \frac{\partial}{\partial x_k}(\langle\omega_k u_i\rangle - \langle u_k\omega_i\rangle) \qquad (5)$$
$$(*)$$

Thus, the unsteady turbulent flow is governed by the same equation as the laminar case, except for an added term (*) standing for the turbulent effects.

Assuming that the fine scale turbulent Reynolds can be connected to the strain rate tensor

$\langle S_{ij}\rangle = \frac{\partial\langle U_i\rangle}{\partial x_j} + \frac{\partial\langle U_j\rangle}{\partial x_i}$ by a simple eddy viscosity concept :

$$-\langle u_i u_j\rangle = \nu_t\langle S_{ij}\rangle - \frac{2}{3}\delta_{ij}\langle k\rangle \qquad (6)$$

equation (5) can be rewritten as :

$$\frac{\partial}{\partial t}\langle\Omega_i\rangle + \langle U_k\rangle\frac{\partial}{\partial x_k}\langle\Omega_i\rangle = \langle\Omega_k\rangle\frac{\partial}{\partial x_k}\langle U_i\rangle + (\nu_t+\nu)\frac{\partial^2\langle\Omega_i\rangle}{\partial x_k\partial x_k} + S_\Omega \qquad (7)$$

where S_Ω is a source term containing derivatives of the turbulent viscosity ν_t.

In a previous work (12), it was shown in the case of steady flows that the source term S_Ω has a minor importance.

Furthermore, if we assume that in a turbulent flow the eddy viscosity is of a higher order of magnitude than the molecular one, it is perfectly legitimate to consider that the actual Reynolds number based on ν_t is in a low range.

Since for viscous flows the Reynolds number is the only governing parameter, it may be inferred that the turbulent flow behaves in a similar way. It is also possible to notice that the constant value of the Strouhal number ($\simeq 0.197$) observed experimentally is due to some "universal" effective Reynolds number independent of the classical one.

Thus, although significant differences between laminar and turbulent flows may be not negligible, since the eddy viscosity is not constant in space and in time, it is yet interesting to compute the laminar case for a Reynolds number corresponding to the same Strouhal number, before introducing a convenient turbulence model allowing the computation of the actual turbulent viscosity in the flow field.

For this purpose, equation (7) (where ν_t = constant and $S_\Omega = 0$) is simultaneously solved with the Poisson equation for the stream function (Helmholtz formulation) :

$$\nabla^2\langle\psi\rangle = -\langle\Omega_3\rangle \qquad (8)$$

for a two dimensional flow.

The initial conditions correspond to a flow at rest and the boundary conditions are those of no slip on the wall and a mixed Neuman-Dirichlet condition at infinity, allowing vortices to go freely out of the downstream boundary (13).

A passive scalar transport equation can be adjoined, the temperature for instance, being of some interest here for a slighty heated cylinder.

Numerical code

Equations (7) and (8) transformed in a logarith-

the polar coordinate system, are approximated by centered space finite difference schemes. An Alternating Direction Implicit (A.D.I.) method is used for the transport equations and the Poisson equation is solved at each time step by an A.D.I. optimized method. Detailed description of the procedure is given by MARTINEZ [19].

The results

The results are given for a Reynolds number of 200 since the corresponding Strouhal number (0.19) is quite closed to those of the turbulent case. (Fig.12)

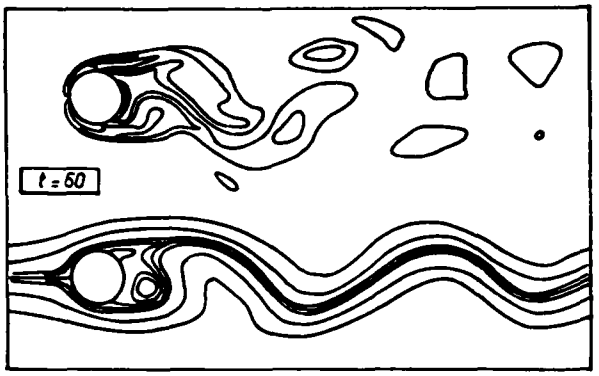

Fig.12. Vorticity contours and streamlines.

The vortex shedding mechanism is clearly apparent and the wavelenght λ calculated from the instantaneous flow is given on table 1 together with the corresponding convection velocity.

Reynolds R_e	Strouhal S_t	Wavelenght λ/D	Convection velocity U_c/U_o
100	0.16	4.57	0.73
200	0.19	4.37	0.83
52300	0.197	4.20	0.82

Table 1.

Thus the examination of these results shows that the differences between two first laminar cases are greater than those of the two last flows (laminar R_e = 200 and turbulent R_e = 52300).

The deep penetration of potential flow inside the wake is obvious from figure 12. However the temperature variations (fig.13) are more suitable for picturing the coherent vortices. Temperature, as a passive scalar, has been currently used for the evaluation of the intermittency function and is considered as a marker of the flow. It can be observed that the flow pattern exhibits the same unsteady features that have been measured previously in the turbulent wake.

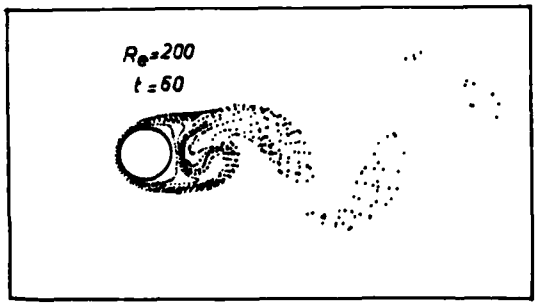

Fig.13. Isothermal curves

CONCLUSION

On a qualitative basis the comparison proves that the approach of the organized modition by an unsteady two dimensional method is valuable for the Reynolds number under study. The measured phase averaged parameters reflect the periodic structure predicted by a constant viscosity model. However, it seems that such a model would probably be unsuitable for predicting the coherent structures of the turbulent flow everywhere.

REFERENCES

1 Davies ME, "A comparison of the wake of a stationary and oscillating bluff body using a conditional averaging technique" Jl of F. Mech. (1976), vol 75, part 2, pp. 209-231

2 Hussain AKMF and Zaman KBMQ, "Vortex pairing in a circular jet under controlled excitation. Part 2 : coherent structure dynamics" Jl of F. Mech (1980), vol 101, part 3, pp 493-544

3 Cantwell BJ, "A flying hot wire study of the turbulent near wake of a circular cylinder at a Reynolds number of 140000" (1975) CALTECH, Ph.D.Thesis

4 Lecnard A, "Turbulent structures in wall-bounded shear flows observed via three dimensional numerical simulation" Proc. of the Inter. Conf. on Turbulent Flows, Madrid (June 1980) session 3

5 Schumann, U. Grötzbach, G. Kleiser, L. "Direct numerical simulation of turbulent" V. Karman Institute L.S. 1979-2 (January 1979)

6 Chorin J. "Numerical study of slightly viscous flow" Jl. of F. Mech. (1972) vol 57, part 4, p.785-796

7 Ashurst WT, "Numerical simulation of turbulent mixing layers via vortex dynamics" Proc. of the Turbulent shear Flow Symp., Pennsylvania Univ. (1977)

8 Hussain AKMF and Reynolds WC, "The mechanics of an organized wave in turbulent shear flow. Jl. of Fluid Mech. (1970) vol 41, part 2, pp 241-258

9 Knight DD and Murray BT, "Theoretical investigation of interaction and coalescence of large scale structures in the turbulent mixing layer" Proc. of the Inter. conf. on turbulent flows, Madrid (1980) ses.3

10 West GS and Apelt AJ, "The effects of tunnel blockage and aspect ratio on the mean flow past a circular cylinder in the range $10^4<R<10^5$". To be published in Jl. of Fluid Mechanics

11 Roshko A, "On the development of turbulent wakes from vortex streets" NACA Rept 1191 (1954)

12 Blackwelder R, "On the role of phase information in conditional sampling" The Physics of Fluids (1977) vol 20, n°10, part II, pp. S232-S242

13 Boisson HC, Chassaing P, Ha Minh H, "Conditional analysis of intermittency in the near wake of a circular cylinder" IMF Toulouse, Rept M3-39 (1981)

14 La Rue JC and Libby PA, "Statistical properties of the interface in the turbulent wake of a heated cylinder" The Physics of Fluids, vol 19, n°212 (1976)

15 Fabris G, "Conditional sampling study of the turbulent wake of a cylinder. Part 1" Jl of F. Mech. (1979) vol 94, part 4, pp 693-709

16 Symes CR and Fink LE, "Effects of external turbulence upon the flow past a cylinder" Lect. notes on Physics (Germany) (1978) n° 75, pp 86-102

17 Ha Minh H, Chassaing P, "Some numerical predictions of incompressible turbulent flows" 1st Inter. Conf. on Numerical Prediction in Laminar and Turbulent Flows, Swansea, UK,

18 Ha Minh H, Boisson H, Martinez G, "Unsteady mixed convection heat transfer around a circular cylinder" ASME annual Winter Meeting (1980) HTD vol 13,

19 Martinez G, "Ecoulement autour d'un cylindre à nombres de Reynolds modérés" INP Toulouse (1979) Thèse Docteur Ingénieur n°48

A THEORETICAL MODEL OF THE COHERENT STRUCTURE OF THE TURBULENT BOUNDARY LAYER IN ZERO PRESSURE GRADIENT

Z. Zhang and G.M. Lilley

University of Southampton, England

SUMMARY

A self-generating deterministic coherent structure is shown to arise in calculations on a model of a turbulent boundary layer. The solution commences with the evaluation of the linear damped periodic eigen mode for the vertical velocity perturbation which leads to an initial growth in the vorticity perturbations. These lead to changes in the Reynolds stresses and hence to a distortion of the time dependent mean velocity distribution. Our analysis in this respect is somewhat similar to the Benny-Lin investigation of the non-linear interaction of two symmetric oblique waves in unstable laminar boundary layers. The distorted mean velocity profile leads to a strong growth in the Reynolds shear stress, provided the initial disturbance exceeds a certain amplitude of the order of 5% of the freestream velocity. The numerical results display a spanwise periodic structure with a spacing of the order of 100 wall units and have the form of side by side ejections and sweeps. The maximum distortion in the mean velocity occurs near $y^+ = 20$ over a wide range of Reynolds numbers. It is concluded that the distorting mean velocity profile in the inner region of the boundary layer is grossly unstable and will lead to a catastrophic breakdown of the flow into smaller scales, which therefore represents the high production of turbulent energy and its dissipation. This process is self-generating and occurs randomly throughout the turbulent boundary layer.

INTRODUCTION

During the past 25 years experimental studies of the incompressible turbulent boundary layer have shown that over a wide range of Reynolds numbers the seemingly random structure of convecting, distorting eddies is nevertheless controlled by repeating, coherent large scale structures which occur naturally and at random.

Many theoretical attempts have been made, based on quasi-laminar linear perturbation theory, to uncover the production and subsequent development of these coherent structures. These have met with only limited success. Some non-linear approaches have been attempted such as in Landahl (1973), Walker (1978) and Hanratty (1979). A detailed commentary on these methods is described elsewhere, Zhang (1981).

In this work we describe a new approach which is based on the full equations of fluid flow in which the small scale turbulence is modelled using an eddy viscosity. Although it is shown that the first order mode is damped, nevertheless there is an initial linear growth in part of the flow structure leading to a strong non-linear interaction and consequent distortion to the mean flow. The distorted mean profile suffers a secondary instability and subsequent breakdown of the flow within a streamwise length scale of the order 3 to 5 boundary layer thicknesses and which is a weak function of Reynolds number. Our work also describes the formation of streamwise vortices which suffer the

secondary instability and breakdown referred to above.

The model is incomplete in that the breakdown of the flow arising from the secondary instability is only described qualitatively. In addition, no attempt is made to model the mean growth of the boundary layer and the necessary entrainment of irrotational fluid from the freestream. Since our model describes the self-generation of unstable and repeatable flow structures as a result of instabilities that arise within the inner region of the boundary layer, the neglect of such features as boundary layer growth and entrainment are, we believe, not of prime importance in the determination of turbulent boundary layer flow structure. However, these features and those relating to the break-up of the secondary instability are subjects for further work.

The preliminary work leading to this model was completed when one of us (GML) was a Visiting Professor in the Department of Aeronautics and Astronautics at Stanford University (1977-1978).

DESCRIPTION OF MODEL

In order to model the self-generated cell-like structure, which we refer to as a coherent structure, in a turbulent boundary layer, as described in Fig.1

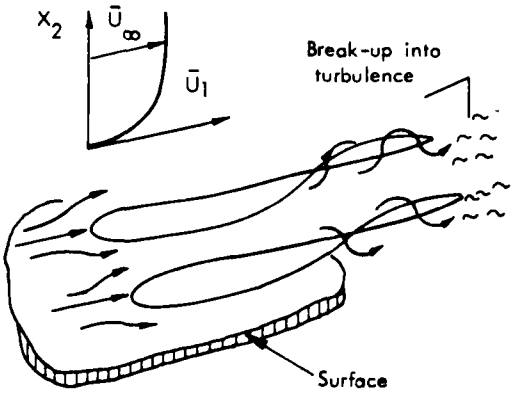

Fig 1 Development of streamwise vortices and the lift-up of wall streaks and their subsequent break-up. (After Kline and Runstadler) (1959)

we have to make several assumptions. These are as follows: (a) the large scale features of the coherent structures are treated as an ensemble average of perturbations to the turbulent flow, (b) three-dimensional linear perturbations are introduced which are composed of a series of eigen functions of a modified Orr-Sommerfeld equation, (c) distortions to the mean flow arise from non-linear interactions between the linear perturbations, (d) the distorted mean profile, which is time dependent, suffers a secondary instability resulting in a flow breakdown, (e) non-linear distortion and energy considerations will lead to a finite maximum amplitude for the secondary instability. All the characteristics of our model, except (e), have been treated in the following sections. An important aspect of our model is the use of an eddy viscosity to model the small scale random disturbances in the flow as well as the non-linear interactions. Several forms of eddy viscosity have been used in predictions of unsteady turbulent flow (Reynolds (1972); Smith and Cebeci (1974)). We have used the Smith and Cebeci model for both the steady and unsteady mean flow. Although other models may have certain advantages, including that of a time dependent eddy viscosity, we believe that the model we have used is plausible and reflects most of the observed features of turbulent flows.

Finally, we note that the non-linear interaction arising from the linear growing modes and the subsequent development of the secondary perturbations and mean flow distortion have a related form to the Benney-Lin analysis (Benney and Lin (1960); Benney (1964)) of non-linear interactions of a pair of symmetrical oblique linear waves in unstable laminar shear flows.

ANALYSIS

Mean flow

The turbulent flow in the boundary layer is assumed to be incompressible (density equal to unity) and Newtonian so that at all $(\underline{x},t)$ the basic equations for the unsteady flow are:-

$$\left(\frac{\partial}{\partial t} - \nu\nabla^2\right)v_i + \frac{\partial}{\partial x_j}\left(p\delta_{ij} + v_i v_j\right) = 0 \; ; \; \frac{\partial v_j}{\partial x_j} = 0 \qquad (1)$$

The ensemble average taken over an infinite number of realisations of the flow reduces these equations to:-

$$\frac{\partial}{\partial x_j}\left(\bar{P}\delta_{ij} + \bar{U}_i\bar{U}_j + \overline{u_i'u_j'}\right) = \nu\nabla^2\bar{U}_i \; ; \; \frac{\partial U_j}{\partial x_j} = 0 \qquad (2)$$

where $\langle v_i\rangle = \bar{U}_i$; $\langle p\rangle = \bar{P}$ and with $v_i = \bar{U}_i + u_i'$, $\langle v_iv_j\rangle = \bar{U}_i\bar{U}_j + \overline{u_i'u_j'}$. We assume the mean flow velocity $\bar{U}_i$ is governed by Prandtl's boundary layer approximations for a two-dimensional mean flow so that $\underset{\sim}{\bar{U}} \equiv (\bar{U}_1, \bar{U}_2, 0)$ with $\bar{U}_1 >> \bar{U}_2$ and $\frac{\partial}{\partial x_2} >> \frac{\partial}{\partial x_1}$. The flow outside the boundary layer is constant and equal to $\bar{U}_\infty$.

For the purpose of evaluating $\bar{U}_i$ we introduce an empirically derived eddy viscosity ν_T for which Cebecci and Smith (1974) suggested the following formula:

$$\frac{\nu_T}{\nu} = K^2y^{+2}\frac{du^+}{dy^+}\left(1 - \exp(-\frac{y^+}{26})\right)^2 \qquad 0\le y\le y_c$$
$$= K_1 R_\theta H \qquad y_c\le y\le\delta \qquad (3)$$

where K is von Karman's constant

$$K_1 = 0.016\left[1 - 0.355\exp(-0.243z^{\frac{1}{2}} - 0.298z)\right]^{-1}$$

with $z = \frac{R_\theta}{425} - 1$

and R_θ, H are the Reynolds number $\left(\frac{\bar{U}_\infty\theta}{\nu}\right)$ based on the momentum thickness, θ and the form factor respectively. In equation (3) $u^+ = \bar{U}_1/u_\tau$ and $y^+ = \frac{x_2u_\tau}{\nu}$ where $u_\tau = \sqrt{\tau_w/\rho}$ is the shear velocity. The same formula for ν_T will be used below for the determination of the Reynolds stress when the mean flow suffers a distortion. In the present case:

$$-\overline{u_i'u_j'} = \nu_T\left(\frac{\partial\bar{U}_i}{\partial x_j} + \frac{\partial\bar{U}_j}{\partial x_i}\right) \qquad (4)$$

The unsteady flow model

We next assume that the turbulent boundary layer develops at each position a repeatable coherent structure which is self-generating. These structures occur randomly in space and time. The coherent structure is of finite amplitude and during its

development a measurable distortion of the mean flow occurs. At any given station within the boundary layer we therefore take a conditionally sampled ensemble average of the flow field such that its trigger is associated with the commencement of a new coherent or cell-like structure. At the commencement of the coherent structure the flow is such that its ensemble average velocity is $\overline{U}_i$ and its Reynolds stress is $\widetilde{u_i' u_j'}$. During the development of the coherent structure the conditionally sampled ensemble average (written $\overline{\overline{\ }}$) shows a slow variation in velocity in space and time given by $\overline{\overline{v_i}} = U_i(\underline{x},t)$ and a fast fluctuation $u_i'(\underline{x},t)$ where $v_i = U_i(\underline{x},t) + u_i'(\underline{x},t)$ and $\overline{\overline{v_i v_j}} = U_i U_j + \widetilde{u_i' u_j'}(\underline{x},t)$. We assume that Reynolds stress $\widetilde{u_i' u_j'}$ can be modelled by the use of the same eddy viscosity ν_T, as was used for the mean flow analysis leading to the evaluation of $\overline{U}_i$. Thus we write

$$-\widetilde{u_i' u_j'} = \nu_T S_{ij} \tag{5}$$

where $S_{ij} = \frac{\partial U_i}{\partial x_j} + \frac{\partial U_j}{\partial x_i}$ is the conditionally sampled ensemble averaged rate of strain tensor. This assumption that ν_T is governed by the mean flow is not critical to the remainder of the analysis and although other approximations may be used, that above is the simplest and most plausible. Hence in terms of these conditionally sampled ensemble averages, equation (1) becomes

$$\frac{\partial U_i}{\partial t} + \frac{\partial}{\partial x_j}\left(P\delta_{ij} + U_i U_j\right) = \frac{\partial}{\partial x_j}(\nu+\nu_T) S_{ij} \tag{6}$$

with

$$\frac{\partial U_j}{\partial x_j} = 0 \tag{7}$$

The mean flow distortion $\Delta U_i = U_i - \overline{U}_i$ is governed both by large scale disturbances of order of the cell size and the more rapid fluctuations which generate the Reynolds stress $\widetilde{u_i' u_j'}$ which itself is governed by the large scale distortion.

So far our model is completely general but being non-linear is incapable of solution. We therefore simplify our model by the introduction of a perturbation scheme taken up to second order. A higher order analysis may have certain advantages over that adopted here. Nevertheless, we have no evidence that a third order analysis will lead to improved results. Thus, the conditionally sampled ensemble averaged velocity and pressure are written:-

$$U_i = \overline{U}_i(\underline{x}) + \varepsilon\, U_i^{(1)}(\underline{x},t) + \varepsilon^2\, U_i^{(2)}(\underline{x},t) \tag{8}$$

$$P = \overline{P}(\underline{x}) + \varepsilon\, P^{(1)}(\underline{x},t) + \varepsilon^2\, P^{(2)}(\underline{x},t) \tag{9}$$

where ε is a small parameter. In our flow model $\overline{P} = 0$ and $\overline{U}_i = \overline{U}_1(x_2)\delta_{i1}$. When substituted into equation (6) we find the zeroth, first and second order approximations give respectively the mean flow, the linear perturbation and the secondary perturbation to the mean flow.

Linear perturbation

The equation for $U_i^{(1)}$ becomes

$$\left(\frac{\partial}{\partial t} + \overline{U}_1(x_2)\frac{\partial}{\partial x_1}\right)U_i^{(1)} + \delta_{i1}U_2^{(1)}\frac{d\overline{U}_1}{dx_2} + \frac{\partial P^{(1)}}{\partial x_i} = \frac{\partial}{\partial x_j}(\nu+\nu_T)\, S_{ij}^{(1)} \tag{10}$$

with $\frac{\partial U_j^{(1)}}{\partial x_j} = 0$ (11)

We next find the Fourier Transformation of these equations with respect to the spatial coordinates x_1, x_3 where

$$U_i^{(1)} = \iint_{-\infty}^{\infty} \hat{U}_i(\alpha,\beta;x_2,t)\exp i(\alpha x_1+\beta x_3)\,d\alpha d\beta \tag{12}$$

and a similar relation for $P^{(1)}$.

The equations for $\hat{U}_i$ are given by:-

$$\left(\frac{\partial}{\partial t} + i\alpha\overline{U}_1\right)\begin{Bmatrix}\hat{U}_1\\ \hat{U}_2\\ \hat{U}_3\end{Bmatrix} + \begin{Bmatrix}\overline{U}_1'\hat{U}_2\\ 0\\ 0\end{Bmatrix} + \begin{Bmatrix}i\alpha\hat{P}\\ \hat{P}'\\ i\beta\hat{P}\end{Bmatrix} = (\nu+\nu_T)\left(\frac{\partial^2}{\partial x_2^2} - k^2\right)\begin{Bmatrix}\hat{U}_1\\ \hat{U}_2\\ \hat{U}_3\end{Bmatrix} + \nu_T'\begin{Bmatrix}\hat{U}_1' + i\alpha\hat{U}_2\\ 2\hat{U}_2'\\ \hat{U}_3' + i\beta\hat{U}_2\end{Bmatrix} \tag{13}$$

with $i(\alpha\hat{U}_1 + \beta\hat{U}_3) + \frac{\partial\hat{U}_2}{\partial x_2} = 0$ (14)

where $k^2 = \alpha^2 + \beta^2$ and primes denote differentiation with respect to x_2.

If we introduce the vertical component of the vorticity $\eta^{(1)}$

where $\eta^{(1)} = \frac{\partial U_1^{(1)}}{\partial x_3} - \frac{\partial U_3^{(1)}}{\partial x_1}$ (15)

and $\eta^{(1)} = \iint_{-\infty}^{\infty}\hat{\eta}(\alpha,\beta;x_2,t)\exp i(\alpha x_1 + \beta x_3)\,d\alpha d\beta$ (16)

it can be shown that since we are dealing with oblique waves, our set of equations for $\hat{U}_1$, $\hat{U}_2$, $\hat{U}_3$ and $\hat{P}$ reduce to two equations in $\hat{U}_2$ and $\hat{\eta}$ only. These equations are

$$\left(\frac{\partial}{\partial t} + i\alpha\overline{U}_1\right)\left(\frac{\partial^2}{\partial x_2^2} - k^2\right)\hat{U}_2 - i\alpha\overline{U}_1''\hat{U}_2 = (\nu+\nu_T)\left(\frac{\partial^2}{\partial x_2^2} - k^2\right)^2\hat{U}_2 + 2\nu_T'\frac{\partial}{\partial x_2}\left(\frac{\partial^2}{\partial x_2^2} - k^2\right)\hat{U}_2 + \nu_T''\left(\frac{\partial^2}{\partial x_2^2} + k^2\right)\hat{U}_2 \tag{17}$$

and

$$\left(\frac{\partial}{\partial t} + i\alpha\overline{U}_1\right)\hat{\eta} - (\nu+\nu_T)\left(\frac{\partial^2}{\partial x_2^2} - k^2\right)\hat{\eta} - \nu_T'\frac{\partial\hat{\eta}}{\partial x_2} = -i\beta\overline{U}_1'\hat{U}_2 \tag{18}$$

In addition $\hat{U}_1 = \left(i\alpha\frac{\partial}{\partial x_2}\hat{U}_2 - i\beta\hat{\eta}\right)/k^2$ (19)

$$\hat{U}_3 = \left(i\beta\frac{\partial\hat{U}_2}{\partial x_2} + i\alpha\hat{\eta}\right)/k^2 \tag{20}$$

Our method of solving these equations is as follows. We assume that at time t=0 an initial disturbance $(U_i^{(1)}(x_2))$ is prescribed. The stability and ultimate growth of that disturbance is then investigated. Now the general properties of equations (13) with constant viscosity and with appropriate boundary conditions have been investigated by several authors. It has been shown by Murdock and Stewartson (1977) and Mark (1976) that the linear operator of these equations has a finite discrete set of eigen modes as well as a continuous

spectrum and moreover the continuous spectrum has higher damping coefficients. We have found similar properties for our equations, with the terms in the eddy viscosity included by direct numerical calculation. Hence we deduce that for any small finite initial disturbance, it is only the least damping mode that can dominate the later development of the disturbance. Thus we choose

$$\hat{U}_2 = \phi(\alpha,\beta;x_2)\exp(-i\omega t) \tag{21}$$

where $\phi(\alpha,\beta;x_2)$ is the least damped eigen function of the modified Orr-Sommerfeld equation derived from equation (17) above. The eigen value is ω and we write

$$c = \omega/\alpha \tag{22}$$

for real α. The real part of ω is the frequency and $c_i < 0$ denotes a damped mode. The least damped mode is denoted by $c_i^*(\alpha,\beta;R)$ where $R = \overline{U}_\infty\delta/\nu$.

Unlike the equation (17) above for $\hat{U}_2$ the vorticity equation (18) is inhomogeneous with the forcing term $-i\beta\overline{U}_1'\hat{U}_2(\alpha,\beta;x_2t)$. It has also been shown by Murdock et al that the spectrum of the linear operator of equation (18) has a similar spectrum to that of the Orr-Sommerfeld equation and thus there are a finite number of discrete eigen modes plus a continuous spectrum. Furthermore, we have found numerically that the least damping mode of the vorticity equation usually has a larger damping coefficient than that of the Orr-Sommerfeld equation. Hence, only the particular solution from the forcing term can play an important role in the later development of the disturbance which we will show involves a non-linear interaction. The particular solution of equation (18) is in the form:

$$\hat{\eta} = H(x_2,t)\exp(-i\omega t) \tag{23}$$

where the amplitude function H satisfies the equation

$$\frac{\partial H}{\partial t} + i\alpha(\overline{U}_1-c)H-(\nu+\nu_T)\left(\frac{\partial^2}{\partial x_2^2}-k^2\right)H-\nu_T'\frac{\partial H}{\partial x_2} = -i\beta\overline{U}_1'\phi(x_2) \tag{24}$$

with the initial and boundary conditions

$$H(0,t) = H(\infty,t) = 0\ ;\ H(x_2,0) = 0$$

The inviscid approximation to equation (24) shows that at the critical layer where $\overline{U}_1 = c_r$ we find

$$H(x_2,t) \sim \frac{i\beta\overline{U}_1'\phi}{\alpha c_i^*}(\exp(-\alpha c_i^* t)-1) \tag{25}$$

showing that for small time $\hat{\eta} \sim t$.

This linear growth in the amplitude of $\hat{\eta}$ has also been found in a related problem investigated by Gustavsson (1980). We find moreover from the numerical solution of equation (24), when viscous terms are included, a similar growth in the vertical component of vorticity during the initial period and that such linear growth makes an important contribution to the developing non-linear interaction. Our solution for the three components of velocity can therefore be written:

$$\begin{aligned}\hat{U}_1 &= (i\alpha\phi - i\beta H)\exp(-i\omega t)\\ \hat{U}_2 &= \phi\exp(-i\omega t)\\ \hat{U}_3 &= (i\beta\phi + i\alpha H)\exp(-i\omega t)\end{aligned} \tag{26}$$

It is easy to show from the Orr-Sommerfeld equation that

$$\phi(x_2,t;\alpha,-\beta) = \phi(x_2,t;\alpha,\beta)$$

and from equation (24)

$$H(x_2,t;\alpha,-\beta) = -H(x_2,t;\alpha,\beta)$$

Thus

$$\hat{U}_1(\alpha,-\beta) = \hat{U}_1(\alpha,\beta) \qquad \hat{U}_2(\alpha,-\beta) = \hat{U}_2(\alpha,\beta)$$

$$\hat{U}_3(\alpha,-\beta) = -\hat{U}_3(\alpha,\beta)$$

showing that $\hat{U}_1$, $\hat{U}_2$ are even functions of β whereas $\hat{U}_3$ is an odd function of β. These properties of $\hat{U}_1$, $\hat{U}_2$, $\hat{U}_3$ will be used in our consideration of the non-linear interaction which is treated in section 3.4 below.

Second order perturbation and mean flow distortion

The equation for the secondary perturbations is derived from equation (6) above, and is

$$\left(\frac{\partial}{\partial t}+\overline{U}_1\frac{\partial}{\partial x_1}\right)U_i^{(2)} + \delta_{i1}\overline{U}_1'U_2^{(2)} + \frac{\partial P^{(2)}}{\partial x_i} = -\frac{\partial}{\partial x_j}U_i^{(1)}U_j^{(1)} + \frac{\partial}{\partial x_j}(\nu+\nu_T)\delta_{ij}^{(3)} \tag{27}$$

with $$\frac{\partial U_j^{(2)}}{\partial x_j} = 0 \tag{28}$$

where $(U_i^{(1)}U_j^{(1)})$ has been derived from section 3.3 for the least damped eigen mode. When we make use of the symmetrical properties found for $U_1^{(1)}$ and $U_2^{(2)}$ and the antisymmetrical properties for $U_3^{(1)}$ with respect to β, we find the following average properties for the Reynolds stress $U_i^{(1)}U_j^{(1)}$ produced by symmetrical oblique waves with given spanwise wave number $\pm\beta$ and streamwise wave number α

$$\begin{aligned}\sigma_{ij} &= U_i^{(1)}U_j^{(1)} = A(\alpha,\beta)(\hat{U}_i\hat{U}_j^* + \hat{U}_i^*\hat{U}_j)\cos^2\beta x_3;\ i,j = 1 \text{ or } 2\\ \sigma_{33} &= U_3^{(1)}U_3^{(1)} = A(\alpha,\beta)2\hat{U}_3\hat{U}_3^*\sin^2\beta x_3\\ \sigma_{k3} &= U_k^{(1)}U_3^{(1)} = A(\alpha,\beta)(\hat{U}_k\hat{U}_3^* + \hat{U}_k^*\hat{U}_3)\sin\beta x_3\cos\beta x_3;\ k = 1 \text{ or } 2\end{aligned} \tag{29}$$

where $A(\alpha,\beta)$ is related to the amplitude of the initial disturbance. These values of the first order Reynolds stresses are all independent of x_1. With these Reynolds stress properties the solution of equation (27) has the form

$$\begin{aligned}U_1^{(2)} &= A(\alpha,\beta)(u_{10} + u_{11}\cos 2\beta x_3)\\ U_2^{(2)} &= A(\alpha,\beta)(\quad u_{21}\cos 2\beta x_3)\\ U_3(2) &= A(\alpha,\beta)(\quad u_{31}\sin 2\beta x_3)\\ P^{(2)} &= A(\alpha,\beta)(p_o + p_1\cos 2\beta x_3)\end{aligned}$$

when we substitute these values into equation (27) above we find writing $\tilde{\sigma}_{ij} = \hat{U}_i\hat{U}_j^* + \hat{U}_i^*\hat{U}_j$ that

$$\frac{\partial}{\partial t}\begin{Bmatrix}u_{10}\\ u_{11}\\ u_{21}\\ u_{31}\end{Bmatrix} = \begin{Bmatrix}0\\ 0\\ -p'\\ 2\beta p_1\end{Bmatrix} + (\nu+\nu_T)\begin{Bmatrix}u_{10}''\\ u_1''-4\beta^2u_1\\ u_{21}''-4\beta^2u_{21}+2\beta u_{31}'\\ u_{31}''-8\beta^2u_{31}-2\beta u_{21}'\end{Bmatrix}$$

$$+\nu_T'\begin{Bmatrix}u_{10}'\\ u_{11}'\\ 2u_{21}'\\ u_{31}'-2\beta u_{21}\end{Bmatrix} - \begin{Bmatrix}\tilde{\sigma}_{12}'/2\\ \tilde{\sigma}_{12}'/2+\beta\tilde{\sigma}_{13}\\ \tilde{\sigma}_{22}'/2+\beta\tilde{\sigma}_{23}\\ \tilde{\sigma}_{32}'/2+\beta\tilde{\sigma}_{33}\end{Bmatrix} \tag{30}$$

with $p_o = \tilde{\sigma}_{22}/2$ (31) and $u_{21}' + 2\beta u_{31} = 0$ (32)

where primes denote differentiation with respect to x_2

The initial and boundary conditions are

$U_i^{(2)}(x_2,0) = 0$; $U_i^{(2)}(0,t) = U_i^{(2)}(\infty,t) = 0$

Of particular interest are the equation for the growth of the streamwise component of vorticity $\xi^{(2)} = \partial U_3^{(2)}/\partial x_2 - \partial U_2^{(2)}/\partial x_3$ which can be found from equation (30) above, and the time dependent distortion of the streamwise component of velocity given by $\epsilon^2 U_1^{(2)}$.

Secondary instability associated with the mean flow distortion

The stability of the 'slowly' varying time dependent conditionally sampled ensemble averaged mean velocity distribution $\overline{U}_1\delta_{i1} + \epsilon^2 U_i^{(2)}(x_2,t)$ can be determined for different values of the initial disturbance amplitude. The equation we use is the modified Orr-Sommerfeld equation (17), including the terms in the eddy viscosity ν_T, as used above in the determination of the eigen modes for the linear perturbation. The only difference is that $\overline{U}_1$ and $\overline{U}_1''$ are to be replaced by $\overline{U}_1 + \epsilon^2 U_1^{(2)}$ and its second derivative with respect to x_2.

NUMERICAL METHOD

All the numerical calculations were performed on the ICL 2970 at Southampton University.

We use an orthogonalized Runge-Kutta integration scheme to evaluate the eigen values and eigen functions of the modified Orr-Sommerfeld equation for the least damped mode of the mean flow and for the most unstable mode of the distorted flow velocity profile.

An explicit finite difference scheme was used to solve the parabolic partial differential equation for the vertical vorticity component. The same integration scheme was used to solve for the velocity distribution.

RESULTS

Stability characteristics of the mean velocity profile

It was found that the mean velocity profile (a typical profile is shown in Fig.2 for R=40,000) was

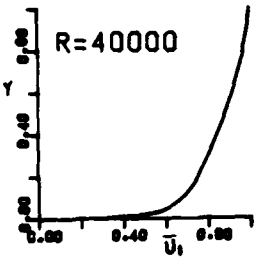

FIG.2 MEAN VELOCITY PROFILE

stable, in agreement with the results of several authors, over a wide range of Reynolds number, $R = \overline{U}_\infty\delta/\nu$, from 6000 to 400,000. However, our results are, we believe, new in that the terms involving a variable eddy viscosity are included in the modified Orr-Sommerfeld equation. We found that the least damping modes have phase (wave) speeds ranging from 0.66 to 0.75 $\overline{U}_\infty$ for wave numbers $\alpha\delta^*$ up to 2 and $\beta\delta^*$ up to 3.5. These results, as shown in Fig.3, are in fair agreement with the corresponding wave speeds

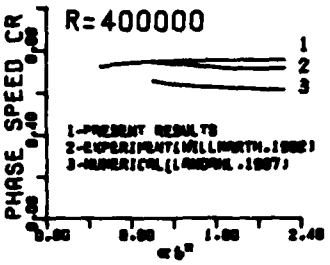

FIG.3 VARIATION OF PHASE SPEED WITH WAVE NUMBER

derived from the experiments of Willmarth and Wooldridge (1962) and others.

Mean flow distortion

The distorted mean velocity profile during the initial development of a coherent structure is shown in Fig.4 for two initial disturbance amplitudes

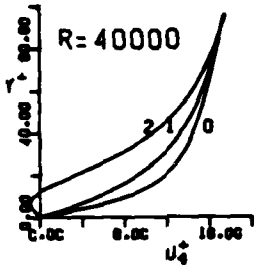

FIG.4 MEAN FLOW DISTORTION
0-NO DISTORTION
1-INITIAL DISTURB. 10%
2-INITIAL DISTURB. 10%

whilst in Fig.5 the distortion and its second derivative are shown for an initial disturbance of 5% of the freestream velocity. It has been shown that these distortions are qualitatively in agreement with the experimental results of Blackwelder et al (1972) and others where results of conditionally sampled flow velocity profiles have been obtained throughout the complete development and decay cycle of coherent structures. It is shown that the distortions are quite marked for initial disturbance amplitudes as low as 5% of $\overline{U}_\infty$. When the initial disturbance amplitude exceeds 10% of $\overline{U}_\infty$ the calculations show a tendency to flow reversal in the region close to the wall within the complete cycle of the coherent structure formation. Since experimental results do not show flow reversal we can only assume that our results for 10% initial disturbance or less are of significance in forming a composite picture of the development of the coherent structure.

Fig.5 shows that the maximum distortion occurs near the wall and for the case shown is at $y^+ = 16$. This result is typical for a large range of Reynolds numbers.

Secondary instability arising from mean flow distortion

In Fig.6 we show the results of phase speed and damping coefficient for R = 40,000 and for various values of $\alpha\delta^*$. Our numerical results show that when the initial disturbance amplitude is of the order of 5% or less, the distorted profile is always stable throughout the cycle of a coherent structure. However, when the initial disturbance amplitude is of order 10% when R = 6000 changing to 5% when R is greater than

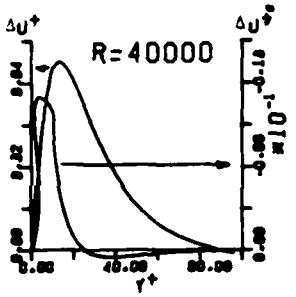

FIG.6 MAX. MEAN FLOW DISTORTION (INITIAL DISTURB. 5%)

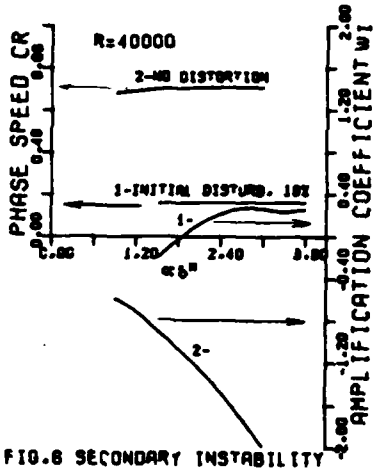

FIG.8 SECONDARY INSTABILITY

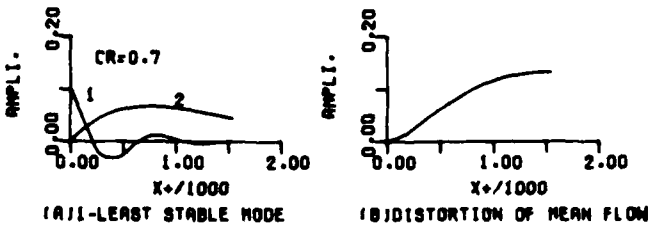

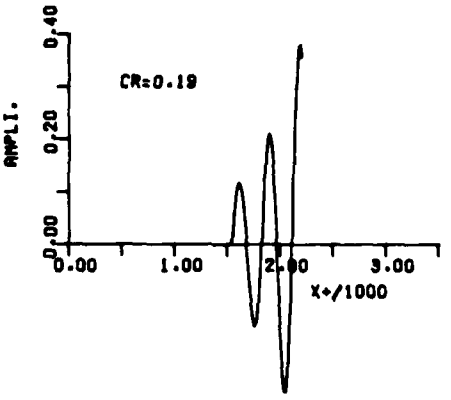

(C)SECONDARY DISTURBANCE

FIG.7 DEVELOPMENT OF FLOW DISTORTION

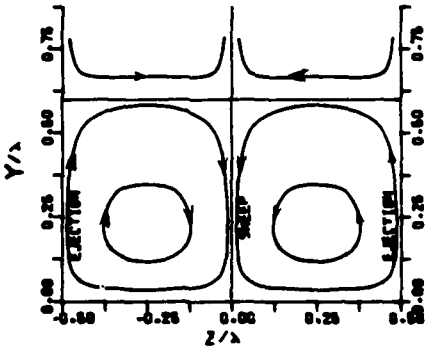

FIG.8 STREAMLINES IN TRANSVERSE PLANE (λ^+=100)

40,000 the distorted profile becomes unstable within the time to reach a maximum distortion. This time is shorter as the Reynolds number is increased.

In Fig.7a we show typical results for the decay of the least stable (linear) mode from an initial disturbance of 10% of $\overline{U}_\infty$, together with the initially linear growth of H. In Fig.7b we show typical values of the mean flow distortion as functions of $x_1 u_\tau/\nu$ on the assumption that the spatial growth can be determined approximately from the calculated temporal growth and assuming the convection speed is equal to the group velocity, which in our case is nearly equal to the phase velocity. In Fig.7c the secondary instability is shown to lead rapidly to a breakdown of the flow and occurs within a distance of about $x_1 u_\tau/\nu$ = 2000 following the commencement of the coherent structure.

The development of strong streamwise vorticity

For a given initial disturbance amplitude we found that a strong streamwise vorticity is generated as a second order effect. A typical result is shown in Fig. 8 in which the calculated streamlines are shown in plane perpendicular to the freestream direction. The non-dimensional spanwise wave length, $\lambda u_\tau/\nu$, of a cell is shown to be of order 100 over a wide range of Reynolds numbers. We note that the flow in transverse planes superimposed on the streamwise component of the distorted mean flow has the appearance of side-by-side ejection events ($\Delta U_1<0, \Delta U_2>0$) with sweep events ($\Delta U_1>0, \Delta U_2<0$) and are similar to the 'finger' structure observed by Brodkey et al (1978).

REFERENCES

Benney, D.J. 1964 Phys. Fluids. Vol.7, 319
Benney, D.J., Lin, C.C 1960 Phys. Fluids Vol.3, 656
Blackwelder, R.F., Kaplan, R.E. 1972 Int. Union Theor. Appli. Mech., 12th, 1972
Cebeci, T., Smith, A.M.O. 1974 Academic Press NY 1974
Gustavsson, L.H., Hultgren, L. 1980 JFM Vol.98, 149
Hatziavramidis, D.T., Hanratty, T.J. 1979 JFM Vol.95, 655
Kline, S.J., Rustadler, P.W. 1959 J.Appl.Mech.Vol.26, 166
Landahl, M.T. 1973 Symp. on Mod.Dev. in Fluid Dyn.
Landahl, M.T. 1967 JFM Vol.29, 441
Mack, L.M. 1976 JFM, Vol.73, 497
Murdock, J.W., Stewartson, K. 1977 Phys.Fluids, Vol.20
Praturi, A.K., Brodkey, R.S. 1978 JFM Vol.89, 251
Reynolds, W.C., Hussain, A. 1972 JFM, Vol.54, 263
Walker, J.D.A., 1978 Proc.R.Soc.Lond.A. Vol.359, 167
Willmarth, S. Wooldridge, C.F. 1962 JFM, Vol.14, 187
Zhang, Z. 1981 Ph.D. thesis Southampton Univ(unpub).

ENTRAINMENT AND MIXING IN PULSATILE JETS

V. Sarohia and L. P. Bernal
Jet Propulsion Laboratory
California Institute of Technology
Pasadena, California 91103

ABSTRACT

A subsonic axisymmetric jet with time-varying velocity profile has been experimentally investigated to determine the influence of pulsations on jet growth and entrainment. The kinematics of the entrained flow were studied by marking the fluid with a sheet of CO_2 gas at approximately the jet spreading angle. The influence of the frequency and amplitude of pulsation on the jet flow was inferred by measuring the mean and fluctuating velocities by constant temperature hot-wire anemometry. The enhanced gro[illegible] of the pulsatile jet as compared to the steady jet was accompanied by a circumferential bulk transport of the fluid entrained by the organized vortices.

NOMENCLATURE

b	width of the jet
d	primary nozzle diameter
f	frequency of pulsations
M_e	nozzle exit flow Mach number
p	static pressure
p_∞	ambient pressure
p_o	stagnation pressure
Q	volumetric jet flow
$Re \equiv \frac{\rho U d}{\mu}$	
$S \equiv \frac{fd}{U_e}$	non-dimensional frequency
u'	longitudinal velocity fluctuation
U	longitudinal mean velocity
U_e	nozzle exit flow velocity
X	longitudinal distance from nozzle exit plane
λ	spacing between the vortices
ρ	gas density
μ	gas viscosity

INTRODUCTION

Recent investigations[1] have revealed that augmentation in the thrust of an ejector can be improved by pulsating the primary jet. It was further observed that over a wide range of primary jet Mach numbers, this improvement in ejector performance was independent of the frequency of pulsations but was directly proportional to their amplitude. To enhance the understanding of the relationship of pulsations to ejector performance, preliminary experiments were performed on entrainment and mixing in pulsatile jets and are reported in this paper.

Experimental investigations by Binder and a Favre-Marinet,[2] Bremhorst and March[3], Crow and Champagne[4], Leister[5], Platzer, et al.[6] and Wygnanski et al.[7] have demonstrated without doubt the importance of organizing the jet with large-scale vortices in order to achieve an increased rate of jet growth and hence increased entrainment of ambient fluid. In the following section, the influence of pulsations (time-varying complete flow) on the jet growth and entrainment is further investigated. The kinematics of the fluid entrained by the pulsatile jet was also studied and is reported below.

EXPERIMENTAL FACILITIES AND INSTRUMENTATION

Subsonic jet flow was generated by expanding air at room stagnation temperature through an axisymmetric convergent nozzle which has an exit diameter d of 2.54 cm. The flow before entering the plenum chamber could be modulated from 20 Hz to 1500 Hz by first passing the flow through a pneumatic transducer. The time-varying primary jet velocity profile (complete jet flow) was achieved by utilizing this pneumatic transducer. To avoid any changes in the mean mass flow rate which may result by the introduction of these modulations, a choked flow condition was maintained in the air supply line upstream of the pneumatic transducer. Constant temperature hot-wire anemometry was utilized to determine the mean and the fluctuating velocity components of the pulsating jet. The data was plotted on x-y plotters and subsequently digitized and processed on the mini-computer data acquisition facility.

The jet flow was visualized by injecting CO_2 gas into the plenum chamber of the nozzle air supply. Still shadowgraphs were taken with a spark source that had a time duration of approximately 1.0 μs. Visualization of the entrained fluid alone was also made by taking spark shadowgraphs of a sheet of fluid marked with CO_2 gas. The results of this flow visualization work are discussed in the following section.

EXPERIMENTAL RESULTS AND DISCUSSION

Flow Visualization

Spark shadowgraphs showing the jet growth without and with upstream pulsations are shown in Figures 1 and 2 respectively. The Reynolds number based on the nozzle exit diameter and mean velocity was $R_e = 0.9 \times 10^5$. In Figures 4 and 5 in which the mean mass flow rates were equal, the spreading angle of the jet is significantly enhanced by the flow pulsations. By the nozzle design and its contraction ratio of 25, the flow was kept laminar at the nozzle exit. As is evident from Figure 1, the roll-up of the shear layer into discrete ring vortices is evident with the flow rapidly becoming turbulent within less than a diameter downstream of the nozzle exit. The spanwise coherency of the initial laminar instability waves is evident in Figure 1. Organization of the jet with upstream pulsations is quite evident in Figure 2. The non-dimensional frequency, fd/U_e was 0.3. It is clear from Figure 2 that the organization was axisymmetric. Observation of vortex spacing in Figure 2 leads to the conclusion that the vortices convected approximately at the mean velocity with spacing $\lambda/d \simeq 1.1$ where λ is the spacing between the vortices. Figure 2 also shows that the wavelength remains constant up to $\lambda/d = 5$.

The changes in entrainment of the jet with and without primary jet pulsations were observed by visualizing the entrained fluid marked by CO_2 gas. A slit of CO_2 gas was introduced at the jet spreading angle all along the jet. Typical results showing the instantaneous behavior of the entrained fluid without pulsation are shown in Figure 3 and with pulsations in Figures 4 and 5. Figures 4 and 5 indicate a sharp interface between the entrained fluid and the organized vortex structure in the jet. From a close look at the entrained fluid in Figures 4 and 5 as compared to Figure 3 it is inferred that the bulk of the entrainment occurs at localized regions within the jet and shear layer for pulsatile jets as compared to non-pulsatile jets.

Influence of Pulsations on Free-Jet Growth

Typical results from hot-wire anemometry of the longitudinal velocity fluctuations are shown in Figure 6. The results obtained by traversing two hot-wires relative to each other at a fixed distance from the nozzle and by looking at the phase of the velocity fluctuations, showed that the pulsations were axisymmetric in nature.

To determine the influence of pulsations of the jet on its growth extensive mean velocity profile measurements were made at various axial locations downstream of the nozzle exit. These measurements were made at a fixed nozzle exit Mach number, $M_{exit} = 0.2$, and over a range of pulsation frequencies from 0 to 1500 Hz. Two linearized constant temperature hot-wires were employed to measure the mean and the fluctuating velocity components in the jet. One wire was fixed and located in the jet at $X/d \simeq 0.5$ and was utilized to control the amplitude of free-jet pulsations. The second wire was traversed across the jet at various axial locations to measure the mean velocity, U, and the velocity fluctuations, u', normal to the wire.

The influence on the free-jet growth rate of the pulsation frequency is shown in Figure 7 for various values of the non-dimensional frequency, fd/U_e. These results were obtained for a series of mean velocity profiles taken at various axial locations, X/d, at a fixed Mach number, $M_{exit} = 0.2$. Throughout these experiments, the rms value of the longitudinal velocity fluctuations, $\sqrt{\overline{u'^2}}/U_e$ were kept at 10% at the nozzle exit. This entrainment is associated with the engulfing action of the large scale vortices. As can be seen in Figure 4 at $f/dn5$ an interaction between the ring vortices occurs which results in an increase vortex spacing.

The decay of center-line velocity in the present experiments at low non-dimensional frequency of excitation, $fd/U_e < 0.05$, does not seem to influence the growth of the free jet. For $fd/U_e > 0.05$, the influence of excitation is to increase the decay of the centerline velocity. Present results further showed this enhanced decay to be independent of the pulsation frequency at least within the accuracy of the present experimental results. The above results were further supported when the influence of various pulsation frequencies on mean velocity profile growth and jet entrainment were determined as shown in Figures 8 and 9. Up to $X/d = 14$, as discussed above, the growth of the jet and its entrainment at low pulsation frequency were not influenced by the pulsations.

The entrainment with pulsations is significantly larger even at the lowest values of x/d explored. The results presented in Figure 9 indicate that the pulsatile flow yields a constant increase in entrained mass flow up to $x/d \sim 5$ where it experiences an additional increase presumably associated with the vortex interaction observed in Figure 4.

The relative large amplitude of forcing used in this investigation results in significant changes in the evolution of the vortices. The formation process is dominated by the forcing with the Kelvin-Helmholtz free shear layer instability appearing as a ripple on the interface between the jet and the surrounding fluid. The interaction process apparent in Figure 4 was not observed in a previous investigation with lower forcing amplitude.[4]

ACKNOWLEDGEMENTS

This paper presents the results of one phase of research carried out at the Jet Propulsion Laboratory, California Institute of Technology, Contract NAS7-100, Task Order RD-182, Amendment 63, sponsored by the Naval Air Systems Command under MIPR No. N00019-80-MP-07850. The authors extend their gratitude to Prof. M. P. Platzer, U. S. Naval Postgraduate School, Monterey, California, for many valuable technical suggestions throughout this program. The assistance of Mr. Stan Kikkert in design, fabrication and assembly of the experimental apparatus is greatly appreciated.

REFERENCES

1. V. Sarohia, L. Bernal, and T. Bui, "Entrainment and Thrust Augmentation in Pulsatile Ejector Flows," Jet Propulsion Laboratory Publication 81-36, February, 1981.

2. G. Binder and M. Favre - Marinet "Mixing Improvement in Pulsating Turbulent Jets" in Fluid Mechanics of Mixing (ed. Uram and Goldschmidt), ASME United Engineering Center, 1973, pp 167-172.

3. Bremhorst, K. and Harch, W. H., "Nearfield Velocity Measurements in a Fully Pulsed Subsonic Air Jet," in Turbulent Shear Flows I ed. by Durst, F., Launder, B. E., Schmidt, F. W., and Whitelaw, J. H., Springer-Verlag, Berlin, Heidelberg, 1979, pp 37-54.

4. Crow, S. C. and Champagne, F. H., "Orderly Structures in Jet Turbulence," J. of Fluid Mechanics, Vol. 48, 1971, pp 547-591.

5. P. Leister, "Experimental Investigation on the Turbulence of an Impinging, Pulsating Jet," Paper presented at the Symposium on Turbulent Shear Flows, April 18-20, 1977, at University Park, PA.

6. M. F. Platzer, J. M. Simmons, and K. Bremhorst, "On the Entrainment Characteristics of Unsteady Subsonic Jets," AIAA Journal, Vol. 16, March 1978, pp 282-284.

7. I. Wygnanski, D. Oster, B. Dziomba and H. Fiedler, "On the Effect of Initial Conditions on Two-Dimensional Turbulent Mixing Layer," Journal of Fluid Mechanics, 1979, Vol. 93, p. 325.

Figure 1. Nozzle Exit Velocity 52 m/s

AD-A111 522 PENNSYLVANIA STATE UNIV UNIVERSITY PARK DEPT OF MECH--ETC F/G 20/4
SYMPOSIUM ON TURBULENT SHEAR FLOWS (3RD), UNIVERSITY OF CALIFOR--ETC(U)
SEP 81 F W SCHMIDT AFOSR-80-0033

UNCLASSIFIED AFOSR-TR-82-0032 NL

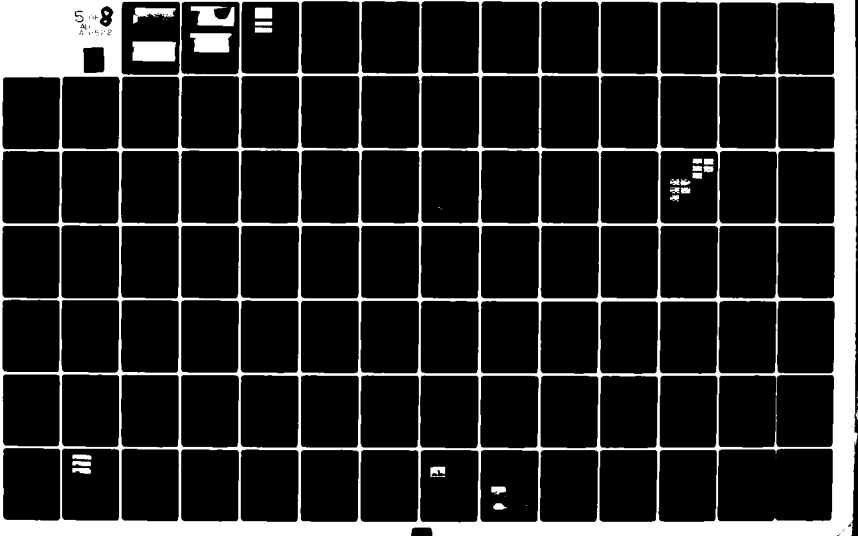

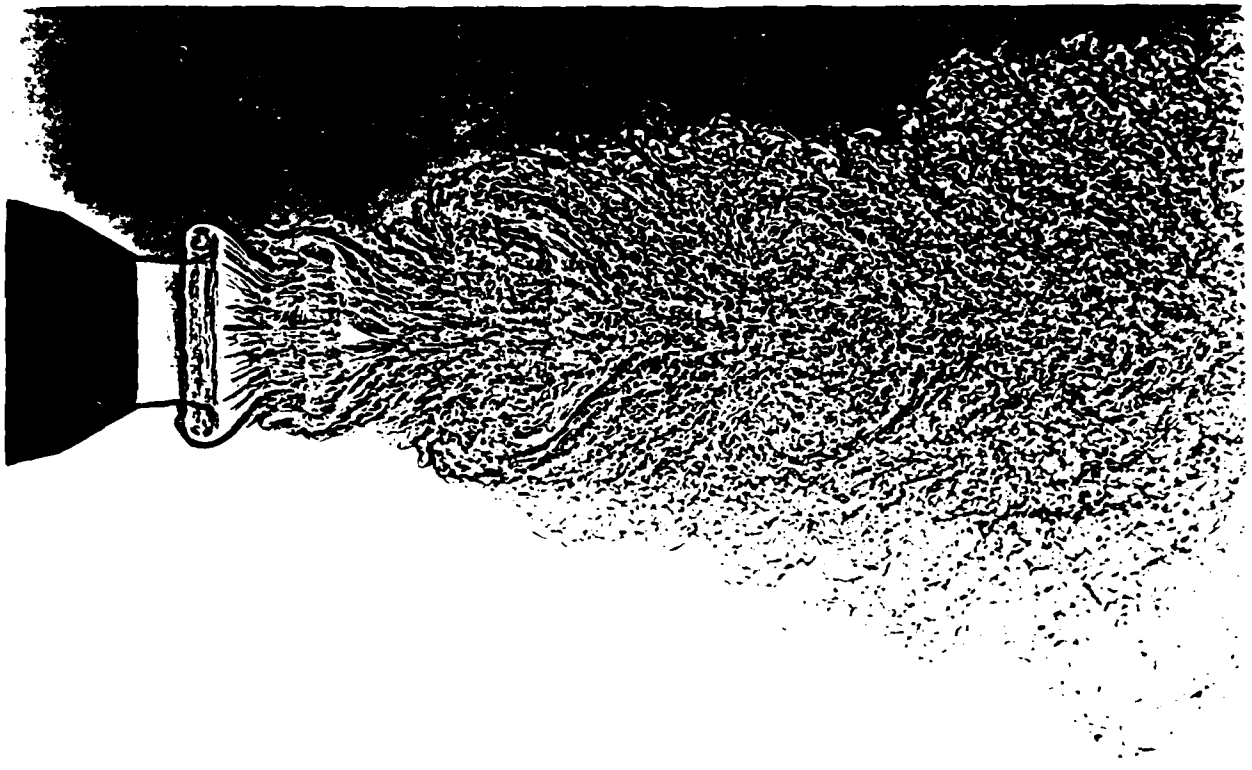

Figure 2. Nozzle Exit Velocity 42 m/s. Frequency fd U_e = .03

Figure 3. Shadowgraph Showing Entrained Flow of a Jet. Velocity at Nozzle Exit = 152 m/s

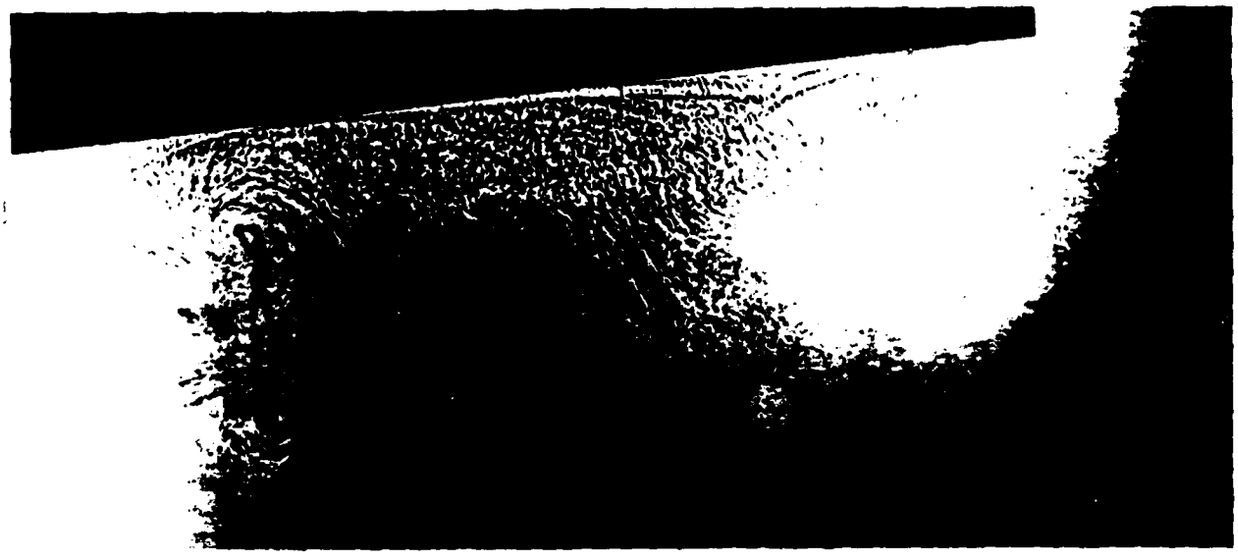

Figure 4. Shadowgraph Showing Entrained Flow of a Pulsed Jet. Nozzle Exit Velocity = 152 m/s. Frequency $fd/U_e = 0.07$

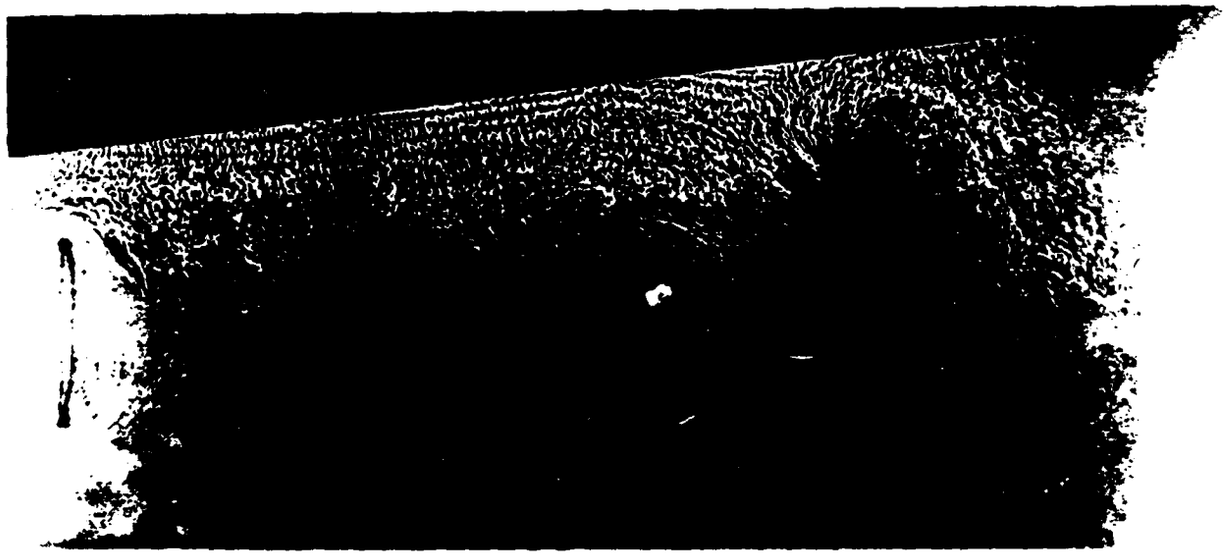

Figure 5. Same conditions as in Figure 4.

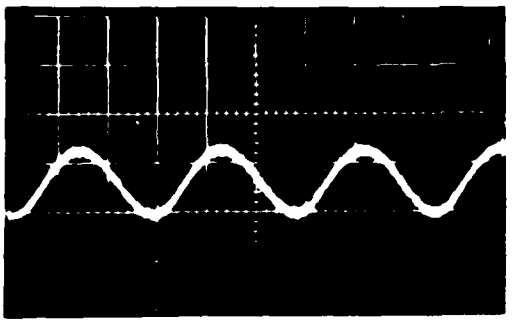

Pulsation Frequency 136 Hz

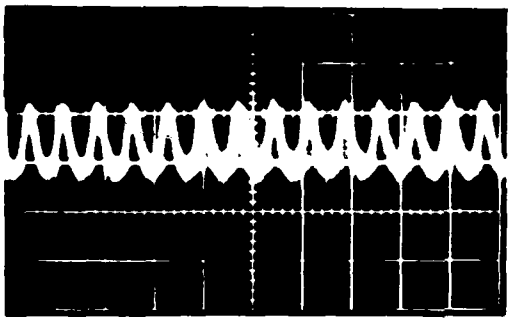

Pulsation Frequency 546 Hz
Horizontal Scale 2 ms/division
Vertical Scale 0.2 Volts/division

Figure 6. Linearized Constant Temperature Hot-Wire Annemometry Output

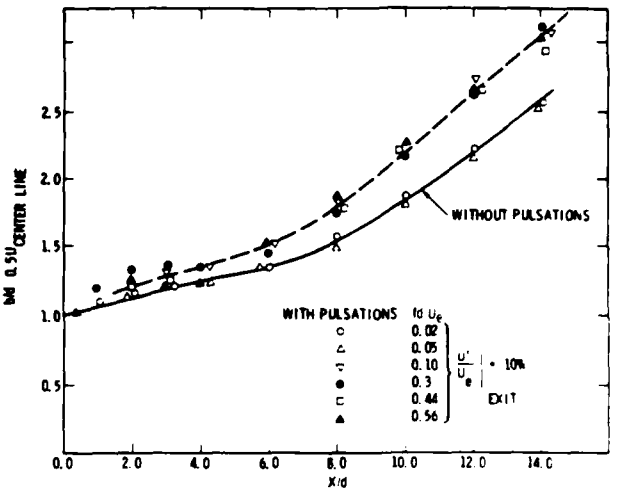

Figure 8. Growth of Jet

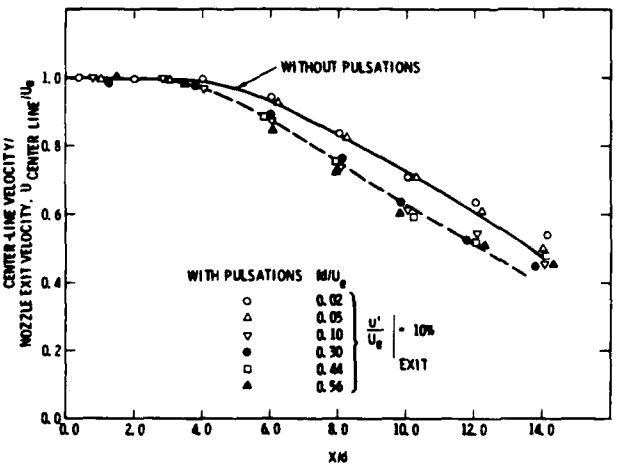

Figure 7. Centerline Velocity Decay

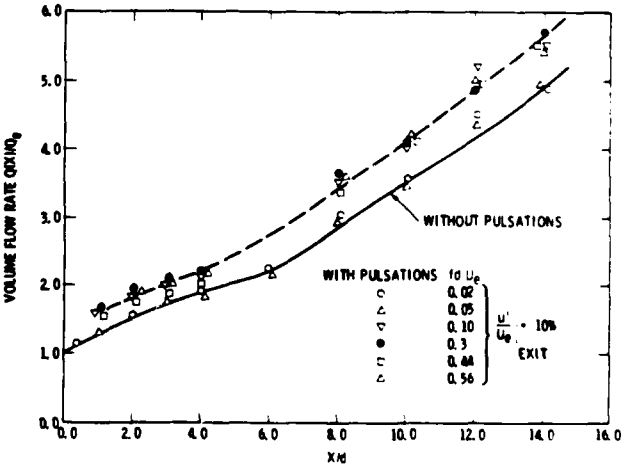

Figure 9. Entrainment of Flow by a Jet

SESSION 12 - GEOPHYSICAL FLOWS II

J.-C. André - Chairman

HOW TIME DEPENDENCE AND VARIABLE FROUDE NUMBER CAN EXPLAIN MORE RAPID ENTRAINMENT OF THE TWO-LAYER SYSTEM IN ANNULUS EXPERIMENTS

J. W. Deardorff
Department of Atmospheric Sciences
Oregon State University
Corvallis, Oregon 97331

ABSTRACT

New experiments on the entrainment rate of a turbulent mixed layer that is stirred by a surface shear stress (u_*^2) permit a new interpretation of annulus experiments for either the two-layer system (2LS) or the system with a stratified outer layer (SOL). The new experiments included measurements of the velocity jump (Δu) across the interfacial or entrainment layer, and the entrainment rate was found to depend on both Δu and u_* in a product form. The greater entrainment rate for the 2LS than for the SOL is found to be associated with greater Δu with the 2LS, for given values of density jump, $\Delta\rho$, and u_*. This paper attempts to explain why, in the two different types of experiment, greater Δu values occur for the 2LS for given values of $\Delta\rho$ and u_*.

NOMENCLATURE

English

B	stabilizing buoyancy parameter
g	gravitational acceleration
h	depth of well mixed layer (does not include mean interfacial layer)
R	overall Richardson number based on surface shear stress
R_V	overall Richardson number based on interfacial velocity jump
t	time
t'	dummy time variable
u	tangential flow speed
u_*	friction velocity
w_e	entrainment rate
z	height (distance from rotating screen)

Greek or other symbol

Δ	change in property across the edge of the mixed layer (except Δr)
Δr	annulus gap width
ρ	density
ρ_o	reference density
$\overline{(\ )}$	mean value

INTRODUCTION

In the past 12 years there have been several experiments on the rate at which a turbulent mixed layer, stirred by the action of a surface shear stress, entrains an adjacent non-turbulent outer fluid layer of contrasting density. This topic is most conveniently studied within an annulus equipped with a rotating screen to provide the shear stress and fluid velocity of the turbulent layer. There are then no tangential end effects, the flow is fully developed, and the tangential mean pressure gradient is zero. The various investigators hope that centrifugal effects are minimal and that the entrainment interface is nearly horizontal in the mean. In order that centrifugal effects not be too severe, rather small screen rotation rates are used.

The first such experiment by Kato & Phillips (1, abbreviated KP) employed a linearly stratified outer layer (abbreviated SOL). The approximate relation they found is

$$w_e/u_* = 2.5R_\tau^{-1} \qquad (1)$$

where w_e is the vertical entrainment rate, u_* is the friction velocity at the rotating screen surface, and R_τ is an overall Richardson number defined by

$$R_\tau = B/u_*^2 \qquad (2)$$

where B is the overall buoyancy parameter:

$$B = gh\Delta\rho/\rho_o$$

with ρ_o being a reference density of one of the layers, $\Delta\rho$ the magnitude of the density jump between the turbulent and non-turbulent layers, g the gravitational acceleration, and h the mixed-layer depth.

Using the same annulus, Kantha et al. (2, abbreviated KPA) explored the two-layer system (abbreviated 2LS) wherein the non-turbulent layer is homogeneous and not stratified. (In both the 2LS and SOL configurations a density jump, $\Delta\rho$, exists or develops.) They found that the normalized entrainment is considerably larger (roughly by a factor of 2) for the 2LS than that given by (1) for the SOL. The discrepancy was disturbing and unexplained; it was speculated that internal gravity waves in the SOL may sap enough turbulence energy from the mixed layer to reduce significantly the entrainment rate. They also noticed that, for a given R_τ, w_e/u_* was reduced when $h/\Delta r$ is greater, where Δr is the annulus gap width, due to the influence of sidewall friction. They therefore attempted to extrapolate their results to the limiting case of no sidewall friction.

Using an annulus only half as large, Kantha (3) also explored the entrainment rate in the 2LS. He found w_e/u_* values significantly smaller than those of KPA for the same system but otherwise following roughly the same R_τ dependence. Confusingly, his w_e/u_* values lay closer to those of KP than KPA. Relatively strong sidewall friction could be invoked as the cause of the reduced entrainment rates.

An explanation for the discrepancy between the

SOL and 2LS results was provided by Price (4) and Thompson (5). They assumed that the inverse Froude number, R_V, was constant (of order 0.6) during most of the entrainment period, where

$$R_V = B/(\Delta u)^2 \qquad (3)$$

and Δu is the magnitude of the velocity jump across the entrainment interface. The R_V = const explanation involved the mixed-layer momentum and salt mass budgets, and predicted a factor of two greater values for w_e/u_* for the 2LS than for the SOL at a given R_τ. In Price's words, "The factor of 2 arises because half the available momentum supply (screen stress minus sidewall drag) must be used to accelerate the mixed layer in the linearly stratified case in order to maintain R_V constant as B increases with h. All of the available momentum supply is used to accelerate entrained fluid in the two-layer case, where B is constant." In the absence of sidewall friction, Price and Thompson also predicted an $R_\tau^{-\frac{1}{2}}$ dependence for R_e/u_* in the laboratory.

In recent annulus experiments by Deardorff and Willis (6) R_V values were measured for the first time. They were found to vary from about 0.7, the smallest value they could achieve in their apparatus, to over 10, depending largely on how great $h/\Delta r$ was. That is, with relatively large sidewall damping Δu was kept small, forcing R_V to be large. Rather than reject all data for which R_V was greater than about 0.6, they found that their observed entrainment rates could be fit by the relationship

$$w_e/u_* = 0.33 R_\tau^{-\frac{1}{2}} R_V^{-1.4} \qquad (4)$$

This $R_\tau^{-\frac{1}{2}}$ dependence was derived solely from the arguments of Price and Thompson, but the circumstance of R_V = const is considered to be only a special case. The exponent in the R_V dependence, determined from their 2LS data using turbulent salt water underneath non-turbulent fresh water, is not yet known to an accuracy better than ± 10%.

Eq. (4) is based on the use of the depth, h, of the well mixed layer as length scale. It was found that, typically, $h \cong 0.8h_2$, where h_2 is the outermost depth reached by mixed-layer fluid at any given time. Thus, $h \cong 0.9h_2$ can be considered a more representative mean mixed-layer depth. Then (4) converts to

$$w_e/u_* = 0.47 R_\tau^{-\frac{1}{2}} R_V^{-1.4} \qquad \text{(based on } \bar{h}\text{)} \qquad (5)$$

Details of their experiments and findings are presented in Deardorff and Willis. Here the emphasis is on explaining why R_V should tend to be larger in laboratory SOL experiments, with consequently reduced w_e/u_* values, than for the 2LS, assuming that in both cases the entrainment obeys (4) or (5).

THE MODEL FOR TESTING (5)

A time dependent numerical model was constructed which obeyed (5) and predicted $\bar{h}$ from

$$\bar{h}(t) = \bar{h}(0) + \int_0^t w_e(t')dt'.$$

The mean mixed-layer momentum, $\bar{u}$, was obtained from the momentum budget taking entrainment and sidewall drag into account.

For the 2LS B was taken constant, equal to its initial value, such as to yield constant R_τ values (in 5 different runs) of 36.2, 70.3, 150, 292 and 523. For the SOL, B was diagnosed from

$$B = \tfrac{1}{2}(g/\rho_o)\left|\partial\rho/\partial z\right| h^2$$

where $|\partial\rho/\partial z|$ is the constant linear stratification of the outer layer.

In all cases, initial conditions included $\bar{u}(0) = 0$, and at all times $u_* = 1.41$ cm s^{-1} and $\Delta r = 22.8$ cm. For the 2LS, $\bar{h}(0) = 5.4$ cm; for the SOL $\bar{h}(0) = 0.5$ cm and $(1/\rho_o)|\partial\rho/\partial z| = 7.67 \times 10^{-3}$ cm^{-1}. Only one SOL numerical run was necessary because R_τ increased with time and covered the range of R_τ values from the five 2LS runs.

MODEL RESULTS

The numerical results are displayed in Fig. 1 on a w_e/u_* versus R_τ diagram. Included are the data from the actual KP and KPA experiments simulated. The model, using (5), does predict substantially greater entrainment rates for the 2LS, indicating that R_V was smaller for the 2LS at the same R_τ value. In addition, the agreement with different experimental results than those from which (4) was derived is probably as close as can be expected. However, the use of (5) did not produce quite as large an entrainment advantage for the 2LS as that observed.

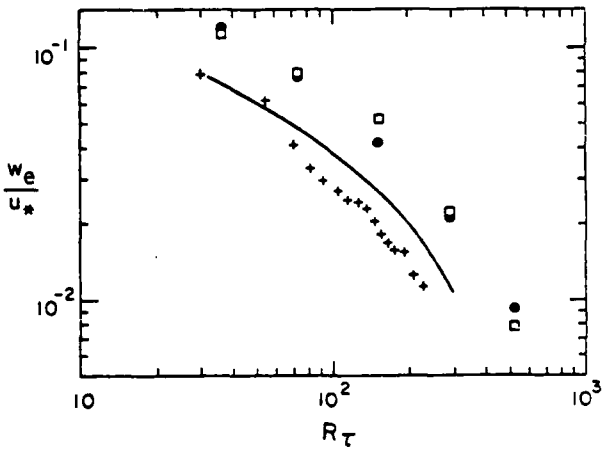

Figure 1. Entrainment rate normalized by friction velocity versus R_τ calculated numerically from a model obeying (5) for the case of the stratified outer layer (SOL, solid curve) and for 5 two-layer systems (2LS, solid circles). The corresponding experimental data from KP (+) and from KPA (□) are also shown.

Fig. 2(a) shows the main dimensionless time-dependent results for the case $(R_\tau)_{2LS} = 36.2$. In this case we see that sidewall friction has had little effect on the $\bar{u}/u_*$ values at the small times at which the simulated KP and KPA runs are compared. Here, $\bar{u}$ is the mixed-layer mean velocity which is slightly larger than $|\Delta u|$, due to some viscous propagation of momentum beyond the mixed-layer interface. Both results follow the expected 1:1 line of $\bar{u}/u_* = (u_*/h)t$ for no sidewall friction at small time. However, when $(R_\tau)_{SOL}$ reaches 36.2 (it grows with time) a smaller dimensionless time has elapsed for the SOL than for the 2LS when the latter's R_V has reached a minimum value. This appears to be the appropriate time to evaluate the 2LS entrainment rate, since 2LS data

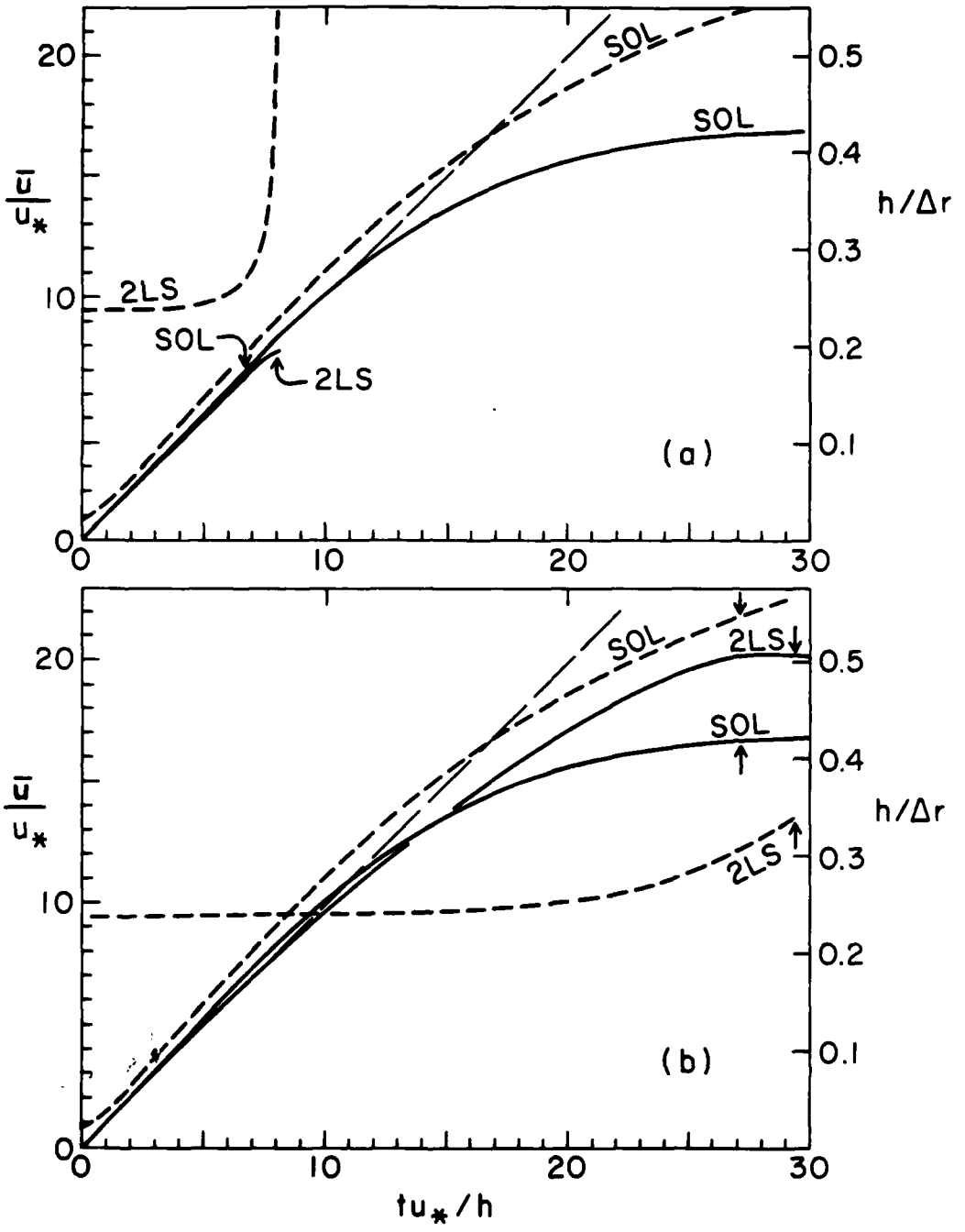

Fig. 2. Numerical simulation of KP (SOL) and KPA (2LS) experiments. Solid curves are $\bar{u}/u_*$, short-dashed are $\bar{h}/\Delta r$, versus $tu_*/\bar{h}$. Long-dash line is 1:1. Arrows denote times of comparison between SOL and 2LS. (a) $(R_T)_{2LS} = 36.2$; (b) $(R_T)_{2LS} = 292$.

occurring before this minimum R_V is reached are usually rejected because the w_e values are then so small. Thus, $\bar{u}/u_*$ is greater, at small times, for the 2LS than for the SOL, for the same R_τ, because of a somewhat greater dimensionless period of acceleration experienced by the 2LS. Hence, by (5) and (3) this difference is amplified into a substantially greater entrainment rate relative to u_*.

At larger times sidewall drag is an important factor because $\bar{h}/\Delta r$ is, and had recently been, larger for the SOL. Fig. 2(b) shows the model results at that stage, for the case $(R_\tau)_{2LS} = 292$. The dimensionless times at which $(R_\tau)_{SOL}$ reaches 292 and $(R_V)_{SOL}$ dips to its minimum value are then roughly the same, but $(\bar{h}/\Delta r)_{SOL}$ is substantially larger because of its earlier history of faster entrainment. Thus, wall friction by this later time has reduced $(\bar{u}/u_*)_{SOL}$ below that of the 2LS, thereby again increasing $(R_V)_{SOL}$ and decreasing $(w_e/u_*)_{SOL}$ relative to the 2LS. This second explanation takes over well before the first leaves off.

In a recent study by Kitaigorodskii (7), it has also been concluded that w_e/u_* should depend on both R_V and R_τ, and that $|\partial\rho/\partial z|$ should not affect the entrainment rate if the latter is expressed as a function of both R_τ and R_V. However, at and before the time of that study there was no experimental guidance on the R_V dependence of w_e/u_*.

SUMMARY

The entrainment rate in rotating-screen annulus experiments was found to depend on the velocity-jump scale, Δu, as well as upon u_*. By treating the inverse Froude number R_V as a variable, the influence of sidewall drag was taken implicitly into account by its influence on R_V. The dependence found is $w_e/u_* = 0.33 R_\tau^{-\frac{1}{2}} R_V^{-1.4}$.

This relationship was used to predict relative entrainment in simulation of some KP and KPA experiments. In the two-layer-system (2LS) smaller R_V values are predicted to occur than in stratified-outer-layer (SOL) experiments, under the different conditions at which R_τ is the same. Hence, the entrainment rate is greater for the 2LS at the time at which the comparison is made. The distinction disappears when both velocity scales are utilized, as in (5), to diagnose the entrainment rate.

ACKNOWLEDGMENTS

This study was supported by the Office of Naval Research. The experiments involved the labors of G. E. Willis and P. Stockton, along with assistance from P. Katen and S. Yoon.

REFERENCES

1 Kato, H. and Phillips, O. M., "On the Penetration of a Turbulent Layer into Stratified Fluid," J. Fluid Mech., Vol. 37, 1969, 643-655.

2 Kantha, L. H., Phillips, O. M. and Azad, R. S., "On Turbulent Entrainment at a Stable Density Interface," J. Fluid Mech., Vol. 79, 1977, 753-768.

3 Kantha, L. H., "On Surface-stress-induced Entrainment at a Buoyancy Interface," Dept. Earth Planet. Sci., Johns Hopkins Univ. Rep. GFDL TR 78-1, 1978.

4 Price, J. F., "On the Scaling of Stress-driven Entrainment Experiments," J. Fluid Mech., Vol. 90, 1979, 509-529.

5 Thompson, R. O. R. Y., "A Re-examination of the Entrainment Process in some Laboratory Flows," Dyn. Atmos. Oceans, Vol. 4, 1979, 45-55.

6 Deardorff, J. W. and Willis, G. E., "Dependence of Mixed-layer Entrainment on Shear Stress and Velocity Jump," to appear in J. Fluid Mech., 1981.

7 Kitaigorodskii, S. A., "On the Theory of the Surface-stress Induced Entrainment at a Buoyancy Interface (toward interpretation of KP and KPA experiments)," Tellus, Vol. 33, 1981, 89-101.

ON THE INFLUENCE OF BUOYANCY ON THE TURBULENT EKMAN LAYER

URBAN SVENSSON
DIVISION OF WATER RESOURCES ENGINEERING
(TECHNICAL) UNIVERSITY OF LULEÅ, SWEDEN

ABSTRACT

A one-dimensional mathematical model of the stratified ocean surface layer is presented. The model is verified against laboratory measurements of the entrainment rate across a density interface. The reduction of the entrainment rate by the earth's rotation is predicted and a comparison with earlier models of this problem is made. Field measurements are used for testing the performance of the model in more complex situations.

The study indicates that the mathematical model, and in particular the turbulence model used, is capable of predicting all the essential features of the flow situations studied. It is the author's view that improved results could not be obtained by employing a more advanced turbulence model.

NOMENCLATURE

B	= buoyancy parameter
D	= depth
f	= Coriolis parameter
g	= gravitational acceleration
k	= turbulent kinetic energy
N	= buoyancy frequency
Ri_o	= Richardson number
S	= salinity
U,V	= components of mean velocity
u,v,w	= components of fluctuating velocity
U_*	= friction velocity
x,y,z	= coordinates
α	= coefficient in density-salinity relation
ϵ	= dissipation rate of k
ν,ν_T,ν_{eff}	= laminar, turbulent and effective viscosity
ρ	= fluid density
$\sigma_k, \sigma_\epsilon$	= constants in turbulence model
$\sigma,\sigma_T,\sigma_{eff}$	= laminar, turbulent and effective Schmidt number
τ_x,τ_y	= shear stresses.

INTRODUCTION

The present paper deals with the structure and dynamics of the stably stratified ocean surface layer. It is a continuation of a study of the homogeneous Ekman layer, Svensson (23); henceforth to be referred to as paper I. In paper I a mathematical model was formulated and verified against laboratory measurements. Different turbulence models were discussed as well as predictions of the homogeneous Ekman layer. The present study extends that mathematical model to stably stratified situations.

Earlier models of the surface layer may be divided into two groups: 1) Integral models, Kraus and Turner (8); Pollard et al. (19); Garwood (2) and 2) Models that use turbulent transport coefficients Mellor and Durbin (14); Marchuk et al. (13); Kundu (9). Integral theories are simpler to use but, as pointed out by Mellor and Durbin (14), disconnected from available information on other turbulent boundary layer flows including neutral flows. The present model belongs to the second group but differs from earlier models both in formulation and, particularly, the extent to which it is verified.

The mathematical formulation of the problem is outlined in Section 2 together with some basic assumptions and a discussion of the way to include terms due to buoyancy. Results are presented in Section 3 starting with a verification study of the shear-induced entrainment experiment by Kantha, Phillips and Azad (6). Thereafter the much studied problem of the deepening of a linearly stratified layer under the influence of the earth's rotation is considered. Finally in Section 3, field measurements

are used for testing the performance of the model in more complex situations. Section 4 finishes the paper with a discussion and some conclusions.

MODEL FORMULATION

Basic Assumptions

The study will restrict attention to horizontally homogeneous flows, which means that terms containing gradients in the horizontal plane are neglected. Boussinesq's approximation is employed and it will also be assumed that no mean vertical velocity is present. The effect of the earth's rotation is described by the Coriolis parameter, f. These assumptions are in geophysical fluid dynamics well known as characterizing the planetary boundary layer equations.

Momentum Equations

Within the assumptions made the momentum equations take the following form:

$$\frac{\partial U}{\partial t} = \frac{\partial}{\partial z}\left(-\overline{uw} + \nu\frac{\partial U}{\partial z}\right) + fV \tag{1}$$

$$\frac{\partial V}{\partial t} = \frac{\partial}{\partial z}\left(-\overline{vw} + \nu\frac{\partial V}{\partial z}\right) - fU \tag{2}$$

where z is the vertical space coordinate, positive upward, t the time coordinate, f the Coriolis parameter, U and V mean velocities in the x and y direction, respectively, $\overline{uw}$ and $\overline{vw}$ the Reynolds stresses and ν the molecular kinematic viscosity.

The surface wind stress, $\vec{\tau}$, specifies the momentum flux at the surface, thus:

$$\left(-\overline{uw} + \nu\frac{\partial U}{\partial z}\right)_{z=0} = \frac{\tau_x(t)}{\rho} \tag{3}$$

$$\left(-\overline{vw} + \nu\frac{\partial V}{\partial z}\right)_{z=0} = \frac{\tau_y(t)}{\rho} \tag{4}$$

where ρ is the density of water. The present analysis assumes an infinitely deep ocean, with zero velocities at the lower boundary. To be able to apply a numerical model it is, however, necessary to specify a depth, D, where zero velocities are prescribed. Thus:

$$(U(t))_{z=-D} = (V(t))_{z=-D} = 0 \tag{5}$$

The depth of vanishing motion must of course be chosen large enough not to influence the predicted results in the region of interest.

Turbulence Model

The turbulence model used is, except for the buoyancy terms, the same as in paper I and will therefore be only briefly described in the present paper.

The kinematic eddy viscosity, ν_T, is calculated from the turbulent kinetic energy, k, and its dissipation rate, ϵ, according to:

$$\nu_T = C_\mu \frac{k^2}{\epsilon} \tag{6}$$

where C_μ is an empirical constant. Transport equations for k and ϵ may be derived in exact form from Navier-Stokes equations and thereafter "modeled" to the following form:

$$\frac{\partial k}{\partial t} = \frac{\partial}{\partial z}\left(\frac{\nu_{eff}}{\sigma_k}\frac{\partial k}{\partial z}\right) + \nu_T\left[\left(\frac{\partial U}{\partial z}\right)^2 + \left(\frac{\partial V}{\partial z}\right)^2\right] + \frac{\nu_T g\alpha}{\sigma_T}\frac{\partial S}{\partial z} - \epsilon \tag{7}$$

$$\frac{\partial \epsilon}{\partial t} = \frac{\partial}{\partial z}\left(\frac{\nu_{eff}}{\sigma_\epsilon}\frac{\partial \epsilon}{\partial z}\right) + C_1\nu_T\frac{\epsilon}{k}\left[\left(\frac{\partial U}{\partial z}\right)^2 + \left(\frac{\partial V}{\partial z}\right)^2\right] + C_3\nu_T\frac{\epsilon}{k}\frac{g\alpha}{\sigma_T}\frac{\partial S}{\partial z} - C_2\frac{\epsilon^2}{k} \tag{8}$$

where ν_{eff} is the effective viscosity $(\nu_T + \nu)$, S salinity, g gravitational acceleration, α coefficient in density-salinity relation, σ_k, σ_ϵ, and σ_T Prandtl/Schmidt numbers, and C_1, C_2 and C_3 empirical constants.

The terms on the right-hand side of (7) and (8) describe diffusion, production due to shear, production or dissipation due to buoyancy and dissipation due to viscous action, respectively. While the k-ϵ model for homogeneous conditions can be claimed to be well established, there are a few different lines of development when it comes to buoyancy affected flows. Gibson and Launder (3) neglected the buoyancy term in the ϵ-equation but derived an extension of (6) which includes buoyancy effects. Hossain and Rodi (4) found that the buoyancy term in the ϵ-equation was needed for the vertical buoyant jet, while the horizontal one was predicted satisfactory by putting $C_3 = 0$. For a further discussion of the buoyance term in the ϵ-equation, see Rodi (21). The inclusion of buoyancy effects in the k-ϵ model is clearly still a matter for basic research. For geophysical flows there is, however, a common situation which demands that $C_3 > 0$. The situation in mind is the unstably stratified boundary layer without any significant mean shear. In this situation the ϵ-equation would otherwise lack a production term which of course is unrealistic. The buoyancy term in the ϵ-equation thus seems to be essential in geophysical flows and a nonzero value of C_3 is therefore required. The actual value of C_3 used is 0.8 which was found to ensure maximum agreement when predicting the experimental results given by Kantha et al. (6). Also the unstably stratified boundary layer experiment by Deardorff et al. (1) was used when the value of C_3 was optimized. For details see Svensson (22). Rodi (21) has optimized C_3 for horizontal buoyant flows and found that $C_3 = 1.0$ ensures maximum agreement with available experimental data on entrainment velocities. The difference between the values adopted is of no practical significance. The reason for not making use of the extension of (6) given by Gibson and Launder (3) is simply that (6) should not be replaced until it proves to be insufficient. The predictions to be presented in this paper did not call for this extension. For further details about the k-ϵ model, see Launder and Spalding (11, 12).

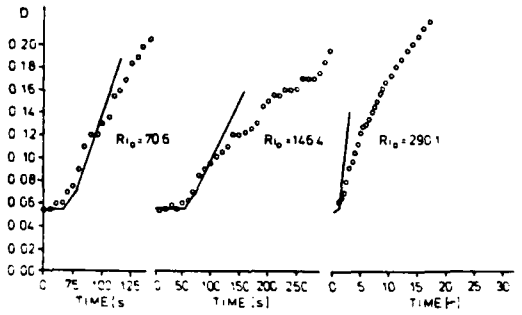

Fig. 1 Entrainment generated by a surface stress. Development of mixed layer depth as a function of time for different Ri-numbers, o-measurements, -calculations.

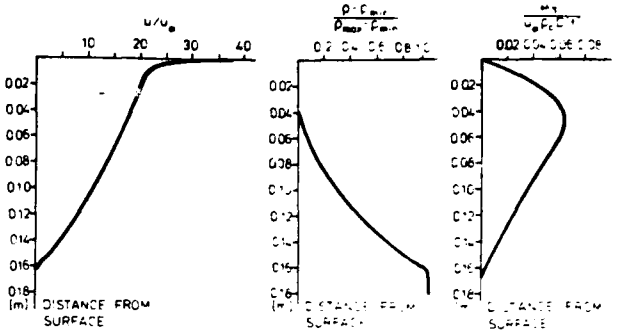

Fig. 2 Entrainment generated by a surface stress. Velocity, density and eddy viscosity profiles for Ri = 146.4 , t = 150 S .

Salinity

For the predictions to be presented it will be assumed that density variations are caused solely by changes in salinity. The inclusion of other buoyancy affecting variables into the model is of course possible.

Within the assumptions made the transport equation for salt, S , reads:

$$\frac{\partial S}{\partial t} = \frac{\partial}{\partial z}\left(\frac{\nu_{eff}}{\sigma_{eff}}\frac{\partial S}{\partial z}\right) \qquad (9)$$

where σ_{eff} is the effective Prandtl/Schmidt number for salt. The value of σ_{eff} is not well established and some rather ad hoc assumptions are needed for its determination. One such assumption is that laminar and turbulent contributions to the effective exchange coefficient are additive, see Patankar and Spalding (17). Thus:

$$\frac{\nu_{eff}}{\sigma_{eff}} = \frac{\nu}{\sigma} + \frac{\nu_T}{\sigma_T} \qquad (10)$$

where σ is the laminar and σ_T the turbulent Prandtl/Schmidt number. The value of σ is well known, but σ_T needs further consideration. Launder (10) has, starting from the exact transport equations for Reynolds stresses and turbulent heat flux, derived an expression for σ_T. With the constants used in modeling of the exact equations the formula reads:

$$\sigma_T = 0.63\ (1 + 0.2\ B)/(1 + 0.06\ B) \qquad (11)$$

where

$$B = -\alpha g \frac{k^2}{\epsilon^2}\frac{\partial S}{\partial z} \qquad (12)$$

is a buoyancy parameter. The expression will thus give $\sigma_T = 0.63$ for nonbuoyant flows and have a limit of $\sigma_T = 2.1$ for strongly stratified flows. Launder showed that this variation is in accordance with available experimental data. The expressions (10), (11) and (12) will provide a way of calculating σ_{eff}, but it is emphasised that further studies of how σ_T is affected by buoyancy are needed.

RESULTS

A Laboratory Experiment

An experiment which closely simulates the shear induced entrainment in the atmosphere and the ocean has been reported by Kantha, Phillips and Azad (6), see also Kantha (5). The salient features of the experiment may be described as follows. At time $t = 0$ a shear stress is applied at the top of a homogeneous layer of depth D_i, resting over a quiescent denser layer. The development of the mixed layer depth, D(t), is studied for different initial and boundary conditions in order to determine the dimensionless entrainment velocity, U_e/U_*, as a function of an overall Richardson number. The formulation of the Richardson number reads:

$$Ri_o = \frac{D_i\, g\Delta\rho}{\rho\, U_*^2} \qquad (13)$$

where $\Delta\rho$ is the initial density jump between the two layers. For a description of the experimental set-up, see Kato and Phillips (7).

In all calculations the shear stress, τ, was 0.109 N/m^2 and the initial depth, D_i, 0.054 m. These conditions are the same as in one of the experimental series. The predicted mixed layer deepening for different Ri-numbers are displayed in Fig. 1, together with the experimental data. The mixed layer depth has to be defined in some way, especially since the model predicts the continuous vertical variation of different variables. Two different definitions were tried: 1) the depth where the laminar viscosity exceeds the calculated eddy viscosity, and 2) the depth of maximum density gradient. The two definitions gave essentially the same depth for Ri_o up to 150, while definition 2 gave a somewhat lower U_e/U_* for higher Ri_o-numbers. The choice of definition is of course a matter of taste, but judging from the profiles of velocity, density, and eddy viscosity shown

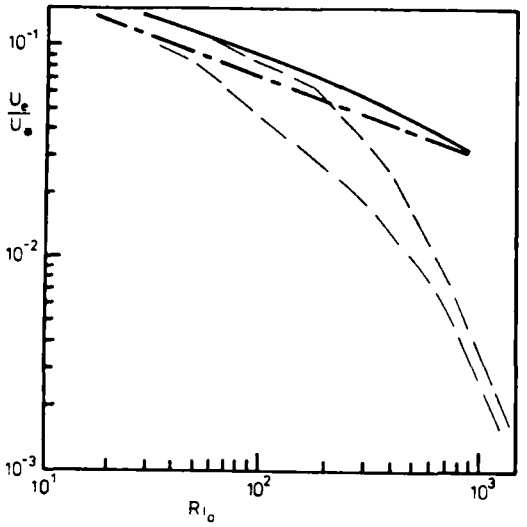

Fig. 3 Entrainment generated by a surface stress. Entrainment velocities versus an overall Richardson number. The shaded area represents the results by Kantha et al. (6), the dashed line is Price's analysis and the solid line present predictions.

in Fig. 2 it is clear that the "turbulence-alternative" offers a more precise definition. So, this is the definition used in Fig. 1 and also in Fig. 3, where the entrainment velocity versus the Richardson number is displayed. The dashed line in this figure represents Price's (20) interpretation of the experimental data. He considered in detail the frictional influence of the sidewalls in the experiment and concluded that the sidewall correction made by Kantha et al. was too small. The present predictions are seen to be in close agreement with Price's analysis and it is concluded that the model predicts the entrainment process in a satisfactory way. As a part of the calculations, the energy balance was studied. The partitioning between the different components is of special interest in integral theories of the mixed layer dynamics. The energy balance for the present case is shown in Fig. 4. It is interesting to note that more energy is spent in creating the velocity field than to change the potential energy of the system. Only a small amount is stored as turbulent kinetic energy, while the bulk of energy supplied is dissipated. The supplied energy was calculated as:

$$\text{supplied energy} = \int_0^t \tau \cdot U_s \, dt \qquad (14)$$

where U_s is the surface velocity.

The deepening of a rotating boundary layer

In paper I it was shown that the depth of vanishing motion is about U_*/f for the homogeneous steady Ekman layer. This depth is thus an upper limit for the deepening of the linearly stratified boundary layer to be investigated in this section. In fact, one would expect the depth to be significantly smaller if a local Richardson number criterion is the relevant parameter for the deepening.

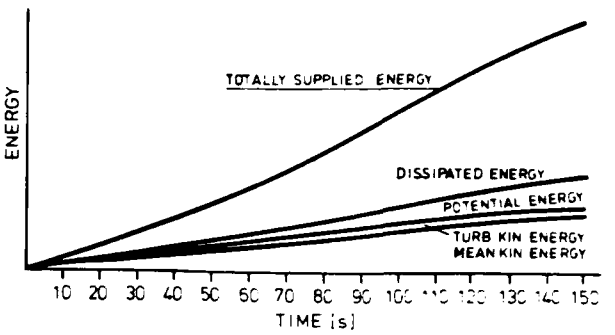

Fig. 4 Entrainment generated by a surface stress. The different components in the energy balance.

Mathematical models describing the response of a linearly stratified layer to a suddenly imposed surface stress under the influence of rotation have been presented, among others, by Pollard et al. (19), Niiler (16), and Phillips (18). As these models produce rather consistent results within themselves, they will be used for a comparison with the present model.

The parameters characterizing the case are the Coriolis parameter, f, the surface friction velocity, U_*, and the initial buoyancy frequency, N, defined by:

$$N^2 = -\frac{g}{\rho}\frac{\partial \rho}{\partial z} \qquad (15)$$

Earlier investigators found that, due to rotation, the deepening will slow down when t is greater than π/f. In table 1 the layer depths at $t = \pi/f$, as predicted by different models, are given for $U_* = 0.0173$ m/s, $N = 5 \cdot 10^{-3} s^{-1}$ and $f = 1.2 \cdot 10^{-4} s^{-1}$. As can be seen the estimates are quite consistent. The present model does not a priori assume the existence of a completely mixed layer and the definition of the layer depth is, as discussed earlier, therefore somewhat arbitrary. The two definitions mentioned earlier gave however for this case the same result and the well mixed layer was therefore easily identified. From Fig. 5 it is found that the predicted depth at $t = \pi/f$ is about 42 m, which certainly is in good agreement with other models.

The mixed layer depth as a function of time is displayed in Fig. 6. The solid line is the formula:

$$D(t) = 0.9 \frac{U_*}{f^{2/3} N^{1/3}} \left[2 - 3\cos\left(\frac{ft}{2}\right) + \cos^3\left(\frac{ft}{2}\right)\right]^{1/6} \qquad (16)$$

given by Phillips (18) and the dashed line represents present calculations. The agreement is almost perfect and it can be concluded that the model presented predicts the same behavior of the wind mixed layer as other more established models. Phillips model is restricted to $t < 2\pi/f$, but the behavior after this time is of course also of interest. Predictions were therefore extended to $4\pi/f$. As can be expected by considering the inertial oscillations, the depth increases after $2\pi/f$ and is once again haltered at $3\pi/f$, see Fig. 6.

Also for this case the components in the energy balance were estimated. The energy supplied was calculated according to (14). This indicates that the energy input is sensitive to the surface roughness, since a logarithmic law is known to be valid close to

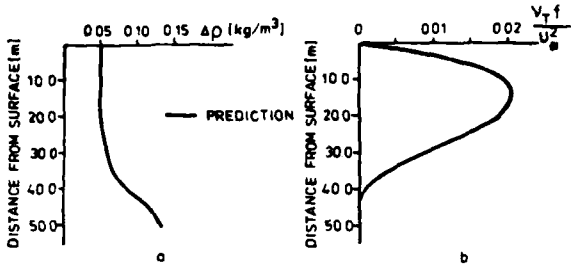

Fig. 5 Deepening of the wind-mixed layer. Density profile (a) and eddy viscosity profile (b) after π/f seconds

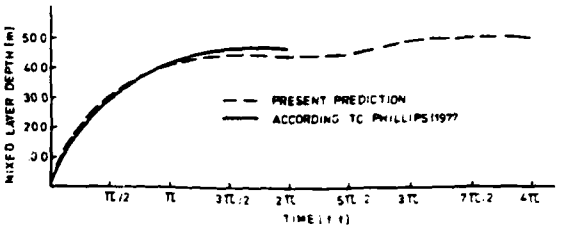

Fig. 6 Deepening of the wind-mixed layer. Mixed layer depth versus time

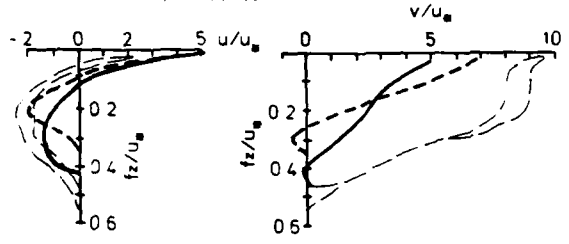

Fig. 7 Measured and predicted mean flow velocities. Shaded area represents measurements, dashed line predictions with density profile "frozen" and solid line predictions with salinity as a prognostic variable

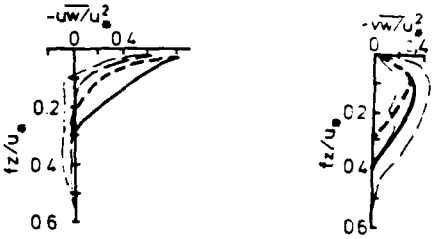

Fig. 8 Measured and predicted distribution of Reynold stresses. For meaning of symbols, see legend to Fig. 7

Table 1. Mixed layer depth after π/f seconds

Investigator	Formula	h_{max} or h after t = π/f
Pollard et al. (19)	$h_{max}=2^{3/4}\cdot u_*/(Nf)^{1/2}$	37.5
Niiler (16)	$h_{max}=1.9(u_*/Nf)^{1/2}$	42.5
Phillips (18)	$h_{max}=0.9\ 2^{1/6}\ u_*/(f^2N)^{1/3}$	41.9

the surface. Assuming a hydrodynamically smooth surface, which is an idealization, it was found from the predictions that roughly 2 % of the energy supplied up to $t = 2\ \pi/f$ was spent on increasing the potential energy.

Comparison With Field Measurements

A most impressive series of measurements of the turbulent boundary layer under pack ice has been reported by McPhee and Smith (15). Mean current, density and turbulence quantities were measured simultaneously throughout the entire boundary layer. A strong pycnocline bounded the mixed layer at a depth of about 35 m. Friction velocities were calculated from the measurements of the Reynolds stresses and found to be about 10^{-2} m/s.

McPhee and Smith also analysed their data and compared the results with recent planetary boundary layer models. They found that the measured lateral velocity component deviated both from theoretical models and from what could be expected from a consideration of the magnitude of the terms in the momentum equation. Also the predictions by the present model will show this discrepancy, which McPhee and Smith attribute to form drag. Another unwanted effect in the measurements was indicated by a weak stable stratification throughout the boundary layer. The authors suggest that convective effects can be the cause of this. In order to investigate the importance of this stratification the predictions to be presented were carried out both with salinity as a prognostic variable and with the density profile frozen at the shape given by the measurements, see Fig. 4 in the paper by McPhee and Smith.

Nondimensional profiles of velocity are compared in Fig. 7. The poor agreement for the lateral velocity component, discussed earlier, is discouraging even if it may be attributed to the measurements. It is interesting to note how the small stable stratification ($\Delta\sigma \approx 0.1$ over the layer) has a clearly recognizable influence on the velocity profiles. Reynolds stress profiles are in satisfactory agreement as can be seen in Fig. 8. The predicted stresses do however cease somewhat faster than the measured ones. The same discrepancy is even clearer in the comparison of turbulent kinetic energy profiles, see Fig. 9. A possible explanation may be that internal waves contribute to the measured fluctuations in the deeper parts, while this effect is not represented in the model. The effect of a mild stratification is also clearly demonstrated in Fig. 10, where eddy viscosity profiles are displayed. The predicted maximum eddy viscosity is seen to be reduced by 60 % when the density profile is frozen. McPhee and Smith calculated the eddy viscosity values from the peaks in the measured spectra of the vertical velocity fluctuations and considered the obtained values as rough estimates. The agreement with the present predictions is therefore as good as can be expected.

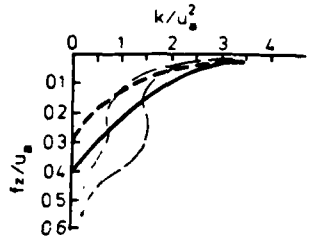

Fig. 9 Measured and predicted turbulent kinetic energy distribution. For meaning of symbols, se legend to Fig. 7

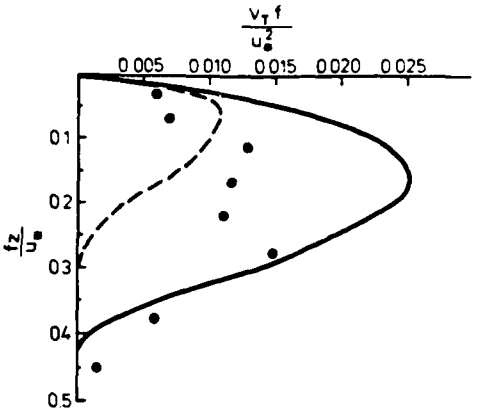

Fig. 10 Measured and predicted eddy-viscosity distribution. Dots represent measurements, lines as in Fig. 7

DISCUSSION AND CONCLUSIONS

Stratification is known to add a number of complicated phenomena to turbulence, i.e. energy radiation, strong anisotropy, step-like density profiles etc. These effects are not taken into account in the mathematical model and the predictions are therefore surprisingly good. A possible explanation is that the gross features of the mixed layer are governed by the momentum balance and the conversion of mechanical energy to heat and potential energy. This conversion is described by the turbulent energy equation and thus represented in the model. It is, however, too early to regard the above mentioned phenomena as unimportant and further investigations are thus needed.

The conclusions emerging from this study can be summarized in the following points:

- An extension of the k-ϵ model to stably stratified flows has been tested and found to reproduce the observed dampening of turbulence in a realistic way.
- Entrainment velocities across a density interface were predicted and regarded to be in satisfactory agreement with the experimental results by Kantha et al. (6).
- Rotation was found to decrease the entrainment rate. Maximum mixed layer depths and transient development were predicted and found to be in agreement with models particularly designed for this problem.
- Field measurements reported by McPhee and Smith (15) were used for a final test of the model. All the essential features of the boundary layer were predicted accurately by the model. It is the author's view that improved results could not be obtained by employing a more advanced turbulence model.

REFERENCES

1 Deardorff, J.W., Willis, G.E., and Lilly, D.K.: "Laboratory investigation of non-steady penetrative convection", Journal of Fluid Mechanics, Vol. 35, 1969, pp. 7-31.

2 Garwood, R.W.: "An oceanic mixed layer model capable of simulating cyclic states", Journal of Physical Oceanography, Vol. 7, 1977, pp. 455-468.

3 Gibson, M.M. and Launder, B.E.: "On the calculation of horizontal turbulent, free shear flows under gravitational influence", Journal of Heat Transfer, 1976, pp. 81-87.

4 Hossain, M.S., and Rodi, W.: "Influence of Buoyancy on the turbulence intensities in horizontal and vertical jets", In: Heat Transfer and Turbulent Buoyant Convection, Hemisphere Publishing Corp., Washington, D.C., 1977.

5 Kantha, L.H.: "Turbulent entrainment at the density interface of a two-layer stably stratified fluid system", Geophys. Fluid Dyn. Laboratory, Technical Report 75-1, 1975.

6 Kantha, L.H., Phillips, O.M., and Azad, R.S.: "On turbulent entrainment at a stable density interface", Journal of Fluid Mechanics Vol. 79, 1977, pp. 753-768.

7 Kato, H. and Phillips, O.M.: "On the penetration of a turbulent layer into a stratified fluid", Journal of Fluid Mechanics, Vol. 37, 1969, pp. 643-655.

8 Kraus, E.B. and Turner, J.S.: "A one-dimensional model of the seasonal thermocline II. The general theory and its consequences", Tellus, Vol. 19, pp. 98-106.

9 Kundu, P.K.: "A numerical investigation of mixed-layer dynamics", Journal of Physical Oceanography, Vol. 10, 1980, pp. 220-236.

10 Launder, B.E.: "On the effects of a gravitational field on the turbulent transport of heat and momentum", Journal of Fluid Mechanics, Vol. 67, 1975, pp. 569-581.

11 Launder, B.E. and Spalding, D.B.: "Mathematical models of turbulence", Academic Press, London and New York., 1972.

12 Launder, B.E. and Spalding, D.B.: "The numerical computation of turbulent flows", Comp. Meth. Appl. Mech. and Eng., Vol. 3, 1974, pp. 269-288.

13 Marchuk, G.I., Kochergin, V.P., Klimok, V.I., and Sukhorukov, V.A.: "On the dynamics of the ocean surface mixed layer", Journal of Physical Oceanography, Vol. 7, 1977, pp. 865-875.

14 Mellor, G.I. and Durbin, P.A.: "The structure and dynamics of the ocean surface mixed layer",

Journal of Physical Oceanography, Vol. 5, 1975, pp. 718-728.

15 McPhee, M.G. and Smith, J.D.: "Measurements of the turbulent boundary layer under pack ice", Journal of Physical Oceanography, Vol. 6, 1976, pp. 696-711.

16 Niiler, P.P.: "Deepening of the wind-mixed layer", Journal of Marine Research, Vol. 33, 1975, pp. 405-422.

17 Patankar, S.V. and Spalding, D.B.: "Heat and mass transfer in boundary layers", 2:nd edition, 1970, Intertext Books, London.

18 Phillips, O.M.: "Entrainment". In "Modelling and Prediction of the Upper Layers of the Ocean", Edited by E.B. Kraus, Pergamon Press, 1977.

19 Pollard, R.T., Rhines, P.B., and Thompson, R.O.R.Y.: "The deepening of the wind-mixed layer", Geophysical Fluid Dynamics, Vol. 3, 1973, pp. 381-404.

20 Price, J.P.: "On the scaling of stress-driven entrainment experiments", Journal of Fluid Mechanics, Vol. 90, 1979, pp. 509-529.

21 Rodi, W.: "Influence of buoyancy and rotation on equations for the turbulent length scale", Paper presented at the 2:nd symposium on turbulent shear flows, Imperial College, London, 1979.

22 Svensson, U.: "A mathematical model of the seasonal thermo-cline", Report No, 1002, Department of Water Resources Engineering, University of Lund, Sweden, 1978.

23 Svensson, U.: "The structure of the turbulent Ekman layer", Tellus, Vol. 31, 1979, pp. 340-350.

SEDIMENT TRANSPORT IN STRATIFIED TURBULENT FLOW

B.A. DeVantier and B.E. Larock
Civil Engineering Department, University of California, Davis

ABSTRACT

A mathematical model of sediment laden, density affected turbulent flows is presented. The finite element technique is used in conjunction with the Newton iterative method to solve the resulting partial differential equations. The model satisfactorily predicts velocity and concentration profiles for unidirectional open channel flows. It is concluded that the model can justifiably be extended to multi-dimensional flows.

NOMENCLATURE

a	Distance from Wall to Edge of Computational Grid
A	Surface Area
c	Constants for k-ε Model
d	Free Surface Height Above Bed
e	Characteristic Roughness Height
E	Turbulent Dispersion Coefficient
f	Volume Fraction of Sediment
F	Finite Element Residual
g	Gravitational Acceleration
G	Buoyant Production of k
k	Turbulence Kinetic Energy
K	Constant in Law of the Wall
ℓ	Outer Unit Normal
N	Basis Function
P	Pressure
Pr	Production of k by Bulk Fluid Motion
p	Turbulent Pressure Fluctuation
q	Vector of Nodal Unknowns
r	Relaxation Factor
s	Surface Force
S	Channel Slope
t	Time
U	Bulk Fluid Horizontal Velocity
u	Bulk Fluid Horizontal Velocity Fluctuation
V	Velocity
v	Velocity Fluctuation
v_α	Point Velocity, α Phase
v_β	Point Velocity, β Phase
$\mathcal{V}$	Volume
W	Bulk Fluid Vertical Velocity
w	Bulk Fluid Vertical Velocity Fluctuation
x	Streamwise Coordinate
y	Transverse Coordinate
z	Vertical Coordinate
γ	Turbulent Dispersion Constant
Γ	Finite Element Domain Boundary
δ	Kronecker Delta
ϵ	Dissipation Rate for k
η	Density Difference Ratio
κ	von Karman Constant
λ	Sediment Volume Fraction Fluctuation
Λ	Mean Sediment Volume Fraction
ν	Fluid Kinematic Viscosity
ρ	Fluid Density
σ	Density Ratio
τ	Shear Stress
Φ	Surface Volume Fluctuation Correlation
ψ	Intrinsic Property Tensor
Ω	Finite Element Domain

Subscripts and Superscripts

b	Bulk Fluid
e	At Element Level
f	Frictional
i	Summation Subscript
j	Summation Subscript
n	Latest Iteration Value
o	Previous Iteration Value
s	Sediment
T	Turbulence (subscript)
T	Transpose (superscript)
α	Fluid Phase
β	Solid Phase
μ	Viscosity

INTRODUCTION

An accurate description of many environmental and industrial processes depends upon a good prediction of sediment transport behavior in fluids. Often sediment concentration gradients create density gradients in the bulk fluid which give rise to density currents or stratified flow. Since many problems of practical interest can not be represented as unidirectional flows, a transport model which can be applied to multidimensional flow problems is needed. It is the writers' goal to use the present model for prediction of these more complicated flows. These preliminary results are restricted to the prediction of concentration and flow properties for a unidirectional case for three reasons: the nonlinear equation set is relatively simpler to solve for this case; the interplay and effects of individual physical processes are simpler to identify and examine; data from controlled laboratory experiments are available for such flows, and are not available for more complex flows.

MODEL THEORY

Sediment transport is a two-phase flow phenomenon, and a proper mathematical description of it must include the motion of particles as well as fluid parcels. Following each sediment particle through a flow domain is conceptually possible but is totally impractical, so some sort of statistical description or averaging is required. Statistical descriptions such as those proposed by Buyevich and Shchelchkova (2) are proper and somewhat more

computationally realistic, but they require correlations which are very difficult if not impossible to obtain for a general problem. The writers have found the volume averaging technique proposed by Whitaker (12) and corrected by Gray (5) to be preferable in a sediment transport description.

If an averaging volume is chosen, Figure 1, which includes moving fluid and particles, the equations describing the fluid motion are

$$\frac{\partial \rho_\alpha}{\partial t} + \frac{\partial}{\partial x_i}(\rho_\alpha v_i) = 0 \tag{1}$$

(mass conservation), and

$$\rho_\alpha \frac{\partial v_{\alpha i}}{\partial t} + \rho_\alpha \frac{\partial}{\partial x_i}(v_{\alpha i} v_{\alpha j}) = - \frac{\partial}{\partial x_i} P_\alpha + \rho_\alpha g_i + \frac{\partial}{\partial x_j} \tau_{ij} \tag{2}$$

(momentum conservation). Although the Einstein summation convention is employed, the subscript α is not summed but is used to denote a property defined only in the α phase.

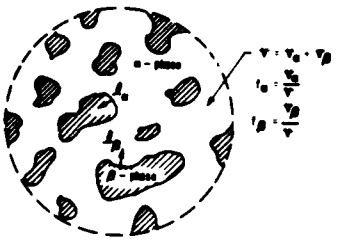

Fig. 1 Schematic of volume averaging region

The volume averaging theorem of Slattery (12) is

$$\frac{1}{V}\int \frac{\partial}{\partial x_i}\psi_\alpha dV = \frac{\partial}{\partial x_i}\frac{1}{V}\int \psi_a dV + \frac{1}{V}\int_{A_{\alpha\beta}(t)} \psi_\alpha \ell_{\alpha i} dA \quad , \tag{3}$$

where ψ_α is an intrinsic α-phase tensor property of indefinite order; the last term is a surface boundary integral computed only on the α-β interfacial area, and $\ell_{\alpha i}$ is the unit normal from the α phase. The volume average of the property ψ_α in the α region is

$$\langle \psi_\alpha \rangle^\alpha = \frac{1}{V}\int \psi_\alpha dV \tag{4}$$

When the averaging theorem and this definition are applied to the momentum conservation equation, the result is

$$\rho_\alpha \frac{\partial}{\partial t}(f_\alpha \langle v_{\alpha i}\rangle^\alpha) + \rho_\alpha \frac{\partial}{\partial x_j}(f_\alpha \langle v_{\alpha i}\rangle^\alpha \langle v_{\alpha j}\rangle^\alpha) = - \frac{\partial}{\partial x_i}\langle P_\alpha \rangle^\alpha + \rho_\alpha g_i + \frac{\partial}{\partial x_j}\langle \tau_{ij}\rangle^\alpha + 2\frac{\partial}{\partial x_j}\Phi_{ij} + s_{\alpha\beta i} - \frac{\partial}{\partial x_j}(f_\alpha \langle v'_{\alpha i} v'_{\alpha j}\rangle^\alpha) \tag{5}$$

Here the last term is the volume-averaging equivalent of the turbulent stress term in the time-averaged Navier-Stokes equations. The other terms are

$$s_{\alpha\beta i} = \frac{1}{V}\int_{A_{\alpha\beta}(t)} (\tau_{ij} - P\delta_{ij})\ell_{\alpha j} dA \tag{6}$$

and

$$\Phi_{ij} = \frac{1}{V}\int_{A_{\alpha\beta}(t)} v_{\alpha i}\ell_{\alpha j} dA \tag{7}$$

which are surface momentum exchange terms.

When the mass conservation equation for the fluid is volume averaged and incompressibility is assumed, then

$$\frac{\partial}{\partial x_i}(f_\alpha \langle v_{\alpha i}\rangle^\alpha) = 0 \tag{8}$$

If the phase average velocity of the solid particles is defined as the β phase momentum divided by its mass and the particles are also assumed to form a continuum, then for the β phase one obtains

$$\frac{\partial}{\partial x_i}(f_\beta \langle v_{\beta i}\rangle^\beta) = 0 \tag{9}$$

The volume averaged momentum conservation equation for the particles is

$$\rho_\beta \frac{\partial}{\partial t}(f_\beta \langle v_{\beta i}\rangle^\beta) + \rho_\beta \frac{\partial}{\partial x_j}(f_\beta \langle v_{\beta i}\rangle^\beta \langle v_{\beta j}\rangle^\beta) = - \frac{\partial}{\partial x_i}\langle P_\beta \rangle^\beta + f_\beta \rho_\beta g_i - s_{\alpha\beta i} - 2\frac{\partial}{\partial x_j}\Phi_{ij} \tag{10}$$

The phase average pressure in the β phase is the result of the continuum assumption.

The motion of the bulk fluid may now be described if equations (8) and (9), and (5) and (10) are combined. Considerable algebraic manipulation and order-of-magnitude analyses leads to this relation for conservation of bulk fluid volume:

$$\frac{\partial}{\partial x_i}\langle v_{bi}\rangle = 0 \tag{11}$$

For conservation of momentum the result is

$$\frac{\partial}{\partial t}(\rho_b \langle v_{bi}\rangle) + \frac{\partial}{\partial x_j}(\rho_b \langle v_{bi}\rangle \langle v_{bj}\rangle) = - \frac{\partial \langle P\rangle}{\partial x_i} + \rho_b g_i - \rho_\alpha \rho_\beta \frac{\partial}{\partial x_3}\left(\frac{f_\beta (1-f_\beta) v_s^2}{\rho_b}\right) - \rho_\alpha \frac{\partial}{\partial x_j}[(1-f_\beta)\langle v'_{\alpha i} v'_{\alpha j}\rangle] + \frac{\partial}{\partial x_j}(\tau_{bij}) \tag{12}$$

where the subscript b denotes bulk fluid properties, and the bulk velocity vector is

$$\langle v_{bi}\rangle = \frac{1}{\rho_b}[(1-f_\beta)\rho_\alpha \langle v_{\alpha i}\rangle^\alpha + f_\beta \rho_\beta \langle v_{\beta i}\rangle^\beta] \tag{13}$$

with $$\rho_b = \rho_\alpha (1-f_\beta) + f_\beta \rho_\beta \tag{14}$$

Here it is assumed that the β phase velocity and the α-phase velocity differ only by v_s, or

$$\langle v_{\beta i}\rangle^{\beta} = \langle v_{\alpha i}\rangle^{\alpha} - v_s \delta_{i3} \tag{15}$$

where v_s is the suspension settling velocity, which is a measured function of concentration, with the x_3-direction being vertical. This relation should be valid when particle relaxation times are small. A third equation for conservation of particle mass

$$\frac{\partial}{\partial x_i}\left(f_\beta \langle v_{bi}\rangle\right) - \frac{\partial}{\partial x_3}\left[f_\beta (1-f_\beta) v_s\right] = 0 \tag{16}$$

is obtained by considering the volume fraction dependence in equations (8) and (9).

Equations (11), (12), and (16) are quite similar to an equation set proposed by Barenblatt (1). These three equations are valid for a suspension in any fluid for which momentum exchange due to particle collision is insignificant and a constitutive relationship is known. However, when turbulent flow is considered, these equations are totally impractical to use. By defining the time averages of volume averaged quantities as

$$V_i = \overline{\langle v_{bi}\rangle} \quad , \quad P = \overline{\langle P\rangle} \quad , \text{ and } \Lambda = \overline{f_\beta} \quad , \tag{17}$$

the Reynolds decomposition can be expressed as

$$\langle v_{bi}\rangle = V_i + v_i \quad , \quad \langle P\rangle = P + p \quad , \text{ and } f_\beta = \Lambda + \lambda . \tag{18}$$

The time-averaged equations for steady flow then become

$$\frac{\partial}{\partial x_i} V_i = 0 \qquad \text{(volume conservation)} \tag{19}$$

$$V_i \frac{\partial \Lambda}{\partial x_i} - \frac{\partial}{\partial x_3}\left[\Lambda(1-\Lambda) v_s\right] = -\frac{\partial}{\partial x_i}\left(\overline{\lambda v_i}\right) - \frac{\partial}{\partial x_3}\left(\overline{\lambda^2 v_s}\right) \qquad \text{(sediment conservation)} \tag{20}$$

and

$$\frac{\partial}{\partial x_j}(V_i V_j) = -\frac{1}{\rho_b}\frac{\partial P}{\partial x_i} + (1+\eta\Lambda) g_i - \frac{\partial}{\partial x_j}\left(\overline{v_i v_j}\right) - \frac{\partial}{\partial x_j}\left[\overline{(1-f_\beta)\langle v'_{\alpha i} v'_{\alpha j}\rangle}\right] \qquad \text{(momentum conservation)} \tag{21}$$

The usual closure problem is visible in the overbarred terms in equations (20) and (21). Because no data exist for the correlation in the last term of equation (21) and measurement is not feasible, it is currently assumed that it may be lumped with the turbulent shear to form an effective $\overline{v_i v_j}$ which can be determined by a k-ε model for density-affected turbulent flow. The direct effect of buoyancy in the momentum equation is seen in the term $n\Lambda g_i$, where

$$\eta = \rho_\beta / \rho_\alpha - 1 \tag{22}$$

The Boussinesq approximation of neglecting density gradients except in buoyancy terms is used, as well as the approximation that the pure-fluid density is approximately that of the bulk fluid.

The sediment conservation equation (20) has two terms which must be modelled to close the equation set. An order-of-magnitude analysis shows the last term on the right to be negligible, and the first term on the right is modeled by the gradient transport relation

$$\overline{\lambda v_i} = -E_s \frac{\partial \lambda}{\partial x_i} \tag{23}$$

where E_s is a mass dispersivity coefficient to be discussed later.

A two-equation turbulence model, the k-ε model, has been proposed and tested by Rodi (7) for density-affected flows; the primary dependent variables are the turbulence kinetic energy k and its dissipation rate ε. This model is used herein. The steady state transport equations for k and ε respectively are

$$V_i \frac{\partial k}{\partial x_i} = \frac{\partial}{\partial x_i}\left(\frac{\nu_T}{\sigma_k}\frac{\partial k}{\partial x_i}\right) + Pr - \varepsilon + G \tag{24}$$

and

$$V_i \frac{\partial \varepsilon}{\partial x_i} = \frac{\partial}{\partial x_i}\left(\frac{\nu_T}{\sigma_\varepsilon}\frac{\partial \varepsilon}{\partial x_i}\right) + c_{\varepsilon 1}\frac{\varepsilon}{k}\left[Pr + (1-c_{\varepsilon 3})G\right] - c_{\varepsilon 2}\frac{\varepsilon^2}{k} \tag{25}$$

where

$$\nu_T = c_\mu \frac{k^2}{\varepsilon} \tag{26}$$

$$Pr = -\overline{v_i v_j}\frac{\partial V_i}{\partial x_j} \tag{27}$$

and

$$G = \overline{(\rho_\beta - \rho_\alpha) v_3 \lambda / \rho_b} = \eta\, \overline{v_3 \lambda} \tag{28}$$

Here ν_T is the kinematic eddy viscosity, Pr is the shear-induced production of k, and G is the buoyancy-induced production. The turbulence kinetic energy k is defined as

$$k \equiv \frac{1}{2}\left(\overline{v_i v_i}\right) \tag{29}$$

and the turbulent kinetic energy dissipation rate is

$$\varepsilon \equiv -\nu \overline{\frac{\partial v_i}{\partial x_j}\frac{\partial v_i}{\partial x_j}} \tag{30}$$

Values for the empirically determined coefficients c_μ, $c_{\varepsilon 1}$, $c_{\varepsilon 2}$, $c_{\varepsilon 3}$, σ_k and σ_ε will be given later in Table I.

In the k-ε model the turbulent viscosity concept is introduced to model the velocity fluctuation terms as

$$\overline{v_i v_j} = \nu_T\left(\frac{\partial V_i}{\partial x_j} + \frac{\partial V_j}{\partial x_i}\right) - \frac{2}{3} k \delta_{ij} \tag{31}$$

The turbulent viscosity is also used in modelling the mass dispersivity factor as

$$E_s = \gamma \nu_T \tag{32}$$

As noted by Graf (4), it is not clear whether γ is a true constant or even if the relation defined by the combination of equations (23) and (32) is valid. This form of modelling the turbulent dispersion term has been chosen, however, because some experimental values do exist for γ, and the inclusion of a transport equation for $\overline{\lambda v_i}$ would increase the complexity of the model to a point where multidimensional flow computations would not be practical.

MODEL APPLICATION TO UNIDIRECTIONAL FLOW

Governing Equations and Boundary Conditions

Steady, unidirectional, open channel flow containing suspended sediment can be modelled with the stated equations when the following assumptions are made: (a) for the purpose of determining the streamwise pressure gradient, pressure can be assumed to be hydrostatic, and so the streamwise gradient can be approximated as the product of gravitational acceleration and the slope S, (b) flow is in the x direction and there is no gradient of any variable in the x or y direction, and (c) the free surface can be modelled as a plane of symmetry. These assumptions reduce the relevant equations to a set of four scalar equations in four unknowns:

$$0 = gS - \frac{\partial(\overline{uw})}{\partial z} \qquad \text{(x-momentum)} \qquad (33)$$

$$0 = Pr - \epsilon + \frac{\partial}{\partial z}\left(\frac{c_\mu}{\sigma_k}\frac{k^2}{\epsilon}\frac{\partial k}{\partial z}\right) + G \qquad \text{(k transport)} \qquad (34)$$

$$0 = c_{\epsilon 1}\frac{\epsilon}{k}[Pr + (1-c_{\epsilon 3})G] - c_{\epsilon 2}\frac{\epsilon^2}{k} + \frac{\partial}{\partial z}\left(\frac{c_\mu}{\sigma_\epsilon}\frac{k^2}{\epsilon}\frac{\partial \epsilon}{\partial z}\right) \qquad \text{(ϵ transport)} \qquad (35)$$

$$0 = \frac{\partial}{\partial z}[\Lambda(1-\Lambda)v_s] + \frac{\partial}{\partial z}\left(\gamma \nu_T \frac{\partial \Lambda}{\partial z}\right) \qquad \text{(Λ transport)} \qquad (36)$$

The horizontal velocity U does not appear in equation (33) as written, but it is included in the turbulent stress term

$$\overline{uw} = -\nu_T \frac{\partial U}{\partial z} \qquad (37)$$

The values of the constants in this equation set are those suggested by Rodi (7) and listed in Table I. Vanoni noted (11) that other researchers have determined values for γ from unity to 1.5, so the writers have arbitrarily set γ at 1.2.

Table I. k-ε model constants

c_μ	$c_{\epsilon 1}$	$c_{\epsilon 2}$	$c_{\epsilon 3}$	σ_k	σ_ϵ
0.09	1.44	1.92	0.8	1.0	1.3

A proper set of boundary conditions will complete the problem description. In wall-bounded turbulent flows the computational region can not extend all the way to the wall (see Figure 2), so a law-of-the-wall boundary condition is applied at a distance a from the physical boundary. This boundary condition is

$$\frac{U}{u_*} = \frac{1}{\kappa} \ln\left(K\frac{z}{e}\right) \qquad (38)$$

where κ is the von Karman constant, e is the characteristic roughness height, and u_* is the friction velocity defined as the square root of the bed shear stress over the bulk density. The constant K is determined from Nikuradse's (6) experiments with sand roughened pipes (the channel bed is assumed to be sand roughened). Rodi (7) suggests that the near-wall boundary conditions on k and ϵ be

$$k|_a = u_*^2/c_\mu^{1/2} \qquad (39)$$

and

$$\epsilon|_a = u_*^3/(\kappa a) \qquad (40)$$

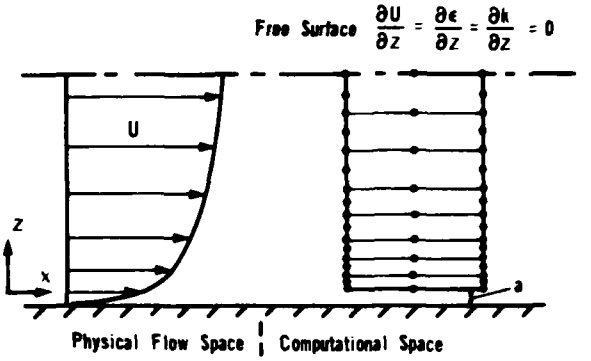

Fig. 2 Schematic of flow domain

These equations arise from the assumption that a is in the constant-stress layer so that the kinetic energy production Pr is balanced by the dissipation ϵ. At the near-wall boundary Λ is set to a prescribed value Λ_o. Since the free surface is modelled as a plane of symmetry, there can be no flux of k, ϵ, or Λ across the boundary. Nor can there be a momentum flux across this boundary; hence $\overline{uw}$ is zero here. The vertical bulk velocity W is zero throughout the flow.

Numerical Solution Methods

The nonlinear partial differential equation set is solved by Newton iteration as applied to the Galerkin finite element method by Schamber and Larock (9). The element residuals for this problem are

$$F_U = \int_{\Omega_e}(-N_i gS + \frac{\partial N_i}{\partial z}\nu_T\frac{\partial U}{\partial z})d\Omega + \int_{\Gamma_e} N_i\,\overline{uw}\,\ell_z\,d\Gamma \qquad (41)$$

$$F_k = \int_{\Omega_e} N_i(P_r + G - \epsilon)d\Omega - \int_{\Omega_e}\frac{c_\mu}{\sigma_k}\frac{k^2}{\epsilon}\frac{\partial k}{\partial z}\frac{\partial N_i}{\partial z}\,d\Omega + \int_{\Gamma_e} N_i\frac{c_\mu}{\sigma_k}\frac{k^2}{\epsilon}\frac{\partial k}{\partial z}\ell_z\,d\Gamma \qquad (42)$$

$$F_\epsilon = \int_{\Omega_e} N_i\{-c_{\epsilon 1}\frac{\epsilon}{k}[P_r + G(1-c_{\epsilon 3})] + c_{\epsilon 2}\frac{\epsilon^2}{k}\}\,d\Omega + \int_{\Omega_e}\frac{c_\mu}{\sigma_\epsilon}\frac{k^2}{\epsilon}\frac{\partial \epsilon}{\partial z}\frac{\partial N_i}{\partial z}\,d\Omega - \int_{\Gamma_e} N_i\frac{c_\mu}{\sigma_\epsilon}\frac{k^2}{\epsilon}\frac{\partial \epsilon}{\partial z}\ell_z\,d\Gamma \qquad (43)$$

and

$$F_\Lambda = -\int_{\Omega_e}\frac{\partial N_i}{\partial z}[\{\Lambda(1-\Lambda)v_s\} + \gamma c_\mu\frac{k^2}{\epsilon}\frac{\partial \Lambda}{\partial z}]\,d\Omega - \int_{\Gamma_e} N_i[\Lambda(1-\Lambda)v_s + \gamma c_\mu\frac{k^2}{\epsilon}\frac{\partial \Lambda}{\partial z}]\ell_z\,d\Gamma \qquad (44)$$

In these integrals Ω_e is the element domain; the boundary terms are only integrated over the portion of the element boundary Γ_e which coincides with part of the global domain boundary Γ. The Galerkin weighting functions are chosen

to be the 8-node basis functions N_j, and ℓ_z is the vertical boundary unit normal. The element discretization of the flow domain is shown in Figure 2. Since the values rather than the derivatives of k, ϵ, and Λ are prescribed at the near-wall boundary, boundary integrals need not be calculated there. Boundary contributions at the vertical boundaries are zero because ℓ_z is zero, and the free surface boundary integrals are all zero due to the no-flux conditions there. Thus the only nonzero boundary integral appears in equation (41), and it is nonzero only at the lower boundary. The law of the wall is then applied, following Schamber (8):

$$\int_{\Gamma_e} N_i \, \overline{uw} \, \ell_z \, d\Gamma = -\int_{\Gamma_{bed}} N_i \, c_f \, U^2 \, \ell_z \, d\Gamma \qquad (45)$$

where U is obtained from equation (41) with

$$c_f = \frac{1}{\kappa} \ln \left(K \frac{z}{e}\right)^{-2} \qquad (46)$$

Newton's method for this problem can be written

$$\frac{\partial F_i^{\,o}}{\partial q_j} \Delta q_j = - F_i^{\,o} \qquad (47)$$

where $q_j = [U_j, k_j, \epsilon_j, \Lambda_j]^T \qquad (48)$

is the column vector of nodal variables. The superscripts "o" indicate that these quantities are evaluated with data for q_j from the previous iteration. The nodal variables can then be updated with

$$q_j^{\,n} = q_j^{\,o} + r\Delta q_j \qquad (49)$$

As an example, one (typical) term in the Jacobian in equation (47) is

$$\frac{\partial F_\epsilon}{\partial k_j} = \int_{\Omega_e} N_i N_j \, c_{\epsilon 1} \frac{\epsilon}{k^2} [Pr + (1 - c_{\epsilon 3})G] \, d\Omega + 2 \int_{\Omega_e} N_j \frac{\partial N_i}{\partial z} \frac{c_\mu}{\sigma_\epsilon} \frac{k}{\epsilon} \frac{\partial \epsilon}{\partial z} \, d\Omega - \int_{\Omega_e} N_i N_j \, c_{\epsilon 2} \frac{\epsilon^2}{k^2} \, d\Omega \qquad (50)$$

Convergence of the computational scheme was not particularly sensitive to closeness of the initial estimates to the final converged solution. A single constant value was used for U, and Λ was estimated to decrease linearly with z to 98% of Λ_o. Based upon nondimensional data for k and ϵ appearing in (7), ϵ was assumed to be a function of z^{-1}, and k was chosen to be a linear function of z^{-1} and z.

Two-dimensional eight-node isoparametric elements were used even though the problem is truly one-dimensional because the intent is to apply this model to two-dimensional flows in the near future. All variables were approximated as quadratic in the element. Pressure need not be approximated because its streamwise gradient is assumed to be constant.

RESULTS

Controlled measurements of mean velocity and sand concentration as functions of depth in a flume have been reported by Vanoni (10) and Einstein and Chien (3). Predictions of the numerical model presented herein have been compared with measured data for six cases which cover a wide spectrum of volume fractions and sediment settling velocities. Concentration profiles for the six cases over the lower 30% of the flow are presented in Figure 3. Einstein and Chien measured concentrations in this domain only, because their equipment was designed to measure high sediment concentrations, and concentrations decreased rapidly above this region. Overall the model does reasonably well in predicting concentration profiles; however, accuracy of the predictions decreases as the bottom volume fraction of sediment increases. This is to be expected because the order of magnitude analysis contained the assumption that volume fraction is O(0.1) or less. This is not, however, the only possible explanation for these predictions. Particle collisions or damping of turbulence due to particles affecting the turbulence length scales could increase the effective settling velocity, which was determined from a quiescent settling test. Modelling the free surface as plane of symmetry will also cause sediment concentration to be a little higher than is proper, because turbulent dispersion will not be damped near the surface. The effect, however, should be small, and changing the model to account for it would require a higher order turbulence closure for turbulent sediment dispersion.

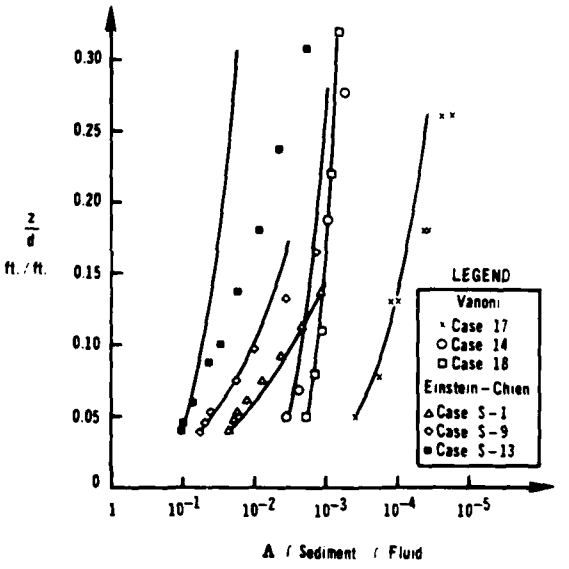

Fig. 3 Comparison of measured and predicted volume fractions

The model did remarkably well in prediction of the mean velocity, considering the uncertainties involved in determining the input data required by the model. Figure 4 is one example of good agreement. The shape of the velocity profiles were predicted well except for those cases involving a high sediment volume fraction, and the values of mean velocity are also predicted reasonably well. The near-wall velocity is not predicted as well as it might be, because the characteristic roughness height is taken to be the largest sieve diameter sand grain glued to the flume bottom. It is well accepted however that the roughness height is not a physically measurable quantity but an effective value. Correct prediction of the shape of the velocity profile is more important than the actual value, because none of the equations have any convective terms

and only derivatives of U appear. Figure 5 presents the worst velocity prediction obtained; in this case, which has the highest volume fraction, the near-wall velocity prediction is in error and the velocity profile is too flat. The next lower volume fraction case also has too flat a velocity profile but is less in error. Damping of turbulence by stratification makes the velocity profile less flat, but this effect is not nearly strong enough to be a complete explanation. Apparently some other mechanism is causing the velocity profile to be less flat as well. A probable mechanism is additional shear due to particle collisions; however, if particle collisions were considered, the assumption that the bulk fluid is Newtonian would have to be reevaluated.

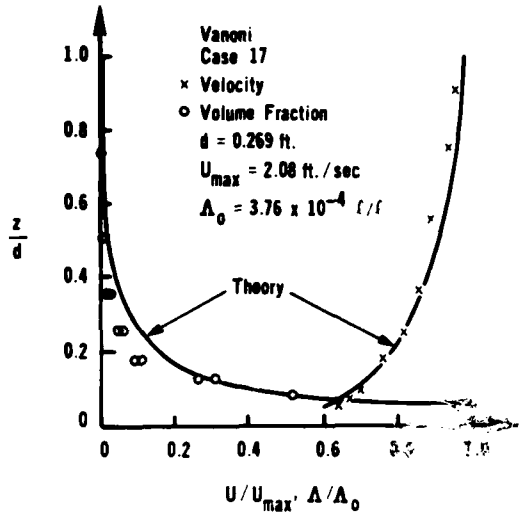

Fig. 4 Comparison of model velocity and volume fraction with measurements for Vanoni data

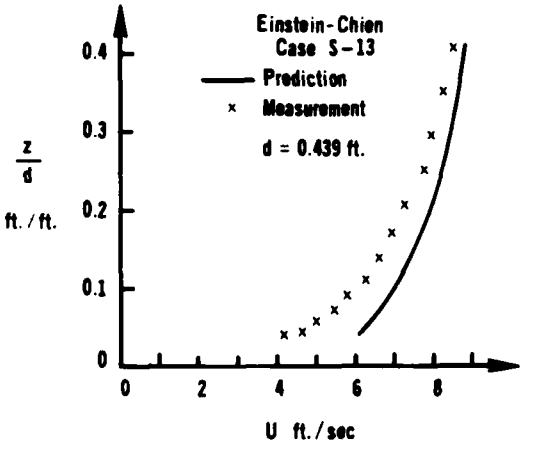

Fig. 5 Comparison with measurement for high volume fraction

If the flow is truly density affected, then decoupling the sediment transport equation from the flow equations should yield a different concentration profile. The decoupling is accomplished by first calculating the flow variables while assuming that the sediment concentration is zero, and then calculating the sediment concentration profile using the clear water values of flow variables as constants in the sediment transport equation. When this is done for Vanoni's case 14, the concentration increases 5-10% throughout the flow field, which is the proper trend. The effect of uncoupling the equations is a slight decrease in the velocity profile. This trend was observed experimentally by Vanoni (11) and Einstein (3) in comparisons of clear water and sediment laden flows.

The numerical computations were accomplished on a CDC 7600 computer in 9-10 CP seconds, with all variables converged to 8 significant figures. A nine element descretization was used for Vanoni's data and ten elements for Einstein and Chien's data. Subdividing and doubling the number of elements produced no change in the results, so they are grid independent.

CONCLUSION

Based on its predictive ability for unidirectional flows, the present model should be applicable to multidimensional flows. Because the model does less well at high volume fractions, improved modelling of particle interactions and a modified settling velocity appear to be needed to improve results. Because the correct trends are noted when velocity and concentration equations are uncoupled, and because the dispersion mechanism has been tested by cases which have no convection effects, the writers feel that extension of the model to more complex flows is warranted.

REFERENCES

1 Barrenblatt, G.I., "Motion of Suspended Particles in Turbulent Flow," Zhurnal Prikladnoi Matematiki i Mechaniki, Vol. 17, No. 3, 1953, pp. 262-265.

2 Buyevich, Y.A., and Shchelchkova, I.N., "Flow of Dense Suspensions," Prog. in Aerospace Sci., Vol. 18, 1978, pp. 121-150.

3 Einstein, H.A., and Chien, N., "Effect of Heavy Sediment Concentration Near the Bed on Velocity and Sediment Distribution," University of California Inst. of Engr. Res., No. 8, 1955.

4 Graf, W.H., Hydraulics of Sediment Transport, McGraw-Hill, New York, 1971, pp. 161-202.

5 Gray, W.G., "A Derivation of the Equations for Multi-phase Transport," Chem. Engr. Sci., Vol. 30, 1975, pp. 229-233.

6 Nikuradse, J., "Strömungsgesetze in rauhen Rohren," VDI-Forschungsheft, No. 361, 1933.

7 Rodi, W., "Turbulence Models for Environmental Problems," Prediction Methods for Turbulent Flow, von Karman Inst. Pub., McGraw-Hill, New York, 1980, pp. 276-281.

8 Schamber, D.R., "Finite Element Analysis of Flow in Sedimentation Basins," Ph.D. Dissertation, University of California, Davis, 1979.

9 Schamber, D.R., and Larock, B.E., "Computational Aspects of Modelling Turbulent Flows by Finite Elements, Computer Methods in Fluids, Pentech Press, London, 1980, pp. 339-361.

10 Vanoni, V.A., "Transportation of Suspended Sediment by Water," Transactions ASCE, Vol. 111, 1946, pp. 67-133.

11 Vanoni, V.A., "Sediment Transportation Mechanics: Suspension of Sediment," Proceedings ASCE, No. HY5, 1963, pp. 45-76.

12 Whitaker, S., "Advances in Theory of Fluid Motion in Porous Media," Ind. and Engr. Chem., Vol. 61, 1969, pp. 14-28.

SESSION 14 - COHERENT STRUCTURES II

A. K. M. F. Hussain - Chairman

EXPERIMENTAL STUDY OF COHERENT STRUCTURES IN MIXING LAYERS OF COAXIAL JETS

by O. LEUCHTER and K. DANG

OFFICE NATIONAL D'ETUDES ET DE RECHERCHES AEROSPATIALES
29 Avenue de la Division Leclerc, 92320 CHATILLON (France)

ABSTRACT

A technique of conditional sampling is used for characterizing the coherent structure of the three-dimensional velocity field in the mixing layer and that of the near pressure field of an unexcited jet of Reynolds number 2.10^5. The sampling technique is based on the use of a trigger probe (hot wire) of fixed position inside the potential core, and the coherent part of the turbulent signals (hot wire or microphone) is extracted by means of ensemble averaging. Phase shift corrections have been applied in order to improve the efficiency of the extraction. Typical results concern the convection velocity of the structures, the characteristic Strouhal number and the energy content of the recovered coherent part compared to the total energy of the signals. The coherent fluctuations are found to be highly anisotropic, the radial component being the most energetic one. The phenomenon of vortex pairing is clearly evidenced. The pressure field outside the jet is shown to contain an ordered wave structure with the wave center located in the near region of the mixing layer.

NOMENCLATURE

D	:	diameter of the jet
E	:	turbulent energy
f	:	frequency
p	:	pressure
R_D	:	Reynolds number, $U_j D/\nu$
S	:	Strouhal number, $f D/U_j$
t	:	time
T	:	characteristic period
x, y	:	coordinates in the axial and radial directions
x'	:	axial position of the detection probe
u, v, w	:	velocity components in the axial, radial and circumferential directions
U_e	:	velocity of the external flow
U_j	:	velocity of the jet
η	:	non dimensional radial coordinate defined as $\eta = (y - D/2)/x$
ν	:	kinematic viscosity
σ	:	rms value (of u if not otherwise specified)
τ	:	delay time

Symbols :

~	:	relative to the coherent part of the signal

INTRODUCTION

Since Brown and Roshko's [1] well known flow visualization experiments some ten years ago, numerous subsequent investigations have confirmed the existence of distinct coherent eddy structures in free and wall bounded turbulent shear flows. The configuration of jet mixing layers, the structure of which exhibits strong analogies with that of the flow cases examined by Brown and Roshko, have been the object of an increased research activity [2] to [5], especially since it has been recognized that coherent structures could there significantly contribute to entrainment, turbulence production and aerodynamic jet noise [6]. The main purpose of the present investigation is to characterize these structures in the near mixing layers of axisymmetric unexcited jets by means of appropriate techniques of signal processing. The final goal is to gather more quantitative information in order to provide a better general understanding of the physics of the coherent large scale phenomena in natural (unexcited) shear flows and to establish guide-lines for subsequent tentatives of numerical modelisation or direct simulation.

Relevant parameters characterizing the behaviour and the strength of the structures are : their characteristic Strouhal numbers and the corresponding convection velocities, the energy content relative to the coherent motion compared to the total energy of the turbulence, the location of the pairing process, the level of anisotropy of the coherent fluctuations,... These parameters depend in general on the initial conditions of the flow : the Reynolds number of the inner jet, the velocity of the outer flow, the initial turbulence level in one or both of the flows,... The study of the effect of these various initial conditions has also been included in the present investigation.

Despite of their quasi deterministic nature as revealed by numerous visualization experiments in jet flows, the detection of the coherent structures as well as their detailed investigation is complicated by the high level of random turbulence prevailing in fully turbulent jet mixing layers at moderate and high Reynolds numbers. The conventional statistical methods become then inefficient and more elaborate procedures employing conditional sampling are required. They are generally based on the use of a reference probe maintained in a fixed position inside the potential flow adjacent to the turbulent shear layer to be explored. This probe is assigned to detect the quasi periodic passage of the large vortex structures imbedded in the turbulent part of the flow and to trigger sampling from the main probe at a definite phase with respect to the occurence of particular events recognized as being relevant to the vortex structure. The coherent part of the main signal can then be extracted by ensemble averaging the individual samples. This procedure which is due to Lau and Fisher [2] has been widely used in studies of jet mixing layers. It is however not completely unambiguous if applied to unexcited flows. This is due to the apparent lack of eddy coherence as well in the spatial as in the temporal sense owing to small deviations (from the mean) of the individual trajectories of the structures, to different individual life histories

and to fluctuations of the individual convection velocities. To overcome this supplementary difficulty, phase shift corrections may be applied to the individual samples before ensemble averaging [7], [8], allowing the efficiency of the eduction process to be highly improved.

Most of the results discussed in the following were obtained in the reference case of zero outer flow at a jet Reynolds number of 2.10^5. In an early stage of this work, single hot wires were used in order to study the influence of the longitudinal position of the detection probe inside the potential core, the effect of the jet Reynolds number and the secondary to primary velocity ratio on the level of the relative coherent energy of the signals. Also the effect of phase shift corrections have been examined in this part of the study. In subsequent stages crossed hot wire probes have been used (with and without phase shift corrections) allowing the radial and circumferential velocity components to be investigated too. The energy and shear stress contribution of the coherent motion could thus be determined as well as its anisotropy. Measurements in the near pressure field outside the reference jet were also performed in order to characterize the coherent pressure waves and their contribution to the near field pressure intensity.

EXPERIMENTAL SET-UP AND PROCEDURE

The experiments were carried out in a coaxial jet facility equiped with two concentric nozzles of exit diameter 3 and 10 cm respectively, with contraction ratios of 16 for the inner jet and of 7.5 for the outer jet. Each of the nozzles is supplied separately with clean air of controlled (ambiant) temperature proceeding from a high pressure storage tank. Before exiting through the nozzles the flows pass through settling chambers equipped with turbulence screens in order to control the initial level of turbulence in the exit plane.

In the present study only turbulence-free jets have been studied, i.e. with residual turbulence levels lower than 1 % in the exit plane. The maximal velocity of the inner jet has been fixed at 100 m/s, the corresponding jet Reynolds number being of 2.10^5. Most of the experiments have been done in these reference conditions. Variation of the Reynolds number is achieved by decreasing the jet velocity. The velocity ratio Ue/Uj can be varied between 0 and 0.5, for the reference conditions of the inner jet. The external nozzle can be prolonged by a cylindrical duct of adjustable length in order to avoid the outer mixing layer to interact with the inner layer to be explored.

For the detection of the velocity signals standard hot wire techniques were employed using linearized constant temperature anemometers (DISA type 55 M). The pressure fluctuations in the near field were detected by Brüel and Kjaer (B&K) microphones of 1/8" equiped with the proper electronics of B&K. All fluctuating quantities were tape recorded on a SCHLUMBERGER tape recorder at the maximum speed of 1.52 m/s.

The principle of the signal processing is as follows : The detection probe (2) is maintained at a fixed position in the potential core, generally on the axis at an axial position of x = 2D. It detects there the quasi periodic fluctuations of the axial velocity induced by the large vortex structures of the mixing layer. The eduction process is initiated by identifying peaks of signal (2) with amplitudes exceeding a given level (of the order of the rms value of signal (2)). At each event of this kind, a sample of a fixed length is taken from the main probe (1) and eduction is achieved by ensemble averaging a large number of those samples. One obtains thus the educed signal $\tilde{u}(\tau)$ which represents the trace of the coherent structure in signal (1). This procedure is repeated for different positions of the main probe (hot wire or microphone).

In the first stages of the study (see [9], [10]), the peak selection was performed by means of an analog circuit and the ensemble average carried out with a numerical correlator of the type SAICOR A43 which was triggered by the peak selector. The correlator delivered 400 equidistant values of $\tilde{u}(\tau)$ which could be transferred into a computer (HP 2100) for further processing. The number of summations was in this case of the order of 16,000. For further details, see [9] and [10]. More recently, the signals have been processed entirely by numerical way, thus allowing phase jitter corrections to be applied. This is achieved by time shifting the individual samples before ensemble averaging. The amount of the time shifting is determined by maximizing the cross correlation between the individual (filtered) samples and the ensemble average. The process is initiated by ensemble averaging in a first step unshifted samples. Due to time and storage constraints, the number of summations was reduced to approximately 2500. The educed signals are further Fourier analysed in order to determine the characteristic period T or the corresponding Strouhal number $S = D/U_j T$, from which the energy content can be deduced by calculating the mean square value of $\tilde{u}(\tau)$ over a characteristic period.

RESULTS AND DISCUSSION

Figures 1 to 4 are relative to the single hot wire (u- component) measurements and concern the influence of various flow conditions and procedures on the coherent energy contribution. This is expressed here in terms of the ratio $(\tilde{\sigma}/\sigma)$ of the rms values relative to the educed $\tilde{u}$-signal and to the original u-signal. Figure 1 shows for the reference jet conditions the influence of the axial position (x'/D) of the detection probe. Three different positions (x'/D = 1, 2, 3) have been examined showing that the results are nearly insensitive to this parameter. The main probe is maintained at a fixed y-position (y ≈ D/2) as it moves downstream in the mixing layer. A maximum contribution of the coherent part of about 20 % (in rms units) is seen to be extracted with the basic (uncorrected) procedure. The maximum is quite flat and occurs in the near region of

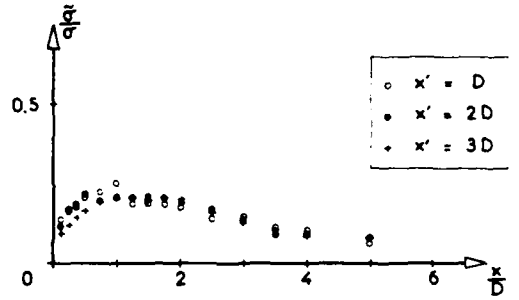

Fig. 1 – Rms contribution of the coherent structures for the reference case.

the mixing layer (about x ≈ 1 D). Figure 2 shows the effect of the jet Reynolds number. A noticeably higher level of coherent energy contribution is extracted for the lower value of the Reynolds number reflecting a smaller damping effect on the developing instability waves owing to the lower level of random eddy viscosity. No significant difference is observed between the two modes of detection examined here (reference probe fi-

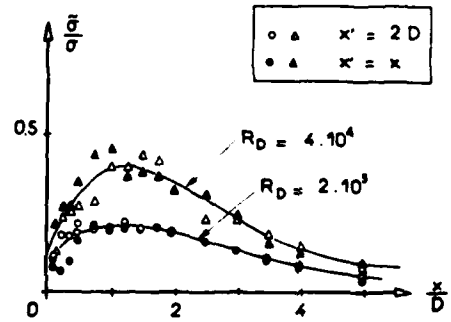

Fig. 2 – Effect of the jet Reynolds number on the rms contribution

xed at x' = 2 D or moving with the main probe, x' = x). Figure 3 shows that increasing the velocity ratio U_e/U_j (for the fixed standard value of U_j) produces a higher level of relative coherent energy with the maximum occuring farther downstream. This could be due to the fact that the turbulent damping effect decreases while the shear layer becomes less instable as the external velocity increases. Again here, as in the previous figures, the influence of the detection mode (fixed or moved detection probe) is insignificant. The improvement of the extraction due to phase shift cor-

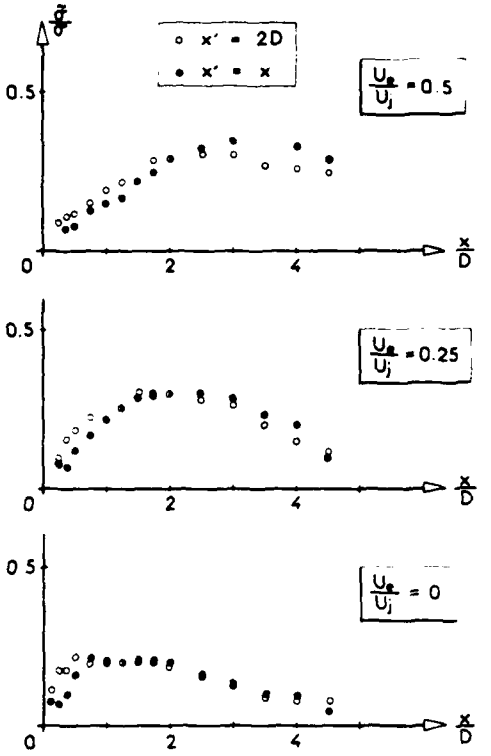

Fig. 3 – Effect of the velocity ratio $U_e \cdot U_j$ on the rms contribution.

rections is clearly evidenced in figure 4 for the standard conditions of the jet, as well for the axial distribution as for the radial one (at x = 2 D). The correction produces a much higher level of the coherent energy contribution especially in the central part of the mixing layer, where the values are roughly doubled. As the potential core is approached, the phase correction has a smaller effect and the $\tilde{\sigma}/\sigma$ - ratio tends to the limiting value of 1, as should be expected. The crossed wire experiments allow the longitudinal and radial (or circumferential) components of the velocity

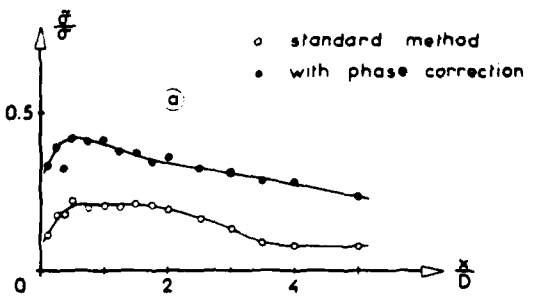

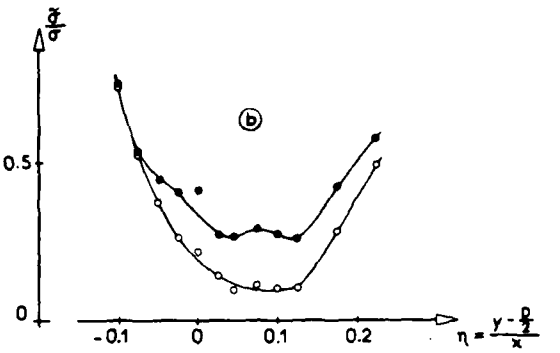

Fig. 4 – Effect of the phase correction on the rms contribution.
a) axial distribution,
b) radial distribution (x = 2 D)

to be analysed simultaneously. Figure 5 shows for the reference jet the ensemble averaged (phase corrected) signatures of the u and v components for various axial positions of the main probe (at a fixed radial position y = 0.5 D). The detector probe was held at a fixed position on the axis (x' = 2 D) allowing convection of the structures to be detected. Both signatures exhibit very similar features : downstream convection of particular phases at a definite speed and doubling of the period as x exceeds 2 D. Close to the nozzle where the Strouhal number is of the order of 0.8, the convection velocity (identical for $\tilde{u}$ and $\tilde{v}$) is of about 0.45 U_j, whereas farther downstream the (common) value is close to that usually deduced from space time correlations (0.6 U_j). The drop of the characteristic Strouhal number from the upstream value of 0.8 to the downstream

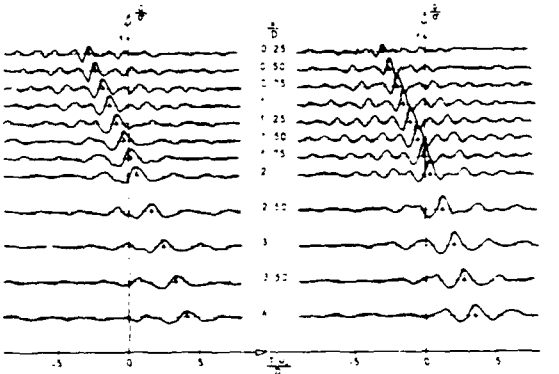

Fig. 5 – Wave diagram for the $\tilde{u}$ and $\tilde{v}$ components.

value of 0.4 is more clearly evidenced in figure 6, where the lines of constant values of the power spectrum of $\tilde{u}$ and $\tilde{v}$ (in arbitrary units) are shown in the x - S plane. The main features of both figures are quite similar : in the initial region ($x \leqslant 1$) the coherent energy is concentrated at S = 0.8, whereas downstream of x = 2 D the dominant Strouhal number is roughly half that value, suggesting that vortex pairing occurs between these two regions. The transition is seen to take place farther downstream for the v - component than for the u - component showing that vortex pairing is a complex and non local process which deserves further detailed investigation.

Figure 7 shows the axial evolutions of the relative coherent rms levels for the three velocity components. Characteristic features are the high relative contribution of the v - component (excepted in the very near re-

gion of the mixing layer) and the low level of the w - component suggesting that the coherent motions are approximately two-dimensional. It can be noticed further that the maximum of the v - contribution occurs farther downstream than that of the u - contribution. This appears to be consistent with the results of figure 6 relative to the location of the Strouhal number jump. The results for the u - component are also compared here to those obtained with the single hot wire.

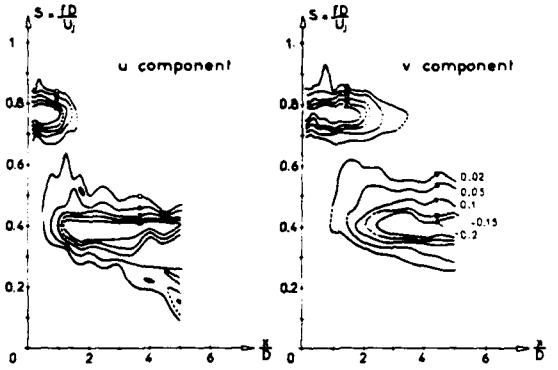

Fig. 6 – Lines of equal power spectrum of $\tilde{u}$ and $\tilde{v}$.

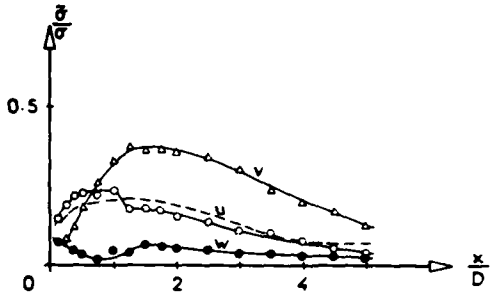

Fig. 7 – Rms contributions for the three velocity components
– – – single wire

Figure 8 gives the axial variation of the coherent energy contribution to the overall turbulent energy. Phase correction is seen to lead to much higher values than the standard method, the results being consistent with those presented in figure 4 for the rms ratio of the u - component. The maximum of the energy contribution of about 20 % occurs in the near mixing layer (x = 1D) and appears therefore to be closely connected to the phenomena of vortex pairing evidenced in figure 6. Further downstream the coherent energy decreases rapidly. Figure 9 illustrates the anisotropy of the coherent motion (Fig. 9b) in comparison to that of the overall random turbulence (Fig. 9a) showing again that the coherent motion is highly anisotropic and dominated by the v - component, excepted in the very near region, where the u - component prevails. In contrary, the w - component remains very small over the whole region implying quasi two dimensionality of the coherent motion. In figure 10, the contribution of the coherent shear stress (defined as $\widetilde{uv}$) to the overall turbulent stress is compared with that of the energy. Both quantities are relative to the uncorrected method. Positive contributions to the shear stress of a level comparable to that of the energy contribution occur only in a limited region centered at x = 1D. Further downstream the contribution is much smaller and becomes negative, but this particular behaviour needs more detailed investigations than could be done in this preliminary study.

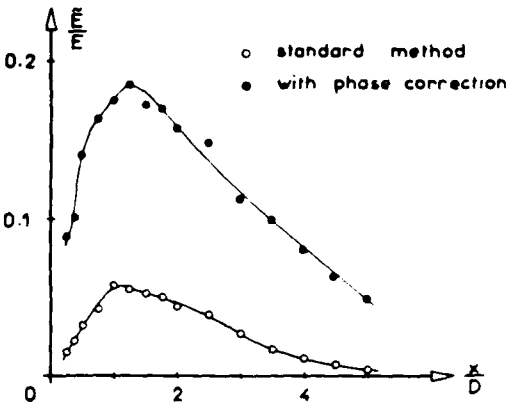

Fig. 8 – Energy contribution of the coherent structures

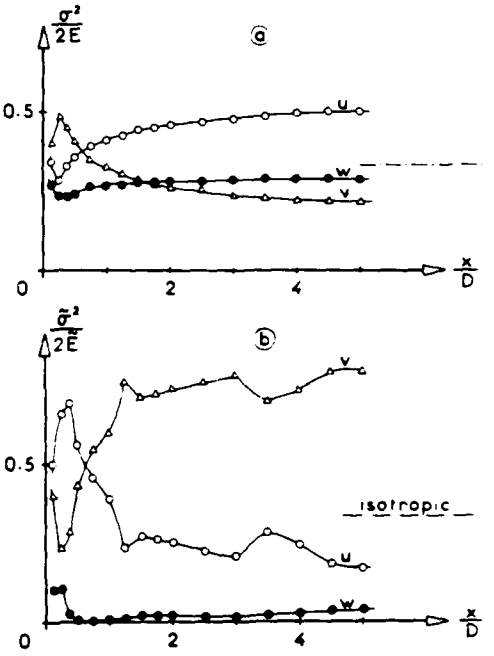

Fig. 9 – Anisotropy of the velocity fluctuations
a) random field,
b) coherent part.

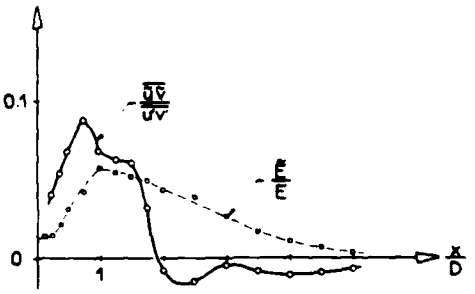

Fig. 10 – Contribution of the coherent shear stress.

The near pressure field outside the jet has been investigated in detail in the domain $x \leq 12\,D$, $y \leq 6.5\,D$, in order to determine how the coherent structure of the pressure may be related to that of the velocity in the mixing layer. Figure 11 shows the lines of equal rms values of the global (unconditioned) pressure signals : the total pressure level is maximum near the jet boundary, where it exceeds 120 dB, and decreases regularly toward the outer region, the highest levels being found in the region facing the potential core. The power spectra of the educed pressure signals revealed distinct peaks occuring at the structures' characteristic Strouhal numbers (0.4 and 0.8) and also at harmonics (S = 1.2 and 1.6) demonstrating clearly the existence of a close connection between the coherent structures in the mixing layer and the coherent part of the pressure field. The contribution of the coherent component to the overall pressure intensity was determined from third octave band filtered signals with the filter centered at the characteristic Strouhal numbers. The relative coherent part expressed in terms of the ratio $\tilde{\sigma}_p/\sigma_p$ of the corresponding rms values was found to increase slightly with the distance from the axis. Maximum values above 0.3 are reached in several isolated areas at axial locations between 2 D and 5 D. The conditional sampling procedure adopted here allows as for the velocity signals, to follow in space and time

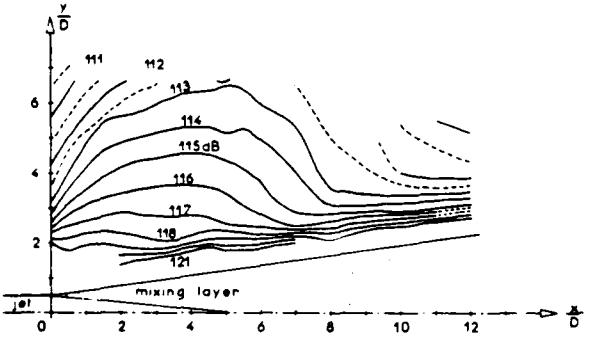

Fig. 11 – Lines of equal pressure level in the near field.

particular phases of the educed pressure signal. Figure 12 shows in the x-y plane lines of constant time delay τ relative to a particular phase of the $\tilde{p}$ - traces. It can be seen that this phase propagates at sound velocity with fronts of approximately circular form and with the corresponding wave center located in the near region of the mixing layer (about x = 1D) where vortex pairing was found to occur. This supports again the assumption [6] that the phenomenon of vortex pairing is strongly involved in the mecanism of noise production in turbulent jet mixing layers.

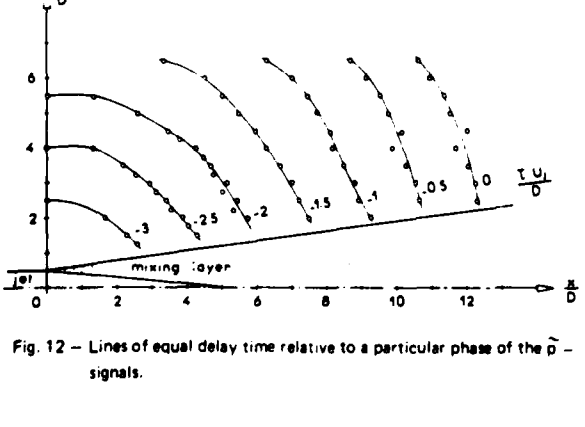

Fig. 12 – Lines of equal delay time relative to a particular phase of the $\tilde{p}$ – signals.

CONCLUDING REMARKS

Detection and detailed investigation of coherent structures in natural turbulent free shear layers are and remain problematic owing to the high level of random turbulence and to the large dispersion in the characteristic properties of the individual structures. The latter difficulty can be efficiently subjugated by exciting the flow periodically in order to organize and to regularize the structures. But if this artifice is to be discarded in order to preserve the natural features of the turbulent structure, then phase-shifting the individual pattern by optimizing the cross correlation with the ensemble average can significantly improve the eduction process.

An attempt was made in the present study to characterize the coherent part of the turbulence in natural jet mixing layers using this technique. It was possible thus to describe quantitatively the contribution of the coherent motion and to examine the effects of various initial conditions applied to the flow.

The most significant results can be resumed as follows : In so far as the level of the extracted coherent energy is concerned, it can be noticed that :

i) the position of the detection probe appears to be irrelevant to the energy level,

ii) substantial benefit is achieved by phase alignment of the samples,

iii) the Reynolds number and the ratio of external to jet velocity have a siginficant influence.

The convection velocities of the structures and the Strouhal numbers are sharply defined by the method and vortex pairing is clearly evidenced. The use of crossed hot wires allowed the three energy components to be specified. The coherent motion is found to be highly anisotropic in comparison to that of the random turbulence. The radial component is predominant and the circumferential negligeable, so that at a first approximation the coherent motion can be qualified as two dimensional. The first pairing process occuring in the near region of the mixing layer between roughly 1 D and 2 D downstream of the nozzle is associated with a high energy level approaching 20 % of the overall turbulence energy and with a high peak value of the relative coherent shear stress. It seems further to be closely connected to the generation of the coherent part of the sound field outside the jet. Further detailed investigation of this particular phenomenon is however needed to assess and to clarify these connections.

REFERENCES

[1] Brown, G L. and Roshko, A. : "The effect of density differences on the turbulent mixing layer", AGARD-CP No 93, 1971

[2] Lau, J C. and Fisher, M J. : "The vortex street structure of turbulent jets Part 1", J. Fluid Mech., Vol 67, 1975, pp 299-337

[3] Bruun, H H. : "A time-domain analysis of large scale flow structure in a circular jet Part 1 Moderate Reynolds number", J. Fluid Mech., vol 83, 1977, pp 641-671

[4] Yule, A J. : "Large-scale structure in the mixing layer of a round jet", J. Fluid Mech., vol 89, 1978, pp 413-432

[5] Hussain, A K M F. : "Coherent structures and studies of perturbed and unperturbed jets", 1980, to appear in Lecture Notes in Physics

[6] Laufer, J., Kaplan, R E. and Chu, W J. : "On the generation of jet noise", AGARD CP 31, 1973

[7] Blackwelder, R. : "On the role of phase information in conditional sampling", The Physics of Fluids, vol 20, No 10 Pt II, 1977, pp S232-S242

[8] Zilberman, M., Wygnanski, I. and Kaplan, R E. : "Transitional boundary layer spot in a fully turbulent environment", The Physics of Fluids, Vol 20, No 10 Pt II, 1977, pp S258-S271

[9] Leuchter, O. and Dang, K., "Recherche expérimentale des structures à grande échelle dans les couches de mélange de jets turbulents", La Recherche Aérospatiale, No 1978-5, pp. 279-282.

[10] Dang, K. and Leuchter, O., "Etude des structures cohérentes dans les couches de mélange de jets coaxiaux", ONERA TP No 1980-33.

A THREE DIMENSIONAL TIME DEPENDENT SIMULATION OF TRANSITION AND EARLY TURBULENCE IN A TIME-DEVELOPING MIXING LAYER

by
A. B. Cain* W. C. Reynolds** and J. H. Ferziger**

ABSTRACT

The primary focus of this study is the physics of the transition and early turbulence regimes in the time-developing mixing layer. In particular, we deal with the sensitivity of the mixing layer to the disturbance field of the initial condition; the disturbance field and the complete computation is three dimensional. The growth of the momentum thickness, the mean velocity profile, the turbulence kinetic energy, the Reynolds stresses, the anisotropy tensor, and particle track pictures of computations are all examined in an effort to better understand the physics of these regimes. The amplitude, spectrum shape, and random phases of the initial disturbance field were varied. A computation simulating the full Navier-Stokes equations was carried out but the grid (16 x 16 x 33) was too coarse for complete resolution. For this reason most of the cases were "Large Eddy Simulations" using the filtered Navier-Stokes equations. In "Large Eddy Simulations" an assay of the subgrid model was made by running two cases with identical initial conditions, one with a subgrid model and one without. The model lowered the kinetic energy by roughly 5% but otherwise had little effect. Due to computational limitations, all cases address the early or near field of the mixing layer.

NUMERICS

In the time-developing mixing layer we have planes of homogeneity. In these planes we use the standard discrete Fourier method for obtaining spatial derivatives in the two homogeneous directions. For the direction of the mean gradient we developed a new non-uniform grid discrete orthogonal function expansion which retains the efficiency of the fast Fourier transform but allows us to treat the region from minus infinity to plus infinity with very high accuracy. The time advance was done with the 4th order Runge-Kutta scheme.

PARAMETERS OF IMPORTANCE

We shall now define the dimensionless quantities represented in the figures and discussions.

1. $U(z,t) = \langle u \rangle / \Delta u$ — mean velocity, where $\langle\ \rangle$ indicates an average plane of constant z and Δu is the velocity difference across the layer.
2. $\theta(t) \equiv \int_{-\infty}^{\infty} [1/4 - U^2(z,t)]\, dz$; $\theta_0 = \theta(0)$ — Momentum thickness
3. $Z = z/\theta$ — Normalized vertical distance
4. $T = t\Delta u/\theta_0$ — Nondimensional time
5. $\Theta = \theta/\theta_0$ — Normalized momentum thickness
6. $u'_i = u_i - \langle u_i \rangle$ — i^{th} component of turbulent fluctuation
7. $k(Z,T) = \frac{1}{2} \langle u'_i u'_i \rangle / (\Delta u)^2$ — Turbulent kinetic energy
8. $B_{ij} \equiv \int_{-\infty}^{\infty} [\langle u'_i u'_j \rangle - \frac{1}{3} \langle u'_\ell u'_\ell \rangle \delta_{ij}]\, dz \Big/ \int_{-\infty}^{\infty} \langle u'_\ell u'_\ell \rangle dz$ — Integrated Reynolds stress anisotropy tensor
9. $K(Z,T) = k(Z,T)/k(0,T)$ — Turbulent kinetic energy distribution

The mixing layer is studied in the laboratory by independently controlling the speed of two parallel streams separated by a splitter plate. As Fig. 1 illustrates, the boundary layers merge as the splitter plate terminates to form a free-shear layer. The spatial development is characterized by a parameter,

$$\lambda \equiv \frac{u_1 - u_2}{u_1 + u_2}$$

As λ goes to zero, the spatial development becomes insignificant and the far field is essentially a time-developing mixing layer, as seen by an observer traveling at $(u_1+u_2)/2$. Unfortunately, the near field is dominated by the splitter plate wake for small λ. Though the spatial development is maximal for $\lambda = 1$, at least the near field has a single inflection point and probably behaves more like the early time-developing layer depicted in Fig. 2.

INITIAL AND BOUNDARY CONDITIONS

The boundary conditions used are the same in all cases and are periodicity in the streamwise and spanwise directions and no stress conditions at $z = \pm\infty$. The mean flow initial condition is an error function velocity profile and the mean flow Reynolds number based on the velocity difference across the layer and the momentum thickness is 12. The grid is proportioned such that 14 modes are amplified according to linear theory. Nine runs are studied in detail; there are 7 different initial conditions, 3 different amplitudes, 2 different spectrum shapes, 3 different sets of random phases. The filtered, homogeneous, isotropic turbulence spectrum of Comte-Bellot and Corrsin (1971) is the spectrum input to the initial disturbance field for all but Case 11. In Case 11, all the amplified and ten of the most slowly decaying computational modes (linear theory) have a non-zero initial amplitude. All other decaying computational modes (linear theory) have no initial amplitude. For further details of the initial conditions, see Cain et al. (1981).

Table 1 provides a more detailed characterization of the different cases.

*Department of Aerospace and Mechanical Engineering, University of Notre Dame, Notre Dame, IN 46556.
**Department of Mechanical Engineering, Stanford University.

Table 1

Descriptions of Cases Run

Case #	Amplitude	Random No. Set
2	High	1
4	Low	1
5	Medium	1
6	Low	2
7	Medium	2
8	High	2
9	Medium	1
10	Medium	1
11	Medium	3

Quantity	Descriptor	Significance
Amplitude:	Low:	$k(0,0) = 3.2 \times 10^{-6}$.
	Medium:	$k(0,0) = 3.2 \times 10^{-4}$.
	High:	$k(0,0) = 3.2 \times 10^{-2}$.
Random No. set 1,2,3.		

FILTERING AND SUBGRID SCALE MODELING

With the exception of Case 9, all cases are large eddy simulations (i.e., filtering was used). The filtering was done in planes of homogeneity (x,z) using a Gaussian convolution filter. In Case 9, no filtering was used in an attempt at a full simulation of the discrete Navier-Stokes equations.

No subgrid scale model was used in Cases 9, 10, and 11. All other cases employed a modified Smagorinski subgrid scale model.

The initial conditions of Cases 5, 9, and 10 are identical, allowing the influence of filtering and modeling to be determined.

RESULTS

Mean Velocity Profiles

In self-similar coordinates, the initial mean velocity profile persists in all cases until the numerics break down (after the layer has thickened by 8 to 10 times). Thus in the computation self-similarity in the mean velocity profile is achieved from the start, in contrast to the spatially-developed mixing layer studied in the laboratory, which does not have near-field similarity.

Momentum Thickness

Figure 3 shows the growth of momentum thickness for the five medium-amplitude cases (5, 7, 9, 10, 11). The most striking difference is Case 11 which grows 30 to 43 percent faster than the other cases. This is due to the initial disturbance spectrum being concentrated in the wavelengths most amplified (according to linear theory). This is in contrast to the other cases which have broader initial disturbance spectra. The experimental momentum-thickness growth rate $d\theta/dx$ is compared to the time growing layer using Taylor's hypothesis giving:

$$\beta \equiv \frac{1}{2\lambda}\frac{d\theta}{dx} = \frac{1}{\Delta u}\frac{d\theta}{dt}$$

Mansour, et. al. (1978; Table 1.1) examined the growth rates of many experiments and found asymptotic growth rates β ranging from 0.015 to 0.022. Winant and Browand's (1974) layer had an initial growth rate of 0.035 and an asymptotic rate of 0.019. The computational cases had early growth rates peaking as high as 0.048 with later declines to as low as 0.014. Hence, the computation is consistent with the experimental behavior.

Turbulent Kinetic Energy

Figure 4 shows the growth in the turbulent kinetic energy at the center of the layer for five medium amplitude initial disturbance fields. All cases show a similar early growth and all overshoot the expected far downstream values by roughly 50%; this is consistent with the experimental observations of Bradshaw (1966) for laminar boundary layer cases. Case 10 is identical to Case 5 except no model was used in Case 10. The high amplitude initial condition also overshoots the expected far downstream value as Fig. 5 shows. This result is not consistent with experiments in which the boundary layer(s) are turbulent. The discrepancy was initially believed to be due to the high obliqueness of boundary layer turbulence; however, data provided by Kim and Moin (1981) show that the most excited mode in boundary layer turbulence would be weakly amplified (linear theory) by a tanh mean velocity profile. Perhaps the amplification is too weak to result in an overshoot of turbulent kinetic energy. Alternatively, the large structures of boundary layer turbulence may not be amplified by the free-shear profile.

Some interesting oscillatory behavior is observed in the turbulent kinetic energy profile history, depending on the initial amplitude. Figure 6 shows the turbulent energy profile of Case 10, a case with a medium initial disturbance amplitude. Note that no attempt was made to make the initial profile at all realistic. The initial profile is much too broad and the early profile at $T = 66.67$ is characteristic of the eigenfunctions of the linearized equations and is narrower than the fully developed profile (Spencer 1971). The vortices for the last two times resemble Spencer's. Though not shown, the turbulent kinetic energy profiles for small amplitude cases are initially too broad; they then become narrow and again to broad before settling down to the proper asymptotic width (in z/θ) after the layer has thickned by 3.5 times. In contrast, the profiles for cases with high initial amplitude go monotonically to the asymptotic shape before the layer has even doubled in thickness.

The Anisotropy Tensor

Figures 7 and 8 show the behavior of the anisotropy tensor for medium amplitude Cases 5 and 7. These cases have the same initial energy spectrum and differ only in the random phases between Fourier modes. Yet the anisotropy tensors are radically different in the first 8-fold thickening of the layer. Thus, while Case 5 might be "fully developed" for $T \geq 200$, Case 7 is not even close to being fully developed at $T = 350$. The authors consider the anisotropy tensor an important measure of the

turbulent structure. Its sensitivity to initial conditions is a clear indication of the strong sensitivity of the structure to initial conditions, since Cases 5 and 7 differ only in their initial random phases.

A significant observation regarding the effect of initial disturbance amplitude on the anisotropy tensor is shown in Figs. 7, and 9. Cases 5, and 4 are identical in all aspects except the amplitude of the initial disturbance field; Case 5 is initially one hundred times as energetic as Case 4. Figure 9 shows the behavior of the anisotropy tensor for Case 4; note the strong early dominance of the streamwise component followed by a period of dominance by the gradient component. This is in contrast to the medium-amplitude case (5) of Fig. 7, in which the gradient component matches the streamwise component briefly, but never dominates. The high-amplitude Case 2 shows a dominance by the streamwise component at all but the earliest times. We thus conclude there is an increased likelihood of a period of dominance by the gradient component of the normal stresses with decreasing initial disturbance amplitude. Cases 6, 7, and 8 have the same trend, but it is not as strong.

Particle Track Pictures

We have tracked intersections of the grid shown in Fig. 10, initially placed in the plane of homogeneity at z = 0. This provides important insight into the processes of streamwise vortex formation in the mixing layer (Konrad 1976). Figures 11, 12, 14, 15 show the development in time for Case 6, a small initial disturbance case. Since the initial disturbance amplitude is small, the initially vertical lines in Fig. 10 are essentially vortex lines. Look at the distortion of the 3 left-most lines in the time sequence and a mechanism for the secondary instability of the mixing layer is suggested. The secondary instability is the array of counter rotating vortices, documented experimentally by Konrad (1976). These are aligned with the stretching direction of the primary straining field, which, in turn, is due to the dominant spanwise vortices; the spanwise vortices are a result of the Kelvin-Helmholtz instability. The mechanism for the secondary instability is due to spanwise irregularities in the stagnation line of the straining field. Figure 13 illustrates the proposed mechanism. Vortices A and B create the straining field shown by the arrows. In a view normal to the stretching plane, the stagnation line may be wavy, due to spanwise variations in strength or position of vortices A and B. This waviness in the stagnation line would result in a portion of the mean-field vorticity forming the secondary vortex structures. The present calculations suggest a secondary vortex circulation of between 12 and 50% of the primary vortex circulation. Figures 14 and 15 (spanview of 14) show the onset of a pairing which is essentially uniform along the span of the vortices. This is not quite as coherent as the pairing observed by Browand but more coherent than the "helical pairing" of Bradshaw. Figures 16 and 17 show Case 11, which is closer to the "Bradshaw helical pairing".

OTHER INFORMATION

For a complete report of this work, see Cain et al. (1981). Key points documented there include:

1) The subgrid scale model has hardly any effect on the results, while filtering has a major effect.

2) A new spectral method which uses the Fast Fourier transform has errors orders of magnitude smaller than the standard finite-difference methods.

3) Application of boundary conditions to a finite domain can strongly alter results.

CONCLUSIONS

The results of these computations show that the mixing layer's development can be strongly affected by the initial disturbance field. The mean velocity profile is not affected by the disturbance field in the time developing case but it may be in the spatially developing case in which the flow originates with boundary layer(s). The momentum thickness growth rate is strongly affected by the initial disturbance wavelengths. We observe an oscillatory approach (of the turbulent kinetic energy profile) to the fully developed profile if the initial disturbance energy is low and a monotonic approach if the initial disturbance amplitude is high. The anisotropy tensor is the most sensitive measure observed and may not reach fully developed values in a tenfold thickening of the mixing layer. Particle tracking has proved an excellent aid in understanding the physics and suggest the mechanism by which the secondary instability is created.

REFERENCES

Bradshaw, P. (1966), "The Effect of Initial Conditions on the Development of a Free Shear Layer," J. Fluid Mech., 26, Part 2, pp. 225-236.

Comte-Bellot, G., and Corrsin, S. (1971), "Simple Eulerian Time Correlation of Full- and Narrow-Band Signals in Grid-Generated Isotropic Turbulence," J. Fluid Mech., 48, Part 2, pp. 273-337.

Kim, J. (1981), private communication, Stanford Univ.

Konrad, J. H. (1976), "An Experimental Investigation of Mixing in Two-Dimensional Turbulent Shear Flows with Applications to Diffusion-Limited Chemical Reactions," Project SQUID, Tech. Rept. CIT-8-PU.

Mansour, N. N., Ferziger, J. H., and Reynolds, W. C. (1978), "Large-Eddy Simulation of a Turbulent Mixing Layer," Rept. TF-11, Mech. Engrg. Dept., Stanford University.

Spencer, B. W. (1970), "Statistical Investigation of Turbulent Velocity and Pressure Fields in a Two-Stream Mixing Layer," Ph.D. thesis, Nuclear Engrg. Program, University of Illinois, Urbana.

Winant, C. D., and Browand, F. K. (1974), "Vortex Pairing: the Mechanism of Turbulent Mixing-Layer Growth at Moderate Reynolds Number," J. Fluid Mech., Vol. 63, Part 2, pp. 237-255.

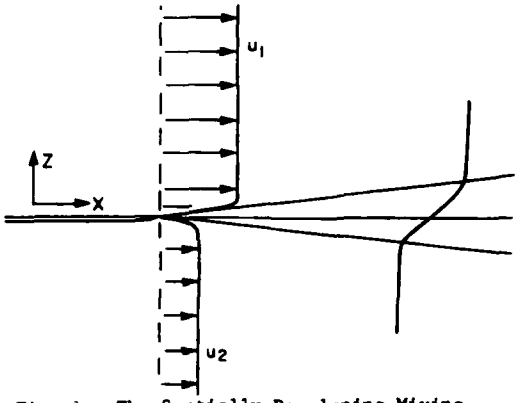

Fig. 1 The Spatially-Developing Mixing Layer as Created in the Laboratory

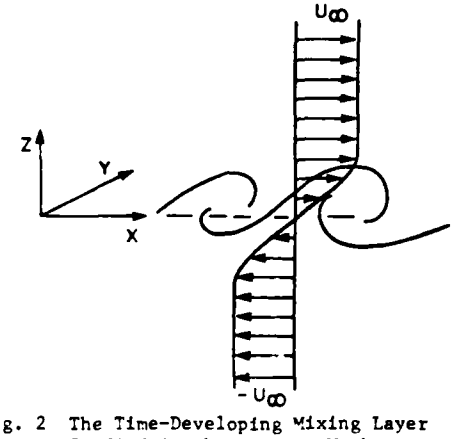

Fig. 2 The Time-Developing Mixing Layer Studied in the Present Work

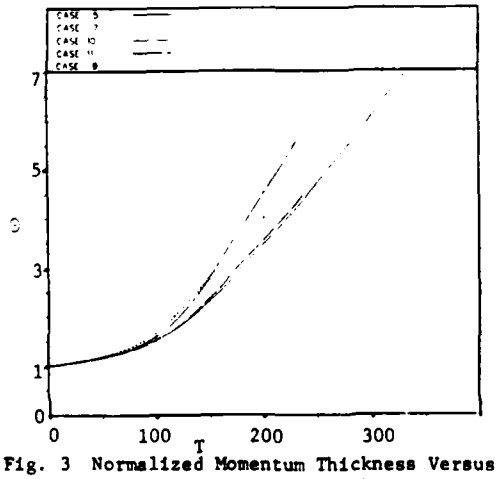

Fig. 3 Normalized Momentum Thickness Versus Dimensionless Time for the Medium Amplitude Cases

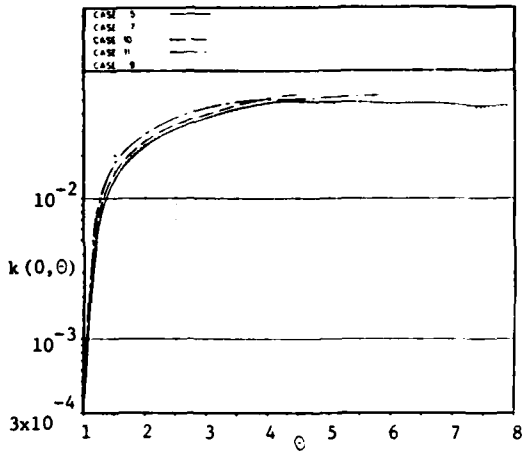

Fig. 4 Dimensionless Turbulent Kinetic Energy at the Center of the Layer Versus Normalized Momentum Thickness for the Medium Amplitude Cases.

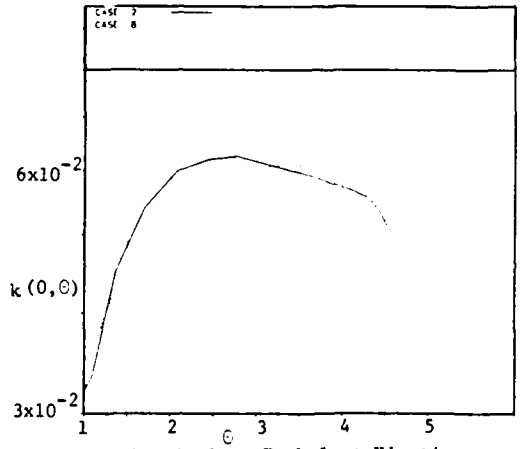

Fig. 5 Dimesionless Turbulent Kinetic Energy at the Center of the Layer Versus Normalized Momentum Thickness for the High Amplitude Cases

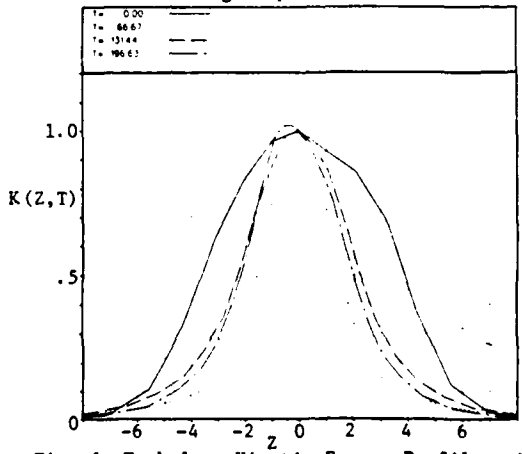

Fig. 6 Turbulent Kinetic Energy Profiles at Various Times for Case 10.

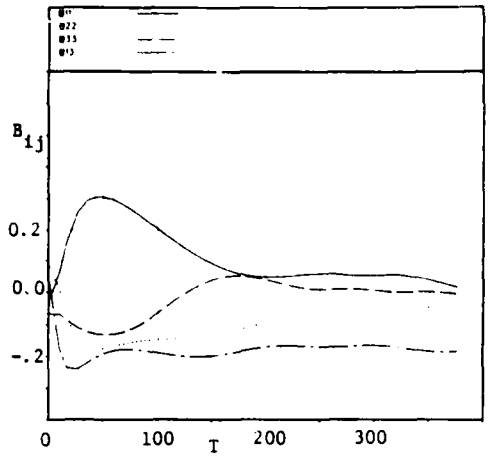

Fig. 7 Integrated Anisotropy Tensor Versus Dimensionless Time for Case 5

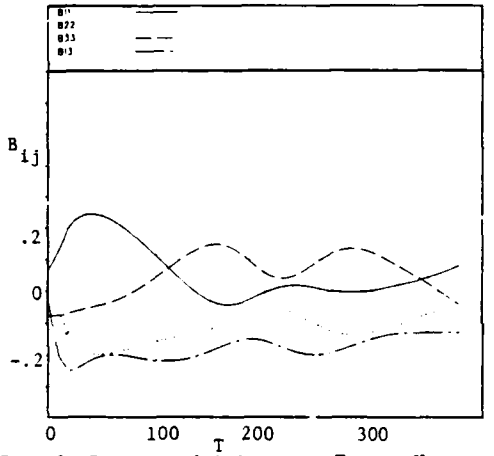

Fig. 8 Integrated Anisotropy Tensor Versus Dimensionless Time for Case 7

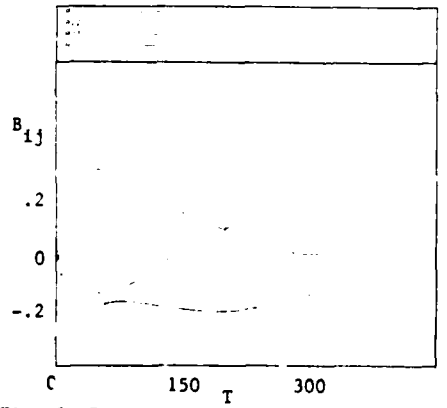

Fig. 9 Integrated Anisotropy Tensor Versus Dimensionless Time for Case 4

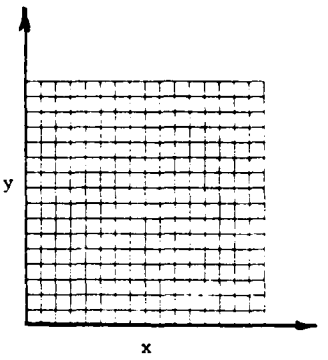

Fig. 10 Particle Tracking Grid; $\bar{z} = 0$, $T = 0$

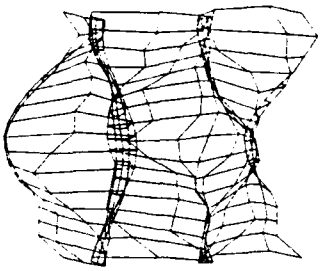

Fig. 11 Particle Tracking Grid at $T = 161$ for Case 6

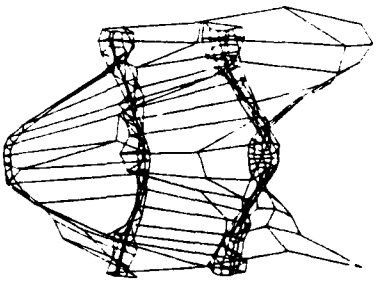

Fig. 12 Particle Tracking Grid at $T = 200$ for Case 6

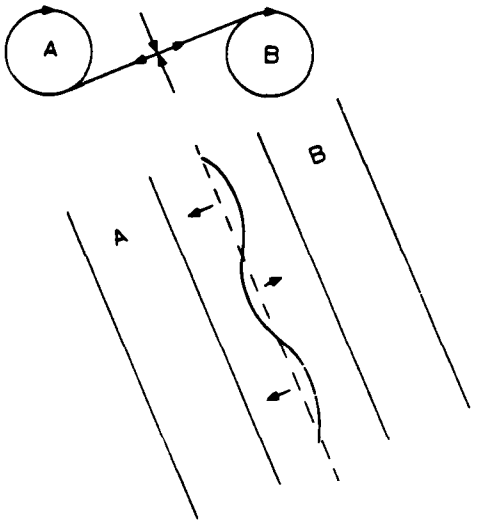

Fig. 13 Primary Straining Field With Schematic Diagram of Proposed Mechanism for the Secondary Instability

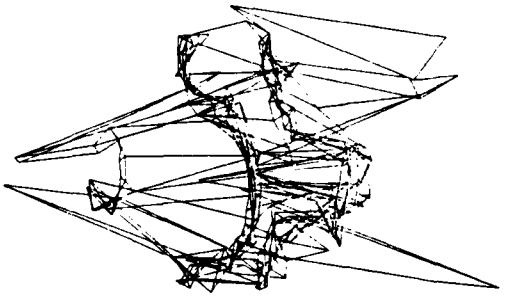

Fig. 14 Particle Tracking Grid at T = 342 for Case 6

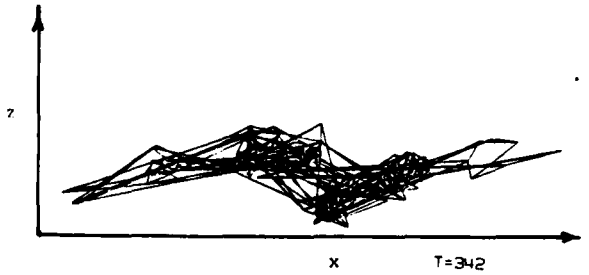

Fig. 15 Span View of Particle Tracking Grid at T = 342 for Case 6

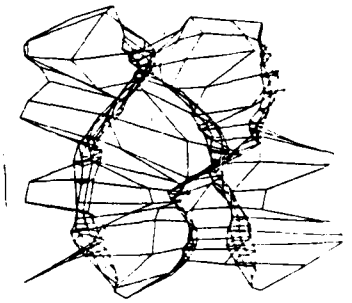

Fig. 16 Particle Tracking Grid at T = 97 for Case 11

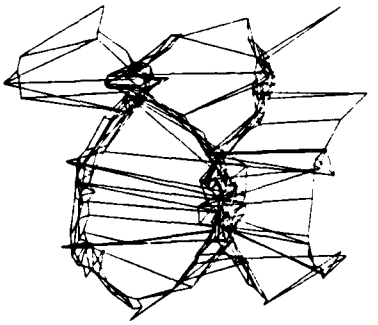

Fig. 17 Particle Tracking Grid at T = 151 for Case 11

SPATIAL GROWTH OF WAVY DISTURBANCES IN A PLANE SHEAR LAYER BETWEEN TWO STREAMS

B. V. Johnson
Fluid Dynamics Laboratory
United Technologies Research Center
E. Hartford, CT. 06108

J. D. Lin
Civil Engineering Department
University of Connecticut
Storrs, CT. 06268

ABSTRACT

An experimental study was conducted to determine the developing character of wavy disturbances put into shear layers between two constant velocity streams. The measured characteristics include the growth or decay rate of the disturbances and the distribution across the shear layer of the fluctuating streamwise velocity amplitude, the fluctuating cross-stream velocity amplitude, and their phase angles. These measurements were obtained for a variety of disturbance frequencies in a free shear layer with Reynolds numbers of the order 10^4. A companion analytical study of the stability of an inviscid shear layer was conducted to guide the experimental effort and to correlate the results. The analysis was conducted for both the experimentally determined velocity profiles and the previously-studied hyperbolic tangent profile. Good agreement was obtained between the results from the experiment and the inviscid stability analysis.

INTRODUCTION

Much of the current interest in fluid dynamic stability is generated by the need to predict when an unavoidable large-scale mixing situation will occur. These situations include the onset of clear air turbulence and mixing in some ocean circulation patterns. There is also a continuing need to develop improved stability analysis and engineering design criteria in technology areas such as aerodynamic noise reduction, jet mixing, boundary layer transition and heat transfer, and plasma containment for fusion nuclear reactions. The complete fluid dynamic stability problem for any of the previously mentioned areas is extraordinarily complicated. Each problem is three-dimensional, viscous, and often has boundary conditions that presently make a complete analytical solution of the steady-state flow field difficult, if not impossible, to obtain. Fortunately, many fluid dynamics problem areas have one or two factors which dominate the flow. Therefore, an understanding of the physical situation can be obtained from a simplified model or experiment. The approach that much can be learned from a simplified flow has been taken by most other fluid stability investigators and will be followed in this work.

The present study is directed toward understanding the development of two-dimensional wavy disturbances in plane shear layers. The study was further restricted to high Reynolds number shear layers with small-scale low-intensity turbulence in the shear layer at the onset of the disturbance location. This class of flows occurs in clear air turbulence and many propulsion applications.

Previous free shear layer experimental studies have been directed toward understanding the development of a shear layer with relatively low initial Reynolds numbers (e.g., Ref. 1). These shear layers have generally had rapid growth of natural occurring turbulent structure. One of the impetuses for the present work was the desire to determine the requirement for impeding or enhancing the development of the large-scale turbulent structure in a plane shear layer.

The objective of the present study was to determine the character of developing wavy disturbances put into the shear layer between two adjacent streams. This was achieved by (1) measuring the spatial growth rates and disturbance velocity profiles, and (2) numerically solving the linearized inviscid stability equation for the spatial growth rates and the disturbance velocity profiles of the measured mean velocity profiles.

EXPERIMENTAL EQUIPMENT

Flow System

A sketch of the flow system is shown in Fig. 1. The motor, fan, and plenum of the system were part of a conventional open circuit wind tunnel. The test section and hot wire probe traverse were also part of the same wind tunnel. However, the system differed from conventional open circuit wind tunnels in that porous media was used to restrict the flow into the test section in a prescribed manner. A porous media assembly consisting of open-pore polyurethane foam (manufactured by the Scott Foam Co.), perforated plate, and screens was assembled to provide the desired velocity ratio and initial shear layer thickness. Using porous media to generate a shear layer velocity profile allowed the instability

characteristics of a high Reynolds number, Re = $(U_1-U_2)\delta/\nu$, shear layer with a relatively low initial turbulence level to be studied in detail.

Disturbance Generator

Wavy disturbances were generated by vibrating a steel ribbon in the center of the shear layer. The ribbon, 1.0-in.-wide and 0.003-in.-thick, was stretched across the test section and held in tension with springs, as shown in Fig. 2. The spring tension was increased on the ribbon until the natural frequency of the vibrating ribbon was more than four times the highest frequency used for any flow disturbance condition. Stroboscopic illumination showed that the ribbon was vibrating in a uniform manner across the test section. For all flow conditions, except those where the disturbance frequency was approximately equal or greater than the neutral stability frequency, the peak-to-peak amplitude was less than 0.030 in.

Measuring Equipment

A 900 series hot wire anemometer manufactured by Datametrics was used for the experiments. The set consisted of two constant temperature anemometers with linearizers, a sum and difference circuit, and a true RMS voltmeter. Cross hot wires, constructed of platinum with a 0.0005-in.-diameter and 0.18-in.-length, were oriented at ±45 degrees to the mean flow direction. The X wires were oriented to measure the streamwise, U, and cross-stream, V, velocities in the plane of the two-dimensionality. A General Radio wave analyzer and a recording wave analyzer were used to measure the amplitude of the hot wire signals. The equipment was connected as shown in Fig. 3. The hot wire probe was held in place with an airfoil-shaped clamp. The clamp was attached to an electrically driven lead screw assembly and digital counter and the hot wire was traversed across the shear layer.

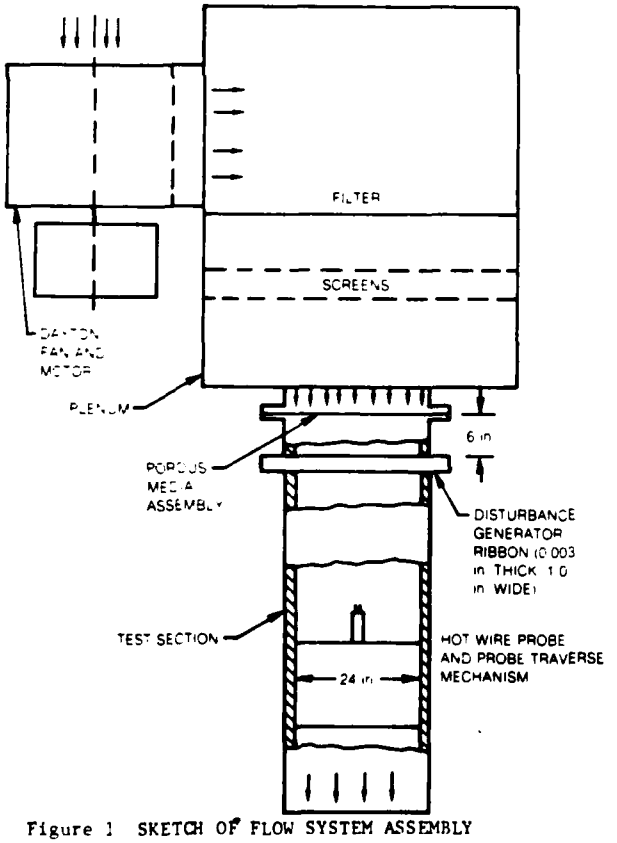

Figure 1 SKETCH OF FLOW SYSTEM ASSEMBLY

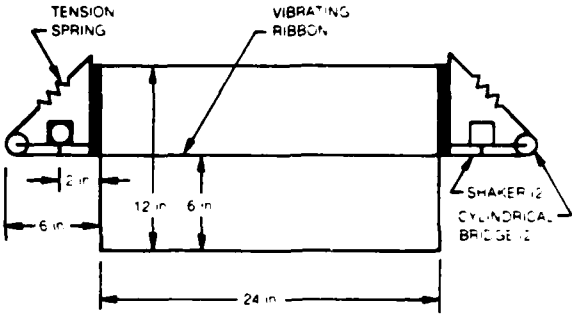

Figure 2 SKETCH OF UPSTREAM END OF TUNNEL SHOWING DISTURBANCE GENERATOR

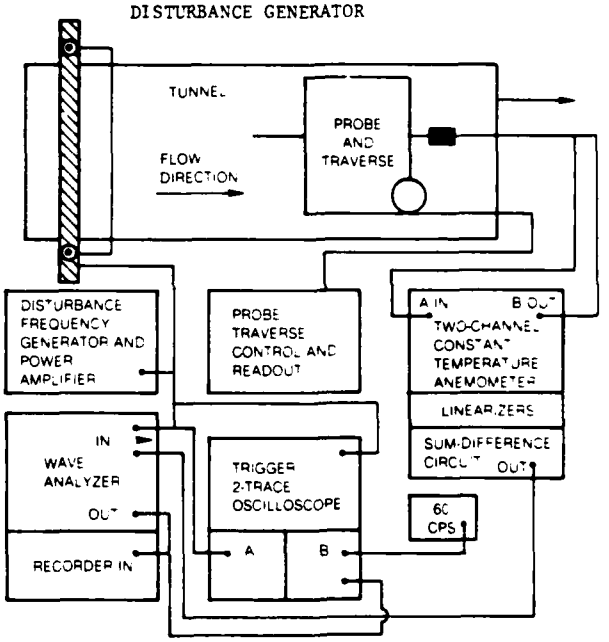

Figure 3 SCHEMATIC OF TEST APPARATUS FOR MEASURING DISTURBANCE CHARACTERISTICS

EXPERIMENTAL RESULTS

Undisturbed Flow

Mean and fluctuating streamwise velocity measurements were obtained (Figs. 4 and 5). The mean velocity profiles have the same approximate shape for a distance of 5 ft from the inlet. However, the turbulence intensity in the undisturbed flow varies in both the streamwise direction and across the shear layer. Note that the turbulence intensities outside the shear layer decrease at x = 3 and 5 ft to approximately one half their respective values at x = 1 ft. The turbulence intensities decrease from 2 to 1 per-

cent in the faster velocity stream; they decrease from 1 to ½ percent in the slower velocity stream. The peak turbulence levels in the undisturbed shear layer increases to 1.4 ft/sec in the shear layer which corresponds to turbulence intensities of 6 to 14 percent based on the local velocity and the shear layer velocity difference, respectively. The latter value is comparable with the turbulence levels in other undisturbed free shear layers.

A shear layer width was defined to compare the experimental results with previous analytical results and the present numerical results which will be discussed later. The growth of the shear layer half width, defined as $L = 0.5\ (U_1-U_2)/(\partial U/\partial y)_{max}$, is given in Fig. 6.

Velocity profiles were also obtained at five spanwise locations at x = 1 ft. The profiles for the three center and one of the end profiles were virtually identical. The largest variation from the centerspan near one wall of the tunnel was 1.8 ft/sec in the faster moving stream. The conclusion from these measurements was that the flow had a sufficiently large two-dimensional region to examine the growth of planar disturbances.

Disturbed Flow

Disturbances were put into the shear layer with various amplitudes and frequencies. Equipment limitations precluded exciting at frequencies less than 10 Hz. The upper limit of the frequency range was determined by increasing the excitation frequency until a frequency was reached where the input disturbance would not grow.

Streamwise and cross stream hot wire traces were obtained for a variety of flow conditions and excitation frequencies. Unfiltered traces were obtained from the hot wire anemometer system at five locations in the shear layer for $U_1/U_2 = 1.7$ and an excitation frequency of 40 Hz (Fig. 7). Voltage traces obtained

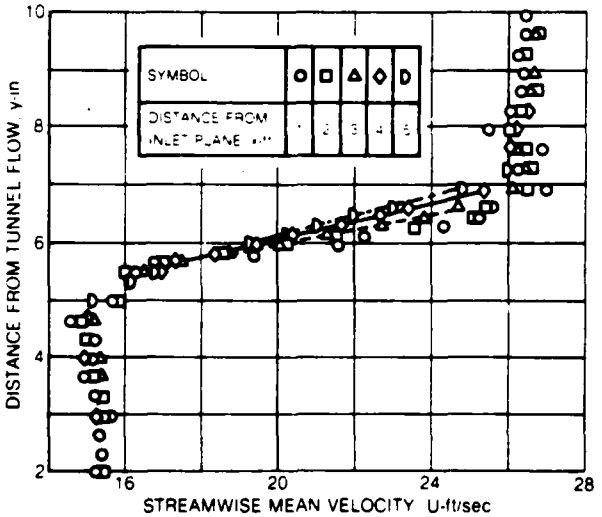

Figure 4 VELOCITY PROFILES FOR $U_1/U_2 = 1.7$ AT FIVE STREAMWISE LOCATIONS

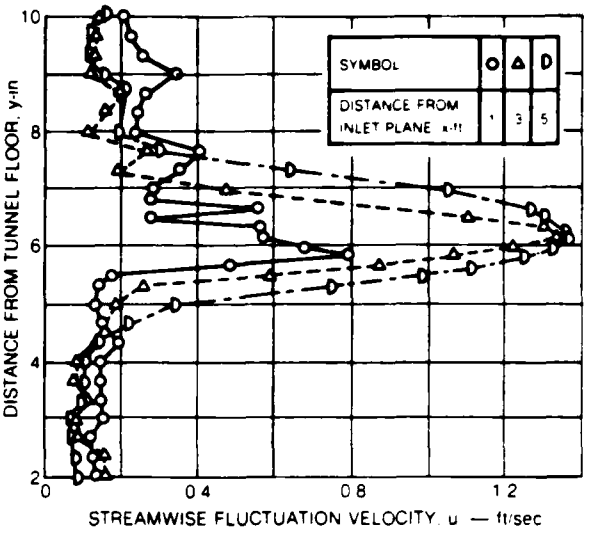

Figure 5 FLUCTUATION VELOCITY PROFILES FOR $U_1/U_2 = 1.7$

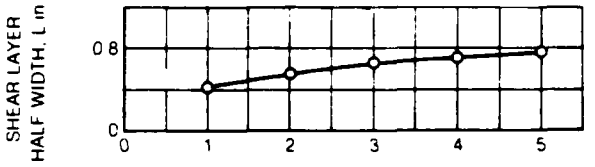

Figure 6 VARIATION OF SHEAR LAYER WIDTH WITH DISTANCE FROM INLET PLANE

during approximately ten cycles of the disturbance ribbon vibration are shown for each velocity component. Note that at the upper (y = 7.5 in.) and lower (y = 4.8 in.) edges of the shear layer both disturbance velocities of the 40 Hz disturbance frequency dominat the unsteady flow. Near the center of the shear layer (y = 6.2 and 6.8 in.) the 40 Hz u' component is less repeatable than the v' component.

Filtered signals from the wave analyzer were obtained (Fig. 8) and used to obtain the phase angles between the excitation signal and the streamwise and cross stream velocity components. This type of data was also used to obtain wave velocities. At y = 6.2 and 6.8 in., the filtered traces for the u' component shift in phase angle and amplitude. Note that cycle-to-cycle variation for the v' component generally vary less than 10 percent from the mean value and that little phase shift occurs.

The relative amplitude variation of the u' and v' signals across the shear layer were obtained by continuously traversing the hot wire probes across the shear layer and recording the wave analyzer output (Fig. 9). Note that the u' disturbances vary rapidly across the shear layer whereas the v' disturbances generally have a monotonic decrease from a peak near the center of the shear layer. The peak amplitude of the v' component was used to determine the disturbance growth rate.

Disturbance growth rates were obtained for a range of disturbance frequencies. Typical data are shown in Fig. 10 along with the experimentally determined spatial growth rate. The faired curves through the disturbance amplitudes were always started at least one wavelength downstream of the disturbance input location. The growth rate, α_i, is determined from a semi-logarithmic fit of the data. Note that for f = 20, 40 Hz and one disturbance amplitude at 60 Hz, the growth rates are positive. For the second input amplitude at f = 60 Hz, and for f = 70 Hz, the amplitude of the disturbance tends to decay. A summary of all the data obtained for the velocity ratio $U_1/U_2 = 1.7$ is presented in TABLE I. Most of the previously undefined parameters are defined in the table. Exceptions include: *, the experimentally determined disturbance wavelength, and Vp*, the experimentally determined phase velocity. The parameters α_r and α_i are the real and imaginary parts of the experimentally determined nondimensional wave number.

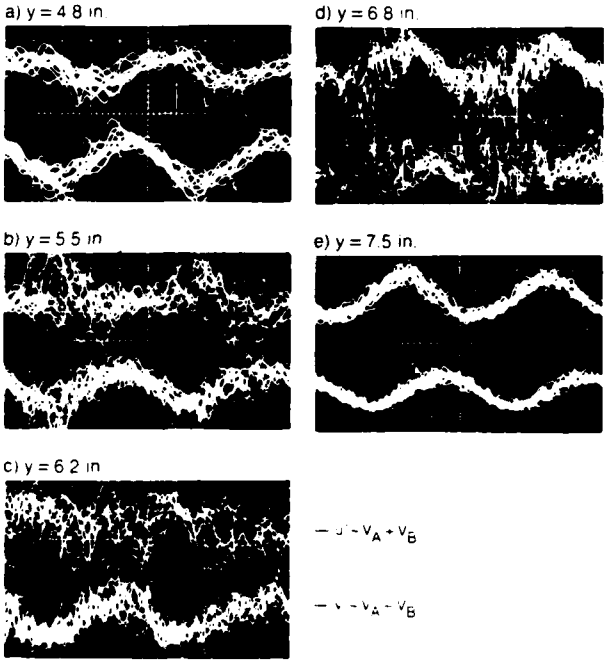

Figure 7 TYPICAL TRACES OF INSTANTANEOUS u' AND v' HOT WIRE SIGNALS OBTAINED AT VARIOUS LOCATIONS IN SHEAR LAYER AT x = 2.6 ft Ratio of u' to v' constant for each photograph; voltage level varied for each photograph; f=40 Hz

LINEAR STABILITY ANALYSIS

A linear inviscid stability analysis of planar shear flow was conducted for the experimentally determined velocity profile and for hyperbolic tangent velocity profiles with the velocity ratio $U_1/U_2 = 1.7$.

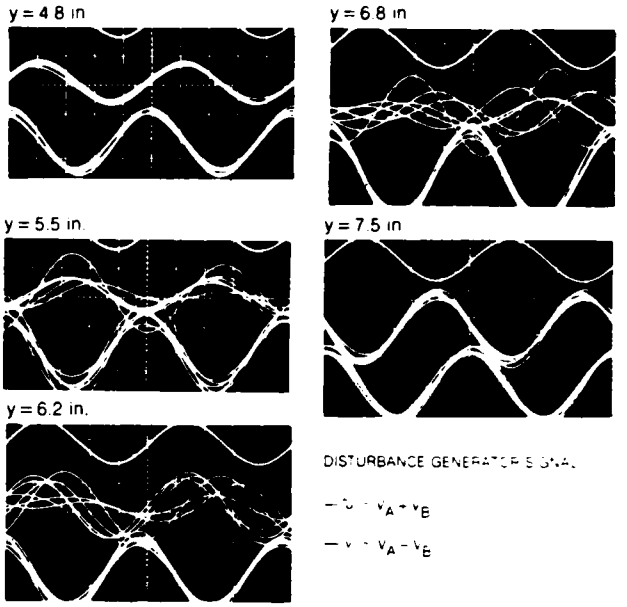

Figure 8 TYPICAL TRACES FROM WAVE ANALYZER OF INSTANTANEOUS u' AND v' HOT WIRE SIGNALS OBTAINED AT VARIOUS LOCATIONS IN SHEAR LAYER, f=40 Hz

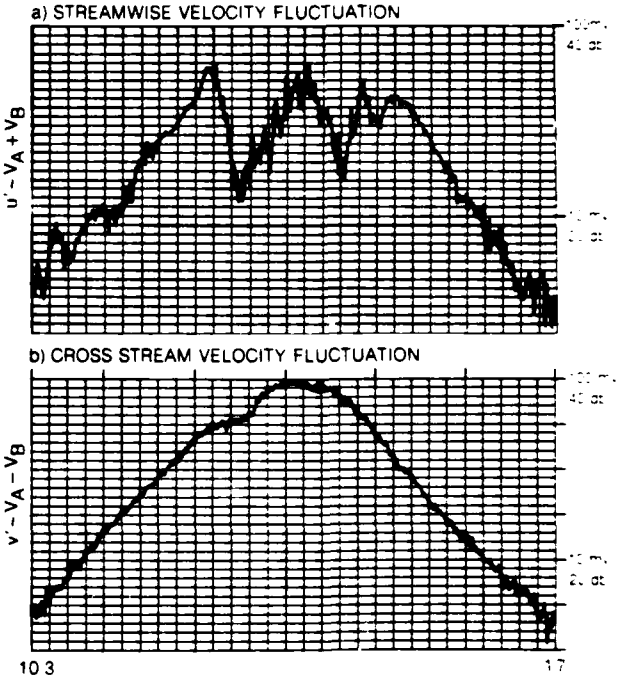

Figure 9 TYPICAL PROFILE OF u' AND v' AMPLITUDE ACROSS SHEAR LAYER FROM RECORDING WAVE ANALYZER, f=40 Hz

The inviscid stability analysis was based on the Rayleigh equation

$$v_1'' = (U''/(U-c) + \alpha^2)\, v_1 \qquad (1)$$

with the spatial growth constraint, $\beta_i = 0$ for disturbances of the form $v_1(y)\exp(i\alpha x - i\beta t)$ where $\alpha = \alpha_r + i\alpha_i$, $\beta = \beta_r + i\beta_i$, and $c = \beta/\alpha$. The velocity profile was nondimensionalized by L and $U_o = 0.5(U_1 - U_2)$ in the form $U = \phi + f(y/L)$ where $\phi = (U_1+U_2)/(U_1-U_2)$. The equation was numerically integrated between two boundary conditions outside the shear layer using the Runge-Kutta method.

Two types of boundary conditions were used for solution of Eq. (1). The first type of boundary condition used an asymmetric wavy disturbance below and above the shear layer of the form

$$v_1 \sim A_1 \exp(\alpha y) \text{ as } y \rightarrow -\infty \qquad (2)$$

and $$v_1 \sim A_2 \exp(-\alpha y) \text{ as } y \rightarrow +\infty$$

This results in the relationships

$$v_1'/(v_1) = 1 \text{ and } v_1'/(v_1) = -1 \qquad (3)$$

below and above the shear layer, respectively. This boundary condition was imposed 3 or 4 shear layer half widths (L) below and above the center of the shear layer. The second type of boundary condition was to set the normal component of the wavy disturbance to vanish on the walls of a planar duct, i.e.,

$$v_1 = 0 \text{ at } y = \pm d \qquad (4)$$

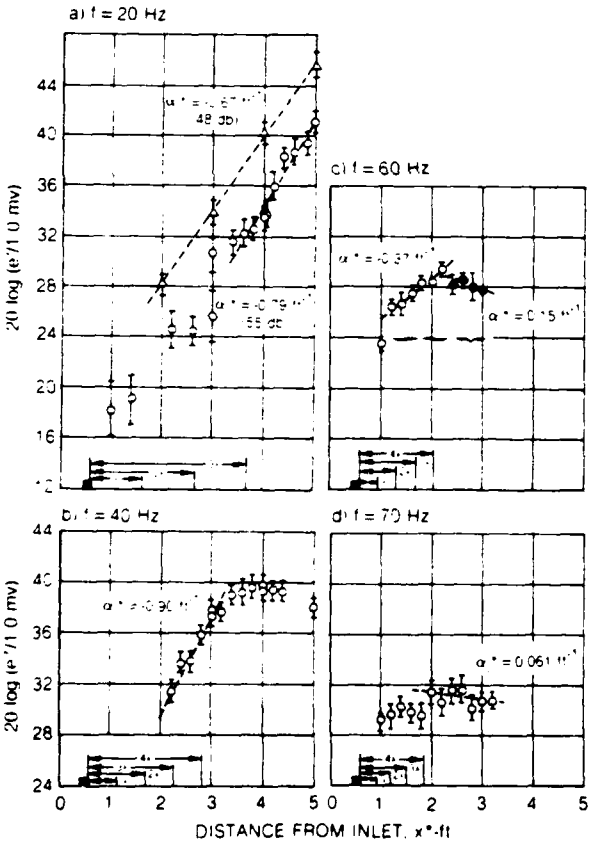

Figure 10 STREAMWISE VARIATION OF MAXIMUM v' AMPLITUDE IN SHEAR LAYER AT SEVERAL EXCITATION FREQUENCIES

f (Hz)	x ft	α_i^* (ft^{-1})	L (in.)	$\alpha_i = \alpha_i^* L$	$\beta_r = 2\pi fL/U_o$	λ^* (ft)
16.67	4.8	-0.95	0.75	-0.059	1.19	
20	3.5	-0.67	0.69	-0.039	1.31	1.036
20	4.0	-0.79	0.71	-0.047	1.35	1.036
30	2.0	-1.38	0.56	-0.064	1.50	0.707
30	2.8	-0.94	0.62	-0.049	1.77	0.707
30	3.3	-0.77	0.68	-0.044	1.94	0.707
40	2.6	-0.91	0.62	-0.047	2.36	0.554
50	1.8	-0.58	0.54	-0.026	2.87	0.437
60	1.5	-0.37	0.50	-0.015	2.36	0.365
60	2.7	+0.15	0.64	+0.008	3.66	0.365
70	2.5	+0.061	0.62	+0.003	4.13	0.309

TABLE I SUMMARY OF EXPERIMENTAL RESULTS FOR FLOW CONDITION $U_1/U_2 = 1.7$ WITH EXCITATION $U_1 = 26.4$ ft/sec; $U_2 = 15.4$ ft/sec; $U_o = (U_1-U_2)/2 = 5.5$ ft/sec

Calculations were made for the hyperbolic tangent velocity profile in a free shear layer with the asymmetric boundary condition and compared with Michalke's results (Ref. 2). The nondimensional profile for this case is $U = 1+\tanh(y/L)$ and corresponds to a plane jet discharging into quiescent fluid. The numerical results from the present calculation procedure agreed with the Michalke results to the third decimal value. Calculations were also made for a shear layer between two walls with the wall spacing, $d = 9L$. Imposing the $v_1 = 0$ boundary condition at these locations caused the disturbance spatial growth rate to decrease approximately 10 and 1 percent for $\beta_r = 0.1$ and 0.2, respectively. The conclusion from these calculations was that for $\beta_r \geq 0.2$, the growth of wavy disturbances in the present experiment was equivalent to the growth in a free shear layer. The locations $d = \pm 9$ were equivalent to the distance of the walls from the center of the shear layer in the present experiment. Therefore, all the calculations described in the subsequent section were made with the asymmetric boundary conditions (Eq. (2)) rather than the wall boundary condition (Eq. (4)).

COMPARISON OF EXPERIMENTAL AND ANALYTICAL RESULTS

The variation of the spatial growth rate with reduced frequency is presented in Fig. 11. The experimental growth rates were obtained for a range of initial disturbance amplitudes. The solid line in Fig. 11 is the analytically determined spatial growth rate for the curve-fitted profile of the velocity measurements in Fig. 4 at x = 3 ft. The dashed line is the analytically determined spatial growth rate for the hyperbolic tangent velocity profile with the respective maximum shear rate

and velocity differences. The data for $U_1/U_2 = 1.7$ are in good agreement with the analytical results for the curve fitted profile. Note that the largest differences between the analytical results for the tanh profile and the curve fitted profile occur as the growth rates decrease toward zero.

The measured nondimensional wave velocities are also compared with the mean shear layer velocities (Fig. 12). The wave velocity is close to that predicted for $\alpha_r \sim 0.4$ but greater at $\alpha_r \sim 0.8$ (the neutral stability value).

A comparison of the experimental and analytical disturbance velocities and phase angles are presented in Figs. 13 and 14 for f = 20, 30, and 40 Hz and $U_1/U_2 = 1.7$. The experimental and analytical disturbance velocities are normalized with respect to the peak cross stream velocity, v', in each profile. For the 20 Hz excitation, the v' profile has the correct shape but an amplitude variation of the order of 10 percent from the predicted profile. The u' profile has the peaks and valleys of the profiles at the cross stream locations predicted but has smaller variations from the mean. For this excitation frequency, the shape of the profile does not have a significant effect on the theoretical shape or relative amplitudes of either the v' or u' disturbance velocity profiles. Matching the asymptotic shape of the v' profile rather than the peak value may have resulted in improved experimental/analytical profile comparisons for this profile. The predicted phase angles are in fair agreement with measured values. These phase angles were graphically determined from oscilloscope photographs similar to those in Fig. 8.

The experimental disturbance velocity profiles for f = 30 Hz have peaks and valleys at the relative locations predicted for this frequency. The shapes of the u' disturbance profiles are a stronger function of the velocity profile than those for f = 20 Hz. The general character of the phase locations are predicted; however, the details of the phase angle shift are significantly different and may be caused by nonparallel or other effects.

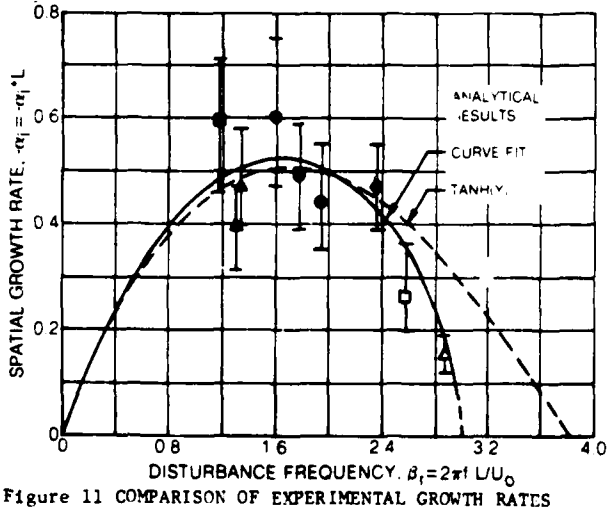

Figure 11 COMPARISON OF EXPERIMENTAL GROWTH RATES WITH ANALYTICAL RESULTS FOR EXPERIMENTAL DATA CURVE FIT AND TANH(Y) VELOCITY PROFILES

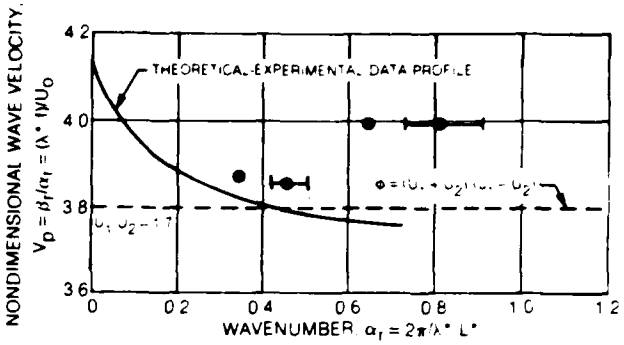

Figure 12 COMPARISON OF EXPERIMENTAL WAVE VELOCITIES WITH ANALYTICAL RESULTS

The analytical disturbance velocities for f = 40 Hz predict the v' disturbance with the same accuracy as the cases for f = 20 and 30 Hz. The u' analytical disturbance profiles also predict the correct relative magnitude of disturbances; however, the detailed relationships vary. Note the significant difference in the predicted phase angles for the tanh and curve fitted profiles for f = 40 Hz. The phase angles for the curve fitted profiles are in good agreement with the data above and below the shear layer, while the measured and predicted phase angles differ considerably near the center of the shear layer. Recall from Fig. 8 that the phase angles varied significantly from cycle-to-cycle in this region. The cycle-to-cycle variation (or nonstationary effect) may also cause some of the differences between the measured and predicted disturbance u' velocity profile for f = 20, 30, and 40 Hz.

Although the exact details of the u' disturbance velocity profile were not predicted, the analysis did predict the major changes in the profile shape over the range investigated. Examination of the filtered and unfiltered hot wire signals (Figs. 7 and 8) for these velocity profiles indicate that nonlinear effects probably were not important. However, the analytical results were obtained here on the basis of parallel flow theory and further examination of Fig. 6 shows that the rapid growth of the shear layer warrants inclusion of nonparallel effects in the analysis.

CONCLUSION

The experimental study showed that, when a high Reynolds number plane shear layer is excited with two-dimensional disturbances, the disturbances will grow with a spatial growth rate and contain the disturbance velocity distributions and phase relationships generally predicted by two-dimensional inviscid stability theory.

REFERENCES

1. Freymuth, L.: On Transition in a Separated Laminar Boundary Layer. J. of Fluid Mech., Vol. 25, Part 4, 1966, pp 683-704.

2. Michalke, A.: On the Spatially Growing Disturbances in an Inviscid Shear Layer. J. of Fluid Mech., Vol. 23, 1965, pp 521-544.

ACKNOWLEDGMENTS

This research was conducted at the University of Connecticut. Financial support for the first author was provided by United Technologies Corporation under a graduate fellowship. Experimental equipment was provided by the Civil Engineering Department of the University. The computer work performed at the University's Computer Center was supported in part by Grant GP-1819 of the National Science Foundation.

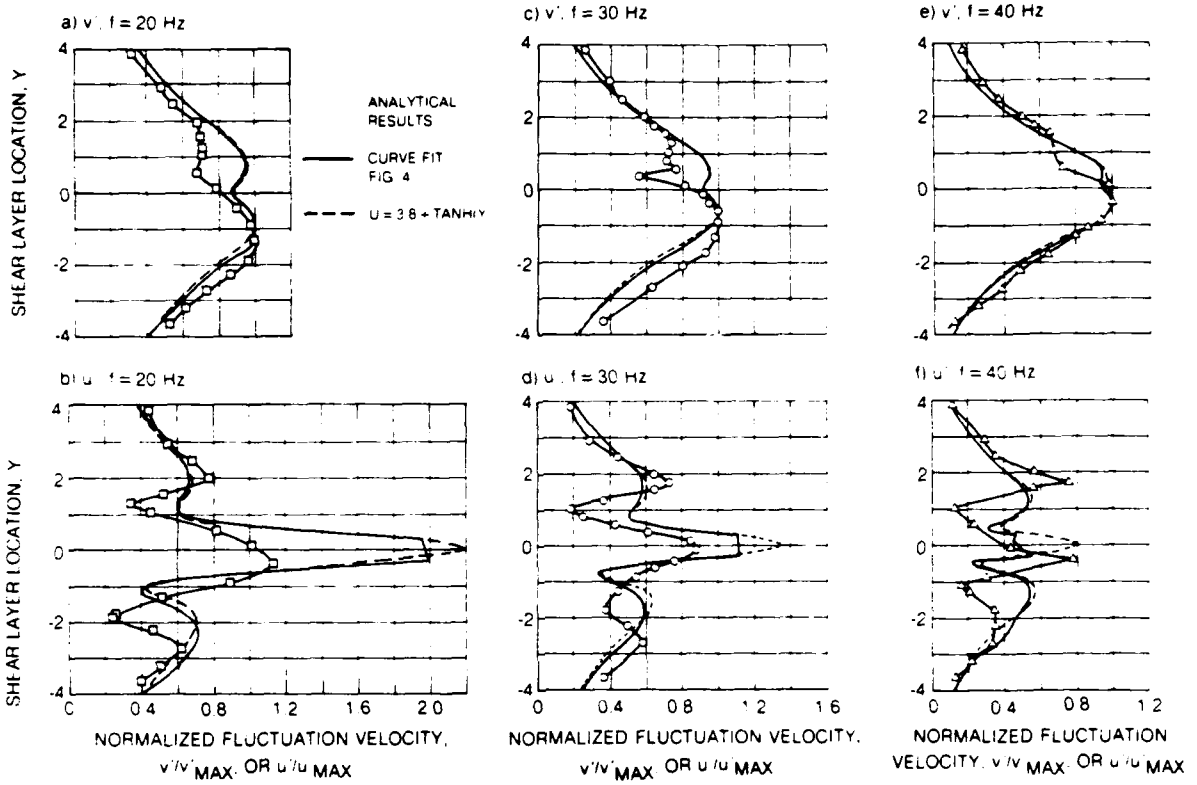

Figure 13 COMPARISON OF v' AND u' AMPLITUDE PROFILES ACROSS SHEAR LAYER WITH ANALYTICAL RESULTS

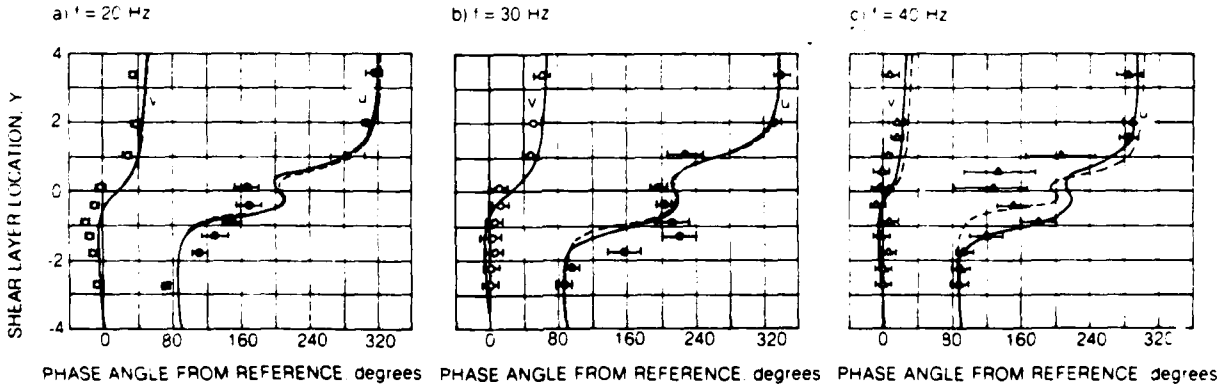

Figure 14 COMPARISON OF v' AND u' PHASE ANGLE PROFILES ACROSS SHEAR LAYER WITH ANALYTICAL RESULTS

SESSION 15 - SCALAR TRANSPORT

R. J. Adrian - Chairman

Further Results on the Thermal Mixing Layer Downstream of a Turbulence Grid

John C. LaRue
Mechanical Engineering
University of California, Irvine
Irvine, California 92717

and

Paul A. Libby and D. V. R. Seshadri[1]
Department of Applied Mechanics and Engineering Sciences
University of California, San Diego
La Jolla, California 92093

ABSTRACT

Simultaneous velocity and temperature measurements in the thermal mixing layer downstream of a partially heated turbulence grid are reported. The temperature data are in good agreement with earlier results. The velocity-temperature correlations are new and permit a systematic assessment of an earlier similarity theory for the region far downstream of the grid. By selecting the virtual origin appropriately and by reconsidering the role of scalar dissipation in that region, agreement between measurement and prediction with respect to temperature intensity and two mean lateral fluxes, that of temperature and of temperature intensity, is achieved.

NOMENCLATURE

D	thermal diffusion coefficient
E_ω	power spectral density of temperature fluctuations
f_c	Kolmogoroff frequency
I_1	nondimensional, asymptotic intensity of temperature fluctuations, $\overline{T'^2}/\bar{T}_\infty^2$
l_c	Kolmogoroff length
M	mesh length of grid
R_M	Reynolds number, UM/ν
T	temperature
u, v	velocity components in the x- and y-directions
U	mean flow velocity
x	spatial coordinate measured from the grid
x_o	location of virtual origin measured from grid
$\bar{x}$	nondimensional coordinate measured from virtual origin, $(x-x_o)/M$
y	spatial coordinate measured from the centerline of the mixing layer
$\bar{y}$	nondimensional transverse coordinate, y/M

Greek

β	empirical constant in model for scalar dissipation
η	similarity variable, $\xi R_M^{1/2}$
ν	kinematic viscosity
ν_t	effective turbulent exchange coefficient
ξ	similarity variable, $\bar{y}\bar{x}^{-1/2}$
χ_θ	scalar dissipation

Subscripts

∞	conditions in fully-heated stream

INTRODUCTION

From a fundamental point of view one of the most interesting turbulent flows involving the transport of a passive scalar is the thermal mixing layer downstream of a turbulence grid which has an appropriate number of its elements heated, e.g., the horizontal rods in the upper half of the tunnel. There result two streams, one fully heated so that it has a uniform mean temperature $\bar{T}_\infty$ and a second unheated so that its temperature may be considered zero. The statistical properties of the temperature in the mixing layer between these two streams vary in both the streamwise and transverse directions while those of the velocity correspond to the usual grid flow and thus vary only in the streamwise direction. The purpose of the present study is to provide data on both the temperature and velocity in this flow and to compare the experimental results with a similarity solution for the thermal mixing layer.

The layer in question has been the subject of several investigations. The earliest experiments are due to Watt and Baines (1) and

[1]The authors are listed in alphabetical order.

Foss *et al.* (2) who measured the mean temperature and the temperature intensity. The former authors deduce that the measured distribution of mean temperature is consistent with a constant thermal diffusivity. In a theoretical analysis of the thermal mixing layer based on the data of Foss *et al.* (2) Libby (3) reaches a similar conclusion by applying the Prandtl-Kolmogoroff model of turbulent transport. Keffer *et al.* (4) use an array of horizontal rods and study the mixing layer which results from heating only those in the upper half of the tunnel. They employ the techniques of conditioned sampling to obtain zone averages for the mean temperature and for the intensity of the temperature fluctuations. Finally, LaRue and Libby (5) provide additional data on the temperature characteristics including probability density functions of the temperature at various locations in the mixing layer and statistical information on the thickness of the superlayer between heated and unheated fluid.

The distributions of mean temperature obtained by the several investigators are in excellent agreement. Such distributions are usually given in terms of a similarity variable $\xi = \bar{y}\,\bar{x}^{-1/2}$ where $\bar{x}$ and $\bar{y}$ are the usual Cartesian coordinates nondimensionalized with respect to the mesh size of the grid denoted M and where $\bar{x}$ is measured from a virtual origin determined experimentally from one or more characteristics of the flow. We show that the conclusions drawn from similarity forms of the statistical characteristics of the flow are in some cases sensitive to the selection of this origin.

The distributions of the intensity of the temperature fluctuations obtained in the various studies cited earlier are usually given in terms of $(\overline{T^2})^{1/2}\,\bar{T}_\infty$ and are somewhat more interesting. All experiments indicate that the peak intensity occurs in the middle of the mixing layer and is essentially constant in the streamwise direction despite the decay of the temperature intensity in the fully heated stream. The data of Foss *et al.* (2) and of LaRue and Libby (5) are in excellent agreement with respect to this peak value while that given by Keffer *et al.* (4) is 25% lower due perhaps to the different configuration of rods used in their study. The value of the peak temperature intensity predicted by the simple gradient transport theory of Libby (3) is 40% higher than that given experimentally by Foss *et al.* (2) and by LaRue and Libby (5) The latter discuss in some detail the possible sources of this discrepancy without resolving the issue. In fact the present study is largely motivated by interest in this discrepancy and by the need for data on both the temperature and velocity characteristics for its resolution. Accordingly, measurements of two velocity components, u and v in the usual notation, and of the temperature T measured relative to the temperature in the unheated stream are made at various locations in the thermal mixing layer downstream of a turbulence grid with half of its horizontal elements heated electrically.

Two sets of measurements are made; in one set the horizontal rods in the upper half of the grid are heated while in the second those in the lower half are heated. We find that within the scatter of the data the results from the two sets are the same and thus that, as estimated by Keffer, buoyancy does not play a significant role in the thermal mixing layer.

ARRANGEMENT AND TECHNIQUES OF THE EXPERIMENT

In this section we discuss the triple sensor probe, the experimental set-up and data collection techniques used in this study.

Calibration of the Probe

A triple sensor probe consisting of two hot-wires in a X-configuration and a cold-wire is used to measure two velocity components u and v and the temperature T. The two hot-wires are approximately mutually perpendicular, are nearly symmetrically oriented relative to the mean streamwise flow, and are placed in a vertical, i.e., x-y, plane. The cold-wire is mounted 0.2 mm upstream of the midpoint of the X-wires and is aligned in the z-direction. The hot-wires are made from tungsten of 2.54 μm diameter approximately 0.51 mm long. The cold-wire is platinum with a diameter of 0.625 μm and a length of 0.5 mm. A heating current of 180 μa is passed through the cold-wire.

The probe is calibrated directly for velocities, temperatures and flow angles from 4 to 11 m/sec, 19 to 31°C and ± 5 degrees respectively. These ranges are adequate to cover all turbulent data obtained from the mixing layer. Calibration is performed both before and after the two sets of measurements are made. The inversion scheme is based on King's law for the hot-wires and on a linear equation between voltage and temperature for the cold-wire.

Spatial Resolution and Frequency Response

The spatial resolution of the triple sensor is estimated to be 0.5 mm while the Kolmogoroff length, l_k, is estimated to vary between 0.25 and 0.49 mm. Therefore, the Kolmogoroff length is at most one-half the characteristic length scale of the sensor. This resolution is adequate for the present results.

The frequency response of the two hot wires and of the cold wire is estimated to be 22 kHz and 3 kHz respectively. The effective digitizing frequency for the signals from the three sensors and their derivatives is 7400 Hz. From an estimate of the Kolmogoroff frequency, f_K, we conclude that our digitizing frequency is 1.45 to 2.84 f_k and is thus adequate.

General Description of the Flow

The measurements are carried out in a low-speed, low-turbulence wind tunnel having a 76 cm × 76 cm cross-section. The turbulence grid consists of eighteen horizontal and eighteen vertical rods 0.665 cm in diameter with a mesh size, $M = 4$ cm. The tunnel and grid are described in detail by Va: Atta and Yeh (7) and Sepri (8). In the separate sets of measurements, nine of the horizontal rods are heated electrically. Each rod consumes 1 kW of power and is heated to about 200°C above ambient. There results a mean temperature $\bar{T}_\infty$ in the fully heated stream of 3.21 ± 0.06°K.

The tunnel is operated in an open circuit mode by installing a flow deflector downstream of the test section. The mean velocity, U, of 7.8 m/sec is monitored by a pressure transducer connected to a Pitot static tube mounted in the unheated stream. The temperature in the unheated stream is measured by a platinum resistance thermometer placed alongside of the Pitot static tube. This temperature is found to be constant to within $\pm 5 \times 10^{-2}$°C during periods of data collection.

The apparent freestream variations (rms) of velocity and temperature in the wind tunnel without the grid in place are found to be 0.01 m/s for u and 0.01°C for T. These apparent intensities are due both to electronic noise and to residual fluctuations in the tunnel

Probe Positioning

The three sensor probe is mounted on a motorized support. A counter provides an output establishing the probe location in the vertical, i.e., y-direction relative to a reference height determined manually from the tunnel floor. The accuracy of our y-coordinates is ± 0.5 mm.

During a data collection period the probe is traversed downward in steps of one cm and held fixed at each position while data is recorded for one minute. After a complete pass through the mixing layer, the probe and probe support are manually moved to the next streamwise station and the procedure repeated.

Data are collected at four x-stations for the first set of measurements, namely at 21, 36, 51 and 67 mesh heights downstream of the grid. For the second set data are collected only at the first three of these stations.

Data Collection and Reduction

We record the following voltages: Those from each of the three sensor circuits and their time derivatives obtained by analog differentiation; the voltage yielding the temperature in the unheated stream; the output from the Pitot static tube determining the mean velocity; and the voltage from the counter related to the probe position. Voltages are stored on tape by means of a FM tape recorder at a tape speed of 38.1 cm/sec corresponding to a maximum recording frequency of 5 kHz.

After being low-pass filtered at 1830 Hz, the voltages on the six channels corresponding to the output from the three sensors and their derivatives are digitized at a rate of 3700 samples/sec/channel and at a playback tape speed of 19.05 cm/sec. There results an effective sampling rate of 7400 samples/sec/channel. As a result of the various steps from recording to digitization the real time increment between samples is 135.1 μsec. At each probe position one hundred records consisting of 1024 samples are digitized so that the results correspond to 13.8 seconds of data and to about one hundred thousand samples. The various time series which result are analyzed on a CDC 3600 computer using standard software.

EXPERIMENTAL RESULTS

The results of the two sets of measurements are identified with the acronyms THG and BHG for top and bottom heated rods respectively. We discuss first the temperature data and then those involving the velocity components.

Virtual Origin

It is convenient to present the data in terms of the similarity variable $\xi = \bar{y}/\bar{x}^{1/2}$. We take the origin of the $\bar{y}$-coordinate to be the point where $\bar{T} = (1/2)\bar{T}_\infty$. The streamwise variation of this origin relative to the tunnel floor is negligible, being less than ± 1.13cm. As indicated earlier the $\bar{x}$-coordinate is defined as $\bar{x} = (x - x_o)/M$ where x_o is the location of the virtual origin measured from the grid. Although x_o can be obtained in a variety of ways, we first follow standard practice relative to grid flows, adopt an idealized rate of decay of the temperature intensity in the fully-heated stream and use our data relative to that intensity to obtain a virtual origin.

The seven data points obtained from the two sets of measurements yield the value $x_o = 6M$. This value is consistent with that found by Van Atta and Yeh (7) and Sepri (8) in experiments involving the same grid, fully-heated, but is not in agreement with the value of $x_o = -9.8M$ found by LaRue and Libby (5) This discrepancy is indicative of the difficulties of determining virtual origins on the basis of the limited data usually available. We note that such discrepancies suitably are not significant if measurements are made at stations which are far downstream. Moreover, they do not appear to be significant relative to comparison among the various sets of experimental results for the thermal mixing layer provided x_o is determined in a consistent fashion. Thus we use the value $x_o = 6M$ determined conventionally to present our data and to compare them with previous results and with the predictions of similarity theory. We then show that an alternative determination of the virtual origin changes sufficiently the display of data to yield reasonable agreement with theory.

Mean Temperature

Figure 1 shows the mean temperature distribution obtained from both the present and previous experiments. We retain the virtual origin of 12M used by Libby (3) for displaying the data of Foss *et al.* (2) and make no correction to the x-values given by Keffer *et al.* (4) We see that all sets of data agree remarkably well with each other. We defer discussion of the prediction of the mean temperature profile but it is clear that an error function distribution as predicted by the simple theory of Libby (3) adequately describes these results provided that the Reynolds number UM/ν, arising in the theory and determining the thermal diffusivity ν, is appropriately chosen.

Temperature Intensity. A similar comparison is shown in Fig. 2 where the distributions of the temperature intensity in the form $\overline{T^2}^{1/2}/\bar{T}_\infty$ given by the four sets of data are shown. We observe that the results of the present study agree very well with those of Foss *et al.* (2) and LaRue and Libby (5) but that there is a discrepancy with the data of Keffer *et al.* (4) as mentioned earlier. It is also to be noted that the intensity predicted by Libby (3) is considerably greater than all the experimental data. We discuss later the reasons for this discrepancy.

The intensity profiles are not strictly similar. This is most obvious in the fully-heated side of the mixing layer. Theory suggests that the temperature intensity in this flow involves two separate components, one representing a simple diffusion of temperature intensity across the mixing layer and thus decreasing in importance with the downstream distance and a second representing production of fluctuations by the mean temperature gradient and thus constant. It is important to note that all the experimental results on the thermal mixing layer, both the earlier and present results, relate to the far downstream region where the first component is significant only near the fully heated stream. Thus in comparing measurement and prediction based on the similarity solution we consider only the second component.

Higher Moments of Temperature Fluctuations

We have analyzed our temperature data to determine the skewness and the kurtosis of the temperature fluctuations. The results are essentially the same as those presented in LaRue and Libby (5) and need not be repeated here. In fact the agreement between the two sets of data is remarkably good. In this regard it is worth noting that there is no significant difference even for these higher moments in

the data obtained with the horizontal rods in the upper half of the tunnel heated and with those in the lower half heated. Thus buoyancy is ineffective and temperature is truly passive.

With respect to the higher moments we note that we have calculated and plotted the probability density functions of the temperature for all of the probe locations. They are fully consistent with the results given in LaRue and Libby (5) and are thus not presented here.

Temperature Dissipation

In Fig. 3 we show the distribution of the nondimensional parameter involving the temperature dissipation, namely $\chi_w \bar{x} M / U \overline{T^2}$, as obtained in the present study and as given by LaRue and Libby (5). In accord with standard practice the dissipation is determined using Taylor's hypothesis and the assumption of local isotropy of the small scales so that

$$\chi_w = \frac{6D}{U^2} \overline{\left[\frac{\partial T}{\partial t} \right]^2} \tag{1}$$

We have checked the accuracy of our determination of χ_w by comparing values of the integral $\int_0^{f_{max}} (2\pi f)^2 E_w(f) df$ with $(1/2)\overline{(dT/dt)^2}$ from a number of locations in the mixing layer. We find that the two values do not differ by more than 10%. In the integral f_{max} is the maximum frequency of interest and $E_w(f)$ is the power spectrum of the temperature.

Several aspects of Fig. 3 call for comment. First the relative constancy of the dissipation parameter across the mixing layer implies consistency of the data with the usual model for the temperature dissipation, namely with $q^{1/2}\overline{T^2}/l$ where q is the turbulent kinetic energy and l is a measure of the scale of the large eddies. It is useful for later developments to exploit this near constancy and to assume further that a constant denoted in Libby (3) as $\hat{\beta}$ can be assigned the dissipation parameter throughout the far downstream region. In reference 3 Libby argued that $\hat{\beta} = 1$ but we see from Fig. 3 that nonunity values are indicated. We note also a significant discrepancy between the $\hat{\beta}$ values obtained in the present study and those of LaRue and Libby (5) the former being smaller by as much as a factor of three. Because of the appearance of $\bar{x}$ in the definition of this dissipation parameter, the presentation of the data in the form shown in Fig. 3 is sensitive to the selection of x_0.

Finally, the present data relative to the skewness of the temperature derivative, a measure of the isotropy of the small turbulence scales, are in accord with those given by LaRue and Libby (5). Although subject to considerable scatter this skewness is generally negative, implying that the factor 6 in Eq. (1) can be somewhat in error. However, it is reasonable to assume that in the absence of any significant spatial variation of this skewness the constancy of the dissipation parameter and thus the selection of a value for $\hat{\beta}$ are not compromised by this error but that values of $\hat{\beta}$ differing somewhat from those shown in Fig. 3 are defensible.

Velocity and Velocity-Temperature Correlations

At all probe locations the ratio of the intensities of the fluctuations of the two velocity components in the form $(\overline{u'^2}/\overline{v'^2})$ is found to be close to 1.1 indicating, as is to be expected, near isotropy of the velocity fluctuations. In addition the correlation coefficient $\overline{u'v'}/(\overline{u'^2}\,\overline{v'^2})^{1/2}$ yields negligibly small values. The data involving the velocity components alone are of little interest and thus are not considered further.

The most interesting correlations of the velocity and temperature relate to the two mean fluxes, $\overline{v'T'}$ and $\overline{v'T'^2}$, which appear in the conservation equations for the mean temperature and temperature intensity. We find that reasonable similarity is achieved for these fluxes and that their distributions are qualitatively as expected on physical grounds, e.g., on the basis of gradient transport. We defer for the moment presentation of these results.

COMPARISON WITH SIMILARITY THEORY

We now turn to comparison between the data of the previous section and the simple theory of Libby (3). The starting point in making such a comparison is the selection of the Reynolds number $R_M = (UM/\nu_t)$ on the basis of the mean temperature distribution shown in Fig. 1. We have

$$\bar{T} = \frac{1}{2} \bar{T}_\infty \left[1 + erf\left(\frac{1}{2} \eta \right) \right] \tag{2}$$

where $\eta = \bar{y} \bar{x}^{-1/2} R_M^{1/2} = \xi R_M^{1/2}$. The comparison between Eq. (2) with $R_M = 142$, the original value used in reference 3, and the data indicates excellent agreement and encourages further comparison.

We next take up comparison relative to the mean flux $\overline{v'T'}$ which enters the conservation equations for the mean temperature and the temperature intensity. Two points of view can be adopted in making a prediction of this quantity; if gradient transport with a constant thermal diffusivity is assumed, $\overline{v'T'}$ can be calculated from Eq. (2) by differentiation. Alternatively, if Eq. (2) is considered an adequate empirical representation of the mean temperature, then the conservation equation in similarity form for that temperature yields by integration without further approximation a solution for the flux. Either point of view results in

$$\frac{\overline{v'T'}\,\bar{x}^{1/2}}{U \bar{T}_\infty} = -\frac{1}{2\pi^{1/2} R_M^{1/2}} \exp\left(-\frac{\eta^2}{4} \right) \tag{3}$$

The comparison between the prediction of Eq. (3) with $R_M = 142$ and the experimental data clearly shows a significant discrepancy of roughly 60%. It follows that an important term, that associated with production of temperature fluctuations, in the balance equation for $\overline{T'^2}$ is in error and thus that further comparison between prediction and measurement is not worthwhile until this discrepancy is removed. The value of simultaneous temperature and velocity data is now obvious. The 40% error in peak intensity shown in Fig. 2 and mentioned earlier can now be attributed at least in part to an error in the production term.

Several explanations of the discrepancy are possible. If the flow is sufficiently nonsimilar, our calculation of the mean flux based on the *a priori* assumption of similarity is in error. However, the mean temperature profiles such as those given in Fig. 1 indicate within the usual experimental error a satisfactory degree of similarity. It does not necessarily follow that the mean flux is also similar since a small degree of nonsimilarity in the mean profiles could lead to significant nonsimilarity in the mean flux. From a careful examination of this possibility we conclude that we must look elsewhere for the source of our error. As indicated earlier we remove the discrepancy by revising the location of the virtual origin. The suggestion is made that the proper virtual origin for the thermal mixing layer is the one making

the measured mean temperature and mean flux profiles consistent with the conservation equation in similarity form and not the one appropriate for the decay of the temperature intensity in the fully-heated stream.

A new virtual origin is found by adjusting x_o and the Reynolds number R_M so that measured and predicted profiles of the mean temperature and mean flux of temperature in terms of the left side of Eq. (3) agree. We find that $x_o = -30M$ and $R_M = 271$ leads to the results for the mean flux shown in Fig. 4; the agreement relative to the mean temperature is essentially the same as shown in Fig. 1 with different values for these two parameters. We see from Fig. 4 that we have achieved consistency between measured and predicted fluxes.

With this advance we take the next step in attempting to bring measurement and prediction of the temperature intensity into agreement. We find that even with the correct production term disagreement such as indicated on Fig. 2 prevails and that a reexamination of our considerations relative to the scalar dissipation is required. If we do not set $\hat{\beta}$ equal to unity but accept the implication of Fig. 3, namely that nonunity values thereof are appropriate in the far downstream region, then we must consider the following revised equation for the temperature intensity:

$$\gamma I_1'' + \frac{\eta}{2} I_1' - \hat{\beta} I_1 = -\frac{1}{2\pi} \exp\left[-\frac{\eta^2}{2}\right] \qquad (4)$$

where $I_1 = I_1(\eta) = \overline{T'^2}/\overline{T}_\infty^2$. Since I_1 describes the asymptotic behavior of the temperature intensity, i.e., the behavior for values of x such that $\overline{T'^2}(\eta = \pm\infty) = 0$, Eq. (4) is to be solved subject to the boundary conditions

$$I_1'(0) = I_1(\infty) = 0 \ .$$

We select both γ and $\hat{\beta}$ so as to achieve agreement as far as possible between experiment and prediction for the far downstream region. We find that $\gamma = 0.89$ and $\hat{\beta} = 2.25$ yield the agreement shown in Fig. 5 in which the experimental data of the present study are replotted to reflect the revised virtual origin. We now see that satisfactory agreement is achieved with respect to both the maximum level and width of the thermal mixing layer. We believe that similar treatment of the data from earlier experiments would lead to corresponding agreement. Note that the value of $\hat{\beta} = 2.25$ is not inconsistent with our experimental results, if the present data shown in Fig. 3 are altered to account for the revised virtual origin, it is found that $1.4 < \hat{\beta} < 2.1$. Our earlier discussion of possible errors in the determination of χ_w suggests that the selected value of $\hat{\beta}$ is reasonable. The disagreement between the data and prediction on the fully-heated side of the mixing layer is due, of course, to neglect of the decaying component of the temperature intensity.

With the solution of Eq. (4) we are able to compare measured and predicted distributions of the flux of the temperature intensities in similarity form as shown in Fig. 6. We see that reasonable agreement with respect to this third-order correlation is achieved, a gratifying result.

The freeing of the value of the dissipation parameter $\hat{\beta}$ from the value of unity calls for comment. In reference 3 Libby argued that the solution of the partial differential equation for the temperature intensity $I = \overline{T'^2}/\overline{T_1'^2}$ close to the virtual origin required $\hat{\beta} = 1$. The present experimental results and those in LaRue and Libby (5) relative to the temperature dissipation support the classical model for that dissipation, at least in the far downstream region, but show that the level differs significantly from that associated with $\hat{\beta} = 1$. We conclude that the classical model for dissipation may be inappropriate for the mixing layer close to the virtual origin. Additional experimental results are called for in order to examine this issue.

CONCLUDING REMARKS

We provide additional data on the temperature characteristics and new data on the velocity-temperature correlations in the thermal mixing layer downstream of a partially heated turbulence grid. The temperature data are largely consistent with earlier results. The velocity-temperature correlations offer no qualitative surprises but permit a detailed examination of the discrepancy between measurements and predictions of the temperature intensity based on a similarity solution for the thermal mixing layer. It is found that the usual method of selecting the virtual origin which is implicit in such solutions, namely on the basis of the rate of decay of the temperature intensity in the fully-heated stream, is inappropriate. By selecting the virtual origin so that the conservation equation for the mean temperature yields a mean flux of temperature consistent with experiment and by taking the level of the dissipation of temperature fluctuations into account, agreement between measurement and prediction with respect to the temperature intensity in the far downstream region of the thermal mixing layer is obtained. Our experience and the simplicity and accuracy of the similarity solution indicate that the thermal mixing layer is a useful flow for the assessment of predictive methods involving passive scalars.

ACKNOWLEDGEMENTS

The authors acknowledge with thanks the assistance of Dr. Kenneth N. Helland, Mr. Ray Hummer, Mr. Jon Haugdahl and Mr. Joe Robison in this research. Special acknowledgments are due to Ms. Barbara Hanson for her excellent typing. This work has been supported by the National Science Foundation under Grant No. CME 78-15712.

REFERENCES

1 Watt, W. E., and Baines, W. D., "Turbulent Temperature Mixing Layer," *J. Hydraulic Research*, Vol. 11, 1973, pp. 157-166.

2 Foss, J., Schlein, J., and Corrsin, S., Private Communication

3 Libby, P. A., "Diffusion of Heat Downstream of a Turbulence Grid," *Acta Astronautica*, Vol. 2, 1975, pp. 867-878.

4 Keffer, J. F., Olsen, G. J., and Kawall, J. G., "Intermittency in a Thermal Mixing Layer," *J. Fluid Mech.*, Vol. 79, 1977, pp. 595-607.

5 LaRue, J. C., and Libby, P. A., "Thermal Mixing Layer Downstream of a Half-Heated Turbulence Grid," *Phys. Fluids*, Vol. 24, 1981, pp 597-603.

6 LaRue, J. C., Deaton, T., and Gibson, C. H., "Measurement of High-frequency Turbulent Temperature," *Rev. Sci. Instrum.*, Vol. 46, 1975, pp. 757-764.

7 Van Atta, C. W., and Yeh, T. T., "Some Measurements of Multi-point Time Correlations in Grid Turbulence," *J. Fluid Mech.*, Vol. 41, 1970, pp. 169-178.

8 Sepri, P., "Two-point Turbulence Measurements Downstream of a Heated Grid," *Phys. Fluids* Vol. 19, 1976, pp. 1876-1884.

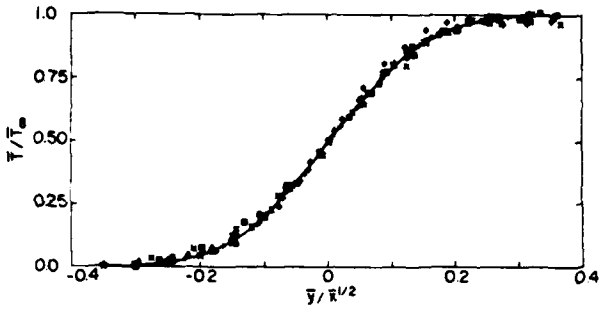

Fig 1 The distribution of mean temperature

- □ $x/M = 21.40$ THG.
- ▲ $x/M = 51.32$ THG.
- ♦ $x/M = 51.32$ BHG.
- × $x/M = 21.40$ BHG.
- ⧖ Keffer *et al.*, Ref. 4.
- —— Theory of Ref. 2.
- ⓘ $x/M = 36.35$ THG
- ◊ $x/M = 67.40$ THG
- ⧖ $x/M = 36.35$ BHG
- ✱ LaRue and Libby, Ref. 5
- + Foss *et al.*, Ref. 2

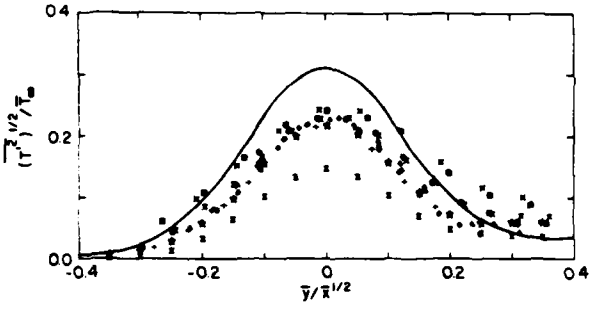

Fig 2 The distribution of temperature intensity. See Fig. 1 for symbol legend.

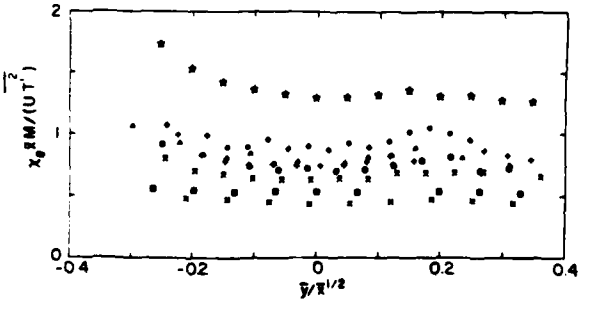

Fig 3 The distribution of the temperature dissipation parameter. See Fig 1 for symbol legend.

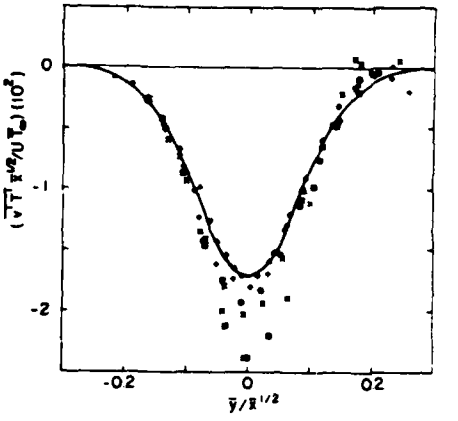

Fig. 4 The distribution of transverse flux of temperature in similarity form. See Fig. 1 for symbol legend

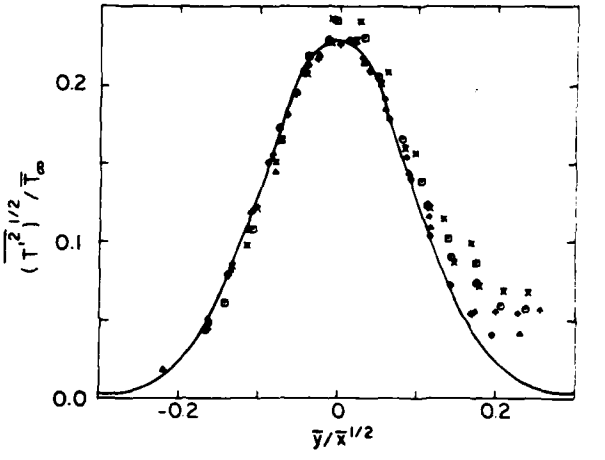

Fig. 5 The distribution of temperature intensity with revised virtual origin and revised prediction. See Fig. 1 for symbol legend.

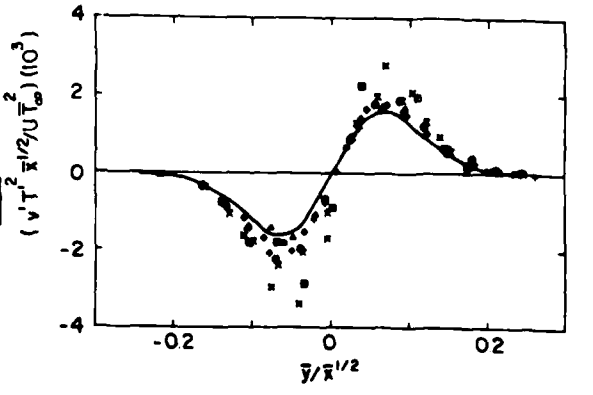

Fig. 6 The distribution of transverse flux of temperature intensity in similarity form. See Fig. 1 for symbol legend

MODELLING OF HOMOGENEOUS TURBULENT SCALAR FIELD DYNAMICS

B.A.Kolovandin, N.N.Luchko and O.G.Martynenko

Heat and Mass Transfer Institute, Minsk, U.S.S.R.

ABSTRACT

The problem of universal (with respect to the turbulent Reynolds and Peclet numbers) modelling of a turbulent passive scalar field dynamics (e.g. temperature or concentration of a contaminant) by means of the second-order model has been studied. In the first part of the paper, a possibility of universal modelling of a homogeneous and isotropic velocity field dynamics using a one-point model of the second order is discussed. The second part deals with the problem of invariant modelling of a homogeneous and isotropic passive scalar field in the asymptotic cases of small and large values of the turbulent Reynolds and Peclet numbers. To check the adequacy of the asymptotic model suggested, a comparison is made of the numerical results on degeneration of a homogeneous and isotropic passive scalar field with the known laboratory experiment data on degeneration of temperature pulsations in the wake behind a heated grid. Finally, in the third part of the paper one of the variants of universal modelling of a turbulent passive scalar field for arbitrary values of the turbulent Reynolds and Peclet numbers and the molecular Prandtl number is suggested.

Modelling of a Homogeneous Velocity Field Dynamics

For a homogeneous and isotropic velocity field, the one-point second-order model may be given by [1]:

$$\dot{\overline{q^2}} + 2\epsilon_u = 0, \qquad (1)$$

$$\dot{\epsilon}_u + F_u(R_\lambda)\epsilon_u^2/\overline{q^2} = 0, \qquad (2)$$

where $\overline{q^2} = \overline{u_i^2}$ is the doubled kinetic turbulence energy, $\epsilon_u = \nu\overline{(\partial u_i/\partial x_k)^2}$ is the kinetic energy dissipation rate, and

$$F_u(R_\lambda) = \frac{7}{15\sqrt{3}}(S_u + S_\nu)R_\lambda,$$

the function of interaction of different-scale velocity pulsations, where

$$S_u = \overline{(\partial u_r/\partial x_r)^3} / \overline{(\partial u_r/\partial x_r)^2}^{\frac{3}{2}},$$

$$S_\nu = 2\nu\cdot\overline{(\partial^2 u_r/\partial x_r^2)^2} / \overline{(\partial u_r/\partial x_r)^2}^{3/2},$$

in which $R_\lambda = \sqrt{\overline{q^2}}\lambda_u/\nu$ is the turbulent Reynolds number, $\lambda_u^2 = 5\nu\overline{q^2}/\epsilon_u$, the squared Taylor's microscale of turbulence.

The problem of modelling of homogeneous and isotropic turbulence dynamics using the momentum equations (1),(2) is reduced to the modelling of F_u as a function of R_λ, provided that the function is universal. For well-known reasons [2], this problem cannot be solved analytically (a solution exists [3] only for the case of weak turbulence, characterized by small values of R_λ).

To date, some attempts have been made [4-8] of semi-empirical modelling of $F_u(R_\lambda)$ using both the limit invariant Loitsyansky's relationships [9], $\overline{q^2}\lambda_u^5 = \text{const}$, for $R_\lambda \ll 1$, and Saffman's relationships [10], $\overline{q^2}L_u^3 = \text{const}$, for $R_\lambda \gg 1$ (here, $L_u = 5\overline{q^2}^{3/2}/\epsilon_u$ is the energy-containing vortex scale), determining asymptotics of the interaction function at $R_\lambda \to 0$ and $R_\lambda \to \infty$:

$$\lim_{R_\lambda \to 0} F_u = 14/5, \quad \lim_{R_\lambda \to \infty} F_u = 11/3, \qquad (3)$$

and treatment of the experimental data on degeneration of $\overline{q^2}$ in the wake behind a grid by means of the power law

$$\overline{q^2} = A(\tau + \tau_0)^{-n} \qquad (4a)$$

Note that (4) is the consequence of the exact solution of the system (1)-(2) with the initial conditions $\overline{q^2}(\tau=0) = \overline{q_0^2}$, $\epsilon_u(\tau=0) = \epsilon_{uo}$ at $F_u = \text{const}$, given by

$$\overline{q^2} = c_{1u}^{F_u/(F_u-2)}\cdot(F_u-2)^{-2/(F_u-2)}\cdot(\tau+\tau_0)^{-2/(F_u-2)}$$

$$\overline{q^2}\epsilon_u^{-2/F_u} = c_{1u}, \qquad (5)$$

where c_{1u} is the integration constant, and

$$\tau_0 = \overline{q_0^2}/(F_u-2)\epsilon_{uo}, \qquad (6)$$

is the origin of turbulence degeneration according to the law (5), i.e. the virtual origin. Comparison of (4) and (5) yields

$$n = 2/(F_u-2)$$

which means that the asymptotic values of kinetic energy degenration exponent "n", according to (3), are the following:

$$\lim n = 5/2, \quad \lim n = 6/5 \qquad (7)$$
$$R_\lambda \to 0 \qquad R_\lambda \to \infty$$

Treatment of the experimental data [11-16] using the relationship (4) shows (see Fig.1) that for an isotropic velocity field, Fu really is the universal function of R_λ, the simplest approximation of which is given by

$$F_u(R_\lambda) = a-b/(1+\beta_u R_\lambda^2) \qquad (8)$$

where, according to (3), a=11/3 and b=13/15, while the numerical value of the constant βu or related constants in the alternative approximations [5-7] should be chosen from the condition of optimum agreement of a corresponding approximation with the experiment at moderate values of R_λ.

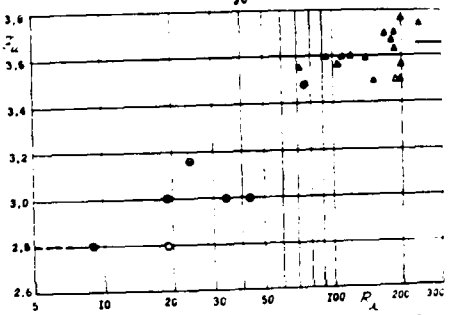

Fig.1 Dependence of the interaction function Fu on the turbulent Reynolds number R_λ: ● - [13]; o - [16]; ⊖ - [14]; ⊖ - [15]; ▲ - [11]; △,▲ - [12]; —— Fu=11/3; - - - Fu=14/5.

Modelling of a Homogeneous Scalar Field Dynamics

Extention of the above approach to the modelling of a homogeneous and isotropic passive scalar field dynamics is not a trivial problem, as could be assumed apriori. Indeed, treatment of the known experimental data [17-20] according to the "law"

$$\overline{t^2} = B\cdot(\tau+\tau_o)^{-m} \qquad (4b)$$

shows that (see Fig.1 in the paper [21] by Warhaft and Lumley), that the exponent "m" of the isotropic temperature pulsation degeneration, in contrast to the exponent "n" of the scalar pulsation degeneration, at $R_\lambda \gg 1$ and $P_\lambda \gg 1$ is noninvariant to the initial conditions. Paradoxical as this fact may appear, it nevertheless can be predicted apriori by means of asymptotic analysis of homogeneous and isotropic scalar field dynamics on the basis of the following one-point second-order model, suggested earlier by B.A.Kolovandin and I.A.Vatutin [22]:

$$\dot{\overline{t^2}} + 2\epsilon_t = 0, \qquad (9)$$

$$\dot{\epsilon}_t + F_t(R_\lambda, P_\lambda)\cdot\epsilon_u\cdot\epsilon_t/\overline{q^2} = 0, \qquad (10)$$

where $\epsilon_t = \varkappa\,\overline{(\partial t/\partial x_k)^2}$ is the function of "smearing" of scalar pulsations, and

$$F_t(R_\lambda, P_\lambda) = 2/3\sqrt{3}(3/2S_t + S_\varkappa)R_\lambda,$$

the interaction function of different-scale velocity and scalar pulsations, consisting of the third-order inertia moment

$$S_t = \overline{(\partial t/\partial x_r)^2\partial u_r/\partial x_r}\ /\overline{(\partial t/\partial x_r)^2}\cdot\overline{(\partial u_r/\partial x_r)^2}^{\,1/2}$$

and the second-order "molecular" moment

$$S_\varkappa = \varkappa\overline{(\partial^2 t/\partial x_r^2)^2}/\overline{(\partial t/\partial x_r)^2}\cdot\overline{(\partial u_r/\partial x_r)^2}^{\,1/2},$$

$$r = (\epsilon_t\overline{q^2})/(\epsilon_u\overline{t^2}) = 6\lambda_u^2/5\sigma\lambda_t^2 = 6L_u/5L_t, \qquad (11)$$

is the scale ratio parameter, $\lambda_t^2 = 6\varkappa\overline{t^2}/\epsilon_t$, squared Taylor's scale of scalar field, $L_t = 6q^{2\,1/2}\,\overline{t^2}/\epsilon_t$, energy-containing "vortices" scale of the scalar field, $\sigma = \nu/\varkappa$, molecular Prandtl number.

At Ft=const, the system (9)-(10), allowing for the asymptotic solution (5) for the velocity field, has the solution

$$\overline{t^2} = \left\{2c_{1t}(F_u-2)/\left[F_t-(F_u-2)\right]\right\}\cdot(\tau+\tau_o)^{-[F_t-F_u-2]/(F_u-2)} + c_{2t}, \qquad (12)$$

$$\epsilon_t/\overline{t^2} = \left\{\left[F_t-(F_u-2)\right]/2(F_u-2)\right\}\cdot(\tau+\tau_o)^{-1},$$

in which τ_o is determined by the relationship (6), i.e. it is assumed that the virtual origin of degeneration of the velocity field and of the scalar one coincide, the constant c_{2t} being identically equal to zero proceeding from the condition at infinity. Since the solution of (12) must satisfy the two initial conditions, $\overline{t^2}(\tau=0)=t_o^2$ and $\epsilon_t(\tau=0)=\epsilon_{to}$, from the second relationship (12) it follows that F_t must be the initial conditions function, i.e.

$$F_t = (F_u-2)+2r_o. \qquad (13)$$

Thus, unlike F_u, the function of F_t cannot be a universal function of R_λ and P_λ. The experimental data [18,21] displayed in Fig.2 confirm this conclusion.

Allowing for (13), the solution of (12) can be represented as

$$\overline{t^2} = 2c_{1t}\cdot\frac{F_u-2}{2}\cdot\frac{1}{r_o}\cdot(\tau+\tau_o)^{-\frac{2}{Fu-2}\cdot r_o} =$$

$$= 2c_{1t}\cdot\frac{1}{n}\cdot\frac{1}{r_o}\cdot(\tau+\tau_o)^{-n\cdot r_o}, \qquad (a)$$

$$r = r_o \qquad (b) \quad (14)$$

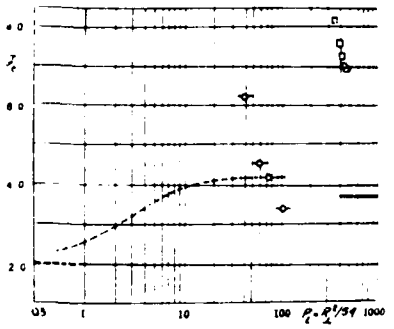

Fig.2 Dependence of the interaction function F_t on the turbulent Peclet number $P_\lambda = R_\lambda^2/54$: □ – [18] ; 0 – [21]; —— $F_t = 11/3$ (r=1); – – – – $F_t = 2$.

A consequence of (13) is the noninvariant nature of the product $\overline{t^2}\,\lambda_t^4$, rejecting reference of this solution to the final stage of degeneration. Thus, solution of (14), obtained on condition that F_t=const, refers only to the asymptotic case of strong turbulence, i.e. $R_\lambda \gg 1$ and $P_\lambda \gg 1$.

As to the case of a "weak" scalar field when $R_\lambda \ll 1$ and $P_\lambda \ll 1$, it can be modelled by the following system of equations:

$$\dot{\overline{t^2}} + 2\epsilon_t = 0 \qquad (9)$$

$$\dot{\epsilon}_t + \psi_t \cdot \epsilon_t^2/\overline{t^2} = 0, \qquad (15)$$

first suggested by Lumley [23] , in which

$$\psi_t = F_t/r \qquad (16)$$

Indeed, at ψ_t= const, the solution of (9)-(15) is given by

$$t^2\epsilon_t^{-2/\psi_t} = c_{1t}, \text{ i.e. } \overline{t^2}\,\lambda_t^{4/(F_t-2)} = \text{const},$$

corresponding at

$$\psi_t = 10/3 \qquad (17)$$

to the Corrsin's invariant of the final stage of degeneration. In this case,

$$r = 3/5 \qquad (18)$$

So, in the case of weak turbulence ($R_\lambda \ll 1$, $P_\lambda \ll 1$) the parameter ψ_t is independent of the initial conditions.

Bearing in mind the expression (13) for F_t and the relationship (16), one may conclude that with the turbulence being strong, the parameter ψ_t is not invariant to the initial conditions, i.e.

$$\psi_t = 2 + (F_u-2)/r_o \qquad (19)$$

That is why the attempts to construct a universal second-order model of the scalar field for $R_\lambda \gg 1$ and $P_\lambda \gg 1$ with the equation (15) (see, for example, the paper by Newman, Warhaft and Lumley [24]) are probably doomed to failure.

Since according to (13) and (19) the parametrs F_t and ψ_t at $R_\lambda \gg 1$ and $P_\lambda \gg 1$ are noninvariant, the equation for ϵ_t in the form (11) or (15) is not acceptable for modelling of scalar field of strong turbulence. The invariant equation for ϵ_t at $R_\lambda \gg 1$ and $P_\lambda \gg 1$ may be obtained by determining of r using the condition (14 b) and the equations (1),(2) and (9). It is easy to show that it is of the form

$$\dot{\epsilon}_t + F_t^{(1)} \cdot \epsilon_u \epsilon_t/\overline{q^2} + F_t^{(2)} \cdot \epsilon_t^2/\overline{t^2} = 0 \qquad (20)$$

in which

$$F_t^{(1)} = F_u - 2 = 5/3, \quad F_t^{(2)} = 2 \qquad (21)$$

Solution of the equations (9), (20) given by

$$\overline{t^2} = [c_{1t}(F_u-2)/r]^{-2/(F_t^{(2)}-2)} \cdot (\tau+\tau_o)^{-2r/(F_u-2)} \qquad (22)$$

$$\epsilon_t/\overline{t^2} = [r/(F_u-2)] \cdot (\tau+\tau_o)^{-1} \text{ or} \qquad (23)$$

$$r = r_o = [F_u - 2 - F_t^{(1)}]/(F_t^{(2)} - 2)$$

leads to the invariant relationship for degeneration of a homogeneous scalar field at $R_\lambda \gg 1$, $P_\lambda \gg 1$

$$\overline{t^2} \cdot L_t^{3r} = \text{const} \qquad (24)$$

The relationship (24) is the extention to the arbitrary values of the rate-scale parameter r of the invariant relationship suggested earlier by Corrsin [25].

Universal Modelling of Degeneration of a Homogeneous and Isotropic Passive Scalar Field

Let us assume that at arbitrary values of R_λ and P_λ , obviously related to each other as

$$R_\lambda^2 = (5r/66) \cdot P_\lambda^2$$

the equation for ϵ_t is given by (20), provided that F_t and F_t are some of universal functions of the turbulent Reynolds and Peclet numbers, when at $R_\lambda \to \infty$ and $P_\lambda \to \infty$, according to (21),

$$F_t \to (F_u-2) = 5/3, \quad F_t^{(2)} \to 2, \qquad (25)$$

and at $R_\lambda \to 0$ and $P_\lambda \to 0$, according to (15) and (17),

$$F_t^{(1)} \to 0, \quad F_t^{(2)} \to 10/3 \qquad (26)$$

Allowing for these asymptotics, we now represent the functions considered in the form:

$$\left.\begin{aligned} F_t^{(1)} &= F_u - 2 - (4/5) f_1(R_\lambda, \sigma), \\ F_t^{(2)} &= 2 + (4/3) \cdot f_2(R_\lambda, \sigma), \end{aligned}\right\} \qquad (27)$$

in which the functions $f_1(R_\lambda, \sigma)$ and $f_2(R_\lambda, \sigma)$, according to the asymptotic relationships (26),(27) at moderate values of σ must have the following limits:

$$\lim f_1 = 1, \quad \lim f_2 = 1, \quad \lim f_1 = 0, \quad \lim f_2 = 0$$
$$R_\lambda \to 0 \qquad R_\lambda \to 0 \qquad R_\lambda \to \infty \qquad R_\lambda \to \infty$$

Besides, according to the solutions of (22), (23), in which, allowing for (27)

$$r = 3f_1/5f_2,$$

the ratio f_1/f_2 must decrease with an increase of the molecular Prandtl number, and increase with a decrease of σ, which corresponds to the intuitive physical picture of a scalar field degeneration in liquids with different physical properties.

The above-mentioned conditions, specifically, are satisfied by the following approximations of the functions considered:

$$\left.\begin{aligned} f_1 &= 1/(1 + \beta_t \cdot \sigma \cdot R_\lambda^2), \\ f_2 &= 1/(1 + \gamma_u \cdot R_\lambda^2), \end{aligned}\right\} \qquad (28)$$

where the constants β_t and γ_u determine the rate of changing of the functions $F_t^{(1)}$ and $F_t^{(2)}$ between the asymptotic values of (25) and (26) in the course of degeneration of t^2. The relation between β_t and γ_u may be determined from the condition of existence of an equilibrium scalar field degeneration regime at moderate values of R_λ and P_λ, which is characterized by the approach, in time, of the r parametr to 1, at $\sigma = 1$, (this regime was discovered by Newman and Herring [26] during numerical modelling of homogeneous vector and scalar field degeneration carried out on the basis of the "test-field" Kreichnan's model), by the obvious relationship

$$\dot{r} = -(4/3) \cdot f_2(r - 3f_1/5f_2) \cdot (\epsilon_t/\overline{t^2})$$

in the form

$$\beta_t \simeq 3\gamma_u/5.$$

In order to check the adequacy of universal modelling of a homogeneous and isotropic scalar field dynamics based on the model equations (1),(2) of the velocity field, assigning $F_u(R_\lambda)$ in the form (8) and equations (9),(20) with $F_t^{(1)}(R_\lambda, \sigma)$ and $F_t^{(2)}(R_\lambda, \sigma)$ being assigned in the form (27), (28), a numerical experiment has been conducted on degeneration of a homogeneous and isotropic scalar field with the assigned initial values of q_o^2, t_o^2, ϵ_{uo} and ϵ_{to}, corresponding to those of the experiment of Warhaft and Lumley [21]. Comparison of numerical and experimental data given in Fig.3

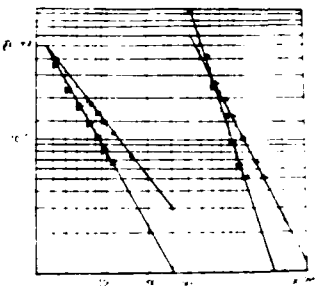

Fig.3 Comparison of numerical modelling of t^2 using (9)-(20)-(27)-(28) at $\beta_u = \gamma_u = 1/150$, $a = 3.52$, $b = 0.72$, $\sigma = 0.73$ with the experiment [21] : • - $m = 1.29$, $r = 0.96$; * - $m = 1.83$, $r = 1.37$; + - $m = 2.06$, $r = 1.54$; 0 - $m = 3.2$, $r = 2.39$.

shows their complete agreement at any of the considered values of r. Figure 4 displays the numerical experiment results on a scalar field degeneration at different values of σ and different initial values of the parameter r. The absence of experimental data on $x/M > 300$, unfortunately, made it impossitle to verify the adequacy of the approximation (28) with respect to both the rate of approach of the degeneration process to the equilibrium ($r \to 1$), and the degree of the molecular Prandtl number effect on degeneration of t^2.

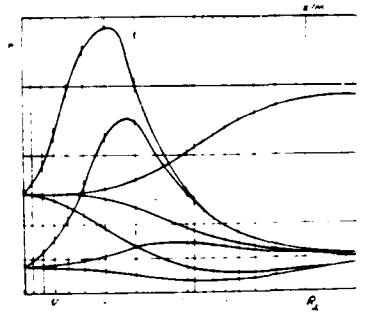

Fig.4 Numerical modelling of the parameters n and r evolution at different values of σ and two different values of r_o (the curves are labelled by the values of the molecular Prandtl number, σ).

Discussion of Results

1. Degeneration of kinetic energy of turbulence in homogeneous and isotropic velocity field is self-similar, i.e. may be represented by the power law (4a) in the asymptotic state of turbulence, at $R_\lambda \gg 1$ or $R_\lambda \ll 1$ only. The empirical curve $F_u(R_\lambda)$ shows that at $R_\lambda \geq 100$, F_u has a platform coinciding with the asymptotic value $F_u = 11/3$, which corresponds to $n = 6/5$. At $0 < R_\lambda < 10$, $F_u(R_\lambda)$ also has a platform coinciding with the asymptotic value $F_u = 14/5$, which corresponds to $n = 5/2$. With the tur-

bulent Reynolds number values being moderate, degeneration of q^2 is not self-similar, hence the power law (4a) may be used for treatment of the experimental data only in a local sense, i.e. over a narrow range of R_λ variation.

For second-order modelling of the turbulence, the information on degeneration of a homogeneous anisotropic velocity field is very important. As shown by Batchelor [27], the weak turbulence asymptotics, n=5/2, in this case is unchanged. At the same time, the preliminary experimental data of Taeker and Ali [28] , demonstrate that the strong turbulence asymptotics is not invariant to the anisotropy degree. For modelling of behaviour of $F_u(R_\lambda$, II,III),the numerical experiment on degeneration of homogeneous anisotropic turbulence following the scheme DNS [29] for small and moderate values of R_λ, and for $R_\lambda \gg 1$, according to the scheme TFM [26] may prove very useful.

2. Degeneration of intensity of a homogeneous and isotropic scalar field is self-similar, i.e. is represented by the power law (4b) only in the asymptotic state of turbulence, $R_\lambda \gg 1$ and $P_\lambda \gg 1$, or $R_\lambda \ll 1$ and $P_\lambda \ll 1$. Asymptotic value of the exponent m of degeneration of t^2 at $R_\lambda \gg 1$ and $P_\lambda \gg 1$, unlike the exponent n of turbulence energy degeneration at $R_\lambda \gg 1$ is not universal but depends on the initial conditions, i.e. $m=m(r_o)$. For the assigned value of r_o, the value of m is constant, until F_t=const. It is probable that at large values of R_λ and P_λ , F_t, like F_u, has a platform with respect to τ (or R_λ). The curve $F_t(P_\lambda)$, calculated from the numerical values of q^2, ϵ_u, t^2 and ϵ_t, is shown in Fig.2. The result (14), i.e. $m= nr_o$ and $r = r_o$ at $R_\lambda \gg 1$ and $P_\lambda \gg 1$, is confirmed by the experimental data of Warhaft and Lumley [21] , but contradicts the results of Newman and Herring[26] Larcheveque et al. [30] and Nelkin and Kerr [31] , according to which the dependence of m (and, hence, of F_t and ψ_t) on the initial conditions is the manifestation of a transient nonself-similar degeneration of t^2, whose relaxation towards equilibrium ($m \to n$, $r \to 1$) occurs very slowly. In contrast, we showed that the dependence of m (and F_t) on the initial conditions is the attribute of a self-similar degeneration regime of a scalar field at $R_\lambda \gg 1$ and $P_\lambda \gg 1$, beginning with $\tau = \tau_o$ and stretching until F_t=const (see the platform in Fig.2 at P_λ). Note that the numerical experiment of Larcheveque et al. rather confirms than rejects this point of view, because for the two realizations of r they obtained different asymptotics of ψ_t (see Fig.6 in Ref.30). As to the change of m and r with respect to τ , according to our data it reflects the process of nonself-similar degeneration of t^2 at moderate values of R_λ and P_λ . In this case F_t (or ψ_t) considerably changes with respect to τ , i.e. the power degeneration law (4b) is not obeyed. At very large values of τ , corresponding to small ones of R_λ and P_λ , degeneration of t^2 becomes self-similar again, with $m \to 3/2$, $r \to 3/5$, $\psi_t \to 10/3$, $F_t \to 2$.

The discussed character of evolution of the exponent m at large, moderate and small values of R_λ and P_λ , is quite similar to the character of variation of the exponent n with a decrease of R_λ , with the only difference that the value of m (and hence of F_t or ψ_t), unlike that of n, at $R_\lambda \gg 1$ and $P_\lambda \gg 1$ is not invariant to the initial conditions. In this respect the behaviour of $m(R_\lambda, P_\lambda, r_o)$ and $F_t(R_\lambda, P_\lambda, r_o)$ is somewhat similar to the behaviour of $n(R_\lambda$,II,III) and $F_u(R_\lambda$,II,III). In its turn, the turbulence anisotropy must probably create an additional invariance of the parameters m and F_t.

Our study of degeneration asymptotics of a homogeneous and isotropic scalar field shows that it is impossible to use in an asymptotic second-order model ($R_\lambda \gg 1, P_\lambda \gg 1$) the equations for ϵ_t either in the form (10) or (15) just because the functions $F_t(R_\lambda, P_\lambda)$ and $\psi_t(R_\lambda, P_\lambda)$ are not universal. A universal asymptotic equation for ϵ_t is given by (20), the solution of which results in the invariant relationship (24) for degeneration of an isotropic scalar field in isotropic turbulence.

3. It should be noted in conclusion that the attempt we have made to construct on intuitive grounds the interaction functions of $F_t^{(1)}$ and $F_t^{(2)}$ for the arbitrary values of σ is preliminary. For a more valid modelling of $F_t^{(1)}(R_\lambda, \sigma)$ and $F_t^{(2)}(R_\lambda, \sigma)$ reliable experimental data on scalar field degeneration at different σ to the weak turbulence asymptotics studied by Corrsin [25]and Deissler [32] are necessary. For solution of this problem, numerical experiment according to the scheme DNS may prove invaluable.

ACKNOWLEDGEMENTS

The authors acknowledge with gratitude the courtesy of Dr.R.Herring who kindly supplied us with a preprint and some of the papers of American and French workers which were not available for the authors.

REFERENCES

1. Karman, Th. and Howarth, L., "On the Statistical Theory of Isotropic Turbulence", Proc. Roy. Soc., A164, 1938, pp.192-215.

2. Monin, A.S. and Yaglom, A.M., "Statistical Hydromechanics", Part II, Fizmatgiz, Moscow, 1967.

3. Deissler, R., "On Decay of Homogeneous Turbulence Before the Final Period", Phys. Fluids, Vol.1, 1958, pp.111-121.

4. Hanja lic, K. and Launder, B.E., "Contribution Towards a Reynolds-Stress Close for Low Reynolds Number Turbulence," J. Fluid Mech., Vol.74, 1976, pp.493-610.

5. Reynolds, W.C., "Computation of Turbulent Flows", Ann. Rev. Fluid Mech., Vol.8, 1976, pp.183-208.

6. Lumley, J.L. and Newman, G.R., "The Return to Isotropy of Homogeneous Turbulence," J. Fluid. Mech., Vol.82, 1977, pp.161-178.

7. Chund, M.K. and Adrian, R.J., "Evaluation of Variable Coefficients in Second-Order Turbulence Models", Preprint of paper, Second Symp. Turb. Shear Flows, London,1979,

pp.10.43-10.48.

8. Kolovandin, B.A., "Asymptotic Correlational Modelling of Nonhomogeneous Turbulence," Preprint of paper, Symp. Turb. Shear Flows, Pennsylvania, 1977, pp.1723-1730.

9. Loitsyansky, L.G., "Some Basic Regularities of an Isotropic Turbulent Flow," Trudy TsAGI, No.440, 1939.

10. Saffman, P.C., "Note on Decay of Homogeneous Turbulence," Phys. Fluids, Vol. 10, 1967, p.1349.

11. Compte-Bellot, G. and Corrsin, S., "The Use of Contraction to Improve the Isotropy of Grid-Generated Turbulence," J.Fluid Mech., Vol.25, 1966, pp.657-682.

12. Gad-El-Hak, M. and Corrsin, S., "Measurements of the Nearly Isotropic Turbulence Behind a Uniform Jet Grid," J. Fluid Mech., Vol.22, 1974, pp.115-143.

13. Batchelor, G.K. and Townsend, A.A., "Decay of Turbulence in the Final Period," Proc. Roy. Soc., A194, 1948, pp.527-543.

14. Ling, S.C. and Huang, T.T., "Decay of Weak Turbulence," Phys. Fluids, Vol.13, 1970, pp.2912-2924.

15. Ling, S.C. and Wan, C.A., "Decay of Isotropic Turbulence Generated by a Mechanically Agitated Grid," Phys. Fluids, Vol. 15, 1972, pp.1363-1369.

16. Bennet, J.C. and Corrsin, S., "Small Reynolds Number Nearly Isotropic Turbulence in a Straight Duct and a Contraction," Phys. Fluids, Vol. 21, 1978, pp.2129-2140.

17. Mills, R.R., Kistler, A.L., O'Brien V. and Corrsin, S., "Turbulence and Temperature Fluctuations Behind a Heat Grid," NACA, No.4288, 1958.

18. Lin, S.C. and Lin, S.C., "Study of Strong Temperature Mixing in Subsonic Grid Turbulence," Phys. Fluids, Vol.16, 1973, pp. 1587-1598.

19. Yeh, T.T. and Ven Atta, C.W., "Spectral Transfer of Scalar and Velocity Fields in Heated-Grid Turbulence," J. Fluid Mech., Vol. 58, 1973, pp. 233-261.

20. Sepri, P., "Two-Point Turbulence Measurements Downstream of Heated Grid," Phys. Fluids, Vol. 19, 1976, pp. 1876-1884.

21. Warhaft, Z. and Lumley, J.L., "An Experimental Study of the Decay of Temperature Fluctuations in a Grid-Generated Turbulence," J. Fluid. Mech., Vol. 88, 1978, pp. 659-684.

22. Kolovandin, B.A. and Vatutin, I.A., "Statistical Transfer Theory in Non-Homogeneous Turbulence," Int. J. Heat Mass Transfer, Vol. 15, 1972, pp. 2371-2383.

23. Lumley, J.L., "A Model for Computation of Stratified Turbulence Flows," Int. Symp. Stratified Flows, Preprint of paper, Novosibirsk, 1972, pp.333-341.

24. Newman, G.R., Warhaft, Z. and Lumley, J.L., "The Decay of Temperature Fluctuations in Isotropic Turbulence," Proc. 6th Australasian Hydraulics and Fluid Mech. Conf., Adelaide, 1977.

25. Corrsin, S., "The Decay of Isotropic Temperature Fluctuations an Isotropic Turbulence," J. Aeronautic. Sci., No.6, 1951, pp. 417-423.

26. Newman, C.R. and Herring, J.R., "A Test Field Model Study of a Passive Scalar in Isotropic Turbulence," J. Fluid Mech., Vol. 94, 1979, pp. 163-194.

27. Batchelor, G.K., "The Theory of Homogeneous Turbulence," University Press, Cambridge, 1959.

28. Taeker, H.J. and Ali, S.F., "Decay of Anisotropic Turbulence," AIAA Journal, Vol. 11, No. 4, 1973, pp. 546-548.

29. McMillan, O.J. and Fersiger, J.H., "Direct Testing of Subgrid-Scale Models," AIAA Journal, Vol. 17, 1979, pp. 1340-1346.

30. Larchevegue, M., Chollet, J.P., Herring, J.R., Lesieur, M., Newman, G.R. and Schertzer, D., "Two-Point Closure Applied to a Passive Scalar in Decaying Isotropic Turbulence," Turbulent Shear Flows II, Springer-Verlag, 1980, pp.50-66.

31. Nelkin, M. and Kerr, R.M., "The Decay of Scalar Variance Interms of a Modified Richardson Law for passive dispersion,"(preprint), 1980.

32. Deissler, R., "Decay of Temperature Fluctuations in Homogeneous Turbulence Before the Final Period," Int. J. Heat Mass Transfer, Vol. 1, 1961, pp.312-324.

MODELLING THE DISSIPATION RATE OF TEMPERATURE VARIANCE IN A THERMAL MIXING LAYER

S. Elghobashi
Mechanical Engineering Department
University of California
Irvine, California

B.E. Launder
Mechanical Engineering Department
University of Manchester
Institute of Science & Technology
Manchester M60 1QD England

ABSTRACT

In a turbulent flow where the mechanisms and/or the importance of the generation processes of turbulent kinetic energy, k, and mean square scalar variance, c^2, are dissimilar, no simple connection exists between the turnover time scale of the fluctuating velocity and fluctuating scalar fields. To allow the computation of the turbulent scalar field in these situations a means of calculating the scalar time is required. Here, in an extension of work by Newman, Launder and Lumley [3], the time scale is obtained via a proposed transport equation for the dissipation rate of mean square scalar variance. The modelled equation has been applied successfully to the calculation of the spread of a thermal mixing layer in grid generated turbulence.

NOMENCLATURE

C	time-mean temperature
c	temperature fluctuation
c_{ϵ_2}	constant appearing in ϵ-equation
c_{D1}, c_{D2}, c_{P1}	constants appearing in ϵ_c-equation
k	kinetic energy of turbulence = $\frac{1}{2}\overline{u_i u_i}$
M	spacing of the turbulence grid
R	time-scale-ratio
T	time scale
U_i, u_i	mean and fluctuating velocities in direction x_i (tensor notation)
$\overline{v^2}$	y-direction component of Reynolds normal stress
$\underline{x}$	distance in mainflow direction
x	x measured from the virtual origin of the turbulent field normalized by M
x_i	Cartesian coordinate (tensor notation)
$\underline{y}$	cross-stream distance coordinate
y	y measured from the point where $C = \Delta C/2$, normalized by M
ΔC	mean temperature difference between the heated and unheated fluid
ϵ	dissipation rate of turbulence energy k
ϵ_c	dissipation rate of $\frac{1}{2}\overline{c^2}$
η	dimensionless cross-stream coordinate; $\eta = \overline{y}/(\overline{y}_{.9} - \overline{y}_{.1})$ where numerical subscript denotes values of $C/\Delta C$
λ	kinematic diffusivity of C

INTRODUCTION

In non-isothermal, turbulent shear flows such as a weakly heated jet mixing in stagnant surroundings or the boundary-layer flow along a heated wall, velocity and temperature fluctuations can be regarded as being created by analogous mechanisms, each associated with the entrainment of free-stream fluid at a different velocity and temperature from that within the shear flow. Moreover, in the balance equations for the turbulent kinetic energy, k, and the mean square temperature variance, $\overline{c^2}$, we find that the generation terms display not only a similar variation across the shear flow but also a comparable degree of importance relative to transport and dissipation processes. In view of this correspondence it is hardly surprising that the ratio of turbulent time scales associated with the velocity and thermal fields should exhibit strong similarity. Beguier et al. [1] showed from a survey of several such flows that the time-scale-ratio R (defined as $\frac{1}{2}\overline{c^2}\epsilon/k\epsilon_c$) was approximately equal to 0.5; here, ϵ and ϵ_c denote respectively the rates of dissipation of k and $\frac{1}{2}\overline{c^2}$ by molecular action.

In fact the implied constancy of R has been basic to nearly all modelling work aimed at calculating scalar variances whether the scalar in question be temperature, chemical species or some other passive marker. By supposing a constant R the level of ϵ_c could be obtined in terms of the other quantities appearing in the definition of R. The supposition of an invariant value of R becomes less tenable, however, in cases where the terms in the respective balance equations for the scalar and mechanical fields are different in character. Warhaft and Lumley's [2] experiment of the decay of temperature fluctuations behind a heated mandoline provides a striking example. The value of R in any experiment remained essentially unchanged througout the development length; its level, however, strongly depended on the proportion of the total number of wires that were heated.* It was to allow the calculation of such phenomena that

* By altering the proportion of the wires that were heated, the ratio of the length scales of the thermal and velocity fluctuations could be varied.

Newman et al. [3] devised a transport equation for ε_c thus removing the need to prescribe R. The present contribution is a continuation of that line of development. The flow of particular interest is grid-turbulence development downstream from a half-heated grid [4,5]. While the turbulence energy, lacking a source, decays monotonically with distance from the grid, the mean temperature gradient sustains the level of $\overline{c^2}$ at an almost constant level.

THE CLOSURE MODEL

The development of the mean square variance $\overline{c^2}$ of a fluctuating scalar in a stationary uniform-density turbulent flow is described by the following coupled system of equations for the mean scalar C, for $\overline{c^2}$ itself and ε_c

$$U_j \frac{\partial C}{\partial x_j} = - \frac{\partial \overline{u_j c}}{\partial x_j} \tag{1}$$

$$U_j \frac{\partial \overline{c^2}}{\partial x_j} = - \frac{\partial \overline{u_j c^2}}{\partial x_j} - 2\overline{u_j c} \frac{\partial C}{\partial x_j} - 2\varepsilon_c \tag{2}$$

$$U_j \frac{\partial \varepsilon_c}{\partial x_j} = - \frac{\partial \overline{u_j \varepsilon_c'}}{\partial x_j} + \left(-\lambda \overline{\frac{\partial c}{\partial x_i} \frac{\partial c}{\partial x_j} \frac{\partial u_i}{\partial x_j}} - \lambda \overline{\left(\frac{\partial^2 c}{\partial x_j \partial x_i} \right)^2} \right) S_{\varepsilon_c} \tag{3}$$

where λ is the kinematic diffusivity of C. In ref. [3], which was concerned exclusively with homogeneous flows, the unknown source/sink terms in equation (3) were approximated by:

$$S_{\varepsilon_c} = - c_{P1} \frac{\varepsilon_c}{\overline{c^2}} \overline{u_j c} \frac{\partial C}{\partial x_j} - c_{D1} \frac{\varepsilon_c^2}{\overline{c^2}} - c_{D2} \frac{\varepsilon \varepsilon_c}{k} \tag{4}$$

for conditions where mean strain is absent. Reference [3] adopts constant values for the coefficients c_{P1} and c_{D1} while c_{D2} is made a function of the anisotropy of the turbulent stress field. In the present work all three coefficients take fixed values since the turbulent stress field is nearly isotropic for the flow situations examined. The scalar fluxes are approximated as follows:

$$\left. \begin{aligned} - \overline{u_j c} &= c_c \overline{u_j u_\ell} T \frac{\partial C}{\partial x_\ell} \; ; \; - \overline{u_j c^2} = c_c \overline{u_j u_\ell} T \frac{\partial \overline{c^2}}{\partial x_\ell} \\ - \overline{u_j \varepsilon_c'} &= c_c \overline{u_j u_\ell} T \frac{\partial \varepsilon_c}{\partial x_\ell} \end{aligned} \right\} \tag{5}$$

Where c_c takes the constant value 0.35 and T denotes a time scale that blends both mechanical and scalar contributions

$$T = \sqrt{\frac{k}{\varepsilon} \frac{\overline{c^2}}{\varepsilon_c}} \tag{6}$$

This blended form, suggested but not used in [3] differs from earlier studies that have adopted

$$T = \text{constant} \; \frac{k}{\varepsilon} \tag{7}$$

The latter form has been used for comparison in the present work where the constant in equation (7) has been taken as unity in order that, in local equilibrium (where $R \approx 0.5$) the time scales given by equations (6) and (7) should be the same. The velocity field is homogeneous in the studies of ref. [4] and [5]; the level of turbulence energy is thus obtained from:

$$U_j \frac{\partial k}{\partial x_j} = - \varepsilon \tag{8}$$

$$U_j \frac{\partial \varepsilon}{\partial x_j} = - c_{\varepsilon 2} \frac{\varepsilon^2}{k} \tag{9}$$

where the quantity $c_{\varepsilon 2}$ takes the value 1.8 which produces a kinetic energy level proportional to x raised to the power -1.25. In the flows considered $\overline{v^2}$, the mean square velocity fluctuations in the direction of the inhomogeneity (y), is the only stress component to enter. Experimental care has ensured that the turbulence produced by the grid is very nearly isotropic; we have accordingly taken.

$$\overline{v^2} = 0.65k, \tag{10}$$

a relationship we assume applies throughout the calculation domain.

Two sets of values have been adopted for the empirical coefficients in the ε_c equation

	c_{P1}	c_{D1}	c_{D2}
Set 1	2.0	2.02	0.89
Set 2	2.0	2.2	2.0

The former are employed in the study of Newman et al. [3] while the latter are the ones giving the best agreement for the cases considered here.

THE TEST FLOWS CONSIDERED

The two best documented experiments of the thermal mixing layer in a homogeneous turbulent field are those of Keffer et al. [4] and La Rue and Libby [5]. The former employed a grid of horizontal bars 9.5 mm in diameter with centres spaced 25 mm apart while the latter adopted a biplanar square mesh of 6.7 mm diameter rods with 40 mm spacing. In each experiment the upper half of the horizontal rods was uniformly heated producing a sharp step in temperature along a vertical section just downstream from the grid (figure 1). As the flow develops downstream turbulent mixing blurs the interface between the hot and cold streams, producing the s-shaped distribution of temperature indicated in figure 1. The effective turbulent diffusivity in grid turbulence is only a weak function of x and thus the mixing layer spread very nearly as $x^{\frac{1}{2}}$.

The numerical simulations of these experiments have been based on the GENMIX two-dimensional parabolic computer program of Spalding [6] using 50 lateral nodes to span the region of thermal inhomogeneity. Unfortunately no experimental data are reported in the vicinity of the grid to serve as starting conditions for the computations. We have accordingly adjusted the initial levels of $\overline{c^2}$ and ε_c in the heated stream to produce so far as possible agreement at the first station for which data are reported. It is thus principally the subsequent development of the mixing layer that reflects the success or otherwise of the chosen model. In the case where the purely mechanical timescale k/ε was used to represent the diffusion process only the peak value of $\overline{c^2}$, not the complete profiles, could be satisfactorily matched with the initial data.

Keffer et al. [4] report profiles only at 41 bar spacings downstream from the grid. In figure 2 one notes almost complete agreement between experimental and computed profiles of mean temperature and rms temperature fluctuations; Set 2 coefficients were used in the ε_c equation. The development of the temperature fluctuations downstream along the line where the mean temperature is the arithmetic mean of that of the two streams ($\eta = 0$), shown in figure 3, indicated a slight increase of $\overline{c^2}$ with distance, again in accord with reported measurements. On the same figure is shown the corresponding development of $\varepsilon_c]_{\eta=0}$ with x. We note a marked decrease in this quantity. Now, both k/ε and $\overline{c^2}$ increase at about the same rate (see figure 3). Thus conventional approaches to approximating ε_c, which assume that quantity to be proportional to $\varepsilon\overline{c^2}/k$, would thus give a virtually uniform ε_c in marked contrast with the behavior here found.

The experiment of LaRue and Libby [5], using a bi-plane grid leads to higher levels of temperature variance at the initial station which are mimicked in the numerical simulation by adjusting appropriately the initial levels of $\overline{c^2}$ and ε_c. The experiments show an almost invariant profile of temperature variance when plotted as a function of $\bar{y}/\bar{x}^2$ ($\bar{x}$ being the distance, normalized by M, measured from the effective origin of the turbulence field, 6 mesh widths upstream of the grid). In particular the maximum intensity of temperature fluctuations $\sqrt{\overline{c^2}}/\Delta C$ is essentially uniform at 0.22. This behavior is extremely well reproduced by the computation with the coefficients of set 2 as seen in figures 4-7. The coefficients proposed by Newman et al. also give a fair account of the development though the peak intensity slowly decays with distance downstream. By comparison, the computed development employing the mechanical timescale k/ε leads to far too rapid rates of dispersion. The computed evolution of the time-scale ratio R obtained with set 2 coefficients is shown in figure 8. There is a virtually linear, unabated growth of this quantity with distance in both sets of computations. Both produce parallel lines of evolution, with no evident tendency either for the curves to converge or, indeed, for asymptotic level of R to be reached. It must be remarked that his development is somewhat surprising and not yet confirmed by experiment. If one takes the view that $\overline{c^2}/\Delta C$ *does* reach an entirely self-similar shape independent of x, it follows from equations (2), (5) and (6) that

$$\varepsilon_c \equiv \frac{\overline{c^2}}{R}\,\frac{\varepsilon}{k} \propto \frac{k^2}{\varepsilon\sqrt{R}}\,\frac{\Delta C^2}{x}$$

and so $R \propto (\varepsilon/k^2)^{2/3}$. Now k^2/ε is proportional to the effective turbulent viscosity and this, as we have remarked is known to change only slowly in grid turbulence.

CONCLUDING REMARKS

It has been shown that the transport equation for ε_c proposed in ref [3] does allow the correct simulation of the evolution of the scalar field in the inhomogeneous flow behind a half-heated grid. A number of uncertainties remain and one should, for the present, exercise due caution in applying the equation to flows substantially different in character from those considered here or in ref [3]. There is an urgent need for a detailed mapping of velocity and scalar statistics in the vicinity of the grid in order to provide a more precise set of starting conditions for the numerical simulation. The absence of such data at present clouds our ability to judge the satisfactoriness of the proposed equation.

REFERENCES

1 Beguier, C., DeKeyser, I. and Launder, B.E., "Ratio of Scalar and Velocity Dissipation Time Scales in Shear Flow Turbulence," Physics of Fluids, Vol. 21, 1978, p. 307.

2 Warhaft, Z. and Lumley, J.L., "An Experimental Study of the Decay of Temperature Fluctations in Grid-Generated Turbulence," Journal of Fluid Mechanics, Vol. 88, 1978, p. 659.

3 Newman, G.R., Launder, B.E., and Lumley, J.L., "Modeling the Behavior of Homogeneous Scalar Turbulence," Journal of Fluid Mechanics, 1981 (in press).

4 Keffer, J.F. Olsen, G.J., and Kawall, J.G., "Intermittency in a Thermal Mixing Layer," Journal of Fluid Mechanics, Vol. 79, 1977, p. 595.

5 LaRue, J.C., and Libby, P.A., "Thermal Mixing Layer Downstream of Half-Heated Turbulence Grid," to appear in Physics of Fluids, 1981.

6 Spalding, D.B., "GENMIX: A General Computer Program for Two-Dimensioonal Parabolic Phenomena," Pergamon Press, 1977.

ACKNOWLEDGEMENTS

Besides the assistance provided by our respective institutions, the research has been supported by the U.S. Department of Energy, (Division of Basic Energy Sciences) through Contract No. AS03-76SFO 0034.

Author's names appear alphabetically.

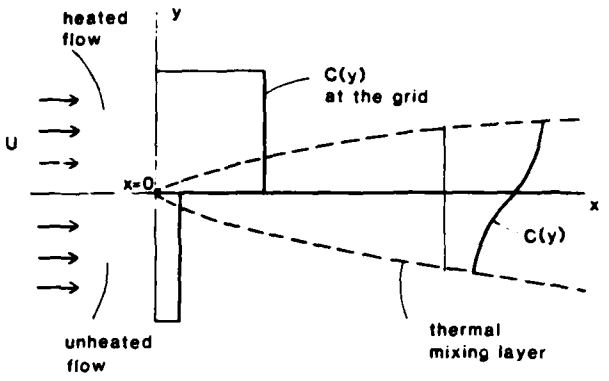

Fig. 1 Schematic of flow

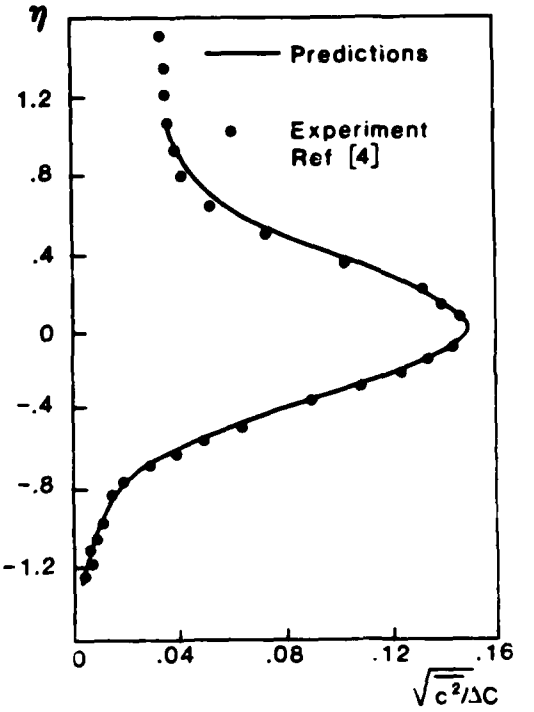

Fig. 2(b) Normalized rms temperature fluctuation at x/M = 41

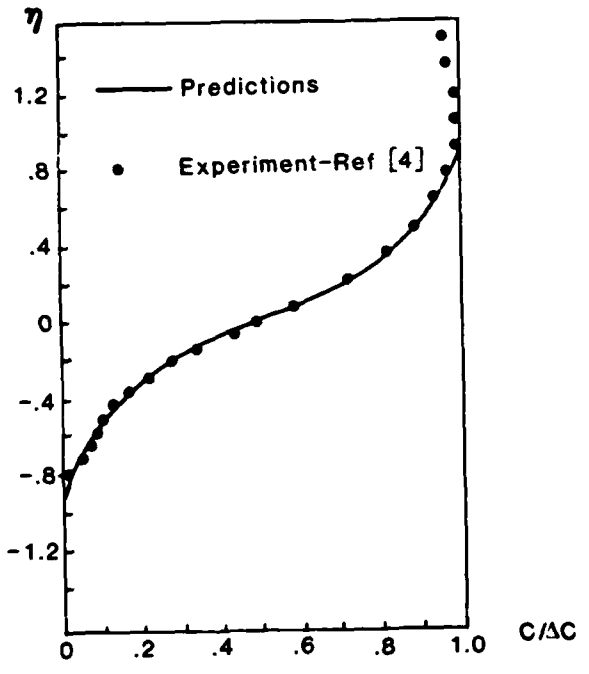

Fig. 2(a) Normalized mean temperature profile at x/M = 41

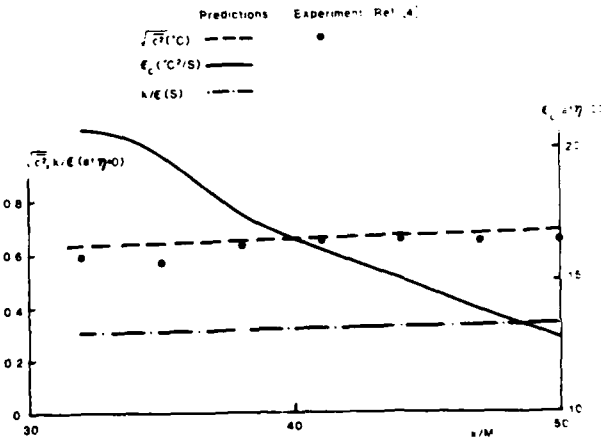

Fig. 3 Variation of $\sqrt{\overline{c^2}}$, ϵ_c and k/ε, at η = 0, with distance downstream of grid

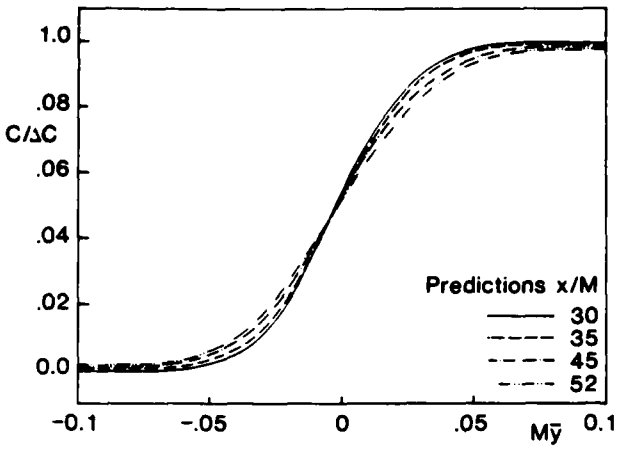

Fig. 4 Development of normalized mean temperature profile in absolute cross-stream distance

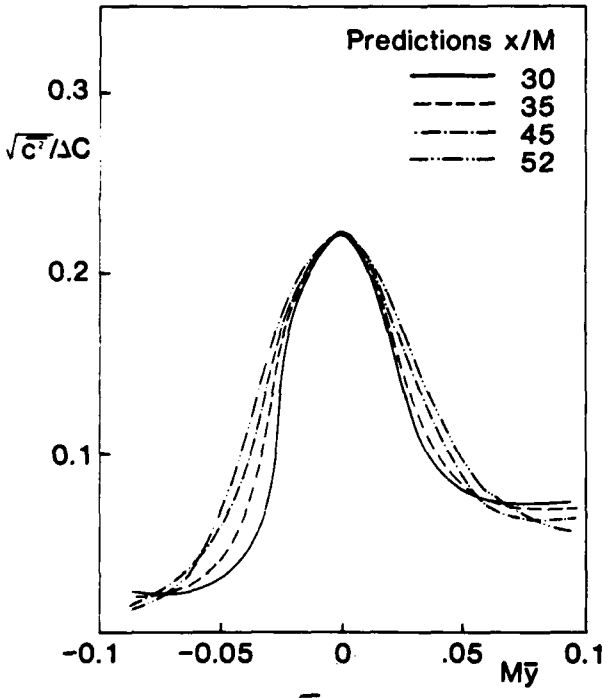

Fig. 5 Development of $\sqrt{\overline{c^2}}/\Delta C$ profile in absolute cross-stream distance

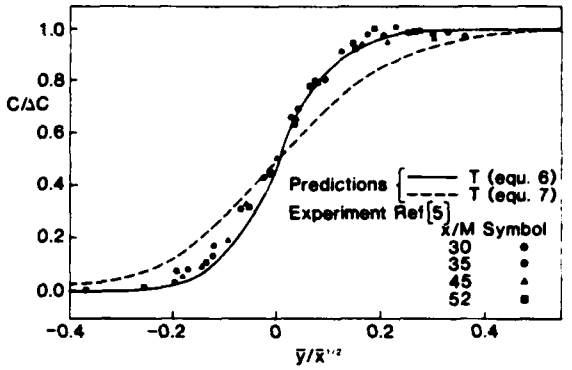

Fig. 6 Normalized mean temperature profile in the similarity coordinate $\bar{y}/\bar{x}^{\frac{1}{2}}$

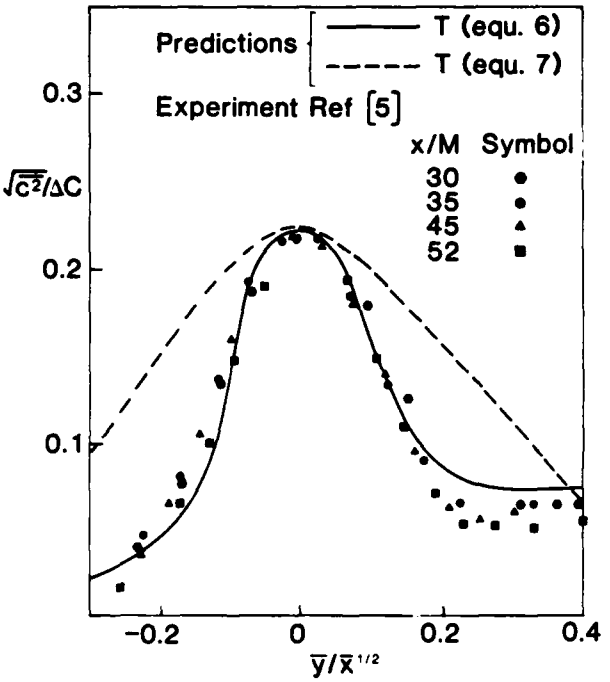

Fig. 7 Normalized rms temperature fluctuation profile in the similarity coordinate $\bar{y}/\bar{x}^{\frac{1}{2}}$

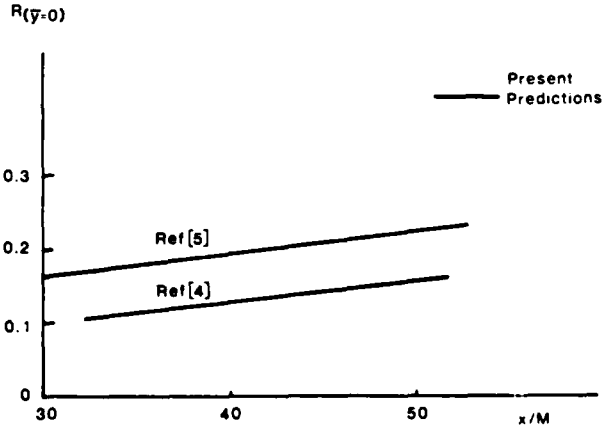

Fig. 8 Development of time-scale-ratio with distance downstream of grid

STRUCTURAL FEATURES OF A UNIFORMLY DISTORTED HEATED PLANE TURBULENT WAKE

J.G. Kawall and J.F. Keffer

Department of Mechanical Engineering
University of Toronto, Toronto, Canada

ABSTRACT

The development of a uniformly distorted, passively heated cylinder-generated wake is investigated experimentally. Characteristic local length and intensity scales for the flow are determined from the experimental data and compared to theoretical expressions derived on the assumption that the uniformly distorted wake is a self-preserving flow. It is found that, although the scales based on mean (streamwise velocity and temperature) profiles and the half-intermittency point length scale are in reasonable agreement with predictions, the scales based on root-mean-square profiles and, in particular, the scale characterizing the lateral extent of the large-scale, intermittent turbulent bulges of the flow deviate from the predicted behaviour, signifying that the distorted wake does not really undergo a truly self-preserving development. Evidence is presented indicating that this lack of self-preservation is the result of amplification, by the distortion field, of coherent structures within the flow. The signatures of these organized motions - which are, in fact, the turbulent bulges - are identified by means of coherence functions and phase spectra.

NOMENCLATURE

- D - cylinder diameter, mm .
- ℓ_o - length scale based on a mean streamwise velocity profile, mm .
- ℓ_o' - length scale based on an RMS streamwise velocity profile, mm .
- ℓ_{o_2} - length scale based on a mean-square streamwise velocity profile, mm .
- $\ell_{\theta'}$ - length scale based on an RMS temperature profile, mm .
- n - frequency, Hz .
- T - local mean temperature, K .
- T_1 - free-stream temperature, K .
- t - time, s .
- U - local mean streamwise velocity, ms^{-1} .
- U_d - mean velocity defect, ms^{-1} .
- U_1 - free-stream velocity, ms^{-1} .
- u' - RMS streamwise velocity, ms^{-1} .
- u_o - intensity scale based on a mean streamwise velocity profile, ms^{-1} .
- u_o' - intensity scale based on an RMS streamwise velocity profile, ms^{-1} .
- u,v - fluctuating velocity components in the x and y directions respectively, ms^{-1} .
- x_s - streamwise distance between the cylinder location and the beginning of the distortion mm .
- x,y,z - Cartesian, streamwise, lateral and spanwise coordinates.
- $\bar{Y}$ - half-intermittency point length scale, mm .
- Γ - coherence function .
- γ - intermittency factor .
- Θ - local mean temperature difference, K .
- θ' - RMS temperature, K .
- θ_o - intensity scale based on a mean temperature profile, K .
- θ_o' - intensity scale based on an RMS temperature profile, K .
- σ - characteristic lateral length of intermittent turbulent bulges, mm .
- ϕ - phase spectrum .

INTRODUCTION

The problem of whether a classical free turbulent shear flow can undergo a simple self-preserving development when a specially aligned strain field is *imposed upon* it has been considered by relatively few investigators, (1), (2), (3), (4). It is, nonetheless, a problem of both practical and intrinsic interest, inasmuch as the reaction of the flow to such a strain field can provide information on the basic structural features of the turbulence.

In the present work, attention is focused upon the spread of a heated cylinder-generated wake subjected to a constant and uniform rate of strain. The strain field was aligned in such a way as to distend the flow in the spanwise direction and simultaneously constrict it laterally - without applying any strain in the streamwise direction. The heat input level was kept sufficiently low so that the temperature could be considered a passive scalar contaminant. Length and intensity scales based upon the lateral distributions of conventional mean and root-mean-square (RMS) streamwise velocities and temperatures and length scales based upon intermittency factor distributions were determined. As well, one point coherence functions and phase spectra of simultaneously-measured streamwise and lateral velocity signals, pertaining to various lateral locations within the vertical centre-plane of the flow, were examined. We note that coherence functions and phase spectra are important statistical tools in the study of turbulent shear flows, as they serve as a means of detecting the presence of coherent structures in such flows, (5), (6), (7), (8).

DESCRIPTION OF THE FLOW

A definition sketch of the flow is shown in Fig. 1. The imposed strain field was effected by means of

a distortion duct with exponentially varying sides and a constant cross-sectional area (see Fig. 2). The flow within such a duct is subjected to a pure strain rate in the cross-stream directions but is not accelerated in the streamwise direction.

It can be shown (9) that if the uniformly strained wake is capable of undergoing a self-preserving development, then, in the plane of symmetry of the flow (z = 0), all characteristic length and intensity scales should be (essentially) directly proportional to exp [-a(x-x_s)/2], where "a" is a positive strain constant for a given distortion duct and "s" pertains to conditions at the entrance to the distortion duct.

DEFINITIONS

The intensity scales based upon the mean and RMS (streamwise velocity and temperature) profiles are given by the center-line values of U_d, U', Θ and Θ'; and the length scales based on these profiles are defined as one-half the distances between the (positive and negative) lateral locations where the various variables assume one-half their center-line values.

The length scales derived from the intermittency factor (γ) profiles are (i) the so-called half-intermittency point, $\bar{Y}$, which is the distance between the center-line of the flow and the lateral location where $\gamma = 0.5$, and (ii) the characteristic lateral extent of the large-scale, intermittent turbulent bulges of the flow, σ. This latter is given by:

$$\sigma^2 = \int_{y_\infty}^{y_o} y\gamma(y)dy - \bar{Y}^2 + y_\infty^2 \quad ,$$

where y_o is the lateral position where γ first attains its maximum value of unity and y_∞, the position at which γ becomes zero.

The one-point coherence function for u(t) and v(t), which describes the coherence or degree of correlation between u(t) and v(t) at frequency n, is defined as:

$$\Gamma_{uv}(n) = \frac{C_{uv}^2(n) + Q_{uv}^2(n)}{E_{uu}(n)E_{vv}(n)} \quad .$$

Here, $C_{uv}(n)$ is the co-spectrum and represents the correlation between in-phase components of u(t) and v(t) at frequency n; $Q_{uv}(n)$ is the quadrature spectrum and represents the correlation between 90° out-of-phase components at frequency n; $E_{uu}(n)$ and $E_{vv}(n)$ are the normalized autospectra of u(t) and v(t) respectively.

The one-point phase spectrum, which describes the phase relationship between the Fourier components of u(t) and v(t) is given by:

$$\phi_{uv}(n) = \tan^{-1}\left[\frac{Q_{uv}(n)}{C_{uv}(n)}\right] \quad .$$

EXPERIMENTAL DETAILS

The wake was generated by a circular heating element (referred to as the cylinder) of diameter, D, equal to 6.6 mm, mounted horizontally in the center of a variable-speed, open-circuit wind tunnel. This tunnel, which is fully described by Kawall (9), has 3 test sections, viz, a pre-strain section, a straining section, similar to the distortion duct described previously, and a post-strain section. The tunnel was operated at a speed, U_1, of about 10 ms^{-1} which resulted in a cylinder Reynolds number of approximately 4200.

The temperature and velocity signals were measured by means of DISA 55 M anemometer systems in conjunction with cold-wire (resistance thermometer), normal hot-wire and X-wire probes. The temperature data were obtained with the cylinder heated to a sufficiently low level so as to ensure that the velocity field was not affected by the temperature filed. The velocity data were obtained with the cylinder unheated in order to simplify the signal processing. All measurements were taken in the vertical center-plane of the tunnel (z = 0) at x/D values of 65, 81, 89, 96, 135, 154, 173, 188 and 212. The first 4 values corresponded to positions within the pre-strain region, the other 5 values, to positions inside the distortion.

The anemometer signals were low-pass filtered and sampled digitally at rates such that the problem of aliasing was effectively eliminated. The digital data were analysed subsequently on a 370-165 digital computer.

RESULTS AND DISCUSSION

The normalized mean profiles for the velocity and temperature fields within the pre-strain and strain regions are indicated in Fig. 3, from which it is clear that these profiles are self-similar. Figures 4 and 5 show the streamwise variations of the mean profile length and intensity scales. The agreement between the measured and predicted variations is seen to be quite good, implying that the mean temperature and streamwise velocity distributions are self-preserving within the distortion.

An inherently more sensitive test for self-preservation of the flow is provided by the behaviour of the RMS quantities. The normalized distributions of RMS streamwise velocites and temperatures are depicted in Figs. 6 and 7. It is apparent that these profiles are not strictly self-similar. Thus, the detailed structure of the distorted wake examined here did not attain the self-preserving state (self-similarity being a necessary condition for self-preservation). Figures 8 and 9 show that, within the distortion, the RMS scales decrease at a rate significantly smaller than that required for self-preservation.

In Fig. 10, RMS streamwise velocity length scales obtained in this study are compared with those found by Reynolds (1) and by Keffer (2) for similar flow situations. (Note that $\hat{r}_o$ in this Figure represents one-half the distance between the half-maximum mean-square velocity points and is, therefore, not equal to r_o'). It can be seen that at all downstream locations, the present scales are larger than those of the other studies. This is probably because x_s and D were, respectively, about 50% and about 40% greater for the present experiments than they were in the case of the Reynolds-Keffer experiments. Yet, the data obtained here and those obtained by Keffer exhibit much the same trends (with respect to the predicted scale behaviour). On the other hand, Reynolds' data and Keffer's data, which were determined under essentially identical experimental conditions are quite different both in trend and in magnitude. We may infer from this that the detailed self-preservation claimed by Reynolds, as revealed by the turbulence (i.e. RMS) quantities, does not really exist for these flows.

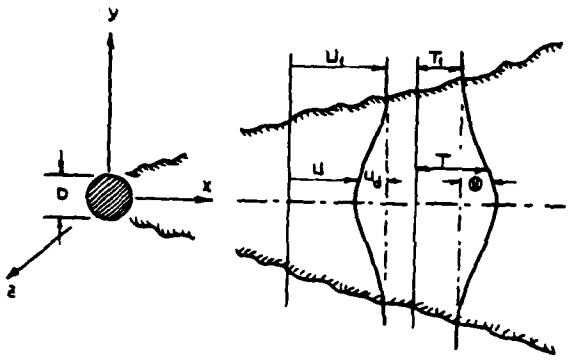

Fig. 1 Definition sketch

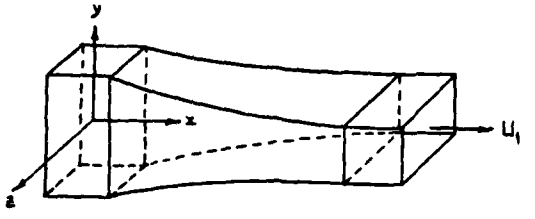

Fig. 2 Schematic diagram of distortion duct

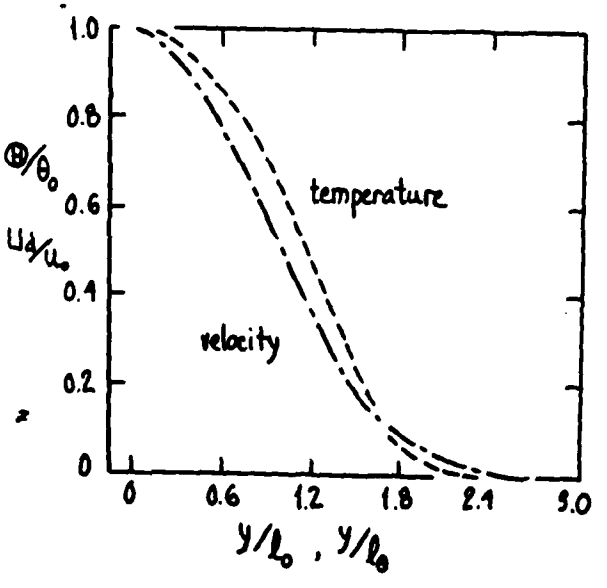

Fig. 3 Normalized mean streamwise velocity and temperature distributions

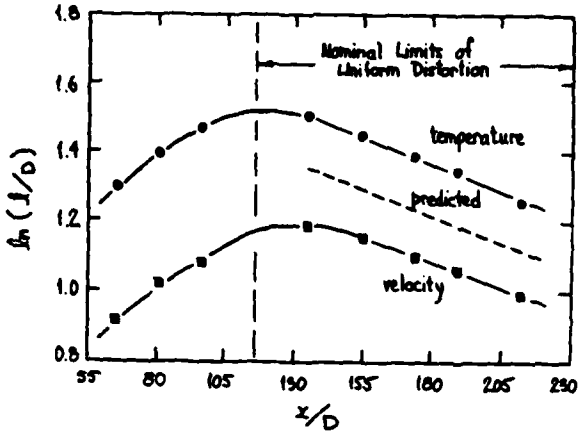

Fig. 4 Mean profile length scales. ■, velocity; ●, temperature; ---, -a/2 slope

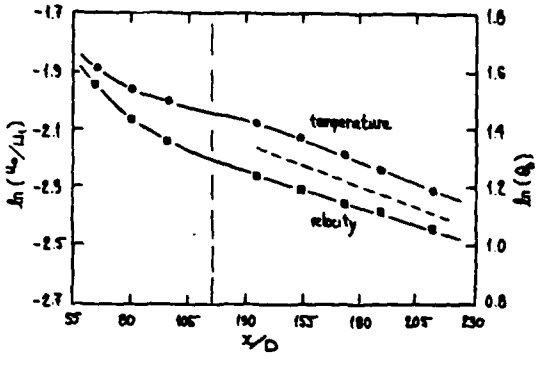

Fig. 5 Mean profile intensity scales. The symbols have the same meaning as in Fig. 4

The normalized intermittency factor profiles were found to be self-similar and well-represented by the Gaussian distribution function (9). The streamwise variations of the lateral length scales ($\bar{Y}$ and σ) that characterize these profiles are presented in Fig. 11. As expected, $\bar{Y}$ (being a measure of the gross width of the flow) conforms well to the "self-preserving" behaviour. In contrast, σ, the characteristic lateral extent of the large-scale, intermittent turbulent bulges, deviates completely from the predicted variation. This behaviour of σ clearly lends support to the view (based on the RMS scale results) that uniformly distorted wakes do not attain a truly self-preserving state.

In Figs. 12 and 13, we present representative one-point uv coherence functions pertaining to the pre-distorted flow and the distorted flow respectively. One notes that these functions exhibit frequency-centred activity, i.e., more or less broad-band peaks, especially in the highly intermittent flow regions (where γ is much less than 0.5). One point uv phase spectra show that there are definite phase differences between the Fourier components of the u and v signals, for the same frequency ranges within which there is significant coherence; for frequencies beyond which the coherence is essentially zero, these phase differences become random. Typical examples of such spectra, pertaining to the distorted wake, are depicted in Fig. 14. A comparison of this latter and Fig. 13 shows that, near the core region of the flow (where $\gamma \simeq 0.99$), the coherence between u and v is due to Fourier components that are essentially 180° out of phase; whereas, in the highly intermittent region ($\gamma \simeq 0.1$), the coherence is due largely to Fourier components that are 90° out of phase, the implication here being that, in this region, the co-spectrum is virtually zero for all frequencies (so that the Reynolds shear stress, $\overline{uv}$, is zero) but the quadrature spectrum is relatively large (i.e., the 90° out-of-phase Fourier components of u and v are relatively highly correlated) over a certain frequency range. We can infer from these phase and coherence results that coherent structures exist within the flow, (5), (6), (7), (8). We thus see that the large-scale bulges are (relatively) highly organized structures, and, as such, they can be amplified by the imposed strain field. It is clearly evident from a comparison of Fig. 12 and Fig. 13 that the bulges become much more organized within the distortion: on the average, the magnitude of the coherence function increases and the frequency-centered activity becomes more localized, i.e., the coherence functions become distinctly more "peaky". This, in conjunction with the behaviour of σ (Fig. 11) leads to the conclusion that the imposed strain field does, indeed, effect an amplification of the bulges - as was originally suggested by Keffer (2). And it is for this reason that the uniformly distorted wake fails, in practice, to undergo the predicted self-preserving development. It should be pointed here that Keffer (2) had speculated that the turbulent bulges occurred in a periodic fashion. But, the results of Kawall and Keffer, (10), (11), concerning the motion of the turbulent/non-turbulent interface, have established that these coherent structures arise randomly within both the undistorted wake and the uniformly distorted wake.

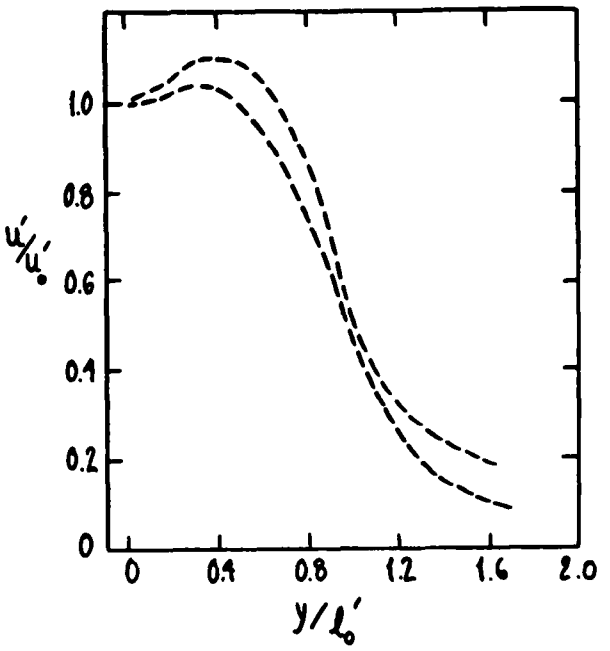

Fig. 6 Normalized RMS streamwise velocity distributions

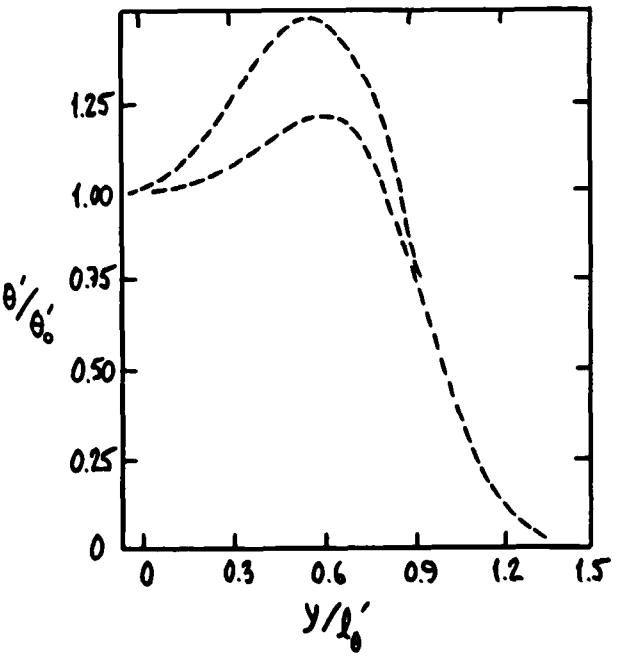

Fig. 7 Normalized RMS temperature distributions

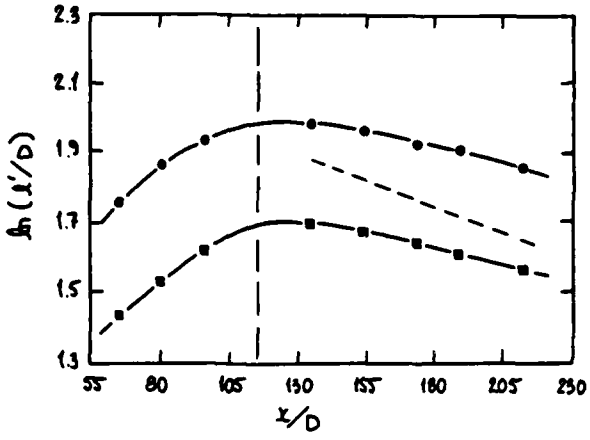

Fig. 8 RMS profile length scales. The symbols have the same meaning as in Fig. 4

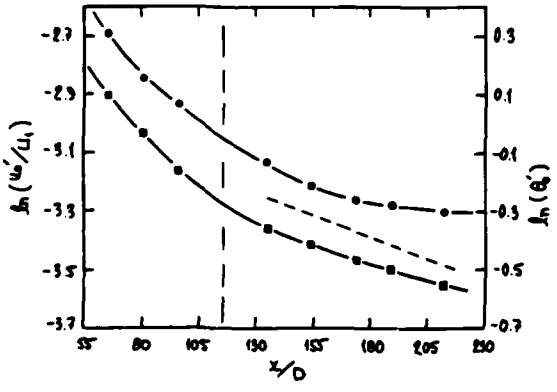

Fig. 9 RMS profile intensity scales. The symbols have the same meaning as in Fig. 4

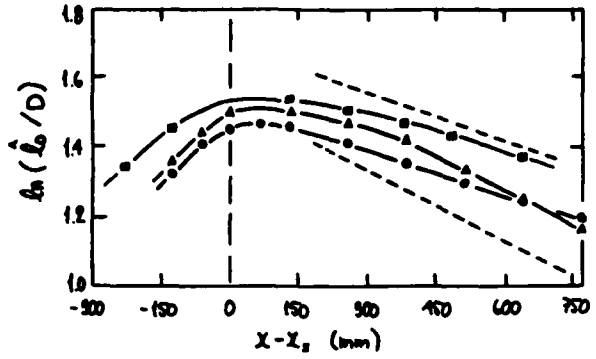

Fig. 10 Comparison of length scales based on mean-square streamwise velocity profiles. ■, present results; ●, Keffer (2); ▲, Reynolds (1); ---, -a/2 slope

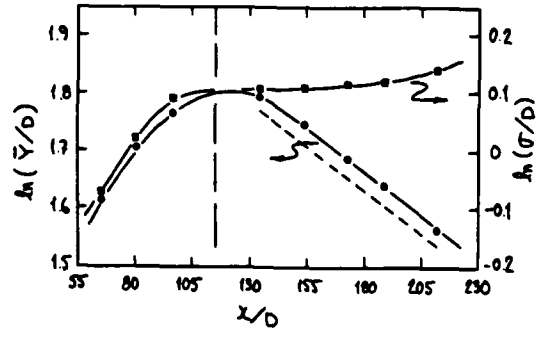

Fig. 11 Length scales based on intermittency factor distributions

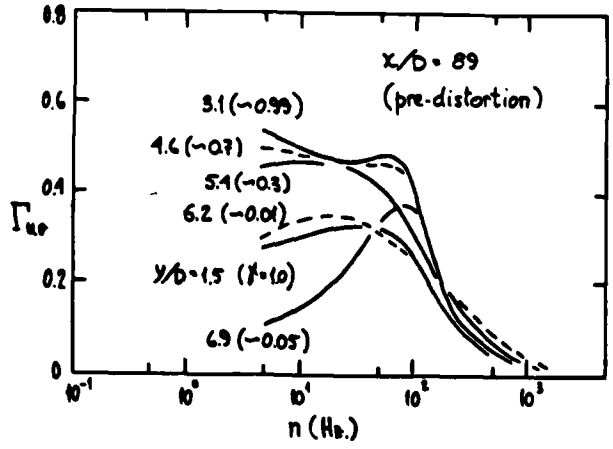

Fig. 12 One-point uv coherence functions

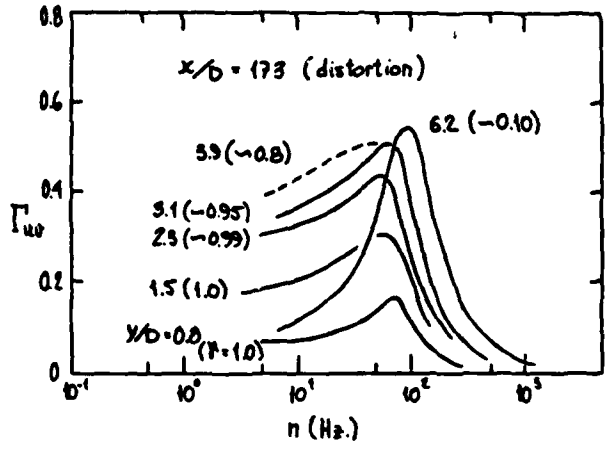

Fig. 13 One-point uv coherence functions

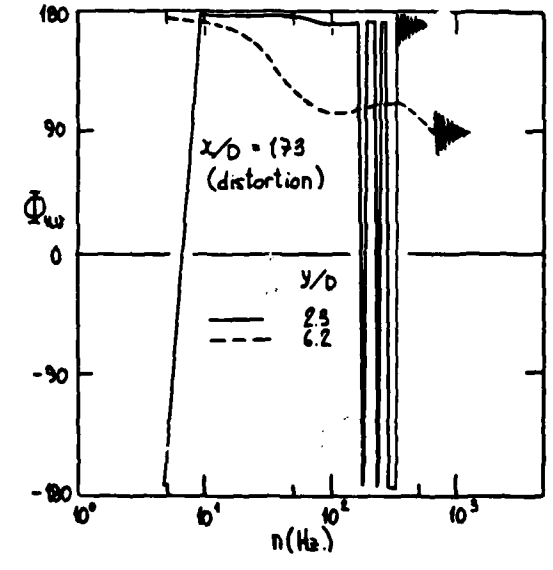

Fig. 14 One-point uv phase spectra

ACKNOWLEDGEMENT

This work was supported by the Natural Sciences and Engineering Research Council of Canada through Grant A-2746.

REFERENCES

1 Reynolds, A.J., "Observations on distorted turbulent wakes," Journal of Fluid Mechanics, Vol. 13, 1962, pp. 333-355.

2 Keffer, J.F., "The uniform distortion of a turbulent wake," Journal of Fluid Mechanics, Vol. 22, 1965, pp. 135-159.

3 Keffer, J.F., "A note on the expansion of turbulent wakes," Journal of Fluid Mechanics, Vol. 28, 1967, pp. 183-193.

4 Keffer, J.F., Kawall, J.G., Hunt, J.C.R. and Maxey, M.R., "The uniform distortion of thermal and velocity mixing layers," Journal of Fluid Mechanics, Vol. 86, 1978, pp. 465-490.

5 Budny, R.S., Kawall, J.G. and Keffer, J.F., "Vortex street evolution in the wake of a circular cylinder," 2nd Symposium on Turbulent Shear Flows, Imperial College, London, 1979.

6 Keffer, J.F., Kawall, J.G., Giralt, F. and Béguier, C., "Analysis of turbulent structures in complex shear flows," 2nd Symposium on Turbulent Shear Flows, Imperial College, London, 1979.

7 Keffer, J.F. and Kawall, J.G., "Structural features of plane turbulent shear flows," AIAA 13th Fluid and Plasma Dynamics Conference, Snowmass, Colorado, 1980.

8 Keffer, J.F., Kawall, J.G., Giralt, F. and Béguier, C., "Characteristics of coherent structures in complex turbulent shear flows," Heat and Mass Transfer and the Structure of Turbulence Joint Symposium, Dubrovnik, Yugoslavia, 1980.

9 Kawall, J.G., "Statistical properties of a slightly heated uniformly distorted plane turbulent wake," Ph.D. Thesis, 1975, University of Toronto.

10 Kawall, J.G. and Keffer, J.F. "Uniform distortion of a heated turbulent wake," Lecture Notes in Physics, Vol. 76, Springer-Verlag, Berlin, Heidelberg, New York, 1978, pp. 85-100.

11 Kawall, J.G. and Keffer, J.F., "Interface statistics of a uniformly distorted heated turbulent wake," The Physics of Fluids, Vol. 22, 1979, pp. 31-39.

THEORETICAL AND EXPERIMENTAL DETERMINATION OF THE TURBULENT DIFFUSIVITY TENSOR IN HOMOGENEOUS TURBULENT SHEAR FLOW

S. Tavoularis
Department of Mechanical Engineering, University of Ottawa, Ottawa, Ontario K1N 6N5, Canada

S. Corrsin
Department of Chemical Engineering, Johns Hopkins University, Baltimore, MD 21218, U.S.A.

ABSTRACT

Earlier measurements of some components of the turbulent diffusivity tensor D_{ij} in a nearly homogeneous turbulent shear flow with constant mean temperature gradient parallel to the mean shear are now supplemented with measurements of additional components in the same flow but with mean temperature gradient perpendicular to both mean velocity and mean shear. A Lagrangian analysis provides expressions for all components of D_{ij} and comfirms the expectation that D_{ij} is non-diagonal and non-symmetric. The available data agree well with the theoretical estimates. Independent estimates of D_{ij}, based on a numerical simulation of homogeneous shear flow as well as on a rapid distortion type analysis, are also reported.

NOMENCLATURE

D_{ij} turbulent diffusivity tensor

M_{ij} Lagrangian velocity correlation moment

$\overline{T}$ mean temperature rise

T_{ij} Lagrangian velocity integral time scale

T_{il}^{*} quasi-Lagrangian velocity integral time scale

$\overline{U}_i$ mean velocity

u_i Eulerian velocity fluctuation

v_i Lagrangian velocity fluctuation

v_i^{*} quasi-Lagrangian velocity fluctuation

x_i Cartesian axis; $i = 1$ is the streamwise direction, $i = 2$ is the direction of mean shear

X_i fluid point position in Lagrangian coordinates
$X_i = X_i(\underset{\sim}{X}_o, t)$

X_{o_i} Lagrangian coordinate

θ temperature fluctuation

Suffixes

$()'$ root-mean-square value

$\overline{()}$ time-averaged quantity

$\underset{\sim}{()}$ vector quantity

INTRODUCTION

The most widely used approximations in the modeling of turbulent heat transport are based on the assumption that the turbulent heat flux, $-\overline{\theta u_i}$ and the mean temperature gradient $\partial\overline{T}/\partial x_i$ are proportional. It has long been known that such a relationship is often wrong in principle, yet can be a useful hypothesis in practice (e.g. Corrsin, 1974). Even a simple scalar proportionality coefficient ("turbulent diffusivity" or "eddy diffusivity") has sometimes been successful in rough predictions of the mean temperature field in some shear flows, but it has been found inadequate for the general modeling of non-isotropic turbulence. The appropriate form of the diffusivity concept, if it is to be used, is a second-rank "turbulent diffusivity tensor", D_{ij} (Batchelor, 1949), defined by

$$-\overline{\theta u_i} \equiv D_{ij}\frac{\partial\overline{T}}{\partial x_j} \qquad (1)$$

As a specially simple example of the detailed determination of the components of D_{ij} we consider a homogeneous turbulent shear flow, e.g. a flow with a constant mean velocity gradient $d\overline{U}_1/dx_2$, and transversely constant turbulent stresses $-\overline{u_i u_j}$.

and velocity integral scales. This flow retains many of the crucial features of more complex common turbulent shear flows while allowing a relatively simple analytical representation and eliminating boundary effects. We shall present measurements of some D_{ij} components in such a flow, as well as estimates based on analytical, numerical and semi-empirical results.

More sophisticated analytical models of scalar transport have recently been reviewed by Launder (1978).

MEASUREMENTS OF CERTAIN COMPONENTS

The nearly-homogeneous turbulent shear flow achieved in the wind tunnel experiments of Harris, Graham and Corrsin (1977) and of Tavoularis and Corrsin (1981) presents a mean shear sufficiently large to allow the attainment of an asymptotic (though evolving) state over an appreciable part of the test section, corresponding to non-dimensional total strains $(x_1/\bar{U}_1)\, d\bar{U}_1/dx_2$ in the range 4.5 to 12.5. In these experiments, the (typically anisotropic) turbulent velocities and the integral scales increased monotonically downstream, but both preserved a reasonable transverse homogeneity over a central core much larger then the integral scales. The shear-stress correlation coefficient was roughly constant, $\overline{u_1u_2}/(u_1'u_2') \approx -.45$. This flow (occasionally with minor variations) will be considered in the following.

The direct measurement of all D_{ij} components would require the generation of mean temperature gradients in all three directions, $x_i = x_1, x_2, x_3$. In the case with $\partial\bar{T}/\partial x_2 \approx$ constant $\neq 0$, and $\partial\bar{T}/\partial x_1 \approx \partial\bar{T}/\partial x_3 \approx 0$ (Tavoularis and Corrsin, 1981), it was found that, like the velocity fluctuations, the temperature fluctuations seemed to be approaching an asymptotic state, with mean squared values and their integral scales monotonically increasing downstream. The two non-zero heat flux correlation coefficients $\overline{\theta u_1}/(\theta' u_1')$ and $\overline{\theta u_2}/(\theta' u_2')$ were roughly 0.56 and -0.44 respectively. The third component of the heat flux vector, ideally zero by symmetry if the fields were perfectly generated, had the negligible normalized value of $|\overline{\theta u_3}|/(\theta' u_3') < .02$. The two non-zero correlation values give two components of the diffusivity tensor D_{12} and D_{22}. It turned out that $D_{12} \approx -2.2\, D_{22}$ $(D_{22} > 0)$, which is roughly the same as the empirical relationship estimated by Yaglom (1969) and Corrsin (1974) from atmospheric and laboratory boundary layer data respectively.

New experiments have now been conducted in the same flow field, but with the mean temperature gradient normal to the mean velocity gradient: $\partial\bar{T}/\partial x_3 \approx$ const. > 0, and $\partial\bar{T}/\partial x_1 \approx \partial\bar{T}/\partial x_2 \approx 0$. The degree of transverse homogeneity achieved was not as good as that in the previous case, but seems adequate. The mean square temperature fluctuation again increases monotonically downstream. The only significant non-zero heat flux correlation co-efficient was $\overline{\theta u_3}/(\theta' u_3') \approx -.45$. The other two components, which should have been zero by symmetry if the fields had been perfectly generated, had appreciably smaller coefficients: $|\overline{\theta u_1}|/(\theta' u_1')$ and $|\overline{\theta u_2}|/(\theta' u_2')$ were $O(0.05)$. The new turbulent diffusivity component evaluated was $D_{33} \approx 1.6\, D_{22}$.

In conclusion, the existing direct measurements of D_{ij} components were

$$[D_{ij}] \approx \begin{bmatrix} \cdots & -2.2 & 0 \\ \cdots & 1.0 & 0 \\ \cdots & 0 & 1.6 \end{bmatrix} D_{22}, \quad (2)$$

where D_{22} is factored out in order to emphasize ratios.

Efforts are under way to create in the same flow field a mean temperature field which, at least locally, will have

$$|\partial\bar{T}/\partial x_1| \gg |\partial\bar{T}/\partial x_2|, |\partial\bar{T}/\partial x_3|$$

This would allow direct evaluation of the remaining three components of D_{ij}.

A THEORETICAL EXPRESSION

A quasi-Lagrangian analysis of fluid point dispersion in stationary, homogeneous, turbulent shear flow (Corrsin, 1953, 1959), was exploited by Riley and Corrsin (1975) to estimate D_{11}, D_{22}, D_{33}, and $D_{12} + D_{21}$. A slightly different application of the same viewpoint allows estimation of the individual off-diagonal components, thus emphasizing the non-symmetry of D_{ij}. The heat flux vector can be expressed as

$$-\overline{\theta u_i} = \frac{\partial\bar{T}}{\partial x_j}\left[\int_0^t \overline{v_i(0)v_j^*(\tau)}\, d\tau + \delta_{j1}\frac{d\bar{U}_i}{dx_2}\int_0^t \tau\, \overline{v_i(0)v_2(\tau)}\, d\tau\right], \quad (3)$$

where v_i is the Lagrangian velocity fluctuation and the quasi-Lagrangian velocity fluctuation v_i^* is defined as

$$v_i^*(\underset{\sim}{X}_0, t) \equiv V_i(\underset{\sim}{X}_0, t) - \frac{d\bar{U}_i}{dx_2}\left[X_2(\underset{\sim}{X}_0, t) - X_{02}\right]\delta_{i1} \quad (4)$$

For large times, the resulting asymptotic expression for D_{ij} is

$$[D_{ij}] = \begin{bmatrix} \overline{v_1v_1^*}\,T_{11}^* + \overline{v_1v_2}\,M_{12}\frac{d\bar{U}_1}{dx_2} & \overline{v_1v_2}\,T_{12} & 0 \\ \overline{v_2v_1^*}\,T_{21}^* + \overline{v_2^2}\,M_{22}\frac{d\bar{U}_1}{dx_2} & \overline{v_2^2}\,T_{22} & 0 \\ 0 & 0 & \overline{v_3^2}\,T_{33} \end{bmatrix}, \quad (5)$$

with T_{ij} being the Lagrangian integral time scales, M_{ij} the Lagrangian correlation moments and T_{i1}^* defined as

$$T_{i1} \equiv \frac{1}{\overline{v_i v_1^*}}\int_0^\infty \overline{v_i(0)\, v_1^*(\tau)}\, d\tau \quad (6)$$

Obviously, expression (5) is in general non-diagonal and non-symmetric.

VARIOUS ESTIMATES

Equation (5) is a theoretical result for the impossible case of homogeneous, stationary shear flow. Further, the Lagrangian and quasi-Lagrangian quantities in (5) have not been measured in the nearly homogeneous shear flow described above. Nevertheless, it seems worthwhile to test (5) crudely by invoking connections, both exact and speculative, with Eulerian quantities. Lumley (1957) has shown that in homogeneous turbulence Lagrangian and Eulerian one-point moments are equal; thus $\overline{v_2^2}$ and $\overline{v_3^2}$ can be replaced by Eulerian

data. Next, we speculate that the statistical properties of v_i^* are the same as in its original Eulerian coordinates, and finally we assume that the T's and M's can be approximated by their Eulerian counterparts in a frame travelling with the mean flow.

With experimental Eulerian data inserted, we get the theoretical estimates

$$[D_{ij}] \approx \begin{bmatrix} (5.7-13.0) & -2.9 & 0 \\ -2.9+1.3 & 1.0 & 0 \\ 0 & 0 & 1.5 \end{bmatrix} D_{22} \quad . \quad (7)$$

D_{11}/D_{22} is bracketed because the net negative value seems physically unlikely; we shall discuss this point further in the next section. The second and third columns are in reasonable agreement with the direct measurements, equation (2). Also D_{12}/D_{21} is not too far from its estimate of 2.0 by Gee and Davies (1964).

Another test of the theoretical estimates in equation (5) can be made by appeal to a crude simulation of homogeneous turbulent shear flow outlined by Riley and Corrsin (1971; details given by Riley, 1971). The direct "experimental" values are

$$[D_{ij}] \approx \begin{bmatrix} 1.9 & \cdots & 0 \\ \cdots & 1.0 & 0 \\ 0 & 0 & 1.2 \end{bmatrix} D_{22} \quad . \quad (8)$$

$D_{12}+D_{21} \approx -0.9\ D_{22}$, but the separate values were not computed. For comparison with (8), we can estimate the asymptotic theoretical terms of equation (5), using the appropriate Lagrangian and quasi-Lagrangian values determined from the simulation:

$$[D_{ij}] \approx \begin{bmatrix} 2.4-0.7 & -0.7 & 0 \\ -0.9+0.5 & 1.0 & 0 \\ 0 & 0 & 1.2 \end{bmatrix} D_{22} \quad . \quad (9)$$

There is good agreement between (8) and (9). Also, $D_{12}+D_{21} \approx -1.1\ D_{22}$ in (9), not far from the "experimental" value.

Finally, independent estimates of D_{ij} components can be based on a rapid distortion type analysis by Kozlov and Sabel'nikov (1977). Isotropic turbulence is subjected to uniform shear rapidly enough for the non-linear interactions to be neglected. The resulting diffusivity ratios do not demonstrate any asymptotic trends in the reported range. D_{33}/D_{22} exceeds 13 at the higest total strain, while D_{11}/D_{22} increases slightly from the isotropic value 1.0 to a maximum of about 1.4, then it decreases monotonically with a value -2.5 at the highest total strain. The ratios D_{12}/D_{22} and D_{21}/D_{22} (assumed to be equal) decrease monotonically from the isotropic value 10.

DISCUSSIONS AND CONCLUSIONS

A re-evaluation and comparison of the results represented earlier appears necessary. The existing measurements (equation 2), which however do not include the D_{i1} components, are in fair agreement with the theoretical estimates (equation 7). Similarly, the "experimental" values in a numerical simulation (equation 8) are close to the corresponding estimates (equation 9). These two results support the validity of the theoretical expression (5). The components of D_{ij} in the numerical simulation demonstrate qualitative similarities with the experimental ones, but the individual values are different. Recalling that the simulation corresponds to a flow (Champagne, et al., 1970) with mean shear about one third of that in the present experiment, it appears that the diffusivity ratios, like the principal stress axes, depend on the total strain imposed on the turbulence. More specifically, the present results support the speculation that the low-shear values of D_{ij} should be closer to the isotropic ones than are those in the high-shear case.

A negative value of D_{11} (equation 7) appears at first glance to be contrary to the intuitive notion of diffusivity. However, although errors resulting from extensive extrapolation used in the M_{12} estimate and from the appreciable downstream inhomogeneity over a T_{12} time scale may be significant in the present D_{11} estimate, the rapid distortion analysis also predicts a negative D_{11}. An explanation can be provided by the theoretical expression (5). Approximating the velocity autocovariances by exponential functions and replacing Lagrangian and quasi-Lagrangian velocities with Eulerian ones, (5) is simplified into

$$[D_{ij}] \approx \begin{bmatrix} \overline{u_1^2}T_{11} + \left(\overline{u_1u_2}T_{12}\right)\left(T_{12}\frac{d\bar{U}_1}{dx_2}\right) & \overline{u_1u_2}T_{12} & 0 \\ \overline{u_1u_2}T_{12} + \left(\overline{u_2^2}T_{22}\right)\left(T_{22}\frac{d\bar{U}_1}{dx_2}\right) & \overline{u_2^2}T_{22} & 0 \\ 0 & 0 & \overline{u_3^2}T_{33} \end{bmatrix} . \quad (10)$$

Since the relative magnitudes of turbulent stresses and of integral scales in different directions are only weak functions of mean shear, it seems plausible that, for large enough $d\bar{U}_1/dx_2$, the (negative) second term in D_{11} may have magnitude larger than the first term.

Another consequence of (10) is that the degree of asymmetry of D_{ij}, expressed as the ratio D_{12}/D_{21}, is also a function of mean shear. Although not observed in the present study, it even appears possible that, for large enough $d\bar{U}_1/dx_2$, D_{12} may become positive, while D_{21} will always remain negative.

The present estimates apply mainly to a hypothetical homogeneous turbulence with a uniform mean shear, but the results should also be applicable to the wider class of nearly parallel flows with small transverse inhomogeneities and slowly variable mean gradients. For example, (Tavoularis and Corrsin, 1981) the ratio D_{12}/D_{22} was roughly the same in the nearly homogeneous turbulent shear flow, in a

turbulent boundary layer at one momentum thickness distance from the wall, and in a turbulent pipe flow at half the radius distance from the axis.

This work was supported primarily by the National Science Foundation, Program on Atmospheric Sciences.

REFERENCES

1. Batchelor, G.K., Austral. J. Sci. Res., Vol. A2, 1949, p. 437.
2. Champagne, F.H., Harris, V.G. and Corrsin, S., J. Fluid Mech., Vol. 41, 1970, p. 81.
3. Corrsin, S., Proc. Iowa Thermodynamics Sympos., Univ. of Iowa, Iowa City, 1953, p. 5.
4. Corrsin, S., Advan. Geophys., Vol. 6, 1959, Academic Press, p.161.
5. Corrsin, S., Advan. Geophys., Vol. 18, 1974, Academic Press, p. 25.
6. Gee, J.H. and Davies, D.R., Quart. J. Roy. Met. Soc., Vol. 90, 1964, p. 478.
7. Harris, V.G., Graham, J.A.H., and Corrsin, S., J. Fluid Mech., Vol. 81, 1977, p. 657.
8. Kozlov, V.E. and Sabel'nikov, V.A., Fluid Dynamics, Vol. 12, 1977, p. 940.
9. Launder, B.E., Turbulence (ed. by P. Bradshaw), Top. in Appl. Phys., Vol. 12, 1978, Springer-Verlag, p. 231.
10. Lumley, J.L., PhD Thesis, Johns Hopkins University, Baltimore, 1957.
11. Riley, J.J., PhD Thesis, Johns Hopkins University, Baltimore, 1971.
12. Riley, J.J. and Corrsin, S., Proc. Conf. on Air Pollution Meteorology, Amer. Meteorol. Soc., 1971, p. 16.
13. Riley, J.J. and Corrsin, S., J. Geophys. Res., Vol. 79, 1975, p. 1768.
14. Tavoularis, S. and Corrsin, S., J. Fluid Mech., Vol. 104, 1981, p. 311.
15. Yaglom, A.M., Fluid Dynamics Transactions, Vol. 4, Inst. Fundam. Tech. Res., Polish Acad. Sci., Warsaw, 1969, p. 801.

TURBULENT TRANSPORT IN PASSIVELY HEATED HOMOGENEOUS AND INHOMOGENEOUS FLOWS

K.R. Sreenivasan
Applied Mechanics, Mason Laboratory, Yale University, New Haven, CT 06520

S. Tavoularis
Mechanical Engineering Dept., University of Ottawa, Canada K1N 6N5

and

S. Corrsin
Chemical Engineering Dept., Johns Hopkins University, Baltimore, MD 21218

ABSTRACT

Heat flux measurements in several specially designed turbulent flows with inhomogeneous temperature field are presented and analyzed with the purpose of evaluating the performance of the gradient transport models (GTM) as well as several of the generalizations. One of the flows considered is a uniform grid-generated flow; two others are shear flows with transverse homogeneity and a constant mean velocity gradient. The fourth is the wake of a circular cylinder in which an asymmetric temperature field is created by heating a combination of thin wires located off-axis. A GTM with a constant turbulent diffusivity adequately describes the turbulent heat flux in all three homogeneous flows, while in the inhomogeneous flow, forcing gradient transport to the measured heat flux results in negative diffusivity over a part of the flow. Direct evaluation from the present and other measurements shows that none of the generalizations of the GTM is adequate. It is suggested that the large eddy transport in inhomogeneous shear flows is the possible cause for the failure of the GTMS, and that its apparent success in symmetrically heated free shear flows is largely due to the imposed boundary conditions.

NOMENCLATURE

d = diameter of the cylinder
D = turbulent diffusivity
h = height of the wind-tunnel test section
L_θ = half the distance between half-maximum θ' points
L_f = longitudinal integral length scale
L_g = transverse integral length scale
L_θ = half the distance between $T_{max}/2$ points
M = mesh size of the grid
q' = $(\overline{u_i u_i})^{1/2}$
T = mean temperature rise above the ambient
u_i = velocity fluctuation in the direction i
U_i = mean velocity in the direction i
V_c = characteristic bulk convection velocity
w = wake defect velocity
x_i = coordinate axes; i=1 is along the flow and i=2 is along the direction of maximum shear.
θ = temperature fluctuation

Suffixes

o = centerline value
max = maximum value
$'$ = root-mean-square value

INTRODUCTION

Virtually all the "classical turbulent theories" model turbulent transport of momentum, heat or a passive contaminant by linear mean gradient models. This hypothesis, probably attributable to de St. Venant or to Boussinesq, has appeared in different forms - usually incorporating an ad hoc estimate of the proportionality coefficient, the "eddy viscosity" or "eddy diffusivity" (for example, (1,2)).

In spite of the enormous development in turbulence modeling witnessed over the last two decades, the simplicity of the gradient transport models (GTM) - often with enough adjustable parameters - appears to be responsible for their persistent use in some areas of engineering practice, especially in meterology and oceanography. Among other things, gradient transport models require that the characteristic scale of the turbulent transporting mechanism must be small compared with the dimension characteristic of the inhomogeneity of the mean transported quantity. It has been pointed out many times (3-5) that nearly all turbulent flows violate this basic *a priori* requirement, and yet a reasonable degree of success has been claimed for the gradient transport models, especially in free shear flows. Therefore, a study directed towards determining the reasons for this (apparent) success of the GTMs appeared to be worthwhile; this is one of the goals of the present study.

Several instances can now be quoted which, over the years, have demonstrated the inadequacies of the GTMs (6-15). Mindful of these inadequacies to turbulence, several formal generalizations have been proposed (5, 16-18). Alternatively, it has been thought that formal generalizations do not address themselves to the heart of the problem, and so some *ad hoc* 'corrections' - which could even be drastic - have also been proposed, for example (19). However, the validity of any of these models in more than one situation remains to be tested. This is the second purpose of the present study. For this purpose, we designed several simple experimental configurations in some of which simple gradient transport models worked well but in some of the others did not. Presentation of the experimental data in these flows - with a possible relevance to turbulence modeling and the computation of complex turbulent flows forms yet another purpose of our paper.

FLOW CONFIGURATION

Figure 1 shows a schematic representation of the experimental configurations used here. The wind tunnel was of the open-return type with a nominal test section 30 cm x 30 cm, and about 3.65 m long. Air

flow was created by two axial fans in tandem. An essentially constant pressure field was created by adjusting the vertical walls.

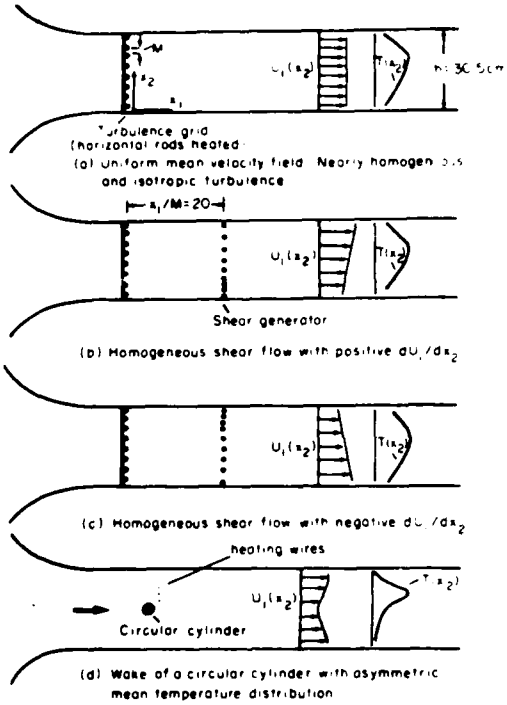

Fig. 1. Schematic of experimental set-up

Three homogeneous flows and one inhomogeneous shear flow were studied. One of the homogeneous flows was the uniform flow produced behind a square-mesh biplane cylindrical-rod grid with 2.54 cm mesh and solidity 0.36. The mean velocity was nominally uniform across the test section. The temperature field was created by electrically heating each of the horizontal rods of the grid separately, so that the desired inhomogeneous mean temperature field could be created (Figure 1a).

The two other homogeneous flows with nominally uniform positive or negative mean velocity gradient were created by placing a shear generator 20 mesh sizes downstream of the turbulence-generating grid (see Figures 1b and 1c). The shear generator is an array of horizontal non-uniformly spaced cylindrical rods (20) and could be inserted in the tunnel such that dU_1/dx_2 could be positive (Figure 1b) or negative (Figure 1c). The temperature field was created exactly as in the uniform flow case.

Lastly, the inhomogeneous shear flow studied here is the wake of a circular cylinder (d = 1.1 cm) in which the temperature field was produced by heating three thin parallel wires (diameter 0.127 mm) mounted asymmetrically with respect to the cylinder on a wooden frame which could be inserted (see Figure 1d) at any of the three locations (x_1/d = 1.2, 2.3, and 46) downstream of the cylinder. Also, the spacing between the wires, their transverse location with respect to the cylinder and the heating current in each of the wires could be adjusted independently to obtain within limits any desired mean temperature distribution.

INSTRUMENTATION

Mean velocity U_{1c} along the tunnel centerline was measured with a pitot-static tube. The mean velocity profile $U_1(x_2)$ and the velocity fluctuations u_1 and u_2 were measured with a DISA 55P51 gold-plated X-wire probe, with sensing elements 5 μm in diameter and 1.25 mm in length, powered by two DISA 55D01 constant temperature anemometers; D.C. power supplies were used to minimize the noise level. The mean temperature profile $T(x_2)$ and the reference temperature upstream of the grid were measured with two Fenwall Electronics GC32M21 thermistor probes. The temperature fluctuation θ was measured with a DISA 55P31 platinum wire probe with the wire length of 0.4 mm and diameter 1 μm. The temperature wire was positioned vertically at a distance of about 0.5 mm from the nearest wire of the X-wire probe, and was operated at a constant current of 0.3 mA on a home-made constant current source (21). The operating current was low enough to render the velocity sensitivity of the temperature wire negligible. The temperature contamination of the velocity signals was eliminated by correcting them with the instantaneous local temperature measured with the temperature wire (22). The vertical position of the probes was adjusted with a variable speed motor and a gear mechanism.

All signals were amplified and low-pass filtered at an upper cut-off frequency of 5 kHz. The signals were also corrected for noise assuming that the noise was statistically independent of the signal. The signals were digitized and processed on a DEC PDP 11/40 digital computer.

RESULTS IN HOMOGENEOUS FLOWS

Mean Velocity and Mean Temperature Distributions

Measurements were made at x_1/M = 60 and 128 but, in most cases, only those made at x_1/M = 60 are reported here. In all the cases, there was a significant region of two-dimensionality in the mean quantities.

Figure 2 shows the distribution of mean velocity and mean temperature rise for the three homogeneous flows. For the uniform flow experiment, the mean velocity was uniform across the test section to within about 2% of the centerline velocity of 17.2 m sec^{-1}. The grid mesh Reynolds number was about 29100. The two other flows had roughly linearly varying mean velocity profiles (except for the last point in each case on the low velocity side). The centerline velocity U_{1_0} in both cases was 16.0 m sec^{-1}, and $|dU_1/dx_2|$ was 17.9 m sec^{-1}.

In all three cases, the mean temperature distributions were quite similar. The maximum mean temperature rise of 2.7°C was low enough to consider heat as a passive scalar. This was also verified by noting that the measured root-mean-square velocity intensities with and without heating were essentially the same. A measure of the inhomogeneity of the temperature field is given by the parameter $(dT/dx_2)\, L_g/T_{max}$. In the present experiments, this parameter was estimated to be as high as 0.5, signifying a sizeable inhomogeneity.

Root-Mean-Square Intensities

Figure 3 shows the transverse distribution of the normalized root-mean-square velocity fluctuations in the central two-thirds of the tunnel height. For the uniform grid flow, both u_1' and u_2' are uniform

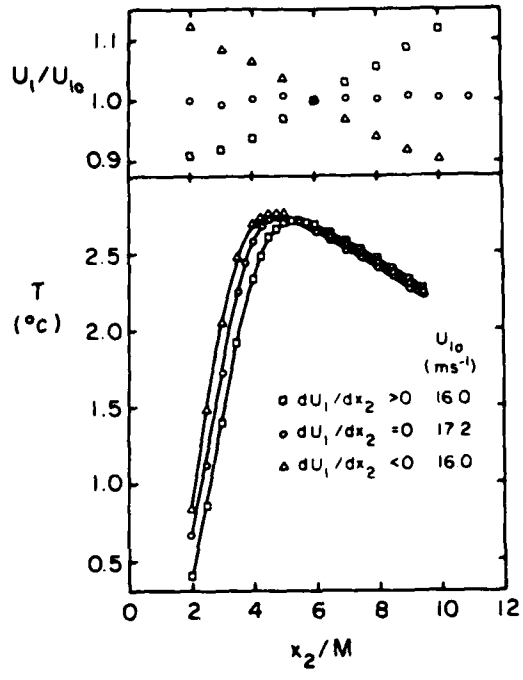

Fig. 2. Transverse distributions of mean velocity and mean temperature rise

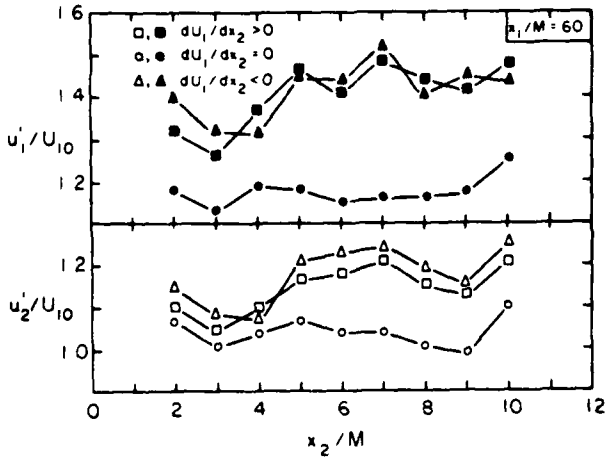

Fig. 3. Transverse variation of turbulence intensities

to within ±5%. The ratio $u_1'/u_2' = 1.15$, quite comparable to that in other similar flows (23). For the shear flows, on the other hand, there is a ±12% variation in u_1'/U_{10} and about ±8% variation in u_2'/U_{10}. For the present purposes, these distributions are considered sufficiently homogeneous in the transverse direction. On the average, $u_1'/u_2' = 1.23$. At $x_1/M = 128$, the turbulence intensity distributions are homogeneous to a somewhat better accuracy. Figure 4 shows the transverse distribution of the normalized root-mean-square temperature fluctuation.

Heat Transport in the x_2-Direction

Figure 5 is a plot of $\overline{u_2\theta}$ against the corresponding local values of dT/dx_2. Data are presented

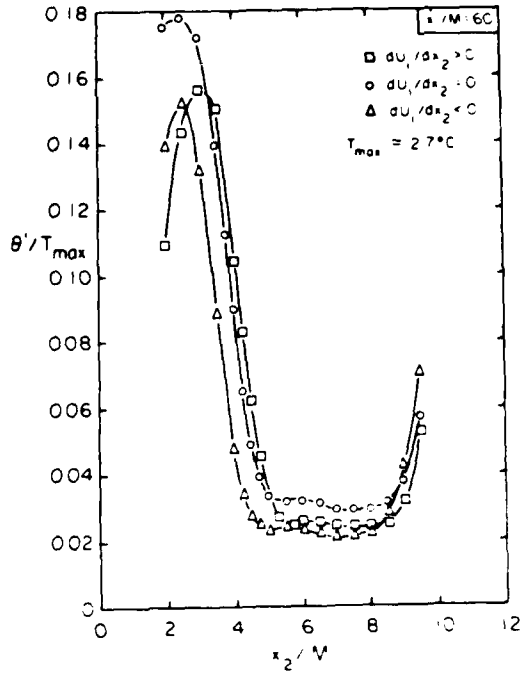

Fig. 4. Transverse variation of the root-mean-square temperature fluctuation

for x_1/M=60 and 128. A 6th order polynomial was fitted to the measured mean temperature distribution to obtain dT/dx_2. The estimated error bounds for both quantities are shown in the figure. It is clear that in all three cases $\overline{u_2\theta}$ is zero when dT/dx_2 is zero, and a gradient transport model with constant diffusivity is quite satisfactory.

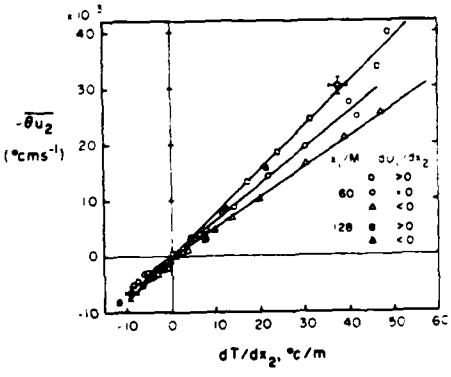

Fig. 5. Variation of heat flux with mean temperature gradient for the homogeneous flows

ASYMMETRICALLY HEATED WAKE

Measurements were made for several configurations of the heating wires and the wake generator, but results are presented here only for that shown in Figure 6. Measurements were made only at one station ($x_1/d = 100$). It would have been desirable to have

made the measurements further downstream (where the flow would be self-preserving to a better degree of approximation), but the limitations of accuracy in heat transport measurements for small T led to this choice. Figure 6 shows transverse profiles of normalized velocity defect w/w_o (w_o = 1.78 ms^{-1}), u_2'/w_o, T, θ'/T_{max} and L_f/d; here L_f was obtained by evaluating the area up to the first crossing under the autocorrelation function of u_1(24) and converting the resulting integral time scale to a length scale via Taylor's "frozen field" approximation. It is seen that even at x_1/d = 100, the presence of the wires in the wake results in a slight asymmetry in the velocity near the maximum defect region, and stronger asymmetries in u_2' and L_f profiles.

Figure 7a shows a plot of the heat flux $-\overline{u_2\theta}$ and the mean temperature gradient $\partial T/\partial x_2$ at several points across the wake. Clearly, there is a small but finite region (the shaded region in the figure) in which the heat flux and the mean temperature gradient are of opposite sign implying negative diffusivity, or heat transport against the mean temperature gradient.

A more direct demonstration of the inadequacy of the GTMs is given in Figure 7b which shows that $-\overline{u_2\theta}$ when plotted against $\partial T/\partial x_2$ forms a closed loop. (If a GTM were applicable the loop would collapse on to a single curve through the origin; if the diffusivity were also constant, the curve would be a straight line.) For the discussion to follow, the rough correspondence between the various key points of this loop and their physical location is indicated by the use of the same letters A,B,C,D and E in Figures 7a,b and the inset to Figure 7b. Large negative x_2/d (say, around A in the inset) correspond to the vicinity of the origin in Figure 7b. As x_2/d increases (algebraically), both $\partial T/\partial x_2$ and $-\overline{u_2\theta}$ increase until at B the (positive) maximum value of $\partial T/\partial x_2$ is reached. Beyond B, $\partial T/\partial x_2$ decreases but $-\overline{u_2\theta}$ does not keep pace with $\partial T/\partial x_2$ and is finite and large even in the vicinity of C where $\partial T/\partial x_2$ is small. For even larger x_2/d, $\partial T/\partial x_2$ is negative (path CD) until the negative maximum of the temperature gradient is attained at D; around D, $-\overline{u_2\theta}$ is still decreasing (see Figure 7a), however. The path DE constitutes the return to $\partial T/\partial x_2$ = 0 as x_2/d approaches large positive values.

Corresponding regions in which the turbulent momentum transport $-\overline{u_1u_2}$ occurs against the direction of mean velocity gradient have been observed in many different flow situations (6-16). These regions have been called regions of "energy reversal" (9) or, more commonly in the later literature, as regions of "negative production", although the appropriateness of either term has been questioned. For example, it has been pointed out (25) that the total production terms are given by $-\overline{u_iu_j}\,\partial U_i/\partial x_j$, and that in the regions where $-\overline{u_1u_2}\,(\partial U_1/\partial x_2)$ is negative, the other production terms $-(\overline{u_1^2}-\overline{u_2^2})\,\partial U_1/\partial x_1 - \overline{u_1u_2}\,\partial U_2/\partial x_1$ are positive and (though small) of the right magnitude to counteract locally the negative values of $-\overline{u_1u_2}\,\partial U_1/\partial x_2$. However, this conclusion is negated by other measurements (10,26) in which all the production terms except $-\overline{u_1u_2}\,(\partial U_2/\partial x_1)$ were measured. In these two latter cases, the magnitude of the negative values of the total production is very small indeed. Lastly, we may mention Hinze's (16) conclusion that even if the sum-total of production terms is negative, it does *not* imply energy transfer back to the mean flow.

In the heat transfer case, there are fewer measurements of the $\overline{\theta^2}$-production terms (14,19,27), but the balance of evidence does suggest that the total thermal production terms

$$-\overline{u_2\theta}\,\partial T/\partial x_2 + \overline{u_1\theta}\,\partial T/\partial x_1$$

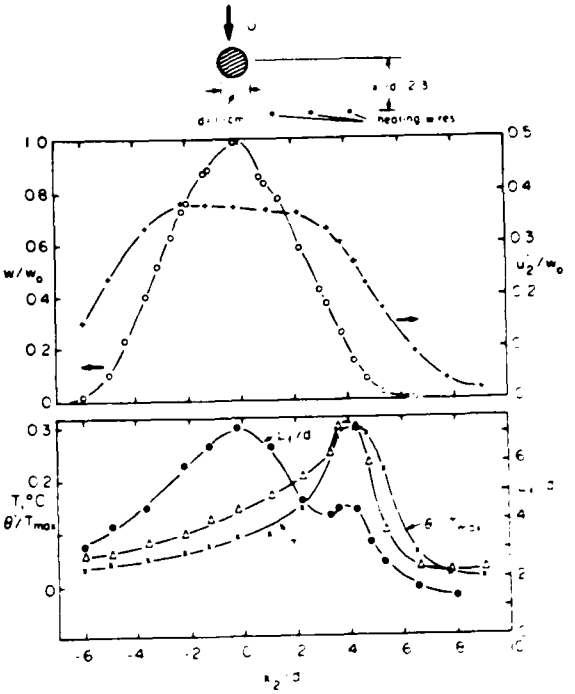

Fig. 6. A representative cylinder/heating wire combination and the resulting transverse distributions of mean defect velocity and temperature rise

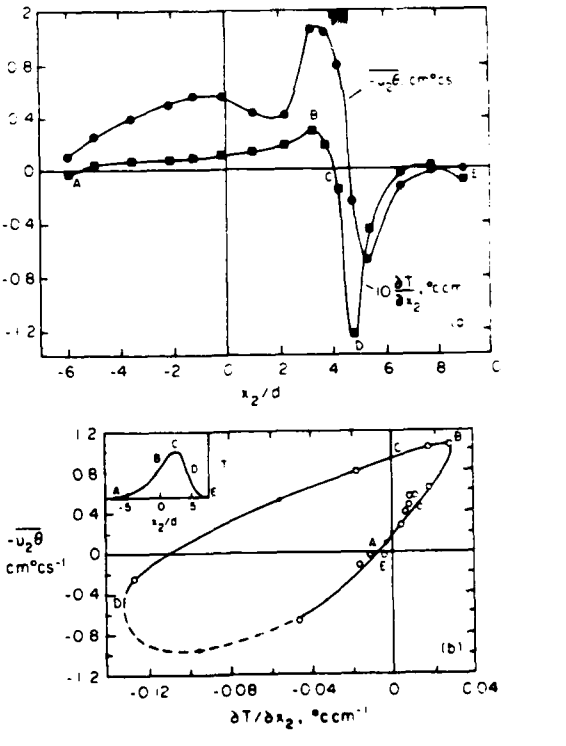

Fig. 7. Variation of heat flux with mean temperature gradient for the asymmetrically heated wake

add up to negative values in some small flow region. In the present wake, mean temperature profiles were not measured sufficiently closely to evaluate $\partial T/\partial x_1$ accurately, but rough estimates suggest that the inclusion of $-\overline{u_1\theta}\,\partial T/\partial x_1$ does not alter the sign of total production in any substantial way.

TEST OF GENERALIZED MODELS

For lack of space, we shall restrict to testing the performance of these models without discussing the basis of their formulation. Specifically, we consider the following models which, in order, are the GTM and models due to Corrsin (5), Lumley (17) Kronenburg (18), Beguier-Fulachier-Keffer (19) - BFK for short-and Townsend (28):

$$-\overline{u_2\theta} = D\,(\partial T/\partial x_2) \equiv R_G \qquad (a)$$

$$-\overline{u_2\theta} = D\,(\partial T/\partial x_2) + L_f T\,(\partial u_2'/\partial x_2) \equiv R_C \qquad (b)$$

$$-\overline{u_2\theta} = D\,(\partial T/\partial x_2) + (T/2)\,(\partial D/\partial x_2) \equiv R_L \qquad (c)$$

$$-\overline{u_2\theta} = D\,(\partial T/\partial x_2) + L_f\,\partial/\partial x_2\,(D\,\partial T/\partial x_2) \equiv R_K \qquad (d)$$

$$-\overline{u_2\theta} = D\,(\partial T/\partial x_2) + K_\theta\,\varepsilon_\theta^{-3}(\partial q'/\partial x_2)\,(\partial^2 T/\partial x_2^2) \equiv R_B \qquad (e)$$

$$-\overline{u_2\theta} = D\,(\partial T/\partial x_2) - V_c\,T_{max} \equiv R_T \qquad (f)$$

All models have been considered to the first order of correction. For convenience in evaluation, we have here replaced D by $L_f\,u_2'$; a more appropriate definition would presumably differ from the present one by a constant factor that is immaterial in the present context.

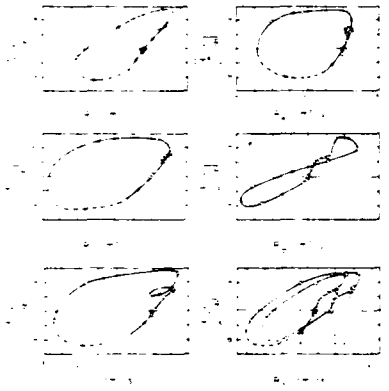

Fig. 8. Test of generalizations of GTM for the present asymmetrically heated wake

Any improved alternative to the GTM must be capable of collapsing the closed loop in Figure 7b on to a single curve or nearly so. From both Figures 8 and 9, the models due to Corrsin (5) and Lumley (17) appear to aggravate rather than improve the situation. The Kronenburg model appears to work reasonably well for the mixing layer data (19), but has poor performance in the present flow. For testing model (e) using the present flow data, we have replaced q' by $\sqrt{3/2(\overline{u_1^2} + \overline{u_2^2})}$. This introduces an uncertainty in the precise value of K_θ, which should be -0.11 according to (19). Several values in the vicinity of -0.11 were tried, but the performance of the model was worse than that of GTM for all negative K_θ. There is no physical or mathematical reason why K_θ must be only negative, and so we tried positive values as well. Figure 8e shows that for $K_\theta = 0.015$, the model performs reasonably well. However, the significance of a model with a coefficient whose sign itself is uncertain is not clear. In Townsend's model, the correction due to the bulk transport is a constant number on the right hand side, and this can only translate the closed loop without either shrinking or enlarging it. The effect is shown in Figure 8f for two values of the correction, and in Figure 9f for one.

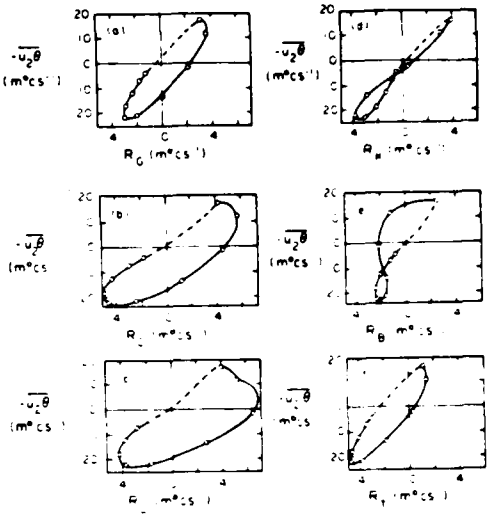

Fig. 9. Test of generalizations of GTM for the asymmetrically heated mixing layer (19)

DISCUSSION

Our experiments have emphasized that the GTM which appears perfectly adequate with a constant diffusivity for the homogeneous flows cannot handle inhomogeneous flows even qualitatively. The chief difference between the homogeneous and inhomogeneous shear flows is the dominance of the large structure in the latter; it appears that the large structures are responsible for a sizeable fraction of the transport process, and it is in the modeling of these effects that none of the generalizations of the GTM discussed earlier has had reliable success. One of the currently held views is that a turbulent shear

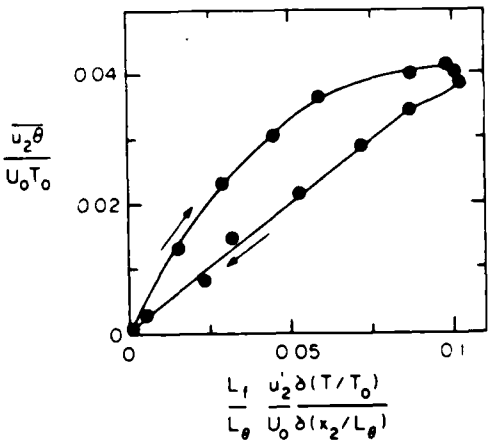

Fig. 10. Variation of heat flux with mean temperature gradient in a symmetrically heated co-flowing jet (29)

flow is essentially a consequence (and not the cause) of these transport-efficient large structures and their mutual interactions. If this view is correct, an altogetherly different approach, which does not even invoke a mean field, is necessary before the problem can be resolved.

Finally, we examine briefly the reason that the GTM seems to work well in free shear flows. Figure 10 shows a plot of $u_2\theta$ vs $(\partial T/\partial x_2)$- now appropriately normalized - for one half of a symmetrically heated co-flowing jet (29). It is again seen that the data form a loop instead of a single curve. However, the flow symmetry about the centerline forces both $u_2\theta$ and $\partial T/\partial x_2$ to be zero at the same point, so that the return part of the loop is now constrained to go through the origin. This results in a much smaller loop than would be the case if asymmetries existed. This is the reason for the apparent success of the GTM in symmetric flows.

ACKNOWLEDGMENT

This research was supported by the Atmospheric Science Division of the National Science Foundation.

REFERENCES

1 Monin, A.S. and Yaglom, A.M. "Statistical Fluid Mechanics: Mechanics of Turbulence," Vol. 1, 1971, M.I.T. Press, Cambridge (Ed. J.L. Lumley).

2 Hinze, J.O.. "Turbulence," 1976, McGraw Hill Co., New York (Second Edition).

3 Batchelor, G.K., "Note on Free Turbulent Flows, with Special Reference to the Two-Dimensional Wake," Journal of Aeronautical Sciences, Vol. 17, 1950, pp. 441-445.

4 Corrsin, S., "Heat Transfer in Isotropic Turbulence," Journal of Applied Physics, Vol. 23, 1952, pp. 113-118.

5 Corrsin, S., "Limitations of Gradient Transport Models in Random Walks and in Turbulence," Advances in Geophysics, Vol. 18A, 1974, pp. 25-60.

6 Eskinazi, S. and Yeh, H. "An Investigation of Fully Developed Turbulent Flows in a Curved Channel," Journal of Aeronautical Sciences, Vol. 23, 1956, pp. 23-31.

7 Mathieu, J. and Tailland, A., "Étude d'un Jet Plan Dirigé Tangentiellement à une paroi," C.R. Academy of Sciences, Vol. 256, 1963 pp. 2768-2771.

8 Gee, M.T., and Bradshaw, P. "Turbulent Wall Jets with and without External Stream," NPL 3252 June 1960, Aeronautical Research Council, England.

9 Eskinazi, S. and Erian, E.F. "Energy Reversal in Turbulent Flows," Physics of Fluids, Vol. 12, 1969, pp. 1988-1998.

10 Erian, E.F., "Influence of Pressure Gradient on Turbulent Flow with Asymmetric Mean Velocity," ASME-Journal of Applied Mechanics, Vol. 91, 1969, pp. 901-904.

11 Hanjalic, K. and Launder, B.E., "Fully Developed Asymmetric Flow in a Plane Channel," Journal of Fluid Mechanics, Vol. 51, 1972, pp. 301-335.

12 Palmer, M.D. and Keffer, J.F., "An Experimental Investigation of an Asymmetrical Turbulent Wake," Journal of Fluid Mechanics, Vol. 53, 1972, pp. 593-610.

13 Fabris, G., "Conditionally Sampled Turbulent Thermal and Velocity Fields in the Wake of a Warm Cylinder and its Interaction with an Equal Cool Wake," Ph.D. dissertation, Illinois Institute of Technology, 1979.

14 Charney, G., Schon, J.P., Alcaraz, E. and Mathieu, J., "Thermal Characteristics of a Turbulent Boundary Layer with Inversion of Wall Heat Flux," Proceedings of the Symposium on Turbulent Shear Flows, Penn. State University, University Park, 1977, pp. 15.47-15.55.

15 Morel, R., Awad, M. Schon, J.P. and Mathieu,J., "Experimental Study of an Asymmetric Thermal Wake," In Structure and Mechanism of Turbulence, Vol. 1 1978, pp. 36-35. Lecture Notes in Physics, Springer-Verlag, Berlin.

16 Hinze, J.O., "Turbulent Flow Regions with Shear Stress and Mean Volocity Gradient of Opposite Sign," Applied Science Research, Vol. 22, 1970, pp. 168-175.

17 Lumley, J.L., "Modeling Turbulent Flux of Passive Scaler Quantities in Inhomogeneous Flows," Physics of Fluids, Vol. 18, 1975, pp. 619-621.

18 Kronenburg, C., "On the Extension of Gradient -Type Transport to Turbulent Diffusion in Inhomogeneous Flows," Applied Science Research, Vol. 33, 1977, pp. 163-175.

19 Beguier, C., Fulachier, L. and Keffer, J.F., "The Turbulent Mixing Layer with an Asymmetrical Distribution of Temperature," Journal of Fluid Mechanics, Vol. 89, 1978, pp. 561-587.

20 Rose, W.G., "Results of an Attempt to Generate a Homogeneous Turbulent Shear Flow," Journal of Fluid Mechanics, Vol. 25, 1966, pp. 97-120.

21 Tavoularis, S., "A Circuit for the Measurement of Instantaneous Temperature in Heated Turbulent Flows," Journal of Physics, E: Scientific Instruments, Vol. 11, 1978, pp. 21-23.

22 Tavoularis, S. and Corrsin, S., "Experiments in Nearly Homogeneous Turbulent Shear Flow with a Uniform Mean Temperature Gradient. Part 1," Journal of Fluid Mechanics, Vol. 104, 1981, pp. 311-347.

23 Comte-Bellot, G. and Corrsin, S., "The Use of a Contraction to Improve the Isotropy of Grid-Generated Turbulence," Journal of Fluid Mechanics, Vol. 25, 1966, pp. 657-682.

24 Comte-Bellot, G. and Corrsin, S., "Simple Eulerian Time Correlation of Full and Narrow-Band Velocity Signals in Grid-Generated, 'Isotropic' Turbulence," Journal of Fluid Mechanics, Vol. 48, 1971, pp. 273-337.

25 Wilson, J.D., "Turbulent Transport of Mean Kinetic Energy in Countergradient Shear Stress Regions," Physics of Fluids, Vol. 17, 1974, pp. 674-675.

26 Beguier, C., "Mesures de Tensions de Reynolds dans un écoulement dissymetrique en régime turbulent incompressible," Journal de Mécanique, Vol. 4, 1965. pp. 319-334.

27 Fulachier, L., Keffer, J.F. and Beguier, C., "Production Negative de Fluctuations Turbulentes de Température dans le case d'un Créneau de Chaleur s'épanouissant dans une Zone de Mélange," C.R. Academy of Sciences, Vol. 280, Series B, 1975, pp.519-522.

28 Townsend, A.A., "The Structure of Turbulent Shear Flows," 1956, University Press, Cambridge, England.

29 Antonia, R.A., Prabhu, A. and Stephenson, S. E., "Conditionally Sampled Measurements in a Heated Turbulent Jet," Journal of Fluid Mechanics, Vol. 72, 1975, pp. 455-480.

SESSION 16 - RECIRCULATING FLOWS I

H. McDonald - Chairman

MOMENTUM, HEAT, AND MASS TRANSFER IN BACKWARD-FACING STEP FLOWS

by

B.F.Armaly*, F. Durst** and V. Kottke***

* Mechanical & Aerospace Engineering Department, University of Rolla, Missouri 56401, USA

** Sonderforschungsbereich 80, University of Karlsruhe, W. Germany

*** Institut für Chemische Verfahrenstechnik, University of Stuttgart, W. Germany

ABSTRACT

Laser Doppler measurements of velocity distributions and reattachment lengths behind a single-backward facing step mounted in a two-dimensional test section are reported together with heat and mass transfer data at the wall downstream of the step. The measuring techniques to obtain the wall values are also described in the paper. Measurements are presented in laminar, transitional and turbulent air flows in a Reynolds number range of $70 < Re < 8000$. The experimental results show that the various flow regimes are characterized by typical variations of the separation length with Reynolds number. Differences between the location of the reattachment line and the lines of maximum heat and mass transfer are stressed.

The measurements do not only show the expected primary zone of recirculating flow attached to the backward-facing step but show additional regions of flow separation, on the wall of the test section located opposite to the step and downstream of the primary separation zone.

NOMENCLATURE

D_a	Diffusion coefficient for ammonia in air
h	height of inlet duct
H	height of outlet duct
Re	Reynolds number, $Re = \bar{U}_m \cdot (2h)/\nu$
s	(H-h), step height
Sh_s	Sherwood number, $Sh_s = \beta \cdot (2h)/D_A$
$\bar{U}_m$	time and bulk average inlet velocity
β	mass transfer coefficient
μ	viscosity of air
ν	kinematic viscosity, $\nu = \mu/\rho$
ρ	density of air

INTRODUCTION

Investigations of momentum, heat and mass transfer in separated flows require the employment of various experimental techniques to quantitatively measure those properties that are of importance to practical engineers and to research workers actively involved in studies of transport phenomena in flows. New experimental techniques have recently become available and have reached a state of development which permits non-intrusive measurements in laminar and turbulent separated flows. Laser Doppler anemometry is one of these techniques. It has been employed by the authors to obtain measurements of velocity distribution and reattachment length behind a single backward-facing step mounted in a two-dimensional test section. This test section is shown in Fig. 1 which provides the major dimensions and also illustrates the flow straightener and settling chamber with inlet test section used to obtain a well controlled inlet flow. The laser-Doppler anemometer consisted of a single-channel optical unit with a double Bragg cell frequency shifting module. A 15mW Helium-Neon laser was employed and light in the forward direction was collected for the measurements. The signals were evaluated by a frequency tracker and also using a transient recorder combined with a digital computer.

In addition to velocity measurements, quantitative investigations of the transport of scalar properties to the wall were performed in the region downstream of the step using three different techniques described in section 2. Mass transfer measurements were carried out using a technique developed by the first author, e.g. see ref.1. Heat transfer measurements were performed using a flash mounted hot-film and a heated insulated element mounted into a copper plate. It is explained in section 2 that the electrical energy supply to this element can be taken as a measure of the local heat transfer obtained for constant temperature wall conditions.

Results of the authors' measurements are summarized in section 3. For more detailed information, suggestions for improving the measurements, and detailed discussions of the results, the reader is referred to a more extended report given in ref. 2.

EXPERIMENTAL TECHNIQUES

Laser-Doppler Anemometers

A LDA-system incorporating a 15mW He-Ne laser, a transmission optics with a double Bragg cell frequency shifter and a light collecting system for forward scattered light, was employed in the present study. This is shown in Fig. 2 which also shows the signal processing equipment consisting of two completely different systems. One system incorporated a frequency tracker to measure the Doppler frequency whereas the other is a transient recorders followed by a digital computer. The transient recorder based processing system was applicable over the entire Reynolds number range. The tracker based system could not be applied at higher Reynolds numbers. It was found to yield erroneous results in the reattachment region of the flow.

MOMENTUM, HEAT, AND MASS TRANSFER IN BACKWARD-FACING STEP FLOWS

by

B.F.Armaly*, F. Durst** and V. Kottke***

* Mechanical & Aerospace Engineering Department, University of Rolla, Missouri 56401, USA

** Sonderforschungsbereich 80, University of Karlsruhe, W. Germany

*** Institut für Chemische Verfahrenstechnik, University of Stuttgart, W. Germany

ABSTRACT

Laser Doppler measurements of velocity distributions and reattachment lengths behind a single-backward facing step mounted in a two-dimensional test section are reported together with heat and mass transfer data at the wall downstream of the step. The measuring techniques to obtain the wall values are also described in the paper. Measurements are presented in laminar, transitional and turbulent air flows in a Reynolds number range of $70 < Re < 8000$. The experimental results show that the various flow regimes are characterized by typical variations of the separation length with Reynolds number. Differences between the location of the reattachment line and the lines of maximum heat and mass transfer are stressed.

The measurements do not only show the expected primary zone of recirculating flow attached to the backward-facing step but show additional regions of flow separation, on the wall of the test section located opposite to the step and downstream of the primary separation zone.

NOMENCLATURE

D_a	Diffusion coefficient for ammonia in air
h	height of inlet duct
H	height of outlet duct
Re	Reynolds number, $Re = \bar{U}_m \cdot (2h)/\nu$
s	(H-h), step height
Sh_s	Sherwood number, $Sh_s = \beta \cdot (2h)/D_A$
$\bar{U}_m$	time and bulk average inlet velocity
β	mass transfer coefficient
μ	viscosity of air
ν	kinematic viscosity, $\nu = \mu/\rho$
ρ	density of air

INTRODUCTION

Investigations of momentum, heat and mass transfer in separated flows require the employment of various experimental techniques to quantitatively measure those properties that are of importance to practical engineers and to research workers actively involved in studies of transport phenomena in flows. New experimental techniques have recently become available and have reached a state of development which permits non-intrusive measurements in laminar and turbulent separated flows. Laser Doppler anemometry is one of these techniques. It has been employed by the authors to obtain measurements of velocity distribution and reattachment length behind a single backward-facing step mounted in a two-dimensional test section. This test section is shown in Fig. 1 which provides the major dimensions and also illustrates the flow straightener and settling chamber with inlet test section used to obtain a well controlled inlet flow. The laser-Doppler anemometer consisted of a single-channel optical unit with a double Bragg cell frequency shifting module. A 15mW Helium-Neon laser was employed and light in the forward direction was collected for the measurements. The signals were evaluated by a frequency tracker and also using a transient recorder combined with a digital computer.

In addition to velocity measurements, quantitative investigations of the transport of scalar properties to the wall were performed in the region downstream of the step using three different techniques described in section 2. Mass transfer measurements were carried out using a technique developed by the first author, e.g. see ref.1. Heat transfer measurements were performed using a flash mounted hot-film and a heated insulated element mounted into a copper plate. It is explained in section 2 that the electrical energy supply to this element can be taken as a measure of the local heat transfer obtained for constant temperature wall conditions.

Results of the authors' measurements are summarized in section 3. For more detailed information, suggestions for improving the measurements, and detailed discussions of the results, the reader is referred to a more extended report given in ref. 2.

EXPERIMENTAL TECHNIQUES

Laser-Doppler Anemometers

A LDA-system incorporating a 15mW He-Ne laser, a transmission optics with a double Bragg cell frequency shifter and a light collecting system for forward scattered light, was employed in the present study. This is shown in Fig. 2 which also shows the signal processing equipment consisting of two completely different systems. One system incorporated a frequency tracker to measure the Doppler frequency whereas the other is a transient recorders followed by a digital computer. The transient recorder based processing system was applicable over the entire Reynolds number range. The tracker based system could not be applied at higher Reynolds numbers. It was found to yield erroneous results in the reattachment region of the flow.

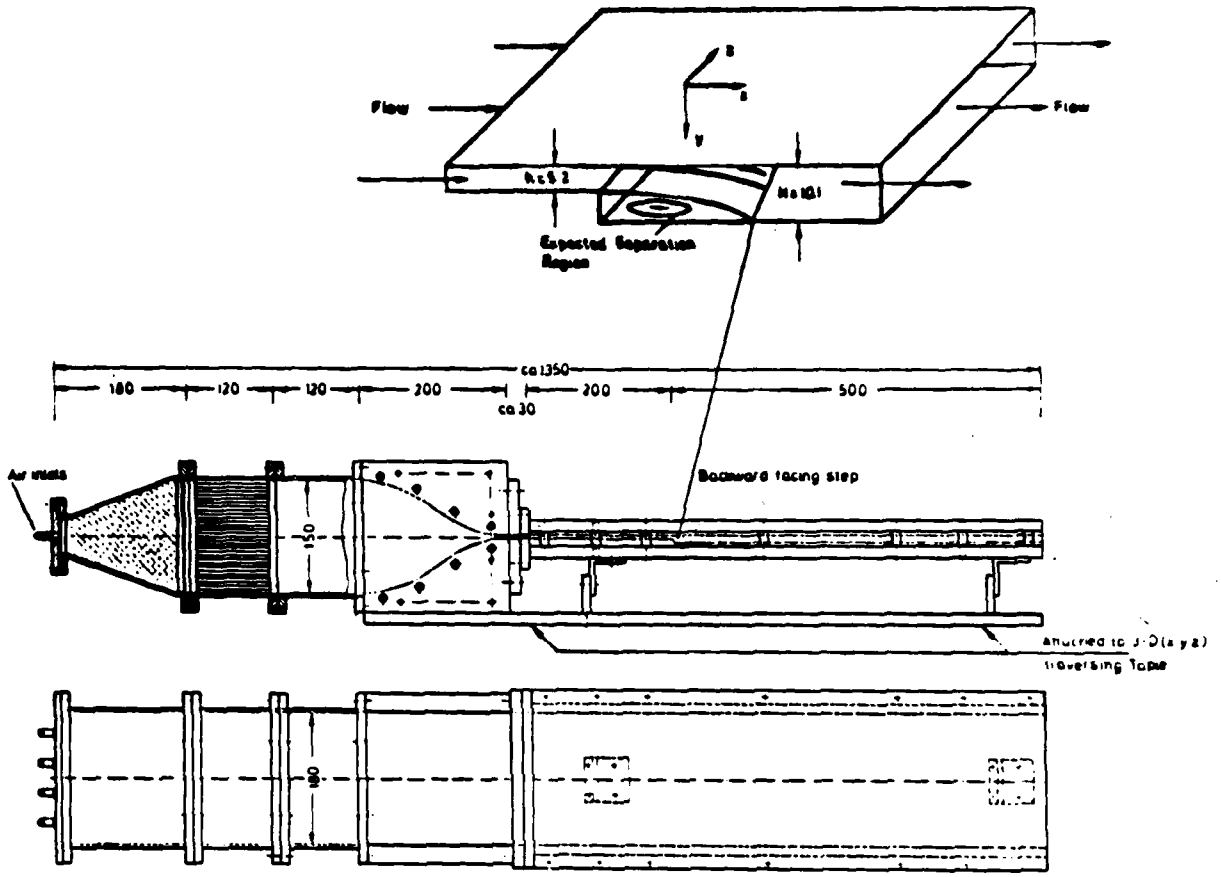

Figure 1: Schematic of air tunnel and test section (mm)

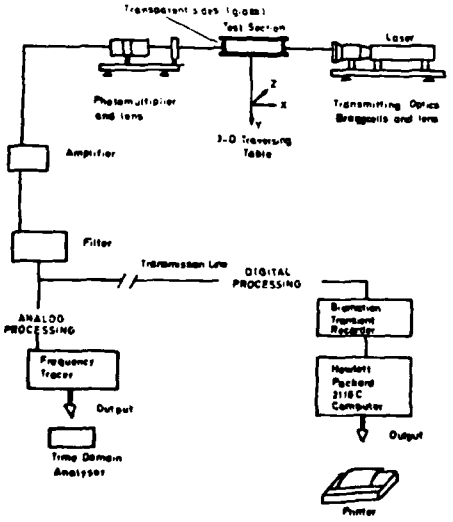

Figure 2: Data acquisition and processing system

Measuring Techniques for Mass Transfer

Quantitative measurements of the wall mass transfer were carried out with a method developed by the first author and described in ref. 1. The method is based on the colour-change that occurs on filter paper soaked with a manganese-chloride solution. If this paper is located downstream of the step and a known dosis of ammonia is added to the flow, the ammonia will be absorbed at the surface of the soaked filtered paper and the following reaction will take place.

$$NH_3 + H_2O \rightleftharpoons NH_4OH \rightleftharpoons NH_4^+ + OH^-$$

$$2NH_4OH + MnCl_2 \rightarrow 2NH_4Cl + Mn(OH)_2 \downarrow \xrightarrow{O_2} H_2O_2$$

$$MnO_2$$

This equation shows that manganese-dioxide remains on the surface of the filter paper yielding a change in colour. The intensity of this change is dependent on the amount of ammonia transported to the wall, and, hence, a measure of the local mass transfer coefficient or the appropriate Sherwoood number.

Measurements of Heat Transfer

Heat transfer measurements were performed in a specially designed test section constructed out of Perspex. The wall on which the step was located consisted of a copper plate with heating elements to adjust the temperature of the plate. In the centre of the copper plate, a separate small copper element was inserted which also contained heating elements thermally isolated from the remainder of the plate. This element was heated so that its temperature agreed with the temperature of the surrounding copper plate. The energy to the surface element was measured and from it the local heat transfer coefficient was deduced and the corresponding Nusselt number computed. The copper plate could be moved in the longitudinal direction in order to allow the measuring element to be located at various distances downstream of the step.

Heat transfer measurements were also carried out from a small hot-film element positioned in a metal wall kept at the temperature of the fluid. The data from this element were compared with measurements of the velocity gradient at the wall in order to confirm that the conditions required to apply Reynolds analogy between heat, mass and momentum transfer are not satisfied in separated flows.

RESULTS OF VELOCITY AND SCALAR TRANSPORT MEASUREMENTS

The application of the laser-Doppler anemometer also permitted accurate measurements of the reattachment length as a function of Reynolds number. The way in which such measurements can be accurately performed has been described by Durst and Tropea (3). Their method of measurement was employed on both walls of the two-dimensional test section downstream of the step. Various regions of separations were found on both walls of the test section with longitudinal dimensions as given in Fig. 3.

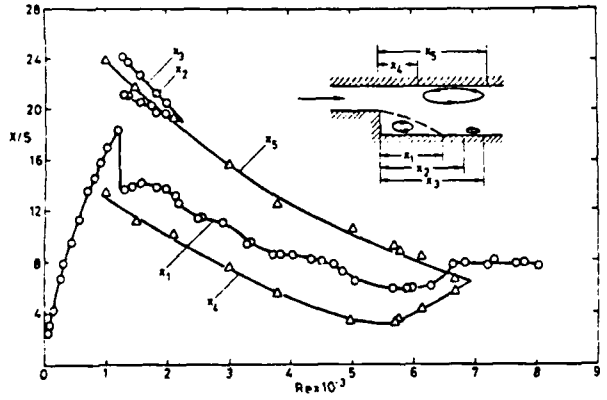

Figure 3: Circulation regions at the upper and lower walls

Measurements of detailed velocity profiles were also performed at various Reynolds numbers and throughout the entire channel. Fig. 4 shows an example of such measurements for a Reynolds number of Re = 1095 indicating the two regions of backflow; one region attached to the backward facing step and the other located on the wall opposite to the step. It was observed that the occurance of the upper region of separated flow causes the flow to become three-

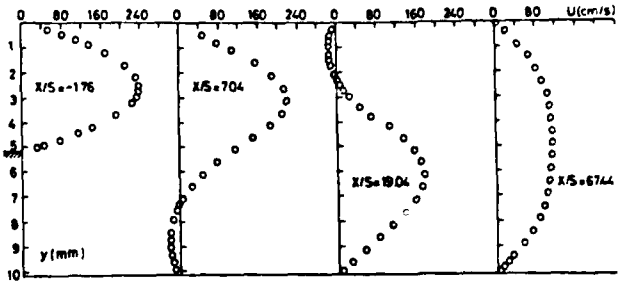

Figure 4: Velocity profiles for Re = 1095

dimensional irrespective of the aspect ratio chosen for the test section geometry, see ref. 4.

Figs. 5 and 6 present a summary of the results of the local mass transfer measurements carried out by the authors for the region downstream of the step. The local Sherwood number is plotted as a function of the longitudinal distance normalized by the test section width downstream of the step. At Reynolds numbers in excess of 400, the longitudinal Sherwood number-distribution shows two maxima up to Reynolds numbers of approximately 4000. With increasing Reynolds numbers, these maxima move closer to the step as indicated in Fig. 5. In the fully developed turbulent flow region, only one maximum exists. This is shown in Fig. 6.

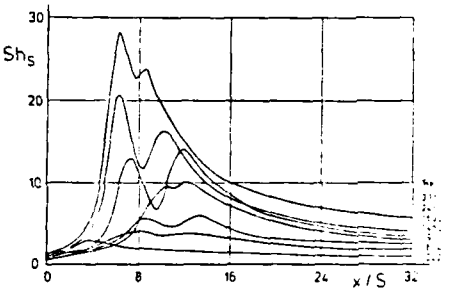

Figure 5: Mass transfer in backward-facing step flows

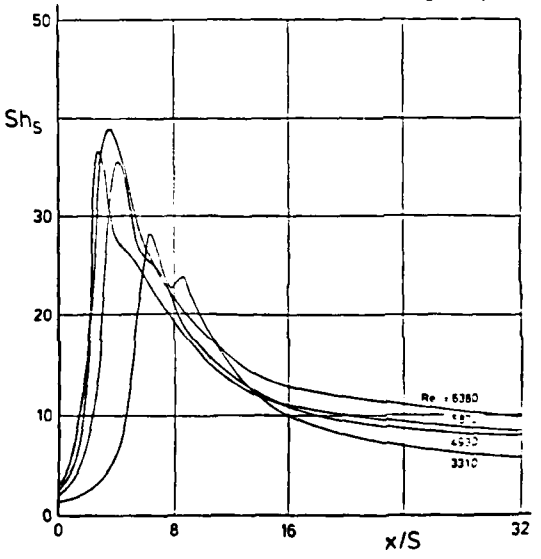

Figure 6: Mass transfer in backward-facing step flows

More detailed results of mass transfer measurements are presented in ref. 5 where also the locations of the maxima and minima of the Sherwood number distributions are explicitly given as functions of Reynolds numbers. Comparison to other measurements are provided and differences explained.

Measurements of heat transfer are only reported for the hot-film element. Figs. 7 and 8 show examples of measurements of heat transfer obtained from the hot film. The diagrams also contain the variation of the velocity gradients along the wall. Both figures clearly indicate that the Reynolds analogy relating the local wall shear stress to the local heat transfer is not applicable. This indicates the difficulty that arises if hot-element wall sensors are used to determine fluid velocity information, e.g. the location of reattachment.

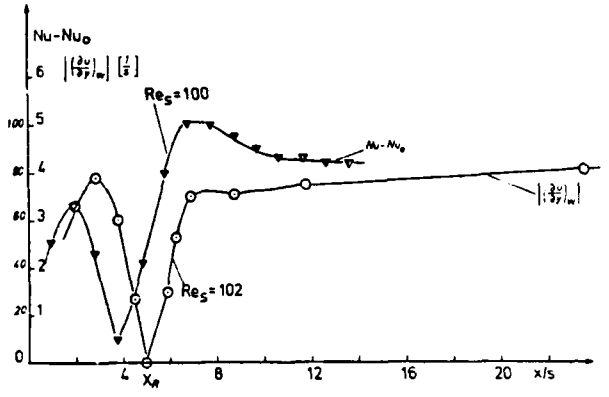

Figure 7:

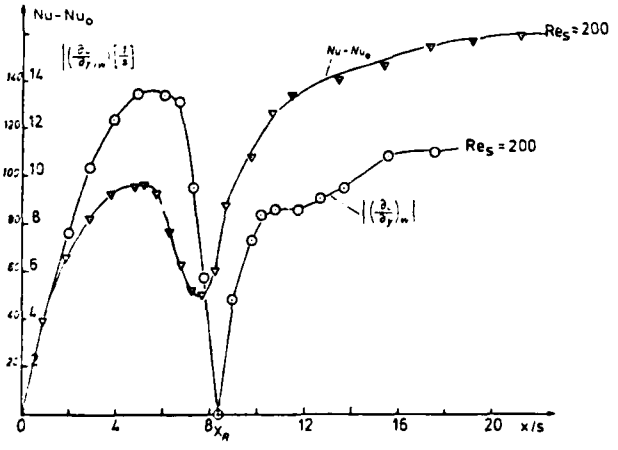

Figure 8:

The reader is referred to ref. 5 for more detailed measurements of heat transfer with the hot element mounted into the cupper plate described in section 2.

FINAL REMARKS

In addition to the measurements summarized in this paper, flow predictions were carried out using computer programs to numerically solve the two-dimensional Navier-Stokes equation. Comparisons between predicted results and measurements showed good agreement up to Reynolds numbers:

$$Re \simeq 400.$$

Thereafter, predicted separation length differed severely from those obtained in the measurements. The predictions also showed the second separation region at the wall opposite to the step but its shape and location differed from those of the measurements. Its difference was carefully investigated and it turned out that the entire flow field turns three-dimensional at Reynolds numbers for which the upper separation bubble occurs.

The second author and his students are continuing the work described in this paper. Measurements at different expansion ratios are planned for the laminar flow regime together with detailed numerical predictions. In addition, measurements are extended into the turbulent range up to Reynolds numbers of 5×10^5.

REFERENCES

1 Kottke, V., Blenke, H., Schmidt, K.G. and "Eine remissionsphotometrische Meßmethode zur Bestimmung örtlicher Stoffübergangskoeffizienten bei Zwangskonvektion in Luft", Wärme- und Stoffübertragung, No. 10, 1977, pp. 9-21.

2 Armaly, B.F., Durst, F. and Kottke, V., "Momentum, Heat and Mass Transfer in Backward-Facing Step Flow", SFB 80 Report, Universität Karlsruhe, in preparation.

3 Durst, F. and Tropea, C., "Turbulent, Backward-facing Step Flows in Two-Dimensional Ducts and Channel Flows", Symposium on Turbulent Shear Flows 3, University of California, Davis, Sept. 1981.

4 Armaly, B.F., Durst, F. Pereira, J.C.F. and Schönung, B., "Flow Downstream of a Single-Backward-Facing Step, Part I: Laminar Flow Regime", SFB 80 Report, University of Karlsruhe, in preparation.

5 Haas, W., Wärmeübertragung in einer Kanalströmung mit plötzlicher Querschnittserweiterung", Studienarbeit, Universität Karlsruhe, Institut für Hydromechanik, 1981.

VELOCITY CHARACTERISTICS IN THE VICINITY OF A TWO-DIMENSIONAL RIB

by

D. Crabb*, D.F.G. Durão** and J.H. Whitelaw
Department of Mechanical Engineering
Imperial College, London SW7 2BX

ABSTRACT

Measurements of the velocity characteristics of the flow in the vicinity of a single rib have been obtained with a laser-Doppler anemometer. They show, for example, that the reattachment length is around 12.3 times the rib height for a 23.5 mm square rib and demonstrate that it depends on the length of the rib and ratio of boundary layer thickness to rib height. Measurements with hot-wire anemometry in the region of the shear layer indicate rapid changes in skewness and small peaks in energy spectra which would not be represented by eddy-viscosity assumptions.

1. INTRODUCTION

The present paper is concerned with the flow in the vicinity of a single, two-dimensional rib and is relevant to a wide range of practical problems including wind breaks, trains and roughness elements. (An earlier and less complete version was presented in reference 1). It describes measurements of velocity and turbulence characteristics of this flow and is intended to contribute to understanding of the related turbulent transfer processes.

Recent attempts to calculate the properties of the flow around obstacles, for example those of Pope and Whitelaw (2), Vasilic-Melling (3) and Castro and Robins (4), have shown that the results do not agree well with corresponding measurements and that the latter are not available in sufficient detail to allow the discrepancies to be explained. In general, present knowledge of the velocity and turbulence characteristics of high-turbulence and recirculating flows is much less than that available for boundary-layer flows even though the former are at least as important. This imbalance is due largely to the availability of appropriate instrumentation.

Previous measurements in the vicinity of ribs have been reported, for example, by Tillman (5) and Plate and Lin (6) and are confined to values of mean velocity and wall pressure. In both cases, the reattachment length, normalised with rib height, was of the order of 15 although one rib was of square cross-section and the other of triangular cross-section with a surface orthogonal to the oncoming flow. Similar measurements around a thin obstacle (a fence) by, for example, Good and Joubert (7) and Sakamoto et al (8) indicate recirculation lengths of around 13, and the backward facing-step measurements of Bradshaw and Wong (9) indicate a length of around 6. Of course, the reattachment length is a time-averaged property and not necessarily representative of all features of the flow. The variation of length with geometry does, however, indicate a considerable dependence of the flow on its upstream characteristics which include the geometry and the ratio of boundary-layer thickness, δ, to bluff-body height, H, at least for small values of the latter quantity.

The measurements referred to in the previous paragraph, with the exception of those of Bradshaw and Wong, are confined to mean properties and those of Bradshaw and Wong, obtained by hot-wire anemometry, are limited to regions of relatively low turbulence intensity. The more recent measurements of Moss, Baker and Bradbury (10) obtained with the pulsed-wire method, and those of Restivo and Whitelaw (11) and Durão and Whitelaw (12), obtained with laser-Doppler anemometry, suggest that accurate measurements can now be made in regions of high turbulence intensity. The laser-Doppler anemometer also removes doubts associated with probe-interference effects. It is useful to note that, in the annular-jet measurements of Durão and Whitelaw, the length of the recirculation region was approximately one disc diameter.

The present measurements were obtained with a combination of laser-Doppler anemometry, hot-wire anemometry and flow visualisation. The helium-bubble was used to provide a visual impression of particular aspects of the flow; observation of surface streaks, obtained with impurities suspended in an oil solution, were used to confirm the two-dimensionality of the flow and to observe the reattachment line. Laser-Doppler anemometry allowed measurements of mean and rms velocities in all regions of the flow including those with high turbulence intensity and recirculation. Hot-wire anemometry was used to measure in locations of lower turbulence intensities.

The flow configuration, experimental methods and procedures are described in the following section and the results presented and discussed in sections 3 and 4. Brief conclusions are presented in section 5.

2. FLOW CONFIGURATION, EXPERIMENTAL METHODS AND PROCEDURES

Most of the measurements were obtained with a single rib, 23.5 mm square, located 430.0 mm downstream of an emery-paper trip in the 0.46 m x 0.9 m

---

* Combustion Engineer, Rolls-Royce Motors, Crewe, Cheshire.

** Professor and Head of Department of Mechanical Engineering, Instituto Superior Tecnico, Lisbon.

wind tunnel previously used, for example, by Kacker and Whitelaw (13) and Vasilic-Melling (3). To study the influence of boundary layer thickness, the same rib was also located 187.3 mm from the trip, a 70.5 mm wide x 23.5 mm high rib was used to provide an indication of the influence of rib dimensions. The two-dimensionality of the tunnel has been extensively tested by previous authors and the present ribs were carefully located across the full 0.46 m width of the tunnel and orthogonal to the flow. The area contraction ratio of the tunnel is 7.1 to 1 and, together with the carefully located upstream screens and honeycomb, ensures a free-stream turbulence intensity of around 0.6%. The present measurements were obtained with a free-stream velocity, $\bar{U}_o$, measured upstream of the rib, of 18 m/s with a corresponding rib-height Reynolds number of 2.7×10^4. The ribs themselves had sharp corners and were rigidly attached to the base plate of the tunnel; the imposed blockage ratio was 12.8.

The use of neutrally buoyant, helium-filled bubbles to visualise details of the flow was used here with a probe arrangement in accordance with the design of Button (14). It comprised a tube, of outer diameter 6 mm and with two concentric tubes of lesser diameter. Helium flowed through the innermost tube with a low velocity; liquid soap passed slowly through the first annulus; and air, at approximately the external stream velocity, through the outer annulus. Careful control of the flow rate of helium allowed the rate of flow of bubbles to be regulated. In the present experiments, the helium-bubbles were released into the stream upstream of the trip and at various distances from the base plate. The flow patterns were lighted from above and recorded with a 35 mm camera. Flow patterns, on the base plate of the wind tunnel, were obtained with thin layers of oil with suspended particles. The oil was spread evenly over the base plate both upstream and downstream of the rib and the flow patterns were formed after the fan had been running for a short period of time.

The hot-wire results were obtained with a crossed hot-wire probe (DISA 55P61), two anemometer bridges (DISA 55M01) and linerarizers (DISA 55D10) interfaced with a 12k storage PDP 8E mini computer and a Racal T7000 magnetic tape system. The final interpretation of the results was made on a CDC 6500 computer. The output signal from a single channel arrangement with a straight wire probe (DISA 55A25) was used to obtained spectrum measurements; in this case, the analogue signal was processed by a General Radio (model 1564-A) spectrum analyser.

The laser-Doppler anemometer comprised an Argon ion laser (Spectra Physics 164) operating at 488 μm and approximately 200 mW. One channel of a two-component water-filled acousto optic cell, based on the arrangement described by Durão and Whitelaw (15) and operated with a frequency shift of 21.0 MHz, was used to divide the laser beam into a zero and +1 order beams of approximately equal intensity. These two beams were focussed to an intersection region and backward-scattered light collected through the same lens. This collected light was focussed by another lens, via a mirror, onto a pinhole immediately prior to the cathode of a photomultiplier (EMI 9815B). The resulting control-volume has a diameter of 0.12 mm and a length of approximately 0.85 mm. The resulting Doppler signal was processed by a spectrum-analyser counter similar to that described by Durão, Laker and Whitelaw (16). The discrimination level of the analysis system slightly reduced the control volume dimensions. To provide a measurable particle-arrival rate, the wind tunnel was seeded with kerosene smoke generated by an evaporation (condensation) arrangement. The resulting droplets were smaller than 5 μm in diameter and allowed the construction of a velocity probability distribution in less than 10 minutes. The average quality of the signals processed, corresponded to a signal-to-noise ratio of approximately 20 db. It is estimated that the mean velocity values are precise to 2% and the turbulence intensity values to better than 5%.

3. RESULTS

The two-dimensionality and symmetry of the flow were examined by hot-wire anemonetry and flow visualization. Values of mean velocity and the rms of the corresponding fluctuations were measured in several planes, in the vicinity of the reattachment line, and across a 200 mm wide central zone; the various profiles were identical within experimental uncertainty. Surface flow-visualisation results were obtained with the square rib located 430.1 mm downstream of the emery-paper trip and confirmed the two-dimensionality of the flow in the central one third of the tunnel. The separation lines, upstream and downstream of the rib, and the reattachment line were clearly visible; they were straight in the central region and curved towards the side walls to give shorter reattachment lines downstream of the rib and larger separation regions upstream and downstream.

Figure 1 consists of three photographs, of helium-bubble traces, selected from a large number of prints, and intended to indicate three features of the flow. The exposure time was 5 ms for photograph a and b and 10 ms for c. Photograph a shows several exposures and provides a general impression of the flow suggesting that the range of instantaneous values of reattachment length is considerable. The trajectory of bubbles immediately above the rib suggests that a region of recirculation could exist there and this is confirmed by photograph b. Photograph c indicates, at closer range, the bubble traces in the vicinity of the shear layer above the rib.

Measurements of longitudinal velocity and the non-dimensional normal stress were obtained in the central plane for the flow conditions of Figure 1 and are presented in Figs. 2 and 3. These on Fig. 2 indicate the flow characteristics upstream and downstream of the rib. The main profile two rib heights upstream of the rib may be compared with the measurements obtained at the same location, but in the absence of the rib. It is clear that, at this location, the rib has already had an effect and caused the flow to respond to an effective adverse pressure gradient. This pressure gradient is confirmed by the wall static pressure distribution on Fig. 4. The values of velocity measured in the free strear also indicate an influence of the rib although the blockage ratio is small. The distribution of normal stress at $x/H = -2.0$ has the form appropriate to an adverse pressure gradient with turbulence intensities less than 25 % at all measuring stations.

Immediately upstream of the rib, i.e. $x/H = -0.4$, the measurements show a region of separated flow

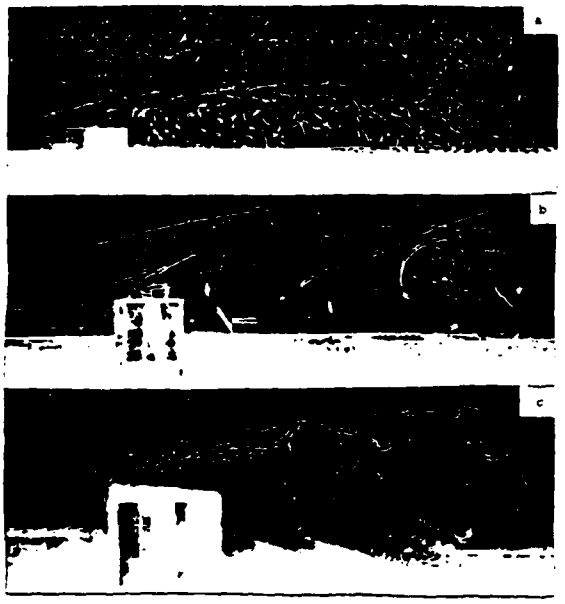

Fig. 1 Photographs of the flow using helium bubbles

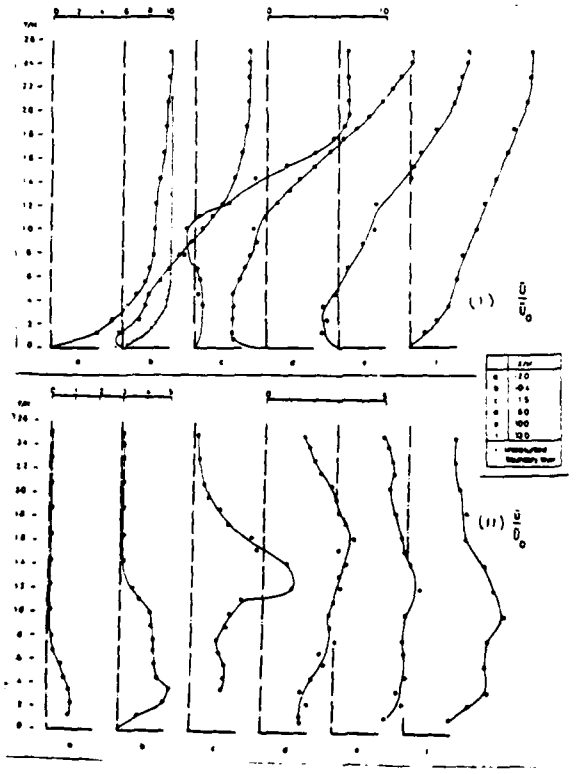

Fig. 2 Mean velocity and normal stress profiles upstream and downstream of the rib

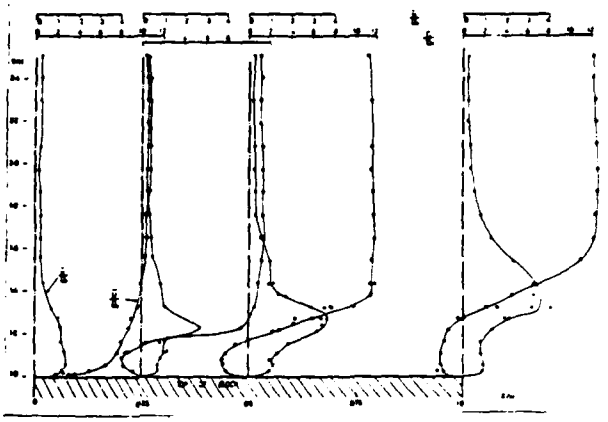

Fig. 3 Mean velocity and normal stress profiles on top of the rib

which is confined to the near-wall region. It is clear from the measurements, and also from the surface flow visualization, that the time-averaged line of boundary-layer separation occurs at a value of x/H of less than -1. The normal stress results suggest an upstream influence of the rib in that the distribution tends to be discontinuous at y/H = 1. For values of y/H less than 1, the turbulence intensity, $\bar{u}/\bar{U}$, increases rapidly to an infinite value at y/H of around 0.14; at this location, the instantaneous velocity is continuously changing sign and has a mean value of zero. The normal stress has a maximum corresponding to a turbulence intensity slightly in excess of 100% and coincides with the inflection in the mean velocity profile. The turbulence energy spectra shown in Fig. 5 at y/H = 1.0 ($\bar{u}/\bar{U}$ = 25%) is similar to that associated with fully developed turbulent flows.

The flow on top of the rib, Fig. 3, indicates a region of near-wall separation from the leading edge to trailing edge. The zero mean velocity streamline is 0.14 and 0.28 rib heights above the rib at 0.25 rib lengths and the trailing edge respectively. The normal stress profiles achieve increasingly high values and have a maximum value immediately downstream of the rib, as can be seen from Fig. 2. Figure 3 shows that the maximum values of normal stress are located close to the points of maximum gradient of the mean velocity profiles. In the recirculation zone the turbulence intensity has minimum values

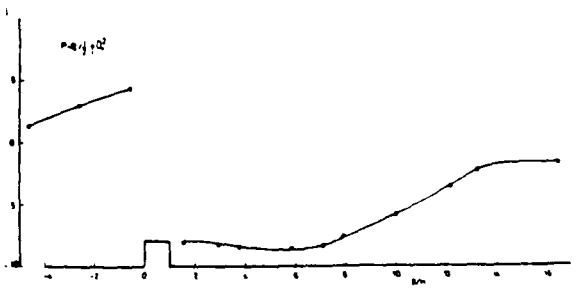

Fig. 4 Wall static pressure distribution

around the maximum reverse mean velocity in each x-plane and the normal stress is comparatively uniform.

In contrast to spectrum 1 of Fig. 5, the power spectra obtained from the straight hot-wire anemometer at x/H of 0.5 and 1.5, spectra 2 and 3, close to the region of maximum normal stress, exhibit maxima around 200 Hz. Spectrum 2 also indicates a shift of turbulent flow fluctuation towards the higher frequencies compared with those measured upstream of the rib; this is consistent with the large shear, caused by the presence of the block, destroying the larger eddies. Downstream of the rib, the sequence of spectra 2, 3 and 4 shows a shift towards the lower frequencies. This variation of eddy scale can also be identified from the helium-bubble visualization as is shown in Fig. 1c; the traces over the block show the presence of much higher frequencies than those observed elsewhere. Velocity probability distributions were also measured with hot-wire probes and typical results are shown on Fig. 6.

The curves referenced 1, 2 and 3 demonstrate a change from positive to negative skewness in a relatively short distance. This variation in the sign of skewness is usually associated with locations of large gradients and inflection points in the mean velocity profile. Distributions 5 and 4 are probability distributions of a U-component of velocity associated respectively with positive and negative values of V component and measured at the same location as distribution 1. They indicate opposite skewness suggesting that, when the velocity vector is upwards, the flow is associated with lower U-component velocities; the reverse holds for negative V. Contours of joint probability distributions of U and V, similar to those presented by Ribeiro and Whitelaw (17), would indicate asymmetry about the point of zero U/σ_U and V/σ_V and higher densities in the first and third quadrants. Comparison of distributions 5 with 2 and 4 with 3 suggests that the flow carries information from previous locations; when the flow moves upwards, the probability characteristics are similar to those measured at lower regions; when the flow moves downwards, the probability characteristics correspond to those in upper regions. The most probable velocities of distributions 4 and 5 correspond closely to the two small kinks of distribution 1.

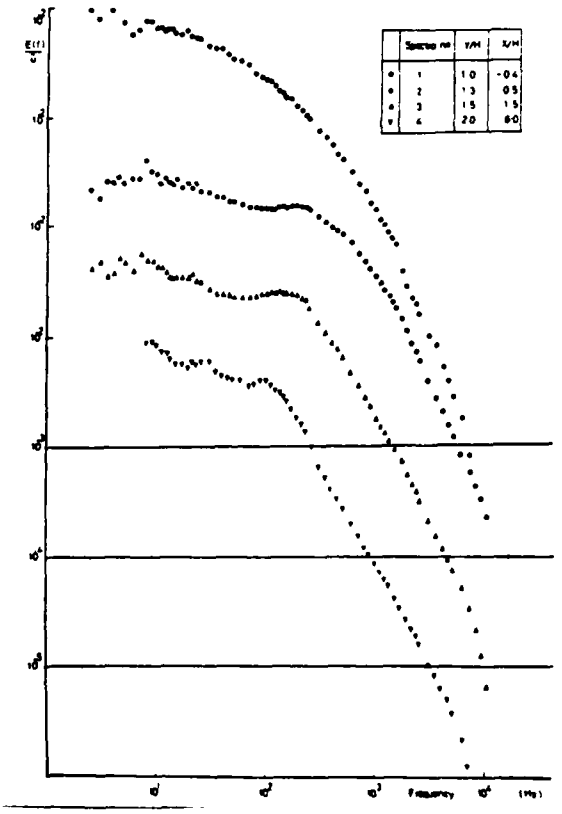

Fig. 5 Turbulence energy spectra

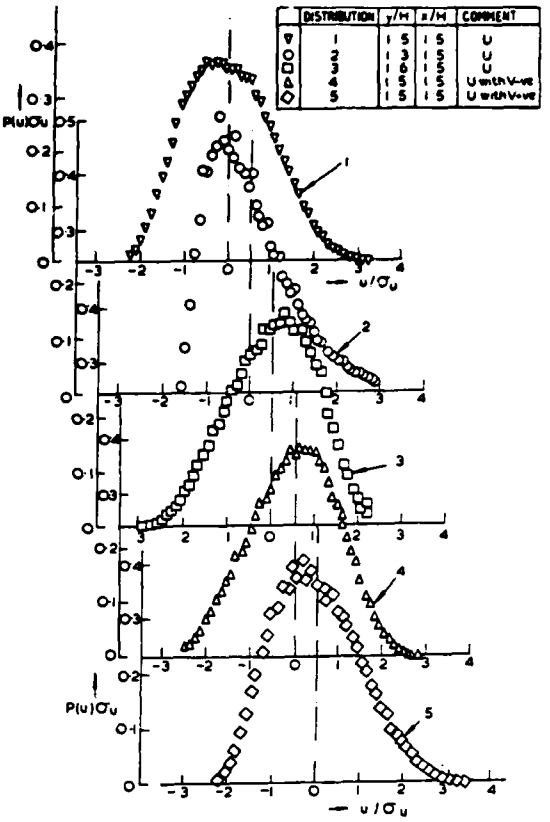

Fig. 6 Velocity probability distributions: obtained with hot-wire anemometer

4. DISCUSSION

The profile c of Fig. 2(i) indicates that the zero velocity streamline beginning at the front edge of the block has a reduction in height (zero velocity at y/H of 1.10 compared with y/H of 1.34 at the trailing edge) caused by the sudden pressure decrease behind the block. The zero velocity line is still at y/H of 1.10 at x/H of 6 and moves to the reattachment point which, for this case (δ/H = 0.55), is approximately 12.3H behind the leading face of the rib. The shape of profile f, figure 2(i), obtained 13H down-

stream, indicates that the mean velocity at this location has already been entirely positive for some distance. For a boundary layer thickness to block height ratio of 0.34 (distance from the trip = 187.3 mm) the measured recirculation length was around 12.9H and indicates the small influence of δ/H. The measured reattachment distances are smaller than those presented by Good and Joubert and Sakamoto et al and this cannot be explained by the differences in the ratio of boundary layer thickness to block height (0.34 and 0.55 in the present case compared with 0.612 and 0.427). However, it has also been found that the rib width has a much larger effect on the length of the recirculation zone length; for δ/H = 0.55 and L/H = 3 (i.e. L = 70.5 mm), the reattachment line was located at 10.2H downstream. It may be expected that the reattachment distance will be longer, therefore, for fences than for square ribs and to be much shorter for a backward-facing step. The difference between the present results and those of Tillman suggests that differing rib geometry may not be the complete answer; however the blockage ratio used by Tillman was much larger (117) and probably accounts for the differences with the present results.

The calculated results of Vasilic-Melling suggest that the length of the rib should have only a small influence on the reattachment length. This is not confirmed by the present results which show that the trajectory of the zero velocity streamline is initially dictated by the rib height and upstream boundary thickness, but the length of the top surface of the rib affects the trajectory and the length of downstream recirculation. This is confirmed by the slope of the dividing streamline which, in Fig. 3, reduced between 0.25H and 0.5H and increased again from 0.5H to 1.0H; the increase is due to the presence of the downstream recirculation zone extending over the top face of the rib, see Fig. 1. The stronger recirculation region immediately downstream of a fence causes a greater initial slope of the dividing streamline and results in a longer reattachment length such as observed by Good and Joubert and Sakamoto et al. The shorter reattachment length of Bradshaw and Wong (6H) downstream of a backward facing step, is consistent with the zero velocity streamline leaving the trailing edge almost horizontally which conforms with the above argument. Between the large recirculation zone downstream of the rib and the downstream plane of the rib, a second and smaller recirculation region can be identified, Fig. 2(i)c, with an opposite rotation to that of the main recirculation. At 0.5H downstream of the downstream face of the block, this recirculation extends vertically to 0.7H from the surface. The corresponding turbulence intensity profile, Fig. 2(ii)c has, therefore, two points of discontinuity and two minima.

5. CONCLUSIONS

The following more important conclusions may be extracted from the preceding text.

(1) The flow characteristics in the vicinity of single roughness ribs have been quantified with a laser-Doppler anemometer. They show, for example and for the case of the 23.5 mm square rib, a region of upstream recirculation of length less than 1H and a downstream reattachment of around 12.3H; the downstream region of recirculation contains two vortices of opposite sense. An influence of boundary-layer thickness to block height ratio on the recirculation length has been detected but is much less than that due to the length to height ratio of the rib.

(2) The trajectory of the streamline dividing forward from backward flow is clearly influenced by the length of the rib and confirms that in contrast of previous calculations, the reattachment length should be different for a rib and a fence.

(3) In the vicinity of the shear layer above the rib, hot-wire measurements indicate small peaks in the energy spectra and rapid changes in the skewness factor which would not be represented by eddy-viscosity type models of turbulence.

ACKNOWLEDGEMENTS

The authors are glad to acknowledge the support from the Science Research Council and the National Gas Turbine Establishment.

REFERENCES

1 Crabb, D., Durão, D.F.G., and Whitelaw, J.H., "Velocity Characteristics in the Vicinity of a Two-Dimensional Rib." Proc. of the 4th Brazilian Congress of Engineering Mechanics, Paper B-3, 415-429, Florianapolis, 1977.

2 Pope, S.B., and Whitelaw, J.H., "The Calculation of Near-Wake Flows." J. Fluid Mech. 73, 9, 1975.

3 Vasilic-Melling, D., "Three-Dimensional Turbulent Flow Passed Rectangular Bluff Bodies." Ph.D. thesis, University of London, 1976.

4 Castro, I.P., and Robins, A.G., "The Flow around a Surface-Mounted Cube in Uniform and Turbulent Streams." J. Fluid Mech. 79, 307, 1977.

5 Tillman, W., "Investigations of some Particularities of Turbulent Boundary Layers on Plates." British Ministry of Aircraft Production, Translation MAP-VG-34-45T, 1945.

6 Plate, E.J., and Lin, C.W., "The Velocity Field Downstream from a Two-Dimensional Model Hill." Colorado State University Report CER65JP14, 1965.

7 Good, M.C., and Joubert, P.N., "The Form Drag of Two-Dimensional Bluff Plates Immersed in Turbulent Boundary Layers." J. Fluid Mech. 31, 547, 1968.

8 Sakamoto, H., Morita, M., and Arie, M., "A Study of the Flow around Bluff Bodies Immersed in Turbulent Boundary Layer." Bulletin JSME 18, 1126, 1975.

9 Bradshaw, P., and Wong, F.Y.F., "The Reattachment and Relaxation of a Turbulent Shear Layer." J. Fluid Mech. 52, 113, 1972.

10 Moss, W.D., Baker, S., and Bradbury, L.J.S., "Measurements of Mean Velocity and Reynolds Stresses in some Regions of Recirculating Flow." Proc. of Turbulent Shear Flow Symposium, the Penn. State University, 13.1, 1977.

11 Restivo, A., and Whitelaw, J.H., "Turbulence Characteristics of the Flow Downstream of a Symmetric

Plane, Sudden Expansion." Journal of Fluids Engineering, 100, 308, 1978.

12 Durão, D.F.G., and Whitelaw, J.H., "Velocity Characteristics of the Flow in the Near-Wake of a Disc." J. Fluid Mech., 85, 369, 1978.

13 Kacker, S.C., and Whitelaw, J.H., "The Turbulence Properties of Wall-Jet and Wall-Wake Flows." J. Appl. Mech., 38E, 239, 1971.

14 Button, B.L., Private Communication, 1976.

15 Durão, D.F.G., and Whitelaw, J.H., "The Performance of Acousto-Optic Cells for Laser-Doppler Anemometry." J. Phys. E. Sci. Instruments, 8, 776, 1975.

16 Durão, D.F.G., Laker, J., and Whitelaw, J.H., "Digital Processing of Frequency-Analysed Doppler Signals." Proc. of LDA-75 Symposium, Technical University of Denmark, 1976.

17 Ribeiro, M.M., and Whitelaw, J.H., "Statistical Characteristics of a Turbulent Jet." J. Fluid Mech., 70, 1, 1975.

TURBULENT SHEAR FLOW BEHIND HEMISPHERE-CYLINDER PLACED ON GROUND PLANE

SHIKI OKAMOTO

DEPARTMENT OF MECHANICAL ENGINEERING,
SHIBAURA INSTITUTE OF TECHNOLOGY,
TOKYO, JAPAN

ABSTRACT

This paper presents an experimental investigation of the flow past a hemisphere-cylinder (a circle whose lower half is replaced by a circular cylinder). The experiment was carried out in an N. P. L. blow-down type wind tunnel having a working section of 400 x 400 x 2000 mm in size at the Reynolds number 4.74×10^4.

The drag and lift coefficients were determined by integration of the surface pressure. It was found that the drag coefficient of a sphere placed on a ground plane is deducted 7.5 percent by fitting up the lower half of sphere with a cylindrical skirt. The velocity and pressure distributions and turbulence intensities in the turbulent shear flow behind a hemisphere-cylinder were measured. Since a hemisphere-cylinder is seen to be a hybrid of sphere and circular cylinder of aspect ratio one, the results of a hemisphere-cylinder were compared with those of a sphere and a circular cylinder of aspect ratio one.

1. NOMENCLATURE

b	:	Position of peak velocity defect [mm]
C_D	:	Drag coefficient
C_L	:	Lift coefficient
C_p	:	Pressure coefficient = $(P-P_\infty)/(\rho U^2_\infty/2)$
D	:	Diameter of cylinder [mm]
H	:	Height of cylinder [mm]
n	:	Frequency of vortex shedding [Hz]
P	:	Static pressure [Pa]
P_∞	:	Free-stream pressure [Pa]
P_0	:	Stagnation pressure [Pa]
r	:	Radial distance from center axis of cylinder [mm]
Re	:	Reynolds number = $U_\infty D/\nu$
St	:	Strouhal number = nD/U_∞
U	:	Time-mean velocity in X-direction [m/s]
U_∞	:	Free-stream velocity [m/s]
u',v',w'	:	Velocity fluctuation in X, Y, Z direction [m/s]
X, Y, Z	:	Coordinates axes [mm]
α	:	Latitude angle [degree]
δ	:	Thickness of shear layer [mm]
θ	:	Longitude angle [degree]
ν	:	Kinematic viscosity of air [m^2/s]
ρ	:	Density of air [kg/m^3]

2. INTRODUCTION

Most of the investigations of the flow past a three-dimensional bluff body placed on a ground plane have been performed concerning with buildings, cooling towers, stacks, and other structures. The bodies hitherto investigated are divided mainly into two groups : the tall bodies of high aspect ratio H/D (for example, tall building, stack) and the short bodies of low aspect ratio (for example, sphere, short circular cylinder). Hunt [1] studied the flow past a building, Peterka-Cermak [2] measured the mean velocity defect and turbulence in the wake behind a building, and Okamoto-Yagita [3] investigated the flow past a circular cylinder of finite length placed on a ground plane.

On the other hand, Schlichting [4] studied the flow past a sphere concerning with the surface roughness, Klemin-Schaefer-Beerer[5] measured the drag of a sphere placed on a ground plane, and Okamoto [6] investigated the flow past a sphere placed on a ground plane. Moreover, Sforza-Mons [7] studied the wall wake behind a rectangular plate placed on the leading edge of a flat plate, and Okamoto et al. [8] investigated the flow past a cone placed on a ground plane. Among the bodies of low aspect ratio, sphere, circular cylinder, and hemisphere-cylinder (a sphere whose lower half is replaced by a circular cylinder) are often seen at the fuel-tank yards and the electric power plants.

This paper presents an experimental investigation of the flow past a hemisphere-cylinder. Since a hemisphere-cylinder is seen to be the hybrid of sphere and circular cylinder, the result of a hemisphere-cylinder was compared with that of a sphere and a circular cylinder of aspect ratio one, which was measured in this experiment.

3. EXPERIMENTAL APPARATUS AND PROCEDURE OF MEASUREMENT

The experiment was carried out in an N. P. L. blow-down type wind-tunnel having a 400 x 400 mm working section of 2000 mm length. The ground plate, an aluminium plate of 4 mm thickness, was set with a spacing of 25 mm from the lower wall of the tunnel

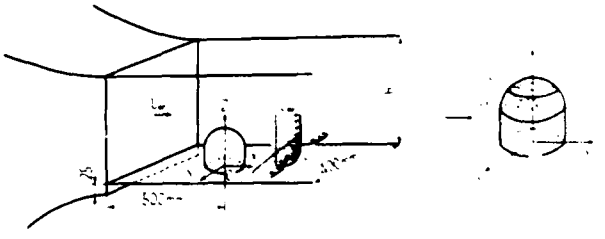

Fig. 1. Schema of apparatus and nomenclature

exit in order to avoid the boundary layer developed on the tunnel wall, as shown in Fig. 1. The model was placed at downstream distance 500 mm from the leading edge of the ground plate. The thickness of boundary layer at the model position was about 4 mm.

The origin of coordinates was taken at the bottom center of the model with the X-axis facing downstream, the Y-axis to the right of downstream, and the Z-axis vertically.

A hemisphere-cylinder and a circular cylinder used in this experiment are shown in Fig. 2. Two kinds of model of 70 mm and 40 mm diameter were used, the former being used for measurement of the surface pressure and the latter used for measurements of velocity, static pressure, and turbulence intesity of the flow. There was no blockage effect even for a model of 70 mm diameter, because the blockage ratio in this case was 0.026 which is less than the limiting value 0.05 obtained by Farell et al. [9].

The pressure holes of 0.5 mm diameter were bored with the angular spacing of α=10 degree on the surface of a hemisphere-cylinder in the vertical plane θ=0. Measurements of the surface pressures for any values of θ were done by rotating the model about the vertical Z-axis. The surface pressures on a circular cylinder were measured through the pressure holes of 0.5 mm diameter bored with 7 mm vertical spacing on the surface in the vertical plane θ=0.

The velocity vector was obtained by use of a cylindrical yawmeter of 6 mm diameter. The time-mean velocity and the static pressure were measured by use of a Pitot and static-pressure tube of 1 mm diameter, and turbulence was measured by a hot wire anemometer of constant temperature type. The flow behind a cylinder was measured at various distances X/D=1~14 at the Reynolds number of 4.74×10^4.

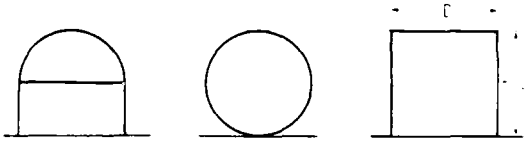

Fig. 2. Models

4. EXPERIMENTAL RESULTS

4. 1. Surface Pressure

The surface-pressure distribution on the upper hemispherical part and the lower cylindrical part of a hemisphere-cylinder are shown in Figs. 3 and 4 respectively, in which the dotted lines represent the theoretical value $C_p=1-(9/4)\sin^2\theta$ of a sphere in the absence of a ground plane and $C_p=1-4\sin^2\theta$ of a two-dimensional circular cylinder obtained by the potential-flow theory. The pressure distributions on the cylindrical surface and the top surface of a circular cylinder of H/D=1 placed on a ground plane are shown in Figs. 5 and 6 respectively.

The dimensionless surface pressures $(P-P_\infty)/(P_0-P_\infty)$ at θ=0 are shown in Fig. 7, from which the stagnation point is seen to be located at Z/D=0.45 for three bodies. This location of the stagnation point is slightly low compared with Z/D=0.6 for two-dimensional fence measured by Good-Joubert [10]. It should be noted that the pressure on the hemispherical surface of a hemisphere-cylinder at θ=0 agrees with that of a sphere and the pressure on the lower cylindrical

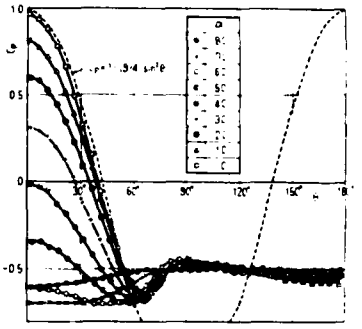

Fig. 3. Surface pressure distribution on upper hemispherical part of hemisphere-cylinder

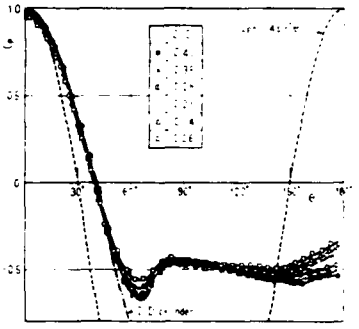

Fig. 4. Surface pressure distribution on lower cylindrical part of hemisphere-cylinder

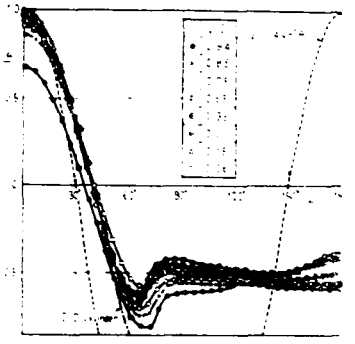

Fig. 5. Pressure distribution on cylindrical surface of circular cylinder

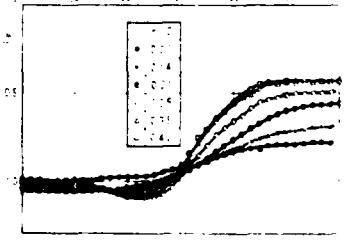

Fig. 6. Pressure distribution on top surface of circular cylinder

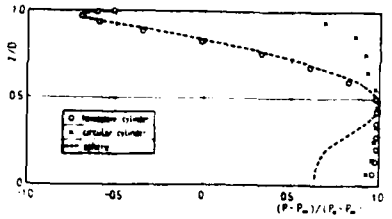

Fig. 7. Pressure at θ=0

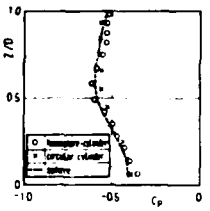

Fig. 8. Pressure at θ=180 deg.

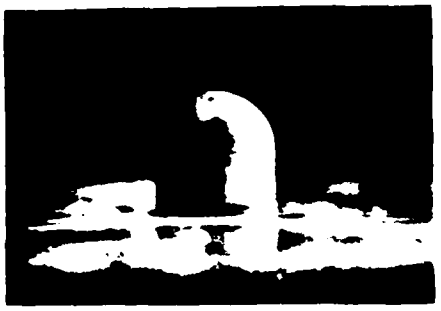

Fig. 9. Separation line on hemisphere-cylinder

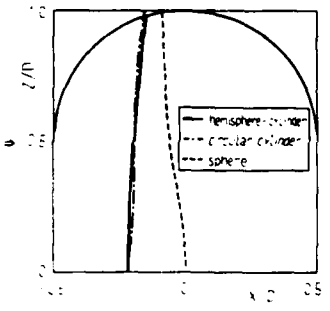

Fig. 10. Separation lines on bluff bodies

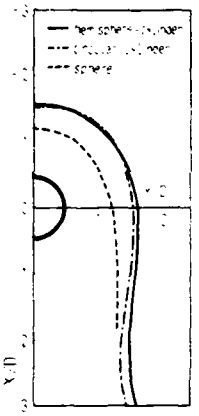

Fig. 11. Separation lins on ground plate

surface is close to that of a circular cylinder of H/D=1, while the pressure at θ=180 degree is nearly equal for three bodies, as seen in Fig. 8.

Fig. 9 shows the separation line obtained by an oil film technique of visualization. It is found that the separation line of a hemisphere-cylinder is close to that of a circular cylinder, but greatly different from that of a sphere, as shown in Fig. 10.

4.2. Drag and Lift

The drag and lift coefficients of a hemisphere-cylinder are determined from the surface pressure by following equations.

$$C_D = \frac{2}{\pi}\int_0^{\frac{\pi}{2}}\int_0^{\pi} C_P \cos^2\alpha \cos\theta \, d\alpha \, d\theta \qquad \text{for hemispherical part}$$

$$C_D = \int_0^{\frac{1}{2}}\int_0^{\pi} C_P \cos\theta \, d\theta \, d(Z/D) \qquad \text{for cylindrical part}$$

$$C_L = -\frac{1}{\pi}\int_0^{\frac{\pi}{2}}\int_0^{\pi} C_P \sin 2\alpha \, d\alpha \, d\theta \qquad \text{for hemispherical part}$$

The above-mentioned drag is, strictly speaking, the pressure drag, but it may be seen to be the total drag, because the frictional drag of a hemisphere-cylinder is negligible compared with the pressure drag. The values of C_D and C_L of hemisphere-cylinder, sphere, and circular cylinder of H/D=1 are shown in Table 1.

Table 1. Values of drag and lift coefficients

Bluff bodies	C_D	C_L
Hemisphere-cylinder	0.580	0.470
Circular cylinder	0.698	0.775
Sphere [6]	0.627	0.242

It is found that the drag is smallest for a hemisphere-cylinder and the lift is greatest for a circular cylinder of H/D=1 among three bodies. It is noteworthy that the drag coefficient of a sphere placed on a ground plane is deducted 7.5 percent and the lift coefficient is increased about 94 percent by fitting up the lower half of sphere with a cylindrical skirt.

The drag coefficient of a sphere at the subcritical Reynolds number ($Re=4.74 \times 10^4$) is increased 30.6 persent by the presence of a ground plate. An increase of C_D due to the presence of a ground plane was pointed out by Klemin et al. [5], whose experiment of a sphere of 609.6 mm diameter at the supercritical Reynolds number ($Re=1.69 \times 10^5$) gave an increase 186.5 percent of C_D by the presence of a gound plane and a collor. An increase of C_D of a sphere due to the presence of a ground plane seems to be remarkable at the supercritical Reynolds numbers compared with at the subcritical Reynolds numbers. The drag coefficients $C_D=0.698$ of a circular cylinder of H/D=1 is in good agreement with $C_D=0.70$ by Okamoto-Yagita [3].

4. 3. Vortices

It has been known from the experiments of a cone [8] and a sphere [6] placed on a ground plane that there exist the vortices of two kinds :

(1) The horse-shoe vortices generated at the corner between the frontal face of obstacle and a ground plane.
(2) The arch vortices generated behind the separation line on the surface of obstacle.

The separation, which induces the horse-shoe vortices, occurs on the ground plate, as shown in Fig. 11. The separation line for a hemisphere-cylinder is close to that of a circular cylinder, but different from that of a sphere.

The arch vortices are shed downstream, inclined and fallen down on the ground plane by a strong downwash behind the obstacle. The movement of the arch vortices can be surmised from the pressure distribution on the ground plane shown in Fig. 12. There are a pair of portions of lowest pressure, at which the roots of arch vortex are seen to be attached to the ground plane. The position of root of an arch vortex is shown in Table 2. It is hence supposed that the arch vortex rotates about the attachment points and falls down.

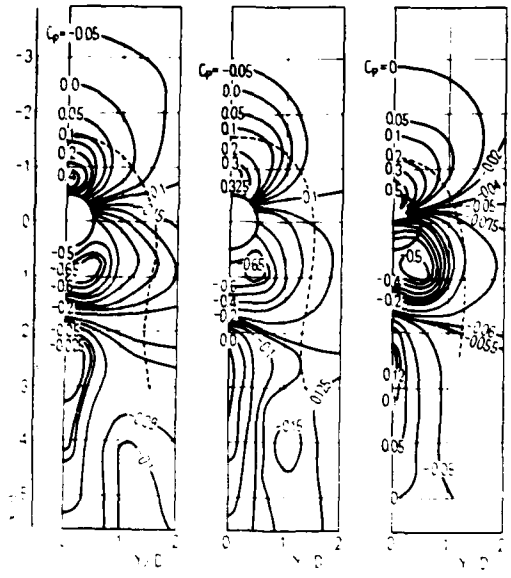

hemisphere-cylinder circular cylinder sphere

Fig. 12. Static pressure distribution on ground plate

Table 2. Position of roots of arch vortices

Bluff bodies	X/D	Y/D
Hemisphere-cylinder	0.95	0.30
Circular cylinder	0.90	0.50
Sphere [6]	0.86	0.35

Fig. 13. Horse-shoe vortices

Fig. 14. Arch vortices

The vortices generation was visualized by the ink shedding in the water tank at the Reynolds number Re=1.06 x 10^3. The horse-shoe and arch vortices in the case of a hemisphere-cylinder are shown in Figs. 13 and 14 respectively. Fig. 14 illustrates that the arch vortices incline and fall down.

The Strouhal number of the arch vortex shedding measured by a hot-wire anemometer is shown in Table 3. It is found that the Strouhal number for a hemisphere-cylinder is small compared with that for a circular cylinder and a sphere.

Table 3. Strouhal number of arch vortex shedding

Bluff bodies	St=nD/U_∞
Hemisphere-cylinder	0.152
Circular cylinder	0.225
Sphere [6]	0.222

The recirculation region is formed behind an obstacle. Because of a strong downwash behind a hemisphere-cylinder, the recirculation region is remarkably reduced compared with a two-dimensional fence. The position of highest pressure on the ground plane is seen to be the point of reattachment of the outer streamline enclosing the recirculation region. The reattachment point is the rear end of recirculation region, which are shown in Table 4. It is found that the recirculation region is reduced for a hemisphere-cylinder compared with a sphere and a circular cylinder. The rear end of recirculation region is located at X/D=2.0 for a hemisphere-cylinder, while X/D=13.2 for two-dimensional fence according to Good-Joubert's experiment [10].

Table 4. Reattachment point

Bluff bodies	X/D
Hemisphere-cylinder	2.00
Circular cylinder	2.92
Sphere [6]	2.50

4. 4. Shear Layer Behind Bluff Body

Fig. 15 shows the distribution of velocity vector past a hemisphere-cylinder in the center section (Y=0). It is found from this figure that the recirculation region ends at X/D=2.0, as surmised from the pressure distribution on the ground plane, and the turbulent shear layer is formed along the ground plane at X/D>4.

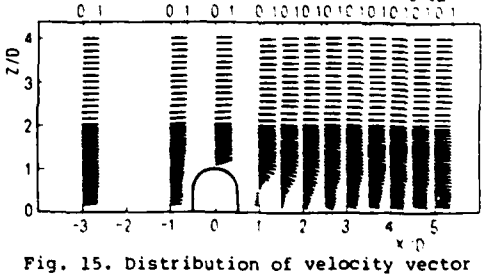

Fig. 15. Distribution of velocity vector in center section (Y=0)

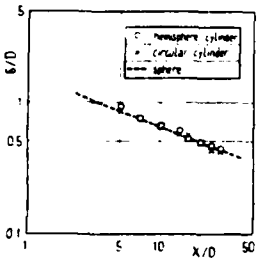

Fig. 16 Thickness of shear layer in center section (Y=0)

Fig. 16 shows the thickness of shear layer in the center section (Y=0), which is expressed as

$$\delta/D=1.63(X/D)^{0.40}$$

for three bluff bodies. It follows that the wall wake behind a three-dimensional obstacle becomes thin with an increase in the downstream distance.

4. 5. Velocity Defect in Horizontal Center Section (Z/D=0.5)

Fig. 17 shows the distribution of mean velocity defect in the horizontal center section (Z/D=0.5). The position of peak velocity defect are shifted in the Y-direction with an increase in the downstream distance. Fig. 18 shows the velocity defect in the center section (Y=0), which is expressed as

$$(U_\infty-U)/U_\infty=0.95(X/D)^{-1.62}$$

at X/D>3.0 for three bluff bodies. This is close to Hunt's result : $(U_\infty-U)/U_\infty \propto X^{-1.5}$ for the wake behind a building [1].

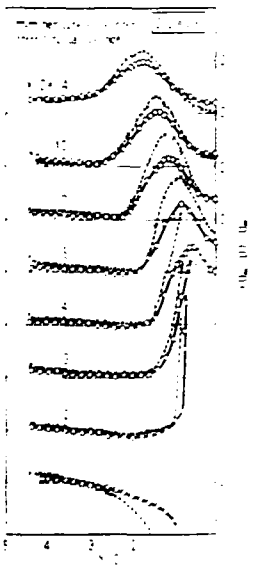

Fig. 17. Profiles of velocity defect in horizontal center section (Z/D=0.5)

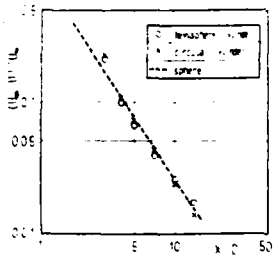

Fig. 18. Velocity defect in center section (Y=0, Z/D=0.5)

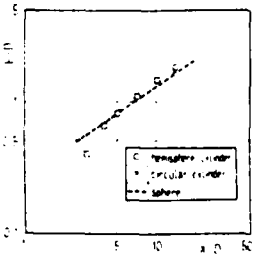

Fig. 19. Position of peak velocity defect (Z/D=0.5)

Fig. 19 shows the position (Y=b) of peak velocity defect, which is expressed as

$$b/D=0.21(X/D)^{0.84}$$

for hemisphere-cylinder and circular cylinder, while

$$b/D=0.26(X/D)^{0.69}$$

for sphere. It is found from Figs. 16 and 19 that the wall wake behind an three-dimensional obstacle becomes thin and spreads transversely with increasing the downstream distance. This change in the wall wake can be seen obviously from the lines of $(U_\infty-U)/U_\infty=0.10$ shown in Fig. 20.

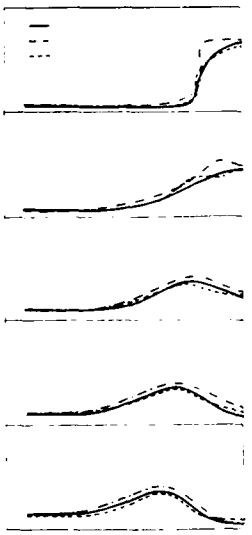

Fig. 20. Lines of $(U_\infty-U)/U_\infty=0.10$

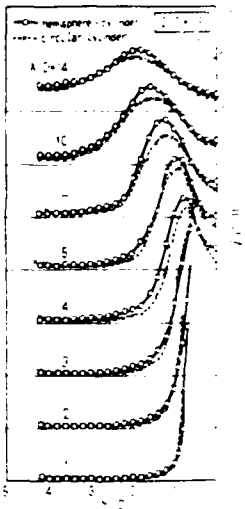

Fig. 21. Turbulence intensity in X-direction (Z/D=0.5)

Fig. 22. Turbulence intensity in Y-direction (Z/D=0.5)

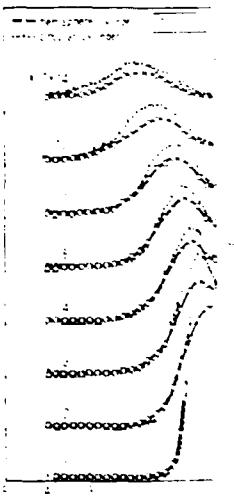

Fig. 23. Turbulence intensity in Z-direction (Z/D=0.5)

4. 6. Turbulence Intensities in Horizontal Center Section (Z/D=0.5)

Figs. 21, 22 and 23 show the turbulence intensities in the X-, Y-, and Z-directions in the horizontal center section (Z/D=0.5) respectively. The position of the peak turbulence intensity is shifted in the Y-direction with increasing the downstream distance. The peak turbulence intensities in the X-, Y- and Z-directions occur at Y/D=1.00, 0.80 and 1.00 for X/D=5, and at Y/D=1.58, 1.50 and 1.45 for X/D=10 respectively.

Fig. 24 shows the decay of the X-component of turbulence intensity in the center section (Y=0), which is expressed as

$$\sqrt{\overline{u'^2}}/U-(\sqrt{\overline{u'^2}}/U)_\infty=A(X/D)^{-1.40},$$

where A=0.85 for hemisphere-cylinder, and A=0.69 for circular cylinder and sphere. Fig. 25 shows the decay of the Y-component of turbulence intensity, which is expressed as

$$\sqrt{\overline{v'^2}}/U-(\sqrt{\overline{v'^2}}/U)_\infty=B(X/D)^{-1.37},$$

where B=1.05 for hemisphere-cylinder and circular cylinder, and B=0.57 for sphere. Fig. 26 shows the decay of the Z-component of turbulence intensity, which is expressed as

$$\sqrt{\overline{w'^2}}/U-(\sqrt{\overline{w'^2}}/U)_\infty=0.55(X/D)^{-1.09},$$

for three bodies.

It follows that the decay of the X- and Z-components of turbulence intensity in the section (Z/D=0.5) for a hemisphere-cylinder are nearly equal to that of a circular cylinder and a sphere, and the decay of Y-component of turbulence intensity of a hemisphere-cylinder is nearly equal to that of a circular cylinder, but different from that of a sphere.

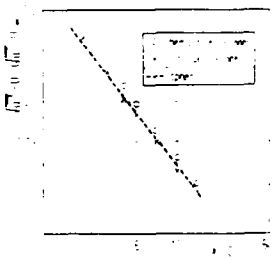

Fig. 24. Decay of X-component of turbulence intensity (Y=0, Z/D=0.5)

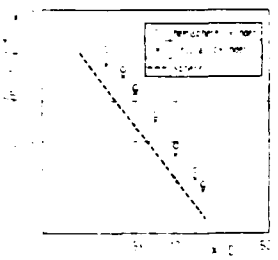

Fig. 25. Decay of Y-component of turbulence intensity (Y=0, Z/D=0.5)

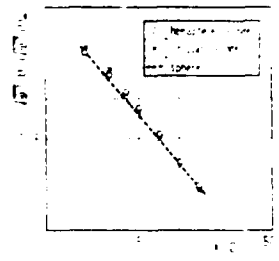

Fig. 26. Decay of Z-component of turbulence intensity (Y=0, Z/D=0.5)

5. CONCLUSION

The experimental results are summarized as follows :

(1) The drag is smallest for a hemisphere-cylinder and the lift is largest for a circular cylinder among three bluff bodies.

(2) The Strouhal number of arch vortex shedding is 0.152 for a hemisphere-cylinder, while it is 0.225 for a circular cylinder and 0.222 for a sphere.

(3) The thickness of shear layer behind a hemisphere-cylinder in the center section (Y=0) is equal to that of a circular cylinder and a sphere.

(4) The velocity defect in the center section (Y=0, Z/D=0.5) of a hemisphere-cylinder is nearly equal to that of a circular cylinder and a sphere.

(5) The decay of the X- and Z-components of turbulence intensity in the section (Z/D=0.5) of a hemisphere-cylinder are nearly equal to that of a circular cylinder and a sphere. And the decay of the Y-component of turbulence intensity is nearly equal to that of a circular cylinder, but different from that of a sphere.

ACKNOWLEDGEMENT

The author expresses his thanks to Dr. Tetsushi Okamoto, professor emeritus of Tokyo Institute of Technology, for his cordial guidance.

REFERENCES

1) Hunt, J. C. R. : "The effect of single buildings and structures", Philosophical Transaction of Royal Society, London, A. 269, 1971, pp. 457-467

2) Peterka, J. A. and Cermak, J. E. : "Turbulence in building wakes", Proceedings of the Fourth International Conference on Wind Effects on Building and Structures, 1977, pp. 447-463

3) Okamoto, T. and Yagita, M. : "The experimental investigation on the flow past a circular cylinder of finite length", Bulletin of the Japan Society of Mechanical Engineers, vol. 16, No. 95, May 1973, pp. 805-814.

4) Schlichting , H. : " Experimentelle Untersuchungen zum Rauhigkeits-Problem", Ingenieur Archiv, vol. 7, 1936, pp. 1-34.

5) Klemin, A, Schaefer, E. B. and Beerer, J. G. : "Aerodynamics of the perisphere and trylon at world's fair",Transactions of the American Society of Civil Engineers, No. 2042, 1939, pp. 1449-1472.

6) Okamoto, S. : "Turbulent shear flow behind a sphere placed on a plane boundary", Proceedings of 2nd symposium on Turbulent Shear Flows,1979, pp. 16.1-16.6 and Turbulent Shear Flows 2, Springer-Verlag, Berlin Heidelberg New York, 1980. pp. 246-256.

7) Sforza, P. M. and Mons, R. F. : "Wall-wake: Flow behind a leading edge obstacle", AIAA Journal, vol.8 December, 1970, pp. 2162-2167.

8) Okamoto, T., Yagita, M. and Kataoka, S. : "Flow past cone placed on flat plate", Bulletin of the Japan Society of Mechanical Engineers, vol. 20, No. 141, March 1977, pp. 329-336.

9) Farell, C., Carrasquel, S., Güven, O. and Patel, V. C. : "Effect of wind-tunnel walls on the flow past circular cylinders and cooling tower models", Transaction of the ASME, Series I, vol. 99, No. 3, 1977, pp.470-479

10) Good, M. C. and Joubert, P. N. : "The form drag of two-dimensional bluff-plates immersed in turbulent boundary layers", Journal of Fluid Mechanics, vol. 31 part 3, 1968, pp. 547-582.

LOW FREQUENCY UNSTEADINESS OF A REATTACHING TURBULENT SHEAR LAYER

By

John K. Eaton, Assistant Professor
James P. Johnston, Professor
Department of Mechanical Engineering
Stanford University

ABSTRACT

Low-frequency unsteadiness of a reattaching shear layer was studied in the flow behind a backward-facing step. Spectral data from a hot-wire probe showed that a substantial fraction of the measured turbulence intensity occurs at frequencies significantly lower than the large eddy passing frequency. Several thermal tuft probes were used simultaneously to identify the source of the low-frequency disturbances. It was concluded that the reattaching free shear layer undergoes a non-periodic flapping motion. The flapping causes the impingement point of the reattaching shear layer to drift slowly up- and downstream over a range of approximately two step heights. The likely cause of the low-frequency flapping is an instantaneous imbalance between the entrainment rate from the recirculation zone and the reinjection rate near reattachment. The existence of the low-frequency motions must be addressed by future model developers.

NOMENCLATURE

F	Frequency (Hz).
h	Step height = 5.08 cm.
U_o	Inlet free stream velocity.
x	Streamwise coordinate.
x_R	Time mean reattachment location.
γ	Percent of time that flow is in downstream direction.
θ	Momentum thickness.

INTRODUCTION

In this paper we shall discuss our observations and measurements of low-frequency motions of a reattaching shear layer in the flow behind a backward-facing step. Low-frequency motions are defined as those motions having time and length scales much longer than the scales of a typical large, turbulent eddy.[1] The time scale for a large eddy in a separated shear layer is approximately equal to the shear layer thickness divided by one-half of the free stream velocity. The length of a separation bubble is typically 5 to 10 times the shear layer thickness. Therefore the low frequency motions have time scales which are greater than or equal to the time it takes the free stream to pass over the separation bubble.

It has long been recognized that low-frequency unsteadiness can occur in separation bubbles bounded by turbulent free shear layers. "Jitter" of the separation point is frequently reported in airfoil experiments [1] and transitory stall behavior is a well-known but poorly understood example of very large-scale, low-frequency unsteadiness [2]. In general, low-frequency unsteadiness has been regarded as a nuisance rather than a topic of scientific interest. To date, there have been few studies of long time-scale motions of separation bubbles. However, low-frequency unsteadiness can cause significant difficulties in engineering equipment such as combustors and wind tunnel nozzles. It is also a major source of uncertainty in single-sample measurements with relatively short averaging times.

Perhaps more important is the fact that low-frequency unsteadiness causes significant difficulties in the measurement, understanding and modeling of turbulent separated flows. Unsteadiness has gone unrecognized in many previous experiments and has, we believe, contaminated the available data base. For example, it has often been stated that the structure of a reattaching free shear layer is fundamentally different from a plane-mixing layer. The major evidence for this conclusion is that the measured turbulence intensity is considerably higher in a reattaching free shear layer. *It is the authors'* contention [3] that this measured difference is caused largely by low-frequency unsteadiness in reattaching flows which has little real effect on the basic structure of the free shear layer.

The contamination of turbulence data by low-frequency unsteadiness could have serious consequences for computational fluid mechanics. In general, turbulence models attempt to represent the effects of eddies up to the scale of the typical "large eddy" described above. However, turbulence data which are used for calibration of models may be strongly biased by low-frequency contributions. It would then be impossible to rationally compare model results to data.

The backward-facing step flow has usually been considered immune from low-frequency unsteadiness of significant magnitude because the separation line is fixed at the sharp corner. It was felt that most unsteadiness of separation bubbles is related to a wandering separation point. Tani et al [4] and Chandrsuda [5] both determined that low frequency motions were not present in their back-step flows by examining the fluctuations of manometers attached to static taps in the separated zone. However, during the course of a recent study of the backward-facing step flow [6], we found significant evidence of low-

[1] Here we refer to large turbulent eddies as the largest structures visible in flow visualization. These typically have a length scale comparable to the shear-layer thickness.

frequency motions which were affecting the time-averaged data. This led us to concentrate in the present study on understanding low-frequency unsteadiness.

Long time scale motions in backward-facing step flows have not been explicitly studied prior to this work. Low-frequency flapping of a plane jet has been studied by Goldschmidt and Bradshaw [7] and by de Gortari [8]. They found that the flapping was quasi-periodic and had an amplitude of approximately 20% of the jet half width. A number of other workers have investigated low frequency oscillations in cavity flows (c.f. Rockwell and Naudascher [9]), Knisely and Rockwell [10] concluded that low frequency oscillations of a cavity flow are caused by feedback of disturbances from the impingement point which are then amplified in the free shear layer. Rockwell [11] suggested that a similar mechanism may cause low frequency motions in the backward-facing step flow. McGuinness [12] observed low-frequency pressure fluctuations in the separation bubble at a pipe entrance. He concluded from spectral data that these fluctuations were caused by eddies moving upstream in the low speed recirculating flow. However, his flow visualization work did not confirm this conclusion.

OBJECTIVES

The objective of the present study is to understand the nature and cause of low-frequency motions of separation bubbles. We hope to obtain data to gauge the effects of unsteadiness on time-averaged turbulence data. We also hope to better understand how very low-frequency unsteadiness can be accounted for in turbulence models which currently ignore its presence.

METHODS

The experiments were conducted in the same low speed air flow facility used by Eaton and Johnston [13] (see Figure 1). After a short entrance duct to develop turbulent boundary layers the flow passes through a two dimensional sudden expansion of area ratio 3:5. The step height was set at 5.04 cm which gave an aspect ratio (channel span/step height of 12). The inlet free stream velocity was approximately 12 m/s for most of the measurements reported here. At that inlet speed the boundary layer at separation was approximately 0.2 step heights thick and turbulent. The momentum thickness Reynolds number of the boundary layer was 950 indicating that the boundary layer was not fully turbulent. Mean velocity and turbulence intensity profiles however did appear quite similar to an ordinary turbulent boundary layer.

Mean velocity and turbulence data for this flow were reported in references 6 and 13. The measurements indicated that two-dimensionality in the channel was good; mass and momentum balances for an integral control volume around the entire separation bubble showed balance to within 0.5% and 1.7% of the inlet mass and momentum flux, respectively. However, Westphal and Johnston [14] in later measurements using the same facility found a narrow region near the channel centerline where the spanwise velocity profile was non-uniform. Although this non-uniformity may have affected some of the quantitative data, it is doubtful that it had a significant effect on the results reported here.

It was desirable to have a laminar boundary layer at separation for some of the experiments. In this case the tunnel was run at an inlet free stream velocity of 3.26 m/s. The boundary layer at separation was then laminar with a thickness of 0.9 cm and a momentum thickness Reynolds number of 240. Transition of the free shear layer to turbulent flow occurred just downstream of separation despite the fact that the upstream boundary layer was laminar.

The primary instrument used in this study was the thermal tuft, a device which indicates the instantaneous flow direction (upstream or downstream) in a thin layer of fluid adjacent to the wall.[2] A sketch of the probe is shown in Figure 2. The center wire is heated with a DC current of 1.5 amperes to create a heated wake which moves back and forth as the flow direction reverses. The outer two wires are operated as resistance thermometers and sense the presence of the hot wake. The control electronics compare the temperatures of the two outer wires and give an output signal of 0 volts or 5 volts depending on which wire is hotter. It should be noted that the electronics will always indicate an instantaneous flow direction. If there is no temperature difference between the wires electronic noise will cause the output to toggle between 0 and 5 volts at high frequency. In practice, such signal dropout rarely occurs. The signal due to the temperature difference is almost always larger than the electronic noise.

Single hotwires were used for the measurement of mean velocity and turbulence intensity near the outer edge of the shear layer, where the turbulence intensity was less than 30-40%. The probes were operated with a TSI 1050 anemometer and the signal was linearized with a TSI Model 1052 linearizer. A pulsed-wire anemometer [16] was used for mean velocity and turbulence intensity measurements in more highly turbulent regions of the flow including the recirculating region.

RESULTS

The thermal tuft was used to measure the percentage of time that the flow near the wall is in the downstream direction. Plots of this quantity for the two cases (laminar and turbulent boundary layers at separation) are shown in Figure 3. Also shown are the time mean reattachment points for the two cases.[3]

The curves show a broad region at least 4 step heights long where the near wall flow can be instantaneously moving either upstream or downstream.

---

[2] Details of thermal tuft construction and operation are described in Ref. 15.

[3] It was shown by Eaton et al. [17] that the point of 50% downstream flow is the same as the point of zero mean skin function in reattaching flows.

This result alone suggests that large scale unsteadiness is present in the flow. However other evidence is far more conclusive. Averaging times of approximately 200 seconds were needed to obtain converged (±1%) data. This was true both for thermal tuft data and velocity data. The largest turbulent eddies in the flow were the spanwise (Brown-Roshko) vortices which had a maximum period of approximately 0.06 seconds or 1/3600th of the averaging time. It was apparent from statistical considerations that unsteadiness was present which had a time-scale much greater than the large-eddy period.

Spectral analysis of the turbulence data was used to quantify the effect of low frequency fluctuations of the time-averaged data. Spectra were computed only from the hot-wire data bacause the pulsed-wire sampling rate was too slow to obtain alias-free spectra. Autocorrelations of the hotwire signal were obtained using a Hewlett Packard Model 3721A Digital correlator. The digital autocorrelation data were then Fourier transformed to obtain the power spectrum of the velocity fluctuations. The autocorrelation was formed at 100 equally spaced time delays and approximately 130,000 samples were taken at each time delay.

A typical spectrum of hot-wire data is shown in Figure 4. This spectrum was measured near the outer edge of the shear layer at x/h=8, very close to reattachment. The broad peak in the spectrum at a non-dimensional frequency of 0.065 is caused by large spanwise vortices in the free shear layer. The spectrum also shows that significant turbulence energy occurs at frequencies much lower than the large eddy frequency. The spectrum in Figure 4 and others shows that more than 30% of the measured turbulence intensity $(\sqrt{u'^2})$ occurred at non-dimensional frequencies below 0.02, considerably lower than the large-eddy passage frequency. The resolution of the spectra was not sufficient to identify any spectral peaks in the low-frequency range.

The above-described results showed that low-frequency motions occur in the separated flow behind a backward-facing step. These motions have a significant effect on the time-averaged turbulence data. Multiple thermal tufts were used simultaneously in an effort to explore the nature of the low-frequency motions. For this set of experiments the tunnel was run at a somewhat higher speed resulting in a reduction of the reattachment length to 7.6 step heights. Three thermal tuft probes were used at x/h = 6, 8 and 9. Thus, all three probes were within the region where flow reversals occurred a significant fraction of the time. Figure 5 is a typical record of output from two of the probes which shows two significant trends. First, at a given x-location flow reversals occur in bursts of rapid activity separated by times when the flow direction is relatively steady. During the bursts of activity, flow reversals occur at roughly twice the passage frequency of the largest turbulent eddies. Secondly, we find that when a burst is occurring at one location the output is relatively quiescent at the other location. These observations taken together suggest that a motion of larger scale than the large turbulent eddies in the flow must be responsible for the wide region of instantaneous flow reversal. A detailed examination of records similar to Figure 5 shows that for any given short time interval a significant number of flow reversals occur in a region which is only about two step heights long. However, over a long period of time flow reversals occur over a region which is approximately 4 step heights long (see Figure 3). Our interpretation of the records is that the impingement point of the free shear layer is moving slowly up- and downstream. When the impingement point is centered on a probe, rapid flow reversals caused by the passage of large turbulence structures will be recorded. When the impingement point is well upstream of the probe, the "mean" velocity (short-time average) would be sufficiently large that turbulent fluctuations could not cause flow reversals.

The existence of large-scale, low-frequency motions seems to be irrefutable. Given their existence, two significant questions are: (i) are the very long time scale motions periodic in nature? and (ii) what causes the motions? We attempted to resolve the first question using short-time averages of thermal tuft data. The outputs of the three thermal tufts were simultaneously sampled at a rate of approximately 1300 Hz using a microcomputer. Data were recorded for approximately 0.2 seconds, and a number indicating the fraction of samples which indicated downstream flow was recorded for each probe. Sampling recommenced after a very short time delay (< 1 ms). This procedure continued for about 30 seconds for a given run. Short time-averaged values (0.2 seconds) of the percent downstream flow time (γ) were then available at each of three steamwise locations as a function of time. For each time interval a parabola was fitted to the three values of γ and a short-time-averaged reattachment length computed. We assumed that the reattachment point is the same as the point where γ is 50%. This assumption was shown to be valid by Eaton et al. [17] for long-time-averaged data. There is considerable statistical scatter in the data because the averaging time of 0.2 seconds would typically include only about eight flow reversal cycles. The short-time-averaged data varied monotonically for every record examined (several thousand) indicating that statistical uncertainty at least did not cause absurd results. We estimate that the results are within about ± 0.3 step heights of the actual short-time-averaged reattachment point.

A section of one of the records is shown in Figure 6. The short-time-averaged reattachment length varies from about 6.5 to 8.5 step heights about the mean reattachment length of 7.6 step heights. No regular periodicity is evident in the record shown or in any of the other records examined. The record also shows that the impingement point may remain nearly stationary for as long as a second before moving to a new location.

DISCUSSION AND CONCLUSIONS

The results reported above show that low-frequency motions occur in reattaching shear layers. These motions have time scales several times longer than the largest turbulent eddies and make substantial contributions to measured turbulence quantities. Several possible descriptions of the nature and cause of the low-frequency motions are discussed below.

AD-A111 522 PENNSYLVANIA STATE UNIV UNIVERSITY PARK DEPT OF MECH--ETC F/G 20/4
SYMPOSIUM ON TURBULENT SHEAR FLOWS (3RD), UNIVERSITY OF CALIFOR--ETC(U)
SEP 81 F W SCHMIDT AFOSR-80-0033

UNCLASSIFIED AFOSR-TR-82-0032 NL

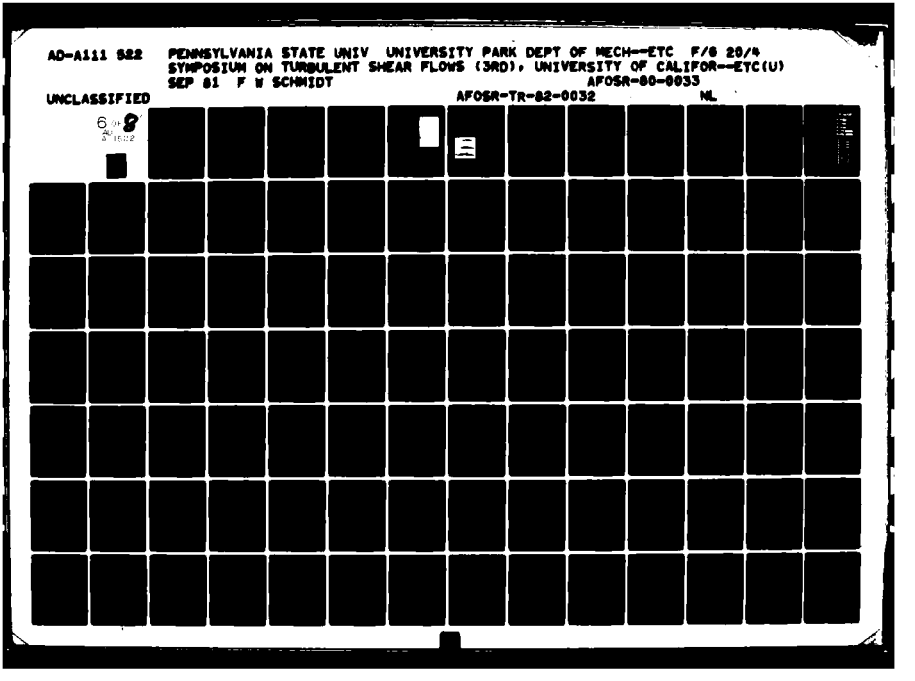

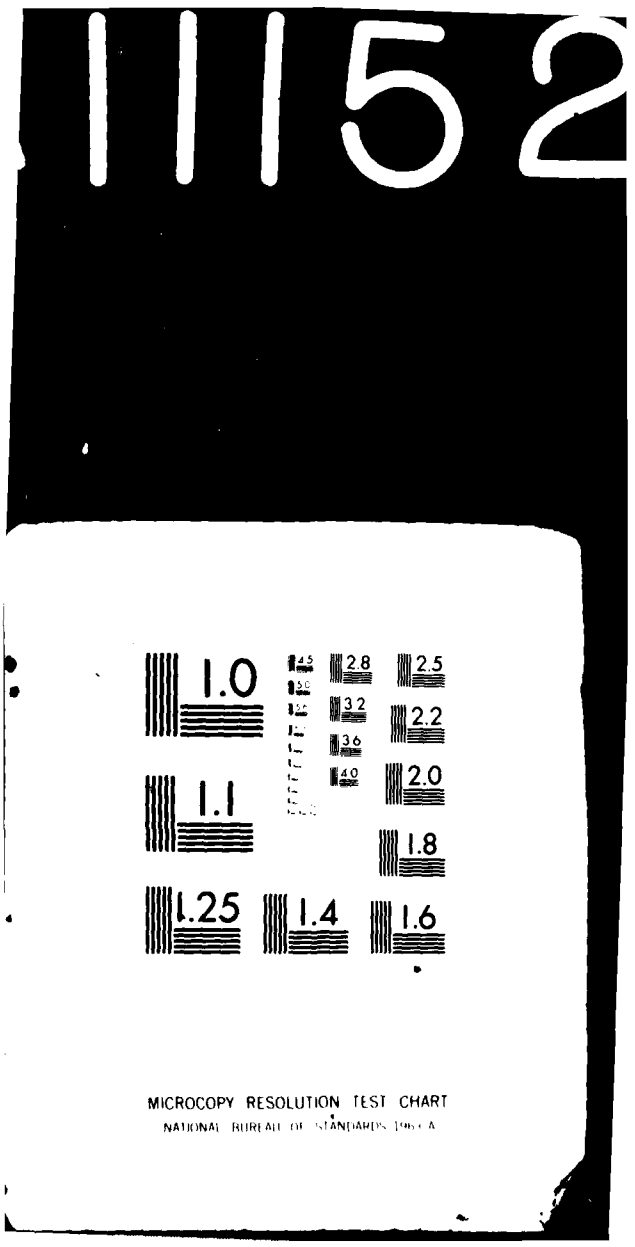
11152
1.0
1.1
1.25
1.4
1.6
1.8
2.0
2.2
2.5
2.8
3.2
3.6
4.0
MICROCOPY RESOLUTION TEST CHART
NATIONAL BUREAU OF STANDARDS 1963-A

Our own opinion is that the motions are long-time-scale, non-periodic flapping of the shear layer. The flapping causes the impingement point of the reattaching shear layer to move up- and downstream over a distance of at least two step heights. We feel that the flapping motion is caused by an instantaneous imbalance between shear-layer entrainment from the recirculating zone on the one hand and reinjection of fluid near reattachment on the other. For example, an unusual event may cause a short-term breakdown of the spanwise vortices in the shear layer. The entrainment rate would be temporarily decreased, while the reinjection rate remained constant. This would cause an increase in the volume of recirculating fluid, thus moving the shear layer away from the wall and increasing the short-time-averaged reattachment length. This conclusion is strongly supported by our thermal tuft data, which show that the impingement point may remain stationary for 10-20 large eddy periods, then move to another location.

Rockwell [11] suggested that the low-frequency motions may be flapping of the shear layer induced by feedback of disturbances from the impingement point to the separation point. The disturbances would appear as a low-frequency modulation of the shear layer downstream of separation which would be amplified by the free shear layer. This is the mechanism responsible for low-frequency motions in cavity flows. However, the present flow is considerably more complex than a cavity flow. Multiple vortex pairings occur upstream of reattachment, and the shear-layer impingement point is not fixed. Resolution of this question may be difficult because of these complexities.

A third possibility is that a section of the recirculating flow could be "divorced" (or cut off) from the separation bubble by a large structure which reaches the wall well upstream of the mean reattachment point. McGuinness [12] observed that the separation bubble was occasionally cut roughly in two and that the downstream half proceeded downstream as a "divorced eddy." McGuinness's observations were made in the separation bubble at the entrance to a pipe, using smoke visualization. We have never observed similar behavior in several experiments on two-dimensional, backward-facing steps, although admittedly the visualization techniques have been crude. A divorced eddy could cause non-monotonic behavior in the short-time-averaged thermal tuft data. The flow sweeping to the wall would cause forward flow, while the divorced eddy would continue to cause flow reversals downstream. Non-monotonic behavior was never observed in the large number of thermal tuft records we examined.

Intermittent separation on the wall opposite the step could also cause the low-frequency motions. Armaly et al. [18] showed that separation could occur on the opposite wall of single-sided sudden expansions at low Reynolds numbers. Opposite wall separation would cause the reattachment length on the step side to shorten. This hypothesis was discounted because thermal tuft results showed that flow reversals never occurred on the opposite wall of the test section.

Finally, the apparent long-time scale could be caused by low-frequency perturbations in the inlet flow. This possibility has been discounted because the wind tunnel has undergone two significant modifications without changing the characteristics of the unsteady motion. These changes included replacing the blower and filter assembly, replacing the inlet diffuser, completely changing the honeycomb and screen arrangement, and lengthening the test-section inlet section downstream of the nozzle. None of these changes caused an appreciable change in the length of the region of flow reversals.

Regardless of their cause, the low-frequency motions can cause serious difficulties for both experimenters and modelers. The spectral data showed that a substantial fraction of the measured turbulence energy is due to the low-frequency unsteadiness. Unfortunately, it is not clear where the low-frequency unsteadiness ends and the turbulence begins. Therefore, an experimenter must be very careful to avoid filtering of low-frequency information. In addition, comparisons among different experiments will be difficult if the unsteadiness is wind tunnel dependent.

The low-frequency motions can probably be ignored by modelers if they need only time-averaged results. One would have to assume that energy is not fed from the low-frequency motions back into the turbulence.

The real problem arises in development and testing of a new model. Models are designed to represent a range of scales which typify the turbulence. If empirical input is used which is biased by very-low-frequency content, one cannot expect the model to correctly represent the turbulence. A model tuned for a given flow configuration could not be expected to work well in another configuration when the low-frequency unsteadiness is different. This problem provides substantial impetus to further investigate low-frequency motions of separated shear layers.

In summary, our data show that a separated and reattaching shear layer undergoes a non-periodic flapping motion of significant amplitude. This motion must be accounted for in future experimental and computational programs if we hope to have a full understanding of reattaching flows.

ACKNOWLEDGMENT

We gratefully acknowledge the support of the Fluid Mechanics Program of the Engineering Division of the National Science Foundation.

REFERENCES

1. Owen, F. K., and Johnson, D. A., "Separated Skin Friction Measurements--Source of Error: An Assessment and Elimination," AIAA Paper No. 80-1409, 1980.

2. Smith, C. R., Jr., and Kline, S. J., "An Experimental Investigation of the Transitory Stall Regime in Two-Dimensional Diffusers, Including the Effects of Periodically Disturbed Inlet Conditions," TASME Journal of Fluids Engineering, Vol. 96(I), 1974, pp. 11-15.

3. Eaton, J. K., and Johnston, J. P., "A Review of Research on Subsonic Turbulent Flow Reattachment," AIAA paper 80-1438, to be published in AIAA Journal, 1981.

4. Tani, I., Iuchi, M., and Komoda, H., "Experimental Investigation of Flow Separation Associated with a Step or Groove," Report No. 364, 1961, Aero Research Institute, Univ. of Tokyo.

5. Chandrsuda, C., "A Reattaching Turbulent Shear Layer in Incompressible Flow," Ph.D. thesis, 1975, Dept. of Aeronautics, Imperial Coll. of Science and Technology.

6. Eaton, J., and Johnston, J. P., "An Evaluation of Data for the Backward-Facing Step Flow," Report prepared for the 1980-81 Conferences on Complex Turbulent Flows, 1980, Stanford Univ.

7. Goldschmidt, V. W., and Bradshaw, P., "Flapping of a Plane Jet," Physics of Fluids, Vol. 16, No. 3, March 1973, pp. 354-355.

8. de Gortari, C. J., "An Experimental Study of the Flapping Motion of a Turbulent Plane Jet," Ph.D. thesis, 1978, Purdue University.

9. Rockwell, D., and Naudascher, E., "Self-Sustained Oscillations of Impinging Free Shear Layers," Annual Review of Fluid Mechanics, Vol. 11, 1979, pp. 67-94.

10. Rockwell, D., and Knisely, C., "Vortex Edge Interaction Mechanisms for Generating Low-Frequency Components," Physics of Fluids, Vol. 23, pp. 239-240.

11. Rockwell, D., private communication, 1980.

12. McGuinness, M., "Flow with a Separation Bubble --Steady and Unsteady Aspects," Ph.D. dissertation, 1978, Cambridge University.

13. Eaton, J. K., Johnston, J. P., and Jeans, A. H., "Measurements in a Reattaching Turbulent Shear Layer," Proceedings of the 2nd Symposium on Turbulent Shear Flows, 1979, London.

14. Westphal, R. V., and Johnston, J. P., unpublished work in progress, 1981.

15. Eaton, J. K., Jeans, A. H., Ashjaee, J., and Johnston, J. P., "A Wall-Flow-Direction Probe for Use in Separating and Reattaching Flows," Journal of Fluids Engineering, Vol. 101, 1979, pp. 364-366.

16. Bradbury, L.J.S., and Castro, I. P., "A Pulsed-Wire Technique for Velocity Measurements in Highly Turbulent Flow," Journal of Fluid Mechanics, Vol. 49, 1971, 657-691.

17. Eaton, J. K., Westphal, R. V., and Johnston, J. P., "Two New Instruments for Flow Direction and Skin-Friction Measurements in Separated Flows," paper submitted to ISA 2nd Int'l. Symposium on Flow, April 1981.

18. Armaly, B. F., Durst, F., and R. Schönung, "Measurements and Predictions of Flow Downstream of a Two-Dimensional Single Backward-Facing Step," Report SFB80/ET/172, SFB80, 1980, Universität, Karlsruhe, Germany.

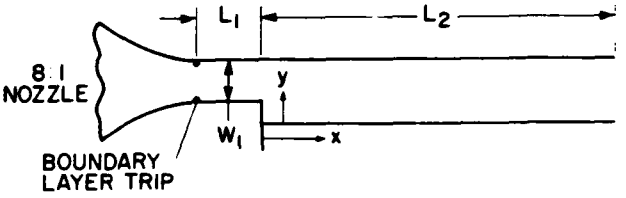

Fig. 1. Sketch of the wind tunnel test section.

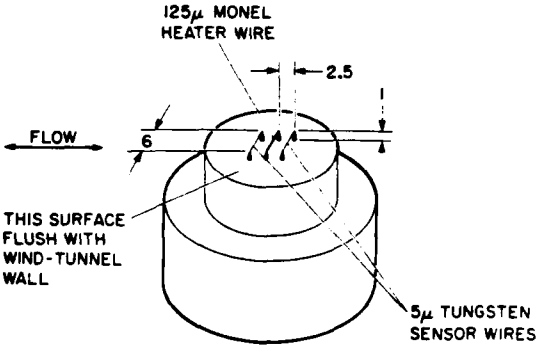

Fig. 2. Sketch of thermal tuft probe (dimensions in mm)

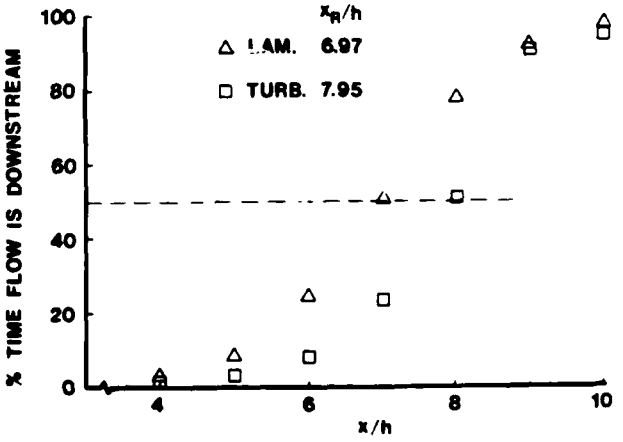

Fig. 3. Time averaged thermal tuft data for laminar and turbulent boundary layers at separation.

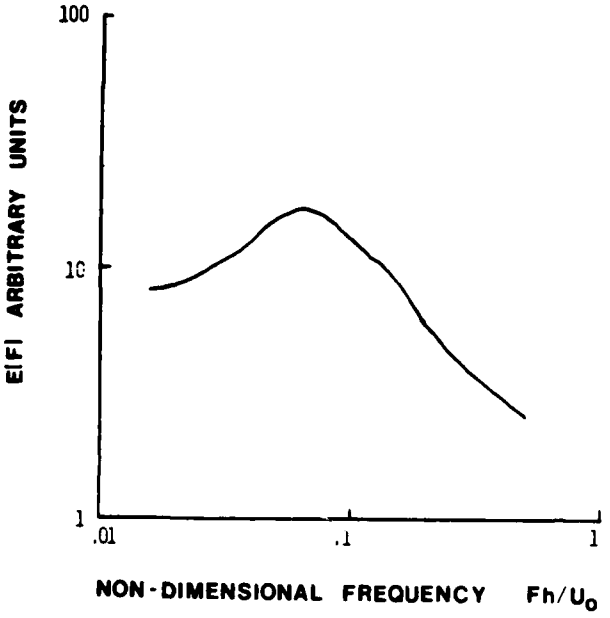

Fig. 4. Power spectrum of streamwise velocity fluctuations near the outer edge of the shear layer at x/h = 8 .

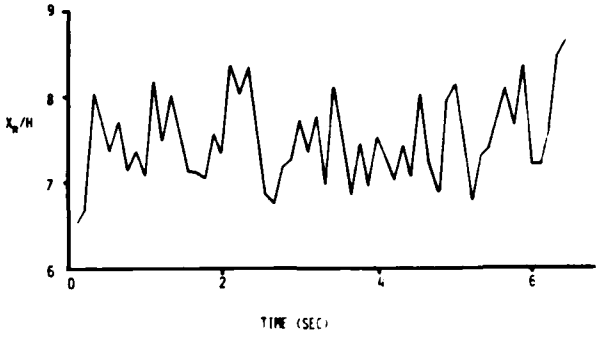

Fig. 6. Variation of the short-time-average (0.2 sec) reattachment length.

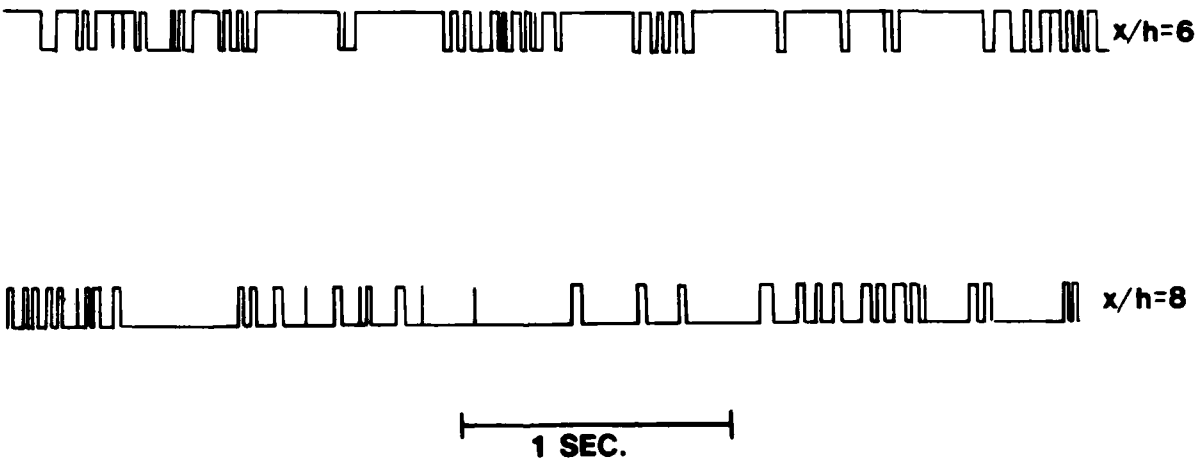

Fig. 5. Simultaneous records of the instantaneous direction of the flow near the wall at two points in the reattachment zone.

PRESSURE FLUCTUATIONS UNDER A TURBULENT SHEAR LAYER

R. Hillier and N.J. Cherry*

Department of Aeronautics, Imperial College, London

*Central Electricity Research Laboratories, Leatherhead

ENGLAND

ABSTRACT

This paper presents experimental measurements of surface pressure fluctuations in a separated-and-reattaching flow. It is shown that near separation pressure spectra are dominated by low wave-numbers and it is only further downstream, where the eddy scales typical of the shear layer have grown, that the contribution from the local shear layer structure becomes apparent. From the mid-bubble position onwards pressure spectra are dominated by wave-numbers corresponding to the shedding of vorticity from the bubble. This exhibits occasional weak periodic bursts, suggesting that there may be some correlation between the shedding of this vorticity and the initiation of the subsequent bubble re-growth cycle. Laterial correlation scales for the surface pressure are comparable to the streamwise spacing between these shedding structures, so that the unsteady flow field appears three-dimensional.

NOMENCLATURE

$\bar{C}_p, C_p'$	mean pressure coefficient, r.m.s. coefficient of fluctuating pressure
D	model thickness (Figure 1)
L_R	mean reattachment length
n	frequency
p'	fluctuating component of pressure
R_{eD}	Reynolds number based on model thickness
S(n)	power spectral density
T	time
U, U_∞, U_c	local mean velocity, free stream velocity, convection velocity
u'	streamwise velocity fluctuations
X,Y,Z	ordinates measured parallel to, normal to and transverse to the flow (Figure 1)
θ_s	momentum thickness at separation

INTRODUCTION

Flow separation, even from a two-dimensional geometry, provides a challenging problem in turbulent shear flows. It presents complications in addition to those found in the associated case of the plane parallel mixing layer. These arise from the mean shear layer curvature (stabilising initially, destabilising near reattachment), from the streamwise pressure gradients, and from the distortions of reattachment and recirculation which feed turbulent fluid back upstream towards the separation region. And just as developments in coherent structures have highlighted the need to study the instantaneous flow field of mixing layers, then so the same arguments apply with equal force to the case of separation bubbles. Unlike the problem of strong periodic vortex shedding from bluff bodies there has been relatively little attempt to investigate the fundamental underlying unsteady structure of reattaching flows, so that basic questions as to the degree of three-dimensionality of the unsteady flow field, or the manner in which vorticity initially shed from the separation edges negotiates the reattachment region and sheds from the bubble are largely left unanswered. The early flow visualisations of Tani et al. (1), for the separation from a rearward facing step, show instantaneous flow fields which depart overwhelmingly from the mean, whilst more recent measurements such as those of Eaton (2), Eaton et al. (3) using "thermal tufts", and Kim et al. (4) using arrays of wool tufts have explored the inherent unsteadiness of the reattachment zone.

The main objective of the present work was to study the flow by way of the fluctuating surface pressure field, both as an experiment in its own right because of an environmental interest in dynamic loading of structures and also because it provided an unobtrusive (although not necessarily easy) method of investigating the larger scale motion in the shear layer, particularly if correlated with velocity fluctuations in the external flow.

EXPERIMENTAL EQUIPMENT AND PROCEDURE

The general schematic of the model is shown in Figure 1, comprising a rectangular forebody (thickness D = 3.85 cm), with separation fixed at the sharp leading edges and with an overall chord sufficiently long (33D) that reattachment occurred well before the trailing edge (at X/D = 4.89). This trailing edge was streamlined to minimise any wake-induced unsteady effects. The model was placed at a nominal zero incidence to the stream, final mean flow symmetry being achieved top-to-bottom by use of a trailing edge flap to equalise pressures at three matching pairs of tappings at various chordwise positions in the bubble region (within 0.01 in C_p). Sideplates were employed for all tests, generally at an aspect ratio of 13.2 (span between end plates/model thickness). The mean reattachment length was repeatable within about 2%. It was found to curve slightly across the span so that the mean flow field cannot be properly regarded as two-dimensional, although aspect ratio changes down to 9.33 produced no systematic effect on the bubble length or on mean and fluctuating quantities, which is similar to the conclusions of Brederode (5) for the

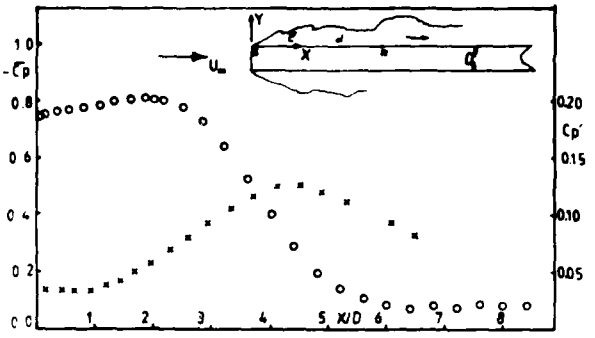

Fig. 1 Schematic of model. Mean pressures ($\bar{C}_p$, o o) and r.m.s. fluctuating pressures (C_p', × ×).

same geometry. The lateral correlation length for the surface pressure fluctuations in the vicinity of reattachment is about 1.5D (it falls to zero by a 4D separation) so that the end-plates are unlikely to two-dimensionalise artificially the unsteady flow field. Tests were conducted in a nominally smooth stream (0.1% turbulence intensity) at a solid blockage of 3.79%, no correction for this being made to any data presented here.

Fluctuating pressures were measured with Setra 237 low pressure transducers mounted internally within the model. These were fitted with caps to minimise internal dead volume and connected by minimum lengths of tubing to short stub (internal diameter = 1.6 mm) pressure tappings. The finite size of the tapping attenuates smaller scales, an effect calculated only to reduce the signal by less than 10% at 500 Hz if the measured convection speed of 0.41 U_∞ is taken for the pressure disturbances. Dynamic calibration of the transducer system also showed a Helmholtz resonance at about 700 Hz, although gain variations were only ±5% up to 350 Hz which is much higher than most energy containing frequencies in the power spectra of Figures 4 and 5 (350 Hz ≡ 1.17 in nD/U_∞). Phase angle changes with frequency are not important for spectra, nor for pressure-pressure correlations since the transducers were quite well matched. The phase angle error in the pressure-velocity correlations is estimated to correspond to a shifting of about 0.03D in the X-direction, barely more significant than probe positioning errors so that no corrections have been made.

Smoke flow visualisation was carried out at identical conditions to the other measurements; that is using the same model, end plates (perspex) and the correct Reynolds number. Smoke was injected from the front face near separation, either as a single filament from a small hole (1.5 mm diameter) or as a sheet from a spanwise slot (1.5 mm by 9 mm). It was illuminated by an intense flash of about 30 μs duration, focussed as a thin sheet of light 1 cm wide oriented along the model centreline in the X-Y plane, so that even at the highest speed motion is probably frozen within a resolution of 0.01D. Hillier and Cherry (6) have shown that the present model is sensitive to stream turbulence, and Laneville et al. (7) suggest that it is the stream turbulence immediately adjacent to the shear layer which provides the interaction, so that there was some concern that smoke injection might interfere with the shear layer development. There was no evidence of any such effect, either in mean pressure distributions or in the visualisations of Figure 2.

SMOKE FLOW VISUALISATION AND REYNOLDS NUMBER VARIATION

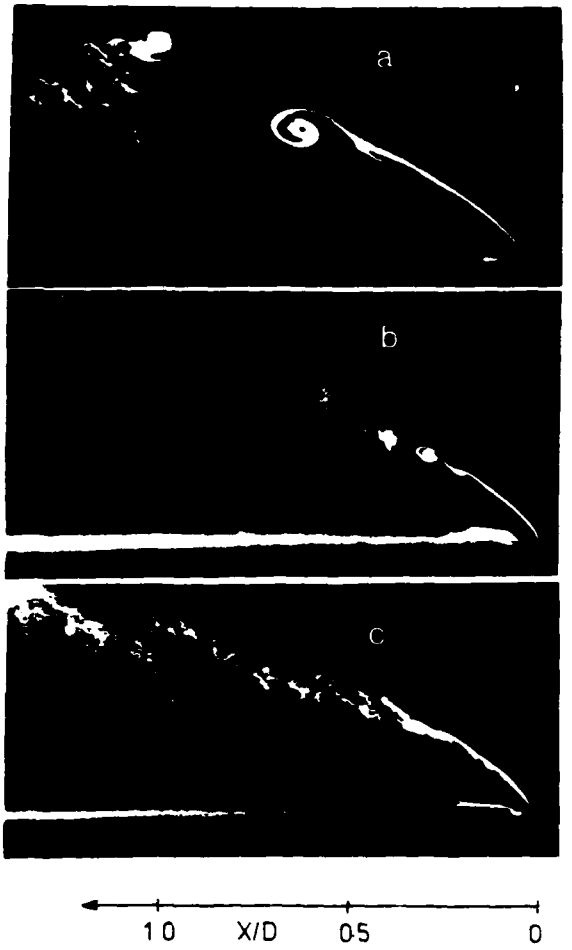

Fig. 2 Smoke flow visualisation of shear layer transition. Smoke injected as a filament (a) $R_{e_D} = 4.6 \times 10^3$, (b) $R_{e_D} = 1.05 \times 10^4$, (c) $R_{e_D} = 3.0 \times 10^4$.

Because the transducer response characteristics meant it was desirable to keep frequencies as low as possible, the bulk of the experiments were conducted at a Reynolds number based upon model thickness of 3.0×10^4. Above this value both mean and fluctuating data (within a few percent which is better than expected from the transducer characteristics) were unchanged by Reynolds number increases up to 6×10^4. Below this value a slight elongation of the bubble became apparent (although accurate oil flow visualisation was more difficult) which probably begins to

indicate the importance of transitional effects in the separated shear layer. The model geometry of course provides a highly favourable pressure gradient on the front face so that separation is always laminar ($\theta_s \triangleq 0.0015$ D, $R_{\theta_s} \triangleq 45$ at the test speed). The development of transition with Reynolds number is shown in the smoke visualisations of Figure 2 where particularly at the two lowest values there is a clear progression from steady laminar flow, through unsteady laminar flow, to transition and turbulence. These photographs can be considered as a typical sequence with Reynolds number, in that there is a clear tendency for all the appropriate scales to reduce, although at a given Reynolds number a wide variability was found between successive photographs. On occasion "pairing" or "coalescing" was evident in the unsteady laminar zone, similar to the visualisations produced by Freymuth (8) for transition in a jet, which in some cases did appear to be associated with the initiation of turbulence. At the test Reynolds number transition is completed by 0.35D or about 7% of the bubble length, with initial disturbances evident within at least half this distance (just over 100 initial momentum thicknesses) so that these observations of early transition follow the general conclusions of Sato (9), Roshko and Lau (10) and others.

When smoke was injected from the spanwise slot the spiral nature of the laminar vortices became more diffuse because of a rather sinuous spanwise development of the vortex cores (this was evident from visualisation above the model although photography was not possible, it is also evident to some extent in the full bubble visualisation of Figure 3(a)).

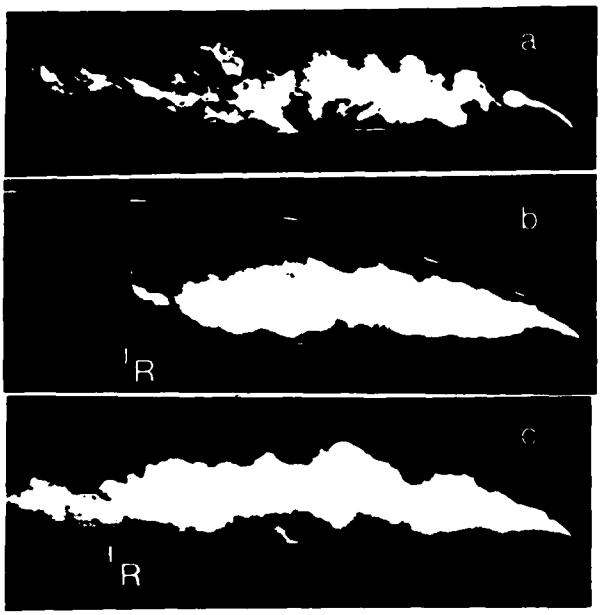

Fig. 3 Visualisation of full bubble. Smoke injected from slot; (a) $R_e = 4.6 \times 10^3$; (b) and (c), $R_e = 3 \times 10^4$.

Figure 3 presents smoke visualisation of the whole bubble length and will be referred to again later in the text. A line is marked on the photograph which indicates, approximately, the contour of 2½% local intensity. This locus was used for hot wire measurements and essentially appears to be the edge of the turbulent flow, turbulent spikes appearing here only very infrequently. In the low Reynolds number case of Figure 3 the rear 80% or so of the bubble can be considered turbulent, but it is clear nonetheless that the effects of the initial laminar roll-up persist for substantial distances along the shear layer. For the higher Reynolds number cases there is no apparent organisation, although as will be noted later clear quasi-periodic bursts appear in the irrotational fluctuations (measurements outside the shear layer spatially filter out the higher frequency turbulence). Large structures are visible in the flow field and, as noted above, on occasion these must penetrate at least as far as the contour drawn.

PRESSURE DISTRIBUTIONS AND SPECTRA

Reattachment in Figure 1 occurs at $X/D = 4.89$ towards the end of the mean pressure recovery region. Near separation C_p' is low and appears to remain more or less constant up to $X/D = 1.0$, well downstream in fact of the observed transition position. Further downstream it rises steadily to reach a maximum somewhat upstream of reattachment, more in the region of the maximum rate of recovery of mean pressure which is similar to work of Emery and Mohsen (11), Fricke (12), Fricke and Stevenson (13) and others. There is little justification, however, in relating any significant reattachment pressure fluctuations to a quasi-steady modulation of the mean pressure distribution. Space-time correlation data identify the main pressure disturbances as convecting at U_c equals $0.41\ U_\infty$, with no evidence in fact of upstream convecting signals, and with streamwise scales generally well less than the bubble length (also see Figure 7), so that the peaks in dC_p/dX and C_p' probably more share some common source in the dynamics of shear layer reattachment rather than that the one drives the other. The peak values of C_p' are nearly an order of magnitude less than those experienced in cases of strong periodic shedding, which reflects the inability of the vorticity shed from the separation edge to concentrate itself into strong discrete structures.

The pressure spectra of figures 4 and 5 nominally divide the flow field into three regions. Near separation, where r.m.s. pressures are low, the spectra are dominated by low wave-numbers centred upon $nD/U_\infty = 0.025$. This low frequency contribution does not arise from tunnel acoustics since the pressure energy is too broad band and low frequency to correspond to any of the very weak acoustic modes detected in a tunnel calibration (weak acoustic spikes, contributing less than 1% to the total energy, have been removed from the spectra). It also appears unlikely that it is a phenomenon of unsteady circulation about the whole model because deliberate extension of the model chord, by nearly 100%, produced no effect upon the r.m.s. values or spectra at separation. Low frequency velocity fluctuations have been observed in the flow over a rearward step by Eaton (2), and in the present work they were particularly apparent in hot-wire signals close to separation. Just outside the shear layer, in the irrotational region, hot-wire signals were almost identically in anti-phase with the surface pressure fluctuations. The low frequency was also the cause of some difficulty in accurately locating a hot-wire in an attempt to correlate velocity fluctuations in the transition region with the observed flows

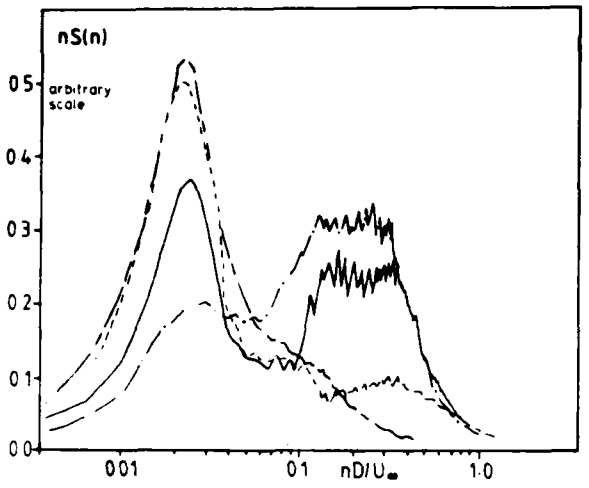

Fig. 4 Surface pressure spectra. $X/L_R = 0.026$ (———— – ————); 0.14, (– – – –); 0.25, (————————); 0.35, (—— . ——).

of Figure 2, since the turbulence signal was modulated by the low frequency unsteadiness rather in the manner noted in Roshko's (14) earlier comments on transition. Clearly the low frequency fluctuations reflect as a weak "flagging" of the shear layer near separation, but as the next section shows this does not appear to produce any well-correlated effect throughout the bubble. The cause of the low frequency is unclear. Since it appears to be associated with the near-wake of separation the possibility always exists that it is associated with laminar/transitional behaviour of the shear layer. Tests at a higher Reynolds number (6×10^6) were inconclusive; the r.m.s. pressure coefficient close to separation ($X/L_R = 0.026$) was unchanged, nor were there significant alterations in the spectra.

By 10% of the bubble length and onwards, where the r.m.s. pressure begins to rise, there is a change of spectral shape as shown by the emergence of, and eventual dominance by, a higher wave number contribution which arises from the increasing nearfield effect of the shear layer. No strong narrow-band spectral peaks were apparent although a large number of samples were required to produce acceptable accuracy, which probably reflects the tendency for the flow field to generate quasi-periodic bursts which will be discussed later. This region can be regarded as a transition between the low frequency dominated flow near separation and the region downstream of (say) the mid-bubble position which is shown in Figure 5. Here there is little change in spectral shape, a broad band energy distribution (centred upon $nD/U_\infty \triangleq 0.14$) becoming established for the shedding of vorticity from the bubble. This agrees with measurements by Katsura (15) on a similar geometry (although his model chord was only 6D so that there is also some question of wake-induced fluctuations), and a "shedding" frequency based upon bubble length ($nL_R/U_\infty \triangleq 0.7$) is the same as the approximate value given by Mabey (16) for various thin aerofoil and spoiler separations. At first sight Figure 5 seems perhaps to suggest that by half the bubble length the growth of the larger scale eddies has become disrupted or stopped by the presence of the surface. This seems unlikely however. A characteristic wavelength for this central frequency (taking a convection speed of $0.41\ U_\infty$) is 2.93 D, which mixing layer data such as those of Brown and Roshko (17) and Dimotakis and Brown (18) show would

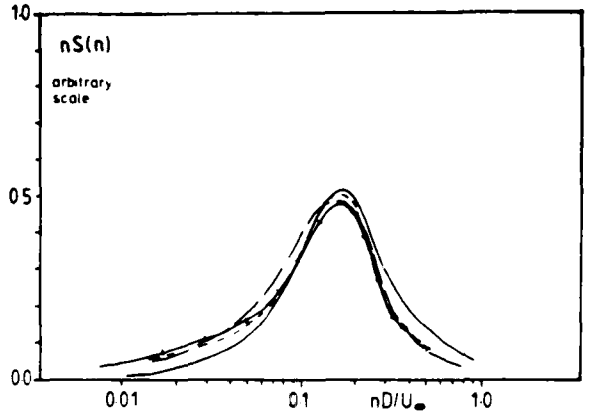

Fig. 5 Surface pressure spectra. $X/L_R = 0.55$, (———— ————); 0.70, (— — — —); 0.94, (—+————+—); 1.35, (————).

be more appropriate for a full shear layer development up to reattachment. Furthermore, Figure 6 presents a measure of large structure growth obtained by traversing a hot-wire along a contour of 2½% local intensity (as shown). This gives a path just along the shear layer edge, only occasional turbulent bursts being detected and the intention being to monitor irrotational fluctuations induced by the local shear layer structure. The typical form of the velocity auto-correlation is shown in the inset to Figure 6, and a measure of the variation of disturbance timescale is obtained by plotting the time to this minimum (which is roughly one half the disturbance period) against distance. This reveals a nearly linear increase, within measurement accuracy, nearly up to reattachment, followed by a surprisingly abrupt plateau, the peak value near reattachment correlating well with the corresponding autocorrelation data for pressure shown. Upstream of reattachment the two sets of data diverge, the pressure reflecting its spectral behaviour in that the time scale remains effectively constant. It therefore appears that the mixing layer probably grows more-or-less linearly from separation to reattachment, and that the shedding frequency is then determined by whatever scale the mixing layer happens to have reached by that stage. Almost certainly the pressure data signify some sort of feedback mechanism, whereby the shedding of vorticity from the bubble can initiate a new growth stage.

CORRELATION MEASUREMENTS

Figures 7 and 8 provide an idea of the scale of the pressure generating disturbances in the vicinity of reattachment, being respectively the unlagged pressure cross-correlation along the model centreline (fixed transducer at X/D = 5.00) together with

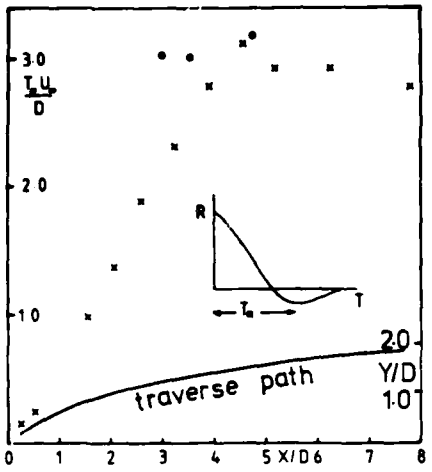

Fig. 6 Shear layer growth; hot-wire traversed along 2½% intensity line. Fluctuating velocity (× ×); fluctuating pressure (o o).

the spanwise correlations of pressure (fixed transducers at X/D = 3.15 and 5.00), and the correlation between the pressure at X/D = 4.74 and a hot-wire traversed vertically above that location. Figure 7 shows the formation of quite pronounced negative lobes in the streamwise cross-correlation, the separation between these (3.2D) agreeing well with the

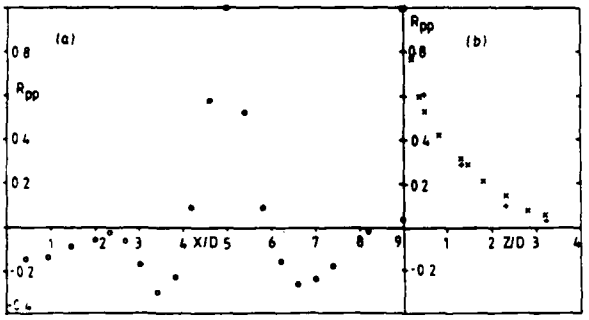

Fig. 7 (a) Cross-correlation along model centreline, transducer fixed at X/D = 5.00.
(b) Spanwise correlation; X/D = 5.00, (× ×); X/D = 3.15, (+ +).

previous wavelength estimates. The correlation shows a slight tendency to overshoot again in the downstream direction, although this is inconclusive since measurements were not continued beyond X/D = 9.0.

Any tendency to overshoot in the upstream direction is suppressed by the formation of a region near separation with a weak negative correlation, which represents the correlated energy at the low frequency shown in the spectra of Figure 4.

The lateral correlation of Figure 7 falls monotonically to about 0.05 by Z/D = 3, which is about four times the maximum slope thickness measured for the shear layer at reattachment. Interestingly the lateral correlation at X/D = 3.15 is virtually indistinguishable from this, either indicating a rapid onset of three-dimensionality as reattachment is approached or that the lateral scales of pressure generating eddies in the rearward half of the bubble are dominated by a common mechanism as for the spectral data. It should not be assumed that a similar development of spanwise correlation would be apparent at the shear layer edge, since we have already noted in Figure 6 that the pressure and velocity autocorrelation data differ. Browand and Troutt (19), in their study of lateral scales in a mixing layer, located their velocity probes at about the same relative position used for Figure 6, producing a correlation falling to 0.2 within three maximum slope thicknesses (compared to 2.46 thicknesses here). Their measurements also show that the lateral correlation only reaches this asymptotic state for Reynolds numbers (based upon maximum slope thickness) of about 3×10^4, compared with 2.26×10^4 in the present work, so that clearly further measurements at higher Reynolds number are needed.

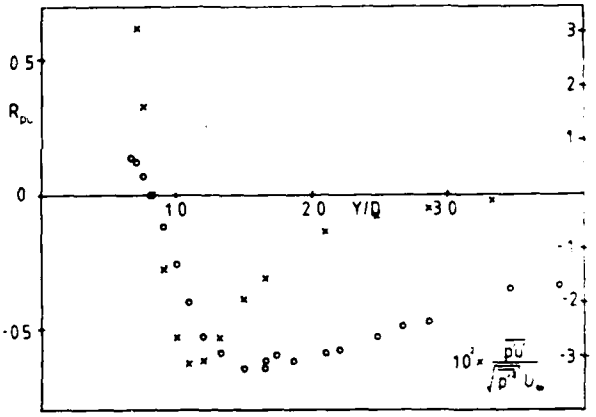

Fig. 8 Cross-correlation between pressure at X/D = 4.74 and hot-wire traversed vertically above that station.
R_{pu}, (o o); $\overline{p'u'}$, (× ×).

Figure 8 shows that streamwise velocity fluctuations in the irrotational region (large Y/D) are negatively correlated with the surface pressure. The correlation coefficient reaches a minimum at about the same position that the first turbulent bursts were detectable (2½% local intensity) and the subsequent variation of the correlation coefficient is determined largely by the rapid increase in intensity so that actually consideration of the term $\overline{p'u'}$ alone is more illuminating. This falls to a minimum well within the turbulent region (Y/D ≙ 1.15, u'/U ≙ 6% followed by a rapid monotonic increase through zero (at u'/U ≙ 19%) to positive values as

the surface is approached. Measurements were terminated at Y/D = 0.715 where the local intensity was 30% and data were therefore becoming increasingly unreliable. The correlation clearly reflects a vortex-like structure, the location of zero correlation indicating a "mean" position for vortex centres and the distance from this zero to the extreme negative value of $\overline{p'u'}$ providing some measure of the vortex core radius and the random modulation in vertical location of vortex centres. This modulation can be seen to some extent in Figure 9, which presents sequences of simultaneous velocity and pressure records taken with a pressure transducer at X/D = 4.74 and with a hot-wire located at the same streamwise position just outside the shear layer in the essentially irrotational region (Y/D = 1.55).

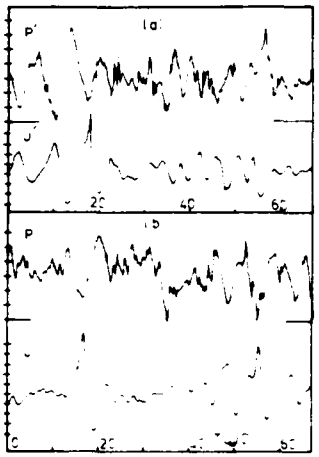

Fig. 9 Simultaneous pressure and velocity records. Amplitude scale marked in steps of one r.m.s. in each case.

The general impression from these traces is that the pressure and velocity are broadly in anti-phase as expected for instantaneous pressure and velocity signals either side of a vortex core. However, the appearance of a strong fluctuation in velocity (say) indicates either that the vortical structure is strong or that it happens to have convected close to the probe. There is no way that the two effects can be separated using a single hot wire, but they can with records of surface pressure as well. In Figure 9(a) the strongest positive velocity fluctuation occurs at TU_∞/D equals 17. The corresponding pressure fluctuation is weak, and this is a case where the effective centre of vorticity for the structure is closer to the probe than the surface. Figure 9(b) shows two equally strong negative pressure fluctuations, at TU_∞/D = 35 and 54. The first corresponds to a quiescent velocity phase, so it derives from an event close to the surface; the second correlates with a significant positive-going velocity (which incidentally shows a pairing is nearing completion) so that the vortex core must be more uniformly positioned between the probe and the wall.

Another feature is the quasi-periodic nature of some of the fluctuations. Figure 9(a) shows a sequence of 3-4 velocity disturbances commencing at $TU_\infty/D = 0$, whilst a similar sequence forms in Figure 9(b) (at $TU_\infty/D = 46$) together with a clear isolated disturbance at $TU_\infty/D = 15$. These tend to be energetic velocity fluctuations, signifying significant excursions of the intermittent interface from the surface. The average period ($\Delta TU_\infty/D$) of about 7-8 corresponds well with the characteristic frequency already noted at reattachment. This produces a wavelength of 3.2D, assuming a convection speed of 0.41 U_∞, or some 65% of the bubble length; typical for example of the structure shedding from the bubble in the visualisation of Figure 3(b). Also visible on the velocity trace of Figure 9(a) is a quasi-periodic burst of disturbances, starting at $TU_\infty/D = 33$, whose frequency is now roughly doubled so that it appears that some mechanism has temporarily interposed to prevent the "pairing" process from taking place. This may reflect the very low frequency modulation; for the bursts of Figure 9 certainly do appear modulated and may be responding to a gentle flagging motion of the shear layer near separation.

CONCLUSIONS

Surface pressure fluctuations near reattachment are closely identified with the passage of vortical structures within the shear layer. These appear at times as quasi-periodic bursts, with modulations in amplitude and frequency which are possibly driven by a low frequency unsteadiness which is easily detectable near separation. The structures appear three-dimensional, taken over long time averages, so that it is unclear whether they can be instantaneously two-dimensional, in the manner of the Browand and Troutt (19) experiments, or whether the distortions and instability of reattachment will prevent this. The data are collected at modest Reynolds numbers, but there is little evidence to suggest that tests at higher values will substantially alter these conclusions.

ACKNOWLEDGEMENT

N.J. Cherry was supported by an SRC Studentship in cooperation with the Building Research Establishment.

REFERENCES

1 Tani, I., Matsusaburo, I. and Hiroyuki, K. "Experimental Investigation of Flow Separation Associated with a Step or Groove". Aeronautical Research Institute, University of Tokyo, Report No. 364, 1961.

2 Eaton, J.K. "An Experimental Study of the Flow and Structure behind a Backward-Facing Step". Ph.D. Thesis, Thermoscience Division, Mechanical Engineering Dept., Stanford University, 1980.

3 Eaton, J.K. and Johnston, J.P. "A Review of Research on Subsonic Turbulent-Flow Reattachment". AIAA 13th Fluid and Plasmadynamics Meeting, 1980.

4 Kim, J., Kline, S.J and Johnston, J.P. "Investigation of a Reattaching Turbulent Shear Layer: Flow over a Backward-Facing Step". Journal of Fluids Engineering, Vol. 102, 1980, p305.

5 Brederode, V.A.S.L. "Three-Dimensional Effects in Nominally Two-Dimensional Flows". PhD Thesis, University of London, 1975.

6 Hillier, R. and Cherry, N.J. "The Effects of Stream Turbulence on Separation Bubbles". 4th Colloquium on Industrial Aerodynamics, Aachen, 1980. Also, Journal of Wind Engineering and Industrial Aerodynamics, Vol.8, No. 1/2, 1981, p49.

7 Laneville, A., Gartshore, I.S. and Parkinson, G.V. "An Explanation of some Effects of Turbulence on Bluff Bodies". 5th Int. Conference on Wind Effects on Buildings and Structures, Heathrow, 1975.

8 Freymuth, P. "On Transition in a Separated Laminar Boundary Layer". Journal of Fluid Mechanics,

Vol.25, 1966, p683.

9 Sato, H. "Experimental Investigation on the Transition of Laminar Separated Layer". Journal Phys.Soc. Japan, Vol. 11, 1956, p702.

10 Roshko, A. and Lau, J.K. "Some Observations on Transition and Reattachment of a Free Shear Layer in Incompressible Flow". Proc. Heat Transfer Fluid Mech. Inst. Vol.18, 1965, p157.

11 Emery, A.F. and Mohsen, A.M. "An Experimental Study of the Separated Flow of very thick Incompressible Turbulent Boundary Layers". ASME, Paper No. 68 - WA/FE-36, 1968, p1.

12 Fricke, F.R. "Pressure Flucutations in a Separated Flow". J. Sound Vib., Vol.17, 1971, p113.

13 Fricke, F.R. and Stevenson, D.C. "Estimation of Wall-Pressure Fluctuations in a Separated Flow". Journal Acous. Soc. America, Vol.50, 1971, p985.

14 Roshko, A. "Transition in Incompressible Near Wakes". Phys. Fluids, 1967, Supplement 10.s181-S183.

15 Katsura, J. "A Wind Tunnel Test of Pressure Distribution on Box Shaped Models". Proc. US-Japan Research Seminar on Wind Loads on Buildings, 1970, NSF 97-103.

16 Mabey, D.G. "Pressure Fluctuations caused by Separated Bubbles at Subsonic Speeds". Royal Aircraft Establishment, Tech.Report 71160, 1971.

17 Brown, G.L. and Roshko, A. "On Density Effects and Large Structure in Turbulent Mixing Layers". Journal of Fluid Mechanics, Vol.64, 1974, p775.

18 Dimotakis, P.E. and Brown, G.L. "The Mixing Layer at High Reynolds Number". Journal of Fluid Mechanics, Vol.78, 1976, p538.

19 Browand, F.K. and Troutt, T.R. "A Note on Spanwise Structure in the Two-Dimensional Mixing Layer". Journal of Fluid Mechanics, Vol.97, 1980, p771.

EXPERIMENTAL INVESTIGATIONS IN TRANSONIC HIGHLY SEPARATED, TURBULENT FLOW

A. Farcy, V. Mercier and R. Leblanc

Laboratoire d'Aérodynamique, LA 191
Centre d'Etudes Aérodynamiques et Thermiques
43 Rue de l'Aérodrome, 86000 Poitiers, France

ABSTRACT

Experimental results in transonic, highly separated, turbulent flow are presented. The model is an air intake of 20×80 mm^2 section set with an angle of attack from 20 to 40° inside à M = 0,7 free jet flow. The Mach numbers and mass flow rates are deduced from pressure measurements. Flow visualizations, laser Doppler and Hot wire anemometries are used to analyse the mean velocity field, unsteadiness and turbulent flow characteristics.

INTRODUCTION

Important difficulties occur in the measurement of the turbulent characteristics in transonic field. The case of the flow inside an air intake set with a large incidence in transonic speed is particularly strong (Fig. 1).

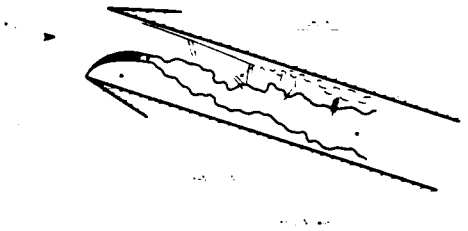

Fig. 1 - Transonic separated flow in air intake

This type of configuration presents a maximum of complexity due to the combination of compressibility, large separation regions and unsteady effects. An important separation bubble occurs at the lower leading edge which involves a turbulent wake with high velocity distorsion and fluctuations baneful for the engine. Then it is of major interest to know the mean velocity field, the unsteady frequencies, the turbulent intensities and the scale of the fluctuations.

This paper describes some results of experimental investigations inside a model of air intake set with an angle of attack α from 20 to 40° in a M = 0,7 stream. Because important difficulties arise in the total and static pressure measurements due to the transonic nature of the flow, laser doppler and hot wire anemometries were used in combination with high speed visualizations.

EXPERIMENTAL SET UP

A 100×40 mm^2 transonic nozzle produces a free jet at M = 0,7 max and Re = 4×10^5/cm for a total temperature maintained approximately to the ambiant conditions. The 20×80 mm^2 air intake model is mounted on a support which can be adjusted in incidence with respect to the axis of the jet (Fig. 2).

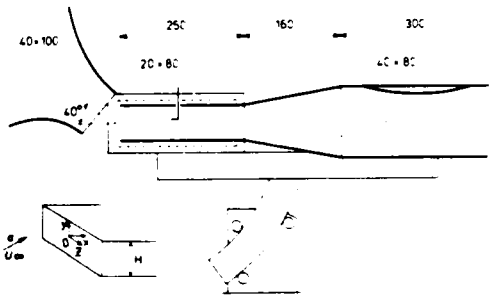

Fig. 2 - Schematic view of the test set up

The side walls of the model exceed the lateral section of 20 mm in order to limit the 3.D effects. The leading edge of the walls is sharp (10°). Optical glasses allow visualizations and laser doppler anemometry. The total angle of the diffuser is 7° and the variable -h throat permits to adjust the mass flow rate σ inside the air intake.

As reported above, the flow configuration is analysed for some values of incidence between 20 and 40°. Preliminary tests (Ref. 1) having shown the effect of mass flow rate, $\sigma = \rho u/\rho_\infty u_\infty$, it was then decided to establish the curves σ(M) as shown Fig. 3. σ and M are deduced from pitot and static pressures measurements in section x/H = 8.

For h = 16 and 20 mm the mass flow rate increases with increasing M and decreasing h. Reverse trend appears at the lower value of h (8 and 12 mm) and for α = 30°. Note, as a possible explanation, the proximity of the critical condition (M^*= 1) for these throat openings. The flow visualizations conducted simultaneously reveal an increasing separation bubble with increasing incidence, without significative effects of h. The major LDA and HW anemometries measurement are then conducted at α = 40° (large separation bubble) for the contractual fixed point P (σ = 0,57, M = 0,39).

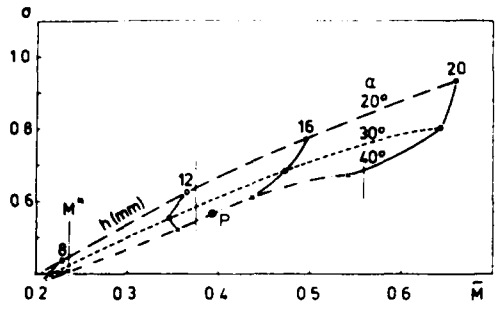

Fig. 3 - Mass flow rate

VISUALIZATIONS OF THE FLOW

It is well known that compressibility allows shadowgraph or strioscopy visualizations. These techniques are used extensively and the pictures are fixed other by magnetoscop, photography or movies.

The magnetoscop is very useful to detect the low frequency instabilities as a function of incidence and mass flow rate. The following graph is a synthesis of the observations.

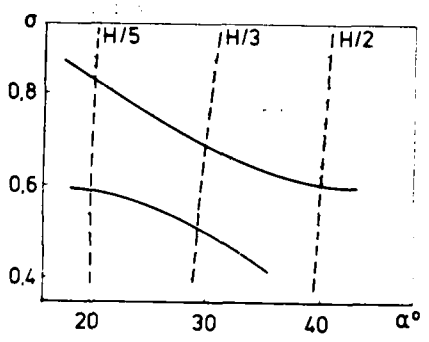

The photographs are realized on 9×10 plates of 400 ASA with a time exposure of 1/500 sec (continuous Hg vapor light) or 1 µs (spark light). The movie of 25 pictures of 15×24 mm^2 is made with a LCA-CI4 high speed camera between 8×10^4 and 10^6 frames/sec. An adjustable flash tube is then used as light. The time exposure is equal to 314 ns for 10^6 fr/s and 1,25 µs for 250.000 fr/sec. Some examples of these different technics are shown on the figures 4. The description of the flow is first issued from the observations of the photographic plates, fig. 4a.

For the incidence of 20° there is a small bubble which produces a sonic throat. A λ-shock lies at the rear part of the bubble and produces an interaction with the upper wall laminar boundary layer. Turbulent flow seems to become uniform after x = 3 to 4H. Major feature at α = 40° is the well established bubble which lies on H/2 in hight and more 2H in length. Its forward limit is clearly laminar and becomes promptly turbulent at x = y ∿ H/2. This shear layer between recirculating and highly accelerated flow spread across the air intake as a turbulent "wake" for the bubble.

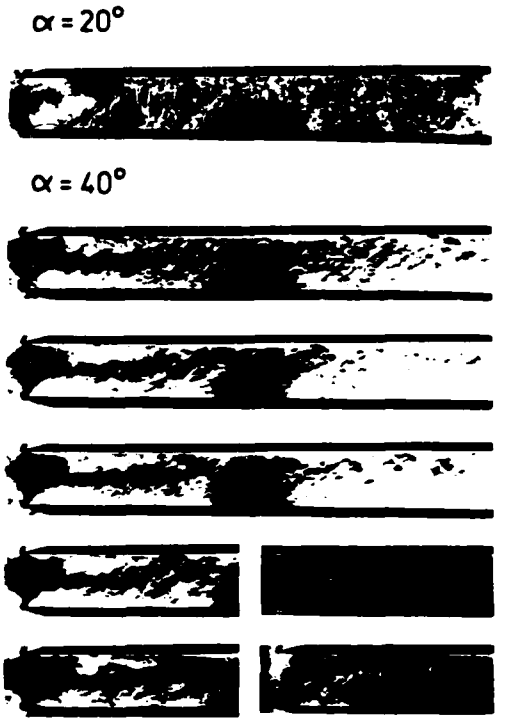

Fig. 4a - 9×12 plates t = 1 µs

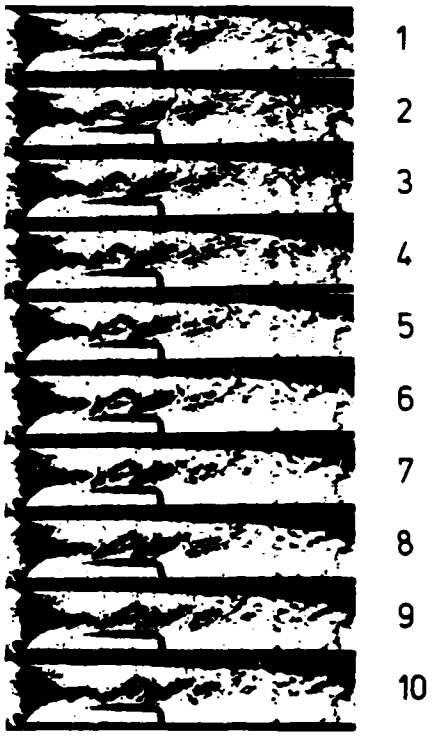

Fig. 4b - High speed movies
(250 000 fr/s, t = 1.25 µs, Δt = 3.88 µs)

After x = 3H inclined large turbulent structures from the wake and the strioscopies reveal clearly these large movements whereas small structures can be seen on the shadowgraph pictures. Normal shocks, in the upper transonic flow, vary in position as also indicated on the shadowgraphs. More informations about the evolution of the turbulent flow are then issued from the pictures movies analysis, Fig. 4b.

Ten successive strioscopic pictures show the evolution of the turbulent shear layer for α = 40°. One see clearly a characteristic "ovoid" structure above the probe (picture 1) with a core which appears on picture 4 and desappears on picture 8. Its persistence is then equal to 20 μs which is a relatively slow variation. Likewise the normal shock position is constant along the sequence which indicate that the frequence of the mean limit oscillations of the shear layer is smaller than 20 kHz.

From a colour "equidensity" exploitation of the picture movies, using the special Agfacontour process, it is concluded, for a sequence at 100 000 fr/s, that the limit of the bubble oscillate at 10-15 kHz with turbulent structure entrainment as result. It is also clear that the position of the transition point vary of some mm (∿H/10) about its mean value x = H/2. Further, the mean stability of the bubble (i.e. no pulsation) was confirmed using a HICAM camera at 8000 fr/s.

Finally it is important to note the limit of the visualizations to show the reattachment point. Such indication with detailed velocity and turbulent intensity fields are obtained with the LDA measurements.

LASER ANEMOMETRY MEASUREMENTS

An home-made Laser Doppler Anemometer (LDA) was developped in 1974 by Ardonceau (Ref. 3). It is make up with a 5W Coherent Radiation Laser, a 40 MHZ TSI-Bragg Cell and a RTC, XP 1110 photomultiplier. The signal is analysed by an home-made digital counter for frequences between 10 kHz and 200 MHz with a 5 ns resolution. A carriage supports the LDA. The air intake traverses as the data acquisitions and reductions are performed through an IBM 1800 computer. The diameter of the measurement volume vary between .3 and .6 mm. Small oil particles (ϕ .7 to 1.3 μm) are injected in the settling chamber of the transonic jet. Detailed measurements are conducted inside the air intake only for α = 40°.

Longitudinal and transversal mean velocities $\bar{u}$ and $\bar{v}$ and corresponding RMS fluctuation values u' and v' are shown on Fig. 5a and 5b as measured in the eight section x = H/4, H/2, H, 2H, 3H, 4H and 8H. The bubble appears clearly with recirculating flow beyond x = 3H. Maximum reversed velocity, larger than 50 m/s, is found at x = 2H. The highly accelerated shear layer above the bubble leads to a maximum velocity of 280 m/s at x = H/4 and H. Considering the high level of the velocity fluctuations (40 m/s for x = H and Y = 12 mm) it is then possible to explain the existence of the shock waves shown in the flow visualizations. The instability of the shock would be due to this continuation of mean and fluctuating velocities with a probable influence on the displacement of the transition point. The u' peak observed at x = H/4, H/2 and H, which spreds across the channel after H, can be born of other the explosion of the highly accelerated shear layer limiting the bubble into a turbulent wake as observed

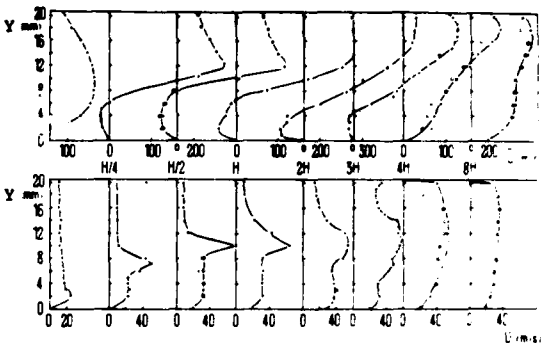

Fig. 5a - Longitudinal velocity

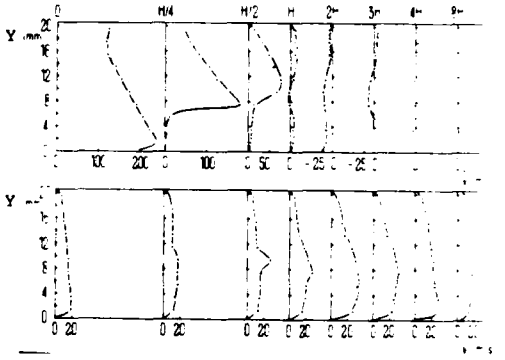

Fig. 5b - Transversal velocity

in the previous section or the bubble frontier oscillations. With this later hypothesis a such peak must appear for the v' component in the three above mentioned sections, that do not occur Fig. 5b. Except this peak, the u' is constant across the bubble equal approximatly three time its value in the upper "potential" flow. The turbulent diffusion across the air intake appears just after the reattachment (between 3H and 4H) and a correct uniformity of both u and u' is seen at x = 8H. At this position, the intensity of the turbulence is two time higher in the x-direction (40%) than in the y-one (20%).

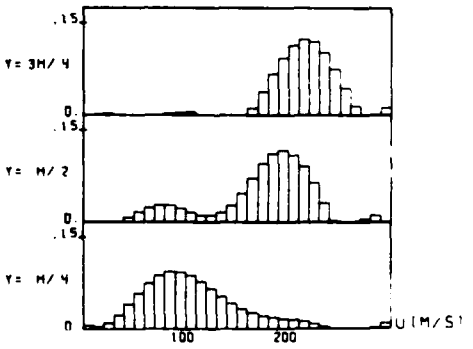

Fig. 6 - Histogram LDA

Three u-velocity histograms are shown on the figure 6 at x = 4H for y = H/4, H/2 and 3H/4. The double maxima of the probability density function is certainly characteristic of the intermittency of the flow.

HOT WIRE ANEMOMETRY RESULTS

It is generally admitted that the velocity and specific mass sensitivity coefficients of the hot wire are equal in supersonic flow (M≥1,2). The hot wire response is then dependant upon two parameters only ρu and T_t and the u component is deduced by using a separation procedure as diagram of fluctuation for example. These properties disappear in transonic flows, and some cautions are necessary, that are :

- to limit the T_t' fluctuations maintaining constant the total temperatures T_t
- to measure with a high overheat ratio (0,8)
- to avoid the pure transonic regions (M~1) and the shock areas.

A subminiature DISA 55A53 probe is used associated to a main unit DISA 55M with a CTA 55M10 bridge. The pass band is higher than 100 kHz. A FM Bell & Howell RD-378/U tape recorder store the output signals with a passband of 500 kHz for a nominal signal/noise of 32 dB at a 120 in/s recording speed. The data are then directly treated with a ND 100 mini-computer through a CAMAC data acquisition system.

The evolution of the power spectra for six longitudinal positions of the hot wire on the line y = H/2, z = 0 is shown on the figure 7.

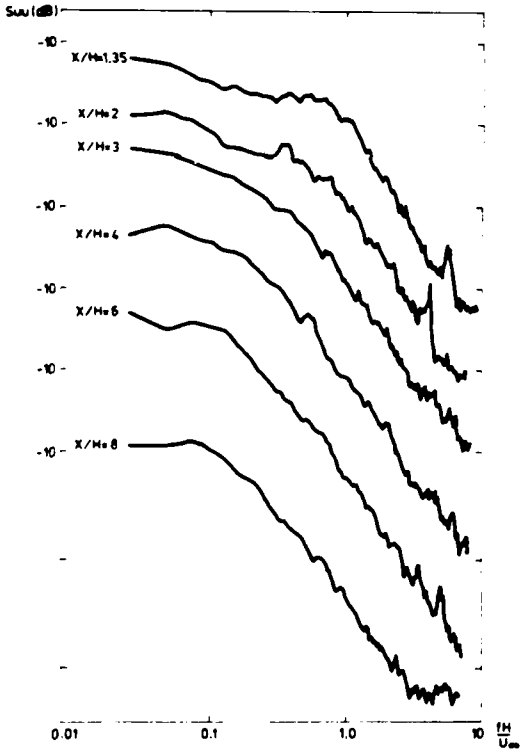

Fig. 7 - Power spectra (y = H/2)

The frequency f is reduced using H and the velocity of the free jet u_∞. The downstream energy damping of the large structures is clearly seen, approximately equal to 8 dB for example in the sections x = 1,35 H and 8H, for the characteristic dimension of the structures about H/2.

The spectrum analysis and the application of the Taylor hypothesis allow to estimate an integral scale Λx which is represented on the figure 8, on the height of the six previous sections. From the section x = 4H the value of Λx vary smoothly, between 0,3 and 0,4 H, both on the height and in the x-direction.

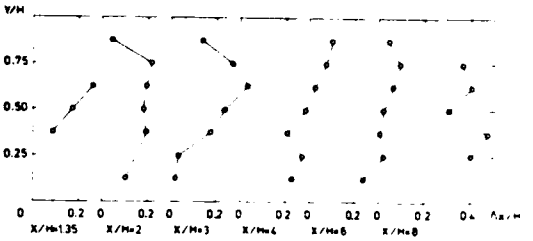

Fig. 8 - Integral scale

Some correlations between two hot wire measurements are shown on the Figure 9. The first probe coordinates are x = H, y = H/2, z = 0 (z = 0 corresponds to the vertical plan of symetry) whereas the second is moving on the half span from the same point.

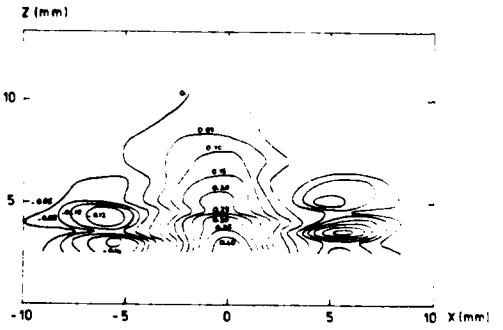

Fig. 9 - Isocorrelations

An interesting feature is the existence of two negative correlation cores in the x-direction which reveal the emission of large vortex structures having a x-scale about H/2 in accordance with the flow visualizations. The integral scale ratio $\Lambda z/\Lambda x$ is approximately equal to 3 which reinforce the two-dimensionality hypothesis. More detailed conclusions would be hazardous because the non linearity of the hot-wire response in transonic speed and the application of the Taylor hypothesis in a such region with high velocity gradients and inhomogeneity.

CONCLUSION

The combination of visualization (V), visualization movies (VM) pressure measurements (P) and Laser Doppler (LDA) and Hot Wire (H.V.) anemometries allows a detailed description of a typical turbulent and highly separated transonic flow inside an air intake set at an angle of attack from 20 to 40° in a M = 0,7 jet flow.

The possible description of the mean features of the configuration is : (1) the shock existence and their stability (V, VM) ; (2) the existence of a bubble (V) and their dimensions (V, LDA) ; (3) the mass flow rate (P).

The analysis of turbulent nature of the flow is more dependent upon these combinations : the burst or transition of the bubble limiting shear layer stay at an unsteady point (V, VM) and induces a turbulence intensity peak which spread across the height of models (LDA, HW). Large inclined structures are observed (V, HW) which promptly evolve (V, VM, HW). The turbulence intensity is constant inside the bubble, outside the shear layer and far downstream.

As conclusion, it seems of large interest, for example, to complete the informations on the high lateral correlation and quasi periodicity of the structure in the transition region issued from H.W. results by LDA transverse W, W' components measurements, or those on velocity field distorsions and high intermittency from LDA by systematic statistic H.W. analysis.

ACKNOWLEDGMENTS

This work was supported by the Grant DRET 79/069 from the French Defense Ministry.

REFERENCES

1. Leblanc, R., Thiebault, P., Ardonceau, P. and Goethals, R., "Etude expérimentale des entrées d'air transsoniques aux grandes incidences", Contrat DRET 77/214, rapport final, Nov. 1978

2. Thiebault, P., Ardonceau, P., Leblanc, R., Goethals, R., "First measurements in highly separated transonic flow", Mechanics Research Communications, Vol.6, No.2, 1979, pp.113-114

3. Ardonceau, P., "Application de l'anémométrie laser à l'aérodynamique supersonique", Thèse de 3ème Cycle, Université de Poitiers, 1974

SESSION 17 - FUNDAMENTALS I

J. Herring - Chairman

A MODEL OF THREE-DIMENSIONAL TRANSFER IN NON-ISOTROPIC HOMOGENEOUS TURBULENCE

::

Jean-Pierre BERTOGLIO
Laboratoire de Mécanique des Fluides
ECOLE CENTRALE DE LYON
36 Avenue Guy de Collongue
69130 ECULLY (France)

ABSTRACT

A model for predicting homogeneous anisotropic turbulence submitted to uniform mean velocity gradients is presented. Equations of second order correlations are used. They are closed in the frame of the E.D.Q.N.M. theory. Since the use of the fully three-dimensional expression for the transfer results in cumbersome computations, a modeled form is proposed to interpolate this term. Then only a few complete calculations are required and computations can be carried out. Our results agree fairly well with the trends predicted by the experiments.

NOMENCLATURE

$D_{ijk\ell mn}$	fonction of $\vec{K}$, $\vec{P}$ and $\vec{Q}$, depending on the geometry of the triad.
$D'_{ijm\ell}, D''_{ijm\ell}$	idem.
$E(K,t)$	kinetic energy spectrum.
κ	structural parameter, $\equiv \dfrac{\overline{u_2^2} - \overline{u_3^2}}{\overline{u_2^2} + \overline{u_3^2}}$.
$\vec{K}$	wave vector .
K	wave number, $= \lvert\vec{K}\rvert$.
$\vec{P}$	wave vector.
P_{ij}^{L}	linear part of the velocity pressure correlation : $\overline{\frac{1}{\rho}\{u_i \frac{\partial p}{\partial x_j} + u_j \frac{\partial p}{\partial x_i}\}}$.
$\vec{Q}$	wave vector.
$\overline{q^2}$	kinetic turbulent energy, $= \frac{1}{2}(\overline{u_1^2} + \overline{u_2^2} + \overline{u_3^2})$.
S	shear, $= \dfrac{\partial \overline{U}_2}{\partial x_3}$.
t	time.
$T_{ij}(\vec{K},t)$, or $\underline{T}$	three-dimensional transfer, $= T_{ij}^{+} + T_{ij}^{-}$.
$T_{ij}^{+}(\vec{K},t)$	part of T_{ij} corresponding to the backscatter.
$T_{ij}^{M+}(\vec{K},t)$	modeled form of T_{ij}^{+}.
$T_{ij}^{-}(\vec{K},t)$	part of T_{ij} corresponding to the drain.
$tr(\lvert\vec{K}\rvert,t)$	isotropic transfer associated with an isotropic turbulence, $= tr^{+} + tr^{-}$.
$tr^{+}(\lvert\vec{K}\rvert,t)$	isotropic backscatter.
$tr^{-}(\lvert\vec{K}\rvert,t)$	isotropic drain.
$u_i(\vec{X})$	velocity fluctuation.
u'_i	$\sqrt{\overline{u_i^2}}$
$\overline{u_i u_j}$	Reynolds stress tensor.
$\overline{U}_i(\vec{X})$	mean velocity.
ϵ	dissipation.
$\eta_{ij}(\vec{K},\vec{P},\vec{Q},t) = -\theta_{KPQ}\{D'_{ijm\ell}\Phi_{m\ell}(\vec{Q}) + D''_{ijm\ell}\Phi_{m\ell}(\vec{P})\}$	
η_{ij}^{M}	modeled form of η_{ij}.
$\Phi_{ij}(\vec{K},t)$, or $\underline{\Phi}$	spectral tensor, Fourier transform of the second order velocity correlation at two points.

μ damping factor.

ν kinematic viscosity.

θ_{KPQ} E.D.Q.N.M. characteristic time.

1. INTRODUCTION

The use of two-point correlations has often been very helpful to predict turbulent flows. In particular, concerning homogeneous anisotropic turbulent fields, the Rapid-Distortion theory has provided satisfactory informations about the interaction between turbulence and mean velocity gradients, which is a linear process. Unfortunately, at the present time, the use of analytical theories, such as D.I.A., T.F.M. and E.D.Q.N.M., to take into account the nonlinear action of turbulence on itself, has essentially been restricted to the area of isotropic turbulence. The main reason for this restriction is that using these theories without simplification to close the rate equation for the three-dimensional second order spectral tensor $\Phi_{ij}(\vec{K},t)$ would result in too cumbersome computations.

One is therefore led to make hypothesis to obtain reduction in computational labor. Two interesting attempts have to be mentioned at this point. The first is due to Herring[1,2] who developed the $\Phi_{ij}(\vec{K},t)$ tensor into a spherical harmonic expansion and retained only low order terms. Computations of the return to isotropy of turbulence then become tractable and have been carried out by using the equations of the D.I.A.. Comparison with direct simulation is fairly good. This study is nevertheless limited to the particular case of an axisymmetrical homogeneous turbulence, and a much larger number of terms would probably be needed if turbulent fields associated with mean velocity gradients were to be studied in that way.

Another interesting approach has recently been developed by Cambon[3]. The idea is to use the equation governing the average of $\Phi_{ij}(\vec{K},t)$ over a sphere of radius K and to close this equation with the E.D.Q.N.M. assumptions. When performing the integration over the sphere, informations concerning the "directivity" of $\Phi_{ij}(\vec{K},t)$ are lost, and a modeled form of Φ_{ij} is needed. $\Phi_{ij}(\vec{K})$ is then expressed as an isotropic function of its average over the sphere and of $\vec{K}$. A good agreement with experiment has been obtained when predicting the classical homogeneous flows with this model, in particular in the case of plane strain. However the model does not seem to fit with every kind of anisotropy, in particular we have pointed out that the presence of rotation affects its validity[4].

In the present paper, we develop a different kind of approach. We propose a model in which hypothesis are not made on the $\Phi_{ij}(\vec{K},t)$ tensor itself, but on the three-dimensional transfer $T_{ij}(\vec{K},t)$. The advantage is that the linear terms are then exactly taken into account. Values of $T_{ij}(\vec{K},t)$ computed by using the complete 3D E.D.Q.N.M. closure are needed only for a restricted number of wavevectors and for a few values of time. In between, a modeled form of T_{ij} is adopted, based on an interpolation between the computed values. The interpolated form is chosen to depend on Φ_{ij} and on the "isotropic" transfer, which is easier to compute.

In order to find a suitable form for the interpolation, which preserves the most important properties of the "true" three-dimensional E.D.Q.N.M. transfer, a preliminary study is made : T_{ij} is computed in particular cases of anisotropy resulting from the action of Rapid-Distortion on an initially isotropic turbulence. The main characteristics of transfer are then examined. A modeled form is thereafter proposed. Agreement between the model and the computed values of $T_{ij}(\vec{K})$ is found to be satisfactory.

Computations using the modeled $T_{ij}(\vec{K})$ are then carried out. The first results and confrontations with experiments are presented here.

2. THE CLOSURE OF THE EQUATION GOVERNING $\Phi_{ij}(\vec{K},t)$ IN THE FRAME OF THE E.D.Q.N.M.

We chose the E.D.Q.N.M. theory (Orszag[5]) as it is the simplest analytical closure and because it has been successfully employed in isotropic turbulence, in particular by Lesieur[6].

Putting an isotropic θ_{KPQ} in the equation of the Test Field Model given by Kraichnan[7], assuming furthermore that θ_{KPQ} can be expressed by using the same function of $|K|$ and $E(|K|)$ as in isotropic E.D.Q.N.M., give :

$$(1)\quad \frac{\partial}{\partial t}\Phi_{ij}(\vec{K},t) + 2\nu K^2 \Phi_{ij}(\vec{K},t) =$$

$$\int_\Delta \theta_{KPQ} D_{ijk\ell mn} \Phi_{k\ell}(\vec{P},t)\,\Phi_{mn}(\vec{Q},t)\,d\vec{P}\,d\vec{Q} \quad (= T_{ij}(\vec{K},t))$$

$$- \int_\Delta [\eta_{ik}(\vec{K},\vec{P},\vec{Q})\Phi_{kj}(\vec{K},t) + \eta^*_{jk}(\vec{K},\vec{P},\vec{Q})\Phi_{ik}(\vec{K},t)]\,d\vec{P}\,d\vec{Q} \quad (= T_{ij}(\vec{K},t))$$

where the integrals extend over the triads $\vec{K} + \vec{P} + \vec{Q} = \vec{0}$, and where

$$\eta_{ij}(\vec{K},\vec{P},\vec{Q}) = -\theta_{KPQ}\{D'_{ijm\ell}\Phi_{m\ell}(\vec{Q}) + D''_{ijm\ell}\Phi_{mi}(\vec{P})\},$$

D, D' and D" being coefficients depending on the geometry of the triad.

Equation (1), in which the terms containing mean velocity gradients have been omitted for the sake of briefness, can be considered as the equation of E.D.Q.N.M. for a non-isotropic turbulence.

The assumptions made on θ_{KPQ} imply that the damping factor μ of the E.D.Q.N.M. is not affected by anisotropy, and furthermore that the mean gradients are neglected in the equation of third-order correlations. From the point of view of the D.I.A., an equivalent of those assumptions is to assume, as suggested by Leslie[8], that Green's function is affected neither by the anisotropy of turbulence, nor by the presence of mean velocity gradients. If we have an idea of the validity of the first part of the proposition, which is probably acceptable (see Schumann and Herring[9]), the influence of the mean gradients is not clear (see Kraichnan[7] and Cambon in the present volume). In the present paper we make the simplest hypothesis on θ_{KPQ} on the basis of a practical consideration.

The right hand side of (1) is the 3D transfer, and we shall call is $T_{ij}(\vec{K},t)$.

3. STUDY OF THE THREE-DIMENSIONAL TRANSFER AND PHENOMENOLOGICAL APPROACH OF ITS MODELED FORM

In order to study the main properties of $T_{ij}(\vec{K},t)$ we have computed the values of this tensor in particular cases of anisotropic turbulence in which $\Phi_{ij}(\vec{K},t)$ can easily be obtained. For practical considerations we have chosen turbulent fields resulting from the action of Rapid-Distortion on the initially isotropic turbulence measured by Comte-Bellot[9]. Obviously the non linear processes are not taken into account when "building" the Φ_{ij} tensor in that way, but it is hoped that the observed properties of the computed form of the 3D transfer will still be valuable for real homogeneous flows, i.e. for less anisotropic turbulence.

The results are presented by using a visualization over spheres of radius $|\vec{K}|$. The principal axes of the tensors are visualized and segments proportional to the eigen values are plotted, as shown on figure 1. T_{ij} has been split into two parts : $T_{ij}^{+}(\vec{K},t)$ usually called backscatter, and $T_{ij}^{-}(\vec{K},t)$ called drain. Each part is visualized, as well as the $\Phi_{ij}(\vec{K},t)$ tensor itself.

Figure 1

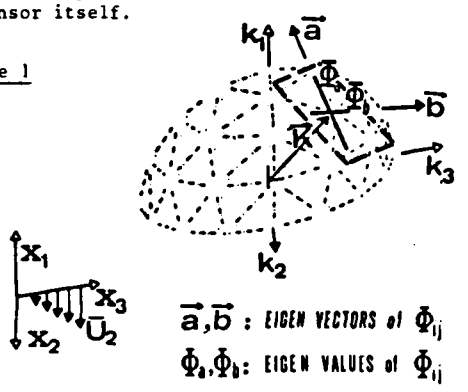

The most important results are that, on the one hand the distributions on the sphere of both T_{ij}^{+} and T_{ij}^{-} are strongly influenced by the distribution of $\Phi_{ij}(\vec{K},t)$, on the other hand that the "local" anisotropy of T_{ij}^{-}, at a given point of the sphere, is strongly influenced by the local anisotropy of Φ_{ij}. Moreover, it appears that T_{ij}^{+} is less connected to $\Phi_{ij}(\vec{K})$ than T_{ij}^{-} is, which is suggested by equation (1). These considerations can be deduced from figure 2 in the case of a uniform shear flow ; they remain true for a pure plane strain.

We now try to find a modeled form for T_{ij} which respects those main features. We try to express $T_{ij}(\vec{K},t)$, for any values of $\vec{K}$ and t, as a functional of $\Phi_{ij}(\vec{K},t)$, of the isotropic transfer $tr(|\vec{K}|,t)$ and of $T_{ij}(\vec{K}',t')$ computed for $\vec{K}$ describing a small set of spheres and for a few values of time. We still make the split $T_{ij} = T_{ij}^{+} + T_{ij}^{-}$ and then model separately.

Calling $(K_1, \ldots K_\alpha \ldots K_\gamma)$ the set of wavenumbers corresponding to the spheres on which the 3D transfer is computed by E.D.Q.N.M. for the set of times $(t_1, \ldots t_\beta \ldots, t)$, we write the functional F^{+} such as :

$$(2)\quad T_{ij}^{M+}(\vec{K},t) = F^{+}\{(\underline{\underline{T}}^{+}(\vec{K}\frac{K_\alpha}{|\vec{K}|}, t_\beta),\ \alpha = 1..\gamma\ ;\ \beta = 1..\delta),$$

$$\vec{K},\ \underline{\underline{\Phi}}(\vec{K},t),\ tr^{+}(|\vec{K}|,t),\ E(|\vec{K}|,t)\}$$

For the drain, it appears that it is better to model η_{ij}^{-} than to directly express T_{ij}^{-} by using a functional like (2).

We finally adopt, for $\eta_{ij}(\vec{K},t)$:

$$(3)\quad \eta_{ij}^{M}(\vec{K},t) = \frac{\overline{tr}(\vec{K},t)}{E(K,t)}\left[\eta_{ij}(K\frac{K_\alpha}{K},t_\beta)\frac{E(K_\alpha,t_\beta)}{\overline{tr}(K_\alpha,t_\beta)}\cdot\frac{K_{\alpha+1}-K}{K_{\alpha+1}-K_\alpha}\right.$$

$$\left. + \eta_{ij}(\vec{K}\frac{K_{\alpha+1}}{K},\ t_\beta)\frac{E(K_{\alpha+1},t_\beta)}{\overline{tr}(K_{\alpha+1},t_\beta)}\cdot\frac{K-K_\alpha}{K_{\alpha+1}-K_\alpha}\right]$$

t_β being the value of the set such as $t_\beta < t < t_{\beta+1}$, and K_α such as $K_\alpha < K < K_{\alpha+1}$. $E(K,t)$, $tr^{+}(K,t)$ and $tr^{-}(K,t)$ are respectively the average of $\Phi_{ij}(\vec{K},t)$ over the direction of $\vec{K}$, and the two parts of the isotropic E.D.Q.N.M. transfer associated with $E(K,t)$.

A similar form of T_{ij}^{M+} is adopted, which is based on the principal directions of Φ_{ij}.

For different values of K, which do not belong to the set of K_α, the modeled forms $T_{ij}^{M+}(K,t)$ and $T_{ij}^{M-}(K,t)$ are tested by comparisons with the true three-dimensional results of the E.D.Q.N.M. computation. An example of such a comparison is given on figure 3. The model can be considered as satisfactory, and no optimization of constant is found to be necessary.

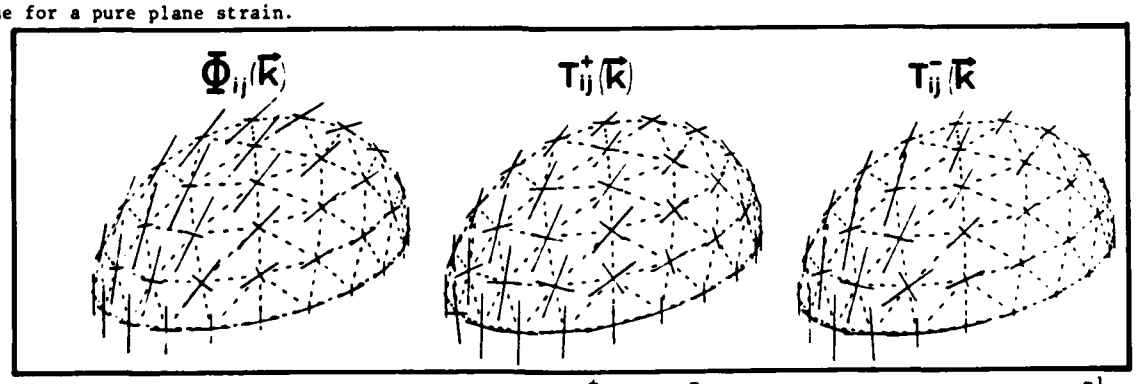

Figure 2 - Visualization of Φ_{ij}, T_{ij}^{+} and T_{ij}^{-} on a sphere of radius $K = 0.45\ cm^{-1}$, in the case of a mean shear $S = 13.6\ s^{-1}$ and for a time $t = 0.07$ s (same conventions as on figure 1).

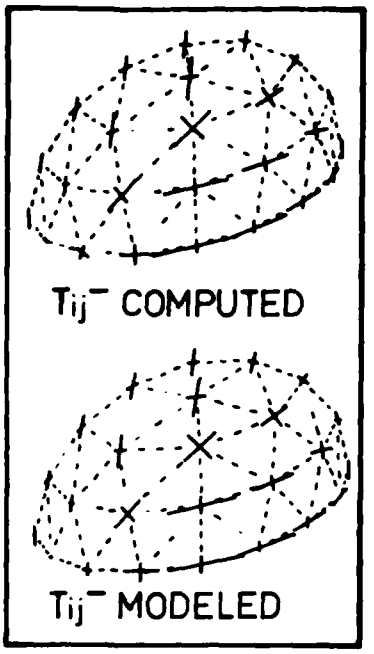

Figure 3 - Comparison between the computed form of of T_{ij}^-, at $K = 0.2\ cm^{-1}$, and its modeled form, interpolated from the results of computations at $K = 0.1\ cm^{-1}$ and $K = 0.5\ cm^{-1}$ ($S = 13.9\ s^{-1}$, $t = 0.1$ s) ; (same conventions as on figure 1).

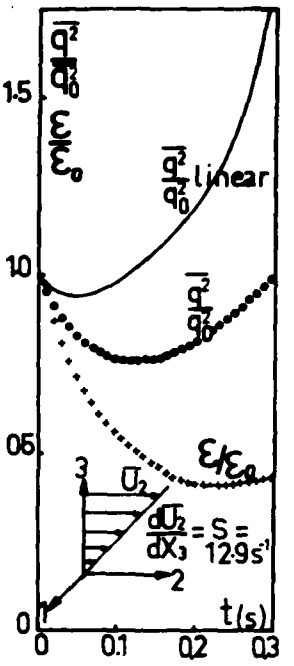

Figure 4 - Evolution with time of the turbulent kinetic energy $\overline{q^2}$, •• present model, —— rapid distortion ; and evolution with time of the dissipation ε, + present model.

4. RESULTS

We now use the modeled form of the transfer in the equation governing T_{ij}. The only constant appearing in the closure is then the usual E.D.Q.N.M. constant determined in isotropic turbulence. The computation time remains tractable since only a few complete 3D values of T_{ij} have to be computed. As typical values corresponding to the results presented here, we can indicate that T_{ij} is computed over 4 spheres of radius K, and every 0.02 second. The modeling form of the transfer being not exactly conservative, the backscatter is adjusted in the code to ensure energy conservation.

The computing method has been tested in the case of isotropic turbulence. It gives good results when compared to the experiment of Comte-Bellot[9].

Two non-isotropic cases are presented. They concern the uniform shear flow and the pure plane strain.

Figure 4 shows the comparison of our results with the effect of Rapid-Distortion on the evolution with time of the turbulent kinetic energy, in the case of a shear flow acting on an initially isotropic turbulence deduced from the measurements of Comte-Bellot. The components of the Reynolds stress tensor are plotted in figure 5 ; it appears, as expected, that anisotropy is smaller than in Rapid-Distortion.

Comparisons with experiment has been carried out in one of the few cases in which an initial spectrum is known : the pure strain distortion of Maréchal[10]. Figure 6 shows that agreement on the evolution of the turbulent kinetic energy is good. As for the structural parameter κ, it reaches 0.56 (figure 7) whereas values of about 0.6 are obtained by Maréchal. The corresponding one-dimensional spectra are plotted in figure 8.

The lack of initial experimental data concerning homogeneous shear flow badly restrains the validity of comparison with experiments in the shear case. A comparison is nevertheless attempted on the correlation coefficient $\overline{u_2 u_3}/\sqrt{\overline{u_2^2}\,\overline{u_3^2}}$ which seems to be less sensitive to initial conditions than the other quantities. Two values of shear are examined, $S = 12.9\ s^{-1}$ and $S = 45\ s^{-1}$, respectively corresponding to the experiments of Champagne, Harris and Corrsin[11] and Harris, Graham and Corrsin[12] (or more recently Tavoularis and Corrsin[13]). In both cases we assume that turbulence is isotropic at the entrance of the wind tunnel and we use the initial spectrum deduced from Comte-Bellot's experiment. In the C.H.C. case, our results tend to a (nearly) asymptotic value of about 0.44 (figure 9). The experimental results reach a slightly higher value, but the evolution with time can be considered to be fairly well predicted. In the high shear case, after reaching a maximum, our values are decreasing with time, which seems to agree with the experiments, especially with the measurements of Tavoularis.

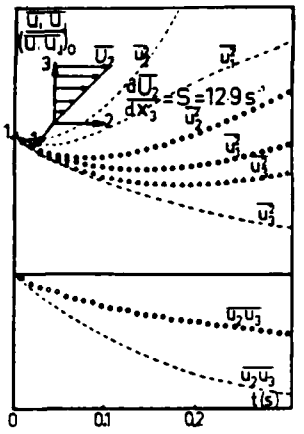

Figure 5 - Evolution with time of the components of the Reynolds stress tensor.●✹△○ Present Model, --- Rapid-Distortion.

Several other features, concerning the behaviour of different turbulent quantities, can be deduced from our computation. As an example, we can mention the results concerning the pressure velocity correlations in presence of shear, because of the importance of carefully modeling these correlations when doing one point closure (Launder[14], Lumley[15]).

Figure 10 shows that the behaviour of the linear part of the pressure velocity tensor P_{ij}^L is found to be very different from what it is in the Rapid-Distortion theory. All the components are found to be increasing with time, for large values of time however P_{33}^L soon becomes negative, which corresponds to a supply of energy to $\overline{u_3^2}$, while it remains positive in Rapid-Distortion. The discrepancy between the behaviours of P_{33}^L in our computation and in linear studies is directly connected to the difference of the distributions of Φ_{ij} on the spheres of radius $|\vec{K}|$ (figure 11).

These remarks concerning P_{ij}^L are important because they point out the danger of modeling the linear part of pressure velocity correlationsonly with reference to Rapid-Distortion theory when doing one points closures.

5. CONCLUSIONS

Even if, at the present time, there are few experimental confrontations because of the difficulty to generate anisotropic initial conditions for the computation, it is shown that when using isotropic initial spectra, a good qualitative and even quantitative prediction of classical homogeneous turbulent flows can be derived from the analytical theories of turbulence by modeling the transfer. As no modeled form of the $\Phi_{ij}(\vec{K},t)$ tensor itself is employed, the method is hoped to be particularly fitting for predicting flows in which the use of isotropic functions is inadequate ; rotating flows for example. The results can be directly used to predict flows, or can provide informations to improve one point closures or other modelings.

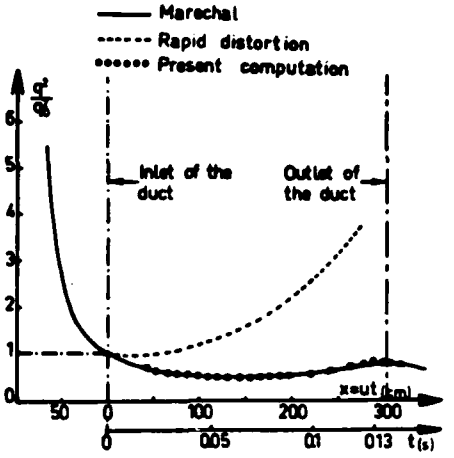

Figure 6 - Evolution with time of the turbulent kinetic energy the case of a plane strain distortion. ($a = \partial \overline{U}_3/\partial X_3 = -\partial \overline{U}_2/\partial X_2 = 19\ s^{-1}$). Comparison with the experimental values of Maréchal.

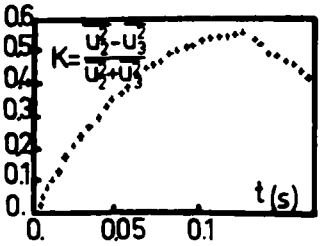

Figure 7 - Evolution with time of the structural parameter in the case of a plane strain distortion ($a = \partial \overline{U}_3/\partial X_3 = -\partial \overline{U}_2/\partial X_2 = 19\ s^{-1}$).

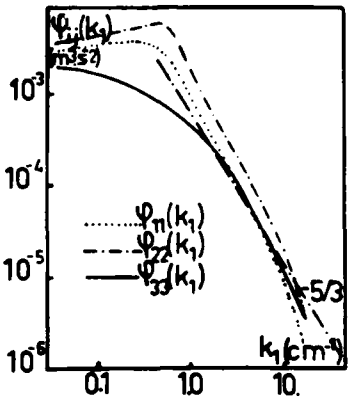

Figure 8 - One-dimensional spectra of the components of the Reynolds stress tensor, t = 0.13 s, $a = 19\ s^{-1}$.

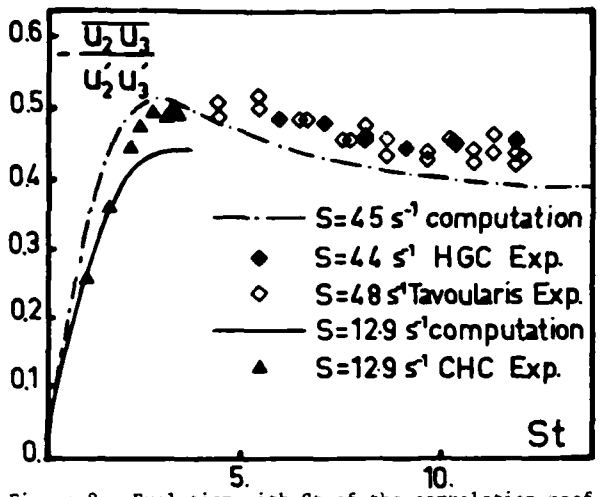

Figure 9 - Evolution with St of the correlation coefficient. Comparison with the experiments of C.H.C., H.G.C. and Tavoularis and Corrsin (St has been evaluated with the mean value S = 45 s^{-1} for both H.G.C. and Tavoularis experiments).

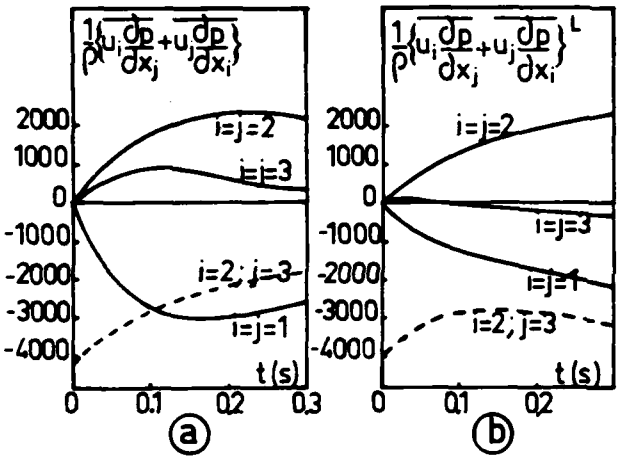

Figure 10 - Evolution of the pressure velocity correlation for S = 13.6 s^{-1}.
a) Rapid-Distortion.
b) Present Model.

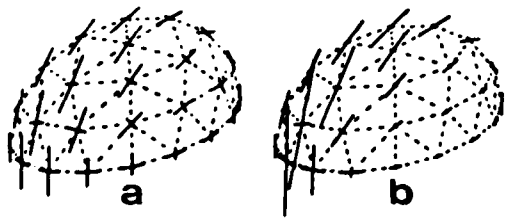

Figure 11 - Visualization of $\Phi_{ij}(\vec{K})$. Comparison between the present model:a, and Rapid disortion:b, in the case of shear S = 13.6 s^{-1}, t = 0.1 s, K = 1 cm^{-1}.

REFERENCES

1. HERRING J.R., "Approach of axisymmetric turbulence to isotropy", Physics of Fluids, Vol. 17, n° 5, 1974.

2. SCHUMANN H. and HERRING J.R., "Axisymmetric homogeneous turbulence : a comparison of direct spectral simulations with the direct-interaction approximation", Journal of Fluid Mechanics, Vol. 76, part 4, 1976, pp. 755-782.

3. CAMBON C., JEANDEL D. and MATHIEU J., "Spectral modeling of homogeneous non isotropic turbulence", Journal of Fluid Mechanics, Vol. 104, 1981, pp. 247-262.

4. BERTOGLIO J.P., "Homogeneous turbulent field within a rotating frame", AIAA 13th Fluid and Plasma Conference, paper 80-1353, 1980.

5. ORSZAG S.A., "Analytical theories of turbulence", Journal of Fluid Mechanics, Vol. 41, part 2, 1970, pp. 363-386.

6. LESIEUR M. and SCHERTZER D., "Dynamique des gros tourbillons et décroissance de l'énergie cinétique en turbulence tridimensionnelle isotrope à grand nombre de Reynolds", Journal de Mécanique, (Paris), Vol. 225, 1978, p. 464.

7. KRAICHNAN R.H., "Test-field model for inhomogeneous turbulence", Journal of Fluid Mechanics, Vol. 56, part 2, 1972, pp. 287-304.

8. LESLIE D.C., "Developments in the theory of turbulence", Clarendon Press, Oxford, 1973.

9. COMTE-BELLOT G. and CORRSIN S., "Simple Eulerian time correlation of full and narrow band velocity signals in grid-generated isotropic turbulence", Journal of Fluid Mechanics, Vol. 48, part 2, 1971, pp. 273-337.

10. MARECHAL J., "Etude expérimentale de la déformation plane d'une turbulence homogène", Journal de Mécanique, Vol. 11, n° 2, 1972, pp. 263-294.

11. CHAMPAGNE F.H., HARRIS V.G. and CORRSIN S., "Experiments on nearly homogeneous turbulent shear flow", Journal of Fluid Mechanics, Vol. 41, part 1, 1970, pp. 81-139.

12. HARRIS V.G., GRAHAM J.A.H. and CORRSIN S., "Further experiments in nearly homogeneous turbulent shear flow", Journal of Fluid Mechanics, Vol. 81, part 4, 1977, pp. 657-687.

13. TAVOULARIS S. and CORRSIN S., "Experiments in nearly homogeneous turbulent shear flow with a uniform mean temperature gradient - Part I", Journal of Fluid Mechanics, Vol. 104, 1981, pp. 311-347.

14. LAUNDER B.E., REECE G.J. and RODI W., "Progress in the development of a Reynolds stress turbulence closure", Journal of Fluid Mechanics, Vol. 68, part 3, 1975, pp. 537-566.

15. LUMLEY J.L., "Prediction methods for turbulent flows", Von Karman Institue, Lecture Series 76, 1975.

APPROACH OF NON ISOTROPIC HOMOGENEOUS TURBULENCE SUBMITTED TO MEAN VELOCITY GRADIENTS

by

C. CAMBON and D. JEANDEL
Laboratoire de Mécanique des Fluides - Ecole Centrale de Lyon - 69130 ECULLY - FRANCE

ABSTRACT

The paper provides an analytical formalism for describing the evolution of non isotropic homogeneous turbulence submitted to mean velocity gradients.

The basic procedure is a polarization vector decomposition of the velocity fluctuation field. Retaining only the linear mechanisms, the general solution for the equation of the fluctuation is derived without restrictive assumptions, for arbitrary realizations. The corresponding solution for the n^{th} order independant statistical moments is simply deduced. As examples, numerical experiments give the effects of plane distortion on second order moments when rotation is acting simultaneously.

Regarding the problem of closure, the extension of this linear analysis is examined from the point of view of statistical turbulence theory.

NOMENCLATURE

F_{ij}	Lagrangian mean strain gradient
k	Wavevector
p	Pressure field
p	Pressure fluctuation field
t	Time
U_i	Velocity field
u_i	Velocity fluctuation field
x	Position
ϱ	Density
ν	Kinematic viscosity
λ_{ij}	Mean velocity gradient

Superscripts

$\hat{}$	Spatial Fourier transform
$\sim$	Matrix transposition
$\langle\ \rangle$	Statistical averaging

FORMALISM FOR NON ISOTROPIC HOMOGENEOUS TURBULENCE

Basic relations

Consider an incompressible velocity field statistically homogeneous, velocity and pressure are splitted in two parts which respectively characterize the mean and the fluctuation fields.

$$U_i(X,t) = \langle U_i(X,t)\rangle + u_i(X,t)$$
$$P(X,t) = \langle P(X,t)\rangle + p(X,t)$$

Furthermore, the mean velocity is given in the following form

$$U_i(X,t) = U_i^{\circ}(t) + \lambda_{ij}(t)X_j$$

where U_i° and λ_{ij} are functions of time only. Consequently, if λ_{ij} is stationary, following Craya (1), compatibilities between the preceding conditions imply the mean field to be irrotational or plane.

The Fourier transforms of the velocity and of the pressure fluctuations are defined by :

$$\hat{u}_i(k,t) = \frac{1}{(2\pi)^3}\int_{R^3} u_i(X,t)e^{-Ikx}\,d^3x$$
$$\left(\frac{\hat{p}}{\varrho}\right) = \frac{1}{(2\pi)^3}\int_{R^3}\frac{p(X,t)}{\varrho}e^{-Ik.x}\,d^3x,\quad I=\sqrt{-1}$$

and the classical statistic spectral tensors of order n are found to be :

$$\langle \tilde{u}_i(p,t)\tilde{u}_j(k,t)\rangle = \Phi_{ij}(k,t)\cdot\delta(k+p)$$

.....

$$\langle \tilde{u}_{i_1}(k_n,t)\,\tilde{u}_{i_2}(k_1,t)\ldots u_{i_n}(k_{n-1},t)\rangle =$$

$$\Phi_{i_1 i_2\ldots i_n}^{(k_1,k_2,\ldots,k_{n-1})}\cdot\delta(k_1+k_2\ldots+k_n)$$

The condition of incompressibility requires :

$$\alpha_i \tilde{u}_i(k,t) = 0 \text{ with } \alpha_i = k_i/k$$

so that, in an orthonormal frame $(\alpha(k),\beta(k),\gamma(k))$ the velocity may be expressed in terms of two components in the form :

$$A_\alpha(k,t) = Q_{\alpha i}(k)\,\tilde{u}_i(k,t)$$

$$\text{or } \tilde{u}_i(k,t) = A_1(k,t)\beta_i(k) + A_2(k,t)\gamma_i(k)$$

(greek indices take only the values one or two). Among other authors, J. LEE (2) used such a polarizat on vector decomposition.

Accordingly, the corresponding reduced spectral tensors are :

$$\langle A_\alpha(p,t)A_\beta(k,t)\rangle = \Psi_{\alpha\beta}(k,t)\delta(k+p)$$

.....

$$\langle A_{\alpha_1}(k_n,t)A_{\alpha_2}(k_1,t)\ldots A_{\alpha_n}(k_{n-1},t)\rangle =$$

$$\Psi_{\alpha_1\alpha_2\ldots\alpha_n}^{(k_1,k_2,\ldots k_{n-1},t)}\delta(k_1+k_2\ldots+k_n)$$

with

$$\Psi_{\alpha\beta}(k,t) = Q_{\alpha i}(-k)Q_{\beta j}(k)\Phi_{ij}(k,t)$$

.....

$$\Psi_{\alpha_1\alpha_2\ldots\alpha_n}^{(k_1,k_2,\ldots k_{n-1},t)} =$$

$$Q_{\alpha_1 i_1}(k_n)Q_{\alpha_2 i_2}(k_1)\ldots Q_{\alpha_n i_n}(k_{n-1})\Phi_{i_1 i_2\ldots i_n}^{(k_1,k_2,\ldots k_n,t)}$$

$$\sum_{p=1}^{n} k_p = 0$$

We find that the moments of order n can be expressed in terms of n+1 independant components only :

$$\Psi_{\alpha_1\alpha_2\ldots\alpha_n}^{(k_1,k_2,\ldots k_n,t)},\ \alpha_1\zeta_{\alpha_2}\ldots\zeta_{\alpha_n}\zeta_2$$

General procedure for solving linear equations

Using the incompressibility condition, the Navier Stokes equation governing the fluctuation field may be written :

$$\Delta_{ij}\left(\frac{\partial \tilde{u}_j}{\partial t} + (\nu k^2 + Ik_1U_1^\circ)\,\tilde{u}_j + \lambda_{j1}\tilde{u}_1 - \lambda_{1m}k_1\frac{\partial \tilde{u}_j}{\partial k_m}\right) = \quad (1)$$

$$\Delta_{ij}\left(Ik_1\int_{p+q=k}\tilde{u}_j(p,t)\tilde{u}_1(q,t)\,d^3p\right)$$

with the projection operator

$$\Delta_{ij} = \delta_{ij} - \frac{k_ik_j}{k^2}$$

Retaining only linear terms, the partial differential equation reduces to :

$$\frac{\partial \tilde{u}_i}{\partial t} - \lambda_{1m}k_1\frac{\partial \tilde{u}_i}{\partial k_m} + (\nu k^2 + Ik_1U_1^\circ)\,\tilde{u}_i + \lambda_{i1}\tilde{u}_1 - \frac{2k_ik_1}{k^2}\lambda_{1m}\tilde{u}_m = 0 \quad (2)$$

the associated characteristic curves are given by :

$$X = \underline{\underline{F}}(t)k \quad (3)$$

where the lagrangian strain gradient $\underline{\underline{F}}(t)$ associated with the mean flow is governed by the equation :

$$\frac{dF_{ij}(t)}{dt} = \lambda_{il}^{(t)}\,F_{lj}(t) \quad (4)$$

Consequently, using the time derivative with respect to X constant (noted by the superscript $^\bullet$), the general solution of equation (2) writes :

$$\tilde{u}_i(k,t) = e^{-\mathcal{F}}G_{il}(k,t)\tilde{u}_l(X,0)$$

with

$$\mathcal{F} = \nu k_1k_n\int_0^t F_{li}(t')F_{ni}(t')dt' + IU_i^\circ k_l\int_0^t F_{li}(t')dt'$$

the solution V(k,t) of the equation

$$\Delta_{ij}(k)\left(\dot{V}_j(k,t) + \lambda_{jl}(t)V_l(k,t)\right) = 0 \quad (5)$$

with the incompressibility condition

$$K_iV_i(k,t) = 0$$

determines the associated tensor $G_{ij}(k,t)$

The linear sotutions of the equations governing the n^{th} order moments (without contribution on $n+1^{th}$ order moments) are then, written concisely as

$$\Phi_{i_1i_2\ldots i_n}^{(k_1,k_2,\ldots k_{n-1},t)} = e^{-\mathcal{F}_n}G_{i_1j_1}(k_n,t)G_{i_2j_2}(k_i,t)\,x \quad (6)$$

$$x\ G_{i_3j_3}(k_2,t)\ldots G_{i_nj_n}(k_{n-1},t)\Phi_{j_1j_2\ldots j_n}^{(X_1,X_2,\ldots X_{n-1},0)}$$

with

$$\mathcal{F}_n = \sum_{p=1}^{n}\mathcal{F}(k_p,t),\quad \sum_{p=1}^{n}k_p = \vec{0}$$

Similarly, the procedure may be described in the typical local frame. The corresponding differential system is deduced, and we have :

$$A_\alpha(k,t) = e^{-\mathcal{F}}q_{\alpha\beta}(k,t)A_\beta(X,0)$$

Likewise, the solution of the equation

$$\dot{W}_\alpha(k,t) + M_{\alpha\beta}(k,t)\,W_\beta(k,t) = 0 \quad (7)$$

gives the corresponding tensor $q_{\alpha\beta}(k,t)$

The general form of the n^{th} order moments

$$\Psi_{\alpha_1\alpha_2\ldots\alpha_n}^{(k_1,k_2,\ldots k_{n-1},t)}$$

is similar to (6).

CHARACTERIZATION OF THE KERNELS

The tensors G_{ij} or $q_{\alpha\beta}$ are calculated for all the mean flows retained by Craya. The resolution of (4) with (3) gives $\underline{F}(t)$ and the characteristic curves $X(k,t)$.

The condition of incompressibility is immediately satisfied by projection in the local frame or by introduction of the new function $\Psi_i(k,t)$ such that :

$$V_i(k,t) = \Delta_{ij}(k)\Psi_j(k,t)$$

In this last case, the equation (5) to be solved may be presented as :

$$\Delta_{ij}\left(\dot{\Psi}_j + \lambda_{jl}\Psi_l + (\lambda_{jl} - \lambda_{lj})\frac{k_l k_n}{k^2}\Psi_n\right) = 0 \quad (8)$$

and the specific feature of irrotational mean flows clearly appears.

Irrotational mean flows

The eigen values of $\underline{\lambda}$ and $\underline{F}$ are respectively a_i and $e^{a_i t}$, $i = 1,3$.

Using (8), the tensor $G_{ij}(k,t)$ is given in the form

$$G_{ij}(k,t) = \Delta_{il}(k)F^{-1}_{jl}(t)$$

The concise form of the n^{th} order moments generalize the expressions given by Batchelor (3) and Courseau-Loiseau (4) (second order moments with isotropic initial conditions). To illustrate the procedure, in the case of arbitrary initial conditions, the solution for the second order moments reduce to the tensorial form

$$\Phi_{ij}(k,t) = \Delta_{ik}(k)F^{-1}_{lk}(t)\Delta_{jn}F^{-1}_{pn}(t) \times$$

$$\times \Phi_{lp}\left\{\underline{\underline{F}}(t)k,0\right\} e^{-\mathcal{F}_2}$$

$$\mathcal{F}_2 = 2\nu k_l k_n \int_0^t F_{li}(t')F_{ni}(t')dt'$$

Plane rotational mean flows

For such flows, it is convenient to use the local frame $\alpha(k)$, $\beta(k)$, $\gamma(k)$). Accordingly, the matrix $M_{\alpha\beta}$ of the linear differential system (7) leading to $q_{\alpha\beta}$ may be written as :

$$\underline{\underline{M}} = \begin{vmatrix} \beta_i\lambda_{ij}\beta_j & \beta_i(\lambda_{ij}-\lambda_{ji})\gamma_j - \dfrac{n_i\lambda_{in}\beta_n}{\sqrt{1-(\alpha_l n_l)^2}} \\ 2\gamma_i\lambda_{ij}\gamma_j + \dfrac{n_i\lambda_{in}\beta_n}{\sqrt{1-(\alpha_l n_l)^2}} & \gamma_i\lambda_{ij}\gamma_j \end{vmatrix}$$

with

$$\alpha_i = k_i/k, \beta_i = \frac{\varepsilon_{ijl}\alpha_j n_l}{\sqrt{1-(\alpha_l n_l)^2}}, \gamma_i = \varepsilon_{ijl}\alpha_j\beta_l, \quad n_i \text{ fixed}$$

Two particular cases lead to analytical solutions for $q_{\alpha\beta}$: the pure rotation and the pure shear flow.

For the pure rotation, choosing n colinear to the rotation vector Ω, the mean velocity gradient

$$\lambda_{ij} = \varepsilon_{ijl}\Omega_l$$

leads to :

$$g = \begin{vmatrix} \cos\varpi t & -\sin\varpi t \\ \sin\varpi t & \cos\varpi t \end{vmatrix} \qquad \varpi = 2\Omega.\alpha$$

In the case of pure shear flow, with

$$\lambda_{ij} = s\cdot\delta_{i2}\delta_{j3} \text{ and } n_i = \delta_{i3}$$

we have :

$$g = \begin{vmatrix} 1 & f(k,t) \\ 0 & |\vec{X}| \,/\, |\vec{k}| \end{vmatrix} \text{ and } X(k_1,k_2,k_3+k_2st)$$

with

$$f(k,t) = \frac{k_1}{k_2}\frac{|\vec{X}|}{\sqrt{k_1^2+k_2^2}}\left(\text{Arctg}\frac{k_3}{\sqrt{k_1^2+k_2^2}} - \text{Arctg}\frac{X_3}{\sqrt{k_1^2+k_2^2}}\right), k_2 \neq 0$$

$$f(k,t) = -\frac{k_1}{k}st, \quad k_2 = 0$$

Using (6), these results will generalize the solution given by Gence (5) and Loiseau.

The general computation of mean rotational flows is performed with the mean velocity gradient

$$\begin{vmatrix} 0 & 0 & 0 \\ 0 & d & \omega \\ 0 & \omega & -d \end{vmatrix}$$

given in the fixed principal axes of the distortion tensor. Without evident analytical solutions, the differential system (7) is numerically solved by Runge Kutta integration.

As examples, using initial isotropic conditions, the evolution of the second order moments Φ_{ij} are calculated for various values of the ratio ω/d. On figure 1, we give the radial tensor, obtained by integration over a spherical shell of radius $|\vec{k}|$

$$\varphi_{ij}(|\vec{k}|,t) .$$

at $d.t = 0.76$ (d fixed), for various values of the ratio ω/d.

The evolution with time of the one point non diagonal component $\langle u_2u_3\rangle$ and the kinetic energy $\langle u_iu_i\rangle$ are shown on the figure 2. From $\omega/d = 0$ to $\omega/d = 1$, $\langle u_2u_3\rangle$ is contineously increasing with time; when $\omega/d > 1$, $\langle u_2u_3\rangle$ is always increasing for small values of d.t, but the level at large values of d.t falls when ω/d is growing. Moreover, an oscillating tendency appears, its period is roughly identical to that of the pure rotation.

CONCLUDING COMMENTS AND APPROACH OF THE NON LINEAR PROBLEM

In the present work, the study of the linear effects on an arbitrary realization of the fluctuation velocity field is readily extended to statistical spectral tensors using the determinist behavior of the operator. Accordingly, the linear problem becomes more tractable than the classical rapid distortion theories and more general results on n^{th} order moments are extracted. Moreover, the numerical solution underlines the consequent qualitative effects of the mean flow : the exact calculation of the linear part of the pressure-strain correlation may be used as a guide for the modeling of the corresponding term in the Reynolds stress equation, (6).

For the approach of the non linear problem, we examine the contribution of the previous analysis to the classical theories of closure starting from a linear gaussian model. Indeed, considering an initial statistical ensemble, such that $\tilde{u}_i(k,0)$ has a multivariate normal law, it is clear that the linear solution preserves this property. The same situation appears in the case of the linear response of the

fluctuation field when a gaussian forcing term take the place of the non linear right hand side of (1).

In the both cases, we can associate a gaussian solution $\tilde{u}_i^\circ$ and a linear problem, characterized by the Green function R_{ij}°.

$$R_{ij}^\circ(k,t,k',t') = G_{ij}(k,t-t')e^{-\mathcal{F}(k,t-t')} \times \delta(k' - \mathcal{F}(t-t')k) \quad (9)$$

The departure from the gaussianity will then essentially be linked to the non-linear terms in (1). Accordingly, the effects of these mechanisms on statistical quantities can be treated formally as weak corrections added to the basic set $(\tilde{u}_i^\circ, R_{ij}^\circ)$.

At first, following the DIA method (7), we let the response tensor be defined by the functional derivative :

$$R_{ij}(k,t,k',t') = \delta\tilde{u}_i(k,t)/\delta f_j(k',t') \text{ or,}$$

$$\delta\tilde{u}_i(k,t) = \iint_{-\infty}^{t} R_{ij}(k,t,k',t')\delta f_j(k',t')d^3k'dt'$$

where f_j represents a forcing term acting on the right hand side of (1).

The DIA algorithm would be the following :
- Considering the equations for the statistical quantities $\langle R_{ij} \rangle$ and Φ_{ij}, close the unknown terms by expanding $\tilde{u}_i$ and R_{ij} around $\tilde{u}_i^\circ$ and R_{ij}° using perturbations.
-Retain only the lowest order terms in these expansions and discard the indice zero.

At this stage, this procedure reveals, among other inconsistencies, a specific problem in our case : the time-dependant shifting between k and k', induced by the Green function (9), can lead to violate spatial homogeneity. Thus, for future investigations, we retain only, in the DIA approach, the sounding concept of response tensor.

Then, comparing characteristic time-scales, of both linear and non-linear mechanisms[1], we can assume that R_{ij}° is a good approximation for R_{ij}, at least in the small wavenumbers range.

Consequently, the abridgment proposed by Leslie (8) for treating shear-flows, appears questionable ; indeed the author choice, "a priori", an isotropic distribution for Φ_{ij}° and a local (in k-space) isotropic form :

$$R_{ij}^\circ = e^{-\mathcal{F}(k,\,t-t')}\Delta_{ij}(k)\,\delta(k'-k)$$

On the other hand, spatial correlations can be used exclusively at the same time, without inconsistency, when applying a quasi-normal hypothesis with an eddy damping (EDQN). Following Orszag(9), this way consists to close the equation of the third-order spectral tensor by splitting the term relative to fourth-order correlations in two parts : the first is expressed in terms of second-order correlations, applying the rules for evaluating moments of normal distributions ; the second one depends linearly on the third order tensor and come in addition to the primitive linear part of the equation. Then, we can define a primitive, or zeroth order, Green function and an enlarged one, characterizing the upper whole linear term. In a previous work, (10), the unknown enlarged function was assumed to be isotropic, with a single damping coefficient. An improvement of such a drastic assumption may be expected starting from the linear exact model : an exact determination of the primitive Green function can be extracted in term of R_{ij}° function products (see relation (9)). This information will be used as the first step for the construction of a suitable enlarged function.

1 - For exemple, we can compare the constant "linear" scale $(\lambda_{ij}\lambda_{ij})^{-1/2}$ with the large eddy turn-over time $\left(\int_0^k p^2 E(p)dp\right)^{-1/2}$

REFERENCES

1. CRAYA,A., "Contribution à l'analyse de la turbulence associée à des vitesses moyennes",P.S.T. du Ministère de l'Air, N° 345, 1958.
2. LEE,J., "Dynamical behavior of the fundamental triad-interaction system in three-dimensional homogeneous turbulence", Physics of Fluids, Vol. 22, (1), 1979
3. BATCHELOR, G.K. and PROUDMAN, I., "The effect of rapid distortion of a fluid in turbulent motion", Quart. J. Mech. and Appl. Math., Vol. 7, Part 1, 1954.
4. COURSEAU, P. et LOISEAU, M., "Contribution à l'analyse de la turbulence homogène anisotrope", J. de Mécanique, Vol. 17, n° 2, 1978.
5. ITSWEIRE, E., CHABERT, L. et GENCE, J.N., "Action d'une rotation pure sur une turbulence homogène anisotrope", Compte-rendu à l'Académie des Sciences de Paris, T. 289, nov. 1979.
6. LAUNDER, B.E., REECE, G.J. and RODI, W., "Progress in the development of Reynolds-stress turbulence closure", Journal of Fluid Mechanics, Vol. 68, Part 3, 1975, pp. 537-566.
7. KRAICHNAN, R.H., "Diagonalizing approximation for inhomogeneous turbulence", Physics of Fluids, Vol. 7, N° 8, Aug. 1964.
8. LESLIE, D.C., "Developments in the theory of turbulence", Clarend on Press, Oxford, 1973, pp. 317-326.
9. ORSZAG, S.A., "Analytical theories of the turbulence", Journal of Fluid Mechanics, Vol. 41, p. 363, 1970.
10. CAMBON, C., JEANDEL, D., and MATHIEU J., "Spectral modelling of homogeneous non-isotropic turbulence", Journal of Fluid Mechanics, Vol.104, 1981, pp. 247-262

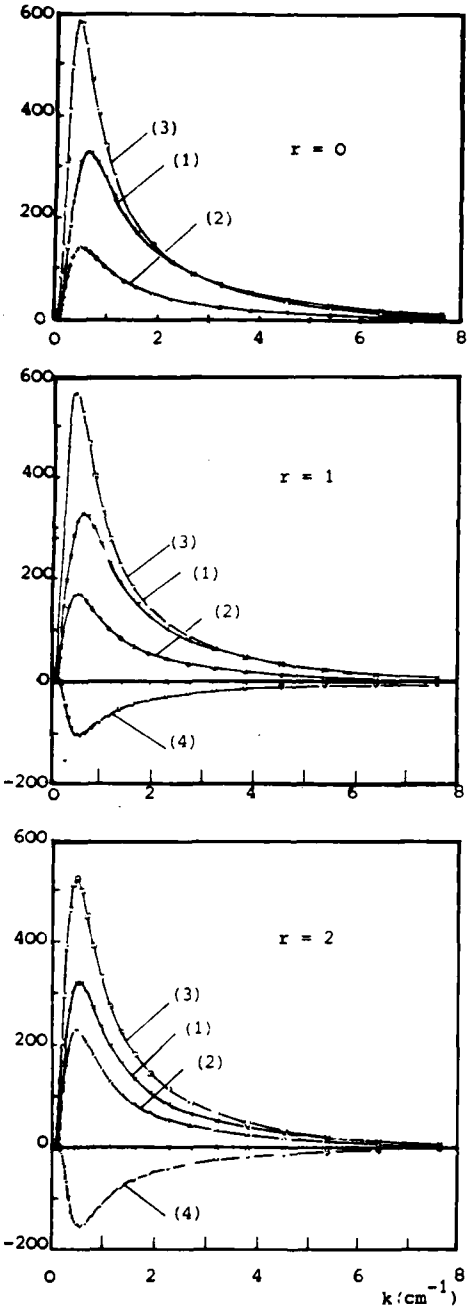

Fig. 1 Radial spectral tensor at d.t = 0.76 for various values of $r = \omega/d$; $d = 19\ s^{-1}$

(1) $\varphi_{11}(k,t)$ (cm^3/s^2)

(2) $\varphi_{22}(k,t)$

(3) $\varphi_{33}(k,t)$

(4) $\varphi_{23}(k,t)$

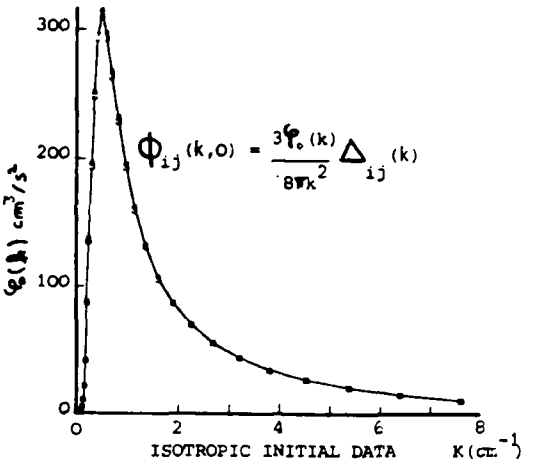

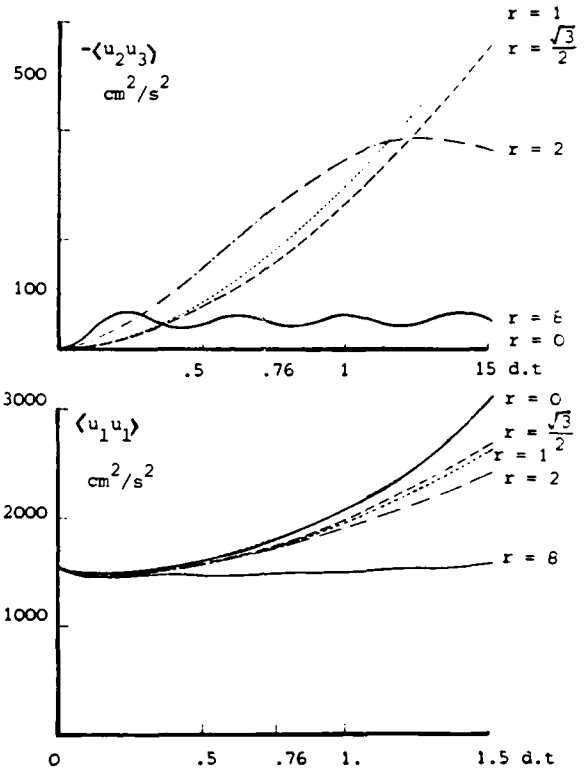

Fig. 2 Non diagonal Reynolds Stress component $\langle u_2u_3\rangle$ and Kinetic energy, for various values of $r = \omega/d$

ENTRAINMENT DIAGRAMS FOR VISCOUS FLOWS

By
Brian Cantwell and Gary Allen
Department of Aeronautics and Astronautics
Stanford University
Stanford, CA 94305

ABSTRACT

A technique is described for visualizing unsteady flows which are self similar in time. The method makes use of a reduction of the equations for unsteady particle paths to an autonomous system in similarity coordinates. The entrainment diagram for a given flow corresponds to the phase portrait of this system and the flow structure is analyzed in terms of its critical points. This approach provides a powerful method for analyzing the dependence of the flow on various governing parameters.

NOMENCLATURE

a,b,c,d - matrix coefficients
f,g - self similar Falkner-Skan stream functions
G - self similar round jet stream function
H - self similar vortex ring stream function
M - governing parameter
p,q - trace and determinant of the matrix of coefficients
Re - Reynolds number
t - time
$\mathbf{u}$ - velocity vector
U_e - free stream velocity
U_o - plate velocity
x_i - spatial coordinates
β - pressure gradient exponent
ξ,η - similarity coordinates
ξ_c,η_c - coordinates of a critical point
θ - polar angle
ξ_c,θ_c - coordinates of a critical point in spherical coordinates
ω - vorticity
τ - $\ln t$

INTRODUCTION

This paper is addressed to the problem of visualizing unsteady fluid motion. Observations of organized structure in turbulence have led to an increased emphasis on direct analysis or measurement of complex unsteady flow fields. An extremely important element in current research is a renewed emphasis on the use of flow visualization and a widespread awareness that flow visualization can play a very broad role in improving our physical understanding of complicated turbulent phenomena (Kline 1978).

The instantaneous streamline patterns which result from these investigations provide a form of flow visualization combined with substantial amounts of quantitative information about the flow. However, there are significant conceptual problems involved in interpreting unsteady streamline patterns as they relate to entrainment. In an unsteady flow, streamlines can move across fluid pathlines; thus the unsteady stream function provides little insight into the behavior of the fluid itself.

Particle trajectories drawn in physical coordinates also present similar conceptual difficulties. If the integration of the particle-path equations is carried out over a volume of particles, then each point in space will be traversed by an infinite set of trajectories, each with a different slope corresponding to the passage of particles through the point at successive instants of time. In addition, the pattern of particle paths, like the pattern of streamlines, depends on the frame of reference.

Certain time-dependent flows can be reduced to a self-similar form. Such flows usually depend on one or two global parameters. In this case, some of the above objections can be removed by reducing the equations for unsteady particle paths

$$\frac{dx_i}{dt} = u_i(\underline{x},t) \qquad (1)$$

to an autonomous system in similarity coordinates. We shall call the phase portrait of this system, the entrainment diagram of the flow. It is a Lagrangian representation of the unsteady flow pattern in a system of scaled spatial coordinates. There are several useful elements of this technique

i) The entrainment diagram provides a visual picture of the flow which is invariant for various moving observers.
ii) The flow structure is described in terms of a limited set of critical points in the entrainment diagram. Thus the technique provides a quantitative scheme for identifying and classifying related features of various classes of self-similar flows.
iii) The entrainment diagram can be used to analyze the dependence of a flow on various governing parameters.

At this point it may be noted that the restriction to flows which are self-similar in time turns out to be remarkably general. Even when we further restrict ourselves to flows which are amenable to

simple stretching transformations[1] the list of cases is quite long and includes virtually all of the flows which we ordinarily think of as self similar in space (Cantwell 1981).

In the present paper we will focus our attention on element (iii) of the entrainment diagram technique and demonstrate its application to the analysis of three flow problems; the classification of Falkner-Skan boundary layers, transition in the axisymmetric jet and reverse transition of the vortex ring. In each case the dependence of the flow pattern on governing parameters will be demonstrated.

EXAMPLE 1.
CLASSIFICATION OF FALKNER-SKAN BOUNDARY LAYERS

These are steady boundary layers with an imposed streamwise pressure gradient which varies according to a power law in the x-direction. Nevertheless we will begin the analysis with a similarity form appropriate to the unsteady boundary layer equations. In terms of the stream function

$$\frac{\partial^2\psi}{\partial y\partial t} + \frac{\partial\psi}{\partial y}\frac{\partial^2\psi}{\partial x\partial y} - \frac{\partial\psi}{\partial x}\frac{\partial^2\psi}{\partial y^2} = U_e\frac{\partial U_e}{\partial x} + \nu\frac{\partial^3\psi}{\partial y^3} \qquad (2)$$

where the free stream velocity U_e is given by

$$U_e(x) = Mx^\beta \qquad (3)$$

The constant, M, determines the rate at which U_e varies and is the parameter which governs the motion in the x-direction. The appropriate similarity form is

$$\psi = \nu^{1/2}\, M^{\frac{1}{1-\beta}}\, t^{\frac{1+\beta}{2(1-\beta)}}\, g(\xi,\eta) \qquad (4)$$

where

$$\xi = \frac{x}{M^{1/(1-\beta)}\, t^{1/(1-\beta)}};\quad \eta = \frac{y}{\sqrt{\nu t}} \qquad (5)$$

Substituting (3), (4) and (5) into (2) leads to

$$\frac{1+\beta}{2(1-\beta)}g\frac{\partial g}{\partial\eta} - \frac{\partial}{\partial\eta}\left[\frac{\xi}{(1-\beta)}\frac{\partial g}{\partial\xi} + \frac{\eta}{2}\frac{\partial g}{\partial\eta}\right] + \frac{\partial g}{\partial\eta}\frac{\partial^2 g}{\partial\xi\partial\eta} - \frac{\partial g}{\partial\xi}\frac{\partial^2 g}{\partial\eta^2} = \beta\,\xi^{2\beta-1} + \frac{\partial^3 g}{\partial\eta^3} \qquad (6)$$

The governing partial differential equation no longer depends on time and thus (4) and (5) are correct forms. When expressed in terms of ξ and η the equations for unsteady particle trajectories become

$$\frac{d\xi}{d\tau} = g_\eta - \frac{\xi}{1-\beta} \qquad (7)$$

$$\frac{d\eta}{d\tau} = -g_\xi - \frac{\eta}{2} \qquad (8)$$

where $\tau = \ell n\, t$.

The Falkner-Skan solutions are usually expressed in the form

$$\psi = \left(\nu M x^{\beta+1}\right)^{1/2} f\left(y\left(\frac{M}{\nu x^{1-\beta}}\right)^{1/2}\right) \qquad (9)$$

One can easily verify that (9) is equivalent to (4) where

$$g(\xi,\eta) = \xi^{(1+\beta)/2}\, f(s) \qquad (10)$$

and $s = \eta/\xi^{(1-\beta)/2}$.

In terms of f(s) the equations (7) and (8) become

$$\frac{d\xi}{d\tau} = \xi^\beta f' - \frac{\xi}{1-\beta} \equiv F_1(\xi,\eta) \qquad (11)$$

$$\frac{d\eta}{d\tau} = -\xi^{-\left(\frac{1-\beta}{2}\right)}\left[\frac{1+\beta}{2}\, f - \frac{(1-\beta)}{2}\, sf'\right] - \frac{\eta}{2} \equiv F_2(\xi,\eta) \qquad (12)$$

In the neighborhood of a critical point (ξ_c,η_c), the above equations may be expanded as

$$\frac{d\xi}{d\tau} = a(\xi-\xi_c) + b(\eta-\eta_c) \qquad (13)$$

$$\frac{d\eta}{d\tau} = c(\xi-\xi_c) + d(\eta-\eta_c) \qquad (14)$$

where

$$a = \left.\frac{\partial F_1}{\partial\xi}\right|_{\xi_c,\eta_c},\quad b = \left.\frac{\partial F_1}{\partial\eta}\right|_{\xi_c,\eta_c},\quad c = \left.\frac{\partial F_2}{\partial\xi}\right|_{\xi_c,\eta_c},$$

$$d = \left.\frac{\partial F_2}{\partial\eta}\right|_{\xi_c,\eta_c} \qquad (15)$$

The nature of the critical point is completely determined by the trace and determinant of the matrix of coefficients.

$$p = -(a+d) \qquad (16)$$

$$q = ad - bc \qquad (17)$$

In order to evaluate p and q we make use of the following relations derived from setting (11) and (12) equal to zero at (ξ_c,η_c). Note $s_c = \eta_c/\xi_c^{(1-\beta)/2}$.

$$f'(s_c) = \frac{\xi_c^{1-\beta}}{1-\beta} \qquad (18)$$

$$f(s_c) = 0 \qquad (19)$$

Using (15), (18) and (19) the coefficients become

$$a = -1-\left(\frac{1-\beta}{2}\right)\eta_c\xi_c^{3(\beta-1)/2} f''(s_c) \qquad (20)$$

$$b = \xi_c^{3\beta/2-\frac{1}{2}}\, f''(s_c) \qquad (21)$$

$$c = -\left(\frac{1-\beta}{2}\right)\frac{\eta_c\xi_c}{2} + \frac{\beta}{2}\frac{\eta_c}{\xi_c} - \left(\frac{1-\beta}{2}\right)^2\frac{\eta_c^2}{\xi_c}\xi_c^{\frac{3}{2}\beta-\frac{3}{2}} f''(s_c) \qquad (22)$$

$$d = -\frac{(1+\beta)}{2(1-\beta)} + \frac{(1-\beta)}{2}\eta_c\xi_c^{3\beta/2-3/2} f''(s_c) \qquad (23)$$

Evaluating p and q we have

$$p = -\frac{(\beta-3)}{2(1-\beta)} \qquad (24)$$

[1] In the general case in two-dimensions the basic similarity variables are of the form (Cantwell 1978)
$\xi = t^{-k}(x-\bar{X}(t))\cos(a\ell nt + bt) - (y-\bar{Y}(t))\sin(a\ell nt + bt)$
$\eta = t^{-k}(x-\bar{X}(t))\sin(a\ell nt + bt) + (y-\bar{Y}(t))\cos(a\ell nt + bt)$
Where k, a and b are arbitrary constants and $\bar{X}(t)$ and $\bar{Y}(t)$ are arbitrary functions of time. In the case of simple stretching transformations $a=b=\bar{X}(t)=\bar{Y}(t)=0$.

$$q = \frac{1+\beta}{2(1-\beta)} \qquad (25)$$

Note that the evaluation of p and q does not require an explicit knowledge of f(s). Figure 1. indicates the various critical points associated with different values of β.

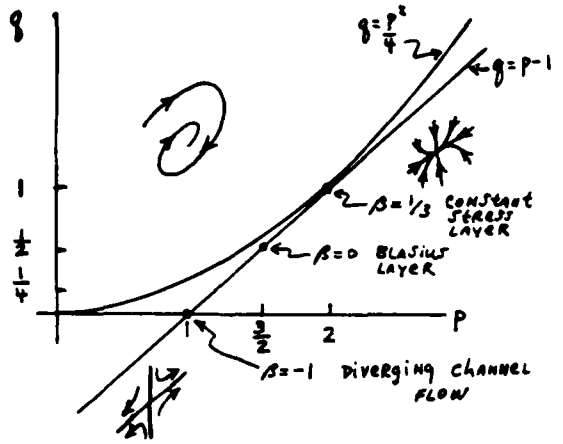

Figure 1. Trajectory of the critical point of the Falkner-Skan solutions in the (p,q) plane.

The line q=p-1 is gotten by eliminating β between (24) and (25). Well known cases include

i) (β=0) The Blasius Layer - the critical point in this case is a stable node with (p,q)= (3/2,1/2). The entrainment diagram for this flow is shown schematically in Figure 2.

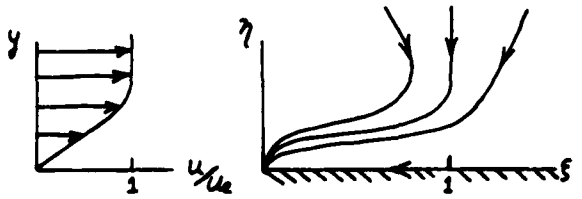

Figure 2. Entrainment diagram for the Blasius Layer.

ii) (β=1/3) Constant stress layer - this occurs where the line q=p-1 osculates with the parabola $q=p^2/4$. It represents a situation in which a mildly favorable pressure gradient balances diffusion from the wall to produce a boundary layer with a wall shear stress which remains constant with x. The entrainment diagram is similar to Figure 2. but with a star point at the leading edge.

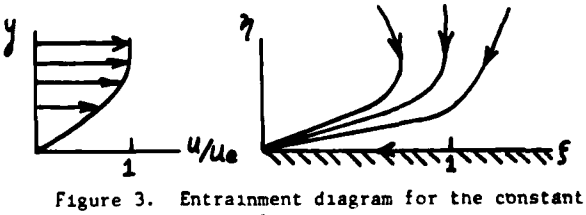

Figure 3. Entrainment diagram for the constant stress layer.

iii) (β=-1) Jeffrey - Hamel Flow - This represents the case of flow in a diverging channel produced by a volume source at the vertex. It happens to be a case where length scales in both coordinate directions vary like $\sqrt{t}$. The entrainment diagram is shown schematically in Figure 4.

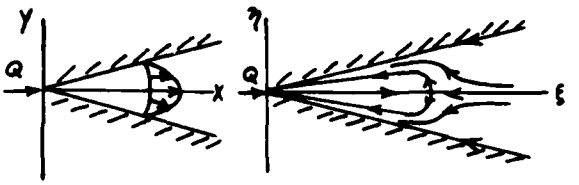

Figure 4. Entrainment diagram for the flow in a diverging channel (ONE POSSIBLE SOLUTION).

In the context of discussing the Blasius Layer we may also consider the case of an impulsively started plate. For this case

$$u = U_o(1-\mathrm{erf}(\tau)); \quad \eta = \frac{y}{\sqrt{4\nu t}} \qquad (26)$$

The particle paths in similarity coordinates are

$$\frac{d\xi}{d\tau} = (1-\mathrm{erf}(\tau)) - \xi \qquad (27)$$

$$\frac{d\eta}{d\tau} = -\frac{\eta}{2} \qquad (28)$$

where $\xi=x/U_o t$, $\eta=y/\sqrt{4\nu t}$ and $\tau=\ln t$.

with a critical point at $(\xi_c,\eta_c) = (1,0)$.

Near the critical point (27) and (28) may be expanded as

$$\begin{bmatrix} \frac{d\xi}{d\tau} \\ \frac{d\eta}{d\tau} \end{bmatrix} = \begin{bmatrix} -1 & 2/\sqrt{\pi} \\ 0 & -1/2 \end{bmatrix} \begin{bmatrix} \xi-1 \\ \eta \end{bmatrix} \qquad (29)$$

The critical point is a stable node with (p,q)=(3/2, 1/2); i.e. the same (p,q) values as for the steady Blasius Layer. The entrainment diagram for this flow is shown schematically in Figure 5.

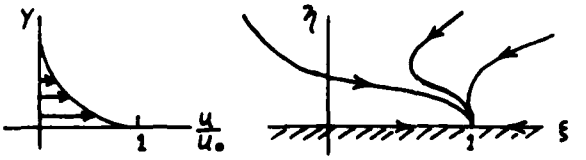

Figure 5. Entrainment diagram for the impulsively started flat plate.

Inclusion of the starting process in the analysis of the phase portrait of the particle path equations leads to a powerful method for analyzing the dynamics of fluid motion. In Example 2 we will briefly review results published previously (Cantwell 1981) for transition in the axisymmetric jet. This will serve to introduce Example 3 in which the application of the entrainment diagram technique to the problem of relaminarization or reverse transition in the impulsively produced vortex ring will be described.

The purpose for contrasting these two examples with each other is to illustrate the fundamentally different nature of the Reynolds number dependence of the two flows.

In each case we will be considering solutions of the linearized equations of motion.

$$\nabla \cdot \bar{u} = 0 \tag{30}$$

$$\nabla \times \bar{u} = \bar{\omega} \tag{31}$$

$$\frac{\partial \bar{\omega}}{\partial t} = \nu \nabla^2 \bar{\omega} \tag{32}$$

EXAMPLE 2.
TRANSITION IN THE IMPULSIVELY STARTED ROUND JET

In this section we will review the behavior of an impulsively started, axisymmetric laminar jet. The Reynolds number is, $Re=(J/\rho)^{1/2}/\nu$, where J/ρ is the strength of the momentum source which produces the jet. Dimensional considerations lead to a formulation of the problem which is self similar in time in the variables $\xi = r/\sqrt{\nu t}$ and θ, where r and θ are the raduis and polar angle in spherical polar coordinates.

We will make use of the analytic solution for the limit $Re \to 0$. The Stokes stream function for this case is given by

$$\Psi = \nu^{3/2} t^{1/2} G(\xi,\theta) \tag{33}$$

Substituting (33) into (30) to (32) and solving for G leads to

$$G(\xi,\theta) = \frac{Re^2}{16\pi} \sin^2\theta \left(2\xi - \frac{4}{\sqrt{\pi}} e^{-\xi^2/4} - \left(2\xi - \frac{4}{\xi}\right)\mathrm{erf}\left(\frac{\xi}{2}\right)\right) \tag{34}$$

By any conventional measure the above solution has only a trivial dependence on Reynolds number. However an examination of particle trajectories associated with (33) and (34) reveals a remarkably complex structure. The equations for particle trajectories are given by

$$\frac{dr}{dt} = u(r,\theta,t;Re) \; ; \; \frac{d\theta}{dt} = \frac{v(r,\theta,t;Re)}{r} \tag{35}$$

where u and v are the radial and tangential velocities. In terms of similarity variables the equations become

$$\frac{d\xi}{d\tau} = U(\xi,\theta;Re) - \frac{\xi}{2} \; ; \; \frac{d\theta}{d\tau} = \frac{V(\xi,\theta;Re)}{\xi} \tag{36}$$

Where

$$U(\xi,\theta;Re) = \frac{1}{\xi^2 \sin\theta} \frac{\partial G}{\partial \theta} \; ; \; V(\xi,\theta;Re) = \frac{-1}{\xi \sin\theta} \frac{\partial G}{\partial \xi} \tag{37}$$

and $\tau = \ln t$. Substitution of (34) into (36) using (37) leads to

$$\frac{d\xi}{d\tau} = \frac{Re^2}{2\pi} \frac{\cos\theta}{\xi^2} \left(\frac{\xi}{2} - \frac{1}{\sqrt{\pi}} e^{-\xi^2/4} - \left(\frac{\xi}{2} - \frac{1}{\xi}\right)\mathrm{erf}\left(\frac{\xi}{2}\right)\right) - \frac{\xi}{2} \tag{38}$$

$$\frac{d\theta}{d\tau} = -\frac{Re^2}{4\pi} \frac{\sin\theta}{\xi^2} \left(\frac{1}{2} + \frac{1}{\xi\sqrt{\pi}} e^{-\xi^2/4} - \left(\frac{1}{2} + \frac{1}{\xi^2}\right)\mathrm{erf}\left(\frac{\xi}{2}\right)\right) \tag{39}$$

The structure of the flow is examined by finding and classifying critical points of (38) and (39); points (ξ_c,θ_c) at which both right hand sides are equal to zero. The zeros of (39) are at ($\theta = 0,\pi$ all ξ) and ($\xi = 1.7633$ all θ) and are clearly the same for all Reynolds numbers. Setting the right hand side of (38) equal to zero gives

$$Re^2 = \frac{\pi \xi_c^3}{\left(\frac{\xi_c}{2} - \frac{1}{\sqrt{\pi}} e^{-\xi_c^2/4} - \left(\frac{\xi_c}{2} - \frac{1}{\xi_c}\right)\mathrm{erf}\left(\frac{\xi_c}{2}\right)\right)\cos\theta_c} \tag{40}$$

Equation (40) defines a family in the (ξ,θ) plane for various values of the Reynolds number. Intersections between (40) and the zeros of (39) locate critical points in the entrainment diagram of the solution (34). Figure 6 below shows schematically the entrainment diagram of (34) at three values of the Reynolds number.

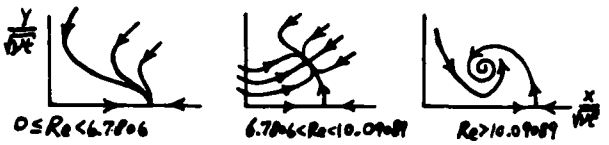

Figure 6. Entrainment diagrams of $G(\xi,\theta)$ (equation 34) for various Reynolds number ranges.

For sufficiently small Reynolds number, pathlines converge to a single stable node which lies on the axis of the jet. At a Reynolds number of 6.7806 the pattern bifurcates to a saddle lying on the axis of the jet, plus two stable nodes lying symmetrically to either side of the axis. At a Reynolds number of 10.09089 the pattern bifurcates a second time to form a saddle and two stable foci. The Reynolds number dependence of the flow is conveniently summarized by the trajectory of the critical points of (38) and (39) in the (p,q) plane shown in Figure 7.

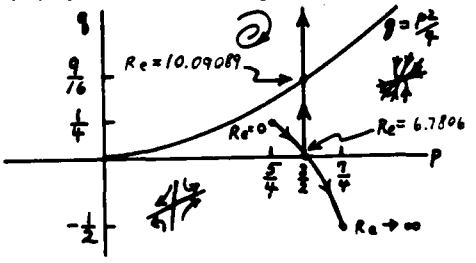

Figure 7. Trajectory of the critical points of (38) and (39) in the (p,q) plane.

Several aspects of this work which have important implications for our understanding of unsteady shear flows should be noted.

i) A vortex rollup such as that depicted in Figure 6 is usually thought of as an essentially nonlinear phenomenon. Yet here we see that a rollup process is contained in the structure of a linearized solution of the equations of motion.

ii) The vortex rollup, or focus forms just one of a family of possible critical points which may describe the structure of a given flow. In two dimensions possible critical points include saddles, nodes and foci. In three

dimensions the entrainment diagram may be very complex.

iii) One can give a physical interpretation to the three flow patterns depicted in Figure 6. Consider an interface between two fluids A and B in physical coordinates. If the momentum source is turned on at t=0 then, depending on the Reynolds number, the interface will distort into one of the three possible patterns depicted below.

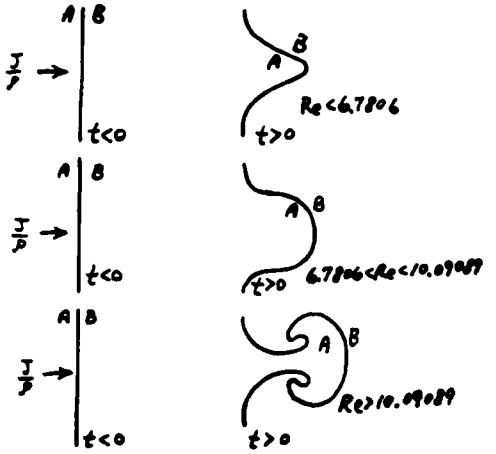

Figure 8. Distortion of fluid interface by $G(\xi,\theta)$ at three Reynolds numbers.

EXAMPLE 3.
RELAXATION OF AN IMPULSIVELY STARTED VORTEX RING

In this section we will examine the behavior of an impulsively started, axisymmetric vortex ring. The Reynolds number of the vortex ring is $Re = (I/\rho t)^{1/2}/\nu$, where I/ρ is the total impulse applied to the fluid,

$$\frac{I}{\rho} = \frac{3}{2}\int_0^{\pi}\int_0^{\infty} (u\cos\theta - v\sin\theta)2\pi r^2\sin\theta\, dr d\theta \qquad (41)$$

Note that, in contrast to the previous example, the Reynolds number in this flow depends on time. The equations of motion in spherical polar coordinates are

$$\frac{1}{r}\frac{\partial}{\partial r}(r^2 u) + \frac{1}{\sin\theta}\frac{\partial}{\partial\theta}(v\sin\theta) = 0 \qquad (42)$$

$$r\omega = \frac{\partial}{\partial r}(rv) - \frac{\partial u}{\partial\theta} \qquad (43)$$

$$\frac{\partial}{\partial t}(r\omega) = \nu\left[\frac{1}{r^2}\frac{\partial}{\partial\theta}\left(\frac{1}{\sin\theta}\frac{\partial}{\partial\theta}(\omega\sin\theta)\right) + \frac{\partial^2}{\partial r^2}(r\omega)\right] \qquad (44)$$

with the Stokes stream function defined by

$$u = \frac{1}{r^2\sin\theta}\frac{\partial\psi}{\partial\theta}\ ; v = \frac{-1}{r\sin\theta}\frac{\partial\psi}{\partial r} \qquad (45)$$

As before particle paths are given by

$$\frac{dr}{dt} = u(r, \theta, t; \frac{I}{\rho}; \nu) \qquad (46)$$

$$\frac{d\theta}{dt} = \frac{v(r, \theta, t; \frac{I}{\rho}; \nu)}{r} \qquad (47)$$

with the parametric dependence of u and v on I/ρ and ν indicated. The variables r, θ, u and v are the same coordinates and velocities used in Example 2. The similarity forms appropriate to this problem are

$$\psi = \frac{I}{\rho}\,\nu^{-1/2}\,t^{-1/2}\,H(\xi,\theta) \qquad (48)$$

$$u = \frac{I}{\rho}\,\nu^{-3/2}\,t^{-3/2}\,U(\xi,\theta) \qquad (49)$$

$$v = \frac{I}{\rho}\,\nu^{-3/2}\,t^{-3/2}\,V(\xi,\theta) \qquad (50)$$

$$\omega = \frac{I}{\rho}\,\nu^{-2}\,t^{-2}\,W(\xi,\theta) \qquad (51)$$

$$r = \nu^{1/2}\,t^{1/2}\,\xi$$

Where U, V, H and W are the self-similar velocities, stream function and vorticity. Note that we have assumed that these functions do not depend on I/ρ or ν. We shall check this assumption a posteriori. In terms of similarity variables, the particle path equations become

$$\frac{d\xi}{d\tau} = Re^2\,U(\xi,\theta) - \frac{\xi}{2}\ ;\quad \xi = \frac{r}{\sqrt{\nu t}} \qquad (52)$$

$$\frac{d\theta}{d\tau} = Re^2\,\frac{V(\xi,\theta)}{\xi} \qquad (53)$$

where $\tau = \ell n\ t$ and $Re^2 = I/\rho\nu^2 t$. These equations should be compared with equivalent equations for the round jet (Equations 36). Note that in this example the particle path equations do not reduce to an autonomous system. Rather the right hand sides of the equations depend on time, with the dependence appearing through the Reynolds number which now comes out as a parameter multiplying the as yet unknown functions $U(\xi,\theta)$ and $V(\xi,\theta)$. The entrainment diagram for this flow evolves with time.

Substituting (51) into (44) and solving the resulting equation by separation of variables leads to

$$W(\xi,\theta) = \frac{1}{16\pi^{3/2}}\sin\theta\ \xi\ e^{-\xi^2/4} \qquad (54)$$

where the constant has been chosen to insure that (41) is satisfied. The stream function is determined using (54), (45) and (43). The result is

$$H(\xi,\theta) = \frac{1}{4\pi}\sin^2\theta\left[\frac{1}{\xi}\,\mathrm{erf}\left(\frac{\xi}{2}\right) - \frac{1}{\sqrt{\pi}}\,e^{-\xi^2/4}\right] \qquad (55)$$

Taking limits gives

$$\lim_{\xi\to\infty} H(\xi,\theta) = \frac{\sin^2\theta}{4\pi\xi} \qquad (56)$$

or, in terms of ψ

$$\lim_{r\to\infty} \psi = \frac{I}{\rho}\,\frac{\sin^2\theta}{4\pi r} \qquad (57)$$

The flow at infinity is that due to a steady dipole of strength I/ρ. Using (45) the particle path equations become

$$\frac{d\xi}{d\tau} = \frac{Re^2}{2\pi}\frac{\cos\theta}{\xi^2}\left[\frac{1}{\xi}\,\mathrm{erf}\left(\frac{\xi}{2}\right) - \frac{1}{\sqrt{\pi}}\,e^{-\xi^2/4}\right] - \frac{\xi}{2} \qquad (58)$$

$$\frac{d\theta}{d\tau} = \frac{-Re^2}{4\pi}\frac{\sin\theta}{\xi^3}\left[\frac{1}{\sqrt{\pi}}\left(1+\frac{\xi^2}{2}\right)e^{-\xi^2/4} - \frac{1}{\xi}\,\mathrm{erf}\left(\frac{\xi}{2}\right)\right] \qquad (59)$$

At this point the analysis follows very closely that used to analyze the round jet. The structure of the vortex ring is examined by finding and classifying critical points of (58) and (59); points (ξ_c,θ_c) at which both right hand sides are equal to zero. The zeros of (59) are at (θ=0, π all ξ) and (ξ=3.022437 all θ) and are clearly the same for all Reynolds numbers. Setting the right hand side of (58) equal to zero gives

$$Re^2 = \frac{\pi\xi_c^3}{\left(\frac{1}{\xi_c}\,\mathrm{erf}\left(\frac{\xi_c}{2}\right) - \frac{1}{\sqrt{\pi}}\,e^{-\xi_c^2/4}\right)\cos\theta_c} \qquad (60)$$

intersections between (60) and the zeros of (59) locate the critical points of the system (58) and (59).

If Re < 18.174936 there is a single node lying on the axis of the vortex ring (θ_c=0). In this Reynolds number range (60) provides a relation between Re and ξ_c, the radial coordinate of the node which moves outward along the axis of the vortex ring as Re is increased.

When Re exceeds 18.174936 the flow splits into three critical points; a saddle situated on the axis of the vortex ring and two stable nodes lying symmetrically about the axis at ξ_c=3.022437 and

$$\theta_c = \pm\cos^{-1}\left[\left(\frac{18.174936}{Re}\right)^2\right] \qquad (61)$$

As the Reynolds number is further increased, the nodes move away from the axis on the circle ξ_c=3.022437. At the same time the ξ_c coordinate of the saddle continues to follow (60) with θ_c=0. For the critical point on the axis, the invariants of the matrix of coefficients are

$$p_{\theta_c=0} = \frac{3}{2} - \frac{Re^2}{4\pi\xi_c^3}\left[\frac{1}{\sqrt{\pi}}\left(1+\frac{\xi_c^2}{2}\right)e^{-\xi_c^2/4} - \frac{1}{\xi_c}\,\mathrm{erf}\left(\frac{\xi_c}{2}\right)\right] \qquad (62)$$

$$q_{\theta_c=0} = \left(p_{\theta_c=0} - \frac{3}{2}\right)\left(\frac{3}{2} - 2\,p_{\theta_c=0}\right) \qquad (63)$$

For the critical point off the axis, the invariants are (ξ_c evaluated as 3.022437)

$$p_{\theta_c\neq 0} = \frac{3}{2} \qquad (64)$$

$$q_{\theta_c\neq 0} = 2.94130154 \times 10^{-6}\;Re^4 - 3.20945389 \times 10^{-1} \qquad (65)$$

The off-axis node changes to a stable focus when $q_{\theta_c\neq 0}$ exceeds 9/16. This occurs at Re=23.410465. Figure 9 shows schematically the entrainment diagram of the vortex ring at three values of the Reynolds number

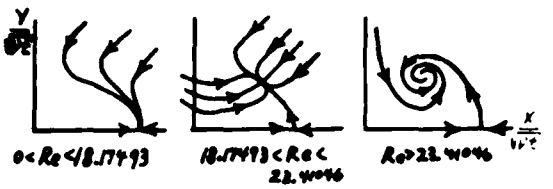

Figure 9. Entrainment diagrams of $H(\xi,\theta)$ (equation 55) for various Reynolds number ranges.

The various patterns and their limiting forms at ξ_c=0 and ξ_c=∞ (Re=0, Re=∞) are summarized in Figure 10 which shows the trajectory of the critical points of the vortex ring in the (p,q) plane.

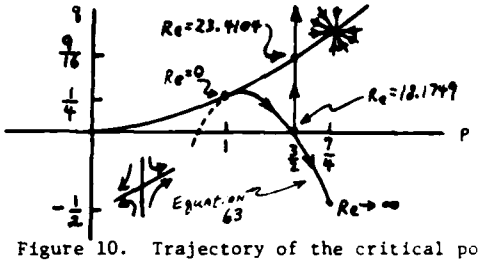

Figure 10. Trajectory of the critical points of (58) and (59) in the (p,q) plane.

Note that the trajectory is almost identical to that of the round jet (Figure 7). The main difference is in the limiting values of p and q as Re→0 (ξ_c→0). In the case of the vortex ring the (p,q) trajectory (Equation (62)) osculates with the parabola q=p/4; i.e. the on-axis critical point becomes a star (p=1, q=1/4) as Re→0. Whereas the zero Reynolds number limit in the case of the round jet was a stable node (p=5/4, q=1/4).

While the similarities between these two examples may be quite striking, the physical interpretation of the results is totally different. In the case of the round jet the pathline equations are strictly autonomous and, in a given realization of the flow the Reynolds number is constant over all space and time. In the case of the vortex ring the pathline equations are not autonomous and, in a given realization all Reynolds numbers are encountered with the Reynolds number decreasing with increasing time ($Re\sim 1/\sqrt{t}$). The appropriate mixing problem to imagine in this case is one in which a series of interfaces is encountered by a single vortex ring as shown schematically in Figure 11.

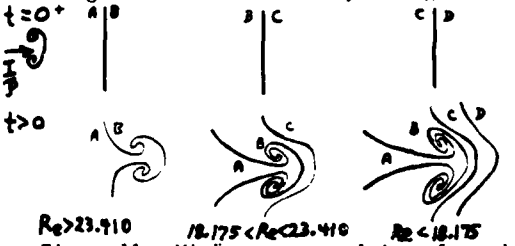

Figure 11. Mixing at several interfaces by a vortex ring.

The first interface encountered by the vortex ring rolls up in the traditional fashion. The second and third interfaces are placed sufficiently far from the origin so that the Reynolds number of the arriving ring has dropped below the appropriate threshold value. These latter two interfaces never roll-up.

ACKNOWLEDGEMENT

This work was supported by NASA Ames Research Center under NASA Grant NSG-2392.

REFERENCES

1) Kline, S.J. 1978. The Role of Visualization in the Study of the Structure of the Turbulent Boundary Layer. Lehigh Workshop on Coherent Structure of Structure of Turbulent Boundary Layers, ed. C.R. Smith, D.E. Abbott pp 1-26.

2) Cantwell, B.J. 1981. Organized Motion in Turbulent Flow. Ann. Rev. Fluid Mech. 13:457-515.

3) Cantwell, B.J. 1978. Similarity Transformations for the Two Dimensional Unsteady Stream Function Equation. J. Fluid Mech. 85:257-271.

4) Cantwell, B.J. 1981. Transition in the Axisymmetric Jet. J. Fluid Mech. 104:369-386.

PREDICTABILITY OF TWO-AND THREE-DIMENSIONAL FREELY DECAYING FLOWS. APPLICATION TO MIXING LAYERS

Marcel LESIEUR and Jean-Pierre CHOLLET
Université de Grenoble
Institut de Mécanique

ABSTRACT

It is suggested that, contrary to what happens for stationary forced homogeneous turbulence, the large scales of three-dimensional freely evolving turbulence may be predictable in the sense that an initial error grows at a rate no faster than the large energetic structures. This conjecture is based on: a) a phenomenological approach, b) results on pair dispersion obtained from two-points closures, c) direct numerical simulations. The same analysis performed in the two-dimensional case seems on the contrary to confirm a rapid contamination of the large scales by an error initially confined to the small scales.

The latter results are used as ingredients of an attempt to describe the dynamics of mixing layers in terms of statistical theories of two-dimensional freely-evolving turbulence. Four steps may be pointed out : i) the build up of the enstrophy cascade, which creates excitation up to the three-dimensional Taylor microscale (equivalent to the two-dimensional enstrophy dissipative wavenumber) ; ii) the establishment of a three-dimensional energy cascade up to the three-dimensional Kolmogorov wavenumber ; iii) a rapid contamination of the large scales by the three-dimensionality induced in the small scales ; iiii) an ultimate state of "equipartition" of energy in the large scales between two-and three-dimensional structures.

NOMENCLATURE

$\mathcal{D}(t)$	enstrophy
$E(k,t)$	energy spectrum
k_I	wavenumber characteristic of large energetic eddies
k_E	wavenumber characteristic of the error spectrum
k_D	two-dimensional dissipative wavenumber
ℓ	integral scale
$P(r,t)$	probability distribution for the two particles of a pair to be distant of $\vec{r}$
R	root mean square separation of the tracers in a pair
Re	Reynolds number
t	time
v	velocity field
β	enstrophy injection rate
$\Delta(k,t)$	error spectrum
ε	energy dissipation rate
λ	three-dimensional Taylor microscale
θ_q	relaxation time for the triple correlations
ν	kinematic viscosity
σ	dispersion coefficient
τ	local turnover time

1. INTRODUCTION

Among the various approaches used to study the stability of a given flow, predictability studies allow one to make a stability analysis "in the mean" of a turbulent flow. The mathematical formalism (see e.g. LORENZ (1) and KRAICHNAN (2)) consists in considering two random fields $u^{(1)}$ and $u^{(2)}$ both satisfying Navier-Stokes equations, having the same statistical properties, and initially completely correlated except in the small scales. It has been shown without ambiguity in the frame of two-point closures such as the quasi-normal theory (LORENZ (1)), the eddy-damped markovian quasi-normal theory (LEITH (3)) or the test field model (LEITH and KRAICHNAN (4)), that an initial error confined to scale sizes greater than the dissipative scales would progressively contaminate larger and larger scales. These results have been obtained with models of homogeneous stationary turbulence supplied by external forces injecting energy at a given wavenumber k_I. From these results the conclusion was made that a turbulent flow is by nature unpredictable, and consequently it is impossible to make a numerical long term deterministic prediction of a flow at high Reynolds number. The dynamics of this inverse cascade of error deduced from the statistical models can be described phenomenologically as follows : let

$k_E(t)$ be the wavenumber characterizing the front of decorrelation. A decorrelation velocity may be defined as $(d/dt)(k_E^{-1})$ and expressed as the ratio $k_E^{-1}/\tau(k_E)$, where $\tau(k_E)$ is the local turnover time at k_E. We then obtain the relation :

$$\frac{dk_E}{k_E} \sim \frac{-dt}{\tau(k_E)} \qquad (1\text{-}1)$$

which governs the inverse cascade of error. Relation (1-1), with $\tau(k) \sim \left\{\int_0^k p^2 E(p)\, dp\right\}^{-1/2}$, implies that a decorrelation initially confined above wavenumber k_2 will reach wavenumber k_1 in a time of the order of :

$$T(k_1,k_2) = \int_{k_1}^{k_2} \tau(p)\, dp/p \quad . \qquad (1\text{-}2)$$

In three dimensions and if k_2 lies in the $k^{-5/3}$ energy cascade, the time required for the uncertainty to reach k_1 is of order $\tau(k_1)$. In two dimensions and if k_2 is in the enstrophy cascade, things are not so simple because of the well known logarithmic correction. Nevertheless if the extent of the enstrophy cascade does not exceed a few decades, the logarithmic correction to the k^{-3} energy spectrum may be neglected, and the predictability time is of the order of the local eddy turnover time, approximately equal to $\beta^{-1/3}$ along the cascade. (β is the enstrophy injection rate).

A consequence of the latter result, mentioned by ALEMANY et al., (5), concerns the return to three-dimensionality of the large scales of a two-dimensional flow perturbed three-dimensionality in the small scales : indeed, the initial three-dimensional perturbation induces a decorrelation in the small scales between two horizontal sections of the flow which otherwise would be completely identical. This decorrelation will then gradually contaminate larger and larger scales, implying the return to three-dimensionality of the large scales.

There seems to be an inconsistency between these theoretical results and the experimental observations of the so-called "large coherent structures". Some authors have suggested that the analytical theories of turbulence mentioned above may be unable to describe such turbulent flows. Our point of view is different : we suggest, using arguments taken from these analytical theories, that some classes of freely evolving flows could be much more predictable than statistically stationary flows. In the three-dimensional case, this predictability is due to a self-similar increase of the large structures which proceeds at a rate comparable to the growth of the error. In the two-dimensional case, the results of unpredictability obtained for stationary flows still hold for unforced freely-evolving flows : consequently the three-dimensionality contained in the small scales rapidly contaminates the large two-dimensional energy-containing eddies. Nevertheless the two-dimensional structures cannot disappear, because their size increases at a rate proportional to t (see BATCHELOR (6)), while the integral scale of a three-dimensional isotropic turbulence increases much slower. We shall then be led to propose a concept of "equipartition of dimensionality". This could be an explanation of the experimental evidence of the persistance of large scale quasi-two-dimensional structures in mixing layers for downstream (BROWAND en TROUTT (7)).

2. PHENOMENOLOGY

In the case of $\ldots$-dimensional turbulence at high Reynolds number, it may be shown assuming a self-similar decay that the integral scale ℓ and the energy $\frac{1}{2} v^2$ evolve like t^{α_ℓ} and $t^{-\alpha_E}$, α_ℓ and α_E satisfying the relation :

$$\alpha_\ell = 1 - \alpha_E/2 \qquad (2\text{-}1)$$

easily obtained from the definition of ℓ by $\ell = v^3/\varepsilon$, where $\varepsilon = -\frac{1}{2}\frac{d}{dt} v^2$ is the energy dissipation rate. More details are given in LESIEUR and SCHERTZER (9) . Eq. (2-1) is then equivalent to :

$$\frac{d}{dt}\left(\ell^{-1}\right) \sim -\varepsilon^{1/3}\left(\ell^{-1}\right)^{5/3} \qquad (2\text{-}2)$$

These results are of course valid for asymptotically high times and Reynolds numbers. More precise calculations using two-point closures such as the Test-Field Model (see LARCHEVEQUE et al. (8), the Eddy-Damped Quasi-Normal Markovian approximation (see LESIEUR and SCHERTZER (9)) or the Quasi-Normal approximation (see TATSUMI, KIDA and MIZUSHIMA (10)) show that, with an energy spectrum behaving like k^4 when $k \to 0$, α_E is of order 1.38 $\sim$ 1.39, and α_ℓ of order 0.31. For a k^4 spectrum, it is well known that $\alpha_E = 1$ and $\alpha_\ell = 0.5$. But since a k^4 energy-spectrum immediately appears in the low-k range when turbulence is induced by a forcing concentrated in a narrow band around an injection wavenumber k_I , it is reasonable to infer that the k^4 shape is the best fitted for grid turbulence experiments. The fact that the values of α_E measured in these experiments are lower than 1.38 (1.26 in COMTE-BELLOT and CORRSIN (11)) is certainly ascribable to insufficient values of the decay times and Reynolds numbers.

We now return to eq.(2-2), which is independent of the value of α_E . On the other hand, when k_E belongs to the $k^{-5/3}$ inertial range of the energy spectrum, (1-1) implies

$$\frac{dk_E}{dt} \sim -\varepsilon^{1/3} k_E^{5/3} \qquad (2\text{-}3)$$

It may be checked easily from (2-2) and (2-3) that for $t \gg t_o$ (t_o is the initial time where complete decorrelation for $k > k_o$ is assumed), k_E^{-1} and ℓ remain in a constant ratio and are both proportional to $t^{1-\alpha_E/2}$. The decorrelation obeys then the same self-similarity law as the energy spectrum and never overtakes the large energy-containing eddies.

A similar phenomenology may be performed for two-dimensional turbulence. The evolving spectrum may then be characterized by two wavenumbers : $k_I(t)$ and $k_D(t)$ characteristic, respectively, of the energy-containing eddies and of the enstrophy-dissipative scales, with :

$$k_I(t) \sim (v_o t)^{-1} \qquad (2\text{-}4)$$

$$k_D(t) \sim (\beta t)^{-1/2} \qquad (2\text{-}5)$$

Between k_I and k_D extends an enstrophy-cascading energy spectrum

$$E(k) \sim t^{-2} k^{-3}$$

(see BATCHELOR (6), TATSUMI and YANASE (12), and BASDEVANT (13)). $\frac{1}{2} v^2$ is the kinetic energy, conserved with time. The enstrophy $D(t)$ varies as t^{-2}. It is interesting to note that k_D corresponds to the Taylor microscale of a three-dimensional turbulence whose energy-containing eddies would correspond to k_I. This result will be shown in section 5. The time $\tau(k)$ is then constant along the cascade and proportional to t. Then eq. (1-1) reads :

$$\frac{dk_E}{k_E} \sim - \frac{dt}{t} \qquad (2\text{-}7)$$

The phenomenology is not completely conclusive, in this case, since knowledge of the constant arising in (2.7) is necessary to determine the law for the time evolution of $k_E(t)$.

3. PAIR-DISPERSION

Preceeding results are complemented by the pair-dispersion studies in freely evolving flows made by LARCHEVEQUE and LESIEUR (14), using the Eddy Damped Quasi-Normal Markovian approximation. In the three-dimensional case, it may be shown that, for pairs of Lagrangian tracers whose initial separation lies in the inertial range and is very small in front of the integral scale , the RICHARDSON's law is still valid, in the form :

$$\dot{R} \sim \varepsilon^{1/3} R^{1/3} \qquad (3\text{-}1)$$

where R is the root mean square separation of the tracers in the pair. Eq. (3-1) is strictly equivalent to (2-2) and shows that R grows proportionally to ℓ . This result may be interpreted as kind of predictability result : indeed, let us consider an eddy of size ℓ, and let $\vec{X}(t)$ be a lagrangian tracer convected by this particular eddy. Then the position of an another lagrangian tracer $\vec{Y}(t)$, distant from $\vec{X}$ of $\vec{R}$, and "close" to $\vec{X}$ ($R \ll \ell$), may be considered as the position that $\vec{X}$ would occupy in a turbulent field perturbed in the small scales. R(t) becomes then a kind of measure of the error between the original flow and the disturbed flow. Since the "error" R(t) grows at the same rate as $\ell(t)$, an eddy of size ℓ will never be destabilized by small scale errors. This is of course strictly valid only in an infinite flow, where the large scales may grow indefinitely. In a real flow limited by boundaries, the error would finally reach the larger eddies, which are limited by the size of the installation.

The same kind of analysis may be attempted for the problem of pair dispersion in two-dimensional freely evolving turbulence. In that case the root mean square distance R between the particles of the pair is a more convincing measure of the error field, since each fluid particle of the flow conserves its own vorticity. We assume a self-similar evolving spectrum $E(k,t) = v_o^3 t\, F(k v_o t)$ (3-2)

where F is a nondimensional function, as predicted by BATCHELOR (6). Then it may be shown, within the same framework as in the three dimensional case, that the probability distribution P(r,t) for the two particles of the pair be distant of $\vec{r}$ satisfies the equation

$$\frac{\partial}{\partial t} P(r,t) = \frac{1}{r} \frac{\partial}{\partial r} \left[r\, K_{//}(r) \frac{\partial P}{\partial r} \right] \qquad (3\text{-}2)$$

with $r = |\vec{r}|$ and

$$K_{//}(r,t) = 2 \int_0^\infty \theta_q(t)\, E_q(t) \left[1 - 2 \frac{J_1(qr)}{qr} \right] \qquad (3\text{-}3)$$

In (3-3), θ_q is the relaxation time for the triple correlations of the velocity field at wavenumbers of order q . Eq. (3-2) had first been given by KRAICHNAN (15), using the Atridged Lagrangian History Direct Interaction approximation. The form (3-3) for $K_{//}(r,t)$ corresponds to the Eddy-Damped-Quasi-Normal Markovian approximation (see LARCHEVEQUE and LESIEUR (14)). From (3-2) the value of the dispersion coefficient is :

$$\sigma = \frac{1}{2} \frac{d}{dt} \iint P(r,t)\, r^2 d^2 r = \iint P(r,t) \frac{1}{r} \frac{\partial}{\partial r} (r^2 K_{//}) d^2 r \qquad (3\text{-}4)$$

The dominant contribution to σ given by (3-4) will come from $r \sim R$. In (3-3), q will be of order k_I, which implies :

$qr \sim qR \sim k_I R \ll 1$. Then $1 - \frac{2J_1(qr)}{qr}$ is equivalent to $q^2 r^2 / 8$, and the diffusion coefficient $K_{//}(r,t)$ is, for $r \sim R$, given by

$$K_{//}(r,t) = \frac{r^2}{4} \int_0^\infty \theta_q(t)\, q^2 E(q,t)\, dq$$

Let $\beta = - \frac{d}{dt} D(t)$ be the enstrophy dissipation rate. Assuming $\theta_q(t) \simeq \beta^{-1/3}$, we then have $K_{//} = \beta^{-1/3} D\, r^2/4$.

Finally the dispersion coefficient σ writes :

$$\sigma = \beta^{-1/3} D(t) \iint r^2 P(r,t) d^2 r = \beta^{-1/3} D\, R^2.$$

It will be seen in section 5 that D(t) varies like

$$D(t) = A\, t^{-2} \qquad (3\text{-}5)$$

where the nondimensional coefficient A is proportional to the square of the logarithm of the Reynolds number (based on initial large energy containing eddies . From (3-5) and (3-4) we have :

$$\sigma = \ell^{-1/3} A^{2/3} t^{-1} R^2 \quad , \text{ which shows}$$

that R increases like :

$$R \sim t^{(A^2/3)^{1/3}} . \qquad (3\text{-}6)$$

It is easily seen that R will catch the large scales $k_I^{-1}(t)$ (which grow proportionally to t) as soon as $A > \sqrt{3}$. This is obtained as far as the value of the Reynolds number exceeds a few hundreds. This calculation seems to indicate that unpredictability still holds for freely-evolving two-dimensional turbulence. Nevertheless we shall show in section 5 that, as far as we are interested in the contamination of large two-dimensional scales by three-dimensional disturbances, these large structures will never be completely destabilized and then they may be considered as predictable (or "coherent").

The utilization of these pair- dispersion results for the predictability problem may of course be questionable. Nevertheless, in the three-dimensional case, there are strong analogies to the case of a stationary turbulence fed by a continuous injection of

energy at a wavenumber k_I : here, where unpredictability has been demonstrated, it is clear that the two tracers become uncorrelated as soon as the separation R is larger than k_I^{-1}, the dispersion law being then $R \sim t^{1/2}$. On the other hand, we have shown above that the two particles of the pair never become decorrelated in a freely evolving turbulence. It seems then quite natural to infer that predictability of large scales should hold in that case. HERRING et al. (15) studied the predictability of a three-dimensional decaying flow using the DIA approximation and direct numerical simulations. Their results seem to disagree with our predictions, since they show an increase with time of the total error energy ratio :

$$k(t) = \frac{\int_0^\infty \Delta(k,t)\, dk}{\int_0^\infty E(k,t)\, dk} \qquad (3\text{-}8)$$

where $\Delta(k,t)$ and $E(k,t)$ are respectively the error and energy spectra. Our conjectures on self-similar evolution of Δ and E would yield a constant value for $r(t)$. The relatively low value of Reynolds number obtained by HERRING et al. makes it difficult to extrapolate their results to high Reynolds number flows.

4. DIRECT NUMERICAL SIMULATIONS

We have made an attempt of studying the predictability of three-dimensional decaying turbulence at high Reynolds number by means of direct numerical simulations. The $(32)^3$ code of SIGGIA and PATTERSON (17) has been used, with an appropriate parameterization of subgridscale based on an eddy-viscosity model taken from LILLY (18) and KRAICHNAN (19). Such a parameterization, which is discussed in CHOLLET and LESIEUR (20), allows one to recover a $k^{-5/3}$ spectrum up to the cutoff wavenumber, with only one adjustable constant arising from the eddy-damped quasi-normal markovian approximation (determined from the value of the Kolmogorov constant). The following figure shows the cross spectrum between two flows corresponding to two calculations made with different resolutions (32^3 and 30^3). It is clearly seen that the error created by the change of resolution does not contaminate significantly the large scales, at least during the 12 large eddy turnover times while the calculation is performed. This result is not really a direct numerical simulation of a high Reynolds number flow because a parameterized subgridscale energy transfer is added to the usual terms of the Navier-Stokes equation. Nevertheless the result favours our conjectures concerning the predictability of large scales of decaying turbulence.

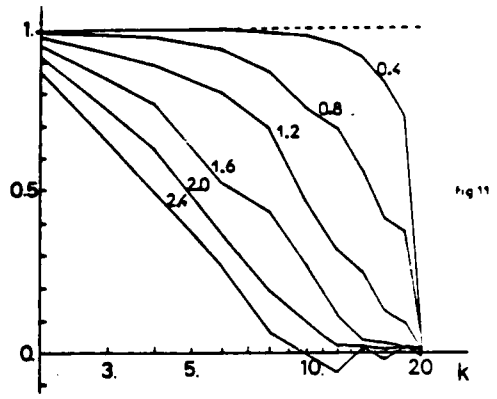

fig 11

Normalized cross-spectrum between two velocity fields: $U^{(1)}$ computed with $2 \leq k \leq 32$ and $U^{(2)}$ computed with $2 \leq k \leq 20$. Initial Reynolds number $R_\lambda = 5.10^3$. Results at t = 0., 0.4, 0.8, 1., 2., 1.6, 2.0, 2.4 seconds ; the large eddy turn over time is about 1.2 second.

5. STATISTICAL THEORIES APPLIED TO MIXING LAYERS

We shall try in that section to interpret the dynamics of mixing layers with the aid of statistical theories of two-and three-dimensional turbulence. Following on approach developed by TAM and CHEN (21), we shall consider the flow initially created in the layer as a particular realization of a freely-evolving two-dimensional turbulence. The numerous experiments performed these past years (see e.g. BROWAND and TROUTT (7) for review) have shown three peculiarities of these mixing layers

i) a pairing mechanism, leading to a growing of the large scales proportionally to t.

ii) the apparition at a finite time of small scale three-dimensional turbulence.

iii) the persistence far downstream of the two-dimensionality of the large scales.

* * *

In this section, these three points will be studied using the statistical theories of two-and three-dimensional turbulence. We have already mentioned that BATCHELOR's (6) theory of two-dimensional evolving turbulence predicts a growing of the integral scale proportionally to t. TATSUMI and YANASE (12) have proposed, on the basis of the Quasi-Normal Markovian Theory, the concept of a critical time t_c before which the enstrophy is (for vanishing viscosity) conserved, and after which the enstrophy is dissipated proportionally to t^{-2}. As shown by BASDEVANT (13), this time t_c corresponds to the build up of the enstrophy cascade : the initial excitation created at a wavenumber $k_I(0)$ will reach, through nonlinear interactions, smaller and smaller scales, up to the two-dimensional dissipation wavenumber

$$k_D \sim \left(\beta/\nu^3\right)^{1/6} . \qquad (5\text{-}1)$$

The time t_c may be evaluated as a result of a summation of the local eddy turnover times $\tau(k_M)$, k_M being the maximum wavenumber of the spectrum above which the excitation is negligible :

$$t_c = \int_{k_I(0)}^{k_D(t_c)} \tau(k_M)\, dk_M/k_M . \qquad (5\text{-}2)$$

$\tau(k_M)$, as given in section 4, is proportional to $D(0)^{-1/2}$ in this preliminary evolution stage. (5-2) yields :

$$t_c \sim D(0)^{-1/2} \log \frac{k_D(t_c)}{k_I(0)} . \qquad (5\text{-}3)$$

Now this initial stage will end when the dissipation will be efficient at k_M. Another estimation of t_c is then given equaling $\tau(k_M)$ and the viscous time $1/\nu k_M^2$. This gives :

$$D(0)^{-1/2} = \left[\nu\, k_D^2(t_c)\right]^{-1} . \qquad (5\text{-}4)$$

Since the initial excitation is concentrated in a narrow spectral band around $k_I(0)$, the initial enstrophy $D(0)$ is of order $k_I(0)^2 E(0)$, where $E(0)$ is the initial kinetic energy. We then obtain

$$t_c \sim D(0)^{-1/2} \log \left[R_e(0)^{1/2} \right]$$

where $R_e(0) = \frac{E(0)^{1/2}}{\nu k_I(0)}$ is the turbulent Reynolds number built on initial large scales. Then t_c increases proportionally to $\log R_e(0)$:

$$t_c \sim D(0)^{-1/2} \text{ Log } Re(0) \quad . \quad (5\text{-}5)$$

This result has been checked by BASDEVANT (13) using the Eddy-Damped Quasi-Normal Markovian Approximation at high Reynolds number. This allows to evaluate the constant A introduced in (3-6) and (3-7). Since $D(t_c) = D(0)$, A is equal to $t_c^2 D(0)$ and proportional to $[\text{Log } Re(0)]^2$. Returning to the mixing layer, this result may be interpreted as follows : the large two-dimensional structures of scale $k_I^{-1}(0)$ created at $t = 0$ degenerate, through nonlinear interactions, into smaller two-dimensional structures, up to the "Kolmogorov" two-dimensional wavenumber k_ν, above which no two-dimensional excitation is any longer possible. At the same time, and as a result of some kind of pairing mechanism, the large structures amalgamate and grow proportionally to t. This first stage ($0 < t < t_c$) is purely two-dimensional. It creates eddies whose minimal length scale is of order $k_\nu(t_c)^{-1}$ is nothing else than the three-dimensional Taylor microscale corresponding to a three-dimensional isotropic turbulence whose large energetic eddies should be of order $k_I(0)^{-1}$. This statistical analysis has to be related to deterministic instability mechanisms proposed by SAFFMAN (22) and CORCOS (23). $k_\nu(t_c)^{-1}$ is the size of the "braids "in the "cat's eye" of the Kelvin-Helmoltz wave.

The next stages in the evolution of the flow may be described as follows : we assume that, due to tiny three-dimensional disturbances, three-dimensionality will contaminate scales from $k_\nu(t_c)^{-1}$ to the three-dimensional Kolmogorov scale. The precise dynamical reason for that is not very clear, but it seems reasonable to think that these three-dimensional disturbances will reinforce three-dimensionally nonlinear interactions for $k > k_\nu(t_c)$, and the flow will naturally become three-dimensional in these scales. The further evolution with time is the following : the two-dimensional "error" in small scales will contaminate larger and larger scales, so as to reach the large scales $k_I^{-1}(t)$. The time necessary for this inverse cascade of three-dimensionality may be evaluated, and we have checked that, for high Reynolds number, it is negligible in front of the critical time t_c corresponding to the initial stage of the evolution. This explains why in the experiments three-dimensionality appears so abruptly in all the scales.

Numerical calculations made by BASDEVANT (13) using the Eddy-Damped Quasi-Normal Markovian approximation, show that the dependence of t_c with respect to Log R(0) is given by :

$$t_c \, D(0)^{1/2} = 2.72 \text{ Log } R_e(0) - 9.12 \quad . \quad (5\text{-}6)$$

This allows to make a comparison with experimental data : JIMENEZ et al. (24) have evaluated the time where three-dimensionality appears, for different Reynolds numbers. With a proper choice of the origin of times and of the initial integral scale and kinetic energy, the critical times t_c obtained in the experiments can be compared to the times predicted by (5-6). These times, in units of large initial eddy turnover times $D(0)^{-1/2}$, are displayed on the following tatle

Re(c)	170	460	562	930
t_c : theory	4.86	7.55	8.10	9.48
t_c : experiments	6.4	7.5	8	12.5

Though the precise dependence (5-6) of t_c on Reynolds number is not shown by the experiments, the agreement with theoretical predictions is nevertheless extremely satisfying.

We finally come to the reasons why the large two-dimensional "coherent" structures of scale $k_\nu(t)^{-1}$ do not disappear once they are overtaken by the inverse cascade of three-dimensionality : the explanation lies in the fact that, as mentioned in section 2, the integral scale of a three-dimensional isotropic turbulence increases much more slowly ($\sim t^{1/2}$) than the large two-dimensional structures which grow like t. So, notwithstanding the fact that the nonlinear inverse cascade of three-dimensionality continuously feeds structures $\sim k_\nu^{-1}$, the three-dimensional structures created at k_ν^{-1} will grow slower than the remaining two-dimensional structures which in turn will overtake the latter. This continuous mutual exchange of energy between two-and three-dimensional structures could at term lead to a kind of state of equipartition of energy among these structures.

VI. CONCLUSIONS

This paper has presented arguments to indicate that the large scales of a homogeneous three-dimensional freely decaying flow can be predictable in the sense that they are free of complete error contamination. This is possible because the large scales grow precisely at the same rate as the propagation decorrelation front. The reasons given to support this assessement are not completely conclusive, since i) the phenomenological analysis of the predictability problem, valid in the case of stationary turbulence, may not hold in the unforced case ; ii) the analogy between the problems of predictability and pair-dispersion may be questionable ; iii) the results from direct numerical simulations must be viewed cautiously due to the small number of computed wavenumbers in the large scales. If valid, this conjecture could have important implications for the numerical modeling of certain classes of turbulent flows not subject to destabilizing external forcing nor to the influence of boundaries. We might then expect to make deterministic predictions for periods much longer than the predictability times generally proposed.

In two-dimensions, it seems that errors in small scales will rapidly contaminate the large structures. In that sense a freely-evolving flow is still unpredictable. Nevertheless, when applied to mixing layers, this results allows to envisage the persistance of the large quasi-two-dimensional coherent structures, whose proper growth proceeds faster than the increase of the three-dimensional structures created at the same length scale.

The authors are indebted to F. BROWAND and G. CORCOS for stimulating discussions, and to E. SIGGIA for having provided us the Navier-Stokes direct numerical simulation code. Computations were carried out at the National Center for Atmospheric Research, sponsored by the National Science Foundation.

REFERENCES

1 Lorenz, E.N., Tellus, vol. 21, 1969, pp. 289-307.

2 Kraichnan, R.H., Phys. Fluids, vol. 13, 1970, pp. 564-575.

3 Leith, C.E., J. Atm. Sci., vol. 28, 1971, pp. 145-161.

4 Leith, C.E. and Kraichnan, R.H., J. Atm. Sci., vol. 29, 1972, pp. 1041-1058.

5 Alemany, A., Moreau, R., Sulem, P.L., Frisch U., J. de Mécanique, vol. 18, 1979, p. 277.

6 Batchelor, G.K., Phys. Fluids, Suppl., vol. 12, part. II, 1969, pp. 233-239.

7 Browand F. and Trowtt, T., J. Fluid Mech., vol. 4 1979, p. 771.

8 Larchevêque, M., Chollet J.P., Herring, J.R., Lesieur, M., Newman, G.R. and Schertzer, D., Turbulent Shear Flow 2, 1980, Springer-Verlag, pp. 53-66.

9 Lesieur, M. and Schertzer, D., J. de Mécanique vol. 17, 1978, pp. 609-646.

10 Tatsumi, T., Kida, S. and Mizushima, J., J. Fluid Mech., vol. 85, 1978, pp. 97-142.

11 Comte-Bellot, G., and Corrsin, S., J. Fluid Mech. vol. 24, 1966, p. 657.

12 Tatsumi, T. and Yanase, S., "The modified cumulant expansion for two-dimensional isotropic turbulence", J. Fluid Mech., 1981, to appear.

13 Basdevant, C. : "Contribution à l'étude numérique et théorique de la turbulence tridimensionnelle", Thèse de Doctorat d'Etat, 1981, Université de Paris VI.

14 Larchevêque, M. and Lesieur, M., J. de Mécanique, vol. 20, 1981, pp. 113-134.

15 Kraichnan, R.H., Phys. Fluids, vol. 9, 1966, pp. 1937-1943.

16 Herring, J.R., Riley, J.J., Patterson, G.S. and Kraichnan, R.H., J. Atm. Sci., vol. 30, 1973, pp. 997-1006.

17 Siggia, E. and Patterson, G.S., J. Fluid Mech., vol. 86, 1978, pp. 567-592.

18 Lilly, D.K. : "On the application of the eddy-viscosity concept in the inertial subrange of turbulence", NCAR Manuscript n° 123, 1966.

19 Kraichnan, R.H., J. Atm. Sci., vol. 33, 1976, pp. 1521-1536.

20 Chollet, J.P. and Lesieur, M. : "Parameterization of small scales of three-dimensional isotropic turbulence utilizing spectral closures", preprint, 1981.

21 Tam, K.W. and Chen, K.C., J. Fluid Mech., vol. 92, 1979, pp. 303-326.

22 Saffman, P.G., in "Topics on nonlinear Physics" 1968, N. Zabusky Ed., Springer-Verlag.

23 Corcos, G. : "La couche de mélange : modèles déterministes d'écoulements turbulents". Thèse de Doctorat d'Etat, 1980, Université de Grenoble.

24 Jimenez, J., Martinez-Val, R. and Rebollo, M., "On the origin and evolution of three-dimensional effects in the mixing layer", 1979, Report of European Research Office, number DA-ERO 78-G-079.

SESSION 18 - RECIRCULATING FLOWS II

A. K. Runchal - Chairman

TURBULENT, BACKWARD-FACING STEP FLOWS IN TWO-DIMENSIONAL DUCTS AND CHANNELS

by

F. Durst and C. Tropea

Institute for Hydromechanics
Section III "Mechanics of turbulent flows"
University of Karlsruhe, FRG

ABSTRACT

This paper summarizes the authors' research work on backward-facing step flows in two-dimensional ducts and channels. A review of results which are available from other research workers is presented in tabular form with notes on the experimental techniques which have been used, the selection and extent of measured quantities and some brief notes on the results. A more detailed discussion presents available data on the length of the reattachment region located behind the step and this is shown to be strongly Reynolds number and geometry dependent.

The authors own studies were carried out in water flows through nominally two-dimensional ducts with backward-facing steps and in open channel flows. A laser-Doppler anemometer operating with forward scattered light and employing a transient recorder and digital computer for signal processing was employed and is described in the paper. Measurements of separation length were obtained for a wide Reynolds number range and for various values of expansion ratio.

NOMENCLATURE

ER = h_2/h_1, expansion ratio

h_1 upstream water height

h_2 downstream water height

H step height, $H = (h_2-h_1)$

Re = $\frac{U_b h_1}{\nu}$ channel Reynolds number

Re_H = $\frac{U_b H}{\nu}$ step-height Reynolds number

U_o centre-line velocity in duct
free-stream velocity in channel

U_b $\frac{1}{h_1}\int_0^{h_1} u\,(y)dy$ bulk velocity

$\overline{U}$ mean velocity in longitudinal direction

$\sqrt{u^2}$ root-mean-square velocity in longitudinal direction

$\overline{V}$ mean velocity in normal direction

$\sqrt{v^2}$ root-mean-square velocity in normal direction

x longitudinal coordinate

x_R mean reattachment position

y normal coordinate

z spanwise coordinate

$\hat{z}$ spanwise coordinate normalized to channel half-width

ν kinematic viscosity

ψ streamline function

I. INTRODUCTION AND SURVEY OF EXISTING RESULTS

The importance of separated flows in the engineering sciences is beyond question and has resulted in a large number of investigations with the aim to provide an insight into the mechanisms of flow separation and reattachment and to yield information on mean flow properties and turbulence characteristics of such flows. Flows over backward-facing steps mounted in two-dimensional ducts and open channels, have been extensively investigated due to the simplicity of test section geometry. Specifically the backward-facing step provides a fixed point of flow separation and hence, a spatially fixed region of separated flow. This simplifies greatly the experimental investigations allowing spatially fixed measuring sensors to be employed. Table 1 provides a summary of those studies known to the authors on backward- facing step flows together with information on the form of their channel geometry before the step, the measuring techniques employed, and the results obtained. A detailed discussion of these studies is provided in refs. (9) and (22). Only a summary of these results that are of significance of to the authors own results is presented below.

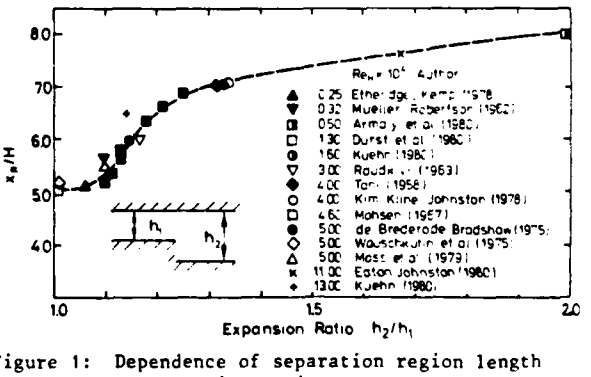

Figure 1: Dependence of separation region length on expansion ratio

One of the integral parameters of the flow that has been measured by most of the authors is the distance of the mean reattachment point of the shear layer behind the step. Fig. 1 shows various measurements available in literature indicating a strong

AUTHOR & REFERENCE	FLOW GEOMETRY	DIMENSIONS (cm)	H (mm)	ER h/h	AR B/H	U_∞	%Tu	Re_H ($\times 10^4$)	δ/H	MEASURING TECHNIQUE	MEASURED QUANTITIES	x_R/H	REMARKS
Tani 1958 Grenzschichtforschung Ed. H. Görtler		l=80 B=100 h_1=55	5 10 (20) 40 60	1.01 1.02 1.04 1.07 1.11	200 100 (50) 25 16	10 m/s 16 22 (28)		0.3 ↓ (4.0) ↓ 11.0	.18 - 6 (.55) (.15)	Pitot Tube Pressure Taps Hot-Wire Probe Flow Visualization	$\bar{U}_1$ P_w (x) $\overline{u_1^2}$(x,y) $\overline{u_1 u_2}$(x,y)	7	B is reference Position for static pressure (3cm upstream of step) At U_∞ 10 m/s B.l. was laminar Trip was used to increase δ sometimes 10 cm from leading edge!
Abbott and Kline 1962 J. of Basic Eng., Sept. Trans. of ASME	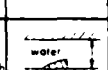	l=2 B=30 h=8.5	10 ↓ 240	1.1 ↓ 4.0	0.8 ↓ 50	20cm/s	1 ↓ 18 (also scale)	0.3 ↓ 10.0	.04 ↓ .75	Inclined Hot Film Probe Flow Visualization (needle trace)	$\bar{U}_1(y)$, $\overline{u_1^2}(y)$ x_R (in three distinct zones of separation)	6 7	B is a trip 45 cm from step No dependence of x_R on Re_τ Inlet Condition was B.L. flow and not f. dev. channel flow.
Mueller and Robertson 1962 Dev. in Th.& App.Mech.	 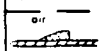	B=5 h_2=14 B=10 h_2=∞	5 6 13 19	1.04 1	10 17 7.7 5.3	61 cm/s 30 m/s	0.3	0.33 1.2 2.4 3.6	.4 1 2 3	Hyperdermic Pitot Tube Dye Pitot Probe Inclined Hot-Wire Probe Hyperdermic Pitot Probe	$U_1(x,y)$ x_R $\bar{U}_1(x,y)$ $\overline{u_1^2}(x,y)$, $\overline{u_2^2}(x,y)$ $\overline{u_1 u_2}(x,y)$ τ_w, Cp	5.62 6.87 6.8 7.0	Test section lined with side panels & placed in open jet
Moheen, Bowie, Lange, Holmann 1967 Boeing Co. Report D6-17094	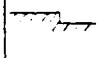	l=60 B=18 h=∞	13 25 38	1.0	14 7.2 4.7	51 m/s 112		4.4 ↓ 28.0	3.8 2 1.3	Pressure Taps (Water Manometer) Pitot Tubes Hot-Wire Probe Flow Visualization Film Wind Vane Microphones	P_w (x) Total & Static Pressure $\bar{U}_1(x,y)$, $\overline{u_1^2}(x,y)$ x_R Zero Velocity line P_w (x)	4.5	Test section has sidewalls Mean and fluctuating wall pressure was found to be independent of Re and step height
Isaacson and Wong 1972 IFM 1972 Vol 52-1	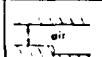	B=75 h_1=10	25	1.25	30	25 m/s	0.07	4.1	.13	Pitot Tube Preston Tube Hot-Wire Probe	$\bar{U}_1$ (y) C_f $\overline{u_1^2}$ (y), $\overline{u_1 u_2}$ (y)		Relaxation of reattached B.L.f is not achieved by x/h = 30 B.L. is laminar at separation
ge Bredcrade and Bradshaw 1972 A.C. Aero. Report 72-19	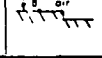	l=15 B=76 h_1=12.7	25	1.2	3 ↓ 30	30 m/s	0.07	5.0	.15	Flow Visualization - Oil Film Pressure Taps Inclined Manometer Diff. Thermocouple	x_R, 3-D Behaviour Base Pressure	6	Investigated influence of AR on flow pattern Flow tested with sidewall suction and blowing Separation at B = 25 cm
Wuschkuhn and Vasanta Ram 1975 Z. f. Flugwissenschft. H. 1	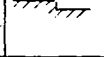	l=45 B=40 h_1=∞	10 20 40	1.0	40 20 10	40 m/s (36)		2.6 4.7 9.7	.11 .14 .03	Pressure Taps B.L.Fence Pitot Tube Inclined and Normal Hot-Wire Probe	P_w (x) τ_w (x) $\overline{u_1^2}$(x,y) $\bar{U}_1(x,y)$, $\overline{u_1^2}(x,y)$ $\overline{u_1 u_2}(x,y)$	5.2	Max. of Cp does not correspond to τ_w = 0 Hot-Wire used without linearizer
Chandrsuda 1975 Phd. Thesis Imperial College	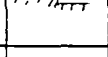	l=84 B=76 h_1=7.6	50	1.65	15.2	31.5m/s	0.07	10	.04	Stanton Tube Hot-Wire Probe X Hot-Wire Probe Pitot Tube Pressure Taps	C_f $\bar{U}_1$ (y), $\overline{u_1^2}$ (y) $\overline{u_1^2}$ (y), $\overline{u_1 u_2}$(y) P (y) Cp	5.85	Upper wall inclined for infinite stream behaviour
[illegible] Kline, Johnston 1968 Stanford Report MD-37	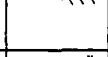	l=30 B=61 h_1=7.6	38 25	1.5 1.3	16 24	18.1m/s		4.6 3.0	.45 .30	Static Pressure Probe Total Pressure Probe X-Array Hot-Wire Probe Flow Visualization Tufts	Cp $p'(y)$ $\bar{U}_1(y)$, $\overline{u_1^2}(y)$, $\overline{u_1^2}(y)$ $\overline{u_1 u_2}(y)$ approx. x_R	7	Used forward pressure tube to measure reverse flow B.L. was tripped upstream of step.
Etheridge and Kemp 1978 JFM Vol 86, pt.3	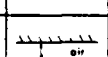	l=75 B=15 h_1=20	13.5	1.07	11	20 cm/s		0.25	2	LDA with Rotating Grating	$\bar{U}_1(y)$, $\overline{u_1^2}(y)$, $\overline{u_2^2}(y)$, $\overline{u_1 u_2}(y)$	5.1	Extensive velocity measurements within recirculation zone
Chun 1979 Internal Report	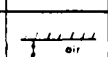	B=140 h_1=66	90	1.14	15	9.7m/s 8.4	0.24 3.5 0.24 3.5	5.9	.09 0.5 .13 .7	Hot-wire probe X-array probe Pulsed wire Pressure taps Twin tube probe	$\bar{U}_1(y)$ no recirc. $U_1(y)$, $U_2(y)$, $u_1 u_2(y)$ $\overline{u_1^2}(y)$, $\overline{u_1 u_2}(y)$, $\overline{u_2^2}(y)$ $P_w(x)$ x_R	5	Grid was used to vary free stream turbulence Boundary layer thickness controlled with sandpaper and suction
Eaton and Johnston 1980 Stanford Report MD-39	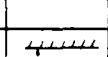	B=61 h_1= 7.6	51	1.67	12	3.2 m/s 6.0 12.2 18.3	0.3	1.1 2.0 4.1 6.2	.22	Thermal tuft Pulsed hot-wire Normal and X-array hot-wire probes	x_R $\bar{U}_1(y)$, $\overline{u_1^2}(y)$ $\overline{u_1 u_2}(y)$	8 (high Re)	Spanwise measurements were taken. Lowest Re had lam. B.L. at separation Emphasis on high measurement accuracy
[illegible], Durst, Schönung 1980 SFB 80, T1, 172 Sonderforschungsbereich 80, Univ., Karlsruhe	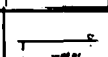	l=23 B 18 h_1= 0.52	4.9	1.94	35	0.15m/s		.004	N/A	LDA with Bragg cells	$\bar{U}_1(y)$, $\overline{u_1^2}(y)$, x_R	8 (high Re)	Inlet profile was fully dev. channel flow. Second separation bubble was detected.
Durst, Papp, Trapea 1980: Sonderforschungsbereich 80, Univ., Karlsruhe	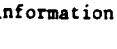	l=350 B=60 h_1= 16-60	40	1.06 ↓ 1.25	15	4 cm/s ↓ (33) 80	3	0.2 ↓ (1.3) 3.0	1	LDA with Bragg cells Flow Visualization	$\bar{U}_1(y)$, $\overline{u_1^2}(y)$, $\overline{u_2^2}(y)$, $\overline{u_1 u_2}(y)$, x_R	5.2 ↓ 8	Influence of Expansion ratio investigated Re in transitional range

Table 1: Tabulated information on studies of backward-facing step flow

dependence of the length of separation region on the expansion ratio (h_2/h_1). The available data also indicates a dependence of the reattachment length on flow Reynolds numbers but insufficient information exists upon which a Reynolds number dependence for various expansion ratio can be derived. It is one of the aims of this paper to extend the existing information in this direction using laser-Doppler anemometers to measure the location of the reattachment point. This is further explained in section 2 and detailed results are provided in section 3 (together with information on local flow properties of the mean velocity field and the turbulence properties).

II EXPERIMENTAL TEST RIG AND EQUIPMENT

The authors' experiments were carried out in a 600mm wide open-water channel with major dimensions given in Fig. 2. The test section was situated near the downstream end of the channel and consisted of a second floor with a leading edge for initiating a new floor boundary layer. For the open channel measurements, a raised backward facing step of 40mm in height was placed at a downstream position from the leading edge such that the boundary layer at separation would be fully developed for all Reynolds numbers investigated. For the two-dimensional flows, 20mm and 40mm step heights were employed with the oncoming flow being that of a laminar, transitional or turbulent channel flow. The expansion ratio of this duct could be changed by mounting the upper channel wall at different heights. Similarly, a downstream weir permitted the water level in the open channel flow to be changed.

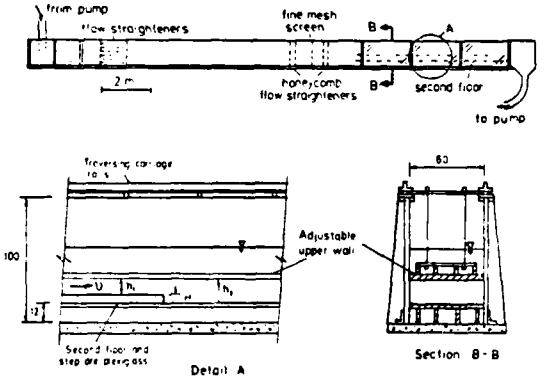

Figure 2: Water channel and details of the test section (dimensions are in cm)

Considerable effort was expended in placing flow straighteners and screens upstream from the test section so that a nominally two-dimensional flow was ensured, at least in the mean properties. The success of these flow straightening devices is shown in Fig. 3, which presents spanwise profiles of the mean longitudinal velocity components at various test section locations and also the root-mean-square of the longitudinal velocity fluctuations at the same locations. The data show that the mean longitudinal velocity before the step edge has spanwise uniformity over at least the centre of the channel. In this region, it also obeyed the law of the wall for the turbulent flow cases and the parabolic velocity profile for the laminar flow, (see Fig. 4).

Flow velocity was measured with a one component forward-scatter laser-Doppler anemometer (LDA)

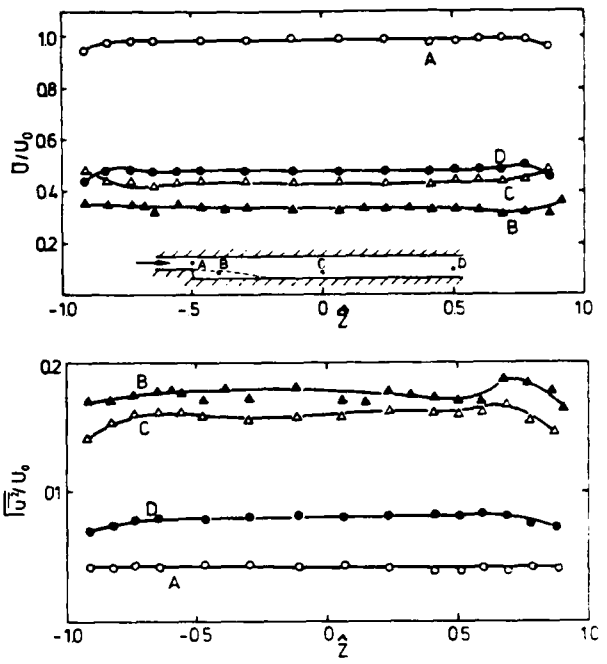

Figure 3: Spanwise profiles of mean and fluctuating longitudinal velocity for a duct configuration with an expansion ratio of 2

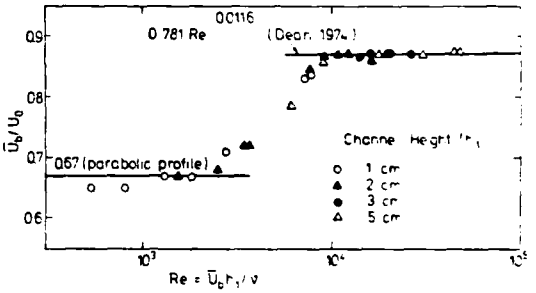

Figure 4: The ratio U_b/U_o for mean velocity prfiles taken 10H upstream of step for various duct geometries

equipped with frequency shifting. Several features of the LDA system make it one of the few devices suitable for velocity measurement in recirculating flow: 1) nonintrusiveness, 2) instantaneous velocity direction resolution, 3) single velocity component measurement without contamination from other components, 4) high spatial and temporal resolution, 5) accurate measurement in regions with very high turbulent levels, and 6) no calibration necessary. The LDA was mounted, in the present experiment, on a cradle-type traversing carriage which straddled the water channel on rails and thus permitted three-dimensional movement of the measuring volume to almost any desired position within the flow. The measuring volume is approximately 0.25 mm in diameter and 1.5mm long. Further details are given in ref. (9).

Signals were processed with a digital processor based on a transient recorder system that was developed at the University of Karlsruhe and is described in detail in ref. (10). This processing system can accurately determine the frequencies of

individual Doppler bursts. Sampling procedures, as outlined by Tropea and Durst (11) ensured nonbiased estimates of the velocity. Measurement times at each point varied from one region of the flow to another, but were generally 15-20 minutes inside the recirculating zone and about 5 minutes in the potential flow region.

III EXPERIMENTAL RESULTS

In order to obtain accurate information on the location of the mean reattachment point, the laser-Doppler anemometer was employed in order to measure the location of the zero velocity line indicated in Fig. 5a. The measuring point was located at a fixed distance y from the wall and measurements were made at various x-locations to obtain the time-averaged velocity for each point. This velocity was plotted as a function of x and for every y-distance from the wall, see Fig. 5b. From this figure the x-locations for zero velocity line were obtained by interpolation and plotted as indicated in Fig. 5c. An extrapolation

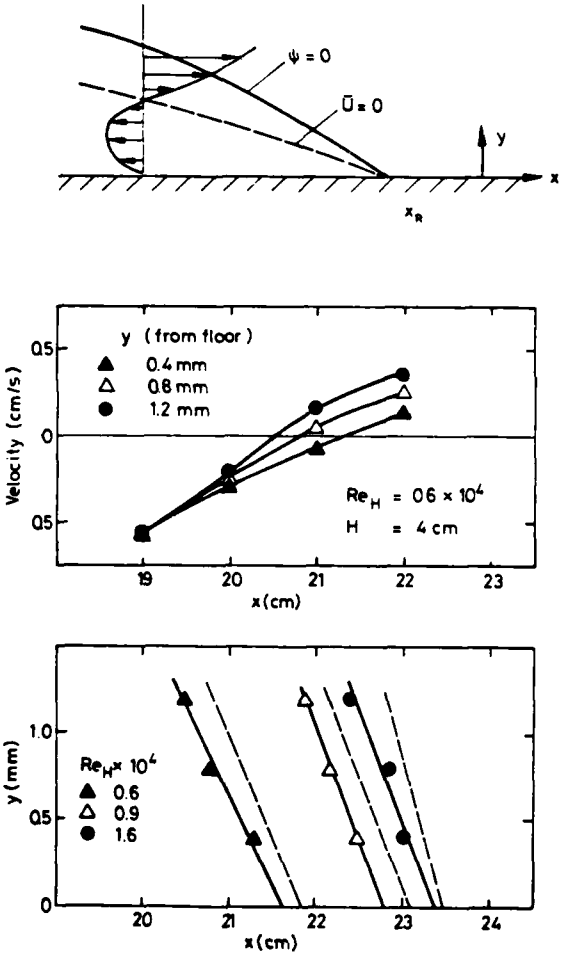

Figure 5: a) Dividing streamline and zero velocity line near reattachment
b) Measurements of zero mean velocity at various heights above floor
c) Zero velocity line at reattachment; --- line representing position at which velocity is 50% positive and negative

of these points permitted the reattachment point to be obtained at the wall. Fig. 5c shows several of these plots for various Reynolds numbers. It also indicates the location of those points at which the number of particles with a positive velocity was equal to the number with negative velocity. This information has been used in (12) in order to measure the location of the mean reattachment point.

Employing the above procedure, reattachment length measurements were performed for various Reynolds numbers, Re_H, and for various expansion ratios, h_2/h_1. A summary of the data is provided in Fig. 6 and indicates that there is strong dependence of the length of the reattchment region after the step on Reynolds number and expansion ratio. Interesting to note is that the step-height Reynolds number is reasonably successful in aligning the results from various expansion ratios. This is not true at the Reynolds number based on the upstream momentum thickness. Plotted with the latter Reynolds number, the curves were shifted to lower values of Reynolds number for increasing expansion ratios. The information obtained

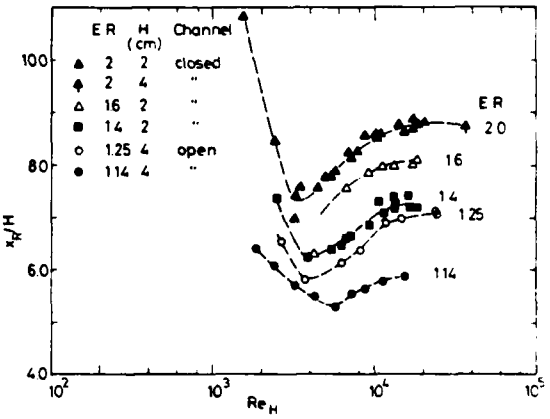

Figure 6: Mean reattachment position as a function of Reynolds number for several expansion ratios.

here is in general agreement with the findings by Armaly et al. (2) who found a strong Reynolds number dependence for Reynolds numbers up to 6000. In the present study measurements concentrated on higher Reynolds numbers. For a Reynolds number of $1.5 \cdot 10^4$ the dependence on expansion ratio is shown in Fig. 7.

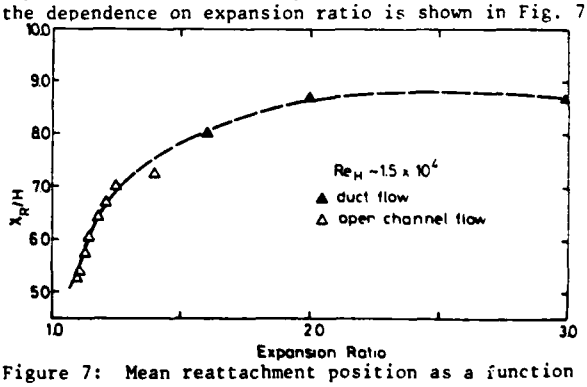

Figure 7: Mean reattachment position as a function of expansion ratio

From this figure it is evident that the expansion ratio transition from an open channel to a duct flow has a small but distinct influence on the mean reattchment length. This is not surprising since in the open channel flow the static pressure can be altered by the free

surface behavior over the step. In performing only low expansion ratio tests in the oepn channel (ER < 1.25) the estimated distortion of the free surface was less than 4%.

In Fig. 8 the authors' results are compared for an expansion ratio of 2 with similar results available in literature. The data by Eaton and Johnston are lower than those obtained in the present investigation the reason for this is the lower expansion ratio which these authirs had available in their study. Their data are in good agreement with the authors' data for an expansion ratio 1.6.

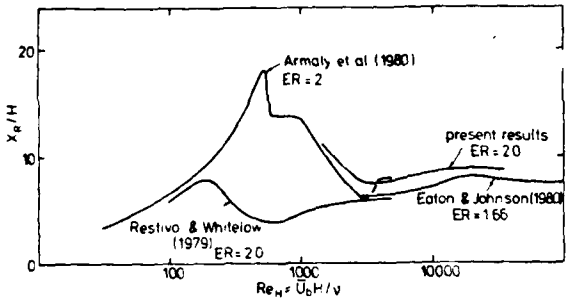

Figure 8: Comparison of present results to those of other authors

Results by Restivo and Whitelaw were obtained in a test section with very small aspect ratio so that three-dimensional effects must have existed also in the center-part where the authors measured. This might be the reason for the difference between the data of ref. (20) and those represented here. In fact other studies carried out with low aspect ratio test sections (4) and (8) seem to confirm that the reattachment length shortens at low aspect ratios. The present data are in very good agreement with those of Armaly et al. (2) obtained in an air flow at least at the higher Reynolds number range. For lower Reynolds numbers the flow is transitional, as Fig. 4 shows and this might explain the differences between the results of ref. (2) and those of the present study in that region.

In addition to measurements of reattachment length the authors have measured in detail mean velocity distributions in backward-facing step flows in open channels and in ducts. Detailed results on the open channel flow are available in ref. (9) and those on ducts are provided in ref. (22). The reader is referred to these publications for further details.

IV CONCLUSIONS AND FINAL REMARKS

Laser-Doppler measurements were carried out to obtain information on the length of reattachment region in backward-facing step flows in ducts and open channels. The measurements showed that the length was strongly dependent on the Reynolds number and expansion ratio. The location of the mean reattachment point was obtained from mean velocity measurements and was found to be different to the point obtained by measuring the 50% time of positive and negative flow direction. However, the differences were found to be small.

ACKNOWLEDGEMENTS

The authors would like to gratefully acknowledge the assistance of Mr. M. Popp who carried out some of the open channel measurements presented here as a part of his Studienarbeit thesis.

REFERENCES

1 Abbott, D.E. and Kline, S.J., "Experimental Investigation of Subsonic Turbulent Flow over Single and Double Backward-Facing Steps", Trans. of ASME, J. of Basic Eng., Sept. 1962, pp. 317-325.

2 Armaly, B.F., Durst, F. and Schönung, B., "Measurements and Predictions of Flow Downstream of a Two-Dimensional Single Backward-Facing Step", SFB 80/ET/172, July 1980, Sonderforschungsbereich 80, Universität Karlsruhe.

3 Bradshaw, P. and Wong, F.Y.F., "The Reattachment and Relaxation of a Turbulent Shear Layer", JFM, Vol. 52, pt. 1, 1972, pp. 113-135.

4 Bremmer, R., Thompson, H.D. and Stevenson, W., "An Experimental and Numerical Comparison of Turbulent Flow over a Step", Techn. Rept. AFWAL-TR-80-2108, Air Force Wright Aeronautical Labs., Dec. 1980.

5 Chandrsuda, C., "A Reattaching Turbulent Shear Layer in Incompressible Flow", Ph.D. Thesis, Dept. of Aeronautics, Imperial College of Science and Technology, London, 1975.

6 Cheun, B.S., "Effect of Upstream Conditions on Turbulent Flow over a Backward-Facing Step", Interim Rept. 1979, private communications.

7 Dean, R.B., "Reynolds Number Dependence of Skin Friction in Two-Dimensional Rectangular Duct Flow and a Discussion of the "Law of the Wall", IC Aero. Rept. 74-11, Dec. 1974.

8 de Brederode, U. and Bradshaw, P., "Three-Dimensional Flow in Nominally Two-Dimensional Separation Bubbles, I. Flow Behind a Rearward Step", I.C. Aero. Rept. 72-19, 1972.

9 Durst, F., Popp, M. and Tropea, C., "Experimentelle Untersuchungen einer turbulenten Strömung mit Ablösung hinter einer Stufe", SFB 80/E/192, May 1981, Sonderforschungsbereich 80, University of Karlsruhe.

10 Durst, F. und Tropea, C., "Processing of Laser-Doppler Signals by Means of a Transient Recorder and a Digital Computer", SFB 80/E/118, Dec. 1977, Sonderforschungsbereich 80, University of Karlsruhe.

11 F. Durst and C. Tropea, "Digital Processing of LDA-Signals by Means of a Transient Recorder and a Computer", Symposium on Long and Short Range Optical Velocity Measurements, German-French Research Institute, ISL, Saint Louis, France. Sept. 1980.

12 Eaton, J.K. and Johnston, J.P., "Turbulent Flow Reattachment: An Experimental Study of the Flow and Structure Behind a Backward-Facing Step", Report MD-39, 1980, Thermoscience Division, Dept. of Mech. Eng., Stanford University.

13 Etheridge, D.W. and Kemp, P.H., "Measurements of Turbulent Flow Downstream of a Rearward-Facing Step", JFM, Vol. 86, pt. 3, 1978, pp. 545-566.

14 Kim, J., Kline, S.J. and Johnston, J.P., "Investigations of Separation and Reattachment of a Turbulent Shear Layer: Flow Over a Backward-Facing Step", Rept. MD-37, 1978, Thermoscience Divsion, Dept. of Mech. Eng., Stanford University.

15 Kuehn, D.M., "Effects of Adverse Pressure Gradient on the Incompressible Reattaching Flow over a Rearward-Facing Step", AIAA Journal, Vol. 18, No. 3, 1980.

16 Mohsen, A.M., "Experimental Investigation of the Wall Pressure Fluctuations in Subsonic Separated Flows", Boeing Co. Rept. No. D6-17094, 1967.

17 Moss, W.D., Baker, S. and Bradbury, L.J.S., "Measurements of Mean Velocity and Reynolds Stresses in Regions of Recirculating Flow", paper presented at Symposium on Turbulent Shear Flows, Penn. State Univ., 1979.

18 Mueller, T.J. and Robertson, J.M., "A Study of Mean Motion and Turbulence Downstream of a Roughness Element", Proc. of the 1st Southeastern Conference on Theoreitcal and Applied Mechanics,Calinberg, Tenn., 1962.

19 Raudkivi, A.J., "Study of Sediment Formation", Proc. of A.S.M.E., J. of the Hydraulics Division,1963.

20 Restivo, A. and Whitelaw, J., "Instability in Sudden-Expansion Flows of Relevance to Room Ventilation", Proc. of Turbulent Shear Flow Conf. II, London, June 1979

21 Tani, I., "Experimental Investigation of Flow over a Step", ed. H. Görtler, Grenzschichtforschung, Springer Verlag, 1958.

22 Tropea, C, "Die turbulente Stufenströmung in Flachkanälen und offenen Gerinnen", Dissertation, Universität Karlsruhe, tentative completion Dec. 1981.

23 Wauschkuhn, H. and Vasanta Ram, "Die turbulente Grenzschicht hinter einem Ablösungsgebiet", Zeitschrift f. Flugwissenschaften, Heft 1, 1975.

PREDICTION OF THE LOW REYNOLDS NUMBER LAMINAR FLOW OVER A NORMAL FLAT PLATE, AND ITS APPLICATION TO TURBULENT FLOW CALCULATIONS

I. P. CASTRO, DEPT. OF MECHANICAL ENGINEERING, UNIVERSITY OF SURREY, ENGLAND.

K. A. CLIFFE, M. J. NORGETT, THEORETICAL PHYSICS DIVISION, A.E.R.E. HARWELL, ENGLAND.

ABSTRACT

The limitations of those numerical methods used increasingly to simulate complex turbulent flows in elliptic regions are best revealed in studies of analogous laminar flows, when results are not obscured by uncertainties in the physical models. We have therefore compared finite-difference and finite-element calculations of steady flow past a flat plate normal to a free stream, with a trailing splitter plate in place to prevent vortex shedding. The chosen Reynolds numbers Re, defined using the plate half-height, ranged up to 100, when the size of the recirculating region resembled that for turbulent flow with Re = $O(10^5)$. Some features of the predicted flows were assessed by comparison with classical solutions of the Navier-Stokes equations. We conclude that present efforts aimed at refining turbulence models deserve a comparable investment in developing improved numerical methods. Otherwise, errors in predictions of bluff-body flows will preclude any detailed comparison of different turbulence models.

NOMENCLATURE

F	non-dimensionalized force
F.D.	finite-difference
F.E.	finite-element
h	plate half-height
ΔH	change in total head
H.D.S.	hybrid-difference scheme
L	length of recirculation zone
p	pressure
Re	Reynolds number
Re_M	mesh Reynolds number
u_o	free stream velocity
u	velocity in x-direction
v	velocity in y-direction
V.D.S.	vector-difference scheme
x,y	cartesian coordinates
δ	thickness of boundary layer on front of plate
δ_ζ	shear-layer thickness
ρ	fluid density
μ	dynamic viscosity
ν	kinematic viscosity.

INTRODUCTION

The application of sophisticated turbulence models in the prediction of those complex flows with regions where the flow equations are principally of elliptic form is not straightforward. For example Leonard et al(1) found, when they made alterations in a turbulence model, that the changes in the calculated flow pattern depended essentially on the method used to represent the flow equations in discrete form. Thus an attempt to discover the limitations of a particular physical model of turbulence may well be thwarted by the inadequacy of the numerical method selected for the computation. There are merits, therefore, as a contribution to improving simulations of turbulent flows, in particular studies of the behaviour of the various numerical methods available for solving the several model equations that aspire to describe turbulence. These several computational schemes may be assessed, without any of that uncertainty as to the validity

of the model that is inevitable in a study of turbulent flow, by examining predictions of carefully chosen laminar flows; these should be selected so that the resulting numerical errors may correspond to those found in the analogous turbulent flows.

We have therefore chosen to study steady laminar flow in two dimensions past a plate normal to a free stream; the geometry of the flow is shown in figure 1. This plate is held at the centre of a channel and imposes a blockage ratio of 1:5; in addition, a central splitter plate behind the obstacle prevents vortex shedding. The flow velocity is fixed at the channel inlet and at the outer boundaries of the channel. This geometry could therefore be conveniently realized in a towing-task experiment, but no appropriate measurements have been made to date.

The flow about such an obstacle has particular advantages for our object of studying the performance of various numerical methods. This is because a wholly satisfactory technique must represent the flow accurately in regions with very different character: that is in an upstream region of irrotational flow; in the separated shear layer; and in the recirculating zone. The complete calculation of the flow pattern is therefore just such a demanding study that we sought, but it has also several convenient features. Separation of the flow necessarily occurs at the tips of the plate; thus there is no difficulty in locating the point of separation, which invariably complicates any simulation of flow over a curved body. Moreover, the grid used to represent the flow equations in discrete form can be immediately refined in those important regions where the flow variables are changing most rapidly.

We need make calculations of course only for half the channel, with appropriate boundary conditions along the symmetry plane upstream of the plate. Parkinson and Jandali(2), in calculations of potential flow past a bluff body, found that the obstacle did not influence flow upstream at distances exceeding 10 times the height of the body. The upstream boundary, with a uniform velocity u_o specified across the channel, was therefore placed at a distance 20 times the half-height h of the plate.

The appropriate downstream boundary condition for our calculation corresponds to no further variation in flow further along the channel. This constraint had no influence on predicted flow if imposed across a plane at a distance from the obstacle about twice that to the point where the flow reattaches to the central splitter plate. The distance to reattachment increases with the Reynolds number Re of the flow; we conveniently use $Re = u_o h/\nu$, where ν is the kinematic viscosity of the fluid. We have made studies with Re ranging from 10 to 100; at Re = 100 the distance L to reattachment is about 25h, and the explicit channel lengths used for this calculation were between 40 and 65h. If we recall our objective of making studies comparable with turbulent flow, we note that Arie and Rouse(3) found L = 18h for this flow geometry at $Re = O(10^5)$; thus the eddy viscosity acting in the turbulent shear layer must be of the order of the laminar viscosities used in this study.

Any assessment of the performance of a numerical method in predicting laminar or turbulent flow requires a practicable standard of achievement. Ideally, we would compare simulation and experiment; but no measurements are recorded for flow in this geometry, although we expect and look forward to publication of appropriate data. An alternative test is therefore to compare detailed calculations with analytic predictions of particular features of the expected flow pattern; for example in the upstream irrotational region, the boundary layer on the face of the plate, and where the shear layer develops. In the next section, therefore, we consider the expected behaviour of flow in these situations.

A more practicable but less rigorous test is a comparison between the predictions of several numerical methods, so that we may perhaps identify unsatisfactory aspects of each of them. To this end, we have chosen to study two finite-difference (F.D.) and one finite-element (F.E.) method. The first difference scheme selected was the hybrid method (H.D.S.) first proposed by Spalding(4), used extensively in subsequent practical studies of flow; and recently, for example by McGuirk and Rodi(5), for simulation of complex turbulent flows.

Leonard(6) and Gresho and Lee(7), however, have emphasized the limitations of this approach, and the advantages of using a higher-order difference scheme. Of various alternatives we have chosen to study a variant of the vector-differencing scheme (V.D.S.), originally devised by Raithby(8), then extended by Castro(9) and subsequently by Lillington(10). The finite-element method we have used is due to Taylor and Hood(11,12), and has been widely applied in studies of fluid flow. The third section of this paper provides a brief outline of particular characteristics of these several methods of calculation. The paper is completed by a discussion of results, and of their significance in developing improved simulations of turbulent flow.

CLASSICAL FLOW PREDICTIONS

Our calculated results, in particular regions of flow and for limiting values of the flow parameters, must approximate certain analytic solutions of the equations of laminar flow; the relevant solutions are for fluid moving towards an infinite boundary, and for the growth of a mixing layer between two uniform streams. We use these analytic solutions explicitly as direct tests of our simulations, but also as frameworks for presenting various aspects of the numerical results.

Flow Towards an Infinite Barrier

Standard texts present the classic analytic solution for viscous flow about a stagnation point on an infinite boundary. This solution has a region of irrotational flow outside a boundary layer adjoining the barrier, in which the flow is strongly affected by the viscosity of the fluid. The thickness δ of the intruded boundary layer depends on the ratio of the viscosity and velocity of the fluid, with $\delta = O(Re^{-\frac{1}{2}})$. We may therefore expect to find, at Re = 100, a significant region of the surface of the finite plate where the flow pattern matches the analytic solution for flow towards an infinite plate; here we may usefully compare numerical and analytic predictions of flow in the boundary layer itself, and out into the surrounding irrotational region of flow. However, we cannot expect any such agreement at low values of the Reynolds number.

The calculation of the change in total head

along the stagnation streamline is another useful indicator as to the validity of any particular method of modelling laminar flow. A single integration of the u-momentum equation with respect to x gives the difference in head between two points on the stagnation streamline as

$$\Delta H_1^2 \equiv \frac{\Delta\{\frac{1}{2}\rho(u^2+v^2)+p\}}{\frac{1}{2}\rho u_o^2}\Bigg|_1^2 = \frac{2\nu}{u_o^2}\left\{\frac{\partial u}{\partial x}\Bigg|_1^2 + \int_1^2 \frac{\partial^2 u}{\partial y^2}\,dx\right\};$$

here p is the pressure and ρ the density of the fluid.

There can be no change in head in the irrotational region of flow, so the two terms on the right-hand side of this expression are equal and opposite if the total head is compared at two points that are both outside the boundary layer. Moreover, for an infinite boundary, each term separately is zero. Thus the only change in total head, for both finite and infinite barriers, occurs across the boundary layer; and in both cases ΔH is given entirely by the change in $\frac{\partial u}{\partial x}$ because $u \neq f(x)$ in the layer adjoining the boundary. Because $\frac{\partial u}{\partial x}$ is zero at the boundary itself, the change in head is determined by the value of $\frac{\partial u}{\partial x}$ at the outside of the boundary layer, where flow must be matched to the irrotational region; hence the change in head is determined by the actual shape of the obstacle.

There is an alternative prescription for calculating the change in head along the stagnation streamline for a finite body. Far upstream from the obstacle, the flow is uniform with $\frac{\partial u}{\partial x}$ zero. Thus the total change in head across the boundary layer is equal to the complete integral of $\frac{\partial^2 u}{\partial y^2}$, from far upstream to the boundary itself, or in fact to the outside of the boundary layer, within which $\frac{\partial^2 u}{\partial y^2}$ is of course zero.

The Separated Shear Layer and Recirculation Zone

We expect the shear layer, which separates from the tip of the plate obstructing the stream, to behave roughly like a classic two-dimensional laminar mixing layer that grows between two uniform streams. In this analogue of our flow geometry, the shear layer grows as $(\nu x/u_o)^{\frac{1}{2}}$; we therefore expect of our own results, at least where the shear layer is unaffected by pressure gradients, that the thickness δ_ℓ of the shear layer should behave thus:

$$\delta_\ell/h \propto \{(x/h)/Re\}^{\frac{1}{2}}$$

If moreover we assume that the growth of the shear layer continues according to this relation until reattachment, then the distance L to reattachment corresponds to $\delta_\ell \sim h$, so

$$\{(L/h)/Re\}^{\frac{1}{2}} = O(1).$$

We may therefore expect L to increase linearly with Re at Reynolds numbers high enough to ensure that L is significantly greater than h.

The viscous force transmitted to any portion of the recirculating zone between x_1 and x_2 can be estimated by integrating the product of the dynamic viscosity μ with the velocity gradient at the centre of the shear layer, which is of order u_o/δ_ℓ. If F_1^2 is this force, brought to dimensionless form by division by $\frac{1}{2}\rho u_o^2$, then

$$F_1^2 = \int_{x_1}^{x_2} \mu(u_o/\delta_\ell)/\tfrac{1}{2}\rho u_o^2 \propto h.\Big[\{(x/h)/Re\}^{\frac{1}{2}}\Big]_1^2$$

The force per unit height of the recirculating zone is balanced by a pressure gradient which we therefore expect to vary as a function of $\{(x/h)/Re\}$. The total pressure change across the region of back-flow, which we can use to estimate the pressure drop across the plate, is obtained by integrating over the complete recirculation zone; the result is independent of Re under conditions where L/Re is constant.

NUMERICAL METHODS

The three numerical methods used in this study are the hybrid-difference scheme, the vector-difference scheme, and the finite-element method. Details of all these techniques can be found in the literature; we consider only those particular aspects of each method that may affect the results of our flow simulation.

Hybrid-Difference Scheme

Straightforward central differencing of the equations of flow is unsatisfactory: if the convective terms are represented in this way, then the finite-difference matrix is not generally diagonally dominant. This occurs if the mesh Reynolds number Re_m exceeds two, where

$$Re_m = u\,\Delta x/\nu$$

is defined in terms of the relevant flow velocity u in a particular finite-difference cell, and the grid spacing Δx. In this circumstance, the usual methods of solving the discrete form of the flow equations are sometimes unstable and may not converge.

The most convenient expedient is to use upwind differences for the convective terms; at least, as in the hybrid scheme, whenever $Re_m > 2$. This prescription introduces first-order error terms, however, which enhance and often dominate the diffusion of the flow variables; this effect is often ascribed to 'numerical viscosity'. The consequence is that the effective Reynolds number of the flow in such regions is determined by the difference grid rather than the physical properties of the fluid. It is therefore conventional to drop actual diffusion terms when $Re_m > 2$, and our hybrid-difference scheme follows this approach. Such numerical viscosity errors will of course increase the spreading rate of the separated shear layer and lead to early re-attachment of the flow.

The character of discrete forms of actual flow equations has been inferred mainly from studies of the one-dimensional, scalar, convection-diffusion equation without source terms; for which it is well-known that upwinding gives exact results as $Re_m \to \infty$. But Castro(13) found the method inaccurate for a non-linear equation; and Lillington(10) that the whole behaviour of the scheme was modified in the presence of significant sources. In two dimensions, moreover, Raithby and Torrance(14) showed that upwinding was unsatisfactory unless the co-ordinate grid was aligned with the direction of flow.

Vector-Difference Scheme

The vector-difference scheme aims to reduce inaccuracies introduced by upwinding convective terms in flow equations. This is achieved by differencing so that leading errors become second derivatives of the field variables along a direction aligned with the flow. This therefore is an advance on an H.D.S.

whenever such terms are less than corresponding derivatives along fixed grid axes. This situation applies in both boundary and shear layers, where we may look for improved performance from a V.D.S. The actual method used in this study is a further refinement of the original vector scheme proposed by Raithby(8).

The difference matrix obtained in a V.D.S. has some terms that link nodes of the grid lying along diagonals rather than the grid axes. The band width of the matrix is increased and it is still not diagonally dominant, although more stable than the matrix obtained by central differencing. It is therefore possible to solve the equations with the usual alternating-direction implicit scheme, with all variables involved with the additional difference terms treated explicitly.

Finite-Element Method

Papers by Taylor and Hood(11,12), Hood(15) and Gresho and Lee(7) describe the application of the finite-element method to simulation of laminar flow. The selection of suitable elements and compatible basis functions severally for the velocity and pressure fields is not straightforward. Our choice of quadratic basis functions for velocity, located at nine nodes in each quadrilateral element, and linear functions for pressure only at four corner nodes, is known to lead to unique solutions of the flow equations. In a Galerkin scheme, with these basis functions used as test functions to establish the weak form of the flow equations, this results in a leading truncation error proportional to the third derivative of the velocity. Oscillating solutions are therefore possible for mesh Reynolds number greater than two in regions of rapidly varying flow. This can be avoided only with a fine grid, particularly with sufficient refinement to resolve the boundary layer at the front of the plate.

Another valuable aspect of the finite-element method is the conservation, to good accuracy, of the total head in the region of irrotational flow; the finite-difference schemes are less successful in this respect. Finally, we note that we have exploited the flexibility of the method to deploy a high density of elements in the separated shear layer; this is straightforward although the shear layer is deflected well above the level of the plate tip.

RESULTS AND DISCUSSION

For this study, we have calculated flows at various Reynolds numbers, using many different grids for each of the three numerical methods. We cannot of course present all such results, or indeed a full description of any particular prediction; rather we intend, as indicated earlier, to pick out the most significant observations and analyse the salient features of the results. We will learn most from calculations at higher Reynolds numbers, particularly for Re = 100, where we expect the numerical errors to be similar to those found in a simulation of turbulent flow. The results will be assessed by comparing them with the analytic predictions set out earlier in the paper, and by posing these questions:

(i) At the highest Reynolds number considered (Re = 100), how do the predictions differ in the region upstream of the fence ($x \leq o$)? If we achieve a reasonable resolution of the upstream boundary layer, and accurately predict variables along, say, $x = o$, then downstream differences must result from local errors rather than convection of errors generated upstream.

(ii) How do the various solutions differ in their detailed description of flow downstream of the fence; in particular, their prediction of the growth of the shear layer as a function of $\{(x/h)/Re\}$; the increase in length of the recirculation region at large Reynolds number; and the variation in surface pressure?

The Upstream Flow ($x \leq o$)

We begin by discussing the numerical errors in the calculations for the irrotational region upstream of the viscous boundary layer on the plate. Figure 2 shows the change in total head ΔH along the stagnation streamline ($y = o$) for two finite-difference and one finite-element simulation at various values of Re. The F.D. predictions were obtained using the vector scheme (hybrid-scheme results were identical along $y = o$ because $v = o$).

Since we expect that the F.E. method will conserve energy to good accuracy, it is not surprising to find that the only significant changes in ΔH occur in the viscous region; but the F.D. results are very different. Since mesh Reynolds numbers are much larger than two, except very close to the plate, upwinding leads to significant errors. These errors appear to be independent of the Reynolds number for a given grid (the results at Re = 50 and Re = 100 are almost identical), and are reduced by refinement of the grid in the region where the mesh Reynolds number is large. The explanation of these results is straightforward: along the stagnation streamline the solution of the upwinded finite-difference form of the flow equations must effectively satisfy the equation

$$u\frac{\partial u}{\partial x} + \frac{1}{\rho}\frac{\partial p}{\partial x} = \nu\nabla^2 u + \frac{1}{\rho}\frac{\partial}{\partial x}\left(\tfrac{1}{2}\rho u \Delta x \frac{\partial u}{\partial x}\right);$$

where, as usual, the last term represents the effect of numerical viscosity, which depends on the grid spacing Δx. In the irrotational region a single integration leads to

$$\Delta H_1^2 = \int_1^2 \frac{\partial}{\partial x}\left(\tfrac{1}{2}\rho u \Delta x \frac{\partial u}{\partial x}\, dx\right)/\tfrac{1}{2}\rho u_o^2,$$

and if limit 1 is sufficiently far upstream, then

$$\Delta H = \frac{u}{u_o} \cdot \frac{\partial(u/u_o)}{\partial(x/h)} \cdot \frac{\Delta x}{h}.$$

At large Reynolds number u/u_o is independent of Re, so the change in head that arises from the use of upwinding does not depend on Re; it is greatest where $u\frac{\partial\theta}{\partial x}$ is largest and decreases with $\Delta x/h$, as the results of figure 2 demonstrate. Notice that the errors depend only on local conditions, and therefore reduce again as $x \to o$. The implications of these errors in the description of the irrotational region, which arise essentially because we must there solve an inviscid flow with a method more suited to viscous flow, will be discussed later.

Our predictions have been compared with the classic solution for the region near the stagnation point on the front of the plate. Good agreement was found for all three methods at the higher Reynolds numbers. More details can be found in Castro et. al.(16).

Whilst it is possible to obtain good resolution

of the viscous layer at Re = 100 with a fine grid, it is obvious that totally impracticable gridding would be required at the much higher Reynolds numbers associated with a turbulent wake flow. It is therefore important to determine whether good resolution of the viscous boundary layer is in fact necessary in order to obtain accurate predictions downstream of the plate. To this end we considered the predictions of the flow in the region of the plate tip, where the boundary layer separates.

Figure 3 shows that the predictions of the flow angle are all very similar, which implies that the streamline directions are reasonably predicted. However, figure 4 shows that the V.D.S. and H.D.S. solutions have a maximum total kinetic energy $(\frac{1}{2}(u^2+v^2)/u_o^2)$ which is about 25% less than that given by the F.E. calculation. The figure also shows that an increased resolution near the plate reduces this difference.

Now we expect that any increase in the energy available in the separated shear layer will increase the distance to the point of reattachment, provided that the flow angles along, say, $y/h = 1$, $x < o$, (or $x = o$, $y/h > 1$) are identical. Thus the F.E. solution predicted reattachment at about $x/h = 25$, compared with the V.D.S. predictions of $x/h \lesssim 20$, for $Re = 100$. Thus the evidence indicates that good resolution of the flow near the plate is necessary for an accurate prediction of the high velocities that occur near separation.

The Separated Shear Layer

Figure 5 shows the growth of the shear layer, as a function of $[(x/h)/Re]^{\frac{1}{2}}$, for all three methods and with Re = 100. The shear-layer thickness, δ_ℓ, was defined as the distance between those points where the axial velocity exceeds u_{min} by 0.05 and 0.95 times the value of $(u_{max}-u_{min})$ at that value of x; u_{min} was of course negative since the shear layer bounds a recirculating region.

Now, as indicated earlier, we expect flow variations downstream of the plate to scale linearly with Reynolds number at sufficiently high values of Re. Both the F.E. and V.D.S. results exhibit this behaviour to reasonable accuracy, whereas the H.D.S. results do not. Further, as can be seen from figure 5, the H.D.S. results predict both a thicker shear layer (at a given x) and a greater rate of growth than either the V.D.S. or F.E. results. This is symptomatic of numerical diffusion and leads to early reattachment. The F.E. results show a greater rate of growth than the V.D.S. in the early part of the shear layer, whereas further downstream this trend is reversed. Since the shear layer in the F.E. calculation is more energetic and more strongly deflected than in the V.D.S. prediction, a simple comparison of the rate of shear-layer growth may be unrealistic.

Surface Pressure and Bubble Length

We expect the surface-pressure coefficient on the splitter plate to be a function only of $(x/h)/Re$, for sufficiently large Re, as indicated earlier. Both the V.D.S. and F.E. results had this property for $Re \geq 50$, whereas there was significantly greater spread in the H.D.S. results. The base pressure was rather lower for the F.E. prediction than either H.D.S. or V.D.S.; this is precisely as expected because the separating boundary layer is significantly more energetic for the F.E. prediction.

Figure 6 shows the normalized distance to reattachment, L/h, of the separated shear layer, plotted against Re for V.D.S., H.D.S. and F.E. simulations. It is clear that differences between the various solutions increase with Reynold number. In particular, hybrid differencing does not lead to a linear growth of L with Re, as originally anticipated; V.D.S. solutions, however, do exhibit the expected behaviour, although the predicted L/Re is not as high as that given by the F.E. calculations. In view of the results discussed earlier we believe that this must be due almost entirely to inadequate resolution near the plate. Since, in the V.D.S. solutions, the downstream surface pressures and shear-layer growth rate have the expected behaviour for $Re \geq 30$, it is difficult to ascribe too low a value of L/Re to deficiencies in the grid downstream of the plate.

DISCUSSION AND IMPLICATIONS FOR TURBULENT FLOW CALCULATIONS

We have remarked that laminar flow over a plate at $Re = O(100)$ is qualitatively similar to turbulent flow at high Reynolds number. It is reasonable to suppose therefore that the numerical errors in this flow will be similar to those in the turbulent flow, at least as far as the momentum equations are concerned. There are of course additional difficulties associated with the turbulent flow calculation, such as additional equations representing transport of turbulence kinetic energy or stress. Nevertheless, we expect the conclusions reached here to have direct application to turbulent flow calculations.

We have seen that the nature and significance of the errors in our calculations depend first on the particular numerical method, but also on the region of the flow where each method is employed. In the irrotational region upstream of the boundary layer on the front of the plate, there is a balance between pressure gradients and the inertial terms. In this region the two finite-difference schemes are inaccurate because they do not conserve energy, and the resulting errors in the predicted flow may subsequently be convected downstream of the barrier. The finite-element method, on the contrary, does not invoke upwinding and therefore behaves more satisfactorily in the irrotational region because the integrals of motion, in particular the kinetic energy, are more nearly conserved. The penalty to pay for this advantage is that it is necessary to use a refined grid that resolves the boundary layer; otherwise, the solution is beset with wiggles.

If there were turbulence in the upstream flow for the high Reynolds number case, the equations would still have the same dominant terms, and would, we believe, require a numerical scheme that conserves energy for their accurate solution. However, it is then still necessary to resolve the much thinner boundary layer at high Reynolds number with a very fine grid, in order to avoid oscillatory solutions. On the other hand, schemes like H.D.S. and V.D.S. maintain stability by introducing dissipation into their description of the convective terms; it is not then essential to resolve the boundary layer. But such methods, as we have seen, introduce significant errors in the upstream region, principally associated with energy loss from the flow. However such errors are bounded, and may not be much larger for $Re = O(10^5)$ than they are in the present case

(figure 2) - they could be reduced by refining the grid. Our results show that flow around separation, which is important in determining the characteristics of the downstream flow, can be predicted with acceptable accuracy using such methods, provided that the grid near the plate is sufficiently fine - it seems to be more important to resolve the flow in the regions of large gradients just outside the boundary layer (e.g. $-1 < x/L < 0$) than further upstream, where mesh Reynolds numbers are actually higher.

An adequate grid must have mesh spacings no larger than a few percent of the plate height in that region. This may not resolve the boundary layer at high Reynolds number, but is sufficient for reasonably accurate prediction of the potential flow around separation.

The characteristics of the flow in the downstream region are quite different: pressure gradients have less significance and the equations of motion impose a balance between viscous and inertial forces, particularly in the shear layer. In fact these differences in the basic character of the flow preclude the choice of a single numerical method that is ideal both in front and behind the barrier. In assessing the performance, in the downstream region, of the various methods considered in this paper, we find that H.D.S. is certainly inadequate in comparison with the other schemes. The simple upwinding technique in the hybrid scheme introduces numerical diffusion that leads to a too rapid spread of vorticity, and as a result to premature reattachment of the separated shear layer. Since the recirculation regions are very similar in size for $Re = O(100)$ and $Re = O(10^5)$, we would expect to find similar numerical errors, so that simple low-order schemes like H.D.S. will not be very satisfactory for calculations of turbulent flow at high Reynolds numbers. A major conclusion of this work is that such schemes should be used with great caution.

We cannot of course infer that the V.D.S. or F.E. methods, which seem to be adequate for predicting laminar flows, will also perform well in studies of turbulent flow. (Indeed, as noted earlier, the latter requires resolution of the boundary layer on the front of the plate, and so would probably be impossible to apply directly at $Re = 10^5$).

We are currently looking at the source-correction scheme proposed by Lillington(10). The initial results are quite encouraging; it seems that the scheme reduces the errors in the irrotational region upstream of the plate, and consequently produces a longer recirculation zone than the standard V.D.S. We hope to give more details at the conference presentation.

In conclusion, we believe that there is a need to develop a more accurate and robust numerical method, which can be applied with confidence to flows that have distinct regions with quite different characteristics.

ACKNOWLEDGEMENT

This work was begun while one of the authors (I.P.C.) was employed at the Marchwood Engineering Laboratory of the Central Electricity Generating Board, and is published by permission of its Director.

REFERENCES

(1) Leonard, B.P., Leschziner, M.A. and McGuirk, J.J., "Third-Order Finite-Difference Method for Steady Two-Dimensional Convection", Proceedings of the 1st International Conference on Numerical Methods in Laminar and Turbulent Flow, Swansea, 1978, p.807.

(2) Parkinson, G.V. and Jandali, T., "A Wake Source Model for Bluff Body Potential Flow", Journal of Fluid Mechanics, 40, 1970, p.577.

(3) Arie, M. and Rouse, H., "Experiments on Two-Dimensional Flow Over a Normal Wall", Journal of Fluid Mechanics, 1, 1956, p.129.

(4) Spalding, D.B., "A Novel Finite Difference Formulation for Differential Expressions Involving both First and Second Derivatives", International Journal for Numerical Methods in Engineering, 4, 1972, p.551.

(5) McGuirk, J.J. and Rodi, W., "A Depth-Averaged Mathematical Model for the Near Field of Side Discharges into Open-Channel Flow", Journal of Fluid Mechanics, 86, 1978, p.761.

(6) Leonard, B.P., "A Survey of Finite-Differences with Upwinding for Numerical Modelling of the Incompressible Convective Diffusion Equation", Computational Techniques for Transient and Turbulent Flow, Pineridge Press, Swansea, 1981.

(7) Gresho, P.M. and Lee, R.L., "Don't Suppress the Wiggles - They're Telling You Something", Computers and Fluids, 9, 1981, p.223.

(8) Raithby, G.D., "Skew Upstream Differencing Schemes for Problems Involving Fluid Flows", Computer Methods in Applied Mechanics and Engineering, 9, 1976, p.153.

(9) Castro, I.P., "The Numerical Prediction of Recirculating Flows", Proceedings of the 1st International Conference on Numerical Methods in Laminar and Turbulent Flow, Swansea, 1978, p.329.

(10) Lillington, J.N., "A Vector Upstream Differencing Scheme for Problems in Fluid Flow Involving Significant Source Terms in Steady-State Linear Systems", International Journal for Numerical Methods in Fluids, 1, 1981, p.3.

(11) Taylor, C. and Hood, P., "A Numerical Solution of the Navier-Stokes Equations Using the Finite Element Technique", Computers and Fluids, 1, 1973, p.73.

(12) Taylor, C. and Hood, P., "Navier-Stokes Equations Using Mixed Interpolation", Proceedings of the 1st International Conference on Finite Element Methods in Flow Problems, 1974, p.121.

(13) Castro, I.P., "Numerical Difficulties in the Calculation of Complex Turbulent Flows", Turbulent Shear Flows I, Springer-Verlag, Berlin, 1979, p.221.

(14) Raithby, G.D. and Torrance, K.E., "Upstream Weighted Differencing Schemes and Their Application to Elliptic Problems Involving Fluid Flow", Computers and Fluids, 2, 1974, p.191.

(15) Hood, P., "Frontal Solution Program for Unsymmetric Matrices", International Journal for Numerical Methods in Engineering, 10, 1976, p.379.

(16) Castro, I.P., Cliffe, K.A. and Norgett, M.J., "Numerical Predictions of the Laminar Flow Over a Normal Flat Plate", International Journal for Numerical Methods in Fluids, to appear.

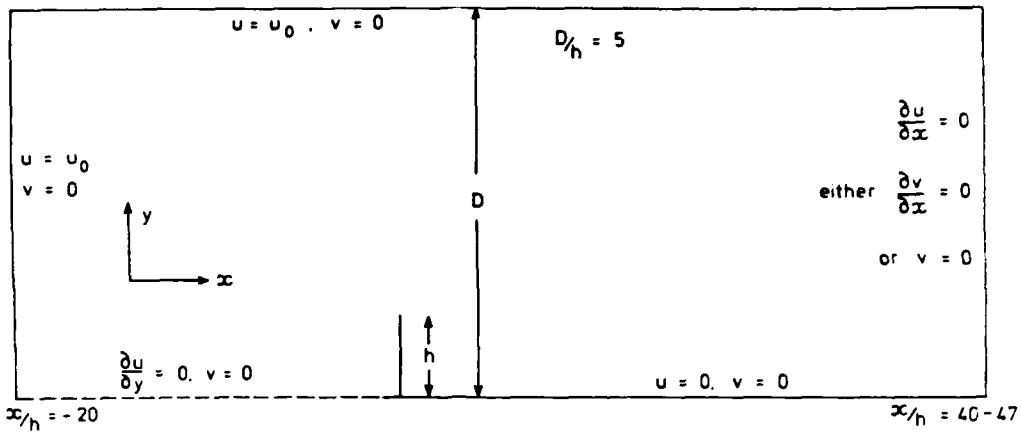

Figure 1. Flow geometry (not to scale) and boundary conditions used for the calculations.

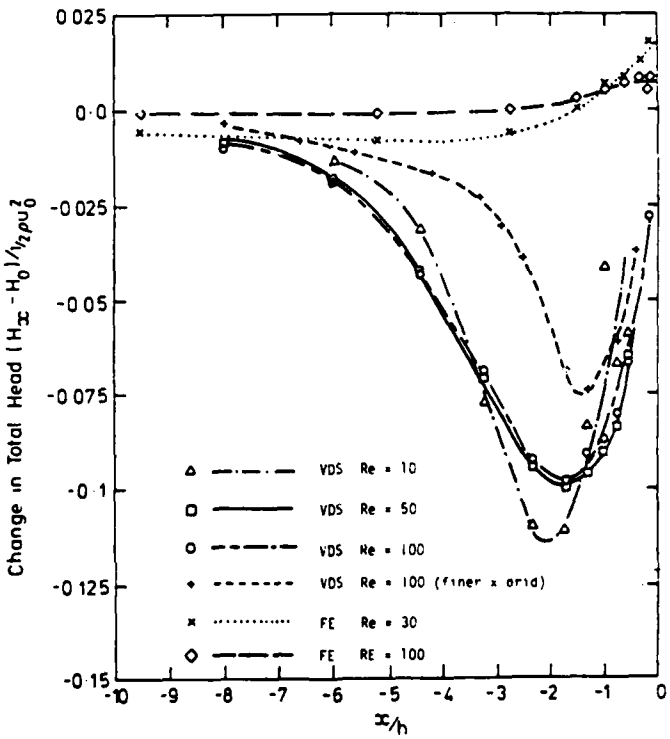

Figure 2. Change in total head along the stagnation streamline, y = 0.

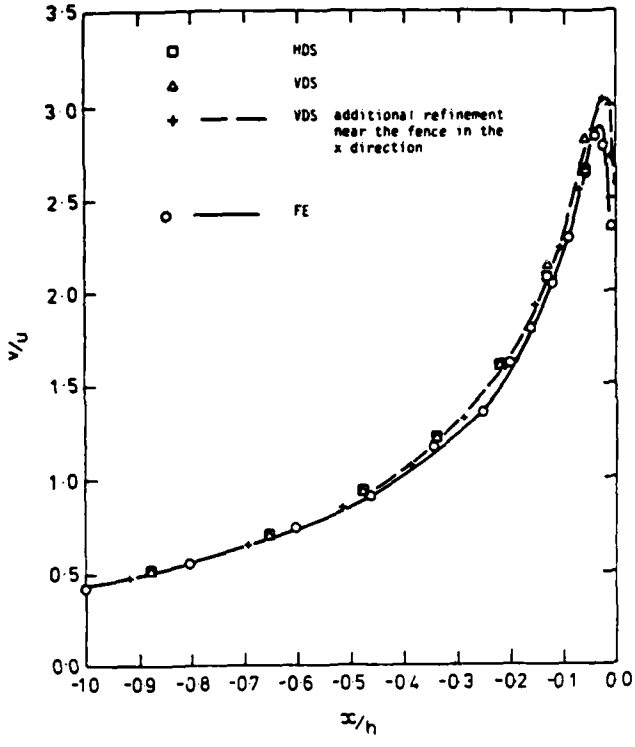

Figure 3. Flow angle v/u upstream of the fence tip (y = 1).

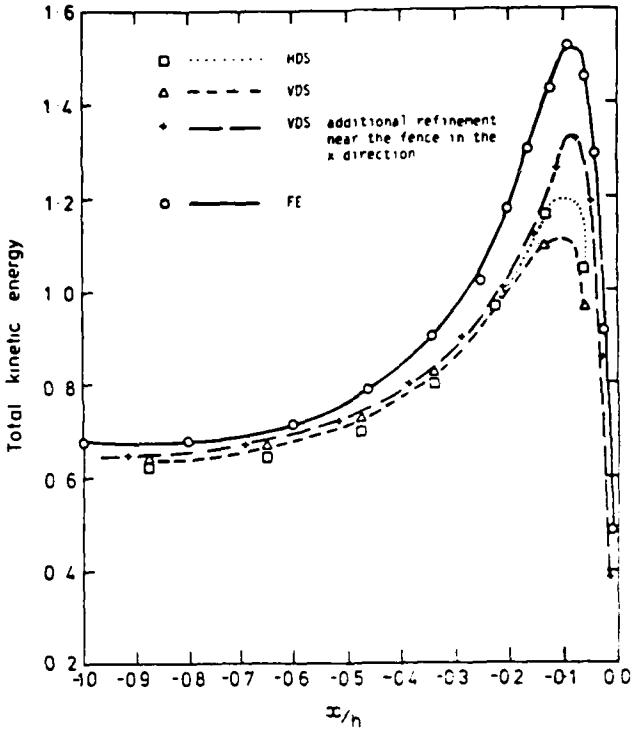

Figure 4. Normalized kinetic energy $(u^2 + v^2)/u_o^2$ upstream of the fence tip.

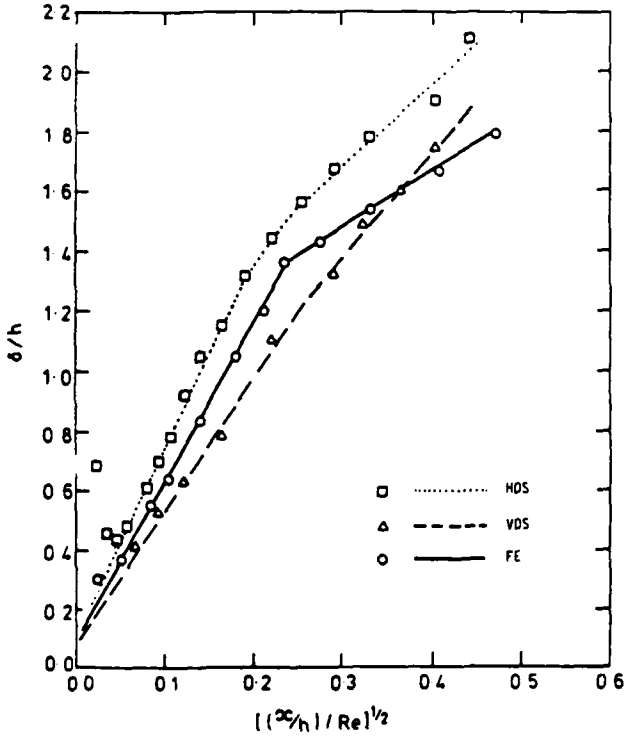

Figure 5. Shear-layer growth at Re = 100.

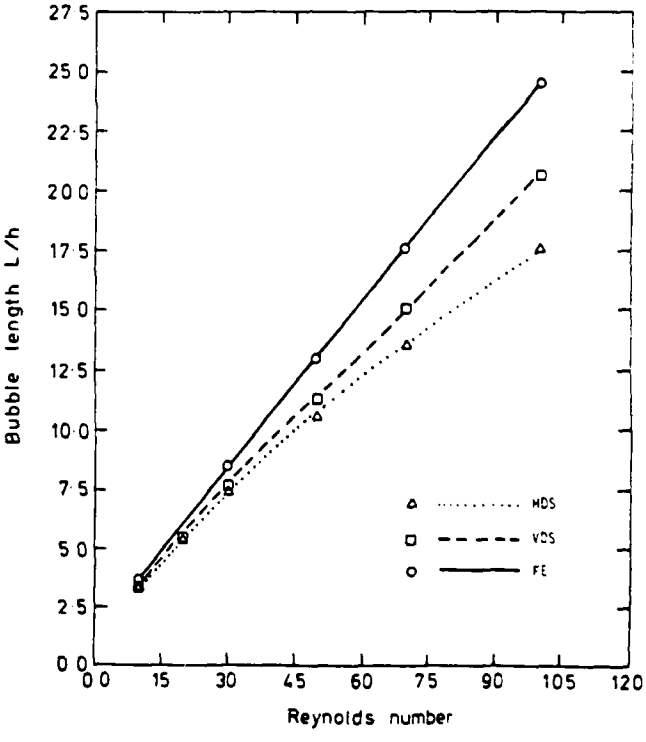

Figure 6. Bubble length L/h against Reynolds number.

TURBULENT FLOW INDUCED BY A JET IN A CAVITY - MEASUREMENTS AND 3-D NUMERICAL SIMULATION.

F. Baron - J.P. Benqué - Y. Coëffé
Electricité de France
Laboratoire National d'Hydraulique
6 quai Watier, 78400 CHATOU (FRANCE)

ABSTRACT

Velocity measurements made by laser anemometry on the turbulent flow induced by a jet in a cubic cavity are presented.

A numerical code solving the instationary Navier-Stokes equations in three dimensions for the large-scale field is described. Subgrid scale turbulence can be modelled by a turbulent viscosity.

The results of two cases of large-eddy simulation made with this code on the flow induced by a jet in the cubic cavity are then compared with measurements.

The same numerical code is applied to large eddy simulation of Plane Poiseuille Flow with periodic boundary conditions. Some results on mean velocities and Reynolds stresses are presented and compared with measurements.

INTRODUCTION

The flow induced by a jet in a cavity is studied as a typical case of industrial flows requiring 3-D numerical prediction with turbulence simulation.

A similar computation was performed on plane Poiseuille Flow in order to understand better the turbulence production mechanism in a simpler case of wall-bounded flow.

MEASUREMENTS IN THE CUBIC BOX

A cubic box (side a = 50 cm) is included in a loop of cold water. The flow enters the box through the window F_1 (see fig. 1) and exits the box through the window F_2. F_1 and F_2 are square windows (side b = 15 cm) and are such that there is no symmetry plane for the flow. The flow consists of a jet entering the box and impinging the opposite wall, generating on each side of the jet a recirculating flow which goes down and progressively moves towards the exit area near F_2.

The flow rate is kept as constant as possible by a free overfall control. The entrance mean velocity is U_0 = 24 cm/s and the entrance Reynolds number is Re = 36,000.

Several flow visualizations are made by taking pictures of particles illuminated when passing through a plane light beam. These visualizations show that except for the planes cutting the jet along its main axis, no big and stable structures are present but mainly middle sized (5 to 10 cm) eddies of relatively short life.

Laser doppler anemometry measurements are performed to obtain simultaneously two components of the velocity in one point of the box. The signals are then treated to get an average value or a filtered value but also the standard deviation and the spectrum of the fluctuations.

NUMERICAL SIMULATION : "TRIDI" CODE

The instationary Navier-stokes equations for the large-scale 3D flow of an incompressible fluid are discretized in a time-advancing finite-difference scheme on two staggered grids.

Large-Scale Field Computation (7) (8)

Velocity field $U_i(\underline{x}, t)$ is separated into a large-scale component $\bar{U}_i(\underline{x}, t)$ and a subgrid-scale component $U'_i(\underline{x}, t)$ by a filtering operation :

$$\bar{U}_i(\underline{x}, t) = \int G(\underline{x} - \underline{x}')\, U_i(\underline{x}', t)\, d\underline{x}'$$

$$U'_i(\underline{x}, t) = U_i - \bar{U}_i$$

Filtered Navier-Stokes equations are :

$$\frac{\partial \bar{U}_i}{\partial t} + \frac{\partial}{\partial x_j}(\bar{U}_i \bar{U}_j) = -\frac{1}{\rho}\frac{\partial \bar{P}}{\partial x_i} - \frac{\partial}{\partial x_j}\left\{L_{ij} + S_{ij} - \nu \frac{\partial \bar{U}_i}{\partial x_j}\right\} \quad (1)$$

$$\frac{\partial \bar{U}_i}{\partial x_i} = 0 \quad (2)$$

Where :

$$L_{ij} = \overline{\bar{U}_i \bar{U}_j} - \bar{U}_i \bar{U}_j \quad (3)$$

is the "Leonard Stress", and

$$S_{ij} = \overline{\bar{U}_i U'_j} + \overline{U'_i \bar{U}_j} + \overline{U'_i U'_j} \quad (4)$$

is the "subgrid stress"

In a finite difference scheme, the

characteristic length λ of the filter has to be several times bigger than the mesh size of the scheme, to make sure that all filtered wavelengths are really computed.

In our wall-bounded flows calculations, this would imply a very large number of grid points if λ is in the inertial subrange, as it has to be.

These are the reasons why we did not use a formal filtering operation, but the inherent filtering effect of the finite difference scheme (MOIN et al (9) did the same in the inhomogenous direction of channel flow, although their number of grid points was quite important).

With this kind of filtering, tests showed that the Leonard stress was within the round-off errors of the finite difference scheme. We have thus neglected these terms.

The subgrid scale stress tensor is modelled with a turbulent viscosity :

$$S_{ij} = -2\nu_T \bar{D}_{ij} + \frac{1}{3} S_{ll} \delta_{ij} \qquad (5)$$

where :

$$\bar{D}_{ij} = \frac{1}{2}\left(\frac{\partial \bar{U}_i}{\partial x_j} + \frac{\partial \bar{U}_j}{\partial x_i}\right) \qquad (6)$$

is the large-scale strain-rate tensor.
We use the Smagorinsky's (11) subgrid model :

$$\nu_T = C_s^2 \lambda^2 (\bar{D}_{ij}\bar{D}_{ij})^{1/2} \qquad (7)$$

(where C_s is a constant and λ a characteristic length of the mesh size)

This model is the most classical one and usually gives rather good results, although it does not reproduce the backscatter transfer from subgrid scales to large scales (8) as it was recently pointed out by a comparison with direct simulations (4).

Note that the spherical part of the subgrid stress tensor is incorporated with the pressure :

$$P = \bar{p} + \frac{1}{3}\rho S_{ll} \qquad (8)$$

Discretization of the Equations

$(n+1)^{th}$ time step is resolved in three steps (The method is on the same pattern as the one proposed by CHORIN (2)) :

Step I : Advection of momentum
(Split into 3 directions)

$$\frac{\tilde{U}_i - U_i^n}{\Delta t} + \left\{U_j \frac{\partial U_i}{\partial x_j}\right\}^n = 0 \qquad (9)$$

This equation is solved by a method of characteristics with third - order interpolation

$$\frac{\partial U_i}{\partial t} + U_j \frac{\partial U_i}{\partial x_j} = 0$$

U_i is constant on the characteristics :

$$dx = U_j\, dt$$

The intersections of one of the axes :

$(t = t^n)$ or $(x = x_n)$

with the characteristics containing the points

$(x_i, t^n + \Delta t)$, $i = 1, --, N$

are computed.

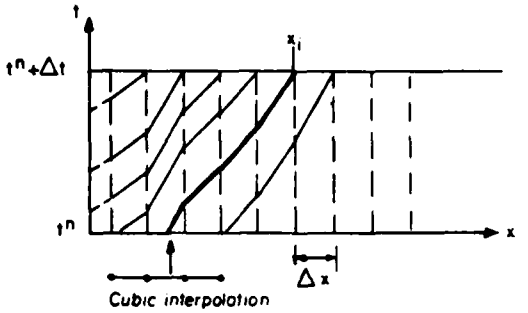

Then $\tilde{\tilde{U}}_i$ is computed with third order interpolation at those intersections.

This method is unconditionnaly stable in each direction, but, due to the splitting in three directions, the Courant criterion has to be observed to insure accuracy. On the other hand this scheme is not energy-conserving, but the third-order interpolation prevents from too important numerical diffusion.

Step II : Diffusion of momentum (split into 3 directions)

$$\frac{\tilde{U}_i - \tilde{\tilde{U}}_i}{\Delta t} = \frac{\partial}{\partial x_j}\left\{(\nu + \nu_T)\bar{D}_{ij}\right\} \qquad (10)$$

This equation is solved by a double-sweep implicit scheme.

Step III : Continuity and pressure

$$\begin{cases} \dfrac{U_i^{n+1} - \tilde{U}_i}{\Delta t} = -\dfrac{1}{\rho}\dfrac{\partial P^{n+1}}{\partial x_i} & (11) \\ \dfrac{\partial U_i^{n+1}}{\partial x_i} = 0 & (12) \end{cases}$$

$$\Longleftrightarrow \begin{cases} \dfrac{\partial \tilde{U}_i}{\partial x_i} = \dfrac{\Delta t}{\rho}\dfrac{\partial^2 P^{n+1}}{\partial x_i\, \partial x_i} & (13) \\ U_i^{n+1} = \tilde{U}_i - \dfrac{\Delta t}{\rho}\dfrac{\partial P^{n+1}}{\partial x_i} & (14) \end{cases}$$

(13) : Poisson equation solved by a Gauss-Seidel iterative method with over-relaxation and Neumann boundary condition :

$$\frac{\partial p}{\partial n}^{n+1} = 0 \quad \text{(see below)}$$

Pressure is defined on a staggered grid ("pressure points" are in the center of "velocity cubes")

Boundary Conditions

Entrance : $U^{n+1} = U_0$ given

Exit : no condition : U^{n+1} is computed assuming that advection is dominating

Walls : The boundary condition should be $U^{n+1} = 0$. But, since the number of grid points we use is not sufficient to allow such a condition, we set : $U^{n+1}.\vec{n} = 0$ for the component normal to the wall and we assume a relationship between total shear stress and instantaneous tangential velocity U_τ^{n+1}.

This relationship, based on the logarithmic law for mean velocity near a rough wall, is quite a crude assumption for instateneous velocities. Schumann (10) had rather good results with similar boundary conditions in channel flow.

In the calculation, we choose arbitrarily as a boundary condition for step II (diffusion) the same condition as for the whole time step :

$\tilde{U}_n = U_R^{n+1} = U_{on}$

then equation (11) yields at boundaries :

$$\frac{\partial p}{\partial n}^{n+1} = -\frac{\rho}{\Delta t}(U_n^{n+1} - \tilde{U}_n) = 0 \qquad (15)$$

(In fact, tests showed that the results are the same with any normal velocity boundary condition for step II).

And then, boundary condition for step III (Poisson equation) is justified :

$$\frac{\partial p^{n+1}}{\partial n} = 0$$

Equation (11) yields also at boundaries :

$$U_\tau^{n+1} - \tilde{U}_\tau = -\frac{\Delta t}{\rho}\frac{\partial p^{n+1}}{\partial \tau} \qquad (16)$$

$$\frac{\partial U_\tau^{n+1}}{\partial n} - \frac{\partial \tilde{U}_\tau}{\partial n} = -\frac{\Delta t}{\rho}\frac{\partial^2 p^{n+1}}{\partial n\, \partial \tau} = 0 \qquad (17)$$

So the boundary condition on shear gradient is also the same for step II and whole time step.

NUMERICAL COMPUTATION OF THE FLOW INDUCED BY A JET IN A CUBIC CAVITY AND COMPARISON WITH MEASUREMENTS

Fig. 2 gives a sample of comparison between measurements and numerical mean flow results in the case of an algebraic turbulent subgrid scale viscosity model. Fig. 3 gives the same comparison for a case with no such viscosity. The full comparison between measurements and numerical results shows that the main aspects of the flow are present even in the no viscosity case ; the turbulent viscosity makes the comparison better in the jet region but some discrepancies remain in the recirculating area under the jet.

These differences between the two cases confirm that the numerical diffusion, inherent to the advection scheme, is not too high : it does not exceed the turbulent diffusion.

But an important feature observed in experiments -the increase of turbulent energy from the entrance to the inside of the box- is not reproduced in this simulation, even with fluctuating boundary conditions at the entrance. This result led us to perform the same simulation scheme on plane Poiseuille flow in order to test its turbulent production mechanism.

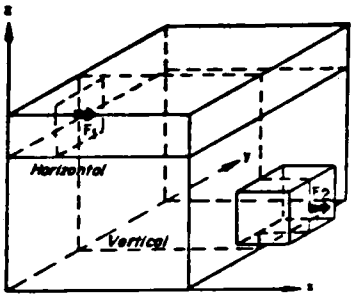

Fig.1. CUBIC BOX GEOMETRY

(and location of the planes of comparison)

LARGE EDDY SIMULATION OF PLANE TURBULENT POISEUILLE FLOW

This calculation aims to improve our LES scheme and its turbulence production mechanism on this simple case of wall-bounded shear flow about which a large amount of measurements -made by G. COMTE-BELLOT (3)- is available.

Computational Specifications for this Flow

The computational domain has the following dimensions

L_x = 8 D in the streamwise direction x

L_y = 4 D in the spanwise direction y

L_z = 2 D in the vertical direction z (perpendicular to the walls)

Boundary conditions in the horizontal directions

According to measurements (3), the double space correlations R_{11} $(L_x/2,\ 0,\ 0)$ and R_{ii} $(0,\ L_y/2,\ 0)$ between the boundaries in these directions are negligible. So the flow between infinite plates can be represented with spatial periodicity for both velocity and pressure fluctuations :

velocity : in the convective operator, a characteristic leaving the domain at one face of the parallelepiped in the X or Y direction re-enters it at the opposite face in the same direction.

pressure fluctuations : $p' = p - P_0$

[P_0 being a given constant gradient pressure field $Po = -\rho U_*^2 \frac{x}{D}$]

The Poisson equation is solved in a domain which is "closed on itself" in two directions.

The number of grid points is

n_x = 65 in the streamwise direction
n_y = 33 in the spanwise direction
} with uniform spacing

n_z = 33 in the vertical direction with variable grid spacing

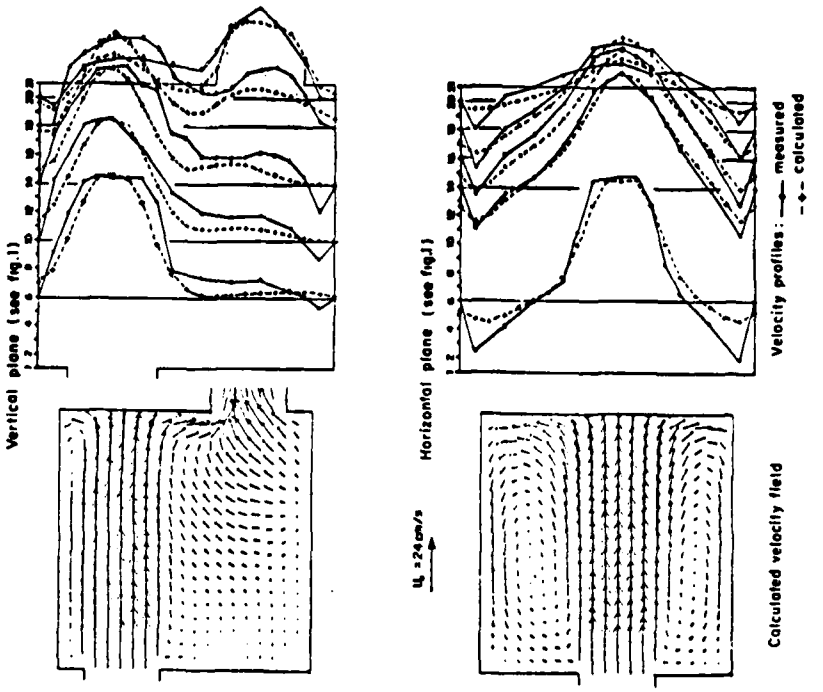

Fig. 2. FLOW IN THE CUBIC BOX (Grid 21x21x27)
With turbulent viscosity

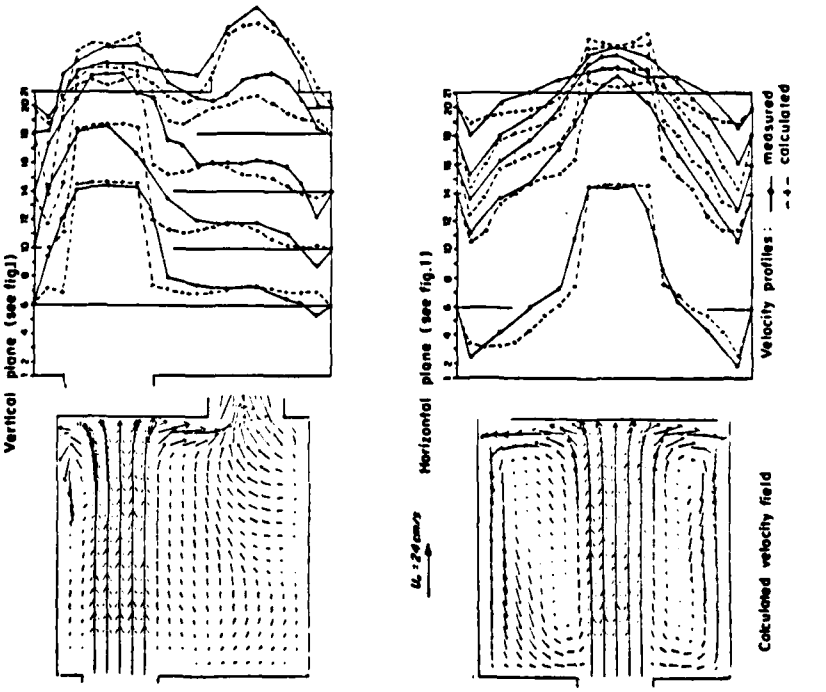

Fig.3. FLOW IN THE CUBIC BOX (Grid 21x21x27)
Without turbulent viscosity

boundary conditions on the walls

- vertical velocity component : $W/_{wall} = 0$
- for the horizontal velocity components, since the above number of grid points is not sufficient to describe a boundary layer with no-slip boundary conditions, we assume a relationship between total shear stress and instantaneous tangential velocity, as described above.

Statistical operator

A statistical operator is needed to compare results with theoretical and experimental data.

We choose to define it-at each time step of the computation-as the mean value over a plane parallel to the walls :

$$\langle Q \rangle (t^n) = \frac{1}{Lx Ly} \int Q\,(t^n, x, y, z)\, dx\, dy$$

and $q = Q - \langle Q \rangle$

(An actual time averaging at one point can be used to study large wave length phenomena, such as pressure-stain correlations...)

Initial Condition

The spatial periodicity implies some equivalence between an entrance boundary condition ($x = 0, 0 < t < T$) and an initial condition function of x ($0 < x < Lx$, $t = 0$).

We thus defined an initial fluctuating velocity field as a serie of periodic functions of x with a (- 5/3) power energy spectrum.

$$\bar{u}_1 = \sum_{i=1}^{n} a_i^1 \cos\,(ik_x x + \phi_i^1(y,z))$$

$$n = \frac{n_x + 1}{2} \quad ; \quad k = \frac{2\pi}{Lx}$$

where : $(a_i^1)^2 = C1(z)\, i^{-5/3}$ and :

$\phi_i^1(y,z)$ are random function

(pressure field and incompressibility are obtained by resolution of Poisson equation (13), as in a time step).

With no more initial correlation between the $\bar{u}_i$, the turbulent energy level had a rapid decrease during the first time steps.

In order to insure a high-level initial turbulent production :

$$P = - \langle \bar{u}_i\, \bar{u}_j \rangle \frac{\partial \langle \bar{u}_i \rangle}{\partial x_j}$$

we add to the initial fluctuating velocities a sheared mean velocity profile $\langle U \rangle$ and we choose the differences :

$$(\phi_i^2 - \phi_i^1) \text{ and } (\phi_i^3 - \phi_i^1)$$

such as the turbulent shear stresses have the theoretical values :

$\langle \bar{u}\bar{w} \rangle = u_*^2 \left(1 - \frac{Z}{D}\right)$ [except near the walls]

$\langle \bar{u}\bar{v} \rangle \cong 0$ and $\langle \bar{v}\bar{w} \rangle \cong 0$

With these initial conditions, the computed energy decrease is much slower.

Computed Turbulent Kinetic Energy

$(k_c = \frac{1}{2} \langle \bar{u}_i\, \bar{u}_i \rangle)$

Despite the improvement on initial condition, the decrease of k_c still remained, due to the advection scheme.

As a first approximation to face this problem, we maintain at a fixed (experimental) level K_c the integral value I_c of k_c over the whole computationnal domain, at each time step :

$$I_c\,(t^n) = \frac{1}{V} \int_D k_c\,(\underline{x}, t^n)\, dV$$

(Practically, we multiply the three components of the fluctuating velocity at each point by the same ratio $\sqrt{K_c / I_c}$).

A few remarks about this operation :

1. the relative change of I_c decreases in time, and, after a few time steps, it becomes :

$$\frac{|K_c - I_c|}{K_c} < 5.10^{-3}$$

It seems that the first time steps can be interpreted as a time scale for the non-linear process.

2. If we stop maintaining I_c, its integral value stays over K_c during 6 crossings of the domain and then decreases very slowly.

Results

Compared with G. COMTE-BELLOT's (3) measurements.

The computed fluctuations (fig. 4) are rather close to measurements in streamwise (u) and spanwise (v) direction. In the vertical (w) direction, there is certainly an incorrect redistribution by the velocity-pressure correlations.

The mean velocity profile $\langle U \rangle$ (fig. 5) is also near the measurements, despite a lack of accuracy on the shear gradient value on the boundary.

The computed part of turbulent shear stress $\langle \bar{u}\bar{w} \rangle$ is about what can be expected. **(fig. 6)**

CONCLUSION

The lack of computed fluctuations observed in the flow induced by a jet in a cubic cavity led us to study the turbulent production in plane Poiseuille flow, and to define on this flow an integral turbulent energy control procedure.

An analogous procedure could be applied to the jet in a cavity (with time-mean statistical operators) in order to obtain, with an improvement on subgrid scale modelling, a more accurate large eddy simulation of that flow with our stable numerical scheme.

REFERENCES

1 BENQUE, J.P. - "Modélisation d'écoulements turbulents isothermes" Rapport EDF-LNH n° HE041/78.12 (1978)

2 CHORIN - "The Numerical Solution of the Navier-Stokes Equations for an Incompressible Fluid" - Bull-Amer/ Math-Soc 73, 928-931 (1967)

3 COMTE-BELLOT, G - "Ecoulement turbulent entre deux parois parallèles" Publications scientifiques et techniques du Ministère de l'Air (1965).

4 FERZIGER, J.H. "Higher-Level simulations of turbulent flows" Von Karman Institute Lecture Series 1981-5

5 GROTZBACH, G. and SCHUMANN, U. "Direct numerical simulation of turbulent velocity-, pressure - and temperature fields in channel flows" Symposium on turbulent shear flows, Pennsylvania State Univ. 14.11 - 14.19 (1977)

6 KIM, J. and MOIN, P., "Large Eddy Simulation of Turbulent Channel Flow", AGARD symposium on Turbulent Boundary layers, The Hague (1979).

7 LEONARD, A "Energy Cascade in Large - Eddy Simulation of Turbulent Fluid Flows" Adv. in Geophys. A18, 237 (1974)

8 LESLIE, D.C. and QUARINI, G.L. "The Application of Turbulence Theory to the Formulation of Subgrid Modelling Procedures" J. Fluid Mech., vol. 91, part1, pp 65-91 (1979).

9 MOIN, P., REYNOLDS, W.C. and FERZIGER, J.H. - "Large Eddy Simulation of Incompressible Turbulent Channel Flow", Report TF-12, Dept. of Mech. Engineering, Stanford University (1978).

10 SCHUMANN, U., "Subgrid Scale Modelling for Finite Difference Simulations of Turbulent Flows in Plane Channels and Annuli", J. Comp. Phys., 18, 376 (1975)

11 SMAGORINSKY, J., "General Circulation Experiments with the Primitive Equations, I. The Basic Experiments" Monthly Weather Review, 91, 99 (1963).

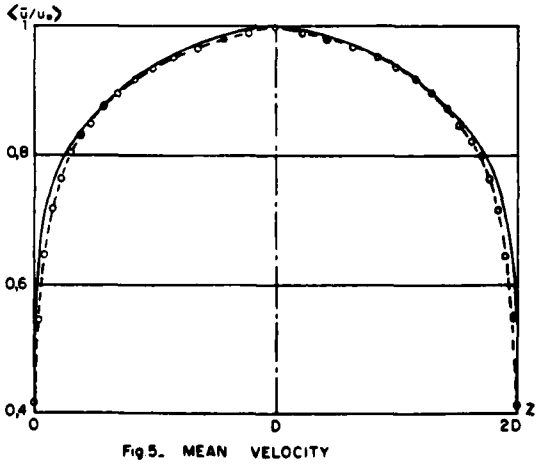

Fig 5. MEAN VELOCITY

—— Measurements

-o- Calculation

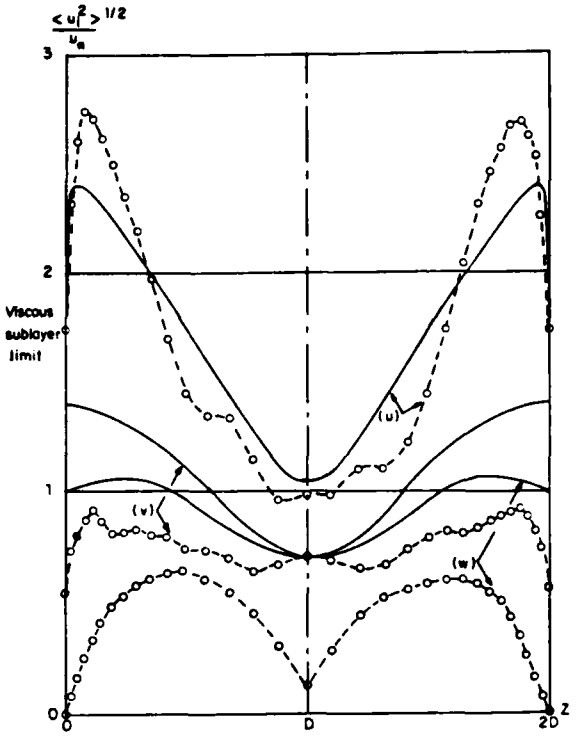

Fig 4. TURBULENCE INTENSITIES IN STREAMWISE (u), SPANWISE (v) AND VERTICAL (w) DIRECTIONS

—— Measurements (3)

-o- Calculations (resolvable part only)

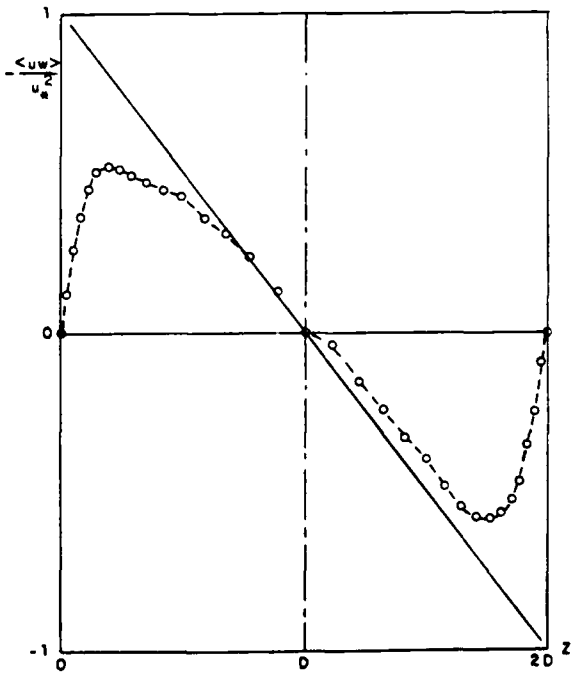

Fig 6. TURBULENT SHEAR STRESS

—— Theoretical value

-o- Computation (resolvable part only)

SESSION 19 - FUNDAMENTALS II

J. L. Lumley - Chairman

PSEUDO-SPECTRAL METHODS FOR HOMOGENEOUS OR INHOMOGENEOUS FLOWS

by Y. MORCHOISNE

OFFICE NATIONAL D'ETUDES ET DE RECHERCHES AEROSPATIALES,
29 Avenue de la Division Leclerc, 92320 CHATILLON (France)

INTRODUCTION

Three dimensional incompressible viscous calculations are done by means of spectral methods.

For time derivatives several schemes have been used :

- finite difference scheme,
- pseudo-spectral scheme.

The solution of Navier-Stokes unsteady equations is obtained by expanding the unknown functions on Fourier series or on a basis of Chebyshev polynomials (e.g. ref. [3], [4]).

Let us set :

$$(1)\quad \begin{cases} (a) & g_i(\vec{U},P) \equiv \dfrac{\partial U_i}{\partial t} + \dfrac{\partial U_i U_j}{\partial x_j} - \nu \Delta U_i + \dfrac{\partial P}{\partial x_i} = 0 \\ (b) & g_4(\vec{U},P) \equiv \dfrac{\partial U_\ell}{\partial x_\ell} = 0 \end{cases}$$

where $\vec{U}$ is the velocity vector, U_i the velocity components and P the pressure (divided by constant density).

For calculations of turbulent flows, a classical space filter is define (ref. [2]) :

$$(2)\quad \overline{\phi}(x,t) = \int_\Omega \phi(x',t)\, G(x,x')\, dx'$$

with $\quad x \in \Omega = [-1,+1]^3$

and $\quad x = \begin{pmatrix} x_1 \\ x_2 \\ x_3 \end{pmatrix}$

Let us set :

$$(3)\quad \phi(x,t) = \overline{\phi}(x,t) + \phi'(x,t)$$

then by applying filter G to equation (1) we obtain :

$$(4)\quad \begin{cases} (a) & \overline{g}_i(\vec{U},P) \equiv \dfrac{\partial \overline{U}_i}{\partial t} + \dfrac{\partial (\overline{U}_i \overline{U}_j + \tau_{ij})}{\partial x_j} - \nu \Delta \overline{U}_i + \dfrac{\partial \overline{\Pi}}{\partial x_i} = 0 \\ (b) & \overline{g}_4(\vec{U},P) \equiv \dfrac{\partial U_\ell}{\partial x_\ell} = 0 \end{cases}$$

with

$$(5)\quad \begin{cases} (a) & \tau_{ij} = \sigma_{ij} - 1/3\, \delta_{ij}\, \sigma_{\ell\ell} \\ (b) & \overline{\Pi} = \overline{P} + 1/3\, \sigma_{\ell\ell} \\ (c) & \sigma_{ij} = \overline{U_i U_j} + \overline{U'_i \overline{U}_j} + \overline{\overline{U}_i U'_j} \end{cases}$$

The Smagorinski closure model is then used :

$$(6)\quad \tau_{ij} = -2\, \nu_T(\overline{S}_{ij})\, \overline{S}_{ij}$$

with

$$(7)\quad \begin{cases} (a) & \overline{S}_{ij} = 1/2 \left(\dfrac{\partial \overline{U}_i}{\partial x_j} + \dfrac{\partial \overline{U}_j}{\partial x_i} \right) \\ (b) & \nu_T = (c\,\Delta_e)^2 \sqrt{2\, \overline{S}_{ij}\, \overline{S}_{ij}} \end{cases}$$

where Δ_e is a length factor

Three cases are now considered :

- the inhomogeneous flow in a cubic domain, with initial and boundary conditions for the velocity components,
- the homogeneous flow in a cubic domain, with initial conditions and periodicity in the space directions,
- the inhomogeneous pipe flow, with initial and boundary conditions.

A pseudo-spectral space-time scheme issued for solving equations (1) (first case) or equation (4) (second case).

In the third case, equations (1) are solved by means of a pseudo-spectral scheme in the space directions and of a finite difference scheme on the time axis.

Other accurate time differencing techniques have been proposed : a technique of Taylor expansion was used by J. Gazdag for the Burgers and Vlasov equations (1973, ref. [1]), by R.M. Morf, S.A. Orszag and U. Frisch for investigating the singularities of Euler equations (1980, ref. [5]) and by P.R. Roy for the incompressible Navier-Stokes equations (1980, ref. [6].

II. INHOMOGENEOUS FLOW IN A CUBIC DOMAIN

Solution of the four equation (1) is obtained as a limit of a sequence of approximate solutions (see ref. [4]) :

$$(8)\quad (\vec{U},P)^0,\ (\vec{U},P)^1,\ \ldots\ (\vec{U},P)^n,\ (\vec{U},P)^{n+1} \ldots \longrightarrow (\vec{U},P)^*$$

At each iteration (calculation of the $(n+1)^{th}$ approximation as a function of the $(n)^{th}$ one, the new set of functions $(\vec{U},P)^{n+1}$ is calculated of the entire space-time domain :

$$(9)\quad (x,t) \in [-1,+1]^3 \cdot [0,T]$$

The limit $(\vec{U},P)^*$ of this sequence is a space-time approximation of the flow solution.

Let us set :

$$(10)\quad \begin{cases} (a) & \tilde{\vec{U}} = \vec{U}^n + \vec{u} \\ (b) & \tilde{P} = P^n + p \end{cases}$$

where $(\vec{u}, p)$ the variation of the solution between iteration (n) and iteration (n + 1) is obtained by means of approximation of equations (1) :

$$(11)\quad \begin{cases} g_i(\tilde{\vec{U}}, \tilde{P}) = 0 & i = 1,2,3 \text{ or } 4 \\ \downarrow \\ g_i(\vec{U}^n + \vec{u}, P^n + p) = 0 \\ \downarrow \\ h_i^n(\vec{u}, p) + g_i(\vec{U}^n, P^n) = 0 \\ i = 1,2,3 \text{ or } 4 \end{cases}$$

The functions h_i^n are finite difference approximations of :

$$(12)\qquad g_i(\vec{U}^n+\vec{u},P^n+p)-g_i(\vec{U}^n,P^n)$$

Each iteration consists of three steps :

- calculation of the residues g_i ($\vec{U}^n$, P^n) by pseudo-spectral expansions on a basis of Chebyshev polynomials of $\vec{U}^n$ and P^n,
- calculation of the variation $\vec{u}$, and p by solving the four equation (11),
- calculation of the new values :

$$(13)\quad \text{(a)}\ \vec{U}^{n+1}=\vec{U}^n+\sigma\vec{u}\qquad \text{(b)}\ P^{n+1}=P^n+\sigma p$$

where σ is under-relaxation coefficient calculated for convergence of the method (e.g. S.A. Orszag [7] and Mc Crory and Orszag [8])

II.1. Residue calculation

For each space or time direction the unknown functions are expanded on a basis of first kind Chebyshev polynomials.

By formal derivation, we obtain then the expansions of the partial derivatives and, by means of Fart Fourier Transform, the values of the partial derivatives at the Chebyshev collocation points.

II.2. Variation calculation

Let us set :

$$(14)\quad \text{(a)}\ D_t \# \frac{\partial}{\partial t}\qquad \text{(b)}\ D_i \# \frac{\partial}{\partial x_i}\qquad \text{(c)}\ D^2 \# \Delta$$

where D_t, D_i, D^2 are finite difference approximations of the corresponding continuous operators.

Then equations (11) become :

$$(15)\quad \text{(a)}\ D_t u_i + D_j(u_i U_j^n + u_j U_i^n + u_i u_j) - \nu D^2 u_i + D_i p + g_i^n = 0$$

$$\text{(b)}\ D_\alpha u_\alpha + g_4^n = 0$$

where $g_i^n = g_i(\vec{U}^n, P^n)$

Instead of solving (15.b), we use the divergence of (15.a) and by taking (15.b) into account, we obtain a Poisson equation for the pressure variation p :

$$(16)\quad D^2 p + D_i g_i^n + \nu D^2 g_4^n - D_t g_4^n + D_i D_j(u_i U_j^n + u_j U_i^n + u_i u_j) = 0$$

The associate boundary conditions are Neumann conditions given by (15.a).

For convergence and cost of the method, the choice of finite difference approximation D_t, D_i and D^2 is important (ref. [4], [7], [8]).

Two kinds of approximations are used for space derivatives :

- central second order approximations on the Chebyshev collocation points,
- same approximations on a finer grid (for these new points, residues are calculated by means of Chebyshev interpolations).

For time derivative, a first order scheme is used :

- implicit for the diffusive term,
- explicit for the convective terms.

III. HOMOGENEOUS FLOW IN A CUBIC DOMAIN

Similarly, the solution of equations (4) can be computed as a limit of the following sequence :

$$(17)\quad (\vec{U},\vec{\pi})^0,\ \ldots\ (\vec{U},\vec{\pi})^n,(\vec{U},\vec{\pi})^{n+1},\ \ldots \to (\vec{U},\vec{\pi})^*$$

Each iteration is slightly modified.

- calculation of residues $\vec{g}_i^n$ by pseudo-spectral Fourier series expansions of $\vec{U}^n$ and $\vec{\pi}^n$,
- calculation of the variation $\vec{u}$, $\vec{\pi}$ by solving the four equations :

$$(18)\qquad \vec{h}_i^n(\vec{u},\vec{\pi})+\vec{g}_i^n=0$$

where

$$(19)\qquad \vec{g}_i^n=\vec{g}_i(\vec{U}^n,\vec{\pi}^n)$$

and where $\vec{h}_i^n$ are approximations of

$$\vec{g}_i(\vec{U}^n+\vec{u},\vec{\pi}^n+\vec{\pi})-\vec{g}_i^n$$

$$(20)\quad \text{(a)}\ \vec{h}_i^n(\vec{u},\vec{\pi}) \# \frac{\partial \vec{u}_i}{\partial t}+\frac{\partial \vec{\pi}_i U_j^n+\vec{U}_j^n\vec{\pi}_i+\vec{\pi}_i\vec{u}_j}{\partial x_j}-\bar{\nu}\Delta\vec{u}_i+\frac{\partial \vec{\pi}}{\partial x_i}$$

$$\text{(b)}\ \vec{h}_\alpha^n(\vec{u},\vec{\pi}) \# \frac{\partial \vec{u}_\beta}{\partial x_\beta}$$

where $\bar{\nu}$ is a mean value (at given t) of $\nu+\nu_T$.

Instead of finite difference schemes for space partial derivative approximations, we use Fourier expansions on the space axes. The only differences between operators $\vec{h}_i^n$ and $\vec{g}_i^n$ are then due to non linearity of the Navier-Stokes equations and to time discretization.

These are calculated by Chebyshev polynomial expansions (for the residues $\vec{g}_i^n$) and by finite difference approximations (for the operators $\vec{h}_i^n$).

The similarity of the operators $\vec{h}_i^n$ and $\vec{g}_i^n$ insures the convergences of the method (e.g. ref [3], [4], [7], [8]).

IV. PIPE FLOW (WITH TRANSVERSAL SQUARE SECTION).

Equations (1) are to be solved in the domain :

$$\Omega=[-1,+1]\times[-1,+1]\times[0,L]$$

with no-slip conditions on the boundaries :

$$x=\pm 1 \quad \text{or} \quad y=\pm 1$$

with up-stream conditions :

$$(21)\qquad \vec{U} \text{ given for } y=0$$

and with down-stream conditions :

$$(22)\qquad \frac{\partial \vec{U}}{\partial y}=0 \quad \text{for } y=L$$

A leap-Frog scheme is used for time discretization and equation (1) gives us :

$$(23)\quad \text{(a)}\ \frac{U_i^{n+1}-U_i^n}{2\delta t}+\frac{\partial (U_i U_j)^n}{\partial x_j}-\frac{\nu}{2}(\Delta U_i^{n+1}+\Delta U_i^{n-1})+\frac{1}{2}\left(\frac{\partial P^{n+1}}{\partial x_i}+\frac{\partial P^{n-1}}{\partial x_i}\right)=0$$

$$\text{(b)}\ \frac{\partial U_\alpha^{n+1}}{\partial x_\alpha}=0$$

with $U_i^n = U_i(n\cdot\delta t)$

where δt is the time step.

Let us set :

$$A_i^{\widetilde{n}} = -U_i^{\widetilde{n-1}}/\delta t + 2\,\frac{\partial (U_i U_j)^{\widetilde{n}}}{\partial x_j} - 2\Delta U_i^{\widetilde{n-1}} + \frac{\partial P^{\widetilde{n-1}}}{\partial x_i} \tag{24}$$

Then equation (23.a) becomes :

$$\frac{U_i^{\widetilde{n+1}}}{\delta t} - \nu \Delta U_i^{\widetilde{n+1}} + \frac{\partial P^{\widetilde{n+1}}}{\partial x_i} + A_i^{\widetilde{n}} = 0 \tag{25}$$

And by taking into account equation (23.b), we obtain a Poisson equation for P^{n+1} :

$$\Delta P^{n+1} + \frac{\partial A_\ell^{\widetilde{n}}}{\partial x_\ell} = 0 \tag{26}$$

with Neumann boundary conditions given by (25).

Because of the boundary conditions for the pressure P^{n+1}, equations (25) and (26) are solved simultaneously (for $t = t_{n+1}$). For each time level, an iterative process, similar to the unsteady previous one (equations (11), (12)), is then developped :

- for a given approximation $(\vec{U}, P)^*$ of $(\vec{U}, P)^{n+1}$, the residual values of equations (25) and (26) are calculated by means of Chebyshev polynomial expansions :

$$\begin{cases} \text{(a)} & R_i^* = \dfrac{U_i^*}{\delta t} - \nu \Delta U_i^* + \dfrac{\partial P^*}{\partial x_i} + A_i^{\widetilde{n}} \\ & \qquad i = 1, 2 \text{ or } 3 \\ \text{(b)} & R_4^* = \Delta P^* + \dfrac{\partial A_\ell^{\widetilde{n}}}{\partial x_\ell} \end{cases} \tag{27}$$

for a given value of $t = t_{n+1}$,

- a better approximation of $(\vec{U}, P)^{n+1}$ is then obtained by solving a set of four partial differential equations for the variation $(\vec{u}, p)$:

$$\begin{cases} \text{(a)} & \dfrac{u_i}{\delta t} - \nu D^2 u_i + D_i p + R_i^* = 0 \\ \text{(b)} & D^2 p + R_4^* = 0 \end{cases} \tag{28}$$

with boundary conditions for $\vec{u}$:

$$\begin{cases} \text{(a)} & \vec{u} = 0 \quad \text{for } |x| = 1 \text{ or } |y| = 1 \text{ or } z = 0 \\ \text{(b)} & \dfrac{\partial \vec{u}}{\partial z} + \dfrac{\partial U^*}{\partial z} = 0 \quad \text{for } z = L \end{cases} \tag{29}$$

and for p :

$$D_i p + \frac{u_i}{\delta t} - \nu D^2 u_i + R_i^* = 0 \tag{30}$$

with :

$$\begin{cases} i = 1 \longleftrightarrow x = \pm 1 \\ i = 2 \longleftrightarrow y = \pm 1 \\ i = 3 \longleftrightarrow z = 0 \text{ or } L \end{cases}$$

D_i and D^2 (see (14)) are finite difference approximations of $\partial/\partial x_i$ and Δ.

The new value of $(\vec{U}, P)^{n+1}$ is then :

$$(\vec{U}^* + \sigma \vec{u},\ P^* + \sigma p) \tag{31}$$

where σ is an under relaxation coefficient.

V. RESULTS

V.1. Non homogeneous flow in a cubic domain

An exact Taylor-Green solution is compared with the results of a pseudo-spectral space-time calculation (with Chebyshev expansions in the four space-time directions).

Let us set :

$$\vec{U} = \overrightarrow{curl}\,(\vec{\psi}) \tag{32}$$

with

$$\vec{\psi} \begin{cases} \psi_x = 0 \\ \psi_y = -\alpha \cos(\lambda x) \cos\left(\lambda \dfrac{z+1}{\sqrt{2}}\right) \\ \psi_z = -\psi_y \end{cases} \tag{33}$$

$$\alpha = \exp(-2\nu t \lambda^2)/2\lambda \qquad \lambda = \pi/2$$

For a Reynolds number of 20 and 9x 9x 9x 5 harmonics, figure (1) shows the variation of the isobaric lines on three faces of the cubic domain. The differences betweer theoretical and computed values are less than 10^{-5}.

Remark .

Calculation of the solution on the entire time domain can be performed successively in time subdomains. Initial conditions in a given subdomain are then the values of the solution, obtained in the previous subdomain, for the final value of t.

V.2. Homogeneous flow in a cubic domain

The pseudo-spectral space-time method has been compared with a finite difference method developed at Stanford University (ref [2]).

A Gaussian filter is used :

$$G(X', X) = \left(\sqrt{\frac{\gamma}{\pi}}\,\frac{1}{\Delta_a}\right)^3 \exp\left(-\gamma \|X - X'\|^2/\Delta_a^2\right) \tag{34}$$

with (ref. [2])

$$\begin{cases} \gamma = 6. \\ \Delta_a = 2 \cdot \Delta \\ \Delta = \text{mesh size} \end{cases} \tag{35}$$

For the Smagorinski closure model, we take (ref. [2])

$$c = .206$$

Starting from the same energy spectrum, calculations are done with 16^3 collocation points for the two methods.

It appears then that skewness but not energy is very sensitive to space-time scheme (see fig. 2 and 3).

When local characteristics of the flow (such as skewness) are needed an accurate calculation of time derivatives is then necessary and a pseudo-spectral space-time formulation answers the requirements of precision.

V.3. Pipe flow (with transversal square section)

The following up-stream condition are used (for $z = 0$) :

$$\begin{cases} \text{(a)} & U_1 = 0 \\ \text{(b)} & U_2 = 0 \\ \text{(c)} & U_3 = (1 - x^{2q}) \cdot (1 - y^{2q}) \cdot \left(1 + \beta(t)\, U_3^*(x, y)\right) \end{cases} \tag{36}$$

where U_3^* is a random function with :

(37) $$|U_3^*(x, y)| < 1$$

and where :

(38) $$f(t) = \lambda \cdot (1 - \cos(\omega_t \cdot t))$$

Calculations are done with :

(39)
$$\begin{cases} R_e = 300 \quad (= 1./\nu) \\ q = 1 \qquad (36\text{-}c) \\ \lambda = .01 \qquad (38) \\ \omega_t = 20.\pi \\ \delta t = .04 \end{cases}$$

For such a laminar flow, figures 4 and 5 show the evolution of isobaric lines (in the plan y = 0) at the beginning of calculation.

More details on the movement of isobaric surfaces during the displacement of perturbations across the pipe are shown in a movie.

For the implementation of turbulent simulation, an important work is actually done :

- the number of harmonics is increased,
- the upstream conditions are modified by introducing an unstable perturbation,
- a closure model is developed.

V. CONCLUSIONS

Some pseudo-spectral formulations have been implemented for resolution of unsteady Navier-Stokes equations. Finite difference scheme as well as pseudo-spectral scheme have been used and compared for calculation of time derivatives.

For inhomogeneous flows (cubic domain or square pipe), both schemes can be used and for given accuracy, it seems that the second one can be competitive.

The implementation of algebraic models has been done (for homogeneous isotropic flows) but with such a small number of harmonics a more elaborate closure technique shall be necessary especially for non isotropic flows.

REFERENCES

[1] GAZDAG, J. - "Numerical convective schemes based on accurate computation of space derivatives", J. Comput. Phys. Vol. 13 (1973), pp. 100-113.

[2] KWAK, D., REYNOLDS, W.C. and FERZIGER, J.H. - "Three dimensional Time Dependent Computation of Turbulent Flow", STANFORD UNIVERSITY, Report n° TF-5, May 1975.

[3] MORCHOISNE, Y.F. - "Résolution des équations de Navier-Stokes par une méthode pseudo-spectrale en espace-temps (Resolution of Navier-Stokes equations by a space-time pseudo-spectral method", La Recherche Aérospatiale n° 1979-5, pp. 293-306 (English translation ESA TT-613).

[4] MORCHOISNE, Y.F. - "Pseudo-spectral space-time calculations of incompressible viscous flows", AIAA 19th Aerospace Sciences Meeting, Saint LOUIS, AIAA paper n° 81-0109 (1981).

[5] MORF, R.H., ORSZAG, S.A., and FRISCH, U. "Spontaneous singularity in three-dimensional, inviscid, incompressible flow", Phys. Review Letters, Vol. 44.9 (1980), pp. 572-575.

[6] ROY, Ph., "Résolution des équations de Navier-Stokes par un schéma de haute précision en espace et en temps (Resolution of Navier-Stokes equations by a method of high accuracy in space and time)", La Recherche Aérospatiale n° 1980-6, pp. 373-385 (English translation).

[7] ORSZAG, S.A., "Spectral Methods for problems in complex Geometries", J. of Comp. Phys., Vol. 37 (1980), pp. 70-92.

[8] Mc CRORY, R.L. and ORSZAG, S.A. - "Spectral Methods for Multidimensional Diffusion Problems", J. of Comp. Phys., Vol. 37,(1980), pp. 93-112.

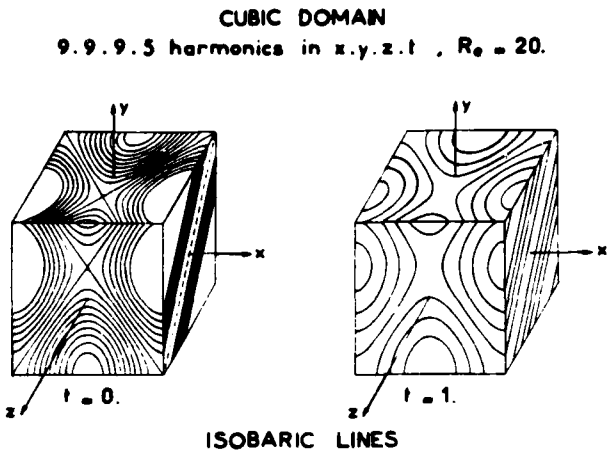

Figure 1

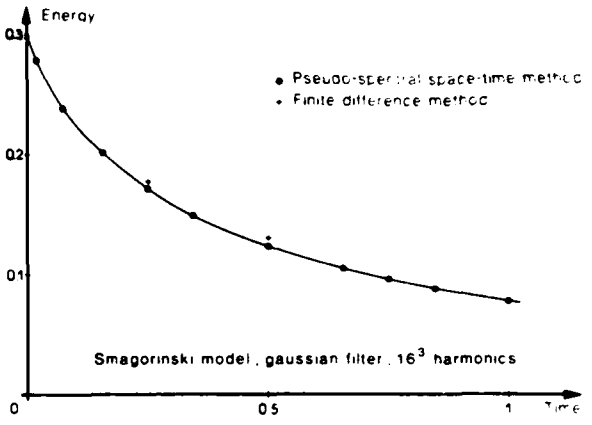

Figure 2

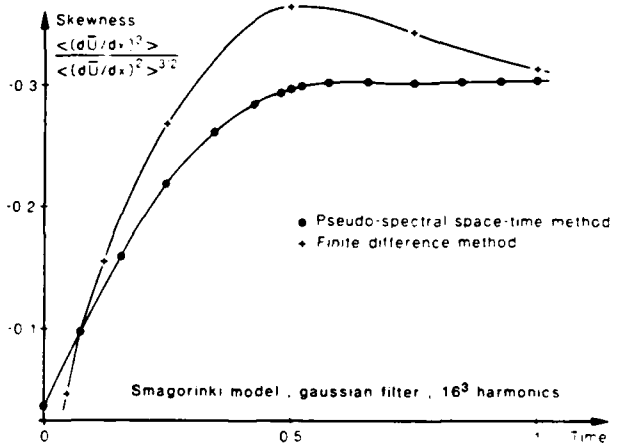

Figure 3

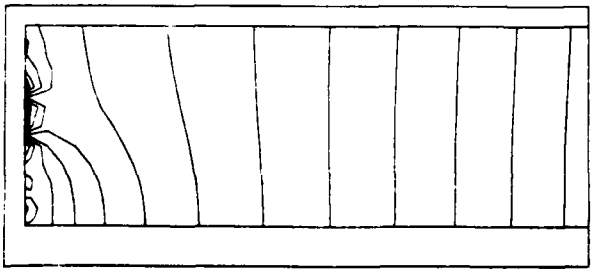

Pipe flow , Re=300
17^3 harmonics , t=.012

Figure 4

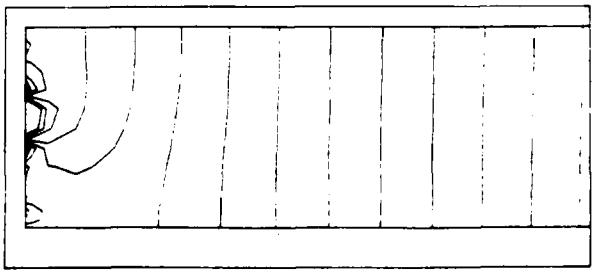

Pipe flow , Re=300
17^3 harmonics , t=.080

Figure 5

THE DISTORTION OF TURBULENT SHEAR FLOW UPSTREAM OF A BODY

J. C. Wyngaard

National Center for Atmospheric Research

P. O. Box 3000, Boulder, Colorado 80307

ABSTRACT

We present a simple method for calculating body-induced flow distortion effects on turbulent flow in the limit of turbulence integral scale very large compared to the body size. The approach is directly applicable to the problem of probe-induced distortion of turbulence measurements. We apply the method to the low Mach number flow approaching a body of revolution, and present contours of the flow-distortion parameters ahead of the body. We show that while second-order models cannot treat this problem, they should be able to treat the other extreme, where the turbulence scale is small compared to the body size.

NOMENCLATURE

a	body length scale
a_{ij}	distortion coefficient tensor, (3)
A_{ij}	angle of attack part of a_{ij}, (8)
F	body fineness ratio, (15)
L	axisymmetric body length
L_x	turbulence integral scale
p	fluctuating pressure
r	radial coordinate
S	body cross-sectional area
t	time
T_{ij}	thickness part of a_{ij}, (8)
U_i	total velocity field, $U_i + u_i$
U_i	mean velocity field
u_i	turbulent velocity field
V	free-stream speed
x_i	spatial coordinate
α	angle of attack of free-stream flow
ϵ_{ij}	deviatoric distortion tensor (4)
ϕ	disturbance velocity potential
ω	angular coordinate

superscripts

$(\tilde{\ })$	distorted quantity

INTRODUCTION

Traditional, <u>in-situ</u> sensors inevitably cause distortion of the velocity field being measured. In geophysical applications, the measuring platform (e.g. aircraft, balloon, towed body, meteorological mast, buoy) also contributes to this distortion, which can be severe enough to induce large errors in turbulence statistics.

Perhaps the most complete study to date of the effect of body-induced flow distortion on turbulence is that of Hunt (1). He showed that flow-distortion effects on turbulence are quite different in the limits $a/L_x \to 0$ and $a/L_x \to \infty$, where a is the body scale and L_x is the integral scale of the approaching turbulence.

Good experimental practice dictates that the scale a of probes and probe supports should be minimized, and since geophysical turbulence tends to have large integral scales, its measurement will almost always involve small values of a/L_x. As Hunt has shown, the flow-distortion theory in this limit is simpler than that for $a/L_x \to \infty$.

We will discuss here an approach to the probe-induced flow-distortion problem for $a/L_x \to 0$ which, while equivalent to Hunt's, seems simpler to apply; we also will show why second-order models cannot calculate flow distortion effects for $a/L_x \to 0$, but suggest that they should be able to do problems with $a/L_x \to \infty$.

A TURBULENCE DISTORTION THEORY FOR $a/L_x \to 0$

Hunt (1) has shown that for turbulence approach flow with $a/L_x \to 0$ the velocity field ahead of the body can be considered irrotational and steady, and Wyngaard (2) has argued that this is true even if the undisturbed flow carries mean shear and turbulent shear stress. Thus one can calculate the distortion effects using potential flow techniques. We will summarize here the method proposed by Wyngaard (2).

We assume that the distorted flow field $\tilde{u}_i(\underset{\sim}{x})$ ahead of the body, having a mean part $\tilde{U}_i$ and a turbulent part $\tilde{u}_i$, is an analytic function of the undistorted oncoming flow:

$$\tilde{U}_i = \tilde{U}_i + \tilde{u}_i = \tilde{U}_i(\underset{\sim}{x}, U_1 + u_1(t), u_2(t), u_3(t)) \qquad (1)$$

By expanding (1) in a Taylor series about the basic state of unidirectional upstream flow, i.e. about $U_i = (U_1,0,0)$ one finds an expression for the distorted turbulence field. Keeping only the first (linear) terms, this is

$$\tilde{u}_i(\underset{\sim}{x},t) = a_{ij}(\underset{\sim}{x})u_j(t) \qquad (2)$$

where we use the summation convention. The a_{ij} are

$$a_{ij}(x) = \left.\frac{\partial \tilde{u}_i(x)}{\partial u_j}\right|_0 \qquad (3)$$

and hence are calculable from potential flow theory. The linear truncation (2) should be adequate for most applications to flow measurements.

In the absence of the body $a_{ij} = \delta_{ij}$, and (2) indicates no distortion, i.e., $\tilde{u}_i(x,t) = u_i(t)$. When a body distorts the flow a_{ij} is no longer diagonal and "crosstalk" is induced among the turbulence components. Thus we express the a_{ij} as

$$a_{ij} = \delta_{ij} + \varepsilon_{ij} \qquad (4)$$

where $\varepsilon_{ij} \to 0$ as distortion effects vanish.

Crosstalk effects are particularly important for shear stress, say u_1u_3. Ahead of a two-dimensional body, for example, the distorted turbulent components are

$$\begin{aligned} \tilde{u}_1 &= (1+\varepsilon_{11})u_1 + \varepsilon_{13}u_3 \\ \tilde{u}_3 &= \varepsilon_{31}u_1 + (1+\varepsilon_{33})u_3 \end{aligned} \qquad (5)$$

Thus the stress in the region of distortion is, to first order in ε_{ij},

$$\begin{aligned} \overline{\tilde{u}_1\tilde{u}_3} = {} & \varepsilon_{31}\,\overline{u_1^2} \\ & + (1+\varepsilon_{11}+\varepsilon_{33})\,\overline{u_1u_3} \\ & + \varepsilon_{13}\,\overline{u_3^2} \end{aligned} \qquad (6)$$

Eq. (6) indicates that a stress will be induced even if the free-stream value $\overline{u_1u_3}$ is zero. This relative stress departure can be quite large if the correlation coefficient between u_1 and u_3 is small. Wyngaard (2) has calculated the ε_{ij} for a circular cylinder (with and without a wake) and for a wakeless sphere.

DISTORTION BY AXISYMMETRIC BODIES

In the case of distortion ahead of axisymmetric bodies (e.g., aircraft nose booms, towed bodies), we write the distorted flow field as

$$\tilde{u}_i = u_i + \phi_{1,i} + \phi_{2,i} \qquad (7)$$

where u_i is the approach flow, and ϕ_1 and ϕ_2 are the disturbance velocity potentials for "thickness" and "angle-of-attack" effects, respectively, and a comma denotes differentiation. Thus

$$\begin{aligned} \left.\frac{\partial \tilde{u}_i}{\partial u_j}\right|_0 &= a_{ij} = \delta_{ij} + \varepsilon_{ij} \\ &= \delta_{ij} + T_{ij} + A_{ij} \end{aligned} \qquad (8)$$

where the thickness and angle-of-attack coefficients are defined by

$$T_{ij} = \left.\frac{\partial \phi_{1,i}}{\partial u_j}\right|_0 \qquad A_{ij} = \left.\frac{\partial \phi_{2,i}}{\partial u_j}\right|_0 \qquad (9)$$

For an axisymmetric body whose axis is along the x_1-direction, T_{ij} and A_{ij} have the forms

$$T_{ij} = \begin{bmatrix} T_{11} & 0 & 0 \\ T_{21} & 0 & 0 \\ T_{31} & 0 & 0 \end{bmatrix} \qquad A_{ij} = \begin{bmatrix} 0 & A_{12} & A_{13} \\ 0 & A_{22} & A_{23} \\ 0 & A_{32} & A_{33} \end{bmatrix} \qquad (10)$$

Symmetries reduce the number of independent components of T_{ij} and A_{ij}. Using Fig. 1, with $x_3 = r\cos\omega$ and $x_2 = -r\sin\omega$, we see that

$$\begin{aligned} T_{21} &= -T(r)\sin\omega \\ T_{31} &= T(r)\cos\omega \end{aligned} \qquad (11)$$

so that there are only two independent components of T_{ij}. Similarly, we see that

$$\begin{aligned} A_{12}(x_1,r,\omega) &= A_{13}(x_1,r,\omega+\pi/2) \\ A_{22}(x_1,r,\omega) &= A_{33}(x_1,r,\omega+\pi/2) \\ A_{32}(x_1,r,\omega) &= -A_{23}(x_1,r,\omega+\pi/2) \end{aligned} \qquad (12)$$

Thus A_{ij} has only three independent components.

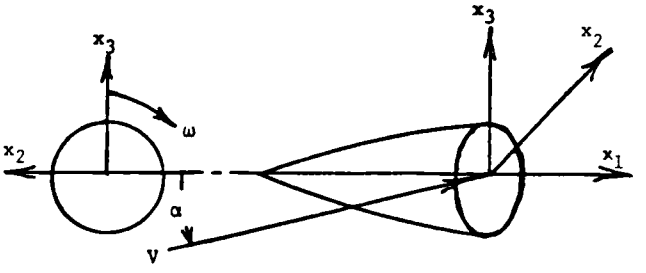

Fig. 1 Coordinate system for axisymmetric body problem

For slender bodies T_{ij} and A_{ij} can be calculated by the methods discussed by Laitone (3,4). We start with the expressions

$$\begin{aligned} \phi_1 &= -\frac{V}{4\pi}\int_0^L \frac{S'(y)}{[(x_1-y)^2+r^2]^{1/2}}\,dy \\ \phi_2 &= -\frac{V\,\alpha r\cos\omega}{2\pi}\int_0^L \frac{g(y)}{[(x_1-y)^2+r^2]^{3/2}}\,dy \end{aligned} \qquad (13)$$

The function g is

$$g(y) = S(y)\left(1 - \frac{S''(y)}{4\pi}\,\mathrm{Ln}\,\frac{S}{\pi L^2}\right) \qquad (14)$$

and the function S represents the cross-sectional area as a function of axial distance; primes denote derivatives.

The differentiation of ϕ_1 and ϕ_2 with respect to x_i is straightforward, as is the differentiation with respect to U_1. By (12) only differentiation with respect to one other velocity component (say U_3) is necessary, and this is done by using $\partial/\partial U_3 = (1/V)\,\partial/\partial\alpha$.

We have done these calculations for a parabola of revolution, whose cross-sectional area S varies as

$$S = \pi L^2(1-(2x_1/L)^2)^2/(4F^2) \qquad (15)$$

The results for the five independent components of T_{ij} and A_{ij}, using the body (15) with F = 6 and x_1 = -0.55 L (i.e., 0.05 body lengths or 0.30 maximum diameters upstream from the leading point) are shown in Figs. 2-5.

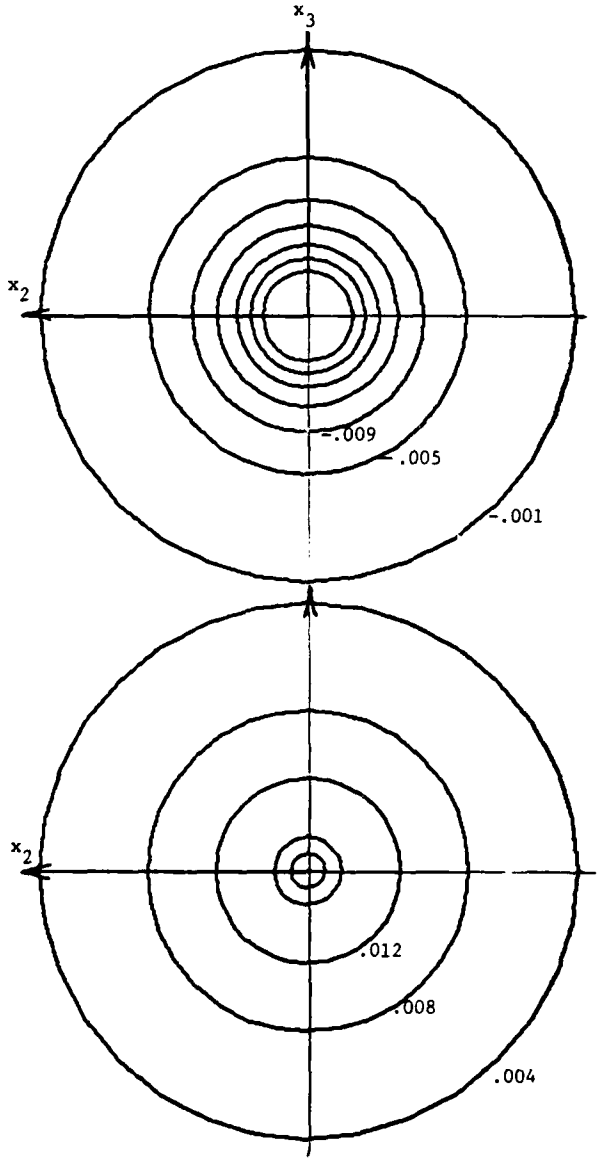

Fig. 2 Upper: T_{11} contours ahead of a parabola of revolution, (15), with F = 6 and x_1 = -0.55 L. Ends of axis arrows are r = L/2. Contour interval 0.004. Lower: same except T(r).

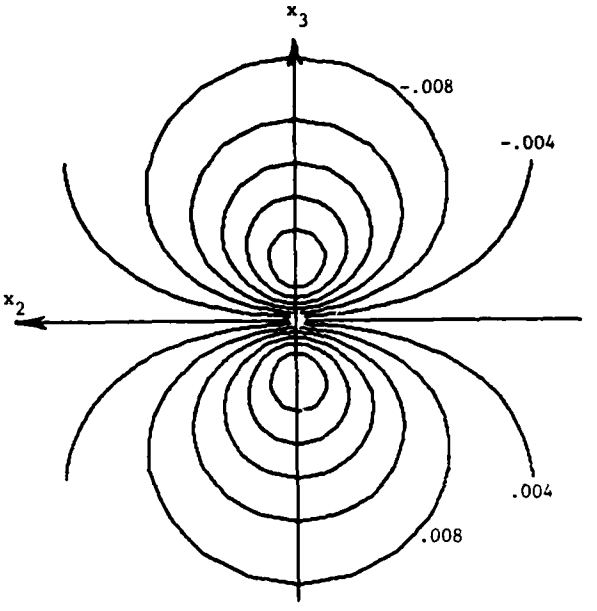

Fig. 3 Same as Fig. 2 except A_{13}. Contour interval 0.004.

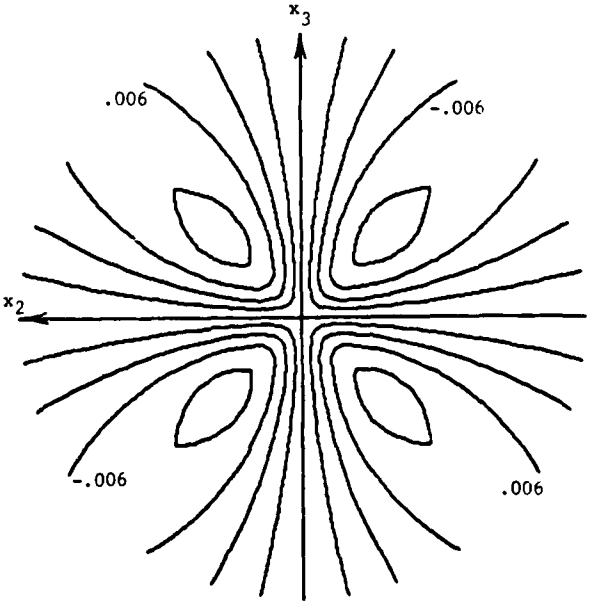

Fig. 4 Same as Fig. 2 except A_{23}. Contour interval 0.002.

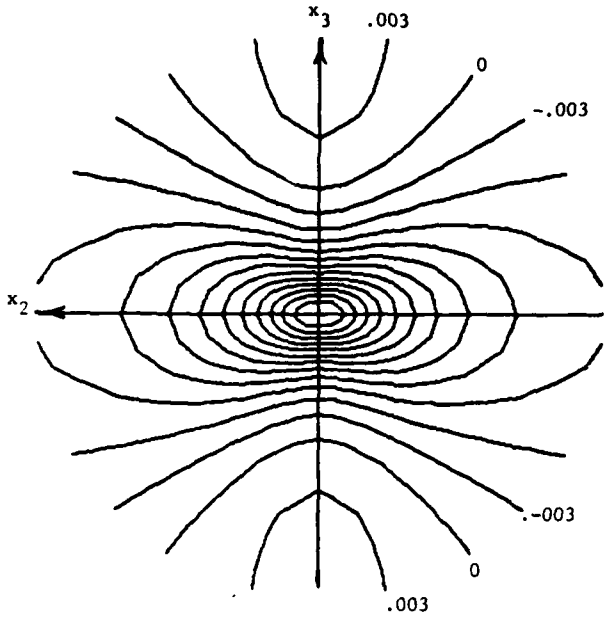

Fig. 5 Same as Fig 2 except A_{33}. Contour interval 0.003.

Results of the type shown in Figs. 2-5 are directly useful in probe design and in the interpretation of existing turbulence data. As an example, in geophysical applications a common problem is the contamination of the vertical velocity component (u_3) with the horizontal ones, which can be much larger in amplitude and have much different low-wavenumber spectral characteristics. From (2), (8), and (10) we see that the measured u_3 component is

$$\tilde{u}_3 = T_{31}\, u_1 + A_{32}\, u_2 + (1 + A_{33})\, u_3 \qquad (16)$$

Our results show that the crosstalk indicated by (16) can be minimized by the body design, or by combining signals from different positions chosen such that the asymmetries in the crosstalk coefficients cause them to vanish identically.

SECOND-ORDER MODELING

In principle one can calculate flow-distortion effects on turbulence variances and covariances through the appropriate second-moment equations. This "second-order modeling" approach is now used in a wide variety of applications, from geophysics (Zeman (6)) to engineering (Reynolds (7)).

Certain second-moment equations, particularly those for turbulent shear stress, are dominated by turbulent pressure covariance terms. Since the turbulent pressure field is also distorted by the body, it is necessary to account for this distortion in parameterizing these pressure terms in second-order models.

The Poisson equation for fluctuating pressure $\tilde{p}$ ahead of a body is

$$\tilde{p}_{,ii} = -2\tilde{U}_{i,j}\tilde{u}_{j,i} - \tilde{u}_{i,j}\,\tilde{u}_{j,i} + \overline{\tilde{u}_{i,j}\,\tilde{u}_{j,i}} \qquad (17)$$

The first term on the right will clearly be important here, since the body generates the mean distortion field $\tilde{U}_{i,j}$. Contemporary second-moment models assume, in their pressure covariance parameterizations, that mean shear varies little over a turbulent integral scale; this allows the mean shear to be taken outside the integral given by the solution of (17). Since in our problem the mean shear $\tilde{U}_{i,j}$ has spatial scale a, this requires a/L_x large. Thus in principle second-order models provide a means of calculating flow-distortion effects on turbulence for large values of a/L_x, but they will fail for small a/L_x.

ACKNOWLEDGEMENTS

I am indebted to Marilyn Hampy, who diligently performed the integrations for the axisymmetric body and prepared the contour plots, and to Dorene Howard, who skillfully typed the manuscript.

REFERENCES

1. Hunt, J.C.R., "A theory of turbulent flow round two-dimensional bluff bodies', J. Fluid Mech., 61, 1973, pp 625-706.
2. Wyngaard, J. C., "The effects of probe-induced flow distortion on atmospheric turbulence measurements", to appear, J. Appl. Meteorology, 20, July 1981
3. Laitone, E. V., "The subsonic flow about a body of revolution", Quart. Appl. Math., 5, No. 2, 1947, pp 227-231.
4. Laitone, E. V., "The linearized subsonic and supersonic flow about inclined slender bodies of revolution", J. Aero. Sci., 14, No. 11, 1947, pp 631-642.
5. Letko, W. and Danforth, E.C.B., "Theoretical investigation at subsonic speeds of the flow ahead of a slender inclined parabolic-arc body of revolution and correlation with experimental data obtained at low speeds", NACA Tech Note 3205, July 1954.
6. Zeman, O., "Progress in the modeling of planetary boundary layers", Ann. Rev. Fluid Mech., 13, 1981, pp 253-272.
7. Reynolds, W. C., "Computation of turbulent flows", Ann. Rev. Fluid Mech., 8, 1976, pp 183-208.

SECOND ORDER CLOSURE FOR VARIABLE DENSITY FREE SHEAR LAYER

Dany Vandromme* & Wolfgang Kollmann**

Von Karman Institute
Belgium

ABSTRACT

A full second order closure turbulence model for the prediction of free shear flows with variable density is developed. The importance of density fluctuations due to inhomogeneities in fluid composition is emphasized. Some simplicity is achieved by using density weighted averaging to account implicitly for density fluctuation effects. Transport equations for various second order correlations - such as Reynolds stress, turbulent mass fluxes or density velocity correlations - are derived, modelled and solved, together with the mean equations for momentum and species conservation. Solutions of these equations are compared with the two different sets of experimental data for low speed free mixing layers (helium into nitrogen and freon 12 into air).

NOMENCLATURE

C_I	I-specie mass fraction
D	velocity divergence
k	turbulent kinetic energy
P	pressure
T_c	triple correlation
v_α/v_β	velocity components
α	Falkner Skan parameter
$\delta_{\alpha\beta}$	Kronecker symbol
δ_1, δ_2	characteristic thicknesses
ε	kinetic energy dissipation rate
$\varepsilon_{\alpha\beta}$	dissipation rate tensor
ϕ_o	velocity ratio
ρ	density
σ	spreading rate parameter
$\tau_{\alpha\beta}$	laminar stress tensor
$\bar{(\ )}, (\ )'$	conventional averaging
$\tilde{(\ )}, (\ )''$	density weighted averaging
$C_\varepsilon, C_{\varepsilon 1}, C_{\varepsilon 2}, C_{\varepsilon 3}, C_{\varepsilon 4}, C_c, C_1, C_2, C_3, C_{\phi 1}, C_{\phi 2}, C_{UDP}, C_{P2}$, $C_{DS}, C_{c1}, C_{c2}, C_c, C_Q, C_{Q1}, C_{Q2}$	modelling constants

* present address: NASA-Ames Research Center, Moffett Field, CA 94035

** present address: Department of Mechanical Engineering, University of California, Davis, California 95616.

INTRODUCTION

The prediction of the mean motion of a chemically homogeneous fluid depends on the evaluation of the Reynolds stress (double velocitiy fluctuation correlations) that appear in the mean momentum equation for turbulent flow. Similarly, the evaluation of the mean species concentrations or temperatures from their conservation equations requires the definition of the local correlations of fluctuations of velocity and temperature and/or species concentration. Early models of turbulence related these correlations (or fluxes of momentum, heat or mass of species) only to the mean values of velocity, temperature or concentration. Many years ago Boussinesq [1] related the flux term of the momentum equation to the mean velocity gradient and an eddy viscosity. Such a relationship functionally similar to the Newton's law of viscosity has been used in a large variety of turbulent models. For all of them the main task is to derive a suitable form for the eddy viscosity. Heat and species flux relationship required further assumptions regarding turbulent Prandtl or Schmidt numbers.

The present paper presents a set of turbulence equations closed at a higher level. Transport equations are derived, modelled and solved directly for second order moments (Reynolds stress and the turbulent mass flux) to avoid the questionable concept of eddy viscosity. Several investigations have dealt with this closure level (e.g., references [2] to [8]) but only two [6,8] have considered variable density flows. This study is restricted to density variations caused by inhomogeneities in fluid composition and does not consider compressibility effects typical of high speed or chemically reacting flows. To achieve checks against experimental data, two different flows are considered:

- low speed mixing layer of helium and nitrogen [9]
- low speed mixing layer of freon 12 and air [10]

In the next section, equations for the different variables and correlations are commented on. Then the necessary modelling assumptions are presented. The fourth section gives some details about the numerical method used to solve the set of equations, the boundary conditions, and the amount of CPU time for a typical run. Then the results are compared with the experimental data

and discussed. The last section summarizes the results obtained so far and suggests future directions for the use of this closure to the solution of more general turbulence problems.

EXACT EQUATIONS

To account implicitly for variable density effects in all the equations, it is helpful to work with mass weighted variables rather than conventionally (time) averaged quantities. This yields a mean mass conservation equation having a similar form to the instantaneous one, and convection terms of all the transport equations forms similar to instantaneous substantial derivatives. The main disadvantage of that averaging is to produce a more complicated equation for turbulent kinetic energy dissipation rate. Nevertheless, since all the terms of the dissipation equation even when conventionally averaged have to be modelled, the additional complications are merely treated as model modifications. Although the main advantage of the mass weighted averaging is to avoid the use of density velocity correlations, it is necessary to evaluate them to refine the determination of third order correlations and to deal with the mean pressure gradient terms. Thus transport equations for density velocity correlations are included in this model. Nevertheless the convective mean terms keep their exact form and stay density correlation free. The exact equations are not reproduced here because of their length but can be found in reference [11].

MODELLING ASSUMPTIONS

Reynolds stress

Diffusion terms

$$- \frac{\partial}{\partial x_\lambda}\left[\bar{\rho}\,\widetilde{v''_\alpha v''_\beta v''_\gamma} + \delta_{\alpha\beta}\overline{v''_\gamma P'} + \delta_{\alpha\gamma}\overline{v''_\beta P'} - \overline{\tau_{\alpha\beta}v''_\gamma} - \overline{\tau_{\alpha\gamma}v''_\beta}\right]$$

The diffusive transport exists in three different forms. The first one can be identified as the turbulent diffusion, the second as the pressure diffusion and the last one as the viscous diffusion.

*Turbulent diffusion. To express this third order correlation, we use a procedure similar to Launder's [2]. Considering the transport equation for the mass weighted third order velocity correlation, we can simplify it by keeping only the leading terms.

$$- \frac{\partial}{\partial x_\delta}\left(\bar{\rho}\widetilde{v''_\alpha v''_\beta v''_\gamma v''_\delta}\right) + \widetilde{v''_\alpha v''_\beta}\frac{\partial}{\partial x_\delta}\left(\bar{\rho}\,\widetilde{v''_\delta v''_\gamma}\right)$$

$$+ \widetilde{v''_\alpha v''_\gamma}\frac{\partial}{\partial x_\delta}\left(\bar{\rho}\,\widetilde{v''_\delta v''_\beta}\right) + \widetilde{v''_\beta v''_\gamma}\frac{\partial}{\partial x_\delta}\left(\bar{\rho}\,\widetilde{v''_\delta v''_\alpha}\right)$$

$$- \overline{v''_\beta v''_\gamma}\frac{\partial P'}{\partial x_\alpha} - \overline{v''_\beta v''_\alpha}\frac{\partial P'}{\partial x_\gamma} - \overline{v''_\gamma v''_\alpha}\frac{\partial P'}{\partial x_\beta} = 0 \qquad (1)$$

As for constant density flows, use is made of the assumption of quasi-normal velocity distribution, also known as the Millionshtchikov approximation. For velocity distribution nearly Gaussian, the triple velocity correlations are small and the fourth order correlation can be expressed in terms of second order correlations only, by the following formulae which is strictly fulfilled for the normal law.

$$\overline{v'_\alpha v'_\beta v'_\gamma v'_\delta} = \overline{v'_\alpha v'_\beta}\cdot\overline{v'_\gamma v'_\delta} + \overline{v'_\alpha v'_\gamma}\cdot\overline{v'_\beta v'_\delta} + \overline{v'_\alpha v'_\delta}\cdot\overline{v'_\beta v'_\gamma} \qquad (2)$$

From the definition of the mass weighted averaging the relationship between the fluctuations is:

$$v'_\alpha = v''_\alpha + \frac{\overline{\rho' v'_\alpha}}{\bar{\rho}} \qquad (3)$$

This equality allows rewriting the equation (2) in terms of mass weighted correlations. The new expression includes a large collection of density correlations, that are mostly negligible (see reference [11]). After reduction to the leading terms the fourth order mass weighted correlation can be expressed as

$$\widetilde{v''_\alpha v''_\beta v''_\gamma v''_\delta} = - k_\alpha \widetilde{v''_\beta v''_\gamma v''_\delta} - k_\beta \widetilde{v''_\alpha v''_\gamma v''_\delta} - k_\gamma \widetilde{v''_\alpha v''_\beta v''_\delta}$$

$$- k_\delta \widetilde{v''_\alpha v''_\beta v''_\gamma} + \widetilde{v''_\alpha v''_\beta}\cdot\widetilde{v''_\gamma v''_\delta} + \widetilde{v''_\alpha v''_\gamma}\cdot\widetilde{v''_\beta v''_\delta} + \widetilde{v''_\alpha v''_\delta}\cdot\widetilde{v''_\beta v''_\gamma} \qquad (4)$$

where $$k_\alpha = \frac{\overline{\rho' v'_\alpha}}{\bar{\rho}} = - \widetilde{v''_\alpha}$$

In case of constant density flows Hanjalić and Launder [2] assume that the last three terms of equation (1) are "adequately represented" by

$$\overline{v'_\beta v'_\gamma}\frac{\partial P'}{\partial x_\alpha} + \overline{v'_\beta v'_\alpha}\frac{\partial P'}{\partial x_\gamma} + \overline{v'_\gamma v'_\alpha}\frac{\partial P'}{\partial x_\beta} \sim \frac{\varepsilon}{k}\overline{v'_\alpha v'_\beta v'_\gamma} \qquad (5)$$

Assuming this relationship holds for constant density, we can obtain the corresponding relationship in terms of mass weighted quantities by using (3). This yields

$$\overline{v''_\beta v''_\gamma}\frac{\partial P'}{\partial x_\alpha} + \overline{v''_\beta v''_\alpha}\frac{\partial P'}{\partial x_\gamma} + \overline{v''_\gamma v''_\alpha}\frac{\partial P'}{\partial x_\beta} \sim \frac{\varepsilon}{k}\widetilde{v''_\alpha v''_\beta v''_\gamma} \qquad (6)$$

Assembling the equations (1), (4), and (6)

$$\widetilde{v''_\alpha v''_\beta v''_\gamma} = - \bar{\rho}\, c\, \frac{k}{\varepsilon}\left[\widetilde{v''_\gamma v''_\delta}\frac{\partial}{\partial x_\xi}\left(\widetilde{v''_\alpha v''_\beta}\right) + \widetilde{v''_\beta v''_\delta}\frac{\partial}{\partial x_\xi}\widetilde{v''_\alpha v''_\gamma}\right.$$

$$\left. + \widetilde{v''_\alpha v''_\delta}\frac{\partial}{\partial x_\delta}\widetilde{v''_\beta v''_\gamma}\right] + \frac{k}{\varepsilon}\frac{\partial}{\partial x_\delta}$$

$$\left[\bar{\rho}k_\alpha \widetilde{v''_\beta v''_\gamma v''_\delta} + \bar{\rho}\, k_\beta \widetilde{v''_\alpha v''_\gamma v''_\delta} + \bar{\rho}k_\gamma \widetilde{v''_\alpha v''_\beta v''_\delta}\right] \qquad (7)$$

c is a constant whose value will be given in the next section. If the density is constant equation (7) is strictly identical to the version of

references [2] and [3]. Thus the third order correlations are determined from a set of first order differential equations, which for boundary layer type flow is

$$A_1 \cdot T_c + A_2 \frac{\partial}{\partial y} (T_c) = A_3 \qquad (8)$$

A_1, A_2 and A_3 are functions of the turbulence time scale, the second order velocity correlations and the density correlations.

*Diffusive transport by pressure fluctuations. So far no satisfactory model has been used for this term. Most authors consider a combined modelling of the triple correlation with the pressure velocity correlation but none have modelled the pressure correlation separately. Lumley [7], Harlow and Nakayama [16] and Donaldson [5] proposed different relationships but none yields improvements of the flow description. Furthermore a number of experiments show that the turbulent energy budget virtually balances without including the unmeasured pressure transport term [17]. Therefore, it is neglected here.

*Diffusive transport by viscous effects. In the assumption of high Reynolds number flow, this contribution is negligible compared to the turbulent diffusive terms. Nevertheless we may ensure a minimal value to the diffusive term by including a constant laminar viscosity in it.

Mean pressure gradient term. As stated previously, the solution of density velocity correlation equations allows dealing with non-zero mean pressure gradient flows. As these terms are exact in the second order moment equations, no modelling assumption is required here.

Pressure-rate of strain correlation. The form to be used here is rewritten from the constant density version of Launder [2,3] in terms of mass weighted averaged quantities. Nevertheless, terms involving the mean dilatation, which do not contribute in constant density flows are retained here. The result is

$$\begin{aligned}
\overline{p'\left(\frac{\partial v''_\beta}{\partial x_\gamma} + \frac{\partial v''_\gamma}{\partial x_\beta}\right)} = & - c_1 \bar{\rho}\, \varepsilon \left[\frac{\widetilde{v''_\beta v''_\gamma}}{k} - \frac{2}{3}\delta_{\gamma\beta}\right] + \frac{c_2 + 8}{11}\bar{\rho} \\
& \cdot \left[\widetilde{v''_\beta v''_\delta}\frac{\partial \tilde{v}_\gamma}{\partial x_\delta} + \widetilde{v''_\gamma v''_\delta}\frac{\partial \tilde{v}_\beta}{\partial x_\delta}\right] - \frac{6\, c_2 + 4}{11}\bar{\rho} \\
& \cdot \left[\widetilde{v''_\beta v''_\gamma}\,\tilde{D} + \delta_{\gamma\beta}\widetilde{v''_m v''_\ell}\frac{\partial \tilde{v}_m}{\partial x_\ell}\right] \\
& + \frac{8\, c_2 - 2}{11}\bar{\rho}\left[\widetilde{v''_\gamma v''_\delta}\frac{\partial \tilde{v}_\delta}{\partial x_\beta} + \widetilde{v''_\beta v''_\delta}\frac{\partial \tilde{v}_\delta}{\partial x_\gamma}\right] \\
& - \frac{30\, c_2 - 2}{55}\left[\frac{\partial \tilde{v}_\beta}{\partial x_\gamma} + \frac{\partial \tilde{v}_\gamma}{\partial x_\beta}\right]\bar{\rho}\, k \\
& - \frac{40\, c_2 + 12}{55}\,\delta_{\gamma\beta}\,\bar{\rho}\, k\, \tilde{D} \qquad (9)
\end{aligned}$$

Dissipation. The last terms appearing in the Reynolds stress equation have a dissipative character. They correspond to the conversion process of mechanical energy into heat due to viscous effects. Arguing for the locally isotropic nature of dissipative processes at high Reynolds number, these terms can be expressed in terms of the dissipation rate of turbulent kinetic energy for which a transport equation is included in the present set.

$$\begin{aligned}
& - \overline{\tau_{\alpha\beta}\frac{\partial}{\partial x_\alpha}v''_\gamma} - \overline{\tau_{\alpha\gamma}\frac{\partial}{\partial x_\alpha}v''_\beta} = \bar{\rho}\,\varepsilon \\
& = -\frac{2}{3}\bar{\rho}\,\delta_{\gamma\beta}\,\varepsilon \qquad (10)
\end{aligned}$$

Modelled Reynolds stress equation. The previous assumptions lead to the following equation for the Reynolds stress:

$$\begin{aligned}
& \frac{\partial}{\partial t}\left(\bar{\rho}\,\widetilde{v''_\gamma v''_\beta}\right) + \frac{\partial}{\partial x_\alpha}\left(\bar{\rho}\,\tilde{v}_\alpha \widetilde{v''_\delta v''_\beta}\right) = -\bar{\rho}\,\widetilde{v''_\alpha v''_\xi}\frac{\partial \tilde{v}_\gamma}{\partial x_\alpha} \\
& - \bar{\rho}\,\widetilde{v''_\alpha v''_\gamma}\frac{\partial \tilde{v}_\beta}{\partial x_\alpha} - \frac{2}{3}\bar{\rho}\,\delta_{\gamma\beta}\,\varepsilon \\
& + \frac{\partial}{\partial x_\alpha}\,\mu_L\frac{\partial}{\partial x_\alpha}\left(\widetilde{v''_\beta v''_\gamma}\right) - \bar{\rho}\,\widetilde{v''_\alpha v''_\beta v''_\gamma} \\
& - \overline{v''_\beta}\frac{\partial \bar{p}}{\partial x_\gamma} - \overline{v''_\gamma}\frac{\partial \bar{p}}{\partial x_\beta} + \overline{p'\left(\frac{\partial v''_\beta}{\partial x_\gamma} + \frac{\partial v''_\gamma}{\partial x_\beta}\right)} \qquad (11)
\end{aligned}$$

in which the pressure-rate of strain correlation is given by equation (9).

Dissipation rate of turbulent kinetic energy

The form of this equation is somewhat similar to the one used in reference [12] with the following differences from the standard k-ε version.

*The diffusivity coefficients allow non-isotropic processes.

$$-\bar{\rho}\,\overline{v''_\beta \varepsilon} = c_\varepsilon \cdot \bar{\rho} \cdot \frac{k}{\varepsilon} \cdot \widetilde{v''_\alpha v''_\beta} \cdot \frac{\partial \varepsilon}{\partial x_\alpha} \qquad (12)$$

*The mean pressure gradients have a form similar to their counterpart in the Reynolds stress equation. S_p represents the set of mean pressure gradient terms in the exact equation.

$$S_p = -c_{\varepsilon 4} \cdot \frac{\varepsilon}{k}\,\overline{v''_\beta}\frac{\partial \bar{p}}{\partial x_\beta} \qquad (13)$$

*The velocity divergence term, called S_d has the form:

$$S_D = -c_{\varepsilon 3} \cdot \bar{\rho} \cdot \varepsilon \cdot \tilde{D} \qquad (13)$$

In which $\tilde{D}$ is the mass weighted velocity divergence. These assumptions yield the following dissipation equation:

$$\frac{\partial}{\partial t}(\bar{\rho}\varepsilon) + \frac{\partial}{\partial x_\alpha}(\bar{\rho}\, u_\alpha \varepsilon) = - c_{\varepsilon 1}\frac{\varepsilon}{k}\bar{\rho}\,\widetilde{v''_\alpha v''_\beta}\frac{\partial \tilde{v}_\alpha}{\partial x_\beta} - c_{\varepsilon 2}\bar{\rho}\frac{\varepsilon^2}{k}$$

$$+ \frac{\partial}{\partial x_\alpha}\left(c_\varepsilon \cdot \frac{k}{\varepsilon}\cdot \widetilde{v''_\alpha v''_\beta}\frac{\partial \varepsilon}{\partial x_\beta}\right)$$

$$- c_{\varepsilon 3}\cdot \bar{\rho}\cdot \varepsilon \cdot \tilde{D} - c_{\varepsilon 4}\frac{\varepsilon}{k}\overline{v''_\beta}\frac{\partial \bar{P}}{\partial x_\beta} \qquad (14)$$

Density velocity correlation

According to the definition of mass weighted averaging, this correlation corresponds to the mean value of the mass weighted fluctuation.

*The diffusive transport term is modelled according to a constant density model for triple correlation [2]

$$\overline{\rho' v''_\alpha v''_\beta} = - c_s \frac{k}{\varepsilon}\left[\widetilde{v''_\alpha v''_\gamma}\frac{\partial}{\partial x_\gamma}(\overline{\rho' v''_\beta}) + \widetilde{v''_\beta v''_\gamma}\frac{\partial}{\partial x_\gamma}(\overline{\rho' v''_\alpha})\right] \qquad (15)$$

This approximation allows permutation of indices of velocity components but no permutation of density and velocity fluctuations.

The next term is approximated by:

$$\overline{v''_\beta \frac{\partial v''_\alpha}{\partial x_\alpha}} = c_{UDP}\frac{\sqrt{\overline{\rho'^2}}}{\bar{\rho}}\,\overline{v''_\beta}\,\frac{\partial}{\partial x_\alpha}(\overline{v''_\alpha}) \qquad (16)$$

There is no precise way to fix the value of c_{UDP} though it may be presumed of order unity.

The basic idea to approximate the pressure term is to use a procedure similar to the pressure-rate of strain modelling in the Reynolds stress equation. Following Lumley [7], the "Rotta" term is approximated by:

$$\Phi_{\beta c,1} = - c_{\phi 1}\cdot \frac{\varepsilon}{k}\cdot \overline{\rho' v''_\beta} - c_{\phi 2}\frac{\varepsilon}{k}\left[\frac{\widetilde{v''_\alpha v''_\beta}}{k} - \frac{2}{3}\delta_{\alpha\beta}\right]\overline{\rho' v''_\alpha} \qquad (17)$$

allowing the anisotropy effects and the rapid part is

$$\Phi_{\beta c,2} = c_{\phi 2}\,\overline{\rho' v''_\beta}\frac{\partial \tilde{v}_\beta}{\partial x_\alpha} \qquad (18)$$

*If the fine scale motion is assumed isotropic the last term

$$\overline{(\rho'/\rho)\ (\partial \tau_{\alpha\beta}/\partial x_\alpha)}$$

is equal to zero. The modelled transport equation for the density velocity correlation is written as:

$$\frac{\partial}{\partial t}(\bar{\rho}\,\overline{v''_\beta}) + \frac{\partial}{\partial x_\alpha}(\bar{\rho}\,\tilde{v}_\alpha\,\overline{v''_\beta}) = - \bar{\rho}\,\overline{v''_\alpha}\frac{\partial \tilde{v}_\beta}{\partial x_\alpha} + \widetilde{v''_\alpha v''_\beta}\frac{\partial \bar{\rho}}{\partial x_\alpha}$$

$$+ c_{UDP}\sqrt{\overline{\rho'^2}}\,\overline{v''_\beta}\frac{\partial}{\partial x_\alpha}(\overline{v''_\alpha})$$

$$- \frac{\partial}{\partial x_\alpha}\left(c_s \frac{k}{\varepsilon}\left(\widetilde{v''_\alpha v''_\gamma}\frac{\partial}{\partial x_\gamma}(\overline{\rho' v''_\beta}) + \widetilde{v''_\beta v''_\gamma}\frac{\partial}{\partial x_\gamma}\right.\right.$$

$$\left.\left.\cdot\,(\overline{\rho' v''_\alpha})\right) + c_{\rho 2}\,\overline{\rho' v''_\alpha}\,\frac{\partial v_\beta}{\partial x_\alpha}\right.$$

$$- c_{\phi 1}\frac{\varepsilon}{k}\overline{\rho' v''_\beta} - c_{\phi 2}\frac{\varepsilon}{k}\left(\frac{\widetilde{v''_\alpha v''_\beta}}{k} - \frac{2}{3}\delta_{\alpha\beta}\right)\overline{\rho' v''_\alpha}$$

(19)

Scalar flux

The modelling assumptions used to close this equation are similar to those for the Reynolds stress equation. Again the production terms are exact.

*The whole diffusive transport process is represented by the following group of terms:

$$\frac{\partial}{\partial x_\gamma}\left(\bar{\rho}\,\widetilde{v''_\beta v''_\gamma c''_I} + \delta_{\beta\gamma}\,\overline{p' c''_I} - \delta_{\gamma\beta}\,\overline{\tau_{\gamma\beta} c''_I}\right)$$

For the triple correlation the assumption concerning the diffusive mass weighted Reynolds stress transport is extended to concentration correlations. The following first order differential equations results:

$$- \bar{\rho}\,\widetilde{v''_\gamma v''_\delta}\frac{\partial}{\partial x_\delta}(\widetilde{v''_\beta c''_I}) - \bar{\rho}\,\widetilde{v''_\beta v''_\delta}\frac{\partial}{\partial x_\delta}\widetilde{v''_\gamma c''_I} - \bar{\rho}\,\widetilde{v''_\delta c_I}\frac{\partial}{\partial x_\delta}$$

$$\cdot\,(\widetilde{v''_\beta v''_\gamma}) + \frac{\partial}{\partial x_\delta}\left[\bar{\rho}\,k_\beta\,\widetilde{v''_\gamma v''_\delta c''_I}) + \bar{\rho}\,k_\gamma\,\widetilde{v''_\beta v''_\delta c''_I}\right]$$

$$\cdot\,\bar{\rho}\,k_c\,\widetilde{v''_\beta v''_\delta v''_\gamma} + \bar{\rho}\,k_\delta\,\widetilde{v''_\beta v''_\gamma c''_I} = - c'\frac{\varepsilon}{k}\bar{\rho}\,\widetilde{v''_\beta v''_\gamma c''_I} \qquad (20)$$

in which

$$k_\alpha = \frac{\overline{\rho' v''_\alpha}}{\bar{\rho}} \quad ; \quad k_c = \frac{\overline{\rho' c''_I}}{\bar{\rho}}$$

The other terms in the diffusive transport contribution correspond to diffusion of concentration by pressure fluctuations and by molecular motion. The pressure effects are neglected here, whereas the molecular effects are represented by a laminar gradient flux law similarly to the Reynolds stress laminar diffusion.

*Redistribution due to pressure fluctuations. Again we use a procedure which is similar to the redistributive term of the Reynolds stress equation, for which we get two different contributions: a fully turbulent and a mean gradient part. The turbulent term may be related to the linear return-to-isotropy approximation of Rotta [13]

$$\Phi_{\beta c,1} = - c_c\frac{\varepsilon}{k}\bar{\rho}\,\widetilde{v''_\beta c''_I} \qquad (21)$$

in which case it must be expected that the time scale (k/ε) used here contains also information about the time scale of the turbulent concentration field $\langle c_i''^2\rangle/\varepsilon_c$, $\langle c_i''^2\rangle$ being the concentration covariance and Epsc its rate of dissipation. Launder [14] and Janicka [15] pointed out that these two time scales are different. In local equilibrium turbulence they may be assumed proportional. Nevertheless an anisotropy term is added to the "Rotta" term, which carries Reynolds stress anisotropy information. This yields to a form similar to Lumley's proposal [7]

$$\phi_{\beta c,1} = - c_{c1} \bar{\rho} \frac{\varepsilon}{k} \widetilde{v''_\beta c''_I} - c_{c2} \bar{\rho} \frac{\varepsilon}{k} \left(\frac{\widetilde{v''_\beta v''_\alpha}}{k} - \frac{2}{3} \delta_{\alpha\beta} \right) \widetilde{v''_\alpha c''_I} \tag{22}$$

The mean gradient part of the pressure term is transposed from the leading term of the pressure-rate of strain term.

$$\phi_{\beta c,2} = c_c \cdot \bar{\rho} \cdot \widetilde{v''_\alpha c''_I} \frac{\partial \tilde{v}_\beta}{\partial x_\alpha}$$

*Dissipation. In the framework of high Reynolds number flows, the fine scale motions are nearly isotropic and the correlation

$$\overline{\left(\tau_{\gamma\beta} \frac{\partial}{\partial x_\gamma} c''_I \right)}$$

which is strictly zero in isotropic turbulence is negligible.

*A mean pressure gradient term exists also in the scalar flux equation. Nevertheless, the isothermal flow assumption avoids the need for a solution of a PDE for the density concentration correlation. It can be expressed in terms of density fluctuations [6,11]

$$\overline{c''_I} = - \frac{\rho_J \rho_I}{(\rho_I - \rho_J)} \frac{\overline{\rho'^2}}{\bar{\rho}^3} \tag{23}$$

This relationship holds only under the assumption of isothermal flow. If heat transfer problems were to be solved with the dynamic field equations, this part would require some modifications for the description of thermal turbulence.

The modelled scalar flux equation is:

$$\begin{aligned} \frac{\partial}{\partial t} (\bar{\rho} \widetilde{v''_\beta c''_I}) + \frac{\partial}{\partial x_\alpha} (\bar{\rho} \tilde{v}_\alpha \widetilde{v''_\beta c''_I}) &= - \bar{\rho} \widetilde{v''_\alpha c''_I} \frac{\partial \tilde{v}_\beta}{\partial x_\alpha} \\ &- \bar{\rho} \widetilde{v''_\alpha v''_\beta} \frac{\partial \tilde{c}_I}{\partial x_\alpha} + \frac{\partial}{\partial x_\alpha} \left(\mu_L \frac{\partial}{\partial x_\alpha} (\widetilde{v''_\beta c''_I}) \right) \\ &- \bar{\rho} \widetilde{v''_\alpha v''_\beta c''_I}) + c_c \bar{\rho} \cdot \widetilde{v''_\alpha c''_I} \frac{\partial \tilde{v}_\beta}{\partial x_\alpha} \\ &+ \frac{\rho_I \rho_J}{\rho_I - \rho_J} \frac{\overline{\rho'^2}}{\bar{\rho}^3} \frac{\partial \bar{P}}{\partial x_\beta} - c_{c1} \bar{\rho} \frac{\varepsilon}{k} \widetilde{v''_\beta c''_I} \\ &- c_{c2} \bar{\rho} \frac{\varepsilon}{k} \left(\frac{\widetilde{v''_\alpha v''_\beta}}{k} - \frac{2}{3} \delta_{\alpha\beta} \right) \widetilde{v''_\alpha c''_I} \end{aligned} \tag{24}$$

Density fluctutions

The derivation of the transport equations for the partial density correlations with the involved modelling efforts has been published in a previous work [12] and thus will not be reproduced here.

COMPARISON WITH EXPERIMENTS

Flow conditions

Two different sets of experimental data were considered to provide a valuable comparison of computational results against physics. The first set of experiments is that of Rebollo [9]. This work emphasizes the influence of non-zero longitudinal mean pressure gradient on a two-dimentional mixing layer. Both adjacent free stream flows have the same dynamic pressure. The gases are helium and nitrogen which yield a density ratio equal to 7. The velocities are 10.9 m/s for the light gas and 4.12 m/s the heavy one. The respective Reynolds numbers

helium ⟶ Re = 3600/cm

nitrogen ⟶ Re = 12000/cm

From his similarity analysis Rebollo has shown that, together with the dynamic pressure equality, a second equilibrium condition concerns the definition of the longtiudinal mean pressure gradient, through the assignment of a constant Falkner-Skan parameter:

$$\alpha = \frac{x}{u} \frac{dU}{dx} \tag{25}$$

The two values considered here are 0. and - 0.18.

The second set of experiments is provided by the thesis of Brown [10]. This set emphasizes the influence of the free stream velocity ratio, and considers air-air and freon 12-air mixings. The density ratio is either 1 or 4 and the velocity ratio 0, 0.3 or 0.6 in the first case and 0.3 and 0.6 in the second case. In both cases the high speed air stream has a velocity equal to 14.0 m/s.

All the boundary layers at the splitter plate trailing edge are laminar and free stream turbulence level is very low (Urms/UE < 1%). Various experimental techniques have been used in these experiments to provide a wide range of information about turbulence quantities such as Reynolds stress, density fluctuations, concentration fluctuations, density velocity correlations, trublent fluxes, etc...

Numerical method

The numerical method which is used for this calculation is a modified version of the Patankar and Spalding method [18], described in detail in reference [11]. All the transport equations are used in their boundary layer form and are solved in a parabolic marching step manner. To start the calculations we must provide the initial values for each transported variable. The given velocity profiles are Blasius-like and agree with the boundary layer thickness values reported by the experiments. The normal Reynolds stresses were assigned to a constant value (isotropic turbulence) in such a way the turbulent kinetic energy remains bounded by the experimentally reported limit. The turbulent shear stress is set to zero and so are all the other turbulent correlations. The dissipation rate is determined to produce a turbulent viscosity equivalent to the laminar one, according to the well known k-ε formula [19].

$$\mu_t = 0.09 \rho k^2 / \varepsilon \tag{26}$$

The boundary conditions are Dirichlet type for the primitive variables such as velocity or concentration and Neumann type (zero gradient) for all the second order moments. When different from

zero, the longitudinal mean pressure gradient must be prescribed analytically as the values of the outer boundaries velocities. The transverse pressure gradient cannot be prescribed but only approximated by a simplified version of the mean transverse momentum equation yielding to

$$\frac{\partial \bar{P}}{\partial y} = - \frac{\partial}{\partial y} \left(\bar{\rho} \widetilde{v''^2} \right) \qquad (27)$$

The set of ordinary differential equations for the triple correlations is solved once at each x-step by a simple centered difference scheme rather than algebraically. The upper bound of the marching step of the main procedure is determined at each forward position with respect to the value of a characteristic thickness of the mixing layer. To solve a typical problem with this 15 equation turbulence model over a distance of 1 meter with 80 node points in the cross direction, the time is about 15 min CPU on a DEC-VAX 11/780 or about 90 seconds CPU on a CDC 7600 computer.

Discussion of the results

Free stream velocity ratio influence. The main results of the comparison against the Brown experiments [10] are summarized in Table 1 for the three different velocity ratios (0.0, 0.3, 0.6) and the two gas compositions (air-air and F12-air). The agreement of the calculations with Brown's numbers is satisfactory except for the following items:

*Virtual origin position. Two different mechanisms establish the virtual origin. First is the spreading rate of the mixing layer - which is properly described by the calculation - and second is the transition process which takes place between the attached laminar boundary layers on the splitter plate and the free turbulent mixing layer developing downstream of it. The second mechanism cannot be predicted by the calculation. The calculations develop a transition-like region but there is no rigorous way to relate that phenomenon to the physical laminar to turbulent transition. The spreading rates are compared through the use of the parameter (σ) which is defined from the velocity profile

$$\sigma = 1.19 \frac{\Delta x}{\Delta y} \qquad (28)$$

This definition is similar to the one given in reference [20] except the characteristic thickness is determined between the bounds (0.2, 0.8) instead of the usual (0.1, 0.9).

*Another point of disagreement concerns the spreading of the F12-air mixing layer with 0.6 velocity ratio. As it is shown on Figure 1, the experimental point is high above the theoretical homogeneous flow curve defined by

$$\sigma = 11.5 \left(\frac{1 + \phi_0}{1 - \phi_0} \right) \quad ; \quad \phi_0 = \frac{U_o}{U_1} \qquad (29)$$

whereas the calculation matches the curve well. Also for this flow case (see Table 1), the measurements show a higher level of V'rms compared to U'rms. This feature does not appear in the calculations for which the ratio U'rms/V'rms remains nearly the same value as for the 0.3 velocity ratio case (=1.6).

The last point of disagreement concerns the turbulence levels for which Brown reports values increasing with the velocity ratio, where one could expect that turbulence increases when the shear increases (or ϕ_0 decreases) as occurs in the calculations.

The main result of this calculation however, is consistent with the observation that density variations do not have significant influence on the spreading rate of a mixing layer if these fluctuations are due only to inhomogeneities in gas composition.

Pressure gradient influence. More extensive calculations were done with the helium-nitrogen flow [11] than with the previous F12-air mixture, but some conclusions are identical.

The virtual origin cannot be determined correctly, because the transitional mechanism which influences it does not exist in this turbulence model. Thus the only way to compare the spreading of the mixing zone is to look at the value of the downstream spreading rate parameter. (Figure 1 shows that for this flow (dP/dX = 0.) the agreement is as good as for the previous one.) The most interesting results are shown in Table 2 for the two cases which are considered here: α=0. and α=-0.18. In both cases the velocity ratio is U_0/U_1=0.378. Globally, the agreement is good for the zero pressure gradient case and weaker for the case with positive pressure gradient, for which the turbulence quantities are underestimated by 25-40%.

No direct comparison of the spreading rate parameter is reported here because it has been found in the calculations that the self-similar region begins only after 7-8 cm from the splitter plate, and no experimental value is given beyond this abscissa. Nevertheless the calculated spreading rate parameter agrees with the results of the previous calculations and with the theoretical curve of Figure 1, when it is calculated further downstream (8<X<30 cm), where the self-similarity is ensured. For the near wake region, two different thicknesses [9] are plotted against experiments and for which the agreement is good (Figure 2). Figures 3, 4, and 5 show some typical results for the shear stress, the density velocity correlation and the density fluctuations, for which the experiments provide information. The results of Table 2 point out that the results are good for all the mean quantities but do not agree with the pressure gradient influence. The experiments show that the pressure gradient tends to increase the spreading rate, the shear stress and the density velocity correlations, but not the density fluctuations whose maximum level remains nearly the same. The calculations show a smaller increase of the shear stress, whereas the density correlations are decreased and do not match at all the results of Rebollo. This weakness is possibly due to the pressure gradient terms in the density correlations equations or in the scalar flux equations. One of these terms is a density concentration equation, for which it would be better to solve a PDE rather than to approximate it from the density fluctuations. Figure 6 gives an estimate of the Schmidt number value across the mixing layer. The straight line represents the constant value which should be used with the two equation model calculations. This shows clearly that even if such value is realistic in the center part of the mixing zone, it becomes completely irrelevant near the edges.

CONCLUSIONS

A full second order closure turbulence model has been set up to describe the low speed mixing of gases with highly different density. Two mixing cases have been studied. In both calculations, the flow predictions are reasonable and promising for future work in that direction. Nevertheless, this turbulence model version fails to predict correctly the pressure gradient influence on the turbulence (Reynolds stress, density correlations). Some further work would be done in this direction, especially the estimate of c''_I through the density fluctuations should be removed.

The main objective of this paper was to demonstrate the value of a second order closure for the prediction of mixing flows where the use of an eddy viscosity with a constant turbulent Schmidt number should fail. Nevertheless, it would be premature to draw any conclusion about universality of such a closure and the values of the constants used here. As some modelling assumptions are based on an analogy with the incompressible Reynolds stress closure [2], future experiments should emphasize measurements on quantities such as turbulent scalar fluxes and density correlations in order to support or to improve these assumptions.

REFERENCES

1. Boussinesq, J., "Theorie de l'ecoulement tourbillonnant et tumultueux des liquides dans les lits rectilignes a grande section", I-II Gauthier-Villars, Paris.

2. Hanjalić, K. and Launder, B. E., "A Reynolds stress model of turbulence and its application to thin shear flows", J. Fluid Mech., 52-4, 1972, pp. 609-638.

3. Launder, B. E., Reece, G. J., and Rodi, W., "Progress in the development of a Reynolds stress turbulence closure", J. Fluid. Mech., 68-3, 1975, pp. 537-566.

4. Wolfshtein, M., Naot, D., and Lin, A., "Models of turbulence", Chapter 1 in Topics in Transport Phenomena, (C. Gutfinger, ed.), Hemisphere Publishing Co, 1975.

5. duPont Donaldson, C., "Atomspheric turbulence and the dispersal of atmospheric pollutants", EPA-R4-73-016a, Office of Research and Monitoring, U.S. Environmental Protection Agency, Washington, D.C., March 1973.

6. Chassaing, P., "Melange turbulent de gas inertes dan un jet de tube libre", These de Doctorat d'Etat, Toulouse, 1979.

7. Lumley, J. L., "Prediction methods for turbulent flows. Introduction", VKI Lectures Series 76, Rhode St. Genese, Belgium, 1975.

8. Lumley, J. L. and Janicka, J., "Second order modelling in non-constant density flows", FDA 81-01, Cornell University, 1981.

9. Rebollo, M., "Analytical and experimental investigation of a turbulent mixing layer of different gases in a pressure gradient", Ph.D. thesis, California Institute of Technology, Pasadena, 1973.

10. Brown, J. L., "Heterogeneous turbulent mixing layer investigations utilizing a 2-D 2-color laser doppler anemometer and a concentration probe", Ph.D. thesis, University of Missouri-Columbia, 1978.

11. Vandromme, D., "Turbulence modelling for avariable density flows", Ph.D. thesis, University of Brussels, 1980.

12. Kollmann, W. and Vandromme, D., "The calculation of free turbulent shear flows with strong density fluctuations", Int. J. Heat Mass Trans., vol. 22, no. 11, 1979, pp. 1557-1565.

13. Rotta, J. C., "Statistische Theorie nichthomogener Turbulenz", Zeitsch. fur Physik, 129 n. 5, pp. 547-572 and 132 n. 1, pp. 51-77, 1951.

14. Launder, B. E., "Heat and mass transport", Chapter 6 in Topics in Applied Physics Vol. 12: Turbulence, (P. Bradshaw, ed.), Springer-Verlag, 1976.

15. Janicka, J., "Berechnung turbulenter Wasserstoff-Luft Diffusions-Flammen", Ph.D. thesis, RWTH, Aachen, 1979.

16. Harlow, F. H. and Nakayama, P. I., "Transport of turbulent kinetic energy decay rate", Los Alamos Scientific Lab Report LA-3854, 1968.

17. Irwin, H. P., "Measurements in blow boundary layers and their prediction by Reynolds stress modelling", Ph.D. thesis, McGill University, 1974.

18. Patankar, S. V. and Spalding, D. B, "Heat and mass transfer in boundary layers", Intertext, London, 1970.

19. Jones, W. P. and Launder, B. E., "The prediction of laminarization with a two equation model of turbulence", Int. J. Heat Mass Trans., vol. 15, 1972, pp. 301-314.

20. Free Turbulent Shear Flows, NASA SP 321, tome. II. p. 14.

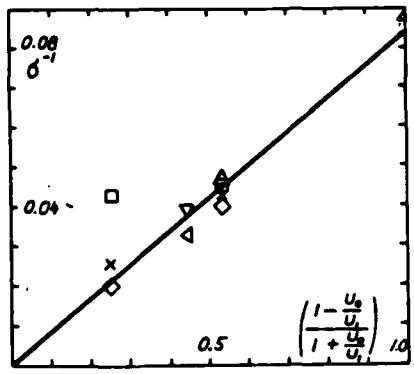

Figure Captions

Fig. 1 - Spreading rate parameter (line:theory)

- × Air-air mxing [10]
- □ Freon 12-air mixing [10]
- △ Air-air mixing
- ◇ Freon 12-air mixing } calculation
- ◁ He-nitrogen dp/dx = 0 } calculation
- ▽ He-nitrogen dp/dx = 0

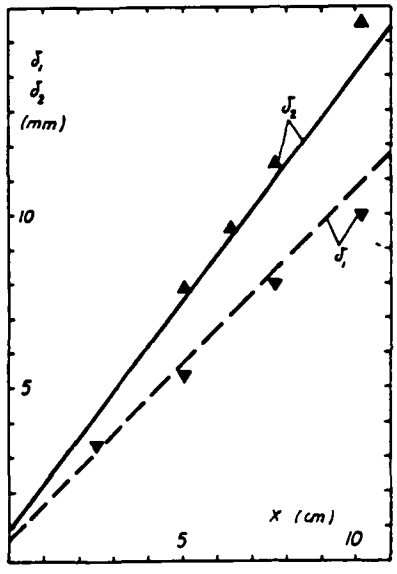

Fig. 2 - Spreading of He-N mixing layer (symbols:[9], lines:calculations)

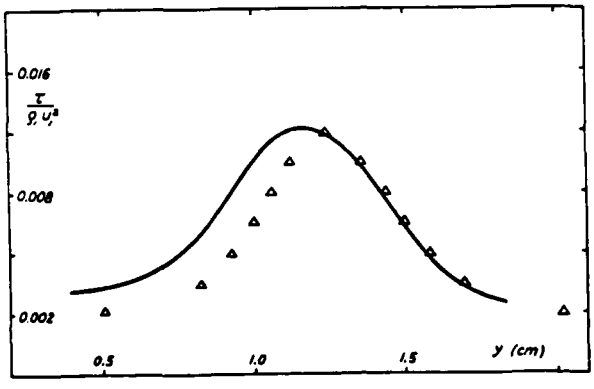

Fig. 3 - Shear stress in H-N mixing layer at x = 5.08 cm for α = 0 (symbols:[9], lines:calculations)

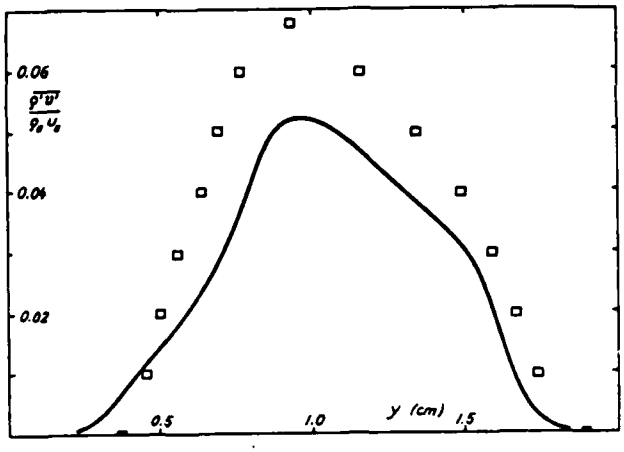

Fig. 4 - Density velocity correlations in He-N mixing layer at x = 5.08 cm for α = 0 (symbols:[9], lines:calculations)

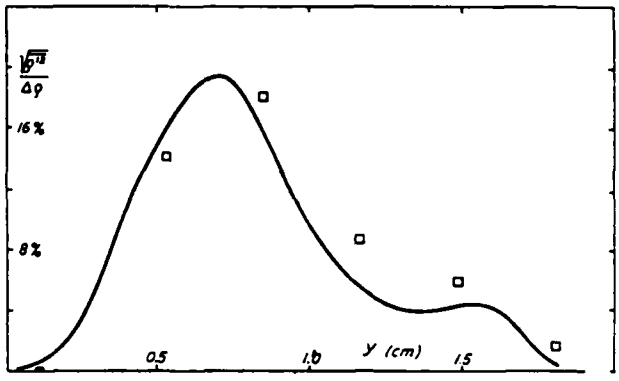

Fig. 5 - Density fluctuation intensity in He-N mixing layer at x = 5.08 cm for α = 0 (symbols:[9], lines:calculations)

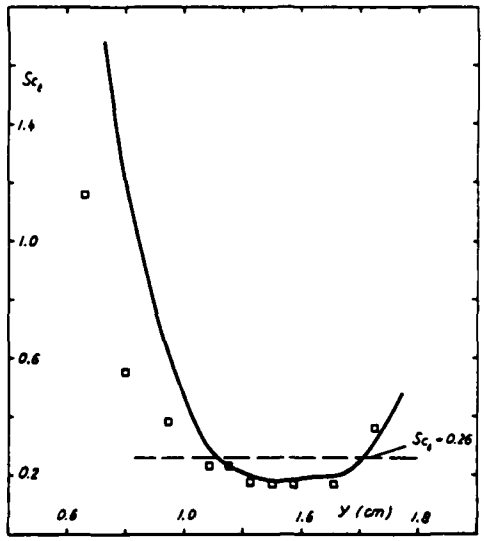

Fig. 6 - Turbulent Schmidt-number in He-N mixing layer at x = 5.08 cm for α = 0 (symbols:[9], lines:calculations)

Table 1 - Velocity ratio influence
(Exp. from Brown [10])

	ρ_0	σ	$\frac{U'rms}{\Delta U}$	$\frac{V'rms}{\Delta V}$	$\frac{-10\langle u'v'\rangle}{\Delta U^2}$	Kuv
	air-air					
exp	0.00	11.97	0.150	-	-	-
calc		11.30	0.192	0.125	0.131	0.548
exp	0.30	23.34	0.165	0.125	0.105	0.509
calc		21.22	0.184	0.120	0.120	0.545
exp	0.60	39.27	0.195	0.165	0.162	0.503
calc		40.37	0.184	0.120	0.120	0.542
	F12-air					
exp	0.30	21.86	0.175	0.125	0.112	0.512
calc		25.67	0.181	0.113	0.112	0.548
exp	0.60	23.76	0.168	0.195	0.180	0.549
calc		54.95	0.198	0.126	0.132	0.532

Table 2 - Pressure gradient effects
(Exp. from Rebollo [9])

$\alpha = \frac{x}{U}\frac{dU}{dx}$	$\alpha = 0.00$		$\alpha = -0.18$	
	exper.	calc.	exper.	calc.
$\delta_1/x-x_o$	0.10	0.10	0.16	0.15
σ	-	31.34	-	25.97
U/U_1	0.70	0.67	0.59	0.59
$\overline{\rho u^2}/\rho_1 U_1^2$	0.87	0.81	0.60	0.59
$\bar{\rho}/\rho_1$	1.78	1.74	1.70	1.62
$\left(\overline{\rho u^2}/\rho_1 U_1^2\right)$	0.52	0.54	0.32	0.31
$\left(\overline{\rho u^2}/\rho_1 U_1^2\right)$	1.22	1.19	1.20	1.22
$\overline{\rho'^2}/\Delta\rho$	1.19	1.18	1.20	1.15
$\overline{\rho u'v'}/\rho_1 U_1^2$	0.012	0.012	0.0205	0.0147
$\overline{\rho' v'}/\rho_1 U_1$	0.068	0.044	0.082	0.040
Scht	0.16	0.22	0.33	0.16

Table 3 - Values of modelling constants

c	0.11	c_1	1.5	c_2	0.4			
c_ε	0.13	$c_{\varepsilon 1}$	1.4	$c_{\varepsilon 2}$	2.1	$c_{\varepsilon 3}$	-1.0	$c_{\varepsilon 4}$	2.0
c_s	0.11	$c_{\phi 1}$	4.0	$c_{\phi 2}$	4.0	c_{UDP}	1.0	$c_{\rho 2}$	0.5
c_{Ds}	0.014	c_{c1}	4.0	c_{c2}	-4.8	c_c	0.5		
c_Q	0.6	c_{Q1}	3.0	c_{Q2}	0.6				

A NEW APPROACH TO THE ANALYSIS OF TURBULENT MIXING IN VARIABLE DENSITY FLOWS

H. Ha Minh,

Institut de Mécanique des Fluides
Institut National Polytechnique
31071 Toulouse
FRANCE

B.E. Launder and J. MacInnes

Mechanical Engineering Department
University of Manchester Institute of Science and Technology
Manchester M60 1QD
ENGLAND

ABSTRACT

A new decomposition is presented of a variable density turbulent field into mean and fluctuating parts which adopts *both* the mass-weighted and the conventional mean velocity as dependent variables. By so doing, the different roles played by the velocity vector in the equations of motion can be properly accommodated. For the mean field conservation equations of momentum and species, the effects of turbulence in each equation are confined to a single correlation between fluctuating quantities; indeed the form is identical to that for a uniform density flow. The transport equations for the turbulent correlations are more complex than when mass weighted averages are adopted but, arguably, the physical processes are easier to approximate. Various extrapolations of uniform-density second-moment closure methodology are discussed in connection with the behaviour observed by Rebollo [1] in the variable density mixing layer. The effective turbulent Prandtl-Schmidt number in a variable density medium is shown to be crucially sensitive to the specific forms of the approximation for correlations containing the fluctuating pressures.

NOMENCLATURE

$\overline{c_i c_j}$	anisotropy of tensor $\overline{a_i b_j}$.
$\tilde{G}_i$	instantaneous mass velocity ($\equiv \tilde{\rho}\,\tilde{U}_i$).
G_i, g_i	mean, fluctuating part of $\tilde{G}_i$ ($\overline{g_i} = 0$).
$\tilde{M}$	instantaneous mass fraction.
M, m	mean, fluctuating part of $\tilde{M}$.
$\tilde{N}$	instantaneous mass-weighted mass fraction ($\equiv \rho M$).
N, n	mean, fluctuating part of $\tilde{N}$.
$\tilde{U}_i$	instantaneous velocity.
U_i, u_i	mean, fluctuating part of $\tilde{U}_i$.
$\tilde{P}$	instantaneous static pressure.
P, p	mean, fluctuating part of $\tilde{P}$.
x_i	cartesian coordinate vector.
ε	dissipation rate of $\overline{g_i^2/2}$.
ε_{ij}^{ab}	dissipation rate of $\overline{a_i b_j}$.
$\tilde{\rho}$	instantaneous density.
ρ, ρ'	mean, fluctuating part of $\tilde{\rho}$.
ϕ_{ij}^{ab}	fluctuating pressure-strain correlation term in transport equation for $\overline{a_i b_j}$.
ϕ_j^{am}	fluctuating pressure-strain correlation term in transport equation for $\overline{a_j m}$.
$\tilde{\tau}_{ij}$	instantaneous Stokes' stress tensor.
τ_{ij}, τ_{ij}'	mean and instantaneous parts of $\tilde{\tau}_{ij}$.

INTRODUCTION

In problems of turbulent combustion, in the mixing of combustion products or in the accidental release of heavy gases into the atmosphere, density fluctuations at a point may be of a magnitude comparable with that of the mean density. In such circumstances any credible turbulence closure must specifically address the influence that the large density excursions will have on the transport processes themselves. Here we consider only those situations where inertial effects entirely swamp contributions due to buoyancy.[1] Until about 1975 nearly all computational studies of variable-density mixing neglected any contribution of density fluctuations to the transport processes. More recently, turbulence closure studies have tended to follow one of two routes. In the first, the instantaneous density is represented as the sum of mean and fluctuating parts so, on averaging the convective transport term, correlations between fluctuating density and velocity appear in addition to the conventional Reynolds stress. This approach, in the context of second-moment closure, has been followed by Donaldson and co-workers [4], Janicka and Kollmann [5] and others. Those following this path have, implicitly, invoked the principle of receding influence since, in the transport equations for the second-moment quantities ($\overline{u_i u_j}$, etc.), *uniform* density forms have been adopted.

The second and increasingly followed approach, originally proposed by Favre [6], adopts a mass weighting of velocity and other dependent variables except pressure. With this arrangement the mean momentum equation, with molecular transport neglected, is analogous in appearance to that for a uniform density flow if the Reynolds stresses, like the velocities, are obtained by taking a density-weighted average. The simplicity of appearance of the resultant equation when mass-weighted averaging is used (a simplicity that also

[1] In many problems gravitational forces will be influential though, to first order, they can be treated by the same approaches adopted when density fluctuations are weak (i.e. when the Boussinesq approximation applies); see, for example, ref. [2] and [3] for a discussion.

carries through to the exact form of the transport equations for turbulence correlations such as the turbulence energy) has encouraged the hope that closure ideas evolved for the invariant density case would be directly applicable to variable density mixing, e.g. Bilger and Kent [7] and Jones [8]. Libby [9], while more cautious about the prospect of direct extrapolation, recommends that closure models be evolved within the framework of mass-weighted averages to keep the computational burden to manageable proportions.

The most decisive set of experimental data for distinguishing between different approaches to closure in variable density flows is that of Rebollo [1] (see also the paper by Brown and Roshko [10]) who in two experiments examined the mixing of helium and nitrogen in a plane mixing layer with velocity ratios adjusted to give uniform dynamic pressure in the two streams. In one case, with zero streamwise pressure gradient, the turbulent Schmidt number in the central part of the layer fell below 0.2, i.e. to about one third the value found in the uniform density case. None of the reported attempts at computing this flow, using either conventional or mass-weighted averaging have, so far as we can judge, been successful in reproducing the measured behaviour unless empirical coefficients are adjusted to values that would give unacceptable predictions in the uniform density case, e.g. [11]. Thus a *direct* application of uniform-density closure methodology in density weighted variables does not account for the observed behaviour.

In principle it would appear possible to extend and generalize the uniform density model in order that the model give satisfactory agreement with measurements for both uniform and variable density mixing. Yet the very simplicity of the exact equations in mass-weighted coordinates gives little guidance on the direction in which to proceed. In the present contribution we have adopted an alternative decomposition which we believe may display more transparently the physical processes at work. We refer to it as "mixed weighting" since, in the momentum equations both conventional velocity and the density weighted velocity appear. The paper is preliminary in character since it could not be claimed that the model is yet ready for widespread application. The various possibilities and consequences are, however, perhaps sufficiently extensively explored for others to be interested in following the line of development further. Before turning to the analysis it remains only to emphasize that there are *many* possible approaches to decomposing variables into mean and fluctuating parts. To underline this fact we note that Janicka and Lumley [12] have very recently proposed a further decomposition no less different from established approaches than that presented herein. It is not yet clear what will eventually represent the best way forward. It could well be the case that the best arrangement for working out the physical modelling is not the best one, from a computational point of view, for calculating inhomogeneous shear flows. Once the physical representation in one decomposition has been settled, however, it should be possible to devise a nearly equivalent form in some other decomposition.

ANALYSIS

The Mean Flow Equations

The Navier Stokes equations for turbulent mixing of a variable density, uniform viscosity[2] stream may be written:

$$\frac{\partial \tilde{\rho}\tilde{U}_i}{\partial t} + \frac{\partial}{\partial x_j}\tilde{\rho}\tilde{U}_j\tilde{U}_i = -\frac{\partial}{\partial x_j}\left[\mu\left(\frac{\partial \tilde{U}_i}{\partial x_j} + \frac{\partial \tilde{U}_j}{\partial x_i} - \frac{2}{3}\delta_{ij}\frac{\partial \tilde{U}_k}{\partial x_k}\right)\right] \quad (1)$$

where tildas denote the instantaneous value (mean plus fluctuating) of the dependent variable in question. We note that the velocity vector in the second term on the left has two roles: $\tilde{\rho}\tilde{U}_j$ represents the mass flow rate per unit area while U_i is the specific x_i-momentum flux. Here these separate roles are brought into prominence by defining

$$\tilde{\rho}\tilde{U}_j \equiv \tilde{G}_j. \quad (2)$$

Let us introduce (2) into (1) and define the mean value Φ of a dependent variable whose instantaneous and fluctuating parts are Φ and ϕ by:

$$\Phi \equiv \frac{1}{2T}\int_{-T}^{T}\tilde{\Phi}dt \; ; \; \tilde{\Phi} \equiv \Phi + \phi. \quad (3)$$

On averaging (1) in the conventional way implied by (3) we obtain for a stationary turbulent flow at high Reynolds number:

$$\frac{\partial}{\partial x_j}G_jU_i = -\frac{\partial P}{\partial x_i} - \frac{\partial}{\partial x_j}\overline{g_ju_i} \; . \quad (4a)$$

The asymmetric, mixed-weighted Reynolds stress, $\overline{g_ju_i}$, is now the quantity for which a turbulence model must be devised and that topic forms the main preoccupation of the remainder of the article. Before considering $\overline{g_ju_i}$ more closely, however, let us note that we could equally have linked $\tilde{\rho}$ with the velocity component U_i. In that case, equation (4a) becomes:

$$\frac{\partial}{\partial x_j}U_jG_i = -\frac{\partial P}{\partial x_i} - \frac{\partial}{\partial x_j}\overline{u_jg_i} \quad (4b)$$

Thus, again the mixed-weighted second-rank tensor appears but note that, in a thin shear flow, a different component of it will make the dominant contribution: $\overline{g_1u_2}$ instead of $\overline{g_2u_1}$. In a uniform density field the correlation is symmetric so the terms are equal but in a strongly stratified medium this may no longer be the case. The distinctions in approach that lead to (4a) and (4b) may appear insignificant but, when carried through to the scalar and, especially, the turbulent transport equations they lead to rather different closed forms for a given set of closure hypotheses.

---

[2] The unrealistic limitation of a stream of uniform viscosity is of no practical consequence since, in a free shear flow at high Reynolds numbers viscous terms only indirectly affect the turbulence structure

We suppose that the density variations arise from the inert mixing of two different gases and that the instantaneous mass fraction $\tilde{M}$ of one of these is governed by

$$\frac{\partial \tilde{\rho}\tilde{M}}{\partial t} + \frac{\partial}{\partial x_j}\tilde{\rho}\tilde{U}_j\tilde{M} = \lambda \frac{\partial^2 \tilde{M}}{\partial x_j^2} . \qquad (5)$$

Introduction of the mass velocity G_j and subsequent averaging, according to equation (3) leads, on neglect of molecular diffusion, to:

$$\frac{\partial}{\partial x_j} G_j M = - \frac{\partial}{\partial x_j} \overline{g_j m} \qquad (6a)$$

for a stationary flow. Alternatively, defining $\rho M \equiv \tilde{N} \equiv (N+n)$ allows us to write (6b) as

$$\frac{\partial}{\partial x_j} U_j N = - \frac{\partial}{\partial x_j} \overline{u_j n} \qquad (6b)$$

The use of (6b) in place of (6a) has certain attractions since N is linearly proportion to density:

$$\tilde{\rho} = a\tilde{N} + b \qquad (7)$$

where a and b are constants. It thus follows from (5) that

$$\frac{\partial}{\partial t}\left(\frac{\tilde{\rho}-b}{a}\right) + \frac{\partial}{\partial x_j}\left(\frac{\tilde{\rho}-b}{a}\tilde{U}_j\right) = \lambda \frac{\partial^2 \tilde{M}}{\partial x_j}$$

$$\text{or } \left(\frac{\partial \tilde{\rho}}{\partial t} + \frac{\partial \tilde{\rho}\tilde{U}_j}{\partial x_j}\right) - b\frac{\partial \tilde{U}_j}{\partial x_j} = \lambda a \frac{\partial^2 \tilde{M}}{\partial x_j} \qquad (8)$$

The term in parentheses on the left is identically zero by continuity and hence, on comparing mean and fluctuating parts of the remaining terms

$$\frac{\partial U_j}{\partial x_j} = - \frac{\lambda a}{b} \frac{\partial^2 M}{\partial x_j^2} \qquad (9a)$$

$$\frac{\partial u_j}{\partial x_j} = - \frac{\lambda a}{b} \frac{\partial^2 m}{\partial x_j^2} \qquad (9b)$$

From (9a) it emerges that at high Peclet numbers the divergence of the velocity field is essentially zero, whether or not the flow is stationary. From the continuity equation the corresponding expressions for the divergence of the mass velocities are:

$$\frac{\partial G_j}{\partial x_j} = - \frac{\partial \rho}{\partial t} \qquad (10a)$$

$$\frac{\partial g_j}{\partial x_j} = - \frac{\partial \rho'}{\partial t} = - a \frac{\partial n}{\partial t} \qquad (10b)$$

Thus the divergence of the mass velocity is exactly zero in a stationary flow but not otherwise. The mean and fluctuating mass velocities are related to the velocity and density through:

$$G_j = \rho U_j + \overline{\rho' u_j}$$

$$g_j = \rho u_j + \rho' U_j + (\rho' u_j - \overline{\rho' u_j})$$

It is evident that the averaged forms of the transport equations governing the velocity and scalar fields which arise from the present decompositions are just as compact as when density-weighted averaging is used for all terms. This compactness does not carry over to the transport equations for turbulence correlations, however. This, we would argue, is a *helpful* feature for, if we are fortunate, the intrinsic physical interactions giving rise to the strong alteration of the turbulent Schmidt number discussed above will become transparent in the additional terms.

Equations Describing the Second-Moment Correlations

Exact transport equations for the second-moment correlations $\overline{g_j u_i}$ and $\overline{g_j m}$ (or $\overline{u_j n}$) may be formed in the conventional way. For example that for the first correlation is obtained by multiplying the equation of motion for $\tilde{U}_i$ by g_j and averaging and adding it to the corresponding equation for $\tilde{G}_j$ multiplied by u_i and averaged. In this connection the "corresponding" $\tilde{G}_j$ equation is formed by multiplying and dividing the $\tilde{U}_i$ equation by density:

$$\frac{\partial \tilde{G}_k \tilde{U}_j}{\partial x_k} = \frac{\partial \tilde{G}_k \tilde{G}_j/\tilde{\rho}}{\partial x_k} = \frac{1}{\tilde{\rho}}\left(\frac{\partial \tilde{G}_k \tilde{G}_j}{\partial x_j} - \tilde{G}_k \tilde{U}_j \frac{\partial \tilde{\rho}}{\partial x_k}\right)$$

Then by straightforward manipulation we find that the transport of $\overline{g_j u_i}$ is described by:

$$\frac{\partial G_k \overline{g_j u_i}}{\partial x_k} = - \overline{g_j g_k}\frac{\partial U_i}{\partial x_k} - \overline{g_k u_i}\frac{\partial G_j}{\partial x_k} - G_j \overline{u_i \frac{\partial g_k}{\partial x_k}} - \overline{g_j u_i}\frac{\partial g_k}{\partial x_k}$$

$$+ \left\{ G_k U_j \overline{u_i \frac{\partial c'}{\partial x_k}} + G_k \overline{u_j u_i}\frac{\partial c}{\partial x_k} + \overline{g_k u_i} U_j \frac{\partial c}{\partial x_k} + G_k \overline{u_i u_j \frac{\partial c'}{\partial x_k}} \right.$$

$$\left. + U_j \overline{u_i g_k \frac{\partial c'}{\partial x_k}} + \overline{g_k u_i u_j}\frac{\partial c}{\partial x_k} + \overline{g_k u_i u_j \frac{\partial c'}{\partial x_k}} \right\}$$

$$- \overline{u_i c'}\frac{\partial p}{\partial x_j} + \mu\left(\overline{\frac{\partial^2 u_j}{\partial x_j} + c'\frac{\partial u_j}{\partial x_j} + u_i \frac{\partial c'}{\partial x_j} + \frac{\partial g_j}{\partial x_i}}\right)$$

$$- \frac{\partial}{\partial x_k}\left(\overline{g_j g_k u_i} + \left[\overline{c u_i p} + \overline{c' u_i p}\right]\delta_{jk} + \overline{g_j p}\,\delta_{ik}\right)$$

$$+ \overline{g_j \frac{\partial \tau_{ik}}{\partial x_k}} + \overline{c' u_i}\frac{\partial \tau_{jk}}{\partial x_k} + c\,\overline{u_i \frac{\partial \tau_{jk}}{\partial x_k}} + \overline{c' u_i \frac{\partial \tau_{jk}}{\partial x_k}} \qquad (11a)$$

The corresponding equation for $\overline{g_j m}$ emerges as:

$$\frac{\partial G_k \overline{g_j m}}{\partial x_k} = - \overline{g_k m}\frac{\partial G_j}{\partial x_k} - \overline{g_j g_k}\frac{\partial M}{\partial x_k} - G_j \overline{m \frac{\partial g_k}{\partial x_k}} - \overline{m g_j}\frac{\partial g_k}{\partial x_k}$$

$$+ \left\{ G_k U_j \overline{m \frac{\partial c'}{\partial x_k}} + G_k \overline{u_j m}\frac{\partial c}{\partial x_k} + \overline{g_k m} U_j \frac{\partial c}{\partial x_k} + G_k \overline{u_j m \frac{\partial c'}{\partial x_k}} \right.$$

$$\left. + U_j \overline{g_k m \frac{\partial c'}{\partial x_k}} + \overline{g_k u_j m}\frac{\partial c}{\partial x_k} + \overline{g_k u_j m \frac{\partial c'}{\partial x_k}} \right\}$$

$$- \overline{c' m}\frac{\partial p}{\partial x_j} + \mu\left(\overline{\frac{\partial u_j}{\partial x_j} + c'\frac{\partial m}{\partial x_j} + m\frac{\partial c'}{\partial x_j}}\right)$$

$$- \frac{\partial}{\partial x_k}\left(\overline{g_j g_k m} + \overline{p'(m-c'm)}\,\delta_{jk}\right)$$

$$+ \overline{c' m}\frac{\partial \tau_{jk}}{\partial x_k} + c\,\overline{m \frac{\partial \tau_{jk}}{\partial x_k}} + \overline{c' m \frac{\partial \tau_{jk}}{\partial x_k}} + \overline{g_j \frac{\partial}{\partial x_k}\left(\tau \frac{\partial m}{\partial x_k}\right)} \qquad (12)$$

These equations are clearly more cumbersome in appearance than their uniform-density counterparts. Moreover, the principal generation terms (involving mean velocity or mass-fraction gradients) introduce a further unknown second-moment tensor, $\overline{g_j g_k}$. Against this somewhat daunting complexity one must set the fact that the observed effects of density stratification are large (as noted above, one experiment showed a three-fold modification in effective Schmidt number). One should therefore be able to make fairly sweeping simplifications to the transport equations on the grounds that certain terms, while not negligible, cannot foreseeably be responsible for changes of such major proportions. We shall therefore assume that the *essential* physics are retained in the local-equilibrium form of the equations and, at the same time, discard all correlations involving terms of similar structure to those associated with the neglected transport terms. In support of the above steps one may note that, in a uniform density mixing layer the net transport of turbulent kinetic energy (convection minus diffusion) is generally an order of magnitude smaller than the rate of energy generation. Unfortunately these steps do not lead, unambiguously, to a suitably truncated (albeit still unclosed) equation set. To illustrate the problem, in forming the $\overline{g_j u_i}$ transport equation we could start with the $\tilde{G}_j$ equation in the form

$$\frac{\partial \tilde{G}_j}{\partial t} + \frac{\partial}{\partial x_k}\tilde{U}_k\tilde{G}_j = -\frac{\partial \tilde{P}}{\partial x_i} + \ldots$$

and this leads, on completing the tensorial algebra, to the following terms arising from the convective transport and pressure gradient

$$\rho U_k \frac{\partial \overline{g_j u_i}}{\partial x_k} = -\left(\overline{\rho u_i u_k}\frac{\partial G_j}{\partial x_k} + \overline{g_j g_k}\frac{\partial U_i}{\partial x_k}\right) - \overline{\rho' u_k}\,\overline{g_j \frac{\partial u_i}{\partial x_k}} - \rho G_j \overline{u_i \frac{\partial u_k}{\partial x_k}} + \overline{g_k g_j \frac{\partial u_i}{\partial x_k}} - \overline{\rho' g_j \frac{\partial u_i}{\partial t}} + \overline{p\left(\frac{\partial \rho u_i}{\partial x_j} + \frac{\partial g_j}{\partial x_i}\right)} + \ldots \qquad (11b)$$

Equation (11b) is considerably simpler in appearance than the corresponding part of (11a). On discarding transport and related terms the respective local-equilibrium equations become:

$$0 = -\left(\overline{g_k u_i}\frac{\partial U_j}{\partial x_k} + \overline{g_j g_k}\frac{\partial U_i}{\partial x_k}\right) - \overline{u_i \rho'}\frac{\partial P}{\partial x_i} + \overline{p\left(\frac{\partial \rho u_i}{\partial x_j} + \frac{\partial g_j}{\partial x_i}\right)} - \epsilon^{gu}_{ji} \qquad (13a)$$

and

$$0 = -\left(\rho\overline{u_i u_k}\frac{\partial G_j}{\partial x_k} + \overline{g_j g_k}\frac{\partial U_i}{\partial x_k}\right) - \overline{\rho' g_j \frac{\partial u_i}{\partial t}} + \overline{p\left(\rho\frac{\partial u_i}{\partial x_j} + \frac{\partial g_j}{\partial x_i}\right)} - \epsilon^{gu}_{ji} \qquad (13b)$$

While the two forms clearly become identical in the uniform-density limit, the approximations made for the unknown correlations in at least one version of equation (13) must introduce quite novel modelling methodology if the closed versions of the two equations are to be equivalent. The correlation involving the time derivative in (13b) is difficult to approximate but its magnitude can (from Taylor's hypothesis) be expected to be of order $\rho' g_j u_i\ |U|/\ell$ where $|U|$ denotes the mean convection velocity and ℓ a representative length scale of the energy-containing motions. It appears likely to be a substantial contributor to (13b) though about only one quarter the size of the largest of the generation terms ($-\overline{g_2^2}\partial U_1/\partial x_2$). As when a fully mass-weighted treatment is employed (see, for example, Rubesin and Rose [13]), mean pressure gradients appear in (13a) though they are absent from (13b). We note that the generation and "pressure-strain" correlations also exhibit differences. Overall, which version is better suited to serve as the basis for closure approximations? We suggest the version that most nearly allows the physical phenomena to be captured by the application of *uniform-density* methodology. This applies particularly to the approximation of the pressure correlations discussed in the next subsection. First, however, let us consider the equations describing other relevant second-moment correlations. Because of space limitations we give here only the severely truncated forms with transport and other terms of the same type discarded. The equation for $\overline{g_i g_j}$ corresponding to (13a) becomes:

$$0 = -\rho\left(\overline{g_j g_k}\frac{\partial U_i}{\partial x_k} + \overline{g_i g_k}\frac{\partial U_j}{\partial x_k}\right) + \overline{p\left(\frac{\partial \rho g_j}{\partial x_i} + \frac{\partial \rho g_i}{\partial x_j}\right)} - \epsilon^{gg}_{ij} \qquad (14a)$$

while the counterpart of (13b) is:

$$0 = -\rho\left(\overline{g_j u_k}\frac{\partial G_i}{\partial x_k} + \overline{g_i u_k}\frac{\partial G_j}{\partial x_k}\right) + \overline{p\left(\frac{\partial g_j}{\partial x_i} + \frac{\partial g_i}{\partial x_j}\right)} - \epsilon^{gg}_{ij} \qquad (14b)$$

where ϵ^{gg}_{ij} represents the dissipation of $\overline{g_i g_j}$ by molecular interactions. An interesting and far-reaching difference appears between the generation terms in the two equations: in the former, mean velocity gradients provide the driving agency for producing $\overline{g_i g_j}$ while in the latter this role is played by mass velocity gradients. Now, consider a flow such as examined by Rebollo[1] where density gradients are in the opposite sense to velocity gradients. In these circumstances the mass velocity may attain one or, indeed, several stationary values within the shear layer (Figure 1 shows the variation of G_1 across Rebollo's flow). In the vicinity of these positions the local-equilibrium concept must fail and equation (14b) becomes highly inappropriate since some of the discarded correlations will exceed the retained generation terms. So, if the strong effect of density gradient on the turbulent Schmidt number can be explained through the local equilibrium equations (in particular, the different contributions of velocity and mass-velocity gradients in the second-moment equations - not just through direct generation but, as we shall shortly see, indirectly via pressure interactions) equation (14a) should be selected.

To complete the equation set for the dynamic variables, the local equilibrium relation for $\overline{u_i u_j}$, using either approach, reduces to:

$$0 = -\left(\overline{u_i g_k}\frac{\partial U_j}{\partial x_k} + \overline{u_j g_k}\frac{\partial U_i}{\partial x_k}\right) + \overline{p\left(\frac{\partial u_j}{\partial x_i} + \frac{\partial u_i}{\partial x_j}\right)} - \epsilon^{uu}_{ij} \qquad (15)$$

The corresponding second-moment equations for the species flux are given below. We use the 'a' and 'b' labelling of the equations to distinguish the paths followed.

$$\overline{g_j m}: \quad 0 = -\left(\overline{g_j g_k}\,\frac{\partial M}{\partial x_k} + \rho\overline{g_k m}\,\frac{\partial U_j}{\partial x_k}\right) - \overline{\rho' m}\,\frac{\partial P}{\partial x_k} + \overline{p\,\frac{\partial \rho m}{\partial x_j}} - \epsilon_j^{gm} \tag{16a}$$

$$\overline{u_j n}: \quad 0 = -\rho\overline{u_j u_k}\,\frac{\partial N}{\partial x_k} - \overline{g_k n}\,\frac{\partial U_j}{\partial x_k} + \overline{p\frac{\partial n}{\partial x_j}} - \epsilon_j^{un} \tag{16b}$$

$$\overline{u_j m}: \quad 0 = -\overline{u_j g_k}\,\frac{\partial M}{\partial x_k} - \overline{g_k m}\,\frac{\partial U_j}{\partial x_k} + \overline{p\frac{\partial m}{\partial x_j}} - \epsilon_j^{um} \tag{17a}$$

$$\overline{g_j n}: \quad 0 = -\rho\overline{g_j u_k}\,\frac{\partial N}{\partial x_k} - \rho\overline{u_k n}\,\frac{\partial G_j}{\partial x_k} + \rho\overline{p\frac{\partial n}{\partial x_j}} - \epsilon_j^{gn} \tag{17b}$$

In practice, one would use (16a) and (17a) *or* (16b) and (17b). Superficially equation (17a) appears unnecessary since $\overline{u_j m}$ does not arise in (16a) - just as equation (15) seems to be unwanted baggage if the 'a' scheme is adopted since $\overline{u_i u_j}$ is absent from (13a) and (14a). In both cases, however, the correlations in question exert an influence via the pressure interactions - at least, if one respects uniform-density approaches to modelling mean-strain effects on the processes.

The Role of Pressure Fluctuations in Variable Density Turbulence

Within the space constraints of the present paper only the barest summary of the approximation of the pressure correlations can be provided. A fuller account is planned.

The equation describing the instantaneous level of pressure fluctuations about its mean value is obtained by taking the divergence of the equation of motion and subtracting its mean part. The resultant equation may be written:

$$-\frac{\partial^2 p}{\partial x_n^2} = \underbrace{\frac{\partial^2}{\partial x_n \partial x_m}\left(u_n g_m - \overline{u_n g_m}\right) + \frac{\partial G_m}{\partial x_n}\frac{\partial u_n}{\partial x_m} + \frac{\partial U_n}{\partial x_m}\frac{\partial g_m}{\partial x_n}}_{A}$$

$$\underbrace{+\frac{\partial}{\partial t}\left(\frac{\partial g_n}{\partial x_n}\right) + G_m\frac{\partial^2 u_n}{\partial x_n \partial x_m} + U_n\frac{\partial^2 g_m}{\partial x_n \partial x_m} + \frac{\partial^2 \tau'_{nm}}{\partial x_n \partial x_m}}_{B} \tag{18}$$

In the above arrangement those grouped as 'A' are clearly recognizable generalizations of terms present in a uniform-density flow; those in group 'B' are non-zero only because of density fluctuations. Though the individual terms in the latter group may be large we here adopt the view that *in correlation with* the fluctuating strain (and similar terms) their overall contribution to the pressure-interaction terms is less significant than that associated with density variations in part 'A'. This point of view is consistent with the dropping of numerous secondary source terms from the second-moment equations themselves. The simplification *may* prove to be an unacceptable one but, if it does, the task of closure would appear to be much more difficult.

If we integrate equation (18) (retaining only part A) the various correlations of interest may, for a homogeneous flow, be expressed in the forms shown in Table 1. The prime superscripts indicate that the quantity in question is evaluated at distance r from the point in question. Two distinctly different types of correlation, purely turbulence interactions (ϕ_1) and mean-gradient contributions (ϕ_2), are clearly evident. A straightforward application of uniform density ideas would suggest that in the equation for $\overline{a_i b_j}$ (a and b standing for either u or g) the ϕ_1 process would be represented as:

$$\phi_{1_{ij}}^{ab} = -\left(\overline{a_i b_j} - \frac{1}{3}\delta_{ij}\overline{a_k b_k}\right)/T_{ab} \tag{19}$$

where T_{ab} denotes a time scale of the interaction. This form has a number of frailties not least of which is the fact that (19) contracts to zero whereas, (as reference to equations (9b) and (10b) indicates) the ϕ_1 processes in Table 1 do not. In fact, the assumption that $\partial u_k/\partial x_k$ is zero is reasonable since the ϕ_1 correlations are predominantly made up of contributions from medium sized eddies in which molecular dispersion (the agency providing divergence) is insignificant. The same argument for simplification does not apply to $\partial g_k/\partial x_k$. Nevertheless, as a starting point, equation (19), and its analogue for the scalar fluxes, has much to commend it.

In uniform density flows there have been two principal approaches to modelling ϕ_2, the "quasi-isotropic" model (QIM) [14,15] and the "re-distribution-of-production" model (RPM) [14,16]. The first provides an exact solution when the 2-point correlation functions, such as appear in the integrals of Table 1, depend on radius only. The second is more intuitive, being based on the simple idea that the stress production rates are redistributed in an analogous way to that in which (19) modifies $\overline{a_i b_j}$. While the former has the clearer pedigree, the latter seems to achieve, overall, slightly better results.

Our studies have considered the application of these two approaches to the case of variable density. Direct application of RPM, together with the supposition that all the time scales T_{ab} etc. for both the "stresses" and the scalar fluxes remain in the same proportion to one another, produces, in conjunction with (19), the result that the turbulent Schmidt number is entirely unaffected by density gradients. This conclusion emerges irrespective of whether the equations relating to the 'a' or the 'b' decomposition are adopted. We note, too, that the same result emerges from conventional mass-weighted averaging.

Investigation with QIM has been limited to the 'a' decomposition since, as discussed above, the 'b' form leads to zero generation of $\overline{g_i g_j}$ where the mass velocity gradient becomes zero. In extrapolating

Equation	Correlation	Approximation ϕ_1	Approximation ϕ_2
$\overline{u_i u_j}$	$\overline{p\left(\frac{\partial u_i}{\partial x_j}+\frac{\partial u_j}{\partial x_i}\right)}$	$\frac{1}{4\pi}\int_V \overline{\left(\frac{\partial^2 g_m u_n}{\partial x_n \partial x_m}\right)'\left(\frac{\partial u_i}{\partial x_j}+\frac{\partial u_j}{\partial x_i}\right)}\frac{dV}{r}$	$+\frac{1}{4\pi}\left\{\frac{\partial G_m}{\partial x_n}\int_V \overline{\left(\frac{\partial u_n}{\partial x_m}\right)'\left(\frac{\partial u_i}{\partial x_j}+\frac{\partial u_j}{\partial x_i}\right)}\frac{dV}{r}+\frac{\partial U_n}{\partial x_m}\int_V \overline{\left(\frac{\partial g_m}{\partial x_n}\right)'\left(\frac{\partial u_i}{\partial x_j}+\frac{\partial u_j}{\partial x_i}\right)}\frac{dV}{r}\right.$
$\overline{g_i g_j}$	$\overline{p\left(\frac{\partial g_i}{\partial x_j}+\frac{\partial g_j}{\partial x_i}\right)}$	$\frac{\rho}{4\pi}\int_V \overline{\left(\frac{\partial^2 g_m u_n}{\partial x_n \partial x_m}\right)'\left(\frac{\partial g_i}{\partial x_j}+\frac{\partial g_j}{\partial x_i}\right)}\frac{dV}{r}$	$+\frac{\rho}{4\pi}\left\{\frac{\partial G_m}{\partial x_n}\int_V \overline{\left(\frac{\partial u_n}{\partial x_m}\right)'\left(\frac{\partial g_i}{\partial x_j}+\frac{\partial g_j}{\partial x_i}\right)}\frac{dV}{r}+\frac{\partial U_n}{\partial x_m}\int_V \overline{\left(\frac{\partial R_m}{\partial x_n}\right)'\left(\frac{\partial R_i}{\partial x_j}+\frac{\partial R_j}{\partial x_i}\right)}\frac{dV}{r}\right.$
$\overline{g_i u_j}$	$\overline{p\left(\frac{\partial g_i}{\partial x_j}+\frac{\partial \rho u_j}{\partial x_i}\right)}$	$\frac{1}{4\pi}\int_V \overline{\left(\frac{\partial^2 g_m u_n}{\partial x_n \partial x_m}\right)'\left(\frac{\partial g_i}{\partial x_j}+\frac{\partial \rho u_j}{\partial x_i}\right)}\frac{dV}{r}$	$+\frac{1}{4\pi}\left\{\frac{\partial G_m}{\partial x_n}\int_V \overline{\left(\frac{\partial u_n}{\partial x_m}\right)'\left(\frac{\partial g_i}{\partial x_j}+\frac{\partial \rho u_j}{\partial x_i}\right)}\frac{dV}{r}+\frac{\partial U_n}{\partial x_m}\int_V \overline{\left(\frac{\partial R_m}{\partial x_n}\right)'\left(\frac{\partial R_i}{\partial x_j}+\frac{\partial \rho u_j}{\partial x_i}\right)}\frac{dV}{r}\right.$
$\overline{g_i m}$	$\overline{p\frac{\partial m}{\partial x_i}}$	$\frac{\rho}{4\pi}\int_V \overline{\left(\frac{\partial^2 g_m u_n}{\partial x_n \partial x_m}\right)'\frac{\partial m}{\partial x_i}}\frac{dV}{r}$	$+\frac{\rho}{4\pi}\left\{\frac{\partial G_m}{\partial x_n}\int_V \overline{\left(\frac{\partial u_n}{\partial x_m}\right)'\frac{\partial m}{\partial x_i}}\frac{dV}{r}+\frac{\partial U_n}{\partial x_m}\int_V \overline{\left(\frac{\partial R_m}{\partial x_n}\right)'\frac{\partial m}{\partial x_i}}\frac{dV}{r}\right.$
$\overline{u_i m}$	$\overline{p\frac{\partial m}{\partial x_i}}$	$\frac{1}{4\pi}\int_V \overline{\left(\frac{\partial^2 g_m u_n}{\partial x_n \partial x_m}\right)'\frac{\partial m}{\partial x_i}}\frac{dV}{r}$	$+\frac{1}{4\pi}\left\{\frac{\partial G_m}{\partial x_n}\int_V \overline{\left(\frac{\partial u_n}{\partial x_m}\right)'\frac{\partial m}{\partial x_i}}\frac{dV}{r}+\frac{\partial U_n}{\partial x_m}\int_V \overline{\left(\frac{\partial R_m}{\partial x_n}\right)'\frac{\partial m}{\partial x_i}}\frac{dV}{r}\right.$

TABLE 1 - Fluctuating - pressure correlations, expressed in terms of the Poisson solution for p, simplified for the case of high Re homogeneous flow

the QIM to the present mixed weighted term we have adopted all but one of the assumptions of the uniform-density development (see [14]) including $\partial u_m/\partial x_m = 0$ (which, as we have remarked, is reasonable) and $\partial g_m/\partial x_m = 0$ (which is not). We have, however, not imposed symmetry in m and n when representing integrals involving the mixed velocity correlation, $\overline{g_m u_n'}$, etc. The outcome is a considerably longer formula for ϕ_2 than in the uniform density case which cannot be included here. Its implications are, however, shown in Figure 2 by the broken line where the turbulent Schmidt number is plotted as a function of d, a dimensionless measure of the density gradient. The resultant linear variation indicates an increase in Sc_t when density gradients oppose velocity gradients and a decrease when they are in the same sense. It must be said that this response is at odds with the experimental data of [1], which gives $Sc_t < 0.2$ for $d = 0.7$.

Launder [17] and Samaraweera [18] have also found the QIM to give unsatisfactory results in predicting heat or mass transfer in *uniform* density flows, at least if the linear return-to-isotropy model were used to represent the ϕ_1 part of the correlation between pressure and mass-fraction fluctuations:

$$\phi_{1j}^{um} = \overline{-u_j m}/T_{um} \qquad (20)$$

Ref. [18] did, however, obtain reasonably good agreement with the QIM if non-linear terms were added

$$\phi_{1j}^{um} = -\left[\overline{u_j m} + C_m \frac{\left(\overline{u_i u_j} - \frac{1}{3}\delta_{ij}\overline{u_k u_k}\right)}{\overline{u_k u_k}}\overline{u_i c}\right]/T_{um} \qquad (21)$$

where the coefficient C_m was chosen as -1.6 in order to produce the correct ratio of scalar fluxes down and at right angles to the mean scalar gradient. We have introduced this non-linear form into the present closure, adding also the corresponding terms for the second-rank "stress" tensors:

$$\phi_{1ij}^{ab} = -\left[\overline{a_i b_j} + C_{ab}\left(\overline{a_i b_k}\,\overline{a_k b_j} - \frac{1}{3}\delta_{ij}\,\overline{a_m b_k}\,\overline{a_m b_k}\right)/\overline{a_k b_k}\right]/T_{ab} \qquad (22)$$

where, for brevity, $\overline{a_i b_j} \equiv \left(\overline{a_i b_j} - \frac{1}{3}\delta_{ij}\,\overline{a_k b_k}\right)$

and C_{ab} takes the value -1.7.

The solid line in Figure 2 shows the predicted variation of turbulent Schmidt number when this non-linearity is introduced. For negative values of d there is little modification to the pattern produced by the linear model for ϕ_1. For positive values, however, there is a very marked effect, with Sc_t falling steeply for $d > 0.5$. Although agreement of the prediction with Rebollo's data is certainly better. The main conclusion to emerge from this computation is that the whole character of the prediction is fundamentally altered by the nature of the approximations made for the pressure-containing interactions. There is the implication that variable density flows offer a more searching test of basic closure ideas than do uniform density flows.

CONCLUSIONS

The use of the mixed weighting of velocities presented in this contribution helps illuminate the different roles that mean velocity and mass velocity gradients play in determining the level of the turbulent stresses and mass fluxes. Our studies

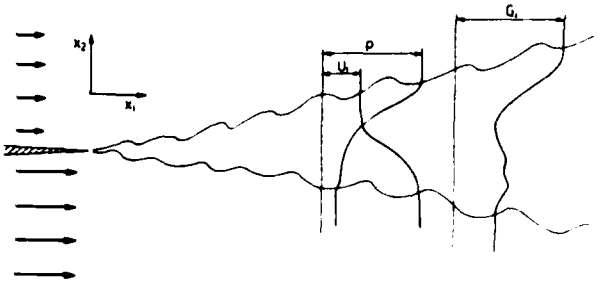

Figure 1. Flow geometry and mean profiles in a variable density mixing layer. From the data of Rebollo [1].

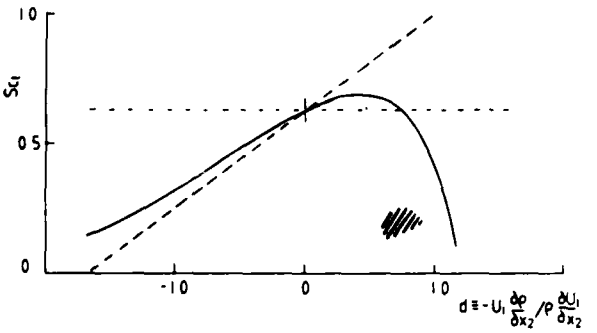

Figure 2 Equilibrium-flow predictions of the turbulent Sc_t number versus dimensionless density gradient parameter d. (1) --- RPM, (2) —— QIM (linear ϕ_1), (3) —— QIM (non-linear ϕ_1); /// Experimental data [1].

suggest that the key to accounting for the observed phenomena is the approximation of the pressure-strain and other pressure-containing correlations. The results obtained for a notionally homogeneous shear flow exhibit strong sensitivity to the nature of these approximations. None of the forms so far considered correctly reproduce the experimental response of the turbulent Schmidt number to mean density gradients. Our current view is that the application of uniform-density ideas to the pressure correlations would be more applicable if the correlations were manipulated so as to eliminate fluctuating mass velocity gradients, $\partial g_k/\partial x_j$, in favour of regular velocity and density gradients; the important distinction in this connection is that while the fluctuations of the energy-containing part of the velocity can be taken as divergence free the corresponding part of the fluctuating mass velocity cannot.

An inescapable conclusion of this study is that there is an urgent need for more experimental data of a fundamental kind that would allow a far more complete guide to the dependence of Sc_t on d (and possibly other factors) than is presently available.

ACKNOWLEDGEMENTS

Besides the assistance provided by our respective institutions, the research has been supported by the US Department of Energy, (Division of Basic Energy Sciences) through Contract No. AS03-76SF0 0034 and continues through the UK Science Research Council Grant, No. GR/B70056.

Authors' names appear alphabetically

REFERENCES

1 Rebollo, R.M., "Analytical and Experimental Investigation of a Turbulent Mixing-Layer of Different Gases in a Pressure-Gradient", Ph.D. Thesis, California Inst. of Technology, Pasadena, 1973.

2 Gibson, M.M., and Launder, B.E., ASME J. Heat Transfer, Vol. 98C, p.81, 1976.

3 Launder B.E., J. Fluid Mech., Vol. 67, p.569, 1975.

4 DuPont-Donaldson, C., Sullivan, R.C., and Rosenbaum, H., AIAA J., Vol. 10, p. 162, 1972.

5 Janicka, J., and Kollmann, W., "A Prediction Model for Turbulent Diffusion Flames Including NO-Formation", AGARD-PEP 54th Meeting, Cologne, 1979.

6 Favre, A., "Statistical Equations of Turbulent Gases", in *Problems of Hydrodynamics and Continuum Mechanics*, Society for Industrial and Applied Mathematics, Philadelphia, PA, pp. 237-266, 1969.

7 Kent, J.H. and Bilger, R.W., "The prediction of turbulent flame fields and nitric oxide formation" Proc. 16th Int. Symp. of Combustion, p. 1643, The Combustion Inst., 1976.

8 Jones, W.P., "Models for Turbulent Flows with Variable Density and Combustion", VKI Lecture Series, 1979-2, Jan. 15-19, 1979.

9 Libby, P.A., "Studies in Variable-Density and Reacting Turbulent Shear Flows," in Studies in Convection, Vol. 2, ed. by B.E. Launder, 1977.

10 Brown, G.L., and Roshko, A., J. Fluid Mech., Vol. 64:4, p. 775, 1974.

11 Kollmann, W., and Vandromme, D., "Turbulent Shear Flow with Fluctuating Density", AIAA 12th Fluid and Plasma Dynamics Conference, Williamsburg, VA, July 23-25, 1979.

12 Janicka, J., and Lumley, J.L., "Second-Order Modelling in Non-Constant Density Flows", Fluid Dynamics and Aerodynamics, Sibley School of Mechanical and Aerospace Engineering, Cornell Univ., Ithaca, NY, Jan. 1979.

13 Rubesin, M.W., and Rose, W.C., "The Turbulent Mean Flow, Reynolds Stress and Heat-Flux Equations in Mass-Averaged Dependent Variables," NASA TNX 62248, 1973.

14 Launder, B.E., Reece, G.J., and Rodi, W., J. Fluid Mech., Vol. 68, p. 537, 1975.

15 Naot, D., Shavit, A., and Wolfshtein, M., Physics of Fluids, Vol. 16, 1973.

16 Naot, D., Shavit, A., Wolfshtein, M., "Interactions Between Components of the Turbulent Velocity Correlation Tensor Due to Pressure Fluctuations", Israel J. Technol., Vol. 8, p.259, 1970.

17 Launder, B.E., "Heat and Mass Transport", *Topics in Applied Physics Vol. 12 "Turbulence"* Ch. 6, Ed. P. Bradshaw, Springer Verlag, Heidelberg, 1976.

18 Samaraweera, D.S.A., "Turbulent Heat Transport in 2- and 3-Dimensional Temperature Fields", Ph.D. Thesis, Faculty of Engineering, University of London, 1978.

PRESSURE STRAIN: EXACT RESULTS AND MODELS

J.J.D. DOMINGOS
Instituto Superior Técnico
Lisbon, Portugal

ABSTRACT

Exact results for pressure velocity correlations are deduced which allow direct measurement using hot wire techniques. Coherent models for linear and non-linear pressure interactions which satisfy realizability and isotropic limits taking into account non-isotropic dissipation, are presented and discussed. Experimental data for weak and strong nearly homogeneous turbulent shear flows are predicted within experimental accuracy.

NOMENCLATURE

A - Fourth order tensor defined by (18)

B - Anisotropy tensor ($B_{ij} = \overline{u_i u_j}/Q - \frac{1}{3}\delta_{ij}$)

F - $\phi + \pi$

G - Generation of turbulence energy

H - Tensor defined by (27)

G - $(G_{ij} = \overline{u_i u_m}\frac{\partial U_j}{\partial x_m} + \overline{u_j u_m}\frac{\partial U_i}{\partial x_m})$

P^+ - Pressure

p - Flutuating pressure

K - $(\overline{u_1^2} + \overline{u_2^2} + \overline{u_3^2})/2$

Q - 2K

r - Distance vector $\sum_m (x_m - x'_m)^2$

R - Stress tensor ($R_{ij} = \overline{u_i u_j}$)

R_{el} - Reynolds number of turbulence ($R_{el} = Q^2/9\epsilon\nu$)

S - Surface enclosing the flow

u - Flutuating velocity

U - Mean velocity

V - Velocity

Greek Symbols

$\alpha, \beta, \gamma, \gamma', \lambda, \alpha_1$ ... scalar functions or constants

ρ - specific mass

ν - kinematic viscosity

δ - kronecker symbol

ϕ_{ij} - defined by (29)

ϕ^+_{ij} - non linear pressure interaction defined by (26)

ψ - scalar function for dissipation, defined by (29)

ϵ_{ij} - half dissipation rate of stress component $u_i u_j$

ϵ - trace of ϵ_{ij}

Ω - surface enclosed by S

π - pressure strain

Subscripts and superscripts

i, j, k, l, m, - vector or tensor component (repeated index means assumption)

$\overline{\quad}$ - (overbar) - ensemble average

' - (prime) - integration variable

Special symbols

∇^2 - Laplacian operator

tr - trace of a sencond order tensor

I_B - first invariant of tensor B($I = t_r B$)

II_B - second invariant of tensor B($II = t_r B^2$)

III_B - third invariant B($III = t_r B^3$)

I_G, II_G, III_G - the same as above for tensor G

$B^2_{ij} = \sum_m B_{im} B_{mj}$

INTRODUCTION

Unsatisfactory performance of Reynolds stress closures are leading to the idea that no improvement is possible within the framework of one point closures. However, a critical review of methods presently in use show that overlooking of crucial terms combined with unnecessary assumptions led to contradictions and global uncoherence on the modelling. Among crucial terms are those involving pressure which are the only ones which introduce two point velocity correlations. Isotropic dissipation, on the other hand, is in formal contradiction with the exact assymptotic limits known as realizability conditions.

In this paper, both question are adressed. New models for linear and non-linear pressure interactionare proposed and the assumption of isotropic dissipation is overcomed without a need to solve more differential equations. The modelling satisfy the exact assymptotic limits of isotropy and maximum anisotropy (realizability conditions) and sets the framework for systematic improvement based on experimental data. The new framework is likely to exaust the predictive capabilities of one point closures.

The first section of the paper presents new exact results expressing the pressure field in terms of the velocity field. From these results, pressure velocity correlations are deduced which stress the local contribution to the correlation. Next, a simple non-linear model for pressure strain is deduced on the assumption of fundamental simmetries relative to the principal axis of the Reynolds stress tensor. In these axis, normal pressure strain components are found to be in agreement with experimental data with no need to adjustable constants.

In section 4, a short critical review is made of linear and non-linear pressure interaction if experimental validation is sought. This leads to discussion of return to isotropy of homogeneous turbulence and the formulation of the most general model of non-linear pressure interaction coupled with non-isotropic dissipation. A rearrangement of terms (and concepts) and use of the trace of the dissipation tensor overcomes the contradictions associated with non-isotropic dissipation and realizability.

It is shown how rate of return to isotropy is likely to depend on the way turbulence is generated. A more complex model for pressure strain is then proposed in conjunction with one for non-linear pressure interaction. Predictions are then compared with experimental data and shown to be within experimental accuracy.

1. EXACT RESULTS

In a cartesian frame of reference the Navier Stokes equations for an incompressible fluid are:

$$\frac{\partial V_i}{\partial t} + \frac{\partial}{\partial x_m} V_m V_i - \nu \nabla^2 V_i = - \frac{1}{\rho} \frac{\partial P^+}{\partial x_i} \qquad (1)$$

$$\frac{\partial V_i}{\partial x_i} = 0 \qquad i,m = 1, 2, 3 \qquad (2)$$

Taking the divergence of 1) and using 2) gives:

$$\nabla^2 \left(\frac{P^+}{\rho}\right) = - \frac{\partial}{\partial x_m} \cdot \frac{\partial}{\partial x_i} V_m V_i \qquad (3)$$

This Poisson equation has the exact solution:

$$\frac{P^+}{\rho} = \frac{1}{4\pi} \iiint_\Omega \frac{1}{r} \left(\frac{\partial}{\partial x'_m} \frac{\partial}{\partial x'_i} V'_m V'_i\right) d\Omega' + P^+_S \qquad (4)$$

$$P^+_s = \frac{1}{4\pi\rho} \iint_S \left[\frac{1}{r} \left(\frac{\partial P^+}{\partial n}\right)_{s'} - \left(P \frac{\partial}{\partial n} \frac{1}{r}\right)_{S'}\right] dS' \qquad (5)$$

As a shorthand notation introduce

$$F_{mi} = V_m V_i \qquad (6)$$

Because the integrand is(4) has no singularity at r = 0, use of Gauss theorem gives:

$$\frac{P^+}{\rho} = - \frac{1}{4\pi} \iiint_\Omega \left(\frac{\partial}{\partial x'_m} F'_{mi}\right) \cdot \frac{\partial}{\partial x'_l} \left(\frac{1}{r}\right) d\Omega' + \qquad (7)$$

$$+ \frac{1}{4\pi} \iint_S \frac{F'_{mi}}{r} \cos \gamma'_i \, dS' + P^+_S$$

where $\cos \gamma'_i$ is the cossinus of the angle between x'_i and the outward normal to S.

Noting that

$$\frac{\partial}{\partial x'_m} \left(\frac{1}{r}\right) = \frac{x_m - x'_m}{r^3}$$

use of Gauss theorem in (7) is not possible because the integrand would become singular at r = 0. This singularity can be overcomed as in [1] or directly taking into account the identity:

$$\frac{\partial}{\partial x'_m} F'_{mi} = \frac{\partial}{\partial x'_m} \left[F'_{mi} - F_{mi}\right] \qquad (8)$$

Introducing (8) in(7), use of Gauss theorem becomes legitimate and then:

$$\frac{P^+}{\rho} = \frac{1}{4\pi} \iiint_\Omega (F'_{mi} - F_{mi}) \frac{\partial^2}{\partial x'_m \partial x'_i} \left(\frac{1}{r}\right) + \qquad (9)$$

$$- \frac{1}{4\pi} \iint_S (F'_{mi} - F_{mi}) \frac{\partial}{\partial x'_i} \left(\frac{1}{r}\right) \cos \gamma'_m \, dS' + (\ldots)$$

Noting again that F_{mi} is not a function of the integration variable:

$$\iint_S F_{mi} \cos \gamma'_m \frac{\partial}{\partial x'_m} \left(\frac{1}{r}\right) dS' = F_{mi} \iint \cos \gamma'_m \left(\frac{\partial}{\partial x'_m}\right) \cdot \frac{1}{r} \, dS' \qquad (10)$$

The surface integral can be evaluated in closed form for any surface and gives $- \frac{4\pi}{3} \delta_{mi}$ for any point inside the domain enclosed by S;the proof can be found in standard texts of Potential Theory.

Using the previous results, (7) becomes:

$$\frac{P^+}{\rho} = -\frac{1}{3} F_{mm} + \frac{1}{4\pi} \iiint_\Omega (F'_{mi} - F_{mi}) \frac{\partial^2}{\partial x'_m \partial x'_i} \cdot$$

$$\cdot \left(\frac{1}{r}\right) d\Omega' + \frac{1}{4\pi} \iint F'_{mi} \left[\frac{\cos\gamma'_i}{r} - \cos\gamma'_m \frac{\partial}{\partial x'_i} \frac{1}{r}\right] \cdot$$

$$\cdot\, dS' + P_S^+ \qquad (11)$$

To find $\frac{\partial P^+}{\partial x_k}$ use can be made of the fact that $\frac{\partial P^+}{\partial x_k}$ obeys itself a Poisson equation and the previous deductions for P^+ are valid, "mutatis mutandis" for $\frac{\partial P^+}{\partial x_m}$. It would be noted, however, that by parts may be used for only two of $\frac{\partial}{\partial x_m}$, $\frac{\partial}{\partial x_i}$, $\frac{\partial'}{\partial x_k}$, which gives rise to the alternative expressions:

integration

$$\frac{1}{\rho} \frac{\partial P^+}{\partial x_k} = -\frac{1}{3} \frac{\partial F_{mm}}{\partial x_k} + \frac{1}{4\pi} \iiint_\Omega \left(\frac{\partial}{\partial x'_k} F'_{mi} -\right.$$

$$\left. + \frac{\partial}{\partial x_k} F_{mi}\right) \frac{\partial^2}{\partial x'_k \partial x'_k} \frac{1}{r}\, d\Omega' + (\ldots) \qquad (12)$$

$$\frac{1}{\rho} \frac{\partial P^+}{\partial x_k} = -\frac{1}{3} \frac{\partial}{\partial x_m} F_{mk} + \frac{1}{4\pi} \iiint_\Omega \left(\frac{\partial}{\partial x'_m} F'_{mi} -\right.$$

$$\left. + \frac{\partial}{\partial x'_m} F_{mi}\right) \frac{\partial^2}{\partial x'_k \partial x'_i} \left(\frac{1}{r}\right) d\Omega' + (\ldots) \qquad (13)$$

where (...) are boundary integrals.

2. Turbulent Flows

The equations for the mean field are:

$$\frac{DU_i}{Dt} + \frac{\partial}{\partial x_m} \overline{u_i u_m} - \nu \nabla^2 U_i = -\frac{\partial P}{\partial x_i} \qquad (14)$$

and for the Reynolds stresses:

$$-\frac{D}{Dt} \overline{u_i u_j} = -\left(\overline{u_i u_m} \frac{\partial U_i}{\partial x_m} + \overline{u_i u_m} \frac{\partial U_i}{\partial x_m}\right) +$$

$$-\frac{\partial}{\partial x_m} \left(\overline{u_i u_j u_m}\right) + \nu \frac{\partial}{\partial x_m} \frac{\partial}{\partial x_m} u_i u_j - 2\nu \cdot$$

$$\cdot \overline{\frac{\partial u_i}{\partial x_m} \frac{\partial u_i}{\partial x_m}} - \left(\overline{u_i \frac{\partial p}{\partial x_j}} + \overline{u_j \frac{\partial p}{\partial x_i}}\right) \qquad (15)$$

The last term on the r.h.s. of 17) is the only one which involves the flutuating pressure. It is also the only one which introduces velocity correlations at two different points.

To eliminate p, use is made of the previously found exact expressions. This can be done introducing 14) and 15) in either 12) or 13). Using 13) and forming the correlation with the velocity gives for unbounded flows the exact results:

$$-\left(\overline{u_j \frac{\partial p}{\partial x_i}} + \overline{u_i \frac{\partial p}{\partial x_j}}\right) = \frac{2}{3} G_{ij} + \frac{1}{3} \frac{\partial}{\partial x_m} \overline{u_i u_j u_m} -$$

$$-\frac{1}{2\pi} \iiint_{-\infty}^{\infty} \left[\overline{u_j u'_m} \frac{\partial U'_\ell}{\partial x'_m} - \overline{u_j u_m} \frac{\partial U_\ell}{\partial x_m}\right] \frac{\partial^2}{\partial x'_i \partial x'_\ell} \frac{1}{r}\, dV' +$$

$$-\frac{1}{2\pi} \iiint_{-\infty}^{\infty} \left[\overline{u_i u'_m} \frac{\partial U'_\ell}{\partial x'_m} - \overline{u_i u_m} \frac{\partial U_\ell}{\partial x_m}\right] \frac{\partial^2}{\partial x'_j \partial x'_\ell} \frac{1}{r}\, dV' +$$

$$-\frac{1}{4\pi} \iiint_{-\infty}^{\infty} \left[\overline{u_j u'_m} \frac{\partial u'_\ell}{\partial x'_m} - \overline{u_j u_m} \frac{\partial u_\ell}{\partial x_m}\right] \frac{\partial^2}{\partial x'_m \partial x'_\ell} \frac{1}{r}\, dV' +$$

$$-\frac{1}{4\pi} \iiint_{-\infty}^{\infty} \left[\overline{u_i u'_m} \frac{\partial u'_\ell}{\partial x'_m} - \overline{u_i u_m} \frac{\partial u_\ell}{\partial x_m}\right] \frac{\partial^2}{\partial x'_j \partial x'_\ell} \frac{1}{r}\, dV' \qquad (16)$$

Boundary integrals do not appear in the expression above because they vanish when the bounding surface is away from the point more than the correlation length.

Besides its theoretical usefulnes, the exact representation for the pressure velocity correlations given by (16) provides also a basis for their experimental measurement because only well mastered techniques for the measurement of two-point velocity correlations are needed.

An approach similar to the one which lead to (16) was independently attempted by A. Lin and M. Wolfsthein [3]. However, the overlooking of the singularities previously noted made their results invalid.

3. PRESSURE STRAIN

In the exact representation of pressure velocity correlations given by (16) the terms involving the mean strain are linear in the Reynolds stresses. Develloping the mean strain in a Taylor series around $x' = x$ and neglecting higher order terms, the pressure strain terms may be represented as:

$$\pi_{jk} = \frac{2}{3} G_{jk} - \left[A^{jl}_{km} + A^{kl}_{jm}\right] \frac{\partial U_m}{\partial x_l} \qquad (17)$$

with

$$A^{jl}_{km} = \frac{1}{2\pi} \iiint_{-\infty}^{\infty} \left(\overline{u_j u'_l} - \overline{u_j u_l}\right) \frac{\partial^2}{\partial x'_k \partial x'_m} d\Omega \qquad (18)$$

A^{jl}_{km} is a fourth order tensor. Because a cartesian frame of reference was assumed, no distinction between covariant and contravariant componentes is needed. Therefore, the arrangement of indices was choosen for the sake of clarity, the lower indices refering to the derivatives of $\left(\frac{1}{r}\right)$.

The tensor has the following exact properties:

$$A^{jm}_{\alpha\alpha} \equiv \sum_\alpha A^{jm}_{\alpha\alpha} = 0 \qquad (19)$$

$$A^{j\beta}_{k\beta} = \sum_\beta A^{j\beta}_{k\beta} = \frac{2}{3} \overline{u_j u_k} \qquad (20)$$

The first relation is a consequence of Green's identities; the second of the incompressibility condition. Besides, continuity of second derivatives of $\frac{1}{r}$ $(r \neq 0)$ gives the following properties:

$$A^{jl}_{km} = A^{lj}_{mk} \qquad (21)$$

If the flow is homogeneous, but only then,

$$A^{jl}_{km} = A^{lj}_{km} \tag{22}$$

The trace of π_{ij} is associated with pressure diffusion and is given by

$$\pi_{kk} = \frac{2}{3} G_{kk} - \left(A^{kl}_{km} + A^{kl}_{km} \right) \frac{\partial U_m}{\partial x_l} \tag{23}$$

If the flow is homogeneous, (20) and (22) give $\pi_{kk} = 0$ showing clearly the pressure diffusion is associated with the non-simmetry of the l,j indices. It also shows the inconsistency of previous modellings which assume the equivalent of (21) and (22) and later attempt to model pressure diffusion. All the previous expressions are exact. However,the number of unknowns exceeds the number of equations and aditional assumptions have to be made. Following Rotta [4],Launder et al [5] have proposed an expression equivalent to A^{ij}_{km} as the most general linear combination of Reynolds stresses at the point. The remaining constant would then be found from experiment. None of these models satisfy the exact assymptotic limits $\pi_{11},\pi_{22},\pi_{33} \to 0$ when $u_1,u_2,u_3 \to 0$, known as realizability conditions. Besides, they are unable to predict, with the same set of constants, known experimental data for weak and strong, nearly homogeneous shear flows.

Using the previously found exact expressions a simple model was deduced on the assumption of simmetries of the correlations similar to the ones of isotropic turbulence when expressed in the principal axis of the Reynolds stresses. The conditions of realizability and convergence to the exact isotropic values completelly specifies the model with no need to adjustable constants. In the principal axis of the Reynolds stress tensor, final expressions are:

$$A^{ij}_{ij} = (3/10)\, u_i^2\, u_j^2 / K \quad \text{(no sum)} \tag{24}$$

with A^{ii}_{ii} (no sum) given by (19), (20). (25)

LINEAR AND NON LINEAR PRESSURE INTERACTION

The simple model refered previously has no adjustable constants, satisfies the assymptotic limits of isotropy and realizability and predicts, within experimental accuracy, known experimental data for weak and strong nearly homogeneous shear flow. However, it can not be considered wholly satisfactory. From a practical point of view, its use requires two coordinate transformations - to and from principal axis of the Reynolds stresses. Besides, its experimental validation and use rests on the assumptions of isotropic dissipation and validity of Rotta's modelling of non linear pressure interaction which are not consistent with the assymptotic limits of one and two dimensional turbulence implied by realizability or by exact mathematical reasoning. To overcome these limitations requires previous consideration of dissipation and Rotta's term.

Return to isotropy of homogeneous turbulence

For decaying, non-istropic, homogeneous and isothermal turbulence the equations for the Reynolds stresses reduce to:

$$\frac{D}{Dt}\overline{u_i u_j} = -\frac{1}{\rho}\left(\overline{u_j \frac{\partial p}{\partial x_i}} + \overline{u_i \frac{\partial p}{\partial x_j}}\right) - 2\nu \overline{\frac{\partial u_i}{\partial x_k}\cdot\frac{\partial u_j}{\partial x_k}}$$

$$= -\phi^{+}_{ij} - 2\varepsilon_{ij} \tag{26}$$

Physical reasoning and the exact expressions found previously sugest ϕ^{+}_{ij} to be related to the anisotropy tensor. Within the scope of one point closures involving no more than double velocity correlations B_{ij} is the only meaninfull second order tensor. Therefore, ϕ^{+}_{ij} may be sought as the most general isotropic dependence on B which is given by

$$-\phi^{+}_{ij} = \lambda\delta_{ij} + \beta' B_{ij} + \gamma B_{im}B_{mj}$$

with λ, β, γ scalar functions. The assymptotic limits imposed by realizability and the condition of zero trace imply

$$\phi^{+}_{ij} = \gamma\left[\left(\frac{1}{3} - II_B\right) B_{ij} + B^2_{ij} - \frac{1}{3} II_B\, \delta_{ij}\right] = \gamma \cdot H_{ij} \tag{27}$$

Regarding anisotropy of dissipation it may be assumed that it may be related to the anisotropy tensor. Considering the most general isotropic relation between both tensors and taking into account the realizability conditions gives:

$$2\varepsilon_{ij} = 2\bar{\varepsilon}\,(B_{ij} + \delta_{ij/3}) + \gamma' H_{ij} \tag{28}$$

Closure of the Reynolds stress system of equations need an equation for $\bar{\varepsilon}$, and the scalar functions γ and γ'. The full set of equations is consistent with the basic assumptions and satisfy the assymptotic limits.

From a computational point of view it is advantageous to rearrange $-\phi^{+}_{ij} - 2\varepsilon_{ij}$ as:

$$-\phi^{+}_{ij} - 2\varepsilon_{ij} = -\bar{\varepsilon}\,\phi_{ij} - \frac{2}{3}\bar{\varepsilon}\,\delta_{ij}$$

$$\frac{D\bar{\varepsilon}}{Dt} = -\psi\frac{\varepsilon^2}{Q} \tag{29}$$

giving:

$$-\phi_{ij} = 2B_{ij} + \beta H_{ij} \tag{30}$$

with β a scalar function of the invariants of B, Reynolds number of turbulence ...

Splitting (29) was a starting expression in Lumley and Newman [9] whose expressions for ϕ_{ij} is different from ours. It must be stressed that (29) does not imply isotropic dissipation but, instead, that change of anisotropy is due to pressure interaction and dissipation. A normalized rate of change of anisotropy may be expressed exactly by

$$\frac{d\log II}{d\log Q} = \beta\,(1/3 - II + III/II) \tag{31}$$

which sugests that rate of change of anisotropy depends on the sign of the third invariant which implies a dependence of the way the turbulent field was generated. This inference agrees with recent experimental observations of Mathieu et al [10]. A discussion of specific functional forms for β is beyond the scope of this paper. Though experimental data is too scarce and mainly confined to III < 0, it seems, however, that a value of $\beta \sim 2$ may be taken in a

first approach. In conclusion, $\bar{\varepsilon}\,\phi_{ij}$ is proposed as a replacement of Rotta's model.

Pressure strain modelling

Exact results given by (16) sugest generation and anisotropy as the two basic second order tensors for modelling pressure strain. The most general isotropic relation between pressure strain (π), generation (G) and anisotropy (B) is:

$$\pi = \alpha_0\delta + \alpha_1 G + \alpha_2 B + \alpha_3 G^2 + \alpha_4 B^2 + \alpha_5(GB + BG) +$$

$$\alpha_6(G^2B + BG^2) + \alpha_7(GB^2 + B^2G) + \alpha_8(B^2G^2 + G^2B^2)$$

where $\alpha_0 \ldots \alpha_8$, are scalar functions of the ten basic invariants given by the trace of G, G^2, G^3, B, B^2, B^3, GB, GB^2, BG^2, B^2G^2. There is no experimental information to justify use of this general relation and a subset will be used. This subset is one of lowest order in G and B which is able to satisfy the basic requirements of realizability, isotropy and zero trace. The subset choosen is:

$$\pi_{ij} = \alpha\,(G_{ij} - \frac{I_G}{3}\,.\,\delta_{ij}) - \alpha\, I_G\, B_{ij} + \lambda'\, H_{ij} \qquad (32)$$

H is defined by (27). It will be noted that H satisfy by itself the basic requirements, and that the term in brackets is "departure from isotropy" of generation.

In the assymptotic limit of isotropy $\alpha \to 0.6$ exactly. Besides, λ' is taken as $\lambda.I_G$, which is the simplest dependence on the invariant of generation which makes λ dimensionless. α and λ are expected to be weak functions of R_{el}, and the invariants of G and B.

Combining (31) and (32) gives for total pressure interaction

$$F_{ij} = \pi_{ij} + \bar{\varepsilon}\phi_{ij} = \alpha\,(G_{ij} - \frac{I_G}{3}\,\delta_{ij} - I_G\,.\,B_{ij}) -$$

$$+ 2\bar{\varepsilon}B_{ij} - (\beta\bar{\varepsilon} - \lambda I_G)\,.\,H_{ij} \qquad (33)$$

In non homogeneous turbulence pressure diffusion is to be modelled separately.

Comparaison with experiment

Experimental data for weak and strong nearly homogeneous shear flows of Corrsin et al refered previously was compared with predictions given by (33). There is only λ to adjust if α is taken at the isotropic value ($\alpha = 0.6$), and $\beta = 2$. λ and β must be optimized. As seen from (33) they act together in defining the coeficient of H. Individual adjustments are not critical. $\lambda = 3$ was chosen.

Measurements and Predictions
$F_{ij} = \pi_{ij} + \phi_{ij}$ (10^4 cm^2 s^{-3})

	F_{11}	F_{22}	F_{33}	F_{12}	
Measured	-.312	.156	.156	.335	WEAK SHEAR [6]
Predicted	-.312	.136	.176	.328	
Error %	0	-13	12.5	2	
Measured	-7.21	3.39	3.83	7.21	STRONG SHEAR [7] [8]
Predicted	-7.32	3.38	3.94	6.52	
Error %	-1.5	-0.05	3	9.5	

Predictions are within experimental accuracy. Compared with other models, for instance Launder et al [5], or D.C. Leslie [8] which used measured anisotropies, errors are smaller. Besides, it predicts correctly the sign of the well observed difference $\overline{u_2^2}$ and $\overline{u_3^2}$. The fact that model (33) satisfies realizability conditions must also be stressed

CONCLUSIONS

A replacement for Rotta's modelling which takes into account non-isotropic dissipation was proposed together with a new model for pressure strain. The new models are the first ones to comply with the exact values at isotropy and maximum anisotropy (realizability conditions). A new and basic second order tensor (H) which automatically satisfies zero trace, isotropy and realizability conditions was introduced.

The models predict within experimental accuracy available data directly relevant to the model.

Rate of change of anisotropy appears to depend on the way decaying turbulence is generated. The need for experimental data with III > 0 must be stressed.

AKNOWLEDGEMENTS

This work was iniciated while visiting at Fluids Section, Dept. Mech. Eng., Imperial College. Support from SRC and from Scientific Affairs Division of NATO though Grant Nº 1586, and the friendly stimulating environment provided by Prof. J.H. Whitelaw are gratefully aknoledged.

REFERENCES

1 Domingos, J.J.D., "Some exact results for the pressure field in viscous incompressible flows", FS/79/6. Report Imperial College (1979).

2 Domingos, J.J.D., "Pressure velocity correlation - a short survey of new results", U.T. Lisbon, Report IST:DTA: TR3/79.

3 Lin, A and Wolfstein, "Theoretical study of the Reynolds stress Equations", Turbulent Shear Flows I, Springer Verlog, 1979.

4 Rotta, J.C., "Statische theorie nichthomogener turbulence", Zeitschrift fur Physik 129, 547 and 131, 51 (1951).

5 Launder, B.E., Reece, G.J. and Rodi, W. "Progress in the devellopment of a Reynolds-stress turbulence closure", J. Fluid Mech. 68, 537, 1975.

6 Champagne, F.H., Harris, V.G. and Corrsin, S., "Experiments on nearly homogeneous turbulent shear flows", J. Fluid Mech 41, 81, 1970.

7 Harris, J.R., Graham, J.A.H., and Corrsin, S. "Further experiments in nearly homogeneous shear flow", J. Fluid Mech. 81, 657, 1977.

8 Leslie, D.C., "Analysis of a strongly sheared, nearly homogeneous turbulent shear flow", Dept. Nuclear Eng., Queen Mary College, 1979.

9 Lumley, J.L., Newman, G.R., "The return to isotropy of homogeneous turbulence", J. Fluid Mech 82, 161, 1977.

10 Gence, J.N., Mathieu, J., "The return to isotropy of an homogeneous turbulence having been submitted to two successive plain strains", J.Fluid Mech. 101, 555, 1980.

11 Schumann, U., "Realizability of Reynolds-stress turbulence models", The Physics of Fluids,20, 721, 1977.

DIRECT SIMULATION OF HOMOGENEOUS TURBULENT SHEAR FLOWS

ON THE ILLIAC IV COMPUTER: APPLICATIONS TO COMPRESSIBLE AND INCOMPRESSIBLE MODELING

W. J. Feiereisen,* E. Shirani,** J. H. Ferziger, and W. C. Reynolds
Department of Mechanical Engineering
Stanford University
Stanford, California

Abstract

Full simulations of sheared homogeneous turbulence were made on the ILLIAC IV computer using 64 × 64 × 64 mesh points; both incompressible and compressible cases were run. The results are validated by comparison with experimental data and are used as the basis for a study of phenomenological turbulence models. A flaw in eddy viscosity models is pointed out. The Rotta pressure-strain model is shown to be reasonably good when one includes the anisotropy of the dissipation in the model. On the other hand, the commonly used model for the rapid pressure-strain term is shown to be not very accurate. Compressibility effects are fairly small, but the acoustic pressure fluctuations in these flows can be quite large. Despite this, little change in the modeling is required.

1. Objectives

The objectives of this paper are to provide guidance to the development of simple phenomenological models of turbulence through comparisons of models against exact numerical simulation of simple turbulent flows. The flow of interest is a homogeneous shear flow in which the mean velocity varies linearly in one direction.

Homogeneous shear flow is of complexity intermediate between unsheared homogeneous turbulence and inhomogeneous turbulent shear flows. Its study can provide better understanding of turbulence and can be used in testing turbulence theories and statistical turbulence models.

2. Review of Previous Work

Reis (1952) studied homogeneous shear flows mathematically. Rose (1966) studied the behavior of the turbulence intensities experimentally at low Reynolds numbers. Champagne, Harris and Corrsin (1970), Harris, Graham, and Corrsin (1976), Rose (1970), Hwang (1971), and Mulhearn and Luxton (1975) studied this flow at higher Reynolds numbers. Tavoularis (1978) studied this flow and included a passive scalar. They all measured the shear stress correlations, various length scales, one- and two-point velocity correlations, spectra, and the kinetic energy of turbulence. Table 1 summarizes some of the basic parameters of these flows.

Numerical simulations of homogeneous shear flow were made by Shaanan, Ferziger, and Reynolds (1975) using large eddy simulation. Rogallo (1977) made full simulations of low Reynolds number homogeneous turbulent shear flows. This paper reports further simulations of this kind.

We also look at the effect of compressibility on homogeneous turbulent shear flow. Early studies of compressible turbulence introduced decomposions of the flow variables into modes and studied their interaction. Kovasznay (1953) and Chu and Kovasznay (1957) derived equations for the vorticity mode, which is responsible for convective and vortical motions, and for the pressure (acoustic) and entropy (temperature) modes. They analytically studied interactions among these modes. Moyal divided the kinetic energy spectra into "eddy turbulence" and "random noise" parts. He did this by Fourier-transforming the velocity vector and decomposing it into vectors that are perpendicular and parallel to the wave-number vector. His analysis, like that of Chu and Kovasznay, is limited to low turbulence levels and therefore not applicable in technologically useful flows. Morkovin (1962) showed that the Reynolds stresses in supersonic boundary layers were structurally similar to those in incompresisble flows. Laufer (1960) used Favre averages and came to the same conclusion. Bradshaw (1977) agreed with Morkovin and showed that incompressible models should not be applied in boundary layers with external Mach numbers greater than five, in shock-boundary layer interactions, nor in free-stream layers with Mach numbers greater than 1.5. The Free Shear Layers Conference (1972) concluded that existing turbulence models were inadequate to predict the decrease in mixing-layer spreading rate with Mach number.

These failures have been attributed to variations in density ratio in mixing layers and concluded that spreading-rate variation must be a "compressibility effect." Oh (1974) simulated a two-dimensional, high-speed mixing layer and proposed a kinetic-energy equation model that provided for a nonzero pressure-dilatation interaction.

3. Review of Turbulence Modeling

Turbulent flows contain a large range of length scales. This causes problems for the flow simulator because the smallest and largest scales of motion in the flow cannot be represented at the same time on a relatively coarse mesh. Only simple flows at low Reynolds numbers can now be simulated.

Most of the fundamental work on turbulence modeling has been based on the incompressible

*Present address: Brown, Boveri et Cie., Baden, Switzerland.
**Present address: Universität Karlsruhe, Karlsruhe, W. Germany.

Table 1

Description of Various Experiments on Homogeneous Shear Flows

Experiment	Shear Rate S (sec^{-1})	Reynolds No. Re_λ †	Shear No. $\mathcal{S}$ ††	Total Shear St
Rose (1966)	13.68	133.0	9.53	3.2
Champagne et al. (1970)	12.90	204.8	7.79	3.2
Harris et al. (1977)	44.0	396.4	8.28	10.81
Tavoularis (1978)	46.8	397.9	14.76	12.65

† The values of Re_λ and $\mathcal{S}$ are given at $x_1/h = 7.5$ for Rose and Harris et al., at $x_1/h = 8.5$ for Champagne et al., and at $x_1/h = 11$ for Tavoularis.

†† The shear number is defined as $\mathcal{S} = SL/q$, where L is integral length scale and $q = \langle u_i u_i \rangle^{1/2}$.

Navier-Stokes equations. For many years, models developed from the incompressible equations have been applied to compressible flows, frequently with great success. At higher Mach numbers, existing turbulence models become increasingly inadequate.

The most common approach to the prediction of turbulent flows is based on Reynolds averaging. The mean equations are not closed, and some terms (principally the Reynolds stresses, $\langle u_i' u_j' \rangle$) need to be modeled. The simplest models for the turbulent Reynolds stress assumes a Newtonian-like constitutive equation--the Boussineq eddy-viscosity concept:

$$\langle u_i' u_j' \rangle = -2\nu_T S_{ij} + \frac{1}{3}\delta_{ij} q^2 \qquad (1)$$

where $\langle\ \rangle$ denotes volume average, u_i' is the velocity fluctuation defined as the difference between the total velocity, u_i, and the ensemble average velocity, $\bar{u}_i$,

$$u_i' = u_i - \bar{u}_i \qquad (2)$$

ν_T is eddy viscosity and itself needs to be modeled. S_{ij} and q are mean strain and r.m.s. turbulent velocity, respectively.

The simplest model represents ν_T in terms of the velocity field. In higher-level models, partial differential equations for the turbulent kinetic energy equation, dissipation, and/or turbulent Reynolds stresses are solved. To close these equations, various terms need to be modeled. In Section 5, we present and test some of the models for these terms.

4. Problem Description and Numerical Methods

In this paper, we consider homogeneous shear flows with the following mean values of velocity components and pressure:

$$\bar{u}_1 = SX_2, \quad \bar{u}_2 = 0, \quad \bar{u}_3 = 0, \quad \bar{p} = \text{const.} \qquad (4)$$

where S is the shear rate. The velocity field is shown in Fig. 1. We choose to simulate a portion of the flow field and impose periodic boundary conditions on the fluctuating quantities. In order to do this, it is necessary to transform to a coordinate system which shears with the mean flow. The physical region being simulated becomes distorted with

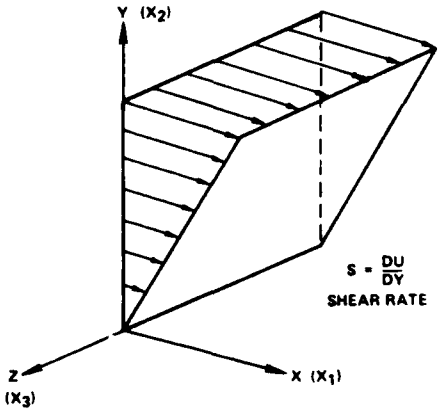

Fig. 1. The mean flow.

time, and, without "remeshing," the simulation, if continued, would become invalid. We "remesh" the coordinate system when St is a half-integer; the sheared coordinate system is replaced by one sheared in the other direction, and the velocity field is placed on the new grid. The mesh points of the "before" and "after" systems are equivalent, but the velocity field needs to be truncated in Fourier space to maintain continuity.

In the compressible flow, the initial condition represents isotropic turbulence with a given spectral shape and intensity, and is divergence-free, i.e., it is an incompressible initial field. Compressibility effects arise from the high shear rate and the fact that the ratio of the turbulence intensity, q, to the mean sound speed is as high as 0.3. The full compressible equations are advanced by means of a fourth-order Runge-Kutta method. Spectral methods are used to evaluate all spatial derivatives; both this and the program described below used 64 mesh points in each spatial direction.

Incompressible flows were simulated both by running the compressible code at low Mach number and

by a separate incompressible code. The latter solves a Poisson equation for the pressure and uses a second-order Adams-Bashforth method for the time advancement. Spectral methods are used for the spatial derivatives. This program also has the ability to include a passive scalar. Further details of these methods can be found in reports by the authors (Feiereisen et al. (1981) and Shirani et al. (1981).

5. The Simulations

Several runs were made with each of the codes described above. In each run, the earliest part of the simulated flow field is not representative of a real flow, because the initial conditions are not sufficiently realistic; at $St = 4$, the flow attains the characteristics observed in the laboratory flow. The length scales grow throughout the simulation; eventually they become long with respect to the size of the region simulated, and the results are no longer realistic. This happens in most cases at approximately $St = 7$. Thus, only the period $4 \leq St \leq 7$ is useful for model testing.

Analysis of the independent variables in these flows shows that there are only two independent, nondimensional parameters (other than the nondimensional time St) in the incompressible flows. We have chosen these to be the Reynolds number $R_\lambda = q\lambda/\nu$ and a quantity we have called the shear number, which is defined as $\mathcal{L} = SL/q$. The range of these parameters is approximately $15 \leq R_\lambda \leq 120$ and $3 < \mathcal{L} < 70$. Here L is the integral scale and λ, the microscale. Due to the restriction on the Reynolds number, the ratio of length scales L/λ is nearly constant in these flows and cannot be considered as an independent, nondimensional variable. In the compressible cases, the Mach number $M = q/c$ is another independent parameter; we have considered the range $0 \leq M < 0.3$.

Detailed comparison of the results with experiments is not possible, because it is impossible to duplicate the initial conditions of the experiments with sufficient precision. We have compared several results with those of experiments, and they appear to agree quite well on a qualitative basis. Some of these will be shown later. For further details, the reader may wish to consult the reports cited earlier.

6. Models for Incompressible Turbulence

This and the following section are devoted to studying turbulence models using the computed results. Incompressible flows and their modeling are considered here, and compressibility effects are considered in the next section.

First, let us consider eddy viscosity models. The usual assumptions are:

$$\tau_{ij} = R_{ij} - \frac{R_{kk}}{3}\delta_{ij} = \langle u_i u_j \rangle - \frac{q^2}{3}\delta_{ij} = -\nu_T S_{ij} \quad ; \quad \nu_T = cqL \tag{5}$$

where L is a length scale which we shall take to be the integral scale (the choice is not critical in view of the above) and c is assumed constant. However, c may be a function of the dimensionless parameters of the problem, so we attempted to fit it as a function of the Reynolds and shear numbers. A power-law fitting function was selected:

$$F = C R_\lambda^{\alpha} \mathcal{L}^{\beta} \tag{6}$$

This function will be used for other parameters as well. It may not be the optimum choice, but there is little theoretical guidance for the selection of a more appropriate function. The intent of this fit is not to develop a model for the term but instead to use the fit to discover which parameter most sensitively affects the quantity under study (e.g., c). The three constants in Eq. (6) were determined by least-squares fitting, and Fig. 2 gives the constants and shows that the results are well fit; three experimental points are also shown, and they agree quite well with the fit. The results show the

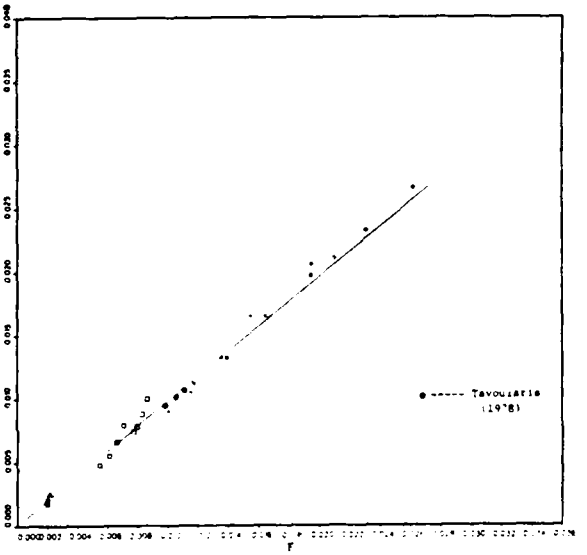

Fig. 2. ν_T/qL vs. the fitting function $0.265\ Re_\lambda^{-0.08}\ \mathcal{L}^{-1.07}$.

eddy viscosity constant c to be nearly inverse to the shear number. This result can be written:

$$\frac{\langle u_1' u_2' \rangle}{q^2} = 0.265\ R_\lambda^{-0.08}\ \mathcal{L}^{-0.07} \tag{7}$$

which agrees quite well with the experimental observation that in many flows $\langle u'v' \rangle/q^2$ is approximately constant. This means that the assumption that c is constant in Eq. (5) is inconsistent with the experimental observation of constant $\langle u_1' u_2' \rangle/q^2$. Furthermore, one can show from these results that the mixing length is given by

$$\ell^2 \equiv \frac{\langle u_1' u_2' \rangle}{S^2} = \frac{\langle u_1' u_2' \rangle}{q^2}\frac{q^2}{S^2} \propto \text{const}\ \lambda^2 \tag{8}$$

Thus, the mixing length appears to grow in proportion to the microscale.

Figure 3 gives a related result. The shear stress correlation $\langle u_1' u_2' \rangle / (\langle u_1'^2 \rangle \langle u_2'^2 \rangle)^{1/2}$ is fitted with the function (6). The fit is not as good as in Fig. 2, but we see that there is little variation of the correlation with Reynolds or shear number.

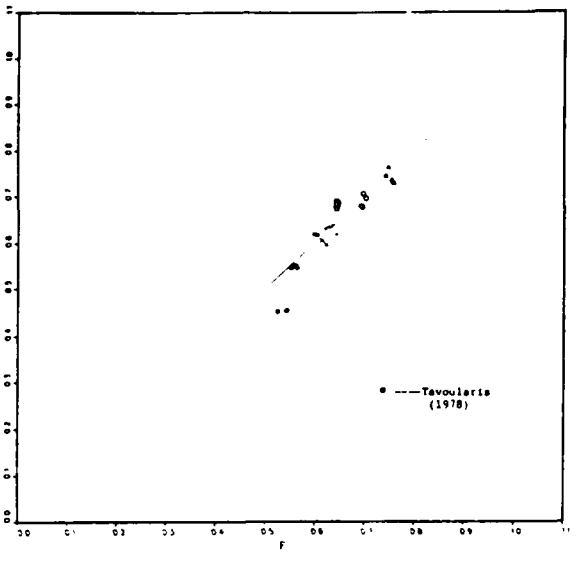

Fig. 3. The Reynolds shear stress correlation vs. the fitting function $0.515\ Re_\lambda^{-0.043}$ $^{0.134}$.

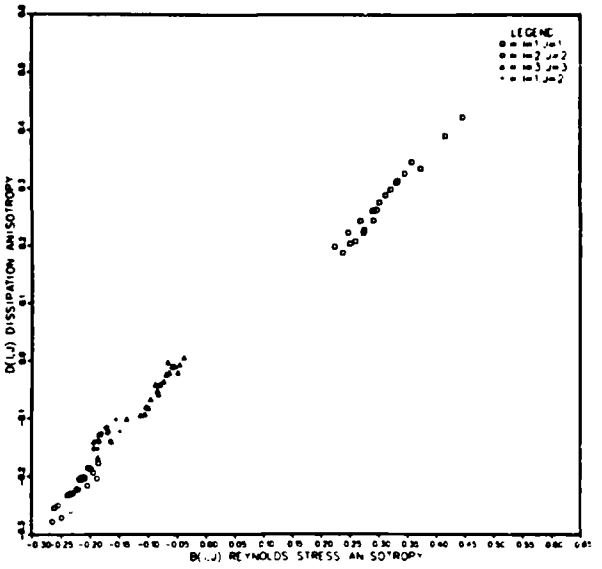

Fig. 4. Dissipation anisotropy vs. Reynolds stress anisotropy. All four nonzero components are shown.

Now let us turn our attention to higher-order models. One common assumption in turbulence modeling is that the dissipation is isotropic. We have looked at the anisotropy of the dissipation defined by:

$$d_{ij} = \left(\varepsilon_{ij} - \frac{\varepsilon_{kk}}{3}\,\delta_{ij}\right)\Big/\varepsilon \qquad (9)$$

where ε_{ij} is the rate of viscous dissipation of $\langle u_i'u_j' \rangle$ and $\varepsilon = \varepsilon_{kk}$. In order to condense the presentation of the results, we plot the dissipation anisotropy vs. anisotropy of the Reynolds stress $b_{ij} = \tau_{ij}/q^2$. Figure 4 shows that the relationship is nearly linear; the slope is approximately 0.85, indicating strong anisotropy of d_{ij}. Although it might be thought that this is attributable to the relatively low Reynolds number of the simulation, we find no systematic variation of the dissipation anisotropy with Reynolds number over the range covered. This result suggests that the assumption of constant d_{ij} be reexamined.

Finally, we have studied the pressure-strain models that are commonly used in a full Reynolds stress models. The pressure obeys the Poisson equation in which the source terms are velocity gradients; the latter can be divided into two groups, depending on whether they contain the mean velocity or not. Following Lumley, we call the terms containing the mean velocity the "rapid" terms and the remainder, the "Rotta" terms.

First, we consider the Rotta terms. The common model is:

$$\tau_{ij}^1 \equiv \left\langle p'\left(\frac{\partial u_i'}{\partial x_j} + \frac{\partial u_j'}{\partial x_i}\right)\right\rangle_{\text{Rotta}} = c\varepsilon b_{ij}/q^2 \qquad (10)$$

The "constant" was evaluated from the computational results and found to be smaller than 1; since the constant must be at least 2 to give relaxation to isotropy, this is unacceptable. The "constant" is also strongly dependent on Reynolds number, as shown in Table 2. When the anisotropy of the dissipation (which acts as a redistribution term) is added to the Rotta term, we get the results shown in Table 3. The best estimate of a single value for the constant is 2.7, and the dependence on Reynolds and shear number is reasonably small. In model calculations, assuming the dissipation isotropy is equivalent to lumping its anisotropy with the Rotta term, and we conclude that, although the arguments used in constructing the model are not correct, the resulting model is reasonable. This provides a reinterpretation of the model and an estimate for the constant that is in good agreement with the ones in common use. We have also tested a correlation suggested by Lumley and Newman (1978) for the Rotta "constant." The results showed large scatter, and some of the coefficients were very large; we cannot recommend this correlation on the basis of our results.

Table 2

"Constant" in the Rotta model, Eq. (10). The "constant" was fit by $c = C\ Re_\lambda^{\alpha}$ $^{\beta}$. The last column is the r.m.s. difference between the "constant" and the fit.

Equation	A	C	α	β	r.m.s. error
i=1, j=1	0.673 ±0.599	1.142	0.678	-1.195	0.15
i=2, j=2	0.673 ±0.570	0.734	0.715	-1.075	0.13
i=1, j=2	0.679 ±0.452	0.238	0.813	-0.776	0.15

AD-A111 582 PENNSYLVANIA STATE UNIV UNIVERSITY PARK DEPT OF MECH--ETC F/G 20/4
SYMPOSIUM ON TURBULENT SHEAR FLOWS (3RD), UNIVERSITY OF CALIFOR--ETC(U)
SEP 81 F W SCHMIDT AFOSR-80-0033

UNCLASSIFIED AFOSR-TR-82-0032 NL

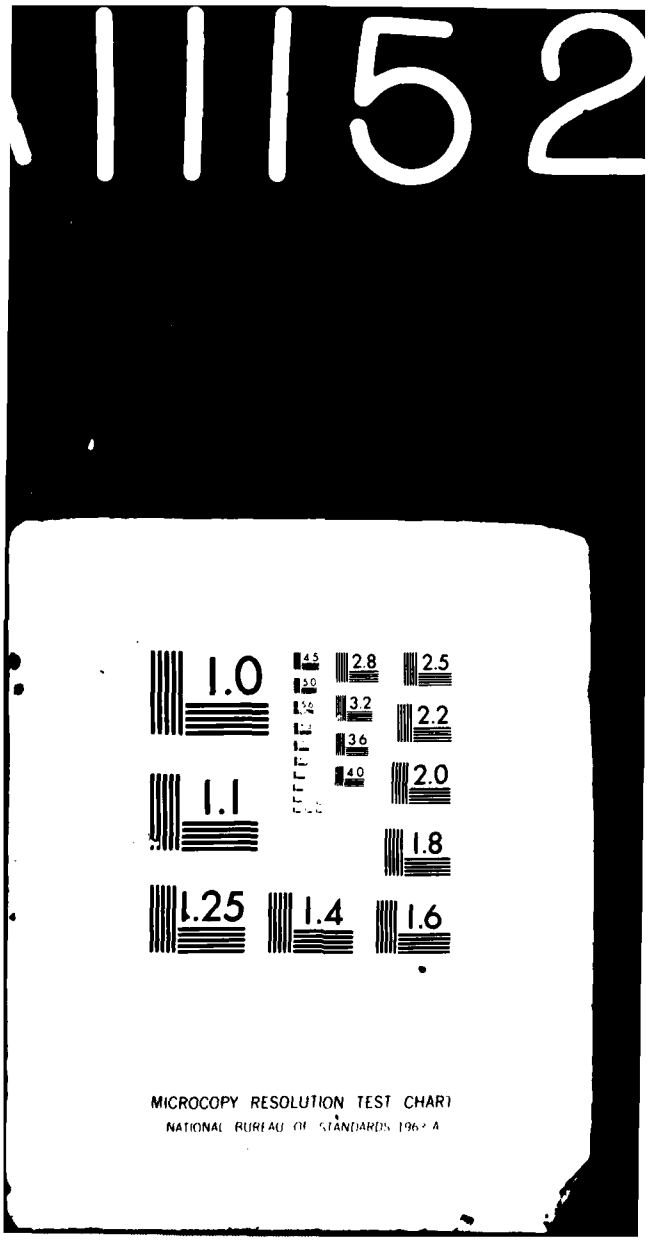
1152
1.0
1.1
1.25
1.4
1.6
1.8
2.0
2.2
2.5
2.8
3.2
3.6
4.0
4.5
5.0
MICROCOPY RESOLUTION TEST CHART
NATIONAL BUREAU OF STANDARDS 1963-A

Table 3

"Constant" in the Rotta model when the anisotropy of the dissipation is included with the pressure-strain term. The meaning of the last four columns is the same as in Table 2.

Equation	A_1	C	α	β	r.m.s. error
i=1, j=1	2.862 ± 0.349	3.342	0.144	-0.225	0.045
i=2, j=2	3.089 ± 0.428	4.200	0.119	-0.245	0.048
i=1, j=2	2.472 ± 0.426	1.633	0.330	-0.266	0.085

Now let us turn to consideration of the rapid term. A model for this term has been given by several authors. They are essentially equivalent, so we shall use the one given by Reynolds (1976):

$$T_{ij}^2 = \frac{2}{5}(1+A_1)\,q^2\delta_{ij} - \frac{3}{5}A_1[R_{ik}S_{kj}R_{jk} + S_{ki} + \frac{2}{3}\mathcal{P}\delta_{ij}]$$

$$- \frac{4}{5}\left(\frac{5}{3} + \frac{7}{12}A_1\right)(R_{ik}\Omega_{kj} + R_{jk}\Omega_{ki}) \qquad (11)$$

where $\mathcal{P} = R_{ik}S_{ki}$ is the production,

$$S_{ij} = \frac{1}{2}\left(\frac{\partial \bar{u}_i}{\partial x_j} + \frac{\partial \bar{u}_j}{\partial x_i}\right)$$

is the strain rate, and

$$\Omega_{ij} = \frac{1}{2}\left(\frac{\partial \bar{u}_i}{\partial x_j} - \frac{\partial \bar{u}_j}{\partial x_i}\right)$$

is the rotation. The "constant" A_1 was computed for each set of tensor indices in each flow for each case, and a remarkable result was found. The "constant" is indeed nearly independent of the Reynolds and shear numbers, but it varies with the tensor index. The results are given in Table 4. We cannot offer an explanation of this result, but people doing model calculations might want to try an ad hoc modification of the model implied by these results, even though is is not in proper tensorial form.

Table 4

"Constant" for the rapid pressure-strain term. The meaning of the last four columns is the same as in the previous tables.

Equation	A_1	C	α	β	r.m.s. error
i=1, j=1	-6.94 ± 0.519	9.75	-0.028	-0.082	0.038
i=2, j=2	-1.83 ± 0.400	1.55	0.038	0.008	0.040
i=3, j=3	-1.57 ± 0.380	6.82	-0.185	-0.282	0.093
i=1, j=2	-1.52 ± 0.077	2.01	-0.082	0.010	0.032

A simplified model by Gibson and Launder (1978) was also tested but did not fare so well as the model represented by Eq. (10).

Finally, fitting the full pressure-strain term to the combined models using a least-squares fit to determine the two constants gives results that are significantly better than either model alone.

7. Compressible Flow

As stated earlier, we also ran several cases in which compressibility is important. The effect of compressibility is indicated by the turbulence Mach number $M = q/c$ differing from zero; we considered values as high as $M = 0.3$, approximately the value found in supersonic shear layers. An alternative measure of the importance of compressibility is the parameter SL/c, the difference in speed across a large eddy divided by the Mach number. This parameter is, of course, the product of the shear and Mach numbers defined above.

In this section, we shall concentrate on the effects produced by the introduction of compressibility into the flow. On the whole, these effects are quite small, but it is instructive to study them in some detail.

One tool for examining the effect of compressibility is the Moyal decomposition. Moyal considers the velocity field to be a combination of a field which contains vorticity but no dilatation and one which has dilation but no vorticity; these two components are called u_i^s (solenoidal) and u_i^d (dilatational), respectively. It turns out that the energy in the dilatational part of the field is always small compared to the energy in the solenoidal component; at the highest Mach number, the former is approximately two orders of magnitude larger than the former. The only exception is the 2-2 component of the dilatation field, which is less than an order of magnitude smaller than the corresponding solenoidal component. This is the gradient direction, and we believe that the relatively large size of $\langle u_2^d u_2^d \rangle$ is associated with sound-wave propagation in the direction normal to the flow. There is also a possibility that this result is connected with the decreased rate of growth of shear layers at high Mach numbers, but it is difficult to offer convincing evidence for this. A typical time history of the flow is given in Fig. 5.

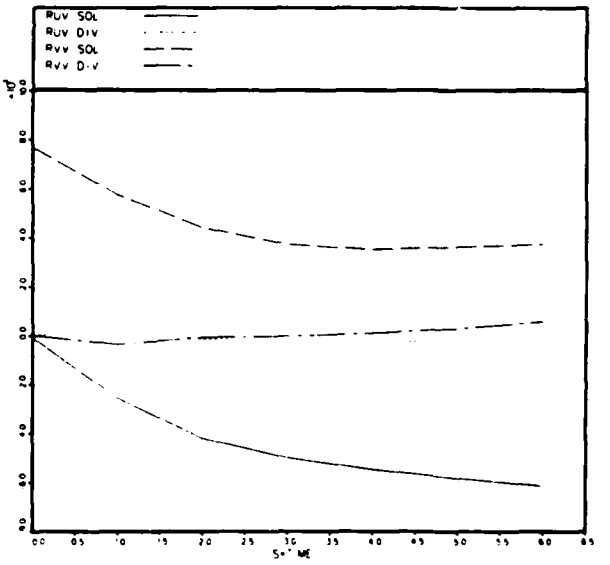

Fig. 5. The solenoidal and dilatational components of the Reynolds stresses $\langle u_1^s u_2^s \rangle$ and $\langle u_1^d u_2^d \rangle$.

We now turn our attention to the pressure field and the pressure-strain terms. In a compressible flow, the pressure obeys the equation:

$$\nabla^2 p = -(\rho u_i u_j)_{,ij} - (\rho u_i)_{,j} u_{j,i} + \frac{\partial^2 \rho}{\partial t^2} \qquad (11)$$

In an incompressible flow, the first two terms give rise to the Rotta and rapid components of the pressure field. In view of what we discovered above, we do not expect these terms to change very much when compressibility is considered. When we note that $\partial^2 \rho / \partial t^2 = c^{-2} \partial^2 p / \partial t^2$, the last term changes the equation from a Poisson equation to a wave equation. Alternatively, we can regard the last term as a new source term due to the compressibility, and the pressure field is then regarded as being composed of three parts--the two used in the incompressible flow and a new compressible term. (There is no need to use the Moyal decomposition here.)

It was expected that the new term would be small, but it turned out that the compressible component of the pressure is surprisingly large. As it is the pressure-strain term that we are primarily concerned with, we present in Fig. 6 the ratio of the mean-square pressure-strain term (the second invariant of the pressure-strain tensor as defined by Lumley) for the compressible and incompressible components of the field. In this figure, the results have been correlated using an extension of Eq. (7) which includes a power of the Mach number. The results are given in the figure, and the size of the new term is indeed much larger than one might have expected. (This term was computed in two different ways which differed by 10%, so we have confidence in the results. We suspect that the results are due to sound waves propagating through the flow. It is worth noting that the ratio of the r.m.s. fluctuations of the components of the pressure field is less than 1%, so there is apparently some mechanism operating which strongly correlates the sound waves with the strain in the field. The origin of the compressible portion of the pressure field was found to be dilatation and not the simple existence of density differences.

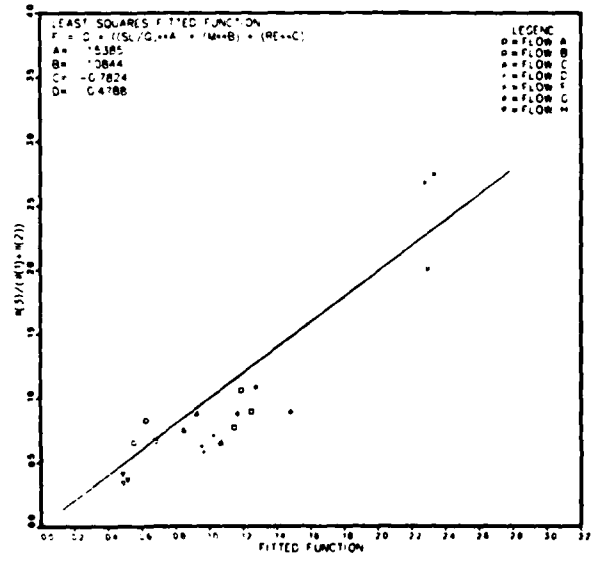

Fig. 6. Ratio of the second invariant of the compressible pressure-strain term to the sum of the second invariants of the rapid and Rotta terms vs. a fitting function.

Finally, we considered the modeling of the compressible term. It was found to behave like the rapid term, and it is preferable to model the sum of the two terms as a unit. When this is done, the result is qualitatively similar to what was found in the incompressible flow; however, the constants are changed somewhat (compare the results in Fig. 7 with those in Table 1). Thus it appears that, the compressible terms have a measurable effect on the pressure-strain term and this may be responsible for the change in $\langle u_1' u_2' \rangle$ noted above.

We have also investigated models in which one assumes structural similarity or constancy of the anisotropic component of the Reynolds stresses. We were unable to find a "constant" for these models which fit the results well.

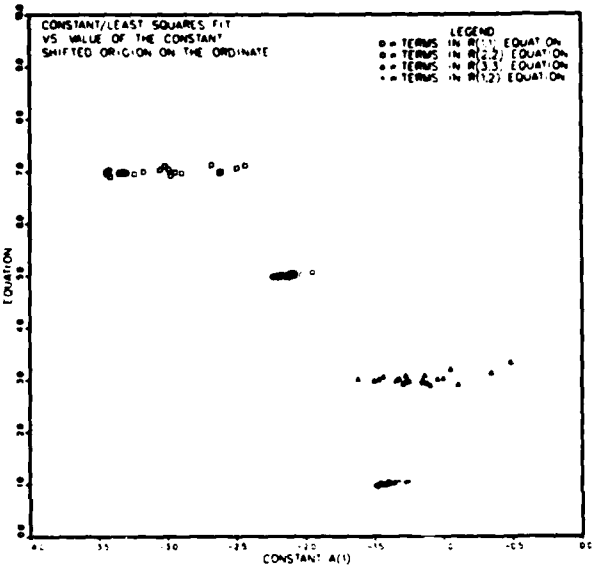

Fig. 7. Test of the model of Eq. (11) in compressible flow. The model is applied to the sum of the rapid and compressible terms. The abscissa is the constant obtained; the ordinate is the ratio of the constant to a correlation fit. The curves are shifted for clarity of presentation.

8. Conclusions

We have shown that it is possible to fully simulate sheared homogeneous turbulence. The results compare quite well with the experiments, at least on a qualitative basis. It is possible to use the results of the simulations to produce information that cannot be obtained directly from experiments. In particular, we have computed the pressure-strain terms and compared them with model predictions. For the Rotta term, good results are obtained, provided that one includes the anisotropy of the dissipation along with the pressure-strain term. For the rapid term, we are unable to produce a good fit between the model and the computational results. Finally, it is shown that the effects of compressibility are small, for the most part. The only effect which was not found to be small is a modification of the pressure term, and this seems to be responsible for producing a change in the normal component of the Reynolds stress.

References

Bradshaw, P., "Compressible Turbulent Shear Layers," Annual Review of Fluid Mechanics, 1977, 33-54.

Champagne, F. H., Harris, V. G., and Corrsin, S., "Experiments on Nearly Homogeneous Turbulent Shear Flow," J. Fluid Mech., 41, 81 (1970).

Chu, B-T, and Kovasznay, L. S. G., "Nonlinear Interactions in a Viscous Heat-Conducting Compressible Flow, J. Fluid Mech., 3, 494, Feb. 1958.

Feiereisen, W. J., "Numerical Simulation of a Compressible, Homogeneous, Turbulent Shear Flow," Ph.D. dissertation, Mech. Engrg. Dept., Stanford University, 1981. (Also published as Report TF-13).

Harris, V. G., Graham, J. A., and Corrsin, S., "Further Experiments in Nearly Homogeneous Turbulent Shear Flow," J. Fluid Mech., 81, 657 (1977).

Hwang, W. S., "Experimental Investigation of Turbulent Shear Flows," Ph.D. dissertation, Univ. of Virginia (1971).

Kovasznay, L. S. G., "Turbulence in Supersonic Flow," J. Aero. Sci., 20, 657 (1953).

Laufer, J., "Thoughts on Compressible Turbulent Boundary Layers," Memorandum RM-5946-PR, RAND Corp., March, 1969.

Lumley, J. L., and G. R. Newman, "The Return to Isotropy of Homogeneous Turbulence," J. Fluid Mech., 82, 161 (1977).

Morkovin, M. V., "Effects of Compressibility on Turbulence," Mechanique de la Turbulence, C.N.R.S., Paris, 1962.

Mulhearn, P. J., and Luxton, R. E., "The Development of Turbulence Structure in a Uniform Shear Flow," J. Fluid Mech., 68, 577 (1975).

Oh, Y. H., "Analysis of Two-Dimensional Free Turbulent Mixing," AIAA 7th Fluid & Plasma Dynamics Conference, AIAA Paper 74-594, 1974.

Reis, F. B., "Studies of Correlation and Spectra in Homogeneous Turbulence," Ph.D. dissertation, MIT, Cambridge, Mass. (1952).

Reynolds, W. C., "Computation of Turbulent Flows," Annual Review of Fluid Mechanics, 8, 183-208 (1976).

Rogallo, R. S., "An ILLIAC Program for the Numerical Simulation of Homogeneous Incompressible Turbulence," NASA TM-73, 203 (1977).

Rose, W. G., "Interaction of Grid Turbulence with a Uniform Mean Shear," J. Fluid Mech., 44, 767 (1970).

Shaanan, S., Ferziger, J. H., and Reynolds, W. C., "Numerical Simulation of Turbulence in the Presence of Shear," Rpt. No. TF-6, Mech. Engrg. Dept., Stanford Univ. (1975).

Shirani-C, E., Ferziger, J. H., and Reynolds, W. C., "Mixing of a Passive Scalar in Homogeneous Turbulent Shear Flows," Ph.D. dissertation, Mech. Engrg. Dept., Stanford Univ. (1981). Also published as Rpt. TF-15.)

Tavoularis, S., "Experiments in Turbulent Transport and Mixing," Ph.D. dissertation, Johns Hopkins Univ. (1978).

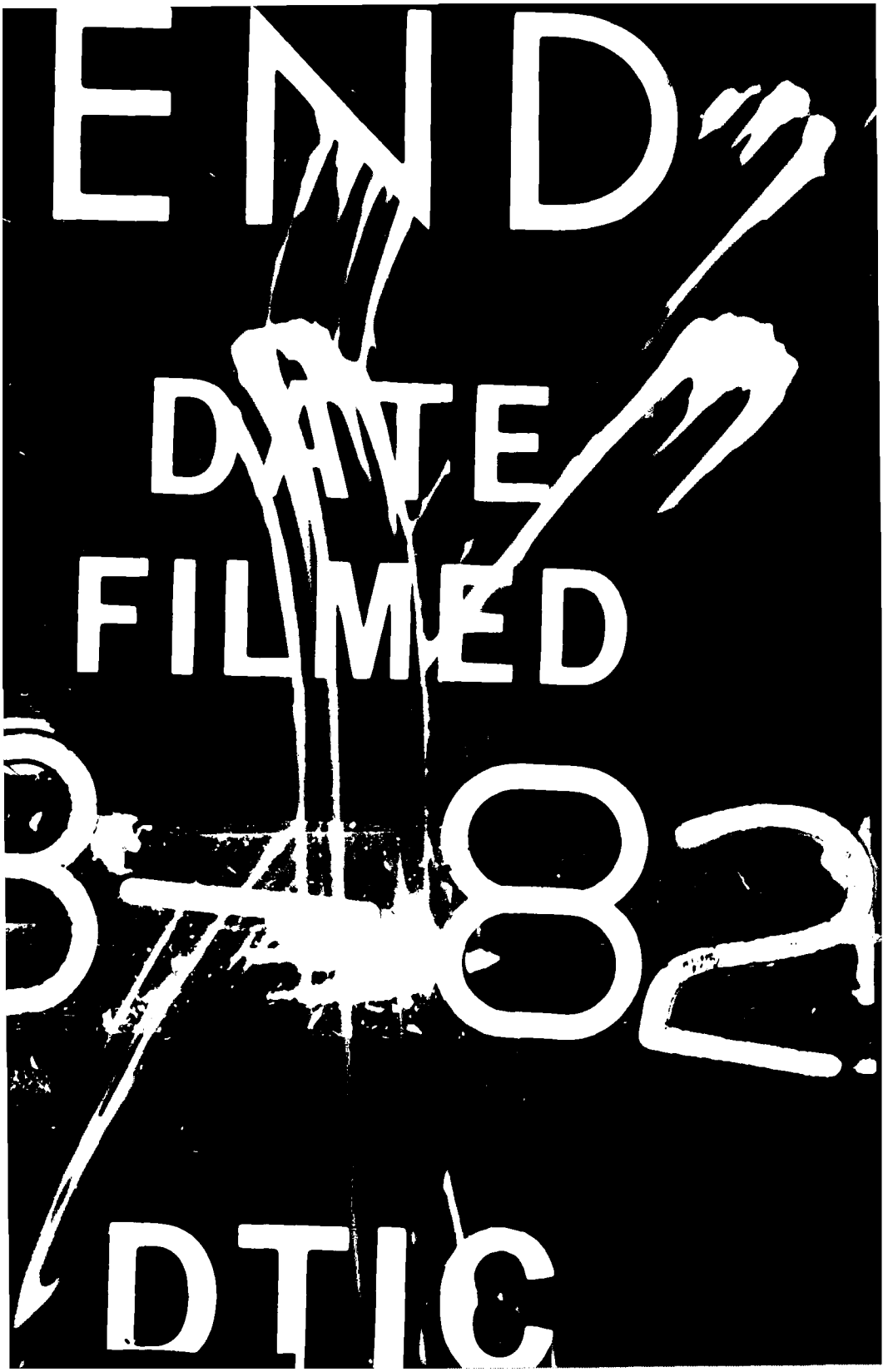
END
DATE
FILMED
82
DTIC

AD-A111 522 SYMPOSIUM ON TURBULENT SHEAR FLOWS (3RD) UNIVERSITY OF CALIFORNIA DAVIS C..(U) PENNSYLVANIA STATE UNIV UNIVERSITY PARK DEPT OF MECHANICAL EN.. F W SCHMIDT

UNCLASSIFIED SEP 81 AFOSR-TR-82-0032 AFOSR-81-0033 F/G 20/4 NL

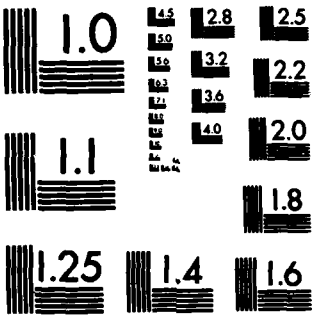

MICROCOPY RESOLUTION TEST CHART
NATIONAL BUREAU OF STANDARDS-1963-A

UNCLASSIFIED

SECURITY CLASSIFICATION OF THIS PAGE (When Data Entered)

REPORT DOCUMENTATION PAGE	READ INSTRUCTIONS BEFORE COMPLETING FORM
1. REPORT NUMBER: AFOSR-TR- 82-0032	2. GOVT ACCESSION NO. AD-A111522 / 3. RECIPIENT'S CATALOG NUMBER
4. TITLE (and Subtitle): THIRD SYMPOSIUM ON TURBULENT SHEAR FLOWS	5. TYPE OF REPORT & PERIOD COVERED: FINAL
	6. PERFORMING ORG. REPORT NUMBER
7. AUTHOR(s): F W SCHMIDT	8. CONTRACT OR GRANT NUMBER(s): Should be -> 81-0033 AFOSR-80-0033 not 80-0033
9. PERFORMING ORGANIZATION NAME AND ADDRESS: THE PENNSYLVANIA STATE UNIVERSITY 308 MECHANICAL ENGINEERING BLDG UNIVERSITY PARK, PA 16802	10. PROGRAM ELEMENT, PROJECT, TASK AREA & WORK UNIT NUMBERS: 61102F 2307/A2
11. CONTROLLING OFFICE NAME AND ADDRESS: AIR FORCE OFFICE OF SCIENTIFIC RESEARCH/NA BOLLING AIR FORCE BASE, DC 20332	12. REPORT DATE: SEPTEMBER 81 / 13. NUMBER OF PAGES: 436
14. MONITORING AGENCY NAME & ADDRESS (if different from Controlling Office)	15. SECURITY CLASS. (of this report): UNCLASSIFIED / 15a. DECLASSIFICATION/DOWNGRADING SCHEDULE

16. DISTRIBUTION STATEMENT (of this Report)

Approved for public release; distribution unlimited.

17. DISTRIBUTION STATEMENT (of the abstract entered in Block 20, if different from Report)

18. SUPPLEMENTARY NOTES

19. KEY WORDS (Continue on reverse side if necessary and identify by block number)

20. ABSTRACT (Continue on reverse side if necessary and identify by block number)

The Third Symposium on Turbulent Shear Flow was held at the University of California, Davis, California on September 9 - 11, 1981. The objective of the symposium was to further advance the understanding of the physical phenomena associated withturbulent flows and the existing capabilities for calculating items such as the transport of heat and mass in such processes. Of the 158 abstracts received by the papers committee, a total of 92 papers were included in the final program. In addition to the 17 paper sessions, an open forum

DD FORM 1 JAN 73 1473 EDITION OF 1 NOV 65 IS OBSOLETE

UNCLASSIFIED

SECURITY CLASSIFICATION OF THIS PAGE (When Data Entered)